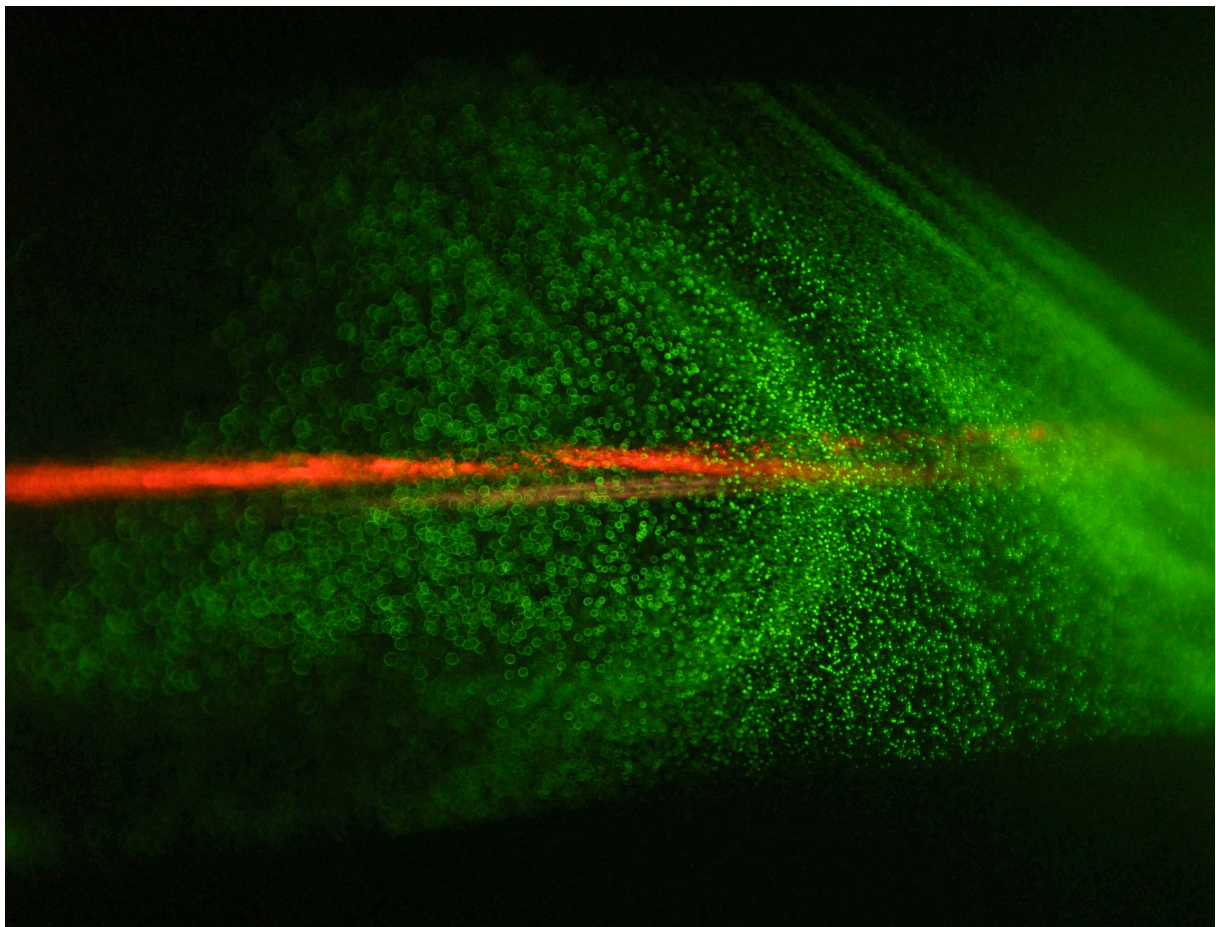


# Teramobile

*Joint French-German project on long-distance fs-laser pulses  
propagation and atmospheric applications*

## List of publications 2000-2011

*Funded by: Centre National de la Recherche Scientifique, Deutsche  
Forschungsgemeinschaft, Ministère des Affaires Étrangères, Deutsche  
Akademische Auslandsdienst, Agence Nationale de la Recherche,  
Swiss National Science Foundation*



*Updated September 2011*

## 2000

1. J. Kasparian, R. Sauerbrey, D. Mondelain, S. Niedermeier, J. Yu, J.-P. Wolf, Y.-B. André, M. Franco, B. Prade, A. Mysyrowicz, S. Tzortzakis, M. Rodriguez, H. Wille and L. Wöste, *Infrared extension of the supercontinuum generated by fs-TW-laser pulses propagating in the atmosphere*, Optics Letters **25**, 1397-1399 (2000).
2. J. Kasparian, R. Sauerbrey and S. L. Chin, *The critical laser intensity of self-guided light filaments in air*, Applied Physics B **71**, 877-879 (2000).

## 2001

1. J. Yu, D. Mondelain, G. Ange, R. Volk, S. Niedermeier, J.-P. Wolf, J. Kasparian and R. Sauerbrey, *Backward supercontinuum emission from a filament generated by ultrashort laser pulses in air*, Optics Letters **26**, 533-535 (2001).
2. G. Faye, J. Kasparian and R. Sauerbrey, *Modifications to the lidar equation due to nonlinear propagation in air*, Applied Physics B **73**, 157-163 (2001).

## 2002

1. M. Rodriguez, R. Sauerbrey, H. Wille, L. Wöste, T. Fujii, Y.-B. André, A. Mysyrowicz, L. Klingbeil, K. Rethmeier, W. Kalkner, J. Kasparian, E. Salmon, J. Yu and J.-P. Wolf, *Triggering and guiding of megavolt discharges using laser-induced ionized filaments*, Optics Letters **27**, 772-774 (2002).
2. H. Wille, M. Rodriguez, J. Kasparian, D. Mondelain, J. Yu, A. Mysyrowicz, R. Sauerbrey, J.-P. Wolf and L. Wöste, *Teramobile: a mobile femtosecond-terawatt laser and detection system*, European Physical Journal - Applied Physics **20**, 183 (2002)

## 2003

1. G. Méjean, J. Kasparian, E. Salmon, J. Yu, J.-P. Wolf, R. Bourayou, R. Sauerbrey, M. Rodriguez, L. Wöste, H. Lehmann, B. Stecklum, U. Laux, J. Eislöffel, A. Scholz and A. P. Hatzes, *Towards a supercontinuum-based infrared Lidar*, Applied Physics B **77**, 357 (2003).
2. J. Yu, D. Mondelain, J. Kasparian, E. Salmon, S. Geffroy, C. Favre, V. Boutou and J.-P. Wolf, *Sonographic probing of laser filaments in air*, Applied Optics **42**, 7117 (2003).
3. J. Kasparian, M. Rodriguez, G. Méjean, J. Yu, E. Salmon, H. Wille, R. Bourayou, S. Frey, Y.-B. André, A. Mysyrowicz, R. Sauerbrey, J.-P. Wolf and L. Wöste, *White light filaments for atmospheric analysis*, Science **301**, 61 (2003).

## 2004

1. M. Rodriguez, R. Bourayou, G. Méjean, J. Kasparian, J. Yu, E. Salmon, A. Scholz, B. Stecklum, J. Eisloffel, U. Laux, A. P. Hatzes, R. Sauerbrey, L. Wöste and J.-P. Wolf, *Kilometer-range non-linear propagation of fs laser pulses*, Physical Review E **69**, 036607 (2004)
2. P. Rohwetter, K. Stelmaszczyk, G. Méjean, J. Yu, E. Salmon, J. Kasparian, J.-P. Wolf, L. Wöste, *Remote LIBS with ultra-short pulses: characteristics in picosecond and femtosecond regimes*, Journal of Analytical Atomic Spectrometry **19**, 437 (2004)
3. G. Méjean, J. Kasparian, J. Yu, S. Frey, E. Salmon, J.-P. Wolf, *Remote Detection and Identification of Biological Aerosols using a Femtosecond Terawatt Lidar System*, Applied Physics B **78**, 535 (2004)
4. L. Bergé, S. Skupin, F. Lederer, G. Mejean, J. Yu, J. Kasparian, E. Salmon, J.-P. Wolf, M. Rodriguez, L. Wöste, R. Bourayou, R. Sauerbrey, *Multiple filamentation of terawatt laser pulses in air*, Physical Review Letters **92**, 225002 (2004)
5. S. Skupin, L. Bergé, U. Peschel, F. Lederer, G. Méjean, J. Yu, J. Kasparian, E. Salmon, J. P. Wolf, M. Rodriguez, L. Wöste, R. Bourayou, R. Sauerbrey, *Filamentation of femtosecond light pulses in the air: Turbulent cells versus long-range clusters*, Physical Review E **70**, 046602 (2004).
6. L. Bergé, S. Skupin, F. Lederer, G. Méjean, J. Yu, J. Kasparian, E. Salmon, J.-P. Wolf, *Spatial break-up of femtosecond laser pulses in the atmosphere*, Physica Scripta **T107**, 135 (2004).
7. G. Méchain, A. Couairon, Y.-B. André, C. D'Amico, M. Franco, B. Prade, S. Tzortzakis, A. Mysyrowicz, R. Sauerbrey, *Long range self-channeling of infrared laser pulses in air: a new propagation regime without ionisation*, Applied Physics B **79**, 379-382 (2004)
8. K. Stelmaszczyk, P. Rohwetter, G. Méjean, J. Yu, E. Salmon, J. Kasparian, R. Ackermann, J.-P. Wolf, L. Wöste, *Long-distance remote laser-induced breakdown spectroscopy using filamentation in air*, Applied Physics Letters **85**, 3977 (2004).
9. R. Ackermann, K. Stelmaszczyk, P. Rohwetter, G. Méjean, E. Salmon, J. Yu, J. Kasparian, G. Méchain, V. Bergmann, S. Schaper, B. Weise, T. Kumm, K. Rethmeier, W. Kalkner, J. P. Wolf, L. Wöste, *Triggering and guiding of megavolt discharges by laser-induced filaments under rain conditions*, Applied Physics Letters **85**, 5781 (2004).

## 2005

1. R. Bourayou, G. Méjean, J. Kasparian, M. Rodriguez, E. Salmon, J. Yu, H. Lehmann, B. Stecklum, U. Laux, J. Eislöffel, A. Scholz, A.P. Hatzes, R. Sauerbrey, L. Wöste, and J.-P. Wolf, *White-light filaments for multiparameter analysis of cloud microphysics*. Journal of the Optical Society of America. **22**, 369 (2005)
2. L. Bergé, S. Skupin, G. Méjean, J. Kasparian, J. Yu, S. Frey, E. Salmon, and J.-P. Wolf, *Supercontinuum emission and enhanced self-guiding of infrared femtosecond filaments sustained by third-harmonic generation in air*. Physical Review E. **71**, 016602 (2005)
3. G. Méchain, C. D'Amico, Y.-B. André, S. Tzortzakis, M. Franco, B. Prade, A. Mysyrowicz, A. Couairon, E. Salmon and R. Sauerbrey, *Range of plasma filaments created in air by a multi-terawatt femtosecond laser*, Optics Communications **247**, 171 (2005)
4. P. Rohwetter, K. Stelmaszczyk, L. Wöste, R. Ackermann, G. Méjean, E. Salmon, J. Kasparian, J. Yu, and J.-P. Wolf, *Filament-induced remote ablation for long range LIBS operation*. Spectrochimica Acta B. **60**, 1025-1033 (2005)
5. G. Méchain, G. Méjean, R. Ackermann, P. Rohwetter, Y.-B. André, J. Kasparian, B. Prade, K. Stelmaszczyk, J. Yu, E. Salmon, W. Winn, L.A.V. Schlie, A. Mysyrowicz, R. Sauerbrey, L. Wöste, and J.-P. Wolf, *Propagation of fs-TW laser filaments in adverse atmospheric conditions*. Applied Physics B. **80**, 785-789 (2005)
6. G. Méjean, J. Kasparian, J. Yu, E. Salmon, S. Frey, J.-P. Wolf, S. Skupin, A. Vinçotte, R. Nuter, S. Champeaux, and L. Bergé, *Multifilamentation transmission through fog*. Physical Review E. **72**, 026611 (2005)
7. A virtual antenna produced in air by intense femtoseconde laser pulses. G. Méchain, A. Mysyrowicz, M. Depiesse, M. Pellet . Proceedings SPIE, 5989 (2005)

## 2006

1. R. Ackermann, G. Méjean, J. Kasparian, J. Yu, E. Salmon, and J.-P. Wolf, *Laser filaments generated and transmitted in highly turbulent air*. Optics Letters. **31**, 86-88 (2006)
2. G. Méjean, R. Ackermann, J. Kasparian, E. Salmon, J. Yu, J.-P. Wolf, K. Rethmeier, W. Kalkner, P. Rohwetter, K. Stelmaszczyk, and L. Wöste, *Improved laser triggering and guiding of megavolt discharges with dual fs-ns pulses*. Applied Physics Letters. **88**, 021101 (2006)
3. G. Méjean, J. Kasparian, J. Yu, S. Frey, E. Salmon, J.P. Wolf, L. Bergé, and S. Skupin, *UV-Supercontinuum generated by long-range filamentation in air*. Applied Physics B. **82**, 341-345 (2006)
4. R. Ackermann, G. Méchain, G. Méjean, R. Bourayou, M. Rodriguez, K. Stelmaszczyk, J. Kasparian, J. Yu, E. Salmon, S. Tzortzakis, Y.-B. André, J.-F. Bourrillon, L. Tamin, J.-P. Cascelli, C. Campo, C. Davoise, A. Mysyrowicz, R. Sauerbrey, L. Wöste, and J-P Wolf, *Influence of negative leader propagation on the triggering and guiding of high voltage discharges by laser filaments*. Applied Physics B. **82**, 561-566 (2006)
5. J. Kasparian, *Filaments of Light*. American Scientist. **94**, 150 (2006)
6. P. Bédot, J. Kasparian, E. Salmon, R. Ackermann, N. Gisin, and J.-P. Wolf, *Laser noise reduction in the air*. Applied Physics Letters. **88**, 251112 (2006)
7. R. Ackermann, E. Salmon, N. Lascoux, J. Kasparian, P. Rohwetter, K. Stelmaszczyk, S. Li, A. Lindinger, L. Wöste, P. Bédot, L. Bonacina, and J.-P. Wolf, *Optimal control of filamentation in air*. Applied Physics Letters. **89**, 171117 (2006)
8. B. Prade, M. Franco, A. Mysyrowicz, A. Couairon, H. Buersing, B. Eberle, M. Krenz, D. Seiffer, O. Vasseur, *Spatial mode cleaning by femtosecond filamentation*, Optics Letters **31**, 2601 (2006)
9. A. Couairon, M. Franco, G. Méchain, T. Olivier, B. Prade, A. Mysyrowicz, *Femtosecond filamentation in air at low pressures: part I: theory and numerical simulations*, Optics Communications **259**, 265 (2006)
10. G. Méchain, T. Olivier, M. Franco, A. Couairon, B. Prade, A. Mysyrowicz *Femtosecond filamentation in air at low pressures: part II: laboratory experiments*, Optics Communications **261**, 322-326 (2006)

## 2007

1. A. Houard, C. D'Amico, Y. Liu, Y.B. Andre, M. Franco, B. Prade, A. Mysyrowicz, E. Salmon, P. Pierlot, and L.-M. Cleon, *High current permanent discharges in air induced by femtosecond laser filamentation*. Appl. Phys. Lett. **90**, 171501 (2007)
2. P. Béjot, J. Kasparian, E. Salmon, R. Ackermann, and J.-P. Wolf, *Spectral correlation and noise reduction in laser filaments*. Applied Physics B. **87**, 1-4 (2007)
3. P. Béjot, L. Bonacina, J. Extermann, M. Moret, J.P. Wolf, R. Ackermann, N. Lascoux, R. Salamé, E. Salmon, J. Kasparian, L. Bergé, S. Champeaux, C. Guet, N. Blanchot, O. Bonville, A. Boscheron, P. Canal, M. Castaldi, O. Hartmann, C. Lepage, L. Marmande, E. Mazataud, G. Mennerat, L. Patissou, V. Prevot, D. Raffestin, and J. Ribolzi, *32 Terawatt Atmospheric White-Light Laser*. Applied Physics Letters. **90**, 151106 (2007)
4. J. Kasparian, *Some properties of femtosecond laser filamentation relevant to atmospheric applications. Part I. The robustness of filamentation*, in *Progress in Ultrafast Intense Laser Science II*, K. Yamanouchi, et al., Editors. 2007, Springer. p. 281-300. *Review article, text not included in the present booklet*
5. J. Kasparian, *Some properties of femtosecond laser filamentation relevant to atmospheric applications II. Large-scale filamentation*, in *Progress in Ultrafast Intense Laser Science II*, K. Yamanouchi, et al., Editors. 2007, Springer. p. 301-318. *Review article, text not included in the present booklet*
6. A. Couairon, A. Mysyrowicz, *Femtosecond filamentation in transparent media*, Physics Reports **441**, 47 (2007) *Review article, text not included in the present booklet*
7. L. Bergé, S. Skupin, R. Nuter, J. Kasparian, J.-P. Wolf, *Ultrashort filaments of light in weakly-ionized, optically-transparent media*. Reports on progress in physics. **70**, 1633-1713 (2007) *Review article, text not included in the present booklet*
8. C. D'Amico, A. Houard, M. Franco, B. Prade, A. Mysyrowicz, *Coherent and Incoherent Radial THz Radiation Emission from Femtosecond Filaments in Air*. Optics Express **15**, 15274-15279 (2007)
9. Y. Liu, A. Houard, B. Prade, S. Akturk, A. Mysyrowicz, V.T. Tikhonchuk, *Terahertz radiation source in air based on bifilamentation of femtosecond laser pulses*, Physical Review Letters **99**, 135002 (2007)
10. C. D'Amico, A. Houard, M. Franco, B. Prade, A. Couairon, V.T. Tikhonchuk, A. Mysyrowicz, *Conical forward THz emission from femtosecond laser filamentation in air*, Physical Review Letters **98**, 235002 (2007)

## 2008

1. C. D'Amico, A. Houard, S. Akturk, Y. Liu, J. Le Bloas, M. Franco, B. Prade, A. Couairon, V.T. Tikhonchuk, and A. Mysyrowicz, *Forward THz radiation emission by femtosecond filamentation in gases: theory and experiment*, New Journal of Physics **10**, 013015 (2008)
2. J. Kasparian, J.-P. Wolf, *Physics and applications of atmospheric nonlinear optics and filamentation*. Optics Express **16**, 466-493 (2008). *Review article, text not included in the present booklet*
3. J. Kasparian, R. Ackermann, Y.-B. André, G. Méchain, G. Méjean, B. Prade, P. Rohwetter, E. Salmon, K. Stelmaszczyk, J. Yu, A. Mysyrowicz, R. Sauerbrey, L. Wöste, and J.-P. Wolf, *Electric Events Synchronized with Laser Filaments in Thunderclouds*, Optics Express **16**, 5757-5763 (2008).
4. J. Kasparian, R. Ackermann, Y.-B. André, G. Méchain, G. Méjean, B. Prade, P. Rohwetter, E. Salmon, K. Stelmaszczyk, J. Yu, A. Mysyrowicz, R. Sauerbrey, L. Wöste, and J.-P. Wolf, *Progress towards lightning control using lasers*. Journal of the European Optical Society: Rapid Publications. **3**, 08035 (2008)
5. P. Béjot, J. Kasparian, and J.-P. Wolf, *Cross compression of light bullets by two-color co-filamentation*. Physical Review A (Atomic, Molecular, and Optical Physics). **78**, 043804 (2008)
6. P. Béjot, J. Kasparian, and J.-P. Wolf, *Dual-color co-filamentation in Argon*. Optics Express. **16**, 14115 (2008)
7. P. Béjot, Y. Petit, L. Bonacina, J. Kasparian, M. Moret, and J.-P. Wolf, *Ultrafast gaseous "half-wave plate"*. Optics Express. **16**, 7564 (2008)
8. J. Extermann, P. Béjot, L. Bonacina, P. Billaud, J. Kasparian, and J.-P. Wolf, *Effects of atmospheric turbulence on remote optimal control experiments*. Applied Physics Letters. **92**, 041103 (2008)

## 2009

1. Y. Petit, P. B ejot, L. Bonacina, J. Kasparian, M. Moret, and J.-P. Wolf, *Filament-Induced Birefringence in Argon*. Laser Physics. **19**, 336-341 (2009)
2. Z.Q. Hao, R. Salam e, N. Lascoux, E. Salmon, P. Maioli, J. Kasparian, and J.-P. Wolf, *Multiple filamentation of non-uniformly focused ultrashort laser pulses*. Applied Physics B. **94**, 243 (2009)
3. P. Maioli, R. Salam e, N. Lascoux, E. Salmon, P. B ejot, J. Kasparian, and J.-P. Wolf, *Ultraviolet-visible conical emission by multiple laser filaments*. Optics Express. **17**, 4726–4731 (2009)
4. J. Kasparian and J.P. Wolf, *Laser beams take a curve*. Science. **324**, 194-195 (2009)
5. O. Graydon and J. Kasparian, *Lightning control by lasers*. Nature Photonics. **3**, 120-121 (2009)
6. K. Stelmaszczyk, P. Rohwetter, Y. Petit, M. Fechner, J. Kasparian, J.-P. Wolf, and L. W oste, *White-light symmetrization by the interaction of multifilamenting beams*. Physical Review A. **79**, 053856 (2009)
7. J. Kasparian and J.P. Wolf, *Curved plasma channels Kerr lens and Airy prism*. Journal of the European Optical Society: Rapid Publications. **4**, 09039 (2009)
8. J. Kasparian, P. B ejot, J.-P. Wolf, and J.M. Dudley, *Optical rogue wave statistics in laser filamentation*. Optics Express. **17**, 12070-12075 (2009)
9. S. Henin, Y. Petit, D. Kiselev, J. Kasparian, and J.-P. Wolf, *Contribution of water droplets to charge release by laser filaments in air*. Applied Physics Letters. **95**, 091107 (2009)

## 2010

1. J. Kasparian and J.P. Wolf, *On lightning control using lasers*, in Progress in Ultrafast Intense Laser Science 5. 2010, Yamanouchi, Kaoru. p. 109-122. *Electronic version not available*
2. P. B ejot, J. Kasparian, S. Henin, V. Loriot, T. Vieillard, E. Hertz, O. Faucher, B. Lavorel, and J.-P. Wolf, *Higher-order Kerr terms allow ionization-free filamentation in gases*. Physical Review Letters. **104**, 103903 (2010)
3. S. Henin, Y. Petit, J. Kasparian, J.-P. Wolf, A. Jochmann, S.D. Kraft, S. Bock, U. Schramm, R. Sauerbrey, W.M. Nakaema, K. Stelmaszczyk, P. Rohwetter, L. W oste, C.-L. Soulez, S. Mauger, L. Berg e, and S. Skupin, *Saturation of the filament density of ultrashort intense laser pulses in air*. Applied Physics B. **100**, 77 (2010)
4. P. Rohwetter, J. Kasparian, K. Stelmaszczyk, Z. Hao, S. Henin, N. Lascoux, W.M. Nakaema, Y. Petit, M. Quei er, R. Salam e, E. Salmon, L. W oste, and J.-P. Wolf, *Laser-induced water condensation in air*. Nature Photonics. **4**, 451 (2010)
5. W. Ettoumi, Y. Petit, J. Kasparian, and J.-P. Wolf, *Generalized Miller Formul e*. Optics Express. **18**, 6613-6620 (2010)
6. J. Kasparian, P. B ejot, and J.-P. Wolf, *Arbitrary-order non-linear contribution to self-steepening*. Optics Letters. **35**, 2795 (2010)
7. Y. Petit, S. Henin, J. Kasparian, and J.-P. Wolf, *Production of ozone and nitrogen oxides by laser filamentation*. Applied Physics Letters. **97**, 021108 (2010)
8. A.G. Stepanov, S. Henin, Y. Petit, L. Bonacina, J. Kasparian, and J.-P. Wolf, *Mobile source of high-energy single-cycle terahertz pulses* Applied Physics B, **101**, 11 (2010)
9. P. B ejot, B. E. Schmidt, J. Kasparian, J.-P. Wolf and F. L egar e, *Mechanism of hollow-core-fiber infrared-supercontinuum compression with bulk material*, Physical Review A, **81**, 063828 (2010)
10. W. Ettoumi, P. B ejot, Y. Petit, V. Loriot, E. Hertz, O. Faucher, B. Lavorel, J. Kasparian, and J.-P. Wolf *Spectral dependence of purely-Kerr-driven filamentation in air and argon*, Physical Review A, **82**, 033826 (2010)
11. B. E. Schmidt, P. B ejot, M. Gigu ere, A. D. Shiner, C. Trallero-Herrero, E. Bisson, J. Kasparian, J.-P. Wolf, D. M. Villeneuve, J.-C. Kieffer, P. B. Corkum & F. L egar e *Compression of 1.8  $\mu\text{m}$  laser pulses to sub two optical cycles with bulk material*, Applied Physics Letters, **96**, 121109 (2010)

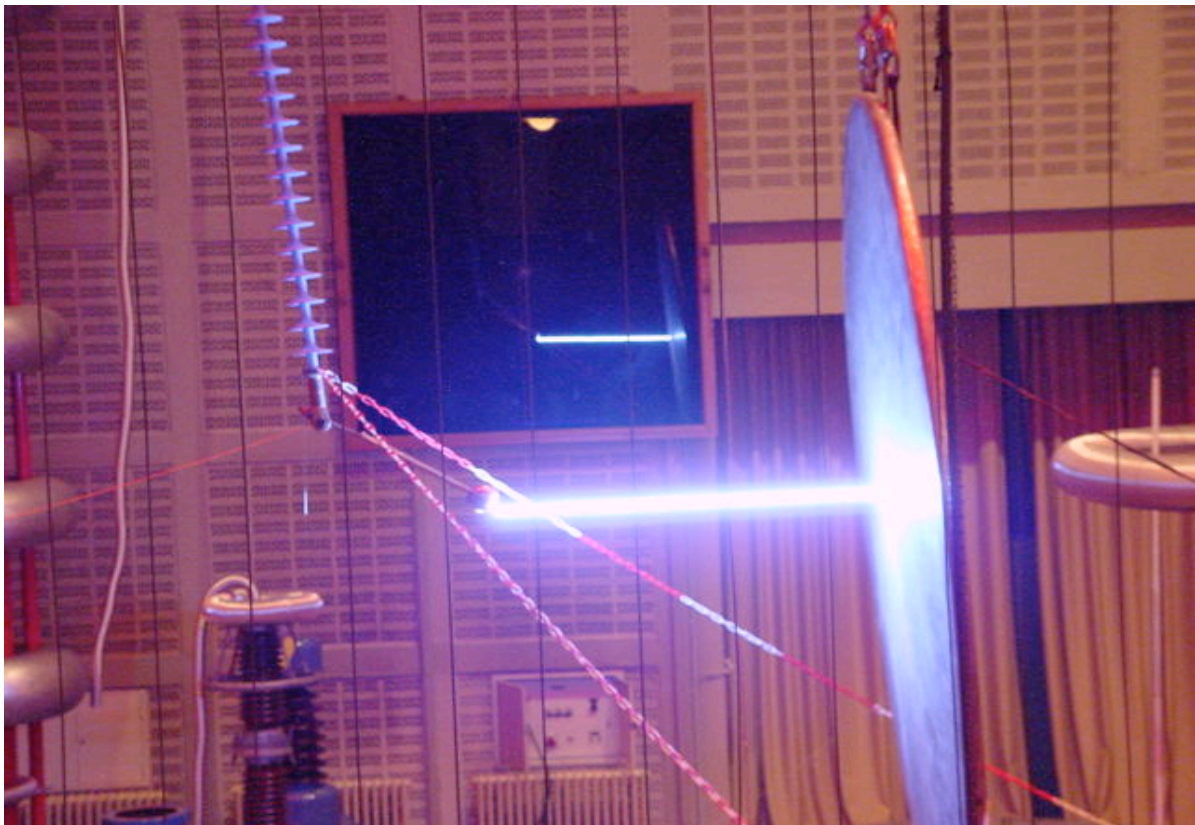
## 2011

1. P. Béjot, E. Hertz, B. Lavorel, J. Kasparian, J.-P. Wolf, and O. Faucher *From higher-order Kerr nonlinearities to quantitative modeling of third and fifth harmonic generation in argon*, Optics Letters, **36**, 828-830 (2011)
2. P. Béjot, E. Hertz, B. Lavorel, J. Kasparian, J.-P. Wolf, and O. Faucher *Transition from plasma- to Kerr-driven laser filamentation*, Physical Review Letters, **106**, 243902 (2011)
3. V. Loriot, P. Béjot, W. Ettoumi, Y. Petit, J. Kasparian, S. Henin, E. Hertz, B. Lavorel, O. Faucher, and J.-P. Wolf *On negative higher-order Kerr effect and filamentation*, Laser Physics, **21**, 1319-1328 (2011)
4. Y. Petit, S. Henin, J. Kasparian, J. P. Wolf, P. Rohwetter, K. Stelmaszczyk, Z. Q. Hao, W. M. Nakaema, L. Wöste, A. Vogel, T. Pohl, and K. Weber *Influence of pulse duration, energy, and focusing on laser-assisted water condensation*, Applied Physics Letters, **98**, 041105 (2011)
5. Y. Petit, S. Henin, W. M. Nakaema, P. Béjot, A. Jochmann, S. D. Kraft, S. Bock, U. Schramm, K. Stelmaszczyk, P. Rohwetter, J. Kasparian, R. Sauerbrey, L. Wöste, and J.-P. Wolf *I-J white-light continuum from 100-TW laser pulses*, Physical Review A, **83**, 013805 (2011)
6. S. Henin, Y. Petit, P. Rohwetter, K. Stelmaszczyk, Z.Q. Hao, W.M. Nakaema, A. Vogel, T. Pohl, F. Schneider, J. Kasparian, K. Weber, L. Wöste, J.-P. Wolf *Field measurements suggest the mechanism of laser-assisted water condensation*. Nature Communications **2**, 456 (2011).

# Teramobile

*Joint French-German project on long-distance fs-laser pulses  
propagation and atmospheric applications*

## List of publications 2000-2010



*Funded by: Centre National de la Recherche Scientifique, Deutsche  
Forschungsgemeinschaft, Ministère des Affaires Étrangères, Deutsche  
Akademische Auslandsdienst, Agence Nationale de la Recherche,  
Swiss National Science Foundation*

*Updated September 2010*

## 2000

1. J. Kasparian, R. Sauerbrey, D. Mondelain, S. Niedermeier, J. Yu, J.-P. Wolf, Y.-B. André, M. Franco, B. Prade, A. Mysyrowicz, S. Tzortzakis, M. Rodriguez, H. Wille and L. Wöste, *Infrared extension of the supercontinuum generated by fs-TW-laser pulses propagating in the atmosphere*, Optics Letters **25**, 1397-1399 (2000).
2. J. Kasparian, R. Sauerbrey and S. L. Chin, *The critical laser intensity of self-guided light filaments in air*, Applied Physics B **71**, 877-879 (2000).

## 2001

1. J. Yu, D. Mondelain, G. Ange, R. Volk, S. Niedermeier, J.-P. Wolf, J. Kasparian and R. Sauerbrey, *Backward supercontinuum emission from a filament generated by ultrashort laser pulses in air*, Optics Letters **26**, 533-535 (2001).
2. G. Faye, J. Kasparian and R. Sauerbrey, *Modifications to the lidar equation due to nonlinear propagation in air*, Applied Physics B **73**, 157-163 (2001).

## 2002

1. M. Rodriguez, R. Sauerbrey, H. Wille, L. Wöste, T. Fujii, Y.-B. André, A. Mysyrowicz, L. Klingbeil, K. Rethmeier, W. Kalkner, J. Kasparian, E. Salmon, J. Yu and J.-P. Wolf, *Triggering and guiding of megavolt discharges using laser-induced ionized filaments*, Optics Letters **27**, 772-774 (2002).
2. H. Wille, M. Rodriguez, J. Kasparian, D. Mondelain, J. Yu, A. Mysyrowicz, R. Sauerbrey, J.-P. Wolf and L. Wöste, *Teramobile: a mobile femtosecond-terawatt laser and detection system*, European Physical Journal - Applied Physics **20**, 183 (2002)

## 2003

1. G. Méjean, J. Kasparian, E. Salmon, J. Yu, J.-P. Wolf, R. Bourayou, R. Sauerbrey, M. Rodriguez, L. Wöste, H. Lehmann, B. Stecklum, U. Laux, J. Eislöffel, A. Scholz and A. P. Hatzes, *Towards a supercontinuum-based infrared Lidar*, Applied Physics B **77**, 357 (2003).
2. J. Yu, D. Mondelain, J. Kasparian, E. Salmon, S. Geffroy, C. Favre, V. Boutou and J.-P. Wolf, *Sonographic probing of laser filaments in air*, Applied Optics **42**, 7117 (2003).
3. J. Kasparian, M. Rodriguez, G. Méjean, J. Yu, E. Salmon, H. Wille, R. Bourayou, S. Frey, Y.-B. André, A. Mysyrowicz, R. Sauerbrey, J.-P. Wolf and L. Wöste, *White light filaments for atmospheric analysis*, Science **301**, 61 (2003).

## 2004

1. M. Rodriguez, R. Bourayou, G. Méjean, J. Kasparian, J. Yu, E. Salmon, A. Scholz, B. Stecklum, J. Eislöffel, U. Laux, A. P. Hatzes, R. Sauerbrey, L. Wöste and J.-P. Wolf,

- Kilometer-range non-linear propagation of fs laser pulses*, Physical Review E **69**, 036607 (2004)
2. P. Rohwetter, K. Stelmaszczyk, G. Méjean, J. Yu, E. Salmon, J. Kasparian, J.-P. Wolf, L. Wöste, *Remote LIBS with ultra-short pulses: characteristics in picosecond and femtosecond regimes*, Journal of Analytical Atomic Spectrometry **19**, 437 (2004)
  3. G. Méjean, J. Kasparian, J. Yu, S. Frey, E. Salmon, J.-P. Wolf, *Remote Detection and Identification of Biological Aerosols using a Femtosecond Terawatt Lidar System*, Applied Physics B **78**, 535 (2004)
  4. L. Bergé, S. Skupin, F. Lederer, G. Mejean, J. Yu, J. Kasparian, E. Salmon, J.-P. Wolf, M. Rodriguez, L. Wöste, R. Bourayou, R. Sauerbrey, *Multiple filamentation of terawatt laser pulses in air*, Physical Review Letters **92**, 225002 (2004)
  5. S. Skupin, L. Bergé, U. Peschel, F. Lederer, G. Méjean, J. Yu, J. Kasparian, E. Salmon, J. P. Wolf, M. Rodriguez, L. Wöste, R. Bourayou, R. Sauerbrey, *Filamentation of femtosecond light pulses in the air: Turbulent cells versus long-range clusters*, Physical Review E **70**, 046602 (2004).
  6. L. Bergé, S. Skupin, F. Lederer, G. Méjean, J. Yu, J. Kasparian, E. Salmon, J. P. Wolf, *Spatial break-up of femtosecond laser pulses in the atmosphere*, Physica Scripta **T107**, 135 (2004).
  7. G. Méchain, A. Couairon, Y.-B. André, C. D'Amico, M. Franco, B. Prade, S. Tzortzakis, A. Mysyrowicz, R. Sauerbrey, *Long range self-channeling of infrared laser pulses in air: a new propagation regime without ionisation*, Applied Physics B **79**, 379-382 (2004)
  8. K. Stelmaszczyk, P. Rohwetter, G. Méjean, J. Yu, E. Salmon, J. Kasparian, R. Ackermann, J.-P. Wolf, L. Wöste, *Long-distance remote laser-induced breakdown spectroscopy using filamentation in air*, Applied Physics Letters **85**, 3977 (2004).
  9. R. Ackermann, K. Stelmaszczyk, P. Rohwetter, G. Méjean, E. Salmon, J. Yu, J. Kasparian, G. Méchain, V. Bergmann, S. Schaper, B. Weise, T. Kumm, K. Rethmeier, W. Kalkner, J. P. Wolf, L. Wöste, *Triggering and guiding of megavolt discharges by laser-induced filaments under rain conditions*, Applied Physics Letters **85**, 5781 (2004).

## **2005**

1. R. Bourayou, G. Méjean, J. Kasparian, M. Rodriguez, E. Salmon, J. Yu, H. Lehmann, B. Stecklum, U. Laux, J. Eislöffel, A. Scholz, A.P. Hatzes, R. Sauerbrey, L. Wöste, and J.-P. Wolf, *White-light filaments for multiparameter analysis of cloud microphysics*. Journal of the Optical Society of America. **22**, 369 (2005)

2. L. Bergé, S. Skupin, G. Méjean, J. Kasparian, J. Yu, S. Frey, E. Salmon, and J.P. Wolf, *Supercontinuum emission and enhanced self-guiding of infrared femtosecond filaments sustained by third-harmonic generation in air*. Physical Review E. **71**, 016602 (2005)
3. G. Méchain, C. D'Amico, Y.-B. André, S. Tzortzakis, M. Franco, B. Prade, A. Mysyrowicz, A. Couairon, E. Salmon and R. Sauerbrey, *Range of plasma filaments created in air by a multi-terawatt femtosecond laser*, Optics Communications **247**, 171 (2005)
4. P. Rohwetter, K. Stelmaszczyk, L. Wöste, R. Ackermann, G. Méjean, E. Salmon, J. Kasparian, J. Yu, and J.-P. Wolf, *Filament-induced remote ablation for long range LIBS operation*. Spectrochimica Acta B. **60**, 1025-1033 (2005)
5. G. Méchain, G. Méjean, R. Ackermann, P. Rohwetter, Y.-B. André, J. Kasparian, B. Prade, K. Stelmaszczyk, J. Yu, E. Salmon, W. Winn, L.A.V. Schlie, A. Mysyrowicz, R. Sauerbrey, L. Wöste, and J.-P. Wolf, *Propagation of fs-TW laser filaments in adverse atmospheric conditions*. Applied Physics B. **80**, 785-789 (2005)
6. G. Méjean, J. Kasparian, J. Yu, E. Salmon, S. Frey, J.-P. Wolf, S. Skupin, A. Vinçotte, R. Nuter, S. Champeaux, and L. Bergé, *Multifilamentation transmission through fog*. Physical Review E. **72**, 026611 (2005)
7. A virtual antenna produced in air by intense femtoseconde laser pulses. G. Méchain, A. Mysyrowicz, M. Depiesse, M. Pellet . Proceedings SPIE, 5989 (2005)

## **2006**

1. R. Ackermann, G. Méjean, J. Kasparian, J. Yu, E. Salmon, and J.-P. Wolf, *Laser filaments generated and transmitted in highly turbulent air*. Optics Letters. **31**, 86-88 (2006)
2. G. Méjean, R. Ackermann, J. Kasparian, E. Salmon, J. Yu, J.-P. Wolf, K. Rethmeier, W. Kalkner, P. Rohwetter, K. Stelmaszczyk, and L. Wöste, *Improved laser triggering and guiding of megavolt discharges with dual fs-ns pulses*. Applied Physics Letters. **88**, 021101 (2006)
3. G. Méjean, J. Kasparian, J. Yu, S. Frey, E. Salmon, J.P. Wolf, L. Bergé, and S. Skupin, *UV-Supercontinuum generated by long-range filamentation in air*. Applied Physics B. **82**, 341-345 (2006)
4. R. Ackermann, G. Méchain, G. Méjean, R. Bourayou, M. Rodriguez, K. Stelmaszczyk, J. Kasparian, J. Yu, E. Salmon, S. Tzortzakis, Y.-B. André, J.-F. Bourrillon, L. Tamin, J.-P. Cascelli, C. Campo, C. Davoise, A. Mysyrowicz, R. Sauerbrey, L. Wöste, and J.-P. Wolf, *Influence of negative leader propagation on the triggering and guiding of high voltage discharges by laser filaments*. Applied Physics B. **82**, 561-566 (2006)

5. J. Kasparian, *Filaments of Light*. American Scientist. **94**, 150 (2006)
6. P. B  jot, J. Kasparian, E. Salmon, R. Ackermann, N. Gisin, and J.-P. Wolf, *Laser noise reduction in the air*. Applied Physics Letters. **88**, 251112 (2006)
7. R. Ackermann, E. Salmon, N. Lascoux, J. Kasparian, P. Rohwetter, K. Stelmaszczyk, S. Li, A. Lindinger, L. W  ste, P. B  jot, L. Bonacina, and J.-P. Wolf, *Optimal control of filamentation in air*. Applied Physics Letters. **89**, 171117 (2006)
8. B. Prade, M. Franco, A. Mysyrowicz, A. Couairon, H. Buersing, B. Eberle, M. Krenz, D. Seiffer, O. Vasseur, *Spatial mode cleaning by femtosecond filamentation*, Optics Letters **31**, 2601 (2006)
9. A. Couairon, M. Franco, G. M  chain, T. Olivier, B. Prade, A. Mysyrowicz, *Femtosecond filamentation in air at low pressures: part I: theory and numerical simulations*, Optics Communications **259**, 265 (2006)
10. G. M  chain, T. Olivier, M. Franco, A. Couairon, B. Prade, A. Mysyrowicz *Femtosecond filamentation in air at low pressures: part II: laboratory experiments*, Optics Communications **261**, 322-326 (2006)

## **2007**

1. A. Houard, C. D'Amico, Y. Liu, Y.B. Andre, M. Franco, B. Prade, A. Mysyrowicz, E. Salmon, P. Pierlot, and L.-M. Cleon, *High current permanent discharges in air induced by femtosecond laser filamentation*. Appl. Phys. Lett. **90**, 171501 (2007)
2. P. B  jot, J. Kasparian, E. Salmon, R. Ackermann, and J.-P. Wolf, *Spectral correlation and noise reduction in laser filaments*. Applied Physics B. **87**, 1-4 (2007)
3. P. B  jot, L. Bonacina, J. Extermann, M. Moret, J.P. Wolf, R. Ackermann, N. Lascoux, R. Salam  , E. Salmon, J. Kasparian, L. Berg  , S. Champeaux, C. Guet, N. Blanchot, O. Bonville, A. Boscheron, P. Canal, M. Castaldi, O. Hartmann, C. Lepage, L. Marmande, E. Mazataud, G. Mennerat, L. Patissou, V. Prevot, D. Raffestin, and J. Ribolzi, *32 Terawatt Atmospheric White-Light Laser*. Applied Physics Letters. **90**, 151106 (2007)
4. J. Kasparian, *Some properties of femtosecond laser filamentation relevant to atmospheric applications. Part I. The robustness of filamentation*, in *Progress in Ultrafast Intense Laser Science II*, K. Yamanouchi, et al., Editors. 2007, Springer. p. 281-300. *Review article, text not included in the present booklet*
5. J. Kasparian, *Some properties of femtosecond laser filamentation relevant to atmospheric applications II. Large-scale filamentation*, in *Progress in Ultrafast Intense Laser Science II*, K. Yamanouchi, et al., Editors. 2007, Springer. p. 301-318. *Review article, text not included in the present booklet*

6. A. Couairon, A. Mysyrowicz, *Femtosecond filamentation in transparent media*, Physics Reports **441**, 47 (2007) *Review article, text not included in the present booklet*
7. L. Bergé, S. Skupin, R. Nuter, J. Kasparian, J.-P. Wolf, *Ultrashort filaments of light in weakly-ionized, optically-transparent media*. Reports on progress in physics. **70**, 1633-1713 (2007) *Review article, text not included in the present booklet*
8. C. D'Amico, A. Houard, M. Franco, B. Prade, A. Mysyrowicz, *Coherent and Incoherent Radial THz Radiation Emission from Femtosecond Filaments in Air*. Optics Express **15**, 15274-15279 (2007)
9. Y. Liu, A. Houard, B. Prade, S. Akturk, A. Mysyrowicz, V.T. Tikhonchuk, *Terahertz radiation source in air based on bifilamentation of femtosecond laser pulses*, Physical Review Letters **99**, 135002 (2007)
10. C. D'Amico, A. Houard, M. Franco, B. Prade, A. Couairon, V.T. Tikhonchuk, A. Mysyrowicz, *Conical forward THz emission from femtosecond laser filamentation in air*, Physical Review Letters **98**, 235002 (2007)

## **2008**

1. C. D'Amico, A. Houard, S. Akturk, Y. Liu, J. Le Bloas, M. Franco, B. Prade, A. Couairon, V.T. Tikhonchuk, and A. Mysyrowicz, *Forward THz radiation emission by femtosecond filamentation in gases: theory and experiment*, New Journal of Physics **10**, 013015 (2008)
2. J. Kasparian, J.-P. Wolf, *Physics and applications of atmospheric nonlinear optics and filamentation*. Optics Express **16**, 466-493 (2008). *Review article, text not included in the present booklet*
3. J. Kasparian, R. Ackermann, Y.-B. André, G. Méchain, G. Méjean, B. Prade, P. Rohwetter, E. Salmon, K. Stelmaszczyk, J. Yu, A. Mysyrowicz, R. Sauerbrey, L. Wöste, and J.-P. Wolf, *Electric Events Synchronized with Laser Filaments in Thunderclouds*, Optics Express **16**, 5757-5763 (2008).
4. J. Kasparian, R. Ackermann, Y.-B. André, G. Méchain, G. Méjean, B. Prade, P. Rohwetter, E. Salmon, K. Stelmaszczyk, J. Yu, A. Mysyrowicz, R. Sauerbrey, L. Wöste, and J.-P. Wolf, *Progress towards lightning control using lasers*. Journal of the European Optical Society: Rapid Publications. **3**, 08035 (2008)
5. P. Bejot, J. Kasparian, and J.-P. Wolf, *Cross compression of light bullets by two-color cofilamentation*. Physical Review A (Atomic, Molecular, and Optical Physics). **78**, 043804 (2008)
6. P. Béjot, J. Kasparian, and J.-P. Wolf, *Dual-color co-filamentation in Argon*. Optics Express. **16**, 14115 (2008)

7. P. B ejot, Y. Petit, L. Bonacina, J. Kasparian, M. Moret, and J.-P. Wolf, *Ultrafast gaseous "half-wave plate"*. Optics Express. **16**, 7564 (2008)
8. J. Extermann, P. B ejot, L. Bonacina, P. Billaud, J. Kasparian, and J.-P. Wolf, *Effects of atmospheric turbulence on remote optimal control experiments*. Applied Physics Letters. **92**, 041103 (2008)

## **2009**

1. Y. Petit, P. B ejot, L. Bonacina, J. Kasparian, M. Moret, and J.-P. Wolf, *Filament-Induced Birefringence in Argon*. Laser Physics. **19**, 336-341 (2009)
2. Z.Q. Hao, R. Salam e, N. Lascoux, E. Salmon, P. Maioli, J. Kasparian, and J.-P. Wolf, *Multiple filamentation of non-uniformly focused ultrashort laser pulses*. Applied Physics B. **94**, 243 (2009)
3. P. Maioli, R. Salam e, N. Lascoux, E. Salmon, P. B ejot, J. Kasparian, and J.-P. Wolf, *Ultraviolet-visible conical emission by multiple laser filaments*. Optics Express. **17**, 4726–4731 (2009)
4. J. Kasparian and J.P. Wolf, *Laser beams take a curve*. Science. **324**, 194-195 (2009)
5. O. Graydon and J. Kasparian, *Lightning control by lasers*. Nature Photonics. **3**, 120-121 (2009)
6. K. Stelmaszczyk, P. Rohwetter, Y. Petit, M. Fechner, J. Kasparian, J.-P. Wolf, and L. W oste, *White-light symmetrization by the interaction of multifilamenting beams*. Physical Review A. **79**, 053856 (2009)
7. J. Kasparian and J.P. Wolf, *Curved plasma channels Kerr lens and Airy prism*. Journal of the European Optical Society: Rapid Publications. **4**, 09039 (2009)
8. J. Kasparian, P. B ejot, J.-P. Wolf, and J.M. Dudely, *Optical rogue wave statistics in laser filamentation*. Optics Express. **17**, 12070-12075 (2009)
9. S. Henin, Y. Petit, D. Kiselev, J. Kasparian, and J.-P. Wolf, *Contribution of water droplets to charge release by laser filaments in air*. Applied Physics Letters. **95**, 091107 (2009)

## **2010**

1. J. Kasparian and J.P. Wolf, *On lightning control using lasers*, in Progress in Ultrafast Intense Laser Science 5. 2010, Yamanouchi, Kaoru. p. 109-122. *Electronic version not available*

2. P. B ejot, J. Kasparian, S. Henin, V. Lorient, T. Vieillard, E. Hertz, O. Faucher, B. Lavorel, and J.-P. Wolf, *Higher-order Kerr terms allow ionization-free filamentation in gases*. Physical Review Letters. **104**, 103903 (2010)
3. S. Henin, Y. Petit, J. Kasparian, J.-P. Wolf, A. Jochmann, S.D. Kraft, S. Bock, U. Schramm, R. Sauerbrey, W.M. Nakaema, K. Stelmaszczyk, P. Rohwetter, L. W oste, C.-L. Soulez, S. Mauger, L. Berg e, and S. Skupin, *Saturation of the filament density of ultrashort intense laser pulses in air*. Applied Physics B. **100**, 77 (2010)
4. P. Rohwetter, J. Kasparian, K. Stelmaszczyk, Z. Hao, S. Henin, N. Lascoux, W.M. Nakaema, Y. Petit, M. Quei er, R. Salam e, E. Salmon, L. W oste, and J.-P. Wolf, *Laser-induced water condensation in air*. Nature Photonics. **4**, 451 (2010)
5. W. Ettoumi, Y. Petit, J. Kasparian, and J.-P. Wolf, *Generalized Miller Formulae*. Optics Express. **18**, 6613-6620 (2010)
6. J. Kasparian, P. B ejot, and J.-P. Wolf, *Arbitrary-order non-linear contribution to self-steepening*. Optics Letters. **35**, 2795 (2010)
7. Y. Petit, S. Henin, J. Kasparian, and J.-P. Wolf, *Production of ozone and nitrogen oxides by laser filamentation*. Applied Physics Letters. **97**, 021108 (2010)
8. A.G. Stepanov, S. Henin, Y. Petit, L. Bonacina, J. Kasparian, and J.-P. Wolf, *Mobile source of high-energy single-cycle terahertz pulses* Applied Physics B. **In press**, DOI: 10.1007/s00340-010-4186-4 (2010)

# Infrared extension of the supercontinuum generated by femtosecond terawatt laser pulses propagating in the atmosphere

J. Kasparian and R. Sauerbrey

*Institut für Optik und Quantenelektronik, Max-Wien-Platz 1, 07743 Jena, Germany*

D. Mondelain, S. Niedermeier, J. Yu, and J.-P. Wolf

*Laboratoire de Spectrometrie Ionique et Moléculaire, Université Claude Bernard Lyon 1, Unité Mixte de Recherche 5579, Centre National de la Recherche Scientifique, F-69622 Villeurbanne Cedex, Lyon, France*

Y.-B. André, M. Franco, B. Prade, S. Tzortzakis, and A. Mysyrowicz

*Laboratoire d'Optique Appliquée, Unité Mixte de Recherche 7639, Centre National de la Recherche Scientifique Ecole Nationale Supérieure des Techniques Avancées—Ecole Polytechnique, Centre de l'Yvette, F-91761 Palaiseau Cedex, France*

M. Rodriguez, H. Wille, and L. Wöste

*Institut für Experimentalphysik, Freie Universität Berlin, Arnimallee 14, D-14195 Berlin, Germany*

Received July 5, 2000

We investigated the spectral behavior of a white-light continuum generated in air by 2-TW femtosecond laser pulses at 800 nm. The spectrum extends at least from 300 nm to 4.5  $\mu\text{m}$ . From 1 to 1.6  $\mu\text{m}$  the continuum's intensity increases strongly with the laser energy and depends on the initial chirp. © 2000 Optical Society of America

OCIS codes: 190.1900, 190.7110, 280.3640, 300.6340.

The propagation of high-peak-power laser pulses in transparent matter gives rise to strong nonlinear effects such as four-wave mixing,<sup>1</sup> stimulated Raman processes,<sup>2</sup> self-focusing,<sup>3</sup> and self-phase modulation (SPM),<sup>4–6</sup> which lead to strong modifications of the pulse characteristics. Self-focusing occurs because of the radial intensity variation in the laser beam, whereas SPM is due to the temporal variation of the laser intensity. Although both effects may be observed in conventional laser pulse propagation experiments, they dominate the behavior of ultrashort terawatt laser pulses. One of the most spectacular features observed is the formation of white-light filaments in air, so-called self-guided channels.<sup>7,8</sup> Self-focusing produces a large increase in rise of intensity in the filaments and permits multiphoton ionization of air and thus the formation of a low-density plasma, as demonstrated by electrical conductivity measurements.<sup>9,10</sup> Therefore self-focusing is balanced by diffraction as well as by refraction from the plasma, and thus the focused laser intensity is limited. The propagation is dynamically guided over distances much longer than the Rayleigh length, as much as several tens of meters,<sup>8,11</sup> with a diameter reported to be  $\sim 100 \mu\text{m}$ .<sup>7</sup>

The spectral content of the white-light supercontinuum generated by high-power lasers has been a subject of interest since 1970.<sup>1,12,13</sup> However, because of limited peak power, experiments then were restricted to condensed media. Recently improvements in ultrashort lasers have permitted the results to

be extended to gases. The spectral content of the supercontinuum generated by a 2-TW laser propagating in atmospheric-pressure rare gases has been measured in the visible and the UV, from 150 to 900 nm.<sup>14</sup> Until now, however, to our knowledge no experiment in the IR part of the supercontinuum generated in atmospheric-pressure gases has been performed.

In this Letter we report the measurement of the spectrum of the white-light continuum, particularly in the IR, up to 4.5  $\mu\text{m}$ . The influence of the laser's initial power and chirp is also investigated. Besides the fundamental interest, that in measuring the IR part of the supercontinuum is stimulated by the potential application of the laser-induced continuum to lidar remote-sensing measurements.<sup>15,16</sup> The laser-induced continuum, as opposed to the traditional lidar technique,<sup>17</sup> allows simultaneous multispectral measurements to be made. This is especially interesting in the 3–3.5- $\mu\text{m}$  IR band, where high-energy tunable laser pulses are difficult to produce and where a number of pollutant gases, in particular, volatile organic compounds have strong overlapping absorption bands.

In our experiments we used two state-of-the-art Ti:sapphire chirped-pulse amplification laser systems that had the following parameters. For system A (located at the École National Supérieure de Techniques Avancées): 60-mJ energy; 35-fs minimal pulse duration after the compressor (corresponding to 86-fs minimal pulse duration after the focusing lens); and beam diameter, 25 mm FWHM. The duration of the

laser pulse was elongated by use of the grating compressor, thus producing chirped pulses. For system B (located at the Institut für Optik und Quantenelektronik): 200-mJ energy; 100-fs minimal pulse duration after the compressor; and beam diameter, 35 mm FWHM. The energy was varied continuously. Both systems provided a peak power of  $\sim 2$  TW at 800 nm (i.e.,  $\sim 10^{16}$  W/cm<sup>2</sup> if it was focused into a single filament), but, because the pulse durations were different, the intensity rise and fall times of the two systems were different.

We used several detection systems to cover the wavelength domain under investigation. For the visible spectral region an optical multichannel analyzer (Chromex 500 IS;  $f/8$ ; spectral range, 400–1000 nm; grating, 150 lines/mm; resolution, 1.28 cm<sup>-1</sup>; cooled; Si-ICCD-576, Princeton Instruments; 576  $\times$  394 pixels) was used. In the IR, a prism spectrometer (Zeiss; 400 nm–2.7  $\mu$ m; resolution,  $<5$  nm) and a Perkin-Elmer double-pass prism spectrometer (focal length, 27 cm; LiF prism; transmission, up to 10  $\mu$ m) were equipped with a germanium detector and a liquid-nitrogen-cooled InSb detector (1.5–5.6  $\mu$ m, Hamamatsu). Additionally, IR interference filters (Corion) suppressed the fundamental wavelength of the laser beam.

In the experiment, the output of the laser was slightly focused with thin fused-silica lenses with 8- and 10-m focal lengths. We verified experimentally that, because of the lenses' large diameter (25 mm FWHM) and small thickness (3 mm), no continuum was generated in the lenses. Generation of the continuum occurred in the focal region, with the broadband continuum propagating farther with nearly the same divergence as the laser beam itself (see below). Power measurements before and after the focus showed that the continuum generation process caused no significant energy loss in the focus.

The spectral measurements took place at a total distance of  $\sim 30$  m from the lens and hence after  $\sim 20$  m of filament propagation. At this position the laser beam had a diameter of 20–25 cm. The angular pattern of white-light generation is beyond the scope of this Letter and is currently under investigation.<sup>18</sup> However, the white light is emitted mainly in the forward direction. Therefore all the spectral measurements were made in the forward direction, with an aluminum-coated mirror reflecting a small portion of the light to the entrance slit of the spectrometer used. The detection setup and the detectors were identical for both laser systems.

Figure 1 shows the spectral distribution of the white-light continuum generated in air by laser system A for a pulse duration of 115 fs after the focusing lens without chirp at the end of the compressor and for an 86-fs pulse duration. The spectrum was assembled from four single spectra (300–900 and 700–1800 nm and 1.5–2.7 and 1.5–4.5  $\mu$ m) taken with four distinct detection systems with overlapping sensibility domains. The continuum band is very broad, extending at least to 4.5  $\mu$ m.

In the IR, a region in which we know of no previous experiments in air, an almost exponential decay over 4

orders of magnitude up to 2.5  $\mu$ m is observed. From 2.5 to 4.5  $\mu$ m a slower decay is recorded, of 1 order of magnitude only. Above 4.5  $\mu$ m, the spectral intensity was too low permit us to discriminate detector noise. Water absorption bands superimposed over a flat continuum spectrum are observed at 1.8 and 2.5  $\mu$ m, suggesting that the use of a white-light continuum as a light source for spectroscopic remote sensing of the atmosphere<sup>16</sup> can be extended to the IR.

The dependence of the signal on the incident laser pulse energy was investigated with laser system B. As shown in the inset of Fig. 1, an initial factor-of-2 variation in intensity leads not to a variation in spectral shape in the 1–1.6- $\mu$ m region to only to an overall decrease in efficiency by almost a factor of 1. Note that the conversion efficiency with laser system B, which provides shorter pulses, is 1 order of magnitude lower than with system A (Fig. 1), although both systems provide the same peak power of 2 TW.

The signal's dependence on the chirp (and thus the pulse duration) was investigated with laser system A. Figure 2 shows the continuum conversion efficiency at two wavelengths (1.7 and 3  $\mu$ m, with 5-nm resolution) as a function of laser chirp. The optimal chirp setting depends on the emission wavelength to be optimized. Moreover, as shown in Fig. 1, the overall conversion efficiency in the near IR changes significantly when the chirp setting is changed.

SPM is generally believed to be the dominant process involved in continuum emission.<sup>4–6,14,19</sup> A simple calculation, with parameters that are typical of our experiments, and with a constant Gaussian beam, showed that SPM alone is in semiquantitative agreement with our experiments: (i) the calculated

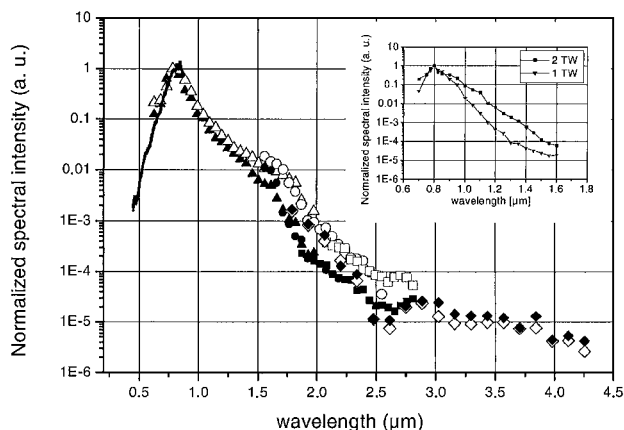


Fig. 1. Measured spectrum of the white-light continuum generated in the center of the beam by 2-TW laser pulses (laser system A). The results are shown for two different chirp settings that correspond to (i) an initial pulse duration of 35 fs without chirp after the compressor (filled symbols) and (ii) a 55-fs initial pulse duration with negative chirp after the compressor (open symbols). These curves are composed of 5 (4) distinct spectra from 5 (4) detection units, respectively, that correspond to the different symbol shapes for each curve. Inset, spectrum of the white-light continuum generated in the center of the beam by 100 fs pulses (laser system B) as a function of pulse power value (200 and 100 mJ for 2 and 1 TW, respectively). The two curves have the same normalization factor.

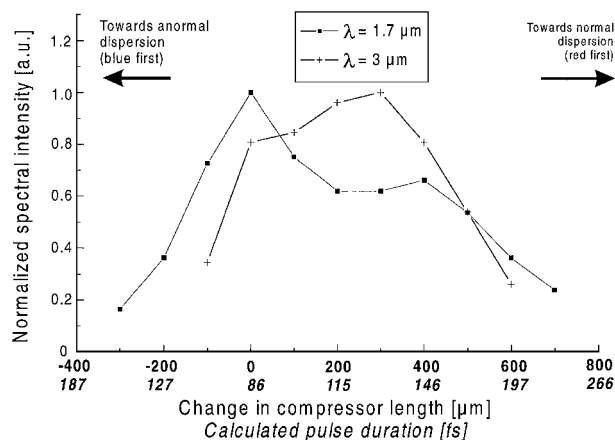


Fig. 2. Initial chirp dependence of the white-light continuum generated by laser system A at two distinct wavelengths (1.7 and 3  $\mu\text{m}$ , with 5 nm resolution). The two curves have the same normalization. The chirp scale is shown as the change in the compressor length, with 0 set arbitrarily, to the chirp value of the curve with open symbols in Fig. 1. Numbers in italics are the corresponding calculated pulse lengths after the exit window and the lens.

spectral content of white light after 20-m propagation in a filament extends from a few hundred nanometers to at least 5  $\mu\text{m}$ ; (ii) laser system A, with shorter pulses, has a larger white-light generation efficiency than system B. This result supports the assumption that SPM is the main process in white-light continuum generation in air. However, a quantitative understanding of the continuum is still a subject for research and needs much more-complex discussion,<sup>19,20</sup> which is beyond the scope of this Letter. Understanding the influence of chirp will require more-detailed calculations.

For atmospheric applications the initial pulse chirp is also critical for the behavior of laser propagation. In particular, because of group-velocity dispersion in air, a negatively chirped pulse will recombine as an ultrashort pulse at a given distance away from the laser,<sup>16,21</sup> giving rise to localized white-light generation. The white-light pulse will also undergo group-velocity dispersion. However, because of tiny changes in the refractive index of air, the pulse broadening will be only 12 ps/km, as calculated with the Rank formula for a pulse ranging from 300 nm to 4.5  $\mu\text{m}$ .

In conclusion, we have measured the wavelength dependence of the white-light continuum emitted from filaments generated in air by high-power femtosecond laser pulses up to 4.5  $\mu\text{m}$  and down to 300 nm. The results show that the shape and the rate of rise in power of the excitation laser pulses have critical effects on conversion efficiency. As far as applications are concerned, a white-light continuum provides broadband pulses with a smooth spectrum up to at least 4.5  $\mu\text{m}$ . It could therefore be used as an *in situ*-produced white lamp, permitting multispectral lidar measurements of atmospheric constituents to be expanded from the visible region<sup>15,16</sup> to the IR.

The authors acknowledge the help of the laser teams at the institutions at Palaiseau and Jena; of

A. Reichmann, who provided the prism spectrometer; and of T. Töpfer, who provided valuable calibrations, tools, and some detectors. This study was done in the framework of the Teramobile project, a joint French–German project funded by the Centre National de la Recherche Scientifique and the Deutsche Forschungsgemeinschaft. R. Sauerbrey's e-mail address is sauerbrey@qe.physik.uni-jena.de.

## References

1. R. R. Alfano and S. L. Shapiro, *Phys. Rev. Lett.* **24**, 584 (1970).
2. L. Smith, P. Liu, and M. Bloembergen, *Phys. Rev. A* **15**, 2396 (1977).
3. D. Strickland and P. B. Corkum, *J. Opt. Soc. Am. B* **11**, 492 (1994).
4. R. Alfano and S. L. Shapiro, *Phys. Rev. Lett.* **24**, 592 (1970).
5. R. R. Alfano and S. L. Shapiro, *Phys. Rev. Lett.* **24**, 1217 (1970).
6. A. Brodeur and S. L. Chin, *J. Opt. Soc. Am. B* **16**, 637 (1999).
7. A. Braun, G. Korn, X. Liu, D. Du, J. Squier, and G. Mourou, *Opt. Lett.* **20**, 73 (1995).
8. E. T. J. Nibbering, P. F. Curley, G. Grillon, B. S. Prade, M. A. Franco, F. Salin, and A. Mysyrowicz, *Opt. Lett.* **21**, 62 (1996).
9. H. Schillinger and R. Sauerbrey, *Appl. Phys. B* **68**, 753 (1999).
10. S. Tzortzakis, M. Franco, Y.-B. Andre, A. Chiron, B. Lamouroux, B. Prade, and A. Mysyrowicz, *Phys. Rev. E* **60**, R3505 (1999).
11. M. Mlejnek, M. Kolesik, J. V. Moloney, and E. M. Wright, *Opt. Lett.* **23**, 2938 (1999).
12. W. Yu, R. R. Alfano, C. L. Sam, and R. J. Seymour, *Opt. Commun.* **14**, 344 (1975).
13. P. B. Corkum, P. P. Ho, R. R. Alfano, and J. T. Manassah, *Opt. Lett.* **10**, 624 (1985).
14. H. Nishioka, W. Odajima, K. Ueda, and H. Takuma, *Opt. Lett.* **20**, 2505 (1995).
15. L. Wöste, C. Wedekind, H. Wille, P. Rairoux, B. Stein, S. Nikolov, Chr. Werner, S. Niedermeier, H. Schillinger, and R. Sauerbrey, *Laser Optoelektron.* **29**, 51 (1997).
16. P. Rairoux, H. Schillinger, S. Niedermeier, M. Rodriguez, F. Ronneberger, R. Sauerbrey, B. Stein, D. Waite, C. Wedekind, H. Wille, and L. Wöste, "Remote sensing of the atmosphere using ultrashort laser pulses," *Phys. B* (to be published).
17. R. M. Measures, *Laser Remote Sensing—Fundamentals and Applications* (Wiley/Interscience, New York, 1984).
18. D. Mondelain, G. Ange, R. Volk, S. Niedermeier, J. Kasparian, J. Yu, R. Sauerbrey, and J. P. Wolf, *Laboratoire Spectrométrie Ionique et Moléculaire, Université Claude Bernard Lyon 1, Unité Mixte de Recherche 5579, Centre National de la Recherche Scientifique, F-69622 Villeurbanne Cedex, Lyon, France*, are preparing a manuscript to be called "Self-reflection-enhanced back scattering from white light filaments induced by high intensity femtosecond laser pulses propagating in air."
19. A. Gaeta, *Phys. Rev. Lett.* **84**, 3582 (2000).
20. I. Golub, *Opt. Lett.* **16**, 305 (1990).
21. J. Kasparian and J.-P. Wolf, *Opt. Commun.* **152**, 355 (1998).

## Rapid communication

# The critical laser intensity of self-guided light filaments in air

J. Kasparian<sup>1,\*</sup>, R. Sauerbrey<sup>1</sup>, S.L. Chin<sup>2</sup>

<sup>1</sup>“Teramobile” project, Institut für Optik und Quantenelektronik, Friedrich Schiller Universität Jena, Max Wien Platz 1, 07743 Jena, Germany (Fax: +49-3641/947-202, E-mail: kasparian@qe.physik.uni-jena.de)

<sup>2</sup>Centre d’Optique, Photonique et Laser (COPL) and Département de Physique, Université Laval, Québec, QC, G1K 7P4 Canada

Received 18 August 2000/Published online: 8 November 2000 – © Springer-Verlag 2000

**Abstract.** The critical intensity inside plasma filaments generated in air by high-power, ultra-short laser pulses is estimated analytically and compared to recent experimental data. The result,  $I_{\text{crit}} \approx 4 \times 10^{13} \text{ W/cm}^2$ , is highly relevant for atmospheric applications.

**PACS:** 42.50.H; 42.68; 42.65.R

When propagating in air, high-power femtosecond laser pulses produce self-guided high-intensity plasma filaments, [1–4] the diameter of which could be as small as 100  $\mu\text{m}$ . These filaments are due to a balance between Kerr self-focusing, and defocusing due to the plasma generated inside the filament. Due to the small value of the nonlinear refractive index of air ( $n_2 = 3 \times 10^{19} \text{ cm}^2/\text{W}$ ), the equilibrium is reached for low plasma densities [5]. A precise description of the filamentation process would need more experimental data relating to parameters such as the intensity inside the filament. Such data would also be useful for atmospheric applications such as lightning control [6] or Lidar [7, 8].

However, due to the very high intensities inside in the filaments (at least  $10^{13} \text{ W/cm}^2$ ), direct measurements are not possible because any device used for that purpose, whether a detector, a reflector or an attenuator, would be damaged. Therefore, only indirect measurements may be performed.

In this short note, we provide an estimation of the intensity inside a filament generated in air by a femtosecond laser pulse, based on recent experimental data obtained by Talebpour et al. [9]. It is well known [10] that the pulse self-focuses until photoionization sets in. Although the detailed propagation dynamics of the pulse may be quite complicated, its propagation and filamentation is dictated by an equilibrium between the focusing Kerr effect and defocusing multiphoton/tunnel ionization. (In the following, the word ionization will be used alone whenever possible for simplicity). It may be shown that diffraction may, to the first approximation, be neglected. We also neglect all non-instantaneous

contributions to nonlinearity, and we shall average all relevant quantities over the whole pulse. Consequently, we obtain a filament whose size and intensity are determined by the following equation, which is a balance between Kerr self-focusing  $\Delta n_{\text{Kerr}}(\text{neutral})$  and defocusing  $\Delta n(\text{plasma})$  contributions to the nonlinear index of refraction [1]:

$$\Delta n_{\text{Kerr}}(\text{neutral}) \approx \Delta n(\text{plasma}) \quad (1)$$

Both changes in the indices of refraction depend on the laser intensity  $I$ :

$$n_2 \times I \approx N_e(I)/2N_{\text{crit}} \quad (2)$$

In this expression,  $n_2$  is the Kerr nonlinear index of refraction of the propagation medium,  $N_{\text{crit}} = \epsilon_0 \times m \times \omega^2/e^2$  is the critical plasma density, with  $m$  being the mass of electron,  $\omega$  the laser angular frequency, and  $e$  the elementary charge.  $N_{\text{crit}} = 1.7 \times 10^{21} \text{ cm}^{-3}$  for a titanium-sapphire laser with a central wavelength of 800 nm. The electron density  $N_e$  is given by ionization:

$$dN_e(z, t)/dt = R(I) \times N(z) \quad (3)$$

where  $N(z)$  is the density of neutrals as a function of the propagation distance  $z$ , and  $R(I)$  is the ionization rate. The results of Talebpour et al. [9] exhibit an effective power law dependence of ionization as a function of intensity. This leads us to write  $R$  as:

$$R(I) = R_T \times (I/I_T)^\alpha \quad (4)$$

where  $R_T$  and  $I_T$  are a pair of experimental values used as a reference point. They can be estimated for nitrogen and oxygen from the ionization data shown in Fig. 1, adapted from [9]. We chose  $I_{T,O_2} = I_{T,N_2} = I_T = 10^{13} \text{ W/cm}^2$ . The corresponding ionization rates are  $R_{T,N_2} = 2.5 \times 10^4 \text{ s}^{-1}$  and  $R_{T,O_2} = 2.8 \times 10^6 \text{ s}^{-1}$ , respectively. A linear fit of the curves gives the slopes  $\alpha_{N_2} \approx 7.5$  for nitrogen and  $\alpha_{O_2} \approx 6.5$  for oxygen for intensities  $I < 10^{14} \text{ W/cm}^2$ . These values are lower than those expected from the number of photons needed for multiphoton ionization, which are 11 and 8 respectively for nitrogen and oxygen at a wavelength of 800 nm, which is

\*Corresponding author.

Present address: LASIM, UMR CNRS 5579, Université Claude Bernard Lyon 1, 69622 Villeurbanne Cedex, France (E-mail: jkaspari@lasim.univ-lyon1.fr)

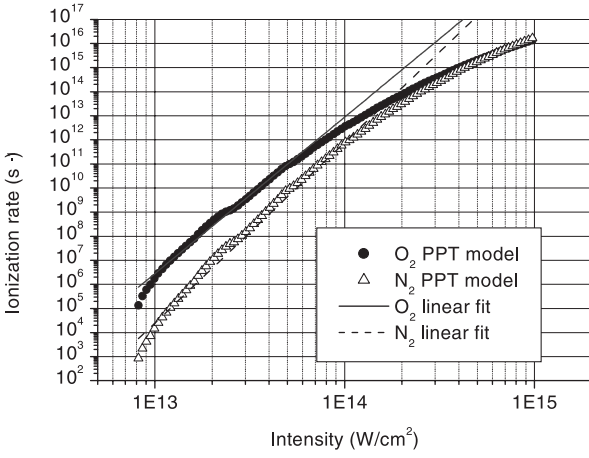


**Fig. 1.** Tunnel ionization rate of  $N_2$  and  $O_2$  molecules as a function of laser intensity, as calculated using the PPT model by Talebhour et al. [9]

an indication of the occurrence of tunnel ionization [11]. We should point out that the ionization rates of oxygen are not much higher than those of nitrogen, even though the ionization potential of oxygen (12.1 eV) is lower than that of nitrogen (15.6 eV) [9]. This is explained by Muth-Böhm et al. [12] as being due to the nature of electron orbitals in the two molecules. In oxygen, with an anti-bonding orbital, electron waves ionized from the two nuclear sites interfere destructively, leading to a significant reduction (suppression) of the ionization probability. In nitrogen, with a bonding orbital, electron waves ionized from the two nuclear sites interfere constructively. Consequently, the probability of ionization is high. As such, in our estimation, we have to keep the contributions to ionization from both  $O_2$  and  $N_2$ , and cannot totally neglect the contribution of  $N_2$ .

As long as the pulse duration remains shorter than the typical collision time in air, which is about 1 ps in standard conditions, only tunnel/multiphoton ionization occurs, and collisional ionization may be neglected. The treatment of  $O_2$  and  $N_2$  can therefore be decoupled. Equation (3) thus becomes:

$$\begin{aligned} dN_e(z, t)/dt &= dN_{e,N_2}(z, t)/dt + dN_{e,O_2}(z, t)/dt \\ dN_e(z, t)/dt &= N_{N_2}(z) \times R_{T,N_2} \times (I/I_T)^{\alpha_{N_2}} \\ &\quad + N_{O_2}(z) \times R_{T,O_2} \times (I/I_T)^{\alpha_{O_2}} \end{aligned} \quad (5)$$

Here,  $N_{N_2}(z) = 0.78 \times N_{air}(z)$  and  $N_{O_2}(z) = 0.21 \times N_{air}(z)$  are the number densities of  $N_2$  and  $O_2$  molecules in air, respectively. At atmospheric pressure, this corresponds to  $N_{N_2}(z) = 2 \times 10^{19} \text{ cm}^{-3}$  and  $N_{O_2}(z) = 5 \times 10^{18} \text{ cm}^{-3}$ , respectively. The relative contribution of both terms, i.e.  $(dN_{e,N_2}(z, t)/dt)/(dN_e(z, t)/dt)$  and  $(dN_{e,O_2}(z, t)/dt)/(dN_e(z, t)/dt)$  as a function of the incident laser intensity using (5) is shown in Fig. 2. Both terms have the same order of magnitude in the intensity range of interest, and their relative contribution to ionization cross each other around  $10^{14} \text{ W/cm}^2$ . This means that in the general case the contributions of both  $O_2$  and  $N_2$  have to be taken into account. The electron density is therefore estimated from (5):

$$N_e = [R_{N_2}(I) \times N_{N_2}(z) + R_{O_2}(I) \times N_{O_2}(z)] \times \tau_1 \quad (6)$$

where  $\tau_1$  is a characteristic ionization time which is on the order of the laser pulse duration. If we neglect the

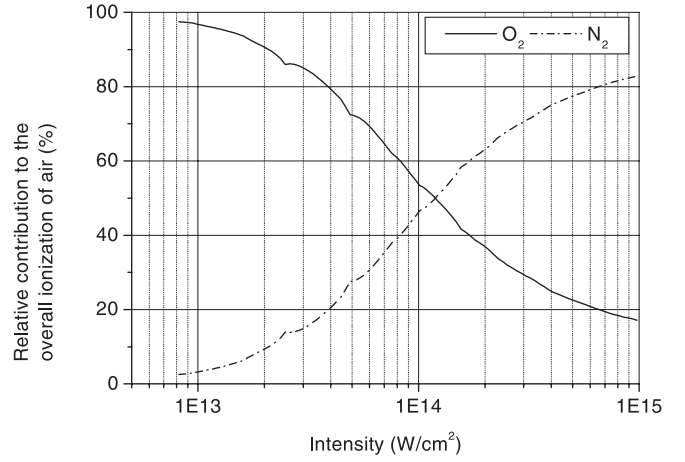


**Fig. 2.** Relative ion densities from  $O_2$  and  $N_2$  with respect to the total number of ions in a laser-generated plasma in air, as a function of the laser intensity after data from [9]. The small dips in the curves are due to dynamic resonances in the ionization process [18]

$z$ -dependence of  $N$  and consider it as a constant, the lowest intensity, or critical intensity  $I_{crit}$ , needed to maintain a filament is the solution of (2):

$$\begin{aligned} n_2 \times I_{crit} &= \frac{\tau_1}{2 \times N_{crit}} \\ (N_{N_2} \times R_{T,N_2} \times (I_{crit}/I_T)^{\alpha_{N_2}} + N_{O_2} \times R_{T,O_2} \times (I_{crit}/I_T)^{\alpha_{O_2}}) \end{aligned} \quad (7)$$

This equation cannot be solved analytically. For our parameters, with  $\tau_1 = 100 \text{ fs}$ , a numerical solution taking into account both  $N_2$  and  $O_2$  gives  $I_{crit} = 4 \times 10^{13} \text{ W/cm}^2$ . At this intensity, Fig. 2 shows that oxygen accounts for more than 80% of the overall plasma. This value is in good agreement with the value of  $I = 4.5 \times 10^{13} \text{ W/cm}^2$  estimated by Lange et al. [13] from the higher harmonics pattern.

Alternatively, we can estimate the intensity in the filament by the following observation. The electron density measured by several groups [5, 14–17] has a wide range of values, ranging from  $10^{12} \text{ cm}^{-3}$  [14] to  $3 \times 10^{16} \text{ cm}^{-3}$  [15]. However, these discrepancies can be explained by the different experimental conditions. In the case of Schillinger et al. [14], the density was averaged over a section with a diameter of 11 mm, containing 10–20 filaments. Taking into account the fact that the plasma is only to be found in the filament, the equivalent plasma density inside the filaments is in the order of  $5 \times 10^{14} \text{ cm}^{-3}$ . The results of Tzortzakis et al. [15] could have been overestimated because they have measured relatively near the focal point of their focusing lens. Therefore, a reasonable range for the free electron density produced by high power ultra-short laser pulses in air is about  $10^{14}–10^{15} \text{ cm}^{-3}$ , corresponding to probabilities of ionization of the order of  $10^{-5}–10^{-4}$ . We can reasonably assume that the focal volume is approximately constant in the filament, and that saturation of the ionization in Figs. 1 and 2 of [9] corresponds to a full ionization of the gases. Therefore an ionization probability of  $10^{-5}–10^{-4}$  corresponds to an intensity of the order of  $4–6 \times 10^{13} \text{ W/cm}^2$  for oxygen as well as for nitrogen. This is in good agreement with the critical intensity calculated above. Due to the high  $\alpha$  value for both  $N_2$  and  $O_2$ ,

even considerable differences in the measured plasma density will not affect the inferred critical intensity substantially.

In conclusion, we have estimated the critical laser intensity in the filaments of intense Ti:Sapphire laser pulses propagating in the atmosphere by two independent methods. Both methods agree with each other and give an intensity in the order of  $4 \times 10^{13}$  W/cm<sup>2</sup>. This result is highly relevant for the study of the propagation of high-power femtosecond laser pulses in air, from a fundamental point of view as well for atmospheric applications such as laser lightning and Lidar.

*Acknowledgements.* S.L. Chin would like to acknowledge the Alexander von Humboldt Foundation for the Humboldt Research Award and the Friedrich Schiller University of Jena for their hospitality in hosting him in the Institute of Optics and Quantum Electronics. J. Kasparian acknowledges financial support of the Deutsche Forschung Gemeinschaft in the framework of the French-German project "Teramobile" (CNRS/DFG).

## References

1. A. Braun, G. Korn, X. Liu, D. Du, J. Squier, G. Mourou: *Opt. Lett.* **20**, 73 (1995)
2. E.T.J. Nibbering, P.F. Curley, G. Grillon, B.S. Prade, M.A. Franco, F. Salin, A. Mysyrowicz: *Opt. Lett.* **21**, 62 (1996)
3. A. Brodeur, C.Y. Chien, F.A. Ilkov, S.L. Chin, O.G. Koserava, V.P. Kandidov: *Opt. Lett.* **22**, 304 (1997)
4. M. Mlejnek, E.M. Wright, J.V. Moloney: *Opt. Lett.* **23**, 382 (1998)
5. A. Talebpour, A. Abdel-Fattah, S.L. Chin: *Opt. Commun.* **183**, 479 (2000)
6. X.M. Xhao, J.-C. Diels, C.Y. Wang, J.M. Elizondo: *IEEE J. Quantum Electron.* **31**, 599 (1998)
7. P. Rairoux, H. Schillinger, S. Niedermeier, M. Rodriguez, F. Ronneberger, R. Sauerbrey, B. Stein, D. Waite, C. Wedekind, H. Wille, L. Wöste: *Appl. Phys. B* **71**, 573 (2000)
8. L. Wöste, C. Wedekind, H. Wille, P. Rairoux, B. Stein, S. Nikolov, Chr. Werner, S. Niedermeier, H. Schillinger, R. Sauerbrey: *Laser Optoelektronik* **29**, 51 (1997)
9. A. Talebpour, J. Yang, S.L. Chin: *Opt. Commun.* **163**, 29 (1999) Note that a typographical error in the vertical axis of Fig. (1) of this paper results in reducing the plotted ionization rate of nitrogen by a factor of 10. This has been corrected in the present paper.
10. Y.R. Shen: *The principles of nonlinear optics* (Wiley, New York 1984)
11. S.L. Chin, F. Yergea, P. Lavigne: *J. Phys. B* **18**, L213 (1985)
12. J. Muth-Böhm, A. Becker, F. Faisal: *Phys. Rev. Lett.* **85**, 2280 (2000)
13. H.R. Lange, A. Chiron, J.-F. Ripoche, A. Mysyrowicz, P. Berger, P. Agostini: *Phys. Rev. Lett.* **81**, 1611 (1998)
14. H. Schillinger, R. Sauerbrey: *Appl. Phys. B* **68**, 753 (1999)
15. S. Tzortzakis, B. Prade, M. Franco, A. Mysyrowicz: *Opt. Commun.* **181**, 123 (2000)
16. B. La Fontaine, F. Vidal, Z. Jiang, C.Y. Chien, D. Comtois, A. Desparois, T.W. Johnston, J.-C. Kieffer, H. Pépin, H.P. Mercure: *Phys. Plasmas* **6**, 1615 (1999)
17. C.Y. Chien, B. La Fontaine, A. Desparois, Z. Jiang, T.W. Johnston, J.C. Kieffer, H. Pépin, F. Vidal, H.P. Mercure: *Opt. Lett.* **25**, 578 (2000)
18. A. Talebpour, C.Y. Chien, S.L. Chin: *J. Phys. B* **29**, 5727 (1996)

# Backward supercontinuum emission from a filament generated by ultrashort laser pulses in air

J. Yu, D. Mondelain, G. Ange, R. Volk, S. Niedermeier, and J. P. Wolf

*Laboratoire de Spectrométrie Ionique et Moléculaire, Unité Mixte 5579, Centre National de la Recherche Scientifique, Université Claude Bernard-Lyon 1, 43, Boulevard du 11 Novembre 1918, F-69622 Villeurbanne Cedex, France*

J. Kasparian and R. Sauerbrey

*Institut für Optik und Quantenelektronik, Friedrich Schiller Universität Jena, Max-Wien-Platz 1, 07743 Jena, Germany*

Received October 16, 2000

Backward emission of the supercontinuum from a light filament induced by high-intensity femtosecond laser pulses propagating in air has been observed to be enhanced compared with linear Rayleigh–Mie scattering. This enhancement is interpreted as a nonlinear scattering process onto longitudinal refractive-index changes induced by the laser pulse itself. The spectral dependence of the supercontinuum angular distribution is also investigated. © 2001 Optical Society of America

OCIS codes: 190.3270, 190.5530, 190.5940, 190.7110, 280.1310, 290.1350.

High-intensity ultrashort laser pulses propagating in air have been observed to self-collimate into long filaments over a distance that substantially exceeds the Rayleigh length.<sup>1</sup> Such light filaments provide long interaction paths, leading to an ultrabroadband continuum from the UV to the IR.<sup>2–4</sup> In the forward direction, this supercontinuum exhibits conical emission with a spectacular pattern of concentric colored rings.<sup>5–7</sup> The self-channeling model interprets filamentation as the result of a balance between self-focusing owing to the Kerr effect and the combined effects of natural diffraction and refraction from a low-density plasma.<sup>1,5</sup> Use of the moving focus model to explain filamentation as well as conical emission in the femtosecond regime has also been proposed.<sup>6,7</sup> More recently, use of the spatial replenishment model<sup>8</sup> to describe the filamentation that results from dynamic guiding has been suggested. Longitudinal effects on a pulse wave packet, such as pulse self-shortening<sup>9,10</sup> and pulse splitting,<sup>11</sup> have been reported. Notice that numeric simulations have been carried out.<sup>12</sup>

Recently, supercontinuum emission and propagation of terawatt laser pulses were observed over several kilometers in air by use of a lidar arrangement.<sup>13,14</sup> For the new applications in atmospheric remote sensing, key issues are the origin and the underlying physical processes of white light detected at large distances. The question is whether this white light is due to *in situ* backward emission from remotely located filaments or to subsequent Rayleigh–Mie backscattering of white light generated in the forward direction by filaments at shorter distances.

In this Letter we show, for the first time to our knowledge, that the supercontinuum emission from a filament is enhanced in the backward direction compared with linear backscattering. This enhancement is interpreted as being due to a backscattering process in laser-induced longitudinal refractive-index changes caused by Kerr and plasma effects.

The experimental setup that we used to measure the angular dependence of the supercontinuum emitted by

a filament in air was based on a chirped-pulse amplification femtosecond laser system providing 6 mJ of energy in 120 fs at 810 nm. The 12 mm-diameter output beam was slightly focused by a spherical mirror of 10-m radius of curvature. The beam propagated in free space over 80 m after the region investigated (1.5 m downstream from the geometrical focus). The direction of propagation of the incident beam was considered the forward-scattering direction and defined as  $\theta = 0^\circ$  (see Fig. 1). The supercontinuum emitted by the filament was collected by a 6-mm-diameter liquid optical fiber with a restricted field of view of  $0.86^\circ$  by a nontransparent guiding tube. The overlap between the field of view of the detection system and the filament (and hence of the signal) is proportional to  $1/\sin(\theta)$ . We mounted the fiber onto a stepper-motor-driven goniometer to measure the angular dependence from  $\theta = 5^\circ$  to  $\theta = 176.5^\circ$ . In most of the experiments the fiber transmitted the collected light to a photomultiplier tube (PMT) through a blue-green color filter, which rejected the fundamental and transmitted the 350–600-nm region. The atmosphere in the region investigated was controlled with a hood that was able to generate a dust-free laminar air flow.

The experimental setup that we used to quantify the contribution of elastic Rayleigh–Mie scattering to the measured signal was identical, except for the input laser beam. Inasmuch as the linear processes had to be investigated in the same blue–green spectral region as the detected part of the supercontinuum, the output beam of the laser was frequency doubled in a KDP crystal. The second harmonic at 405 nm was separated from the fundamental by a dichroic mirror ( $\sim 200 \mu\text{J}$  after the dichroic mirror), which provided a low-intensity and linearly propagating blue beam. The divergence of this beam was  $0.065^\circ$  (half-angle).

The results obtained for linear Rayleigh–Mie scattering are shown in Fig. 1. The raw data are divided by the geometric overlap function  $1/\sin(\theta)$ . The use of the laminar flow provided dust-free air, giving access to pure Rayleigh scattering. The experimental data

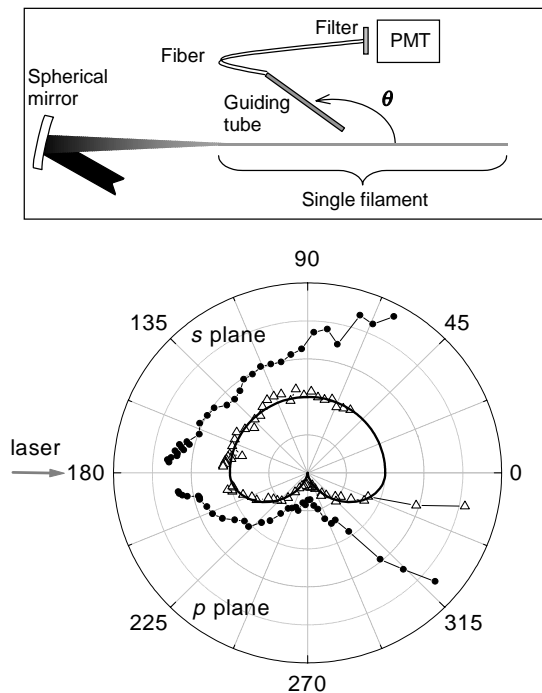


Fig. 1. Experimental setup and angular distributions of linear scattering from a low-energy blue beam. Filled circles, dusty air; open triangles, clean air. The clean-air data are fitted with a Rayleigh distribution (solid curves).

(open triangles) reproduce well the expected Rayleigh scattering angular pattern for both *s*-plane (displayed from  $0^\circ$  to  $180^\circ$ ) and *p*-plane (from  $180^\circ$  to  $360^\circ$ ) polarizations. The filled circles in Fig. 1 display the results for an atmosphere containing aerosol particles (laminar flow off). The angular distributions are thus representative of the combination of Rayleigh and Mie scattering.

The angular distributions of the supercontinuum emitted by a filament were then measured and compared with the linear data. With pulses of 50-GW peak power at 810 nm, a single filament started slightly before the geometrical focal point with conical emission, which had a divergence of  $0.12^\circ$  (half-angle) for its outer ring, in agreement with former observations.<sup>5-7</sup> The angular distributions obtained are shown in Fig. 2 for both clean and aerosol-containing atmospheres. In view of nonlinear lidar applications,<sup>13,14</sup> for which the ratio ( $\alpha/\beta$ ) is the relevant parameter<sup>15</sup> (here  $\alpha$  is the overall extinction coefficient and  $\beta$  is the backscattering coefficient) we need to compare the shapes of the angular patterns, rather than the absolute intensities, of linear and nonlinear signals. Therefore we arbitrarily normalized the linear and the nonlinear signals to the same intensity at  $90^\circ$  in each polarization plane. A remarkable result is that the supercontinuum emission from the filament is greater (factor of 2) in the near-backward direction ( $176.5^\circ$ ) than Rayleigh-Mie scattering. The intensity rises steeply in the near-backward direction, which should lead us to extrapolate even stronger enhancements at  $180^\circ$ . These measurements demonstrate that self-generated enhancement of backward emission occurs within the filament. This discovery

implies that the supercontinuum detected in the backward direction in a white-light lidar experiment not only is the result of linear Rayleigh-Mie backscattering but is also due to the nonlinear backscattering. The fact that a similar enhancement is observed in clean and in dust-containing air implies that aerosols do not contribute significantly to the nonlinear backscattering enhancement.

Compared with elastic scattering, the additional nonlinear scattering is thus of the same order of magnitude at  $176.5^\circ$ . We interpret this nonlinear backscattering enhancement as a consequence of laser-induced longitudinal refractive-index changes. These changes in the index can occur in a dynamic guided structure<sup>8,16</sup> in which the filament diameter, and hence the intensity, undergoes oscillations. The leading edge of a high-peak-power pulse produces long-period gratinglike index changes in the longitudinal direction (as a result of Kerr and plasma effects), which then backscatter white light generated from the trailing part of the pulse. The order of magnitude of the index changes in our experimental conditions is estimated to be  $10^{-5}$  when the nonlinear refractive index of air is used<sup>17</sup> and for the measured plasma density.<sup>18-20</sup> A rough estimation from the Fresnel formula, and assuming a step-shaped refractive-index change, yields an upper limit for the self-reflection factor of  $10^{-5}$ . This value is much larger than the Rayleigh backscattering efficiency of  $2.5 \times 10^{-7}$  in our experimental conditions in the blue-green band

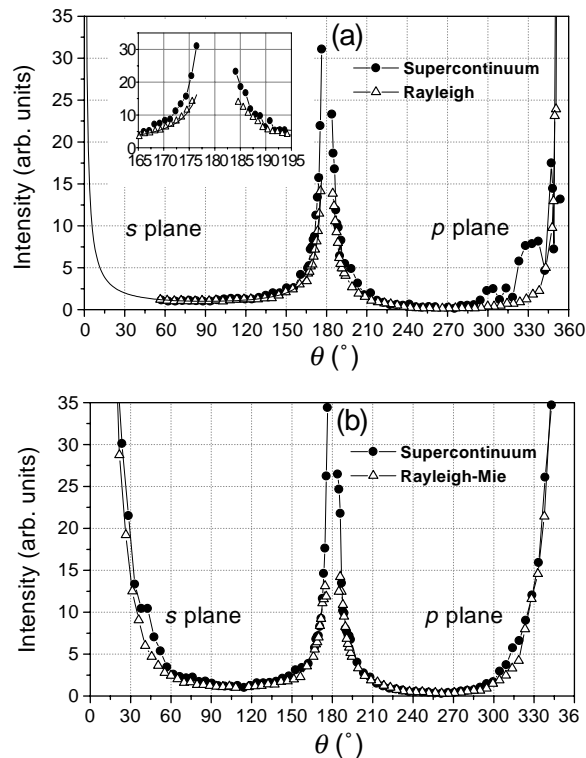


Fig. 2. Angular distributions of the supercontinuum emitted from a filament detected in the blue-green band compared with linear scattering: (a) clean air, (b) dusty air. In clean air and the *s* plane, the linear data are fitted and extrapolated by a Rayleigh distribution [ $1/\sin(\theta)$ ]. Inset, zoomed-in view of the details from  $165^\circ$  to  $195^\circ$ .

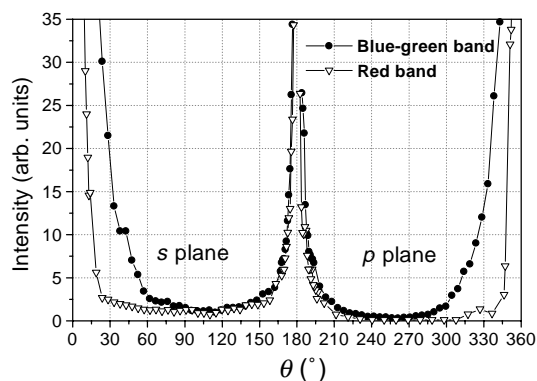


Fig. 3. Angular distributions of the supercontinuum scattered from a filament detected in the red band compared with those in the blue-green band.

[calculated with a 50-cm-long scattering volume, a 0.1-sr detection solid angle, and a Rayleigh backscattering coefficient  $\beta = 4.9 \times 10^{-8} \text{ cm}^{-1} \text{ sr}^{-1}$  at 405 nm (Ref. 15)]. This estimated value is also 2 orders of magnitude higher than the experimentally observed value at  $176.5^\circ$ . This result should suggest a much larger nonlinear self-reflection coefficient at  $180^\circ$ . We remark, however, that the step-shaped index change is an assumption that is not verified in reality. The actual smooth change of index leads to a smaller reflection coefficient than for a step change.

The spectral dependence of the supercontinuum angular distribution was also investigated (in aerosol-rich air) with a bandpass filter from 600 to 650 nm. In Fig. 3 the results obtained are compared with the blue-green data. We can notice first that in the red band the forward peak is much narrower than in the blue-green region. This can be explained by the angular dispersion in the conical emission: The radius of color rings decreases with increasing wavelength.<sup>5</sup> In these plots, data were normalized in each polarization plane to yield identical signals in the near-backward direction for both spectral bands. This representation shows that, for the same near-backward signal, scattering about  $90^\circ$  decreases in the red band. This behavior is easily explained as being due to the decrease of the efficiency of both Rayleigh and Mie scattering when the wavelength increases. This observation implies that the importance of nonlinear self-reflection relative to linear Rayleigh-Mie scattering increases for longer wavelengths. This statement has important implications for lidar measurements in the mid and far infrared, where Rayleigh-Mie scattering decreases dramatically. We may expect that nonlinear self-reflection will then greatly dominate elastic backscattering and permit infrared lidar measurements at larger distances.

In conclusion, we have demonstrated that the supercontinuum emitted by a filament is enhanced in the backward direction because of longitudinal refractive-index changes induced by the laser pulse itself. These results have strong implications for lidar ap-

plications based on high-intensity femtosecond laser pulses.

The present study was made within the framework of the joint French-German Teramobile project, cofinanced by the Deutsche Forschungsgemeinschaft and the Centre National de la Recherche Scientifique. We acknowledge valuable assistance in a part of this research from Stefan Düsterer and Falk Ronneberger. J. Yu's e-mail address is jinyu@lasim.univ\_lyon1.fr.

## References

1. A. Braun, G. Korn, X. Liu, D. Du, J. Squier, and G. Mourou, *Opt. Lett.* **20**, 73 (1995).
2. P. B. Corkum, C. Rolland, and T. Srinivasan-Rao, *Phys. Rev. Lett.* **57**, 2268 (1986).
3. H. Nishioka, W. Odajima, K.-I. Ueda, and H. Takuma, *Opt. Lett.* **20**, 2505 (1995).
4. J. Kasparian, R. Sauerbrey, D. Mondelain, S. Niedermeier, J. Yu, J. P. Wolf, Y. B. André, M. Franco, B. Prade, S. Tzortzakis, A. Mysyrowicz, M. Rodriguez, H. Wille, and L. Wöste, *Opt. Lett.* **25**, 1399 (2000).
5. E. T. J. Nibbering, P. F. Curley, G. Grillon, B. S. Prade, M. A. Franco, F. Salin, and A. Mysyrowicz, *Opt. Lett.* **21**, 62 (1996).
6. A. Brodeur, C. Y. Chien, F. A. Ilkov, S. L. Chin, O. G. Kosareva, and V. P. Kandidov, *Opt. Lett.* **22**, 304 (1997).
7. O. G. Kosareva, V. P. Kandidov, A. Brodeur, C. Y. Chien, and S. L. Chin, *Opt. Lett.* **22**, 1332 (1997).
8. M. Mlejnek, E. M. Wright, and J. V. Moloney, *Opt. Lett.* **23**, 382 (1998).
9. J. H. Marburger and W. G. Wagner, *IEEE J. Quantum. Electron.* **QE-3**, 415 (1967).
10. G. L. McAllister, J. H. Marburger, and L. G. DeShazer, *Phys. Rev. Lett.* **21**, 1648 (1968).
11. J. K. Ranka, R. W. Schirmer, and A. L. Gaeta, *Phys. Rev. Lett.* **77**, 3783 (1996).
12. See, for example, X. Liu and A. Braun, in *Conference on Lasers and Electro-Optics*, Vol. 9 of 1996 OSA Technical Digest Series (Optical Society of America, Washington, D.C., 1996), paper JTUF5.
13. L. Wöste, C. Wedekind, H. Wille, P. Rairoux, B. Stein, S. Nikolov, Chr. Werner, S. Niedermeier, F. Ronneberger, H. Schillinger, and R. Sauerbrey, *Laser Optoelectron.* **29**, 51 (1997).
14. P. Rairoux, H. Schillinger, S. Niedermeier, M. Rodriguez, F. Ronneberger, R. Sauerbrey, B. Stein, D. Waite, C. Wedekind, H. Wille, and L. Wöste, *Appl. Phys. B* **71**, 573 (2000).
15. R. M. Measures, *Laser Remote Sensing* (Krieger, Malabar, Fla., 1992).
16. N. Aközbek, C. M. Bowden, A. Talebpour, and S. L. Chin, *Phys. Rev. E* **61**, 4540 (2000).
17. C. H. Lin, J. P. Heritage, T. K. Gustafson, R. Y. Chiao, and J. P. McTague, *Phys. Rev. A* **13**, 813 (1976).
18. H. Schillinger and R. Sauerbrey, *Appl. Phys. B* **68**, 753 (1999).
19. B. La Fontaine, F. Vidal, Z. Jiang, C. Y. Chien, D. Comtois, A. Desparois, T. W. Johnston, J. C. Kieffer, H. Pépin, and H. P. Mercure, *Phys. Plasmas* **6**, 1615 (1999).
20. S. Tzortzakis, B. Prade, M. Franco, and A. Mysyrowicz, *Opt. Commun.* **181**, 123 (2000).

# Modifications to the lidar equation due to nonlinear propagation in air

G. Faye\*, J. Kasparian, R. Sauerbrey

Institut für Optik und Quantenelektronik, Friedrich Schiller Universität Jena, Max Wien Platz 1, 07743 Jena, Germany

Received: 2 January 2001/Revised version: 8 June 2001/Published online: 18 July 2001 – © Springer-Verlag 2001

**Abstract.** We study how the well-known lidar equation is affected by the use of ultra-short, high-power laser pulses. Because of the self-focusing and self-guiding, the overlap function  $\xi$ , representing the reduction fraction of the signal resulting from geometrical effects inside the experimental system, needs to be reconsidered. The losses due to multi-photon ionisation in the filament entail a heavy weakening of the return signal. We also investigate the contribution of the white-light components generated by self-phase modulation.

**PACS:** 42.50.H; 42.68; 42.65.R; 42.68.W

Light detection of ranging (lidar) [1, 2], an optical analogue of radar, is now a classical technique for atmospheric remote sensing, with unique versatility and three-dimensional (3D) mapping abilities. However, retrieving the atmospheric composition from a lidar signal is not straightforward. Gases with narrow absorption lines may be detected by the Differential Absorption Lidar (DIAL) technique. For gases with overlapping absorption bands leading to interference in the measurements, or for aerosols [3], strong assumptions regarding the particles at play are necessary in order to determine absolute concentrations.

Recently, it has been proposed [4] and demonstrated [5, 6] that nonlinear lidar measurements based on high-power femtosecond laser pulses could provide more information than their linear counterparts. A white-light supercontinuum generated by high-power laser pulses propagating in air provides a broadband pulsed light source from the ultraviolet (UV) [7] to the infrared (IR) [8]. The IR wavelengths, which have been measured up to 4.5  $\mu\text{m}$ , open the way to measurements of pollutants absorbing in this spectral domain such as methane, or with overlapping spectra, such as volatile organic compounds, which could be resolved through multi-spectral lidar measurements [5]. A white light supercontinuum lidar signal was observed up to 13 km [5, 6]. Ultra-short pulses could also give rise to significant size effects in the microcavities formed by spherical, transparent aerosols such as cloud

droplets. When the pulse is shorter than the cavity length, it can be localised in the aerosol cavity. This so-called ballistic mode may lead to a strong enhancement of the lidar signal received from the smallest particles [4, 25].

Nonlinear lidar requires high-power, ultra-short (femtosecond) laser pulses which have a very complex behaviour when propagating in air. Basically, they first undergo self-focusing due to the Kerr effect, giving rise to a sharp increase in the intensity. Then, ionisation takes place and induces defocusing. The equilibrium between these two processes leads to a self-guided filament [9–12] with a diameter of about 100  $\mu\text{m}$ , and which can expand over distances of at least 200 m [13]. Due to the high intensities in the filament, a strong self-phase modulation occurs, which entails a wide spectral broadening, i.e. the supercontinuum generation mentioned above.

On the other hand, losses due to the ionisation in the filament lead to a decrease of the pulse energy. When this intensity has fallen below a critical value [24], the balance between Kerr focusing and plasma defocusing can no longer be maintained and the self-focused filament ends. Then the beam undergoes a so-called conical emission [10, 14, 15] with a typical divergence of 0.1°. The precise mechanism of the filament propagation is not yet clear. At least three models have been proposed: moving focus [11], the self-wave-guiding model [9, 10] and the spatial replenishment model [12]. Analytical [16–18] as well as numerical [19–23] computations simulating the propagation of high-power laser pulses in air are difficult because of the high nonlinearity of the processes at play. This leads to typical computing times of 1 h per calculated metre of propagation, which would correspond to 1 year for a 10-km path. Such values illustrate the need for a more phenomenological description allowing a numerical treatment of the propagation of high-power laser pulses over the several-kilometre ranges involved in lidar experiments, and hence for a computationally efficient nonlinear lidar equation.

The first nonlinear extension to the lidar equation was proposed by Kasparian and Wolf [4]. However, this work focused mainly on the changes to the backscattering term due to transient size effects in aerosols. Propagation effects such as self-focusing were not considered there; hence the extinction term

\*Corresponding author.

(Fax: +49-3641/947-102, E-mail: g.faye@tpi.uni-jena.de)

was left unchanged, which is physically unrealistic in view of the high power at play. In this Letter, we investigate the modifications to the geometrical and propagation/extinction terms due to nonlinear propagation of high-power laser beams, assuming an idealised shape.

At this stage, it is worth recalling the usual linear lidar equation [1]. The detected power  $E$  collected by a detector with surface  $A_0$  after the backscattering of a laser beam of initial power  $E_L$  and wavelength  $\lambda_0$  is given by

$$E(\lambda_0, z) = E_L \frac{A_0 c \tau_d}{z^2} \frac{1}{2} \xi(\lambda_0, z) \times \beta(\lambda_0, z) \exp\left(-2 \int_0^z \alpha_\ell(\lambda_0, z') dz'\right). \quad (1)$$

Here,  $z$  denotes the distance from the detector to the atmosphere slice where the light backscatters;  $\alpha_\ell$  and  $\beta$  are the extinction and the backscattering coefficients respectively. The overlap function  $0 \leq \xi(\lambda_0, z) \leq 1$  includes the various signal losses due to the specific geometrical configuration of the system laser/detector. As for  $\tau_d$  and  $c$ , they are respectively the length of the pulse and the speed of light in air. The meaning of the different contributions in (1) is rather clear. A part of the laser power  $E_L$  is absorbed or scattered according to the Beer–Lambert (exponential) law during the forward travel. Then, a part  $\beta A_0/z^2$  of the power available at distance  $z$  is re-emitted back to the detector, and exponentially attenuated again (hence the factor 2 in front of  $\alpha_\ell$ ) before reaching the telescope. The appearance of the factor  $c \tau_d/2$  is related to the fact that the power recovered immediately after the backscattering is proportional to the thickness of the atmospheric slice coming into play.

In the present paper, we shall modify the standard lidar equation (1) in order to describe both geometrical beam-shape influence (Sect. 1) and extinction due to multi-photon ionisation (Sect. 2), which are the two main effects at play in the propagation of high-power laser pulses. From this, we shall deduce an approximate expression for the signal produced by the individual spectral components of the white light (Sect. 3). As for the geometrical effect, our assumptions are as follows: after self-focusing at a distance  $z_f$  from the source, the laser beam gives rise to a filament of length  $z_{fil}$  that spreads out along the first tens or hundreds of metres and, finally, diverges like a spherical wave (conical emission). As a first approximation, we consider that this filament is a cylinder of diameter  $2a \sim 100 \mu\text{m}$  [9]. On the other hand, following [15], we assume that, after diverging, the beam actually becomes a cone with half top angle  $\theta_{CE} \sim 0.1^\circ$ . From the previous hypothesis, we evaluate the factor  $\xi$  in the case where it is solely due to the default of overlap with the viewing cone of the detector, neglecting in particular the specific features coming from the design of the telescope. In our notation,  $\theta_T$  represents the half opening angle of the telescope field of view, and  $\psi$  the possible deviation of its axis from the laser direction. The horizontal separation between both devices is denoted by  $D$  (see Fig. 1). In the following, we shall always suppose that  $\psi$  is positive or null (i.e. the telescope is either parallel to or inclined towards the laser beam), and that  $\theta_{CE}$ , as well as  $\theta_T$ , are (strictly) positive.

In order to evaluate the overall extinction term, we assume that during the back-travel of light, the intensity of the

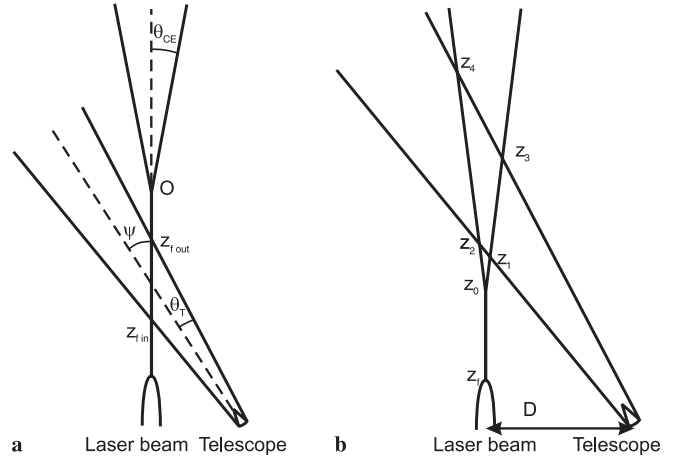


**Fig. 1a,b.** Two possible geometries of the relative positions of the telescope field of view and the laser beam: **a** the telescope sees only a section of the filament, as detailed in case (3) in the text; **b** the telescope intercepts only a part of the conical emission (case (1) in the text)

beam is sufficiently small so that we can neglect the nonlinear effects, and consider that only the forward-beam propagation is submitted to a nonlinear absorption regime resulting from multi-photon ionisation (which entails extra losses). The corresponding term in the local energy balance equation is proportional to a certain power  $n > 1$  of intensity  $I$ , thus depending on the cross-section (and therefore the shape) of the beam. Notice that the pulse attenuation due to other mechanisms such as spectral broadening are neglected here. This is supported notably by spectral measurements of the supercontinuum [8], which exhibit no significant energy loss caused by the continuum-generation process, and show a steep decrease of the spectrum on both sides of the fundamental wavelength.

## 1 Geometrical effects

We first consider the fact that nonlinearity gives rise to a change in the shape of the laser beam, which leads to a modification in the overlap function  $\xi$ . It is easy to convince oneself that this represents merely the fraction of the beam cross-section, with radius  $R_L(z)$  at a distance  $z$ , intersecting the viewing cone of the telescope. Provided  $\psi$  does not exceed a few degrees, the horizontal section of the viewing cone is nearly circular, with radius  $R_T$ , and the problem amounts to computing the overlap area  $\mathcal{A}(R_L, R_T, d)$  of two coplanar disks, with radii  $R_L$  and  $R_T$ , having their centres located at a distance  $d$  from each other (as represented in Fig. 2). If  $(R_L + R_T) \leq d$ , the disks have at most one point in common and  $\mathcal{A}(R_L, R_T, d)$  reduces to zero. As soon as the circles are secant,  $\mathcal{A}(R_L, R_T, d)$  is given by

$$\begin{aligned} \mathcal{A}(R_L, R_T, d) &= f(R_L, R_T, d) \\ &\equiv R_L^2 \arccos\left(\frac{a_L}{R_L}\right) - a_L \sqrt{R_L^2 - a_L^2} \\ &\quad + R_T^2 \arccos\left(\frac{a_T}{R_T}\right) - a_T \sqrt{R_T^2 - a_T^2}, \quad (2) \end{aligned}$$

where the auxiliary length  $a_L = (d^2 + R_L^2 - R_T^2)/(2d)$  measures the algebraic distance between the centre of the first

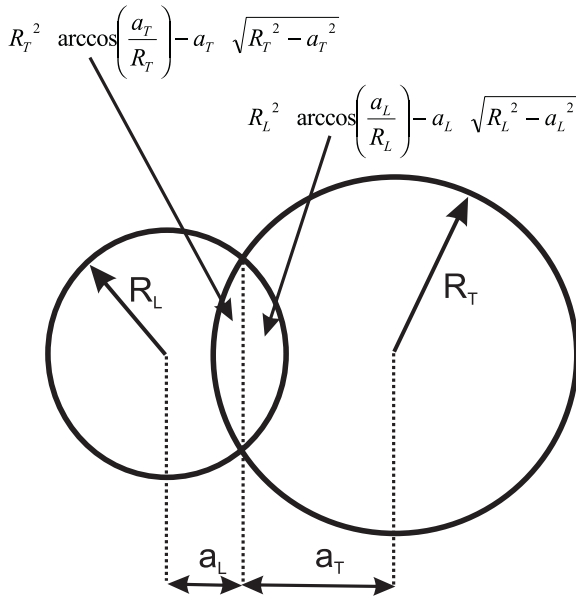


**Fig. 2.** Two secant circles with radii  $R_L$ ,  $R_T$ ;  $a_L$  and  $a_T$  are the same distances as defined in the text; the central overlap region is split into two parts by the string joining the intersecting points; the arrows indicate their respective areas

circle (with radius  $R_L$ ) and the string joining the two intersecting points (see Fig. 2); it is actually a function of the three variables  $d$ ,  $R_L$  and  $R_T$ . The definition of  $a_T$  is similar with the role of  $R_L$  and  $R_T$  exchanged, hence  $a_T = d - a_L = (d^2 + R_T^2 - R_L^2)/(2d)$ . Finally, when one of the disks contains the other one, i.e.  $|R_L - R_T| \geq d$ , then  $\mathcal{A}(R_L, R_T, d) = \min(\pi R_L^2, \pi R_T^2)$ .

All what we need now for getting  $\xi_{NL} \equiv \mathcal{A}(R_L, R_T, d)/(\pi R_L^2)$  is to replace  $R_L$ ,  $R_T$  and  $d$  in the expression of  $\xi_{NL}$  by their actual values, in view of the geometrical configuration of our system. Since the angles  $\theta_T$ ,  $\theta_{CE}$  and  $\psi$  have small values (typically less than a few degrees), it is not worth working beyond the first order in any of these quantities. We shall write:

$$R_T \approx z\theta_T, \quad d \approx |D - z\psi|. \quad (3)$$

The expression of  $R_L$  as a function of  $z$  depends on whether  $z \leq z_f$ ,  $z_f \leq z \leq z_{fil}$  or  $z_{fil} \leq z$  (three segments). The shortest distances are of little interest in lidar measurements; moreover, in this range, the geometry of the telescope has a strong influence on the overlap function. Hence, we will not consider them in the following, and assume that  $\xi_{NL}(z) = 0$  for  $z \leq z_f$ . Moreover, the radius  $a$  of the filament is indeed much smaller than the length  $z_0 = z_f + z_{fil}$  and can be taken to be zero. Therefore,  $R_L = a \approx 0$  in the filament ( $z \leq z_0$ ). Above it,  $R_L \approx (z - z_0)\theta_{CE}$ . Now, the function  $f$  can be viewed as a function of  $z$  only, and more precisely we shall define  $\tilde{f}(z) = f((z - z_0)\theta_{CE}, z\theta_T, |D - z\psi|)$ .

Like the radius  $R_L$ , the overlap function has to be derived by segment. In the filament, it is convenient to define two particular distances  $z_{fin} = D/(\psi + \theta_T)$  and  $z_{fout} = D/(\psi - \theta_T)$ , where the filament enters and exits the viewing cone of the telescope (see Fig. 1). Clearly, those distances can have a meaning only if they are below the end of the filament, i.e. provided  $z_{fin} \leq z_{fout} \leq z_0$ . Then, in the altitude range cor-

responding to the filament, we have  $\xi_{NL}(z) = 1$  for  $z_{fin} \leq z \leq \max(z_{fout}, z_0)$  and  $\xi_{NL}(z) = 0$  everywhere else. After the conical emission ( $z \geq z_0$ ), more geometrical combinations can occur, leading to more cases.

To go further in the study of these different cases, we introduce the altitudes of the four intersection points between the conical emission and the viewing cone of the telescope, as shown in Fig. 1:  $z_1 = (D + z_0\theta_{CE})/(\psi + \theta_T + \theta_{CE})$ ,  $z_2 = (D - z_0\theta_{CE})/(\psi + \theta_T - \theta_{CE})$ ,  $z_3 = (D + z_0\theta_{CE})/(\psi - \theta_T + \theta_{CE})$  and  $z_4 = (D - z_0\theta_{CE})/(\psi - \theta_T - \theta_{CE})$ . Again, those definitions only make sense when the corresponding points are above  $z_0$ . Values less than  $z_0$  lead to no crossing points. In that case, they can be cast to  $+\infty$  for our discussion.

We have to distinguish between three cases.

1. If  $z_1 \geq z_0$  (or equivalently if  $z_{fin} \geq z_0$ ) then the field of view of the telescope intersects only with the conical emission; it is always the case for linear lidar, where results can be obtained from the above discussion by choosing  $z_0 = 0$ .

- (a) under ( $z \leq z_1$ ) or above ( $z \geq z_4 \geq z_0$ ) the field of view of the telescope, we have  $\xi_{NL}(z) = 0$ ;
- (b) if  $z_0 \leq z_2 \leq z \leq z_3$ , the laser beam is included in the field of view of the telescope and  $\xi_{NL}(z) = 1$ ;
- (c) if  $z_0 \leq z_3 \leq z \leq z_2$ , then the field of view of the telescope is included in the laser beam, so that  $\xi_{NL}(z) = [z\theta_T/((z - z_0)\theta_{CE})]^2$ ;
- (d) everywhere else, i.e. for  $z_1 \leq z \leq \min(z_2, z_3)$  or for  $\max(z_2, z_3) \leq z \leq z_4$  (remember that  $z_4$  is taken to be  $+\infty$  if  $z_4 \leq z_0$ ), the two cones cross each other; hence  $\xi_{NL}(z) = \tilde{f}(z)$ .

2. If  $z_{fin} \leq z_0 \leq z_{fout}$  (which implies that  $z_1 \leq z_0$ ), then the field of view of the telescope includes the point O where the beam starts diverging. In this second case:

- (a) under ( $z \leq z_{fin}$ ) or above ( $z \geq z_4 \geq z_0$ ) the field of view of the telescope, we have  $\xi_{NL}(z) = 0$ ;
- (b) if  $z_{fin} \leq z \leq \min(z_2, z_3)$ , the laser beam is included in the field of view of the telescope and  $\xi_{NL}(z) = 1$ ;
- (c) Above  $\max(z_2, z_3) \geq z_0$ , the field of view of the telescope remains inside the laser beam and  $\xi_{NL}(z) = [z\theta_T/((z - z_0)\theta_{CE})]^2$ ;
- (d) If  $\min(z_2, z_3) \leq z \leq \min(\max(z_2, z_3), z_4)$ , then the overlap function is given by  $\xi_{NL}(z) = \tilde{f}(z)$ ;

In the two latter cases, one has again to keep in mind the convention that any  $z_i$  smaller than  $z_0$  must equal  $+\infty$ .

3. If  $z_{fin} \leq z_{fout} \leq z_0$ , the viewing cone completely crosses the filament under the point O. However, it may intersect afterwards with the conical emission, provided  $z_4 \geq z_0$ . Again, four sub-cases have to be distinguished:

- (a) under the intersection with the field of view of the telescope ( $z \leq z_{fin}$ ) and over this intersection up to the possible intersection with the conical emission ( $z_{fout} \leq z \leq z_4$ ), we have  $\xi_{NL}(z) = 0$ ;
- (b) in the section of the filament that is intercepted by the telescope field of view ( $z_{fin} \leq z \leq z_{fout}$ ), we have  $\xi_{NL}(z) = 1$ ;
- (c) for  $z \geq z_2 \geq z_0$ , the field of view of the telescope completely enters the conical emission and  $\xi_{NL}(z) = [z\theta_T/((z - z_0)\theta_{CE})]^2$ ;

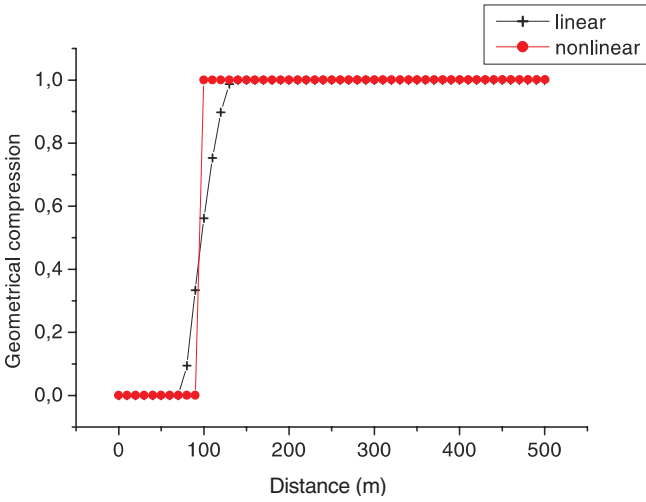


**Fig. 3.** Overlap function  $\xi_{\text{NL}}(z)$  (*thick points*) in the case where the viewing cone contains a part of the filament and the whole conical emission;  $D = 0.33$  m;  $z_{\text{f}} = 1.00$  m;  $z_{\text{fil}} = 100$  m;  $\psi = 1 \times 10^{-3}$ ;  $\theta_{\text{T}} = 2.5 \times 10^{-3}$ ;  $\theta_{\text{CE}} = 1 \times 10^{-3}$ . Compare to the standard situation for  $z_0 = 0$  m (*crosses*)

- (d) for  $z_4 \leq z \leq z_2$  (with, again,  $z_2$  equal to  $+\infty$  if  $z_2 < z_0$ ), the field of view of the telescope intersects the conical emission, hence  $\xi_{\text{NL}}(z) = \tilde{f}(z)$ .

The complication of the result is only apparent, and comes from the high number of geometrical configurations occurring in each case, according to the relative values of the various angles. However, given a specific set of parameters, the function  $\xi_{\text{NL}}(z)$  takes a very simple form. Note that when the cone of view contains a part of the filament as well as the whole conical emission,  $\xi_{\text{NL}}(z)$  jumps abruptly from 0 to 1, and then remains constant (see the ‘step’ in Fig. 3). This leads to a much simpler overlap function than for the linear case, where  $\xi_{\text{NL}}(z)$  rises more slowly from 0 to 1. However, when the cone of view of the telescope intersects with the laser beam above the filament, the geometrical term becomes quite similar to that of the linear case, with only an offset  $z_0$  in the distance  $z$  and both expressions even coincide for  $z_0 = 0$ . In this respect, all the nonlinear effects arise through the filament length, which is actually an implicit (unspecified) function of initial intensity  $z_0 = z_0(I_0)$ ;  $z_0(I_0)$  goes to zero when  $I_0$  becomes small enough, since we must then come back to the linear regime.

## 2 Effect of the nonlinear absorption

Apart from modifying the overlap function  $\xi_{\text{NL}}$ , as already mentioned, the main nonlinear corrections to the lidar equation affect the exponential extinction factor in (1). Indeed, during the forward travel when the intensity is extremely high, a part of the energy of the laser pulse is used to ionise the atmosphere, and the absorption due to multi-photon ionisation losses adds up to the usual linear (Mie and Raleigh) scattering. If  $n$  represents the number of photons that are necessary to ionise one molecule, the corresponding intensity losses (for a plane wave) read

$$\left(\frac{dI}{dz}\right)_{\text{MPI}} = \alpha_{\text{ref}} \left(\frac{I}{I_{\text{ref}}}\right)^n, \quad (4)$$

with  $\alpha_{\text{ref}} = nh\nu_{\text{L}}R_{\text{ref}}N$ , where  $h\nu_{\text{L}}$  is the laser photon energy,  $N$  the ionising molecule density and  $R_{\text{ref}}$  a reference ionisation rate of the considered species, which has to be determined experimentally as does the reference intensity  $I_{\text{ref}}$  [24]. As a matter of fact, the values of  $n$  are given by experiment, and are rather effective values taking all ionisation processes into account. In particular, tunnel ionisation may lead to fractional values lower than those expected from the ratio of the ionisation potential to the photon energy. As the number  $n$  differs from one type of ionised molecule to another, the complete losses are made up of a sum of terms such as the one given by (4) with various values for  $\alpha_{\text{ref}}$ ,  $I_{\text{ref}}$  and  $n$ . However, provided the intensity remains below  $10^{18}$  W/m<sup>2</sup>, the contribution of oxygen dominates in air [24], so that we are allowed to keep only one term in the sum as a first approximation. Higher intensities would moreover produce the saturation of ionisation and alter (4). Besides, our assumption leads us to an analytical solution for the intensity, which provides quite a realistic description of the main changes induced by nonlinearity.

Now, a laser beam can be seen as a divergent wave, emitted by a fictitious point O in a cone of solid angle  $\Omega$ . The energy-density variation in the spherical slice of centre O, radius  $r$  ( $\approx z$  in our case) and thickness  $dr$  is assumed to be entirely due to scattering or absorption. We look for  $I$  as a function of  $r$  only, hence the balance equation:

$$I(r+dr)(r+dr)^2\Omega - I(r)r^2\Omega = -\alpha_{\ell}(r)Ir^2dr\Omega - \alpha_{\text{ref}}(r)\left(\frac{I}{I_{\text{ref}}}\right)^n r^2dr\Omega, \quad (5)$$

where  $\alpha_{\ell}$  denotes the linear scattering coefficient. The differential equation obeyed by the intensity function then reads:

$$\frac{dI}{dr} = -\frac{2}{r}I - \alpha_{\ell}I - \alpha_{\text{ref}}\left(\frac{I}{I_{\text{ref}}}\right)^n, \quad (6)$$

where we immediately recognise a Bernoulli equation. The solution is readily obtained by introducing the intermediate unknown function  $y(r) = I^{1-n}(r)$ . We find after easy calculations

$$I(r) = I_0 \left(\frac{r_0}{r}\right)^2 \exp\left(-\int_{r_0}^r \alpha_{\ell}(\lambda_0, r')dr'\right) \times \left[1 + (n-1)\left(\frac{r_0^2 I_0}{I_{\text{ref}}}\right)^{n-1} \int_{r_0}^r \varrho^{-2(n-1)} \left(\frac{\alpha_{\text{ref}}(\varrho)}{I_{\text{ref}}}\right) \times \exp\left(-\int_{r_0}^{\varrho} \alpha_{\ell}(\lambda_0, \varrho')d\varrho'\right) d\varrho\right]^{-1/(n-1)}. \quad (7)$$

The parameter  $I_0$  can be interpreted as the intensity of the beam at a distance  $r = r_0$  from the point O. The solution  $I(r)$  behaves as  $1/r^2$  when  $r$  goes to zero and, therefore, it represents the propagation of a spherical wave outward from the source. The first exponential factor is mainly responsible for the energy decrease for large values of  $\alpha_{\ell}$  in agreement with

the Beer–Lambert law. The new feature comes from the contribution appearing between the square brackets. The second term inside the brackets represents the correction due to non-linear absorption during the propagation process. It can be seen as resulting from the multi-photon ionisation (4) applied to the linearly attenuated beam. It is of course negligible when the intensity of the beam  $I$  becomes small with respect to the reference intensity  $I_{\text{ref}}$ , but at the exit of the laser, we may have  $I \gg I_{\text{ref}}$  if the initial power  $E_L$  is high enough, so that the ionisation effect dominates. On the other hand, at short distance, i.e. for  $r \ll 1/\alpha_\ell$ , the exponential factor modulating the integrand  $\varrho^{-2(n-1)}\alpha_{\text{ref}}(\varrho)/I_{\text{ref}}$  as well as the one of the Beer–Lambert extinction are close to 1. In summary, we can distinguish between three different absorption regimes provided the initial power is sufficient: (i) for  $r \ll 1/\alpha_\ell$  the absorption is dominated by multi-photon ionisation, (ii) for  $r \gg 1/\alpha_\ell$  it obeys the Beer–Lambert law, (iii) for  $r \sim 1/\alpha_\ell$  we have an intermediate regime where the full expression of the intensity should be used. Note that if we make  $n$  formally go to 1 in (7), the bracket tends towards an exponential function, which is not surprising, since then both energy-loss terms in the balance equation (5) are proportional to the intensity.

In the filament, the beam has to be treated as a plane wave (along the  $z$  axis). Starting from the energy-conservation equation

$$\frac{dI}{dz} = -\alpha_\ell I - \alpha_{\text{ref}} \left( \frac{I}{I_{\text{ref}}} \right)^n \quad (8)$$

and following the same method as the one sketched above, we get the alternative solution, valid for plane propagation:

$$\begin{aligned} I(z) = & I_0 \exp \left( - \int_{Z_0}^z \alpha_\ell(\lambda_0, z') dz' \right) \\ & \times \left[ 1 + (n-1) \left( \frac{I_0}{I_{\text{ref}}} \right)^{n-1} \int_{Z_0}^z \left( \frac{\alpha_{\text{ref}}(\zeta)}{I_{\text{ref}}} \right) \right. \\ & \left. \times \exp \left( -(n-1) \int_{Z_0}^{\zeta} \alpha_\ell(\lambda_0, \zeta') d\zeta' \right) d\zeta \right]^{-1/(n-1)}. \quad (9) \end{aligned}$$

There are only a few changes with respect to the spherical-wave case: the factor  $1/r^2$  has disappeared, and the source inside the integral over  $d\zeta$  has been modified by removing the singular factor  $\varrho^{-2(n-1)}$  appearing in (7).

Combining both results, we obtain the intensity of the laser beam inside the filament as well as after the conical emission. Over the first centimetres or metres of the light travel, i.e. just before the self-focusing, the power losses are nearly negligible with respect to the total available energy per time unit  $E_L$ ; thus, the power at the beginning of the filament  $P(z_f) \equiv \pi a^2 I(z_f)$  is almost equal to  $E_L$ . Now, the intensity of the laser as a function of  $z$  is given for  $z \leq z_0$  by the relation (9), where  $Z_0$  is taken to be equal to  $z_f$  in order to have  $I_0 = E_L/(\pi a^2)$ . This leads to a transmission coefficient in the filament

$$\begin{aligned} T_{\text{NL}}(\lambda_0, I_0, z) = & \exp \left( - \int_{z_f}^z \alpha_\ell(\lambda_0, z') dz' \right) \\ & \times \left[ 1 + (n-1) \left( \frac{I_0}{I_{\text{ref}}} \right)^{n-1} \int_{z_f}^z \left( \frac{\alpha_{\text{ref}}(\zeta)}{I_{\text{ref}}} \right) \right. \\ & \left. \times \exp \left( -(n-1) \int_{z_f}^{\zeta} \alpha_\ell(\lambda_0, \zeta') d\zeta' \right) d\zeta \right]^{-1/(n-1)}, \quad (10) \end{aligned}$$

with the restriction  $z \leq z_0$ . The intensity near the top of the emitting cone is then straightforwardly deduced from the value of the light power at the end of the filament:  $P(z_0) = \pi a^2 I(z_0)$ . If  $r_0$  is a small arbitrary length as compared to  $z_0$ , say  $r_0 \sim a/\theta_{\text{CE}}$ , there is very little absorption or backscattering between  $z_0$  and  $z_0 + r_0$ , and we can write  $\pi \theta_{\text{CE}}^2 r_0^2 I(z_0 + r_0) \approx P(z_0)$ . As a consequence, we determine the intensity  $I(z)$  in the region of the conical emission by substituting  $(a/\theta_{\text{CE}})^2 I(z_0)$  with  $r_0^2 I_0$  as well as  $(z - z_0)$  with  $r$  in (7). We must also replace the backscattering coefficient  $\alpha_\ell(\varrho)$  by  $\alpha_\ell(z_0 + \varrho)$  (and the same for  $\alpha_{\text{ref}}$ ).

$$\begin{aligned} I(z) = & I_0 \left( \frac{a}{\theta_{\text{CE}}(z - z_0)} \right)^2 \exp \left( - \int_{z_f}^z \alpha_\ell(\lambda_0, r) dr \right) \\ & \times \left[ 1 + (n-1) \left( \frac{I_0}{I_{\text{ref}}} \right)^{n-1} \int_{z_f}^{z_0} \left( \frac{\alpha_{\text{ref}}(\varrho)}{I_{\text{ref}}} \right) \right. \\ & \times \exp \left( -(n-1) \int_{z_f}^{\varrho} \alpha_\ell(\lambda_0, \varrho') d\varrho' \right) d\varrho \\ & + (n-1) \left( \frac{a^2 I_0}{\theta_{\text{CE}}^2 I_{\text{ref}}} \right)^{n-1} \\ & \times \exp \left( -(n-1) \int_{z_f}^{z_0} \alpha_\ell(\lambda_0, r') dr' \right) \\ & \times \int_{z_0+r_0}^z \frac{\alpha_{\text{ref}}(\varrho)}{I_{\text{ref}}(\varrho - z_0)^{2(n-1)}} \\ & \left. \times \exp \left( -(n-1) \int_{z_0}^{\varrho} \alpha_\ell(\lambda_0, \varrho') d\varrho' \right) d\varrho \right]^{-1/(n-1)}. \quad (11) \end{aligned}$$

The constant  $r_0$  has been neglected everywhere except in the lower bound of the second integral over  $d\varrho$ , which happens to diverge when  $r_0$  goes to zero. Such a behaviour is not surprising, since in the case of a rigorously spherical wave, the intensity becomes infinite at the origin, which would imply a total nonlinear absorption in the framework of classical electromagnetism. Of course, this situation is not physical and, to a certain extent, the filament ‘matches’ the emitting cone. Setting  $r_0 = a/\theta_{\text{CE}}$  amounts to imposing the continuity of the section radius, but this choice is arbitrary. However, as soon as the diameter of the conical emission is significantly larger than that of the filament, the pre-factor of the

latter integral becomes negligible, and the numerical result should not be notably modified. Again, the first (exponential) factor accounts for linear extinction; the second term of the factor between brackets is associated with the multi-photon ionisation inside the filament, while the last term describes the multi-photon ionisation after the conical emission as obtained from (7) and (9). Neglecting the latter contribution, we define the transmission factor for  $z \geq z_0$  (beyond the conical emission) as

$$\begin{aligned} T_{\text{NL}}(\lambda_0, I_0, z) &\equiv \left( \frac{\theta_{\text{CE}}(z - z_0)}{a} \right)^2 \frac{I(z)}{I_0} \\ &\approx \exp \left( - \int_{z_f}^z \alpha_\ell(\lambda_0, r) dr \right) \left[ 1 + (n-1) \left( \frac{I_0}{I_{\text{ref}}} \right)^{n-1} \right. \\ &\quad \left. \times \int_{z_f}^{z_0} \left( \frac{\alpha_{\text{ref}}(\varrho)}{I_{\text{ref}}} \right) \exp \left( -(n-1) \int_{z_f}^{\varrho} \alpha_\ell(\lambda_0, \varrho') d\varrho' \right) d\varrho \right]^{-1/(n-1)}. \end{aligned} \quad (12)$$

To get the nonlinear lidar equation, it only remains to perform the replacement

$$\begin{aligned} \exp \left( -2 \int_0^z \alpha_\ell(\lambda_0, z') dz' \right) &\rightarrow \\ \exp \left( - \int_0^z \alpha_\ell(\lambda_0, z') dz' \right) &T_{\text{NL}}(\lambda_0, I_0, z) \end{aligned} \quad (13)$$

in (1), remembering that  $I_0 = E_L/(\pi a^2)$ , and using a suitable overlap factor. We finally arrive at

$$\begin{aligned} E(\lambda_0, z) &= E_L \frac{A_0}{z^2} \frac{c\tau_d}{2} \xi_{\text{NL}}(\lambda_0, I_0, z) \\ &\quad \times \beta(\lambda_0, z) \exp \left( - \int_0^z \alpha_\ell(\lambda_0, z') dz' \right) T_{\text{NL}}(\lambda_0, I_0, z), \end{aligned} \quad (14)$$

where  $\xi_{\text{NL}}$  is that of Sect. 1 and  $T_{\text{NL}}$  is given by (10) or (12) depending on whether  $z_f \leq z \leq z_0$  or  $z_0 \leq z$  respectively.

If we compare this nonlinear lidar equation with the linear one (1), it is clear that the effect of the pulse extinction due to multi-photon ionisation results in a heavy reduction (up to several orders of magnitude) of the available power at the end of the filament. However, in the diverging region, where the beam section is much larger, multi-photon ionisation is negligible and, thus, the distance-dependence of the lidar return is similar to that of the linear case. Of course, in the extreme situation where the intensity tends to zero,  $T_{\text{NL}}$  reduces to the Beer–Lambert absorption coefficient. As we also have  $\xi_{\text{NL}} \rightarrow \xi$  in this limit, we recover the linear lidar equation (1) for small values of  $I$ .

### 3 Multi-spectral lidar signal

Due to spectral broadening resulting from self-phase modulation, a nonlinear lidar offers a unique opportunity to perform

multi-spectral experiments. In this purpose, we shall derive here the lidar signal produced at a wavelength  $\lambda$  different from the wavelength  $\lambda_0$  of the laser.

If multiple scattering is neglected, there are two different ways for the white light to reach the detector at time  $t = 2z/c$ : (i) a direct backward emission at altitude  $z$ , which may be treated as in [4] (see (5) therein), with  $T_{\text{NL}}$  given by (12) above, or (ii) a forward white-light emission at a distance  $z_{\text{em}} \leq z$ , followed by a backscattering at distance  $z$ . Recent measurements [26] suggest that the white-light energy is negligible outside the conical emission [10, 14, 15], i.e. we can consider that the white light is emitted forward in a cone with half top angle  $\theta_{\text{em}} \approx \theta_{\text{CE}}$ . The geometrical factor  $\xi_{\text{NL}}(\lambda, I_0, z_{\text{em}}, z)$  thus has the same form as the one of Sect. 1 in the case  $z \geq z_0$ , but the role of  $z_0$  is now held by  $z_{\text{em}}$ .

The white-light intensity travelling in the backward direction is small enough to consider its propagation as linear. In contrast, nonlinearities may affect the forward propagation via the influence of the co-propagating pump pulse. In that case, obtaining an analytical expression of the transmission factor for the white light is an extremely difficult task, due to the numerous processes to be taken into account. We shall neglect all effects of that kind in our simple model. Under this hypothesis, the extinction of forward-travelling (as well as backward-travelling) white light is correctly described by the Beer–Lambert law. If we denote by  $\beta_{\text{for}}(\lambda, \lambda_0, I_0, z_{\text{em}})$  the conversion coefficient from wavelength  $\lambda_0$  to wavelength  $\lambda$ , at distance  $z_{\text{em}}$  from the source with initial intensity  $I_0$ , the contribution to the intensity  $dI_{\text{for}}(\lambda, I_0, z)$  at altitude  $z$  generated on a shell of thickness  $dz_{\text{em}}$  at altitude  $z_{\text{em}}$  reads

$$\begin{aligned} dI_{\text{for}}(\lambda, I_0, z) &= E_L \beta_{\text{for}}(\lambda, \lambda_0, I_0, z_{\text{em}}) \\ &\quad \times \exp \left( - \int_{z_{\text{em}}}^z \alpha_\ell(\lambda, z') dz' \right) T_{\text{NL}}(\lambda, I_0, z_{\text{em}}) dz_{\text{em}}. \end{aligned} \quad (15)$$

Of course, both processes described above occur simultaneously so that their contributions add, which leads to

$$\begin{aligned} E(\lambda, I_0, z) &= E_L \frac{A_0}{z^2} \frac{c\tau_d}{2} \exp \left( - \int_0^z \alpha_\ell(\lambda, z') dz' \right) \\ &\quad \times \left\{ \xi_{\text{NL}}(\lambda, I_0, z) \beta_{\text{back}}(\lambda, \lambda_0, I_0, z) + \pi(\theta_{\text{CE}})^2 \beta(\lambda_0, I_0, z) \right. \\ &\quad \times \int_0^z \left[ \xi_{\text{NL}}(\lambda, I_0, z_{\text{em}}, z) \beta_{\text{for}}(\lambda, \lambda_0, I_0, z_{\text{em}}) \right. \\ &\quad \left. \left. \times \exp \left( - \int_{z_{\text{em}}}^z \alpha_\ell(\lambda, \varrho) d\varrho \right) T_{\text{NL}}(\lambda_0, I_0, z_{\text{em}}) \right] dz_{\text{em}} \right\}. \end{aligned} \quad (16)$$

Note that the signal  $E(\lambda, I_0, z)$  actually represents a spectral density since  $[\beta_{\text{back}}] = [\beta_{\text{for}}] = [\beta]/[\text{length}]$ .

The determination of  $\beta_{\text{back}}$  and  $\beta_{\text{for}}$  for white-light generation as well as their angular dependence is not straightforward. Spectral broadening depends on several processes such as plasma ionisation or self-phase modulation. For this reason, the efficiency of the frequency conversion from  $\lambda_0$  to  $\lambda$  can only be defined under strong assumptions. Moreover,

recent experimental measurements [5, 6, 25] show inconsistencies about the shape of the white-light spectrum in the visible domain. This point is beyond the scope of the paper, but it should be clarified before issuing some definite expression for  $\beta_{\text{for}}$  and  $\beta_{\text{back}}$  and obtaining a more explicit version of (16).

#### 4 Conclusion

Gathering the results for the overlap function and the intensity attenuation, we finally find the main changes to the lidar equation implied by nonlinear propagation of high-power ultrashort laser pulses, for both mono- and multi-spectral lidar configurations. This propagation entails a modification of the geometrical factor  $\xi$  because of self-focusing and subsequent filamentation. The high intensities that are reached in the filaments also result in a strongly nonlinear extinction of the pulses, thus modifying the scattering ( $\alpha$ ) term. The changes proposed in this paper can combine with the modifications described by Kasparian et al. [4] for the backscattering ( $\beta$ ) term. Actually, such a nonlinear lidar equation is essential for the interpretation of lidar signals from femtosecond pulses [5, 6], which could permit a more complete remote sensing of the atmosphere.

*Acknowledgements.* J. Kasparian acknowledges financial support of the Deutsche Forschungsgemeinschaft in the framework of the French–German project ‘Teramobile’ (CNRS/DFG).

#### References

1. R.M. Measures: *Laser remote sensing – Fundamentals and applications* (Wiley Interscience, New York 1984)
2. E. Frejafon, J. Kasparian, P. Rambaldi, B. Vezin, V. Boutou, J. Yu, M. Ulbricht, D. Weidauer, B. Ottobriani, E. de Saeger, B. Krämer, T. Leisner, P. Rairoux, L. Wöste, J.-P. Wolf: *Eur. Phys. J. D* **4**, 231 (1998)
3. J. Kasparian, E. Frejafon, P. Rambaldi, J. Yu, B. Vezin, J.-P. Wolf, P. Ritter, P. Viscardi: *Atmos. Environment* **31**, 2957 (1998)
4. J. Kasparian, J.-P. Wolf: *Opt. Commun.* **152**, 355 (1998)
5. P. Rairoux, H. Schillinger, S. Niedermeier, M. Rodriguez, F. Ronneberger, R. Sauerbrey, B. Stein, D. Waite, C. Wedekind, H. Wille, L. Wöste: *Appl. Phys. B* **71**, 573 (2000)
6. L. Wöste, C. Wedekind, H. Wille, P. Rairoux, B. Stein, S. Nikolov, Chr. Werner, S. Niedermeier, H. Schillinger, R. Sauerbrey: *Laser Optoelektronik* **29**, 51 (1997)
7. P.B. Corkum, C. Rolland, T. Srinivasan-Rao: *Phys. Rev. Lett.* **57**, 2268 (1986)
8. J. Kasparian, R. Sauerbrey, D. Mondelain, S. Niedermeier, J. Yu, J.-P. Wolf, Y.-B. André, M. Franco, B. Prade, S. Tzortzakis, A. Mysyrowicz, M. Rodriguez, H. Wille, L. Wöste: *Opt. Lett.* **25**, 1397 (2000)
9. A. Braun, G. Korn, X. Liu, D. Du, J. Squier, G. Mourou: *Opt. Lett.* **20**, 73 (1995)
10. E.T.J. Nibbering, P.F. Curley, G. Grillon, B.S. Prade, M.A. Franco, F. Salin, A. Mysyrowicz: *Opt. Lett.* **21**, 62 (1996)
11. A. Brodeur, C.Y. Chien, F.A. Ilkov, S.L. Chin, O.G. Koserava, V.P. Kandidov: *Opt. Lett.* **22**, 304 (1997)
12. M. Mlejnek, E.M. Wright, J.V. Moloney: *Opt. Lett.* **23**, 382 (1998)
13. B. La Fontaine, F. Vidal, Z. Jiang, C.Y. Chien, D. Comtois, A. Desparois, T.W. Johnson, J.-C. Kieffer, H. Pépin, H.P. Mercure: *Phys. Plasmas* **6**, 1615 (1999)
14. A. Brodeur, F.A. Ilkov, S.L. Chin: *Opt. Commun.* **129**, 193 (1996)
15. O.G. Kosareva, V.P. Kandidov, A. Brodeur, C.Y. Chien, S.L. Chin: *Opt. Lett.* **22**, 1332 (1997)
16. N. Aközbek, C.M. Bowden, A. Talebpour, S.L. Chin: *Phys. Rev. E* **61**, 4540 (2000)
17. Y. Silberberg: *Opt. Lett.* **15**, 1282 (1990)
18. E.E. Fill: *J. Opt. Soc. Am. B* **11**, 2241 (1994)
19. A. Chiron, B. Lamouroux, R. Lange, J.-F. Ripoche, M. Franco, B. Prade, G. Bonnaud, G. Riazuelo, A. Mysyrowicz: *Eur. Phys. J. D* **6**, 383 (1999)
20. S. Trillo, A.V. Buryak, Y.Z. Kivshar: *Opt. Commun.* **122**, 200 (1995)
21. L. Torner, J.P. Torres, C.R. Menyuk: *Opt. Lett.* **21**, 462 (1996)
22. P.M. Goorjian, A. Taflove, R.M. Joseph, S.C. Hagness: *IEEE J. Quantum Electron.* **QE-28**, 2416 (1992)
23. V.P. Kandidov, O.G. Kosareva, S.A. Shlyonov: *Nonlinear Opt.* **12**, 119 (1995)
24. J. Kasparian, R. Sauerbrey, S.L. Chin: *Appl. Phys. B* **71**, 877 (2000)
25. J.-P. Wolf, Y. Pan, G.M. Turner, M.C. Beard, C.A. Schmuttenmaer, S. Holler, R.K. Chang: Ballistic trajectories of optical wavepackets circulating within microcavities, *Phys. Rev. A*, in press (2001)
26. J. Yu, D. Mondelain, G. Ange, R. Volk, S. Niedermeier, J.-P. Wolf, J. Kasparian, R. Sauerbrey: Backward supercontinuum emission from filaments generated by ultrashort laser pulses in air, *Opt. Lett.* **26**, 533 (2001)

# Triggering and guiding megavolt discharges by use of laser-induced ionized filaments

**M. Rodriguez and R. Sauerbrey**

*Teramobile Project, Institut für Optik und Quantenelektronik, Friedrich-Schiller-Universität Jena, Max-Wien-Platz 1, D-07743 Jena, Germany*

**H. Wille and L. Wöste**

*Teramobile Project, Institut für Experimentalphysik, Freie Universität Berlin, Arnimallee 14, D-14195 Berlin, Germany*

**T. Fujii**

*Electrical Physics Department, Central Research Institute of Electric Power Industry, 2-11-1 Iwado Kita, Komae-shi, Tokyo, 201-8511, Japan*

**Y.-B. André and A. Mysyrowicz**

*Teramobile Project, Laboratoire d'Optique Appliquée, Unité Mixte de Recherche, Centre National de la Recherche Scientifique 7639, Ecole Nationale Supérieure des Techniques Avancées–Ecole Polytechnique, Centre de l'Yvette, F-91761 Palaiseau Cedex, France*

**L. Klingbeil, K. Rethmeier, and W. Kalkner**

*Institut für Elektrische Energietechnik, Technische Universität Berlin, Einsteinufer 11, D-10587 Berlin, Germany*

**J. Kasparian, E. Salmon, J. Yu, and J.-P. Wolf**

*Teramobile Project, Laboratoire de Spectrométrie Ionique et Moléculaire, Unité Mixte de Recherche, Centre National de la Recherche Scientifique 5579, Université Claude Bernard Lyon 1, 43 db du 11 Novembre 1918, F-69622 Villeurbanne Cedex, France*

Received October 8, 2001

We have demonstrated the ability to trigger and guide high-voltage discharges with ionized filaments generated by femtosecond terawatt laser pulses. The plasma filaments extended over the whole gap, providing a direct ohmic connection between the electrodes. Laser-guided straight discharges have been observed for gaps of as much as 3.8 m at a high voltage reduced to 68% of the natural breakdown voltage. The triggering efficiency was found to depend critically on the spatial connection of the laser filaments to the electrode as well as on the temporal coincidence of the laser with the peak of the high voltage. © 2002 Optical Society of America

OCIS codes: 010.1300, 140.7090, 190.5940, 190.7110, 350.5400.

The possibility of triggering and guiding lightning by using laser beams has been discussed for more than 25 years.<sup>1,2</sup> The main motivation for manipulating lightning is to protect sensitive installations such as strategic sites, including nuclear, biological, and chemical plants and airports from direct strikes and electromagnetic perturbations. Whereas early studies in the 1970s and 1980s with nanosecond lasers<sup>3,4</sup> suffered from severe limitations, the advent of high-power femtosecond lasers has opened new perspectives in this research. In particular, recent studies demonstrated that high voltage (HV) discharges can be triggered and guided over distances of as much as 3 m by use of ultrashort laser pulses (0.3 TW, 600 fs) focused between two electrodes and creating a local plasma at the focus.<sup>5</sup> Similar experiments have been conducted in the UV,<sup>6</sup> in which multiphoton ionization was significantly enhanced by the shorter wavelength. In those experiments the laser produced a medium-density plasma (typically  $10^{17}$  cm<sup>-3</sup>), from which ionization waves (streamers), accelerated by the electric field, propagated toward the electrodes.

A remarkable property that has been observed in high-power femtosecond pulse propagation is filamentation. For a pulse propagating in air, a dynamic equilibrium between Kerr self-focusing and plasma-induced diffraction yields a narrow ( $\sim 100$   $\mu$ m in diameter<sup>7,8</sup>), low-impedance<sup>9,10</sup> ionized filament that can be as much as 200 m long.<sup>11</sup> Such long plasma filaments provide a real possibility of triggering and guiding lightning. Experiments that exploited the potential of the laser-induced filaments for HV discharge control without focusing the laser between the electrodes were recently conducted with 600-fs pulses.<sup>12</sup> Discharges guided by filaments have been successfully demonstrated over a gap of 2 m between two plane electrodes. However, these discharges were not triggered, in the sense that the breakdown voltage was not reduced by the presence of filaments.

In this Letter we report, for the first time to our knowledge, triggering and guiding of HV discharges by laser-induced filaments over large gaps (as long as 3.8 m). Our experiments showed that aiming the laser beam in the vicinity of two charged electrodes allows filaments to ohmically bridge the electrodes,

trigger the electric discharge, guide it along a straight way, and reduce the buildup time of the discharge.

In our experiments a standardized negative HV lightning pulse (as much as 2 MV; rise time, 1.2  $\mu\text{s}$ ; decay time to half-maximum, 50  $\mu\text{s}$ ) created by a pulsed voltage generator (Marx multiplier circuit) was applied to a 12-cm-diameter spherical electrode. A plane electrode with a diameter of 3 m was used as ground. Other electrode geometries, such as torus-torus, were tested and yielded similar results. The HV pulses were synchronized to the laser with an adjustable delay.

The laser used for this experiment was the Teramobile system,<sup>13</sup> a container-integrated mobile femtosecond Ti:sapphire laser system. During this experiments the laser provided 150-fs pulses with as much as 300 mJ of energy at 790 nm and 10 Hz. We could vary the output energy continuously by detuning the pulse extraction from the regenerative amplifier. Its unique mobility feature permitted us to locate the laser system inside the HV laboratory, with its horizontal output beam in line with the electrodes, at a distance of 20 m from the HV electrode (Fig. 1). The laser beam was expanded to an initial diameter of 15 cm and slightly focused ( $f \sim 15\text{--}20$  m) with an adjustable telescope. Typically, with 300 mJ we observed a filament bundle with a length of 4–5 m, a 0.5–1-cm diameter, and  $\sim 15$  filaments at the HV electrode. In most of the experiments the filaments started before the HV electrode and spanned the whole gap, as was verified on a screen. To ohmically bridge the electrodes with the filaments we shot the laser beam close to the HV electrode, at a typical distance of 1 cm and against the ground electrode.

We investigated the influence of the delay between the HV and the laser pulses. No successful event was observed for laser pulses before the HV (negative delay), whereas successful triggering and guiding over the whole gap was observed for laser pulses from 0 to 15  $\mu\text{s}$  after the maximum of the HV pulse. These results are in contrast to those of La Fontaine *et al.*,<sup>12</sup> who observed laser-guided discharges for a negative delay as long as 15  $\mu\text{s}$ .

We checked the importance of the ohmic contact between the plasma filaments and the electrodes in two ways. First, we observed qualitatively, in a torus-torus configuration, that the discharge could not be triggered if the laser beam was moved several centimeters away from the HV electrode. This result is consistent with recent observations with a 1.5-cm-long gap.<sup>10</sup> Moreover, we moved the starting position of the filamentation axially over some meters by adjusting the focus of the sending telescope. The laser-induced breakdown (LIB) smoothly decreased to 0 if the starting point of the filament was moved inside the gap between the electrodes. When we moved the filamentation starting point a few meters in the opposite direction from the HV electrode, the end of the filament bundle no longer reached the ground electrode, and the probability of breakdown decreased as well. The optimal filament's starting position was found to be  $\sim 1$  m upstream of the HV electrode, with the filaments spanning the whole gap.

The HV-discharge triggering ability was demonstrated by systematic measurement of the breakdown voltage with and without the laser for several electrode gap distances ( $L$ ), as shown in Fig. 2.  $U_{50}$  values are those of the voltages at which the breakdown probability occurs for 50% of the events tested. Some single LIB events, corresponding to the lowest observed voltages, are also displayed. These results demonstrate that laser-induced filaments do trigger the HV discharge over distances up to 3.8 m: The laser significantly reduced the breakdown voltage. The reduction ratio  $[(U_{50,\text{free}} - U_{50,\text{laser}})/U_{50,\text{free}}]$  was typically  $32(\pm 1)\%$ .

Some discharges were guided over only a fraction  $\eta$  of the gap and continued with an irregular path as in the case of a natural discharge [Fig. 1, inset (b)]. To get insight into the mechanism of the laser-triggered HV discharge we measured breakdown delay  $\tau$  between the arrival of the laser pulse and the actual breakdown as a function of  $\eta$ . For these measurements the laser pulses passed the electrodes typically 1–2  $\mu\text{s}$  after the HV pulse reached its maximum level, and we used a 2-m gap and four HV values, as shown in Fig. 3. The  $\tau$  values do not significantly depend on the HV (which is kept sufficiently below the natural breakdown voltage) when the dispersion in the experimental data is taken into account, especially for small values of  $\eta$ .

For a setup such as ours (negative tip/plane, 1.2/50- $\mu\text{s}$  HV pulse) the literature predicts free discharges without a laser with  $U_{50}$  of 700–1000 kV/m

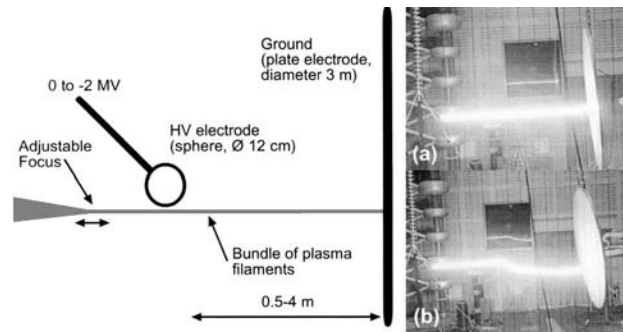


Fig. 1. Schematic of the experimental setup. (a) Photo of a guided discharge, (b) photo of a partly guided discharge.

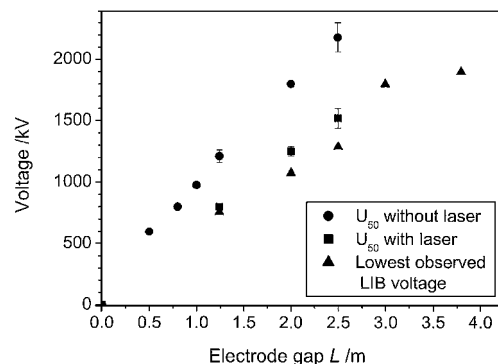


Fig. 2.  $U_{50}$  as a function of the electrode gap. Circles, natural breakdown; squares, laser-triggered discharge; triangles, single LIB events, the lowest observed voltage at each distance.

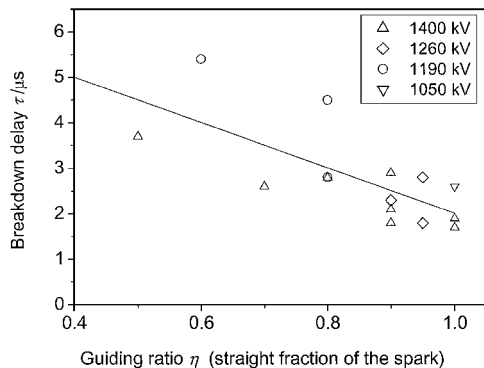


Fig. 3. Breakdown delay  $\tau$  as a function of the guided fraction of spark  $\eta$  measured with an electrode gap of 2 m. The linear fit yields a velocity  $v_g = (1.0 \pm 0.2) \times 10^6$  m/s for the guided propagation and a velocity  $v_f = (2.9 \pm 0.5) \times 10^5$  m/s for free streamer propagation.

(consistent with our results in Fig. 2) conducted by a negative streamer that propagates toward the plane electrode at a velocity  $v_f$  of approximately  $10^5$  m/s.<sup>14</sup> Modification of this process by the laser can be explained as follows: The laser-induced plasma filaments (impedance in the range  $10^5$ – $10^6$   $\Omega$  for a gap of several meters<sup>9,10</sup>) connect with the corona near the HV sphere electrode. The available free charges enhance the electric field locally and initiate electron avalanches along the plasma filaments. Therefore the avalanche threshold of  $\sim 25$  kV cm<sup>-1</sup> atm<sup>-1</sup> is reached with a reduced voltage between the electrodes. At a velocity  $v_g$  the discharge channel grows straight, guided by the laser plasma along a fraction  $\eta$  of the gap. Thereby  $\eta$  fluctuates from 100% to lower values. Finally, if  $\eta < 100\%$ , a dominant streamer leaves the laser channel and propagates freely toward the ground electrode at velocity  $v_f$ , causing a spark. No LIB has been observed with  $\eta$  less than one third, which suggests that a certain guiding length is needed for free bridging of the remaining gap.

This simple model leads to an estimation for the breakdown delay of  $\tau = L[\eta/v_g + (1 - \eta)/v_f]$ . A linear fit to the experimental data shown in Fig. 3 yields  $v_g = (1.0 \pm 0.2) \times 10^6$  m/s and  $v_f = (2.9 \pm 0.5) \times 10^5$  m/s. These values are of the same order of magnitude as those found by La Fontaine *et al.*<sup>12</sup> Furthermore, our guiding velocity is similar to the observed velocities of afterstrikes passing through the same path as a preceding negative cloud-to-ground discharge,<sup>14</sup> which suggests that the laser filaments replace the initial creation of free charges in a natural discharge process.

In conclusion, we have successively triggered and guided HV discharges by using laser filaments ohmically bridging gaps as large as 3.8 m between two electrodes. The sphere–plane electrode configuration

that we used provides a laboratory model of real-scale lightning control experiments. In such experiments a classic lightning conductor installed near the laser system will act as an electrode, which will allow a corona to develop at the conductor's tip as a reaction to a highly charged cloud. With the mobility of our terawatt laser system taken into account, these results promise to be useful in field experiments.

We acknowledge support of the Teramobile project by the Centre National de la Recherche Scientifique (France) and the Deutsche Forschungsgemeinschaft. J.-P. Wolf acknowledges financial support from the Institut Universitaire de France. We acknowledge a constructive discussion with M. Miki of Criepti, Japan, and with S. Martin of Lasim. M. Rodriguez's e-mail address is rodriguez@ioq.uni-jena.de (www.teramobile.org).

## References

1. D. W. Koopman and T. D. Wilkerson, *J. Appl. Phys.* **42**, 1883 (1971).
2. L. M. Ball, *Appl. Opt.* **13**, 2292 (1974).
3. M. Miki, Y. Aihara, and T. Shindo, *J. Phys. D* **26**, 1244 (1993).
4. M. Miki, T. Shindo, and Y. Aihara, *J. Phys. D* **29**, 1984 (1996).
5. H. Pépin, D. Comptois, F. Vidal, C. Y. Chien, A. Desparois, T. W. Johnston, J. C. Kieffer, B. L. Fontaine, F. Martin, F. A. M. Rizk, C. Potvin, P. Couture, H. P. Mercure, A. Bondiou-Clergerie, P. Lalande, and I. Gallimberti, *Phys. Plasmas* **8**, 2532 (2001).
6. P. Rambo, J. Schwartz, and J.-C. Diels, *J. Opt. A* **3**, 146 (2001).
7. A. Braun, G. Korn, X. Liu, D. Du, J. Squier, and G. Mourou, *Opt. Lett.* **20**, 73 (1995).
8. E. T. J. Nibbering, P. F. Curley, G. Grillon, B. S. Prade, M. A. Franco, F. Salin, and A. Mysyrowicz, *Opt. Lett.* **21**, 62 (1996).
9. H. Schillinger and R. Sauerbrey, *Appl. Phys. B* **68**, 753 (1999).
10. S. Tzortzakis, M. A. Franco, Y.-B. André, A. Chiron, B. Lamouroux, B. S. Prade, and A. Mysyrowicz, *Phys. Rev. E* **60**, R3505 (1999).
11. B. La Fontaine, F. Vidal, Z. Jiang, C. Y. Chien, D. Comptois, A. Desparois, T. W. Johnston, J.-C. Kieffer, and H. Pépin, *Phys. Plasmas* **6**, 1615 (1999).
12. B. La Fontaine, D. Comptois, C. Y. Chien, A. Desparois, F. Gérin, G. Jarry, T. W. Johnston, J. C. Kieffer, F. Martin, R. Mawassi, H. Pépin, F. A. M. Rizk, F. Vidal, C. Potvin, P. Couture, and H. P. Mercure, *J. Appl. Phys.* **88**, 610 (2000).
13. H. Wille, M. Rodriguez, J. Kasparian, D. Mondelain, J. Yu, A. Mysyrowicz, R. Sauerbrey, J. P. Wolf, and L. Wöste, "Teramobile: a mobile femtosecond-terawatt laser and detection system," *Eur. Phys. J.* (to be published).
14. M. Beyer, W. Boeck, K. Möller, and W. Zaengl, *Hochspannungstechnik: theoretische und praktische Grundlagen für die Anwendung* (Springer-Verlag, Berlin, 1986), pp. 100–136.

# Teramobile: A mobile femtosecond-terawatt laser and detection system

H. Wille<sup>1</sup>, M. Rodriguez<sup>1,2</sup>, J. Kasparian<sup>2,3,a</sup>, D. Mondelain<sup>3</sup>, J. Yu<sup>3</sup>, A. Mysyrowicz<sup>4</sup>, R. Sauerbrey<sup>2</sup>, J.P. Wolf<sup>3</sup>, and L. Wöste<sup>1</sup>

<sup>1</sup> “Teramobile” project, Institut für Experimentalphysik, Freie Universität Berlin, Arnimallee 14, 14195 Berlin, Germany

<sup>2</sup> “Teramobile” project, Institut für Optik und Quantenelektronik, Friedrich-Schiller-Universität Jena, Max-Wien-Platz 1, 07743 Jena, Germany

<sup>3</sup> “Teramobile” project, LASIM, UMR CNRS 5579, Bât. A. Kastler, Université Claude Bernard Lyon 1, 43 Bd du 11 novembre 1918, 69619 Villeurbanne Cedex, France

<sup>4</sup> “Teramobile” project, LOA, ENSTA – École Polytechnique, Chemin de la Hunière, 91761 Palaiseau Cedex, France

Received: 10 December 2001 / Received in final form: 29 January 2002 / Accepted: 18 February 2002

Published online: 15 November 2002 – © EDP Sciences

**Abstract.** We describe the Teramobile system, a new mobile femtosecond multi-terawatt laser and detection system based on a state-of-the art CPA laser system embedded in a standard freight container, as well as a mobile detection unit allowing a characterization of the nonlinear propagation of high power laser pulses over long horizontal distances. The unique mobility feature of the whole system opens the way to previously unreachable applications for high-power laser pulses in the field of atmospheric research (lidar, laser-triggered lightning), which are also briefly reviewed.

**PACS.** 42.60.By Design of specific laser systems – 42.65.-k Nonlinear optics – 42.68.Wt Remote sensing: LIDAR and adaptive systems

## 1 Introduction

The interest in nonlinear pulse propagation has been significantly renewed since 1985, when the development of the chirped pulse amplification (CPA) technique [1,2] permitted to produce ultra-short laser pulses which now reach powers in excess of  $10^{14}$  W. At those power levels, nonlinear phenomena dominate pulse propagation even in diluted media such as atmospheric pressure gases, opening the way to applications in atmospheric research. However, current high-power lasers are restricted to laboratory experiments due to their size and delicate operation. For the first time we developed a mobile laboratory hosting a CPA fs-TW laser system as well as detection and analysis tools.

In the following, we shall briefly describe relevant properties of nonlinear propagation of ultra-intense pulses in air, showing the need for a mobile high-power laser system. The subsequent section will be dedicated to a detailed description the main components of the Teramobile system: the laser system, the container laboratory and the mobile diagnostics unit. The last section is dedicated to a review of some of the applications as well as the first results obtained by the Teramobile team with our unique tool in its first months of life.

Nonlinear self-action leads to strong modifications of the spatial [3–5], spectral [6,7] and temporal [8–11] characteristics of the pulse. The propagation medium is also affected. It undergoes multiphoton ionization and plasma production [12–15]. One of the most spectacular processes under such conditions is filamentation, which mechanism is described *e.g.* in [16]. Briefly, a dynamical equilibrium between self-focusing due to the Kerr effect and ionization of air leads to a defocusing effect. This equilibrium results in a self-trapping of the beam lasting for a distance of at least 200 m, *i.e.* much longer than the Rayleigh length [17,18], with a diameter reported to be about  $100\ \mu\text{m}$  [4,19]. In those filaments, the intensity reaches  $10^{13}$ – $10^{14}$  W/cm<sup>2</sup> [20], sufficient to generate significant self-phase modulation (SPM), yielding a bright white light supercontinuum [21]. However, the propagation properties of high-power laser pulses over long distances is still unknown. Up to now, the filamentation has been mainly studied in the laboratory over a maximum distance of several tens of meters. Measurements over km-range paths require field experiments, while theoretical simulations, even over distances of one meter, require unreasonable computing time at present.

Recently, interest in long-range propagation of fs-pulses was strongly enhanced when Rairoux *et al.* demonstrated a supercontinuum-based multispectral lidar

<sup>a</sup> e-mail: jerome.kasparian@lasim.univ-lyon1.fr

(Light Detection and Ranging) technique [22,23]. Emitting fs-TW laser pulses in the atmosphere and collecting the backscattered white light, they detected a supercontinuum signal from distances up to 13 km, opening the way to a multi-wavelength atmospheric remote sensing. Since the white light supercontinuum covers the whole visible and near-IR range up to 4  $\mu\text{m}$  [24], it might permit to detect many constituents of the earth atmosphere.

Besides lidar, the broadband supercontinuum generation may be used to excite multiwavelength guide stars, which are needed to correct the large-scale inhomogeneities of the atmosphere at large astronomical telescopes using adaptive optics [25]. Other applications are based on the ionization induced in the air by the self-guided high-power pulses. The plasma channels behave as conducting wires. High power lasers may therefore trigger lightning [26–29]. Also, it is well known that ions can act as condensation nuclei [30], which could lead to laser-triggered rain nucleation in over-saturated atmospheres.

Hence, the need for a femtosecond-terawatt laser system suited for field experiments emerged. For the first time, we developed a fully standalone multi-terawatt laser system, based on a fs-TW laser system integrated in a mobile laboratory built in a standard-dimensioned sea container. This mobile laboratory provides the necessary infrastructure for the laser system as well as the sending and the receiving optics and the detection electronics for lidar. It is supplemented by a mobile beam characterization unit, which is itself a second standalone optics laboratory constructed in a trailer. This infrastructure is obviously suited for km-range propagation experiments, since the mobile system can be installed on long horizontal spots such as the runway of an airfield, permitting to study the beam continuously along its propagation path with the characterization unit.

The mobility also has the big advantage to allow further evaluation of the potential of fs-TW pulses for specific applications or experiments, without permanently installing an expensive and complex system at the place of interest. For example, short test experiments at large facilities such as synchrotrons are made possible at a reasonable investment.

## 2 The Teramobile system

The Teramobile laser is the first mobile femtosecond-terawatt laser system. This unique mobility feature imposed a particularly compact design for the laser. The environmental requirements of such a system determined the conception of a mobile standalone laboratory, including all the sending and receiving optics as well as diagnostics and detection systems. The system as a whole was designed as a versatile tool intended for fundamental as well as atmospheric applied research, and finally as an open system for further improvements of experiments in other scientific fields.

**Table 1.** Laser characteristics.

Center wavelength	793 nm
Bandwidth	16 nm
Pulse energy	350 mJ
Pulse duration	70 fs sech <sup>2</sup>
Peak power	5 TW
Repetition rate	10 Hz
Output beam diameter	50 mm
Chirped pulse duration adjustment	70 fs to 2 ps, positive or negative chirp
Energy stability	2.5% RMS over 400 shots
Dimensions	3.5 × 2.2 m

### 2.1 Laser system

#### 2.1.1 Laser setup

The Teramobile laser is based on the well-known chirped pulse amplification (CPA) technique [1,2]. However, its integration in the reduced space of the mobile laboratory required a particularly compact design, which was developed in cooperation with Thales Laser (formerly BMI division, Thomson CSF, Orsay, France). Its main characteristics are summarized in Table 1. Briefly, the system consists of a compact Ti:Sapphire oscillator (Compact Pro, Femtosource, Vienna, Austria) and a Nd:YAG pumped Ti:Sapphire amplification chain including a regenerative amplifier and two 4-pass amplifiers. A T-shaped table yielded an optimal compactness together with a reasonable access to the system for alignment and operation. The laser can be monitored with the usual diagnostics installed in a rack fixed above the laser table (Fig. 1). Spare space has been reserved for diagnostics to be made available in the future, either permanently or for a specific experiment.

#### 2.1.2 Compensation of the group velocity dispersion

Since atmospheric applications imply the propagation of ultrashort laser pulses over long distances in the atmosphere, group velocity dispersion (GVD) has to be taken into account. In the first order, GVD results in the temporal broadening of the laser pulse, stretching our 70 fs long, 16 nm broad pulse into a strongly chirped, 1 ps long pulse with a 10-fold reduced peak power after 1 km propagation. However, it was shown [22,31] that a negatively chirped pulse is temporally recompressed by GVD, leading to an ultrashort pulse after a propagation distance depending on the initial chirp (Fig. 2). To perform this precompensation of the GVD, we installed one of the compressor gratings on a long-course (40 mm) motorized translation stage. Its translation yields a pulse stretching of 43 fs per mm detuning, hence allowing to precompensate the GVD in up to 1.5 km of air. Further compensation as well as the compensation for higher order dispersion can be provided using a pulse shape modulator.

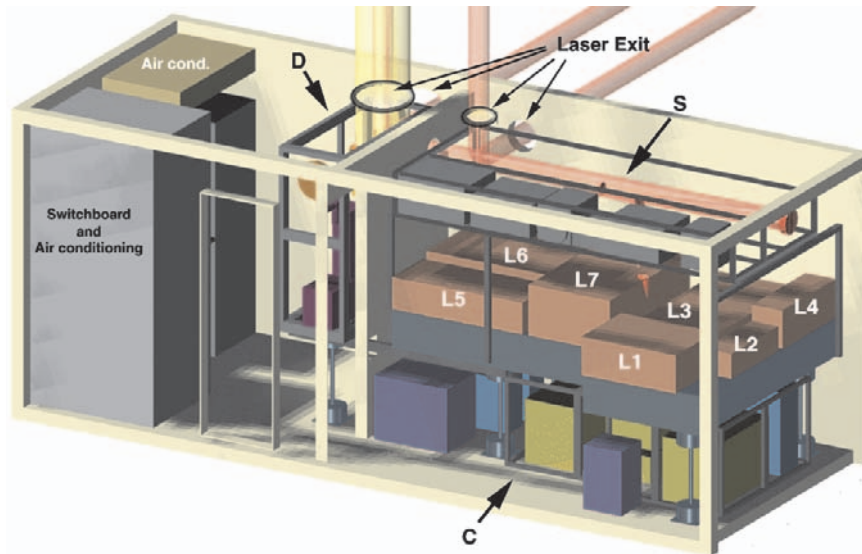


**Fig. 1.** Three-dimensional view inside the Container. The beam expanding system (S) (see also Fig. 3), controllers and power supplies for the laser system are installed on the rack mounted on top of the laser table. The laser system is composed of an oscillator (Femtosource) with a YAG pump laser (Verdi) (L1), a stretcher (L2), regenerative amplifier, multipass preamplifier (L3) and their Compact YAG pump laser (L4). A multipass main amplifier (L5) is pumped by two SAGA-YAG units (L6). The final part is the compressor (L7). The main power supplies of the laser system are installed together with a dedicated water-air heat exchanger in a closed isolation box under the table (C). Details of the Teramobile Detection (D) are shown in Figure 4.

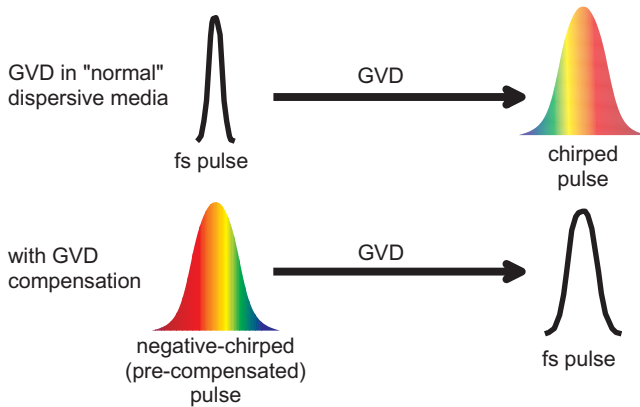


**Fig. 2.** Principle of the compensation of the group velocity dispersion.

### 2.1.3 Sending optics system

Besides transporting the beam directly to the output windows of the mobile laboratory, the sending optics permits to vary its beam diameter and focus. The beam diameter has a critical influence on the distance at which filamentation will occur. Expanding the beam, and hence reducing its intensity, can be favorable to prevent unwanted self-focusing after short distances of propagation through air, which would damage the output windows or sending mirrors. Moreover, controlling the initial focus or divergence of the beam is a key parameter to study the propagation of ultrashort laser pulses as well as to control the filamentation distance.

The geometrical control of the beam is achieved by an off-axis sending telescope (Fig. 3 and Tab. 2) based only

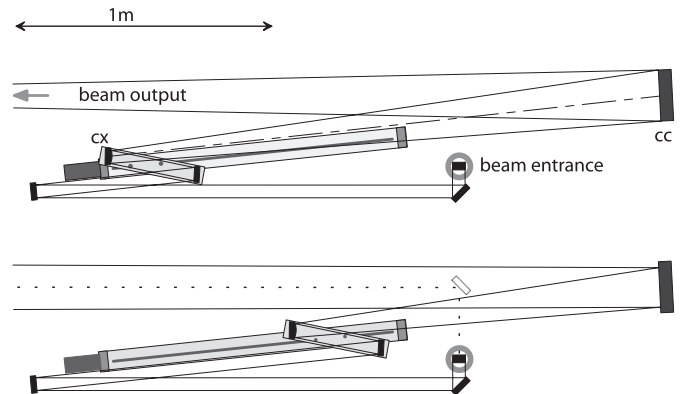


**Fig. 3.** Variable off-axis sending telescope. Up: setting for strongest focus ( $< 10\text{ m}$ ). cx: 75 mm convex mirror, cc: 200 mm concave mirror; - - - indicates the optical axis between the spherical mirrors giving the translation path. Down: setting for slight divergence; - - - indicates the direct sending option bypassing the telescope.

on reflective optics with dielectric coatings, to preserve the temporal and spectral pulse characteristics. To keep the aberration negligible, the telescope extends over the whole available length in the mobile laboratory. It is installed in a rack which is rigidly attached above the laser system (Fig. 1 (S)). The special Z-geometry of the optical path permits to set the focal length of the telescope with a single translation stage (isel automation). The telescope can also be by-passed to use the original 5 cm beam diameter of the laser. The beam can be sent either horizontally to continuously characterize its propagation over long distances, or vertically, *e.g.* for lidar measurements.

**Table 2.** Sending telescope characteristics.

Focal length	10 m to slightly divergent
Magnification	2.7
Output beam diameter	15 cm
Pointing stability	0.1 mrad over the whole focusing range
Off-axis angle	6°
Length	2.5 m
Translation stage precision	12.5 $\mu\text{m}$

**Table 3.** Mobile laboratory specifications.

External dimensions	Standard ISO 20 ft Container
Internal dimensions	5.70 m $\times$ 2.15 m $\times$ 2.20 m
Weight including equipment	10 tons
Power consumption during full operation	30 kW (380 V, 63 A, 3P connector)
Storage power connection	240 V, 16 A
Temperature stability (laser room)	$\pm 1$ °C
Outer temperature range	-20 °C to +35 °C
Humidity range	0 to 100%
Sending, receiving ports	2 $\times$ $\varnothing 25$ cm, 2 $\times$ $\varnothing 45$ cm
Certificates	DIN, IEC, VDE, CEE, NEMKO, CSC

Moreover, the beam can also be emitted through the detection box to permit coaxial lidar experiments. Each of the 4 ports is equipped with a 2-D steering capability over  $\pm 10^\circ$ , as well as the option to attach a full 3-D steering system to the frame of the windows on the roof or the outer wall of the mobile laboratory.

## 2.2 The mobile laboratory

The Teramobile laser system and its equipment are build in a standard sea container (see Tab. 3 for detailed specifications). Since TW-class laser systems are very sensitive to mechanical vibrations and shocks, the optical system as a whole (including the laser, sending and receiving optics) was designed as a single rigid unit smoothly linked to the outer structure of the container through special damping elements. This makes it possible to transport the system to virtually any place in the world and operate it provided climatic conditions permit the operation of the laser system.

The Teramobile mobile laboratory itself, as the infrastructure for the scientific equipment, was designed in a cooperation between the Freie Universität Berlin and Impres GmbH (Bremen, Germany) and was build by TSU (Bremerhaven, Germany). Figure 1 gives an overview of the main structure of the system. The mobile laboratory is divided into two rooms. The partition wall acts as a thermal insulation and electromagnetic shielding. The first room hosts the laser system including all the power supplies of the pump lasers, the driving electronics as well as the sending optics and the diagnostics systems (Fig. 4). The other room contains mainly the detection system, as

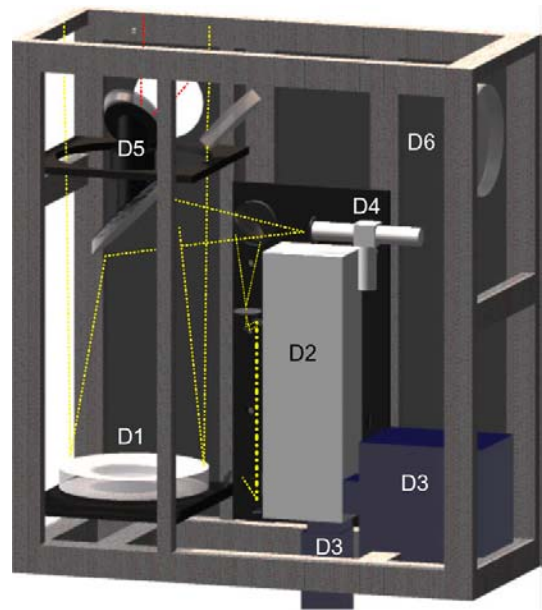


**Fig. 4.** Detection system: the detection system inside the container consists of a 40 cm receiving telescope for lidar measurements (D1), a 50 cm spectrograph (Chromex 500ism) mounted vertically (D2) with two outputs: ICCD (Princeton) and photomultiplier/avalanche photodiode (Hamamatsu/Licel) (D3), a second optical path to measure the depolarization (D4), the on-axis sending mirror (D5) and a horizontal telescope to follow the long-path horizontal propagation experiments (D6).

well as most of the technical functions such as the power distribution, air conditioning devices, storage, control of water supplies. This room is also used as the control room during the experiments.

To ensure the stable operation of the femtosecond laser system, the temperature control is separated into three uncoupled volumes: (i) the control room which acts as an air lock, (ii) the laser room and (iii) a closed isolation box containing all the power supplies of the lasers, cooled by a dedicated water-air exchanger. Under reasonable outdoor conditions, the strongly dimensioned air conditioning even permits to remove the sending windows from their frame to avoid non-linear effects in their glass.

Eye-safety is always a key issue when dealing with lasers. Since a TW laser can not be eye-safe, a security system controls the operation of the laser. Hence, the laser can be blocked by a shutter which is controlled by suitable detectors according to the type of experiment, like a motion detector, hand controller, as well as an additional safety lidar, which are upgradeable to future applications.

## 2.3 Detection units

### 2.3.1 Detection system inside the container

The detection system inside the Teramobile (Fig. 4) is mainly designed to perform lidar measurements and can work in an off-axis or on-axis mode with respect to the emitted beam. The detection consists of a vertically

mounted 40 cm receiving telescope and two detection channels. The first channel consists of a spectrograph for spectrally and temporally resolved measurements. The second one is used to measure depolarization for fundamental investigations of the white light generation and scattering in the filaments, as well as for atmospheric particles characterization. The unit also contains a horizontal telescope aimed at comparing the backscattered light to the forward emission detected by the mobile detection unit described in the next section. Both telescopes and both detection channels can be connected either directly or through fiber couplings. The wavelength range of the detection system ranges from 190 nm to 2.5  $\mu\text{m}$ , using a spectrometer with three integrated gratings and four possible detectors (ICCD 190–950 nm, Hamamatsu PMT 350–1700 nm, Si APD: 700–1100 nm and InSb 1.5–2.5  $\mu\text{m}$ ). With interference filters and the depolarization path, the wavelength range may be extended up to 5  $\mu\text{m}$ .

### 2.3.2 Mobile detection unit

In order to permit the characterization of the laser beam at an arbitrary and large distance, we developed a mobile characterization unit mounted inside a trailer, which can be moved continuously along the beam. It contains a stand-alone optics laboratory equipped with air conditioning, breadboard, desktop and its own power generator.

For safety reasons, since the mobile detection unit is placed inside the laser beam path, it has no window. The only input port is a sampling device, made of a diffuser and a collecting fiber, which can be scanned in two dimensions across the laser beam by a 1.5 m long articulated arm, remote controlled from the inside of the mobile unit. The trailer is also equipped with a screen and an attached video camera, to perform far-field imaging of cross-sections of the laser beam at various distances, up to several km. Since the trailer can be moved along the laser beam on a straight road or an airfield runway, it provides an axially resolved sampling of the beam propagation. Combined with the radial and angular move of the sampling device, this gives access to a full 3D characterization of the laser beam over its propagation path.

## 3 Applications and first results of the Teramobile system

### 3.1 Control of the filamentation distance

As pointed out in the introduction, atmospheric applications of the nonlinear propagation of ultrashort laser pulses rely on white-light continuum and plasma generation in self-guided filaments. Therefore, long range studies of the propagation of high-power laser pulses have to be performed to be able to understand and control the beam propagation, *e.g.* the filamentation distance.

The mobility of the Teramobile system permits such studies, for instance by installing the system at one end

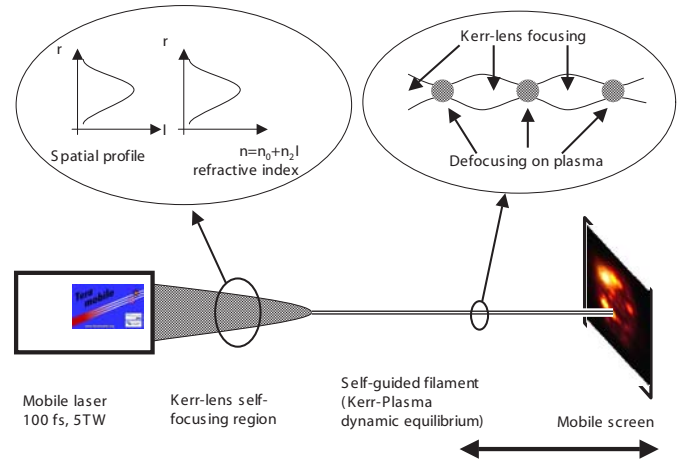


**Fig. 5.** Principle of filamentation and experimental setup to study the filamentation distance.

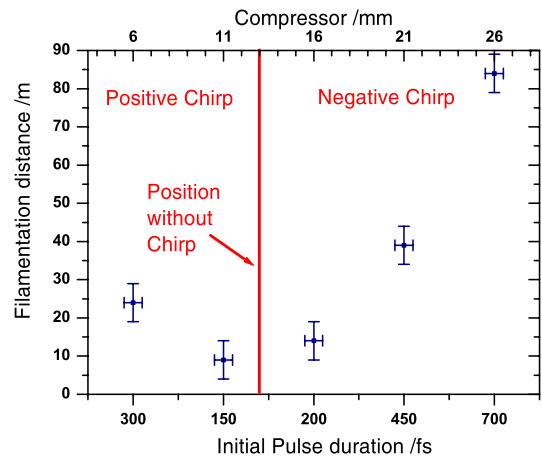


**Fig. 6.** Filamentation distance as a function of the laser chirp. Uncertainties are  $\pm 10\%$  for pulse duration and  $\pm 5$  m for the filamentation distance. Note that the horizontal axis is not linear. The minimum pulselength corresponds to approximately 100 fs.

of an airfield runway, and scanning along the beam with the mobile characterization unit. Here, we shall describe preliminary results about the formation and length of self-guided filaments obtained over 100 m distance, as a function of the initial chirp. In this experiment, pulses with 330 mJ energy and a minimum pulselength of 100 fs were emitted as a 5-cm diameter beam. The filament formation was observed as bright spots on a screen placed in the laser path (Fig. 5).

The high power of the Teramobile system (4 TW), much above the critical power  $P_{\text{crit}} = \lambda^2 / (4\pi n_2) \approx 1$  GW, leads to multifilamentation of the laser beam. The filamentation distance, *i.e.* the distance between the output of the compressor and the beginning of the filaments, strongly varies with the initial chirp of the emitted pulse, as shown in Figure 6. Filamentation occurs much before the pulse is temporally recompressed by GVD. For example, a 16 nm broad pulse is only expanded by 1 ps/km in air by linear dispersion.

This can be understood considering that even with a strong chirp, the pulse power keeps much above the critical power, allowing self-focusing and filamentation to occur before the short pulse is temporally recombined at a remote location. Moreover, in a multi-filamentation regime, the dynamics of the filament formation strongly depends on the laser beam profile because filaments start at slight inhomogeneities of the beam profile. This shows the need to use an expanded and/or slightly divergent beam with a good control of the beam profile in order to further increase the filamentation distance. However, this experiment illustrates the possibility to control the filament distance by adjusting the laser parameters, which is a key issue for long-range atmospheric experiments.

### 3.2 Lidar

Lidar [32] is an efficient technique in atmospheric research. It permitted to understand many important atmospheric phenomena, such as the mechanism of stratospheric ozone depletion [33]. The main advantage of lidar over other remote sensing techniques – as DOAS [34], FTIR [35] or satellite based spectroscopy [36] – is the high range resolution over long distances, which is achieved by the use of short pulse laser (typically a few nanoseconds or less) and fast electronics to record the signal of the light backscattered by molecules and aerosols. However, the number of the detectable species is limited by the availability of narrow-lined pulsed laser sources at suitable wavelengths, especially in the IR. Moreover, since the laser has to be tuned on an absorption band of the species to be measured, only one molecule can be measured at once, and interference between molecules having overlapping spectra are difficult to correct.

Other techniques such as DOAS or FTIR overcome this limitation through a wide available spectral range, but at the cost of a range-integrated measurement. The use of the laser-generated white light continuum in a nonlinear lidar would combine the advantages of both techniques. White light pulses generated by laser-induced filaments in the sky should simultaneously provide range and spectral resolutions. Moreover, the supercontinuum emission covers the near- and mid-infrared [24], where many important pollutants, such as the volatile organic compounds (VOCs), have their absorption bands. Approaches which have been made in remote sensing of VOCs, *e.g.* to use broad bandwidth (dye) laser sources with FTIR detection [37] or to do DIAL with OPO lasers [38], have their limits in the tunability of the lasers or the spectral resolution. The latter is needed to be able to retrieve concentrations of trace gases, while their bands overlap and strongly interfere with absorption lines of water and  $\text{CO}_2$ .

The Teramobile could overcome some of those limits and provide a multi-component analysis, by implementing the first mobile white-light lidar system based on highly nonlinearly propagating pulses. Briefly, the TW laser beam is sent into the atmosphere, and the

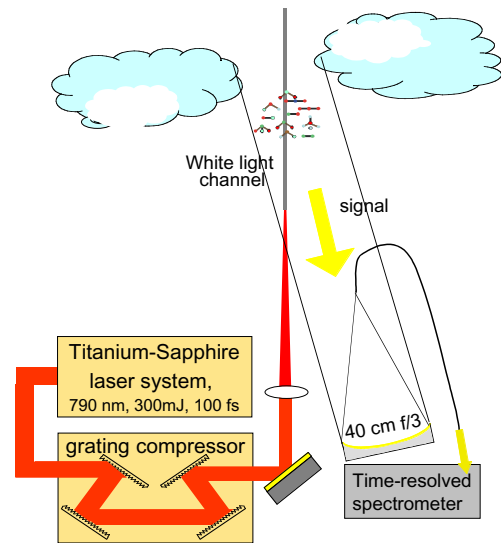


Fig. 7. Setup for white-light lidar experiments.

backscattered light is detected on a spectrometer-photomultiplier combination (Fig. 7). The laser parameters and GVD precompensation can be set to optimize the supercontinuum generation in filaments, which leads to a highly collimated white-light beam. This can be used to measure range resolved broadband absorption spectroscopy of trace gases, as has been showed for water vapor in preliminary experiments [22]. Here the narrowness of the water absorption lines was not a difficulty, as it is for the differential absorption lidar (DIAL) technique using two single wavelengths.

Besides the use of the white-light supercontinuum, two processes could significantly improve non-linear lidar. On one hand, due to local laser-induced refractive index gradients, the backward supercontinuum emission is significantly enhanced, *i.e.* more supercontinuum is emitted towards the lidar detection system than would be by elastic backscattering [39]. This leads to a significantly improved lidar signal.

On the other hand, theoretical studies [31] and laboratory experiments [40,41] have shown strongly non-linear interaction of fs-pulses with aerosols, particularly spherical droplets. Processes like Raman scattering [31], multiphoton-excited fluorescence [41] or plasma emission shall lead to a remote analysis of the characteristics, *e.g.* the chemical composition, of atmospheric aerosols.

### 3.3 Laser-triggered and -guided high voltage discharges

Another application of the Teramobile system was successfully demonstrated in collaboration with the Institute for High Voltage at the Technical University of Berlin. We showed that filaments created by high peak power laser pulses can trigger and guide a discharge between two electrodes. Figure 8 shows the setup used for this experiment.

The mobility of the Teramobile system permitted to install it in the high-voltage hall of the TUB. A high-voltage

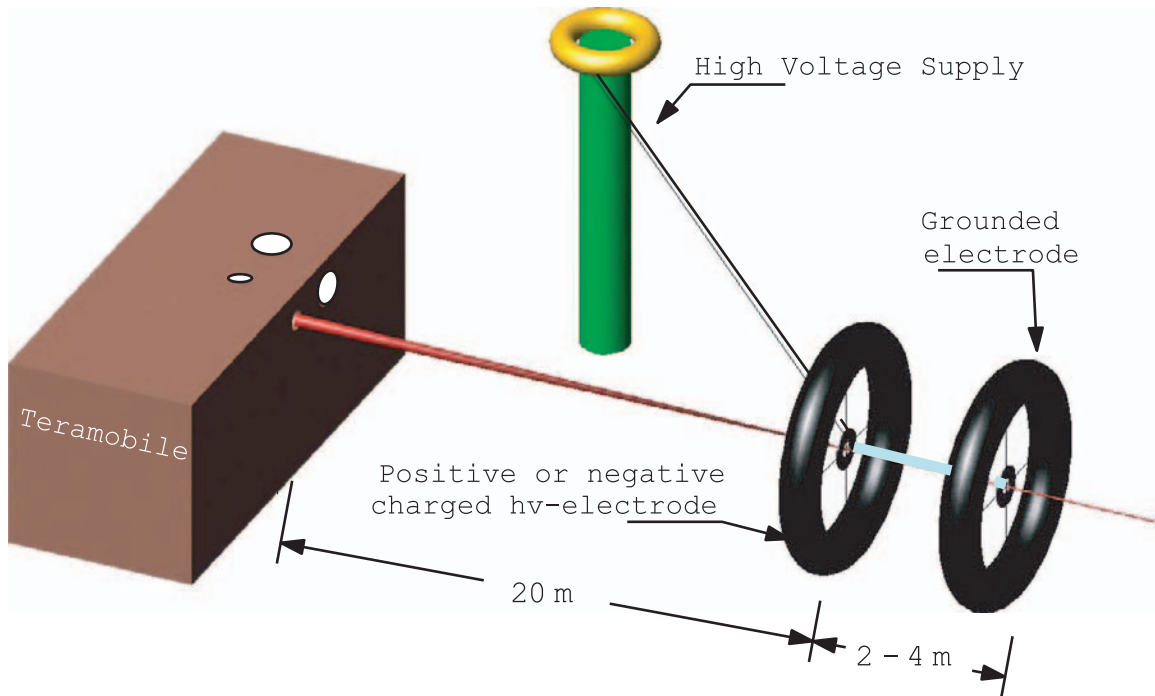


**Fig. 8.** Experimental setup of the high voltage experiment.

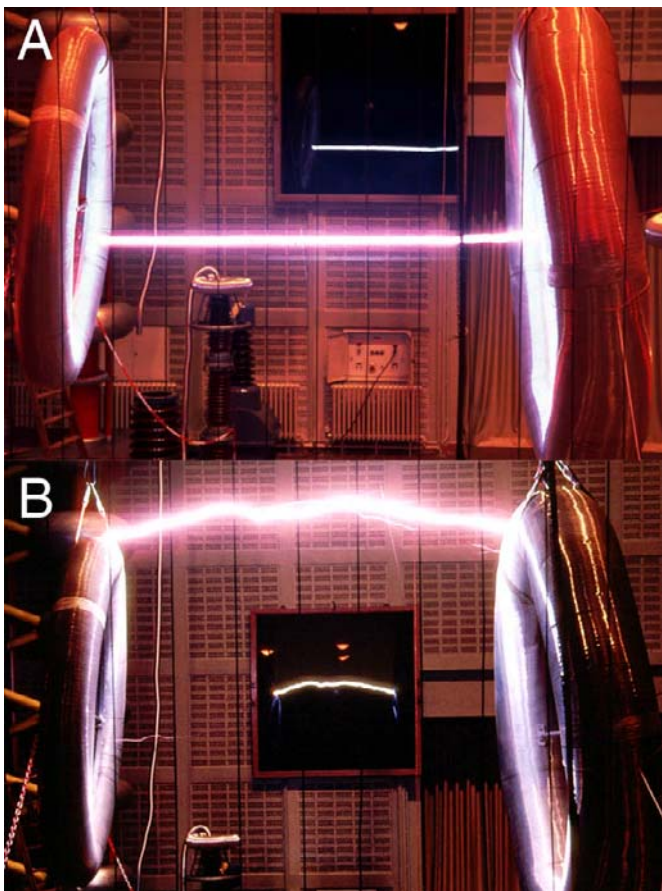


**Fig. 9.** Discharges with (A) and without (B) laser in a 3.2 m gap between toroidal electrodes. On the laser-triggered discharge (A) the guiding is clearly visible.

(HV) generator (Marx multiplier circuit) provided up to 2 MV pulses (with  $1.2 \mu\text{s}$  rise time) between electrodes separated by a gap, which was adjusted between 1 and 4 m. The laser beam (300 mJ and 100 fs) was aligned to pass successively through holes in the center of the two electrodes. It was focused slightly before the high-voltage electrode, so that the focus was outside the gap, while the generated filaments spanned over the whole gap. Successful guiding and triggering (*i.e.* occurrence of discharges at voltage that do not permit discharges without laser) of discharges has been achieved for various electrode setups, laser and high voltage parameters.

Figure 9 (A) and (B) respectively show a triggered and guided discharge and a free discharge without laser between two toroidal electrodes of 2.2 m and 3 m diameter. Detailed results of these experiments for different laser and high-voltage parameters will be published elsewhere [42].

## 4 Conclusion

We successfully integrated a multi-terawatt laser system and a detection unit for lidar, together with their full technical support in a standard 20' freight container. This system, called Teramobile, has been demonstrated to run as stable as under laboratory conditions. The first obtained results include high-power laser propagation studies, lidar, and high-voltage discharge triggering.

In the near future, the mobility of the Teramobile system will allow us to investigate long distance formation and propagation of self-guided plasma filaments up to several kilometers, as well as lidar measurements optimized for different altitudes and spectral regions or studies of larger distance lightning guiding.

The Teramobile project is funded jointly by the German Deutsche Forschungsgemeinschaft (DFG) and the French Centre National de la Recherche Scientifique (CNRS). J.P. Wolf acknowledges support from the Institut Universitaire de France. We acknowledge a strong support from the technical staffs in the universities of Berlin, Jena and Lyon. We would particularly mention the invaluable help of M. Barbaire, M. Kerleroux, M. Néri, W. Ziegler and M. Kregielski. For the good and fair teamwork in the container planning we like to thank I. Beninga and W. Ruhe from Impres GmbH, J.C. Luderer for his helpful hands and S. Niedermeier for his work in the beginning of the project. Due to the very good collaboration with W. Kalkner's group at the Technical University of Berlin, and particularly Lars Klingbeil and Kay Rethmeier, our first high voltage discharge experiment was a great success. The Teramobile web site is [www.teramobile.org](http://www.teramobile.org).

## References

1. D. Strickland, G. Mourou, *Opt. Commun.* **56**, 219 (1985)
2. P. Maine, D. Strickland, P. Bado, M. Pessot, G. Mourou, *IEEE J. Quantum Electron.* **24**, 398 (1988)
3. D. Strickland, P.B. Corkum, *J. Opt. Soc. Am. B* **11**, 492 (1994)
4. A. Braun, G. Korn, X. Liu, D. Du, J. Squier, G. Mourou, *Opt. Lett.* **20**, 73 (1995)
5. L. Roso-Franco, *Phys. Rev. Lett.* **55**, 2149 (1985)
6. R.R. Alfano, S.L. Shapiro, *Phys. Rev. Lett.* **24**, 584, 592, 1217 (1970)
7. A. Brodeur, S.L. Chin, *J. Opt. Soc. Am. B* **16**, 637 (1999)
8. Y. Shen, *The principles of nonlinear optics* (John Wiley and Sons, 1984)
9. G. Yang, Y. Shen, *Opt. Lett.* **9**, 510 (1984)
10. A.L. Gaeta, *Phys. Rev. Lett.* **84**, 3582 (2000)
11. J.K. Ranka, R.W. Schirmer, A.L. Gaeta, *Phys. Rev. Lett.* **77**, 3783 (1996)
12. A. Proulx, A. Talebpour, S. Petit, S.L. Chin, *Opt. Commun.* **174**, 305 (2000)
13. S. Tzortzakis, M.A. Franco, Y.-B. André, A. Chiron, B. Lamouroux, B.S. Prade, A. Mysyrowicz, *Phys. Rev. E* **60**, R3505 (1999)
14. S. Tzortzakis, B. Prade, M. Franco, A. Mysyrowicz, *Opt. Commun.* **181**, 123 (2000)
15. H. Schillinger, R. Sauerbrey, *Appl. Phys. B* **68**, 753 (1999)
16. A. Chiron, B. Lamouroux, R. Lange, J.-F. Ripoche, M. Franco, B. Prade, G. Bonnaud, G. Riazuelo, A. Mysyrowicz, *Eur. Phys. J. D* **6**, 383 (1999)
17. B. La Fontaine, F. Vidal, Z. Jiang, C.Y. Chien, D. Comtois, A. Desparois, T.W. Johnston, J.-C. Kieffer, H. Pépin, H.P. Mercure, *Phys. Plasmas* **6**, 1615 (1999)
18. M. Mlejnek, M. Kolesik, J.V. Moloney, E.M. Wright, *Opt. Lett.* **23**, 2938 (1999)
19. E.T.J. Nibbering, P.F. Curley, G. Grillon, B.S. Prade, M.A. Franco, F. Salin, A. Mysyrowicz, *Opt. Lett.* **21**, 62 (1996)
20. J. Kasparian, R. Sauerbrey, S.L. Chin, *Appl. Phys. B* **71**, 877 (2000)
21. P.B. Corkum, C. Rolland, T. Srinivasan-Rao, *Phys. Rev. Lett.* **57**, 2268 (1986)
22. P. Rairoux, H. Schillinger, S. Niedermeier, M. Rodriguez, F. Ronneberger, R. Sauerbrey, B. Stein, D. Waite, C. Wedekind, H. Wille, L. Wöste, *Appl. Phys. B* **71**, 573 (2000)
23. L. Wöste, C. Wedekind, H. Wille, P. Rairoux, B. Stein, S. Nikolov, Ch. Werner, S. Niedermeier, H. Schillinger, R. Sauerbrey, *Laser Optoelektron.* **29**, 51 (1997)
24. J. Kasparian, R. Sauerbrey, D. Mondelain, S. Niedermeier, J. Yu, J.-P. Wolf, Y.-B. André, M. Franco, B. Prade, A. Mysyrowicz, S. Tzortzakis, M. Rodriguez, H. Wille, L. Wöste, *Opt. Lett.* **25**, 1397 (2000)
25. J.R. Morris, *J. Opt. Soc. Am. A* **11**, 832 (1994)
26. S.L. Chin, K. Miyazaki, *Jap. J. Appl. Phys.* **38**, 2011 (1999)
27. B. La Fontaine, D. Comtois, C.Y. Chien, A. Desparois, F. Gérin, G. Jarry, T.W. Johnston, J.C. Kieffer, F. Martin, R. Mawassi, H. Pépin, F.A.M. Rizk, F. Vidal, C. Potvin, P. Couture, H.P. Mercure, *J. Appl. Phys.* **88**, 610 (2000)
28. H. Pépin, D. Comtois, F. Vidal, C.Y. Chien, A. Desparois, T.W. Johnston, J.C. Kieffer, B. La Fontaine, F. Martin, F.A.M. Rizk, C. Potvin, P. Couture, H.P. Mercure, A. Boudiou-Clergerie, P. Lalanden, I. Gallimberti, *Phys. Plasmas* **8**, 2532 (2001)
29. P. Rambo, J. Schwartz, J.-C. Diels, *J. Opt. A: Pure Appl. Opt.* **3**, 146 (2001)
30. K.J. Oh, G.T. Gao, X.C. Zeng, *Phys. Rev. Lett.* **86**, 5080 (2001)
31. J. Kasparian, J.-P. Wolf, *Opt. Commun.* **152**, 355 (1998)
32. R.M. Measures, *Laser Remote Sensing – Fundamental and Applications* (Wiley Interscience, New York, 1984)
33. B. Stein, C. Wedekind, H. Wille, F. Immler, M. Müller, L. Wöste, M. del Guasta, M. Morandi, L. Stefanutti, A. Antonelli, P. Agostini, V. Rizi, G. Readelli, V. Mitev, R. Matthey, R. Kivi, E. Kyrö, *J. Geophys. Res.* **104**, 23983 (1999)
34. U. Platt, in *Air Monitoring by Spectroscopic Techniques* (Chem. Anal., Vol. 127), edited by M.W. Sigrist (Wiley-Interscience, 1994)
35. J. Notholt, *J. Geophys. Res.* **99**, D2, 3607 (1994)
36. J.P. Burrows, M. Weber, M. Buchwitz, V.V. Rozanov, A. Ladstädter-Weissenmayer, A. Richter, R. de Beek, R. Hoogen, K. Bramstedt, K.-U. Eichmann, M. Eisinger, D. Perner, *J. Atmos. Sci.* **56**, 151 (1999)
37. M. Douard, R. Bacis, P. Rambaldi, A. Ross, J.-P. Wolf, G. Fabre, R. Stringat, *Opt. Lett.* **20**, 2140 (1995)
38. T.D. Gardiner, M.J.T. Milton, F. Molero, P.T. Woods, in *Advances in atmospheric remote sensing with lidar*, edited by A. Ansmann, R. Neuber, P. Rairoux, U. Wandinger (Springer, 1996), p. 451
39. J. Yu, D. Mondelain, G. Ange, R. Volk, S. Niedermeier, J.P. Wolf, J. Kasparian, R. Sauerbrey, *Opt. Lett.* **26**, 533 (2001)
40. W. Zimmer, Nichtlineare optische Effekte bei der Wechselwirkung von Femtosekundenlaserpulsen mit Mikrotropfen, Doctoral thesis, Freie Universität Berlin, 2001
41. S.C. Hill, V. Boutou, J. Yu, S. Ramstein, J.-P. Wolf, Y.-L. Pan, S. Holler, R.K. Chang, *Phys. Rev. Lett.* **85**, 54 (2000)
42. M. Rodriguez, R. Sauerbrey, H. Wille, L. Wöste, T. Fujii, Y.-B. André, A. Mysyrowicz, L. Klingbeil, K. Rethmeier, W. Kalkner, J. Kasparian, E. Salmon, J. Yu, J.-P. Wolf, *Opt. Lett.* **27**, 772 (2002)

G. MÉJEAN<sup>1</sup>  
J. KASPARIAN<sup>1</sup>  
E. SALMON<sup>1</sup>  
J. YU<sup>1</sup>  
J.-P. WOLF<sup>1</sup>  
R. BOURAYOU<sup>2,3,✉</sup>  
R. SAUERBREY<sup>2</sup>  
M. RODRIGUEZ<sup>3</sup>  
L. WÖSTE<sup>3</sup>  
H. LEHMANN<sup>4</sup>  
B. STECKLUM<sup>4</sup>  
U. LAUX<sup>4</sup>  
J. EISLÖFFEL<sup>4</sup>  
A. SCHOLZ<sup>4</sup>  
A.P. HATZES<sup>4</sup>

## Towards a supercontinuum-based infrared lidar

<sup>1</sup> Teramobile, LASIM, UMR CNRS 5579, Université Claude Bernard Lyon 1, 43 bd du 11 Novembre 1918, F-69622 Villeurbanne Cedex, France  
<sup>2</sup> Teramobile, Institut für Optik und Quantenelektronik, Friedrich-Schiller-Universität Jena, Max-Wien-Platz 1, 07743 Jena, Germany  
<sup>3</sup> Teramobile, Institut für Experimentalphysik, Freie Universität Berlin, Arnimallee 14, 14195 Berlin, Germany  
<sup>4</sup> Thüringer Landessternwarte Tautenburg (TLS), Karl-Schwarzschild-Observatorium, Sternwarte 5, 07778 Tautenburg, Germany

Received: 31 January 2003/Revised version: 14 April 2003  
Published online: 24 June 2003 • © Springer-Verlag 2003

**ABSTRACT** Lidar signals were obtained for the first time in the near-infrared using the supercontinuum generated by the terawatt femtosecond laser of the Teramobile system. A signal up to 4 km in altitude, in the band 1–1.7  $\mu\text{m}$ , was collected using a 2 m astronomical telescope. We observed a 10-fold enhancement of the infrared signal backscattered from the atmosphere compared with that expected using a previously measured laboratory spectrum. This suggests a more efficient frequency conversion into the infrared (typically 7% into the 1–1.5  $\mu\text{m}$  band) under long-distance propagation conditions.

PACS 42.65.Jx; 42.68.Wt; 42.65.Ky

### 1 Introduction

The Lidar (LIght Detection And Ranging) [1] technique has become a routinely employed tool for providing atmospheric pollution monitoring. The technique is, however, limited, especially for DIAL (Differential Absorption Lidar), to the measurement of one pollutant at a time, since the laser wavelength is tuned to an absorption line of the species being measured. Femtosecond lasers have recently raised hopes for the simultaneous detection of several pollutants [2, 3], based on white-light radiation through the physical process of supercontinuum generation (SCG).

SCG results from the non-linear propagation of femtosecond pulses with peak powers up to the terawatt level, even in a transparent and dilute medium such as air. The propagation of the pulse results in the creation of a self-induced guiding structure called a filament, interpreted as the manifestation of a dynamic equilibrium between Kerr lens focusing and ionization-induced defocusing (self-channeling [4]). Self-phase modulation (SPM) and possibly four-wave mixing

occur, leading to spectral broadening around the frequency of the initial pulse. The supercontinuum spectral extent has been determined to reach from the UV to the near-infrared up to 4.5  $\mu\text{m}$  [5].

Such bright thin filaments have been observed to develop over tens to hundreds of meters [6, 7], making them extremely promising for lidar applications in the visible spectral range, as shown by Wöste et al. [2, 3]. Extension of investigations to the infrared for possible atmospheric applications is desirable for the characterization of aerosol and gaseous species such as methane or volatile organic compounds (VOCs). However, lidar applications using the near-infrared side of the filament-generated supercontinuum remain a challenge, because of the rapid decrease of the infrared content of the supercontinuum and the  $\lambda^{-4}$  dependence of Rayleigh backscattering.

In this Letter, we report the detection of lidar signals in the near-infrared region up to 1.7  $\mu\text{m}$  using the supercontinuum emitted from light filaments propagating in the atmosphere. This has been made possible by the combined operation of the container-embedded femtosecond terawatt laser of the Teramobile system [8] and an astronomical telescope. After suitable treatment, the detected backscattered band-integrated infrared radiation was compared with the spectrum measured in previous laboratory-scale experiments. Results show a strongly enhanced infrared spectrum from open-path propagation in the atmosphere, and therefore a more efficient frequency conversion than observed in laboratory-scale experiments.

### 2 Experimental set-up

The emitter of the lidar setup was the mobile femtosecond terawatt laser designed and built in the framework of the Teramobile project. This Ti:Sapphire-based laser chain delivered 290 mJ pulses, with a diameter of 9 cm, centered at 795 nm, at a repetition rate of 10 Hz. The initial pulse was slightly negatively chirped to compensate for the atmospheric group velocity dispersion, leading to an initial pulse dura-

✉ Fax: +49-3641/947-202, E-mail: bourayou@physik.fu-berlin.de

tion of 200 fs. The output 1.5 TW beam, sent vertically, was focused a few tens of meters high in the atmosphere through a telescope of adjustable focal length.

The receiver consisted of the 2 m primary mirror telescope [9] of the Thüringer Landessternwarte (TLS) observatory located 30 m from the laser. The Coudé configuration telescope had a field-of-view of 1.2 mrad (full aperture).

The collected light was imaged with an apparent aperture number of  $f/92$  onto a liquid-nitrogen-cooled photomultiplier tube (PMT, Hamamatsu R 5509-72, sensibility range 300 nm–1.7  $\mu\text{m}$ ). To analyze the IR white-light lidar return, we recorded the signals in several spectral bands by using 4 filter sets: (i) no filter, (ii) 1–1.7  $\mu\text{m}$  by use of a long-pass filter (Corion), (iii) 1.2–1.7  $\mu\text{m}$  by use of a combination of two 1 mm thick Schott glass filters UG7 and VG12, and (iv) 1.5–1.7  $\mu\text{m}$  by use of a long-pass filter (Corion). The signal was acquired and averaged over 16 shots on a digital oscilloscope, triggered by the laser pulses. The chirp in the laser compressor and the focus of the sending telescope were optimized to give the maximal detected signal at high altitude. The astronomical telescope was pointed towards the laser beam at about 4 km altitude, at the bottom of a cloud layer.

### 3 Results and discussion

Infrared backscattered signals could be detected with all filter sets used, even for the 1.5–1.7  $\mu\text{m}$  range (Fig. 1). This is, to our knowledge, the first observation of an infrared lidar signal based on supercontinuum generation.

Because of the very limited spectral resolution of the measurement, we compared the actual lidar data with a simulation of the lidar signal that would have been observed if the initial IR spectrum was the same as measured in the laboratory [5]. The simulation also assumed that the previously measured supercontinuum spectrum was generated at low altitude and then propagated linearly over the 8 km forward and return path to the cloud. Since the sky was clear from the ground to the cloud, we neglected any interaction between the laser beam and low-altitude aerosols. We took into account

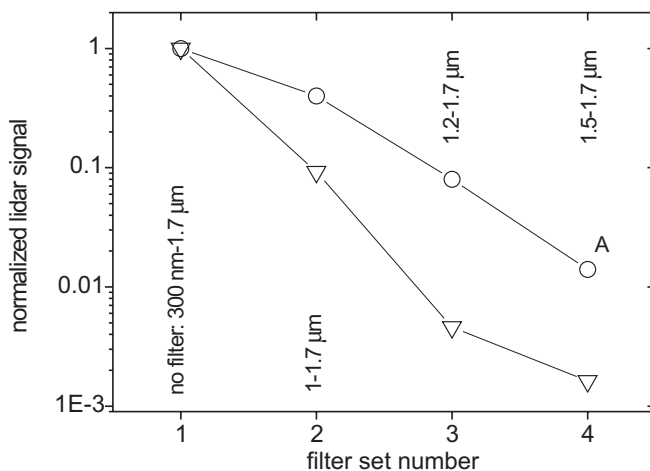


**FIGURE 1** IR lidar signal for each filter set (circles) and expected values calculated from the laboratory spectrum [5], using a C.1 cloud size distribution centered at  $r_0 = 4 \mu\text{m}$  (V). Each curve is normalized to 1 at the fundamental wavelength (filter set 1)

the transmission functions of the diverse filter combinations that we used, the PMT spectral response, and the transmission of the (fully gaseous) atmosphere. This atmospheric transmission was calculated using HITRAN, assuming a mean value for the relative humidity (80%) and the temperature (270 K), both inferred from radiosonde data. The interaction with the cloud was modeled using Mie scattering calculations, and the contribution of multiple scattering was evaluated following a method derived from Bissonnette's multiple-scattering lidar equation (MSLE) [10]. This model only considers the forward and backward lobes of the angular Mie scattering pattern and approximates them by Gaussian curves, thus allowing a quasi-analytical calculation. In our calculations, the backward peak was modeled by a polynomial instead, in order to take into account the ripple structures in the backward direction due to large particles. Besides the density of the cloud, the MSLE requires the particle size distribution as an input parameter. From the altitude and opacity of the cloud, we considered as a first approach an altocumulus cloud of spherical water droplets with radii that follow a C.1 Deirmendjian size distribution [1]:

$$dN/dr = CN_0/r_0(r/r_0)^6 \exp(-6r/r_0), \quad (1)$$

where  $N$  is the concentration,  $r$  is the particle radius,  $r_0 = 4 \mu\text{m}$  is the mode of the size distribution,  $C = 388.8$  is a normalizing factor, and  $N_0$  is the overall aerosol density, which was determined using a self-consistent method applied to the elastic lidar signal. More precisely, the applied procedure was as follows: (1) a first estimate  $N_0^{(1)}$  was obtained from the backscattered signal, neglecting multiple scattering; (2)  $N_0^{(1)}$  was used to compute the multiple scattering contribution; (3) this multiple scattering contribution was used to retrieve a second estimate  $N_0^{(2)}$  from the measured lidar signal; (4) the procedure was iterated until convergence was achieved. After 4 iterations, this algorithm converged to a particle density of  $N_0 = 1.2 \text{ cm}^{-3}$ , corresponding to an aerosol extinction of  $16.3 \text{ km}^{-1}$  at 800 nm, and a relative contribution of multiple scattering evaluated to be 30% at the fundamental laser wavelength, and decreasing to 15% at  $\lambda = 2 \mu\text{m}$ . The retrieved extinction value corresponds to a dense altocumulus cloud. For all of the calculations, only the real part of the refractive index was taken into account, which is not expected to significantly affect the results, since we measured at the bottom of the cloud and the backscattering coefficient is only weakly modified by the absorption.

The simulated IR lidar signals calculated from laboratory spectral measurements lie much below the measured results (respectively  $\nabla$  and  $\circ$  symbols on Fig. 1), with a ratio of about one order of magnitude above 1.5  $\mu\text{m}$ . This indicates that the frequency conversion into the spectral region 1–1.7  $\mu\text{m}$  was significantly more efficient in our large-scale experiment than in previous laboratory measurements. This is due to the much longer interaction path in the atmosphere. Notice that differences between long-range propagation and focused geometries have also been observed in the visible: a plateau has been observed in the visible side of the spectrum emitted by filaments generated by slightly focused beams (see e.g. [3] and [7]), while a sharp decrease has been observed in the case of stronger focusing (such as e.g. in [5]). Moreover, the at-

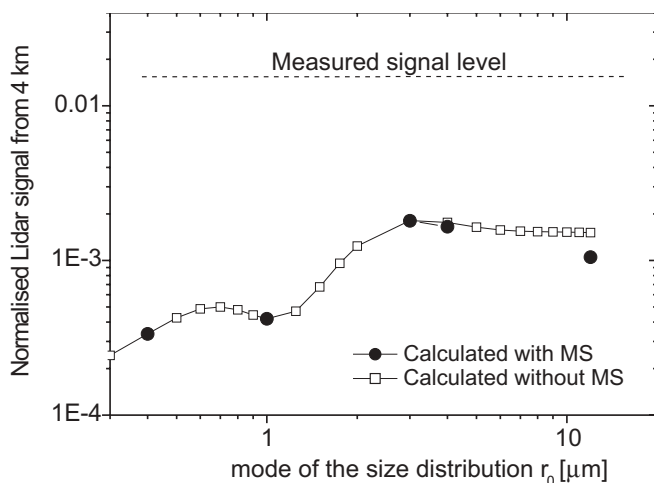


**FIGURE 2** Influence of mode of the C.1 size distribution of the cloud on the calculated lidar intensity with filter set 4 (1.5–1.7  $\mu\text{m}$ ). Calculations both with and without multiple scattering are presented. The normalization is the same as in Fig. 1. The horizontal dotted line is the relative intensity of the measured lidar signal (point A of Fig. 1)

mosphere is clear below the cloud layer. Hence, no influence from low-altitude atmospheric aerosols on the SCG was expected in our experiment.

Since the cloud size distribution was set to a plausible value, we checked the influence of the mode  $r_0$  of the particle size distribution on the retrieved intensity in a fixed wavelength range of filter set 4 (1.5–1.7  $\mu\text{m}$ ). For values of  $r_0$  above 2  $\mu\text{m}$ , the calculated intensity backscattered from the cloud exhibits a weak dependence and reaches a maximum for  $r_0 = 3 \mu\text{m}$ . Below 3  $\mu\text{m}$ , it drops significantly as a consequence of the lower Mie scattering efficiency in the IR. Results of the calculations are presented in Fig. 2, both with and without taking multiple scattering into account. Even in the worst case situation ( $r_0 = 3 \mu\text{m}$ ) the observed IR signal is 7 times larger than the signal expected from the laboratory spectrum [5]. Similar behavior was observed for the other filter sets. The same calculation was performed with and without taking multiple scattering into account, showing that the multiple scattering is negligible for size distributions centered below several microns, while for larger particles, its effect is an enhancement of the difference between the measured and calculated signals.

In order to get more insight into the spectral dependence of our lidar measurement, we assumed that the decrease of the supercontinuum spectral profile generated in the atmosphere follows an exponential decay on the IR side, as observed in the measurements under laboratory conditions [5]. By adjusting the corresponding exponential slope factor to the experimental data, we obtained a decrease of 1 decade per micron, instead of 3 decades as for the laboratory-scale spectrum. This corresponds to a 7% energy conversion efficiency into the

1–1.7  $\mu\text{m}$  band, instead of 0.5% in the laboratory spectrum of [5]. This high efficiency conversion would make the IR part of the SCG a good candidate for many applications requiring ultrashort pulsed IR broadband sources, such as lidar or time-resolved spectroscopy.

#### 4 Conclusion

Near-infrared lidar signals have been recorded from an altitude of up to 4 km, using the broadband white light generated from filaments propagating in the atmosphere. The signal measured for infrared wavelengths is about ten times stronger than expected from simulations from previous laboratory experiments [5]. This result could be attributed to the longer interaction path that results from a weaker focusing. Signal extension to the mid-infrared spectral range can be valuable for the detection and identification of atmospheric pollutants (particularly VOCs) that display characteristic absorption bands in this spectral region. The knowledge of the white-light spectral density is a key feature, as it constitutes the background spectrum of potential altitude-resolved absorption spectra for multi-pollutant detection. This work yields interesting insights for the application of supercontinuum-based LIDAR systems.

**ACKNOWLEDGEMENTS** We acknowledge the support of the Teramobile project, jointly funded by the Centre National de la Recherche Scientifique (France) and the Deutsche Forschungsgemeinschaft (Germany). J.-P. Wolf acknowledges financial support from the Institut Universitaire de France. The Teramobile members would like to thank the technical staff of the Thüringer Landessternwarte Tautenburg, Bernd Furhmann, Jürgen Haupt, Axel Kirchhof, Michael Pluto, Jörg Schiller, and Johannes Winkler, for their assistance in installing the laser at TLS and helping to solve technical problems. We also thank Eike Guenther, Sylvio Klose, and Helmut Meusinger for useful discussions on conducting the observations with the 2 m telescope. The Teramobile web site is [www.teramobile.org](http://www.teramobile.org).

#### REFERENCES

- 1 R.M. Measures: *Laser Remote Sensing – Fundamental and Applications* (Wiley Interscience, New York 1984)
- 2 L. Wöste, C. Wedekind, H. Wille, P. Rairoux, B. Stein, S. Nikolov, C. Werner, S. Niedermeier, H. Schillinger, R. Sauerbrey: *Laser Optoelektronik* **29**, 51 (1997)
- 3 P. Rairoux, H. Schillinger, S. Niedermeier, M. Rodriguez, F. Ronneberger, R. Sauerbrey, B. Stein, D. Waite, C. Wedekind, H. Wille, L. Wöste: *Appl. Phys. B* **71**, 573 (2000)
- 4 A.L. Gaeta: *Phys. Rev. Lett.* **84**, 3582 (2000)
- 5 J. Kasparian, R. Sauerbrey, D. Mondelain, S. Niedermeier, J. Yu, J.-P. Wolf, Y.-B. André, M. Franco, B. Prade, S. Tzortzakis, A. Mysyrowicz, M. Rodriguez, H. Wille, L. Wöste: *Opt. Lett.* **25**, 1397 (2000)
- 6 B. La Fontaine, F. Vidal, Z. Jiang, C.Y. Chien, D. Comtois, A. Desparois, T.W. Johnson, J.-C. Kieffer, H. Pépin: *Phys. Plasmas* **6**, 1615 (1999)
- 7 T.J. Nibbering, P.F. Curley, G. Grillon, B.S. Prade, M.A. Franco, F. Salin, A. Mysyrowicz: *Opt. Lett.* **21**, 62 (1996)
- 8 H. Wille, M. Rodriguez, J. Kasparian, D. Mondelain, J. Yu, A. Mysyrowicz, R. Sauerbrey, J.P. Wolf, L. Wöste: *EPJ-AP* **20**, 3 (2002)
- 9 H. Lehmann: <http://www.tls-tautenburg.de/telesc.html> (2002)
- 10 L.R. Bissonnette: *Appl. Opt.* **35**, 6449 (1996)

# Sonographic probing of laser filaments in air

Jin Yu, Didier Mondelain, Jérôme Kasparian, Estelle Salmon, Sylvain Geffroy, Catherine Favre, Véronique Boutou, and Jean-Pierre Wolf

The acoustic wave emitted from the plasma channel associated with a filament induced by a femtosecond laser pulse in air was detected with a microphone. This sonographic detection provides a new method to determine the length and the spatial profile of the free-electron density of a filament. The acoustic wave is emitted owing to the expansion of the gas in the filament, which is heated through collisions with high-energy photoelectrons generated by multiphoton ionization. Compared with other methods, the acoustic detection is simpler, more sensitive, and with higher spatial resolution, making it suitable for field measurements over kilometer-range distances or laboratory-scale studies on the fine structure of a filament. © 2003 Optical Society of America

OCIS codes: 010.1300, 190.4180, 190.5940, 190.7110, 350.5400.

## 1. Introduction

**Fn1** High-energy femtosecond laser pulses propagating in air form long filaments, owing to an equilibrium between Kerr focusing and defocusing on laser-induced plasma.<sup>1</sup> The properties of the filaments open exciting perspectives for applications, such as white-light lidar<sup>2</sup> and laser lightning control.<sup>3,4</sup> These applications in turn stimulate the need for better characterization of the filamentation propagation, especially the need of the precise determination of the length and the spatial profile of the free-electron density of a filament. Not only is the laser triggering and guiding of high voltage discharge based on the plasma channel associated to a filament, but also the backscattering enhancement of the white light, interesting for lidar applications, is considered to be due to the refractive-index gradient induced by free-electron distribution.<sup>5</sup> Some methods have been used to measure the free-electron density in a filament. An electric field induced by free electrons has been detected by an antenna.<sup>6,7</sup> Fluorescence from excited  $N_2$  molecules and  $N_2^+$  ions has been measured with a spectrometer along a filament<sup>8</sup> and more recently in

the backscattering direction.<sup>9</sup> A diffraction interferometer has been used to determine the decay of the free electrons.<sup>10</sup> More recently, subterahertz radiation from a filament has been detected with a heterodyne detector.<sup>11</sup> The application of these current methods, however, is mainly limited to laboratory-scale experiments. On the atmospheric scale,<sup>12</sup> a slightly focused or a collimated beam lead to long filaments (length exceeding 10 m). A more sensitive and simpler operational method is therefore needed.

In this paper, we demonstrate that the acoustic wave emitted from a long plasma channel associated to a filament can be detected with a microphone with high sensitivity, low noise, and high spatial resolution. Furthermore, the acoustic detection presents a large dynamic range, exceeding 3 orders of magnitude.

## 2. Experimental Setup and Results

**F1** In our experiments (Fig. 1), a chirped pulse amplification (CPA) laser delivered pulses of 120 fs in duration and 8 mJ in energy with a 20-Hz repetition rate at 810 nm. The output beam was focused by a spherical mirror with a focal length of 5 m to initiate a filament in the laboratory. The beam diameter was  $\sim 7$  mm (1/e level) on the spherical mirror. A microphone (bandwidth,  $\sim 15$  kHz together with its amplifier) was installed inside a shielding tube oriented perpendicularly toward the filament at a distance of 10 cm from it. The tube had a length of 7 cm and an inner diameter of 0.6 cm, restricting the directly measured filament to a length of 1.1 cm.

A pulsed acoustic signal was detected by the microphone and recorded by a digital oscilloscope syn-

The authors are with the Laboratoire de Spectrométrie Ionique et Moléculaire, Unité Mixte de Recherche, Centre National de la Recherche Scientifique 5579, Université Claude Bernard-Lyon 1, 43, Bd. Du 11 Novembre 1918, F-69622 Vaulleurbanne Cedex, France. J. Yu's e-mail address is jinyu@lasim.univ-lyon1.fr.

Received 11 April 2003; revised manuscript received 23 July 2003.

0003-6935/03/360001-04\$15.00/0

© 2003 Optical Society of America

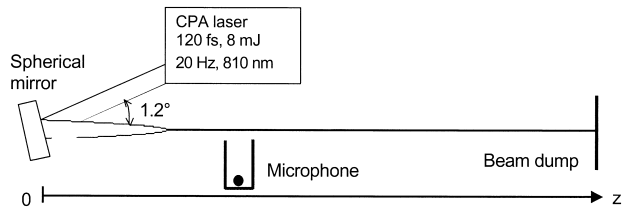


Fig. 1. Experimental setup. The spherical mirror (with 5-m focal length) was used with a small incident angle ( $1.2^\circ$ ) to reduce the astigmatism. The laser beam had a diameter of 7 mm ( $e^{-1}$  level) at the spherical mirror. The origin of the  $Oz$  axis corresponds to the location of the spherical mirror. The beam dump was located 14 m from the spherical mirror.

chronized to a laser pulse by use of a photodiode that detected scattered light from the spherical mirror. In Fig. 2 a typical acoustic signal is shown with an average over 256 laser pulses. The acoustic signal exhibits an overpressure followed by an underpressure, typical for a shock wave due to an explosion. After the initial shock wave some secondary peaks are also detected owing to echo from the surrounding natural reflectors near the setup. The voltage of the first peak as a function of the propagation distance  $z$  is shown in Fig. 3. One first notices the slope changes and signal jumps on the curve at 2.5 and 7 m, as indicated by the arrows. The beam profile was checked with impacts on a black paper. The highest intensity spots in the filament drilled holes in the paper, while the surrounding intensity whitewashed the paper. The impacts showed that three small filaments started around 2.5 m and that beyond 7 m, the beam intensity was not powerful enough to drill the black paper. The profile checks also showed the fusion<sup>13</sup> of the three initial filaments into a single filament around 4.2 m. The jump on the signal around 2.5 m thus indicates the starting of the plasma channel (the Kerr focusing collapse point), and the rapid decrease of the signal around 7 m the ending of it. That allows us to determine the length of the plasma channel of 4.5 m. Before and after the

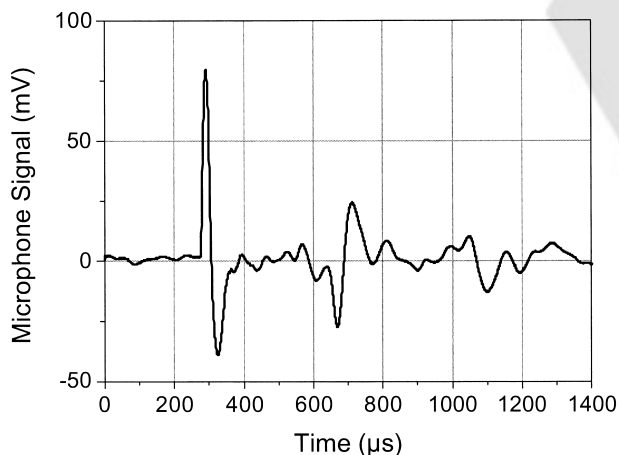


Fig. 2. Acoustic signal recorded by a digital oscilloscope synchronized on laser pulses with an average over 256 shots. The origin of the time axis is the laser pulse.

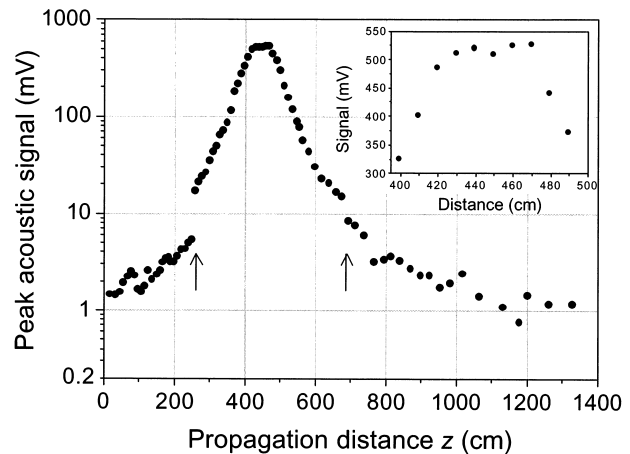


Fig. 3. Peak acoustic signal as a function of the propagation distance  $z$ . The arrows show the starting and the ending points of the plasma channel. The insert presents a detail of the signals between 400 and 500 cm from the spherical mirror.

plasma channel, a pulsed acoustic signal was still detected over the background acoustic noise, which was estimated to 0.2 mV in our laboratory. This noise level is 3 orders of magnitude under the maximal acoustic signal ( $\sim 500$  mV) that we detected at the center of the filament, corresponding to a plasma density 3 orders of magnitude lower than that measured in the center part of the filament, as we will see in Section 3. We interpret the signals detected outside the filament as being due to the ionization of dust particles in air. In a dust-free, clean laboratory we observed a much lower background and, as a consequence, much larger jumps of the acoustic signal in the starting and the ending points of the filament. Once the filaments start, the signal increases exponentially [ $S(z) \sim \exp(0.021z)$ ] and reaches a plateau at 4.2 m, before the geometrical focal point (see the insert in Fig. 3), where the three initial filaments collapse into a single filament. After the plateau, the decrease of the signal is quite similar to the increase [ $S(z) \sim \exp(-0.022z)$ ]. A check of the black paper showed a minimal filament diameter in the range of 100–150  $\mu\text{m}$  in the plateau, where the acoustic signal reached its maximal value. An energy in the filament of  $\sim 0.8$  mJ ( $\sim 10\%$  of the total energy) was determined by use of a power meter and a diaphragm that allowed only the filament through.

### 3. Discussions

It is well known that in a filament with a femtosecond laser pulse, air molecules (nitrogen and oxygen) are partially ionized through the multiphoton ionization (MPI). The photoionization dynamics in an intense laser field has been extensively studied.<sup>14</sup> It has been shown that photoelectrons are ejected from molecules with an initial kinetic energy of a few electron volts,<sup>15</sup> which corresponds to an initial free-electron temperature in the order of  $10^4$ – $10^5$  °K. An energy transfer occurs between the free electrons and the background gas (ions and neutral molecules) owing to

elastic and inelastic collisions. The gas in the filament is then heated to a high temperature when thermal equilibrium is reached in the filament. The heated gas expands, leading to a shock wave emission.

Detailed theoretical analysis of the energy transfer between free electrons and heavy species (ions and neutral molecules) in a femtosecond pulse-induced plasma has been given by V. E. Gusev<sup>16</sup> for solid-state targets and by F. Vidal *et al.* for the air.<sup>17</sup> The authors estimated the time of the energy transfer from electrons to heavy species in the order of  $10^{-11}$  s for typical solid-state targets and in the range of  $10^{-9}$ – $10^{-8}$  s in the air. Especially a final equilibrium temperature of approximately 0.1 eV (corresponding to a temperature of 1200 °K) is reached in a filament in air  $10^{-6}$ – $10^{-5}$  s after the exciting laser pulse.<sup>17</sup>

The relationship between the acoustic signal and the initial free-electron density has been studied by some authors. For example, when the acoustic technique was used to measure the multiphoton absorption by polyatomic molecules, it has been demonstrated that the first peak in the acoustic waveform is proportional to the optical energy absorbed by the gas.<sup>18</sup> For a given gas and a given excitation wavelength, the absorbed energy is in turn proportional to the initial free-electron density generated by the MPI. Therefore in our experiments, the microphone signal shown in Fig. 3 provides a direct measurement on the free-electron density profile in the plasma channel. If we define the beginning and the end of a filament as the points where the acoustic signal jumps and where the slope of the electron density profile changes (i.e., where the signal due to the plasma generated in the filament overrides the noise from the background aerosols), the simple and reproducible sonometric experiments yield a clear measurement of the filament length.

In Fig. 3, we remark that the free-electron density varies over nearly 2 orders of magnitude along the channel (actually,  $\sim 50$  times). This large dynamic range is due to the high-order nonlinearity of the MPI process: A small variation of the light intensity in the filaments leads to a large variation in the free electron density. By use of an effective power-law dependence of  $I^\alpha$  for the ionization rate on the light intensity  $I$ , and taking a value of 7.5 for  $\alpha$ ,<sup>19</sup> the measured variation for the free-electron density corresponds to a variation of a factor 1.7 only in light intensity, which is consistent with the expected intensity clamping in a filament.<sup>20</sup>

To determine the absolute free-electron density, a calibration with cross-check measurements is needed. The calibration can be provided in laboratory experiments, for example by the fluorescence<sup>8</sup> of  $N_2$  or  $N_2^+$ , or the electric conductivity measurements.<sup>21</sup> However the cross-check calibration might not be always necessary, because of the self-organized nature of the filaments, in which the maximum free-electron density is determined by the equilibrium between Kerr self-focusing and defocusing on the plasma. An universal value, or at least a

universal order of magnitude, is found for the maximal value of the free-electron density, independently of the input laser pulse parameters. This maximal value for the free-electron density can also be considered as a consequence of the intensity clamping in the filaments, which limits the free-electron density to a typical value of  $3 \times 10^{16} \text{ cm}^{-3}$  (Ref. 21). In most experiments, when the input laser pulse parameters (energy, duration, chirp, or focusing) are changed, the resulting filaments can have different locations (starting and ending positions), lengths, and free-electron density profiles. The sonographic detection provides a precise and simple method to determine these filament parameters.

The particular spatial plasma profile observed in our experiment is due to our experimental configuration. In particular, the use of a focusing mirror, which was needed to observe filaments in a short propagation distance inside of our laboratory, made the filament diverge rapidly after the geometrical focus point. That corresponds to the quick decay of the observed acoustic signal. Even though refocusing<sup>8</sup> after the geometrical focus can be observed, a filament formed with the use of a focusing lens is in general shorter than a filament formed by a pure self-focusing in a collimated beam. Before the geometric focus, the filament starts owing to the Kerr focusing, as described by the moving focus model.<sup>22</sup>

#### 4. Conclusion

We have demonstrated that the acoustic wave emitted by a filament is a suitable observable for a non-destructive determination of the presence of the plasma channel, its length, and its free-electron density profile. The advantages of the sonographic method are the simplicity, the sensitivity, and the high spatial resolution, thanks to the low speed of the sound. In a field experiment one could take advantages of this simple and sensitive detection method to perform long-distance propagation measurements, while in a laboratory-scale experiment one could benefit from the high spatial resolution (within one centimeter) to study the fine structure in a filament. However, the propagation of the acoustic wave is essentially transverse to the axis of the filament, owing to the cylindrical form of a filament. This limits the use of the acoustic detection in the backwards remote-sensing configuration.

This work was performed in the framework of the Teramobile project, funded jointly by the Centre National de la Recherche Scientifique and the Deutsche Forschungsgemeinschaft. J.-P. Wolf acknowledges financial support from the Institut Universitaire de France.

#### References

1. A. Braun, G. Korn, X. Liu, D. Du, J. Squier, and G. Mourou, "Self-channeling of high-peak-power femtosecond laser pulses in air," *Opt. Lett.* **20**, 73–75 (1995).
2. P. Rairoux, H. Schillinger, S. Niedermeier, M. Rodriguez, F. Ronneberger, R. Sauerbrey, B. Stein, D. Waite, C. Wedekind,

AQ: B

- H. Wille, and L. Wöste, "Remote sensing of the atmosphere using ultrashort laser pulses," *Appl. Phys. B* **71**, 573–580 (2000).
3. B. La Fontaine, D. Comptois, C. Y. Chien, A. Desparois, F. Gérin, G. Jarry, T. W. Johnston, J. C. Kieffer, F. Martin, R. Mawassi, H. Pépin, F. A. M. Rizk, F. Vidal, C. Potvin, P. Couture, and H. P. Mercure, "Guiding large-scale spark discharges with ultrashort pulse laser filaments," *J. Appl. Phys.* **88**, 610–615 (2000).
  4. M. Rodriguez, R. Sauerbrey, H. Wille, L. Wöste, T. Fujii, Y.-B. André, A. Mysyrowicz, L. Klingbeil, K. Rethmeier, W. Kalkner, J. Kasparian, E. Salmon, J. Yu, and J.-P. Wolf, "Triggering and guiding megavolt discharges by use of laser-induced ionized filaments," *Opt. Lett.* **27**, 772–774 (2002).
  5. J. Yu, D. Mondelain, G. Ange, R. Volk, S. Niedermeier, J.-P. Wolf, J. Kasparian, and R. Sauerbrey, "Backward supercontinuum emission from filaments generated by ultrashort laser pulses in air," *Opt. Lett.* **26**, 533–535 (2001).
  6. H. Schillinger and R. Sauerbrey, "Electrical conductivity of long plasma channels in air generated by self-guided femtosecond laser pulses," *Appl. Phys. B* **68**, 753–756 (1999).
  7. A. Proulx, A. Talebpour, S. Petit, and S. L. Chin, "Fast pulsed electrical field created from the self-generated filament of a femtosecond Ti:sapphire laser pulse in air," *Opt. Commun.* **174**, 305–309 (2000).
  8. A. Talebpour, S. Petit, and S. L. Chin, "Re-focusing during the propagation of a focused femtosecond Ti:sapphire laser pulse in air," *Opt. Commun.* **171**, 285–290 (1999).
  9. A. Iwasaki, N. Aközbek, B. Ferland, Q. Luo, G. Roy, C. M. Bowden, and S. L. Chin, "A LIDAR technique to measure the filament length generated by a high-peak power femtosecond laser pulse in air," *Appl. Phys. B* **76**, 231–236 (2003).
  10. S. Tzortzakis, B. Prade, M. Franco, and A. Mysyrowicz, "Time-evolution of the plasma channel at the trail of a self-guided IR femtosecond laser pulse in air," *Opt. Commun.* **181**, 123–127 (2000).
  11. S. Tzortzakis, G. Méchain, G. Patalano, Y.-B. André, B. Prade, M. Franco, A. Mysyrowicz, J.-M. Munier, M. Gheudin, G. Beaudin, and P. Encrenaz, "Coherent subterahertz radiation from femtosecond infrared filaments in air," *Opt. Lett.* **27**, 1944–1946 (2002).
  12. H. Wille, M. Rodriguez, J. Kasparian, D. Mondelain, J. Yu, A. Mysyrowicz, R. Sauerbrey, J.-P. Wolf, and L. Wöste, "Teramobile: a mobile femtosecond-terawatt laser and detection system," *Eur. Phys. J. A* **20**, 183–190 (2002).
  13. S. Tzortzakis, L. Bergé, A. Couairon, M. Franco, B. Prade, and A. Mysyrowicz, "Breakup and fusion of self-guided femtosecond light pulses in air," *Phys. Rev. Lett.* **86**, 5470–5473 (2001).
  14. A. D. Bandrauk, ed. *Molecules in Laser Fields* (Marcel Dekker, New York, 1994).
  15. G. N. Gibson and R. R. Freeman, "Dynamics of the high-intensity multiphoton ionization of N<sub>2</sub>," *Phys. Rev. Lett.* **67**, 1230–1233 (1991).
  16. V. E. Gusev, "Estimate of parameters for shock waves excited by femtosecond laser pulses," in *BRAS Physics Supplement, Physics of Vibrations*, Vol. 57, pp. 1–10. AQ: A
  17. F. Vidal, D. Comtois, C. Y. Chien, A. Desparois, B. La Fontaine, T. W. Johnston, J. C. Kieffer, H. P. Mercure, H. Pépin, and F. A. Rizik, "Modeling the triggering of streamers in air by ultrashort laser pulses," *IEEE Trans. Plasma Sci.* **28**, 418–433 (2000).
  18. S. L. Chin, D. K. Evans, R. D. McAlpine, and W. N. Selander, "Single-pulse photoacoustic technique for measuring IR multiphoton absorption by polyatomic molecules," *Appl. Phys.* **21**, 65–68 (1982).
  19. J. Kasparian, R. Sauerbrey, and S. L. Chin, "The critical laser intensity of self-guided light filaments in air," *Appl. Phys. B* **71**, 877–879 (2000).
  20. A. Becker, N. Aközbek, K. Vijayalakshmi, E. Oral, C. M. Bowden, and S. L. Chin, "Intensity clamping and re-focusing of intense femtosecond laser pulses in nitrogen molecular gas," *Appl. Phys. B* **73**, 287–290 (2001).
  21. S. Tzortzakis, M. A. Franco, Y. B. André, A. Chiron, B. Lamouroux, B. S. Prade, and A. Mysyrowicz, "Formation of a conducting channel in air by self-guided femtosecond laser pulses," *Phys. Rev. E* **60**, R3505–R3507 (1999).
  22. A. Brodeur, C. Y. Chien, F. A. Ilkov, S. L. Chin, O. G. Kosareva, and V. P. Kandidov, "Moving focus in the propagation of ultrashort laser pulses in air," *Opt. Lett.* **22**, 304–306 (1997).

## White-Light Filaments for Atmospheric Analysis

J. Kasparian,<sup>1\*</sup> M. Rodriguez,<sup>2</sup> G. Méjean,<sup>1</sup> J. Yu,<sup>1</sup> E. Salmon,<sup>1</sup> H. Wille,<sup>2</sup> R. Bourayou,<sup>2,3</sup> S. Frey,<sup>1,2</sup> Y.-B. André,<sup>4</sup> A. Mysyrowicz,<sup>4</sup> R. Sauerbrey,<sup>3</sup> J.-P. Wolf,<sup>1</sup> L. Wöste<sup>2</sup>

Most long-path remote spectroscopic studies of the atmosphere rely on ambient light or narrow-band lasers. High-power femtosecond laser pulses have been found to propagate in the atmosphere as dynamically self-guided filaments that emit in a continuum from the ultraviolet to the infrared. This white light exhibits a directional behavior with enhanced backward scattering and was detected from an altitude of more than 20 kilometers. This light source opens the way to white-light and nonlinear light detection and ranging applications for atmospheric trace-gas remote sensing or remote identification of aerosols. Air ionization inside the filaments also opens promising perspectives for laser-induced condensation and lightning control. The mobile femtosecond-terawatt laser system, Teramobile, has been constructed to study these applications.

Remote sensing of the atmosphere is necessary for determining both the chemical and dynamic processes that affect problems such as global warming, ozone loss, tropospheric pollution, and weather prediction. Some approaches bring the instrument to the remote sample, for example, balloon- and aircraft-borne instruments that analyze composition through techniques like mass spectrometry (*1*). The variety of data provided by this type of instrument is difficult to achieve with other methods, but those local methods can be expensive for routine daily studies needed to create archival data sets. The other main approach is to use optical spectrometry to probe a long path through the atmosphere. The path can be fixed, as is the case with Fourier-transform infrared spectroscopy (FTIR) and differential optical absorption spectroscopy (DOAS). These methods allow us to retrieve precise data about the abundance of a large group of atmospheric constituents from the optical absorption of the sunlight or moonlight along its path across the atmosphere (*1*). The light detection and ranging (LIDAR) method, based on atmospheric backscatter signals from actively emitted light pulses, is free from such predetermined absorption

paths and provides three-dimensional distributions of atmospheric trace gases, as well as aerosol abundance, size, and phase information (*1*). LIDAR, however, is generally restricted to the detection of only one substance at a time. For example, in differential absorption LIDAR (DIAL), two lasers are used to monitor trace gases. One emits at the wavelength of peak absorption of the target trace gas, and the other emits at a nearby wavelength where the target gas does not absorb radiation. The difference in the decay between the signals from both lasers will reflect the target gas's concentration.

The main limitation of these long-path absorption methods is that they are constrained by their light sources. Methods that use the Sun or Moon as light sources are path- or intensity-limited, and laser sources are wavelength-limited and hence require multiple instruments for what is essentially the same experiment. Finally, LIDAR is not well suited for the analysis of aerosol compositions such as the identification of bioagents.

The need for an atmospheric sensor that combines the advantages of DOAS, FTIR, and LIDAR resulted in the idea of producing a remote “white lamp” by generating a laser-induced plasma focus in the atmosphere. Recent advances in ultrafast lasers have shown that high-power laser light can, under certain power and focusing conditions, create extended regions of ultra-intense illumina-

tion (*2–4*). To reach the required power at the remote location, we designed an experiment to send a slightly focused, high-power femtosecond laser pulse (100 fs, 3 TW) into the atmosphere with an initial negative chirp, that is, with the shorter wavelengths emitted before the longer ones. Instead of a small spot of a plasma focus, an extended white-light channel was observed (*5, 6*) (Fig. 1), similar to previous observations on shorter scales in the laboratory (*2–4*). Unlike the fundamental infrared laser wavelength ( $\sim 800$  nm), the white-light channel was clearly visible to the naked eye (*5, 6*). [See the photograph on page 54 of this issue (*4*).] The phenomenon also occurred with a spatially unfocused laser beam. The spectrum of the emitted light covered the entire visible range from the ultraviolet (UV) to the infrared (IR), and its signal could be detected from altitudes beyond 10 km.

The fundamental aspects of the observed nonlinear optical phenomena and their potential application for optical remote sensing (fs LIDAR) provide the basis for the Teramobile

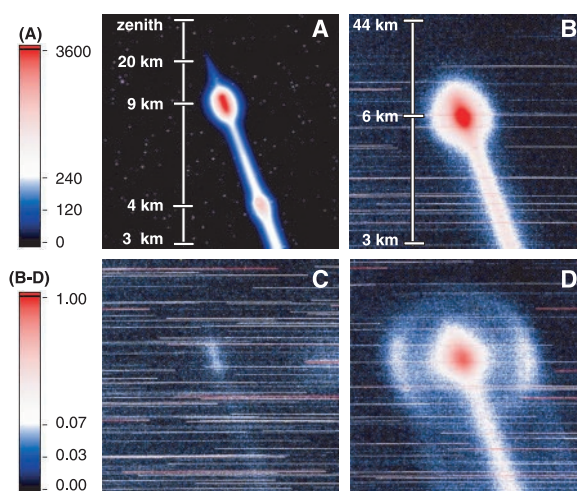


**Fig. 1.** Long-distance white-light propagation and control of nonlinear optical processes in the atmosphere. Images of the Teramobile fs laser beam propagating vertically were taken with the charge-coupled device camera at TLS observatory. (A) Fundamental wavelength, exhibiting signals from more than 20 km and multiple-scattering halos on haze layers at 4- and 9-km altitudes. (B to D) White light (385 to 485 nm) emitted by the fs laser beam. These images have the same altitude range, and their common color scale is normalized to allow direct comparison with that of (A). (B) With GVD precompensation. (C) Without GVD precompensation. (D) With slight GVD precompensation. The conical emission imaged on a haze layer is apparent.

<sup>1</sup>Teramobile project, Laboratoire de Spectrométrie Ionique et Moléculaire, UMR CNRS 5579, Université Claude Bernard Lyon 1, 43 boulevard du 11 novembre 1918, F-69622 Villeurbanne Cedex, France. <sup>2</sup>Teramobile project, Institut für Experimentalphysik, Freie Universität Berlin, Arnimallee 14, D-14195 Berlin, Germany. <sup>3</sup>Teramobile project, Institut für Optik und Quantenelektronik, Max-Wien-Platz 1, D-07743 Jena, Germany. <sup>4</sup>Teramobile project, Laboratoire d'Optique Appliquée, UMR CNRS 7639, ENSTA-Ecole Polytechnique, Centre de l'Yvette, Chemin de la Hunière, F-91761 Palaiseau Cedex, France.

\*To whom correspondence should be addressed. E-mail: jkaspari@lasim.univ-lyon1.fr

## REVIEW

project. Among the main goals of the project are the demonstration of a multicomponent LIDAR and the remote composition analysis of aerosols. Because these filaments are conducting (7, 8), they have applicability in the field of lightning research.

### Filamentation

Filamentation occurs when adequate high-power fs laser pulses propagate across transparent media such as glass or air (2–4, 9, 10). It is initiated by Kerr-lens self-focusing due to an intensity-dependent refractive index of matter:  $n = n_0 + \Delta n_{\text{Kerr}}(I) = n_0 + n_2 I$ , where  $n_2 = 3 \times 10^{-19} \text{ cm}^2/\text{W}$  in air. As a consequence of the usually Gaussian transverse intensity distribution  $I$  in the laser beam, the refractive-index profile behaves like a focusing lens. When the beam power exceeds the critical power  $P_{\text{crit}} = (1.22 \cdot \lambda)^2 / 128 n_2$  of several GW in air (11), the Kerr lens overcomes diffraction and leads to a beam collapse, with all the energy concentrated close to the axis. This strong focusing combined with the high power of femtosecond pulses yields high intensities, leading to high-order multiphoton ionization of air. The resulting free-electron density of  $10^{16}$  to  $10^{17} \text{ cm}^{-3}$  contributes negatively to the index of refraction and has the effect of creating a defocusing plasma lens. From this point, the Kerr and plasma contributions to the refractive index balance out, resulting in a dynamic guiding of the light as thin filaments with a typical diameter of  $100 \mu\text{m}$ . The filaments propagate over distances of hundreds of meters, exceeding the Rayleigh length by orders of magnitude (12–15). The high intensity in the filaments ( $\sim 4 \times 10^{13}$  to  $6 \times 10^{13} \text{ W/cm}^2$ ) (16, 17) induces strong self-phase modulation, leading to the emission of a broadband white-light continuum ranging from 230 nm to  $4.5 \mu\text{m}$  (18, 19).

A certain amount of this white light is emitted in a narrow cone in the forward direction, with a typical cone half-angle of  $0.1^\circ$ , ranging from longer wavelengths in the center to shorter wavelengths at the cone edges (3, 20). However, it has been shown in

the laboratory that a considerable portion of the white light is scattered preferentially in the backward direction (21). This phenomenon is of particular importance for LIDAR applications. For powers much larger than the critical power, the modulational instability breaks the beam into several filaments. Hence, the beam propagates as a bundle of parallel filaments, which vanish and reappear in new patterns over long distances (7, 22).

tion, which allows focal lengths of some hundred meters at best, and at the cost of focusing optics such as large-aperture telescopes with adaptive optics.

However, using filamentation requires control of group velocity dispersion (GVD), which normally increases the duration of short laser pulses propagating across the atmosphere. This duration increase is due to their intrinsic pulse bandwidth of typically 20

nm and occurs because the spectral components with longer wavelengths (“red” components) of the laser spectrum propagate faster than those with shorter wavelengths (“blue”). This effect, however, can be turned into an advantage by launching negatively chirped pulses, for which the blue component precedes its red component at the output of the fs-laser compressor. Such a negatively chirped pulse shortens temporally while propagating, and its intensity increases until the conditions for filamentation, which generates the white light, are reached (6).

The chirp-based control of the white-light supercontinuum has been demonstrated by using the Teramobile laser placed near the 2-m telescope of the Thüringer Landessternwarte Tautenburg (TLS) observatory in Germany. The laser beam was launched vertically, and the backscattered light was imaged through the telescope. Figure 1A shows a typical image obtained at the fundamental wavelength (800 nm) of the laser. Multiple scattering halos are observed on two haze layers at altitudes of 4 and 9 km, and the beam is visible up to more than 20 km in altitude. Tuning the same observation to the white-light continuum in the blue-green band (385 to 485 nm) and comparing images taken with different initial chirp settings (Fig. 1, B and C) shows that the white-light signal can

only be observed with adequate GVD precompensation. In Fig. 1D, the image of the conical emission of the filament appears projected on a haze layer.

### The Teramobile

Field experiments require mobility to perform investigations at adequate locations. Studies of high-power fs-laser beam propaga-

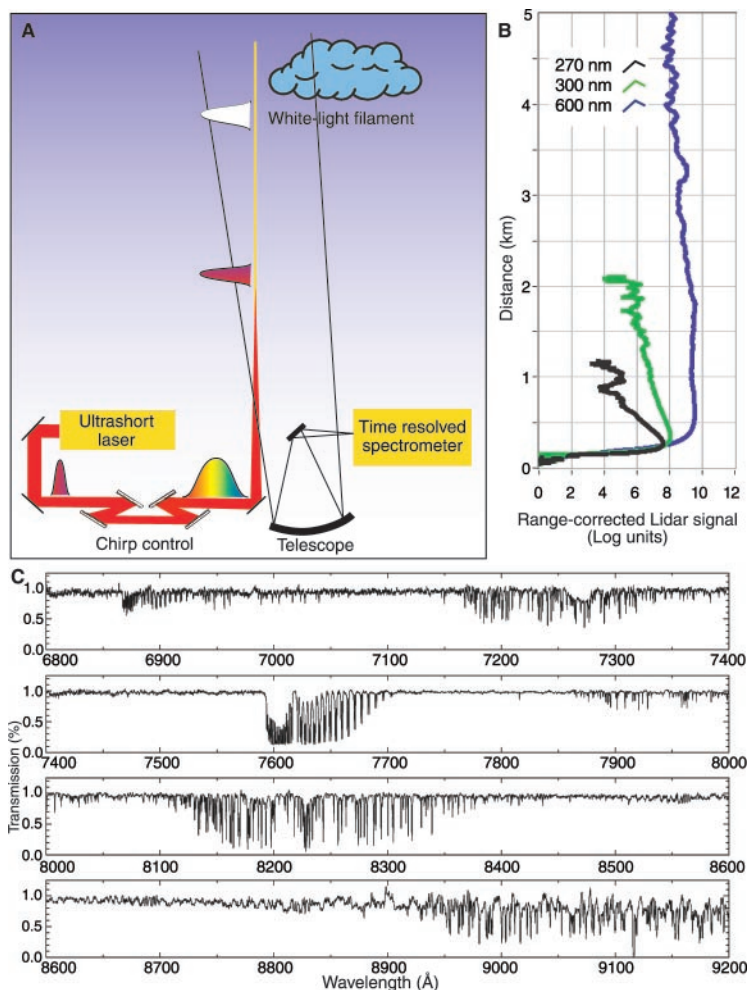


**Fig. 2.** White-light LIDAR. (A) Schematic of the LIDAR experimental setup. Before launch into the atmosphere, the pulse is given a chirp, which counteracts GVD during its propagation in air. Hence, the pulse recombines temporally at a predetermined altitude, where white-light continuum is produced, and then is backscattered and detected by LIDAR. (B) Vertical white-light LIDAR profile at three wavelengths: 270 nm (third harmonic), 300 nm, and 600 nm. (C) High-resolution atmospheric absorption spectrum from an altitude of 4.5 km measured in a LIDAR configuration.

### Atmospheric Experiments

Atmospheric diagnostics based on nonlinear optical processes like white-light generation, multiphoton-induced fluorescence, or harmonic generation require the delivery of high laser intensities at remote distances and high altitudes. Because filamentation counteracts diffraction over long distances, it is better suited to that purpose than is linear propaga-

tion over km-range distances can only be performed realistically in outdoor experiments. The fs-LIDAR measurements have to be performed where relevant gaseous or aerosol pollutants occur, for example, in urban areas or at industrial sites. Laser-lightning studies require spots where the lightning probability is high, as well as test experiments at high-voltage facilities. These considerations clearly define the need for a mobile fs-TW laser system embedded in a standard freight container-integrated laboratory equipped with the necessary LIDAR detection, power and cooling supplies, temperature stabilization, vibration control, and an additional standard LIDAR system to ensure eye safety.

These requirements were achieved by the Teramobile system (23). The laser itself is based on the chirped-pulse amplification technique (24), with a Ti:sapphire oscillator and a Nd-yttrium aluminum garnet (YAG)-pumped Ti:sapphire amplification chain. It provides 350-mJ pulses with a 70-fs duration, resulting in a peak power of 5 TW at a wavelength of  $\sim 800$  nm and a repetition rate of 10 Hz. Its integration in the reduced space of the mobile laboratory required a particularly compact design. The classic compressor setup has been improved into a chirp generator to precompensate the GVD in air. Combined with an adjustable focus, this setup permits us to control the distance of the onset of filamentation and its length. The LIDAR detection chain is based on a 40-cm receiving telescope, a high-resolution spectrometer equipped with a set of gratings, and detectors allowing simultaneous temporal and spectral analysis of the return signal in a wavelength range between 190 nm and 2.5  $\mu\text{m}$ .

## LIDAR

The principle of standard LIDAR systems is based on the effect of optical scattering of emitted light on atmospheric constituents. The Rayleigh-, Raman-, fluorescence, or Mie-scatter processes at a distance  $R$  all return a small portion of the emitted light back to the observer. This necessarily leads to an unfavorable  $1/R^2$  dependency of the received light. Arc lamp-based LIDAR experiments have shown previously that the spectrally dispersed signal on the receiver is usually too weak to allow identification of atmospheric trace substances. The same question must be raised for the fs-LIDAR measurements as well because of the broad spectrum of the white-light supercontinuum. However, the strong backward component of the supercontinuum (21) opens the opportunity to establish a directional, white-light source in the atmosphere, radiating predominantly in the backward direction.

The fs-LIDAR experimental setup is shown in Fig. 2A. After passing a (negative) chirp generator, the fs-laser pulses are launched into the atmosphere. As a result, filaments are generated at a predetermined distance. The backscattered white light is then collected by a telescope and focused through a spectrometer on a time-resolved detector. Figure 2B shows three transients of spectrally filtered return signals recorded in the time window after the laser was fired: two, as an indicator for white light, were recorded at  $\lambda = 300$  and 600 nm; the other was recorded at the third-harmonic (TH) wavelength ( $\lambda = 270$  nm) (25). The vertical axis indicates the altitude at which the signals were backscattered. The initial strong signal increase is due to the progressive overlap between laser and telescope field of view. The white-light signal at 600 nm reaches an altitude of  $>5$  km. Stronger Rayleigh scattering at shorter wavelengths causes the UV wavelengths to vanish shortly above 1 km. The strong decrease of the TH signal is due to a high tropospheric ozone concentration (typically 100  $\mu\text{g}/\text{m}^3$ ) at the time of measurement.

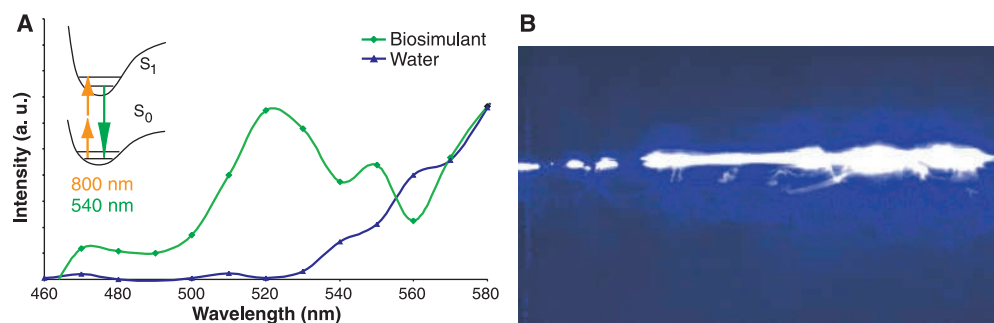


**Fig. 3.** Analysis (A) and synthesis (B) of aerosols with ultrashort laser. (A) LIDAR signal of the two-photon excited fluorescence from a biosimulant (riboflavin-doped water droplets) at a 50-m distance. (B) Laser-induced nucleation of water droplets in a cloud chamber. Nucleated aerosols are visible as a bright line over several tens of cm along the laser beam because they scatter light from the subsequent laser pulses.

The ability to perform high-resolution measurements over a wide spectral range using white-light LIDAR is illustrated in Fig. 2C. The measurement was recorded at an altitude of 4.5 km; it presents the highly resolved optical fingerprints of the atmosphere along this very long absorption path, allowing us to record extremely weak lines. The richness of the apparent atmospheric absorption lines represents, for example, extended ro-vibrational progressions of highly forbidden transitions of  $\text{O}_2$  (with cross sections in the range of  $10^{-25}$  to  $10^{-24}$   $\text{cm}^2$ ). Simulations based on the high-resolution transmission (HITRAN) molecular absorption database of the water lines yield almost perfect agreement with the measured result (6). The experimental data also reveal lines that are not tabulated in the database. The achievable resolution sug-

gests the possibility of retrieving even humidity and temperature profiles. The use of white-light LIDAR has been demonstrated in the UV, where extended sequences of tropospheric-ozone profiles have been deduced from multispectral measurements, as well as in the infrared, where higher conversion efficiencies have been observed (26). White-light LIDAR might also simultaneously yield wind profiles through the measurement of Doppler shifts.

## Aerosols

Aerosols are a key component of atmospheric pollution. They can act, for example, as catalysts for heterogeneous chemistry or as carriers for adsorbed carcinogenic species into the lungs. More recently, the prospect of bioterrorist attacks has increased the urgency for an early-warning system based on selective remote sensing of aerosols. The strong scattering by atmospheric aerosols allows ready LIDAR observation. However, their diversity of size, shape, and composition makes their remote identification a difficult challenge. Using multispectral LIDAR techniques (27), we can retrieve the abundance, particle size, and refractive index, but at

present this can only be done with aerosol models. No remote-sensing method yet allows us to determine the composition of aerosols. The high peak power of the fs pulses offers the possibility of achieving this goal by generating nonlinear effects directly inside the aerosol particles. Ultrashort pulses are focused onto a bright hot spot inside a liquid droplet as it forms a spherical microcavity. At this location, the cross section for nonlinear processes like multiphoton-excited fluorescence (MPEF) is enhanced (28). Although this fluorescence light is emitted isotropically from the hot spot, the reciprocity principle ensures that it is refocused into the backward direction by the droplet itself, favoring its detection by LIDAR. Moreover, signal optimization by pulse shaping would yield unique shaping signatures for individual fluorophores (29). This signature could allow us

## REVIEW

to identify species despite their similar fluorescence spectra.

We recently applied the MPEF process to the remote identification of clean and contaminated water particles (30). In the experiment, we produced a controlled distribution of water droplets of about 1.5  $\mu\text{m}$  diameter in an open cloud chamber, which was placed 50 m away from the Teramobile system. The droplets were doped with the biosimulant riboflavin, which exhibits a characteristic fluorescence emission around 540 nm. When the cloud was illuminated with adequate peak power (250 GW), a two-photon excited fluorescence signal (Fig. 3A) emerged from the riboflavin-containing droplets, allowing us to unambiguously identify the signature of the biosimulant. This result demonstrates the ability of nonlinear LIDAR to distinguish bio-aerosols from natural background aerosols of the same size (Fig. 3A).

The ionized laser-induced filaments also provide the opportunity to detect supersaturation of the atmosphere directly. Supersaturation refers to an atmosphere in which water vapor has not condensed to form clouds, despite thermodynamic conditions (humidity, temperature, and pressure) that imply condensation at equilibrium. Condensation requires sufficient nucleation germs, either natural or artificial, for example, heavy molecules such as AgI. Charges induced by laser filaments—instead of the commonly used ionizing radiation from a radioactive source—can serve as nucleation germs. In our experiments, we sent fs-laser pulses into a fog chamber, allowing the supersaturated water vapor to nucleate around the radiation-induced charges. Strong droplet formation was observed inside the chamber after each laser shot (Fig. 3B). This result demonstrates the possibility of creating laser-induced nucleation germs at distances that can be controlled by the laser chirp. The ability to determine by remote probing whether the atmosphere is supersaturated is of great importance for the prediction of rain, hail, or snow.

### Toward Lightning Control

The possibility of triggering and guiding lightning with laser beams has been debated for more than 30 years (31). The main concern is to protect sensitive sites, such as electrical installations or airports, from direct strikes and electromagnetic perturbations. Early studies in the 1970s and 1980s with nanosecond lasers (32) showed severe limitations arising from the lack of connected plasma channels. However, the advent of high-power fs lasers, which produce ionized plasma channels with electron densities several orders greater than that required for lightning initiation in the atmosphere,  $N_{\text{init}} \approx$

$5 \times 10^{11} \text{ cm}^{-3}$  (33), opened new opportunities in this domain (34).

Rodriguez *et al.* recently demonstrated simultaneous triggering and guiding of large gap discharges in air by laser filaments (35). The Teramobile system was placed inside the high-voltage (HV) facility of the Technical University of Berlin, with its horizontal output beam in line with the electrodes. The filament spanned the whole 1- to 3-m gap between the electrodes (Fig. 4A). Figure 4B shows a typical erratic discharge between the two electrodes when no laser filament is present. Once the filaments are properly located and timed with respect to the HV pulse, a fully guided straight discharge (Fig. 4C) is obtained. Moreover, the breakdown voltage is reduced by  $>30\%$ , demonstrating the abil-

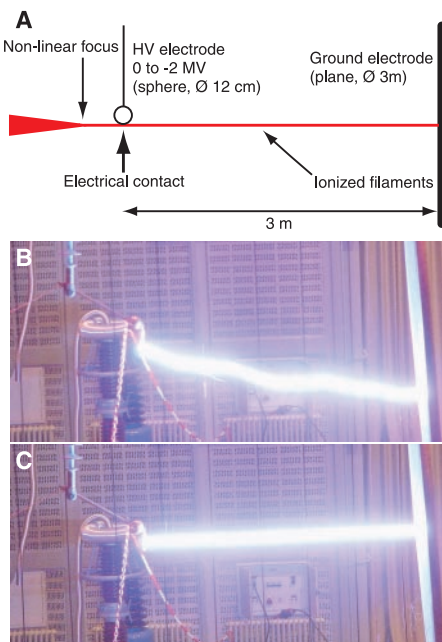


**Fig. 4.** Laser control of high-voltage discharges. (A) Experimental setup. (B) Free discharge over 3 m, without laser filaments. Note the erratic path. (C) Straight discharge guided along laser filaments.

ity of fs-laser filaments to trigger HV discharges by ohmic bridging of the electrodes. The experiment opens fascinating perspectives with regard to fs filament-induced triggering of lightning.

### Conclusion

In the past few years, knowledge about the propagation of ultrashort laser pulses in air and the related nonlinear optical effects has progressed steadily. In particular, the extended fs laser-induced white-light filaments hold promise for applications in atmospheric science. Several encouraging experiments have raised hopes for fs laser-based lightning control and protection, as well as for remote analysis of the atmosphere in the fields of

multicomponent trace-gas diagnosis by fs white-light LIDAR, composition analysis of aerosols, and detection of atmospheric supersaturation. The development of these applications will further be assisted by the expected progress in ultrafast laser technology, such as direct diode pumping, miniaturization, and the development of two-dimensional beam profile and pulse-shaping techniques. Such innovations will greatly improve the versatility, reliability, and ease of operation of fs laser sources and hence make them even more valuable for atmospheric applications.

### References and Notes

1. R. A. Meyers, Ed., *Encyclopedia of Analytical Chemistry* (Wiley, Chichester, UK, 2000), vol. 3.
2. A. Braun *et al.*, *Opt. Lett.* **20**, 73 (1995).
3. E. T. J. Nibbering *et al.*, *Opt. Lett.* **21**, 62 (1996).
4. A. L. Gaeta, *Science* **301**, 54 (2003).
5. L. Wöste *et al.*, *Laser Optoelektron.* **29**, 51 (1997).
6. P. Rairoux *et al.*, *Appl. Phys. B* **71**, 573 (2000).
7. H. Schillinger, R. Sauerbrey, *Appl. Phys. B* **68**, 753 (1999).
8. S. Tzortzakos *et al.*, *Opt. Commun.* **181**, 123 (2000).
9. A. Brodeur *et al.*, *Opt. Lett.* **22**, 304 (1997).
10. M. Mlejnek *et al.*, *Opt. Lett.* **23**, 382 (1998).
11. Y. R. Shen, *The Principles of Nonlinear Optics* (Wiley, New York, 1984).
12. M. Mlejnek, E. M. Wright, J. V. Moloney, *Opt. Express* **4**, 223 (1999).
13. N. Aközbeek, C. M. Bowden, A. Talepbour, S. L. Chin, *Phys. Rev. E* **61**, 4540 (2000).
14. A. Couairon, S. Tzortzakos, L. Bergé, M. Franco, B. Prade, A. Mysyrowicz, *J. Opt. Soc. Am. B* **19**, 1117 (2002).
15. P. Sprangle, J. R. Peñano, B. Hafizi, *Phys. Rev. E* **66**, 046418 (2002).
16. H. R. Lange *et al.*, *Phys. Rev. Lett.* **81**, 1611 (1998).
17. J. Kasparian, R. Sauerbrey, S. L. Chin, *Appl. Phys. B* **71**, 877 (2000).
18. J. Kasparian *et al.*, *Opt. Lett.* **25**, 1397 (2000).
19. N. Aközbeek *et al.*, *Opt. Commun.* **191**, 353 (2001).
20. O. G. Kosareva, V. P. Kandidov, A. Brodeur, C. Y. Chen, S. L. Chin, *Opt. Lett.* **22**, 1332 (1997).
21. J. Yu *et al.*, *Opt. Lett.* **26**, 533 (2001).
22. M. Mlejnek, M. Kolesik, J. V. Moloney, E. M. Wright, *Phys. Rev. Lett.* **83**, 2938 (1999).
23. H. Wille *et al.*, *Eur. Phys. J. Appl. Phys.* **20**, 183 (2002).
24. D. Strickland, G. Mourou, *Opt. Commun.* **56**, 219 (1985).
25. N. Aközbeek *et al.*, *Phys. Rev. Lett.* **89**, 143901 (2002).
26. G. Méjean *et al.*, *Appl. Phys. B*, in press.
27. B. Stein *et al.*, *J. Geophys. Res.* **104**, 23983 (1999).
28. V. Boutou *et al.*, *Appl. Phys. B* **75**, 145 (2002).
29. T. Brixner, N. H. Damrauer, P. Niklaus, G. Gerber, *Nature* **414**, 57 (2001).
30. G. Méjean, J. Kasparian, S. Frey, E. Salmon, J. Yu, J.-P. Wolf, in preparation.
31. D. W. Koopman, T. D. Wilkerson, *J. Appl. Phys.* **42**, 1883 (1971).
32. M. Miki, Y. Aihara, T. Shindo, *J. Phys. D: Appl. Phys.* **26**, 1244 (1993).
33. X. M. Zhao, J.-C. Diels, C. Y. Wang, J. M. Elizondo, *IEEE J. Quantum Electron.* **31**, 599 (1995).
34. H. Pépin *et al.*, *Phys. Plasmas* **8**, 2532 (2001).
35. M. Rodriguez *et al.*, *Opt. Lett.* **27**, 772 (2002).
36. The Teramobile project is funded by the Centre National de la Recherche Scientifique (France) and the Deutsche Forschungsgemeinschaft (Germany). We thank C. Bréchnignac for discussions. We are grateful to the Humboldt Foundation (A.M.) and the Institut Universitaire de France (J.-P. W.) for financial support. The team at the Thüringer Landessternwarte Tautenburg helped with vertical imaging experiments. We acknowledge support by the technical staffs in Berlin, Jena, and Lyon, and in particular by M. Barbaire, M. Kerleroux, M. Kregielski, M. Néri, F. Ronneberger, and W. Ziegler. The Teramobile Web site is at [www.teramobile.org](http://www.teramobile.org).

**Kilometer-range nonlinear propagation of femtosecond laser pulses**

Miguel Rodriguez,<sup>1</sup> Riad Bourayou,<sup>1,2</sup> Guillaume Méjean,<sup>3</sup> Jérôme Kasparian,<sup>3,\*</sup> Jin Yu,<sup>3</sup> Estelle Salmon,<sup>3</sup> Alexander Scholz,<sup>4</sup> Bringfried Stecklum,<sup>4</sup> Jochen Eislöffel,<sup>4</sup> Uwe Laux,<sup>4</sup> Artie P. Hatzes,<sup>4</sup> Roland Sauerbrey,<sup>2</sup> Ludger Wöste,<sup>1</sup> and Jean-Pierre Wolf<sup>3</sup>

<sup>1</sup>*Teramobile, Institut für Experimentalphysik, Freie Universität Berlin, Arnimallee 14, D-14195 Berlin, Germany*

<sup>2</sup>*Teramobile, Institut für Optik und Quantenelektronik, Friedrich-Schiller-Universität Jena, Max-Wien-Platz 1, D-07743 Jena, Germany*

<sup>3</sup>*Teramobile, LASIM, UMR CNRS 5579, Université Claude Bernard Lyon 1, 43 boulevard du 11 Novembre 1918, F-69622 Villeurbanne Cedex, France*

<sup>4</sup>*Thüringer Landessternwarte Tautenburg (TLS), Karl-Schwarzschild-Observatorium, Sternwarte 5, D-07778 Tautenburg, Germany*

(Received 30 September 2003; published 30 March 2004)

Ultrashort, high-power laser pulses propagating vertically in the atmosphere have been observed over more than 20 km using an imaging 2-m astronomical telescope. This direct observation in several wavelength bands shows indications for filament formation at distances as far as 2 km in the atmosphere. Moreover, the beam divergence at 5 km altitude is smaller than expected, bearing evidence for whole-beam parallelization about the nonlinear focus. We discuss implications for white-light Lidar applications.

DOI: 10.1103/PhysRevE.69.036607

PACS number(s): 42.68.Wt, 42.68.Ay, 42.65.Jx, 42.65.Re

**INTRODUCTION**

High-power ultrashort (femtosecond) laser pulses propagate in air in a self-guided mode due to a dynamic balance between Kerr-lens focusing and defocusing on laser-induced plasma [1]. This results in a breakup of the beam in one or several filaments of about 100  $\mu\text{m}$  in diameter that propagate over distances much longer than the Rayleigh length. Each filament contains a very high, quasiconstant, intensity of typically  $10^{14}$  W/cm<sup>2</sup> [2,3], which allows efficient self-phase modulation and generation of a broadband white-light continuum spanning from the UV [4] to the mid-IR [5].

These properties open exciting perspectives for applications [6] such as white-light Lidar (light detection and ranging) [7,8] and laser lightning control [9,10]. These applications in turn stimulate the need for a better characterization of the filament formation over atmospheric scales, i.e., in the km range. In particular, the filaments onset and length are key parameters for spectroscopic measurements of atmospheric compounds and for depositing the desired intensities on remote targets. Wille *et al.* [11] have shown that the filament location strongly depends on the peak power and initial chirp. A negative chirp (i.e., launching the blue part of the spectrum before the red part) can be used to compensate group-velocity dispersion (GVD) in air, and thus to select the distance at which the Fourier components will recombine, leading to high intensity. Together with spatial focusing using a sending telescope, this “temporal focusing” allows us to select the distance at which filamentation will start. Filamentation lengths up to 200 m have been reported by La Fontaine *et al.* [12] on a horizontal optical path. Conversely, in vertical propagation, Rairoux *et al.* [7] have detected white light from altitudes as high as 13 km, but without evidence that the continuum was generated at that altitude rather than near to the ground, with subsequent linear propagation and elastic backscattering.

Vertical propagation is of particular interest because (1) the gradients in pressure and temperature with altitude modify the nonlinear propagation process [13] and (2) most of the atmospheric applications such as Lidar profiling and lightning control require a vertical laser emission. However, characterizing vertical propagation at high altitude is a difficult task because the strong nonlinearity of the problem prevents extrapolation from experimental results at short distances and/or reduced peak powers. Moreover, most numerical simulations [14,15,16] require unreasonable times to get insight in the km-range propagation. First theoretical results about propagation over kilometer-range distances have been reported recently, predicting an overall collapse of the pulse above 20 km altitude under adequate laser parameters [17]. However, this long-distance result was obtained at the cost of a simplified variational calculation, illustrating how difficult exact long-distance propagation simulations are. Propagation experiments at long distance are needed to validate such emerging numerical simulations, and to develop simpler models allowing reasonable computing times usable for applications. The current filament characterization techniques are based on filament conductivity [18,19], nitrogen fluorescence [20], sonometry [21], or terahertz radiation [22], which are local measurements, and thus unpractical for very-long distance measurements, especially in the vertical direction.

In this paper, we investigate the vertical propagation of ultrashort, high-power laser pulses over more than 20 km in the atmosphere. Spectral as well as geometrical data have been acquired using a large scale (2 m) imaging telescope and permit us to fully characterize the beam geometry, showing evidence of anomalous beam propagation on km scales. These measurements constitute a data set for nonlinear propagation in a gaseous medium with (known) decreasing pressure and temperature gradients. Moreover, the white-light generation at high altitudes is investigated as a function of the laser parameters, especially chirp and initial focusing. These data are used for the optimization of white-light Lidar configurations.

\*Email address: jkaspari@lasim.univ-lyon1.fr

## EXPERIMENTAL SETUP

Experiments were performed using the Teramobile system as ultrashort laser source. This mobile femtosecond laser system is described in detail elsewhere [11]. Briefly, it consists of a Ti:sapphire oscillator and CPA amplification chain integrated in a mobile laboratory. It also includes a full Lidar detection equipment. The Teramobile laser provides 100 fs pulses with a peak power of 3 TW in the near infrared (800 nm), at a repetition rate of 10 Hz. In most of the experiments, the laser beam was emitted vertically as a parallel beam with a typical  $1/e^2$  diameter of 3 cm. However, in some of the experiments, an off-axis sending telescope with a tunable focal length was used to expand the beam by a factor of 3, and focus it, with an adjustable focal length. In addition to focusing and initial diameter, the initial laser chirp was varied during the experiments by moving a grating in the compressor. Three chirp values have been used: a short pulse with slight GVD precompensation (150 fs pulse duration), as well as long pulses with strong GVD precompensation and anticompensation (both with 600 fs pulse duration). The focus and chirp changes did not alter the alignment of the laser beam, which remained vertical within  $\pm 0.3$  mrad along the whole experiment.

The Teramobile system was installed at a distance of 30 m from the  $f=4$  m, 2-m diameter telescope [23] of the Thüringer Landessternwarte (Thuringian State Observatory/TLS) in Tautenburg (Germany), used in its Schmidt (imaging) configuration. The imaging device was a CCD with  $2048 \times 2048$  pixels, providing an angular resolution of  $6 \mu\text{rad}/\text{pixel}$ . The sensitivity range of the CCD is 350 to 1000 nm. Integration times between 1 s and 1 h have been used, although typical exposure times ranged between 1 and 360 s. The good linearity of the 16-bit CCD camera allowed us to intercalibrate the relative intensity between images with different integration times.

The slightly off-axis position of the Teramobile, 30 m away from the telescope, allowed both (i) cross-section images of the beam on the bottom of clouds or haze layers acting as screens and (ii) side imaging of the Rayleigh-scattered light from the beam over large altitude ranges (Fig. 1). In the latter case, the precise altitude was retrieved using adequate triangulation. This range was cross checked by precise classical Lidar measurements of the cloud height in the near-IR channel. The astronomical telescope is always focused to infinity, generating a blur on the images, especially at low altitudes. When using the images to retrieve the beam divergence, the beam profiles measured are deconvolved with the blur function of the telescope at the considered distance.

Images have been taken with several glass filter sets (Table I), covering the visible and infrared sides of the white-light continuum, as well as the fundamental wavelength. To take into account the high dynamics of the white-light spectrum [5], the contribution of the fundamental to the overall signal going through each filter is estimated, based on an integration of the spectrum previously measured in the laboratory [5]. Filters B and BG, which have rejections of better

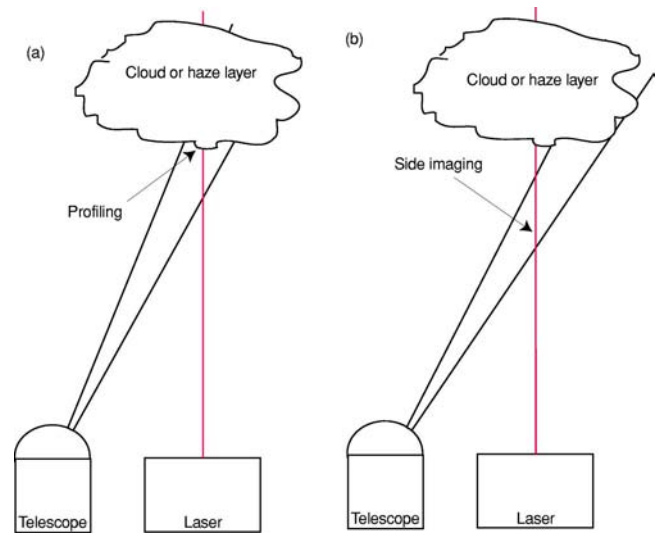


FIG. 1. (Color online) Principle of beam imaging. (a) Beam profiling on a cloud or haze layer. (b) Side imaging of the beam with Rayleigh scattering. In real pictures (see also Fig. 3), a combination of both components is visible together.

than  $10^{-15}$  around 800 nm, block the fundamental completely.

## RESULTS AND DISCUSSION

### Nonlinear propagation and filamentation

Nonlinear propagation and filamentation of ultrashort lasers in air have recently been studied both theoretically [15,24,25] and experimentally [26,27,28]. However, most of the studies were limited to short distance (up to some tens of m) and/or low pulse energy. When the laser pulse power is of the order of the critical power  $P_c \approx 3$  GW [29] the beam forms a single filament of typically  $100 \mu\text{m}$  in diameter, which can propagate over several meters. 10–20% of the total pulse energy (i.e., a few mJ) is then localized in the filamentary structure [30], while the rest of the energy remains in the surrounding unfocused beam that propagates with it. This surrounding “energy reservoir” dynamically feeds the filament [16,30] and allows it to propagate over long distances. The high intensity inside the filament ( $10^{14} \text{ W}/\text{cm}^2$ ) generates new frequencies in the laser spectrum by self-phase modulation (SPM), leading to a broad supercontinuum [Fig. 2(a)]. Part of this supercontinuum is, however, emitted in a narrow cone around the filament. The angle of this conical emission decreases with wavelength, contrary to usual diffraction [26,31,32].

When the laser pulse power reaches several  $10\text{--}100P_c$ , as is the case for TW lasers, the beam breaks up in many “cells,” which each contain about the critical power and generates a filament. The whole beam is formed of a large number of filaments, interacting with a surrounding “photon bath” containing the rest of the pulse energy. It has been predicted numerically that the beam as a whole, including the photon bath, propagates nonlinearly, with a turbulent energy exchange between permanently nucleating and dying filaments and the photon bath itself [16]. Figure 2(b) shows

TABLE I. Filters used.

Symbol	Filter	Wavelength range (combined with CCD efficiency, nm)		Contribution of the fundamental wavelength to the overall transmitted signal	Description
		10% of $T_{\max}$	50% of $T_{\max}$		
B	Johnson B+BG39, 8+2 mm	370–510	390–480		Blue white light
BG	BG39, 3 mm	340–610	370–580		Visible (green) white light
I	Johnson I, 8 mm	750–1000	770–950	50%	Fundamental wavelength
RG	RG850, 3 mm	830–1000	840–970	15%	IR white light

an experimental cross section of such a TW laser beam, after 15 m propagation. In this picture, an IR filter has been used to cut off the white-light continuum generated by each filament. Light emission from the different filaments has been found to be coherent [33]. Recent high-level three-dimensional (3D) [34] and 4D calculations (3D+time) [16] have been able to successfully simulate this behavior over ten to several tens of meters. Numerical instability related to the high nonlinearity of the nonlinear Schrödinger equation prevented simulations over longer distances. The propagation over longer (km-range) distances, and related questions such as (1) the filamentation length, (2) the propagation characteristics (e.g., divergence) of the whole beam including photon bath, and (3) the effect of pressure and temperature gradients are unknown so far.

#### Long-distance–high-resolution imaging of nonlinearly propagating TW lasers

Figure 3(a) displays a typical image in the fundamental wavelength channel of the femtosecond-TW laser beam, emitted as an initially parallel beam with 3 cm diameter. Elastic scattering is detected from the ground to an altitude of at least 25 km (integration time of 1 s). Similar measurements in the white-light band [BG filter, Fig. 3(b)] demonstrate efficient supercontinuum generation by SPM. Under haze-free conditions, white-light signals in the blue region (B filter) have been detected from altitudes beyond 18 km (exposure time of 360 s).

The image of the beam impact on the bottom boundary of the aerosol layer (e.g., cirrus clouds) can be seen as a remote

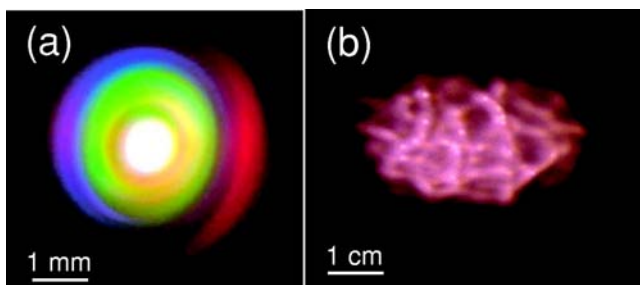


FIG. 2. (Color online) (a) Conical emission from a femtosecond laser beam in air, near the critical power  $P_{\text{cr}}$ . (b) Beam profile of a high-power beam ( $1000 P_{\text{cr}}$ ) after 15 m propagation. Multiple filamentation is clearly visible.

beam profiler. The depth of this nonopaque screen can lead to some slight image distortion and it decreases the image resolution. With higher aerosol density, multiple scattering induces some errors in the profile and affects the image resolution too. In our conditions, numerical simulations showed that the multiple scattering contribution distorts the beam profile on the cloud by less than 10%. Fluctuations due to cloud inhomogeneity are mainly smoothed out by time averaging. An example of such a remote profile of an initially focused ( $f=25$  m) beam, measured in the RG band (near infrared), is shown in Fig. 4. In this profile, taken from a cloud at an altitude of 9.6 km, a structure with two maxima is clearly visible. It is very interesting to notice that although the beam experienced nonlinear propagation and filamentation at lower altitude, this remote profile reflects the initial profile of the beam, which also exhibited a two-peaks mode (see inset). The beam seems therefore to keep a long term memory of its initial characteristics, which survived nonlinearity and modulational instability. Two key parameters are used to control the non-linear propagation and filamentation processes: temporal focusing (impinging an initial chirp to the pulse) and spatial focusing using the variable focal length sending telescope.

#### Filamentation altitude and control by temporal focusing

Beam profile images have been taken on a cloud at 6 km altitude in the white-light *B* band. The beam is sent parallel and with a very low GVD precompensation (corresponding to an initial duration of 150 fs of the launched pulse). The observed images on the cloud exhibit a ring structure around the laser beam, with a diameter of 32 m and a typical ring width of 6 m [Fig. 5(a)]. This ring is clearly the projection of conical emission from the filaments formed at lower altitudes. This allows us to estimate the altitude at which filamentation ends. In our case, the ring structure on the cloud leads to an half angle from ground of about 2.7 mrad and a ring width of 1 mrad. As this angle is typical for the angle of conical emission in this spectral region [27,31,32], we can conclude that the filaments are generated (and end) close to the ground level [see Fig. 5(b)]. This is consistent with previous short distance horizontal measurements, where filamentation started at 8 m and ended at 35 m from the system for a parallel beam with similar chirp configuration [11].

Figure 5(c) shows a transversal cut of the beam profile intensity [horizontal, passing through the maximum in Fig.

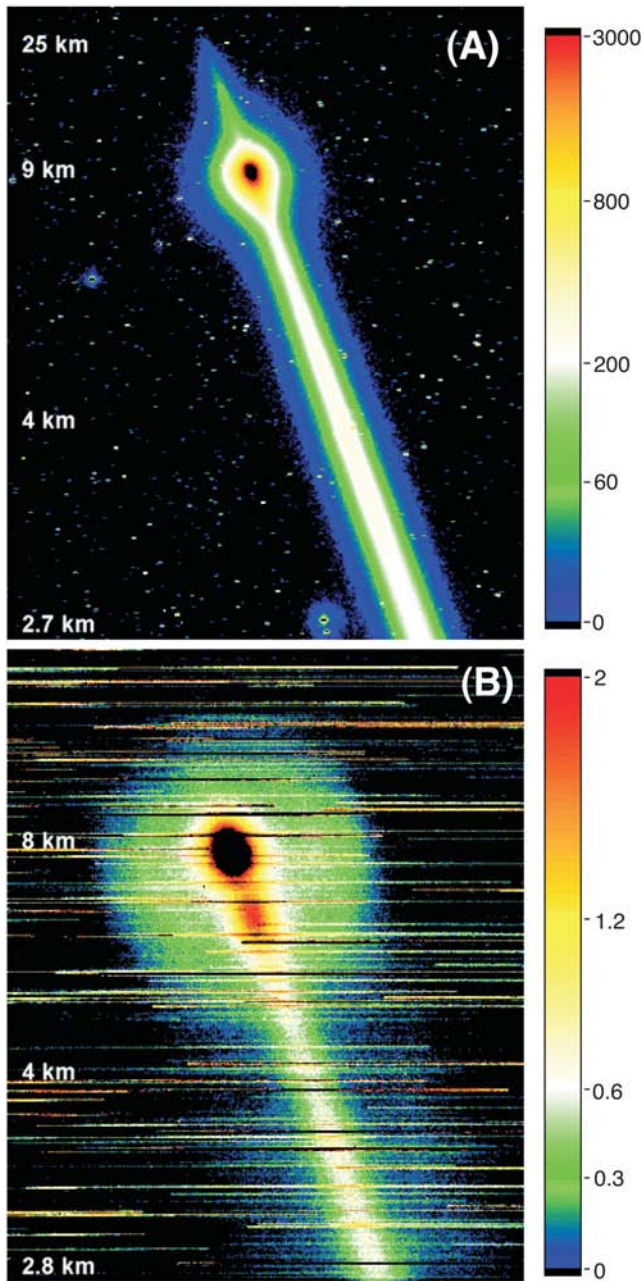


FIG. 3. (Color online) Typical fs beam image taken with the CCD camera of the Tautenburg observatory. (a) Fundamental wavelength, 1 s exposure time, (b) in the BG band, 180 s. The color scales indicate the signal intensities, normalized to the exposure time. The horizontal strips across the pictures are stars passing through the telescope field of view. Note the strongly nonlinear altitude scale due to triangulation. Both images correspond to slight GVD precompensation.

5(a)]. This curve can easily be reproduced by a simulated beam profile, calculated as follows. The white-light is assumed to have a flat wavelength dependence within the transmission window of the B filter. Hence, the measured spectrum is the transmission curve of the B filter. On the other hand, the wavelength dependence of the conical emission from the literature [27,31,32], can be seen as an inverse dispersion relationship, which, combined with the spectrum,

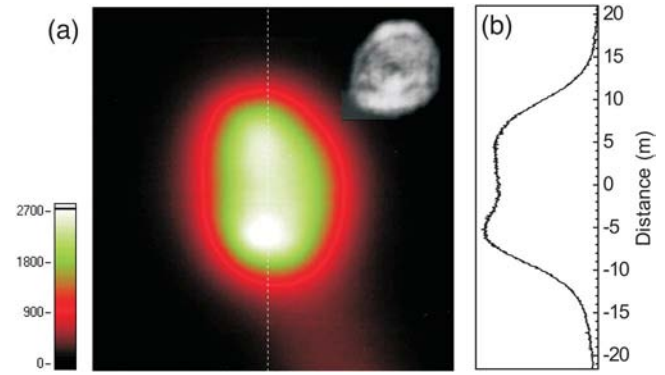


FIG. 4. (Color online) (a) Beam profile on an aerosol layer (thin cirrus) at 9.6 km altitude, showing a double structure in the beam (after focusing with  $f=25$  m). Inset: initial beam profile. (b) Intensity cut across the dotted line of image (a).

yields a spatial profile of the conical emission. Once superimposed with the central peak, this simulated beam profile fits the experimental one very well. Note that the lower contrast of the experimental data is due to the unsharpness of the image.

Radially integrating the simulated curve allows us to estimate that the ring structure accounts for 65% of the overall white-light energy in this band. This is the first time, to our knowledge, that the amount of white light emitted into the conical emission by long filaments has been estimated. Also notice that in our multifilamentation case, the observed conical emission is generated by the overlap of the conical emission of many filaments, forming a bundle inside the main laser beam, as shown above in Fig. 2(b).

A second set of images has been obtained using an initial negative chirp, corresponding to 600 fs pulse duration, to compensate GVD on longer distances. In this case the rings merge to the central peak, forming a narrow pedestal [Fig. 5(d)]. Considering that the initial chirp of the pulse does not affect the angle of conical emission [31], this reduced projected radius of conical emission is the signature for an emission occurring nearer to the cloud, i.e., at higher altitude [Fig. 5(e)]. The height of the conical emission has been fitted from the experimental curves, and amounts to  $2 \text{ km} \pm 0.5 \text{ km}$ . The uncertainty on the measurement is mainly due to the narrowness of the pedestal.

The same altitude change with chirp has been confirmed by results in the blue-green spectral region (BG filter). An independent estimation based on the reduction of the diameter of the central peak of the beam profile, as imaged on high-altitude clouds, also yield filaments in the range of 2 km altitude when GVD is adequately compensated. These estimations provide the first evidence, to our knowledge, of filamentation at km-range altitudes.

#### Beam divergence and spatial focusing effects

Outside the aerosol layers, Rayleigh scattering provides a side image of the beam. This allowed us to measure the divergence of the whole beam (which contains the filament bundle and the photon bath) by measuring its cross-section dimension as a function of altitude. Divergence measure-

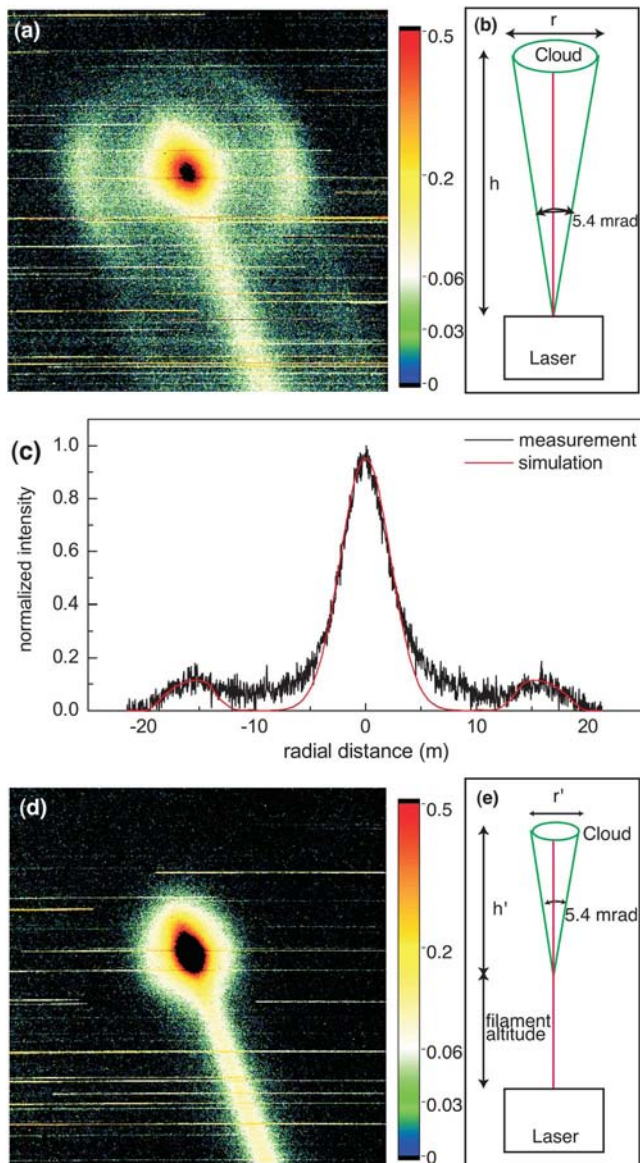


FIG. 5. (Color online) (a) Beam impact on a haze layer and cut across the impact, in the blue (B) band of the white light, with slight GVD precompensation. The conical emission ring is clearly visible. (b) Schematic of the ring emitted from low-altitude filaments imaged on high-altitude clouds. (c) Cross section profile through the intensity maximum of the image (a), and simulation of conical emission (for details see text). (d), (e) Same as (a) and (b) for a stronger GVD precompensation, pushing the filamentation to higher altitudes, and reducing the apparent diameter of the imaged conical emission.

ments were performed for both the fundamental wavelength and the white-light continuum.

By sweeping the telescope vertically along the beam and assembling eight images, we were able to determine the beam size from 600 m to 20 km altitude. For the first measurement of the beam divergence at the fundamental wavelength (I filter), the beam was sent parallel and with a slight GVD precompensation corresponding to an initial pulse duration of 150 fs. The beam divergence is found to be almost constant over the whole altitude range with a value of 0.16

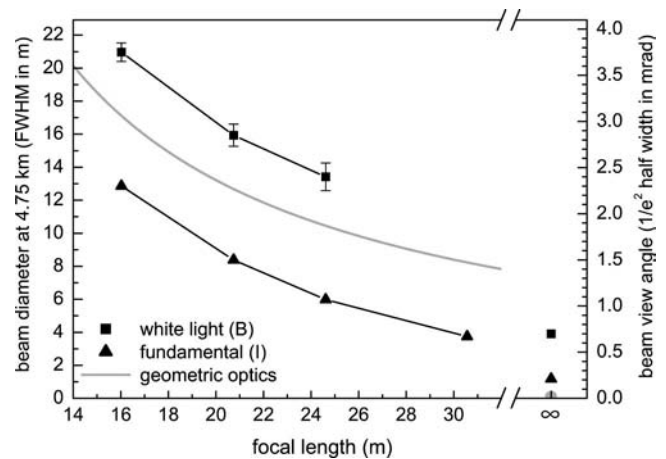


FIG. 6. Focus dependence of the beam divergence for filters B and I at 4.8 km altitude, with slight GVD precompensation. Both vertical scales (left: FWHM in meter, right:  $1/e^2$  half angle in mrad) are valid for all the points. The error bars in the range of the symbol sizes have been omitted. For infinite focal length, the gray dot indicates the diffraction limit.

mrad (half angle at  $1/e^2$ ), three times the specified divergence of the laser output.

No significant effect on the whole fundamental wavelength beam divergence was observed by changing the initial chirp settings. We evaluated the effect of initial spatial focusing, by varying the transmitter focal length from 16 to 30 m. The results are summarized in Fig. 6. The divergence of the beam at 800 nm steadily decreases with focal length from 2.3 mrad to 0.6 mrad, respectively. Geometric optics predicts that the respective opening angle (divergence) after focus (see the gray line in Fig. 6) is significantly larger than the observed divergence. The difference between the two curves is almost constant and amounts to 0.6 mrad. This is the signature for an overall nonlinear parallelization of the whole beam near the focus, showing evidence for a nonlinear propagation not only of the filaments, but of the beam as a whole, as predicted by Mlejnek *et al.* [16]. However, no further anomalous divergence of the beam as a whole was observed at high altitude (measured up to 18 km), as was, for example, predicted theoretically by Sprangle *et al.* [17]. Their simulation yields a collapse of the whole beam around 20 km altitude. However, their simulations are not directly comparable to our experimental results since they use longer, slightly focused pulses with much lower peak power, resulting in predicted self-focusing lengths in the 100-km range.

Divergence measurements were also performed for the white-light supercontinuum generated by SPM. When the beam is sent parallel, the white light contained in the whole beam is significantly more divergent than the fundamental, e.g., 0.7 mrad in the B band instead of 0.16 mrad. This value is larger than a diffraction-limited behavior of the whole 3 cm beam, but still much smaller than would be expected from diffraction at the exit of a commonly considered 100  $\mu\text{m}$  filament. This suggests that the filaments vanish gradually, with their diameter increasing up to about 300  $\mu\text{m}$  near their end, where the white light is released. Note that such a large diameter was observed by Lange *et al.* in a gas cell

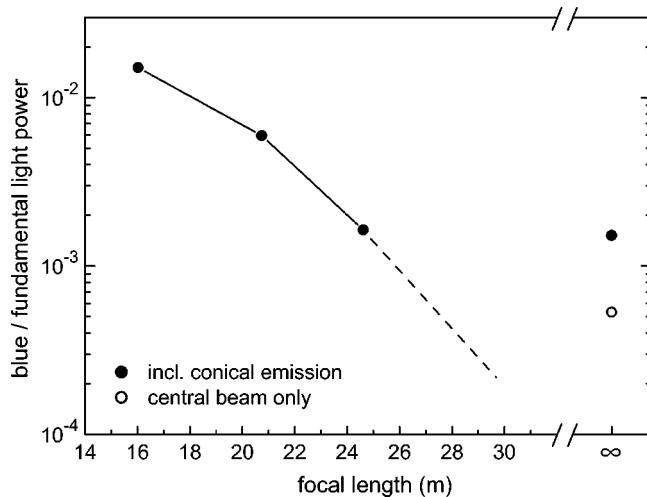


FIG. 7. Conversion efficiency at 4.8 km of the ultrashort pulses into the blue (B) band of the white-light continuum, as a function of focus. Note that the collimated beam (infinite focal length) has a smaller diameter than focused ones (3 cm instead of 10–12 cm), resulting in a more intense white-light generation. The signal for  $f=30$  m lies below detection limit, which amounts to  $2 \times 10^{-4}$ .

[35]. The small divergence of the white light might also be related to a recollimation by the Kerr effect after it exits the filament, or to multiple filaments acting as several coherent, in-phase point sources interfering to generate a narrow emission lobe. Anyway, this small divergence of the white light is favorable in view of Lidar applications, since the 0.7 mrad (half angle) value is in the same range or smaller than the field of view of typical Lidar receivers. This relatively collimated emission is consistent with the fact that the supercontinuum consists of coherent light [33].

The white-light divergence has also been measured as a function of the initial beam focusing (Fig. 6). It was derived in the blue band (B filter set) from the beam diameter on images far beyond the geometrical focus (at 4750 m distance). The white light is, again, more divergent than the fundamental wavelength. Its divergence is equal to that of conical emission from a single filament [27,31,32], convoluted with the divergence of the fundamental beam. This behavior is consistent with the idea that the white light is emitted by each filament with the same angular distribution as from single filaments, while the divergence of the filament bundle itself is imposed by the initial focusing.

#### White-light generation efficiency

In view of Lidar applications, the white-light generation efficiency is a key parameter. We have systematically studied the influence of GVD precompensation (chirp) and of the initial beam focusing on the white light conversion efficiency in the visible range at a remote location (4750 m altitude). We used I as the fundamental wavelength band and B as the white-light indicator. The intensity was estimated from a transverse integration of the beam profile on the haze layer. Figure 7 displays this white-light conversion efficiency into the B band as a function of the initial beam focus. Obviously, strong focusing yields more efficient white-light generation,

up to a factor of 50 compared to an initially parallel beam. Note that, in our experiment, the diameter of the parallel beam is 3 times smaller than the focused beam. This increases the incident intensity, causing stronger SPM and more filaments than for slightly focused beams with a larger initial diameter.

The effect of chirp was investigated by comparing the white-light generation efficiency of the unfocused laser into the BG band, for pulses with 600 fs initial pulse duration, but opposite chirps. The conversion efficiency is at least 6 times more efficient when the initial chirp compensates the GVD, than for GVD anticompensation. In the B band the factor seems to be larger, although it could not be measured precisely.

The above results show that the nonlinear process can be controlled and optimized by adjusting the initial chirp and focus of the laser beam. Even for the shortest focal lengths used, the white-light divergence is smaller than the typical Lidar receiver field of view (several mrad), which allows us to take benefit of the much higher conversion efficiency into the white light. Note that this behavior was actually observed in the UV [36]. Further investigation is required, however, to determine the optimal focus, which would correspond to a white-light divergence comparable to the Lidar receiver field of view.

#### CONCLUSION

As a conclusion, direct imaging observation of femto-second-terawatt laser pulses propagating in the atmosphere have shown evidence for remote nonlinear propagation of high-power ultrashort laser pulses in the atmosphere. Especially, we observed a nonlinear behavior of the beam as a whole [16], since the whole laser beam is partly recollimated near the nonlinear focus and filamentation occurs up to 2 km altitude. The focus dependence of the white-light generation efficiency and divergence yields indications for the optimization of white-light Lidar signals.

Remote imaging gives access to long-range observation of the nonlinear propagation of ultraintense laser beams as shown in this work, e.g., with the analysis of conical emission. Further work is required to characterize the propagation at medium-range distances, typically between 500 m and 5 km. Especially, *in situ* measurements would adequately complement our remote analysis. Moreover, extension of our results to the infrared side of the white-light continuum would allow us to compare the processes at play in its generation on both sides of the fundamental wavelength and the corresponding parameters for Lidar optimization.

#### ACKNOWLEDGMENTS

This work was performed in the framework of the Teramobile project, funded jointly by the Deutsche Forschungsgemeinschaft (Germany) and the Centre National de la Recherche Scientifique (France). We acknowledge support from the TLS technical team, especially J. Haupt, A. Kirchhof, M. Pluto, J. Winkler, and help from K. Stelmaszczyk and H. Wille. The Teramobile web site is [www.teramobile.org](http://www.teramobile.org)

- [1] A. Braun, G. Korn, X. Liu, D. Du, J. Squier, and G. Mourou, *Opt. Lett.* **20**, 73 (1995).
- [2] J. Kasparian, R. Sauerbrey, and S. L. Chin, *Appl. Phys. B: Lasers Opt.* **71**, 877 (2000).
- [3] A. Becker, N. Aközbeke, K. Vijayalakshmi, E. Oral, C. M. Bowden, and S. L. Chin, *Appl. Phys. B: Lasers Opt.* **73**, 287 (2001).
- [4] N. Aközbeke, A. Iwasaki, A. Becker, M. Scalora, S. L. Chin, and C. M. Bowden, *Phys. Rev. Lett.* **89**, 143901 (2002).
- [5] J. Kasparian, R. Sauerbrey, D. Mondelain, S. Niedermeier, J. Yu, J.-P. Wolf, Y.-B. André, M. Franco, B. Prade, A. Mysyrowicz, S. Tzortzakis, M. Rodriguez, H. Wille, and L. Wöste, *Opt. Lett.* **25**, 1397 (2000).
- [6] J. Kasparian, M. Rodriguez, G. Méjean, J. Yu, E. Salmon, H. Wille, R. Bourayou, S. Frey, Y.-B. André, A. Mysyrowicz, R. Sauerbrey, J.-P. Wolf, and L. Wöste, *Science* **301**, 61 (2003).
- [7] P. Rairoux, H. Schillinger, S. Niedermeier, M. Rodriguez, F. Ronneberger, R. Sauerbrey, B. Stein, D. Waite, C. Wedekind, H. Wille, and L. Wöste, *Appl. Phys. B: Lasers Opt.* **71**, 573 (2000).
- [8] G. Méjean, J. Kasparian, E. Salmon, J. Yu, J.-P. Wolf, R. Bourayou, R. Sauerbrey, M. Rodriguez, L. Wöste, H. Lehmann, B. Stecklum, U. Laux, J. Eislöf, A. Scholz, and A. P. Hatzes, *Appl. Phys. B: Lasers Opt.* **77**, 357 (2003).
- [9] B. La Fontaine, D. Comtois, C. Y. Chien, A. Desparois, F. Gérin, G. Jarry, T. W. Johnston, J. C. Kieffer, F. Martin, R. Mawassi, H. Pépin, F. A. M. Rizk, F. Vidal, C. Potvin, P. Couverture, and H. P. Mercure, *J. Appl. Phys.* **88**, 610 (2000).
- [10] M. Rodriguez, R. Sauerbrey, H. Wille, L. Wöste, T. Fujii, Y.-B. André, A. Mysyrowicz, L. Klingbeil, K. Rethmeier, W. Kalkner, J. Kasparian, E. Salmon, J. Yu, and J.-P. Wolf, *Opt. Lett.* **27**, 772 (2002).
- [11] H. Wille, M. Rodriguez, J. Kasparian, D. Mondelain, J. Yu, A. Mysyrowicz, R. Sauerbrey, J.-P. Wolf, and L. Wöste, *Eur. Phys. J.: Appl. Phys.* **20**, 183 (2002).
- [12] B. La Fontaine, F. Vidal, Z. Jiang, C. Y. Chien, D. Comtois, A. Desparois, T. W. Johnston, J.-C. Kieffer, H. Pépin, and H. P. Mercure, *Phys. Plasmas* **6**, 1615 (1999).
- [13] M. Mlejnek, E. M. Wright, and J. V. Moloney, *Phys. Rev. E* **58**, 4903 (1998).
- [14] A. Couairon and L. Bergé, *Phys. Rev. Lett.* **88**, 135003 (2002).
- [15] M. Mlejnek, E. M. Wright, and J. V. Moloney, *Opt. Express* **4**, 223 (1999).
- [16] M. Mlejnek, M. Kolesik, J. V. Moloney, and E. M. Wright, *Phys. Rev. Lett.* **83**, 2938 (1999).
- [17] P. Sprangle, J. R. Peñano, and B. Hafizi, *Phys. Rev. E* **66**, 046418 (2002).
- [18] H. Schillinger and R. Sauerbrey, *Appl. Phys. B: Lasers Opt.* **68**, 753 (1999).
- [19] A. Proulx, A. Talebpour, S. Petit, and S. L. Chin, *Opt. Commun.* **174**, 305 (2000).
- [20] A. Talebpour, S. Petit, and S. L. Chin, *Opt. Commun.* **171**, 285 (1999).
- [21] J. Yu, D. Mondelain, J. Kasparian, E. Salmon, S. Geffroy, C. Favre, V. Boutou, and J. P. Wolf, *Appl. Opt.* **42**, 7117 (2003).
- [22] S. Tzortzakis, G. Méchain, G. Pantalano, Y.-B. André, B. Prade, M. Franco, A. Mysyrowicz, J.-M. Munier, M. Gheudin, G. Beaudin, and P. Encrenaz, *Opt. Lett.* **27**, 1944 (2002).
- [23] H. Lehmann, URL <http://www.tls-tautenburg.de/telesc.html>
- [24] M. Mlejnek, E. M. Wright, and J. V. Moloney, *Opt. Lett.* **23**, 382 (1998).
- [25] L. Berge and A. Couairon, *Phys. Rev. Lett.* **86**, 1003 (2001).
- [26] A. Braun, G. Korn, X. Liu, D. Du, J. Squier, and G. Mourou, *Opt. Lett.* **20**, 73 (1995).
- [27] E. T. J. Nibbering, P. F. Curley, G. Grillon, B. S. Prade, M. A. Franco, F. Salin, and A. Mysyrowicz, *Opt. Lett.* **21**, 62 (1996).
- [28] A. Brodeur, C. Y. Chien, F. A. Ilkov, S. L. Chin, O. G. Kosareva, and V. P. Kandidov, *Opt. Lett.* **22**, 304 (1997).
- [29] Y. R. Shen, *The Principles of Nonlinear Optics* (Wiley, New York, 1984).
- [30] F. Courvoisier, V. Boutou, J. Kasparian, E. Salmon, G. Méjean, J. Yu, and J. P. Wolf, *Appl. Phys. Lett.* **83**, 213 (2003).
- [31] O. G. Kosareva, V. P. Kandidov, A. Brodeur, C. Y. Chen, and S. L. Chin, *Opt. Lett.* **22**, 1332 (1997).
- [32] J. Zhang, H. Yang, J. Zhang, X. Lu, Y. Li, Y. Li, H. Teng, Z. Chen, Z. Wei, and Z. Sheng (unpublished).
- [33] S. L. Chin, S. Petit, F. Borne, and K. Miyazaki, *Jpn. J. Appl. Phys.* **38**, L126 (1999).
- [34] L. Bergé, S. Skupin, F. Lederer, G. Méjean, J. Yu, J. Kasparian, E. Salmon, J. P. Wolf, M. Rodriguez, L. Wöste, R. Bourayou, and R. Sauerbrey, *Phys. Rev. Lett.* (to be published).
- [35] H. R. Lange, G. Grillon, J.-F. Ripoche, M. A. Franco, B. Lamouroux, B. S. Prade, A. Mysyrowicz, E. T. J. Nibbering, and A. Chiron, *Opt. Lett.* **23**, 120 (1998).
- [36] G. Méjean, R. Bourayou, S. Frey, M. Rodriguez, J. Yu, J. Kasparian, E. Salmon, R. Sauerbrey, L. Wöste, and J.-P. Wolf (unpublished).

# Remote LIBS with ultrashort pulses: characteristics in picosecond and femtosecond regimes†

Ph. Rohwetter,<sup>a</sup> J. Yu,<sup>\*b</sup> G. Méjean,<sup>b</sup> K. Stelmaszyk,<sup>a</sup> E. Salmon,<sup>b</sup> J. Kasparian,<sup>b</sup> J.-P. Wolf<sup>b</sup> and L. Wöste<sup>a</sup>

<sup>a</sup>Fachbereich Physik der Freien Universität Berlin, Institut für Experimentalphysik, Arnimallee 14, D-14195 Berlin, Germany

<sup>b</sup>Laboratoire de Spectrométrie Ionique et Moléculaire (LASIM), UMR CNRS 5579, Université Claude Bernard-Lyon 1, 43, Bd. du 11 Novembre 1918, F-69622 Villeurbanne Cedex, France. E-mail: jinyu@lasim.univ-lyon1.fr

Received 15th December 2003, Accepted 23rd February 2004  
First published as an Advance Article on the web 4th March 2004

Using a container-integrated mobile femtosecond terawatt laser system with integrated detection unit (Teramobile), we have demonstrated remote laser-induced breakdown spectroscopy (R-LIBS) on copper and aluminium samples with targets located at 25 m away from the container. The ability of our laser system to generate pulses in the femtosecond, picosecond and nanosecond regimes allowed us to perform direct comparisons between these three pulse durations. The dependence of the fluorescence signal on laser pulse energy showed a nonlinear behavior with a threshold, which is consistent with the previous observations for laser ablation. Such nonlinear behavior leads to a dependence of the LIBS signal on the temporal-spectral shape of the laser pulse. We showed especially that the transform-limited pulse does not optimize the fluorescence. A properly applied chirp allows an increase of the LIBS signal. Understanding and optimization of the chirp effect would improve the detection limit of the LIBS using a femtosecond laser (Femto-LIBS) and lead to a larger detection distance. Furthermore the use of pulse shaping should enhance the detection specificity for the cases of spectral overlapping between several elements to be identified.

## 1 Introduction

Laser-induced breakdown spectroscopy (LIBS) (known also as laser-induced plasma spectroscopy, LIPS) is a versatile analytical method which involves the interaction of a target with an intense laser pulse and the spectral analysis of the fluorescence emission from the generated plasma plume.<sup>1–4</sup> Since plasma production is possible with a sample without any preparation, LIBS is applied on gas, liquid, solid or particle state samples.<sup>5</sup> The applications of the LIBS technique are very broad.<sup>5</sup> They cover environmental monitoring (soil contaminations, air or water quality surveillance...), industrial processing by materials analysis (mineral resources, impurities, quality control, sorting...), biomedical studies (teeth, bones...), military and safety needs, space exploration, and art works analysis. Recent progress has enabled the LIBS techniques to go from laboratory to field applications: long-range open-path LIBS<sup>6</sup> as well as mobile LIBS<sup>7</sup> devices have been realized.

The detection limit of the LIBS technique actually lies in the range from 1 to 100 ppm for most of the elements,<sup>8,9</sup> much higher compared with other laser-based analytical methods, such as LIDAR (down to the ppb level, but only for gases).<sup>10</sup> Remote detection or element identification with LIBS is further limited by the difficulty of delivering high laser intensities over long distances in order to induce ionisation on the target. Increasing the efficiency and measurement range and lowering the LIBS detection limit are important issues for LIBS applications.

Besides the usual IR (typically Nd:YAG: 1064 nm) and visible (typically doubled Nd:YAG: 532 nm) pulse excitations, UV pulses (typically KrF: 248 nm) have been demonstrated to be able to achieve the same detection limit with much lower

laser pulse energy.<sup>11,12</sup> Double-pulse schemes have been proposed to improve the LIBS detection sensitivity. In such configurations, either a pre-ablation air plasma created near the sample surface by a first pulse depletes locally ambient air and enhances the ablation rate of the second pulse,<sup>13,14</sup> or the interaction between the second pulse and the plasma plume generated by the first pulse leads to a more efficient fluorescence emission.<sup>15</sup>

Ultrashort laser pulses with duration in the picosecond or femtosecond ranges represent attractive laser sources to design new and more sensitive LIBS systems. Not only have the advantages of such pulses in laser ablation and laser micro-machining been clearly demonstrated with lower ablation threshold and less thermal damages on the sample,<sup>16–18</sup> but also the development of laser diode pumping and of fibre systems promise compact and reliable ultrashort laser sources.<sup>19,20</sup> Recently 100 ps duration pulses obtained using compression by stimulated Brillouin scattering (SBS) has been applied to LIBS.<sup>21</sup> Picosecond or femtosecond pulse induced LIBS has been studied using mode-locked laser systems in laboratory experiments. Some comparisons have been performed in the ultrashort pulse regime with respect to the classical nanosecond regime.<sup>22,23</sup> Remote LIBS (R-LIBS) with pico- or femto-second laser systems had not been demonstrated so far, partially because usual ultrashort laser systems, especially those which deliver high pulse energy (suitable for remote detections), need a well controlled laboratory environment to run properly.

In this paper we show that using a container-integrated mobile terawatt femtosecond laser, together with the associated detection system (telescope, spectrometer, ICCD camera), it is possible to remotely induce and detect LIBS signals with signal to noise ratios allowing analytical applications. Systematic studies have been carried out with standard industry quality metallic samples (copper and aluminium) at a distance of 25 m to characterise the R-LIBS signal in the picosecond and femtosecond regimes. Comparisons are shown with the

† Presented at the Second Euro-Mediterranean Symposium on Laser Induced Breakdown Spectroscopy, Hersonissos, Crete, Greece, September 30th–October 3rd, 2003.

nanosecond regime. The dependences of the R-LIBS signal on the pulse energy and pulse chirp are experimentally studied, showing interesting results. The applications of these effects should lead to a more efficient LIBS with a lower detection limit and longer detection distance. Although a full understanding of the mechanisms involved is not achieved yet, we provide ideas to interpret the observed spectra or dependences. For applications, the obtained experimental data are very useful for the design of new LIBS systems based on ultrafast lasers. These data should also stimulate the development of new theoretical models in order to reach a better understanding of the LIBS in ultrashort and/or ultraintense pulse regimes.

## 2 Experimental set-up

As shown in Fig. 1, the experimental set-up consisted in two main parts: the laser system and the detection system. The ensemble is called a Teramobile<sup>24</sup> system. Both parts were contained in a standard container of 6 m length and 2.5 m width. The container is transportable and provides a stable environment for a proper operation of the both laser and detection systems under various climatic conditions. Once installed in an experimental site, only standard electricity and water supplies are needed for the stand-alone operation of the Teramobile system.

### 2.1 Laser system

A detailed description of the laser system can be found elsewhere.<sup>25</sup> Briefly, a commercial chirped-pulse-amplification (CPA)<sup>26</sup> chain (Thales Laser Company) was integrated in a standard container. The laser chain consisted of an oscillator, a

stretcher, a regenerative amplifier, a preamplifier, a main amplifier and a compressor. Operating at a wavelength of 795 nm and a repetition rate of 10 Hz, the chain delivered pulses of up to 350 mJ in energy and compressed to 75 fs minimal pulse duration.

One of the gratings in the compressor was mounted on a micro-displacement stage, enabling the control of the pulse duration from sub-100 fs to several ps. In the cases where output pulses were not compressed to their minimal duration, the pulses were temporally chirped. We could get either a positive chirp: the red components preceding the blue ones (the red first), or a negative chirp with a reverse ordering of different spectral components of the pulse (the blue first). The output pulse energy could be varied by rotating a  $\lambda/2$  plate associated with a polarizer, without any change in the pulse duration or in the pulse spatial profile. That allowed us to have a change of laser intensity on the samples linearly proportional to the change of the pulse energy.

The same laser provided pulses with 200 ps or 5 ns durations. Picosecond pulses were obtained by bypassing the compressor, while ns pulses were generated when the seeding of the regenerative amplifier by the oscillator pulses was removed. This specific feature of our laser allowed us to compare easily R-LIBS signals in the three pulse duration regimes. We remark that ps pulses were actually long positively chirped pulses with a perfect coherence between different spectral components. Spatial beam profiles for the three above pulse durations were quite similar and presented a flat-top form.

Output pulses were transmitted horizontally into the atmosphere after passing through a three-times beam expander with a convex and a concave mirror (Fig. 1, sending telescope). The convex mirror was mounted on a stepper motor, which precisely set the distance between the two mirrors to focus the output beam at a remote distance. At the output window of the container, the beam diameter was 15 cm. In our experiments, the laser beam was focused on the targets located 25 m away from the container.

### 2.2 Detection system

For the measurements presented in this paper, the detection system was located beside the laser in the container (Fig. 1). It consisted of a  $f/5$  aperture Newtonian telescope with a primary mirror of 10 cm in diameter. Light collected at the focus of the telescope was coupled into a bundle of fibres with a circular section for the input end and a rectangular section for the output end. The  $f$ -number of the fibre output was adapted to the input of a  $f/8$  ( $f = 500$  mm) spectrometer (Chromex 500IS/SM). An ICCD camera (Stanford Research Inc.) was mounted on the reciprocal plane to record spectra. With a 600 lines  $\text{mm}^{-1}$  grating, our detection had a resolution of about 0.0862  $\text{nm pixel}^{-1}$  on the ICCD. Typically we applied an entrance slit of 100  $\mu\text{m}$  aperture, which led to a final resolution of our detection of 0.34 nm. The ICCD camera was triggered by a photodiode detecting scattered light on the sending mirror due to output laser pulses. The gating of the intensifier of the camera was delayed with respect to the laser pulse by a delay generator (Stanford Research Inc.).

The spectral detectivity of our detection system was measured with a halogen lamp considered as a black-body source at a temperature of 3000 K. The detection system used was sensitive and calibrated between 450 and 950 nm.

The alignment of the detection system was performed with a low energy frequency-doubled YAG laser shooting on a target 25 m away from the container. The visible image of the impact spot of the laser on the target allowed us to set precisely the input end of the fibre on the focal point of the telescope. The initial distance between the laser and the telescope axis was 0.85 m. To increase the signal to noise ratio and to overcome the fluctuations due to laser pulse to pulse jitter, we typically

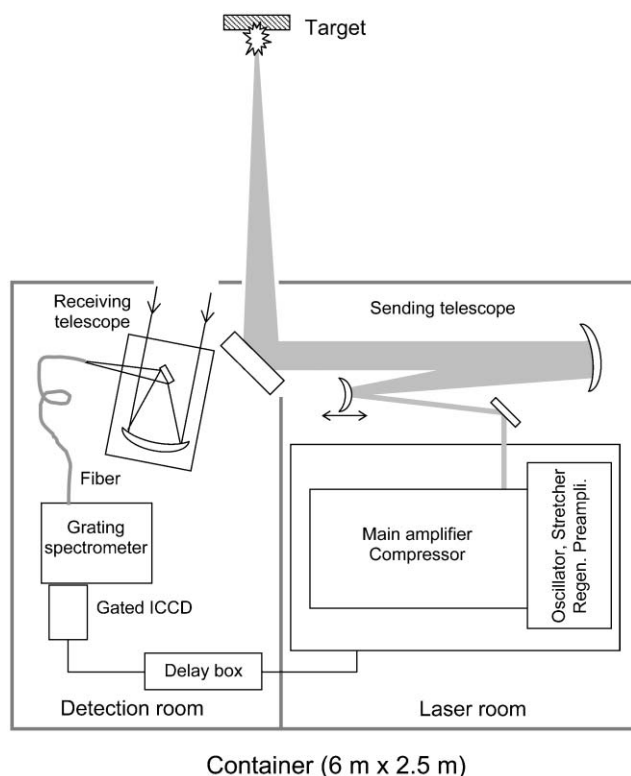


**Fig. 1** Schematic diagram of the experimental set-up including the stand-alone container divided inside into a laser room and a detection room, the femtosecond terawatt laser system, the reflective sending telescope, the receiving telescope, the transmitting fibre, the grating spectrometer, the gated ICCD camera, and the synchronization delay generator. The target was located at a distance of 25 m from the container. The output laser beam was focused by the sending telescope with a movable convex mirror to ensure an optimised beam focusing on the target.

took spectra with an accumulation of hundreds of laser shots, which represented an accumulation time of typically 0.5 min.

### 3 Experimental results

In this section the results are presented in the following way: in section 3.1, R-LIBS spectra from copper and aluminium samples are presented. We compare the spectra obtained with femtosecond, picosecond and nanosecond pulses. The decay of the R-LIBS signal as a function of the detection delay is presented in section 3.2. Section 3.3 is devoted to the dependences of the R-LIBS signal on the laser parameters. We especially discuss dependences of the fluorescence yield on the pulse energy and pulse chirp.

#### 3.1 Characteristics of R-LIBS spectra in the natural atmosphere

**3.1.1 Remote ablation with femtosecond and picosecond pulses.** We used industry-grade copper and aluminium bulk samples without any surface cleaning. Very small aging effects were observed on the copper sample. The recorded LIBS signal stabilized after the first several laser shots. Contrary to copper, the aging effect was clearly observed in aluminium. During the first minutes of laser shooting, the observed spectral intensity varied as a consequence of the surface cleaning by laser pulses. Afterwards the signal stabilized showing only small variations during further laser excitations. Photographs of laser impacts on the sample surfaces are shown in Fig. 2. For the same beam focusing, the laser craters are larger for femtosecond pulses. The observed difference in crater dimensions can be explained by an intensity threshold for laser ablation: the short duration of femtosecond pulses allows even the edge of the beam profile to reach the intensity threshold. For an estimation of the laser intensity deposited on the sample, we use the surface of the crater on the aluminium sample due to femtosecond pulses. The photograph (Fig. 2(b)) shows a surface of about  $34 \text{ mm}^2$  ( $8 \text{ mm} \times 4.2 \text{ mm}$ ). For the pulse energy of 225 mJ (corresponding to a fluence of  $0.66 \text{ J cm}^{-2}$ ) used to obtain the spectra shown in this section, an intensity of  $8.8 \times 10^{12}$ ,  $3.3 \times 10^9$  and  $1.3 \times 10^8 \text{ W cm}^{-2}$ , respectively, is associated with the femtosecond, picosecond and nanosecond pulses. It should be noted that these values correspond to averaged intensities (or fluence) over the beam profile. Much higher

intensities (or fluences) are reached at the center of the focused spot. Except for the results presented in the section 3.3.2, femtosecond pulses were always compressed to their minimal duration of 75 fs.

From Fig. 2, for picosecond pulses, a polished surface is observed in the center of the craters, testifying the melting phase of the surface following the interaction with a laser pulse. In the literature, temperatures exceeding 3000 K are reported in ns pulse produced plasma,<sup>27</sup> much higher than the melting temperatures of copper (1365 K) and aluminium (930 K). For femtosecond pulses, the observed craters show a rough aspect in the central part, with fringe-like structure (several 100  $\mu\text{m}$  period) for the copper sample.

By weighing the aluminium sample before and after 22 000 shots of femtosecond laser pulses, we found an ablated mass of 0.014 g, which corresponds to an ablation of about 640 ng per femtosecond pulse. This value is quite similar to that found for a thin aluminium film (500 nm thickness) ablated by femtosecond pulses.<sup>28</sup> A mass ablation rate can be calculated from the mass removed per pulse (for the pulse parameters of 75 fs duration, focused on a  $0.34 \text{ cm}^2$  spot, 150 mJ pulse energy,  $5.9 \times 10^{12} \text{ W cm}^{-2}$  average intensity), leading to a value of  $2.5 \times 10^7 \text{ g (cm s)}^{-1}$ . This value is more than two orders of magnitude higher than the value for nanosecond pulses at the same intensity.<sup>29,30</sup>

**3.1.2 Copper spectrum.** In Fig. 3 spectra obtained with femtosecond (Fig. 3(a)), and picosecond (Fig. 3(b)) pulses are presented. The delay and the gate width applied on the ICCD camera were 10 ns and 10  $\mu\text{s}$ , respectively, for femtosecond pulses, and 345 ns and 1  $\mu\text{s}$  for picosecond pulses. In the case of

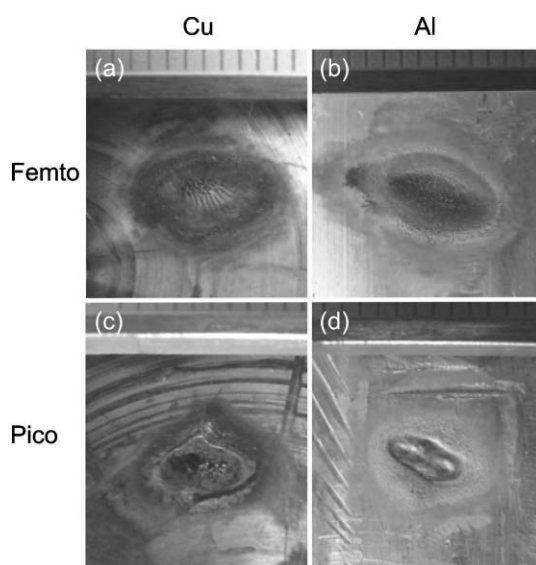


**Fig. 2** Photographs showing laser impacts on the targets: femtosecond pulses on the copper (a) and the aluminium (b) samples; picosecond pulses on the copper (c) and the aluminium (d) samples. The scales appearing on the tops of the photographs are in mm. All of the four photographs are presented in the same scale.

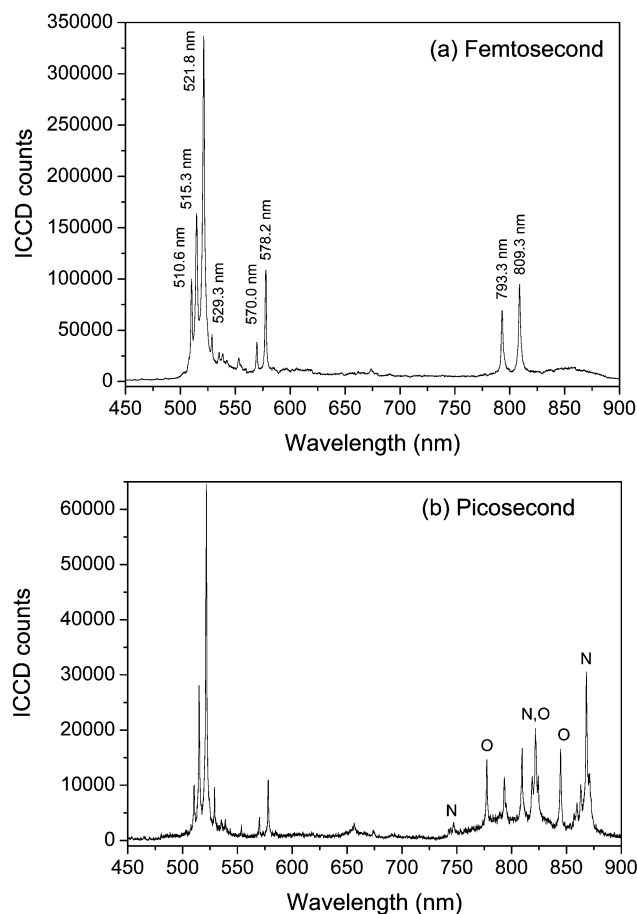


**Fig. 3** R-LIBS spectra for the copper sample at 25 m: (a) using 75 fs pulses, (b) using 200 ps pulses. Wavelengths of observed copper lines are indicated in (a), positions of observed atomic oxygen and nitrogen lines are indicated in (b).

femtosecond pulses, 400 laser shots were accumulated for each spectrum, while in the case of picosecond pulses, 150 shots were accumulated. The zero delay is defined as the arrival time of elastically scattered light from the target.

Using femtosecond pulses, atomic copper lines are well observed over a weak continuum. No ionic lines are observed in this spectral range in spite of the presence of ionic lines as indicated by the spectral database provided by the NIST.<sup>31</sup> Using picosecond pulses, additional lines are detected in the range between 700 and 900 nm. These additional lines are identified as belonging to atomic oxygen or atomic nitrogen. Using the NIST database, the corresponding lines are indicated in Fig. 3(b). The presence of these additional lines can be considered as due to a secondary plasma generated by the breakdown in air near the sample surface induced by the fast jet of laser-ablated material.<sup>32</sup> Direct breakdown in air induced by a laser pulse is not considered here, because of the small intensity in a picosecond pulse. The secondary air plasma also indicates a higher temperature in the plasma plumes induced by picosecond pulses than in those due to femtosecond pulses, which is consistent with the observation from the photographs of laser-induced craters. From the application point of view, femtosecond pulses induce a cleaner spectrum independent of the ambient gas, which is an appreciable quality for quick and precise identifications of elements in an unknown environment.

Starting from the signal to noise of the spectrum (521.82 nm line) shown in Fig. 3(a), which can be measured to be 110 (400 laser shots average), we can deduce a signal to noise ratio of 5.5 for a single shot spectrum. A single-pulse analysis capability of about a few 100 ng of copper can thus be expected for a sample at 25 m away from the laser, if we assume a similar mass ablation rate between copper and aluminium. Such an assumption is quite reasonable because similar mass ablation rates between copper and aluminium have been measured in the nanosecond regime.<sup>33</sup>

**3.1.3 Aluminium spectrum.** In Fig. 4 spectra obtained with femtosecond (Fig. 4(a)), picosecond (Fig. 4(b)) and nanosecond (Fig. 4(c)) pulses are presented. The delay and the gate width applied on the ICCD camera were 345 ns and 10  $\mu$ s, respectively. 400 shots were accumulated for the femtosecond spectrum and 200 shots for the picosecond and nanosecond ones.

For femtosecond pulses, in the spectral range of the detection, only lines belonging to the molecule AIO were observed ( $\text{AIO: B}^2\Sigma^+ \rightarrow \text{X}^2\Sigma^+$ ). No atomic or ionic Al lines were observed in spite of the presence of lines in this spectral range as indicated by the NIST database. The sodium 589 nm line is observed in the spectrum due to a contamination of the aluminium sample by salt.

The detection of the fluorescence of aluminium monoxide in a laser-ablated aluminium plasma has been reported previously with ns pulses.<sup>27,34</sup> AIO molecules are found to be either produced from laser ablation of alumina ( $\text{Al}_2\text{O}_3$ )<sup>27</sup> or formed in a gas-phase chemical reaction of Al vapor with a gas of atomic oxygen.<sup>34</sup> For an aluminium sample exposed in the atmosphere, the surface is quickly oxidized within the interval between two successive laser pulses. Moreover, the highly energetic material jet<sup>32</sup> ablated by a laser pulse produces near the aluminium surface an oxygen plasma, in which  $\text{Al} + \text{O} \rightarrow \text{AIO}$  reactions take place. The absence of atomic and ionic aluminium lines can be explained by either fast oxidation of the aluminium sample surface or fast chemical reaction between Al and O to form AIO. A white-light continuum is also observed in the spectrum, indicating the high temperature reached in the laser-induced plasma.

For picosecond pulses (Fig. 4(b)), in addition to the AIO lines, atomic oxygen and nitrogen lines are observed similarly as for the copper sample. However, two atomic aluminium lines (669.6 and 877.3 nm) are observed in the spectrum. The presence of these lines suggests a post-ablation interaction

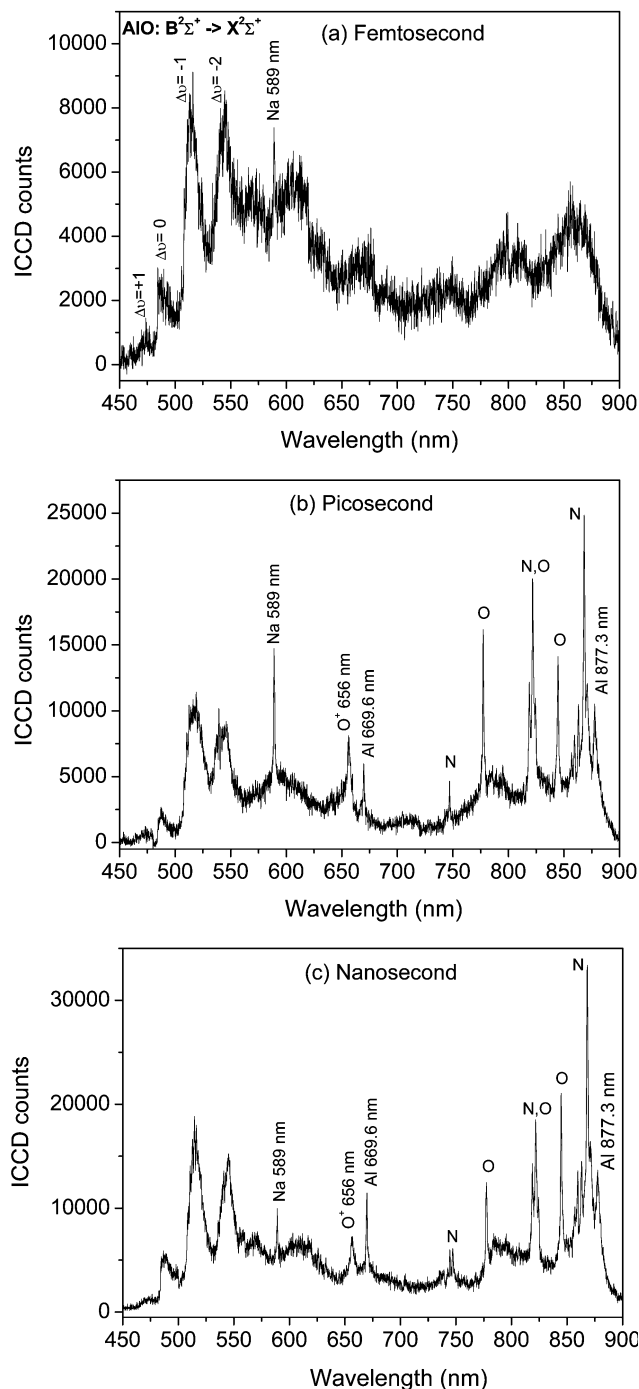


**Fig. 4** R-LIBS spectra for the aluminium sample at 25 m: (a) using 75 fs pulses, (b) using 200 ps pulses, (c) using 5 ns pulses. The observed AIO lines belong to the transition  $\text{B}^2\Sigma^+ \rightarrow \text{X}^2\Sigma^+$  with  $\Delta v = 1, 0, -1, -2$ . The observed atomic and ionic oxygen and nitrogen lines are indicated in (b) and (c). Note also two Al atomic lines as indicated in (b) and (c).

between the plasma plume and the tailing part of the laser pulse in the picosecond regime. With nanosecond pulses, the spectrum (Fig. 4(c)) has a similar behavior to the picosecond spectrum. This is not really a surprise because as for picosecond pulses, the post-ablation interaction plays an important role in the fluorescence generation in the nanosecond regime.

The signal to noise ratio is smaller for aluminium than for copper because our detection did not allow the measurements of intense Al lines in the blue and UV regions.

### 3.2 Decay of the R-LIBS signals

The decay of the laser induced fluorescence was studied using 160 mJ femtosecond and picosecond pulses. Spectra were

recorded with a fixed gate width of 10  $\mu\text{s}$  and an increasing detection delay. The large gate width of 10  $\mu\text{s}$  was used to increase the detected signal. However, since the used gate width is larger than the time constant of the LIBS signal decay, the detected signal is related to the integral of the instantaneous fluorescence from the target:  $S(\tau) = \int_0^\infty s(t)dt$ , where  $s(t)$  is the instantaneous signal at a time  $t$ ,  $S(\tau)$  the integrated signal detected with a delay  $\tau$  and a gate width much larger than the signal decay time constant. In such a mode of detection, the instantaneous signal  $s(t)$  can be extracted from the detected signal  $S(\tau)$ , by a derivation. Moreover if an exponential decay is assumed, either the instantaneous or integrated fluorescence signals have the same decay time constant. We remark here that the temporal behavior of the fluorescence might also be directly measured by applying a gate width much shorter than the time constant of the signal decay.

Fig. 5 shows normalized line intensities for the copper 510.6 and 515.3 nm lines, and the AlO  $B^2\Sigma^+ \rightarrow X^2\Sigma^+$ ,  $\Delta v = -1$  line induced by femtosecond pulses as a function of the detection delay. We note that the copper atomic lines decay faster than the AlO molecular line. For the two studied copper lines, the decay time constants are slightly different. This difference is not observed for the different AlO lines. For all lines studied, a decay time constant of several  $\mu\text{s}$  is observed, which is one order of magnitude longer than previously reported values obtained with low energy femtosecond pulses (1 mJ, 140 fs).<sup>35</sup> This difference indicates different interaction regimes with different fluences for femtosecond pulses.

The results in the picosecond regime are presented in Figs. 6 and 7. In Figs. 6(a) and 7(a), full spectra (with 400 laser shot accumulations), respectively, of copper and aluminium are presented for different delays from 10 ns up to 6  $\mu\text{s}$ . Differential decays are clearly observed between the copper or AlO/Al lines and the air plasma lines. With a large delay, a clean copper or AlO/Al spectrum is observed while air plasma lines almost completely disappear. Line intensities are extracted from the full spectra, and are presented, respectively, in Figs. 6(b) and 7(b) for copper and aluminium, and differential decays are shown clearly between metallic plasma fluorescence and air plasma fluorescence. The observed air plasma lifetime is already much longer than that of the air plasma (in the order of nanoseconds) induced directly by femtosecond laser pulses at the same intensity level as in our experiments.<sup>36</sup>

The generation of a secondary plasma in air in the vicinity of a solid or liquid surface by means of laser ablation provides also a means to chemically analyse the ambient air. An efficient fluorescence generation with a much longer lifetime compared to the direct plasma generation in air is expected.

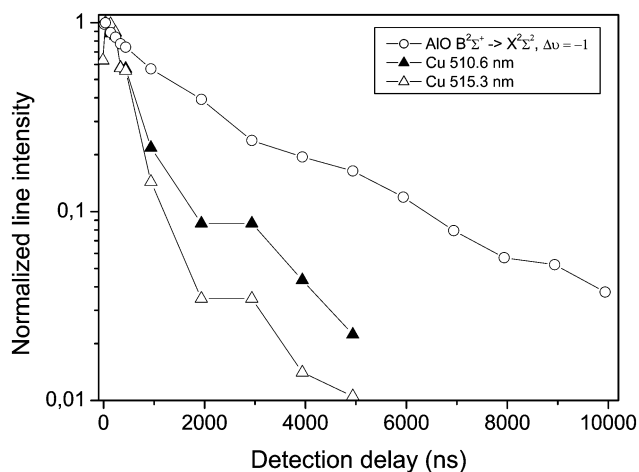


Fig. 5 Normalized spectral line intensities as a function of the detection delay with femtosecond pulse excitation for copper and aluminium.

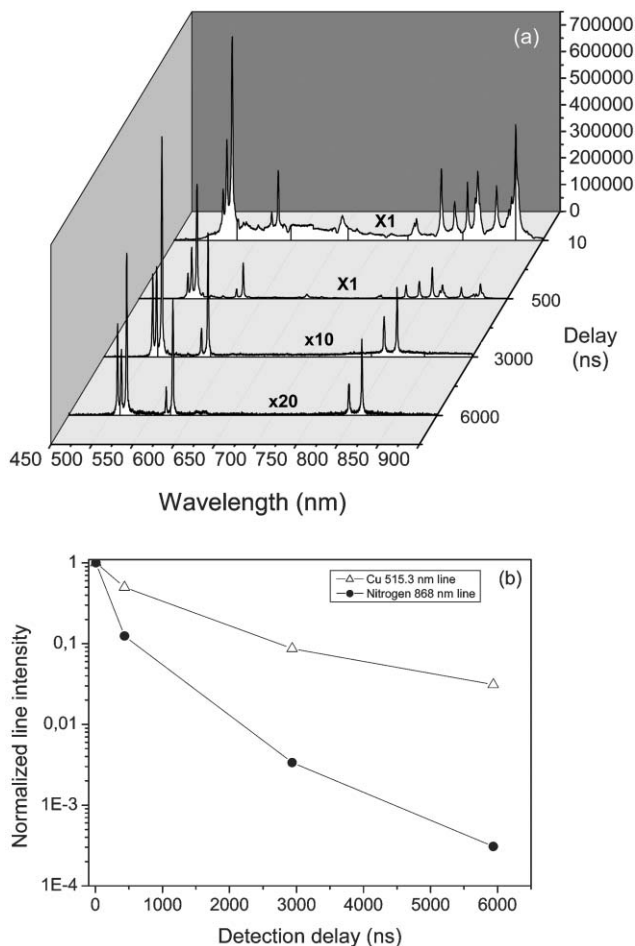


Fig. 6 (a) Full spectra obtained from the copper target with picosecond pulses at different detection delays. (b) Normalized intensities of the copper 515.3 nm line and the nitrogen 868 nm line as a function of the detection delay.

We conclude for this section, that with ultrashort pulses in the high fluence regime, the induced plasma fluorescence has a lifetime of several  $\mu\text{s}$ , which is orders of magnitude longer than the lifetimes in the low fluence regime. Such long fluorescence lifetimes allow the use of slower and less expensive gated detectors to get clean spectra, as well as a long integration time to increase the signal. The air plasma due to the ejection of laser-ablated material could be used to chemically analyse the ambient air with a high sensitivity.

### 3.3 R-LIBS signal vs. laser parameters

**3.3.1. Pulse energy dependence.** Pulse energy dependence of the R-LIBS signal was investigated in the femtosecond and picosecond regimes. Signals from copper were detected for pulse energies as low as 15 mJ (corresponding to an average fluence of 45  $\text{mJ cm}^{-2}$ ) in the femtosecond regime.

Fig. 8 shows the intensity of the copper 521.8 nm line in the femtosecond regime as a function of the laser pulse energy. The experimental data fit well with the model of Hashida *et al.*<sup>18</sup> This model takes two contributions into account: 3-photon absorption, and thermal processes involving the thermal energy of the free electrons and the lattice, respectively. The fit parameters yield a threshold of 40 mJ pulse energy for the thermal ablation process, corresponding to an average fluence of 120  $\text{mJ cm}^{-2}$  over the beam profile, slightly lower than the 180  $\text{mJ cm}^{-2}$  value determined by Hashida *et al.* This slight discrepancy could be due to the different criteria used for the threshold and the imprecision on the beam focus diameter estimation in our experiments. While Hashida *et al.* are interested in laser ablation and characterize threshold as the

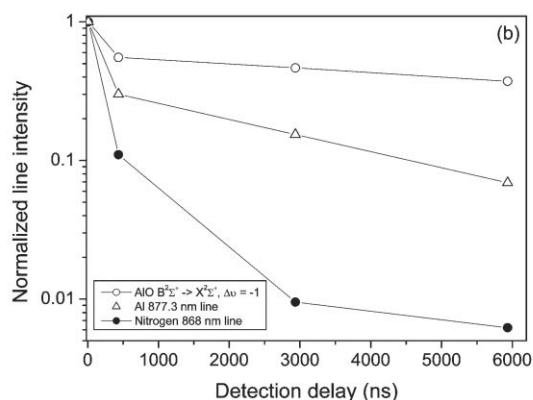
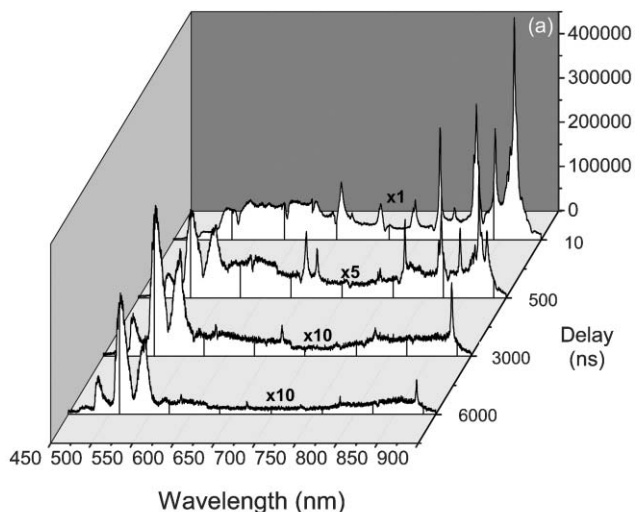


**Fig. 7** (a) Full spectra obtained from the aluminium target with picosecond pulses at different delays. (b) Normalized intensities for the AlO  $\Delta\nu = -1$ , Al 877.3 nm and nitrogen 868 nm lines as a function of the detection delay.

fluence yielding craters of measurable diameters, we detected fluorescence emission instead. However, like these authors, we find that, above this threshold, the 3-photon excitation has a negligible contribution to the overall signal.

In the picosecond regime with copper, the same treatment yields a threshold value of 100 mJ ( $300 \text{ mJ cm}^{-2}$ ), more than twice as high as using femtosecond pulses. This 2.5-fold ratio is similar to that observed by Hashida *et al.* under comparable

conditions. Hence, femtosecond pulses exhibit a reduced threshold as compared with picosecond pulses, allowing measurements at lower laser energies, thus limiting damage on the sample. Alternatively, this lower threshold may permit to focus the beam less tightly, opening the way to operate at longer focal lengths. Moreover the fact that we observed a signal with femtosecond pulses significantly below the threshold for thermal ablation shows that, in the low energy regime, the 3-photon excitation is efficient enough to provide a signal. This feature is a unique advantage of femtosecond pulses for R-LIBS, since the 3-photon ionisation threshold for picosecond pulses is above, not below, the threshold for thermal effects.<sup>18</sup>

Similar results were obtained with aluminium, in the AlO  $B^2\Sigma^+ \rightarrow X^2\Sigma^+$ ,  $\Delta\nu = -1$  line. In the femtosecond regime, the threshold for thermal ablation was determined as 60 mJ ( $180 \text{ mJ cm}^{-2}$ ), similar to the value determined by Furukawa and Hashida.<sup>17</sup> The threshold for picosecond pulses is quite comparable, 70 mJ, corresponding to  $210 \text{ mJ cm}^{-2}$ .

**3.3.2. Pulse shape dependence.** The temporal-spectral shape is an important parameter for a femtosecond pulse because of its short duration and its large spectral extent in the order of tens of nm. The chirp (linear temporal displacement of the different spectral components of a laser pulse) provides a simple case of pulse shaping. In general, a nonlinear optical process depends on the chirp when excited by a femtosecond pulse, which is basically due to the quantum interference between multiple possible paths for a system to undergo a transition involving several photons (more than one).<sup>37,38</sup> Pulse chirping or more generally pulse shaping (a generalized pulse chirping process that produces an arbitrary temporal-spectral form of a pulse), have been demonstrated to be able to optimise multiphoton transitions in an atomic or molecular system.<sup>38,39</sup> It has also been demonstrated that the transform-limited pulse does not optimise multiphoton transitions in an atomic system.<sup>39</sup> In our experiments, we generalize this property to the interaction between a chirped femtosecond pulse and a metallic sample. We demonstrated clearly, for the first time to our knowledge, that the transform-limited pulse does not produce an optimal LIBS signal, and that the optimisation occurs for a properly chirped pulse. We mention here that shaped femtosecond pulses have been used to improve laser ablation performances with successful results.<sup>40</sup>

Experimentally we studied the evolution of the R-LIBS signal as a chirp was applied to femtosecond pulses with an energy fixed at 250 mJ. For copper as well as for aluminium

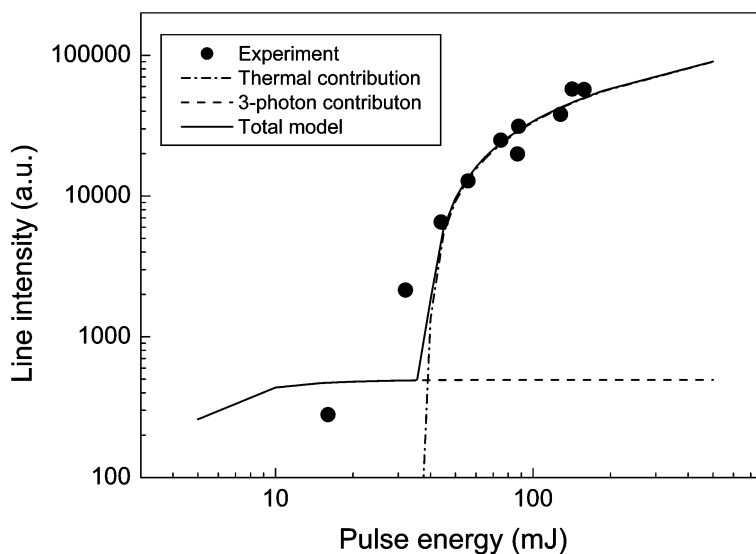


**Fig. 8** Intensity of the copper 521.8 nm line induced by femtosecond pulse as a function of laser pulse energy. The experimental data are fitted to the model proposed by Hashida *et al.* The two significant processes contributing to the fit are also presented.

samples, spectra were recorded around 520 nm as a function of the chirp. The pulse duration that we investigated ranged from 75 fs to about one picosecond.

The obtained results are presented in Fig. 9: the intensities of the copper 521.8 nm line are shown in Fig. 9(a) and those of the  $\text{AlO } B^2\Sigma^+ \rightarrow X^2\Sigma^+, \Delta v = -1$  line in Fig. 9(b). The pulse duration used in the figures are those on the sample. The GVD (group velocity dispersion) effect in air over the 25 m propagation distance are taken into account. Such effect is to stretch a positively chirped pulse and to compress a negatively chirped one. The GVD in air can be calculated using the air dispersion property.<sup>41</sup> For a short propagation distance and a moderate pulse intensity (far from the focus, propagation considered as linear), pulse duration variation is proportional to the propagation distance and the dispersion of the group refractive index. Using the data from ref. 41, for the 16 nm spectral bandwidth of the used femtosecond pulses, we get a pulse duration variation of  $\Delta\tau = 1.01 \times D$  (fs), with  $D$  the propagation distance in m, which leads to a stretching or a compression of 25 fs for positively or negatively chirped pulses.

With both samples, the chirp effect was clearly observed: for the same pulse duration, the line intensity is higher for a positive chirp (red first) than for a negative chirp. The Fourier transform-limited minimal duration pulse does not induce an optimal signal similar to the observation on a Rb vapor.<sup>38,39</sup> When the pulse duration is increased with an applied chirp, the LIBS signal increases. In particular, the LIBS signal increase is

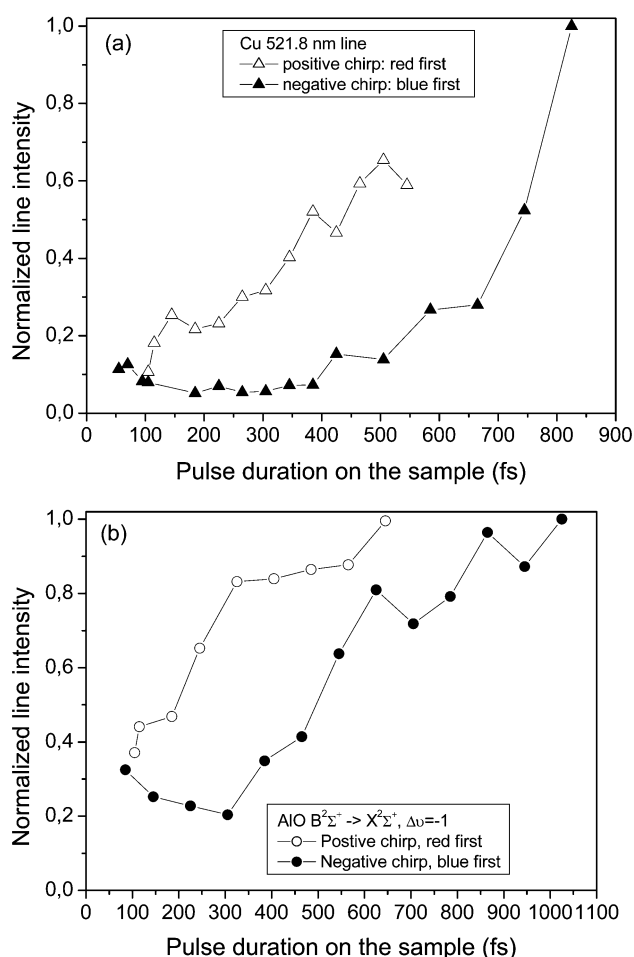


**Fig. 9** Effect of the pulse chirp on the R-LIBS signals with femtosecond pulses. Normalized intensities of (a) the copper 521.8 nm and (b) the  $\text{AlO } \Delta v = -1$  line as a function of the pulse duration. Data for different chirps (positive or negative) are presented in two different branches in each figure. Pulse durations refer to those on the sample. Pulse stretching or compression due to the GVD (group velocity dispersion) in air over the 25 m propagation distance are taken into account.

not symmetric with respect to the minimal duration pulse. Such dissymmetry excludes a pulse duration effect (or power/intensity effect for a fixed pulse energy). In the studied pulse duration range the ratio between the signals for positive and negative chirps is found at maximum to be about 6.5 for copper and 4.1 for aluminium. The observed chirp effect is also consistent with what we found for the energy dependence concerning the nonlinear nature of the plasma generation in the ultrashort and ultraintense pulse regime.

The chirp effect in optimising the fluorescence yield from a quantum system has been previously observed in atomic or molecular systems.<sup>38,39</sup> For such simple systems, the interpretation is based on a multiphoton transition *via* an intermediary level (situated out off the exact middle position from the fundamental to the excited level). With a properly designed pulse temporal-spectral shape, one can first induce a transition from the fundamental to the intermediary level with the first arrived spectral components. Then the delayed spectral components subsequently excite the transition from the intermediary level to the excited state. For a complicated process such as LIBS on solid state materials, new theoretical models are needed to describe in detail the mechanism.

The observed chirp effect appears very important for Femto-LIBS applications. It opens the perspective for optimising the fluorescence signal according to a specific sample or even a specific emission line. Such a material-dependent optimisation process is not only crucial for increasing the detection sensitivity, but also could be a powerful means to enhance the specificity of Femto-LIBS detection in the case, for example, of overlapping between the spectra of several elements to be identified.

## 4 Conclusion

We have demonstrated R-LIBS with metallic samples (copper and aluminium). Our measurements showed that the LIBS spectra in the femtosecond and picosecond regimes with a high signal to noise ratio and a low background can be successively detected at a remote distance. In particular, femtosecond pulses induce a cleaner spectrum independent of the ambient gas. Moreover the high signal to noise ratio of recorded signals would allow us to detect as little as 100 ng of copper from a sample at a distance of 25 m.

Femtosecond as well as picosecond pulse induced fluorescence has been found to decay slowly with a time constant of several  $\mu\text{s}$ . Such long fluorescence lifetimes allows the application of standard gated detectors and have a long integration time. The secondary air plasma induced in the vicinity of the sample surface would provide a sensitive chemical analysis method for the ambient air.

The dependences on pulse energy and pulse chirp have been studied revealing interesting properties. The energy dependence has been found to be nonlinear and fits well to the model developed by Hashida *et al.*<sup>18</sup> As we can expect for a nonlinear optic process, an effect of the pulse chirp has been observed on the LIBS signal. The evidence of this effect has been provided in our experiments by a dissymmetrical LIBS signal increasing with respect to the minimal pulse duration. Our results show clearly that an intense femtosecond pulse with Fourier transform-limited minimal duration does not optimise the fluorescence signal. Instead a material-dependent optimisation process with a specific pulse shape would lead to a more efficient and more selective Femto-LIBS detection. Such improvements promise a longer detection distance for R-LIBS, as well as a high selectivity in the case of overlapping emission of various elements.

Our data does not only provide necessary parameters for the design of new LIBS devices with femtosecond or picosecond lasers, but also an experimental database for the establishment

of models describing the mechanisms involved in the LIBS process in such a new interaction regime with ultrashort and ultraintense laser pulses.

The application of the R-LIBS using ultra-short laser pulses would interest a large area covering for example, environmental monitoring (air, water or soil pollutions, heavy metal contamination...); *in-situ* and real time element detection and analysis of hazardous materials in difficult-access environments (high-temperature, radioactive, chemically toxic materials); mineral resource inspection; civil security and military defence (chemical, biological or nuclear contaminations...); and space missions. All these applications acquire a large detection distance using a mobile unit containing the laser system and the detection system. The need of scanning over a large detection area would be satisfied by the development of a motorised beam steering system, which would be synchronized with the orientation of the receiving telescope, in order to keep the alignment of the telescope at the laser beam impact on the targets. Starting from a versatile laser-detection unit such as the Teramobile system, engineering developments are certainly required to achieve a task-specified unit designed for a special application. Improvements in terms of the compactness of the system, the detection distance and the detection sensitivity can be expected.

## Acknowledgements

This work has been performed within the framework of the Teramobile project, jointly funded by the French CNRS and the German DFG, and the French and the German Ministries of Research and of Foreign Affairs.

## References

- 1 L. J. Radziemski, *Microchem. J.*, 1994, **50**, 218–234.
- 2 L. J. Radziemski and D. A. Cremers, Spectrochemical analysis using laser plasma excitation, in *Laser-induced Plasma: Physical, Chemical and Biological Applications*, ed. L. J. Radziemski and D. A. Cremers, Marcel Dekker, New York, 1989.
- 3 D. A. Rusak, B. C. Castle, B. W. Smith and J. D. Winefordner, *Crit. Rev. Anal. Chem.*, 1997, **27**, 257–290.
- 4 I. Schechter, *Rev. Anal. Chem.*, 1997, **16**, 173–298.
- 5 For a recent review of the fundamentals as well as applications of LIBS, see the special issue on laser-induced plasma spectroscopy, *Spectrochim. Acta, Part B*, 2002, **56**(6), 565–1034.
- 6 S. Palanco, S. Conesa and J. J. Laserna, Field deployable or remote enabled? A portable laser-induced plasma spectrometer for field remote sensing, paper Th-B2, ENSLIBS II, Hersonissos, Crete, Greece, 30 September–3 October 2003.
- 7 K. Kincaid, *Laser Focus World*, 2003, **39**(8), 71–80.
- 8 D. Body and B. L. Chadwick, *Rev. Scient. Instrum.*, 2000, **72**, 1625–1629.
- 9 An introduction to laser-induced breakdown spectroscopy, Information from APPLIED PHOTONICS and BNFL Instruments, <http://www.bnflinstruments.com/products/libl.pdf>.
- 10 R. M. Measures, in *Laser Remote Sensing*, Wiley, New York, 1992.
- 11 R. J. Locke, J. B. Morris, B. E. Forch and A. W. Miziolek, *Appl. Opt.*, 1990, **29**, 4987–4992.
- 12 G. W. Rieger, M. Taschuk, Y. Y. Tsui and R. Fedosejevs, *Appl. Spectrosc.*, 2002, **56**, 689–698.
- 13 D. N. Stratis, K. L. Eland and S. M. Angel, *Appl. Spectrosc.*, 2002, **55**, 1297–1303.
- 14 R. Noll, R. Sattmann, V. Sturm and S. Winkelmann, Space- and time-resolved dynamics of plasmas generated by laser double pulses interacting with metallic samples, paper W-A1, ENSLIBS II, Hersonissos, Crete, Greece, 30 September–3 October 2003.
- 15 M. Corsi, G. Cristoforetti, M. Giuffrida, M. Hidalgo, S. Legnaioli, V. Palleschi, A. Salvetti, E. Tognoni and C. Vallebona, Spatially resolved analysis of single and double pulse laser induced plasma from a brass sample, paper W-A2, ENSLIBS II, Hersonissos, Crete, Greece, 30 September–3 October 2003.
- 16 See, for example: J. Kruger and W. Kautek, *Laser Phys.*, 1999, **9**, 30–40.
- 17 H. Furukawa and M. Hashida, *Appl. Surf. Sci.*, 2002, **197–198**, 114–117.
- 18 M. Hashida, A. F. Semerok, O. Gobert, G. Petit, Y. Izawa and J.-F. Wagner, *Appl. Surf. Sci.*, 2002, **197–198**, 862–867.
- 19 F. Brunner, T. Sudmeyer, E. Innerhofer, R. Paschotta, F. Morier-Genoud, U. Keller, J. Gao, K. Contag, A. Giesen, V. Kisel, V. G. Shcherbitsky and N. V. Kuleshov, 240-fs pulses with 22-W average power from a passively mode-locked thin-disk Yb:KY(WO<sub>4</sub>)<sub>2</sub> laser”, in *Techn. Digest Conf. Laser Electro-Opt.*, Optical Society of America, Washington DC, 2002, paper no. 02CH37337, 24 vol. 1.
- 20 A. Isemann, H. Hundertmark and C. Fallnich, *Appl. Phys. B*, 2002, **74**, 299–306.
- 21 T. Ueda, V. Yashin, M. Wakamatsu and A. Andreev, *Trans. Inst. Electr. Eng. Jpn., E*, 2002, **122**(5), 244–248.
- 22 K. L. Eland, D. N. Stratis, T. Lai, M. A. Berg, S. R. Goode and S. M. Angel, *Appl. Spectrosc.*, 2001, **55**, 279–285.
- 23 K. L. Eland, D. N. Stratis, D. M. Gold, S. R. Goode and S. M. Angel, *Appl. Spectrosc.*, 2001, **55**, 286–291.
- 24 For a review of the results obtained by the Teramobile team, see for example: J. Kasparian, M. Rodriguez, G. Méjean, J. Yu, E. Salmon, H. Wille, R. Bourayou, S. Frey, Y.-B. André, A. Mysyrowicz, R. Sauerbrey, J.-P. Wolf and L. Wöste, *Science*, 2003, **301**, 61–64.
- 25 H. Wille, M. Rodriguez, J. Kasparian, D. Mondelain, J. Yu, A. Mysyrowicz, R. Sauerbrey, J.-P. Wolf and L. Wöste, *Eur. Phys. J. A*, 2002, **20**, 183–190.
- 26 D. Strickland and G. Mourou, *Opt. Commun.*, 1985, **56**, 219–221.
- 27 I. G. Dors, C. Parigger and J. W. Lewis, *Opt. Lett.*, 1998, **23**, 1778–1781.
- 28 B. Le Drogoff, F. Vidal, Y. von Kaenel, M. Chakern, T. W. Johnston, S. Laville, M. Sabsabi and J. Margot, *J. Appl. Phys.*, 2001, **89**, 8247–8252.
- 29 A. Ng, D. Pasini, P. Celliers, D. Parfenuik, L. Da Silva and J. Kwan, *Appl. Phys. Lett.*, 1984, **45**, 1046–1048.
- 30 F. Dahmani, *J. Appl. Phys.*, 1993, **74**, 622–634.
- 31 The NIST spectral databass is available at the website: [http://physics.nist.gov/cgi-bin/AtData/main\\_asd](http://physics.nist.gov/cgi-bin/AtData/main_asd).
- 32 S. S. Mao, Xianglei Mao, Ralph Greif and Richard E. Russo, *Appl. Phys. Lett.*, 2000, **77**, 2464–2466.
- 33 K. Shigemori, H. Azechi, M. Nakai and K. Mima, *Rev. Sci. Instrum.*, 1998, **69**, 3942–3944.
- 34 C. H. Ching, R. M. Gilgenbach and J. S. Lash, *J. Appl. Phys.*, 1995, **78**, 3408–3410.
- 35 S. M. Angel, D. N. Stratis, K. L. Eland, T. Lai, M. A. Berg and D. M. Gold, *Fresenius' J. Anal. Chem.*, 2001, **369**, 320–327.
- 36 S. Tzortzakis, B. Prade, M. Franco and A. Mysyrowicz, *Opt. Commun.*, 2000, **181**, 123–127.
- 37 D. Meshulach and Y. Silberberg, *Nature*, 1998, **396**, 239–242.
- 38 B. Chatel, J. Degert, S. Stocok and B. Girard, *Phys. Rev. A*, 2003, **68**, 41402(R).
- 39 N. Dudovich, B. Dayan, S. M. Gallagher Faeder and Y. Silberberg, *Phys. Rev. Lett.*, 2001, **86**, 47–50.
- 40 R. Stoian, M. Boyle, A. Thoss, A. Rosenfeld, G. Korn, I. V. Hertel and E. E. B. Campbell, *Appl. Phys. Lett.*, 2002, **80**, 353–355.
- 41 J. C. Owens, *Appl. Opt.*, 1967, **6**, 51–59.

G. MÉJEAN  
J. KASPARIAN  
J. YU  
S. FREY  
E. SALMON  
J.-P. WOLF<sup>✉</sup>

## Remote detection and identification of biological aerosols using a femtosecond terawatt lidar system

Teramobile Project, LASIM, UMR CNRS 5579, Université Claude Bernard Lyon 1, 43 bd. du 11 Novembre 1918, 69622 Villeurbanne Cedex, France

Received: 30 January 2004

Published online: 24 February 2004 • © Springer-Verlag 2004

**ABSTRACT** We demonstrate experimentally the first range-resolved detection and identification of biological aerosols in the air by non-linear lidar. Ultra-short terawatt laser pulses are used to induce two-photon-excited fluorescence (2PEF) in riboflavin-containing particles at a remote location. We show that, in the case of amino acid detection, 2PEF-lidar should be more efficient than linear 1PEF-lidar beyond a typical distance of 2 km, because it takes advantage of the higher atmospheric transmission at the excitation wavelengths. 2PEF-lidar moreover allows size measurement by pump-probe schemes, and pulse shaping may improve the detection selectivity.

PACS 33.50.-j; 33.80.Wz; 42.65.-k; 42.68.Wt; 92.60.Mt

The early detection and identification of potentially harmful bioagents in the air has become a major issue for both defence and public security reasons. This requires fast detection of the outbreak location, 3D mapping of the plume as it propagates, and unambiguous identification of the agents among the broad variety of atmospheric background aerosols. In this letter, we study the application of fluorescence-based lidar (light detection and ranging) [1] towards these goals. We demonstrate experimentally the first remote detection and identification of bioagent simulants (riboflavin-doped microparticles) in the air by non-linear lidar. We used ultra-short laser pulses from the Teramobile [2, 3] to induce in situ two-photon-excited fluorescence (2PEF) [4] in the aerosol particles. Two major reasons motivate the use of ultra-short multiphoton excitation: (1) the better atmospheric transmission at longer wavelengths (decrease of Rayleigh scattering and prevention of molecular absorption such as ozone) and (2) the possibility of simultaneous size measurement by pump-probe schemes [5, 6] and coher-

ent excitation with shaped pulses [7, 8] to improve the detection selectivity.

Most of the bioagents, like the bacillus anthracis (anthrax), are bacteria of typically 1  $\mu\text{m}$  in size [9]. Depending on the spread conditions, they can agglomerate in clusters of sizes up to 10  $\mu\text{m}$ . They contain natural fluorophores, like amino acids (e.g. tryptophan), nicotine amides (NADH), and flavins (e.g. riboflavin (RBF) and flavoproteins), which can be used as characteristic tracers of their biological nature [10]. We used the specific fluorescence signature at 540 nm of riboflavin, which we excited with two photons at the fundamental wavelength (800 nm) of the first terawatt lidar system, the Teramobile [2, 3]. The Teramobile is based on a chirped pulse amplified (CPA) laser that delivers 5-TW pulses (80 fs, 400 mJ) at a 10-Hz repetition rate. The laser pulses are sent into the atmosphere using an all-reflective beam expander. The backward-emitted fluorescence and scattered signals are collected by a 40-cm or 20-cm telescope depending on the application (longer or shorter distance measurements), which focuses

the light on a spectrally resolved detector. The returns are recorded as a function of the photons' flight time, providing distance resolution.

The bioagent simulants were produced with an aerosol generator located at 45 m from the Teramobile. Their size distribution and concentrations were monitored using an optical sizer (Grimm model G 1-108). They consisted of water droplets of 1- $\mu\text{m}$  size on average containing 0.02 g/l riboflavin.

A key parameter to efficiently excite 2PEF in the microparticles is the control of the laser pulse intensity at the target location, because of the non-linear nature of the excitation process. For this, the pulses were shaped using a negative linear chirp (shorter wavelengths of the 20-nm broad laser spectrum are launched before the longer wavelengths) in order to compensate the air group-velocity dispersion (GVD) and reduce the initial pulse peak intensity to prevent early filamentation. The best negative chirp value, which corresponds to a 1-ps pulse, leads to the results shown in Fig. 1a. The corresponding intensity on the target is  $10^{11} \text{ W/cm}^2$ . The detected 2PEF spectrum clearly identifies the presence of riboflavin-containing particles, and the lidar range resolution (via the measurement of the flight time of the light) allows the precise spatial localization of the biological aerosol plume. The plume is measured to be spread over some 10 m. The spatial resolution is 45 cm, limited by the fluorescence lifetime of 3 ns for this transition [11]. Notice that the contrast against fluorescence of the background aerosols present in the air at the time of the measurement is excellent. The 2PEF signature of riboflavin was compared to the spectrum from pure wa-

✉ Fax: +33-4724/45871, E-mail: wolf@lasim.univ-lyon1.fr

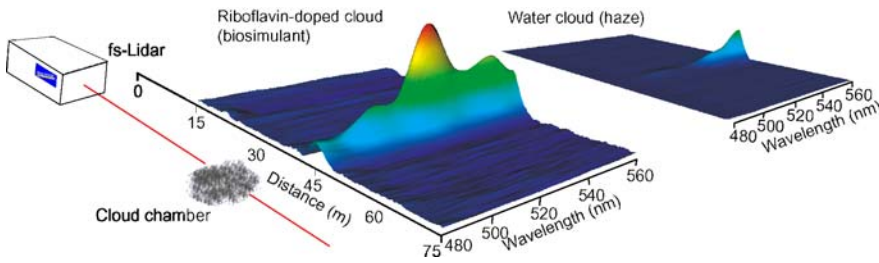


**FIGURE 1** Remote detection and identification of bioaerosols. The femtosecond laser illuminates a plume of riboflavin (RBF)-containing microparticles 45-m away (left). The backward-emitted two-photon-excited fluorescence (2PEF), recorded as a function of distance and wavelength, exhibits the specific RBF fluorescence signature for the bioaerosols (middle) but not for pure water droplets (simulating haze, right)

ter microdroplets (Fig. 1b). This clearly demonstrates the capability of identifying biological particles from background non-biological ones of the same size. A smooth increase of the backscattered signal is observed over 600 nm for both bioagent simulants and pure water due to self-phase modulation (SPM) of the pulse as it propagates in air to the target. The spectrally broadened pulse is elastically scattered by the aerosol particles in the plume. If filamentation was not controlled using a negative chirp, the SPM broadening would extend towards UV-blue, which could partially mask the fluorescence signature of the bioparticles. These experiments also show that the one photon per pulse detection limit corresponds to a concentration as low as 10 particles per cubic centimeter, for a 10-m spatial resolution.

Using shorter-wavelength excitation (around 530 nm) would provide significant advantages as compared to the 800-nm wavelength: (1) the already high sensitivity would be further enhanced by using 2PEF from the amino acid tryptophan (Trp) [9, 10], the concentration of which is typically  $10^4$  times higher than riboflavin in bacteria ( $10^8$  Trp molecules in a 1- $\mu\text{m}$  particle [11]) and (2) two photons at 530 nm would not only excite tryptophan, but also NADH and riboflavin, whose fluorescence features around 320–370 nm, 420–500 nm, and 520–620 nm, respectively, would provide multiple cross-checking biological signatures of the particle [10].

We performed numerical simulations to estimate the performance of a non-linear 2PEF-lidar, compared to a linear 1PEF-lidar (emission wavelength 266 nm), in the case of tryptophan fluorescence detection. Although ultra-short terawatt lasers that emit

around 530 nm are not commercially available yet, recent developments in ytterbium-based lasers are very encouraging, reaching up to the petawatt level (at the fundamental wavelength, to be frequency doubled) in the laboratory. In these simulations, we assumed that the laser intensity decreases only by linear extinction processes (Rayleigh–Mie scattering and absorption from atmospheric molecules) as it propagates in air to the aerosol plume. The number  $N_f(R)$  of  $n$ -photon-excited fluorescence ( $n$ PEF,  $n = 1$  or 2 in the calculations below) photons/pulse detected from the distance  $R$  can be described by the following equation:

$$N_f(R) = \varrho(R) \sigma^{(n)} \eta I_0^n \tau \zeta(R, \lambda) \frac{A}{4\pi R^2} \times S \Delta R \exp \left( - \int_0^R \alpha(R, \lambda_f) - n\alpha(R, \lambda_p) dR \right),$$

where  $\varrho(R)$  is the concentration of aerosol particles,  $\sigma^{(n)}$  is the  $n$ -photon absorption cross section for one mi-

croparticle,  $\eta$  is the fluorescence yield,  $I_0$  is the initial laser pulse intensity,  $\tau$  is the pulse duration,  $A$  is the receiver telescope area,  $\zeta$  is the detection efficiency,  $S$  is the beam surface,  $\Delta R$  is the spatial resolution, and  $\alpha$  is the atmospheric extinction at the fluorescence and excitation wavelengths  $\lambda_f$  and  $\lambda_p$ , respectively.  $\alpha$  widely favors longer wavelengths, because of the  $\lambda^{-4}$  dependence of Rayleigh scattering and molecular absorption in the UV. Around 266 nm, the major absorbing molecule in the atmosphere is ozone.

In the simulations, we used the following parameters: particle size 1  $\mu\text{m}$  (average diameter),  $10^8$  Trp molecules/particle,  $\sigma^{(1)} = 2 \times 10^{-17} \text{ cm}^2$  [11],  $\sigma^{(2)} = 1 \times 10^{-50} \text{ cm}^4 \text{ s/photon}$  [12, 13],  $\eta = 0.13$  [11, 12],  $\zeta = 0.2$ ,  $A = 0.125 \text{ m}^2$  (40-cm-diameter telescope), and  $S = 10 \text{ cm}^2$ . The 1PEF-lidar simulations used the specifications of best commercially available Nd:Yag lasers (fourth harmonic), with 100 mJ at 266 nm and 10-ns pulse duration, while for the 2PEF simulations we used the Teramobile laser specifications (400 mJ, 80 fs). The cross sections are  $\alpha_{1P} = \alpha_{\text{Rayleigh}}(266 \text{ nm}) + N_{\text{Ozone}} \sigma_{\text{Ozone}}(266 \text{ nm}) = 1.6 \times 10^{-4} \text{ m}^{-1} + N_{\text{Ozone}} \sigma_{\text{Ozone}}(266 \text{ nm})$  with  $\sigma_{\text{Ozone}}(266 \text{ nm}) = 1 \times 10^{-17} \text{ cm}^2$ ,  $\alpha_{2P} = \alpha_{\text{Rayleigh}}(530 \text{ nm}) = 1 \times 10^{-5} \text{ m}^{-1}$  (for atmospheric transmission parameters see [14]). Figure 2 shows the results of our simulations ( $N_f(R)$ /pulse from Trp, for 1PEF- and 2PEF-lidars in the case of a 10-m-diameter plume containing 100 bacteria/ $\text{cm}^3$ ), as a function of the distance  $R$  between the plume and the lidar system. The ozone concentration of  $50 \mu\text{g}/\text{m}^3$  (full line) is typical for populated areas (urban or peri-urban conditions). Because of the strong UV extinction, 2PEF-lidar is

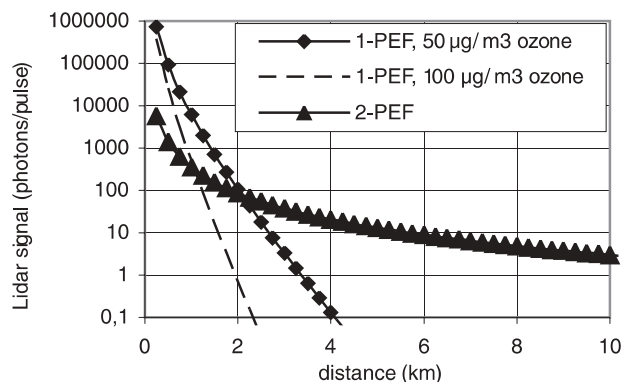


**FIGURE 2** Simulated fluorescence lidar signal for tryptophan detection in bioaerosols. The collected 2PEF intensity is higher than 1PEF for distances over 1–2 km, due to the lower atmospheric transmission in the UV (Rayleigh scattering and ozone absorption, here typically 50 and 100  $\mu\text{g}/\text{m}^3$ )

much more efficient than IPEF-lidar for distances beyond 2 km. The distance  $R_0$  beyond which 2PEF is more efficient than IPEF strongly depends on the ozone concentration. In particular, IPEF-lidar will not be practicable (limited to only a few hundred meters) in urban conditions in summer, where average  $O_3$  concentrations very often exceed  $100 \mu\text{g}/\text{m}^3$  (dashed line in Fig. 2; in ozone episodes up to  $360 \mu\text{g}/\text{m}^3$ , corresponding to the CEE 99 standard alarm level).

The simulations also provide estimations of the typical 2PEF-lidar detection limits. As  $N_f(R)$  is proportional to the product  $\rho(R)\Delta R$ , the longer the integration distance, the better the sensitivity. As an example, for the average ozone concentration of  $50 \mu\text{g}/\text{m}^3$ , we obtain a minimum detectable concentration (corresponding to one fluorescence photon/pulse) as low as four bacteria/ $\text{cm}^3$  at 3 km or 10 bacteria/ $\text{cm}^3$  at 4 km with a 10-m distance resolution. At these distances and ozone concentrations, IPEF-lidar detection is almost useless. Saturation and bleaching [12] do not affect these remarkable 2PEF-lidar sensitivities, as each two-photon-excited Trp molecule only emits typically 0.1 photon per exciting cycle. The estimated detection limit might strongly vary from one type of bacteria to another, because of the variations of the fluorescence quantum yield  $\eta$  [13]. Even for the values taken here [11], which correspond to fluorescence measurements of *bacillus subtilis* and *bacillus cereus*, variations of up to an order of magnitude have been observed. These varia-

tions in  $\eta$ , however, affect the absolute detection limits for a type of bacteria, but not the IPEF- or 2PEF-lidar comparison.

The main limitation of 2PEF-lidar is, however, the ability to deliver the required intensity at the target plume location. In our simulations, we assumed the optimum situation where a successful control of the non-linear propagation (Kerr focusing and pulse compression) in air until the target was realized by using both spectral and spatial phase control. Although phase control could be demonstrated on distances in the 100-m range [3], and chirp-induced effects could be observed on self-phase modulation up to 10 km [2], no systematic investigation could be performed so far on the evolution of the beam intensity profile on the km scale. Further investigations, both theoretical and experimental, are therefore needed to better control the propagation of the ultrashort pulses to the target location. Sophisticated shaping techniques that allow us to precisely set the spectral and spatial phases of the laser pulse (temporal shaping and adaptive optics) will be of great use, as demonstrated for fusion applications [15]. Shaping the pulses in 2PEF experiments and using genetic algorithms moreover recently showed that two species exhibiting the identical linear fluorescence spectrum [7] can be efficiently distinguished. This remarkable experiment opens new perspectives in identifying bioagents from other fluorescing particles using 2PEF-lidars.

**ACKNOWLEDGEMENTS** Teramobile is a French–German project jointly funded by

the CNRS and the DFG. The authors wish to thank Steven C. Hill at ARL, Adelphi (MD) for very fruitful discussions, Marc Néri for helpful technical support, and Matthieu Jomier for assistance in preparing Fig. 1.

## REFERENCES

- 1 J.-P. Wolf: in *Encyclopedia of Analytical Chemistry*, ed. by R.A. Meyers (Wiley, Chichester 2000) pp. 2226–2245
- 2 J. Kasparian, M. Rodriguez, G. Méjean, J. Yu, E. Salmon, H. Wille, R. Bourayou, S. Frey, Y.B. Andre, A. Mysyrowicz, R. Sauerbrey, J.P. Wolf, L. Woeste: *Science* **301**, 61 (2003)
- 3 H. Wille, M. Rodriguez, J. Kasparian, D. Mondelain, J. Yu, A. Mysyrowicz, R. Sauerbrey, J.P. Wolf, L. Woeste: *Eur. Phys. J. D* **20**, 183 (2002)
- 4 S.C. Hill, V. Boutou, J. Yu, S. Ramstein, J.P. Wolf, Y. Pan, S. Holler, R.K. Chang: *Phys. Rev. Lett.* **85**, 54 (2000)
- 5 J.P. Wolf, Y. Pan, S. Holler, G.M. Turner, M.C. Beard, R.K. Chang, A. Schmuttenmaer: *Phys. Rev. A* **64**, 023 808-1 (2001)
- 6 L. Méès, J.P. Wolf, G. Gouesbet, G. Gréhan: *Opt. Commun.* **208**, 371 (2002)
- 7 T. Brixner, N. Damrauer, P. Niklaus, G. Gerber: *Nature* **414**, 57 (2001)
- 8 R.J. Levis, G.M. Menkir, H. Rabitz: *Science* **292**, 709 (2001)
- 9 Y.S. Cheng, E.B. Barr, B.J. Fan, P.J. Hargis, D.J. Rader, T.J. O'Hern, J.R. Torczynski, G.C. Tisone, B.L. Preppernau, S.A. Young, R.J. Radloff, S.L. Miller, J.M. Macher: *Aerosol Sci. Technol.* **30**, 186 (1999)
- 10 S.C. Hill, R.G. Pinnick, S. Niles, Y.L. Pan, S. Holler, R.K. Chang, J.R. Bottiger, B.T. Chen, C.S. Orr, G. Feather: *Field Anal. Chem. Technol.* **3**, 221 (1999)
- 11 G.W. Faris, R.A. Copland, K. Mortelmans, B.V. Bronk: *Appl. Opt.* **36**, 958 (1997)
- 12 M. Lippitz, W. Erker, H. Decker, K.E. van Holde, T. Basche: *Proc. Natl. Acad. Sci.* **99**, 2772 (2002)
- 13 A. Rehms, P. Callis: *Chem. Phys. Lett.* **208**, 276 (1993)
- 14 R.M. Measures: *Laser Remote Sensing, Fundamentals and Applications* (Wiley–Interscience, New York 1984)
- 15 B. Wattelier, C. Sauteret, J.-C. Chanteloup, A. Migus: *Opt. Lett.* **27**, 213 (2002)

## Multiple Filamentation of Terawatt Laser Pulses in Air

L. Bergé,<sup>1</sup> S. Skupin,<sup>1,2</sup> F. Lederer,<sup>2</sup> G. Méjean,<sup>3</sup> J. Yu,<sup>3</sup> J. Kasparian,<sup>3</sup> E. Salmon,<sup>3</sup> J. P. Wolf,<sup>3</sup> M. Rodriguez,<sup>4</sup> L. Wöste,<sup>4</sup>  
R. Bourayou,<sup>2</sup> and R. Sauerbrey<sup>2</sup>

<sup>1</sup>*Département de Physique Théorique et Appliquée, CEA/DAM Ile de France, B.P. 12, 91680 Bruyères-le-Châtel, France*

<sup>2</sup>*Friedrich-Schiller-Universität Jena, Max-Wien-Platz 1, 07743 Jena, Germany*

<sup>3</sup>*Laboratoire de Spectrométrie Ionique et Moléculaire, Université Cl. Bernard Lyon 1, UMR-CNRS 5579, F-69622 Villeurbanne cedex, Lyon, France*

<sup>4</sup>*Institut für Experimentalphysik, Freie Universität Berlin, Arnimallee 14, D-14195 Berlin, Germany*

(Received 11 July 2003; published 2 June 2004)

The filamentation of femtosecond light pulses in air is numerically and experimentally investigated for beam powers reaching several TW. Beam propagation is shown to be driven by the interplay between intense, robust spikes created by the defects of the input beam and random nucleation of light cells. Evolution of the filament patterns can be qualitatively reproduced by an averaged-in-time (2D + 1)-dimensional model derived from the propagation equations for ultrashort pulses.

DOI: 10.1103/PhysRevLett.92.225002

PACS numbers: 52.38.Hb, 42.65.Tg, 42.65.Jx, 42.68.Ay

The self-guiding of femtosecond laser pulses in air is a well-known phenomenon nowadays exploited in, e.g., remote sensing techniques [1,2]. Infrared pulses with about 100 fs duration indeed produce narrow light filaments over long distances, along which self-phase modulation and ionization processes promote white-light emission allowing high-altitude spectroscopy experiments [2]. Self-channeling of light follows from the early self-focusing of laser radiation, caused by the Kerr response of air and leading to a sharp increase of the beam amplitude. This growth is next arrested by the electron plasma created by photoionization of air molecules, which limits the maximum intensity in the filament to  $\sim 10^{14}$  W/cm<sup>2</sup>. If the peak power does not exceed a few tens of critical powers for self-focusing in air ( $P_{\text{cr}} \sim 2\text{--}6$  GW at 800 nm), one or two filaments are created [3–6]. At much higher powers, many of them can be generated by modulational instability of the input beam. This mechanism produces small-scale cells with each conveying a power  $P_{\text{fil}} \approx \pi^2 P_{\text{cr}}/4$  [7,8], which severely degrades the homogeneity of the focal spot.

In this regard, Mlejnek *et al.* [9] proposed, from numerical inspection of a central portion of the beam, that collapsing light cells are randomly nucleated and defocused by plasma generation over short distances (<1 m) in air. Recurrence of such events then seeds a bath of short-living spiky filaments with few-critical powers and produces an optically turbulent light guide in the medium. To our knowledge, this scenario has received no experimental confirmation so far. Besides this pioneering work, a challenging issue in this field has also been to describe the evolution of an entire cm-waisted beam filamenting along extended paths at TW power levels. Although the equations governing ultrashort pulses in the atmosphere are well established, their solution requires high-performance computer machines, whose capacities are still limited for holding the fine resolution needed to resolve accurately the numerous sharp spikes

created inside broad beams, upon propagation distances covering hundreds of meters. In particular, the numerical computation of ionization channels each exhibiting a thin size of  $\sim 50$   $\mu\text{m}$  implies that, for an input beam waist of a few cm only, the required resolution in  $(x, y, t)$  can consume several terabytes of memory for a single run. Such constraints are costly in CPU time, even by using a parallel code turning on many processors. So, it may be highly beneficial to overcome this problem by integrating an alternative model that accounts, e.g., for the spatial distortions of the pulse only.

The purpose of this Letter is to elucidate, on the basis of experiments and numerical simulations, how filaments impact on the long-distance propagation of TW pulses. First, to circumvent the above numerical obstacle, we derive a reduced 2D model achieved by averaging in time the (3D + 1)-dimensional equations for ultrashort pulses in air. This simpler model is validated over meter-range distances by comparison with 3D simulations of mm-waisted pulses. It describes soliton-like states representing short-range filaments. These structures, although emitted at random, are able to confine themselves into a limited number of clusters that drive the pulse dynamics over long distances. Second, we examine two series of experiments involving the Teramobile facility [2] that delivers TW beams with either moderate ( $P_{\text{in}} = 120P_{\text{cr}}$ ) or high ( $P_{\text{in}} = 700P_{\text{cr}}$ ) input powers. We compare each series with results yielded by the averaged-in-time model, which restores the principal features in the experimental patterns. High-intensity defects in the spatial distribution of the input beam generate distinct zones of filaments that persist over several tens of meters, while they can excite secondary turbulent light cells.

To start with, we consider the standard propagation model, which couples an extended nonlinear Schrödinger equation for the electric field envelope  $\mathcal{E}$ , to a Drude model for the local plasma density  $\rho$ :

$$i\partial_z \mathcal{E} + \frac{1}{2k_0} \nabla_{\perp}^2 \mathcal{E} + \frac{k_0 n_2}{2} \left( |\mathcal{E}|^2 + \tau_K^{-1} \int_{-\infty}^t e^{-(t-t')/\tau_K} |\mathcal{E}(t')|^2 dt' \right) \mathcal{E} - \frac{k''}{2} \partial_t^2 \mathcal{E} - \left( \frac{k_0}{2\rho_c} - i \frac{\sigma}{2} \right) \rho \mathcal{E} + i \frac{\beta^{(K)}}{2} |\mathcal{E}|^{2K-2} \mathcal{E} = 0, \quad (1)$$

$$\partial_t \rho = \sigma_K \rho_{\text{nt}} |\mathcal{E}|^{2K} + (\sigma/U_i) \rho |\mathcal{E}|^2. \quad (2)$$

These equations, justified in [9–11], apply to fs pulses moving in their group-velocity frame, characterized by a beam waist  $w_0$ , half-width duration  $t_p$ , central wave number  $k_0$ , and critical power for self-focusing  $P_{\text{cr}} = \lambda_0^2/2\pi n_2 = 3.3$  GW for the laser wavelength  $\lambda_0 = 800$  nm and Kerr refraction index  $n_2 = 3.2 \times 10^{-19}$  cm<sup>2</sup>/W. In Eq. (1),  $\nabla_{\perp}^2 \equiv \partial_x^2 + \partial_y^2$  and the Kerr response of air involves a delayed (Raman) contribution where  $\tau_K = 70$  fs.  $\rho_c \approx 1.8 \times 10^{21}$  cm<sup>-3</sup> is the critical plasma density, and power dissipation is assured by multiphoton absorption (MPA) with coefficient  $\beta^{(K)} \approx 4.25 \times 10^{-98}$  cm<sup>2K-3</sup>/W<sup>K-1</sup>. Plasma defocusing is mainly induced by ionization of oxygen molecules with gap potential  $U_i = 12.1$  eV and neutral density  $\rho_{\text{nt}} = 5.4 \times 10^{18}$  cm<sup>-3</sup>. Plasma formation is essentially driven by multiphoton ionization (MPI) with coefficient  $\sigma_K = 2.88 \times 10^{-99}$  s<sup>-1</sup> cm<sup>2K</sup>/W<sup>K</sup> and number of photons  $K = 8$ . Equations (1) and (2), moreover, include avalanche ionization ( $\sigma = 5.44 \times 10^{-20}$  cm<sup>-2</sup>) and group-velocity dispersion (GVD) with  $k'' = 0.2$  fs<sup>2</sup>/cm.

We now derive a reduced model, which follows from freezing the temporal dependencies of  $\mathcal{E}$  in Eq. (1). For subpicosecond durations, avalanche ionization and related absorption are ignored. We also omit GVD whose coefficient  $k''$  is weak and assume that MPI counterbalances Kerr focusing at a time slice  $t \approx t_c(z)$ , where a dominant spike with temporal extent  $T$  emerges from the pulse profile and keeps the same order of magnitude along propagation. Because there exists evidence [12] that MPI shortens pulses to 1/10 of their initial duration, we choose  $T = t_p/10$ . Setting  $\mathcal{E}(x, y, z, t) = \psi(x, y, z) \times \chi[t, t_c(z)]$ , where the function  $\chi$  is modeled by the Gaussian  $\chi[t, t_c(z)] = e^{-[t-t_c(z)]^2/T^2}$ , we plug this ansatz into Eqs. (1) and (2) and use the expression of  $\rho \approx \sqrt{\pi/(8K)} T \sigma_K \rho_{\text{nt}} |\psi|^{2K} \{\text{erf}[\sqrt{2K}(t-t_c(z))/T] + 1\}$ , where  $\text{erf}(x)$  denotes the error function. We next integrate Eq. (1) over the entire time domain after multiplying it by  $\chi$ . The equation for  $\psi$  thus reads

$$i\partial_z \psi + \frac{1}{2k_0} \nabla_{\perp}^2 \psi + \alpha k_0 n_2 |\psi|^2 \psi - \gamma |\psi|^{2K} \psi + i\nu |\psi|^{2K-2} \psi = 0, \quad (3)$$

with  $\alpha = [1/\sqrt{8} + D(t_p)/4\tau_K]$ ,  $\nu = \beta^{(K)}/2\sqrt{K}$ , and  $\gamma = k_0 \sigma_K \rho_{\text{nt}} \sqrt{\pi/8KT}/2\rho_c$ . Here, the function

$$D(t_p) \equiv \int_{-\infty}^{+\infty} e^{(T^2/8\tau_K^2) - (u/\tau_K) - (2u^2/T^2)} \times \left\{ \text{erf}\left(\frac{\sqrt{2}u}{T} - \frac{T}{\sqrt{8}\tau_K}\right) + 1 \right\} du \quad (4)$$

follows from averaging in time the delayed Raman response. For durations  $85 \leq t_p \leq 510$  fs,  $D(t_p)$  varies between  $0.0868t_p$  and  $0.117t_p$  while  $0.39 \leq \alpha \leq 0.51$ , respectively. Note that this model does not depend on the longitudinal location of the time slice  $t = t_c(z)$ .

For testing the reliability of Eq. (3), we first simulate with Eqs. (1) and (2) the evolution of an anisotropic  $N$ th-order super-Gaussian (SG) input pulse,  $\mathcal{E}_0 = \sqrt{I_0} e^{-(x^2/w_0^2 + 2y^2/w_0^2)^N - t^2/t_p^2}$ , perturbed in space and time by an isotropic 10% random amplitude noise. Figure 1(a) shows the plasma strings ( $\max_t \rho \propto |\mathcal{E}|_{\text{max}}^{2K}$ ) produced by this pulse with the beam parameters  $w_0 = 0.2$  cm,  $t_p = 85$  fs,  $N = 2$ , and  $P_{\text{in}} \approx 88P_{\text{cr}}$ . Integration along the  $z$  axis is performed with a spectral code in  $(x, y, t)$  running over 128 processors and using an adaptive step in  $z$  tuned on the intensity growth. Because of their dependence over  $|\mathcal{E}|^{2K}$ , the plasma strings, having a size in ratio  $1/\sqrt{K}$  of the filament waist, provide direct information on the beam isointensities and on the location of the filaments in the  $(x, y)$  plane. The simulation shows an early disordered emission of short-scale cells nucleated at different locations, as observed in [9]. At later distances, however, these cells self-organize into three distinct channels, which do not interact significantly and conserve their

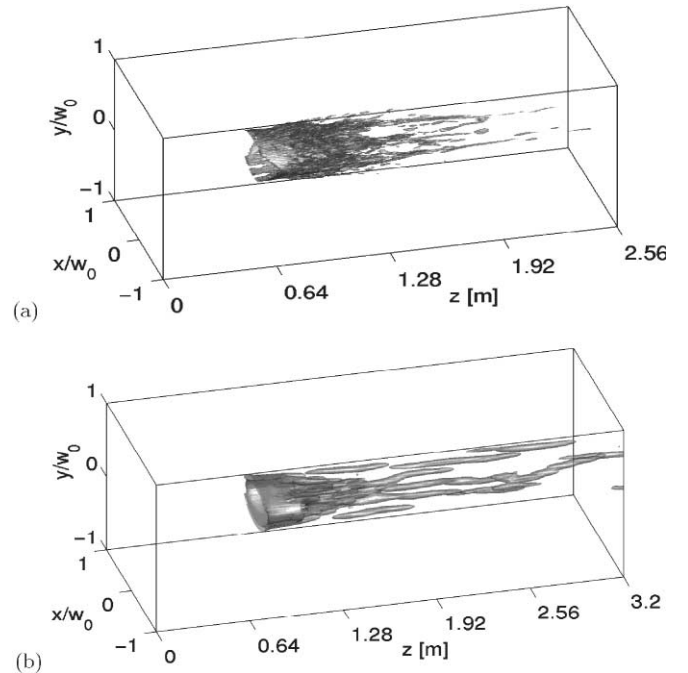


FIG. 1. (a) Plasma strings produced by a perturbed SG pulse governed by Eq. (1) with  $N = 2$ ,  $P_{\text{in}} = 88P_{\text{cr}}$ , and  $w_0 = 0.2$  cm. (b) Isointensity pattern of the filamentary structures created by the same pulse averaged in time following Eq. (3).

mean transverse position. For comparison, we use the fluence distribution  $[\mathcal{F} = \int_{-\infty}^{+\infty} |\mathcal{E}|^2 dt]$  of the same pulse as an input datum for Eq. (3). Figure 1(b) shows the corresponding isointensity plot. Intermittency in filament nucleation occurs again in the early propagation over short ranges  $\leq 0.5$  m, before the filaments gather into a limited number of channels. Short-scale filaments self-attract around specific points in the diffraction plane and produce three clusters of light. These sustain a longer propagation while they still continue to excite short-living cells in their vicinity. This dynamics is qualitatively similar to that developed in Fig. 1(a).

Although restrained to a single time slice, the 2D model reproduces qualitative behaviors of the original 3D Eqs. (1) and (2). Therefore, we find it worth mentioning some major properties of the reduced equation. In the absence of MPA, Eq. (3) admits soliton solutions exhibiting an SG shape with waist  $w_s$ ,  $|\psi_s| \sim A_s e^{-(r/w_s)^{2N}}$ , where  $A_s^2 \sim (\gamma/\alpha k_0 n_2)^{1/(1-K)}$  and  $N$  decreases with the soliton power. When MPA comes into play, it is then easy to evaluate from the power conservation law the maximum dissipation range along which the power in one soliton goes below critical. This length,  $\Delta z_{\text{MPA}} \approx 0.4$  m, does not depend on the beam waist and is compatible with the short “life range” of one isolated filament simulated in [9]. In contrast, when several filaments are confined in the same neighborhood, Eq. (3) predicts that they can interact and self-maintain over much longer distances ( $>1$  m), which explains the apparent robustness of the asymptotic channels in Fig. 1.

To check this concept, we investigate some evolution stages in the filamentation patterns produced by the Teramobile laser [2]. This system delivers 10-Hz rated pulses in collimated geometry with energy up to 0.5 J, transverse diameter equal to 5 cm ( $w_0 \approx 2.5$  cm), and FWHM durations ( $\equiv \sqrt{2 \ln 2} t_p$ ) tunable from 100 to 600 fs. The coming experiments show photos taken from a white screen positioned in the plane orthogonal to the beam path. A filter with narrow bandwidth around  $\lambda_0 = 800$  nm was put in front of a CCD camera.

Figure 2 details the growth of the experimental filaments (colored figures) over 55 m for pulses with 230 mJ energy and duration of 600 fs. Modulations induced by caustics in the spatial beam profile develop as follows: At the edge of the beam where fluctuations are the most intense, filaments occur along a flattened ring inside the focal spot. More filaments are then generated around this ring, which degenerates into a three-pronged fork shape before the final spreading of the beam.

For comparison, we integrated the (2D + 1)-dimensional Eq. (3) from a digitized file of the experimental input beam profile. With a pulse duration of 600 fs ( $t_p \approx 510$  fs), the coefficient  $\alpha$  in Eq. (3) takes the value  $\alpha = 0.51$ . Very high spatial resolution [i.e.,  $8192^2$  points in the  $(x, y)$  plane for a box length of  $6w_0$ ] was required, in order to solve narrow optical structures reaching  $\sim 10^3$  times the input intensity  $I_0$ . In Fig. 2, black and white

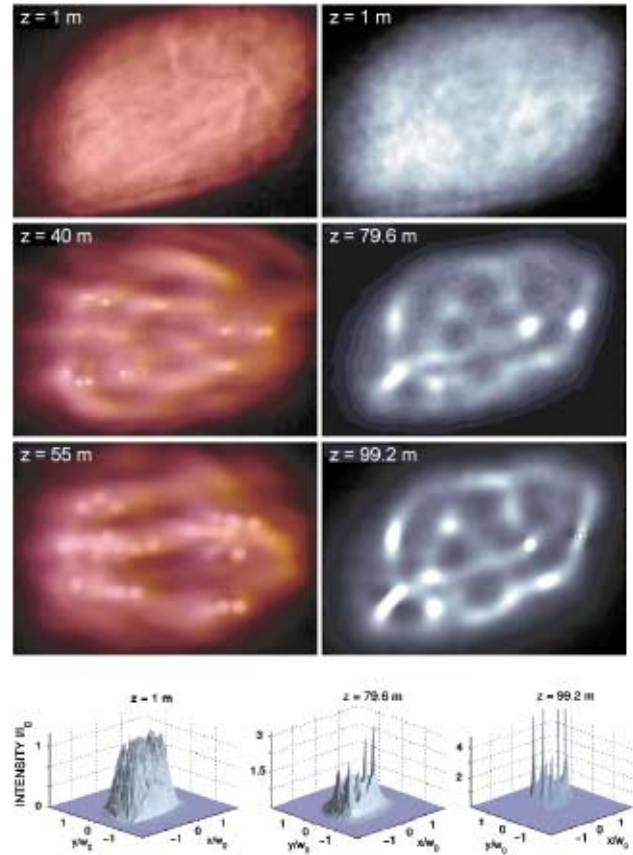


FIG. 2 (color). Left: Filamentation patterns produced experimentally for the  $120P_{\text{cr}}$  beam at different propagation distances. Right: Numerical computations of the same beam from Eq. (3). Bottom row shows the major peaks forming the pattern. For clarity, the maximum intensity is limited to four times the input intensity.

figures illustrate the results of these numerical simulations. The beam containing  $\approx 120$  critical powers begins to form local clots from the highest intensity regions of the beam. Then, others emerge along a ring inside the lower half plane of the focal spot. The final pattern results in a trident-shaped figure, as experimentally observed. Discrepancies in the filamentation distances are attributed to our former choice  $T = 0.1t_p$ , which suits in the ionization regime but cannot restore the early self-focusing distances requiring rather  $T = t_p$ . For such beams with a few tens of critical powers only, Eq. (3) describes a disordered optical distribution having an effective power ratio of  $\sim \alpha P_{\text{in}}/P_{\text{cr}} \approx 60$ . This limits to 24 at the very most the number of genuine filaments reaching the ionization threshold. From these patterns, we can observe that some filamentary channels persist over several meters, whereas others are randomly nucleated over shorter longitudinal scales. The bottom row in Fig. 2 illustrates the numerically computed spatial distortions in the beam profile. These favor the growth of intense peaks that imprint the filamentation figure and locate clusters near which light cells may aggregate.

Let us notice that the resemblance between the experimental and numerical patterns does not lie, of course, in the exact position and number of the filaments, which undergo fluctuations owing to, e.g., atmospheric turbulence or local diffusive processes as they propagate. Instead, qualitative similarities occur in the following sense: Starting with an input coarse profile, the beam amplifies its initial inhomogeneities, and, through modulational instability, it produces bright spots connected by lower-intensity bridges. A “global” pattern then emerges from the zones of highest concentration of light, which form characteristic figures (ring/trident). These aspects are actually well restored by the 2D simulations, using the digitized fluence of the experimental input beam.

Figure 3 displays filamentation stages for pulses delivered by the Teramobile system, with a shorter FWHM duration of 100 fs ( $t_p = 85$  fs) and 230 mJ energy. The power range here accesses 2.3 TW, i.e., about 700 critical powers. A ring-shaped zone supports major spots initiated by the highest-intense defects of the initial beam [ $z \approx 30$  m]. These “hot” spots self-focus more and more over several meters, while they excite secondary smaller-scaled filaments in their vicinity [ $z \approx 35$  m]. Evacuation of power excess (MPA, collapse dynamics) undergone by the primary filaments finally allows the transfer of power to the central zone of the beam, which serves as an energy reservoir for exciting new sequences of small spots [ $z \approx 50$  m]. Equation (3) computed with  $\alpha = 0.39$  ( $t_p = 85$  fs) restores these features with less discrepancy in the filamentation distances, since the beam contains much higher power than in the previous case. From these results, we can examine specific geometrical zones in the beam pattern. Characteristic examples are indicated by the labels 1–3: (1) points to a couple of hot spots surviving at further distances; (2) indicates an active region of the beam, where intense filaments decay into cells of lesser intensity; (3) identifies an area including a cross-wise structure that keeps some filaments robust over 5 m. Spatial distortions in the 2D simulations qualitatively agree with the experimental features. The beam breaks up into more cells ( $\alpha P_{in}/P_{fil} \sim 110$ ) than in the previous lower-power case. Note that even if some filaments are still able to survive over several meters at the most powerful regions of the pulse, random nucleation of optical cells seems here more developed than in the patterns shown in Fig. 2. At high powers, clusters of filaments cannot, indeed, propagate independently due to their smaller separation distance. They experience more substantial power transfers through the overall surface of the beam, which, therefore, increases the number of secondary cells.

In summary, we have investigated the multiple filamentation of collimated beams delivered by the Teramobile laser, for powers up to several TW. Long-range filaments are initiated by the most intense fluctuations of the input beam, and these may persist over several

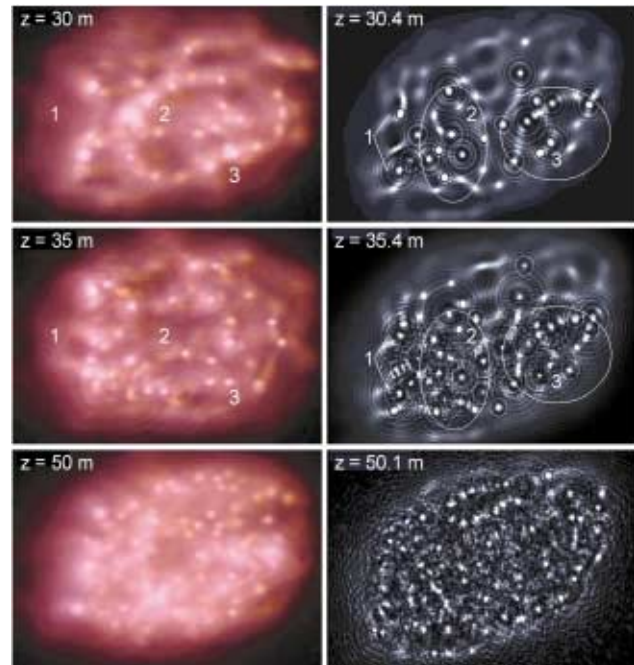


FIG. 3 (color). Left: Filamentation patterns of the  $700P_{cr}$  beam delivered by the Teramobile laser. Right: Numerical computations performed with Eq. (3). Labels 1–3 spot specific beam zones commented on in the text.

tens of meters. Small-scale spots arise and recur rapidly at other places in the diffraction plane, in agreement with the scenario of “optically turbulent light guides” proposed in Ref. [9]. The long-living primary filaments, as well as unstable randomly nucleated ones, can be described by the reduced 2D model [Eq. (3)], which reproduces qualitative events in the filamentation patterns.

Experiments were realized in the framework of the Teramobile Project, funded jointly by CNRS and DFG.

- 
- [1] L. Wöste *et al.*, *Laser Optoelektron.* **29**, 51 (1997).
  - [2] H. Wille *et al.*, *Eur. Phys. J. Appl. Phys.* **20**, 183 (2002); J. Kasparian *et al.*, *Science* **301**, 61 (2003).
  - [3] A. Braun *et al.*, *Opt. Lett.* **20**, 73 (1995); E. T. J. Nibbering *et al.*, *Opt. Lett.* **21**, 62 (1996); A. Brodeur *et al.*, *Opt. Lett.* **22**, 304 (1997).
  - [4] B. LaFontaine *et al.*, *Phys. Plasmas* **6**, 1615 (1999).
  - [5] S. L. Chin *et al.*, *Appl. Phys. B* **74**, 67 (2002).
  - [6] S. Tzortzakis *et al.*, *Phys. Rev. Lett.* **86**, 5470 (2001).
  - [7] V. I. Bespalov and V. I. Talanov, *JETP Lett.* **3**, 307 (1966).
  - [8] L. Bergé, Cl. Gouédard, J. Schjødt-Eriksen, and H. Ward, *Physica (Amsterdam)* **176D**, 181 (2003).
  - [9] M. Mlejnek, M. Kolesik, J. V. Moloney, and E. M. Wright, *Phys. Rev. Lett.* **83**, 2938 (1999).
  - [10] M. Mlejnek, E. M. Wright, and J. V. Moloney, *Opt. Lett.* **23**, 382 (1998).
  - [11] A. Couairon *et al.*, *J. Opt. Soc. Am. B* **19**, 1117 (2002).
  - [12] H. Ward and L. Bergé, *Phys. Rev. Lett.* **90**, 053901 (2003).

**Filamentation of femtosecond light pulses in the air: Turbulent cells versus long-range clusters**S. Skupin,<sup>1,2,\*</sup> L. Bergé,<sup>1</sup> U. Peschel,<sup>2</sup> F. Lederer,<sup>2</sup> G. Méjean,<sup>3</sup> J. Yu,<sup>3</sup> J. Kasparian,<sup>3</sup> E. Salmon,<sup>3</sup> J. P. Wolf,<sup>3</sup> M. Rodriguez,<sup>4</sup> L. Wöste,<sup>4</sup> R. Bourayou,<sup>5</sup> and R. Sauerbrey<sup>5</sup><sup>1</sup>*Département de Physique Théorique et Appliquée, CEA/DAM Ile de France, Boîte Postale 12, 91680 Bruyères-le-Chatel, France*<sup>2</sup>*Institut für Festkörperteorie und Theoretische Optik, Friedrich-Schiller-Universität Jena, Max-Wien-Platz 1, 07743 Jena, Germany*<sup>3</sup>*Laboratoire de Spectrométrie Ionique et Moléculaire, Université Cl. Bernard Lyon 1, UMR-CNRS 5579, F-69622 Villeurbanne Cedex, Lyon, France*<sup>4</sup>*Institut für Experimentalphysik, Freie Universität Berlin, Arnimallee 14, D-14195 Berlin, Germany*<sup>5</sup>*Institut für Optik und Quantenelektronik, Friedrich-Schiller-Universität Jena, Max-Wien-Platz 1, 07743 Jena, Germany*

(Received 30 January 2004; revised manuscript received 13 May 2004; published 5 October 2004)

The filamentation of ultrashort pulses in air is investigated theoretically and experimentally. From the theoretical point of view, beam propagation is shown to be driven by the interplay between random nucleation of small-scale cells and relaxation to long waveguides. After a transient stage along which they vary in location and in amplitude, filaments triggered by an isotropic noise are confined into distinct clusters, called “optical pillars,” whose evolution can be approximated by an averaged-in-time two-dimensional (2D) model derived from the standard propagation equations for ultrashort pulses. Results from this model are compared with space- and time-resolved numerical simulations. From the experimental point of view, similar clusters of filaments emerge from the defects of initial beam profiles delivered by the Teramobile laser facility. Qualitative features in the evolution of the filament patterns are reproduced by the 2D reduced model.

DOI: 10.1103/PhysRevE.70.046602

PACS number(s): 52.38.Hb, 42.65.Tg, 42.65.Jx, 42.68.Ay

**I. INTRODUCTION**

First experiments on the long-range propagation of femtosecond (fs) laser pulses were performed in the mid-1990s [1–3]. In these experiments, infrared laser pulses with duration of about 100 fs produced narrow filaments of several meters, along which more than 10% of the energy was observed to be localized in the near-axis area. This phenomenon is attributed to the early self-focusing of laser radiation, which originates from the Kerr response of air and leads to an increase of light intensity. This growth is then saturated by the defocusing action of the electron plasma created by photoionization of air molecules. As a result, the maximum light intensity in the filament does not exceed  $10^{14}$  W/cm<sup>2</sup> for infrared pulses. If the pulse power is less than a few critical powers for self-focusing ( $P_{cr}$ ) in air [1,2], only one filament is created. At higher powers, two or more filaments can be produced [3–7]. Knowing that novel optical sources nowadays access the terawatt (TW) range, it is thus timely to understand the dynamics of fs light pulses when they decay into multiple small-scale structures, in view of improving, e.g., atmospheric remote sensing techniques [8].

Filaments originate from the modulational instability (MI) triggered by the nonlinear response of air. Applied to an optical background, MI breaks up high-power beams into small-scale cells that each convey a power close to  $P_{fil} \approx \pi^2 P_{cr}/4$  [9–11]. These cells are then amplified through the collapse dynamics and relax their inner power to the critical one, until they reach the ionization threshold near which they give rise to various transverse patterns and undergo strong temporal distortions [11,12]. At relatively low energies

( $\leq 5$  mJ), a beam can decompose only into a couple of small spots that fuse as they attain a full ionization regime [5]. This fusion mechanism reduces the final number of output filaments along the propagation axis. For broader beams conveying much higher energies, another scenario [13], elaborated from three-dimensional (3D) numerical simulations of a central portion of the pulse over a dozen of meters, emphasizes a propagation sustained by random nucleation of small-scale filaments: Collapsing cells resulting from MI are regularized via plasma defocusing with very weak losses from multiphoton absorption (MPA). Recurrent collapse events, which are fed by the energy reservoir created from anterior defocused filaments, then form an “optically turbulent light guide,” which drives the pulse dynamics. This latter scenario contrasts with the simple picture of light guides that stay robust over long distances.

The goal of this work is to clear up this apparent controversy by investigating pulse filamentation up to the Rayleigh range for high input powers ( $10 < P_{in}/P_{cr} < 1000$ ). To address this issue, we first briefly recall the fundamental equations governing the atmospheric propagation of ultrashort pulses. Because the numerical integration of these equations over long distances in full (3D+1)-dimensional geometry is mostly limited by the available computer capacities, we propose a (2D+1)-dimensional model derived by averaging all time dependencies in the laser envelope and the plasma response. This reduced model [7] admits solitonlike states that describe short-range “randomly-nucleated” filaments. We show that these structures confine themselves into a limited number of long-range coherent objects, termed as “optical pillars.” Besides transient stages where turbulent cells recur, these new structures around which filaments self-organize drive the pulse dynamics. This property is confirmed by the direct solving of the (3D+1)-dimensional equations applied

\*Electronic address: stefan@pinet.uni-jena.de

to mm-waisted ultrashort pulses. Second, we compare experiments with numerical simulations in order to understand how filaments are produced and how they impact on the long-distance propagation of TW pulses with peak powers as high as 1000 times  $P_{\text{cr}}$ . To do so, three series of experiments involving the Teramobile facility [14] are performed in parallel geometry, with beam powers varying between 120 and 1000  $P_{\text{cr}}$ . Each series of experiments is numerically simulated by means of the averaged-in-time approach. This model is found to reproduce the qualitative features of the experimental patterns. High-intensity defects in the spatial distribution of the input beam generate “optical pillars” persisting over several tens of meters through the propagation. By “optical pillars” we mean discrete light spots capable of amalgamating short-living solitonlike cells that self-attract around specific points in the diffraction plane. The resulting structure then sustains a long-range propagation, while it can still continue to excite short-range cells in its vicinity. Optical pillars indeed evacuate power as they collapse, so that randomly nucleated filaments may recur more and more along the optical path, in accordance with the scenario of [13]. The major difference between the concept of “optical pillars” and both the “optically-turbulent light guide” [13] and “self-waveguiding” [1] models lies in the following: The possibility of guiding the beam through a small number of quasicontinuous long-range clusters created from its most intense regions. A last experiment realized in converging geometry validates this concept: A focused beam is observed to decay into several tens of small-scale cells before the focal point of the beam. The linear lensing shrinks all filaments at the focal point, after which only three quasicontinuous channels of light keeping the same average direction propagates over almost 10 m.

The paper is organized as follows. In Sec. II we briefly recall the model equations. Section III is devoted to the derivation of the reduced (2D+1)-dimensional model and to the analysis of its solitonlike solutions. Emphasis is put on soliton interactions in the conservative regime and on the action of MPA which damps the soliton profiles and decreases their power over a generic distance. In spite of natural limitations owing to the averaging in time, the spatial dynamics described by this model is found to be qualitatively close to that provided by the original (3D+1)-dimensional equations. Direct comparisons between both models are commented on in Sec. IV, where the limits of applicability for the 2D reduction are thoroughly discussed. Differences between an averaged-in-time filament compared with its (3D+1) counterpart developing a two-peaked temporal profile [15,16] are discussed. Section V concerns experimental observations of filaments evolving from terawatt pulses delivered by the Teramobile facility. By means of classical charge coupled device (CCD) imaging, the filamentation figures are collected over regular distances upon the propagation axis. They emphasize the early amplification of the initial beam defects. These defects then serve as central “hot” spots around which short-scale light cells arise and rapidly recur over 1 m-range distances. The local zones formed by a central spot surrounded by short-living cells are able to propagate much farther and meet the definition of an “optical pillar” given above. The qualitative events developed in the experimental

patterns are shown to agree with numerical computations realized from the 2D reduced model, using a digitized file of the input beam profile. Different input powers comprised between 100 and 1000 times  $P_{\text{cr}}$  are investigated for collimated beams. A special experiment involving a focused beam achieves to confirm both the validity of the 2D model and the existence of “optical pillars.”

## II. THE PHYSICAL MODEL

The equations describing the propagation of ultrashort pulses with intensities limited to  $10^{14}$  W/cm<sup>2</sup> at infrared wavelengths are nowadays classical. As already justified in anterior references [5,7,12,13,15–17], the fundamental model consists of a (3D+1)-dimensional extended nonlinear Schrödinger (NLS) equation for the electric field envelope  $\mathcal{E}(x, y, z, t)$  moving with the group velocity  $v_g$ , coupled to a Drude model for the local plasma density  $\rho(x, y, z, t)$ :

$$\frac{\partial \mathcal{E}}{\partial z} = \frac{i}{2k_0} \nabla_{\perp}^2 \mathcal{E} - i \frac{k''}{2} \partial_t^2 \mathcal{E} + ik_0 n_2 \mathcal{R}(t) \mathcal{E} - \left( \frac{\sigma}{2} + i \frac{k_0}{2\rho_c} \right) \rho \mathcal{E} - \frac{\beta^{(K)}}{2} |\mathcal{E}|^{2K-2} \mathcal{E}, \quad (1a)$$

$$\mathcal{R}(t) = (1 - \theta) |\mathcal{E}|^2 + \frac{\theta}{\tau_K} \int_{-\infty}^t e^{-(t-t')/\tau_K} |\mathcal{E}(t')|^2 dt', \quad (1b)$$

$$\partial_t \rho = \sigma_K \rho_{\text{nl}} |\mathcal{E}|^{2K} + \frac{\sigma}{U_i} \rho |\mathcal{E}|^2. \quad (1c)$$

These equations apply to fs pulses moving in their group-velocity frame ( $t \rightarrow t - z/v_g$ ), with the central wave number  $k_0 = 2\pi/\lambda_0$ . The critical power for self-focusing is defined by  $P_{\text{cr}} = \lambda_0^2 / 2\pi n_2$  and in air it takes the value  $P_{\text{cr}} \approx 3.3$  GW for the laser wavelength  $\lambda_0 = 800$  nm and Kerr refraction index  $n_2 = 3.2 \times 10^{-19}$  cm<sup>2</sup>/W. In Eq. (1a),  $z$  is the longitudinal distance of propagation while  $\nabla_{\perp}^2 = \partial_x^2 + \partial_y^2$  accounts for optical diffraction in the  $(x, y)$  plane. The second-order temporal derivative refers to normal group-velocity dispersion (GVD) with the coefficient  $k'' = 0.2$  fs<sup>2</sup>/cm. The complete Kerr response of air, defined by Eq. (1b), is composed of an instantaneous contribution and a delayed part in ratio  $\theta$ , with a relaxation time  $\tau_K = 70$  fs [5,17]. The quantity  $\rho_c = 1.8 \times 10^{21}$  cm<sup>-3</sup> is the critical plasma density beyond which the beam no longer propagates. Power dissipation is assured by multiphoton absorption (MPA) with coefficient  $\beta^{(K=8)} = 4.25 \times 10^{-98}$  cm<sup>13</sup>/W<sup>7</sup> [15,17]. In Eq. (1c), plasma defocusing is mainly induced by ionization of oxygen molecules with gap potential  $U_i = 12.1$  eV, contributing to 20% of the neutral density  $\rho_{\text{at}} = 2.7 \times 10^{19}$  cm<sup>-3</sup> [17], so that the effective density of neutral molecules is given by  $\rho_{\text{nt}} = 5.4 \times 10^{18}$  cm<sup>-3</sup>. The number of photons  $K$  needed to extract electrons from neutral atoms is then  $K = 8$ . The electron plasma is essentially driven by multiphoton ionization (MPI) with coefficient  $\sigma_{K=8} = 2.88 \times 10^{-99}$  s<sup>-1</sup> cm<sup>16</sup>/W<sup>8</sup>. Avalanche (cascade) ionization and plasma absorption identified by the cross section for inverse bremsstrahlung  $\sigma = 5.44 \times 10^{-20}$  cm<sup>2</sup> complete this model.

### III. THE REDUCED 2D MODEL

In the following, we consider input electric field distributions characterized by a beam waist  $w_0$ , half-width duration  $t_p$ , and Rayleigh length  $z_0 = \pi w_0^2 / \lambda_0$ .

#### A. Derivation

Current limitations of even the most modern, massively parallel computer machines still prevent us from accessing a complete description of a km-range propagation of broad, cm-waisted beams as a whole, in reasonable CPU times. For, e.g., a beam waist of about 2.5 cm only and a pulse duration  $\sim 100$  fs, the appropriate resolution would require at least  $2^{37}$  mesh points for numerical box lengths in  $(x, y, t)$  of  $15 \times 15 \text{ cm}^2$  and 600 fs, respectively. In addition, it is often necessary to employ an adaptively refined step along  $z$  able to resolve correctly the sharp peaks coupled to narrow plasma channels with size  $\leq 50 \mu\text{m}$ , emerging along the filamentation process. Numerical simulations fulfilling these needs then consume several Terabytes in memory for a single run, which we have to avoid. For this reason, we may alternatively derive a reduced model from the original (3D+1)-dimensional equations. This model amounts to reducing the number of effective dimensions by freezing suitably the temporal dependencies of the wave field. Even though this reduction is primarily motivated by technical constraints, it also allows us to gain a deeper insight into the transverse dynamics of the filamentation phenomenon.

To establish the 2D model, we first apply some preliminary approximations. Considering subpicosecond durations, avalanche ionization and related plasma absorption have a weak incidence on the pulse dynamics for the parameters examined below and we thus ignore them. We can also omit group-velocity dispersion, whose physical coefficient  $k'' = 0.2 \text{ fs}^2/\text{cm}$  makes it too weak for being a key player competing with ionization of air molecules over filamentation distances limited to 100 m. Former numerical simulations in this field showed that femtosecond filaments result from the competition between Kerr self-focusing and MPI. We thus assume that MPI mainly counterbalances Kerr self-focusing at a time slice  $t \approx t_c(z)$  where a dominant spike with temporal extent  $T$  emerges in the pulse temporal profile. This duration  $T$  is conjectured to keep the same order of magnitude along propagation. Therefore we decompose  $\mathcal{E}$  as follows:

$$\mathcal{E}(x, y, z, t) = \psi(x, y, z) \times \chi[t, t_c(z)], \quad (2)$$

where the temporal distribution for the highest-intensity peak is modeled by the Gaussian  $\chi[t, t_c(z)] = e^{-[t - t_c(z)]^2 / T^2}$ . Under the previous hypotheses, we can plug the above expression of  $\mathcal{E}$  into Eq. (1), use the expression of

$$\rho \approx \sqrt{\frac{\pi}{8K}} T \sigma_K \rho_{\text{nl}} |\psi|^{2K} \left\{ \text{erf} \left[ \frac{\sqrt{2K}[t - t_c(z)]}{T} \right] + 1 \right\}$$

where  $\text{erf}(x)$  denotes the usual error function, and integrate Eq. (1a) over the entire time domain after multiplying it by  $\chi$ . The resulting equation for  $\psi$  reads

$$\frac{\partial \psi}{\partial z} = \frac{i}{2k_0} \nabla_{\perp}^2 \psi + i \alpha k_0 n_2 |\psi|^2 \psi - i \gamma |\psi|^{2K} \psi - \frac{\beta^{(K)}}{2\sqrt{K}} |\psi|^{2K-2} \psi, \quad (3)$$

where  $\alpha = (1 - \theta + \theta D) / \sqrt{2} \tau_K / \sqrt{2}$ ,  $\gamma = \sqrt{\pi / 8K} (T k_0 \sigma_K \rho_{\text{nl}}) / (2\rho_c)$ , and

$$D = \int_{-\infty}^{+\infty} e^{T^2/8\tau_K^2 - u/\tau_K - 2u^2/T^2} \left[ \text{erf} \left( \frac{\sqrt{2}u}{T} - \frac{T}{\sqrt{8}\tau_K} \right) + 1 \right] du.$$

Here, the integral  $D$  follows from averaging in time the delayed Kerr component, where, in agreement with antecedent studies (see, e.g., Refs. [5,17]), we shall henceforth impose  $\theta = 1/2$ . Equation (3) describes the transverse dynamics of fs beams, with appropriate coefficients  $\alpha$ ,  $\gamma$  keeping the trace of averaged variations in time of the pulse. It is worth noticing that this model does not depend on the longitudinal location of the time slice  $t = t_c(z)$ . The only arbitrariness is the choice of the peak duration  $T$ . On the one hand, a natural assumption would be to opt for  $T = t_p$ , i.e., an ionization front raises from a wave structure with mean duration comparable to that of the input pulse. For example, when  $t_p = 85$  fs and  $\tau_K = 70$  fs, this choice leads to  $D \approx 0.707$  and  $\alpha \approx 0.57$ . On the other hand, there now exists evidence [15,18] that MPI can shorten pulses to mean duration reaching 1/10 of their initial values. Setting  $T = 0.1 t_p$  with  $t_p = 85$  fs then provides the coefficients  $D = 0.117$ , so that  $\alpha = 0.39$ . Note from these estimates that the global effect of the delayed Kerr component is to increase the effective power for self-focusing to some extent. This property may explain former experimental observations [1], following which powers above three times  $P_{\text{cr}}$  are often necessary to create one localized filament. Because we wish to describe filamentation patterns in a full ionization regime, we henceforth assume  $T = t_p/10$ . This value was found to provide the best approximations of fluence patterns developed by (3D+1)-dimensional fs pulses.

Let us now discuss inherent properties to Eq. (3) before proceeding to comparisons of this 2D approach with direct simulations of Eq. (1).

#### B. Solitonlike dynamics

For technical convenience, we express Eq. (3) into a dimensionless system of units. Only employed in this section, this change of variables and fields fixes the saturation intensity ( $I_{\text{max}}$ ) realizing an equilibrium between Kerr and MPI nonlinearities to the unity. By introducing the rescaled variables  $Z = z[(\alpha k_0 n_2)^K / \gamma]^{1/(K-1)}$ ,  $X = x \sqrt{2k_0} [(\alpha k_0 n_2)^K / \gamma]^{1/(2K-2)}$ ,  $Y = y \sqrt{2k_0} [(\alpha k_0 n_2)^K / \gamma]^{1/(2K-2)}$ , the rescaled field  $A = \psi (\gamma / \alpha k_0 n_2)^{1/(2K-2)}$ , and the parameter  $\nu = (\beta^{(K)} / 2\sqrt{K}) \times (\alpha k_0 n_2 \gamma^{K-2})^{1/(1-K)}$ , it is straightforward to rewrite Eq. (3) in the form

$$\frac{\partial A}{\partial Z} = i \Delta_{\perp} A + i |A|^2 A - i |A|^{2K} A - \nu |A|^{2K-2} A, \quad (4)$$

where  $\Delta_{\perp} = \partial^2 / \partial X^2 + \partial^2 / \partial Y^2$  and the parameter  $\nu$  takes the value  $\nu = 0.154$  with the above choices of  $\alpha = 0.39$ ,  $t_p = 85$  fs, and  $T = t_p/10$ .

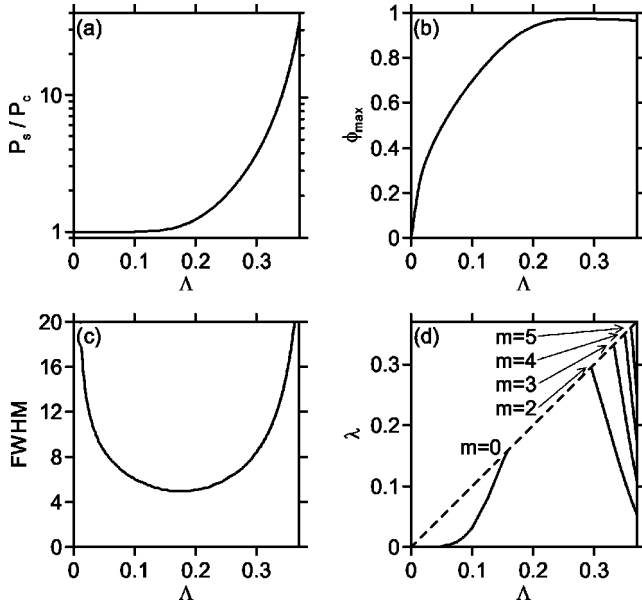


FIG. 1. (a) Soliton power vs  $\Lambda$ , (b) soliton amplitude vs  $\Lambda$ , (c) soliton width vs  $\Lambda$ , and (d) eigenvalues of the internal modes  $\delta\phi$  vs  $\Lambda$ . The dashed line marks the maximum value of  $\lambda$  for which discrete (localized) perturbative modes exist, i.e.,  $\lambda \leq \Lambda$ .

### I. Conservative case $\nu=0$

In the nondissipative regime ( $\nu=0$ ), Eq. (4) admits soliton solutions in the form  $A = \phi(X, Y)\exp(i\Lambda Z)$ , where the soliton shape  $\phi$  is real-valued and satisfies

$$-\Lambda\phi + \Delta_{\perp}\phi + \phi^3 - \phi^{K+1} = 0. \quad (5)$$

Here, we restrict ourselves to the single-hump, nodeless ground state soliton solution. Figures 1(a)–1(c) show the basic properties of this soliton family characterized by  $P_s$ , i.e., the power  $P = \int |A|^2 d\vec{R}$  computed on the shape  $\phi$ , its maximum amplitude  $\phi_{\max}$  and full width at half-maximum (FWHM) over the soliton parameter  $\Lambda$ . Low-power solitons are close to the Townes mode of the cubic NLS equation [corresponding to  $|A|^2 \gg |A|^{2K}$  in Eq. (4)], with power  $P_c = 11.68$  and near-Gaussian spatial shape [19]. High-power ones exhibit a shape resembling high-order super-Gaussians (SG). Their respective intensity  $\phi_{\max}^2$  is always below (although close to) the saturation threshold  $I_{\max} = 1$ .

An important feature is the monotonous increase of  $P_s$  vs  $\Lambda$ , which implies orbital stability of these nonlinear objects, in accordance with the so-called Vakhitov-Kolokolov criterion  $dP_s/d\Lambda > 0$  [20] (see also Refs. [21–23]). Figure 1(d) confirms the stability of such stationary-wave structures from a numerical computation of azimuthal perturbations  $\delta\phi \sim e^{im\theta + i\lambda Z}$  acting against the ground state  $\phi$ , with angular number  $m$  and eigenvalue  $\lambda$  (see details on the related spectral problem in Appendix A). First, we observe that all eigenvalues  $\lambda$  are real-valued, so this family of solitons is linearly stable. Second, in the parameter range  $0.16 < \lambda < 0.29$  ( $1.05 < P_s/P_c < 3.2$  respectively) there are no internal modes, i.e., breather modes characterized by periodic oscillations in their amplitude. Therefore, in this regime we expect the solitons to be particularly robust due to the lack of internal os-

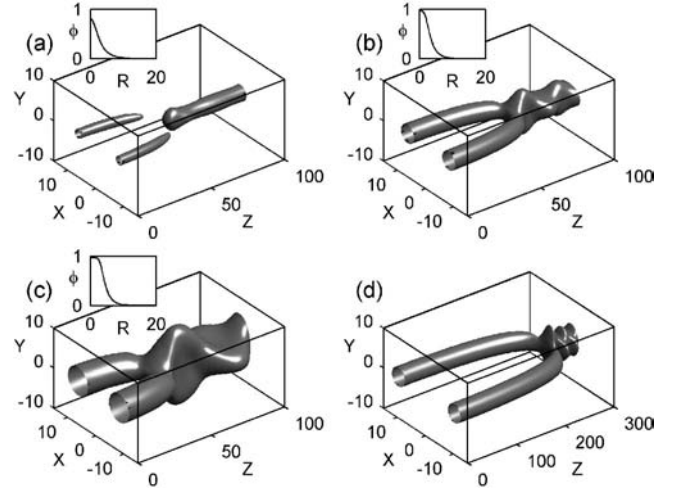


FIG. 2. Isointensity plots [ $I_{\text{iso}}=0.5$ ] of the fusion of conservative solitons ( $\nu=0$ ) with individual power  $P_{\text{fil}}$  and separation distance  $\Delta$ . The insets show the radial shape of the respective soliton. (a)  $P_{\text{fil}} = 1.02P_c$  ( $\Lambda=0.137$ ) and  $\Delta=15$ . (b)  $P_{\text{fil}} = 1.92P_c$  ( $\Lambda=0.254$ ) and  $\Delta=15$ . (c)  $P_{\text{fil}} = 3.84P_c$  ( $\Lambda=3.02$ ) and  $\Delta=15$ . (d) Same parameters as in (b), but with  $\Delta=20$ .

cillations. The corresponding FWHM and intensity maxima expressed in physical units are 150–200  $\mu\text{m}$  and  $(5\text{--}7) \times 10^{13} \text{ W/cm}^2$ , which is in excellent agreement with the usual waist and intensities reached by femtosecond filaments in air [16,17,24].

Solitons are strong nonlinear attractors. Starting with any low intensity field distribution containing sufficient power, self-focusing always leads to the formation of one or more solitons. Another consequence of this dynamics is that these objects attract each other and can mutually fuse. Figure 2 shows iso-intensity plots of the merging of two identical solitons with individual power  $P_{\text{fil}}$  and separation distance  $\Delta$ .

From the above analysis, we expect solitons with powers  $1.05 < P_{\text{fil}}/P_c < 3.2$  to be specifically robust (absence of internal modes). Indeed, for fixed  $\Delta=15$ , solitons without internal modes [Fig. 2(b)] merge at larger distances  $Z$  than those capable of internal oscillations [Figs. 2(a) and 2(c)]. Moreover, if we look at the final states after the fusion processes, only in Fig. 2(a) a robust, new fused static waveguide emerges, starting from  $2P_{\text{fil}}/P_c \approx 2 < 3.2$ . In Figs. 2(b) and 2(c), the opposite condition  $2P_{\text{fil}}/P_c > 3.2$  leads to “breathing” solutions due to the internal mode with  $m=2$ . For an increased separation,  $\Delta=20$ , the point of fusion shifts to significant higher values of  $Z$  [Fig. 2(d)]. Reexpressed in physical units, two filaments separated from each other by a distance  $\sim 0.6 \text{ mm}$  can propagate over more than 3 m before merging.

Using virial arguments detailed in Appendix B, these behaviors can receive a theoretical justification. Two Gaussian-like filaments (which is a reasonable approximation for  $P_{\text{fil}} < 3P_c$ ) with an amplitude close to saturation may merge even without dissipation, provided that both their individual powers and mutual separation distance are below some thresholds. Whenever  $\nu=0$ , this property can indeed be anticipated from the dynamical relation governing the mean-square radius of the beam,  $\langle R^2 \rangle = \int R^2 |\phi|^2 d\vec{R} / P$ . Analyzing

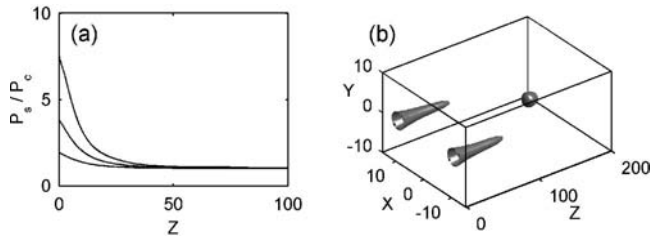


FIG. 3. (a) Decrease of soliton power  $P_s$  vs  $Z$ ,  $\nu=0.154$ , for solitons with  $P_s=1.92P_c$  ( $\Lambda=0.254$ ),  $P_s=3.84P_c$  ( $\Lambda=3.02$ ), and  $P_s=7.56P_c$  ( $\Lambda=3.32$ ). (b) Same as in Fig. 2(d), but with  $\nu=0.154$ . In the region  $100 < z < 150$  preceding the fusion event, beam components slightly diffract with an intensity going below the selected isointensity level [ $I_{\text{iso}}=0.5$ ].

specific regimes for which the interaction terms entering the dynamical relation for  $\langle R^2 \rangle$  remain relevant while the overall radius of the two-component beam decreases, it is found that merging applies in particular to Gaussian-shaped solitons with waist  $W_{\text{fil}}$  and power  $P_{\text{fil}}$  satisfying  $\Delta \leq \Delta_{\text{lim}} = \sqrt{10} W_{\text{fil}}$  and  $P_{\text{fil}} \leq 1.35P_c$ . For wider separation distances ( $\Delta \gg \Delta_{\text{lim}}$ ), the interaction terms vanish and the solitons should in principle cease to interact. Up to discrepancies linked to the starting assumptions (see Appendix B), these expectations are compatible with the results shown in Fig. 2.

### 2. Dissipative case $\nu \neq 0$

When MPA is introduced, Eq. (4) no longer admits stationary solutions. Nevertheless, especially for  $\nu \ll 1$ , the system still holds certain features, deducible from the conservative case. First, for intensities far below the threshold  $\sim 1$ , the dissipative term is irrelevant anyway. So, in the self-focusing regime, formation of “solitons” can proceed as without losses. After reaching a “quasi-soliton” state with an intensity  $\sim 1$ , dissipation comes into play. Since there exists a conservative ground state for all  $P_s \geq P_c$ , the “quasi-soliton” slides “adiabatically” down the curve in Fig. 1(a) until reaching the effective collapse threshold  $P_c$  of the cubic Schrödinger equation. Figure 3(a) shows this property for different powers of the initial soliton. Due to their “flat top” shape, high-power ground states undergo higher losses. As a consequence, starting with high power does not significantly enlarge the dissipation range, which was found numerically  $< 70$  for input powers up to  $20P_c$ . Reexpressed in physical units using the above parameters  $\alpha$ ,  $t_p$ , and  $T$ , this value predicts a maximum filament length  $< 1$  m per pulse, which agrees with the short “life-time” along  $z$  of the recurrent filaments observed in [13].

Modeling the solitons  $\phi$  close to the saturation threshold as  $\phi = \exp[-(R/W_{\text{fil}})^{2N}]$  with  $N \geq 1$ , it is possible to solve approximately the power relation  $d_z P \approx -2\nu \int \phi^{2K} d\vec{R}$ . By using  $\int \phi^{2K} d\vec{R} = K^{-1/N} \int \phi^2 d\vec{R} \approx K^{-1/N} P_s$ , we can evaluate the dissipation range  $\Delta Z_{\text{MPA}}$ , along which the beam power persists above  $P_c$ , as

$$\Delta Z_{\text{MPA}} = \frac{K^{1/N}}{2\nu} (1 - P_c/P_s), \quad (6)$$

where  $P_s$  is the initial soliton power. This estimate takes the maximum value  $\Delta Z_{\text{MPA}} \approx 25$  when  $P_s \gg P_c$  and  $N \rightarrow 1$ . In

physical units,  $\Delta z_{\text{MPA}}$  predicts a maximum filament length of  $\approx 0.35$  m, which is in the same order of magnitude as our numerical result.

Last but not least, dissipation has a significant influence on the fusion dynamics. By comparing Fig. 3(b) to Fig. 2(d), we see that the presence of MPA promotes the mutual coalescence of filaments. The point of fusion shifts to significantly smaller propagation distances. This behavior is understandable in the sense that MPA shifts the “quasi-solitons” to the low power regime  $P_{\text{fil}} < 1.05P_c$ , where we expect an easier merging. Another interesting point is that the dissipation range can be enlarged with the help of the fusion mechanism. The central beam, visible in Fig. 3(b) at  $Z \approx 150$ , indeed clearly exceeds the predicted dissipation range of a single filament.

In summary, Eq. (4) stresses that spatial solitons are the natural objects modeling self-guided femtosecond filaments in the transverse plane. Although their individual range of propagation may be limited to short distances  $< 1$  m by MPA, their capability of merging at relatively low powers enables them to propagate over more extended ranges.

## IV. (2D+1)- VERSUS (3D+1)-DIMENSIONAL NUMERICAL SIMULATIONS

In this section, we return to physical units and compare results of our reduced 2D model [Eq. (3)] with corresponding space-time resolved 3D simulations [Eq. (1)].

### A. 2D simulations

Reframed in the present context, Fig. 4 illustrates filamentation patterns in the 2D approximation, for which different beams undergo random perturbations. Because realistic perturbations mostly differ from oscillatory modulations lined on the maximum MI growth rate [11], we opted, by comparison with antecedent experimental data [5,6], for an input anisotropic  $N$ th-order SG beam in the form  $\psi = \sqrt{I_0} \exp[-(x^2 + 2y^2)^N / w_0^{2N}]$ , perturbed at  $z=0$  m by an isotropic 10% random noise in amplitude and multiplied by a 10% noisy Gaussian temporal profile ( $t_p=85$  fs). The fluence distribution [ $F = \int_{-\infty}^{+\infty} |\mathcal{E}(t)|^2 dt$ ] of the resulting beam is then employed as the input condition for the 2D model. Figure 4(a) shows the isointensity plots for a perturbed beam with  $N=3/2$ ,  $w_0=1$  mm, and  $P_{\text{in}}=20.5P_{\text{cr}}$ . The beam first forms a ring giving rise to two filaments. These merge and reform during a transient stage before they refocus into a robust lobe at center. Intermittency in filament nucleation occurs in the early propagation stage over short ranges, which can be compared with the scenario of the optically turbulent light guide proposed in [13]. However, at larger distances, the filaments relax to a single one in the  $(x, y)$  plane. This waveform afterwards does not change until the Rayleigh length ( $z \rightarrow 4$  m), beyond which it diffracts slowly. Filaments reach the maximum intensity  $I_{\text{max}} \sim 7 \times 10^{13}$  W/cm<sup>2</sup> over distances  $\sim \Delta z_{\text{MPA}} < 1$  m, but they asymptotically remain captured in longer soliton envelopes that locate “optical pillars” in the medium. Similar patterns of two main filaments fusing into one were observed to generically occur with different beam

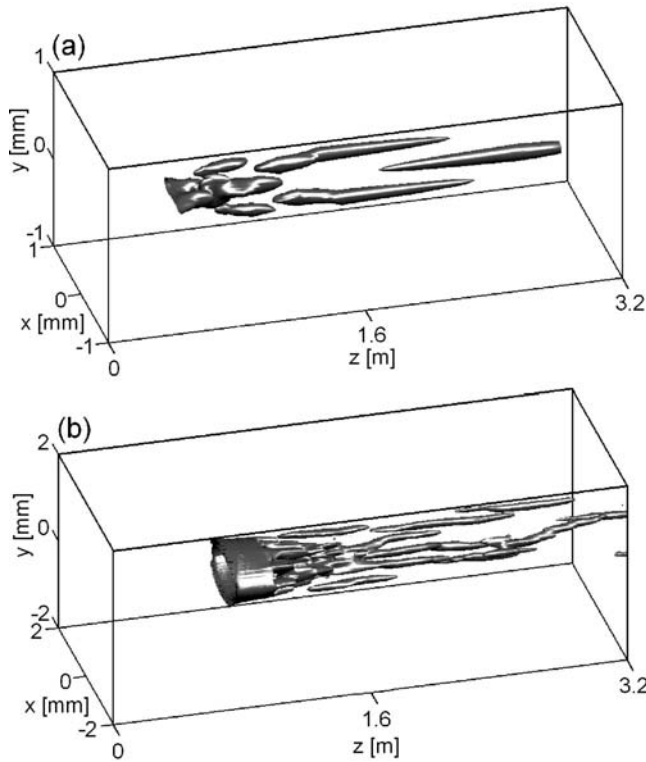


FIG. 4. Isointensity patterns ( $I_{\text{iso}} \approx 10^{12}$  W/cm<sup>2</sup>) of filamentary structures described by Eq. (3) and created from a SG beam with (a)  $N=3/2$ ,  $P_{\text{in}}=20.5 P_{\text{cr}}$  and  $w_0=1$  mm, and (b)  $N=2$ ,  $P_{\text{in}}=88 P_{\text{cr}}$  and  $w_0=2$  mm.

shapes and peak powers comprised between  $15P_{\text{cr}}$  and  $40P_{\text{cr}}$ . This dynamics fully agrees with previous experimental observations [5]. For higher powers, Fig. 4(b) shows a broader ( $N=2$ ) SG beam with  $88P_{\text{cr}}$  and wider waist  $w_0=2$  mm. Filamentary structures with the largest separation distances create strong individual attractors which organize the beams into three major long-range pillars composed of solitonlike filaments. An early stage of “random nucleation” precedes the formation of these three filamentary channels, which may move in the  $(x, y)$  plane while they attempt to attain an equilibrium position.

Like the soliton pattern shown in Fig. 3(b), these two simulations confirm that the mutual interaction between optical cells helps in maintaining the robustness of the beam envelope over several meters.

### B. 3D simulations

For comparison, Eqs. (1) are now solved by means of a spectral code using fast Fourier transforms in the  $(x, y, t)$  variables. Integration along the longitudinal axis ( $z$ ) is performed with an adaptive step tuned on the intensity growth. In the transverse dimensions, a fixed mesh with  $\Delta t \leq 0.5$  fs and  $\Delta x = \Delta y \leq 15$   $\mu\text{m}$  was used. Simulations were realized on the massively parallel machine (TERA) of the CEA, where we used up to 128 processors per run. Details on further numerical aspects and limitations in (3D+1)-dimensional computing are given in Appendix C.

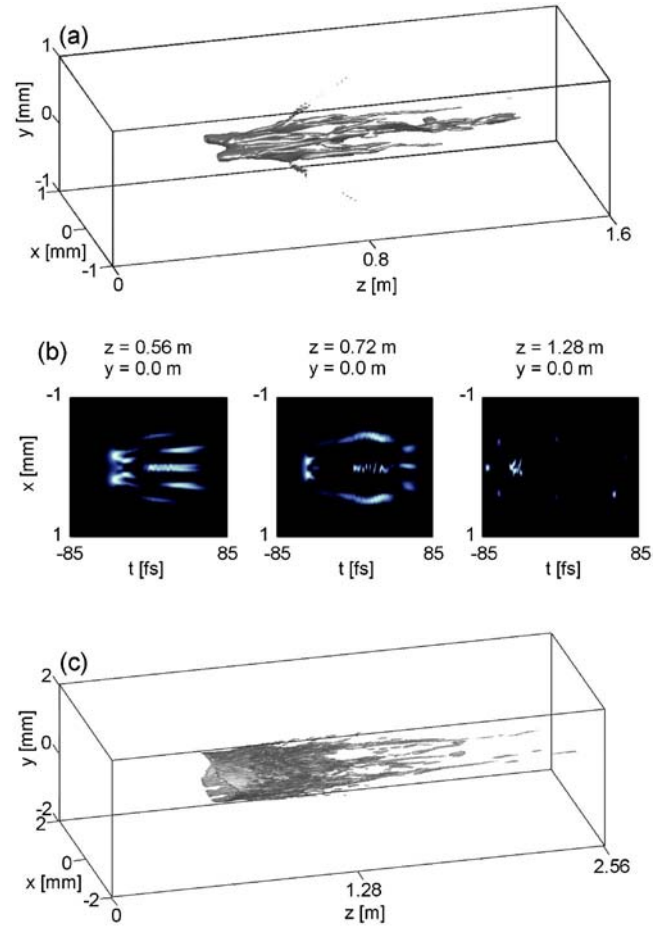


FIG. 5. (a) (Color online) Plasma strings [ $\max_t \rho(x, y, z, t) \geq 10^{15}$  cm<sup>-3</sup>] of the  $20.5P_{\text{cr}}$  SG beam used in Fig. 4(a). (b)  $|\mathcal{E}|^2$  vs  $(x, 0, t)$  for the same beam. (c) Plasma strings from the  $88P_{\text{cr}}$  SG beam of Fig. 4(b).

Figure 5 shows the filamentation of pulses with the same input distributions as the ones used in Fig. 4. In Fig. 5(a) we display the plasma strings produced by the beam with  $20.5P_{\text{cr}}$ . Figure 5(b) shows their associated intensity profiles in the plane  $(x, y=0, t)$  at different  $z$  positions, along the  $y$  axis crossing the two primary spots condemned to merge. The temporal pulse profile, even subject to strong distortions, does not prevent the transverse dynamics of the pulse from developing as in Fig. 4, up to second-order discrepancies in the focus point linked to the choice of  $T$  (see Sec. IV C). Although different temporal slices come into play, all of them support the propagation of cells first nucleated at different locations, then remaining localized around the *same* place in the  $(x, y)$  plane. Plasma strings associated with pulse components of maximum intensity and duration nearby  $1/10$  of the input pulse dominate, which makes our previous assumption for averaging the (3D+1)-dimensional equations valid. Finally, Fig. 5(c) depicts the plasma strings created by the SG pulse with 88 critical powers,  $N=2$  and  $w_0=2$  mm. Three distinct channels clearly emerge in the  $(x, y)$  plane. They do not interact significantly but remain almost robust at their transverse position, in agreement with the filamentation pattern of Fig. 4(b).

### C. Limitations of the reduced model

Major advantages in employing the 2D model concern, of course, the gain in computation time when we only focus on the spatial dynamics of the pulse (see Appendix C). With this aim, Eq. (3) has been successfully employed for clearing up alternative problems, such as, e.g., the interaction of an ultrashort filament with an opaque droplet [24,25]. Experiments on this topic [24] revealed the remarkable robustness of femtosecond filaments with typical waists  $\sim 150 \mu\text{m}$  when they hit a micrometric droplet with a diameter as large as  $2/3$  the filament size. The collision results in a minimal loss of energy and the filament self-heals over very short distances. Recent numerical investigations [25] analyzed this intriguing property. The interaction pattern, simulated from the full 3D system, displayed evidence of the complete rebuilding of the pulse over 2 cm only. The same filament modeled by solitons of Eq. (3) restored an identical pattern within the same longitudinal interval.

Besides such convenient aspects, a 2D reduction of the propagation equations cannot, unfortunately, avoid certain weaknesses. Identifying a 3D, time-resolved filament with a 2D “soliton” means that we only focus on the core of the filament and discard its different time slices [15]. Indeed, Eq. (3) accounts for the time slice with maximum intensity only. For describing, e.g., the self-healing of a fs filament with a micrometric droplet, this simplification has almost no incidence because the interaction length of the beam with the obstacle is short along the  $z$  axis. However, when we simulate long-range propagations, certain concessions in the agreement with fully time-resolved computations have to be made.

(i) The arbitrary choice of the temporal extent  $T=0.1t_p$  prevents us from restoring quantitatively the early self-focusing distances of a beam at relatively low powers ( $\leq 100P_{\text{cr}}$ ), as can be seen by comparing Figs. 4 and 5. Indeed, this choice determines the value of the parameter  $\alpha$  [Eq. (3)] that fixes the effective critical power in the pulse time slice under consideration. Setting  $T=0.1t_p$  is suitable for describing filamentation patterns evolving in ionization regimes, but this choice can lead to visible discrepancies in the location of the first focus point, for which the value  $T=t_p$  yielding a higher  $\alpha$  would be more adapted. Remembering Marburger’s formula [10] that evaluates the collapse point,  $z_c$ , of collimated Gaussian beams in the self-focusing regime:

$$z_c = \frac{0.367z_0}{\sqrt{(\sqrt{\alpha P_{\text{in}}/P_{\text{cr}}} - 0.852)^2 - 0.0219}}, \quad (7)$$

it is seen right away that the differences in the location of the self-focus point indeed become more pronounced at low ratios  $P_{\text{in}}/P_{\text{cr}}$  and for low values of  $\alpha$ .

(ii) Experimental setups for femtosecond pulse propagation are currently based on chirped-pulse amplification (CPA) Ti:sapphire laser sources. CPA techniques allow us to modify the effective initial pulse duration by varying the distance between the gratings of the pulse compression system. These variations also entail a chirp onto the input pulse phase ( $\mathcal{E} \rightarrow \mathcal{E}e^{iCr^2}$ ,  $C=\text{const}$ ), which can lead to noticeable changes in the early self-focusing distances by GVD com-

ensation [26]. Pulse chirping is used to monitor the onset of filamentation [14,27]. Since Eq. (3) ignores the temporal dynamics, applying this model to pulses with an initially large chirped phase may then enhance the differences with the experimental observations.

(iii) Because the averaging procedure involves a single time slice only, the 2D model cannot describe the second focusing of pulses (see, e.g., [16]), which characterizes femtosecond filaments and enables the latter to pursue their propagation over about 1 m. This second refocusing is associated with the late growth of the trailing edge of the pulse. Although it concerns a residual propagation interval in which the pulse intensity noticeably decreases, this process allows one to maintain a femtosecond filament over larger distances than those accessible by the reduced model. In connection with this point, the 2D model also overestimates the losses due to MPA. In full 3D configurations, defocused time slices with lower intensities can maintain a nearly constant power upon propagation until they may focus again. The reliability of the reduced model may thus be limited in, e.g., examining some postionization regimes.

The above discrepancies must not, however, elude the major advantage of the 2D model, which can describe the qualitative dynamics of ultrashort, high-power pulses with broad waists over considerable distances of propagation.

Keeping these limitations in mind, but aware of the information conveyed by the 2D model, we can outline, on the basis of the previous 2D and 3D numerical results, a generic scenario for the filamentation of terawatt fs pulses as follows: (i) Beam modulations give rise to short-range filaments that grow in intensity until reaching the ionization threshold  $I_{\text{max}}$ . In this limit, near-soliton filaments, searching for an equilibrium position, recur in the diffraction plane within an optically turbulent regime during the early stage of propagation [13]. (ii) As they attain a quasistable configuration with respect to their neighbors, short-range filaments either amalgamate or self-attract without merging, depending on their inner power and separation distances, in order to form a limited number of clusters, named as “optical pillars.” These optical pillars then continue the propagation over longer distances.

Note that this scenario applies to input beams where an isotropic random noise first creates short-scale cells that next relax to quasicohherent structures. For experimental beams exhibiting salient defects, it is not excluded that optical pillars are fixed by the most intense defects of the input beam profile, which further excite turbulent cells in their vicinity, as evidenced below (see also [7]).

## V. LONG-DISTANCE PROPAGATION EXPERIMENTS

To figure out how terawatt laser pulses degenerate into multiple filaments over long distances, we investigate some evolution stages in the filamentation patterns produced by the Teramobile laser [14]. This laser system delivers at the 10-Hz rate pulses with energy up to 0.5 J, transverse diameter equal to 5 cm ( $w_0 \approx 2.5$  cm), and FWHM duration tunable from 100 fs (minimal chirp) to 600 fs (large negative chirp) by detuning the compressor with a chirp opposite to

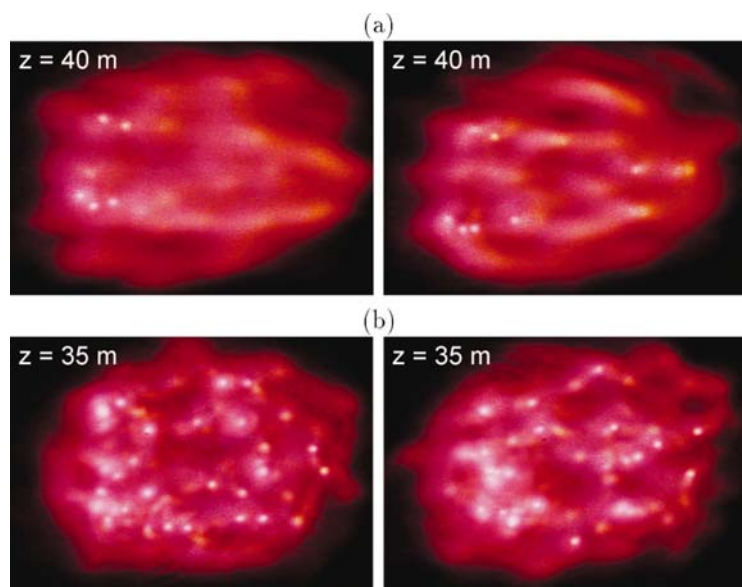


FIG. 6. (Color) Shot-to-shot fluctuations in the filamentation pattern of the 10-Hz rated Teramobile laser delivering 230-mJ pulses with (a) 600 fs duration ( $P_{\text{in}} \approx 120P_{\text{cr}}$ ) at  $z=40$  m, and (b) 100 fs duration ( $P_{\text{in}} \approx 700P_{\text{cr}}$ ) at  $z=35$  m.

air dispersion. The collected experimental data consist of photos taken from a white screen positioned in the plane orthogonal to the beam path. In the first two series of experiments (Figs. 6–8), a filter with narrow bandwidth around  $\lambda_0=800$  nm was put in front of the camera. Two photos with exposure time of 1/8th s were taken at each distance, so that pictures mostly show single-shot beam patterns. Pictures featuring double-pulse images did not present qualitative change from shot to shot, up to slightly more visible filaments or more pronounced ones at certain distances (see Fig. 6). Although the number of “visible” filaments may vary to some extent, the zones at which distinct clusters of filaments develop remain identical and only the relative intensity of certain spots exhibit differences. We consider these fluctuations as being of second-order importance in the global evolution of the filamentation pattern.

Concerning this point, let us emphasize that the resemblance between the experimental and numerical patterns in the forthcoming analysis will not lie in the exact position and number of the filaments, which may undergo similar fluctuations and are subject to atmospheric turbulence or local diffusive processes as they propagate. Instead, qualitative similarities occur in the following sense: Starting with an input coarse profile, the beam amplifies its initial inhomogeneities and, through modulational instability, it produces bright spots connected by lower-intensity bridges. A “global” pattern then emerges from the zones of highest concentration of light, which create characteristic figures (ring/trident/cross). These aspects are actually well restored by the 2D simulations, using the digitized fluence of the experimental input beam.

#### A. “Low”-power filamentation regime

To start with, we examine the filamentation dynamics of terawatt beams with about 100 critical powers only. Figure 7 shows the occurrence of light filaments over 55 m from the Teramobile beam with 230 mJ energy and pulse duration of 600 fs. Modulations induced by caustics distributed in the

spatial beam profile develop as follows: In the early propagation stage, the broad (SG-like) beam tends to develop a ring-shaped zone by diffraction. At the edge of the beam where fluctuations are the most intense, filaments emerge from local defects. Next, several cells occur along a flattened ring inside the focal spot. More filaments are then generated around this ring. They finally self-organize into a three-pronged fork shape.

For comparison, we integrated the (2D+1)-dimensional Eq. (3) from a data file of the experimental input beam measured at the distance  $d=1$  m after the laser exit. With a pulse duration of 600 fs ( $t_p \approx 510$  fs), the coefficient  $\alpha$  in Eq. (3) takes the value  $\alpha=0.51$ . With a beam waist of 2.5 cm, a very high spatial resolution [namely,  $8192^2$  in the  $(x,y)$  plane for a box length of  $6w_0$ ] was required in order to solve narrow optical structures reaching 1000 times the input beam intensity  $I_0$ . Figure 7(b) illustrates the results of numerical simulations. The beam containing  $\sim 120$  critical powers begins to form local clots from the highest intensity regions. Then, others emerge along a ring inside the focal spot. The final pattern, involving several small-scale spots, results in a trident-shaped figure, comparable with the experimental one. For such beams with a few tens of critical powers only, Eq. (6) describes the filamentation of a disordered optical distribution having an effective ratio of input power over critical of about  $\sim \alpha P_{\text{in}}/P_{\text{cr}} \approx 60$ , which limits at the very most to  $P_{\text{in}}/P_{\text{fil}} \approx 24$  the number of genuine filaments reaching the ionization threshold. Filaments develop as asymptotic states and become decoupled from the initial amplitude and phase of the wave field. The discrepancy existing in the distance where the first filaments occur,  $z_c \approx 50$  m, and the experimental measurement,  $z_c \approx 30$  m, is attributed to the pulse chirping, which Eq. (3) ignores, and to our former choice  $T=0.1 t_p$ . As underlined in Sec. IV C, this value suits the experimental development of filaments in the ionization regime, but it cannot restore the early self-focusing distances of the beam requiring rather  $T=t_p$ . Keeping  $T \ll t_p$  is, however, necessary to approach a suitable averaged power ratio in the ionization regime, where filaments mostly evolve.

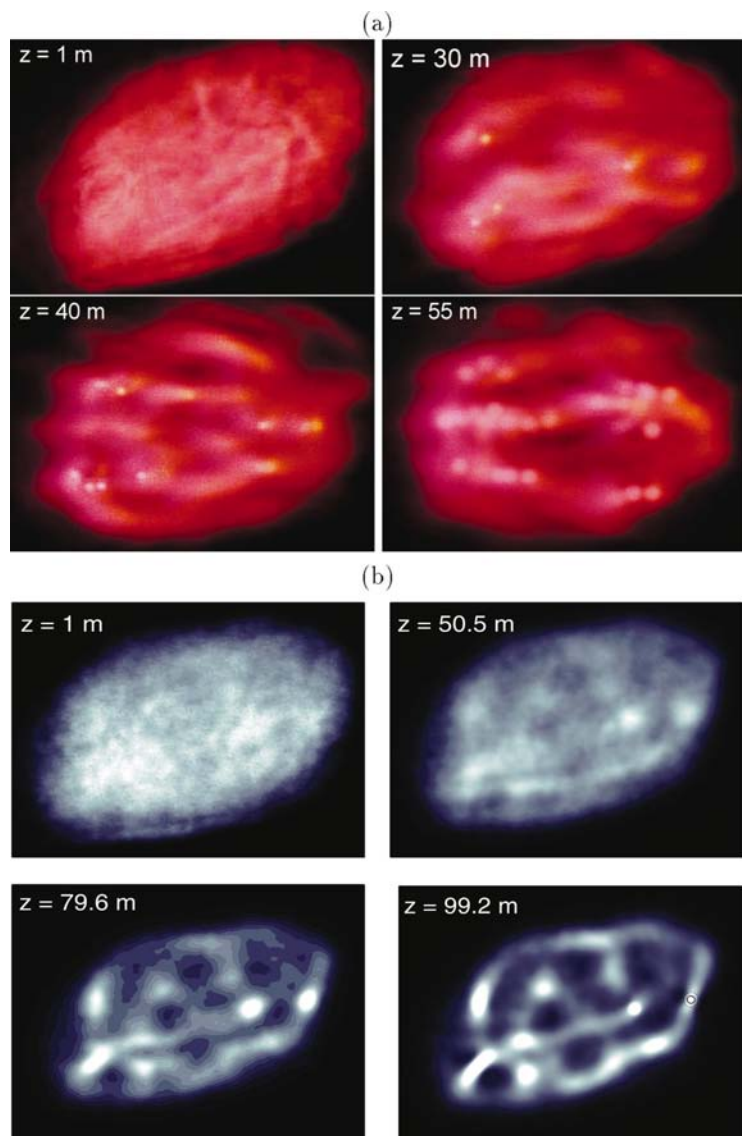


FIG. 7. (Color) Filamentation patterns (a) produced experimentally for the  $120 P_{cr}$  beam at  $z = 1, 30, 40,$  and  $55$  m. (b) Numerical computations of the same beam from Eq. (3). Maximum intensity is limited to twice the input intensity. In this figure as well as in Figs. 8 and 9, the image scale is about  $1.5 w_0 \times 1.5 w_0$  ( $w_0 =$  input beam waist), for both the experimental and numerical snapshots.

From the numerical as well as experimental patterns, we can observe that some filamentary channels persist from the first focus point over several meters, whereas others are randomly nucleated over shorter longitudinal scales.

**B. “Moderate”-power filamentation regimes**

Reducing the pulse duration to 100 fs ( $t_p = 85$  fs) makes it possible to investigate filamentary patterns promoted by fs beams with powers as high as  $700 P_{cr}$ , i.e., 2.3 TW. In this case, displayed in Fig. 8(a), the beam breaks up into more cells than in the previous lower-power case. Following the estimate recalled in the Introduction, up to  $\alpha P_{in}/P_{fil} \sim 110$  light cells may form in principle with  $P_{fil} \approx \pi^2 P_{cr}/4$ . Figure 8(b) reproduces these experimental patterns from a numerical integration of Eq. (3) performed with the parameter  $\alpha = 0.39$  fixed by  $t_p = 85$  fs. Note that the discrepancies in the early self-focusing distances signaled in the previous case almost completely disappear at higher powers. Here, a minimal pulse chirping was used. The agreement between the experimental and numerical results is thus quite satisfactory.

The labels (1)–(3) locate active zones in the beam, which can clearly be identified in both the experimental and numerical patterns: (1) points out a couple of bright, robust filaments, (2) restores an arch of the diffraction ring pattern supporting primary hot spots while (3) indicates a crosswise configuration of filaments. By comparing the four snapshots with those displayed in Fig. 7, these patterns reveal that, although some filaments are able to survive over several meters at the most powerful regions of the pulse, random nucleation of filaments in the entire focal spot seems more privileged, compared with the break-up of the former  $120 P_{cr}$  beam. We explain this property by the high power density. “Optical pillars” cannot propagate independently due to their smaller separation distance. The primary filamentary cells experience more substantial power transfers through the overall surface of the beam.

**C. “High”-power filamentation regimes**

Concerning now higher power levels, Fig. 9(a) displays filamentation stages for pulses delivered by the Teramobile

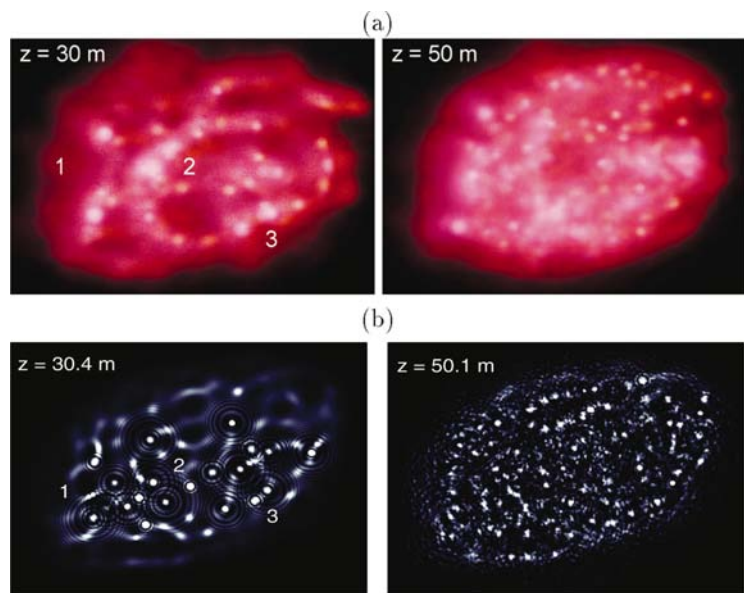


FIG. 8. (Color) Filamentation patterns (a) produced experimentally for the  $700 P_{cr}$  beam at  $z = 30$  and  $50$  m. (b) Numerical computations of the same beam from Eq. (3). Labels (1)–(3) indicate beam zones discussed in the text.

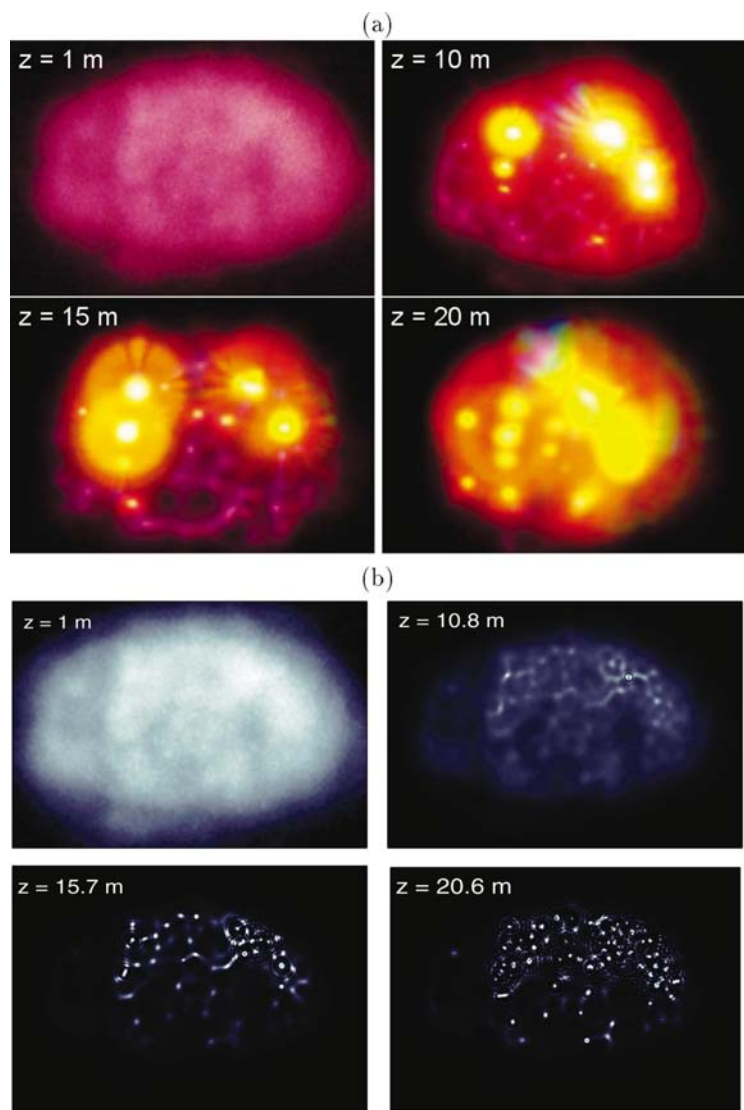


FIG. 9. (Color) Filamentation patterns of the  $1000 P_{cr}$  beam delivered by the Teramobile at different propagation distances: (a) Experimental transverse distributions. (b) Image plots from numerical computations performed with Eq. (3).

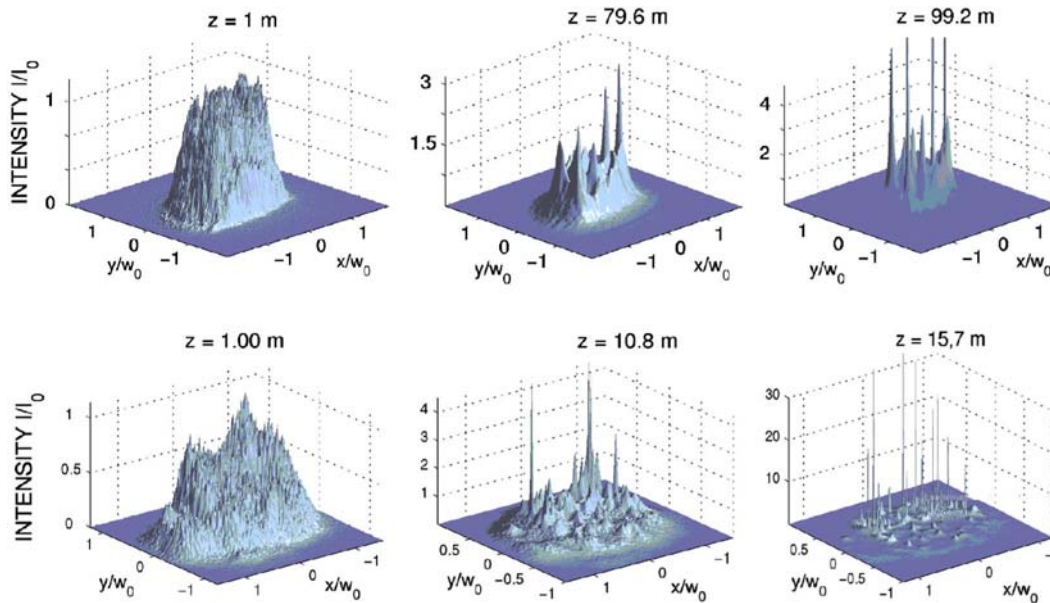


FIG. 10. (Color online) Intensity vs  $(x,y)$  for the beams shown in Fig. 7(b) (top row) and Fig. 9(b) (bottom row).

system, with a FWHM duration of 100 fs ( $t_p=85$  fs) and 330 mJ energy. The power range thus accesses 3 to 4 TW, i.e., about 1000 critical powers. No filter was used in this series of experiments. Although a nontrivial level of overexposure cannot be avoided from the most intense regions of the beam, removing the 800 nm filter makes it possible to exhibit true-colored filaments and to emphasize major optical pillars through the white-light conical emission which signals the presence of nonlinear self-focusing and subsequent plasma generation [14,27]. The filamentation scenario follows the former one: A ring-shaped zone supports a few big spots initiated by the highest-intense defects of the input beam. These “hot” spots self-focus more and more over several tens of meters, while white light occurs on the detection screen. MPA dissipation and evacuation of power excess due to the collapse dynamics undergone by the primary filaments allows one to transfer power to the central zone of the beam, which serves as an energy reservoir for exciting secondary filaments. Equation (3) computed with  $\alpha=0.39$  ( $t_p=85$  fs) restores these features with almost no discrepancy in the first focus point [ $z_c \approx 10$  m], as the beam contains very higher power. Figure 9(b) reproduces the experimental images in the same longitudinal interval.

From the numerical computation, the bright spots observed in the experiments appear to be first excited by an intense primary filament, which afterwards give rise to a bunch of secondary ones emerging as smaller-scale cells located near the central spot. We can observe how the local defects rapidly generate intense spots along a ring. In the upper arch of this ring, the most intense filaments, either as individual entities or gathered in clusters of a few cells, produce  $\sim 4$  distinct active zones, in agreement with Fig. 9(a). These zones actually consist of robust optical pillars, following the definition given above. They persist over several tens of meters, whereas secondary filaments rapidly recur first around them, and next in the central part of the beam.

Figure 10 details the spatial distortions undergone by the

lowest ( $120 P_{cr}$ , top row) and highest ( $1000 P_{cr}$ , bottom row) power beams, computed with the 2D reduced model. It displays evidence in both cases of the early amplification of the initial beam defects, which serve as central spots around which short-living filaments develop into an optical pillar. Note the growth of intense spikes that remain in a self-focused state over several tens of meters, while secondary peaks attain similar intensities at later distances.

#### D. “Moderate”-power beams in focused geometry

While the previous observations on screens provided detailed information about the beam structure at a given distance, they were, however, limited to semiquantitative observations. Fluctuations in the initial beam as well as from the atmosphere let the profile vary from shot to shot (see Fig. 6), so that successive images at different distances cannot be taken as quantitative information providing a complete propagation sequence over long distances. Moreover, the continuity and length of the individual filaments could not be assessed with accuracy.

In order to circumvent this limitation, we used a spatially extended, single shot characterization of the beam profile. The Teramobile laser was slightly focused ( $f=40$  m) from a larger beam waist ( $w_0 \approx 5$  cm) and emitted an energy of 250 mJ in 100 fs pulses (2.5 TW,  $760 P_{cr}$ ). It was installed outdoors on flat humid ground and shot against the wind direction into an aerosol generator producing a thin haze at a distance of 48 m from the laser exit. With a soft regular wind, this setup produced a pretty homogeneous light haze along a distance of up to 10 m towards the laser beam. The haze density was adjusted so that beam scattering was efficient enough to detect the filaments, with limited perturbation on the beam propagation itself. In those conditions, image blurring by multiple scattering was negligible [24].

The beam was imaged with a CCD camera in true colors, from a near-forward direction. More precisely, the CCD

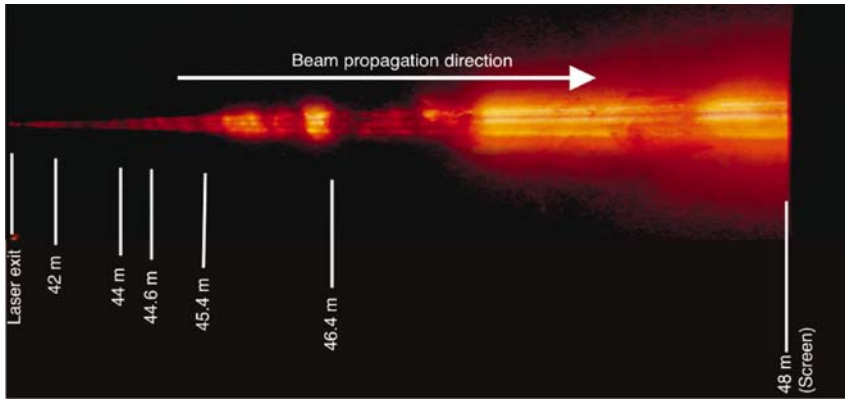


FIG. 11. (Color) Three “robust” filamentary structures propagating over  $\sim 8$  m from the focal point ( $f \approx 40$  m) of a converging beam with  $760 P_{cr}$  delivered by the Teramobile laser system.

camera was placed over the aerosol generator, about 25 cm above the center of the laser beam, and directed to the laser output of the Teramobile system. This setup allowed us to acquire single shot (exposure time 1/8 s) pictures of a long section (up to 10 m) of the beam (Fig. 11). Triangulation, calibrated with reference points along the laser path, enabled us to retrieve the distance calibration indicated in Fig. 11. Note that the beam was imaged with a very strong parallax, since the camera was placed at only 25 cm above it. Hence the triangulation yielding the distance scale is not linear and explains the apparent short distance between the laser exit and the first marked distance (42 m).

Figure 11 exhibits a quasicontinuous three-pillar structure that emerges from  $z > 40$  m and was reproducible from image to image. In this figure, the fluctuating intensity along the beam path is due to inhomogeneities in the haze, as was checked by visual inspection. Here, the observation of seemingly continuous structures along several meters on a single-shot image is evidence for the occurrence of optical pillars within femtosecond laser beams. In the present configuration, the beam self-organizes into three major, distinct clusters of light after passing through the focal point of the long-range converging lens.

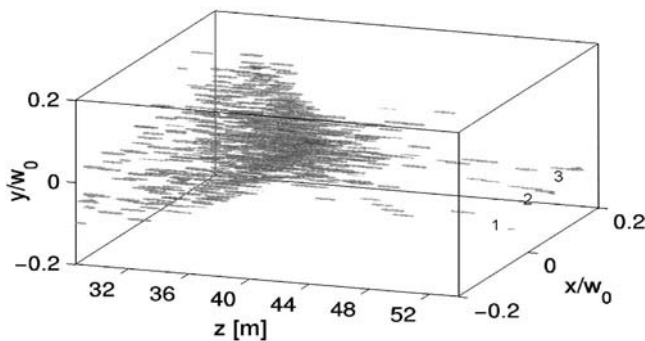


FIG. 12. Propagation of the same beam as in Fig. 11, numerically computed from Eq. (3) with a digitized data file of the input beam intensity profile affected by a spatially parabolic phase. Three filaments, identified by the labels 1, 2, and 3, can develop long sequences ( $\geq 2$  m) after the focus. Although partly disconnected over  $\sim 10$  m, their strong directivity yields the appearance of quasicontinuous strings of light. The numerous filaments occurring at  $z < 40$  m are not visible in Fig. 11 due to the strong parallax in the beam imaging.

Figure 12 shows a 3D plot issued from a direct numerical integration of Eq. (3), using the same input intensity distribution multiplied by the parabolic phase  $e^{-ik_0 r^2/2f}$  that accounts for the lens curvature ( $f=40$  m). As seen from this figure, many filaments arise as the beam approaches the focal length  $z \approx f=40$  m, where its minimum waist is attained. Remarkably, few filamentary structures emerge after this point: Only three of them propagate over  $\sim 10$  m, under the form of sequences of quasicontinuous channels having the same direction and capable of covering more than 2 m as a whole. We attribute the transverse deflection of the most external filaments to the natural divergence of the beam envelope after the focus. This result again confirms the validity of the (2D+1)-dimensional model, together with the concept of “optical pillars”: Long-range filaments can develop as individual entities located in the same region of the transverse plane, where a few intense cells are recurrently emitted as they propagate in a quasicontinuous way.

## VI. CONCLUSION

In summary, we have investigated the multiple filamentation of infrared femtosecond pulses in air, engaging high powers in parallel and focused geometries. Although intermittency of filaments affects the pulse dynamics, turbulent cells can converge towards long-range envelopes. These maintain the propagation over long distances while keeping an intensity close to the ionization threshold.

To understand these behaviors, we elaborated on a 2D model [Eq. (3)] describing the spatial dynamics of fs pulses, even when they undergo a delayed Kerr response. First, we thoroughly discussed the major properties of this reduced model by specifying both conservative and dissipative fundamental solitonlike solutions and their mutual interaction regimes. A noticeable enhancement of the propagation range through fusion processes combined with MPA was put in evidence. Second, we tested this model over a few meters for ultrashort mm-waisted pulses. By fixing the effective pulse temporal extent  $T$  to 1/10 of the input duration in ionization regimes, results from this simplified model were observed to reasonably agree with the transverse patterns of (3D+1)-dimensional pulses. For narrow beams ( $w_0=1$  mm) and weak powers ( $\leq 40P_{cr}$ ), two filaments form and merge into one central lobe. For broader beams ( $w_0=2$  mm) up to

90  $P_{cr}$ , several filaments propagate almost independently of their neighbors. The physical length of each asymptotic filament is of the same order ( $\leq 1$  m) in both configurations. This result is important, since Eq. (3) provides an easy model to integrate, which can be useful for estimating the number and position of filamentary channels created by high-power fs pulses.

Next, we investigated experimentally the multiple filamentation of collimated beams delivered by the Teramobile laser, for powers up to 3 to 4 TW. Experimental patterns were then simulated by means of the previous 2D reduced equation, using a digitized file of the input beam fluence as an initial datum. Along distances limited to 100 m, long-range filaments were observed to be initiated by the most intense fluctuations of the input beam and those may persist over several tens of meters. From these “optical pillars,” small-scale spots arise and recur rapidly at other places in the diffraction pattern, in agreement with the scenario of “optically-turbulent light guides” proposed in Ref. [13]. The long-living primary filaments, as well as unstable randomly nucleated ones, can be described by the 2D model, which reproduces the qualitative behaviors in the filamentation patterns. Direct confrontations of terawatt ultrashort pulses and their numerical simulations revealed the existence of active optical zones keeping the beam collimated over considerable distances.

Finally, focused beams were investigated over several tens of meters along a complete propagation sequence. By optical coalescence, reduction of the beam waist in linearly focused geometry allowed us to form very long light channels over almost 10 m by gathering all filamentary components into a limited number of light strings. These strings, although longer than one elementary filament and keeping the same direction, were numerically revealed to still develop from intermittent cells remaining localized in the same region of the diffraction plane. This observation thereby confirms the concept of “optical pillars” supporting the long propagation of quasicontinuous light tubes.

#### ACKNOWLEDGMENTS

The authors thank Dr. S. Champeaux for preliminary works during a stay at Jena University and Cl. Gouéard for preparing data files of the experimental input beams. L.B. thanks Dr. M. Kolesik from Tucson University for fruitful discussions. Experiments were performed in the framework of the Teramobile project, funded jointly by CNRS and DFG.

#### APPENDIX A: SPECTRAL PROBLEM FOR SOLITON STABILITY AGAINST NONISOTROPIC PERTURBATIONS

We briefly sketch the spectral equations for the ground state stability versus nonisotropic perturbations with azimuthal number  $m$ . According to the standard procedure for linear stability analysis we introduce a small perturbation  $\delta\phi$  on the soliton shape  $\phi$ . We plug  $A = (\phi + \delta\phi)\exp(i\Lambda Z)$  into Eq. (4) and linearize it with respect to the perturbation. The resulting evolution equation for the perturbative mode  $\delta\phi$  is then given by

$$\frac{\partial}{\partial Z}\delta\phi = i\Delta_{\perp}\delta\phi - i\Lambda\delta\phi + i2\phi^2\delta\phi + i\phi^2\delta\phi^* - i(K+1)\phi^{2K}\delta\phi - iK\phi^{2K}\delta\phi^*. \quad (\text{A1})$$

In order to separate azimuthal eigenfunctions of the transverse Laplacian, we transform Eq. (A1) from Cartesian  $(X, Y)$  to polar  $(R, \Theta)$  coordinates. With the ansatz  $\delta\phi(R, \Theta, Z) = \delta\phi_1(R)\exp(im\Theta + i\lambda Z) + \delta\phi_2^*(R)\exp(-im\Theta - i\lambda^*Z)$ , the eigenvalue problem is then derived under the form:

$$\begin{pmatrix} \hat{L}_{11} & \hat{L}_{12} \\ \hat{L}_{21} & \hat{L}_{22} \end{pmatrix} \begin{pmatrix} \delta\phi_1 \\ \delta\phi_2 \end{pmatrix} = \lambda \begin{pmatrix} \delta\phi_1 \\ \delta\phi_2 \end{pmatrix}, \quad (\text{A2})$$

where  $\delta\phi_1$  and  $\delta\phi_2$  are independent complex functions,  $\hat{L}_{11} = -\hat{L}_{22} = \Delta_{\perp} - \Lambda + 2\phi^2 - (K+1)\phi^{2K}$  and  $\hat{L}_{12} = -\hat{L}_{21} = \phi^2 - K\phi^{2K}$ .

Figure 1(d) in Sec. III B shows the eigenvalues  $\lambda$  of the discrete (localized) perturbation modes  $(\delta\phi_1, \delta\phi_2)$  of Eq. (A2), numerically identified for different values of  $m$ . All modes have zero growth rate ( $\text{Im } \lambda = 0$ ), which implies linear stability.

#### APPENDIX B: VIRIAL ARGUMENTS FOR THE FUSION OF CONSERVATIVE SOLITONS

By repeating the analysis proposed in [11], the merging of nonlinear filaments follows from the dynamical relation governing the mean-square radius of the beam,  $\langle R^2 \rangle = \int R^2 |\phi|^2 d\vec{R} / P$ , whenever  $\nu = 0$ :

$$P d_Z^2 \langle R^2 \rangle = 8 \int |\nabla_{\perp} A|^2 d\vec{R} - 4 \int |A|^4 d\vec{R} + \frac{8K}{K+1} \int |A|^{2(K+1)} d\vec{R}, \quad (\text{B1})$$

and applied to two Gaussianlike solitons with waist  $W_{\text{fil}}$ , power  $P_{\text{fil}}$ , and intensity close to saturation. After inserting the two-component trial solution

$$A_{\text{in}} = \sqrt{\frac{2P_{\text{fil}}}{\pi W_{\text{fil}}^2}} \left[ e^{-|\vec{R} + \vec{\Delta}/2|^2 / W_{\text{fil}}^2} + e^{-|\vec{R} - \vec{\Delta}/2|^2 / W_{\text{fil}}^2} \right],$$

expanding Eq. (B1) enables us to predict that well-separated filaments ( $\Delta > \sqrt{2}W_{\text{fil}}$ ) should fuse into a single lobe if the total beam radius decreases in self-compression regimes ( $d_Z^2 \langle R^2 \rangle < 0$ ) where the exponentially decreasing interaction terms remain dominant. When the beamlet intensities attain their saturation level ( $2P_{\text{fil}} / \pi W_{\text{fil}}^2 \rightarrow 1$ ), Eq. (B1) reduces to the interplay between linear ( $\mathcal{F}_{\text{lin}}$ ) and nonlinear ( $\mathcal{F}_{\text{nl}}$ ) contributions, i.e.,  $P d_Z^2 \langle R^2 \rangle \approx (32P_{\text{fil}} / W_{\text{fil}}^2)(\mathcal{F}_{\text{lin}} - \mathcal{F}_{\text{nl}})$  with

$$\mathcal{F}_{\text{lin}} = 1 + (1 - X)e^{-X}, \quad (\text{B2})$$

$$\mathcal{F}_{\text{nl}} = 0.93 \frac{P_{\text{fil}}}{P_c} \left[ 1 + 3e^{-2X} + 4e^{-3X/2} - \frac{2K}{(K+1)^2} \times [1 + 2(K+1)e^{-(2K+1)X/(K+1)}] \right],$$

where  $X \equiv \Delta^2 / 2W_{\text{fil}}^2$ . The requirement that interaction terms

dominate (mostly through linear diffraction in  $\mathcal{F}_{\text{lin}}$ ) while the beam still self-compresses imposes certain constraints on the power level, which must not be too high for avoiding strong localization of the solitons at their own centroids. This need particularly applies to Gaussian-shaped solitons satisfying  $\Delta \leq \Delta_{\text{lim}} = \sqrt{10} W_{\text{fil}}$  and  $P_{\text{fil}} \leq 1.35 P_c$ . For wider separation distances ( $\Delta \gg \Delta_{\text{lim}}$ ), exponential terms in Eq. (B2) vanish and the solitons are expected to no longer interact mutually.

These predictions reasonably agree with the results of Fig. 2. Note, nonetheless, that the previous restrictions inferred on the power bounds and separation distances are subject to discrepancies linked to the modeling of soliton shapes by Gaussian functions with saturated intensities. Figure 2(d) shows, for instance, that solitons with powers exceeding  $1.35 P_c$  and separation distances  $\Delta > \Delta_{\text{lim}}$  ( $\Delta_{\text{lim}} \approx 15$ ) are still able to merge at long propagation distances. However, those distances are large compared with the dissipation ranges limiting the filament self-guiding when we introduce  $\nu \neq 0$  (see Fig. 3).

### APPENDIX C: COMPLEMENTARY NUMERICAL ASPECTS

In this appendix we shortly discuss some specifications related to our numerical codes. A spectral split-step scheme was employed for solving Eqs. (1) and (3). Fast Fourier transformations were performed along the space-time directions  $(x, y, t)$  by routines of the FFTW library, version 3. All codes were parallelized for distributed memory architecture by using the MPI (message passing interface) library. Throughout the simulation, the increment along the  $z$  axis adapted itself as a function of the wave field intensity computed from the nonlinear phase variations, i.e.,  $\Delta z / 4z_0 < a I_0 / I_{\text{max}}$  with  $a$  remaining weaker than  $10^{-3}$ . Relaxation to larger steps  $\Delta z$  was monitored by an upper limit  $\Delta z / 4z_0 > b I_0 / I_{\text{max}}$  with  $b \geq a / 2.5$ . Absorbing boundary conditions and a sufficiently large numerical box with characteristic lengths  $L_t \geq 6t_p$ ,  $L_x, L_y \geq 6w_0$  guaranteed an undisturbed propagation of the pulse. The number of points required for an adequate resolution currently attained 512–1024 in space and 2048 in the temporal direction for the (3D+1)-dimensional numerical runs. The code integrating the 2D reduced model was elaborated on the same architecture, with one dimension suppressed.

Simulations were realized on the massively parallel Compaq alpha-cluster (TERA) of the CEA. Up to 128 processors were employed for runs consuming several thousands of

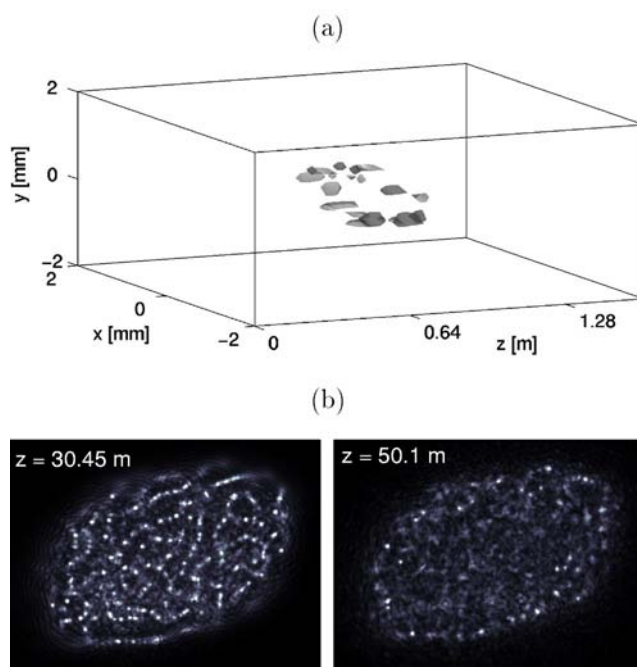


FIG. 13. Underresolved (3D+1) numerical results with spatial stepsize  $\Delta x = \Delta y \approx 100 \mu\text{m}$  for the multiple filamentation patterns shown in Figs. 5(c) and 8.

CPU hours. In spite of these substantial capacities, (3D+1)-dimensional simulations of broad (cm-waisted) pulses over several tens of meters could not be properly achieved in reasonable time. As mentioned in Sec. III A, one of the sharpest constraints met in 3D numerical computing is to solve accurately individual plasma channels, whose typical size reaches a few tens of microns only. In this regard, we find it instructive to show plots of underresolved filamentary patterns corresponding to Figs. 5(c) and 8, respectively (see Fig. 13). In this latter case, the input beam amplitude has been multiplied by a perturbed temporal Gaussian profile. Figure 13 illustrates the results of (3D+1)-dimensional simulations performed with spatial steps limited to  $\sim 100 \mu\text{m}$  along the  $x$  and  $y$  directions. Underresolution leads to an artificial increase of the number of small-scale cells, caused by the coarse plasma response that cannot hold a robust channel. Energy is dissipated outwards, which contributes to increase falsely the number of light cells. The filaments finally spread out too early, compared with the experimental data and with the results yielded by the 2D model [Eq. (3)], integrated with much higher spatial resolution.

- [1] A. Braun, G. Korn, X. Liu, D. Du, J. Squier, and G. Mourou, *Opt. Lett.* **20**, 73 (1995); E. T. J. Nibbering, P. F. Curley, G. Grillon, B. S. Prade, M. A. Franco, F. Salin, and A. Mysyrowicz, *ibid.* **21**, 62 (1996).  
 [2] A. Brodeur, C. Y. Chien, F. A. Ilkov, S. L. Chin, O. G. Kosareva, and V. P. Kandidov, *Opt. Lett.* **22**, 304 (1997).  
 [3] B. LaFontaine, F. Vidal, Z. Jiang, C. Y. Chien, D. Comtois, A.

Desparois, T. W. Johnston, J.-C. Kieffer, H. Pépin, and H. P. Mercure, *Phys. Plasmas* **6**, 1615 (1999).

- [4] S. L. Chin, A. Talebpour, J. Yang, S. Petit, V. P. Kandidov, O. G. Kosareva, and M. P. Tamarov, *Appl. Phys. B: Lasers Opt.* **74**, 67 (2002).  
 [5] S. Tzortzakis, L. Bergé, A. Couairon, M. Franco, B. Prade, and A. Mysyrowicz, *Phys. Rev. Lett.* **86**, 5470 (2001).

- [6] D. Mondelain, Ph.D. thesis No. 212-2001, Université Cl. Bernard, Lyon 1, France 2001, p. 121.
- [7] L. Bergé, S. Skupin, F. Lederer, G. Méjean, J. Yu, J. Kasparian, E. Salmon, J. P. Wolf, M. Rodriguez, L. Wöste, R. Bourayou, and R. Sauerbrey, *Phys. Rev. Lett.* **92**, 225002 (2004).
- [8] L. Wöste, C. Wedekind, H. Wille, P. Rairoux, B. Stein, S. Nikolov, Ch. Werner, St. Niedermeier, F. Ronneberger, H. Schillinger, and R. Sauerbrey, *Laser Optoelektron.* **29**, 51 (1997).
- [9] V. I. Bespalov and V. I. Talanov, *JETP Lett.* **3**, 307 (1966).
- [10] J. H. Marburger, *Prog. Quantum Electron.* **4**, 35 (1975).
- [11] L. Bergé, Cl. Gouédard, J. Schjødt-Eriksen, and H. Ward, *Physica D* **176**, 181 (2003).
- [12] S. Skupin, U. Peschel, C. Etrich, L. Leine, D. Michaelis, and F. Lederer, *Opt. Lett.* **27**, 1812 (2002).
- [13] M. Mlejnek, M. Kolesik, J. V. Moloney, and E. M. Wright, *Phys. Rev. Lett.* **83**, 2938 (1999).
- [14] H. Wille, M. Rodriguez, J. Kasparian, D. Mondelain, J. Yu, A. Mysyrowicz, R. Sauerbrey, J.-P. Wolf, and L. Wöste, *Eur. Phys. J.: Appl. Phys.* **20**, 183 (2002); J. Kasparian, M. Rodriguez, G. Méjean, J. Yu, E. Salmon, H. Wille, R. Bourayou, S. Frey, Y. B. André, A. Mysyrowicz, R. Sauerbrey, J.-P. Wolf, and L. Wöste, *Science* **301**, 61 (2003).
- [15] M. Mlejnek, E. M. Wright, and J. V. Moloney, *Opt. Lett.* **23**, 382 (1998).
- [16] S. L. Chin, A. Brodeur, S. Petit, O. G. Kosareva, and V. P. Kandidov, *J. Nonlinear Opt. Phys. Mater.* **8**, 121 (1999).
- [17] A. Couairon, S. Tzortzakis, L. Bergé, M. Franco, B. Prade, and A. Mysyrowicz, *J. Opt. Soc. Am. B* **19**, 1117 (2002).
- [18] H. Ward and L. Bergé, *Phys. Rev. Lett.* **90**, 053901 (2003).
- [19] R. Y. Chiao, E. Garmire, and C. H. Townes, *Phys. Rev. Lett.* **13**, 479 (1964).
- [20] N. G. Vakhitov and A. A. Kolokolov, *Izv. Vyssh. Uchebn. Zaved., Radiofiz.* **16**, 1020 (1973) [*Radiophys. Quantum Electron.* **16**, 783 (1975)]; A. A. Kolokolov, *ibid.* **17**, 1332 (1974) [*Radiophys. Quantum Electron.* **17**, 1016 (1976)].
- [21] E. A. Kuznetsov, A. M. Rubenchik, and V. E. Zakharov, *Phys. Rep.* **142**, 103 (1986).
- [22] M. I. Weinstein, *Commun. Pure Appl. Math.* **39**, 51 (1986).
- [23] See, for review, L. Bergé, *Phys. Rep.* **303**, 259 (1998).
- [24] F. Courvoisier, V. Boutou, J. Kasparian, E. Salmon, G. Méjean, J. Yu, and J.-P. Wolf, *Appl. Phys. Lett.* **83**, 213 (2003).
- [25] S. Skupin, L. Bergé, U. Peschel, and F. Lederer, *Phys. Rev. Lett.* **93**, 023901 (2004).
- [26] G. P. Agrawal, *Nonlinear Fiber Optics*, 3rd Ed. (Academic Press, New York, 2001), p. 274; L. Bergé, J. Juul Rasmussen, E. A. Kuznetsov, E. G. Shapiro, and S. K. Turitsyn, *J. Opt. Soc. Am. B* **13**, 1879 (1996).
- [27] M. Rodriguez, R. Bourayou, G. Méjean, J. Kasparian, J. Yu, E. Salmon, A. Scholz, B. Stecklum, J. Eisloffel, U. Laux, A. P. Hatzes, R. Sauerbrey, L. Wöste, and J.-P. Wolf, *Phys. Rev. E* **69**, 036607 (2004).

# Spatial Break-up of Femtosecond Laser Pulses in the Atmosphere

L. Bergé<sup>1,\*</sup>, S. Skupin<sup>1,2</sup>, F. Lederer<sup>2</sup>, G. Méjean<sup>3</sup>, J. Yu<sup>3</sup>, J. Kasparian<sup>3</sup>, E. Salmon<sup>3</sup> and J. P. Wolf<sup>3</sup>

<sup>1</sup>Département de Physique Théorique et Appliquée, CEA/DAM Ile de France, B.P. 12, 91680 Bruyères-le-Châtel, France

<sup>2</sup>Friedrich-Schiller-Universität Jena, Max-Wien-Platz 1, 07743 Jena, Germany

<sup>3</sup>Laboratoire de Spectrométrie Ionique et Moléculaire, Université Cl. Bernard Lyon 1, UMR-CNRS 5579, F-69622 Villeurbanne cedex, Lyon, France

Received September 8, 2003

PACS Ref: 42.65.Tg, 42.68.Ay, 42.65.Jx

## Abstract

The filamentation of femtosecond pulses in air is investigated experimentally and numerically for beam powers accessing several hundreds of critical powers for self-focusing. First, evolution of the filament patterns is approached by an averaged-in-time  $(2D + 1)$ -dimensional model derived from the standard propagation equations for ultrashort pulses. Elementary processes such as soliton generation, dissipation by multiphoton absorption and coalescence of filamentary cells are discussed. Second, the  $2D$  model is employed for reproducing filament patterns of femtosecond pulses delivered by a mobile TW laser source (TERAMOBILE). Beam propagation is shown to be driven by the interplay between intense, robust spikes aggregated around the defects of the beam and random nucleation of light cells.

## 1. Introduction

The long-range propagation of femtosecond (fs) laser pulses in air is a well-known phenomenon currently exploited in, e.g., remote sensing techniques [1–3]. Infrared pulses with about 100 fs duration indeed generate narrow filaments of light over long distances, which promote white-light emission allowing high-altitude absorption spectroscopy experiments [3]. This self-guiding originates from the early optical self-focusing caused by the Kerr response of air and leading to an increase of the light intensity. The beam collapse is then saturated by the electron plasma created by ionization of air molecules, when the pulse intensity reaches  $\sim 10^{14}$  W/cm<sup>2</sup>. For moderate input powers,  $P_{\text{in}}$ , below a few tens of critical powers for self-focusing,  $P_{\text{cr}}$ , one or two filaments are created [4–7]. At much higher powers, many filaments can be produced. This process is initiated by the modulational instability, which tends to break up the beam into small-scale cells conveying each a power close to  $\pi^2 P_{\text{cr}}/4$  [8,9]. Several important mechanisms have been proposed to anticipate the dynamics of filamentary cells. On the one hand, a beam can split into a couple of spots that persist over several meters before fusing into a robust central lobe [7]. On the other hand, it has been numerically predicted [10] that collapsing light cells may be nucleated at random and defocused by plasma generation over short distances ( $\ll 1$  m). Recurrent sequence of collapse events then seeds a sea of spiky filaments, which support an “optically turbulent light guide” in the medium. To the best of our knowledge, a scenario unifying both these aspects is still missing. To be valid, this scenario should be confronted with direct experimental observations.

The present work outlines major features in the filamentation dynamics of fs pulses with relatively high powers ( $P_{\text{in}}/P_{\text{cr}} > 100$ ). To address this issue, we first derive a  $(2D + 1)$ -dimensional model where solitonlike states describe short-range “randomly-nucleated” filaments. We show that these structures confine themselves into a limited number of long-range coherent objects, termed as “optical pillars”. Besides transient stages where turbulent cells recur, these new structures around which filaments self-organize drive the pulse dynamics, which is confirmed by the direct solving of the  $(3D + 1)$ -dimensional equations for short-pulse propagation. Next, two series of experiments involving the Teramobile facility [2,3] are performed, engaging either moderate ( $P_{\text{in}} = 120 P_{\text{cr}}$ ) or high powers ( $P_{\text{in}} = 700 P_{\text{cr}}$ ). We compare each filamentation figure with results yielded by the  $(2D + 1)$ -dimensional model, which faithfully restores the experimental patterns.

From the numerical point of view, we consider standard propagation equations [7,10,11]:

$$\begin{aligned} \frac{\partial \mathcal{E}}{\partial z} = & \frac{i}{2k_0} \nabla_{\perp}^2 \mathcal{E} - i \frac{k''}{2} \partial_t^2 \mathcal{E} + i \frac{k_0 n_2}{2} \\ & \times \left( |\mathcal{E}|^2 + \tau_K^{-1} \int_{-\infty}^t e^{-(t-t')/\tau_K} |\mathcal{E}(t')|^2 dt' \right) \mathcal{E} \\ & - \left( \frac{\sigma}{2} + i \frac{k_0}{2\rho_c} \right) \rho \mathcal{E} - \frac{\beta^{(K)}}{2} |\mathcal{E}|^{2K-2} \mathcal{E}, \end{aligned} \quad (1)$$

$$\partial_t \rho = \sigma_K \rho_{\text{nt}} |\mathcal{E}|^{2K} + \frac{\sigma}{U_i} \rho |\mathcal{E}|^2, \quad (2)$$

which couple an extended nonlinear Schrödinger (NLS) equation for the electric field envelope  $\mathcal{E}$ , to a Drude model for the local plasma density  $\rho$ . These equations apply to fs pulses moving in their group-velocity frame ( $t \rightarrow t - z/v_g$ ), characterized by a beam waist  $w_0$ , half-width duration  $t_p$ , Rayleigh length  $z_0 = \pi w_0^2/\lambda_0$ , and the central wavenumber  $k_0 = 2\pi/\lambda_0$ . The critical power for self-focusing in air takes the value  $P_{\text{cr}} = \lambda_0^2/2\pi n_2 = 3.3$  GW at the laser wavelength  $\lambda_0 = 800$  nm. The Kerr refraction index is  $n_2 = 3.2 \times 10^{-19}$  cm<sup>2</sup>/W and the coefficient for group-velocity dispersion (GVD) reads as  $k'' = 0.2$  fs<sup>2</sup>/cm. In Eq. (1),  $\nabla_{\perp}^2 = \partial_x^2 + \partial_y^2$  accounts for optical diffraction in the  $(x, y)$  plane and the complete Kerr response of air is composed of an instantaneous contribution and a delayed part in ratio 1/2, with a relaxation time  $\tau_K = 70$  fs [7,12].  $\rho_c \simeq 1.8 \times 10^{21}$  cm<sup>-3</sup> is the critical plasma density beyond which the medium becomes opaque. Power dissipation is

\*To whom correspondence should be addressed:  
e-mail: luc.berge@cea.fr

assured by multiphoton absorption (MPA) with coefficient  $\beta^{(K)} \simeq 4.25 \times 10^{-98} \text{ cm}^{2K-3} / W^{K-1}$  [11,12]. In Eq. (2), plasma defocusing is mainly induced by ionization of oxygen molecules with a gap potential  $U_i = 12.1 \text{ eV}$  and an initial density  $\rho_{\text{nt}} = 0.2 \times \rho_{\text{at}}$ , contributing to 20% of the total neutral density  $\rho_{\text{at}} = 2.7 \times 10^{19} \text{ cm}^{-3}$  [12]. Plasma formation is expected to be essentially driven by multiphoton ionization (MPI) with coefficient  $\sigma_K = 2.88 \times 10^{-99} \text{ s}^{-1} \text{ cm}^{2K} / W^K$ , where the number of photons  $K$  needed to extract electrons from neutral atoms is  $K = 8$ . Avalanche ionization involving the cross-section for inverse bremsstrahlung  $\sigma = 5.44 \times 10^{-20} \text{ cm}^{-2}$  and related plasma absorption, although of weaker influence for fs pulses, have been included for completeness of the model.

## 2. Nonlinear dynamical aspects

Before proceeding, we elaborate from Eq. (1) on a reduced model constructed by averaging the temporal dependencies of  $\mathcal{E}$ . Considering subpicosecond durations, avalanche ionization and plasma absorption are here ignored. We moreover omit GVD, whose coefficient  $k'' = 0.2 \text{ fs}^2 / \text{cm}$  makes it too weak for being a key-player over filamentation distances limited to 100 m. Under these approximations, we assume that MPI counterbalances Kerr self-focusing at a time slice  $t \simeq t_c(z)$  where a dominant spike with temporal extent  $T$  emerges among other time slices in the pulse temporal profile. This extent keeps the same order of magnitude along propagation, i.e., filaments arise as optical structures coupled with an ionization front that shrinks the pulse to the same mean duration. Because there exists evidence [13] that MPI shortens pulses to 1/10 of their initial length, we choose  $T = t_p/10$ , which was also recently justified in [14]. We thus set  $\mathcal{E}(x, y, z, t) = \psi(x, y, z) \times \chi[t, t_c(z)]$ , where the temporal distribution for the highest-intensity peak is modeled by the Gaussian  $\chi[t, t_c(z)] = e^{-[t-t_c(z)]^2/T^2}$  with  $T = 0.1t_p$ . Plugging this expression of  $\mathcal{E}$  into Eq. (1), integrating the equation for  $\rho$  and averaging Eq. (1) over the whole time domain then provides the equation for the transverse component  $\psi$ :

$$i\partial_z \psi + \frac{1}{2k_0} \nabla_{\perp}^2 \psi + \alpha k_0 n_2 |\psi|^2 \psi - \gamma |\psi|^{2K} \psi + i\nu |\psi|^{2K-2} \psi = 0, \quad (3)$$

with  $\alpha = \frac{1}{4}(\sqrt{2} + D(t_p)/\tau_K)$ ,  $\nu = \beta^{(K)}/2\sqrt{K}$  and  $\gamma = k_0 \sigma_K \rho_{\text{nt}} \sqrt{\pi/8KT}/2\rho_c$ . Here, the function

$$D(t_p) \equiv \int_{-\infty}^{+\infty} e^{T^2/8\tau_K^2 - u/\tau_K - 2u^2/T^2} \times \left\{ \text{Erf} \left( \frac{\sqrt{2}u}{T} - \frac{T}{\sqrt{8}\tau_K} \right) + 1 \right\} du \quad (4)$$

follows from averaging in time the delayed Kerr contribution of Eq. (1).

Equation (3) is instructive for understanding the transverse dynamics of filamentary structures. Three key-processes must indeed be emphasized for this purpose.

- (i) In the non-dissipative case ( $\nu = 0$ ), Eq. (3) admits soliton solutions in the form  $\psi = \phi(x, y)e^{i\Lambda z}$ . Characterized by an intensity reaching the saturation

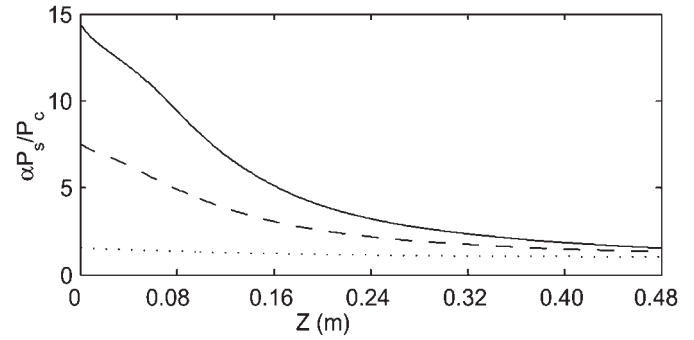


Fig. 1. Decrease of  $P_s$  versus  $z$  for the soliton states engaging  $1.5 P_c/\alpha$  (dotted curve),  $7 P_c/\alpha$  (dashed curve) and  $15 P_c/\alpha$  (solid curve), as they undergo MPA for beam waist  $w_0 = 1 \text{ mm}$ .

threshold  $I_{\text{max}} \sim (\gamma/\alpha k_0 n_2)^{1/1-K}$ , these solitons satisfy the criterion for orbital stability  $dP_s/d\Lambda > 0$  [15], where  $P_s$  is the power  $P \equiv \int |\psi|^2 dr$  computed on the function  $\phi$ . As detailed in [14], low-power solitons ( $\alpha P_s/P_c < 1.5$ ) are close to the Townes mode of the cubic NLS equation with power  $P_c \simeq 0.93 \times P_{\text{cr}}$ . High-power ones ( $\alpha P_s/P_c > 1.5$ ) exhibit a shape resembling high-order super-Gaussians (SG).

- (ii) When adding MPA ( $\nu \neq 0$ ), the soliton power decreases continuously until reaching the effective collapse threshold  $P_c/\alpha$ . This property is shown in Fig. 1. By modelling  $\phi$  like  $\phi = A_s e^{-(r/w_0)^{2N}}$  in monofilamentation regime ( $r^2 = x^2 + y^2$ ,  $N \geq 1$ ), the power relation  $d_z P \simeq -2\nu \int \phi^{2K} dr$  can be solved perturbatively, in order to evaluate the dissipation range along which self-focusing persists with beam powers above critical. Computed in the limit  $\alpha P_s \gg P_c$ , this range:

$$\Delta z = K^{1/N} (\gamma/2\nu\alpha k_0 n_2) (1 - P_c/\alpha P_s), \quad (5)$$

is found to only vary with the laser wavelength, but not with the beam waist. It predicts a maximum filament length of 0.4 m per pulse with, e.g.,  $t_p = 85 \text{ fs}$  at the central wavelength  $\lambda_0 = 800 \text{ nm}$ , which is compatible with the short “life-time” of the recurrent filaments observed in [10] along the propagation axis.

- (iii) Solitons can mutually fuse. It can indeed be shown from the mean-square radius of the beam,  $\langle r^2 \rangle \equiv \int r^2 |\psi|^2 dr / P$ , that two Gaussianlike solitons with waist  $w_{\text{fil}}$  and intensity close to saturation are able to merge, even without dissipation [9]. To show this property, the two-component trial solution  $\psi_{\text{in}} = \sqrt{2P_{\text{fil}}/\pi w_{\text{fil}}^2} (e^{-|r+\Delta/2|^2/w_{\text{fil}}^2} + e^{-|r-\Delta/2|^2/w_{\text{fil}}^2})$  is inserted into the “virial” expression

$$\frac{k_0}{4} P d_z^2 \langle r^2 \rangle = \frac{1}{2k_0} \int |\nabla_{\perp} \psi|^2 dr - \frac{\alpha k_0 n_2}{2} \int |\psi|^4 dr + \frac{K\gamma}{K+1} \int |\psi|^{2(K+1)} dr. \quad (6)$$

Expanding Eq. (6) by using  $\psi_{\text{in}}$  then enables us to predict that well-separated filaments ( $\Delta > \sqrt{2}w_{\text{fil}}$ ) should fuse into a single lobe, if the total beam radius decreases in self-compression regime ( $d_z^2 \langle r^2 \rangle < 0$ ) with dominant, exponentially-decreasing interaction terms. When the beamlet intensities attain their saturation level ( $2P_{\text{fil}}/\pi w_{\text{fil}}^2 \rightarrow I_{\text{max}}$ ), this condition applies in particular to Gaussian-

shaped solitons satisfying

$$\alpha \frac{P_{\text{fil}}}{P_c} \leq \frac{[1 + (1 - X)e^{-X}]/0.93}{1 + 3e^{-2X} + 4e^{-3X/2} - \frac{2K}{(K+1)^2}(1 + 2(K+1)e^{-(2K+1)X/(K+1)})}, \quad (7)$$

where  $X \equiv \Delta^2/2w_{\text{fil}}^2$ . Plotting Eq. (7) would show that coalescence occurs between filaments mutually separated by the distance  $\Delta \leq \Delta_{\text{lim}} = \sqrt{10}w_{\text{fil}}$ , provided their individual powers are below a threshold evaluated nearby  $1.35 \times P_c/\alpha$ . For wide separation distances ( $\Delta \gg \Delta_{\text{lim}}$ ), exponential terms in Eq. (6) vanish and the solitons should in principle cease to interact.

To illustrate this property, Figs. 2(a)–(d) show iso-intensity plots of two identical solitons with  $P_{\text{fil}} = 1.3 P_c/\alpha$ ,  $w_{\text{fil}} = 0.12$  mm (Fig. 2(a)) and  $P_{\text{fil}} = 4 P_c/\alpha$ ,  $w_{\text{fil}} = 0.2$  mm (Fig. 2(b)–(d)). The total beam waist enclosing both filaments is  $w_0 = 1$  mm ( $z_0 \simeq 4$  m). Two separation distances are selected, namely,  $\Delta = 0.8$  mm and  $\Delta = 0.6$  mm. For the first separation, lower-power solitons with no MPA were observed to evolve without interaction like stable, uncorrelated waveguides over at least 8 m (not shown here). In contrast, for the second distance approaching the critical value  $\Delta_{\text{lim}} \sim 0.4$  mm, the same

solitons start to fuse at large distances  $z \sim z_0$  (Fig. 2(a)). With  $\Delta = 0.6$  mm, higher-power solitons do not form a steady-state waveguide by coalescence ( $\Delta \sim \Delta_{\text{lim}}$ ). Instead, they combine into a breatherlike structure having a stable internal oscillating mode (Fig. 2(b)). This mode generically takes place at high power levels and disappears to the benefit of a stationary waveguide as soon as  $P_{\text{fil}} < 2P_c/\alpha$ . When  $\Delta = 0.8$  mm exceeds  $\Delta_{\text{lim}} \simeq 0.6$  mm, solitons with four critical powers propagate without correlation (Fig. 2(c)). In the presence of MPA (Fig. 2(d)), however, the power in each of those solitons rapidly decreases below  $2P_c/\alpha$ , which finally promotes their mutual coalescence. These behaviors are in reasonably-good agreement with the previous theoretical expectations. Nonetheless, discrepancies arised, which are linked to the modeling of soliton shapes by Gaussian functions with saturated intensities. More precisely, the self-compression requirement  $d_z^2 \langle r^2 \rangle < 0$ , computed with real soliton profiles instead of Gaussians, was found to hold over a large interval of powers, even for separation distances satisfying the criterion  $\Delta \leq \Delta_{\text{lim}}$ . The upper bound of power for coalescence suggested by Eq. (7) could not be verified numerically and direct simulations showed that solitons with powers clearly above  $1.35 P_c/\alpha$  were indeed able to merge when  $\nu = 0$ .

The last configuration shown in Fig. 2(d) deserves a special comment: As can be seen from this figure, the propagation length of the solitons before their merging

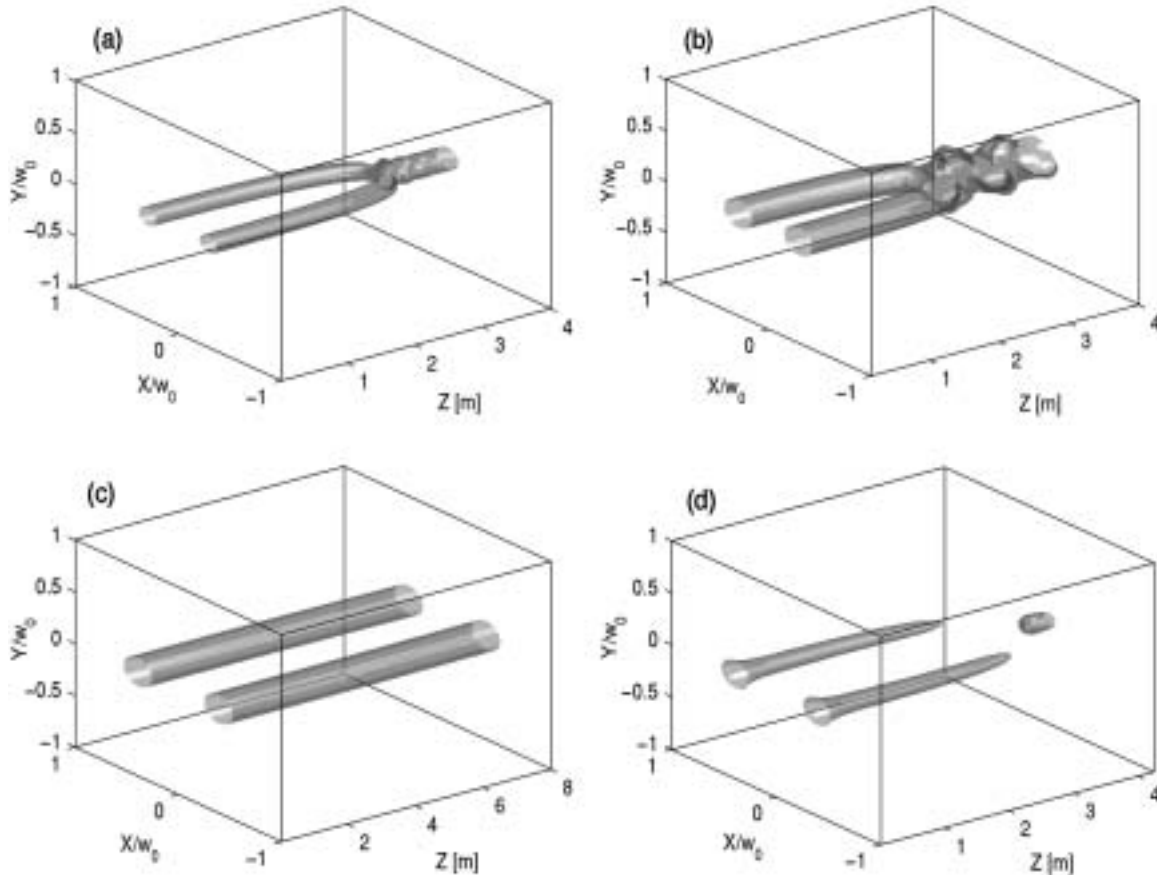


Fig. 2. Interaction of two solitons for different powers and separation distances. (a) Fusion of conservative solitons with individual power  $P_{\text{fil}} = 1.3 P_c/\alpha$  ( $w_{\text{fil}} = 0.12$  mm) and  $\Delta = 0.6$  mm. Filaments were observed to propagate without fusing for  $\Delta = 0.8$  mm. (b) Oscillations of merging solitons when their power is increased to  $4 P_c/\alpha$  for the small separation  $\Delta = 0.6$  mm and no MPA. (c) Uncorrelated propagation of two conservative solitons with  $4 P_c/\alpha$  when their separation distance is increased to  $\Delta = 0.8$  mm. (d) Fusion of solitons subject to MPA with  $P_{\text{fil}} = 4 P_c/\alpha$  and  $\Delta = 0.8$  mm.

widely exceeds (by almost one decade) the damping length (5) computed for one isolated waveguide (Fig. 1). Visual inspection of the soliton shapes allows us to justify this surprising behavior. As power goes down to critical through MPA dissipation, the solitons glide down along the curve  $(P_s, \Lambda)$  by modifying their spatial shape, whose tail becomes more and more extended in space. They can thereby overlap and produce a third lobe at center, which will raise all the farther along  $z$  as the initial separation  $\Delta$  is large. This particular dynamics can help groups of neighboring filaments to survive over several meters in filamentation patterns.

The above properties dictate the filament dynamics. As an example, Fig. 3 illustrates filamentation patterns in the 2D approximation, for which the input beam shape undergoes random, isotropic perturbations. By comparison with antecedent experimental data [7,16], we opted for an input anisotropic  $N$ th-order SG beam in the form  $\psi = \sqrt{I_0} e^{-(x^2/w_0^2 + 2y^2/w_0^2)^N}$ , perturbed at  $z = 0$  by an isotropic 10% random noise in amplitude, multiplied by a 10% noisy Gaussian temporal profile with  $t_p = 85$  fs. The fluence distribution  $[F = \int_{-\infty}^{+\infty} |\mathcal{E}(t)|^2 dt]$  of the resulting beam is then employed as the input datum for Eq. (3). Figure 3(a) shows the iso-intensity plots for a perturbed beam with waist  $w_0 = 2$  mm,  $N = 2$  and  $P_{in} = 95P_c$ . The beam first gives rise to several short-scale collapsing filaments. Intermittency in filament nucleation occurs in the early propagation stage over short ranges  $\leq 0.5$  m, which can be compared with the scenario of optical

turbulence proposed in [10]. Nevertheless, at larger distances, the filaments gather into a limited number of channels. The output filaments reach the maximum intensity  $I_{max}$  over distances  $\sim \Delta z$ , but they asymptotically remain captured in longer soliton envelopes that form “optical pillars” in the medium. By “optical pillars”, we mean discrete light spots capable of amalgamating solitonlike cells that self-attract around specific points in the diffraction plane. The resulting structure then sustains a long-range propagation, while it can still continue to excite short-living cells in its neighborhood. In the present configuration, the filamentary structures organize the entire beam into three major long-range pillars composed of solitonlike filaments.

By comparison, Eqs. (1) and (2) are now resolved in  $(3D + 1)$ -dimensional geometry by means of a spectral code using fast Fourier transforms in the  $(x, y, t)$  variables. Integration along the longitudinal axis ( $z$ ) is performed with an adaptive step tuned on the intensity growth. 2048 points in the time direction and 1024 points along both transverse axes were required for a numerical box with length of  $8w_0$ . Figure 3(b) represents the plasma strings produced by the previous beam. The temporal pulse profile, even subject to strong distortions, does not prevent the transverse dynamics of the pulse from developing as in Fig. 3(a), up to second-order discrepancies in the focus point linked to the choice of  $T$ . Although different temporal slices come into play, all of them support the propagation of cells first nucleated at different locations, then remaining localized around the *same* place in the  $(x, y)$  plane. Three distinct channels clearly emerge: They do not interact significantly but remain almost robust at their transverse position.

In view of the above results, the multiple filamentation of fs pulses can be sketched as follows: (i) Beam modulations give rise to short-range filaments that grow in intensity until reaching the ionization threshold  $I_{max}$ . In this limit, near-soliton filaments, searching for an equilibrium position, recur in an optically-turbulent regime during the early stage of propagation [10]. (ii) As they attain a quasi-stable configuration with respect to their neighbors, short-range filaments either fuse or self-attract without merging, depending on their inner power and mutual separation distance, in order to form a limited number of clusters named “optical pillars”. These propagate over longer distances. It is important to note that the present scenario applies to input beams where *an isotropic random noise* first creates short-scale cells, which afterwards relax to quasi-coherent structures. For experimental beams exhibiting salient defects at  $z = 0$ , the location of optical pillars in the transverse plane may be preconditioned by the most intense defects, which can further excite turbulent cells in their vicinity, as seen below.

### 3. Numerical simulations versus experiments

From the experimental point of view, we investigate evolution stages in the filamentation pattern produced by the TERAMOBILE laser [2]. This system delivers at the 10 Hz rate pulses with energy up to 0.5 J, transverse diameter equal to 5 cm ( $w_0 \simeq 2.5$  cm), and FWHM durations ( $= \sqrt{2 \ln 2} t_p$ ) tunable from 100 fs to 600 fs by

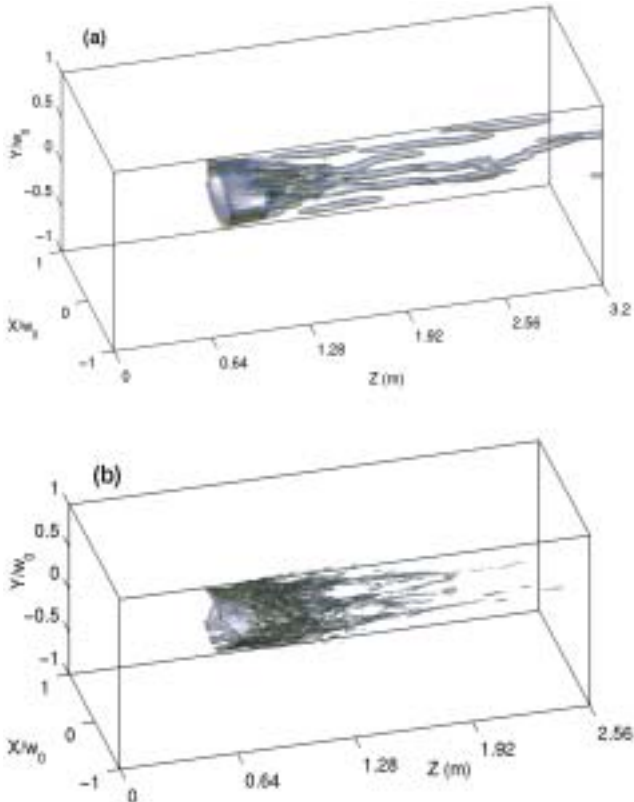


Fig. 3. (a) Iso-intensity patterns of filamentary structures created from an SG beam governed by the 2D reduced model with  $N = 2$ ,  $P_{in} = 95 P_c$  and  $w_0 = 2$  mm. (b) Plasma strings produced by the same beam integrated from the  $(3D + 1)$ -dimensional Eqs. (1) and (2).

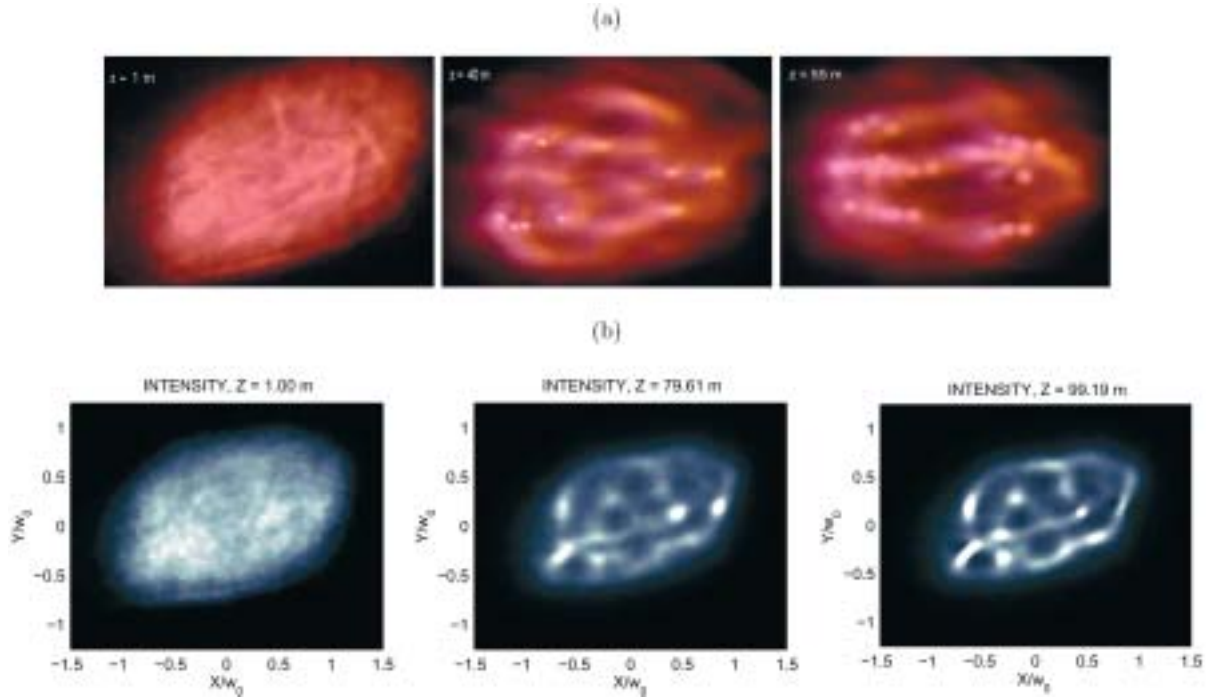


Fig. 4. Filamentation patterns (a) produced experimentally for the  $120 P_{\text{cr}}$  beam at  $z = 1, 40$  and  $55$  m. (b) Numerical computations of the same beam from Eq. (3). Maximum intensity is limited to twice the input intensity, in order to clearly underline the positions of the optical pillars arising from the beam defects.

detuning the compressor with a chirp opposite to air dispersion. Experiments show photos taken in open air from a white screen positioned in the plane orthogonal to the beam path. A filter with narrow bandwidth around the fundamental wavelength  $\lambda_0 = 800$  nm was put in front of the camera. Two photos with exposure time of  $1/8$ th second were taken in sequence at each longitudinal distance, so that two pulses could alter the pattern in some pictures. No qualitative change, however, was observed, up to slightly more visible filaments at certain distances.

Figure 4(a) details the growth of light filaments over  $55$  m with  $230$  mJ energy and pulse duration of  $600$  fs ( $P_{\text{in}} \approx 120 P_{\text{cr}}$ ). At the edge of the beam where fluctuations are the most intense, filaments emerge from local defects and several cells occur along a flattened ring inside the focal spot [ $z = 40$  m]. More filaments are then generated around this ring: They aggregate around the spots created at  $z = 40$  m and finally evolve into a three-pronged fork shape at  $z = 55$  m.

Figure 4(b) illustrates numerical simulations obtained by solving the  $(2D + 1)$ -dimensional Eq. (3) from a data file of the experimental input beam. With a pulse duration of  $600$  fs ( $t_p \approx 510$  fs), the coefficient  $\alpha$  in Eq. (3), computed from Eq. (4), takes the value  $\alpha = 0.51$ . The beam begins to form local clots from the highest intensity regions in a fashion similar to Fig. 4(a). The final pattern, involving several small-scale spots, results in a trident-shaped figure, restoring thereby the experimental observation. The discrepancy existing between the experimental distances and their numerical counterparts is attributed to our former choice  $T = 0.1 t_p$ . This choice suits the experimental development of filaments in ionization regime, but cannot restore the early self-focusing distances of beams with moderate powers,

requiring rather  $T = t_p$ . For such beams engaging  $120$  critical powers only, Eq. (3) describes the filamentation of a disordered optical distribution with an effective ratio of input power over critical of about  $\sim \alpha P_{\text{in}}/P_{\text{cr}} \approx 60$ . This limits to about  $24$  the number of genuine filaments reaching the ionization threshold. From the numerical as well as experimental images, we can observe that the most intense filamentary channels, forming “optical pillars” in the medium, persist over several tens of meters, whereas secondary light cells are randomly nucleated over shorter longitudinal scales.

Reducing the pulse duration to  $100$  fs ( $t_p = 85$  fs) makes it possible to investigate filamentary patterns promoted by fs beams with powers as high as  $700 P_{\text{cr}}$ . In this case displayed in Fig. 5(a), the beam breaks up into more cells than in the previous lower-power case. Following the estimate recalled in the introduction, up to  $\alpha P_{\text{in}}/P_{\text{fil}} \sim 110$  light cells may form in principle with  $P_{\text{fil}} \approx \pi^2 P_{\text{cr}}/4$ . Figure 5(b) reproduces these experimental patterns from a numerical integration of Eq. (3) performed with the parameter  $\alpha = 0.39$  fixed by  $t_p = 85$  fs. The agreement between the experimental and numerical results is quite satisfactory. These patterns reveal that, although some filaments are able to survive over several meters at the most powerful regions of the pulse [ $z = 30$  m and  $35$  m], random nucleation of filaments in the entire focal spot seems more privileged, compared with the break-up of the former  $120 P_{\text{cr}}$  beam. We explain this property by the partial inhibition of the fusion mechanism between filamentary cells (see Section 2), which convey each a higher power and experience more substantial power transfers through the overall surface of the beam. Finally, we can remark that robust filaments surviving over longitudinal distances  $\geq 5$  m evolve in correlation with close, but spatially-separable

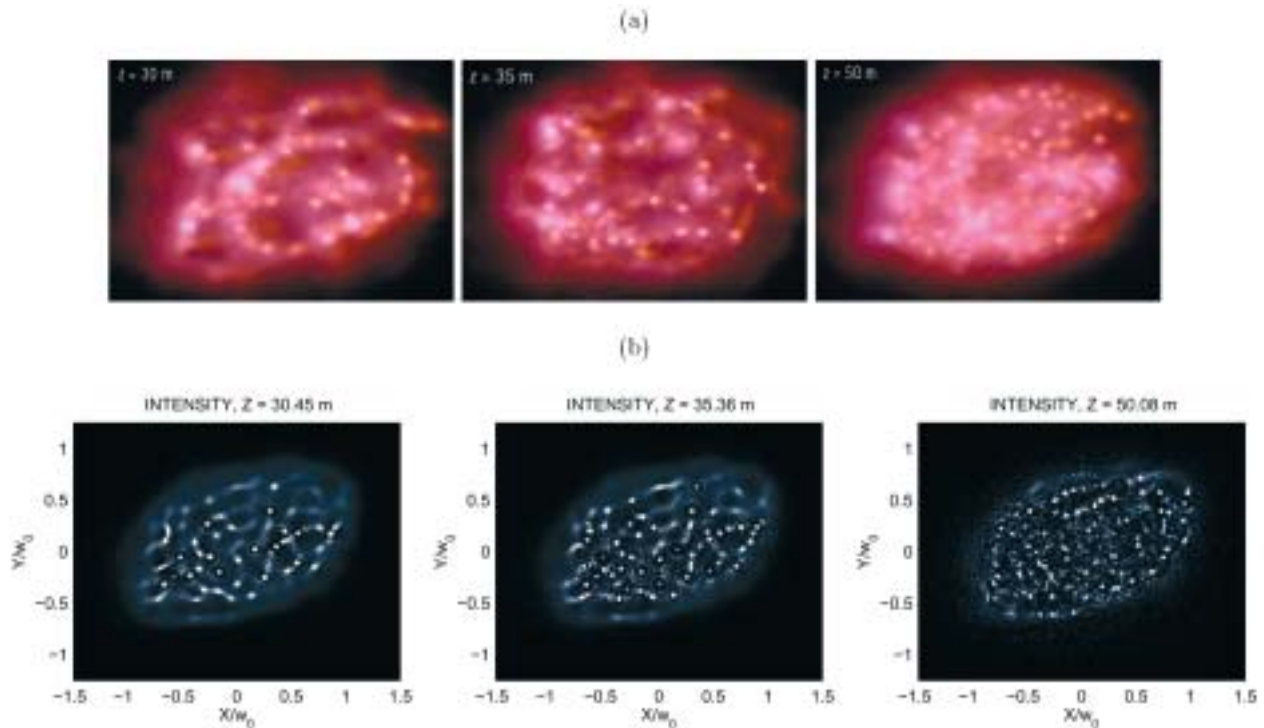


Fig. 5. Filamentation patterns (a) produced experimentally for the  $700 P_{cr}$  beam at  $z = 30, 35$  and  $50$  m. (b) Numerical computations of the same beam from Eq. (3).

neighbors, from which they can develop a long-range propagation dynamics resembling that displayed by Fig. 2(d).

#### 4. Conclusion

In summary, we have investigated the multiple filamentation of high-power beams, both theoretically and numerically. In the experiments, pulses were delivered by the TERAMOBILE laser able to access TW powers. Recent experiments on the beam break-up were already performed by means of the same facility for pulse powers as high as  $1000 P_{cr}$  and compared with numerical simulations [14]. In the present scope, we analyzed intermediate power levels limited to  $700 P_{cr}$  and concentrated more thoroughly on the various interaction regimes that filaments may undergo. Generic features are refound throughout both these works. Long-range filaments are initiated either asymptotically after an early stage of random nucleation for isotropically-perturbed beams or by the most intense defects of experimental beams. The resulting channels, termed as “optical pillars”, can persist over several tens of meters. Around these channels, small-scale spots arise and recur rapidly at other places in the diffraction plane, in agreement with the scenario of “optically-turbulent light guides” proposed in [10]. Long-living filaments, as well as unstable randomly-nucleated ones, can be described by the reduced 2D model [Eq. (3)], which reproduces the experimental patterns. To conclude, let us emphasize that, throughout this investigation, the beams were emitted in parallel geometry. It is thus not excluded that a reduction of the beam waist through an appropriate

convergent lens may allow to generate longer light channels, by gathering all filamentary components into a single central spot. This point, requiring a parametric study depending on the beam aperture, will be addressed in a forthcoming work.

#### Acknowledgements

The authors thank Cl. Gouédard for preparing data files of the experimental input beams. Experiments were performed in the framework of the TERAMOBILE project, funded jointly by CNRS and DFG.

#### References

1. Wöste, L. *et al.*, *Laser Optoelektronik* **29**, 51 (1997).
2. Wille, H. *et al.*, *Eur. Phys. J. Appl. Phys.* **20**, 183 (2002).
3. Kasparian, J. *et al.*, *Science* **301**, 61 (2003).
4. Braun, A. *et al.*, *Opt. Lett.* **20**, 73 (1995).
5. LaFontaine, B. *et al.*, *Phys. Plasmas* **6**, 1615 (1999).
6. Chin, S. L. *et al.*, *Appl. Phys. B* **74**, 67 (2002).
7. Tzortzakis, S. *et al.*, *Phys. Rev. Lett.* **86**, 5470 (2001).
8. Bespalov, V. I. and Talanov, V. I., *J. Exp. Theor. Phys. Lett.* **3**, 307 (1966).
9. Bergé, L., Gouédard, Cl., Schjødt-Eriksen, J. and Ward, H., *Physica D* **176**, 181 (2003).
10. Mlejnek, M., Kolesik, M., Moloney, J. V. and Wright, E. M., *Phys. Rev. Lett.* **83**, 2938 (1999).
11. Mlejnek, M., Wright, E.M. and Moloney, J. V., *Opt. Lett.* **23**, 382 (1998).
12. Couairon, A. *et al.*, *J. Opt. Soc. Am. B* **19**, 1117 (2002).
13. Ward, H. and Bergé, L., *Phys. Rev. Lett.* **90**, 053901 (2003).
14. Skupin, S. *et al.*, submitted to *Phys. Rev. E* (2003).
15. See for review: Bergé, L., *Phys. Rep.* **303**, 259 (1998).
16. Mondelain, D., PhD Thesis No. 212-2001, Université Cl. Bernard—Lyon 1—France, p. 121 (2001).

G. MÉCHAIN<sup>1</sup>  
A. COUAIRON<sup>2,✉</sup>  
Y.-B. ANDRÉ<sup>1</sup>  
C. D'AMICO<sup>1</sup>  
M. FRANCO<sup>1</sup>  
B. PRADE<sup>1</sup>  
S. TZORTZAKIS<sup>1</sup>  
A. MYSYROWICZ<sup>1</sup>  
R. SAUERBREY<sup>3</sup>

## Long-range self-channeling of infrared laser pulses in air: a new propagation regime without ionization

<sup>1</sup> Laboratoire d'Optique Appliquée, École Nationale Supérieure des Techniques Avancées – École Polytechnique, CNRS UMR 7639, 91761 Palaiseau Cedex, France

<sup>2</sup> Centre de Physique Théorique, École Polytechnique, CNRS UMR 7644, 91128 Palaiseau Cedex, France

<sup>3</sup> Institut für Optik und Quantenelektronik, Max-Wien-Platz 1, 07743 Jena, Germany

Received: 18 March 2004/Revised version: 28 April 2004

Published online: 23 June 2004 • © Springer-Verlag 2004

**ABSTRACT** We report long-range self-channeling in air of multiterawatt femtosecond laser pulses with large negative initial chirps. The peak intensity in the light channels is at least one order of magnitude lower than required for multiphoton ionization of air molecules. A detailed comparison is made between experiments and realistic 3 + 1-dimensional numerical simulations. It reveals that the mechanism limiting the growth of intensity by filamentation is connected with broken revolution symmetry in the transverse diffraction plane.

**PACS** 42.65.Sf; 42.25.Bs; 42.65.Jx; 52.38.Hb

Understanding the nonlinear propagation of powerful ultra-short laser pulses in the atmosphere has become important in view of several applications. For instance, remote multicomponent pollutant detection [1–3], lightning protection [4, 5], long-range propagation of light bullets [6] and production of secondary sources rely on femtosecond filamentation [7–13]. This term refers to the self-channeling of femtosecond laser pulses in the form of stable high-intensity light filaments. This phenomenon was discovered in the late 1990s with lasers emitting at infrared (IR) wavelengths [7, 14]. Filaments with diameters around 100  $\mu\text{m}$  and peak intensities below  $10^{14}$  W/cm<sup>2</sup> were observed, sufficient to leave in their wake plasma strings with a density around  $10^{16}$  cm<sup>-3</sup>.

For many applications, a control of femtosecond filamentation over long distances is crucial. A considerable literature has been devoted to the properties of single light filaments with energies in the range 1–10 mJ. They are typically obtained when subpicosecond pulses at near-IR wavelength, with a peak power slightly above a minimum value  $P_{\text{cr}} \sim 5$  GW, are launched in air. Femtosecond filamentation in such a case relies on a competition between well-identified nonlinear effects. The whole beam first undergoes self-focusing until the intensity reaches a sufficiently high value to trigger ionization. Plasma defocusing then stops the collapse that would have occurred in the absence of any saturating mechanism. A plasma string is formed at the beginning of the filamentation process, followed further down by occasional ionization

spikes that prevent beam collapse, resulting in a self-guided light pulse over several tens of meters. Characteristics of filaments such as the beam diameter, the self-guided pulse intensity, the time profile or the plasma string density are well reproduced by numerical simulations [8, 15].

The propagation of ultra-short pulses with a higher laser power  $P \gg P_{\text{cr}}$  is less understood. It has been reported by several groups that the inhomogeneous input beam typically breaks up into several spots during the self-focusing stage. Each filament carries about the same energy as in the case of a single filament. A model has been developed to explain this behavior, although no detailed comparison between numerical and experimental results is yet available. In the model, short-scale multifilamentation occurs, due to unavoidable beam irregularities, giving rise to  $N$  filaments, with  $N \sim P/P_{\text{cr}}$ . Collapse of each filament is limited by ionization. Each filament eventually gives back most of its energy through diffraction to a common laser-energy pool [16]. Successive multifilamentary patterns with decreasing numbers of filaments are formed, until the reservoir energy is exhausted. The typical distance over which ionizing filaments subsist is of the order of a hundred meters [17, 18].

This letter reports experimental results concerning the propagation of intense short laser pulses along a horizontal path ranging over long distances  $d > 500$  m. We observe stable millimeter-size light channels extending over a range of several km [20]. However, in contrast to the usual filaments obtained with small chirp, we find no evidence of ionization in the channels, showing that another mechanism is limiting their peak intensity. In order to obtain insight into this regularizing mechanism, we have compared the experimental results with realistic numerical results, using a nonlinear propagation code which describes successfully the regime  $P \gtrsim P_{\text{cr}}$ . We find that it is not necessary to add any new saturation mechanism to reproduce the experimental results, provided the full three-dimensional aspect of the beam-intensity profile is correctly taken into account. Numerical simulations performed in an ideal case with the addition of small perturbations reveal a crucial feature for regularizing the light channeling over long distances. Each light channel breaks up and nucleates subchannels which compete for the available laser energy. In the absence of an initial intensity perturbation breaking the axial symmetry, the usual ionization-limited filamentation is recovered.

✉ Fax: +33-1/69333008, E-mail: couairon@cph.t.polytechnique.fr

Experiments were performed with a CPA (chirped pulse amplification) multiterawatt laser system, called “teramobile” [21]. It consists of a Ti:S oscillator followed by several stage amplifiers, delivering pulses of 200-mJ energy and a minimum duration of about 100 fs at a repetition rate of 10 Hz. The pulse is stretched in time before amplification to avoid damage in the amplifiers and then is recompressed at the output by a compressor stage consisting of a pair of gratings. This scheme allows us to easily adjust the initial pulse duration before launching the laser pulse in the atmosphere, by imparting a residual linear frequency chirp (either positive or negative) to the emitted pulse. The beam diameter at the output of the compressor is 3.4 cm, with a marked top-hat intensity profile. The laser path propagated 3 m above the ground, during a period of the night when air turbulence was minimal.

Measurements of the beam energy and beam-intensity profile were performed at various locations along the propagation path, up to a distance of 2300 m, for various initial chirps. The beam energy was detected with a calorimeter, over a surface of 15-cm diameter. The intensity distribution in the beam was recorded either by direct single-shot exposure of calibrated photographic plates, or by forming the image of a white diffuser put in the path of the beam. In addition, detection of air ionization was performed using different techniques developed for single filaments: direct electrical conductivity [22, 23], detection of low-frequency radiation from the plasma column [24] or detection of the luminescence from ionized nitrogen molecules [25]. Most experiments were performed with a collimated beam with a 3.4-cm-diameter size. Some experiments were also performed using an expanding telescope and a focusing beam geometry, without significant improvements on the peak intensity at long distances ( $> 500$  m). Collimated beam experiments are discussed here.

Highest laser intensities at long distances were found only when the redder spectral components of the pulse were initially retarded from the bluer components (large negative chirp). For a 200-mJ pulse with a chirp set at or close to its minimum, strong ionization of air was observed over a distance of up to 100 m, starting after a few meters of propagation in air. The beam emerging from the ionization region had a large fraction of its energy converted into a white continuum extending from the ultraviolet to the infrared. The beam also had a significant divergence of the order of 1 mrad, such that the beam intensity rapidly decreased at long distances  $d > 500$  m. On the other hand, a strong negatively chirped pulse prevented early filamentation, yet could deliver high intensity at long distances, because of pulse compression due to the group-velocity dispersion of air [1, 26]. The polarization of the laser beam was measured step by step along the propagation axis and remained linear.

Figure 1a and b show single-shot exposures on calibrated photographic plates recorded at 630 and 1010 m. The initial pulse duration was 9.5 ps with negative chirp. The millimeter-size high-intensity spots were rather reproducible from shot-to-shot except for small fluctuations in the transverse position, presumably due to air turbulence, and tended to align along the periphery of a circle approximately equal to that of the initial beam dimension, as can be seen from the image of successive laser shots recorded at 830 m (Fig. 1c–f). Similar

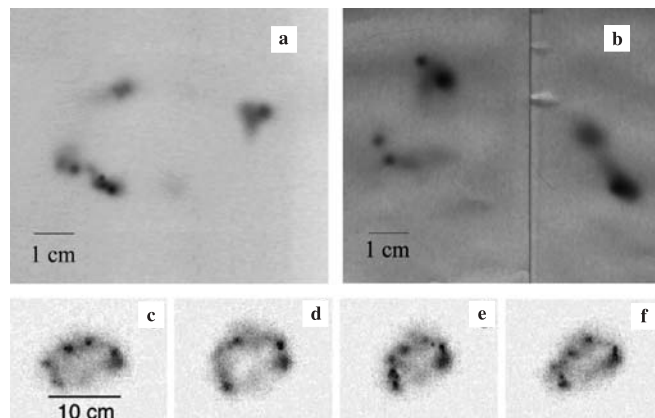


**FIGURE 1** Transverse flux recorded by photographic plates. The initial pulse duration was 9.5 ps with negative chirp. **a** 630 m, **b** 1010 m, **c–f** laser shots taken at 0.1-s interval. The image from a diffuser is recorded from a CCD camera at a distance of 830 m

results were obtained with pulse durations ranging between 3 and 10 ps, up to our longest path of 2350 m. More than 80% of the initial pulse energy was still present at a distance of 1 km. Inspection of photographs taken with a smaller contrast showed that most of the laser energy is distributed unevenly between the light channels, with connecting paths between them. We scanned step by step the propagation distances from 0 to 2350 m by our three methods to measure air ionization. Except for a few sporadic events, we were unable to detect ionization signals for large negative chirps (input durations (FWHM)  $\tau_p \geq 6$  ps). By decreasing the input duration, ionization could be detected occasionally at some specific propagation distances in the range of large chirps ( $1.2 \text{ ps} \leq \tau_p < 6 \text{ ps}$ ). For smaller negative chirps, more intense ionization signals could readily be observed over distances up to 100 m, which corresponds to the classical filamentation regime [7]. From a comparison of the darkening of the photographic plates with that obtained with well-characterized laboratory filaments, we estimated that the peak intensity in the millimeter-size light channels observed up to 2 km is at most  $10^{11} \text{ W/cm}^2$ , insufficient to induce multiphoton ionization of air molecules.

We have calculated the long-range beam propagation in air using our code, which was modified to properly take into account the realistic beam profile. To our knowledge, genuine three-dimensional simulations of multifilamentation have been performed only twice [16, 19]. Our newly developed 3 + 1-dimensional numerical code relies on an extended paraxial model which describes the propagation along the  $z$  axis of the slowly varying envelope  $E(x, y, z, t)$  of the linearly polarized laser pulse, according to the nonlinear envelope equation [15, 27, 28]. The equation accounts for the following effects. (i) Diffraction. (ii) Group-velocity dispersion and higher-order dispersive terms (exactly computed in Fourier space by means of a Sellmeier dispersion relation for the linear index). (iii) The optical Kerr effect with an instantaneous (electronic) and a delayed component due to stimulated molecular Raman scattering. (iv) Plasma absorption and defocusing. (v) Energy absorption due to photo-ionization. (vi) Deviations from the slowly varying envelope approximation due to space–time focusing and self-steepening of the pulse. Since the measured polarization of the beam remains linear,

the effect of cross-phase modulation is not taken into account, in contrast to [28]. At the same time, the generation of the plasma by an optical field and avalanche ionization is described by the evolution equation for the electron density. The photo-ionization rate is computed from the full Keldysh formulation [29] with a recently determined pre-exponential factor [30].

The measured input-beam profile in the form of a data table was adopted as an initial condition. Negative chirps corresponding to an input duration from its minimum  $\tau_p = 120$  fs (without chirp) up to 3 ps were considered, which covers both the small and large negative chirp regimes. We present generic results in the range of negative chirps with  $0.5 \text{ ps} \leq \tau_p \leq 3 \text{ ps}$ . The beam energy was 150 mJ. The results for the fluence distribution  $F(x, y, z) \equiv \int_{-\infty}^{+\infty} |\mathbf{E}(x, y, z, t)|^2 dt$ , after a propagation distance of 50 m, are compared in Fig. 2 to the measurements. Figure 2 shows several hot spots resulting from the amplification of the inhomogeneities in the input beam. During the self-focusing, the flat-top beam produces rings still visible in the figure. The hot spots develop on these rings that store the main part of the beam energy. In agreement with the experimental results, a significant part of the energy is found unevenly distributed between the light channels. The overall beam-intensity distribution as well as the hot-spot positions and sizes are rather well reproduced. Slight discrepancies between experiments and simulations appear in the azimuthal symmetry. Shot-to-shot fluctuations produce slightly different input beams that generate similar but not rigorously identical patterns after propagating over 50 m. The effect of air turbulence might also induce these differences without destroying the global organization of the light channels. Beyond 60 m, the intensity in the spots falls below  $10^{12} \text{ W/cm}^2$ . No ionization is detectable after 100 m. These numerical results show that the nonlinear envelope equation satisfactorily describes the experiments even for  $P \gg P_{cr}$ .

In order to obtain a better insight into the mechanism preventing long-range beam collapse, we have performed simulations assuming a super-Gaussian beam profile that mimics our diaphragmed beam  $\mathbf{E}(x, y, z = 0, t) \propto \exp[-(x^2 + y^2)^3/w_0^6]$ , with a transverse waist  $w_0 = 17 \text{ mm}$ , upon which irregularities in the form of different orders of perturbation are added.

First, radially symmetric, super-Gaussian unperturbed input beams remain symmetric during the propagation. As in 2 + 1-dimensional simulations, spatial rings are formed that fuse into one central filament but the rings do not break up into smaller spots. Peak intensities are sufficient to ionize air and

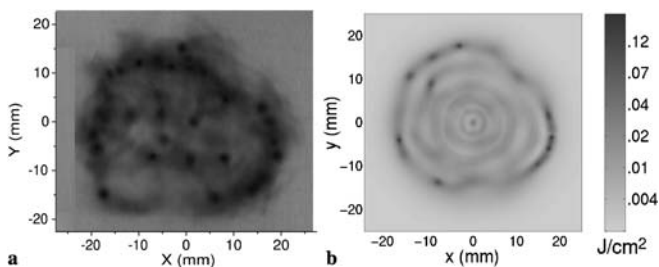


**FIGURE 2** **a** Measured beam profile and **b** computed distribution of the fluence at 50 m for  $\tau_p = 1.5 \text{ ps}$

the classical filamentation model is recovered, including saturation of self-focusing by a plasma density with peaks around  $10^{16} \text{ cm}^{-3}$ . Then, we have studied numerically the multifilamentation process occurring from perturbed input beams. Azimuthal perturbations in the form of a mode with a specific order were added to symmetric super-Gaussian input beams. Gaussian input pulses with decreasing negative chirps (pulse durations from 120 fs to 3 ps) were used. The perturbation contains 1% of the energy of the input pulses. The perturbations are amplified preferentially on the ring that develops in the self-focusing stage, leading to its break up into several spots.

Generic results are shown in Fig. 3 for  $\tau_p = 1.5 \text{ ps}$  (Fig. 3a and b) and 0.5 ps (Fig. 3c and d) and perturbations in the form of an azimuthal mode of orders nine (Fig. 3a) and ten (Fig. 3c and d). Figure 3a shows isosurfaces of the fluence distribution over a distance of 300 m. A very regular multifilamentation pattern with well-organized light channels is obtained on the ring formed in the first stage. Nine light channels propagate over several tens of meters. The diameters are nearly constant in the millimeter range. The channels are located on

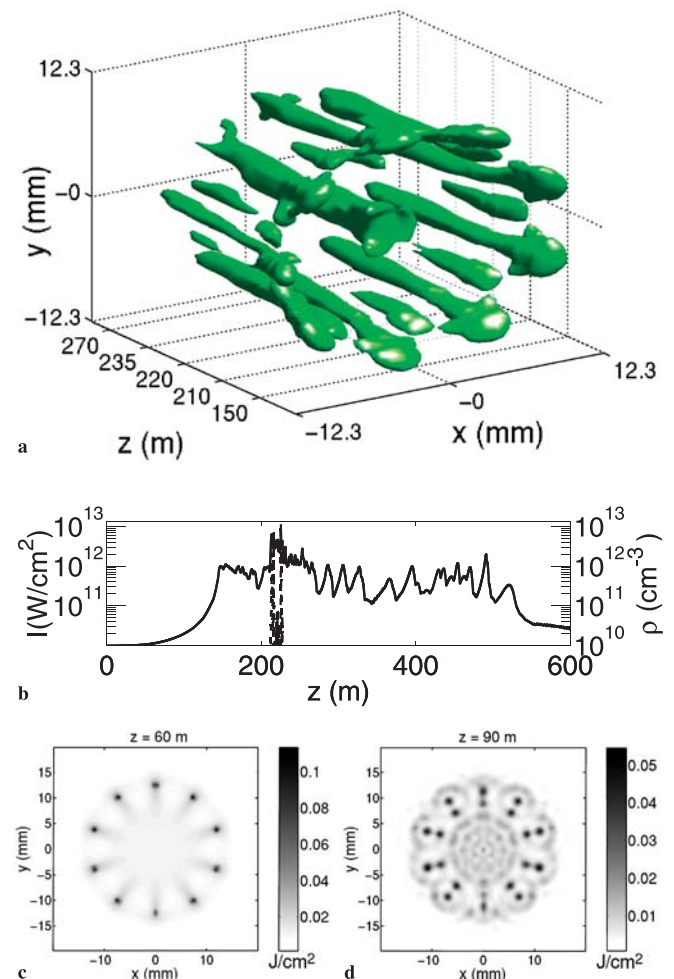


**FIGURE 3** **a** Isosurface of the fluence distribution for  $0.03 \text{ J/cm}^2$ . **b** Maximum intensity (continuous curve, left-hand axis) and electron density (dashed curve, right-hand axis) as a function of the propagation distance for  $\tau_p = 1.5 \text{ ps}$  with negative chirp. **c** and **d** Fluence distributions computed with  $\tau_p = 0.5 \text{ ps}$  at  $c$   $z = 60 \text{ m}$  and **d**  $z = 90 \text{ m}$

a ring slightly smaller than the input-beam radius and regularly spaced like the maximum intensities in the input beam. The pulse duration in the light channels is found to be about 100 fs before a splitting into several subpulses occurs. The same phenomenon is recovered over larger distances from simulations with larger negative chirps.

It is also a generic result that the number of light channels initially follows the order of azimuthal perturbations. When higher-order azimuthal modes are excited, a pattern with a larger number of spots is eventually obtained. Each light channel is well separated and seems to evolve independently from its neighbors. This reflects a competition between the light channels for the surrounding energy. In this respect, the model of the energy reservoir proposed by Mlejnek et al. [16] fully applies except that, in our case, multiphoton ionization does not play a dominant role. Figure 3b shows that the maximum intensity (solid curve, left-hand axis) in the light channels does not exceed a few  $10^{12}$  W/cm<sup>2</sup>. The first stage up to 150 m corresponds to the formation of the light channels under the modulational instability due to the Kerr self-focusing [31]. In the most intense part of the light channels around 210 m, tenuous localized plasma channels of density around a few  $10^{12}$  cm<sup>-3</sup> are triggered (dashed curve, right-hand axis). When the duration of the input pulse is increased, the maximum electron density keeps the same level over a few meters but these localized plasmas are located at increasing distances on the propagation axis. Ionization therefore does not saturate self-focusing as in classical femtosecond filamentation. Yet, it acts locally as a necessary regularizing process during the propagation of the light channels. Simulations performed by unplugging ionization indeed show that the maximum intensity follows the solid curve in Fig. 3b except for slightly higher peaks in the region of the plasma and an eventual catastrophic collapse before  $z = 210$  m. Figure 3c and d show the evolution of the fluence distribution from 60 to 90 m for  $\tau_p = 0.5$  ps. A break up of each filament into two smaller light channels occurs around 60 m. Beyond 90 m, each pair of these co-propagating channels merge (pattern similar to Fig. 3c). This shows nicely how daughter channels are formed along light tracks due to interference in the coherent beam. In this sense, both interference and the nonlinear Kerr effect act to redirect the energy from parent to daughter light channels.

In conclusion, long-range-propagation studies of intense laser pulses in the atmosphere reveal the existence of stable non-ionizing channels extending over km distance. For the first time, their spatial and temporal dynamics is compared to genuine 3 + 1-dimensional numerical simulations. Well-ordered filamentation patterns exhibit a beautiful organization of the spots on concentric rings, which reproduce the patterns obtained in the experiments. Such results are described by using the same nonlinear propagation equation that describes the filamentation at low input power, without the necessity to add a new physical mechanism to limit the growth of laser intensity. Model simulations uncover the complexity of the nonlinear system, where initial conditions play a crucial role for the later evolution of the system.

**ACKNOWLEDGEMENTS** This work was made within the framework of the joint French–German teramobile project funded by the CNRS and the DFG. A.M. acknowledges support from the Humboldt Foundation. We also acknowledge partial support from NATO program TG31.

## REFERENCES

- P. Rairoux, H. Schillinger, S. Neirdeimer, M. Rodriguez, F. Ronneberger, R. Sauerbrey, B. Stein, D. Waite, C. Wedekind, H. Wille, L. Wöste, C. Ziener: *Appl. Phys. B* **71**, 573 (2000)
- L. Wöste, C. Wedekind, H. Wille, P. Rairoux, B. Stein, S. Nikolov, C. Werner, S. Neirdeimer, F. Ronneberger, H. Schillinger, R. Sauerbrey: *Laser Optoelectron.* **29**, 51 (1997)
- J. Kasparian, M. Rodriguez, G. Méjean, J. Yu, E. Salmon, H. Wille, R. Bourayou, S. Frey, Y.-B. André, A. Mysyrowicz, R. Sauerbrey, J.-P. Wolf, L. Wöste: *Science* **301**, 61 (2003)
- F. Vidal, D. Comtois, C.-Y. Chien, A. Desparois, B. La Fontaine, T.W. Johnston, J.-C. Kieffer, H.P. Mercure, F.A. Rizk: *IEEE Trans. Plasma Sci.* **28**, 418 (2000)
- X.M. Zhao, J.-C. Diels, C.Y. Wang, J.M. Elizondo: *IEEE J. Quantum Electron.* **31**, 599 (1995)
- Y. Silberberg: *Opt. Lett.* **15**, 1282 (1990)
- E.T.J. Nibbering, P.F. Curley, G. Grillon, B.S. Prade, M.A. Franco, F. Salin, A. Mysyrowicz: *Opt. Lett.* **21**, 62 (1996)
- O.G. Kosareva, V.P. Kandidov, A. Brodeur, C.Y. Chien, S.L. Chin: *Opt. Lett.* **22**, 1332 (1997)
- N. Aközbebek, M. Scalora, C.M. Bowden, S.L. Chin: *Opt. Commun.* **191**, 353 (2001)
- S. Tzortzakis, G. Méchain, G. Palatano, Y.-B. André, M. Franco, B. Prade, A. Mysyrowicz: *Opt. Lett.* **27**, 1944 (2002)
- C.-C. Cheng, E.M. Wright, J.V. Moloney: *Phys. Rev. Lett.* **87**, 213001 (2001)
- V.S. Letokhov: in *Proc. XXII Solvay Conf. Physics* (World Scientific 2001)
- H.R. Lange, A. Chiron, J.-F. Ripoche, A. Mysyrowicz, P. Breger, P. Agostini: *Phys. Rev. Lett.* **81**, 1611 (1998)
- A. Braun, G. Korn, X. Liu, D. Du, J. Squier, G. Mourou: *Opt. Lett.* **20**, 73 (1995)
- A. Couairon, S. Tzortzakis, L. Bergé, M. Franco, B. Prade, A. Mysyrowicz: *J. Opt. Soc. Am. B* **19**, 1117 (2002)
- M. Mlejnek, M. Kolesik, J.V. Moloney, E.M. Wright: *Phys. Rev. Lett.* **83**, 2938 (1999)
- A. Iwasaki, N. Aközbebek, B. Ferland, Q. Luo, G. Roy, C.M. Bowden, S.L. Chin: *Appl. Phys. B* **76**, 231 (2003)
- B. La Fontaine, F. Vidal, Z. Jiang, C.Y. Chien, D. Comtois, A. Desparois, T.W. Johnston, J.-C. Kieffer, H. Pépin: *Phys. Plasmas* **6**, 1615 (1999)
- S.L. Chin, A. Talebpour, J. Yang, S. Petit, V.P. Kandidov, O.G. Kosareva, M.P. Tamarov: *Appl. Phys. B* **74**, 67 (2002); V.P. Kandidov, O.G. Kosareva, M.P. Tamarov, A. Brodeur, S.L. Chin: *Quantum Electron.* **29**, 911 (1999)
- Millimeter-sized filaments at a distance of 200 m have been reported by several groups [18, 19]
- H. Wille, M. Rodriguez, J. Kasparian, D. Mondelain, J. Yu, A. Mysyrowicz, R. Sauerbrey, J.-P. Wolf, L. Wöste: *Eur. Phys. J.: Appl. Phys.* **20**, 183 (2002)
- S. Tzortzakis, B. Lamouroux, A. Chiron, M. Franco, B. Prade, A. Mysyrowicz, S.D. Moustazis: *Phys. Rev. E* **60**, R3505 (1999)
- H.D. Ladouceur, A.P. Baronavski, D. Lohrmann, P.W. Grounds, P.G. Girardi: *Opt. Commun.* **189**, 107 (2001)
- H. Schillinger, R. Sauerbrey: *Appl. Phys. B* **68**, 753 (1999)
- A. Talebpour, S. Petit, S.L. Chin: *Opt. Commun.* **171**, 285 (1999)
- P. Sprangle, J.R. Peñano, B. Hafizi: *Phys. Rev. E* **66**, 046418 (2002)
- T. Brabec, F. Krausz: *Phys. Rev. Lett.* **78**, 3282 (1997)
- A. Couairon, G. Méchain, S. Tzortzakis, M. Franco, B. Lamouroux, B. Prade, A. Mysyrowicz: *Opt. Commun.* **225**, 177 (2003)
- L.V. Keldysh: *ZhETF* **47**, 1945 (1964); *Sov. Phys. JETP* **20**, 1307 (1965)
- K. Mishima, M. Hayashi, J. Yi, S.H. Lin, H.L. Selzle, E.W. Schlag: *Phys. Rev. A* **66**, 033401 (2002)
- V.I. Bespalov, V.I. Talanov: *JETP Lett.* **3**, 307 (1966)

# Long-distance remote laser-induced breakdown spectroscopy using filamentation in air

Kamil Stelmazczyk and Philipp Rohwetter

*Teramobile, Institut für Experimentalphysik, Freie Universität Berlin, Arnimallee 14, D-14195 Berlin, Germany*

Guillaume Méjean, Jin Yu, Estelle Salmon, Jérôme Kasparian,<sup>a)</sup>

Roland Ackermann, and Jean-Pierre Wolf

*Teramobile, LASIM, UMR CNRS 5579, Université Claude Bernard Lyon 1, 43 bd du 11 Novembre 1918, F-69622 Villeurbanne Cedex, France*

Ludger Wöste

*Teramobile, Institut für Experimentalphysik, Freie Universität Berlin, Arnimallee 14, D-14195 Berlin, Germany*

(Received 22 March 2004; accepted 15 September 2004)

We demonstrate remote elemental analysis at distances up to 90 m, using a laser-induced breakdown spectroscopy scheme based on filamentation induced by the nonlinear propagation of unfocused ultrashort laser pulses. A detailed signal analysis suggests that this technique, remote filament-induced breakdown spectroscopy, can be extended up to the kilometer range. © 2004 American Institute of Physics. [DOI: 10.1063/1.1812843]

Laser-induced breakdown spectroscopy (LIBS)<sup>1</sup> provides a versatile analytical tool for real-time surface analysis of metals,<sup>2</sup> plastics,<sup>3,4</sup> minerals,<sup>5,6</sup> aerosols, biological tissues<sup>7</sup> or liquids. LIBS relies on local plasma generation using a strongly focused laser beam, generally a *Q*-switched Nd:yttrium–aluminum–garnet laser. The emission spectrum of the plasma is used for fast and quantitative elemental analysis, with typical detection limits in the range of several to several hundreds of ppm for most elements. To improve the ablation rates in LIBS measurements, subpicosecond laser pulses have been recently used,<sup>2,8–10</sup> with a strong improvement of the measurement reproducibility. The use of a broadband detection system makes the technique versatile, since there is no need for *a priori* knowledge of the species to be detected. The versatility and ease of use of LIBS led to practical applications such as the control of industrial processes,<sup>11</sup> environmental monitoring,<sup>12</sup> waste management,<sup>3,4</sup> medical diagnostics,<sup>7</sup> or space research.<sup>5,6</sup>

Moreover, supported by the development of compact and reliable spectrometers as well as diode-pumped solid-state lasers, portable LIBS systems<sup>6,13</sup> emerged for *in situ* field applications such as the analysis of old painting for archaeology<sup>14</sup> or food analysis. However, applications in hostile environments, for example, the identification of highly radioactive nuclear waste<sup>15</sup> or the monitoring of molten alloys,<sup>16</sup> require remote analysis. LIBS is particularly suitable for such purposes, since the samples need no preparation and must only be directly visible from the operation site. A remote-sensing LIBS technique, based on long-range focusing and remote light collection, has recently been demonstrated to reach distances up to 80 m.<sup>17</sup> But diffraction limits the delivery of high laser intensity (at least  $10^{12}$  W/cm<sup>2</sup> in the femtosecond regime<sup>2</sup>) at further distances using linear optics, which would require even longer focal lengths and prohibitively large optics. Moreover, atmo-

spheric turbulence may reduce the intensity at the focus.

In this letter, we show that the self-guided filaments generated by high-power, ultrashort laser pulses<sup>18–23</sup> can overcome the diffraction limit and deliver high laser intensities at remote locations without focusing, allowing a remote filament-induced breakdown spectroscopy (R-FIBS) scheme. Filaments arise in nonlinear propagation of ultrashort laser pulses, due to the balance between Kerr self-focusing and defocusing caused by the tiny plasma generated in the air. They carry intensities in the range of  $10^{13}$  W/cm<sup>2</sup> (Ref. 19) over several kilometers.<sup>24,25</sup> Such intensity is above the threshold for laser ablation on metal samples using femtosecond pulses.<sup>26,27</sup> We demonstrate R-FIBS measurements at distances up to 90 m, limited in our experiment by the available free space in front of the laser. Our data suggest, however, that R-FIBS can be successfully applied up to the kilometer range.

The experimental setup is depicted in Fig. 1. The *Teramobile*<sup>28</sup> laser source provided 250 mJ pulses centered at 800 nm, at the repetition rate of 10 Hz. The beam was

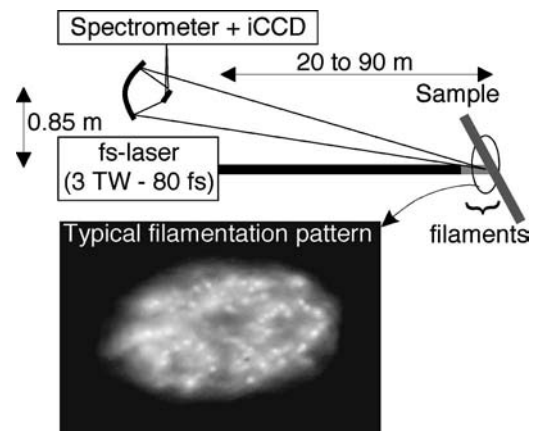


FIG. 1. Experimental setup. Right: beam profile near to the sample showing multifilamentation with typically 30 filaments across the beam.

<sup>a)</sup> Author to whom correspondence should be addressed; electronic mail: jkaspari@lasim.univ-lyon1.fr

emitted collimated, with a diameter of 3 cm. It hit the sample after propagating 20–90 m. The minimum pulse duration at the exit of the compressor was 80 fs. However, to set the position of the filament onset several meters (typically 7–8 m) before the sample, the pulses were shaped with a tunable negative chirp,<sup>23,28</sup> corresponding to pulse durations up to 800 fs. A typical multiple-filamentation pattern, exhibiting around 30 filaments across the beam profile, was observed on the sample (see Fig. 1). The optimal chirp also corresponded to the most intense acoustic shockwave, i.e., to the most intense ablation on the material. The shot to shot excursion of the filament across the large beam cross section spread the damage region on the material over a surface of several cm<sup>2</sup>. Therefore, the ablated depth was negligible, even after as many as several 10<sup>5</sup> shots. This allows for non-invasive analysis. Two samples were investigated: raw, industrial-grade copper and steel plates without any surface preparation.

The backward-emitted signal was collected with a 20 cm telescope and analyzed with a time-gated optical multichannel analyzer (Chromex IS-SM 500 imaging spectrometer and Princeton PI Max 1024 HQ ICCD camera), located near the laser. An adequate time gating of the detector eliminated the white-light continuum generated in the filaments by self-phase modulation in air, and reflected elastically on the sample. Contrary to the results of Angel *et al.* with a focused femtosecond beam,<sup>2</sup> we observed no broadband blackbody emission on the 100 ns time scale, showing that the filament-excited plasma is cold, providing a better contrast than in classical LIBS. The FIBS emission was found to be anisotropic with respect to the tilt angle of the sample. However, in order to demonstrate the capability of the R-FIBS also under adverse conditions, we used tilt angles away from the maximum for our measurements.

Figure 2 presents the emission spectra obtained from copper and steel samples located 90 m away from the laser and detection systems. The typical lines of Cu I and Fe I in the 520 nm region are clearly visible, showing that R-FIBS can perform remote elemental analysis at a distance of 90 m. Although these spectra have been integrated over 10 000 shots, unambiguous spectra could be obtained with only 1000 shots, i.e., less than 2 min at 10 Hz, allowing almost real-time monitoring. Under the same conditions, uncompressed (200 ps) and unseeded (typically 5 ns) laser pulses yield neither ablation nor LIBS signal. Moreover, signal with the femtosecond beam was only observed when the chirp was adjusted so that filaments actually hit the sample. This proves that the observed signal has been generated by the filaments, defining a LIBS scheme for remote analysis.

The measured R-FIBS signal did not depend on the sample distance  $R$ , besides the  $1/R^2$  geometrical term due to the solid angle collected by the telescope (Fig. 3). However, due to the  $1/R^2$  term, the signal-to-noise ratio decreases with the detection distance, and its extrapolated value drops to 1 around 150 m (see dash-dotted line in Fig. 3). This distance must be seen as a lower limit, since the poor coupling into our detection system could be improved, with an expected signal enhancement by a factor of 100, hence allowing R-FIBS measurements at distances up to the kilometer range, comparable with the filament propagation distance.<sup>25</sup> This range opens the way for applications in hostile environments.

We further checked that no intrinsic signal loss occurs, by performing a local measurement, hence without the geo-

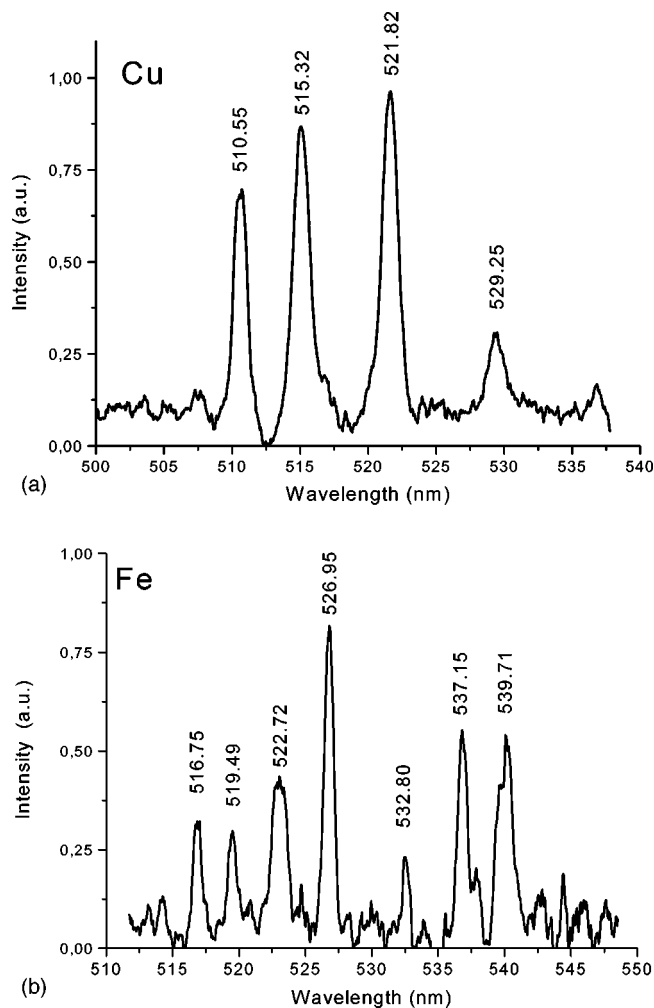


FIG. 2. R-FIBS spectra of copper (a) and steel (b), measured at 90 m distance.

metrical term. In that purpose, we kept a fixed, short distance (7 m) between the detection system and the sample, and we moved the laser away. As expected, the measured signal did not depend significantly on the propagation distance of the laser pulses before the filaments hit the sample, at least up to 90 m of propagation. Such behavior is in strong contrast with remote-LIBS excited by a focused beam.<sup>8,16</sup> Here, the incident fluence on the sample decreases with focusing distance since diffraction leads to a beam waist proportional to the measurement distance. Hence, the ionization efficiency falls down when the distance is increased. Since the plasma generation is a multiphoton process, this decrease is not fully balanced by the increase in the illuminated surface on the sample. The simulation of such distance dependence, in the case of the three-photon ionization of Cu at 800 nm,<sup>29</sup> is displayed for comparison in Fig. 3 (solid curve).

As a conclusion, we have demonstrated a noninvasive, remote optical analysis technique, R-FIBS, up to 90 m, with possible extension up to the kilometer range. This technique is based on filamentation induced by the nonlinear propagation of ultrashort laser pulses. The filaments are able to overcome linear focusing limits of longer pulses, and deliver extremely high laser intensities ( $10^{13}$  W/cm<sup>2</sup>) at remote distances. This technique, which only requires reasonable laser energies, can be practical for versatile remote analysis on hazardous or unreachable spots, such as polluted sites, nuclear plants or chemical leakages.<sup>30</sup>

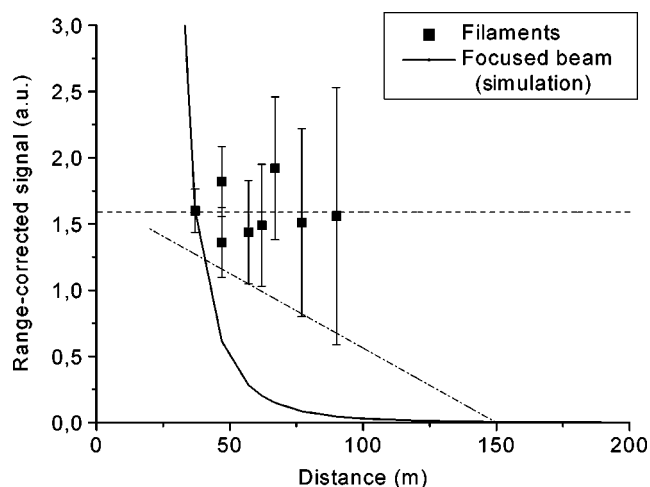


FIG. 3. Distance dependence of the range-corrected R-FIBS signal from the 521.8 nm line of copper.

This work has been performed within the framework of the *Teramobile* project, funded jointly by the CNRS, DFG, and French and German ministries of Research and of Foreign affairs. K.S. acknowledges financial support by the Alexander von Humboldt Stiftung. The *Teramobile* web site is [www.teramobile.org](http://www.teramobile.org).

<sup>1</sup>D. A. Cremers and A. K. Knight, in *Encyclopedia of Analytical Chemistry* (Wiley, New York, 2000), Vol. 11, p. 9595.

<sup>2</sup>S. M. Angel, D. N. Stratis, K. L. Eland, T. Lai, M. A. Berg, and D. M. Gold, *Fresenius' J. Anal. Chem.* **369**, 320 (2001).

<sup>3</sup>R. Niessner, *Proc. SPIE* **2360**, 254 (1994).

<sup>4</sup>Y. Jong-Il, R. Klenze, and J. I. Kim, *Appl. Spectrosc.* **56**, 852 (2002).

<sup>5</sup>A. K. Knight, N. L. Scherbarth, D. A. Cremers, and M. J. Ferris, *Appl. Spectrosc.* **54**, 331 (2000).

<sup>6</sup>R. C. Wiens, R. E. Arvidson, D. A. Cremers, M. J. Ferris, J. D. Blacic, and F. P. Seelos IV, *J. Geophys. Res., [Planets]* **107**, 8003 (2002); S. K. Sharma, P. G. Lucey, M. Ghosh, H. W. Hubble, and K. A. Horton, *Spectrochim. Acta, Part A* **59**, 2391 (2003).

<sup>7</sup>S. Kyuseok, L. Yong-Il, and J. Sneddon, *Appl. Spectrosc. Rev.* **32**, 183 (1997).

<sup>8</sup>P. Rohwetter, K. Stelmaszczyk, G. Méjean, J. Yu, E. Salmon, J. Kasparian, J.-P. Wolf, and L. Wöste, *J. Anal. At. Spectrom.* **19**, 437 (2003).

<sup>9</sup>O. Albert, S. Roger, Y. Glinec, J. C. Loulergue, J. Etchepare, C. Boulmer-

Leborgne, J. Perrière, and E. Millon, *Appl. Phys. A: Mater. Sci. Process.* **76**, 319 (2003).

<sup>10</sup>K. Dou, E. T. Knobbe, R. L. Parkhill, B. Irwin, L. Matthews, and K. H. Church, *Appl. Phys. A: Mater. Sci. Process.* **76**, 303 (2003).

<sup>11</sup>M. Kraushaar, R. Noll, and H.-U. Schmitz, *Appl. Spectrosc.* **57**, 1282 (2003).

<sup>12</sup>J. E. Carranza and David W. Hahn, *Anal. Chem.* **74**, 5450 (2002).

<sup>13</sup>R. A. Walters and J. B. Rose, "Man portable LIBS system with high-resolution broadband spectrometer and active Q-switched laser," presented at EMSLIBS, Hersonissos, Greece, September 2003.

<sup>14</sup>K. Melessanaki, M. P. Mateo, S. C. Ferrence, P. Betancourt, and D. Anglos, *Appl. Surf. Sci.* **197,198**, 156 (2002).

<sup>15</sup>A. I. Whitehouse, J. Young, I. M. Botheroyd, S. Lawson, C. P. Evans, and J. Wright, *Spectrochim. Acta, Part B* **56**, 821 (2001).

<sup>16</sup>S. Palanco, L.M. Cabalin, D. Romero, and J. J. Laserna, *J. Anal. At. Spectrom.* **14**, 1883 (1999).

<sup>17</sup>S. Palanco, S. Conesa, and J. J. Laserna, *J. Anal. At. Spectrom.* **19**, 462 (2003).

<sup>18</sup>J. Kasparian, R. Sauerbrey, and S. L. Chin, *Appl. Phys. B: Lasers Opt.* **71**, 877 (2000).

<sup>19</sup>A. Becker, N. Aközbe, K. Vijayalakshmi, E. Oral, C. M. Bowden, and S. L. Chin, *Appl. Phys. B: Lasers Opt.* **73**, 287 (2001).

<sup>20</sup>A. Couairon and L. Bergé, *Phys. Rev. Lett.* **88**, 135003 (2002).

<sup>21</sup>M. Mlejnek, E. M. Wright, and J. V. Moloney, *Opt. Express* **4**, 223 (1999).

<sup>22</sup>M. Mlejnek, M. Kolesik, J. V. Moloney, and E. M. Wright, *Phys. Rev. Lett.* **83**, 2938 (1999).

<sup>23</sup>J. Kasparian, M. Rodriguez, G. Méjean, J. Yu, E. Salmon, H. Wille, R. Bourayou, S. Frey, Y.-B. André, A. Mysyrowicz, R. Sauerbrey, J.-P. Wolf, and L. Wöste, *Science* **301**, 61 (2003).

<sup>24</sup>B. La Fontaine, F. Vidal, Z. Jiang, C. Y. Chien, D. Comtois, A. Desparois, T. W. Johnston, J.-C. Kiefer, H. Péepin, and H. P. Mercure, *Phys. Plasmas* **6**, 1615 (1999).

<sup>25</sup>M. Rodriguez, R. Bourayou, G. Méjean, J. Kasparian, J. Yu, E. Salmon, A. Scholz, B. Stecklum, J. Eislöffel, U. Laux, A. P. Hatzes, R. Sauerbrey, L. Wöste, and J.-P. Wolf, *Phys. Rev. E* **69**, 036607 (2004).

<sup>26</sup>J. Kruger and W. Kautek, *Laser Phys.* **9**, 30 (1999).

<sup>27</sup>F. Garrelie, A. S. Loir, C. Donnet, F. Rogemond, R. Le-Harzac, M. Belin, E. Audouard, and P. Laporte, *Surf. Coat. Technol.* **163,164**, 306 (2003).

<sup>28</sup>H. Wille, M. Rodriguez, J. Kasparian, D. Mondelain, J. Yu, A. Mysyrowicz, R. Sauerbrey, J.-P. Wolf, and L. Wöste, *Eur. Phys. J.: Appl. Phys.* **20**, 183 (2002).

<sup>29</sup>M. Hashida, A. F. Semerok, O. Gobert, G. Petite, Y. Izawa, and J. F. Wagner, *Appl. Surf. Sci.* **197,198**, 862 (2002).

<sup>30</sup>Since this letter was accepted, we have detected the 395 plasma line from an aluminium sample located 180 m away from the laser source. This demonstrates further the capability of R-FIBS to perform experiments at long distances.

## Triggering and guiding of megavolt discharges by laser-induced filaments under rain conditions

R. Ackermann

*Teramobile, LASIM, UMR CNRS 5579, Université Lyon 1, 43 bd du 11 Novembre 1918, F-69622 Villeurbanne Cedex, France*

K. Stelmaszczyk and P. Rohwetter

*Teramobile, Institut für Experimentalphysik, FU Berlin, Arnimallee 14, D-14195 Berlin, Germany*

G. Méjean, E. Salmon, J. Yu, and J. Kasparian<sup>a)</sup>

*Teramobile, LASIM, UMR CNRS 5579, Université Lyon 1, 43 bd du 11 Novembre 1918, F-69622 Villeurbanne Cedex, France*

G. Méchain

*Teramobile, LOA, UMR CNRS 7639, ENSTA-Ecole Polytechnique, Centre de l'Yvette, Chemin de la Hunière, F-91761 Palaiseau Cedex, France*

V. Bergmann, S. Schaper, B. Weise, T. Kumm, K. Rethmeier, and W. Kalkner

*Institut für Energie- und Automatisierungstechnik, TU Berlin, Einsteinufer 11, D-10587 Berlin, Germany*

L. Wöste

*Teramobile, Institut für Experimentalphysik, FU Berlin, Arnimallee 14, D-14195 Berlin, Germany*

J. P. Wolf

*Teramobile, LASIM, UMR CNRS 5579, Université Lyon 1, 43 bd du 11 Novembre 1918, F-69622 Villeurbanne Cedex, France*

(Received 1 July 2004; accepted 5 October 2004)

We demonstrate laser control of high-voltage discharges over a gap of 1.2 m filled with a dense water cloud. Self-guided filaments generated by ultrashort laser pulses are transmitted through the cloud and ionize a continuous plasma channel. The cloud typically reduces the discharge probability in given experimental conditions by 30%, but has almost no influence on the threshold required to trigger single discharge events, both in electrical field and laser energy. This result is favorable for real-scale lightning control applications. © 2004 American Institute of Physics.

[DOI: 10.1063/1.1829165]

The possibility of triggering and guiding lightning by means of pulsed laser beams has been debated for more than 30 years.<sup>1</sup> The main motivation is to protect sensitive sites, like electrical installations or airports, from direct strikes and electromagnetic perturbations. Studies using nanosecond lasers<sup>2</sup> exhibited severe limitations due to the lack of connected plasma channels. However, high-power femtosecond lasers, which produce ionized plasma channels, have opened new opportunities in this domain.<sup>3</sup> Two approaches have been investigated. In the first approach, strongly focused ultrashort laser pulses produce strongly ionized plasma channels near to the focus.<sup>4–6</sup>

In the second approach, long self-guided filaments generated by a slightly focused or parallel laser beam are used to ohmically bridge (i.e., to short-circuit) the electrodes and trigger and guide the high-voltage pulses.<sup>7,8</sup> Filaments<sup>9–11</sup> arise from a nonlinear propagation of ultraintense laser pulses, when Kerr-lens focusing dynamically balances defocusing by the ionized plasma produced within the filaments. Filaments can propagate over several hundreds of meters,<sup>12</sup> up to the kilometer range.<sup>13,14</sup> Moreover, the filaments survive the interaction with aerosol particles, even of large diameter.<sup>15,16</sup> This makes them suitable candidates for real-scale atmospheric applications<sup>17</sup> such as lightning control,

where conducting over long distances in raining conditions is necessary.

Such outdoor experiments require knowledge about the influence of rain over laser triggering of high-voltage discharges. On one hand, even though self-guided filaments can survive the interaction with droplets,<sup>15,16</sup> the aerosol induces losses in the photon bath and perturbs the laser propagation. On the other hand, a water aerosol is generally considered to reduce the breakdown voltage due to a lower ionization potential. Water or ice particles are also necessary not only to generate the charge within the cumulo-nimbus cloud when they collide, but also to initiate natural lightning discharges.<sup>18</sup> However, due to the technical difficulty of both high-voltage and laser operation in humid conditions, the effect of rain and clouds on laser-triggered discharges has only been investigated with CO<sub>2</sub> lasers,<sup>19</sup> and is mostly focused on fog rather than rain. In this letter, we investigate the effect of rain on discharge guiding by ultrashort self-guided filaments.

The main parts of the experimental setup have been described in detail elsewhere.<sup>8</sup> Briefly, the *Teramobile*<sup>20</sup> laser system provided 170 fs pulses of 230 mJ centered at 800 nm, fired typically 5  $\mu$ s after the peak voltage of a Marx shock generator (1.2  $\mu$ s voltage rise time). We used a tip-plane electrode configuration with a gap of 1.2 m.

On demand, we sprayed water droplets before and in the gap between the electrodes, at a flow corresponding to a heavy rain (1.4 mm/min). The cloud extinction coefficient

<sup>a)</sup> Author to whom correspondence should be addressed; electronic mail: jkaspari@lasim.univ-lyon1.fr

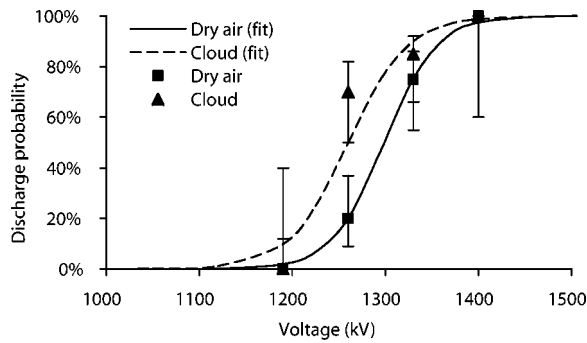


FIG. 1. Influence of a water cloud on free discharges. The solid lines are hyperbolic tangent fits used to determine the  $U_{50}$  values.

was  $0.14 \text{ m}^{-1}$  over 3 m, corresponding  $0.3 \text{ droplets/cm}^{-3}$ , with a mean diameter of 0.5 mm. The beam profile on the ground electrode confirmed that filaments survive the interaction with water droplets, as previously demonstrated on a shorter scale.<sup>15,16</sup> The relative humidity (RH) within the aerosol cloud was 48% at a temperature of 19 °C (1% volume mixing ratio, VMR). Reference measurements have been conducted in dry air (34 % RH at 22 °C, corresponding to 0.9% VMR).

Since the occurrence of discharges in given conditions is stochastic, the estimation of the confidence interval is crucial to assess for significant effects when comparing different experimental conditions. Each data point is assigned a confidence interval at  $\alpha=10\%$ , which was calculated using a binomial probability law, based on the assumption that successive shots are independent from each other.

We first characterized the effect of the cloud on free discharges: the cloud reduces the 50% flashover voltage, i.e., the voltage yielding 50% probability of free discharges ( $U_{50}$ ) by 3% (Fig. 1). This statistically significant positive contribution of water aerosol may be qualitatively understood as the effect of the lower ionization potential of water, compared to oxygen and nitrogen. The low RH in the cloud excludes effects of the water vapor itself.

While a cloud slightly reduces the free breakdown voltage, it does not prevent the filaments from triggering high-voltage discharges (Fig. 2). Triggered discharges have been observed down to 910 kV in cloudy conditions, compared to 850 kV in dry air and 1260 kV without laser. Conversely, the triggered discharge probability decreases by typically 30% in

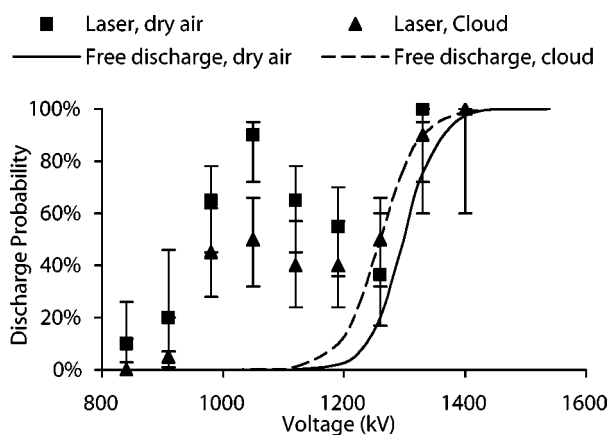


FIG. 2. Discharge probability as a function of voltage, for both dry and cloudy atmosphere. The fitted transition curves for free discharges (see Fig. 1) are plotted for comparison.

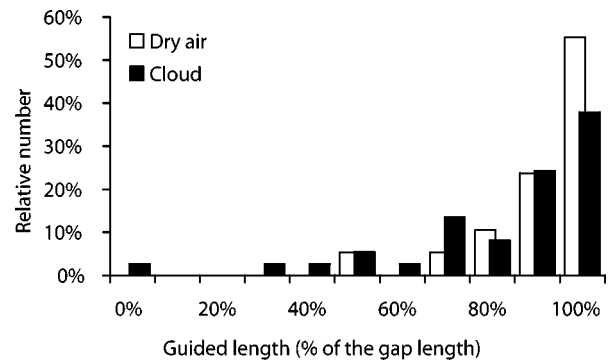


FIG. 3. Guided length (expressed as a fraction of the 1.2 m gap) in dry air and in cloud condition for triggered discharges.

the cloud. However, once triggered, the discharges are guided almost as efficiently as in dry air. Figure 3 displays statistics about the guided length for voltages below 1260 kV, where only triggered discharges can occur. While a dense cloud slightly decreases the number of fully guided discharges and allows guiding over less than 70% of the gap, 90% of the triggered discharges are guided over at least 50% of their length, and 60% of them over more than 90% of their length.

The maintained triggering and guiding effect can be understood by the fact that a cloud with the same transmission (65%) as that of our experiment is known to transmit self-guided filaments.<sup>15</sup> Moreover, considering the droplet size and density, only half of the filaments hit a droplet. They are then replenished by the photon bath acting as an energy reservoir around them. Therefore, the linear extinction of the photon bath within the cloud plays an important role, especially over the long distances required for real-scale lightning control applications.

To quantify the effect of this extinction, we varied the laser pulse energy, at a fixed voltage (1050 kV) well below  $U_{50}$  for natural discharges. Reducing the laser energy decreases the triggering efficiency in both dry air and in a cloud, but the decrease is faster in the cloud (Fig. 4). However, even in the cloud, pulse energies as low as 60 mJ are sufficient to trigger discharges, although with a low probability. But in the context of real-scale lightning control, such low probability for single shots is balanced by the 10 Hz repetition rate of the laser (or by the kilohertz repetition rates of lasers which can be expected in the future). Hence, reasonable event occurrences can be expected for applications such as studies of lightning strikes as long as the energy threshold is not strongly affected by the cloud.

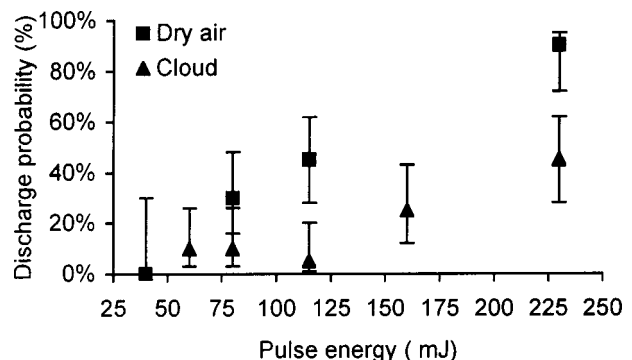


FIG. 4. Laser energy dependence of the triggering at 1050 kV voltage.

As a conclusion, we have demonstrated that self-guided filaments generated by ultrashort laser pulses can trigger and guide high-voltage discharges over a 1.2 m gap even in a dense cloud. The cloud reduces the discharge probability for given electrical field and laser energy conditions, and slightly favors free discharges. However, the presence of a cloud increases neither the electrical field nor the laser energy thresholds allowing single triggering and guiding events. Since real-scale applications can be performed with typical repetition rates of 10 Hz, or even in the kilohertz range in the near future, the reduced event probability near to the threshold should not be critical in applications.

This work has been performed within the *Teramobile* project, funded jointly by the CNRS, DFG, and French and German ministries of Research and of Foreign affairs. The Teramobile web site is [www.teramobile.org](http://www.teramobile.org). K.S. acknowledges support from Humboldt Foundation. We acknowledge the help of L. Gras (Ineris, Verneuil en Halatte, France) in measuring the droplet size distribution.

<sup>1</sup>D. W. Koopman and T. D. Wilkerson, *J. Appl. Phys.* **42**, 1883 (1971).

<sup>2</sup>M. Miki, Y. Aihara, and T. Shindo, *J. Phys. D* **26**, 1244 (1993).

<sup>3</sup>H. Pépin, D. Comtois, F. Vidal, C. Y. Chien, A. Desparois, T. W. Johnston, J. C. Kieffer, B. L. Fontaine, F. Martin, F. A. M. Rizk, C. Potvin, P. Couture, H. P. Mercure, A. Bondiou-Clergerie, P. Lalande, and I. Gallimberti, *Phys. Plasmas* **8**, 2532 (2001).

<sup>4</sup>D. Comtois, C. Y. Chien, A. Desparois, F. Gérin, G. Jarry, T. W. Johnston, J. C. Kieffer, B. L. Fontaine, F. Martin, R. Mawassi, H. Pépin, F.

A. M. Rizk, P. Couture, H. P. Mercure, C. Potvin, A. Bondiou-Clergerie, and I. Gallimberti, *Appl. Phys. Lett.* **76**, 819 (2000).

<sup>5</sup>D. Comtois, H. Pépin, F. Vidal, F. A. M. Rizk, C.-Y. Chien, T. W. Johnston, J.-C. Kieffer, B. La Fontaine, F. Martin, C. Potvin, P. Couture, H. P. Mercure, A. Bondiou-Clergerie, P. Lalande, and I. Gallimberti, *IEEE Trans. Plasma Sci.* **31**, 377 (2003).

<sup>6</sup>D. Comtois, H. Pépin, F. Vidal, F. A. M. Rizk, C.-Y. Chien, T. W. Johnston, J.-C. Kieffer, B. La Fontaine, F. Martin, C. Potvin, P. Couture, H. P. Mercure, A. Bondiou-Clergerie, P. Lalande, and I. Gallimberti, *IEEE Trans. Plasma Sci.* **31**, 387 (2003).

<sup>7</sup>B. La Fontaine, D. Comtois, C. Y. Chien, A. Desparois, F. Gérin, G. Jarry, T. W. Johnston, J. C. Kieffer, F. Martin, R. Mawassi, H. Pépin, F. A. M. Rizk, F. Vidal, C. Potvin, P. Couture, and H. P. Mercure, *J. Appl. Phys.* **88**, 610 (2000).

<sup>8</sup>M. Rodriguez, R. Sauerbrey, H. Wille, L. Wöste, T. Fujii, Y.-B. André, A. Mysyrowicz, L. Klingbeil, K. Rethmeier, W. Kalkner, J. Kasparian, E. Salmon, J. Yu, J.-P. Wolf, *Opt. Lett.* **27**, 772 (2002).

<sup>9</sup>G. A. Askar'yan, *Sov. Phys. JETP* **15**, 1088 (1962).

<sup>10</sup>R. Y. Chiao, E. Garmire, and C. H. Townes, *Phys. Rev. Lett.* **13**, 479 (1964).

<sup>11</sup>A. Braun, G. Korn, X. Liu, D. Du, J. Squier, and G. Mourou, *Opt. Lett.* **20**, 73 (1995).

<sup>12</sup>B. La Fontaine, F. Vidal, Z. Jiang, C. Y. Chien, D. Comtois, A. Desparois, T. W. Johnston, J.-C. Kieffer, and H. Pépin, *Phys. Plasmas* **6**, 1615 (1999).

<sup>13</sup>M. Rodriguez *et al.*, *Phys. Rev. E* **69**, 036607 (2004).

<sup>14</sup>G. Méchain *et al.*, *Appl. Phys. B: Lasers Opt.* **79**, 379 (2004).

<sup>15</sup>F. Courvoisier *et al.*, *Appl. Phys. Lett.* **83**, 213 (2003).

<sup>16</sup>M. Kolesik, J. V. Moloney, *Opt. Lett.* **29**, 590 (2004).

<sup>17</sup>J. Kasparian *et al.*, *Science* **301**, 61 (2003).

<sup>18</sup>M. Baker and J. Nelson, *C. R. Phys.* **3**, 1293 (2002).

<sup>19</sup>T. Shindo *et al.*, *IEEE Trans. Power Deliv.* **8**, 2016 (1993).

<sup>20</sup>H. Wille *et al.*, *Eur. Phys. J.: Appl. Phys.* **20**, 183 (2002).

# White-light filaments for multiparameter analysis of cloud microphysics

**Riad Bourayou**

*Teramobile, Institut für Optik und Quantenelektronik, Friedrich Schiller Universität Jena, Max Wien Platz 1, D-07743 Jena, Germany*

**Guillaume Méjean and Jérôme Kasparian**

*Teramobile, Laboratoire de Spectrométrie Ionique et Moléculaire, Unité Mixte de Recherche (UMR 5579) Centre National de la Recherche Scientifique, Université Claude Bernard Lyon 1, 43 Boulevard du 11 Novembre 1918, F-69622 Villeurbanne Cedex, France*

**Miguel Rodriguez**

*Teramobile, Institut für Experimentalphysik Freie Universität Berlin, Arnimallee 14, D-14195 Berlin, Germany*

**Estelle Salmon and Jin Yu**

*Teramobile, Laboratoire de Spectrométrie Ionique et Moléculaire, Unité Mixte de Recherche (UMR 5579) Centre National de la Recherche Scientifique, Université Claude Bernard Lyon 1, 43 Boulevard du 11 Novembre 1918, F-69622 Villeurbanne Cedex, France*

**Holger Lehmann, Bringfried Stecklum, Uwe Laux, Jochen Eislöffel, Alexander Scholz, and Artie P. Hatzes**

*Thüringer Landessternwarte Tautenburg, Karl Schwarzschild Observatorium, Sternwarte 5, D-07778 Tautenburg, Germany*

**Roland Sauerbrey**

*Teramobile, Institut für Optik und Quantenelektronik, Friedrich Schiller Universität Jena, Max Wien Platz 1, D-07743 Jena, Germany*

**Ludger Wöste**

*Teramobile, Institut für Experimentalphysik Freie Universität Berlin, Arnimallee 14, D-14195 Berlin, Germany*

**Jean-Pierre Wolf**

*Teramobile, Laboratoire de Spectrométrie Ionique et Moléculaire, Unité Mixte de Recherche (UMR 5579) Centre National de la Recherche Scientifique, Université Claude Bernard Lyon 1, 43 Boulevard du 11 Novembre 1918, F-69622 Villeurbanne Cedex, France*

Received March 19, 2004; revised manuscript received September 15, 2004; accepted September 21, 2004

We present a lidar technique using femtosecond-terawatt laser pulses to perform a multiparameter analysis of cloud microphysics. Particle size and density within the cloud are deduced from the multispectral multiple scattering pattern of an ultrashort laser pulse. Furthermore, the spectral analysis of the atmospheric transmission of the white-light continuum from the same laser source yields temperature and relative humidity.

© 2005 Optical Society of America

OCIS codes: 120.0280, 190.7110, 260.5950, 280.3640, 290.1090.

## 1. INTRODUCTION

Cloud nucleation and maturation processes play a key role in atmospheric modeling, both in the meteorological and climatological time and space scales.<sup>1</sup> In particular, both the droplet growth within the cloud and their number density have a strong influence on the Earth albedo

and precipitation forecast. Their characterization requires continuous measurements of the droplet size distribution within the cloud, with a time resolution on the order of several tens of minutes, compatible with the growth and evaporation rates. Besides delicate airborne or balloon-borne *in situ* sampling, the most promising techniques are multispectral or multiple-field-of-view

(MultiFOV) lidars.<sup>2</sup> These techniques rely on the critical dependence of the Mie scattering efficiency (backscattering and extinction cross sections of the particles) and angular pattern, respectively, with the wavelength and the particle size. Most suited for optically thin clouds where multiple scattering is negligible, multispectral lidars<sup>3,4</sup> use several wavelengths, typically the harmonics of Nd:YAG lasers. Comparing the corresponding lidar returns, one can fit parameters such as the width and the mean size of a predefined size distribution. Hence, this technique requires *a priori* knowledge about the shape of the size distribution as well as the type of the particles themselves. Adding a depolarization channel moreover allows one to distinguish between spherical and nonspherical particles.

Optically thick (i.e., dense) clouds, as relevant for precipitation studies, can be better characterized by MultiFOV<sup>5–8</sup> techniques. Here, the multiple-scattering pattern is recorded for several FOV values by masking parts of the detector to select specific ranges of detection angle. The FOV dependence of the signal can be used to gain information about the size distribution. However, the limited number of FOV values as well as the use of one single wavelength can yield only unambiguous particle sizes if the fitting interval is restricted by use of *a priori* knowledge of the cloud of interest. For the improvement of the sensitivity and reliability of the measurements, new remote particle-sizing techniques are required.

The ultimate goal for a full characterization of the cloud microphysics and micrometeorology, e.g. droplet growth, includes knowledge of the thermodynamic parameters of the atmosphere, and especially the relative humidity and temperature, with a reasonable vertical resolution. Balloon-borne radiosondes have limited horizontal and time-resolution coverage, because of the limited amount of balloons that can be launched, and the lack of control over their trajectory. Differential absorption lidars have long been developed that provide good quality data, even in airborne<sup>9–12</sup> or spaceborne<sup>4,13–15</sup> conditions. They can measure both water vapor mixing ratio and the temperature profile from the Rayleigh profile across an adiabatic atmospheric model.<sup>16</sup> Alternative to these very-narrow linewidth (0.01 Å) developments, some groups tried to circumvent the vertical gradients in the Doppler shift and the broadening of the measured line<sup>17</sup> by using broadband (several nanometers) laser sources.<sup>18,19</sup> The emitted spectrum in these experiments is limited, however, intrinsically by the laser process to some tens of nanometers. Efforts to accurately measure water vapor in the atmosphere have also been directed towards Raman lidar.<sup>20,21</sup>

Ultrashort lasers could contribute to a better characterization of the cloud microphysics. In the nonlinear propagation of terawatt-femtosecond laser pulses, filamentation<sup>22–25</sup> generates a white-light continuum extending from the ultraviolet<sup>26,27</sup> to the infrared.<sup>28</sup> This directional, broadband emission provides a basis for white-light lidar, i.e. multispectral lidar measurements with high spectral resolutions over a bandwidth of several hundreds of nanometers. White-light lidar was recently demonstrated to allow the simultaneous range-resolved

detection of several atmospheric species,<sup>29–33</sup> including the atmospheric water vapor volume mixing ratio (VMR).<sup>30</sup> However, simultaneous temperature measurement could not be achieved together with the water VMR to allow the determination of the relative humidity.

In this paper, we show that the multiple-scattering pattern around the white-light beam impact on the bottom of the cloud can yield a measurement of its droplet size distribution and density. Moreover, high-resolution broadband spectra obtained in the white-light lidar returns by use of the same laser source provide the water vapor VMR and temperature of the atmosphere below the cloud layer, which in turn yield the relative humidity of the atmosphere. Although this demonstration was performed in two successive experiments, these experiments both use the same laser source and could be driven simultaneously, opening the potential for a multiparameter remote characterization of cloud microphysics.

## 2. EXPERIMENTAL SETUP

The experiments reported in this paper were performed with the mobile femtosecond terawatt laser Teramobile.<sup>34</sup> This chirped-pulse amplification Ti:sapphire-based laser chain delivered 300-mJ pulses centered at 795 nm at a repetition rate of 10 Hz. The minimum pulse duration (Fourier limited) was 70 fs. However, for the measurements presented here, the pulses were slightly negatively chirped in the compressor, i.e. the shorter wavelength (blue) component of the laser pulse, which intrinsically has a 15-nm broad spectrum, was emitted ahead of the redder one, to compensate for the atmospheric group velocity dispersion. Adjustment of the chirp permits us to control the range and the onset position of filamentation.<sup>34</sup> The corresponding initial pulse duration was 150 fs for multiple-scattering measurements and 300 fs for spectral measurements. The terawatt output beam was sent collimated with a diameter of 3 cm.

Contrary to early white-light lidar experiments using flashlamps, or more recent demonstrations where a femtosecond continuum was generated in a nonlinear medium at ground level,<sup>35</sup> our experiment was based on white light generated *in situ* by filaments in the atmosphere. Therefore the light source can be characterized only indirectly by observations from the ground. Four key parameters are the white-light spectrum, its angular distribution (wavelength-dependent divergence), the altitude of the source (filament height), and the backscatter function, including the backward-enhanced white-light emission.<sup>36</sup>

The spectrum can be inferred from ground measurements,<sup>27,28</sup> although it has been recently suggested that at least the conversion efficiency into the white-light continuum may be affected by the generation over long distances in the atmosphere.<sup>32</sup> Moreover, we have measured that the white-light divergence in the same experimental conditions is slightly below 1 mrad,<sup>37</sup> much wider than the 1.2-arcsec FOV of the telescope used in the spectral measurements. Therefore the wavelength dependence of the divergence and the backscatter function distort the observed spectrum, preventing us from considering the spectrum of our white-source to be pre-

cisely known. Nevertheless, it is well known that the continuum spectrum is smooth, whereas we measure narrow absorption lines. This permits us to deconvolve the partly unknown spectrum of the light source, as detailed in Section 4. Also, the filament height can be controlled and adjusted up to several kilometers through adjustment of the initial chirp of the laser.<sup>34,37</sup> However, we cross checked the filament altitude by fitting the oxygen absorption spectrum during some measurements.

The receiving system consisted of the 2-m primary mirror telescope<sup>38</sup> of the Thüringer Landessternwarte observatory (341-m altitude), located 30 m away from the laser. For this demonstration experiment, where no range resolution was sought, the telescope was aimed at the impact of the laser beam on the bottom of the cloud layer, which was imaged on a time-integrating CCD camera (SITE, 16 bit dynamic range, time integrated) with 0.006-mrad resolution in the Schmidt configuration (optical aperture of 1.34 m, FOV 0.6° full angle, 30 times the laser beam diameter).

Spectral measurements of the backscattered light have been performed with the same telescope in a Coudé configuration with 1.2-arcsec full aperture and an apparent aperture number of  $f/46$ . The signal was analyzed with an Echelle spectrograph<sup>39</sup> with a dispersion of 0.042–0.073 Å per 15 μm CCD pixel (EEV limited, 16-bit dynamic range, time integrated) in the spectral range of interest (538–927 nm). The instrument-broadening function has been measured to be Gaussian, with a typical resolution of 0.1 Å ( $0.1 \text{ cm}^{-1}$ ). The signal was averaged over several minutes (3000 to 12,000 laser shots at 10 Hz). All measurements were correlated with the results of an auxiliary, classical lidar detection providing real-time measurement of the height and thickness of the clouds.

### 3. PARTICLE SIZE DISTRIBUTION FROM MULTIPLE-SCATTERING PATTERN

Cloud characterization requires the measurement of the droplet size distribution and number density. Recent experiments have shown that clouds or aerosol layers located at an altitude of several kilometers yield valuable signals when backscattered photons<sup>37</sup> are imaged (Fig. 1). Such images bear two types of information. On the one hand, differentiating the beam diameter as a function of altitude below the cloud (see arrow in Fig. 1) yields the beam divergence, which amounts to 0.16 mrad in the fundamental wavelength.<sup>37</sup> On the other hand, the wide-scattering halo on the cloud is a clear signature for strong multiple scattering within it. Once corrected with the parallax induced by the experimental configuration, a cut across this halo provides us with the angular pattern of the multiple scattering, bearing information about the cloud itself. Since the ionization of self-guided filaments generated by high-intensity femtosecond lasers have been shown to trigger condensation in supersaturated atmospheres,<sup>31</sup> we ascertained that no filamentation occurred at the cloud altitude, in order to avoid affecting the droplet formation.

High-resolution images of the pattern around 800 nm provide for the first time a multi-FOV<sup>5–8</sup> lidar at this an-

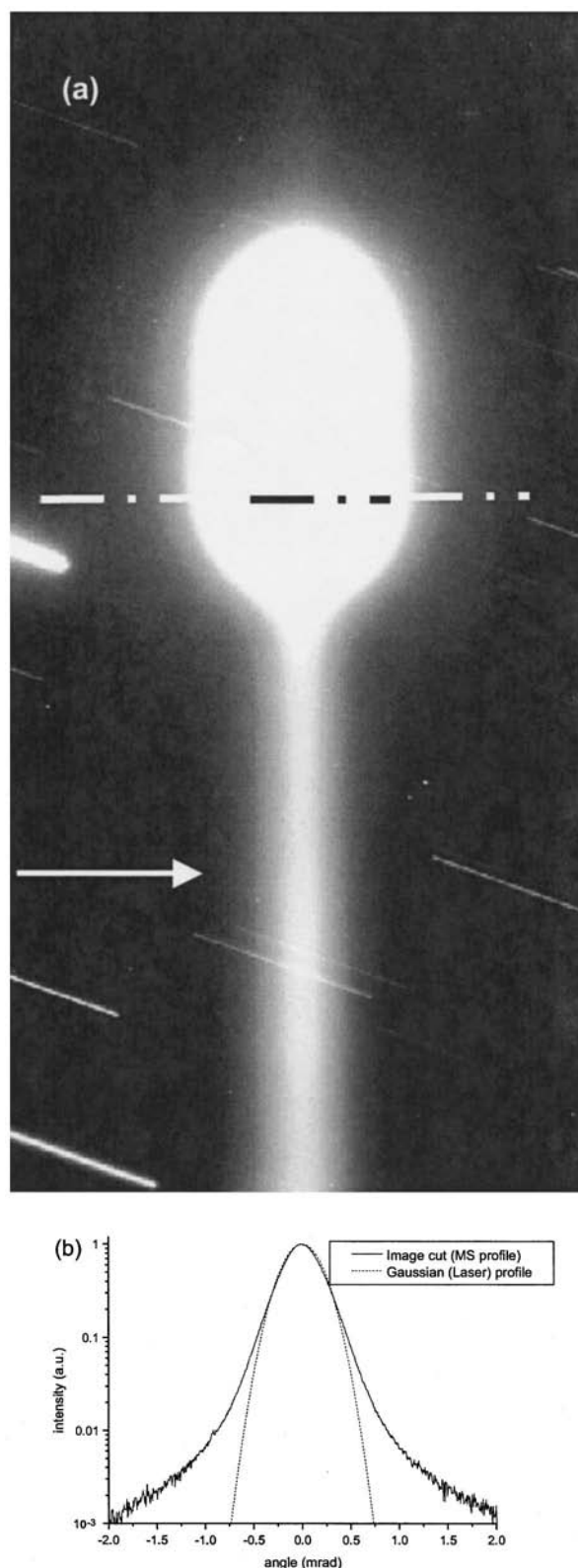


Fig. 1. (a) Beam image observed from the ground in a spectral band near the fundamental wavelength (800 nm). The lower part of the image (see arrow) corresponds to Rayleigh scattering of the beam below the cloud. The halo is due to multiple scattering in the cloud at 6-km altitude. (b) Multiple scattering patterns obtained by geometry-corrected cuts across the halo (see dotted line), and Gaussian profile corresponding to the laser beam. The difference between the two profiles stems from multiple scattering.

gular resolution, which allowed us to fit the droplet size distribution within the cloud using a genetic algorithm.<sup>40</sup> The particle size distribution was modeled by 18 size classes between 0.1 and 20  $\mu\text{m}$ . The weights of each size class were the free parameters. Since we rely on laser beam images on the cloud, we obtained depth-integrated data, which led us to consider that the size distribution is homogeneous within the cloud depth. To avoid possible slight errors induced by multiple scattering on the measurement of the beam divergence,<sup>37</sup> we also left the exact beam divergence as a free parameter. The genetic algorithm used to determine the size distribution works as follows. A set of 100 “individuals,” i.e., tentative solutions (size distribution and laser divergence) was randomly generated, and the corresponding theoretical multiple-scattering patterns were computed, as detailed below. Then the 30 best solutions, i.e., those who fit the experimental pattern better, were selected and combined to form 100 new (“children”) tentative solutions, and the algorithm was iterated until convergence was achieved after 580 iterations.

To compute the theoretical multiple-scattering pattern corresponding to a given size distribution, we first averaged the calculated Mie scattering angular pattern over each size class. The use of Mie scattering is supported by temperatures of  $-25^\circ\text{C}$  to  $-20^\circ\text{C}$  measured at the cloud height (6 km) by radiosondes during the multiple-scattering measurement. This temperature is well above the  $-35^\circ\text{C}$  threshold for a full freezing of the water particles, allowing us to consider the particles as spherical droplets. To model a smooth size distribution, we used a Gaussian shape for each class, and the width was chosen so that the wings of neighboring classes slightly overlapped. Then we generated an effective overall angular Mie scattering pattern by averaging the contribution of each size class, weighted according to the tentative solution under consideration. This angular pattern was then used to simulate the multiple-scattering pattern, treating the  $n$ th-order scattering as  $n$  individual scattering event, with the angular probability given by the effective Mie scattering pattern of the size distribution.<sup>41</sup> Between the scattering events, we considered propagation segments of a length equal to the mean free path of a photon in the cloud  $L_{\text{mfp}} = 1/[2\pi\sum N_i r_i^2 Q_s(r_i)]$ , where  $N_i$  is the particle density of class  $i$ ,  $r_i$  is its droplet radius, and  $Q_s(r_i)$  is the corresponding scattering coefficient calculated from Mie theory for water droplets with refractive index  $n = 1.334$ . The auxiliary lidar provided a cloud altitude of 6 km and a thickness of  $\sim 1$  km, much more than the mean free path of photons within it (10–1000 m for the considered ranges for particle densities and optical thicknesses), so we were able to neglect rays lost by scattering beyond the top of the cloud. Since we deal with relatively dense clouds, Rayleigh scattering from air molecules is neglected. As measured below the cloud, the incident laser beam is considered Gaussian, with a divergence of several tenths of a milliradian.

Tests within the entire parameter range of interest showed that the orders beyond fourth-order scattering had a negligible contribution to the scattering pattern ( $<5\%$ ). Hence, calculations are restricted to the orders 1 (single scattering) through 3 in the following, reducing

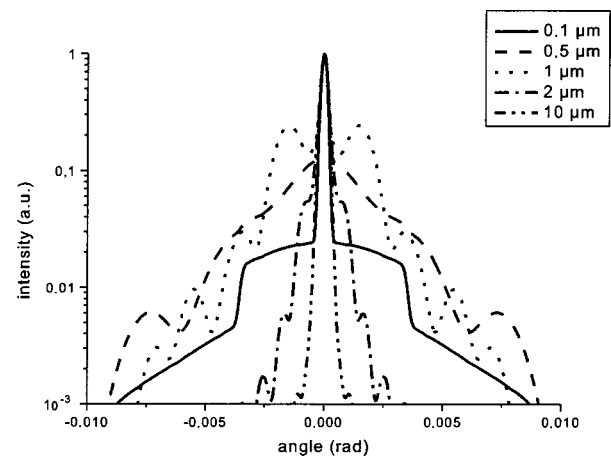


Fig. 2. Simulated angular multiple scattering profiles at 800 nm for monodisperse clouds composed of 0.1-, 0.5-, 1-, 2-, and 10- $\mu\text{m}$  water droplets, with an extinction coefficient of  $\alpha = 3.27 \times 10^{-2} \text{ m}^{-1}$ , corresponding to a cloud penetration depth of  $\sim 30$  m.

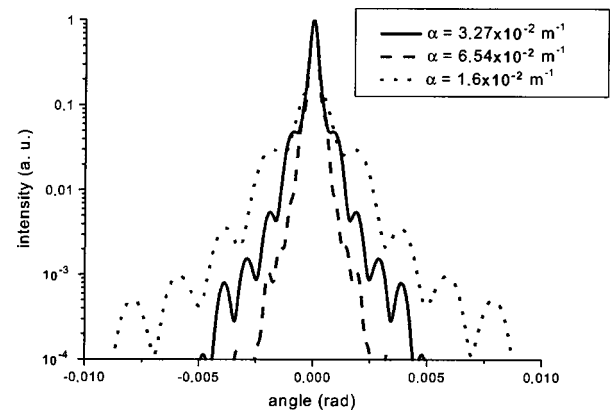


Fig. 3. Simulated angular multiple scattering profiles at 800 nm for monodisperse clouds composed of 2- $\mu\text{m}$  water droplets, as a function of the extinction coefficient  $\alpha$ . The corresponding penetration depths are 30, 15 and 60 m.

the computing time and allowing iterative fitting of the experimental pattern. As shown in Figs. 2 and 3, the simulated radial multiple-scattering profile of individual size classes critically depends on the particle size and density within the cloud, allowing to determine the average particle size within the cloud.

Figure 4 shows the obtained fitted size distribution. Its maximum is peaked around 5  $\mu\text{m}$ , in line with median values reported in the literature for continental stratus clouds.<sup>42,43</sup> The corresponding mean free path  $L_{\text{mfp}} = 700$  m and extinction coefficient  $\alpha = 1.4 \times 10^{-3} \text{ m}^{-1}$  are qualitatively compatible with both the intense signal in the auxiliary lidar detection system and the fact that the auxiliary lidar signal can be received through the 1-km-thick cloud layer.

The droplet size distribution and the cloud density retrieval over more than 15 size classes were made possible by the high-resolution multi-FOV data available from the images of the laser beam on the bottom of the clouds. Moreover, we also recorded similar multi-FOV data in the 400–500 spectral region of the white-light continuum.<sup>37</sup> The simultaneous analysis of the multiple-scattering pat-

terns in two or several spectral regions, with different penetration depths, may provide an opportunity for one to circumvent the intrinsic depth integration of each of our monochromatic data, yielding layered size-distribution data. Independent fits at several wavelengths could also help validate the technique by providing data about the same size distribution.

#### 4. RELATIVE HUMIDITY RETRIEVAL

Besides the droplet size distribution, characterization of the cloud microphysics requires knowledge of the thermodynamical parameters of the atmosphere around it, including relative humidity and temperature. We achieved this measurement with the same laser source as the multiple-scattering study for droplet sizing described in Section 3, thus prouiding the potential for a simultaneous measurement.

More precisely, we analyzed the range-integrated spectrum of the white-light continuum backscattered from clouds located 4.5 km above the ground level, as measured by the auxiliary lidar. The cloud is treated as a hard target, neglecting the penetration depth of less than  $100\text{ m} \ll 4.5\text{ km}$  measured by the auxiliary lidar. The spectrum of the backscattered white light was recorded between 680 and 920 nm,<sup>31</sup> thus encompassing in the same measurement the rotational-vibrational band of H<sub>2</sub>O centered at 820 nm, as well as the O<sub>2</sub> A band around 762 nm.

Since the available spectral range covers lines of different intensities, the bands used in the fit have been chosen to optimize the signal while avoiding saturation, in relation to the actual concentration of the species to be measured. Two fitting procedures, both benefitting from the wide available spectral interval, have been applied independently to two spectra acquired under different laser parameters, to crosscheck the results. The fits are based on HITRAN 2000<sup>44</sup> high-resolution database. The instrumental resolution is ten times broader than that required for differential absorption lidar measurements of pressure or temperature profiles by use of water vapor lines or the O<sub>2</sub> A band.<sup>17,45</sup> However, since the fit is performed over a broad spectral range, we were able to convolve each synthetic spectrum with the known instrumental-broadening function in the fitting procedure. The accuracy of this technique was also checked numerically over simulated spectra. The broad spectral range, together with the narrowness of the absorption lines that we considered, permitted us to circumvent the poor characterization of the white-light continuum source and of the backscatter spectral efficiency on the cloud. Since these functions are known to be smooth, we fitted them as a smooth baseline on the recorded spectrum, as is common e.g., in astronomy. Then this baseline is used to normalize the absorption spectrum over the entire spectral range.

The first procedure was applied to a spectrum acquired at 22:00 UT. The temperature was retrieved from the O<sub>2</sub> A band spectrum and subsequently used to fit the water vapor VMR of the atmosphere from water absorption band of the same spectrum. More precisely, the stable meteorological conditions allowed us to consider a stan-

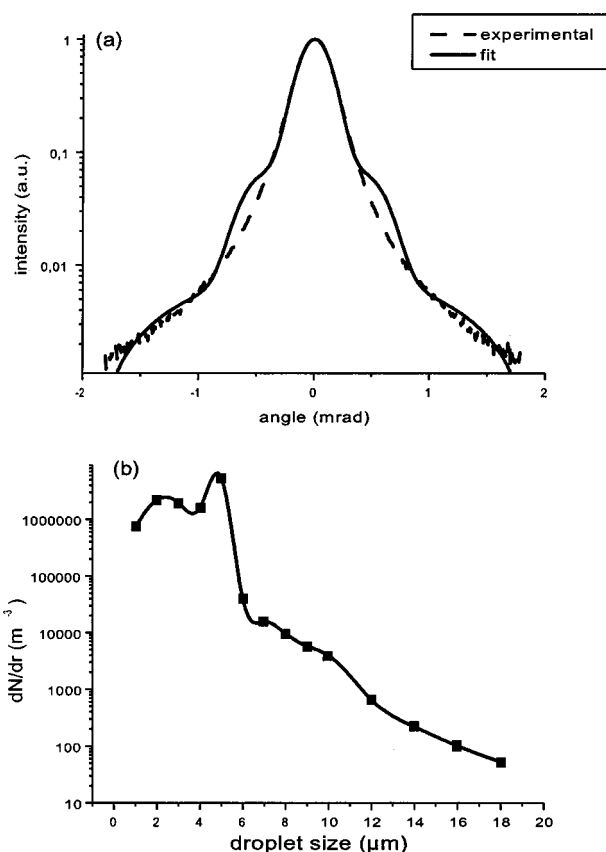


Fig. 4. (a) Experimental and fitted angular distribution of multiple scattering, corresponding to the data of Fig. 1. (b) Corresponding droplet size distribution in the cloud retrieved with the genetic algorithm.

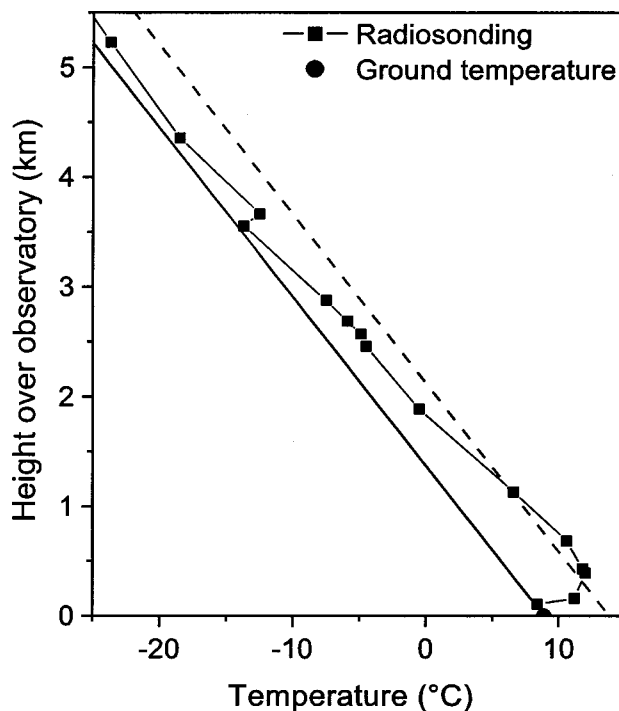


Fig. 5. Temperature determined by a fit of the O<sub>2</sub>A band on the white-light absorption spectrum, and the nearest radiosonde data available (Meiningen, 23:00 UT).

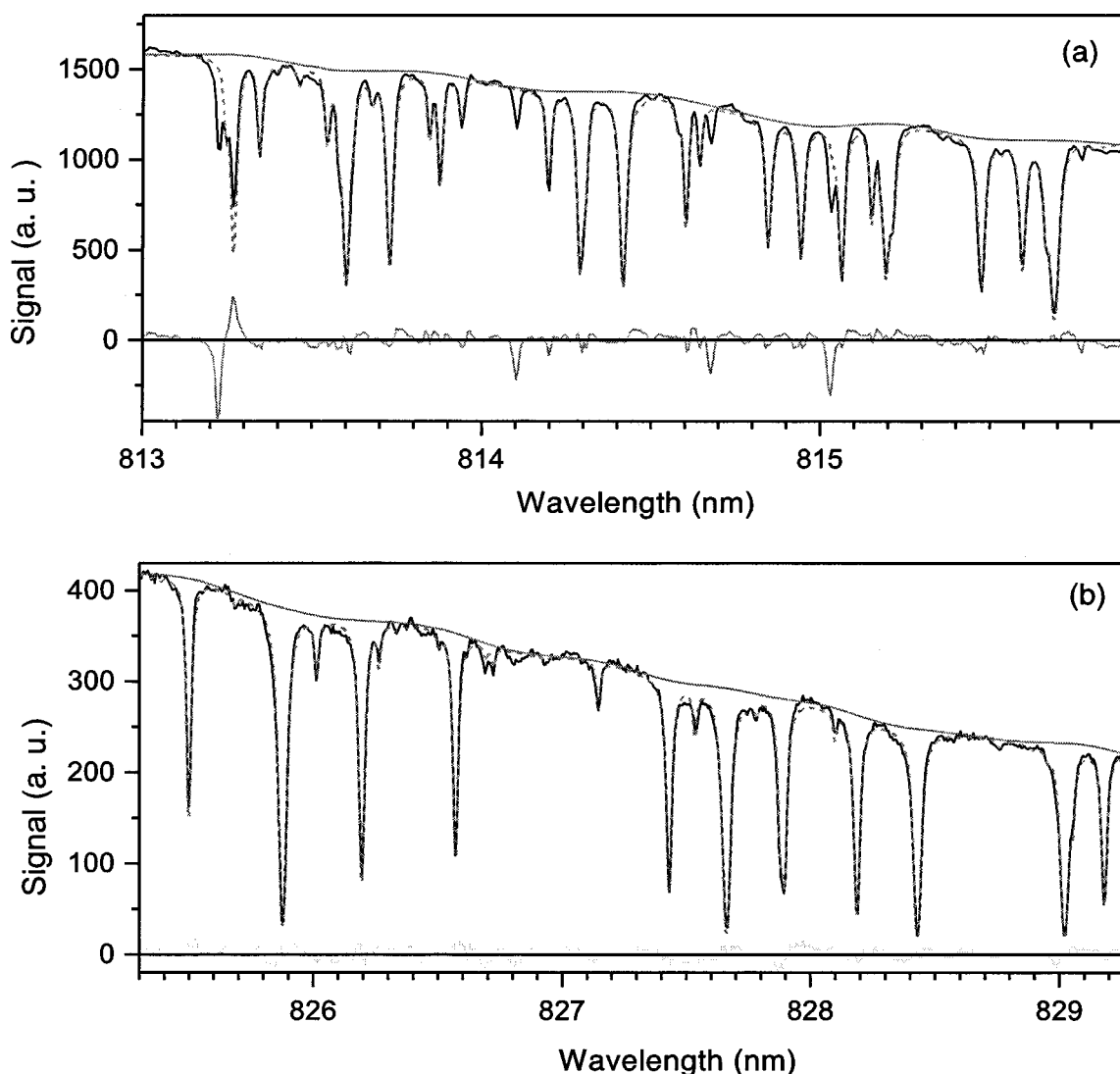


Fig. 6. Fit of the water absorption spectrum in the  $4\nu$ -overtone band in the (a) 813–816 nm and (b) 825–829 nm regions. Black solid curve, measurement; gray dotted curve, fit; lower gray solid curve, residuum of the fit. The lower black line is the estimation of the baseline. Note that the extremely long absorption path allows us to measure weak lines not tabulated in the HITRAN 2000 database.

standard vertical pressure profile and a typical temperature decrease by 6.5 K/km (treated with a vertical resolution of 100 m), and the known VMR of oxygen in the atmosphere (20.9%) was considered. The fitting parameters were the ground temperature ( $T_g$ ) and the emission altitude of the white light ( $z_{WL}$ ). The filament length is neglected, since we have found that it is much shorter than the absorption length under our experimental conditions.<sup>37</sup> Fits in the 761–764 nm and the 766–769 nm ranges both yield  $T_g = 287 \pm 1$  K and  $z_{WL} = 550 \pm 100$  m. Note that the filament altitude obtained for a medium group velocity dispersion precompensation (300 fs initial pulse duration) is in line with data obtained independently with a geometrical method.<sup>37</sup> The ground temperature is slightly higher than measured at ground level during the experiment (282 K). However, the nearest radiosonde temperature profile available (23:00 UT, Meiningen, at 100-km distance, Fig. 5) shows that this discrepancy is due to a sharp temperature gradient near to the ground, below the white-light emission altitude. Therefore the retrieved temperature is reasonable.

This profile and white-light emission altitude were used as references to determine the relative humidity, which was supposed to be constant over the considered altitude range. More precisely, the above-determined temperature and pressure profiles were used to get the relative humidity values from the corresponding water vapor VMR, with the same 100-m resolution. The fit was performed in the water vapor  $4\nu$ -overtone band in both the 813–816 nm and the 825–829 nm regions (Fig. 6). This fit yields a relative humidity of  $(49 \pm 3)\%$ , in good agreement with the vertical average of the radiosonde data (Fig. 7). Hence, white-light lidar data have, for the first time, allowed multicomponent measurements yielding both temperature profile and relative humidity data, which are key parameters in the understanding of the physics of cloud formation and precipitation.

This result was cross checked by a second independent fitting procedure in which both the mean temperature and the water mixing ratio (VMR) of the atmosphere were obtained simultaneously from the same fit of the experimental spectrum over the 815–840 nm spectral region

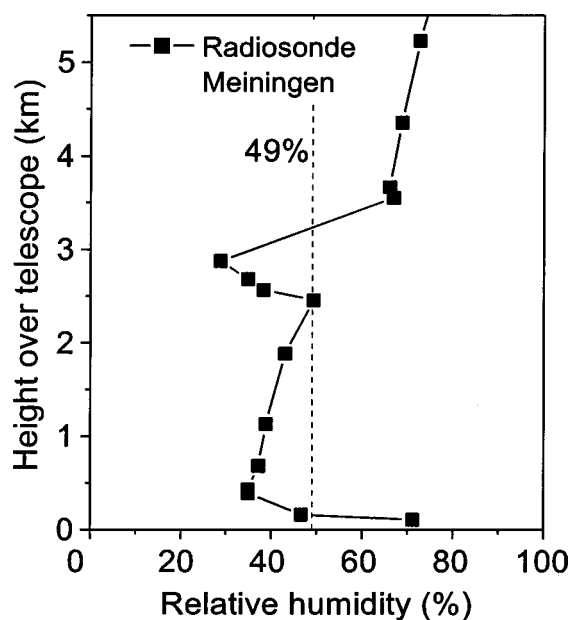


Fig. 7. Retrieved average relative humidity (dotted line) and RH profile measured by radiosonde (solid line). Note that a cloud layer around 3 km at the radiosonde site perturbs the corresponding measurement.

(4 $\nu$ -overtone band). Here, the filaments are considered to span over a short altitude range near the laser output.<sup>34</sup> Hence, the absorption length of the white light is fixed to 9 km. The fit yields a vertically averaged humidity and temperature of  $0.38 \pm 0.01\%$  and  $279.2 \pm 0.4$  K, respectively. The resulting relative humidity at ground level is therefore estimated to be  $42 \pm 3\%$ , comparable with the result of the first fit.

Spectral measurements thus simultaneously yielded the temperature and the relative humidity of the air mass under the clouds, within an error compatible with the requirements of meteorological or climatological modeling purposes. Two variants have been demonstrated in which multiple parameters are retrieved either from distinct spectral regions or from one single, broad wavelength interval. Since the presented results are range-integrated measurements, the analysis required assumptions about the vertical profile of both water vapor and temperature in the atmosphere. Although these assumptions are validated by radiosonde data in the case of our experiments, in principle deviations from the standard models used will cause errors in the data analysis. However, this range integration and the use of a cloud as a target are not intrinsic to the white-light lidar technique, since the CCD detectors can be time gated. Although Rayleigh backscattering in free atmosphere is 100 to 1000 times less efficient than Mie backscattering from a typical cloud, a better fitting of the telescope field of view with the laser divergence, i.e., 1 mrad instead of 6  $\mu$ rad, would improve the signal by a factor of  $3 \times 10^4$ . Hence, the signal would still be ten times more intense, allowing us to reduce the integration time by a factor of 10. Then differentiating the backscattered white light with respect to altitude would yield altitude-resolved relative humidity profiles, therefore allowing for humidity mapping across the atmosphere.

## 5. CONCLUSION

In conclusion, we have shown that a lidar technique using the supercontinuum generated by the filamentation of femtosecond pulses during their vertical propagation in the atmosphere can be used to analyze both the clouds (droplet size distribution and number density) and the thermodynamical properties of the atmosphere in their vicinity, such as the temperature and relative humidity. Since both of these measurements use the same laser source equipped with suitable diagnostics for imaging and spectral analysis, they are suitable for a simultaneous operation. Although preliminary, they open the way to a multiparameter analysis of the cloud microphysics by combined white-light differential absorption and multi-FOV lidar. Routinely obtaining such data about the cloud microphysics would be of high relevance for atmospheric modeling, especially considering the two-dimensional and three-dimensional mapping capability of lidar.

However, the present experiment does not fully use the potential of the described technique. The use of several wavelengths in multi-FOV aerosol analysis would yield more-precise size distributions of the aerosols in the clouds and may even allow us to determine layered size-distribution data. Also, range-resolved spectral measurements using time-gated multichannel detectors would yield relative humidity profiles and release the need for assumptions about the atmospheric temperature and water VMR profiles in the data analysis. Moreover, the practical use of the technique described in this paper, e.g., for routine measurements, requires eye safety, which drastically limits the laser power at 800 nm. However, the white-light lidar measurements are performed at a wavelength that is independent of the laser source. Therefore the currently developing high-power, ultrashort lasers in both the UV and in the telecom window raise the hope of application of the white-light lidar techniques to laser sources in wavelength bands where eye safety can be achieved at much higher powers, compatible with that required for nonlinear effects.

## ACKNOWLEDGMENTS

The Teramobile project acknowledges support of the Center National de la Recherche Scientifique (France) and the Deutsche Forschungsgemeinschaft (Germany). The Teramobile members would like to thank the technical staff of the Thüringer Landessternwarte Tautenburg (TLS), Bernd Fuhmann, Jürgen Haupt, Axel Kirchhof, Michael Pluto, Jörg Schiller, and Johannes Winkler, for their assistance in installing the laser at TLS and helping to solve technical problems. We also thank Eike Guenther, Sylvio Klose, and Helmut Meusinger for helpful discussions on conducting the observations with the 2-m telescope. The Teramobile web site is [www.teramobile.org](http://www.teramobile.org).

## REFERENCES

1. H. R. Pruppacher and J. D. Klett, *Microphysics of Clouds and Precipitation* (Reidel, Dordrecht, The Netherlands, 1978).
2. R. M. Measures, *Laser Remote Sensing—Fundamental and Applications* (Wiley Interscience, New York, 1984).

3. B. Stein, M. Del Guasta, J. Kolenda, M. Morandi, P. Rairoux, L. Stefanutti, J. Wolf, and L. Wöste, "Stratospheric aerosol size distribution from multispectral lidar measurements at Sodankylä during EASOE," *Geophys. Res. Lett.* **21**, 1311–1314 (1994).
4. D. M. Winker and M. P. McCormick, "Aerosol and cloud sensing with the Lidar In-space Technology Experiment (LITE)," in *Lidar Techniques for Remote Sensing*, C. Weiner, ed., Proc. SPIE **2310**, 98–105 (1994).
5. S. R. Pal and A. I. Carswell, "Multiple scattering in atmospheric clouds: lidar observations," *Appl. Opt.* **15**, 1990–1995 (1976).
6. J. S. Ryan, S. R. Pal, and A. I. Carswell, "Laser backscattering from dense water-droplet clouds," *J. Opt. Soc. Am.* **69**, 60–67 (1979).
7. L. R. Bissonnette and D. L. Hutt, "Multiply scattered aerosol lidar returns: inversion method and comparison with in-situ measurements," *Appl. Opt.* **34**, 6959–6975 (1995).
8. L. R. Bissonnette, "Multiple-scattering lidar equation," *Appl. Opt.* **35**, 6449–6465 (1996).
9. R. A. Ferrare, E. V. Brownell, S. Ismail, V. G. Brackett, M. B. Clayton, M. Fenn, L. Heilman, S. A. Kooi, D. D. Turner, M. J. Mahoney, R. E. Newell, Y. Zhu, E. Jensen, J. Barrick, and G. Sachse, "Lidar measurements of relative humidity and ice supersaturation in the upper troposphere," presented at the International Laser Radar Conference, Vichy, France, July 10–14, 2000.
10. S. Ismail and E. V. Brownell, "Airborne and spaceborne lidar measurements of water vapor profiles: a sensitivity analysis," *Appl. Opt.* **28**, 3603–3615 (1989).
11. G. Ehret, C. Liemle, W. Renger, and G. Simmet, "Airborne remote sensing of tropospheric water vapor with a near-infrared differential absorption lidar system," *Appl. Opt.* **32**, 4534–4551 (1993).
12. C. Flamant, J. Pelon, L. Eymard, and J. Tournadre, "SSM/I integrated water vapor content measurements in coastal regions: a comparison with shipborne and airborne remote sensing measurements, radiosonde measurements, and NWP model retrievals," *J. Geophys. Res.* **108**(C3), FET4-1-20 (2003).
13. L. Garand, E. Gerard, D. Tan, V. Wulfmeyer, G. Ehret, and P. Di Girolamo, "WALEs (Water Vapour Lidar Experiment in Space): impact of space borne measurements on NWP and climate research," in *Proceedings of Twenty-First International Laser Radar Conference*, Vol. 2, pp. 755–758.
14. A. Heliere, J. L. Bezy, P. Bensi, and P. Ingmann, "System definition of the ESA Earth Explorer WALEs mission," in *Sensors, Systems, and Next-Generation Satellites VI*, H. Fujisada, J. B. Lurie, M. L. Aten, and K. Weber, eds., Proc. SPIE **4881**, 24–32 (2003).
15. A. J. Wimmers, J. L. Moody, E. V. Browell, J. W. Hair, W. B. Grant, C. F. Butler, M. A. Fenn, C. C. Schmidt, J. Li, and B. A. Ridley, "Signatures of tropopause folding in satellite imagery," *J. Geophys. Res.* **108**(D4), 8360 (2003).
16. D. D. Turner, R. A. Ferrare, L. A. Heilman, and T. P. Tooman, "A two year climatology of water vapor and aerosols in the lower troposphere measured by a Raman lidar," presented at the International Laser Radar Conference, Vichy, France, July 10–14, 2000.
17. J. Bösenberg, "Measurements of the pressure shift of water vapor absorption lines by simultaneous photoacoustic spectroscopy," *Appl. Opt.* **24**, 3531–3534 (1985).
18. M. Douard, R. Bacis, P. Rambaldi, A. Ross, J.-P. Wolf, G. Fabre, and R. Stringat, "Fourier-transform lidar," *Opt. Lett.* **20**, 2140–2142 (1995).
19. F. A. Theopold, C. Weitkamp, and W. Michaelis, "Double-cavity étalon in the near infrared," *Opt. Lett.* **18**, 253–255 (1993).
20. C. R. Philbrick, "Application of Raman lidar advancements in meteorology and air quality monitoring," in *Lidar Remote Sensing for Industry and Environment Monitoring III*, U. N. Singh, T. Itabe, and Z. Liu, eds., Proc. SPIE **4893**, 61–69 (2003).
21. G. Pappalardo, A. Amodeo, S. Amoroso, V. Cuomo, P. Di Girolamo, F. Esposito, L. Leone, L. Mona, M. Pandolfi, G. Pavese, R. Restieri, and C. Serio, "Measurement campaign of atmospheric water vapor and aerosols in southern Italy," in *Optical Remote Sensing of the Atmosphere and Clouds III*, H.-L. Huang, D. Lu, and Y. Sasane, eds., Proc. SPIE **4891**, 353–360 (2003).
22. A. Braun, G. Korn, X. Liu, D. Du, J. Squier, and G. Mourou, "Self-channeling of high-peak-power femtosecond laser pulses in air," *Opt. Lett.* **20**, 73–75 (1995).
23. E. T. J. Nibbering, P. F. Curley, G. Grillon, B. S. Prade, M. A. Franco, F. Salin, and A. Mysyrowicz, "Conical emission from self-guided femtosecond pulses in air," *Opt. Lett.* **21**, 62–64 (1996).
24. A. Brodeur, C. Y. Chien, F. A. Ilkov, S. L. Chin, O. G. Kosareva, and V. P. Kandidov, "Moving focus in the propagation of ultrashort laser pulses in air," *Opt. Lett.* **22**, 304–306 (1997).
25. M. Mlejnek, E. M. Wright, and J. V. Moloney, "Dynamic spatial replenishment of femtosecond pulses propagating in air," *Opt. Lett.* **23**, 382–384 (1998).
26. N. Aközbeke, A. Iwasaki, A. Becker, M. Scalora, S. L. Chin, and C. M. Bowden, "Third-harmonic generation and self-channeling in air using high-power femtosecond laser pulses," *Phys. Rev. Lett.* **89**, 143901 (2002).
27. G. Méjean, J. Kasparian, J. Yu, S. Frey, E. Salmon, J. P. Wolf, L. Bergé, and S. Skupin, "UV-supercontinuum generated by kilometer-range filamentation in air," *Phys. Rev. Lett.*, submitted for publication.
28. J. Kasparian, R. Sauerbrey, D. Mondelain, S. Niedermeier, J. Yu, J.-P. Wolf, Y.-B. André, M. Franco, B. Prade, S. Tzortzakakis, A. Mysyrowicz, M. Rodriguez, H. Wille, and L. Wöste, "Infrared extension of the supercontinuum generated by fs-TW-laser pulses propagating in the atmosphere," *Opt. Lett.* **25**, 1397–1399 (2000).
29. L. Wöste, C. Wedekind, H. Wille, P. Rairoux, B. Stein, S. Nikolov, Ch. Werner, S. Niedermeier, H. Schillinger, and R. Sauerbrey, "Femtosecond atmospheric lamp," *Laser Optoelektron.* **29**, 51–53 (1997).
30. P. Rairoux, H. Schillinger, S. Niedermeier, M. Rodriguez, F. Ronneberger, R. Sauerbrey, B. Stein, D. Waite, C. Wedekind, H. Wille, and L. Wöste, "Remote sensing of the atmosphere using ultrashort laser pulses," *Appl. Phys. B* **71**, 573–580 (2000).
31. J. Kasparian, M. Rodriguez, G. Méjean, J. Yu, E. Salmon, H. Wille, R. Bourayou, S. Frey, Y.-B. André, A. Mysyrowicz, R. Sauerbrey, J.-P. Wolf, and L. Wöste, "White-light filaments for atmospheric analysis," *Science* **301**, 61–64 (2003).
32. G. Méjean, J. Kasparian, E. Salmon, J. Yu, J.-P. Wolf, R. Bourayou, R. Sauerbrey, M. Rodriguez, L. Wöste, H. Lehmann, B. Stecklum, U. Laux, J. Eislöffel, A. Scholz, and A. P. Hatzes, "Towards a supercontinuum-based infrared lidar," *Appl. Phys. B* **77**, 357–359 (2003).
33. G. G. Matvienko, V. V. Veretennikov, G. M. Krekov, and M. M. Krekova, "Remote sensing of atmospheric aerosols with a white-light femtosecond lidar," *Atmos. Oceanic Opt.* **16**, 1013–1019 (2003).
34. H. Wille, M. Rodriguez, J. Kasparian, D. Mondelain, J. Yu, A. Mysyrowicz, R. Sauerbrey, J.-P. Wolf, and L. Wöste, "Teramobile: a mobile femtosecond-terawatt laser and detection system," *Eur. Phys. J.: Appl. Phys.* **20**, 183–190 (2002).
35. M. C. Galvez, M. Fujita, N. Inoue, R. Moriki, Y. Izawa, and C. Yamanaka, "Three-wavelength backscatter measurement of clouds and aerosols using a white light lidar system," *Jpn. J. Appl. Phys. Part 2* **41**, L284–L286 (2002).
36. J. Yu, D. Mondelain, G. Ange, R. Volk, S. Niedermeier, J.-P. Wolf, J. Kasparian, and R. Sauerbrey, "Backward supercontinuum emission from a filament generated by ultrashort laser pulses in air," *Opt. Lett.* **26**, 533–535 (2001).
37. M. Rodriguez, R. Bourayou, G. Méjean, J. Kasparian, J. Yu, E. Salmon, A. Scholz, B. Stecklum, J. Eislöffel, U. Laux, A. P. Hatzes, R. Sauerbrey, L. Wöste, and J.-P. Wolf, "Kilometer-range non-linear propagation of fs laser pulses," *Phys. Rev. E* (to be published).
38. H. Lehmann, "The 2m telescope," <http://www.tls-tautenburg.de/telesc.html>.
39. H. Lehmann, "Coudé Echelle Spectrograph," [http://www.tls-tautenburg.de/coude/echelle\\_spectrograph.html](http://www.tls-tautenburg.de/coude/echelle_spectrograph.html).

40. T. Back and H. Schwefel, "An overview of evolutionary algorithms for parameter optimization," *Evol. Comput.* **1**, 1–23 (1993).
41. O. B. Toon and T. P. Ackerman, "Algorithms for the calculation of scattering by stratified spheres," *Appl. Opt.* **20**, 3657–3660 (1981).
42. A. V. Korolev, G. A. Isaac, I. P. Mazin, and H. W. Barker, "Microphysical properties of continental clouds from *in situ* measurements," *Q. J. R. Meteorol. Soc.* **127**, 2117–2151 (2001).
43. N. L. Miles, J. Verlinde, and E. E. Clothiaux, "Cloud droplet size distributions in low-level stratiform clouds," *J. Atmos. Sci.* **57**, 295 (2000).
44. L. S. Rothman, A. Barbe, D. C. Benner, L. R. Brown, C. Camy-Peyret, M. R. Carleer, K. Chance, C. Clerbaux, V. Dana, V. M. Devi, A. Fayt, J.-M. Flaud, R. R. Gamache, A. Goldman, D. Jacquemart, K. W. Jucks, W. J. Lafferty, J.-Y. Mandin, S. T. Massie, V. Nemtchinov, D. A. Newnham, A. Perrin, C. P. Rinsland, J. Schroeder, K. M. Smith, M. A. H. Smith, K. Tang, R. A. Toth, J. Vander Auwera, P. Varanasi, and K. Yoshino, "The HITRAN Molecular Spectroscopic Database: Edition of 2000 Including Updates of 2001," *J. Quant. Spectrosc. Radiat. Transf.* **82**, 5–44 (2003).
45. G. Mégie, "Mesure de la pression et de la température atmosphériques par absorption différentielle lidar: influence de la largeur d'émission laser," *Appl. Opt.* **19**, 34–43 (1980).

# Supercontinuum emission and enhanced self-guiding of infrared femtosecond filaments sustained by third-harmonic generation in air

L. Bergé,<sup>1,\*</sup> S. Skupin,<sup>1,2</sup> G. Méjean,<sup>3</sup> J. Kasparian,<sup>3</sup> J. Yu,<sup>3</sup> S. Frey,<sup>3</sup> E. Salmon,<sup>3</sup> and J. P. Wolf<sup>3</sup>

<sup>1</sup>*Département de Physique Théorique et Appliquée, CEA/DAM Ile de France, Boîte Postale 12, 91680 Bruyères-le-Châtel, France*

<sup>2</sup>*Institute for Condensed Matter Theory and Solid State Optics, Friedrich-Schiller-Universität Jena, Max-Wien-Platz 1, 07743 Jena, Germany*

<sup>3</sup>*Laboratoire de Spectrométrie Ionique et Moléculaire, Université Claude Bernard Lyon 1, UMR-CNRS 5579, F-69622 Villeurbanne cedex, Lyon, France*

(Received 15 July 2004; published 5 January 2005)

The long-range propagation of two-colored femtosecond filaments produced by an infrared (IR) ultrashort pulse exciting third harmonics (TH) in the atmosphere is investigated, both theoretically and experimentally. First, it is shown that the coupling between the pump and TH components is responsible for a wide spectral broadening, extending from ultraviolet (UV) wavelengths (220 nm) to the mid-IR (4.5  $\mu\text{m}$ ). Supercontinuum generation takes place continuously as the laser beam propagates, while TH emission occurs with a conversion efficiency as high as 0.5%. Second, the TH pulse is proven to stabilize the IR filament like a saturable quintic nonlinearity through four-wave mixing and cross-phase modulation. Third, the filamentation is accompanied by a conical emission of the beam, which becomes enlarged at UV wavelengths. These properties are revealed by numerical simulations and direct experimental observations performed from the Teramobile laser facility.

DOI: 10.1103/PhysRevE.71.016602

PACS number(s): 42.65.Tg, 52.38.Hb, 42.65.Jx, 42.68.Ay

## I. INTRODUCTION

Femtosecond laser pulses are well known to propagate over several Rayleigh lengths as robust filamentary channels in the atmosphere [1–3]. The basic principle of this self-guiding relies on a delicate balance between the nonlinear Kerr response of air, which focuses the beam and produces optical intensities as high as  $10^{14}$  W/cm<sup>2</sup>, and the defocusing action of ionization of air molecules, which arrests the beam collapse and excites a tenuous plasma with electron densities limited to  $10^{16}$ – $10^{17}$  cm<sup>-3</sup>. Apart from this principle, additional mechanisms, such as higher-order terms in the nonlinear index of refraction, have been proposed as stabilizers for femtosecond filaments, not only in the atmosphere [4,5], but also in various transparent media [6]. Plasma defocusing creates ring structures in the pulse spatial profile and damps the latest time slices in the temporal profiles. Because of this complexity, several scenarios have been elaborated to explain the nature of the filamentation process, such as the self-channeling model [1,2,7], the moving focus picture [8], and the spatial replenishment [9]. Recently [10], it was proposed that the complex dynamics of filamentation could mainly be inferred from the latter scenario, the former ones clearing up intermediate stages in the filament formation according to the input beam power.

This filament process has been put in evidence both for near IR [1–3] and UV wavelengths [11–13]. In the IR domain (800 nm), femtosecond pulses were shown to undergo a strong spectral broadening caused by the following: In the early propagation, the pulse is subject to self-phase modulation (SPM) in regimes for which Kerr compression (self-focusing) dominates, starting with beam powers ( $P_{\text{in}}$ ) well

above the critical power for self-focusing ( $P_{\text{cr}}$ ). SPM symmetrically increases the pulse spectrum to some extent, until plasma generation comes into play. Self-induced ionization then depletes the back of the pulse and keeps untouched its leading edge, which creates a redshift in the pulse spectrum [14,15]. This redshift has also been observed in dielectrics such as fused silica or sapphire samples [16,17]. It was explained by the same cause, namely, the occurrence of a steep leading edge in the pulse temporal profile (see, e.g., Agrawal [18]). According to the number of critical powers in the initial beam, femtosecond pulses can undergo distinct sequences of focusing/defocusing events, triggered by the refocusing time slices (back or front) raising in the pulse. Such sequences favor multi-peaked temporal profiles which participate in enlarging more and more the spectra. In addition to these distortions, there exists a significant broadening of the angular spectrum dictated by the spatial variations of the pulse phase. These variations are responsible for conical emission (CE) [2,19] through which the beam diverges as a concentric rainbow with colors ranging from red to green.

These two effects, i.e., spectral broadening and CE, constitute the key tools currently used for atmospheric remote sensing by ultrashort laser pulses [20–26]. Temporal variations in the pulse profile indeed induce a very broad spectral continuum, spanning from the UV (350 nm) to the mid-IR ( $\sim 4.5$   $\mu\text{m}$ ) [20], so that the broadened laser beam is often termed as “white-light laser” [21,22]. Long-distance nonlinear propagation of terawatt (TW) laser pulses was found to significantly enhance such a supercontinuum generation. Filamentation could be observed up to 2 km altitudes via a detailed analysis of the conical emission. Compared with laboratory experiments limited to meter scales, the spectrum intensity was found to be enhanced up to two orders of magnitude in the IR domain [26]. This enabled the improvement of Lidar (light detection and ranging) performances through

\*Electronic address: luc.berge@cea.fr

white-light emission, as many important pollutants cover large absorption bands [27].

So far, investigations on the self-channeling of femtosecond pulses have mostly concerned the central component of infrared beams (800 nm). Only recently [29,30] has the question of the coupling between this IR component and self-induced third-harmonic generation (THG) been raised. While THG is nowadays a well-known mechanism [18,31], less attention has been paid to its implications in the propagation of ultrashort laser pulses in the atmosphere. Among the references available in the literature, we can mention the works [32–35], where there has been considerable interest in high harmonic generation using intense femtosecond laser pulses focused into gases. In [32], a conversion efficiency as high as 0.1% was reported for THG in air. Higher conversion efficiency, up to 0.2%, was measured in [29,30] and the coupling of TH with the pump IR beam was shown to produce a “two-colored” femtosecond filament.

The former pioneering references, however, were limited to propagation distances never exceeding a few tens of cm and using tightly focused beams. It is thus worthwhile studying THG in the framework of long-distance propagation, involving the development of femtosecond filaments over several meters and beyond. In this respect, several points deserve to be addressed, such as determining the spectral broadening promoted by THG, understanding the influence of the third harmonics onto the self-channeling characteristics, and the incidence of THG on the conical emission.

In the present work, we numerically and experimentally investigate third-harmonic generation in air and its incidence on the filamentation of femtosecond pulses over several meters. We report a new phenomenon: The supercontinuum generation at UV-visible wavelengths produced by infrared ultrashort laser pulses in air. Implications of this UV continuous emission are very important for white-light Lidar experiments [27], as numerous atmospheric pollutants (NO<sub>x</sub>, SO<sub>2</sub>, O<sub>3</sub>, benzene, toluene, xylene, PAHs, formaldehyde, Hg, etc.) have strong specific UV absorption bands. Aerosol fluorescence is also excited in this region (e.g., for bioaerosol detection using amino acids as tracers [28]).

The paper is organized as follows. The model equations are first derived (Sec. II). Emphasis is then given on the superbroadband continuum in the UV-visible domain of wavelengths admitting a cutoff as low as 230 nm and an IR tail as far as 4.5 μm. By means of numerical simulations, long-distance propagation is shown to lead to a smooth continuous UV-IR broadening. This phenomenon is explained in terms of SPM of the pump wave being amplified by the TH pulse, which is locked at the constant π phase shift with the fundamental (Sec. III). Effects of THG on conical emission are also discussed (Sec. IV). Both this spectacular broadening and conical emission are experimentally reported from direct measurements and analysis of the white-light laser formed by cm-waisted pulses delivered by the Teramobile system [23] (Sec. V). An important consequence of THG is moreover the stabilization of the two-colored femtosecond filament, whose length is shown to be increased by almost one meter (Sec. VI). Long-distance propagation allows the beam to preserve part of its energy by converting the pump wave into TH with an efficiency as high as 0.5%. With a

large wave-vector mismatch ( $\sim 5 \text{ cm}^{-1}$ ), harmonic generation acts on the pump field as a quintic saturation nonlinearity. Implications of these new results on the current modeling of fs pulses in air are finally discussed (Sec. VII).

## II. MODEL EQUATIONS FOR ATMOSPHERIC THG BY FEMTOSECOND IR PULSES

The derivation of equations describing third-harmonic generation (THG) from an infrared pump follows the classical steps when deducing nonlinear Schrödinger (NLS) wave equations for different optical components [18]. With the ansatz

$$E \rightarrow \mathcal{E}_\omega e^{i[k(\omega)z - \omega t]} + \tilde{\mathcal{E}}_{3\omega} e^{i[k(3\omega)z - 3\omega t]} \quad (1)$$

for the complex field, we get two equations for the slowly varying envelopes  $\mathcal{E}_\omega$  and  $\tilde{\mathcal{E}}_{3\omega}$ . These equations are coupled via cross-phase modulation (XPM) and four-wave mixing (FWM) due to the cubic nonlinearity. Further on, we substitute  $\tilde{\mathcal{E}}_{3\omega} \rightarrow \mathcal{E}_{3\omega} e^{i\Delta k z}$ , taking into account the linear wave-vector mismatch parameter  $\Delta k = 3k(\omega) - k(3\omega)$ . After transforming to a reference frame moving with the group-velocity  $v_g(\omega)$  of the pump wave, our propagation equations for THG in air read

$$\left( i\partial_z + \frac{1}{2k_0} \nabla_\perp^2 - \frac{k''_\omega}{2} \partial_t^2 \right) \mathcal{E}_\omega + k_0 n_2 [R(t) \mathcal{E}_\omega + 2|\mathcal{E}_{3\omega}|^2 \mathcal{E}_\omega + \mathcal{E}_\omega^{*2} \mathcal{E}_{3\omega}] - \left[ \left( \frac{k_0}{2\rho_c} - i\frac{\sigma_\omega}{2} \right) \rho - i\frac{\beta_\omega^{(K\omega)}}{2} |\mathcal{E}_\omega|^{2K_\omega - 2} \right] \mathcal{E}_\omega = 0, \quad (2)$$

$$\left( i\partial_z + i\Delta v^{-1} \partial_t + \frac{1}{6k_0} \nabla_\perp^2 - \frac{k''_{3\omega}}{2} \partial_t^2 - \Delta k \right) \mathcal{E}_{3\omega} + 3k_0 [n_2^{3\omega} |\mathcal{E}_{3\omega}|^2 \mathcal{E}_{3\omega} + 2n_2 |\mathcal{E}_\omega|^2 \mathcal{E}_{3\omega} + n_2 \mathcal{E}_\omega^3 / 3] - \left[ \left( \frac{k_0}{6\rho_c} - i\frac{\sigma_{3\omega}}{2} \right) \rho - i\frac{\beta_{3\omega}^{(K_{3\omega})}}{2} |\mathcal{E}_{3\omega}|^{2K_{3\omega} - 2} \right] \mathcal{E}_{3\omega} = 0, \quad (3)$$

$$R(t) = \frac{1}{2} |\mathcal{E}_\omega|^2 + \frac{1}{2} \tau_K^{-1} \int_{-\infty}^t e^{-(t-t')/\tau_K} |\mathcal{E}_\omega(t')|^2 dt'. \quad (4)$$

The physical parameters are defined by  $k_0 = 2\pi/\lambda_0 = \omega/c$ ,  $\Delta k = -5 \text{ cm}^{-1}$ , while  $k''_\omega = 0.2 \text{ fs}^2/\text{cm}$  and  $k''_{3\omega} = 1 \text{ fs}^2/\text{cm}$  are the coefficients for normal group-velocity dispersion (GVD).  $\Delta v = [v_g(3\omega)^{-1} - v_g(\omega)^{-1}]^{-1} = 0.44 \text{ cm/fs}$  is the group-velocity mismatch responsible for temporal walk-off. The terms induced by the coupling between the two components involve self- and cross-phase modulations together with the FWM, allowing energy transfer between fundamental and TH fields. Here,  $n_2 = 4 \times 10^{-19} \text{ cm}^2/\text{W}$  denotes the nonlinear Kerr index for the IR component, while  $n_2^{3\omega} = 8 \times 10^{-19} \text{ cm}^2/\text{W}$  is that experienced by TH. The IR Kerr response of air, defined by Eq. (4), is composed of an instantaneous contribution and a delayed part with a relaxation

time  $\tau_K=70$  fs [12,14,36]. The free electron density  $\rho$  increases in time as

$$\partial_t \rho = \sum_{j=\omega,3\omega} (\rho_{\text{nt}} - \rho) \sigma_{(K_j)} |\mathcal{E}_j|^{2K_j} + (\sigma_j/U_i) \rho |\mathcal{E}_j|^2, \quad (5)$$

where the index  $j$  refers to  $\omega$  and  $3\omega$  components, respectively. In Eq. (5),  $K_j$  and  $\sigma_{(K_j)}$  denote the number of photons for IR (800 nm,  $K_\omega=8$ ) and UV wavelengths (266 nm,  $K_{3\omega}=3$ ), and their respective multiphoton ionization (MPI) rates  $\sigma_{(8)}=2.88 \times 10^{-99} \text{ s}^{-1} \text{ cm}^{16}/\text{W}^8$ ,  $\sigma_{(3)}=1.91 \times 10^{-28} \text{ s}^{-1} \text{ cm}^6/\text{W}^3$  [13]. Plasma response has been completed by inclusion of avalanche ionization with the inverse bremsstrahlung cross sections  $\sigma_\omega=5.44 \times 10^{-20} \text{ cm}^2$  and  $\sigma_{3\omega}=6.044 \times 10^{-21} \text{ cm}^2$ . Only oxygen ionization with gap potential  $U_i=12.1$  eV is considered for a neutral medium with density  $\rho_{\text{nt}}=5.4 \times 10^{18} \text{ cm}^{-3}$ ;  $\rho_c=1.8 \times 10^{21} \text{ cm}^{-3}$  is the plasma critical density defined at 800 nm. Because avalanche ionization is weak for pulse duration  $<1$  ps, MPI is the principal actor in generating an electron plasma. Multiphoton absorption (MPA) intervenes through the coefficients  $\beta_j^{(K_j)} = \hbar \omega_j K_j \rho_{\text{nt}} \sigma_{(K_j)}$ , yielding  $\beta_\omega^{(8)}=3.1 \times 10^{-98} \text{ cm}^{13}/\text{W}^7$  and  $\beta_{3\omega}^{(3)}=2.31 \times 10^{-27} \text{ cm}^3/\text{W}^2$ .

This system of equations resembles that proposed by Aközbek *et al.* in [29], apart from the following points: First, plasma generation by avalanche and related absorption have been included. Second, in the equation for the IR pump, the Raman-delayed Kerr response [14,36] has been taken into account. We assumed a zero delayed response for the UV component, as chosen in [13,29]. Third, MPI and MPA for the TH component have been tuned on their appropriate cross sections ( $K_{(3)}$ ,  $\sigma_{(3)}$ ,  $\beta_{3\omega}^{(3)}$ ), while SPM, XPM, and FWM contributions in Eq. (3) possess different nonlinear Kerr indices.

These changes are, however, minor and preliminary simulations using the pulse parameters of Ref. [29] restored a propagation dynamics close to that commented on in this reference. In addition, we verified that simulations performed with halved nonlinear coefficients for XPM and FWM, and involving also  $R(t)$  in the  $3\omega$  component, led to results comparable with the coming ones.

### III. METER-RANGE PROPAGATION OF FUNDAMENTAL AND TH PULSES IN PARALLEL GEOMETRY

Equations (2)–(5) are numerically integrated by means of a parallel radial code for pulses propagating in collimated geometry, in order to produce femtosecond filaments keeping a quasiconstant diameter over several meters. Two input beam configurations are investigated: (a) Sub-mm pulses ( $w_0=0.5$  mm) conveying a ratio of input power over critical  $P_{\text{in}}/P_{\text{cr}}=4$  and (b) broader beams with waist  $w_0=0.25$  cm containing 50 critical powers. The critical power for self-focusing is defined by  $P_{\text{cr}}=\lambda_0^2/2\pi n_2$  and it takes the value  $P_{\text{cr}}=2.55$  GW at  $\lambda_0=800$  nm.

#### A. Femtosecond pulses with moderate powers

To start with, we first solve Eqs. (2)–(5) for an input pulse having a Gaussian shape

$$\mathcal{E}_\omega(z=0, r, t) = \sqrt{\frac{2P_{\text{in}}}{\pi w_0^2}} e^{-r^2/w_0^2 - t^2/t_p^2}, \quad (6)$$

with power  $P_{\text{in}}=4P_{\text{cr}}$ , waist  $w_0=0.5$  mm, and temporal half-width  $t_p \approx 127$  fs [ $\equiv$ full width at half maximum (FWHM) duration/ $\sqrt{2 \ln 2}$ ]. The beam is launched into the atmosphere in a collimated way (no focusing lens). At  $z=0$ , there is no third-harmonic component ( $\mathcal{E}_{3\omega}=0$ ). Figure 1 summarizes the results of the numerical simulations. Figures 1(a) and 1(b) show the peak intensities of the fundamental ( $\omega$ ) and TH ( $3\omega$ ) pulses. Figures 1(c) and 1(d) represent the on-axis fluence distribution [ $\mathcal{F}=\int_{-\infty}^{+\infty} (|\mathcal{E}_\omega|^2 + |\mathcal{E}_{3\omega}|^2)(r=0, z, t) dt$ ] and the mean radius of the two-colored filament taken as the FWHM of the fluence, respectively. Figures 1(e) and 1(f) illustrate the maximum plasma density ( $\max_t \rho$ ) excited by ionization of air molecules and the energy loss upon the propagation axis, computed throughout the entire simulation box. All dashed curves refer to the same quantities plotted for an IR pulse only, i.e., while maintaining  $\mathcal{E}_{3\omega}=0$  along the  $z$  axis.

From these figures, a couple of important features can already be emphasized.

(i) The ratio of peak intensities  $I_\omega/I_{3\omega}$  ( $I_j \equiv |\mathcal{E}_j|^2$ ;  $j = \omega, 3\omega$ ) mostly remains  $\geq 50$ . This observation can be explained by the large phase mismatch  $\Delta k$  between the pump and TH components: The characteristic coherence length  $L_c = \pi/|\Delta k| \approx 0.63$  cm is rather small, so the evolution of the TH peak intensity almost follows that of the fundamental. Generated TH field experiences down-conversion after a short propagation length  $<1$  cm, which significantly limits the growth of its intensity over larger distances.

(ii) There is a noticeable enlargement of the filament range in the presence of THG: Self-guiding is enhanced by a multiplicative factor of  $\sim 1.5$  compared with the case where TH is omitted. Note the smoother decrease in energy when both IR and UV components couple, which allows the filament to survive over longer distances and stay clamped with a longer plasma channel reaching a peak electron density  $\sim 10^{16} - 10^{17} \text{ cm}^{-3}$ .

In order to get a deeper insight into the nonlinear dynamics of the two-colored filament, we display in Fig. 2 information related to the on-axis temporal distortions undergone by the two components [Figs. 2(a) and 2(b)] and by an IR pulse only [Fig. 2(c)]. Here, the red zones correspond to intensity levels  $60 \text{ TW}/\text{cm}^2 \leq I_{\text{max}} \leq 80 \text{ TW}/\text{cm}^2$ , while yellow and green zones correspond to lower ones, i.e.,  $40 \text{ TW}/\text{cm}^2 \leq I_{\text{max}} < 60 \text{ TW}/\text{cm}^2$ . Some temporal profiles are illustrated in Fig. 2(d) at different propagation distances. Figure 2(e) supplies information about the dephasing  $\Delta\phi = 3\phi_\omega - \phi_{3\omega}$  between the components at two different instants, namely,  $t=0$  and  $t=t_{\text{max}}$  when the pulse intensity is maximum. Figure 2(f) finally shows the energy conversion efficiency between the fundamental and the TH pulses, inside a contour of  $300 \mu\text{m}$  in diameter around the filament core (dashed line) and over the whole simulation box (solid line). This conversion efficiency is defined by the ratio between the energy in the TH component and the energy of both components. It attains values as high as 0.5% over 5 m of propagation.

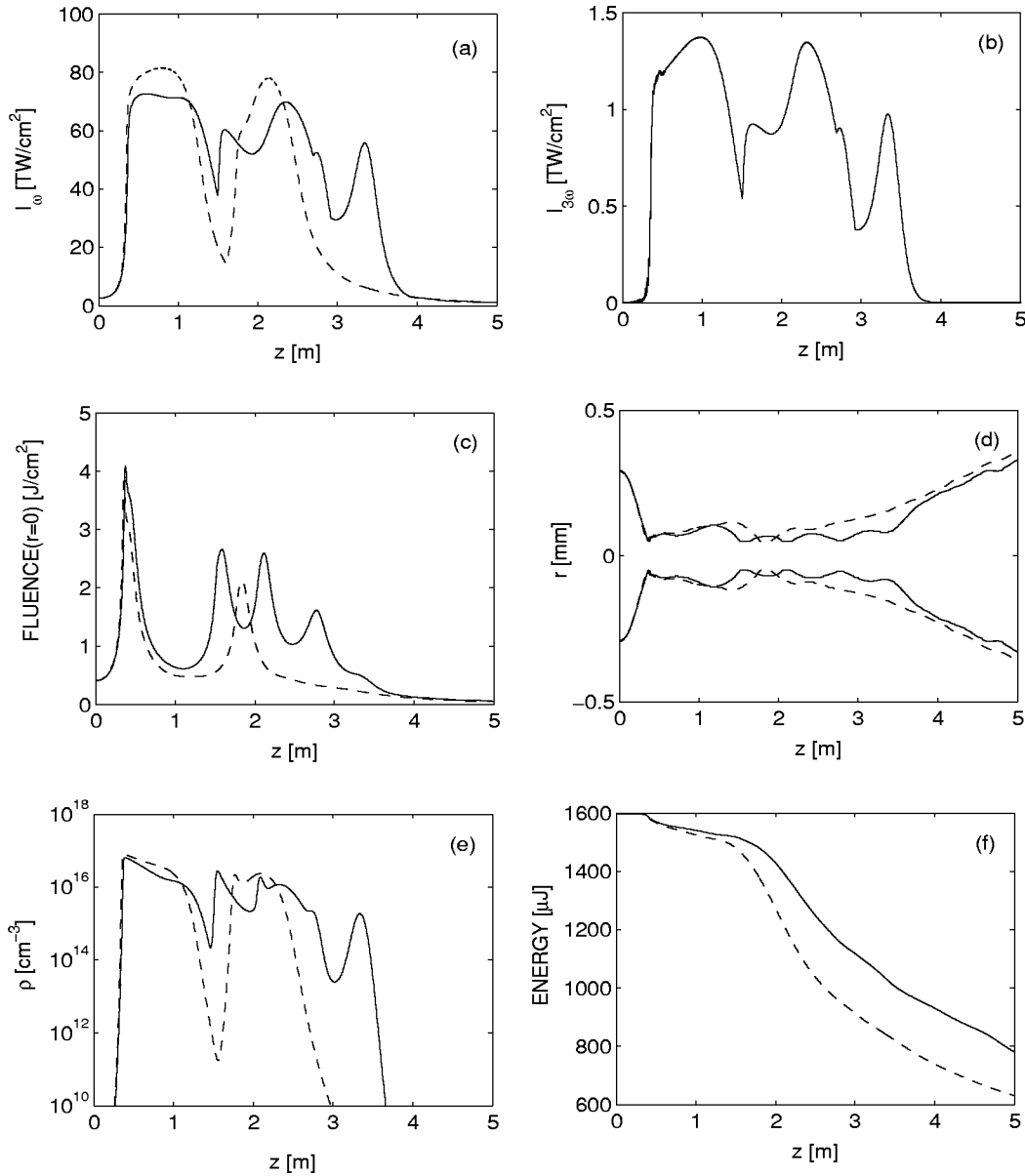


FIG. 1. (a) Peak intensities for the fundamental and (b) TH components, (c) fluence distribution, (d) mean radius (FWHM of the fluence distribution), (e) peak electron density, and (f) energy losses for a Gaussian pulse with  $P_{in}=4P_{cr}$ . Dashed lines represent the same quantities without THG.

Again we may underline important points revealed by these computations.

(iii) Temporal walk-off, which should promote the displacement of the TH component to positive times compared with the fundamental pulse profile, is negligible. The walk-off length,  $L_{\Delta v} \approx 66$  cm, is about 100 times higher than the coherence length  $L_c \approx 0.63$  cm, so the TH component is located at the instants when the pump field develops.

(iv) Following the “spatial replenishment dynamics” model [9], when a single component propagates, plasma generation defocuses the back of the pulse and thereby forms a leading edge ( $t < 0$ ). Afterwards, plasma partly turns off and provokes the refocusing of the trailing edge ( $t > 0$ ). This standard scenario is refound in Fig. 2(c). Note that the trail is here directed to  $t=0$  at  $z \approx 2.5$  m. We attribute this reconfinement

to center to the Raman-delayed Kerr response, which smooths the back of the pulse and lowers the number of peaks arising at positive times [37]. When both IR and UV components couple, we rediscover this temporal evolution, up to  $\sim 2$  m only. Next, the dynamics changes: Temporal fluctuations develop in the pulse profile at  $z \sim 2.2$  m. Two new cycles of focusing/defocusing events occur, connected with the oscillations seen in Fig. 1(c). These new events go on feeding the interplay between the leading and trailing edges in the pulse, before only one temporal peak is confined around  $t=0$  at the distance  $z=3.24$  m. When the pulse temporal profile relaxes to a single peak, it exhibits a typical duration  $\approx t_p/10$ .

(v) The phase difference is quasiconstant and keeps the value  $\Delta\phi \approx \pi$  almost all along the self-guiding range, up to

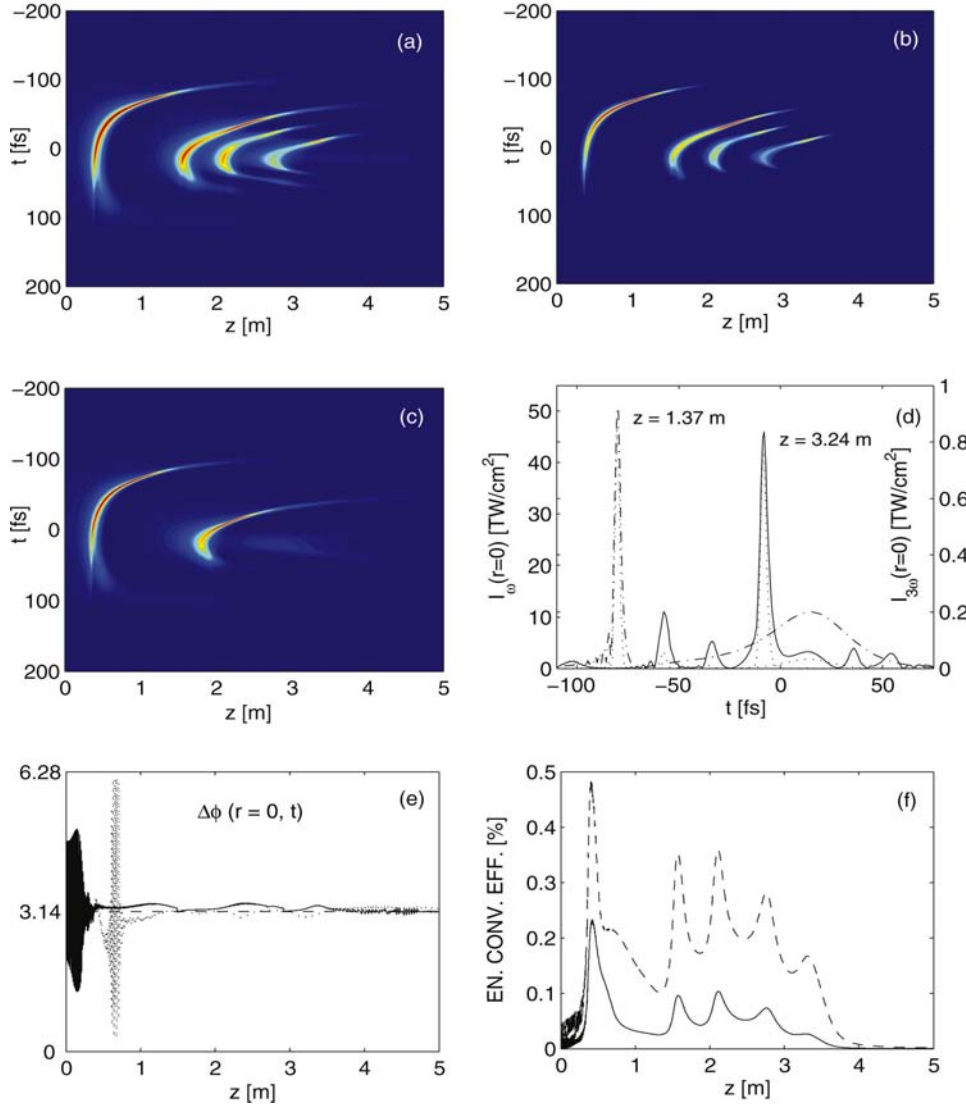


FIG. 2. (Color) Image plots of the temporal distributions for  $4P_{\text{cr}}$  mm-waisted pulses: (a) fundamental pulse; (b) TH pulse; (c) IR component alone; (d) temporal profiles from the coupling between both components at  $z = 1.37$  m and  $z = 3.24$  m (TH intensity must be read on the right-hand side axis); (e) dephasing  $\Delta\phi$  at  $t = t_{\text{max}}$  (solid line) and  $t = 0$  (dashed line); (f) energy conversion efficiency around the filament core (dashed curve) and over the entire simulation box (solid curve).

few intervals in  $z$ . This property, first discovered in [29] upon a few cm only, is hence confirmed for collimated beams propagating over meter-range distances.

To understand this latter point, we may follow the procedure proposed in [29]. We decompose the pump and TH fields in phase and amplitude ( $\mathcal{E}_j = A_j e^{i\phi_j}$ ,  $j = \omega, 3\omega$ ). Discarding transverse diffraction, walk-off, and GVD in regimes mainly driven by the nonlinearities that involve relatively weak losses [see Fig. 1(f)], we find

$$\partial_z \phi_\omega \approx -\frac{k_0 \rho}{2\rho_c} + k_0 n_2 [R(t) + 2A_\omega^2 + A_\omega A_{3\omega} \cos(\Delta\phi)], \quad (7)$$

$$\begin{aligned} \partial_z \phi_{3\omega} \approx & -\Delta k - \frac{k_0 \rho}{6\rho_c} + 3k_0 n_2^3 A_\omega^2 + 3k_0 n_2 \\ & \times \left( 2A_\omega^2 + \frac{A_\omega^3}{3A_{3\omega}} \cos(\Delta\phi) \right), \end{aligned} \quad (8)$$

$$\frac{1}{2} \partial_z A_\omega^2 \approx k_0 n_2 A_\omega^3 A_{3\omega} \sin(\Delta\phi), \quad (9)$$

$$\frac{1}{2} \partial_z A_{3\omega}^2 \approx -k_0 n_2 A_\omega^3 A_{3\omega} \sin(\Delta\phi). \quad (10)$$

The demand that the spatial profiles of both coupled components remain steady-state in the self-channeling regime suggests  $\sin \Delta\phi = 0$ . Hence, the dephasing  $\Delta\phi = 3\phi_\omega - \phi_{3\omega}$  should be close to either 0 or  $\pi$ . The fact that only a dephasing of  $\pi$  is possible follows immediately from  $\partial_z \Delta\phi \approx 0$ : At leading order,  $\Delta\phi$  satisfies

$$\partial_z \Delta\phi \approx \Delta k - \frac{4k_0 \rho}{3\rho_c} - 3k_0 n_2 [2A_\omega^2 - R(t)] - k_0 n_2 \frac{A_\omega^3}{A_{3\omega}} \cos(\Delta\phi), \quad (11)$$

where one may further approximate the Kerr response  $R(t)$  by identifying the time  $t_{\text{max}}$  for which the temporal dependencies in Eq. (4) are maximum at  $z=0$  [43]. For instance, when  $t_p = 127$  fs, this instant is  $t_{\text{max}} \approx 13$  fs and yields  $R(t_{\text{max}}) \approx 0.83A_\omega^2$ , i.e., the effective Kerr index,  $n_2^{\text{eff}}$ , is equal to  $0.83n_2$  in this approximation, so that  $2A_\omega^2 - R(t) \approx 1.17A_\omega^2$ . Setting  $\cos \Delta\phi \approx -1$  ( $\Delta\phi \approx \pi$ ) is then necessary to reach a balance between the mismatch parameter  $\Delta k = -5 \text{ cm}^{-1}$  and the nonlinear contributions. At certain instants, Fig. 2(e)

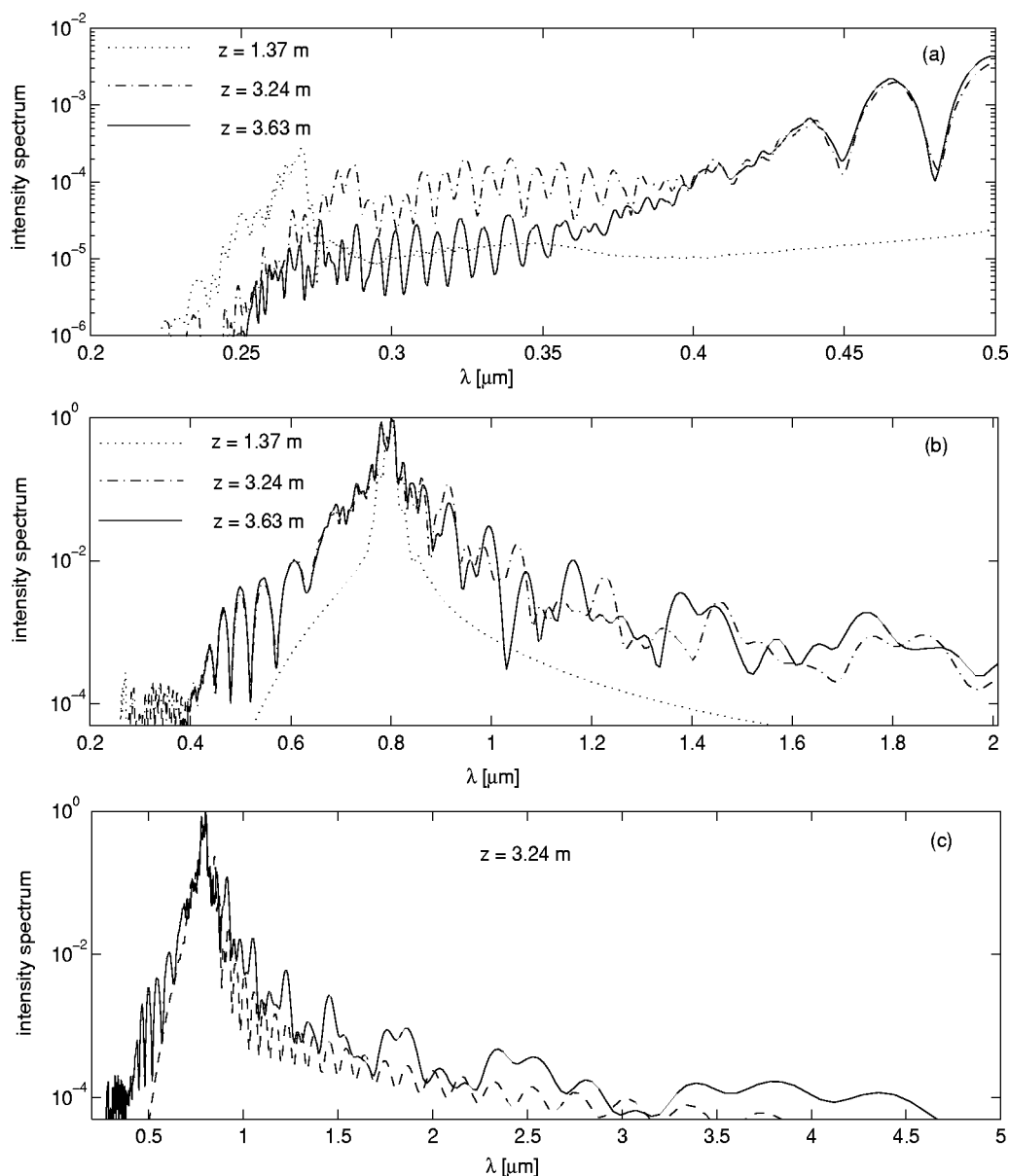


FIG. 3. (a) Intensity spectra up to 500 nm. (b) Same spectra, but extended to 2  $\mu\text{m}$ . (c) Spectra enlarged to 5  $\mu\text{m}$  at  $z=3.24$  m with (solid curve) and without (dashed curve) THG.

shows that this balance, however, drops inside short longitudinal intervals. Visual inspection of the numerical results reveals that here either  $\mathcal{E}_{3\omega}=0$  or  $\mathcal{E}_\omega=0$ . Such zero-valued components cannot support the previous phase balance. These rapid drops of  $\pi$ -phase shift are responsible for a significant decrease in the energy conversion efficiency [see Fig. 2(f)].

Let us now emphasize one of the most important results of this analysis: The supercontinuum induced by third-harmonic generation.

Figure 3 shows the intensity spectra of the previous pulse. The plotted quantity is the spectral intensity,  $\tilde{I}(r,\lambda)$ , expressed in Fourier space and integrated over the diffraction plane. Three characteristic stages of pulse broadening in the presence of plasma generation are illustrated. After a Kerr-induced SPM stage (not shown here), a redshift signals the

emergence of a leading edge in the pulse temporal profile created by plasma defocusing ( $z=1.37$  m). Then, the spectrum is continuously enhanced into a hump of wavelengths in the UV-visible domain ( $z=3.24$  m). At larger distances, this hump persists, although the UV components become more damped ( $z=3.63$  m). These spectral distortions amplify oscillations mainly caused by constructive/destructive interference between different temporal peaks emerging in the pulse profile and altering consequently the Fourier transform ( $\omega_{\text{osc}} \sim 2\pi/\Delta t$ , where  $\Delta t$  is the interpeak interval).

These three phases can briefly be explained by the elementary theory for SPM [18], predicting that a Gaussian pulse  $\mathcal{E}_\omega(L,t) = \mathcal{E}_\omega(L_0,t)e^{i\phi(L,t)}$  keeping a nearly constant temporal profile will undergo spectral broadening characterized by a maximum phase shift  $\phi_{\text{max}} \sim (I_\omega^{\text{max}}/I_0) \times (L/L_{\text{NL}})$ , where  $L_{\text{NL}} = (k_0 n_2^{\text{eff}} I_0)^{-1}$  is the nonlinear length scale ( $L_{\text{NL}} \sim 13$  cm;

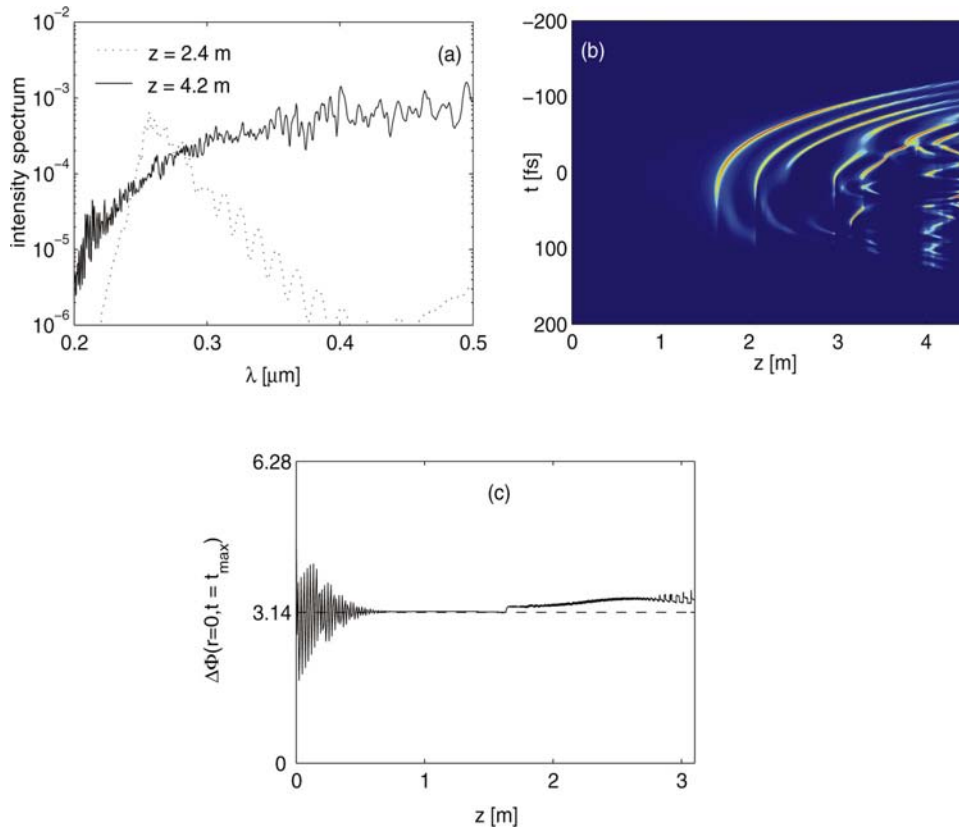


FIG. 4. (Color) (a) Intensity spectra, (b) temporal distribution of the  $\omega$  component and (c) dephasing of coupled  $\omega/3\omega$  pulses formed from a 2.5-mm, high-power ( $P_{\text{in}}=50 P_{\text{cr}}$ ) beam.

$I_0=2.6 \text{ TW/cm}^2$ ). The frequency variations  $\Delta\omega=\omega-\omega_0$  dictating the spectral enlargement are given by  $\Delta\omega=-\partial\phi/\partial t$  with maximal value  $\Delta\omega_{\text{max}}\approx 0.86\phi_{\text{max}}/T$ , where  $T$  is the pulse duration kept quasiconstant along the propagation length  $L$ . Applying these estimates to Fig. 3, we find that the competition between Kerr focusing and MPI forms a “constant” leading spike with  $T\sim t_p/10$  at  $z\sim 1.3 \text{ m}$ , where  $I_{\text{max}}$  attains 20 times  $I_0$  over the distance  $L\sim 0.5 \text{ m}$ . This leads to the frequency broadening  $\Delta\omega_{\text{max}}\approx 5\times 10^{15} \text{ Hz}$ , with a pronounced redshift. Further focusing/defocusing sequences occurring from  $z\geq 2 \text{ m}$  and achieved by the formation of a central spike close to  $t=0$  induce a more symmetric enlargement ( $z=3.24 \text{ m}$ ). The UV components amplify this spectral dynamics as  $\partial_t\phi_{3\omega}\approx 3\partial_t\phi_\omega$  ( $\Delta\omega_{3\omega}\approx 3\Delta\omega_\omega$ ).

Spectral broadening in wavelength follows the same distortions in the proportion  $\Delta\lambda_j=-\lambda_j^2\Delta\omega_j/(2\pi c)$ , where  $c$  is the speed of light in vacuum. Deviations in wavelengths are found to attain  $\Delta\lambda_\omega\approx 2 \mu\text{m}$  for the IR pulse and  $\Delta\lambda_{3\omega}=\Delta\lambda_\omega/3\approx 0.6 \mu\text{m}$  for the TH one. At  $z=3.24 \text{ m}$ , the deviations  $\Delta\lambda_j$  overlap in the region separating the  $3\omega$  and  $\omega$  spectra, which become the locus of an important superimposition of wavelengths. This results in an UV-visible supercontinuum generation in the domain  $200 \text{ nm}\leq\lambda\leq 500 \text{ nm}$  revealed by Fig. 3(a). Figure 3(b) extends the same spectral evolution, up to  $2 \mu\text{m}$ , while Fig. 3(c) depicts the complete spectrum at  $z=3.24 \text{ m}$  with and without THG. From this latter figure, one can conclude that, actually, the hump in wavelength below  $500 \text{ nm}$  is caused by THG. Moreover, the IR content of the spectrum reaches  $4.5 \mu\text{m}$ , in agreement with experimental observations [20].

## B. Broad pulses with high power

To prove that the supercontinuum generation revealed in Fig. 3(a) is generic, we briefly examine the dynamics of a broader Gaussian beam, starting with the input datum (6) having the bigger waist  $w_0=2.5 \text{ mm}$  and containing 50 critical powers. The other pulse parameters are kept unchanged. Again, the build-up of UV-visible wavelengths appears over a couple of meters, as displayed by Fig. 4. Figure 4(a) puts in evidence two different stages in the spectral broadening attained at high power levels, for which the nonlinear focus is formed at  $z\approx 1.5 \text{ m}$ . The same “spectral” dynamics characterizes these propagation scales: The TH component widely broadens towards its red direction at  $z=2.4 \text{ m}$ , as plasma generation defocuses the back of the pulse. At  $z=4.2 \text{ m}$ , a significant “symmetric” enlargement of both pulses results from a distorted temporal distribution mixing leading and trailing peaks. Spectral enlargements strongly superimpose at this distance and promote a salient hump in the wavelength domain  $200 \text{ nm}\leq\lambda\leq 500 \text{ nm}$ . The temporal evolution of the pulse profile along the  $z$  axis can be followed in Fig. 4(b). Over this propagation range, the dephasing  $\Delta\phi$  is again clamped around the value  $\pi$ , as seen in Fig. 4(c).

From Fig. 4(b), one can notice how the temporal pulse profiles become distorted at large distances. We must, however, keep in mind that spherically symmetric filaments keeping 50 critical powers during their early propagation are not very realistic, as the focal spot should break up into multiple filaments at powers  $\geq 20P_{\text{cr}}$  [38]. Figure 4 shows, nevertheless, that supercontinuum generation occurs over a few meters in the UV-visible domain, even for broad beams

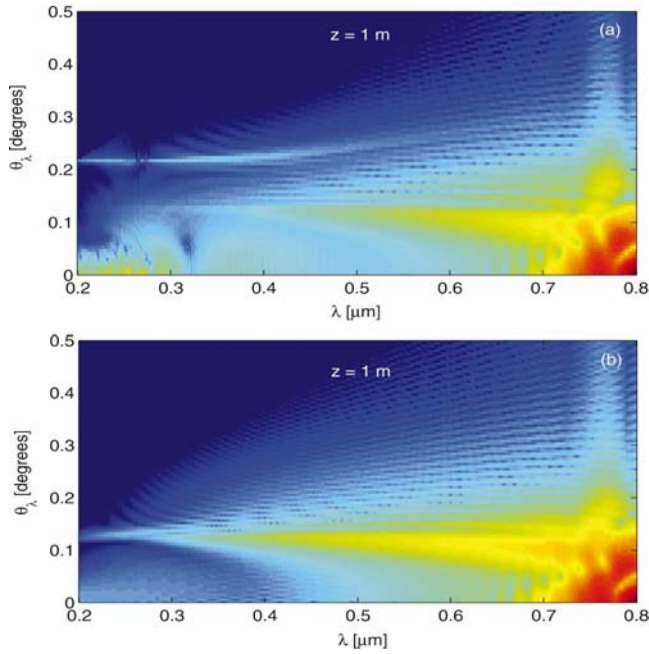


FIG. 5. (Color) Numerically computed CE for the same pulse used in Sec. III, (a) with and (b) without THG, at  $z=1$  m.

conveying initially an important ratio of input power over critical.

#### IV. CONICAL EMISSION

If spectral broadening is linked to the temporal variations of the pulse phase, the conical emission, which manifests as an angular emission of shifted radiation at specific wavelengths, is currently justified by the spatial variations of the same phase. As examined in [19], CE originates from the SPM of an IR pulse. Its half-angle of divergence,  $\theta_\lambda$ , is generally measured as the ratio of the radius of a given colored ring to the distance from the middle of the CE source to the screen. This angle does not depend on the longitudinal position where it is measured. Whereas CE has been observed many times for various waists in the range of wavelengths  $500 \text{ nm} \leq \lambda \leq 800 \text{ nm}$  [2,19], little information has been reported for the complementary domain  $200 \text{ nm} \leq \lambda \leq 500 \text{ nm}$ .

Since CE originates from the nonlinear phase shifts in one filament, it is worth computing it from the mm-waisted beam ( $w_0=0.5$  mm) simulated in Sec. III. For any pulse component, CE follows from the broadening of the angular spectrum defined by  $k_\perp = |\partial\phi/\partial r|$ , which is mainly driven by the spatial variations of the plasma density ( $\sim |\partial\rho/\partial r|$ ). Along the self-focusing process, radial compression and longitudinal steepening occur simultaneously at the pulse front, which results in a salient increase of the nonlinearities interplaying in the phase [see, e.g., Eq. (7)]. For TH generation, CE is reinforced by the FWM source contribution for the  $3\omega$  component. This angular divergence is plotted in Fig. 5 at  $z \approx 1$  m, where the pulse intensity attains its maximum in both components. Figure 5(a) shows the angular divergence computed from the spatio-temporal Fourier spectrum of the total

pulse intensity  $|\tilde{\mathcal{E}}_\omega(k_\perp, \omega) + \tilde{\mathcal{E}}_{3\omega}(k_\perp, \omega)|^2$ , from which the half-angle of propagation at given wavelength  $\lambda$  is  $\theta_\lambda \approx k_\perp/k_z \times (360/2\pi)$  (degrees), where  $k_z \approx 2\pi/\lambda$ . For wavelengths above 400 nm, an “inner” bright curve occurs in the plane  $(\theta_\lambda, \lambda)$ , which is caused by the fundamental pulse. At smaller wavelengths, a second “outer” curve arises because of the influence of THG. For  $\lambda=500$  nm, this angle reaches the value  $0.12^\circ$ , in agreement with available experimental data [2,19]. Figure 5(b) illustrates the CE for the same pulse without THG ( $\mathcal{E}_{3\omega}=0$ ), for which  $\theta_\lambda$  slightly increases with decreasing  $\lambda$ , but with an angular growth limited to  $\theta_\lambda \sim 0.15^\circ$ . In contrast, when TH is generated, CE is noticeably enhanced by about  $0.1^\circ$ . The divergence is steeply augmented to  $0.23^\circ$ – $0.25^\circ$  in the range  $200 \text{ nm} \leq \lambda \leq 400 \text{ nm}$ , as the angular contribution from the pump wave becomes more and more extinguished. This angular growth is linked to additional (FWM) nonlinearities coming from the coupling  $\omega/3\omega$  ( $\partial_r\phi_{3\omega} \approx 3\partial_r\phi_\omega$ ) and making the TH spectrum in  $k_\perp$  wider than the fundamental.

#### V. EXPERIMENTAL LIDAR SENSING REVEALS UV-VISIBLE SUPERCONTINUUM GENERATION

Since supercontinuum generation in the UV-visible wavelength domain was numerically evidenced over meter-range propagation scales for mm-waisted beams, we may expect to detect the same phenomenon over several hundreds of meters by using cm-waisted pulses. With this aim, experiments were performed by means of the Teramobile laser system [23], delivering pulses with waist  $w_0$  as large as 5 cm from the laser exit.

The Teramobile system is the first mobile femtosecond TW-laser based Lidar system [23]. It involves a chirped pulse amplified (CPA) Ti:sapphire laser source that delivers 5 TW pulses (70 fs, 350 mJ) at 10 Hz repetition rate. The laser pulses are sent vertically into the atmosphere using an all-reflective beam expander ( $3\times$ ). The photons backscattered from the atmosphere are collected by a 40-cm-diam telescope, which focuses the light onto a spectrally resolved detector. The Lidar returns are recorded as a function of the photon flight time using a 500 MHz digital oscilloscope, which provides distance resolution. The initial chirp of the pulse can be modified by varying the grating distance in the compressor, in order to limit the initial optical intensity and to compensate for group-velocity dispersion (GVD) in air as the laser beam propagates. This allows us to modify the distance at which the onset of filamentation occurs.

The UV-visible content of the supercontinuum was measured at different altitudes by using the Lidar arrangement and by scanning the spectrometer. The wavelength increment was 10 nm from 230 nm to 600 nm. For each spectral interval, averaging over 1000 shots was performed. The white light intensity was optimized by changing the initial chirp and geometrical focusing. Optimal white-light emission was found for an initial GVD precompensation chirp of  $-150$  fs ( $t_p \approx 127$  fs) and a linear focusing of  $f=10$  m. De-

convolution of the spectral dependence of the apparatus response was applied. Correction over the Rayleigh-Mie backscattering/extinction efficiencies was performed by analyzing the individual Lidar returns. Moreover, correction over the ozone absorption, present in the atmosphere at a concentration of  $100 \mu\text{g}/\text{m}^3$ , was applied to the spectra.

Lidar signals contain information about the intensity profile in a cross section of the beam depending on the altitude [39]. Because of the Lidar optical arrangement, the overlap between the laser beam and the telescope field varies with altitude and strongly depends on the laser divergence. In particular, Lidar signals become very sensitive to this overlap function at low altitude. To correct this function, the whole detection system geometry, including the collecting telescope, the monochromator, and the detector, has been designed in three dimensions in order to calculate the geometrical compression, and hence the overlap function. This function was integrated over the whole beam section. In this integration, following the results of [25], we modeled the laser beam profile at each wavelength as a central emission peak, surrounded by conical emission bearing 70% of the energy. The divergence angle of the conical emission at each wavelength, as well as the laser angle relative to the telescope axis that could not be measured directly, were left as free parameters. These parameters have been determined by fitting the simulated signal as a function of the altitude at each wavelength with the experimental ones. The strongest weight in this fit was given at the lowest altitudes, where the geometrical compression effect is higher, and, therefore, where the signal is more sensitive to the parameters. This fit allowed us to access the white light spectrum at low altitude (100 m–200 m) and the supercontinuum divergence related to conical emission as a function of the wavelength.

The results at 105 m, 135 m, and 195 m altitudes are shown in Fig. 6(a). At 105 m, SPM widely broadens the fundamental laser spectrum and THG appears as a band of some 50 nm around 265 nm. At 135 m, however, the observed spectrum changes into an ultrabroadband and continuous UV-visible plateau down to 230 nm. At 195 m, TH spectral contribution relaxes to some extent, while the hump at visible wavelengths still persists.

This spectral dynamics agrees with the previous numerical results. Some discrepancies, however, deserve special comments. First, experimental and numerical spectra are quite similar, up to the oscillations created by interference between different peaks appearing in the pulse profile (see Fig. 3). Such oscillations are smoothed in the experimental spectra, measured with a resolution of 10 nm, and averaged over 1000 shots. Second, differences also occur in the longitudinal scales. Whereas our numerics emphasizes a spectral dynamics taking place over 2.5 m (see Sec. III), identical spectral distortions develop over several tens of meters in the experiments. We attribute these discrepancies to the large increment ( $\approx 10$  m) limiting the number of available experimental data, where the build-up in wavelengths arises as a cumulative effect from all filaments in the entire laser focal spot. A majority of filaments should indeed be aligned on the same spectral profile to modify noticeably the overall laser spectrum, which can happen after several tens of meters along the propagation axis. This conjecture received confir-

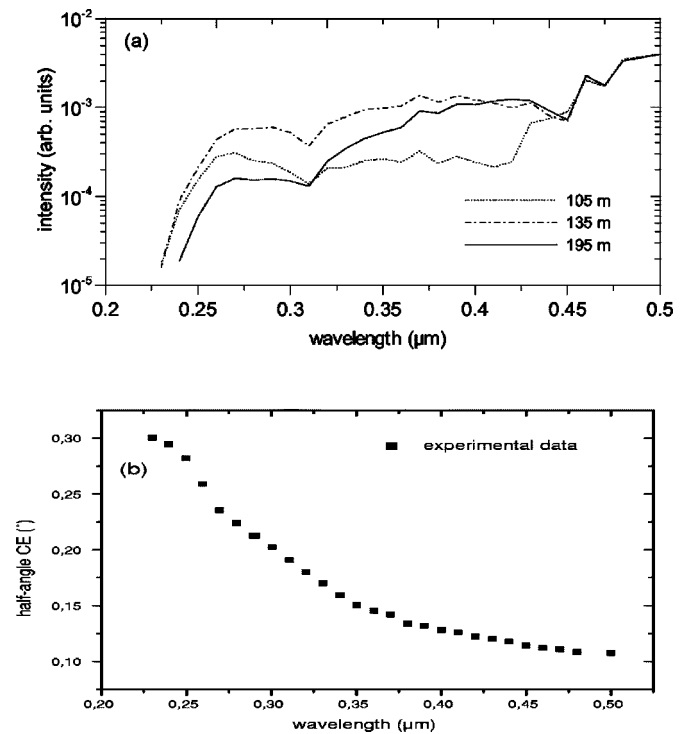


FIG. 6. (a) Spectral evolution measured at different propagation distances. Intensity at 500 nm is fixed at  $4 \times 10^{-3}$  times the intensity in the fundamental [40]. (b) Conical emission experimentally reported at 200 m altitude for  $\lambda < 500$  nm.

mation in a very recent investigation [44], where UV spectral measurements were performed on a single filament over laboratory scales and restored a supercontinuum similar to Figs. 3(a) and 4(a) over a few meters of propagation only.

Figure 6(b) shows the conical emission detected from the same experimental setup. The observed divergence can be explained as the convolution of CE from each filament in the bundle (overall beam) and the linear divergence of the Tera-mobile bundle itself [25]. This latter angle corresponds to the whole beam divergence governed by geometrical optics, due to the 10-m focusing geometry. It is determined by subtracting the CE angles known from the literature in the domain of 500–600 nm from the global divergence of the beam. The resulting value is then used to deduce the CE angles at lower wavelengths, which are presented in Fig. 6(b) (squares). Basically, the conical emission in the UV-visible wavelength domain prolongs almost linearly that known from IR pulses at relatively larger wavelengths [19]. This behavior is true, up to an important deviation of the half-angle  $\theta_\lambda$  at UV wavelengths  $\lambda < 350$  nm. This deviation increases the CE by more than  $0.1^\circ$  and reaches  $0.28^\circ$  at 250 nm, which reasonably agrees with the simulations of Sec. IV.

Note that, whereas IR and UV components are connected in Fig. 6(b), they look disconnected in Fig. 5(a). We believe that this discrepancy originates from the lack of higher-order dispersion and space-time focusing terms in our model equations. These effects are indeed awaited to match the two spectral components by increasing their own angular divergence (see, e.g., Ref. [45]).

## VI. THG IS A NONLINEAR SATURATION MECHANISM FOR THE PUMP WAVE

As revealed by Fig. 1(d), THG enables the two-colored filament to propagate further by keeping a quasiconstant waist of  $\sim 100 \mu\text{m}$ . This phenomenon is compatible with the weaker energy loss undergone by the filament when TH is emitted, compared with the propagation of an IR pulse alone [Fig. 1(f)]. By computing the continuity relations for the wave densities, Eqs. (9) and (10) indeed show that generation of third harmonics takes place by FWM through up- and down-conversion cycles, which, on the whole, do not affect the global energy content. Converting part of the fundamental energy into TH thus limits the energy loss undergone by plasma formation.

To understand the self-channeling enhancement, we can first notice the order of magnitude of the wave-vector mismatch parameter:  $|\Delta k|=5 \text{ cm}^{-1}$ . This parameter is large compared with the typical “nonlinear wave vector” associated with the peak intensity of the  $\omega$  component:  $n_2 k_0 A_\omega^2 < 2.5 \text{ cm}^{-1}$ . More precisely,  $|\Delta k|$  has an order of magnitude comparable with the XPM and FWM contributions of Eq. (3), so that we can apply the so-called “cascading” limit which consists in setting  $\Delta k$  equal to the leading-order nonlinearities, i.e.,

$$\mathcal{E}_{3\omega} \approx - \frac{k_0 n_2}{|\Delta k| + 6k_0 n_2 A_\omega^2} \mathcal{E}_\omega^3. \quad (12)$$

As long as  $A_\omega^2 < |\Delta k|/6k_0 n_2 = 2.7 \times 10^{13} \text{ W/cm}^2$ , the approximation  $\mathcal{E}_{3\omega} \approx -k_0 n_2 \mathcal{E}_\omega^3/|\Delta k|$  holds. Once Eq. (12) is plugged into the pump wave equation, Eq. (2) simplifies at leading order into

$$\begin{aligned} \partial_z \mathcal{E}_\omega \approx & \frac{i}{2k_0} \nabla_\perp^2 \mathcal{E}_\omega - \frac{i}{2} k''_\omega \partial_t^2 \mathcal{E}_\omega + ik_0 n_2 R(t) \mathcal{E}_\omega \\ & - i \left( \frac{k_0}{2\rho_c} - i \frac{\sigma_\omega}{2} \right) \rho \mathcal{E}_\omega - \frac{\beta_\omega^{(K_\omega)}}{2} |\mathcal{E}_\omega|^{2K_\omega-2} \mathcal{E}_\omega \\ & - ik_0 n_2 \left[ \frac{k_0 n_2}{|\Delta k|} \right] \frac{|\mathcal{E}_\omega|^4}{(1+C|\mathcal{E}_\omega|^2)} \mathcal{E}_\omega, \end{aligned} \quad (13)$$

where  $C \equiv 6k_0 n_2/|\Delta k|$ . The TH nonlinearities thus combine into a defocusing quintic saturation, which becomes itself saturated at high enough intensities ( $I_\omega \rightarrow I_\omega^{\text{max}}$ ). Therefore, THG acts in the sense of “delaying” the collapse of the pump wave and stabilizes the self-guided filament to some extent. A similar phenomenon was earlier discovered in [41] for cw beams without plasma generation: At large, negative mismatch values  $\Delta k/(n_2 k_0 A_\omega^2) < -1$ , THG promoted the arrest of beam collapse and contributed to form  $\chi^{(5)}$ -like spatial solitons ( $C \rightarrow 0$ ) characterized by periodic oscillations. Such oscillations, which anticipate the convergence of nonlinear beams to solitary-wave structures over long ranges [42], are visible in Figs. 1(c) and 1(d) from  $z=1 \text{ m}$ . In the present context, they decrease in amplitude until MPA dissipates the filament.

Let us estimate the intensity threshold for the  $\omega$  component resulting from the interplay between MPI and Kerr focusing. The order of magnitude of the laser intensity,  $I_\omega$

$\equiv |\mathcal{E}_\omega|^2$ , when it becomes saturated by MPI takes the value  $I_{\omega, \text{MPI}}^{\text{max}} \approx (2\rho_c n_2^{\text{eff}}/t_p \sigma_{(K_\omega)} \rho_{\text{nt}})^{1/(K_\omega-1)} \approx 48 \text{ TW/cm}^2$ , where  $n_2^{\text{eff}} \approx 0.83n_2$ . In the absence of THG, the typical length for self-channeling is then given by

$$\Delta z_{\text{MPA}} \sim \frac{2}{\beta_\omega^{(K_\omega)} (I_{\omega, \text{MPI}}^{\text{max}})^{K_\omega-1}} \approx 1.1 \text{ m}. \quad (14)$$

If we now consider the role of TH in the limit  $C \rightarrow 0$ , the third harmonics couples with the fundamental like an effective  $\chi^{(5)}$  nonlinearity [4] with related coefficient  $n_4$ ,

$$n_4 = \frac{n_2^2 k_0}{|\Delta k|} \approx 2.513 \times 10^{-33} \text{ cm}^4/\text{W}^2, \quad (15)$$

which is about a quarter of the value often proposed in the literature (see, e.g., [4]). In spite of the smallness of  $n_4$ , one can see that such quintic nonlinearities are active in stabilizing the filament for the following reason.

When we analyze the effective nonlinear index of refraction associated with Eq. (13), i.e.,

$$\begin{aligned} \Delta n = & n_2 R(t) - n_4 |\mathcal{E}_\omega|^4 - \rho_{\text{max}}/2\rho_c \\ \approx & n_2^{\text{eff}} I_\omega - n_4 I_\omega^2 - \frac{t_p \sigma_{(8)} \rho_{\text{nt}}}{2\rho_c} I_\omega^{K_\omega}, \end{aligned} \quad (16)$$

the combination of nonlinearities can be rewritten as

$$\Delta n = n_2^{\text{eff}} I_{\omega, \text{MPI}}^{\text{max}} (1 - y^{K_\omega-1} - \alpha y). \quad (17)$$

Here,  $y \equiv I_\omega/I_{\omega, \text{MPI}}^{\text{max}}$  and  $\alpha \equiv I_{\omega, \text{MPI}}^{\text{max}}/I_{\omega, \chi^{(5)}}^{\text{th}}$  involves the saturation threshold owing to TH-induced quintic saturation,

$$I_{\omega, \chi^{(5)}}^{\text{th}} = \frac{n_2^{\text{eff}}}{n_4} = 1.32 \times 10^{14} \text{ W/cm}^2. \quad (18)$$

Even higher than  $I_{\omega, \text{MPI}}^{\text{max}}$ , quintic saturation still plays a significant role in lowering the overall intensity threshold. Computing the zeros of  $\Delta n$ , for which MPI and  $\chi^{(5)}$  nonlinearities both saturate Kerr focusing, no longer yields the solution  $y=1$ , but instead  $y=0.94$ , which lowers  $I_\omega^{\text{max}}$  below  $4.5 \times 10^{13} \text{ W/cm}^2$ . The self-guiding length is then enhanced accordingly,

$$\Delta z_{\text{MPA}} \sim \frac{2}{\beta_\omega^{(K_\omega)} (I_{\omega, \text{MPI}}^{\text{max}})^{K_\omega-1}} \approx 1.63 \text{ m}. \quad (19)$$

It becomes augmented by the multiplicative factor  $y^{-7} \sim 1.5$ , which agrees with Fig. 1(d).

Figure 7 shows the peak intensity [7(a)], mean beam radius [7(b)], temporal distribution [7(c)], and averaged spectra at  $z=3.24 \text{ m}$  [7(d)] from the input beam (6) used as an initial condition for Eq. (13). In Figs. 7(a) and 7(b), the dashed lines report the peak intensity and mean radius plotted in Fig. 1(a), while the dotted curve represents the same quantities computed from Eq. (13) in the pure  $\chi^{(5)}$  limit,  $C \rightarrow 0$ . Remarkably, this equation restores nearly the same pulse dynamics as that observed in Figs. 1(a), 1(b), and 3(c). Even though THG is “formally” not existing in Eq. (13), its corresponding quintic saturation promotes close temporal distortions [Fig. 7(c)]. It helps in symmetrizing the pulse spectra and in enhancing spectral enlargement towards the blue side,

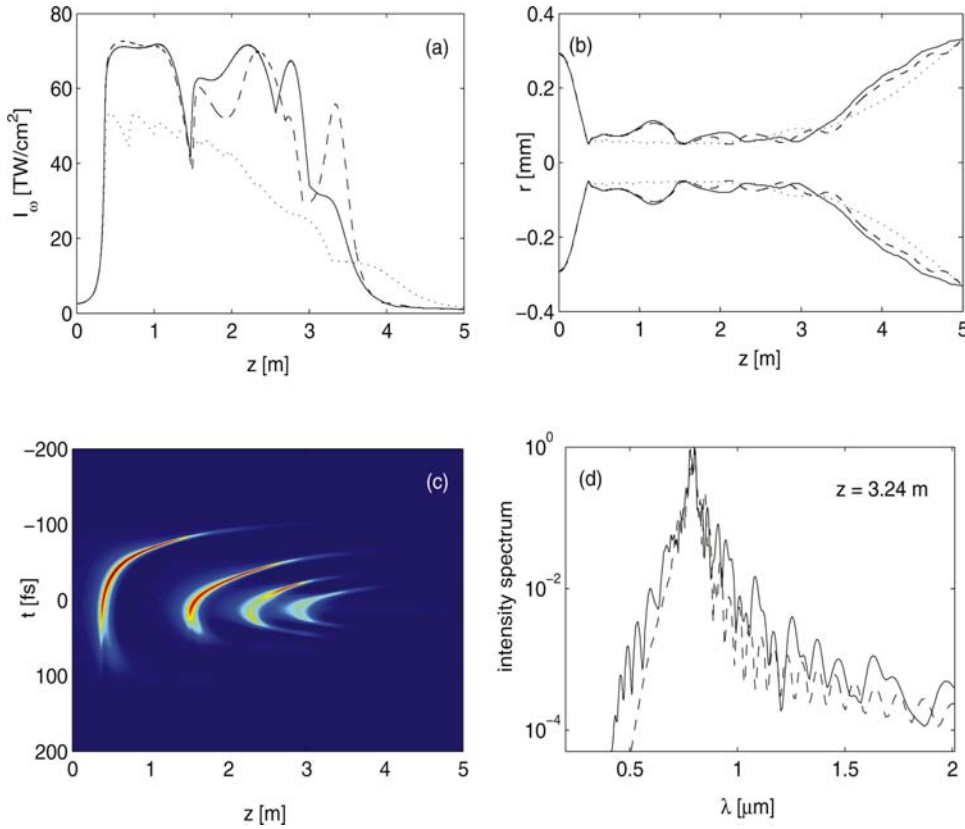


FIG. 7. (Color) (a) Peak intensities for a 0.5 mm-waisted pulse with  $4P_{cr}$  taken as the input condition for Eq. (13) (solid curve), for Eqs. (2) and (3) (dashed curve) and in the pure  $\chi^{(5)}$  limit  $C \rightarrow 0$  (dotted curve). (b) Mean FWHM radius of the same solutions. (c) Temporal distribution corresponding to the dynamics described by Eq. (13). (d) Averaged spectrum at  $z = 3.24$  m computed from Eq. (13) (solid curve) and from Eq. (2) without THG (dashed curve).

compared with an IR pulse undergoing plasma defocusing alone [Fig. 7(d)]. These last numerical results reproduce spectra resembling those depicted in Fig. 3, apart from the UV broadband earlier excited by THG which is, of course, absent here. They suggest that, even if current models of pulses propagating in air may not account for TH excitation and discard integration of Eq. (3), they should at least include a saturated quintic nonlinearity [last term in Eq. (13)] with the effective  $n_4$  given by Eq. (15).

## VII. CONCLUSION

In summary, we have investigated the influence of phase-locked propagation of TH pulses on the white-light continuum spectrum generated by the fundamental IR pulse over meter-range propagation distances. From numerical computations supported by theoretical estimates, we demonstrated that the third-order harmonics significantly contributes to the supercontinuum generation. As already expected in [29,30], TH is generated and maintains the beam energy and intensity over long distances within a two-colored filament. In this filament, the IR pulse is subject to SPM which broadens the spectrum asymmetrically towards the red direction, caused by the early plasma defocusing of the back of the pulse. Simultaneously, the UV spectral region undergoes a wide broadening, as the dephasing between the two components stays locked at  $\Delta\phi = \pi$  all along the self-channeling process. This property, discovered in [29] over a few cm, has been put in evidence upon several meters of filamentation. The  $\pi$ -phase locking guarantees that SPM of the dominant IR pulse has a direct incidence on the UV part in the spectrum,

which becomes three times more enlarged in frequency. This mechanism finally results in a superimposition of the blue-shifted IR spectrum with the strongly redshifted UV one and to the build-up of novel wavelengths in the intermediate range  $200 \text{ nm} \leq \lambda \leq 500 \text{ nm}$ . This phenomenon was experimentally confirmed by atmospheric sensing experiments performed with the Teramobile laser facility. By means of chirped (150 fs), cm-waisted pulses delivering several TW in power, vertical shots in the atmosphere allowed us to display evidence of this supercontinuum generation starting from the deepest UV wavelengths.

Next, we analyzed the conical emission induced by the spatial variations occurring in the nonlinear phase of the two-colored filament. Numerical computations of the CE revealed that the angular divergence still increases at decreasing wavelengths going down to the UV region, in the same proportions as inside the Teramobile bundle. A steep angular deviation of  $0.1^\circ$  produced at  $\lambda \sim 250 \text{ nm}$  was revealed by both the experiment and numerical computations, which clearly proves that the TH component undergoes a more important spectral diffraction. Increase of the CE angle at UV wavelengths is also a consequence of the  $\pi$ -phase locking. It can also be attributed to the additional saturable nonlinearity originating from THG, which reinforces the defocusing action of MPI.

In connection with this point, the last—but not least—important result consisted in the partial stabilization of the two-colored filament by THG, whose principal effect on the IR pulse dynamics is to introduce a quintic, defocusing nonlinearity at large wave-vector mismatch values. This extra defocusing contribution arises as a saturating nonlinearity in

the form  $-n_4|\mathcal{E}_\omega|^4\mathcal{E}_\omega/(1+6k_0n_2|\mathcal{E}_\omega|^2/|\Delta k|)$ , which lowers the maximum intensity threshold reached by the  $\omega$  component and, thereby, enhances the self-guiding range by an efficient decrease of the MPA damping of the filament. Even weak, this stabilization mechanism participates in making SPM-broadened spectra more symmetric and prolonging the lifetime of the filament.

The question of knowing whether  $\chi^{(5)}$  saturation is important or not was raised in several recent papers (see, e.g., [4,5]), where quintic saturations were suggested to influence the propagation dynamics. However, no precise evaluation of the quintic coefficient  $n_4$  was given, as no specific measurement of higher-order nonlinearities was realized nowadays at

800 nm for di-oxygen molecules. Our present investigation clearly shows that THG can be a key player in stabilizing femtosecond filaments in air by acting like a  $\chi^{(5)}$  defocusing nonlinearity with a quite definite  $n_4$  coefficient proposed in Eq. (15). Further models of femtosecond pulse propagation in air should be modified accordingly.

#### ACKNOWLEDGMENTS

The authors thank Professor Falk Lederer and Professor Ulf Peschel for fruitful discussion. Experiments were realized in the framework of the Teramobile Project, funded jointly by CNRS and DFG.

- 
- [1] A. Braun, G. Korn, X. Liu, D. Du, J. Squier, and G. Mourou, *Opt. Lett.* **20**, 73 (1995).
- [2] E. T. J. Nibbering, P. F. Curley, G. Grillon, B. S. Prade, M. A. Franco, F. Salin, and A. Mysyrowicz, *Opt. Lett.* **21**, 62 (1996).
- [3] B. LaFontaine, F. Vidal, Z. Jiang, C. Y. Chien, D. Comtois, A. Desparois, T. W. Johnston, J. C. Kieffer, H. Pépin, and H. P. Mercure, *Phys. Plasmas* **6**, 1615 (1999).
- [4] N. Aközbek, C. M. Bowden, A. Talebpour, and S. L. Chin, *Phys. Rev. E* **61**, 4540 (2000).
- [5] N. Aközbek, M. Scalora, C. M. Bowden, and S. L. Chin, *Opt. Commun.* **191**, 353 (2001).
- [6] I. G. Koprnikov, A. Suda, P. Wang, and K. Midorikawa, *Phys. Rev. Lett.* **84**, 3847 (2000).
- [7] H. R. Lange, G. Grillon, J. F. Ripoche, M. A. Franco, B. Lamouroux, B. S. Prade, A. Mysyrowicz, E. T. J. Nibbering, and A. Chiron, *Opt. Lett.* **23**, 120 (1998).
- [8] A. Brodeur, C. Y. Chien, F. A. Ilkov, S. L. Chin, O. G. Kosareva, and V. P. Kandidov, *Opt. Lett.* **22**, 304 (1997).
- [9] M. Mlejnek, E. M. Wright, and J. V. Moloney, *Opt. Lett.* **23**, 382 (1998).
- [10] S. Champeaux and L. Bergé, *Phys. Rev. E* **68**, 066603 (2003).
- [11] J. Schwarz, P. Rambo, J. C. Diels, M. Kolesik, E. M. Wright, and J. V. Moloney, *Opt. Commun.* **180**, 383 (2000).
- [12] S. Tzortzakis, B. Lamouroux, A. Chiron, M. Franco, B. Prade, A. Mysyrowicz, and S. D. Moustazis, *Opt. Lett.* **25**, 1270 (2000).
- [13] A. Couairon and L. Bergé, *Phys. Rev. Lett.* **88**, 135003 (2002).
- [14] A. Couairon, S. Tzortzakis, L. Bergé, M. Franco, B. Prade, and A. Mysyrowicz, *J. Opt. Soc. Am. B* **19**, 1117 (2002).
- [15] Th. Lehner and N. Aubry, *Phys. Rev. E* **61**, 1996 (2000).
- [16] H. Ward and L. Bergé, *Phys. Rev. Lett.* **90**, 053901 (2003).
- [17] A. L. Gaeta, *Phys. Rev. Lett.* **84**, 3582 (2000).
- [18] G. P. Agrawal, *Nonlinear Fiber Optics*, 3rd ed. (Academic, New York, 2001), pp. 274.
- [19] O. Kosareva, V. P. Kandidov, A. Brodeur, C. Y. Chien, and S. L. Chin, *Opt. Lett.* **22**, 1332 (1997).
- [20] J. Kasparian, R. Sauerbrey, D. Mondelain, S. Niedermeier, J. Yu, J. P. Wolf, Y. B. André, M. Franco, B. Prade, S. Tzortzakis, A. Mysyrowicz, M. Rodriguez, H. Wille, and L. Wöste, *Opt. Lett.* **25**, 1397 (2000).
- [21] L. Wöste, C. Wedekind, H. Wille, P. Rairoux, B. Stein, S. Nikolov, C. Werner, S. Niedermeier, F. Ronneberger, H. Schillinger, and R. Sauerbrey, *Laser Optoelektron.* **29**, 51 (1997).
- [22] S. L. Chin, S. Petit, F. Borne, and K. Miyazaki, *Jpn. J. Appl. Phys., Part 2* **38**, L126 (1999).
- [23] H. Wille, M. Rodriguez, J. Kasparian, D. Mondelain, J. Yu, A. Mysyrowicz, R. Sauerbrey, J. P. Wolf, and L. Wöste, *Eur. Phys. J.: Appl. Phys.* **20**, 183 (2002).
- [24] J. Kasparian, M. Rodriguez, G. Méjean, J. Yu, E. Salmon, H. Wille, R. Bourayou, S. Frey, Y. B. André, A. Mysyrowicz, R. Sauerbrey, J. P. Wolf, and L. Wöste, *Science* **301**, 61 (2003).
- [25] M. Rodriguez, R. Bourayou, G. Méjean, J. Kasparian, J. Yu, E. Salmon, A. Scholz, B. Stecklum, J. Eislöffel, U. Laux, A. P. Hatzes, R. Sauerbrey, L. Wöste, and J. P. Wolf, *Phys. Rev. E* **69**, 036607 (2004).
- [26] G. Méjean, J. Kasparian, E. Salmon, J. Yu, J. P. Wolf, R. Bourayou, R. Sauerbrey, M. Rodriguez, L. Wöste, H. Lehmann, B. Stecklum, U. Laux, J. Eislöffel, A. Scholz, and A. P. Hatzes, *Appl. Phys. B: Lasers Opt.* **77**, 357 (2003).
- [27] J. P. Wolf, *Encyclopedia of Analytical Chemistry*, edited by R. A. Meyers (Wiley, Chichester, 2000), Vol. 3, pp. 2226–2245.
- [28] G. Méjean, J. Kasparian, J. Yu, S. Frey, E. Salmon, and J. P. Wolf, *Appl. Phys. B: Lasers Opt.* **78**, 535 (2004).
- [29] N. Aközbek, A. Iwasaki, A. Becker, M. Scalora, S. L. Chin, and C. M. Bowden, *Phys. Rev. Lett.* **89**, 143901 (2002).
- [30] H. Yang, J. Zhang, J. Zhang, L. Z. Zhao, Y. J. Li, H. Teng, Y. T. Li, Z. H. Wang, Z. L. Chen, Z. Y. Wei, J. X. Ma, W. Yu, and Z. M. Sheng, *Phys. Rev. E* **67**, 015401(R) (2003).
- [31] Y. R. Shen, *The Principles of Nonlinear Optics* (Wiley, New York, 1984).
- [32] S. Backus, J. Peatross, Z. Zeek, A. Rundquist, G. Taft, M. M. Murnane, and H. C. Kapteyn, *Opt. Lett.* **21**, 665 (1996).
- [33] A. B. Fedotov, N. I. Koroteev, M. M. T. Loy, X. Xiao, and A. M. Zheltikov, *Opt. Commun.* **133**, 587 (1997).
- [34] G. Marcus, A. Zigler, and Z. Henis, *J. Opt. Soc. Am. B* **16**, 792 (1999).
- [35] C. J. Zhu, Y. D. Qin, H. Yang, S. F. Wang, and Q. H. Gong, *Chin. Phys. Lett.* **18**, 57 (2001).
- [36] J. F. Ripoche, G. Grillon, B. Prade, M. Franco, E. Nibbering, R. Lange, and A. Mysyrowicz, *Opt. Commun.* **135**, 310 (1997).
- [37] L. Bergé and A. Couairon, *Phys. Plasmas* **7**, 210 (2000).
- [38] L. Bergé, S. Skupin, F. Lederer, G. Méjean, J. Yu, J. Kaspar-

- ian, E. Salmon, J. P. Wolf, M. Rodriguez, L. Wöste, R. Bourayou, and R. Sauerbrey, *Phys. Rev. Lett.* **92**, 225002 (2004); S. Skupin, L. Bergé, U. Peschel, F. Lederer, G. Méjean, J. Yu, J. Kasparian, E. Salmon, J. P. Wolf, M. Rodriguez, L. Wöste, R. Bourayou, and R. Sauerbrey, *Phys. Rev. E* **70**, 046602 (2004).
- [39] R. M. Measures, *Laser Remote Sensing—Fundamentals and Applications* (Wiley Interscience, New York, 1984).
- [40] P. Rairoux, H. Schillinger, S. Niedermeier, M. Rodriguez, F. Ronneberger, R. Sauerbrey, B. Stein, D. Waite, C. Wedekind, H. Wille, L. Wöste, and C. Ziener, *Appl. Phys. B: Lasers Opt.* **71**, 573 (2000).
- [41] A. V. Buryak, V. V. Steblina, and R. A. Sammut, *Opt. Lett.* **24**, 1859 (1999).
- [42] L. Bergé, Cl. Gouédard, J. Schjødt-Eriksen, and H. Ward, *Physica D* **176**, 181 (2003).
- [43] L. Bergé, *Phys. Rev. E* **69**, 065601(R) (2004).
- [44] G. Méjean, J. Kasparian, J. Yu, S. Frey, E. Salmon, R. Ackermann, J. P. Wolf, L. Bergé, and S. Skupin (unpublished).
- [45] M. Kolesik, G. Katona, J. V. Moloney, and E. M. Wright, *Phys. Rev. Lett.* **91**, 043905 (2003); M. Kolesik, E. M. Wright, and J. V. Moloney, *ibid.* **92**, 253901 (2004).



ELSEVIER

Available online at [www.sciencedirect.com](http://www.sciencedirect.com)

SCIENCE @ DIRECT®

Optics Communications 247 (2005) 171–180

OPTICS  
COMMUNICATIONS

[www.elsevier.com/locate/optcom](http://www.elsevier.com/locate/optcom)

## Range of plasma filaments created in air by a multi-terawatt femtosecond laser

G. Méchain<sup>a,\*</sup>, C.D'Amico<sup>a</sup>, Y.-B. André<sup>a</sup>, S. Tzortzakis<sup>a,1</sup>, M. Franco<sup>a</sup>,  
B. Prade<sup>a</sup>, A. Mysyrowicz<sup>a</sup>, A. Couairon<sup>b</sup>, E. Salmon<sup>c</sup>, R. Sauerbrey<sup>d</sup>

<sup>a</sup> *Laboratoire d'Optique Appliquée, Centre National de la Recherche, Unité Mixte de Recherche 7639, Ecole Nationale Supérieure de Techniques Avancées – Ecole Polytechnique, Chemin de la Lumière, F-91761 Palaiseau Cedex, France and Teramobile project*

<sup>b</sup> *Centre de Physique Théorique, Ecole Polytechnique, CNRS UMR 7644, Palaiseau 91128, France*

<sup>c</sup> *Laboratoire de spectrométrie ionique et moléculaire, CNRS UMR 5579, Université Lyon I, 69622 Villeurbanne, France and Teramobile project*

<sup>d</sup> *Institut für Optik und Quantenelektronik, Jena, 07743, Germany and Teramobile project*

Received 8 July 2004; received in revised form 9 November 2004; accepted 11 November 2004

### Abstract

The propagation of a multi-terawatt femtosecond laser pulse in air is studied as a function of initial chirp. The chirp conditions for optimising air ionisation at long distance are presented. Ionisation channels are observed over a distance reaching 400 m.

© 2004 Elsevier B.V. All rights reserved.

PACS: 42.25.Bs; 42.65.Re; 42.65.Jx; 52.38.Hb; 52.35.Mw

Keywords: Femtosecond filamentation; Ultrashort laser pulses

### 1. Introduction

There is increasing interest in the study of femtosecond laser self-guiding (filamentation) in air

and other transparent media. The physical processes underlying this effect are now well understood. Filamentation arises predominantly from a dynamic competition between the optical Kerr effect, which leads to beam self-focusing and air ionisation by multi-photon absorption, preventing beam collapse by beam defocusing [1,2]. Air ionisation involves the simultaneous absorption of at least 8 infrared photons, so that it occurs for a threshold like intensity  $I \sim 10^{13} \text{ W/cm}^2$ . In the case of an input power close to the critical power for

\* Corresponding author. Tel.: +33 1693 19702; fax: +33 1693 19996.

E-mail addresses: [mechain@ensta.ensta.fr](mailto:mechain@ensta.ensta.fr) (G. Méchain), [stzortz@greco2.polytechnique.fr](mailto:stzortz@greco2.polytechnique.fr) (S. Tzortzakis).

<sup>1</sup> Present address: Laboratoire d'Utilisation des Lasers Intenses, UMR 7605, CNRS-CEA-Université Paris VI- Ecole Polytechnique, 91128 Palaiseau, France.

filamentation ( $P_{\text{cr}} \approx 5$  GW for air at normal pressure and a laser central wavelength of 800 nm), the main features of the filament which is formed, such as spectral broadening, pulse shortening, beam contraction and plasma channel formation, are in good agreement with numerical simulations that solve a non linear Schrödinger equation for the envelope of the propagating field [3–6]. At higher input power,  $P \gg P_{\text{cr}}$ , the beam splits into a large number  $N$  of filaments, with  $N \approx P/P_{\text{cr}}$  [7–9]. This situation is less well understood, due on the one hand to the complexity of numerical simulations which require a full “3d + 1” treatment over a long path [5,10,30] and on the other hand to the difficulty in measuring the beam characteristics over long propagation distances  $D > 100$  m, due to the sensitivity of the multifilamentary pattern on the initial beam characteristics and on atmospheric turbulence.

Long-range filamentation of femtosecond laser pulses in air can lead to several applications [11]. The broad white continuum generated during self-guided propagation can be exploited for multi-component LIDAR studies of air pollution [12–14]. The creation of plasma column can be used to trigger and guide electric discharge, and eventually can lead to a new type of lightning rod [15–17]. Finally, the high local intensity of the self-guided laser pulse can be used for laser-induced plasma spectroscopy (LIPS) of remote targets [18]. Thus, depending on the particular application, it is important to maximise either continuum generation, the length of ionisation channels or the laser intensity at long distance.

One important laser parameter in this respect is the initial chirp of the laser pulse. For ultra-short pulses at 800 nm, the pulse duration is expected to increase because of group velocity dispersion of air. This detrimental effect can be precompensated by imparting a negative initial chirp [19,20]. Initial chirped laser pulse has another effect. By increasing the pulse duration at constant pulse energy, it decreases its peak power [21]. This is expected to increase the distance necessary for the onset of filamentation [23] and also to reduce the number  $N$  of generated filaments.

In this paper, we report experimental results concerning the long propagation of IR multi-tera-

watt laser pulses on a horizontal path. Measurements are performed as a function of initial laser chirp. We are particularly interested in measuring the length over which ionised plasma channels are formed. We also investigate the conditions for optimal continuum generation at long distance  $D > 600$  m.

## 2. Experimental procedure

The experiments have been performed with a Ti:Sapphire multi-terawatt laser system, called Teramobile. A detailed description of the laser is given in [21]. The laser operates with a central wavelength at 800 nm and an energy per pulse of up to 190 mJ at a repetition rate of 10 Hz. The beam diameter at the output of the compressor is 34 mm with a pronounced top-hat profile, as shown in Fig. 1. Since the laser is based on the chirped pulse amplification (CPA) technique [24,25], the initial chirp of the laser pulse can be easily adjusted. For the present campaign, the laser final compression stage was modified so that it could produce pulses with a negative chirp (shorter wavelength first) varying between 0.2 and 9.6 ps pulses. This corresponds to respectively 190 and 4 times the critical value  $P_{\text{cr}} = 5$  GW for

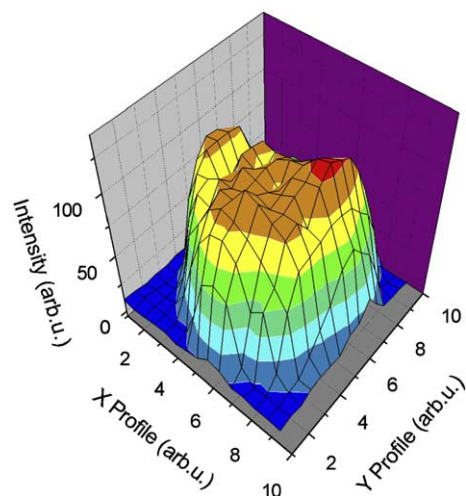


Fig. 1. Profile of the beam. Intensity recorded at the output of the compressor.

laser pulses at 800 nm. This implies that the initial power of the laser is always higher than the critical power necessary to create filaments in air. In order to obtain large negative chirps, one of the gratings of the compressor was mounted on a 40-mm translation stage. The compressor was calibrated with an autocorrelator measuring the pulse duration as a function of the distance between the gratings, yielding the value 241 fs/mm. The collimated laser beam was launched horizontally 3 m above a paved road to a maximum distance of 600 m. Longer distances of 1000 and 2350 m were also available.

Measurement of the beam intensity in a filament is a difficult task, even in the case of a well-controlled single filament in the laboratory. The most reliable method, which is based on the generation by a filament of high order odd harmonics in an atomic gas cell [26], requires an elaborate set-up with precise alignment. Additional difficulties in the present case are the high input power, leading to multifilamentary structures that may vary from shot to shot, and the effect of air turbulence [29], which produces fluctuations in the position of the beam at long distance.

In view of these difficulties, we have adopted the following procedure. We first measure the occurrence of air ionisation as a function of distance for a given initial laser chirp. Optical field ionisation of air is detected with two electric techniques described below. The onset of ionisation yields a precise value of the laser intensity, which is independently known both from experiments in single filament and from simulations. Next we correlate the ionisation signal measured as a function of distance with the darkening of preexposed photographic paper (Kodak linagraph paper, type 1895). To confirm this calibration, the same procedure is repeated in the laboratory using a well-characterized single filament. This procedure allows us to determine in a single shot the intensity profile in a complex multifilamentary pattern at a given distance with an order-of-magnitude accuracy.

Calibration of the photographic paper in the laboratory proceeds as follows. First, we measure the electric conduction of the plasma channel using the method described in [27]. Two electrodes with

small holes in their centre and separated by 3 cm are placed in the filament path. A potential difference of 1000 V is applied between the electrodes. The conducting channel formed by the filament between the electrodes closes the electric circuit and induces a current that is monitored across a load resistance of 8.2 k $\Omega$ . Keeping constant the interelectrode distance and moving the circuit along the propagation axis, one obtains a characteristic ionisation curve as shown in Fig. 2(b) (black squares). A second technique measures directly the electric signal obtained when the filament impinges on the exposed copper tip of a coaxial cable connected to an oscilloscope [28]. This induces a voltage measured with a low inductance electric circuit (grey triangles).

Both types of signals recorded as a function of distance, are shown in Fig. 2(b). For comparison, we also show in Fig. 2(c) the calculated length of the plasma channel and the corresponding laser intensity in the filament for the same experimental conditions. These results have been obtained by solving numerically the non-linear Schrödinger equation governing the slowly varying envelope of the laser field [6]. Various physical effects are taken into account: diffraction, group velocity dispersion and higher-order dispersive terms, self-focusing, stimulated Raman scattering, plasma absorption and defocusing, space-time focusing and self-steepening. More details on the physical model used in the code can be found in [6]. Since the results in Fig. 2 correspond to single filaments produced in laboratory experiment, 2 + 1 dimensional simulations were performed by assuming revolution symmetry around the propagation axis. Usually, a resolution of 10 microns in the transverse direction and 1–3 fs in the time direction is sufficient but much higher resolution can be achieved with fixed step size or with adaptative mesh if necessary. As can be seen in Fig. 2(c), there is a sharp threshold-like onset of ionisation when the laser intensity reaches the value  $10^{13}$  W/cm<sup>2</sup>; this correspond to an electric signal of 10–30 mV induced in the coaxial cable. For the same points in the path of the filament, pictures of the beam profile were also recorded on a photosensitive paper in single shot exposures. The black spot recorded on the photographic paper was scanned

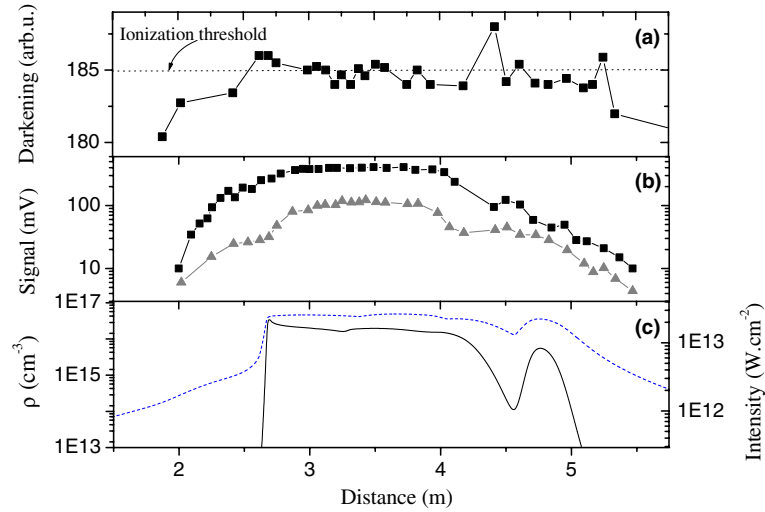


Fig. 2. (a) Darkening of a photographic papers measured along the laser propagation axis. (b) Electric conductivity of air (black square) and induced voltage on a coaxial detector (grey triangle) measured along the laser propagation axis. (c) Numerical simulation. The black continuous line represents the electron density ( $\rho$ ) (scale on the left axis). The dotted line gives the intensity in the core of the filament (scale on the right axis).

and its darkening was plotted as a function of propagation distance. The value of darkening corresponding to the ionisation threshold is given at the extremities of the plasma string at  $z = 2.6$  and at  $z = 5.1$  m. This corresponds to a value around 185 (in arbitrary units) for the darkening curve of the photographic paper (see Fig. 2(a)). It is adopted as the minimum value for which ionisation of air occurs in long-range propagation experiments. In this range of value the photographic paper is in a saturated regime.

The same procedure relating electric and photographic exposure traces has been applied to outdoor, long distance experiments for two different laser chirps. First, the electric conductivity of the plasma channel was measured for a pulse duration stretched to 0.2 ps. For this chirp value, the observed filaments are rather reproducible in position from shot to shot and can be tracked over several tens of meters of propagation. Measurements recorded at several points along the propagation are reported in Fig. 3(a). To assess the darkening of the photographic papers that corresponds to the ionisation threshold, the last value of the plateau on the electric signal has been related to the degree of darkening at the same distance. The de-

duced value is about 185 in arbitrary units, consistent with the value obtained in the laboratory experiment.

We have also measured the electric signal for an initial pulse stretched to 2.4 ps. In this case, fluctuations in position become more important, making the electric conductivity measurement unreliable. We have instead recorded the electric signal produced by the central wire of the coaxial cable placed on the beam (see Fig. 3(b)). As discussed above, the ionisation threshold is reached for an electric signal of about 10 mV. This corresponds to a darkening of about 188 in arbitrary units, as shown in Fig. 3, in accordance with the previous results. We have therefore used the darkening of the paper as method to characterize the multi-filamentary-pattern, for various initial chirps on the beam path.

### 3. Long-range beam characterisation

One series of photographic exposures recorded at four distances, 21, 50, 68, and 109 m is shown in Fig. 4 for a negative initial pulse duration of 1.2 ps. One can clearly observe in the transverse

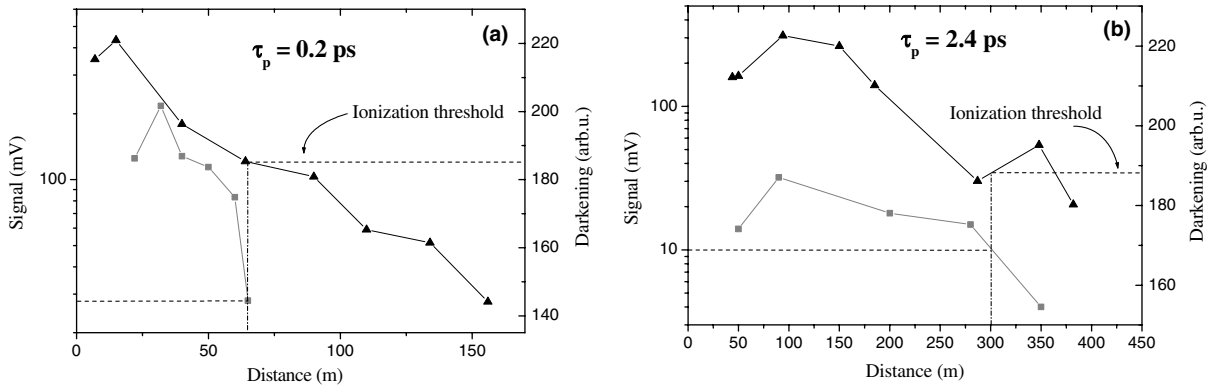


Fig. 3. (a) Comparison of the darkening between photosensitive paper (black triangle) and electric conductivity measurements (grey square) for a pulse duration stretched to 0.2 ps. (b) Comparison between photosensitive paper (black triangle) and coaxial cable measurements (grey square) for a pulse duration stretched to 2.4 ps.

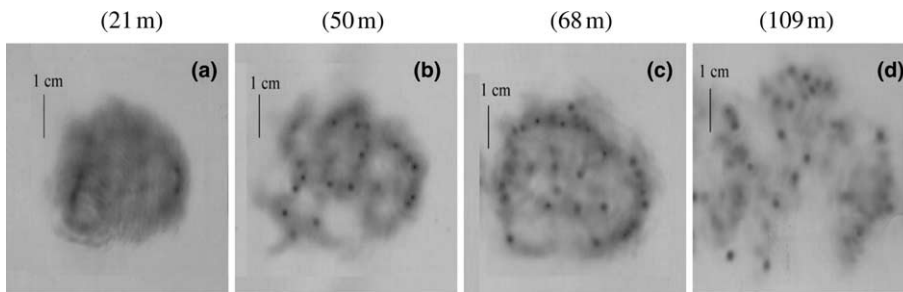


Fig. 4. Measured beam profile at various distances with a initial pulse duration stretched to 1.2 ps.

section of Fig. 4(a)–(c) the appearance of a number of high intensity channels that tend to appear on a ring at the periphery of the beam. This highly uneven intensity distribution of the beam intensity profile persists after a hundred meters of propagation (Fig. 4(d)). High intensity channels are also linked by an energy web organization. The ring like multi-filamentary structure can be understood, by considering the initial superGaussian beam profile (see Fig. 1). Since the self-focusing process initiates filamentation by excitation of a limited range of transverse wavenumbers [7], one expects few filaments in the centre of the beam, because of its flat intensity profile corresponding to wavenumbers having a weak amplification rate, and an accumulation of filaments around the beam edge, where intensity gradients are maximum. As shown in Fig. 5, this behaviour is well reproduced numerically by the same three-dimensional + time propa-

gation code used in [10,30]. The physical model is that described in [30] and takes account of the afore mentioned effects. The code follows a split step Crank–Nicholson, Fourier (in time) scheme. Unevenly distributed adaptative mesh grids allow us to adjust the resolution to the wide range of spatial and temporal scales. The initial beam intensity profile at  $d = 0$  (see Fig. 1) is introduced in the code as an initial condition.  $10^5$  spatial grid points in the transverse dimension were sufficient to reproduce the light tubes shown in Fig. 5(a) with a resolution of 100  $\mu\text{m}$ . The temporal resolution was varied in the range 3–15 fs. No atmospheric turbulence is included in these calculations, first because the patterns recorded experimentally were rather reproducible from shot to shot, second because the scale of viscous dissipation is about 1 mm [29] which is slightly larger than the light tubes and third because it is mainly the intensity

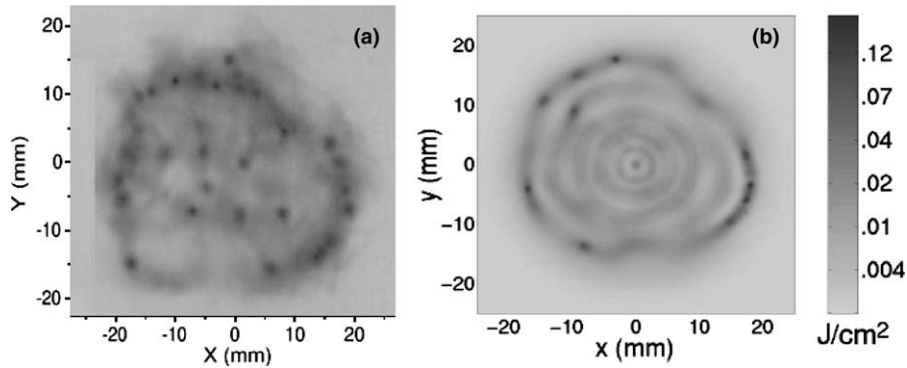


Fig. 5. Comparison between experiment and simulation after 68 m of propagation for a beam initially stretched to 1.2 ps. (a) Beam cross-section recorded with a photosensitive paper. (b) Computed distribution of fluence.

gradients in the nearly top hat beam profile (see Fig. 1) which are responsible of the organization of the light channels on the periphery of the input beam. A much cleaner beam with regular azimuthal perturbations was numerically shown to produce similar patterns except that the light tubes are regularly located on polygonal figures [30].

The photographic papers have been scanned in a densitometer through the highest intensity spots. Results are shown in (Fig. 6). Between  $d = 50$  and 68 m, the trace is saturated or even burned (Fig. 6(a)). At longer distances, one observes a broadening of the spot size and a decrease of the darkening.

From such measurements, one deduces that air ionisation takes place over a distance of up to 100 m.

In Fig. 7, a count of the number of hot spots giving a signal exceeding the ionisation threshold and a count of the number of light channels are given for three representative chirps as a function of distance. Light channels are defined here to be high intensity spots within the beam profile with insufficient intensity to ionise air. The intensity of light channels is in the range  $5 \times 10^{10}$ – $10^{13}$  W/cm<sup>2</sup> as deduced from the darkening of photographic plates comprised between 145 and 185

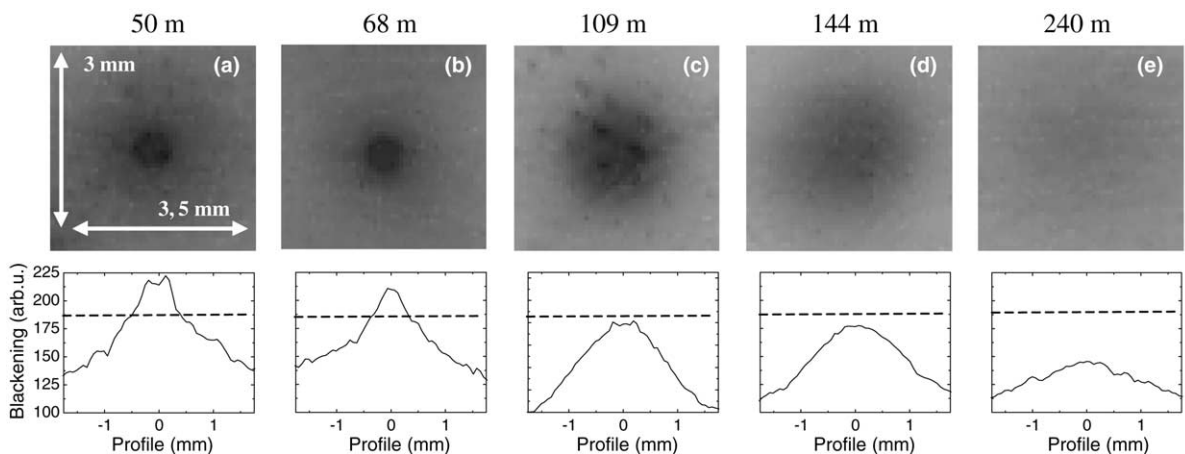


Fig. 6. Experimental burning spots of the laser on photographic paper at five various distances and for an initial pulse duration of  $\tau_p = 1.2$  ps. For each distance, the intensity profile has been reported below, dotted lines show the ionisation threshold (in arbitrary units).

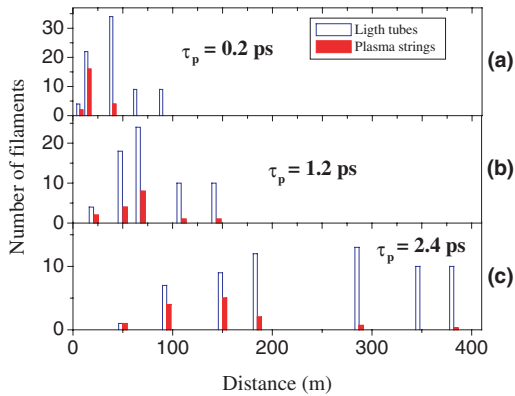


Fig. 7. Evolution of the number of filaments in step with distance for three consecutive pulse duration: (a) 0.2 ps, (b) 1.2 ps, (c) 2.4 ps.

(see Fig. 11(c)). Adopting the criterion that an ionising filament is formed if, at least one hot spot has a peak intensity exceeding the threshold value for ionisation (darkening  $>185$ , see Fig. 6), one can draw the filament length as a function of laser chirp. It is plotted in Fig. 8 as black lines. When the initial pulse duration is increased by introducing a negative chirp the peak power decreases. Filamentation occurs later but over a longer distance and with less plasma strings. For the pulse duration  $\tau_p = 2.4$  ps the length where ionisation occurs has been increased by more than a factor of 5 and

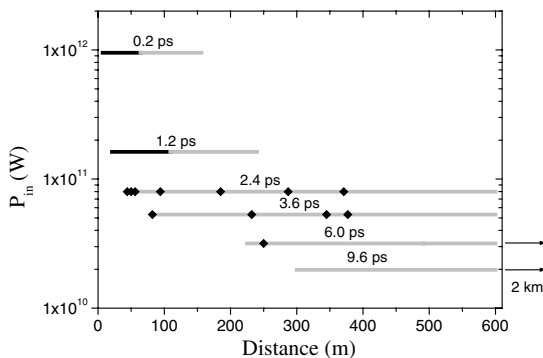


Fig. 8. Evolution of the length of filamentation by varying the initial chirp of the laser pulse. The pulse without chirp has a duration of 100 fs. The black lines and black points refer to locations where air ionisation could be detected, grey lines to distances where bright light channels are observed.

the number of filaments has been divided by 3. In a recent work, Golubtsov et al. [22] reported numerical simulations on the control of filamentation and the generation of supercontinuum by also varying the initial pulse-phase modulation (PPM). They predicted that a negative PPM shift the beginning of filamentation [16,21–23,31] and significantly extend the length of plasma channels. With an initial pulse duration of 800 fs and a negative PPM, the filamentation length reaches 800 m and is 2.5 times longer than with the transform-limited pulse ( $\tau_0 = 21$  fs). Our results are qualitatively comparable to most of the predictions made from the calculations of Golubtsov et al. [22]. Nevertheless, the calculated length of plasma channels is much longer than our experimental optimum. The numerical ionisation length reaches 800 m with a pulse duration of 800 fs, even though we find a maximum length of 300 m for a pulse duration of 2.4 ps. Numerical results sensitively depends on the specific shape of the input beam, the initial pulse parameters and experimental results depend also on the dynamics of plasma detection. This explains discrepancies between their simulations and our experiments, despite clear common general trends. Finally, the grey lines in Fig. 8 correspond to the formation of intense light channels, without occurrence of detectable ionisation. As reported recently, such bright light channels without measurable ionisation propagate over at least 2350 m [10].

The procedure using photosensitive paper has been repeated for various initial pulse duration with the results summarized in Fig. 9. The degree of darkening of papers corresponding each time to the strongest spots within the entire beam profile has been traced as a function of distance for different initial negative chirps. In the same figure, the value of the ionisation threshold is plotted as a horizontal dashed line. The degree of darkening for each curve above the ionisation value should be considered with circumspection, because the paper becomes saturated or even burned. However, it gives a rather reliable criterion for the onset of ionisation and therefore allows us to extract the distance over which air is ionised. An optimum was found for a negatively chirped pulse (duration of 2.4 ps). For this value, ionisation was observed

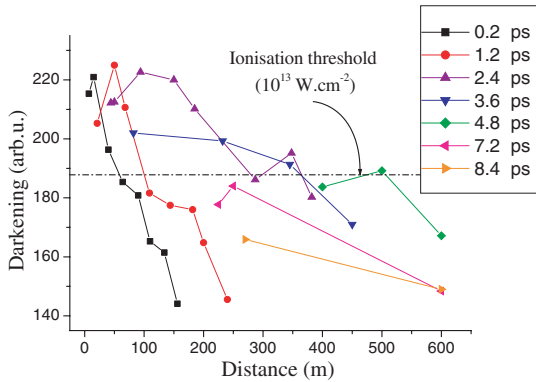


Fig. 9. Measurement of maximum of intensity in light filament as a function of distance for various stretched pulse durations.

over more than 300 m with a maximum of five ionising filaments in the beam profile.

Finally, we briefly address the question of optimising white continuum generation at long distance. The beam intercepted by a white screen was photographed with a digital camera at several distances. In Fig. 10, the beam cross-section recorded at 1000 m is compared for two values of the chirp, 0.2 and 9.6 ps. The first corresponds to the smallest duration of the pulse that can be realized with the modified compressor stage, the second gives the highest negative chirp achievable. One notices in the first case a bright continuum generation, without discernible hot spots, with a beam divergence of 1 mrad. In the second case, the whole beam profile is slightly compressed, and bright channels (which persists beyond 2350 m) are clearly observable.

For the longest pulse duration, 9.6 ps, photographs of the beam profile recorded at a distance of 2350 m are shown in Fig. 11(a) and (b). As discussed earlier, we were not able to measure reliable evidence of air ionisation under these conditions. An estimate of the laser intensity from the darkening of the photographic paper gives a peak value of about  $10^{12}$  W/cm<sup>2</sup>.

Assuming a conversion efficiency of 1–10% between the initial pulse and the broadband continuum, we can now estimate the total power as well as the fluence of the continuum on a distance of 1 km, since we know the white continuum beam divergence. We find an energy of 2–20 mJ in a continuum comprise between 300 and 950 nm and a fluence of  $2 \times 10^{-7}$ – $2 \times 10^{-6}$  J/cm<sup>2</sup> for an initial pulse duration close to minimum. On the other, with a negative chirp giving a pulse duration of 9.6 ps, we have typically between 5 and 7 light channels at 1 km. Only the bright channels generate continuum in this case. Assuming the same conversion efficiency into continuum of 1–10%, the continuum energy is in the ratio of (total surface of light tubes/beam surface)  $\sim 10^{-6}$ . However, the fluence is the same. Therefore, we conclude that a small negative chirp is better suited for applications where the continuum emission must be maximized.

The fact that ionisation is usually needed for balancing self-focusing is a physical picture that emerged from works on filaments generated by unchirped pulses at moderate powers. With multiple filaments generated by high-power beams, this picture is expected to be still correct for indepen-

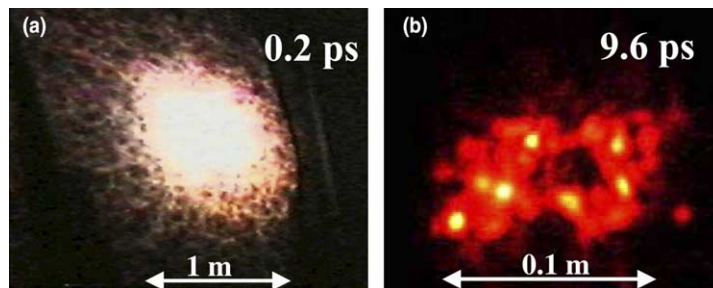


Fig. 10. Comparison between two beam cross-section at 1000 m. (a) minimum negative chirp: 0.2 ps, (b) maximum negative chirp: 9.6 ps.

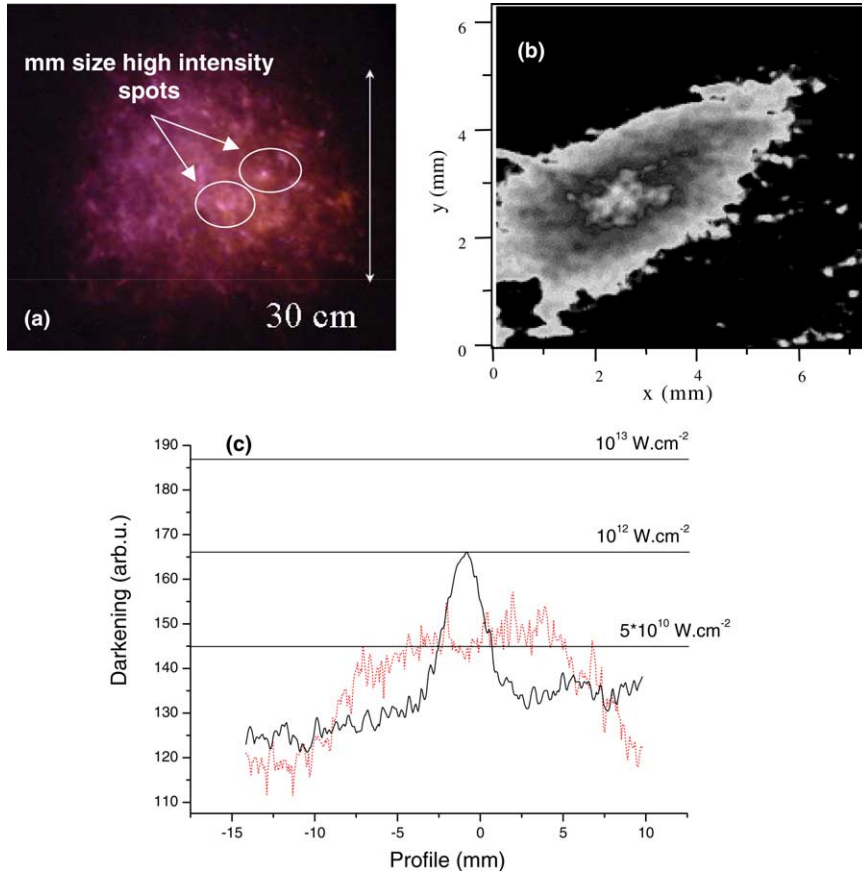


Fig. 11. Experiment at 2350 m. The beam had initial chirp of 9.6 ps. (a) Photography of the beam cross-section intercepted by a white screen. Exposure time of a few second. (b) Detail of a single shot light tube recorded with photosensitive paper. (c) Transverse profile (continuous curve) of the light tube at 2350 m. The dash curve represents the measured curve in laboratory (energy  $E = 20$  mJ, pulse duration 130 fs, diameter  $\Phi = 2$  cm) to determine the lower intensity limit of the light tubes.

dent filaments collapsing on themselves, a situation favoured with unchirped pulses. With powerful beams and large chirps, a large number of light tubes compete for the available laser energy over extended distance. The validity of this powerful concept of the energy reservoir, originally proposed in [5], was shown in detail for a single filament [32]. The collapse of a specific light channel into a plasma filament is more difficult when surrounding light channels prevent a fast concentration of power, which makes other mechanism such as, e.g., GVD, more efficient to arrest the collapse before ionisation occurs [33].

In conclusion, we have studied the beam profile of an intense IR femtosecond laser pulse as a function of distance, up to 2350 m, for different initial chirps. Using electric measurements and photographic recordings, we estimated the distance over which air ionisation was occurring. A maximum ionisation distance of 370 m was found for a laser with a negative chirp of 2.4 ps. A shorter pulse duration favoured the amount of broadband continuum detected at long distance, while longer negative chirps led to the appearance of bright light channels at 2350 m, the longest distance for which measurements were performed. The peak

intensities of such bright light spots was estimated to be around  $10^{12}$  W/cm<sup>2</sup>.

### Acknowledgements

This work has been funded by a special CNRS-DFG program, called Teramobile. A.M. is grateful to the Humboldt foundation for support.

### References

- [1] A. Braun, G. Korn, X. Liu, D. Du, J. Squier, G. Mourou, *Opt. Lett.* 20 (1995) 73.
- [2] E.T.J. Nibbering, P.F. Curley, G. Grillon, B.S. Prade, M.A. Franco, F. Salin, A. Mysyrowicz, *Opt. Lett.* 21 (1996) 62.
- [3] O.G. Kosareva, V.P. Kandidov, A. Brodeur, C.Y. Chien, S.L. Chin, *Opt. Lett.* 22 (1997) 1332.
- [4] M. Mlejnek, E.M. Wright, J.V. Moloney, *Opt. Lett.* 23 (1998) 382.
- [5] M. Mlejnek, M. Kolesik, E.M. Wright, J.V. Moloney, *Phys. Rev. Lett.* 83 (15) (1999) 2938.
- [6] A. Couairon, G. Méchain, S. Tzortzakis, M. Franco, B. Lamouroux, B. Prade, A. Mysyrowicz, *Opt. Commun.* 225 (2003) 177.
- [7] V.I. Bespalov, V.I. Talanov, *JETP Lett.* 3 (1966) 307.
- [8] B. LaFontaine, F. Vidal, Z. Jiang, C.Y. Chien, D. Comtois, A. Desparois, T.W. Johnson, J.-C. Kieffer et, H. Pépin, *Phys. Plasmas* 6 (1999) 1615.
- [9] Miguel Rodriguez, Riad Bourayou, Guillaume Méjean, Jérôme Kasparian, Jin Yu, Estelle Salmon, Alexander Scholz, Bringfried Stecklum, Jochen Eisloffel, Uwe Laux, Artie P. Hatzes, Roland Sauerbrey, Ludger Wöste, Jean-Pierre Wolf, *PRE* 69 (2004) 036607.
- [10] G. Méchain, A. Couairon, Y.-B. André, C. D'Amico, M. Franco, B. Prade, S. Tzortzakis, A. Mysyrowicz, R. Sauerbrey, *Appl. Phys. B* 79 (2004) 379.
- [11] J. Kasparian, M. Rodriguez, G. Méjean, J. Yu, E. Salmon, H. Wille, R. Bourayou, S. Frey, Y.-B. André, A. Mysyrowicz, R. Sauerbrey, J.-P. Wolf, L. Wöste, *Science* 301 (2003) 61.
- [12] L. Wöste, C. Wedekind, H. Wille, P. Rairoux, B. Stein, S. Nikolov, Ch. Werner, St. Niedermeier, F. Ronneberger, H. Schillinger, R. Sauerbrey, *Laser Optoelektron.* 29 (1997) 51.
- [13] J. Yu, D. Mondelain, G. Ange, B. Volk, S. Niedermeier, J.P. Wolf, J. Kasparian, R. Sauerbrey, *Opt. Lett.* 26 (2001) 533.
- [14] G. Méjean, J. Kasparian, J. Yu, S. Frey, E. Salmon, J.-P. Wolf, *Appl. Phys. B* 78 (2004) 535.
- [15] X.M. Zhao, J.-C. Diels, C.Y. Wang, J.M. Elizondo, *IEEE J. Quantum Electron.* 31 (1995) 599.
- [16] M. Rodriguez, R. Sauerbrey, H. Wille, L. Wöste, T. Fujii, Y.-B. André, A. Mysyrowicz, L. Klingbeil, K. Rethmeier, W. Kalkner, J. Kasparian, E. Salmon, J. Yu, J.-P. Wolf, *Opt. Lett.* 27 (2002) 772.
- [17] D. Comptois, et al., *IEEE Trans. Plasmas Sci.* 31 (2003) 377.
- [18] Ph. Rohwetter, J. Yu, G. Méjean, K. Stelmasczyk, E. Salmon, J. Kasparian, J.-P. Wolf, L. Wöste, *J. Anal. Atom Spectrom.* 19 (2004) 437.
- [19] G. Yang, Y. Shen, *Opt. Lett.* 9 (1984) 510.
- [20] A.L. Gaeta, *Phys. Rev. Lett.* 84 (2000) 3582.
- [21] H. Wille, M. Rodriguez, J. Kasparian, D. Mondelain, J. Yu, A. Mysyrowicz, R. Sauerbrey, J.-P. Wolf, L. Wöste, *Eur. Phys. J. AP* 20 (2002) 183.
- [22] I.S. Golubtsov, V.P. Kandidov, O.G. Kosareva, *Quantum Electron.* 33 (2003) 525.
- [23] J.H. Marburger, *Prog. Quantum Electron.* 4 (1975) 35.
- [24] D. Steickland, G. Mourou, *Opt. Commun.* 56 (1985) 219.
- [25] P. Maine, D. Strickland, P. Bado, M. Pessot, G. Mourou, *IEEE J. Quantum Electron.* 24 (1988) 398.
- [26] H.R. Lange, A. Chiron, J.-F. Ripoche, A. Mysyrowicz, P. Breger, P. Agostini, *Phys. Rev. Lett.* 81 (1998) 1611.
- [27] S. Tzortzakis, M.F. Franco, Y.-B. André, A. Chiron, B. Lamouroux, B.S. Prade, A. Mysyrowicz, *Phys. Rev. E* 60 (1999) 3505.
- [28] H.D. Ladouceur, A.P. Baronavski, D. Lorhmann, P.W. Grounds, P.G. Girardi, *Opt. Commun.* 189 (2001) 107.
- [29] S.L. Chin, A. Talebpour, J. Yang, S. Petit, V.P. Kandidov, O.G. Kosareva, M.P. Tamarov, *Appl. Phys. B* 74 (2002) 67.
- [30] G. Méchain, A. Couairon, M. Franco, B. Prade, A. Mysyrowicz, *Phys. Rev. Lett.* 93 (2004) 035003.
- [31] J. Kasparian, R. Sauerbrey, D. Mondelain, S. Niedermeier, J. Yu, J.-P. Wolf, Y.-B. André, M. Franco, B. Prade, S. Tzortzakis, A. Mysyrowicz, M. Rodriguez, H. Wille, L. Wöste, *Opt. Lett.* 25 (2000) 1397.
- [32] V.P. Kandidov, O.G. Kosareva, A.A. Koltun, *Quantum Electron.* 33 (2003) 69.
- [33] G. Fibich, G.C. Papanicolaou, *Opt. Lett.* 22 (1997) 1379.

# Filament-induced remote surface ablation for long range laser-induced breakdown spectroscopy operation<sup>☆</sup>

Ph. Rohwetter<sup>a</sup>, K. Stelmaszczyk<sup>a</sup>, L. Wöste<sup>a</sup>, R. Ackermann<sup>b</sup>, G. Méjean<sup>b</sup>, E. Salmon<sup>b</sup>,  
J. Kasparian<sup>b</sup>, J. Yu<sup>b,\*</sup>, J.-P. Wolf<sup>b</sup>

<sup>a</sup>*Fachbereich Physik der Freien Universität Berlin, Institut für Experimentalphysik, Arnimallee 14, D-14195 Berlin, Germany*

<sup>b</sup>*Laboratoire de Spectrométrie Ionique et Moléculaire (LASIM), UMR CNRS 5579, Université Claude Bernard-Lyon 1, 43, Bd. du 11 Novembre 1918, F-69622 Villeurbanne Cedex, France*

Received 13 December 2004; accepted 22 March 2005

Available online 16 June 2005

## Abstract

We demonstrate laser induced ablation and plasma line emission from a metallic target at distances up to 180 m from the laser, using filaments (self-guided propagation structures  $\sim 100\ \mu\text{m}$  in diameter and  $\sim 5 \times 10^{13}\ \text{W/cm}^2$  in intensity) appearing as femtosecond and terawatt laser pulses propagating in air. The remarkable property of filaments to propagate over a long distance independently of the diffraction limit opens the frontier to long range operation of the laser-induced breakdown spectroscopy technique. We call this special configuration of remote laser-induced breakdown spectroscopy “remote filament-induced breakdown spectroscopy”. Our results show main features of filament-induced ablation on the surface of a metallic sample and associated plasma emission. Our experimental data allow us to estimate requirements for the detection system needed for kilometer-range remote filament-induced breakdown spectroscopy experiment. © 2005 Elsevier B.V. All rights reserved.

*Keywords:* Laser filaments; Remote laser-induced surface ablation; Remote laser-induced breakdown spectroscopy

## 1. Introduction

Laser-induced breakdown spectroscopy (LIBS) is a laser-based versatile elemental analysis tool which attracts increasing attention today because of broad range of applications [1,2]. The increasing interest in the LIBS techniques is certainly due to their inherent features: atmospheric pressure all-optical excitation and detection, no need for sample preparation, multi-element analytical capability [1–3]. The recent progresses in the fundamentals of the LIBS technique, such as dual-pulse configuration [4]

or femtosecond LIBS (Femto-LIBS) [5], and the introduction into the market of new types of spectrometers (multi-spectrometers [6], or échelle spectrometers [7]), do contribute to the evolution of the LIBS technique toward a more powerful analytical tool, allowing quantitative analysis or complex sample analysis including organic and biological samples [2].

The possibility of remote operation of LIBS is one of the properties which enlarge field of applications of this technique. Remote operation is required when samples to be analysed are difficult to access or located in hazardous areas. Examples would be minerals in a geological site, a chemically or nuclearly polluted industrial or urban site, or simply an edifice with polluted surface. Classical approach using a nanosecond pulsed laser for excitation is limited in range of operation by difficulty to tightly focus exciting laser beam at long distances. Obeying the laws of classical optics, diameter of focus linearly increases with focusing distance as a consequence of the

<sup>☆</sup> This paper was presented at the 3rd International Conference on Laser Induced Plasma Spectroscopy and Applications (LIBS 2004), held in Torremolinos (Málaga, Spain), 28 September – 1 October 2004, and is published in the special issue of *Spectrochimica Acta Part B*, dedicated to that conference.

\* Corresponding author.

*E-mail address:* jin.yu@lasim.univ-lyon1.fr (J. Yu).

diffraction. Remote LIBS measurements performed at distances up to 120 m using nanosecond pulses have been reported by the group of Prof. Laserna in Malaga [8]. However, further increase of operation distance would require exorbitant large laser energy and large focusing optics which would become prohibitive for practical uses. Therefore carrying high laser fluence beyond the limitation of the diffraction to generate strong sparks on a sample at a long distance is a key point for a remote chemical identification and furthermore a remote chemical analysis by LIBS.

In this paper we demonstrate a new approach for long distance remote operation of LIBS technique. This approach is based on use of filaments formed by ultra-short and ultra-intense laser pulses propagating in air. We call this configuration remote filament-induced breakdown spectroscopy (R-FIBS) [9]. Briefly, filaments appear as a result of a dynamic equilibrium between Kerr lens focusing and defocusing on laser-induced micro-plasma. More precisely, due to nonlinear part of the refractive index, a laser pulse with peak power larger than a critical power (several GW in air) undergoes self-focusing and tends to collapse after a certain distance of propagation [10]. However, self-focusing goes into competition with a defocusing effect due to a partial ionization of air once self-focused laser intensity becomes high enough. Experimental observation [11] and theoretical calculation [12] show that a dynamic equilibrium establishes at an intensity of  $\sim 5 \times 10^{13}$  W/cm<sup>2</sup> and a free electron density of  $\sim 10^{16}$  cm<sup>-3</sup> in laser-induced plasma [13,14]. Such equilibrium leads to a self-guided channel, called filament, with a diameter on the order of 100  $\mu$ m. A single filament carries typically 1 mJ of pulse energy. The length of filaments has been observed exceeding 100 m [15]. With an initial focusing and/or initial pulse chirp, starting point of filaments can be controlled [16]. Filaments have been observed propagating at a distance of few kilometers from the laser [17]. High intensity inside the core of a filament leads to ablation on a target. The subsequent plasma line emission can then be detected by a suitable detection system coupled to a telescope remotely collecting light emitted from the plasma.

In following sections we first describe our experimental setup. In Experimental results, we present characteristics of the surface of a copper sample ablated by filaments together with the associated plasma emission spectra. The dependences of plasma line emission intensity as a function of an initial chirp of laser pulses are then presented for different distances between the laser and the sample. We show especially that for an increasing sample distance,  $R$  (up to 90 m limited by the available space in our experiments), it is always possible to optimize plasma emission with an adequate negative chirp. In such way, the plasma emission detected by a fixed detection system nearby the laser only decreases with the geometrical factor  $1/R^2$ . That means a constant plasma emission from the sample ablated by

filaments independently on the sample distance. As an example of filament-induced ablation at long distance, we present the evidence of line emission from a plasma induced on an aluminum sample located at a distance of 180 m from the laser. In Section 4, we provide an estimation of requirements for the detection system to reach 1-km operation of LIBS using filaments.

## 2. Experimental setup

In our experiments, a container-integrated femtosecond terawatt laser system (Teramobile [18] system) was used. A detailed description of the laser system can be found elsewhere [16]. Briefly, a commercial chirped-pulse-amplification (CPA) [19] chain (Thales Laser Company) was integrated in a standard ISO container. The laser chain consisted of an oscillator, a stretcher, a regenerative amplifier, a preamplifier, a main amplifier and a compressor. Operating at a wavelength of 795 nm and a repetition rate of 10 Hz, the chain delivered pulses of up to 350 mJ energy and of 75 fs minimal duration.

The laser beam was sent towards the target collimated with a beam diameter of about 4.5 cm. An initial chirp was applied to laser pulses in order to initiate filaments at a defined distance to the sample. In order to have a precise control of chirp setting, one of the gratings in the compressor was mounted on a motorized linear translation. Initial pulse duration could be set from less than 100 fs to several picoseconds with either positive or negative chirps. Picosecond ( $\sim 200$  ps) or nanosecond ( $\sim 5$  ns) pulses at same energy per pulse as femtosecond pulses can also be generated from our system, by bypassing the compressor or by removing the injection from the oscillator, respectively.

A detection system was located beside the laser in the container. It consisted of a  $f/4$  aperture Newtonian telescope with a primary mirror of 20 cm diameter. Light collected at the focus of the telescope was coupled into an optical fiber bundle. The output  $f$ -number of the fiber bundle was matched to the input of a  $f/8$  ( $f=500$  mm) spectrometer (Chromex 500IS/SM) equipped with a 1200 lines/mm diffraction grating. The detector of an ICCD camera (Princeton Instruments PI-MAX 1024HQ) was placed in the reciprocal plane of the spectrometer. The ICCD camera was triggered with a selectable delay with respect to the emission of a laser pulse. This detection system was used for the results presented in Sections 3.1, 3.2, and 3.3.

In a second detection system, a lens of 50 mm diameter and 250 mm focal focused plasma emission on the input end of a fiber. The fiber was directly connected to the input slit of a 250 mm focal length  $f/4$  aperture grating spectrometer (Oriol MS257) equipped with a UV grating ruled with 600 lines/mm. At the output of the spectrometer, light was detected by a photomultiplier (PM) module (Hamamatsu

6780-03). This detection system could be placed near a sample to be able to locally detect plasma line emission. The result presented in Section 3.4 was obtained with this detection system.

### 3. Experimental results

#### 3.1. Characteristics of filament-induced remote surface ablation on a metallic sample and associated plasma line emission

##### 3.1.1. Remote surface ablation induced by filaments

As laser pulses were sent towards a sample in a parallel beam, ablation on the sample was induced by filaments only. With a pulse energy exceeding several tens of millijoules, multi-filamentation occurs, which denotes breaking up of the beam into a large number of self-guided substructures, carrying about 1 mJ energy in each filament. Multi-filamentation must be distinguished from collapse of a beam as a whole into one single filament. Filaments emerge from hot spots or generally from non-uniformities in the initial beam profile [20]. Fig. 1(a) shows a picture of a typical beam profile with many filaments (about 15 filaments) which appear as bright spots. Fig. 1(b) shows a picture of a copper sample irradiated by both a parallel laser beam containing filaments, and a focused laser beam for comparison. The black spot in the centre is due to a focused beam hitting the sample at a distance of 25 m from the laser. Other grey spots are caused by filaments contained in a parallel beam hitting the sample at a distance of 90 m from the laser. Spots due to filaments exhibit a diameter larger than filament diameter of about 100  $\mu\text{m}$ , that is because of random walks around the mean position of a filament due to turbulent nature of filamentation process [20] and inhomogeneities in air. Such random walks lead to a superficial ablation of the sample even after a long time irradiation. Our previous works [16] (see also Section 3.2 below) show a dependence of the filament starting position on the initial pulse duration. To avoid a filamentation very close to the laser, which leads to weaker filaments at long distance, we applied a negative chirp on the pulse to increase its initial duration. The initial pulse duration for a filamentation at around 90 m is about 400 fs. When a filament starts, the laser pulse undergoes strong spectral and temporal modulations as shown by numerical simulations [21,22]. However, due to extreme high intensity inside of a filament, a direct measurement of pulse profile by the means of autocorrelation for example, is quite difficult.

We have inspected the surface of a copper sample irradiated by filaments with a scanning electron microscope (SEM). A corresponding SEM micrograph is shown in Fig. 2(a). For comparison, an SEM micrograph of a crater made by focused laser pulses is shown in Fig. 2(b). As one can see, the surface ablated by filaments exhibits a regular quasi-periodical ripple structure. The orientation of the

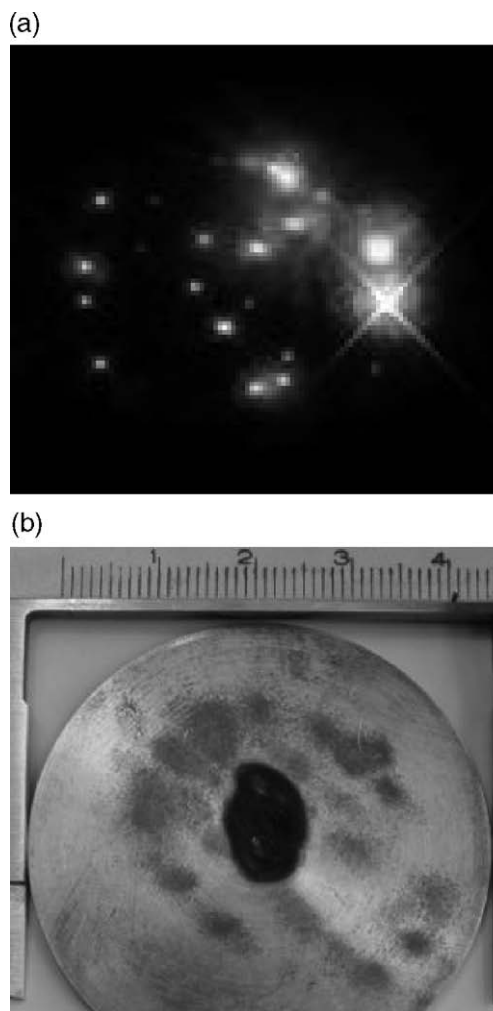


Fig. 1. (a) Picture of a typical laser beam profile with many filaments (single shot picture). On the picture, filaments appear as bright spots. Notice that each filament is surrounded by a conical emission in the visible range that increases the apparent size of the filaments on the picture to the order of mm. The whole beam had a diameter of 5 cm. (b) Picture of a copper sample irradiated by a large number of laser pulses. The black spot in the middle is due to irradiation with a focused beam from a distance of 25 m. Other grey spots are results of filament irradiation of the sample placed at a distance of 90 m. Random walks of a filament around its mean position due to inhomogeneities in air lead to a superficial ablation on a surface much larger than filament diameter. The scale of this picture is indicated by a ruler with a cm graduation in the upper part of the picture.

ripples is perpendicular to the polarization of incident laser light. In our experiments, laser light was horizontally polarized. Observed ripples are then oriented in the vertical direction. Dominant spatial ripple is a sub-wavelength structure of period about 0.64  $\mu\text{m}$ . In contrast, metal surfaces ablated by focused high-energy femtosecond laser pulses exhibit irregular microscopic structure due to higher fluence deposited on the sample in this configuration.

Similar ripple structures have been also reported for nanosecond pulse surface ablation [23]. According to the theory developed for long pulse duration laser irradiation [24], such patterns are due to interferences between incoming and anisotropically scattered light on surface

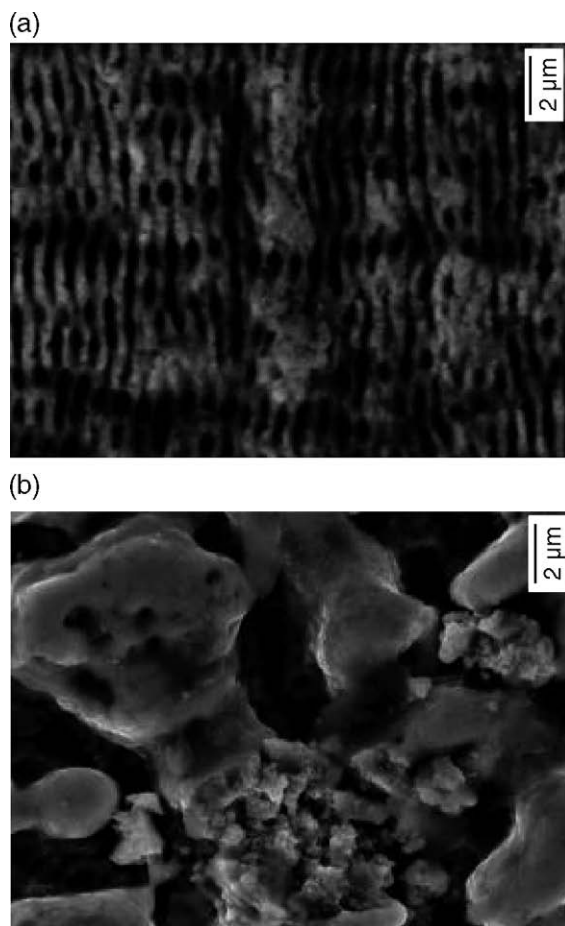


Fig. 2. SEM images of laser-ablated surface of a copper sample after a large number of laser pulse irradiation. (a) Irradiated by filaments, target at 90° from the laser, (b) irradiated by focused pulses, target at 25° from the laser. A grating like ripple structure is clearly observed on the surface ablated by filaments. Ripples are oriented perpendicular to laser polarisation with a period of 0.64 μm. In contrast, focused pulses lead to a chaotic ablated surface at the microscopic scale.

roughness with sub-wavelength dimension. Such interferences result in inhomogeneous energy deposition on the surface. This process involves a feedback mechanism between evolving surface sub-wavelength structure and anisotropic energy deposition which leads to the observed steady-state surface pattern under certain threshold for laser fluence. This model predicts a sub-wavelength period for ripples when incident pulses are not in the normal direction with respect to the sample surface. Orthogonal direction of ripples with respect to laser polarization is also predicted by the model.

In ultra-short pulse regime, ripple structures have been recently reported for dielectric substrates such as BaF<sub>2</sub> or CaF<sub>2</sub> ablated by focused femtosecond pulses [25–27]. In this regime, the model based on interferences discussed above cannot be applied because of either short pulse duration or associated large pulse spectrum excluding any steady-state interference. The proposed model for ripple in ultra-fast regime is a self-organization from a chaotic state [25–27]. In

this model, rapid excitation of electrons and surface ionization by the incident laser pulse induce a massive instability in the crystal lattice due to a perturbation of the interatomic bonds. The resulted instability characterized by positive charge accumulation and explosive emission of massive particles leads to a relaxation of the highly perturbed surface through surface reorganization by atomic diffusion. Such reorganization results mostly in regular and periodic structure. This model is supported by experimental observations [25–27] such as sensitivity to both wavelength and incident angle, observed ripple period significantly smaller than the incident wavelength, and bifurcations (also visible on our copper sample shown in Fig. 2(a)). Theoretical simulations of femtosecond ablation [28,29] support also the self-organization model. Our observation reported here provides the first evidence of surface ripples induced by femtosecond pulses on a metallic sample.

### 3.1.2. Filament-induced plasma emission spectra

Emission spectra of plasma induced by femtosecond laser pulses on metal samples in ambient air have been compared to those induced by picosecond or nanosecond pulses of same energy under the same atmospheric conditions. With femtosecond pulses, in focused geometry as well as in collimated ‘filament’ configuration, plasma line emission have been observed on a clean background, free from spectral emission of ambient air species. As shown in Fig. 3(a), in the spectral range between 700 nm and 900 nm, two atomic copper lines are observed without any background lines. In the same spectral range, with picosecond (or nanosecond) pulses additional non-copper lines are observed (Fig. 3(b)). These background lines represent atomic oxygen and atomic nitrogen emission. They are due to diffusive mixing of the expanding hot metal vapour with ambient gas [30] in the nanosecond pulse regime. In the picosecond pulse regime, emission from ambient gas is due to the interaction of the trailing part of the laser pulse with an early stage electron plasma leading to inverse bremsstrahlung heating of the plasma plume [31]. We interpret the absence of background lines in femtosecond pulse induced LIBS spectra as being a consequence of fundamental differences of laser-surface interaction in the different regimes of laser pulse duration. Especially, in the femtosecond regime, produced plasma plume is not enough energetic to excite ambient gas. A spectrum without background lines is highly appreciable for analysis and identification of complex biological samples such as bacteria [32]. Background lines overlapping with emission from sample can induce ambiguity in the analysis.

## 3.2. Optimizing filaments with a chirped pulse

### 3.2.1. Control of filament starting position by an initial negative chirp

Filament-induced plasma line emission intensity has been observed to depend critically on an initial chirp

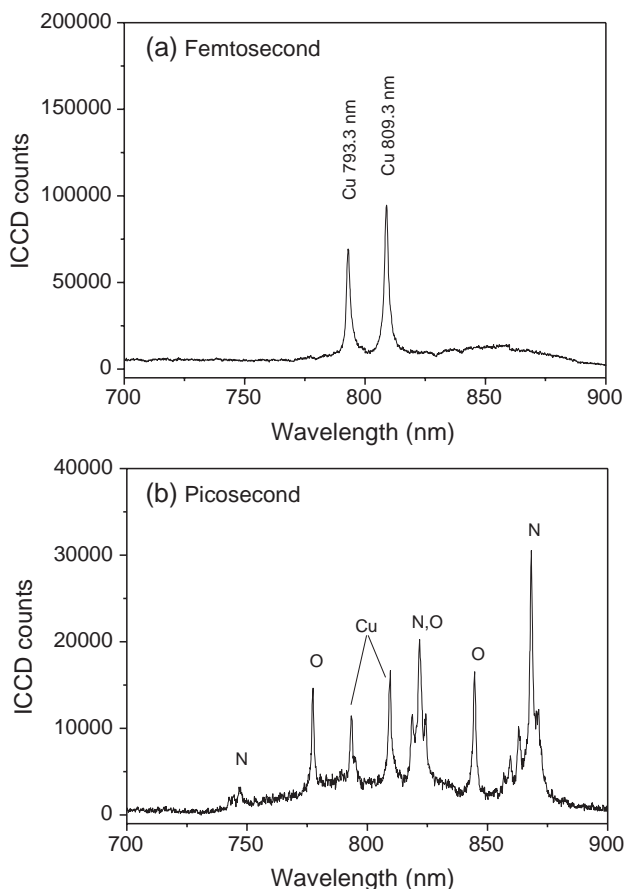


Fig. 3. Plasma line emission spectra from a copper sample excited by femtosecond pulses (a), and by picosecond pulses (b). With femtosecond pulses, two copper atomic lines in the spectral range from 700 nm to 900 nm are observed without any background lines. In contrast, with picosecond (or nanosecond pulses), the copper lines are mixed with background lines from ambient air: atomic oxygen (O) and atomic nitrogen (N) lines.

applied to laser pulses. That is because the starting position of filaments can be controlled by an initial chirp [16], and light intensity inside a filament varies as the filament propagates. Fig. 4 shows the result of an acoustic measurement on longitudinal profile of filaments induced by initially compressed 350 mJ femtosecond pulses. As we have shown elsewhere [33,34], measured acoustic signal is proportional to free electron density in the filaments. And via equilibrium between Kerr focusing and plasma defocusing, detected acoustic signal is finally related to light intensity in filaments.

From the result shown in Fig. 4, we can consider the development of filaments in three steps: onset of the filaments where the intensity increases, saturation of the filaments where the intensity reaches a maximum and remains constant, and finally damping of the filaments where the intensity decreases gradually. For initially compressed pulses, filaments build up quickly after travelling a short distance from the output of the laser, and reach the saturation at a distance of about 3.5 m from the window of

the container. At a distance of about 12.5 the filament intensity starts to decrease. At a distance of about 40 m, free electron density falls down to a 10th of its maximal value.

In a remote LIBS experiment, for a certain distance between the laser and the sample, it is desirable to have the filaments hitting the target in their most intense phase. Imposing a negative chirp (“blue” first) on initial laser pulses is a suitable means for achieving a control of filamentation [16]. An initial negative chirp has in fact two effects: (1) it leads to a larger pulse duration and lower pulse peak power. This reduces initial Kerr-focusing and delays the onset of filamentation. (2) It pre-compensates the GVD of air. The negatively chirped pulse gets recompressed by the positive GVD of air, i.e. its peak power increases during propagation through air, in turn leading to increased Kerr focusing. The interplay of both effects allows prolonging the starting position of filaments to a long distance near the target.

### 3.2.2. Optimization of plasma line emission by an initial negative chirp

In Fig. 5, intensity of remotely detected line emission from filament-induced copper plasma is plotted versus initial duration of negatively chirped laser pulses for three different distances between the laser and the sample. We arbitrarily normalize the maximal intensities at different distances in order to focus attention on effects of the initial pulse duration due to a negative chirp for a given sample distance.

In Fig. 5, dashed parabolas do not represent theoretical fitting curves, but are intended to guide the eye. As can be seen in the figure, line emission intensity for different distance peaks at specific pulse durations corresponding to specific negative chirps. The larger the sample distance is, the longer is the initial pulse duration which optimizes plasma emission, that corresponds to the fact that a larger

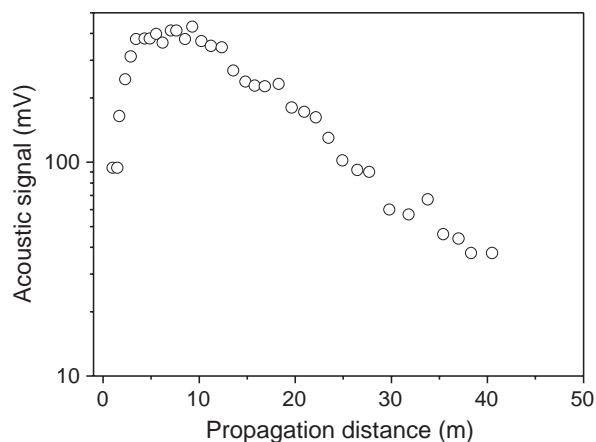


Fig. 4. Acoustic signal versus propagation distance for initially fully compressed pulses. Acoustic signal being proportional to the local peak free electron density is related to the light intensity in the filaments via the condition of equilibrium between Kerr focusing and plasma defocusing. Distance is measured relative to the output window of the container.

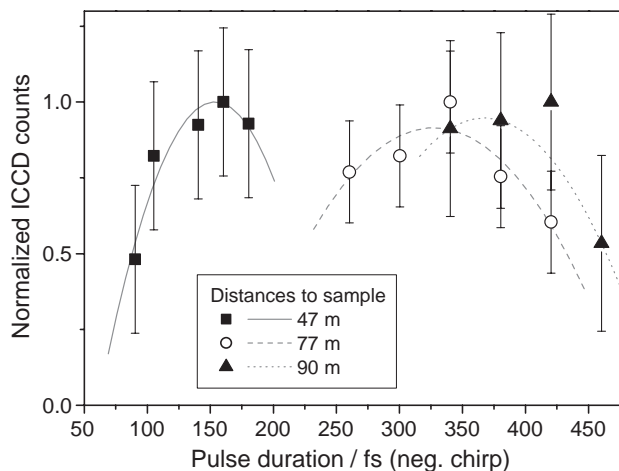


Fig. 5. Intensity of remotely detected copper line emission vs. negatively chirped pulse duration for three different sample distances. The maximums for different distances are arbitrarily normalized in order to plot experimental data in the same graph. Dashed parabolas are intended to guide the eye.

negative chirp leads to a longer filament starting distance. The following observations are common to optimum chirp settings at different distances: (a) onset of filamentation could be observed about 7 m before the sample, which corresponds well to what is indicated by the acoustic measurement (Fig. 4). Corresponding to this, (b) the filaments strong enough to ablate material from the sample were accompanied by bright white light spots on the sample, which are due to supercontinuum generated in the filaments before they hit the sample. (c) Ablating filaments could be

identified by the clicking noise caused by shockwaves in consequence of ablations. Intense plasma line emission was expected when a high percentage of the filaments incident on the target were such strong ablating filaments.

The observed chirp dependence of LIBS signal can be explained by the dynamic nature of the process of multifilamentation. During the life cycle of a filament, the peak intensity in its core can vary considerably, as shown by our acoustic measurement. Our experiments show that for a given sample distance, a suitable initial chirp allows a maximal plasma emission from the sample. They also confirm that the range of initial pulse durations which allows optimizing plasma emission becomes larger for a longer sample distance.

### 3.3. Filament-induced plasma emission as a function of sample distance

As discussed in the preceding paragraph, it is possible with an increasing negative chirp, to initiate filaments several meters before a sample is placed at an increasing distance. This procedure ensures a constant fluence contained in the filaments on a sample independently on its distance from the laser, provided that filaments are properly set to be initiated in the front of the sample. For a fixed detection system located nearby the laser, one expects a decrease of the detected signal due to geometrical factor  $1/R^2$ , where  $R$  denotes sample distance (or range of detection).

In Fig. 6 range-corrected plasma spectra from copper are shown for three different sample distances. These spectra

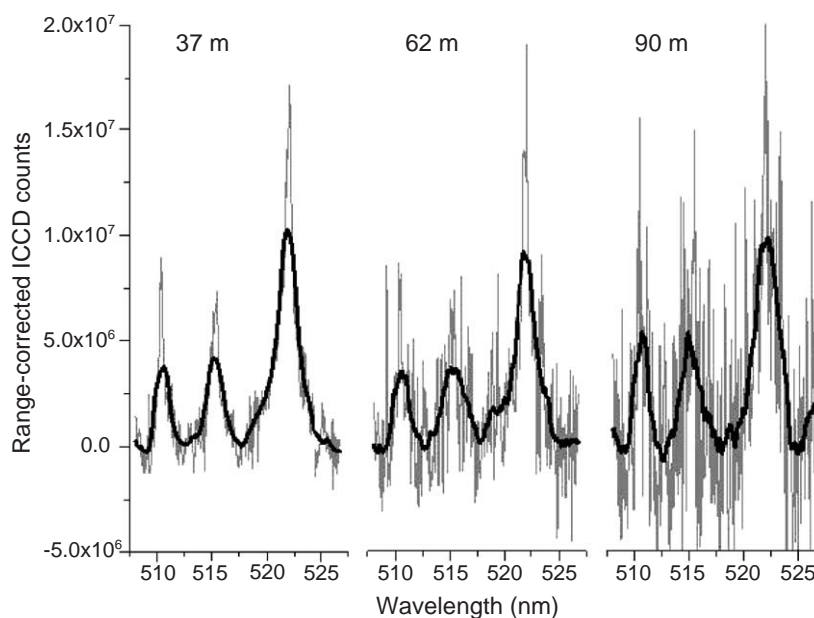


Fig. 6. Background- and range-corrected spectra of remotely detected copper plasma line emission (510.55 nm, 515.32 nm, and 521.82 nm) from three sample distances, 37 m, 62 m, and 90 m. Raw signals are plotted in grey. Thick black curves are obtained by smoothing raw spectra using an average of 32 adjacent points. All three spectra have been integrated over 1000 shots with an ICCD gate width of 10  $\mu$ s. Despite the decrease of signal to noise ratio, the plot shows that there is no decrease of number of photons emitted by filament-induced plasma as sample distance increases.

have been acquired with an integration time of 100 s. Spectra have been multiplied by a factor of  $R^2$  to compensate for the geometrical decrease. As it can be seen from the figure, range-corrected spectra have the same intensity for 37 m, 62 m and 90 m. This result demonstrates clearly that the number of initially emitted photons from the plasma is independent on the distance between laser and sample. This holds at least for a distance up to 90 m, which was limited by the available experimental space. Due to  $1/R^2$  decrease of the number of collected photons, signal to noise ratio (SNR) decreases as sample distance increases. Assuming the number of photons emitted by plasma is the same at even longer distances, extrapolation of the spectra in Fig. 6 leads to an estimated maximal sample distance of 150 m for the used detection system, where the SNR reaches the value 1.

#### 3.4. Filament-induced remote ablation at a distance of 180 m

In order to investigate the capability of filaments to generate plasma at distances exceeding the estimated limit of 150 m imposed by the used detection system, an aluminum sample was positioned at a distance of 180 m from the laser. Due to limitations inherent to the new target location (in an office at the fifth floor of a building), the second detection system was used to detect plasma emission near the sample.

The aluminum sample was irradiated by filaments. We optimized ablation by varying initial chirp. The supercontinuum generated in filaments by self-phase modulation being enough weak in the blue-UV region, plasma line emission from the aluminum sample at 394.4 nm and 396.1 nm could be detected without temporally gating the detection system. Elastic scattering of the supercontinuum from the sample was used to trigger a digital oscilloscope connected to the output of the PM. The wavelength

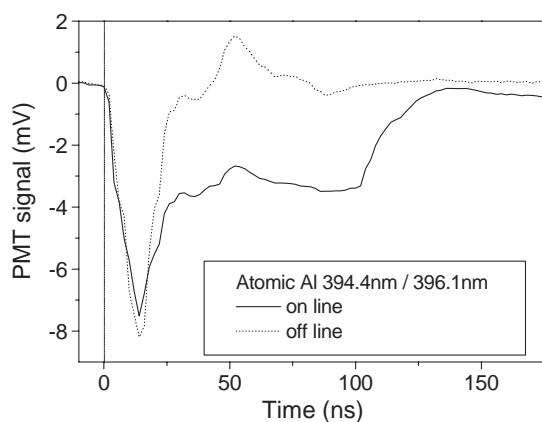


Fig. 7. Transient signals from filament-induced plasma emission from an aluminium target placed at 180 m from the laser. The on-line transient corresponds to the spectrometer tuned to one of aluminium lines. The off-line transient corresponds to the spectrometer tuned out of aluminium lines. The decay time of plasma emission can be estimated from the PM signal to be about 130 ns.

transmitted by the spectrometer was scanned in steps of 1 nm in the region of the two strong atomic aluminum emission lines around 395 nm. The transient PM signals were averaged over 100 shots for each wavelength. Two representative transient signals are shown in Fig. 7, one corresponding to on-resonance setting of the spectrometer, and the second off-resonance spectrometer setting. The off-resonance curve represents elastically scattered supercontinuum. On the on-resonance curve, plasma line emission appears with a lifetime of about 130 ns. This decay time is much shorter than microsecond decay times that we observed with focused pulses (femtosecond, picosecond or nanosecond duration) at shorter distances [5].

#### 4. Discussion: towards the kilometer-range LIBS

Our results show that remote ablation can be induced by filaments at long distances. This opens the way to kilometer-range LIBS. In this section, we provide a parameter estimation for detection system required for the detection of plasma emission induced by filaments on a metallic sample placed at 1 km from the laser. Here we assume that filaments can be induced at distances of the order of 1 km, which is supported by experimental observations [17,35] and theoretical calculations [36].

The detection system used in present experiments (telescope, spectrometer, and ICCD camera) offers good spectral resolution and ease of use at the cost of low light throughput. The major bottlenecks are represented by the fiber bundle and the spectrometer itself. The fiber bundle unavoidably introduces Fresnel (reflection) losses and damping (transmission losses), which lead to a net transmittance of the fiber bundle of 55% around 520 nm (manufacturer data). Including the necessary  $f$ -number matching of the fiber output, light passing through the Czerny–Turner spectrometer suffers a total of five reflections from aluminum coated mirrors. Consequently, at wavelengths under consideration, the transmittance of the sequence of optical elements before the detector is at best 14%, including the spectral efficiency of the diffraction grating and assuming optimum coupling into the fiber bundle.

From the filament-induced plasma copper spectrum acquired from 90 m distance, one can estimate average number of photons originating from the copper 521.8 nm line and reaching the detector after each laser shot. This has been done by integrating the background-removed ICCD counts which can be attributed to this emission line, and by taking into account the spectral efficiency of the ICCD photocathode and the gain of the intensifier. Such estimation leads to an average of 19 photons reaching the detector at each laser shot. As it was mentioned before, such a small number of detected per-shot photons are due to the low transmittance of the used detection system.

For longer operation ranges, a dedicated detection system offering high light collection efficiency has to be designed.

Besides increasing the transmittance of the spectrometer, the aperture of the telescope has also to be increased. We propose an integrated combination of a Cassegrainian reflector telescope, a flat-field spectrograph and an ICCD detector. Compared to Newtonian design, folded Cassegrainian design offers compactness and a location of the focal plane situated behind the primary mirror, more convenient for attaching further instrumentation. A flat-field spectrograph has a flat-field imaging grating as its single optical element, which reduces the number of optical elements to a minimum and allows transmittance of the spectrometer to be practically given by grating reflectivity. A flat-field imaging grating is a holographically structured concave grating with modulated non-uniform line spacing allowing the spectrum to be imaged on a plane (i.e. the ICCD) instead on an arc on Rowland's circle. Such a design requires a telescope of far better imaging quality and pointing stability than the approach utilizing a fiber bundle.

High throughput is essentially achieved by reducing number of reflections, i.e. by keeping light path as direct as possible. However, that allows more direct paths for stray light as well. A challenge is to keep the rejection rate of stray light comparable to that of the present setup in order to finally improve the overall SNR. In this condition and assuming a realistic transmittance of 50% for the discussed telescope–spectrometer combination, the SNR can be increased from 1 to 3.57 (50:14%) for a sample distance of 150 m with the same ICCD detector as used in the present experiments. A larger primary mirror with diameter of 70 cm can be used to further increase the solid angle of the detection system by a factor of  $(70/20)^2 = 12.25$ . That would lead to a theoretical SNR of  $\sim 46$  ( $12.25 \times 3.57$ ) for a sample distance of 150 m. It means that copper line emission from filament-generated plasma would be detectable with a SNR of 1 at a distance of  $\sim 1000$  m ( $150 \text{ m} \times \sqrt{46}$ ) with an integration time comparable to that used in the present experiments.

Another approach to dramatically increase the sensitivity of the detection system with relatively small telescope (primary mirror diameter 40 cm for example) consists of the use of a single element detector such as a photomultiplier tube (PMT) coupled to a monochromator. This setup is actually similar to a LIDAR [37] detection with a well-known high sensitivity allowing an easy access to a multiple kilometer detection range. Our observation on transient plasma emission at a distance of 180 m from the laser demonstrates that due to low supercontinuum emission in the near UV range (especially interesting for LIBS), plasma emission can be detected by a PMT without any optical or electronic gating. Even though the low spectral resolution of PMT detection could limit analytical capability in this configuration, an elemental identification can be carried out with a compact detection system over a distance as far as filaments can propagate. In this case, the detection would not be the limiting factor for a long-range kilometer LIBS elemental identification.

## 5. Conclusion

We have demonstrated ablation of the surface of a metallic target placed at a distance up to 180 m using filaments induced by high intensity femtosecond pulses propagating in air. A quasi-periodical grating like ripple structure has been observed on the surface irradiated by filaments. Spatial period of the ripples is estimated to be  $0.64 \mu\text{m}$ . Our observation provides the evidence of ripple structure on metallic sample induced by ultra-short laser pulses. The detection of plasma emission from the target corresponds to remote filament-induced breakdown spectroscopy, that we call R-FIBS. A remarkable property of a LIBS spectrum induced by femtosecond pulse is the absence of emission from ambient air, which is particularly interesting in case of analysis of a complex sample by the method of spectral correlation. For an increasing distance between the laser and the target, we have demonstrated that a properly increasing negative chirp leads to a constant plasma emission from the target, which means that for a detection system located nearby the laser system, LIBS signal only decreases as  $1/R^2$ , where  $R$  is the distance between the laser and the target. Finally, a parameter estimation based on our experimental data at 90 m shows that kilometer-range R-FIBS operation would be possible with an improved high-throughput spectrometer coupled to a telescope with a primary mirror of 70 cm diameter and an ICCD camera. Furthermore, a LIDAR type detection system including a monochromator and a PMT would allow a R-FIBS elemental identification over a very long distance, as far as filaments propagate in the atmosphere, with a detection system based on a compact telescope.

## Acknowledgements

This work has been carried out within the framework of the Teramobile Project funded by Centre National de la Recherche Scientifique (CNRS), Deutsche Forschungsgemeinschaft (DFG), Ministère des Affaires Étrangères Français (MAE), Deutsche Akademische Austauschdienst (DAAD). The website of the Teramobile project is [www.teramobile.org](http://www.teramobile.org). We would like to thank Dr. R. Bourayou for his contribution in the acoustic measurement of longitudinal plasma profile in filaments. Kamil Stelmaszczyk would like to acknowledge the fellowship of Alexander von Humboldt Foundation.

## References

- [1] Special issue on laser-induced breakdown spectroscopy, *Spectrochim. Acta B* 56 (2002).
- [2] Special issue on laser-induced breakdown spectroscopy, *J. Anal. At. Spectrom.* 19 (2004).
- [3] L.J. Radziemski, D.A. Cremers, Spectrochemical analysis using laser plasma excitation, in: L.J. Radziemski, D.A. Cremers (Eds.), *Laser-*

- Induced Plasma: Physical, Chemical and Biological Applications, Marcel Dekker, New York, 1989.
- [4] S. Michael Angel, Dimitra N. Stratis, Kristine L. Eland, Tianshu Lai, Mark A. Berg, David M. Gold, LIBS using dual- and ultra-short laser pulses, *J. Anal. Chem.* 369 (2001) 320–327.
- [5] P. Rohwetter, K. Stelmaszczyk, G. Méjean, J. Yu, E. Salmon, J. Kasparian, J.P. Wolf, L. Wöste, Remote LIBS with ultrashort pulses: characteristics in picosecond and femtosecond regimes, *J. Anal. At. Spectrom.* 19 (2003) 437–444.
- [6] Homeland security drives LIBS forward, *Opto- and -Laser-Europe*. 112 (Dec. 2003) 13–15.
- [7] S. Hamilton, R. Al-Wazzan, A. Hanvey, A. Varagnat, S. Devlin, Fully integrated wide range LIBS system with high UV efficiency and resolution, *J. Anal. At. Spectrom.* 19 (2003) 479–482.
- [8] Santiago Palanco, Simon Conesa, Javier Laserna, Pulse energy requirements for remote analysis with LIBS beyond the 100 meter range paper W3-2, 3rd International Conference, LIBS 2004, September 28–October 1 2004, Torremolinos (Malaga), Spain, 2004.
- [9] K. Stelmaszczyk, P. Rohwetter, G. Méjean, J. Yu, E. Salmon, J. Kasparian, R. Ackermann, J.-P. Wolf, L. Wöste, Long-distance remote laser-induced breakdown using filamentation in air, *Appl. Phys. Lett.* 85 (2004) 3977–3979.
- [10] J.H. Marburger, Self-focusing: theory, *Prog. Quantum Electron* 4 (1975) 35.
- [11] A. Braun, G. Korn, X. Liu, D. Du, J. Squier, G. Mourou, Self-channeling of high-peak-power femtosecond laser pulses in air, *Opt. Lett.* 20 (1995) 73–75.
- [12] A. Chiron, B. Lamouroux, R. Lange, J.F. Ripoche, M. Franco, B. Prade, G. Bonnaud, G. Riazuelo, A. Mysyrowicz, Numerical simulations of the nonlinear propagation of femtosecond optical pulses in gases, *Eur. Phys. J. D* 6 (1999) 383–396.
- [13] J. Kasparian, R. Sauerbrey, S.L. Chin, The critical laser intensity of self-guided light filaments in air, *Appl. Phys.*, B 71 (2000) 877–879.
- [14] A. Becker, N. Aközbeke, K. Vijayalakshmi, E. Oral, C.M. Bowden, S.L. Chin, Intensity clamping and re-focusing of intense femtosecond laser pulses in nitrogen molecular gas, *Appl. Phys.*, B 73 (2001) 287–290.
- [15] B. La Fontaine, F. Vidal, Z. Jiang, C.Y. Chien, D. Comtois, A. Desparois, T.W. Johnston, J.-C. Kieffer, H. Pépin, H.P. Mercure, Filamentation of ultrashort pulse laser beam resulting from their propagation over long distance in air, *Phys. Plasmas* 6 (1999) 1615–1621.
- [16] H. Wille, M. Rodriguez, J. Kasparian, D. Mondelain, J. Yu, A. Mysyrowicz, R. Sauerbrey, J.P. Wolf, L. Wöste, Teramobile: a mobile femtosecond–terawatt laser and detection system, *Eur. Phys. J.*, Appl. Phys. 20 (2002) 183–190.
- [17] M. Rodriguez, R. Bourayou, G. Méjean, J. Kasparian, J. Yu, E. Salmon, A. Scholz, B. Stecklum, J. Eislöffel, U. Laux, P. Hatzes, R. Sauerbrey, L. Wöste, J.-P. Wolf, Kilometer-range non-linear propagation of fs laser pulses, *Phys. Rev.*, E 69 (2004) 036607.
- [18] J. Kasparian, M. Rodriguez, G. Méjean, J. Yu, E. Salmon, H. Wille, R. Bourayou, S. Frey, Y.B. Andre, A. Mysyrowicz, R. Sauerbrey, J.P. Wolf, L. Wöste, White light filaments for atmospheric analysis, *Science* 301 (2003) 61–64.
- [19] D. Strickl, G. Mourou, Compression of amplified chirped pulses, *Opt. Commun.* 56 (1985) 219.
- [20] S. Skupin, L. Bergé, U. Peschel, F. Lederer, G. Méjean, J. Yu, J. Kasparian, E. Salmon, J.-P. Wolf, M. Rodriguez, L. Wöste, R. Bourayou, R. Sauerbrey, Filamentation of femtosecond light pulses in the air: turbulent cells versus long-range clusters, *Phys. Rev.*, E 70 (2004) 046602.
- [21] M. Mlejnek, E.M. Wright, J.V. Moloney, Power dependence of dynamic spatial replenishment of femtosecond pulses propagating in air, *Opt. Express* 4 (1999) 223–228.
- [22] N. Aközbeke, M. Scalora, C.M. Bowden, S.L. Chin, White-light continuum generation and filamentation during the propagation of ultra-short laser pulses in air, *Opt. Commun.* 191 (2001) 353–362.
- [23] Jeff F. Young, J.S. Preston, H.M. van Driel, J.E. Sipe, Laser-induced periodic surface structure: II. Experiments on Ge, Si, Al, and brass, *Phys. Rev.*, B 27 (1983) 1155–1172.
- [24] J.E. Sipe, J.F. Young, J.S. Preston, H.M. van Driel, Laser-induced periodic surface structure: I. Theory, *Phys. Rev.*, B 27 (1983) 1141–1153.
- [25] F. Costache, M. Henyk, J. Reif, Modification of dielectric surface with ultra-short laser, *Appl. Surf. Sci.* 186 (2002) 352–357.
- [26] J. Reif, F. Costache, M. Henyk, S.V. Pandelov, Ripple revisited: non-classical morphology at the bottom of femtosecond laser ablation craters in transparent dielectrics, *Appl. Surf. Sci.* 197–198 (2002) 891–895.
- [27] F. Costache, M. Henyk, J. Reif, Surface patterning on insulators upon femtosecond laser ablation, *Appl. Surf. Sci.* 208–209 (2003) 486–491.
- [28] H.O. Jeschke, M.E. Garcia, K.H. Bennemann, Theory for the ultrafast ablation of graphite film, *Phys. Rev. Lett.* 87 (2001) 015003.
- [29] H.O. Jeschke, M.E. Garcia, K.H. Bennemann, Time-dependent energy absorption changes during ultrafast lattice deformation, *J. Appl. Phys.* 91 (2002) 18–23.
- [30] A. Gomes, A. Aubreton, J.J. Gonzalez, S. Vacquie, Experimental and theoretical study of the expansion of a metallic vapour plasma produced by laser, *J. Phys. D: Appl. Phys.* 37 (2004) 669–689.
- [31] Samuel S. Mao, Xianglei Mao, Ralph Greif, Richard E. Russo, Initiation of an early-stage plasma during picosecond laser ablation of solids, *Appl. Phys. Lett.* 77 (2000) 2464–2466.
- [32] Alan C. Samuels, Frank C. DeLucia Jr., Kevin L. McNesby, Andrzej W. Miziolek, Laser-induced breakdown spectroscopy of bacterial spores, molds, pollens, and protein: initial studies of discrimination potential, *Appl. Opt.* 42 (2003) 6205–6209.
- [33] J. Yu, D. Mondelain, J. Kasparian, E. Salmon, S. Geffroy, C. Favre, V. Boutou, J.P. Wolf, Sonographic probing of laser filaments in air, *Appl. Opt.* 42 (2003) 7117–7120.
- [34] S.A. Hosseini, J. Yu, Q. Luo, S.L. Chin, Multi-parameter characterization of the longitudinal plasma profile of a filament: a comparative study, *Appl. Phys.*, B 97 (2004) 519–523.
- [35] G. Méchain, A. Couairon, Y.B. André, C. D’Amico, M. Franco, B. Prade, S. Tzortzakis, A. Mysyrowicz, R. Sauerbrey, Long-range self-channeling of infrared laser pulses in air: a new propagation regime without ionization, *Appl. Phys.*, B 79 (2004) 379–382.
- [36] P. Sprangle, J.R. Peñano, B. Hafizi, Propagation of intense ultrashort pulses in the atmosphere, *Phys. Rev.*, E 66 (2002) 046418.
- [37] Raymond M. Measures, *Laser Remote Sensing*, Wiley, New York, 1992.

G. MÉCHAIN<sup>1</sup>  
G. MÉJEAN<sup>2</sup>  
R. ACKERMANN<sup>2</sup>  
P. ROHWETTER<sup>3</sup>  
Y.-B. ANDRÉ<sup>1</sup>  
J. KASPARIAN<sup>2</sup>, ✉  
B. PRADE<sup>1</sup>  
K. STELMASZCZYK<sup>3</sup>  
J. YU<sup>2</sup>  
E. SALMON<sup>2</sup>  
W. WINN<sup>4</sup>  
L.A. (VERN) SCHLIE<sup>5</sup>  
A. MYSYROWICZ<sup>1</sup>  
R. SAUERBREY<sup>6</sup>  
L. WÖSTE<sup>3</sup>  
J.-P. WOLF<sup>2</sup>

## Propagation of fs TW laser filaments in adverse atmospheric conditions

<sup>1</sup>Teramobile, Laboratoire d'Optique Appliquée, UMR CNRS 7639, ENSTA – Ecole Polytechnique, Centre de l'Yvette, Chemin de la Hunière, 91761 Palaiseau Cedex, France

<sup>2</sup>Teramobile, LASIM, UMR CNRS 5579, Université Claude Bernard Lyon 1, 43 bd du 11 Novembre 1918, 69622 Villeurbanne Cedex, France

<sup>3</sup>Teramobile, Institut für Experimentalphysik, Freie Universität Berlin, Arnimallee 14, 14195 Berlin, Germany

<sup>4</sup>Langmuir Laboratory for Atmospheric Research, Geophysical Research Center, New Mexico Institute of Mining and Technology, Socorro, New Mexico, USA

<sup>5</sup>Directed Energy Directorate (AFRL/DELS), Air Force Research Laboratory, 3550 Aberdeen Blvd, SE, Kirtland AFB, NM 87117, USA

<sup>6</sup>Teramobile, Institut für Optik und Quantenelektronik, Friedrich Schiller Universität, Max-Wien-Platz 1, 07743 Jena, Germany

Received: 1 April 2005 / Published online: 9 May 2005 • © Springer-Verlag 2005

**ABSTRACT** The propagation of femtosecond terawatt laser pulses at reduced pressure (0.7 atm) is investigated experimentally. In such conditions, the non-linear refractive index  $n_2$  is reduced by 30%, resulting in a slightly farther filamentation onset and a reduction of the filament number. However, the filamentation process, especially the filament length, is not qualitatively affected. We also show that drizzle does not prevent the filaments from forming and propagating.

**PACS** 42.65.Jx; 42.68.Ge; 42.68.-w

### 1 Introduction

Femtosecond (fs) laser pulses can propagate in air as self-guided filaments [1] as soon as the beam power exceeds a so-called critical power  $P_{cr} \sim \lambda^2 / (2\pi n_0 n_2)$  (e.g.  $P_{cr} = 3.37\lambda^2 / (8\pi n_0 n_2)$  for a Gaussian beam) [2]. In air, with a refractive index  $n_0 \sim 1$  and a non-linear refractive index  $n_2 = 3 \times 10^{-23} \text{ m}^2/\text{W}$ ,  $P_{cr} = 3 \text{ GW}$  at a wavelength  $\lambda = 800 \text{ nm}$ . Under these conditions, Kerr-lens self-focusing overcomes diffraction, so that one or several filaments are formed and propagate with a typical diameter of  $100 \mu\text{m}$  over distances much longer than the Rayleigh length, up to several hundreds of meters [3]. Filaments have been observed at distances up to several kilometers [4–6]. The intensity within the filaments is in the order of  $10^{14} \text{ W/cm}^2$  [7, 8], allowing self-phase modulation

and generation of a broadband white-light continuum spanning from ultraviolet [9] to the mid infrared [10]. Ionization of the air [11–16] in the filaments crucially contributes to their self-guiding as it allows a dynamic balance with the Kerr effect.

These properties of filaments open exciting perspectives for atmospheric applications [17], such as white-light lidar (light detection and ranging) [4, 18–20], high-voltage discharge switching and guiding or even laser lightning control based on continuous air ionization [21–23], optical telecommunications, or laser-induced breakdown spectroscopy for remote elemental analysis based on the remote delivery of high intensities [24]. Large-scale outdoor applications in turn raise interest for a full characterization of the filament propagation in real atmospheric conditions,

including the low-pressure conditions encountered at high altitudes. The influence of the gas pressure has been investigated on the laboratory scale in several media, especially in rare gases [25–29] and air [30]. Pressure variations induce proportional changes in the group-velocity dispersion (GVD), the non-linear refractive index, and the molecule density available for ionization. Besides this, atmospheric pressure influences the processes of plasma formation and laser–plasma interaction in an essentially non-linear way, mainly by affecting collisional absorption efficiency [31]. On the laboratory scale, pressure mainly affects the relative ionization level, and hence the intensity, within the filaments. However, up to now, little work has been dedicated to the influence of low pressure or pressure gradients [4] at longer scales, although interesting processes like full-beam refocusing have been predicted by some theoretical calculations [32]. Besides effects of reduced pressure, a realistic model for the real-scale propagation of filaments in the atmosphere must take into account the influence of water droplets (i.e. haze, clouds, or rain) on the non-linear propagation of high-power laser pulses. It has recently been shown that single [33–35] and multiple [36] filaments can survive their interaction with dense clouds or fog. However, the possibility of initiating filaments in the

✉ Fax: +33-472445871, E-mail: jkaspari@lasim.univ-lyon1.fr

rain itself, rather than propagating pre-formed filaments in a subsequent cloud, has never been demonstrated to date. Moreover, previous experiments have been performed on synthetic rain, which could result in a biased droplet-size distribution.

In this paper, we characterize the multifilamenting propagation of a fs terawatt (TW) laser beam in adverse conditions at high altitude. In particular, we show that the reduced pressure reduces the filament number without qualitatively affecting the filamentation process, and that filaments can actually be generated and propagated in natural rain.

## 2 Experimental setup

The laser source used in the experiments was the *Teramobile* mobile femtosecond terawatt laser system [37]. This system allows outdoor experiments under virtually any atmospheric conditions, as was required for measurements over an extended period of two months under various meteorological conditions at a high-altitude location. The *Teramobile* delivers 280-mJ pulses centered at 800 nm, with a repetition rate of 10 Hz. The beam is emitted parallel or slightly focused, with an initial beam diameter of 3 cm. The minimum pulse duration was 150 fs, although a chirp can be applied to the pulses in order to pre-compensate for GVD in air, resulting in initial pulse durations up to 1.5 ps. In that case, the pulses are refocused temporarily by GVD after a given propagation distance [38].

The *Teramobile* beam was propagated horizontally over 325 m on the Magdalena Mountain ridge (New Mexico, 3230-m altitude above sea level). The standard pressure at this altitude is 0.67 atm, i.e.  $6.8 \times 10^4$  Pa. The laser beam propagation was characterized by recording beam profiles. They were acquired by taking photographs of the beam on a screen using a digital camera. The exposure time of 1/8 s was chosen to assure that each picture corresponds to a single-shot picture. Images have been taken over both the whole spectrum, with high sensitivity to the white-light continuum and to the conical emission, and in the infrared (fundamental) region of the spectrum, yielding a good approximation of the beam profile

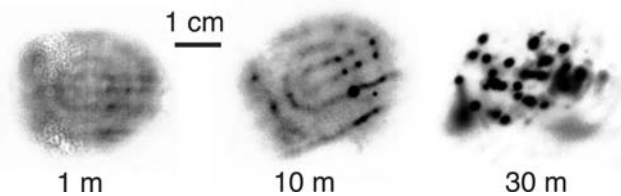


FIGURE 1 Grey-scale intensity profiles of the laser beam on a screen for three propagation distances

at the considered distance, as demonstrated in Ref. [39]. The occurrence of filaments at a given distance was also characterized by single-shot burns on impact paper (Kodak Linagraph, 1895). The darkening of the photosensitive paper yields the intensity profile, while ablation craters in the center of a hot spot characterize a plasma string.

## 3 Results and discussion

### 3.1 Propagation at reduced pressure

Figure 1 shows beam profiles after propagation over 1 to 30 m. These profiles are qualitatively similar to equivalent profiles acquired at sea level [6, 39]. More specifically, high-intensity ‘fork’ structures appear within the beam profile, and filaments are later generated on these intensity ridges.

The position of the filament onset ( $z_f$ ) provides a good characterization of the first phase of filamentation, namely the self-focusing (Kerr) region. It is given by the Marburger formula [2]

$$\frac{1}{z_f(P)} = -\frac{1}{R} \pm \frac{\sqrt{(\sqrt{P/P_{\text{crit}}} - 0.852)^2 - 0.0219}}{0.367ka^2}, \quad (1)$$

where  $R$  is the initial wavefront curvature (in our case,  $R = f \sim 50$  m),  $P$  is the laser power,  $k$  is the wave number, and  $a$  is the radius of the beam, defined as the half width at  $e^{-1/2}$ .

In the self-focusing region, the propagation is governed by Kerr self-focusing and hence by the non-linear refractive index  $n_2$  of the air, which is proportional to the pressure [40]. Therefore, the critical power is inversely proportional to the air pressure, and  $z_f$  is strongly affected in the low-power regime, when  $P \sim P_{\text{cr}}$ . However, the asymptotic behavior of Eq. (1) for high powers ( $P \gg P_{\text{cr}}$ ) leads to a square-root pressure dependence so that, in our experiment, a 30% reduction in the atmospheric pressure only results in 15% shortening of  $z_f$ . Such an estimation cannot be compared with the experimental data (see Fig. 2), due to the limited range resolution (5 m). However, the reduced pressure does not significantly affect the filamentation length. The length observed in Fig. 2 is comparable with measurements performed under similar conditions close to sea level (155-m altitude), suggesting that the loss due to the multiphoton ionization of air is not significantly different from its value at sea level. [6]

Another key parameter is the number of filaments. A multifilamenting beam breaks up into cells containing several

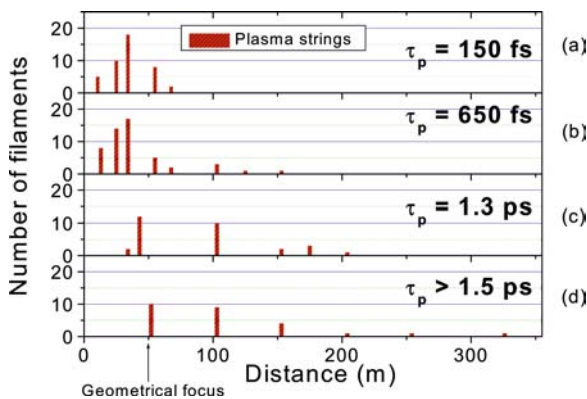
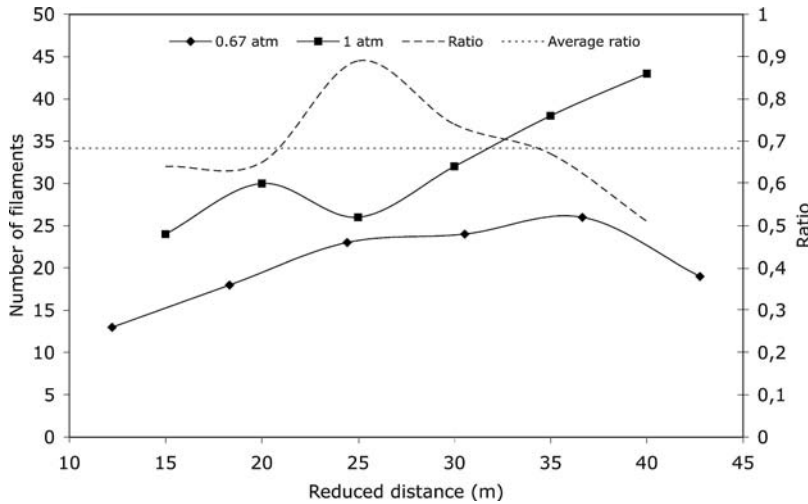


FIGURE 2 Filamentation range for 280-mJ pulses, with an initial pulse duration of a)  $\tau_p = 150$  fs, b)  $\tau_p = 650$  fs, c)  $\tau_p \sim 1.3$  ps, and d)  $\tau_p \sim 1.5$  ps



**FIGURE 3** Comparison of the filament number generated by 2.5-TW pulses at 0.67 atm (3200-m altitude) and 1 atm (sea level) for corresponding reduced propagation distances (*left-hand scale*). The ratio of the filament numbers in both conditions is plotted relative to the *right-hand scale*. See the text for the definition of reduced distances

(typically 1 to 10) critical powers [36]. Hence, the number of filaments is inversely proportional to  $P_{cr}$ , and therefore proportional to the pressure. Figure 3 correlates the filament numbers observed at 0.67-atm air pressure with those observed under similar conditions (2.5 TW, 150 fs) at sea level (Lyon, France, 170-m altitude) [36], for several propagation distances. Here, filaments have been identified as localized, high-intensity hot spots in the beam profiles. To compare filament numbers at similar stages of filamentation, the data are plotted as a function of the reduced propagation distance  $\hat{z} = z/\sqrt{p/p_0} = zz_f/z_f(p_0)$ , where  $z$  is the propagation distance and  $p$  the atmospheric pressure, and the 0 subscript corresponds to the standard atmospheric pressure. The square root of  $p$  stems from the asymptotic behavior of Eq. (1). A fairly good proportionality is observed between the filament numbers at 1 and 0.67 atm, and the average reduction of the filament number (32%) corresponds to the pressure reduction and hence to the drop in the critical power. It indeed shows that the beam breaks up into cells containing some  $P_{cr}$  each [36].

We further investigated the influence of power on the filament number by varying the chirp and observing the beam profile on photographic paper [6]. Figure 2 displays the number of plasma strings (filaments) as a function of the propagation distance for various pulse durations. The lower peak power of

longer pulses results in a farther filamentation onset (i.e. closer to the geometrical focus,  $z \sim 50$  m). A stronger chirp also results in fewer plasma channels, but over a longer filamentation range. Filaments could be observed up to 325-m distance for chirps corresponding to  $\sim 1.5$ – $1.8$ -ps pulse length.

The present observation of filamentation at a high altitude confirms a recent observation of filamentation in air at pressures as low as 0.2 atm, corresponding to an altitude over 11 km [30]. Moreover, our results extend this observation to the high-power, multifilamentation regime over several hundreds of meters. The fact that the filaments themselves are not qualitatively affected shows that the expected slightly lower free electron density in the plasma channels, due to the lower air-molecule density, does not have a significant effect.

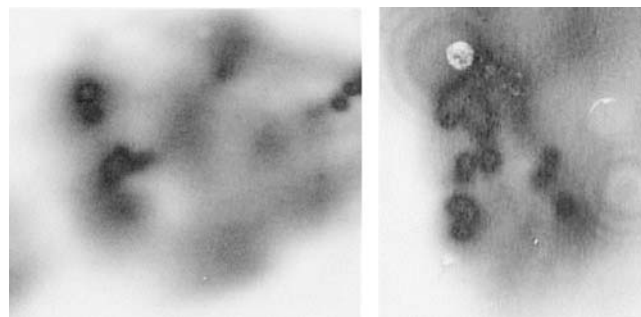


**FIGURE 4** Single-shot beam impacts on photosensitive papers after 75-m propagation in dry air (*left*) and in rain (*right*). The air pressure is 0.67 atm (altitude 3230 m). Filaments are clearly visible in both cases. The ring patterns on the profile in rain are due to the diffraction of the beam on the rain droplets

### 3.2 Filament generation in rain

Besides reduced pressure at high altitudes, the filamentation under real atmospheric conditions includes the propagation in water clouds and rain. The interaction of a fs TW laser beam with rain was investigated by propagating the strongly chirped Teramobile beam over 150 m in drizzle consisting of small ( $< 0.5$  mm) droplets with a rain flow of several mm per hour. The estimated visibility was 150 m, i.e. an extinction coefficient of  $6.6 \text{ km}^{-1}$  or 37% transmission over 150 m. In the cloud, the estimated droplet density is  $1.7 \times 10^4 \text{ m}^{-3}$  so that the 3-cm beam hits approximately one droplet for every cm propagation. Contrary to previous experiments [33, 36], where previously formed filaments interacted with a synthetic cloud, in the present experiment the whole beam interacted with water droplets, even before the filaments were initiated.

Figure 4 compares impacts on photosensitive paper at 75-m distance with and without rain. Filaments are clearly identified as intense spots on the impact paper, with ablation of the paper in their center. This provides evidence for the ability of the filaments to form in rain. The comparison between both images shows that filamentation was not perturbed by the rain, even at reduced pressure, i.e. under conditions of weaker Kerr effect. Further propagation of the filamentation process in rain was also observed up to 150 m (Fig. 5).

Therefore, rain does not prevent the filaments from being generated in the propagation of ultra-short, high-power laser pulses. Since the beam used in our experiments is much above the critical power, the losses induced by the

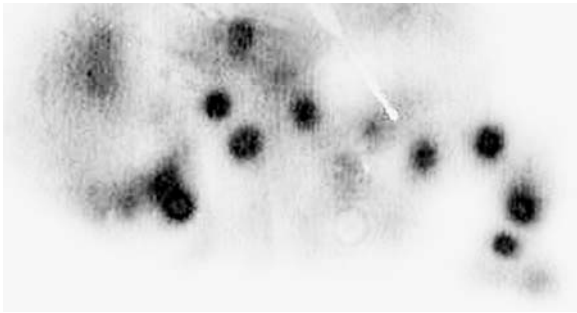


**FIGURE 5** Beam impacts on photosensitive paper after 150-m propagation in rain

scattering on the water droplets in the self-focusing (prefilamentation) region are not sufficient to prevent the self-focusing process. Moreover, one can expect that diffraction on water droplets deforms the beam profile and could generate local transverse intensity gradients. Since the self-focusing action of the Kerr effect is due to such gradients, the local intensity dips caused by the droplets could even provide nucleation centers for self-focusing and filamentation. Our observation shows that this possible positive contribution to filamentation roughly balances that of the power losses by diffraction. Once the filamentation is established, the survival of the filaments can be understood by the continuous feeding by the photon bath, as on the laboratory scale [33–35]. Filaments can therefore form and propagate in spite of rain.

#### 4 Conclusion

As a conclusion, we have presented the first experimental data about the propagation of high-power ultrashort laser pulses at reduced pressure over atmospheric scale distances. Lower pressures result in fewer filaments forming at longer distances, but without qualitatively affecting the filamentation process. Moreover, the reduced Kerr effect at high altitude does not prevent filamentation from being initiated and propagating in natural rain. The limited perturbation of both altitude and rain on filamentation is favorable for real-scale applications, which require actual filamentation at remote distances and/or high altitudes or vertical propagation in the case of atmospheric profiling, in clear atmosphere as well as under adverse weather.

**ACKNOWLEDGEMENTS** This work has been performed within the framework of the *Teramobile* collaboration, funded jointly by the CNRS, DFG, and French and German Ministries

of Foreign Affairs. The authors also acknowledge AFOSR and AFRL/DE for their financial support of the experimental campaign. K.S. acknowledges financial support by the Alexander von Humboldt Foundation. We would like to warmly thank the team of the Langmuir Laboratory at the New Mexico Institute of Mining and Technology, and especially Graydon Aulich, Gary Coppler, James Dinallo, Steven Hunyady, Sandy Kieft, Dan Klinglesmith, William Rison, and William Winn for their constant support all along the campaign. The efficient administrative support by Anne Gourlan at Lasim was also highly appreciated. The *Teramobile* web site is [www.teramobile.org](http://www.teramobile.org).

#### REFERENCES

- 1 A. Braun, G. Korn, X. Liu, D. Du, J. Squier, G. Mourou, *Opt. Lett.* **20**, 73 (1995)
- 2 J.H. Marburger, E.L. Dawes, *Phys. Rev. Lett.* **21**, 556 (1968)
- 3 B. La Fontaine, F. Vidal, Z. Jiang, C.Y. Chien, D. Comtois, A. Desparois, T.W. Johnston, J.-C. Kieffer, H. Pépin, *Phys. Plasmas* **6**, 1615 (1999)
- 4 M. Rodriguez, R. Bourayou, G. Méjean, J. Kasparian, J. Yu, E. Salmon, A. Scholz, B. Stecklum, J. Eislöffel, U. Laux, A.P. Hatzes, R. Sauerbrey, L. Wöste, J.-P. Wolf, *Phys. Rev. E* **69**, 036607 (2004)
- 5 G. Méchain, A. Couairon, Y.-B. André, C. D'Amico, M. Franco, B. Prade, S. Tzortzakis, A. Mysyrowicz, R. Sauerbrey, *Appl. Phys. B* **79**, 379 (2004)
- 6 G. Méchain, C. D'Amico, Y.-B. André, S. Tzortzakis, M. Franco, B. Prade, A. Mysyrowicz, A. Couairon, E. Salmon, R. Sauerbrey, *Opt. Commun.* **247**, 171 (2005)
- 7 J. Kasparian, R. Sauerbrey, S.L. Chin, *Appl. Phys. B* **71**, 877 (2000)
- 8 A. Becker, N. Aközbe, K. Vijayalakshmi, E. Oral, C.M. Bowden, S.L. Chin, *Appl. Phys. B* **73**, 287 (2001)
- 9 N. Aközbe, A. Iwasaki, A. Becker, M. Scalora, S.L. Chin, C.M. Bowden, *Phys. Rev. Lett.* **89**, 143901 (2002)
- 10 J. Kasparian, R. Sauerbrey, D. Mondelain, S. Niedermeier, J. Yu, J.-P. Wolf, Y.-B. André, M. Franco, B. Prade, A. Mysyrowicz, S. Tzortzakis, M. Rodriguez, H. Wille, L. Wöste, *Opt. Lett.* **25**, 1397 (2000)
- 11 H. Schillinger, R. Sauerbrey, *Appl. Phys. B* **68**, 753 (1999)
- 12 S. Tzortzakis, B. Prade, M. Franco, A. Mysyrowicz, *Opt. Commun.* **181**, 123 (2000)
- 13 B. La Fontaine, F. Vidal, Z. Jiang, C.Y. Chien, D. Comtois, A. Desparois, T.W. Johnston, J.-C. Kieffer, H. Pépin, H.P. Mercure, *Phys. Plasmas* **6**, 1615 (1999)
- 14 A. Talebpour, A. Abdel-Fattah, S.L. Chin, *Opt. Commun.* **183**, 479 (2000)
- 15 J. Kasparian, R. Sauerbrey, S.L. Chin, *Appl. Phys. B* **71**, 877 (2000)
- 16 A. Talebpour, J. Yang, S.L. Chin, *Opt. Commun.* **163**, 29 (1999)
- 17 J. Kasparian, M. Rodriguez, G. Méjean, J. Yu, E. Salmon, H. Wille, R. Bourayou, S. Frey, Y.-B. André, A. Mysyrowicz, R. Sauerbrey, J.-P. Wolf, L. Wöste, *Science* **301**, 61 (2003)
- 18 P. Rairoux, H. Schillinger, S. Niedermeier, M. Rodriguez, F. Ronneberger, R. Sauerbrey, B. Stein, D. Waite, C. Wedekind, H. Wille, L. Wöste, *Appl. Phys. B* **71**, 573 (2000)
- 19 G. Méjean, J. Kasparian, E. Salmon, J. Yu, J.-P. Wolf, R. Bourayou, R. Sauerbrey, M. Rodriguez, L. Wöste, H. Lehmann, B. Stecklum, U. Laux, J. Eislöffel, A. Scholz, A.P. Hatzes, *Appl. Phys. B* **77**, 357 (2003)
- 20 G. Méjean, J. Kasparian, J. Yu, S. Frey, E. Salmon, J.-P. Wolf, *Appl. Phys. B* **78**, 535 (2004)
- 21 B. La Fontaine, D. Comtois, C.Y. Chien, A. Desparois, F. Gérin, G. Jarry, T.W. Johnston, J.C. Kieffer, F. Martin, R. Mawassi, H. Pépin, F.A.M. Rizk, F. Vidal, C. Potvin, P. Couture, H.P. Mercure, *J. Appl. Phys.* **88**, 610 (2000)
- 22 M. Rodriguez, R. Sauerbrey, H. Wille, L. Wöste, T. Fujii, Y.-B. André, A. Mysyrowicz, L. Klingbeil, K. Rethmeier, W. Kalkner, J. Kasparian, E. Salmon, J. Yu, J.-P. Wolf, *Opt. Lett.* **27**, 772 (2002)
- 23 R. Ackermann, K. Stelmaszczyk, P. Rohwetter, G. Méjean, E. Salmon, J. Yu, J. Kasparian, G. Méchain, V. Bergmann, S. Schaper, B. Weise, T. Kumm, K. Rethmeier, W. Kalkner, J.P. Wolf, L. Wöste, *Appl. Phys. Lett.* **85**, 5781 (2004)
- 24 K. Stelmaszczyk, P. Rohwetter, G. Méjean, J. Yu, E. Salmon, J. Kasparian, R. Ackermann, J.-P. Wolf, L. Wöste, *Appl. Phys. Lett.* **85**, 3977 (2004)
- 25 M. Mlejnek, E.M. Wright, J.V. Moloney, *Phys. Rev. E* **58**, 4903 (1998)
- 26 S. Champeaux, L. Bergé, *Phys. Rev. E* **68**, 066603 (2003)
- 27 A. Becker, N. Aközbe, K. Vijayalakshmi, E. Oral, C.M. Bowden, S.L. Chin, *Appl. Phys. B* **73**, 287 (2001)
- 28 N. Kortsalioudakis, M. Tatarakis, N. Vakakis, S.D. Moustazis, S. Tzortzakis, M. Franco, B. Prade, A. Mysyrowicz, N. Papadogiannis, A. Couairon, *Appl. Phys. B* **80**, 211 (2005)
- 29 C.P. Hauri, W. Kornelis, F.W. Helbing, A. Couairon, A. Mysyrowicz, J. Biegert, U. Keller, *Appl. Phys. B* **79**, 673 (2004)
- 30 G. Méchain, T. Olivier, M. Franco, A. Couairon, B. Prade, A. Mysyrowicz, Femtosecond filamentation in air at low pressure, part II: laboratory experiments in preparation
- 31 P. Chylek, M.A. Jarzembki, V. Srivastava, R.G. Pinnick, *Appl. Opt.* **29**, 2303 (1990)
- 32 P. Sprangle, J.R. Peñano, B. Hafizi, *Phys. Rev. E* **66**, 046418 (2002)
- 33 F. Courvoisier, V. Boutou, J. Kasparian, E. Salmon, G. Méjean, J. Yu, J.-P. Wolf, *Appl. Phys. Lett.* **83**, 213 (2003)
- 34 M. Kolesik, J.V. Moloney, *Opt. Lett.* **29**, 590 (2004)

- 35 S. Skupin, L. Bergé, U. Peschel, F. Lederer, Phys. Rev. Lett. **93**, 023901 (2004)
- 36 G. Méjean, J. Kasparian, J. Yu, E. Salmon, S. Frey, J.-P. Wolf, S. Skupin, A. Vinçotte, R. Nuter, S. Champeaux, L. Bergé, submitted to Phys. Rev. E
- 37 H. Wille, M. Rodriguez, J. Kasparian, D. Mondelain, J. Yu, A. Mysyrowicz, R. Sauerbrey, J.P. Wolf, L. Wöste, Eur. Phys. J. – Appl. Phys. **20**, 183 (2002)
- 38 J. Kasparian, J.-P. Wolf, Opt. Commun. **152**, 355 (1998)
- 39 L. Bergé, S. Skupin, F. Lederer, G. Méjean, J. Yu, J. Kasparian, E. Salmon, J.P. Wolf, M. Rodriguez, L. Wöste, R. Bourayou, R. Sauerbrey, Phys. Rev. Lett. **92**, 225 002 (2004)
- 40 E.R. Peck, J.D. Fischer, J. Opt. Soc. Am. **54**, 1362 (1964)

**Multifilamentation transmission through fog**

G. Méjean, J. Kasparian,\* J. Yu, E. Salmon, S. Frey, and J.-P. Wolf  
*Teramobile, LASIM, UMR CNRS 5579, Université Claude Bernard Lyon 1, 43 bd du 11 Novembre 1918,  
 F-69622 Villeurbanne Cedex, France*

S. Skupin,† A. Vinçotte, R. Nuter, S. Champeaux, and L. Bergé  
*Département de Physique Théorique et Appliquée, CEA/DAM Ile de France, B.P. 12, 91680 Bruyères-le-Châtel, France*  
 (Received 11 April 2005; revised manuscript received 15 June 2005; published 19 August 2005)

The influence of atmospheric aerosols on the filamentation patterns created by TW laser beams over 10 m propagation scales is investigated, both experimentally and numerically. From the experimental point of view, it is shown that dense fogs dissipate quasi-linearly the energy in the beam envelope and diminish the number of filaments in proportion. This number is strongly dependent on the power content of the beam. The power per filament is evaluated to about 5 critical powers for self-focusing in air. From the theoretical point of view, numerical computations confirm that a dense fog composed of micrometric droplets acts like a linear dissipator of the wave envelope. Beams subject to linear damping or to collisions with randomly-distributed opaque droplets are compared.

DOI: [10.1103/PhysRevE.72.026611](https://doi.org/10.1103/PhysRevE.72.026611)

PACS number(s): 42.68.Ay, 42.68.Ge

**I. INTRODUCTION**

High-power, ultrashort (femtosecond) laser pulses can propagate in air within a self-guided mode. This regime is often referred to as “filamentation” [1]. It requires that the beam power exceeds a critical power  $P_{cr}=3.7\lambda_0^2/8\pi n_2$ , where  $n_2$  denotes the nonlinear Kerr index coefficient of dioxygen molecules and  $\lambda_0$  the central laser wavelength ( $P_{cr} \approx 3$  GW at  $\lambda_0=800$  nm with  $n_2 \sim 3 \times 10^{-19}$  cm<sup>2</sup>/W). This condition allows Kerr-lens self-focusing to overcome diffraction. For beam powers widely above  $P_{cr}$ , several filaments with about 150  $\mu$ m in diameter, forming localized structures inside the transverse beam pattern, are nucleated and can propagate over distances much longer than the Rayleigh length, from several hundreds of meters [2] up to the kilometer range [3,4]. Their very high, quasiconstant intensity lying in the order of 10<sup>14</sup> W/cm<sup>2</sup> [5,6] allows efficient self-phase modulation and generation of a broadband white-light continuum spanning from the ultraviolet [7] to the mid-infrared [8]. Ionization of air molecules [2,9–12] in the vicinity of the filaments crucially contributes to their self-guiding, as the resulting electron plasma defocuses the pulse and keeps up a dynamic balance with the Kerr focusing response of the medium.

The main properties of the filaments (white-light generation, air conductivity, and high intensities at remote distances) open exciting ways for atmospheric applications [13]. The broad white-light continuum allows to extend the Lidar (light detection and ranging) technique with nonlinear and multispectral measurements [3,14–16]. The continuously ionized plasma channels generated in the filaments are also

suitable for high-voltage discharge switching and guiding, opening the perspective for laser lightning control [17–20]. Finally, the ability of filaments to deliver high intensities at long distances permits remote elemental analysis by laser-induced breakdown spectroscopy techniques [21].

The above open-field applications stimulate the need for a better knowledge of the filament propagation in perturbed atmospheres, such as adverse weather, and especially through clouds and rain. Recent results on laboratory scales, both experimental [22] and theoretical [23,24], have shown that single filaments can survive their interaction with obscuring droplets of diameters up to  $\sim 100$   $\mu$ m, comparable with the filament size. They have also shown that the filamentation of a GW beam can survive the transmission through a cloud with an optical thickness as high as 3, corresponding to 5% transmission. Filament robustness is due to the refocusing of some beam components that are kept untouched after the collision and whose power remains above critical. These components again self-focus onto the beam axis and replenish the filament within a few cm. In connection with this aspect, the role of elastic losses inside the overall beam envelope (i.e., the whole focal spot playing the role of an “energy reservoir” or “photon bath” for the enclosed filaments) is crucial for maintaining the filamentary dynamics over longer distances. In Refs. [25,26], high-power beams were shown to freely propagate through long-range clusters of filaments (so-called “optical pillars”) created from the initial fluctuations of the beam. Such clusters are capable of covering several tens of meters, while their constituent filaments appear and disappear recurrently over  $\sim 1$  m by exchanging energy with the surrounding photon bath, in agreement with the scenario proposed in Ref. [27]. In the presence of water droplets, the survival of multiple filaments has been observed qualitatively. The propagation through 5 m of a water cloud with 0.3 droplets/cm<sup>3</sup> having a mean diameter of 0.5 mm reduces only slightly the efficiency of a  $\sim 1.5$  TW beam to trigger and guide high-voltage discharges [20]. However, neither systematic experimental data nor numerical simula-

\*Electronic address: [jkaspari@lasim.univ-lyon1.fr](mailto:jkaspari@lasim.univ-lyon1.fr)

†Also at: Institute for Condensed Matter Theory and Solid State Optics, Friedrich-Schiller-Universität Jena, Max-Wien-Platz 1, 07743 Jena, Germany

tions are available to date concerning the multifilamentation of TW-class beams propagating in clouds or rain over propagation scales relevant for atmospheric applications.

In this work, we investigate for the first time the influence of a 10 m long fog on multifilamenting TW beams that propagate upon 50 m. Section II presents the experimental setup and main observations. Section III is devoted to numerical computations performed in this field.

## II. EXPERIMENTAL RESULTS

### A. Experimental setup

The experiments were conducted with the mobile femtosecond-Terawatt “*Teramobile*” laser system [28], allowing for outdoor experiments under any weather condition. The *Teramobile* produces 220 mJ pulses at 10 Hz repetition rate, centered at 800 nm. The beam is emitted in collimated geometry, with an initial diameter of 3 cm. The minimum pulse duration is 80 fs, although a chirp enlarging it up to 1 ps can be applied, in order to precompensate for group velocity dispersion (GVD) in air. In that case, the pulses are refocused temporally after a given propagation distance [29,30].

The *Teramobile* beam was propagated horizontally at the sea level (Lyon, 170 m altitude). After 40 m of free propagation, it hit a synthetic fog of water droplets produced in an open cloud chamber, already depicted in Ref. [16]. The initial laser chirp was adjusted, so that filamentation began shortly before the beam enters the cloud. This corresponds to an initial pulse duration of 600 fs. Then, the filaments propagated over 10 meters through a quasihomogeneous cloud. The cloud density was estimated by measuring the elastic transmission of a low-power He:Ne laser. Its droplet size distribution was centered at 1  $\mu\text{m}$  radius (i.e., much smaller than the filament size), as monitored by using an optical sizer (Grimm model G 1-108).

Propagation in cloudy atmosphere was characterized by recording beam profiles. These were acquired by taking photographs of the beam imaged on a screen, using a digital camera. The exposure time of 1/8 s was chosen to assure that each picture corresponds to a single-shot picture. Images have been taken both over the whole spectrum, with high sensitivity to the white-light continuum and to the conical emission, and in the infrared (fundamental) region of the spectrum, yielding a good approximation of the beam profile at the considered distance, as demonstrated in Refs. [25,26].

### B. Results and discussion

In a first series of experiments, we analyzed the beam pattern at the exit of the cloud chamber for high droplet densities (not shown here). The minimal input power required for observing transmission of light by one filament at the chamber exit was about 28 GW, i.e., close to  $9P_{\text{cr}}$ . At higher powers, filaments were clearly transmitted through the cloud and the transmitted beam energy lied above 25 mJ (power  $\sim 45$  GW). For a cloud length of 10 m crossed by pulses with 220 mJ incident energy, this corresponds to 12% transmission, i.e., a dense fog with an extinction coefficient

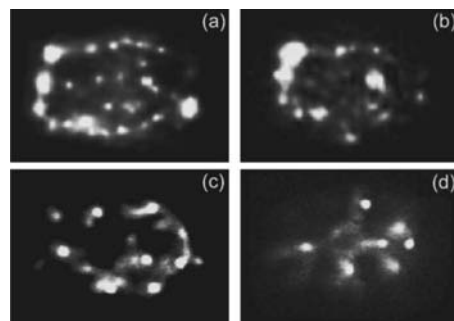


FIG. 1. Beam profiles at the exit of the 10 m long cloud chamber, in the case of both free propagation [(a) and (c)] at the respective powers of  $123P_{\text{cr}}$  (220 mJ, 600 fs) and  $51P_{\text{cr}}$  ( $\sim 90$  mJ, 600 fs), and propagation through 10 m of a dense fog [(b) and (d)] with the same powers. Subplot dimensions are about  $5 \times 3.5$  cm<sup>2</sup>.

of  $\epsilon \approx 0.21$  m<sup>-1</sup>. Thus, filamentation can survive the propagation in a fog over a distance comparable with the fog visibility. In the cloud, the droplet density is  $N = 6.7 \times 10^4$  cm<sup>-3</sup>, so that the photon mean free path (MFP) is about 5 m. Here, MFP is the average longitudinal length  $L_M$ , along which an optical object of radius  $r$  will collide a droplet of radius  $R$ ,  $L_M = 1 / \pi(r+R)^2 N$ . For an optical ray, we have  $r \rightarrow 0$ , so that  $L_M = 5$  m guarantees a weak interaction of photons with droplets. In contrast, a femtosecond filament with radius  $r \sim 100$   $\mu\text{m}$  has a MFP of only  $\sim 0.5$  mm, so that one individual filament hits about 2000 particles per meter of propagation. This may possibly induce substantial damage on the filamentary structure. However, the droplet radius (1  $\mu\text{m}$ ) is typically 100 times smaller than the filament size. Since much larger droplets are not sufficient to block the filaments [22–24], these may not be destroyed by the cloud used in our experiment, as long as droplets have a small enough mean size. With that condition, the cloud influence can be expected to occur mainly through the energy losses escaping from the overall beam envelope.

We investigated this effect with a second series of experiments by recording beam profiles at the exit of the cloud chamber for two incident laser energies, both in the free propagation regime and with the synthetic cloud with 50% transmission. This higher transmission corresponds to an extinction coefficient of  $\epsilon = 0.07$  m<sup>-1</sup>, i.e., to a droplet density of  $2.2 \times 10^4$  cm<sup>-3</sup> and a photon MFP of 14 m. As shown in Fig. 1, the transmitted beam energy strongly influences the spatial distribution of filaments, and especially their number. The filamentation patterns for close transmitted energies (90 mJ [Fig. 1(c)], and 220 mJ with 50% attenuation, i.e., 110 mJ transmitted energy [Fig. 1(b)]) indeed look similar, with most of the filaments located on a ring at the edge of the beam profile, and several of them arising inside this ring. Only a few filamentary sites have disappeared along the optical path through the fog [see Figs. 1(a)–1(d)]. The number of filaments decreases accordingly with the power left at the output of the cloud chamber. This shows that the cloud globally acts like a power attenuator on the beam as a whole. It promotes elastic extinction of the “photon bath” and its embedded filaments.

To confirm this finding, we investigated the dependency of the transmitted power on the number of filaments. It is

TABLE I. Average filament number vs input beam power after 50 m of propagation, thereof 10 m in free or foggy atmospheres.

$P_{in}/P_{cr}$	123		51	
Propagation	Free	Fog	Free	Fog
Filament No.	24	13	11	6

generally known that beams highly exceeding the critical power for self-focusing break up into many self-focusing cells, each containing several critical powers. Typically, the modulational instability theory predicts that about  $3P_{cr}$  is engaged in each cell [31], which holds as long as a single filament experiences the surrounding background field as a uniform plane wave. For each experimental condition of Fig. 1, the filament number has been averaged over four to seven recorded profiles. Results have been summarized in Table I. Assuming weak absorption caused by plasma generation [27], the beam power transmitted over 50 m of free propagation is almost constant, whereas that crossing the cloud chamber upon the same propagation distance can be estimated by  $P_{tr} \approx P_{in}/2$ . A linear fit shows in Fig. 2 a ratio of one filament cell for every 15 GW of transmitted power with  $P_{cr} \approx 3$  GW. This curve clearly indicates that about five critical powers are engaged in each filament, regardless of whether the beam propagates through a cloud or not. This estimate is in reasonably good agreement with previous expectations. It lies between the theoretical evaluations applying to purely Kerr media ( $P_{fil} \sim 3P_{cr}$ ) [31] and recent (3+1)-dimensional simulations of femtosecond filaments self-channeling in air ( $P_{fil} \sim 7P_{cr}$ ) [24].

Furthermore, besides energy losses, the cloud may reduce the peak power by increasing the pulse duration, because of multiple scattering. We estimated this effect by means of ray-tracing techniques and Monte Carlo simulations. Multiple scattering induced by  $1 \mu\text{m}$  large droplets results in random trajectories, modeled as successive segments, whose length is the photon MFP deflected by a small angle with respect to the beam propagation axis. Differences in the trajectory lengths of rays remaining near axis at the exit of the cloud chamber yield a direct information on the modal (temporal) dispersion produced by the droplets. The rays scattered out of the beam axis are considered as lost and are discarded by the calculation. With a cloud transmission of 50%, the pulse stretching is around 100 fs, negligible for the 600 fs pulse used in the present experiment. However, at the

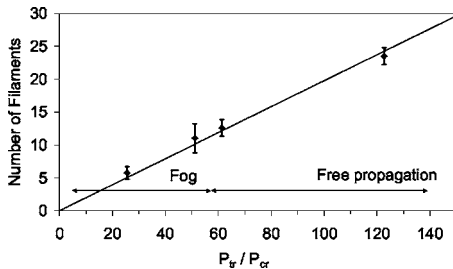


FIG. 2. Dependence of the transmitted power ( $P_{tr}$ ) on the filament number for free or humid propagation [ $P_{cr} \approx 3$  GW].

filamentation threshold (12% transmission), the broadening is in the order of 500 fs, thus doubling the effective pulse duration. The effect would be even stronger in the case of shorter incident pulses. This semiquantitative argument indicates that the cloud affects the filamentation by reducing the laser power together with the beam energy.

### III. NUMERICAL ANALYSIS

The extinction of filaments through a dense cloud is now numerically investigated. Our physical model, which captures the essential features of long-distance propagation in air, has been described in Refs. [25,26]. Originally derived in (3+1) dimensions, it consists of an extended nonlinear Schrödinger equation for the laser electric field envelope  $\mathcal{E}$ , coupled with a Drude model describing the growth of free electron density. These equations apply to pulses moving in their group-velocity frame, and characterized by a beam waist  $w_0$ , half-width duration  $t_p$  and central wave number  $k_0 = 2\pi/\lambda_0$ . They include effects of transverse diffraction, self-focusing, stimulated Raman scattering, plasma gain and losses that are mainly induced by multiphoton ionization (MPI) of dioxygen molecules.

Because experiments involve broad beams with cm waists, direct simulations in (3+1)-dimensional geometry are costly in computation time and require Terabyte storage systems when propagating the entire pulse over several tens of meters. Moreover, simulating collisions with micrometric droplets become even impossible to deal with, since the requested spatial resolution should typically access the tenth of micron for a numerical box close to  $6 \times 6 \text{ cm}^2$ . Therefore, the present issue will be addressed in the framework of a reduced (2+1)-dimensional model, which freezes the temporal dependencies of  $\mathcal{E}$ . After substituting the *ansatz*  $\mathcal{E}(x, y, z, t) = \psi(x, y, z) \times e^{-[t-t_c(z)]^2/T^2}$  whose temporal extent,  $T \approx t_p/10$ , is assumed constant in the filamentation regime, the model equations are averaged in time following the analytical procedure described in Ref. [25], in order to establish the equation for the spatial envelope  $\psi$  as

$$\frac{\partial \psi}{\partial z} = \frac{i}{2k_0} \nabla_{\perp}^2 \psi + i\alpha k_0 n_2 |\psi|^2 \psi - ik_0 \frac{n_4}{\sqrt{3}} |\psi|^4 \psi - i\gamma |\psi|^{2K} \psi - \frac{\beta^{(K)}}{2\sqrt{K}} |\psi|^{2K-2} \psi - \frac{\epsilon}{2} \psi, \quad (1)$$

with  $\alpha = 1/\sqrt{8} + D/4\tau_K$ ,  $\gamma = k_0 \sigma_K \rho_{nt} \sqrt{\pi/8KT}/2\rho_c$  and

$$D \equiv \int_{-\infty}^{+\infty} e^{(T^2/8\tau_K^2) - (u/\tau_K) - (2u^2/T^2)} \left[ \text{erf} \left( \frac{\sqrt{2}u}{T} - \frac{T}{\sqrt{8}\tau_K} \right) + 1 \right] du. \quad (2)$$

The function  $D$  depends on the relaxation time ( $\tau_K = 70$  fs) of the Raman-delayed Kerr response and it takes the value of 44 fs (resulting  $\alpha = 0.51$ ) for a temporal duration of  $t_p \approx 510$  fs [full width at half-maximum (FWHM) = 600 fs]. The other coefficients of Eq. (1) involve parameters appropriate to air, namely, the neutral density of dioxygen molecules  $\rho_{nt} = 5.4 \times 10^{18} \text{ cm}^{-3}$ , the critical plasma density at

800 nm,  $\rho_c \approx 1.8 \times 10^{21} \text{ cm}^{-3}$ , the multiphoton absorption (MPA) coefficient  $\beta^{(K)} \approx 3.1 \times 10^{-98} \text{ cm}^{2K-3} / \text{W}^{K-1}$ , the MPI rate  $\sigma_K = 2.9 \times 10^{-99} \text{ s}^{-1} \text{ cm}^{2K} / \text{W}^K$  and number of photons  $K=8$ . For completeness, quintic susceptibility has been introduced with weak coefficient  $n_4 = 2.5 \times 10^{-33} \text{ cm}^4 / \text{W}^2$ , which was justified by recent studies [32,33]. The damping term with coefficient  $\epsilon$  (in  $\text{m}^{-1}$ ) describes the linear extinction of power in a beam propagating through the cloud chamber. We recall that Eq. (1) restores quantitative features in the long-range evolution of TW filamentation patterns issued from realistic broad beams [25,26]. It is, however, constrained to the approximation limiting the temporal pulse profile to one narrow time slice ( $T=0.1t_p$ ) and cannot account for, e.g., the variations of the nonlinear focus caused by the introduction of a temporally chirped phase [30].

#### A. Filament decay by linear damping and random collisions with obscurants

We examine the changes occurring in filamentation patterns caused either by a linear damping or by collisions with droplets randomly distributed in the  $(x, y)$  plane. Such collisions are currently modeled by means of the Mie theory [34] for light scattering by spheres. Since Mie scattering is almost independent of the optical properties of the scatterers, it is possible to model droplets by opaque screens of suitable size in the simulations. This property was exploited in Ref. [24], where droplets were numerically designed as a circular amplitude mask with radius  $R$  and maximum opacity (zero transmission) at their center  $(x_0, y_0)$ . This modeling provides good results for the interaction of one filament with a single droplet. For example, simulations proved that a single filament self-heals over only 2 cm of propagation with an energy loss limited to around 10%, which agrees with the experimental observations of Ref. [22]. This property, however, does not guarantee that many filaments can survive sharp interactions with thousands of small obscurants placed upon a long optical path.

To address this point, we first integrate Eq. (1) for a mm-waisted Gaussian beam ( $w_0=2 \text{ mm}$ ) having a FWHM duration of 600 fs and  $\sim 110$  critical powers perturbed by a 20% random noise. On the one hand, we let the beam propagate freely over 1 m, before it reaches a 10 m long zone in which linear dissipation becomes active with  $\epsilon=0.07 \text{ m}^{-1}$ . This value insures in principle an attenuation rate of 50% over 10 m. On the other hand, we impose  $\epsilon=0$ , but model the random collisions of the beam with the micrometric obstacles used in Ref. [24]. In this case, a random number of droplets located at random positions is computed at each  $z$  step. These positions are assumed to be uniformly distributed with respect to  $x$  and  $y$ . Hence, for each droplet we generate two random numbers between  $-0.5$  and  $0.5$  and multiply them by  $L_x$  and  $L_y$ , that denote the sizes of the computation window. Since the number of droplets in one  $z$  step is small compared to their total number, a Poisson statistics may be used. We fix the expected average number of droplets at a  $z$  step,  $\Delta z$ , by  $\lambda = \Delta z L_x L_y N$ , where  $N$  is the droplet density. Then, the Poisson density function  $\mathcal{P}(l) = \lambda^l / l! \times \exp(-\lambda)$  gives the probability to find exactly  $l$  droplets between  $z$  and

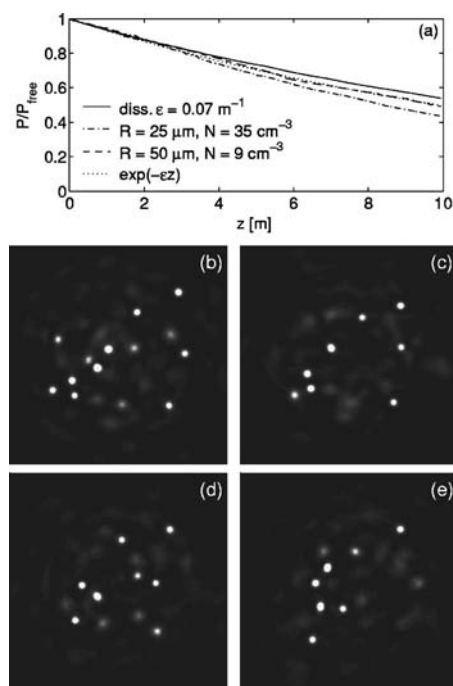


FIG. 3. (a) Numerically computed beam power scaled by the power of a freely propagating narrow beam ( $w_0=2 \text{ mm}$ ) of  $\sim 110P_{\text{cr}}$  through a 10 m long fog with linear damping ( $\epsilon = 0.07 \text{ m}^{-1}$ , solid curve), random distributions of  $25 \mu\text{m}$  droplets (dashed-dotted curve), and of  $50 \mu\text{m}$  droplets (dashed curve). The distance  $z=0$  marks the entrance into the cloud chamber. (b)–(e) Filamentation patterns at 4 m inside the cloud chamber. Subplots correspond to (b) free propagation, (c) linear damping, random droplets with radii of (d)  $25 \mu\text{m}$ , and (e)  $50 \mu\text{m}$ , respectively. Subplot dimensions are  $7 \times 7 \text{ mm}^2$ . Intensity levels are twice higher than the initial intensity.

$z + \Delta z$ . The number  $l$  is computed from the Poisson distribution function  $\mathcal{F}_{\mathcal{P}}(l) = \sum_{l'=0}^l \mathcal{P}(l')$  by means of the standard probability theory. Following this procedure, the average droplet number  $\lambda$  is linked to the dissipation parameter  $\epsilon$ , when we specify the average relative loss induced by a single droplet. Assuming that droplets do not overlap, the rate of losses caused by the obstacles along one  $z$  step can be evaluated by  $\lambda \pi R^2 / L_x L_y$ . Besides, the equivalent loss rate induced by the extinction coefficient  $\epsilon$  is  $\epsilon \Delta z$ , since  $\exp(-\epsilon \Delta z) \approx 1 - \epsilon \Delta z$ . Identifying both contributions leads to  $\epsilon = N \pi R^2$ , which agrees with the experimental estimates for  $\epsilon$ ,  $N$  and  $R$  given in Sec. II.

Because computer limitations prevented us from resolving obstacles of 1 micron large, we adopted the density for larger droplets with different radius  $R \geq 25 \mu\text{m}$  by means of the direct rescaling  $N \rightarrow N/R^2 [\mu\text{m}]$ , in order to keep the average losses constant. Results are illustrated in Fig. 3. Figure 3(a) shows the power decrease inside the cloud chamber, normalized with respect to the power of the freely propagating beam. All curves lie closely to each other, within a margin less than  $\pm 5\%$  around the exponential decrease  $e^{-\epsilon z}$  (note that the curve for linear damping also accounts for Kerr, MPI, and MPA nonlinearities and cannot exactly fit this exponential function). This property was retrieved when using different densities  $N$  and adapted values of  $\epsilon$ . Here, the decrease of

power undergone by the 2 mm beam from random collisions with droplets of  $25 \mu\text{m}$  as well as  $50 \mu\text{m}$  radius almost superimposes with that induced by linear dissipation over 4 m. Beam profiles at this distance are detailed in Figs. 3(b)–3(e). After only 4 m of “humid” propagation, the filamentation patterns remain similar in linearly damped regime and in the presence of random droplets ( $\sim 8$  cells). Compared with the free propagation regime [Fig. 3(b)], the number of filaments has already decreased by a factor  $\sim 3/2$  [Figs. 3(c)–3(e)]. Analogy in the power losses and filament number between droplets of different sizes follows from the fact that, even if small droplets embark half-energy of the big ones per collision event (see, e.g., Ref. [22]), their density is four times higher and cause equivalent damage on the filamentation patterns.

At further distances ( $z \rightarrow 10$  m), the filaments decrease in number, but this number is preserved with linear dissipation and random droplets (not shown here). This confirms the good agreement between the power losses induced by random collisions with micrometric obscurants and those induced by linear damping. Note, however, that the power lost from random droplets can reach  $\sim 55\%$  at large distance. Although small, these discrepancies are related to the finiteness of the numerical box, from which escaping field components increases the losses. This tendency is amplified by the opacity of the droplets, which favors large-angle diffraction to the boundaries.

In summary, droplet-induced losses are identical at constant product  $N \times R^2$ , i.e., they are similar for droplets with different radii, provided that the density  $N$  is tuned accordingly. They follow an exponential-like decrease comparable with the energy fall produced by a linear damping. These findings confirm the equivalence between collisions of an optical beam with randomly distributed droplets and exponential attenuation of its power.

### B. Linear damping vs filamentation patterns

Because linear damping and droplet collisions induce analogous power losses, we investigate the consequences of a linear damping on broad beams inside a 10 m dense fog after a 40 m long stage of free propagation, in conditions close to the experimental setup. We enlarge the beam waist to the value  $w_0 = 1$  cm, applied to a digitized file of the experimental input beam fluence. This value is willingly chosen smaller than the experimental beam waist, in order to compensate for the limitations of Eq. (1) recalled above. This model cannot indeed account for the temporal compression induced by pulse chirping (see Sec. II) and it artificially decreases the effective ratio of power over critical when imposing  $T = 0.1t_p$  (see Ref. [30]). The need to make a fully bloomed filamentation pattern emerge before the cloud chamber ( $z < 40$  m) implies us to select a Rayleigh length smaller than the experimental one, which justifies the choice of  $w_0 = 1$  cm. Figure 4 shows the filamentary patterns outgoing from the fog tube at  $z = 50$  m, after crossing the 10 m long water cloud with 50% transmission. These patterns are in qualitatively good agreement with their experimental counterparts shown in Fig. 1. In the absence of fog, the trans-

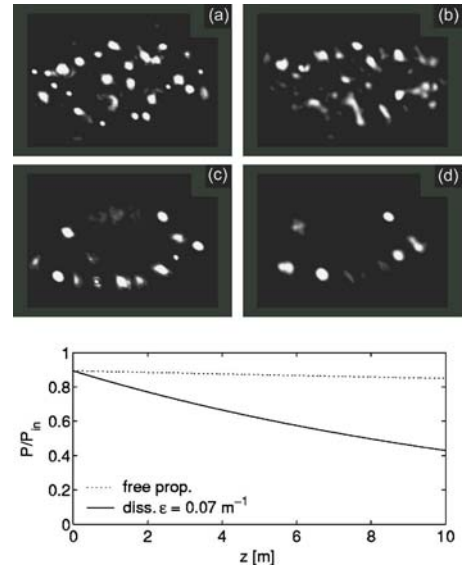


FIG. 4. Numerically computed beam profiles at the exit of the cloud chamber ( $z = 50$  m), in the case of both free propagation [(a) and (c)] at the respective powers of  $123P_{\text{cr}}$  and  $51P_{\text{cr}}$  and propagation through 10 m of a dense fog [(b) and (d)] with the same powers. Window scales are  $2.3 \times 1.6 \text{ cm}^2$ . Intensity levels correspond to twice the initial intensity. Bottom inset compares the power losses normalized to  $P_{\text{in}}$  between free propagation and linearly damped regimes for  $P_{\text{in}} \approx 123P_{\text{cr}}$ .  $z = 0$  marks the entrance of the cloud chamber.

verse profile of the beam still contains about 25 filaments [Fig. 4(a)]. This number is almost halved when the beam undergoes linear damping [Fig. 4(b)]. The resulting number of filaments (12–15) is of the same order as that obtained over a 50 m long free propagation range, when the beam only involves an initial power divided by a factor  $\sim 2$  [Fig. 4(c)]. The same beam with 51 critical powers undergoes a drastic reduction of filaments when it propagates through the 10 m tube with a 50% linear damping [Fig. 4(d)]. The bottom inset of this figure demonstrates that MPA losses remain weak over 50 m compared with linear damping, which supports the approximation on the transmitted power  $P_{\text{tr}} \approx P_{\text{in}}/2$  made in Sec. II. The counted filaments then correspond to the bright spots visible in Fig. 4. Their number, summarized in Table II, is in very good quantitative agreement with the data mentioned in Table I. Differences in the exact number and location of the filaments compared with the experimental profiles are attributed to the smaller beam waist and to fluctuations of secondary importance (local diffusion, atmospheric turbulence, see Ref. [26]), which we ignore.

TABLE II. Filament number vs input beam power provided by numerical computations. The additional datum with 62 critical powers concerns filaments counted from the same beam in free propagation regime (not shown in Fig. 4).

$P_{\text{in}}/P_{\text{cr}}$	123		62		51	
Propagation	Free	Fog	Free	Free	Free	Fog
Filament No.	25	12–15	13	12	12	6

These last results are instructive: They validate the experimental estimate of about 5 critical powers per filament. In free propagation regime, they also highlight the strong correlation between the number of critical powers in the starting beam and the number of filaments formed along the course of the pulse. They finally confirm again that the effect of a dense cloud enclosing sufficiently small droplets (compared with the filament size) is equivalent to a linear dissipation source acting on the energy reservoir formed by the beam envelope and its filaments.

#### IV. CONCLUSION

In summary, we have studied both experimentally and numerically the propagation of ultrashort laser pulses with powers much above critical in multifilamentation regimes through dense fogs. We showed that filament transmission through clouds is not restricted to the laboratory scale [22], but also occurs when multiple filaments take place over a distance comparable with the visibility length of the fog.

From the theoretical point of view, we examined differences in the transmitted light, when the model equations account for either linear damping or a stochastic hitting of the beam by micrometric obstacles. Because of computer limitations, we could not access the interaction of femtosecond pulses with  $1\ \mu\text{m}$  large droplets. However, our simulations revealed that randomly distributed opaque droplets with ra-

dius  $\geq 25\ \mu\text{m}$  induce comparable energy losses, with an exponential fall. The equivalence between linear damping and losses caused by micrometric droplets enabled us to numerically reproduce the experimental filamentation patterns and achieve a very good agreement on their number of filaments.

As a conclusion, the fact that clouds do not significantly affect the filamentation process (only the number of filaments is reduced quasilinearly by power extinction) is of high interest for applications, because it implies that the filament features such as white-light generation, ionization of air or the delivery of high intensities at long distances are not forbidden inside or beyond clouds, as long as their density permits to transmit several critical powers. Therefore, the corresponding applications, respectively, multicomponent Lidar, lightning control or remote laser-induced breakdown spectroscopy (LIBS or RFIBS [20]) are still feasible within cloudy atmospheres.

#### ACKNOWLEDGMENTS

This work has been carried out within the framework of the Teramobile project, funded jointly by the CNRS, DFG, and French and German Ministries of Foreign Affairs. The Teramobile website is [www.teramobile.org](http://www.teramobile.org). Numerical simulations were performed on the COMPAQ alpha cluster (TERA) of CEA-France and on the IBM p690 cluster (JUMP) of the Forschungs-Zentrum in Jülich-Germany.

- 
- [1] A. Braun, G. Korn, X. Liu, D. Du, J. Squier, and G. Mourou, *Opt. Lett.* **20**, 73 (1995).
  - [2] B. La Fontaine, F. Vidal, Z. Jiang, C. Y. Chien, D. Comtois, A. Desparois, T. W. Johnston, J.-C. Kieffer, H. Pépin, and H. P. Mercure, *Phys. Plasmas* **6**, 1615 (1999).
  - [3] M. Rodriguez, R. Bourayou, G. Méjean, J. Kasparian, J. Yu, E. Salmon, A. Scholz, B. Stecklum, J. Eislöffel, U. Laux, A. P. Hatzes, R. Sauerbrey, L. Wöste, and J.-P. Wolf, *Phys. Rev. E* **69**, 036607 (2004).
  - [4] G. Méchain, A. Couairon, Y.-B. André, C. D'amico, M. Franco, B. Prade, S. Tzortzakis, A. Mysyrowicz, and R. Sauerbrey, *Appl. Phys. B: Lasers Opt.* **B79**, 379 (2004).
  - [5] J. Kasparian, R. Sauerbrey, and S. L. Chin, *Appl. Phys. B: Lasers Opt.* **B71**, 877 (2000).
  - [6] A. Becker, N. Aközbeke, K. Vijayalakshmi, E. Oral, C. M. Bowden, and S. L. Chin, *Appl. Phys. B: Lasers Opt.* **B73**, 287 (2001).
  - [7] N. Aközbeke, A. Iwasaki, A. Becker, M. Scalora, S. L. Chin, and C. M. Bowden, *Phys. Rev. Lett.* **89**, 143901 (2002).
  - [8] J. Kasparian, R. Sauerbrey, D. Mondelain, S. Niedermeier, J. Yu, J.-P. Wolf, Y.-B. André, M. Franco, B. Prade, A. Mysyrowicz, S. Tzortzakis, M. Rodriguez, H. Wille, and L. Wöste, *Opt. Lett.* **25**, 1397 (2000).
  - [9] H. Schillinger and R. Sauerbrey, *Appl. Phys. B: Lasers Opt.* **B68**, 753 (1999).
  - [10] S. Tzortzakis, B. Prade, M. Franco, and A. Mysyrowicz, *Opt. Commun.* **181**, 123 (2000).
  - [11] A. Talebpour, A. Abdel-Fattah, and S. L. Chin, *Opt. Commun.* **183**, 479 (2000).
  - [12] A. Talebpour, J. Yang, and S. L. Chin, *Opt. Commun.* **163**, 29 (1999).
  - [13] J. Kasparian, M. Rodriguez, G. Méjean, J. Yu, E. Salmon, H. Wille, R. Bourayou, S. Frey, Y.-B. André, A. Mysyrowicz, R. Sauerbrey, J.-P. Wolf, and L. Wöste, *Science* **301**, 61 (2003).
  - [14] P. Rairoux, H. Schillinger, S. Niedermeier, M. Rodriguez, F. Ronneberger, R. Sauerbrey, B. Stein, D. Waite, C. Wedekind, H. Wille, and L. Wöste, *Appl. Phys. B: Lasers Opt.* **B71**, 573 (2000).
  - [15] G. Méjean, J. Kasparian, E. Salmon, J. Yu, J.-P. Wolf, R. Bourayou, R. Sauerbrey, M. Rodriguez, L. Wöste, H. Lehmann, B. Stecklum, U. Laux, J. Eislöffel, A. Scholz, and A. P. Hatzes, *Appl. Phys. B: Lasers Opt.* **B77**, 357 (2003).
  - [16] G. Méjean, J. Kasparian, J. Yu, S. Frey, E. Salmon, and J.-P. Wolf, *Appl. Phys. B: Lasers Opt.* **B78**, 535 (2004).
  - [17] B. La Fontaine, D. Comtois, C. Y. Chien, A. Desparois, F. Gérin, G. Jarry, T. W. Johnston, J.-C. Kieffer, F. Martin, R. Mawassi, H. Pépin, F. A. M. Rizk, F. Vidal, C. Potvin, P. Couture, and H. P. Mercure, *J. Appl. Phys.* **88**, 610 (2000).
  - [18] B. La Fontaine, F. Vidal, D. Comtois, C. Y. Chien, A. Desparois, T. W. Johnston, J.-C. Kieffer, H. P. Mercure, H. Pépin, and F. A. M. Rizk, *IEEE Trans. Plasma Sci.* **27**, 688 (1999).
  - [19] M. Rodriguez, R. Sauerbrey, H. Wille, L. Wöste, T. Fujii, Y.-B. André, A. Mysyrowicz, L. Klingbeil, K. Rethmeier, W. Kalkner, J. Kasparian, E. Salmon, J. Yu, and J.-P. Wolf, *Opt. Lett.* **27**, 772 (2002).
  - [20] R. Ackermann, K. Stelmaszczyk, P. Rohwetter, G. Méjean, E.

- Salmon, J. Yu, J. Kasparian, G. Méchain, V. Bergmann, S. Schaper, B. Weise, T. Kumm, K. Rethmeier, W. Kalkner, J.-P. Wolf, and L. Wöste, *Appl. Phys. Lett.* **85**, 5781 (2004).
- [21] K. Stelmaszczyk, P. Rohwetter, G. Méjean, J. Yu, E. Salmon, J. Kasparian, R. Ackermann, J.-P. Wolf, and L. Wöste, *Appl. Phys. Lett.* **85**, 3977 (2004).
- [22] F. Courvoisier, V. Boutou, J. Kasparian, E. Salmon, G. Méjean, J. Yu, and J.-P. Wolf, *Appl. Phys. Lett.* **83**, 213 (2003).
- [23] M. Kolesik and J. V. Moloney, *Opt. Lett.* **29**, 590 (2004).
- [24] S. Skupin, L. Bergé, U. Peschel, and F. Lederer, *Phys. Rev. Lett.* **93**, 023901 (2004).
- [25] L. Bergé, S. Skupin, F. Lederer, G. Méjean, J. Yu, J. Kasparian, E. Salmon, J.-P. Wolf, M. Rodriguez, L. Wöste, R. Bourayou, and R. Sauerbrey, *Phys. Rev. Lett.* **92**, 225002 (2004).
- [26] S. Skupin, L. Bergé, U. Peschel, F. Lederer, G. Méjean, J. Yu, J. Kasparian, E. Salmon, J.-P. Wolf, M. Rodriguez, L. Wöste, R. Bourayou, and R. Sauerbrey, *Phys. Rev. E* **70**, 046602 (2004).
- [27] M. Mlejnek, M. Kolesik, J. V. Moloney, and E. M. Wright, *Phys. Rev. Lett.* **83**, 2938 (1999).
- [28] H. Wille, M. Rodriguez, J. Kasparian, D. Mondelain, J. Yu, A. Mysyrowicz, R. Sauerbrey, J.-P. Wolf, and L. Wöste, *Eur. Phys. J.: Appl. Phys.* **20**, 183 (2002).
- [29] J. Kasparian and J.-P. Wolf, *Opt. Commun.* **152**, 355 (1998).
- [30] R. Nuter, S. Skupin, and L. Bergé, *Opt. Lett.* **30**, 917 (2005).
- [31] L. Bergé, Cl. Gouédard, J. Schjødt-Eriksen, and H. Ward, *Physica D* **176**, 181 (2003), and references therein.
- [32] A. Vinçotte and L. Bergé, *Phys. Rev. A* **70**, 061802(R) (2004).
- [33] L. Bergé, S. Skupin, G. Méjean, J. Kasparian, J. Yu, S. Frey, E. Salmon, and J.-P. Wolf, *Phys. Rev. E* **71**, 016602 (2005).
- [34] G. Mie, *Ann. Phys.* **25**, 337 (1908).

# Laser filaments generated and transmitted in highly turbulent air

R. Ackermann, G. Méjean, J. Kasparian, J. Yu, E. Salmon, and J.-P. Wolf

Laboratoire de Spectrométrie Ionique et Moléculaire, Unité Mixte de Recherche Associée au Centre National de la Recherche Scientifique 5579, Université Claude Bernard Lyon 1, 43 bd du 11 Novembre 1918, F-69622 Villeurbanne Cedex, France

Received July 28, 2005; accepted July 28, 2005

The initiation and propagation of a filament generated by ultrashort laser pulses in turbulent air is investigated experimentally. A filament can be generated and propagated even after the beam has propagated through strongly turbulent regions, with structure parameters  $C_n^2$  as many as 5 orders of magnitude larger than those encountered in the usual atmospheric conditions. Moreover, the filament's position within the beam is not affected by the interaction with a turbulent region. This remarkable stability is allowed by the strong Kerr refractive-index gradients generated within the filament, which exceed the turbulence-induced refractive-index gradients by 2 orders of magnitude. © 2006 Optical Society of America  
OCIS codes: 010.7060, 010.3310, 190.5940, 190.3270, 190.7110.

High-power, ultrashort (femtosecond) laser pulses can propagate in air in a strongly nonlinear mode; such propagation is referred to as filamentation<sup>1</sup> if the beam reaches a critical power [e.g.,  $P_{cr} = 3.37 \lambda^2 / (8\pi n_2)$  for Gaussian beams, i.e.,  $P_{cr} = 3$  GW in air at 800 nm, with  $n_2 = 3 \times 10^{-23}$  m<sup>2</sup>/W], allowing Kerr-lens self-focusing to overcome diffraction. Then a dynamic balance<sup>2,3</sup> between the Kerr effect and the defocusing on the plasma generated by multiphoton ionization<sup>4,5</sup> in air results in one or several filaments with diameter  $d \sim 100$   $\mu$ m. Although the Rayleigh length for such a diameter is only 4 cm, the filamentation can be observed over many tens of meters<sup>6</sup> and generated at several kilometers' distance.<sup>7</sup> Their high intensity [ $\sim 10^{14}$  W/cm<sup>2</sup>; Ref. 8] permits efficient self-phase modulation and generation of a broadband white-light continuum spanning the ultraviolet<sup>9</sup> to the mid infrared.<sup>10</sup>

These properties open exciting prospects for atmospheric applications.<sup>11</sup> The broad supercontinuum facilitates nonlinear and multispectral lidar remote sensing for detection of multiple pollutants and identification of aerosols.<sup>12</sup> The plasma channels generated in the filaments are suitable for high-voltage discharge switching and guiding, opening prospects for lightning control.<sup>13,14</sup> Finally, the possibility of remotely delivering high intensities permits remote elemental analysis.<sup>15</sup> Open-field applications in turn stimulate the need for better knowledge of filament propagation in perturbed atmospheres.

Recent results, both experimental<sup>16</sup> and theoretical,<sup>17</sup> have shown that filaments can survive their interaction with aerosols. Yet, in dry atmospheres, the main optical perturbation is turbulence, which strongly affects beam profiles and pointing stabilities. The effect of turbulence on the filaments and their pointing stability has been observed and modeled in air<sup>18,19</sup> and in water<sup>20</sup> by several groups of scientists, but no comprehensive data sets to characterize the effect of turbulence in various conditions have been reported. In this Letter we characterize the

threshold of the structure parameter for the refractive index,  $C_n^2$ , for which filamentation in air can occur and survive, depending on the position of the perturbation relative to the filament's onset.  $C_n^2$  is defined from the Kolmogorov theory for turbulence as

$$C_n^2(r) = \frac{\langle [n(r) - n(r + \Delta r)]^2 \rangle}{\Delta r^{2/3}}, \quad (1)$$

where  $r$  is the location of the perturbation and separation  $\Delta r$  is a length scale within the inertial range, i.e., a few millimeters in typical atmospheric conditions near the ground.<sup>21</sup>

In our experiments (Fig. 1), a chirped-pulse amplification Ti:sapphire laser system delivered 300 pulses of 8 mJ energy at a 22.5 Hz repetition rate, centered at 810 nm, with  $\sim 20$  mm beam diameter (at  $1/e^2$  level). The beam was focused by a spherical mirror with 5 m focal length. The origin for the propagation axis ( $z=0$ ) was taken at the nonlinear focus (filament onset,  $\sim 2.5$  m downstream of the spherical mirror). The filament length was  $\sim 2$  m. At a given position  $z$ , the beam crossed a perpendicular hot air flow (up to 500°C and 500 l/min flow at 20 m/s at the exit port, with a divergence of 20° full angle). Varying distance  $d$  between the air blower and the beam from 1 mm to 2 m permitted us to reach  $C_n^2$  values up to  $10^{-8}$  m<sup>-2/3</sup>, as monitored by use of the pointing stability of an elastically transmitted low-power laser. Pointing stabilities were characterized on series of 50 pictures on a screen ( $z=7.6$  m) of the lasers transmitted through the turbulent region. The images were

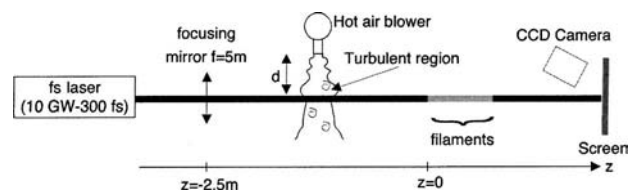


Fig. 1. Experimental setup.

**Table 1. Standard Deviation ( $\mu\text{rad}^2$ ) of the Beam Pointing and of the Filament Position Relative to the Beam on a Screen at  $z=2.6$  m.**

Title	Unperturbed Beam	Turbulence ( $C_n^2=6 \times 10^{-10} \text{ m}^{-2/3}$ at $z=1$ )
Whole beam pointing	351	856
Filament position relative to the beam	243	224

recorded by a (RGB) red–green–blue CCD camera (10.6  $\mu\text{m}/\text{pixel}$  resolution, i.e., typically 10  $\mu\text{rad}$  on the laser beam deflection) equipped with an RG780 colored glass filter to block the fundamental wavelength. First we investigated possible beam stabilization by nonlinear propagation by comparing the pointing stability in the same turbulence conditions of three laser beams: (i) the filamenting beam; (ii) the same ultrashort, infrared laser at a reduced power below filamentation threshold ( $\sim 1$  mJ, i.e., 3 GW peak power); and (iii) a cw 10 mW He–Ne laser beam. We defined the beam position as the center of gravity of the region within the beam profile where the intensity was more than 70% of the maximum on the red layer of the images. The resulting accuracy of a few pixels was comparable to the unperturbed beam-pointing stability. Then the variances  $\sigma_x^2$  and  $\sigma_y^2$  in both the  $x$  and  $y$  positions of the beam yield the average  $C_n^2$  structure parameter for the refractive index through the relation<sup>22</sup>

$$C_n^2 = \sigma^2 \phi^{1/3} / (2.91l), \quad (2)$$

where  $\phi$  is the beam diameter and  $l$  is the length of the turbulent path. Here  $\sigma^2$  ( $\sigma^2 = \sigma_x^2, \sigma_y^2$ ) is expressed in squared radians and  $C_n^2$  is in units of  $\text{m}^{-2/3}$ . The factor of 2.91 is derived for plane waves, and applies with a good approximation to the beams used in these experiments. The three laser configurations had the same pointing stability for identical perturbations. Therefore nonlinear propagation does not improve the pointing stability of the overall beam.

We then characterized the stability of the filament itself by installing the screen in the filamenting region ( $z=2.6$  m). The screen was continually moved during the acquisitions such that each shot met a new screen region. An unperturbed He–Ne beam shone on the screen served as a reference for the beam's position. The center of the overall beam and the filament's position were located by use of the blue and green layers of the RGB images, respectively. We assessed the beam's position by thresholding a noise-filtered image and then determining the center of gravity of the beam's contour. Whereas the turbulence generates random shot-to-shot pointing fluctuations of the overall beam, the pointing stability of the filament relative to the beam is unaffected by the perturbation located both at the onset of filamentation ( $z=0$ ) and in the filament ( $z=1$ ; Table 1). This stabilization raises the hope that beam profiles can be transmitted nonlinearly with reduced blur through turbulent regions and could, e.g., permit spatial multiplexing in open-space laser telecommu-

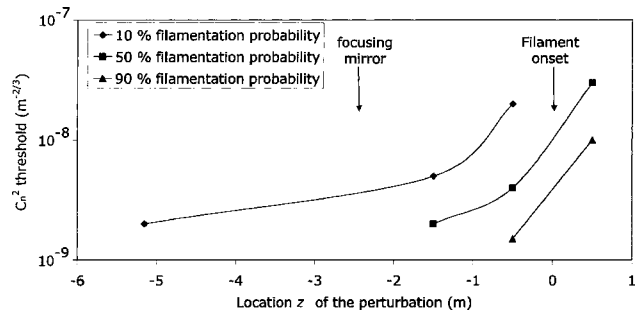


Fig. 2.  $C_n^2$  threshold for 90%, 50%, and 10% probability of generating a filament as a function of location  $z$  of the turbulent region.

nications. It may have contributed to the beam-profile memory effect observed after several kilometers' vertical propagation.<sup>7</sup>

However, a key feature for atmospheric applications is the ability of the filaments to survive their propagation through turbulence. We characterized the occurrence of a filament in given conditions by setting a threshold value on the integrated contribution of the green layer of the recorded RGB beam profiles. This automated criterion corresponded well to visual observation of a filament. A statistical analysis based on the binomial law shows that, for 50 pictures in each condition, the confidence interval for the rate of filament occurrence is limited to  $\pm 10\%$  in the worst case (50% occurrence rate). Therefore the observed changes in filament occurrence rates are statistically significant. The  $C_n^2$  parameter was monitored by use of the main laser beam ( $\phi=10$  mm) on the same records. This procedure limits the influence of fluctuations and drifts, knowledge of which is crucial to the study of turbulence, which is a stochastic phenomenon.

The influence of turbulence on the probability of filamentation is found to decrease steeply near nonlinear focus (Fig. 2). Although a moderate perturbation at the exit of the laser can significantly hinder the formation of a filament 5 m downstream, a filament once formed needs a considerable perturbation to be destroyed. Moreover, the  $C_n^2$  values that permit a 90% probability of occurrence of a filament are orders of magnitude greater than any real atmospheric condition [ $10^{-15}$  to  $10^{-13} \text{ m}^{-2/3}$  (Ref. 22)]. Although atmospheric applications of filaments require much longer length scales than in our experiments, and although the scaling of laboratory results for strongly nonlinear processes such as turbulence and filamentation are not straightforward, our results suggest that turbulence should not be the limiting factor for applications that require propagation of filaments

across the atmosphere. The high turbulence threshold for filamentation also opens the way to specific applications that may require propagating filaments through highly turbulent regions. Such applications include the new filament-based laser-induced breakdown spectroscopy technique,<sup>15</sup> in the context of combustion metrology, implying highly turbulent fluid flows.<sup>23</sup>

The small effect of turbulence on an already formed filament highlights the intrinsic stability of the filament structure, which can also withstand the interaction with large obscurants<sup>16,17</sup>. In a filament, the phase perturbations induced by the turbulence may be smoothed out. Moreover, we can compare the refractive-index gradients induced by both turbulence,  $\nabla n_T \approx 9.1 \times 10^{-5} \times T_s / (T \Delta r)$ , and filamentation,  $\nabla n_{\text{fil}} \approx n_2 I / d$ , where  $I = 10^{14} \text{ W/cm}^2$  is the typical intensity within the filament,  $d \sim 100 \mu\text{m}$  is the filament's diameter,  $T_s = 288.15 \text{ K}$  is the standard temperature,  $T$  is the temperature, and  $\Delta r$  is the scale of the temperature gradients within the hot air beam. The dimensionless  $9.1 \times 10^{-5}$  factor stems from the Rank formula evaluated at  $800 \text{ nm}$ .<sup>24</sup> Considering  $T = 500^\circ\text{C}$  as an upper bound for the temperature at the exhaust of the hot air blower and estimating that  $\Delta r \sim 1 \text{ cm}$ , we get  $\nabla n_T \approx 6 \times 10^{-3} \text{ m}^{-1} \ll \nabla n_{\text{fil}} \approx 0.3 \text{ m}^{-1}$  such that, even for strong structure parameter values, the contribution of turbulence to the refractive-index gradient is negligible compared with that induced by the Kerr effect within the filament. Note that, when lasers are propagated over large distances in the atmosphere, the air pressure varies to a large extent. However, because the distances involved are large, the corresponding index gradients are negligible.

In contrast, an early perturbation in the beam profile will develop further during subsequent propagation because of its nonlinearity and will give rise to turbulent cells within the beam profile, each one generating one or several local intensity maxima. These turbulent cells propagate almost independently of one another.<sup>25</sup> Therefore they can generate filaments only if they contain several critical powers. If they are too small, filamentation will be impossible.

In conclusion, we have shown that filamentation is not affected by turbulence in the ranges that can be encountered in the atmosphere. For stronger turbulence, filamentation may be stopped or prevented, with a relatively sharp cutoff of the filamentation when turbulence increases. The effect of the perturbation is greater when the turbulent region is located at the early stages of propagation of the laser beam.

We acknowledge helpful discussions with Matthieu Jomier about the image analysis. J. Kasparian's e-mail address is jkaspari@lasim-univ-lyon1.fr.

## References

1. A. Braun, G. Korn, X. Liu, D. Du, J. Squier, and G. Mourou, *Opt. Lett.* **20**, 73 (1995).
2. A. Brodeur, C. Y. Chien, F. A. Ilkov, S. L. Chin, O. G. Kosareva, and V. P. Kandidov, *Opt. Lett.* **22**, 304 (1997).
3. M. Mlejnek, E. M. Wright, and J. V. Moloney, *Opt. Lett.* **23**, 382 (1998).
4. H. Schillinger and R. Sauerbrey, *Appl. Phys. B* **68**, 753 (1999).
5. J. Kasparian, R. Sauerbrey, and S. L. Chin, *Appl. Phys. B* **71**, 877 (2000).
6. B. La Fontaine, F. Vidal, Z. Jiang, C. Y. Chien, D. Comtois, A. Desparois, T. W. Johnston, J.-C. Kieffer, H. Pépin, and H. P. Mercure, *Phys. Plasmas* **6**, 1615 (1999).
7. M. Rodriguez, R. Bourayou, G. Méjean, J. Kasparian, J. Yu, E. Salmon, A. Scholz, B. Stecklum, J. Eisloffel, U. Laux, A. P. Hatzes, R. Sauerbrey, L. Wöste, and J.-P. Wolf, *Phys. Rev. E* **69**, 036607 (2004).
8. A. Becker, N. Aközbeek, K. Vijayalakshmi, E. Oral, C. M. Bowden, and S. L. Chin, *Appl. Phys. B* **73**, 287 (2001).
9. N. Aközbeek, A. Iwasaki, A. Becker, M. Scalora, S. L. Chin, and C. M. Bowden, *Phys. Rev. Lett.* **89**, 143901 (2002).
10. J. Kasparian, R. Sauerbrey, D. Mondelain, S. Niedermeier, J. Yu, J.-P. Wolf, Y.-B. André, M. Franco, B. Prade, A. Mysyrowicz, S. Tzortzakis, M. Rodriguez, H. Wille, and L. Wöste, *Opt. Lett.* **25**, 1397 (2000).
11. J. Kasparian, M. Rodriguez, G. Méjean, J. Yu, E. Salmon, H. Wille, R. Bourayou, S. Frey, Y.-B. André, A. Mysyrowicz, R. Sauerbrey, J.-P. Wolf, and L. Wöste, *Science* **301**, 61 (2003).
12. G. Méjean, J. Kasparian, J. Yu, S. Frey, E. Salmon, and J.-P. Wolf, *Appl. Phys. B* **78**, 535 (2004).
13. B. La Fontaine, D. Comtois, C. Y. Chien, A. Desparois, F. Gérin, G. Jarry, T. W. Johnston, J. C. Kieffer, F. Martin, R. Mawassi, H. Pépin, F. A. M. Rizk, F. Vidal, C. Potvin, P. Couture, and H. P. Mercure, *J. Appl. Phys.* **88**, 610 (2000).
14. R. Ackermann, K. Stelmaszczyk, P. Rohwetter, G. Méjean, E. Salmon, J. Yu, J. Kasparian, G. Méchain, V. Bergmann, S. Schaper, B. Weise, T. Kumm, K. Rethmeier, W. Kalkner, J. P. Wolf, and L. Wöste, *Appl. Phys. Lett.* **85**, 5781 (2004).
15. K. Stelmaszczyk, P. Rohwetter, G. Méjean, J. Yu, E. Salmon, J. Kasparian, R. Ackermann, J.-P. Wolf, and L. Wöste, *Appl. Phys. Lett.* **85**, 3977 (2004).
16. F. Courvoisier, V. Boutou, J. Kasparian, E. Salmon, G. Méjean, J. Yu, and J.-P. Wolf, *Appl. Phys. Lett.* **83**, 213 (2003).
17. M. Kolesik and J. V. Moloney, *Opt. Lett.* **29**, 590 (2004).
18. V. P. Kandidov, O. G. Losareva, E. I. Mozhaev, and M. P. Tamarov, *Atmos. Ocean. Opt.* **13**, 394 (2000).
19. S. L. Chin, A. Talebpour, J. Yang, S. Petit, V. P. Kandidov, O. G. Kosareva, and M. P. Tamarov, *Appl. Phys. B* **74**, 67 (2002).
20. W. Liu, O. Kosareva, I. S. Golubtsov, A. Iwasaki, A. Becker, V. P. Kandidov, and S. L. Chin, *Appl. Phys. B* **75**, 595 (2002).
21. V. I. Tatarskii, *The Effects of the Turbulent Atmosphere on Wave Propagation* (Keter, Jerusalem, 1971).
22. S. Bendersky, N. S. Komeika, and N. Blaunstein, *Appl. Opt.* **43**, 4070 (2004).
23. V. Sturm and R. Noll, *Appl. Opt.* **42**, 6221 (2003).
24. D. H. Rank, in *Advances in Spectroscopy I*, H. W. Thompson, ed. (Interscience, 1959), Chap. 10.
25. M. Mlejnek, M. Kolesik, E. M. Wright, and J. V. Moloney, *Phys. Rev. Lett.* **83**, 76 (1999).

## Improved laser triggering and guiding of megavolt discharges with dual fs-ns pulses

Guillaume Méjean, Roland Ackermann, Jérôme Kasparian,<sup>a)</sup> Estelle Salmon, Jin Yu, and Jean-Pierre Wolf

*Teramobile, LASIM UMR CNRS 5579, Université Lyon 1, 43 bd du 11 Novembre 1918, F-69622 Villeurbanne Cedex, France*

Kay Rethmeier and Wilfried Kalkner

*Institut für Energie- und Automatisierungstechnik, TU Berlin, Einsteinufer 11, D-10587 Berlin, Germany*

Philipp Rohwetter, Kamil Stelmaszczyk, and Ludger Wöste

*Teramobile, Institut für Experimentalphysik, FU Berlin, Arnimalle 14, D-14195 Berlin, Germany*

(Received 19 September 2005; accepted 16 November 2005; published online 9 January 2006)

We demonstrate that the capacity of ultrashort high-power laser pulses to trigger and guide high-voltage discharges can be significantly enhanced by a subsequent visible nanosecond laser pulse. The femtosecond pulse induces a bundle of filaments, which creates a conducting channel of low density and cold plasma connecting the electrodes. The subsequent laser pulse photodetaches electrons from  $O_2^-$  ions in the electrode leader. The resulting electrons allow efficient heating by Joule effect in a retroaction loop, resulting in a 5% reduction of the breakdown voltage. © 2006 American Institute of Physics. [DOI: 10.1063/1.2162430]

Triggering and guiding of lightning using laser beams has been considered for more than 30 years.<sup>1</sup> The main motivation is to protect sensitive sites, such as electrical installations or airports, from direct strikes and electromagnetic perturbations. Early studies in the 1970s and 1980s using nanosecond laser pulses of high energy (in the kJ range),<sup>2</sup> have shown severe limitations due to the lack of connected plasma channels and the large absorption of the laser pulse by the induced hot and dense plasma. In contrast, ultrashort (femtosecond) lasers can generate efficient multiphoton/tunnel ionization even at moderate energy (typically 0.1 J per pulse), while they are too short to induce cascading ionization. The weak absorption of the laser energy results in long channels of cold plasma with an electron density as low as  $N_e \approx 10^{15} \text{ cm}^{-3}$ ,<sup>3</sup> still several orders of magnitude above the required free-electron density for lightning initiation in the atmosphere ( $N_{\text{init}} \approx 5 \times 10^{11} \text{ cm}^{-3}$ ).<sup>4</sup> This promising approach has been demonstrated in the ultraviolet (UV) over short scales (typically 30 cm),<sup>4,5</sup> as well as with infrared lasers, both focused to form a short plasma channel of 5 to 20 cm length<sup>6,7</sup> or longer, using multiple focusing,<sup>8,9</sup> and in the filamentation regime.<sup>10,11</sup> In the latter approach, collimated or slightly focused infrared (IR) femtosecond pulses generate long plasma channels (filaments) that ohmically connect the electrodes. Filaments<sup>12</sup> result from the dynamic balance between Kerr-lens focusing and the defocusing by the laser-induced plasma. In the atmosphere, filaments have been observed over several tens of meters, up to a few kilometers away from the laser source.<sup>13</sup> Therefore, they are good candidates to extrapolate laboratory results to the atmospheric scale (>100 m), especially since rain does not prevent the triggering effect of the filaments.<sup>14</sup>

A strong limitation for lightning control by filaments stems from the limited lifetime of the generated plasma, which amounts to only a few  $\mu\text{s}$ .<sup>15,16</sup> At a typical speed of

$10^6 \text{ m/s}$ ,<sup>17</sup> the discharge can thus only propagate over a few meters,<sup>9,11</sup> which limits the effective guiding length to the meter scale and prevents a direct extrapolation of the laboratory results to the atmospheric scale. Hence, the key issue to trigger lightning discharges resides in increasing the plasma lifetime. For this purpose, it has been shown that the use of a train of ultrashort pulses<sup>18</sup> can prolong the plasma lifetime. Also, it has been suggested that a second, relatively long (ns) laser pulse of high energy (several tens of J),<sup>4,5</sup> referred to as the maintaining pulse, could sustain the plasma density through both photodetachment from  $O_2^-$  ions, and plasma heating by inverse bremsstrahlung. The absorption coefficient for inverse bremsstrahlung is  $\alpha = \nu_{ei} \omega_p^2 / c \omega^2$ , where  $\omega$  represents the laser frequency,  $\omega_p = \sqrt{N_e e^2 / m_e \epsilon_0}$  is the plasma frequency,  $\nu_{ei} = 3 \times 10^{-6} N_e \ln(\Lambda) / T_e^{1.5}$  is the electron-ion collision frequency, and a typical range for the Coulomb integral is  $1 < \ln(\Lambda) < 10$ .<sup>5,8</sup> Treating the plasma as an ideal gas and assuming that all the deposited energy heats it, an upper bound for the plasma heating is only 4 K per Joule of laser energy at  $\lambda = 532 \text{ nm}$  when considering an upper limit for the electron density  $N_e = 10^{21} \text{ m}^{-3}$ ,<sup>3</sup> with  $\ln(\Lambda) = 5$ ,<sup>4,5</sup> and an electron temperature ( $T_e = 1 \text{ eV}$ ), corresponding to the excess energy of the free electrons after photodetachment and multiphoton ionization. Therefore, the electron density in a filament is not sufficient for a maintaining a laser pulse of reasonable energy to significantly heat the plasma.

The main electron sink in the filaments is the attachment to  $O_2$  molecules.<sup>19</sup> Since the photodetachment energy of  $O_2^-$  (0.54 eV) is well below the considered photon energies ( $E_{\text{photon}} = 2.3 \text{ eV}$  at 532 nm), the single-photon photodetachment rate is  $\gamma_l = \sigma_{O_2^-} I_l / \hbar \omega$ , where  $I_l$  is the intensity of the maintaining pulse (in  $\text{W}/\text{cm}^2$ ),  $\sigma_{O_2^-,532} = 1.5 \times 10^{-19} \text{ cm}^2$ , and  $\sigma_{O_2^-,1064} = 4.6 \times 10^{-21} \text{ cm}^2$  at 532 and 1064 nm, respectively.<sup>19</sup> In standard conditions ( $T = 300 \text{ K}$ ,  $P = 1 \text{ atm}$ ), under an electric field  $E = 500 \text{ kV/m}$ , the attachment coefficient of electrons to  $O_2$  molecules is  $\eta = 2.5 \times 10^7 \text{ s}^{-1}$ . Therefore, pulse

<sup>a)</sup>Electronic mail: jkaspari@lasim.univ-lyon1.fr

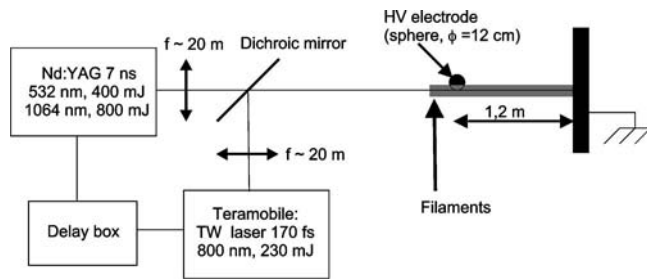


FIG. 1. Experimental setup for high-voltage discharges guiding and triggering with a double pulse configuration

energies as high as  $E_{532}=0.7$  J and  $E_{1064}=2$  J are required for the photodetachment to overcome attachment (i.e.,  $\gamma_1 > \eta$ ). Detailed simulations based on a kinetic analysis show a maximum efficiency when the ns laser pulse is fired when the  $O_2^-$  concentration is maximum in the filaments, i.e., 10 ns after the ultrashort laser pulse.<sup>15</sup> However, in view of field experiments, efficiently coupling a high-energy laser on self-guided filaments may not be straightforward. In this letter, we show that a maintaining laser pulse of moderate (subjoule) energy is sufficient to significantly improve the triggering and guiding of the high-voltage discharges, because it improves the ohmic contact between streamers and filaments.

The experimental setup (Fig. 1) is similar to that of previous experiments.<sup>11</sup> The impulse generator (Marx multiplier circuit) of the high-voltage facility of the Technical University of Berlin provided up to 2 MV negative pulses with a rise time of 1.2  $\mu$ s and an exponential decay time of 50  $\mu$ s. We used a spherical high-voltage electrode of 12 cm diameter and a plane ground electrode of 3 m diameter, with a gap of 1.2 m. Prior to the experiments, the 50% flashover voltage ( $U_{50}$ ) without laser has been measured to be 1300 kV.<sup>14</sup>

The *Teramobile* (Ref. 20) provided 100 fs pulses of 230 mJ centered at 800 nm at a repetition rate of 10 Hz. In order to optimize filamentation between the electrodes, the laser beam of 10 cm initial beam diameter was slightly focused ( $f \sim 20$  m), and properly antichirped with an initial pulse duration of 170 fs. The high-voltage pulse was synchronized so that the laser was fired typically 5  $\mu$ s after the maximum voltage was reached, on the voltage plateau. After an adjustable delay, the maintaining laser pulse of 7 ns duration was shot by a Nd:YAG laser (Spectra-Physics, Quanta-Ray) providing 800 mJ pulses at 1064 nm, or 400 mJ pulses at 532 nm. A telescope focused the YAG beam (initial beam diameter  $\sim 5$  cm) to match its profile with that of the femtosecond beam between both electrodes. Both beams were shot onto the center of the ground electrode by passing very close to the tip electrode (1 cm, comparable with the beam diameter). The filament started some meters before the tip electrode and spanned over the whole gap. No triggered discharge could be observed with the nanosecond pulse only.

Since the occurrence of discharges in given conditions is stochastic, the effect of the lasers is characterized by accumulating statistics over 10 to 20 shots in each experimental condition. The confidence interval for the measured discharge probability is estimated by using a binomial law, based on the assumption that successive shots are independent from each other.

Figure 2 shows the discharge probability for a set of voltages well below the  $U_{50}$  for natural discharges, for both

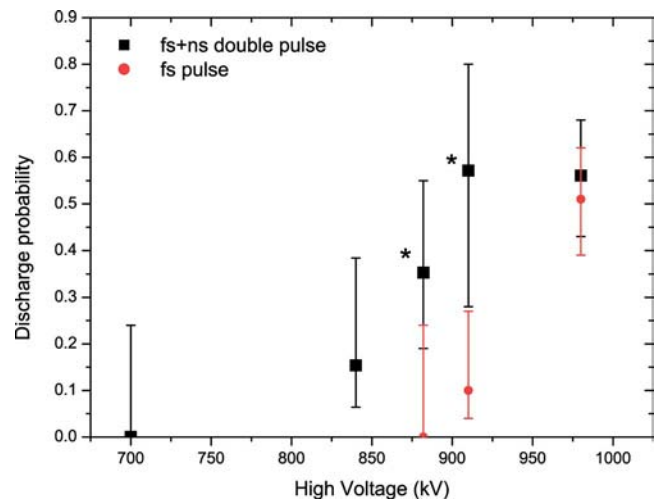


FIG. 2. Triggering probability of high-voltage discharges with both a single fs pulse alone and a dual (fs+ns) pulse with the maintaining pulse at 532 nm. The astrisk (\*) denotes a statistically significant effect of the maintaining laser for individual points.

fs pulses alone, and dual pulses, with the maintaining pulse at  $\lambda=532$  nm temporally overlapping the fs pulses.

The effect of the nanosecond pulse is greater for low voltages, at which the triggering probability of the femtosecond pulse alone falls down. At 880 kV and 910 kV, the effect of the YAG has a statistical significance higher than 98% even for individual points, with more than a five fold increase of the discharge probability at these voltages (Fig. 2). Moreover, the second pulse decreases the voltage required to trigger discharges by at least 40 kV, i.e., more than 5%, compared to the femtosecond laser alone. It allows discharge events at 65% of the natural  $U_{50}$ .

With the fundamental wavelength of the YAG, at 1064 nm, no significant effect could be observed although the pulse energy is twice (800 mJ) as high as the second harmonic. Also, the maintaining pulse has no significant effect when shot before the femtosecond pulse, nor when the pulses had no temporal overlap at all, i.e., when the maintaining laser pulse does not meet the plasma produced by the femtosecond pulse and cannot therefore have any action on it.

The effect of a maintaining pulse with moderate energy can be understood if considering that under similar conditions but without laser, no breakdown occurs and leaders propagate only a few centimeters within several  $\mu$ s.<sup>21</sup> Therefore, when arriving at the high-voltage electrode, the maintaining pulse crosses the leader head, with  $10^{14}\text{cm}^{-3}$   $O_2^-$  ion density<sup>9</sup> and atomic temperatures between 300 K and 1500 K. These elevated temperatures lead to significant drop of the attachment rate. For example, after 5  $\mu$ s, the temperature amounts to 1200 K and the attachment rate drops by a factor of 2. Since the detachment rate is not affected by the atomic temperature, the reduced attachment rate does not balance thermal detachment any more, so that the *net* detachment rate of electrons from  $O_2^-$  ions rises by six orders of magnitude, from  $\gamma_{\text{net},300\text{K}}=1.2 \times 10^{-6} \text{ s}^{-1}$  to  $\gamma_{\text{net},1200\text{K}}=2.7 \text{ s}^{-1}$ .<sup>9</sup> Therefore, the maintaining pulse is able to efficiently detach electrons from  $O_2^-$  ions, and the resulting higher electron density leads to more efficient heating by the Joule effect, which in turn favors photodetachment, launching a positive retroaction loop which lasts even after the end

of the maintaining pulse. The resulting enhanced electron density within the streamer improves the electrical connection between the streamer and the filament. Due to the retroaction loop, the new maintaining mechanism described here is efficient at much lower laser pulse energies than those proposed earlier,<sup>4,6</sup> which rely on either photodetachment or heating.

In conclusion, we have demonstrated an improved triggering of high-voltage discharges by femtosecond laser pulses using a second, maintaining ns laser pulse of moderate energy. The effect is due to a positive retroaction loop involving photodetachment, improved Joule heating, and a better ohmic bridging, suggesting that the electron density keeps above  $5 \times 10^{11} \text{ cm}^{-3}$  for a longer time. This longer lifetime could provide a way to circumvent the main limitation of the extrapolation of laboratory results to real lightning experiments. Together with recent demonstrations of high-voltage discharges triggered and guided under rain,<sup>14</sup> it improves the evaluation of the feasibility of a real-scale lightning control experiment. Besides increased energy for the maintaining pulse, further improvement can be reached by using a maintaining pulse of a shorter wavelength providing a more efficient photodetachment, and by optimally matching the profile of the maintaining pulse with that of the plasma channel. In that regard, the thermal expansion of the plasma channel generated by the laser<sup>22</sup> is favorable since it increases the active volume and reduces both the criticality of the alignment and the limitations induced by the diffraction on the propagation of a collimated maintaining pulse of small diameter.

This work has been performed within the *Teramobile* project, funded jointly by the CNRS, DFG, and French and German ministries of Research and of Foreign affairs. The *Teramobile* web site is [www.teramobile.org](http://www.teramobile.org). One of the authors (K. S.) acknowledges support from the Humboldt Foundation.

<sup>1</sup>D. W. Koopman and T. D. Wilkerson, *J. Appl. Phys.* **42**, 1883 (1971).

<sup>2</sup>M. Miki, Y. Aihara, and T. Shindo, *J. Phys. D* **26**, 1244 (1993).

<sup>3</sup>J. Kasparian, R. Sauerbrey, and S. L. Chin, *Appl. Phys. B: Lasers Opt.* **71**, 877 (2000).

<sup>4</sup>X. M. Zhao, J.-C. Diels, C. Y. Wang, and J. M. Elizondo, *IEEE J. Quantum Electron.* **31**, 599 (1995).

<sup>5</sup>P. Rambo, J. Schwarz, and J.-C. Diels, *J. Opt. A, Pure Appl. Opt.* **3**, 146 (2001).

<sup>6</sup>H. Pépin, D. Comtois, F. Vidal, C. Y. Chien, A. Desparois, T. W. Johnston, J. C. Kieffer, B. L. Fontaine, F. Martin, F. A. M. Rizk, C. Potvin, P. Couture, H. P. Mercure, A. Bondiou-Clergerie, P. Lalande, and I. Gallimberti, *Phys. Plasmas* **8**, 2532 (2001).

<sup>7</sup>D. Comtois, C. Y. Chien, A. Desparois, F. Gérin, G. Jarry, T. W. Johnston, J. C. Kieffer, B. L. Fontaine, F. Martin, R. Mawassi, H. Pépin, F. A. M. Rizk, F. Vidal, P. Couture, H. P. Mercure, C. Potvin, A. Bondiou-Clergerie, and I. Gallimberti, *Appl. Phys. Lett.* **76**, 819 (2000).

<sup>8</sup>D. Comtois, H. Pépin, F. Vidal, F. A. M. Rizk, C.-Y. Chien, T. W. Johnston, J.-C. Kieffer, B. La Fontaine, F. Martin, C. Potvin, P. Couture, H. P. Mercure, A. Bondiou-Clergerie, P. Lalande, and I. Gallimberti, *IEEE Trans. Plasma Sci.* **31**, 377 (2003).

<sup>9</sup>D. Comtois, H. Pépin, F. Vidal, F. A. M. Rizk, C.-Y. Chien, T. W. Johnston, J.-C. Kieffer, B. La Fontaine, F. Martin, C. Potvin, P. Couture, H. P. Mercure, A. Bondiou-Clergerie, P. Lalande, and I. Gallimberti, *IEEE Trans. Plasma Sci.* **31**, 387 (2003).

<sup>10</sup>B. La Fontaine, D. Comtois, C. Y. Chien, A. Desparois, F. Gérin, G. Jarry, T. W. Johnston, J. C. Kieffer, F. Martin, R. Mawassi, H. Pépin, F. A. M. Rizk, F. Vidal, C. Potvin, P. Couture, and H. P. Mercure, *J. Appl. Phys.* **88**, 610 (2000).

<sup>11</sup>M. Rodriguez, R. Sauerbrey, H. Wille, L. Wöste, T. Fujii, Y.-B. André, A. Mysyrowicz, L. Klingbeil, K. Rethmeier, W. Kalkner, J. Kasparian, E. Salmon, J. Yu, and J.-P. Wolf, *Opt. Lett.* **27**, 772 (2002).

<sup>12</sup>A. Braun, G. Korn, X. Liu, D. Du, J. Squier, and G. Mourou, *Opt. Lett.* **20**, 73 (1995).

<sup>13</sup>M. Rodriguez, R. Bourayou, G. Méjean, J. Kasparian, J. Yu, E. Salmon, A. Scholz, B. Stecklum, J. Eislöffel, U. Laux, A. P. Hatzes, R. Sauerbrey, L. Wöste, and J.-P. Wolf, *Phys. Rev. E* **69**, 036607 (2004).

<sup>14</sup>R. Ackermann, K. Stelmaszczyk, P. Rohwetter, G. Méjean, E. Salmon, J. Yu, J. Kasparian, G. Méchain, V. Bergmann, S. Schaper, B. Weise, T. Kumm, K. Rethmeier, W. Kalkner, J.-P. Wolf, and L. Wöste, *Appl. Phys. Lett.* **85**, 5781 (2004).

<sup>15</sup>B. La Fontaine, F. Vidal, D. Comtois, C.-Y. Chien, A. Desparois, T. W. Johnston, J.-C. Kieffer, H. P. Mercure, H. Pépin, and F. A. M. Rizk, *IEEE Trans. Plasma Sci.* **27**, 688 (1999).

<sup>16</sup>S. Tzortzakakis, B. Prade, M. Franco, A. Mysyrowicz, *Opt. Commun.* **181**, 123 (2000).

<sup>17</sup>M. Rodriguez, R. Sauerbrey, H. Wille, L. Wöste, T. Fujii, Y.-B. André, A. Mysyrowicz, L. Klingbeil, K. Rethmeier, W. Kalkner, J. Kasparian, E. Salmon, J. Yu, and J.-P. Wolf, *Opt. Lett.* **27**, 772 (2002).

<sup>18</sup>Z. Q. Hao, J. Zhang, Y. T. Li, X. Lu, X. H. Yuan, Z. Y. Zheng, Z. H. Wang, W. J. Ling, and Z. Y. Wei, *Appl. Phys. B: Lasers Opt.* **80**, 627 (2005).

<sup>19</sup>F. Vidal, D. Comtois, C.-Y. Chien, A. Desparois, B. La Fontaine, T. W. Johnston, J.-C. Kieffer, H. P. Mercure, H. Pépin, and F. A. Rizk, *IEEE Trans. Plasma Sci.* **28**, 418 (2000).

<sup>20</sup>H. Wille, M. Rodriguez, J. Kasparian, D. Mondelain, J. Yu, A. Mysyrowicz, R. Sauerbrey, J.-P. Wolf, and L. Wöste, *Eur. Phys. J.: Appl. Phys.* **20**, 183 (2002).

<sup>21</sup>Les Renardieres Group, *Electra* **75**, 67 (1981).

<sup>22</sup>S. Tzortzakakis, M. A. Franco, Y.-B. André, A. Chiron, B. Lamouroux, B. S. Prade, and A. Mysyrowicz, *Phys. Rev. E* **60**, R3505 (1999).

G. MÉJEAN<sup>1</sup>  
J. KASPARIAN<sup>1</sup>  
J. YU<sup>1</sup>  
S. FREY<sup>1</sup>  
E. SALMON<sup>1</sup>  
R. ACKERMANN<sup>1</sup>  
J.P. WOLF<sup>1</sup>  
L. BERGÉ<sup>2,✉</sup>  
S. SKUPIN<sup>2,3</sup>

# UV–Supercontinuum generated by femtosecond pulse filamentation in air: Meter-range experiments versus numerical simulations

<sup>1</sup>Laboratoire de Spectrométrie Ionique et Moléculaire, Université Cl. Bernard Lyon 1, UMR-CNRS 5579, 69622 Villeurbanne cedex, Lyon, France

<sup>2</sup>Département de Physique Théorique et Appliquée, CEA/DAM Ile de France, B.P. 12, 91680 Bruyères-le-Châtel, France

<sup>3</sup>Friedrich-Schiller-Universität Jena, Max-Wien-Platz 1, 07743 Jena, Germany

Received: 25 October 2005

Published online: 11 January 2006 • © Springer-Verlag 2005

**ABSTRACT** We report new experimental and numerical results on supercontinuum generation at ultraviolet/visible wavelengths produced by the propagation of infrared femtosecond laser pulses in air. Spectral broadening is shown to similarly affect single filaments over laboratory distance scales, as well as broad beams over long-range propagation distances. Numerical simulations display evidence of the crucial role of third harmonic generation in the build-up of UV–visible wavelengths, by comparison with current single-envelope models including chromatic dispersion and self-steepening.

PACS 52.38.Hb; 42.65.Tg; 42.65.Jx; 42.68.Ay

## 1 Introduction

While propagating in air, ultrashort laser pulses undergo filamentation [1] due to the dynamic interplay between Kerr focusing and self-induced plasma defocusing. Depending on the beam power, this subtle balance generates light filaments, which can develop over several hundreds of meters [2] and even kilometers in the vertical direction [3]. Associated with this property, the temporal variations experienced by the pulse produce a very broad spectral continuum, spanning from UV to IR wavelengths. Coherence is preserved between the different spectral components, so that the broadened pulse is often referred to as a “white light laser” [4]. Part of this supercontinuum leaks out from the beam as a narrow cone in the forward direction, called “conical emission” [5], with a typical half-angle of  $\sim 0.12^\circ$  at  $0.5 \mu\text{m}$ .

Most experimental and theoretical investigations using femtosecond Ti:Sa laser sources ( $0.8 \mu\text{m}$ ) reported spectral broadening extending from  $4.5 \mu\text{m}$  to a UV cut-off around  $0.35 \mu\text{m}$  [6]. However, a few years ago pioneering results demonstrated that another emission peak around  $0.27 \mu\text{m}$  arises from an additional process: third harmonic generation (THG) [7, 8]. Although these studies were limited to low energies (few mJ) and short propagation distances (tens of cm), THG conversion efficiencies as high as 0.2% were measured. More recently, a couple of publications appeared in this field [9, 10]. In [9], supercontinuum generation (SCG) extending up to  $0.23 \mu\text{m}$  in air was experimentally observed over laboratory scales. As the beam energy was increased from  $250 \mu\text{J}$  to 10 mJ, the TH spectrum was seen to merge into the blue side of the supercontinuum generated by the IR pump, resulting in a con-

tinuous broad spectral band in the UV-visible wavelength domain. Frequency variations of the TH component, mainly dictated by cross-phase modulation induced by the pump, were expected to produce this effect, to the detriment of self-steepening and chromatic dispersion. In [10], the same phenomenon of UV-visible SCG in air was reported over much longer distances ( $\sim 200 \text{m}$ ), by means of a light detection and ranging (Lidar) experimental setup. From the theoretical point of view, numerical simulations evidenced the following properties: (i) UV-visible spectral broadening is created by the overlap of redshift from the TH component and blueshift from the IR pump. Frequency shifts depend on the component phases ( $\phi_j$ ,  $j = \omega, 3\omega$ ), such as  $\Delta\omega_j = -\partial_t\phi_j$ , subject to the phase-locking constraint  $\Delta\phi = 3\phi_\omega - \phi_{3\omega} \simeq \pi$  in the filamentation regime (see also [7]). (ii) The TH component behaves as a weak quintic-type defocusing nonlinearity on the fundamental dynamics. This saturation lowers the maximum intensity of the IR component and significantly increases the filament range by  $\sim 1 \text{m}$ . (iii) TH-induced saturation superimposes with plasma generation to defocus the pulse and enlarge the conical emission to  $\sim 0.25^\circ$  at  $0.25 \mu\text{m}$ .

In spite of these investigations, two questions remain open. First, numerical limitations prevented realistic simulations of broad beams [10] from accessing Lidar propagation ranges. Although differences between meter-range simulations and Lidar data ( $\geq 100 \text{m}$ ) oc-

✉ Fax: (+33) 1 69 26 71 06, E-mail: luc.berge@cea.fr

curred in the longitudinal scales, the spectral dynamics, however, looked similar, which received no explanation. Second, the role of chromatic dispersion and self-steepening compared with THG remains unclear. Whereas the former processes are capable of enlarging the fundamental spectrum to the UV regions [11, 12], their relative strength compared with THG deserves a special investigation.

Therefore, the issues addressed in this paper are twofold. Firstly, because a direct comparison between spectral dynamics on laboratory scales and over Lidar ranges is missing, we experimentally demonstrate that filaments lead to analogous supercontinua in long-range Lidar propagation as well as in laboratory-scaled experiments. Emphasis is next given to the spectral distortions developing along meter-range distances from the second experimental setup as well as in numerical computations. We investigate this spectral dynamics by means of two models, one involving THG without self-steepening and chromatic dispersion, the other one describing the pump wave including these effects. THG equations are shown to yield more accurate results than the latter model.

## 2 Experiments

Range resolved spectra have been measured using two different setups. For long scales, the Teramobile laser system [13] was arranged in a Lidar-based configuration, delivering 10-Hz rated, 5 TW pulses (70 fs, 350 mJ) cen-

tered at  $0.8\ \mu\text{m}$ . A beam with 10 cm diameter was sent vertically into the atmosphere. The Rayleigh–Mie scattering signals were inverted with standard algorithms [14]. Chirp and beam focusing produced a pulse duration of 150 fs and 10 m focal length, which optimized white-light generation at long distances. Spectra were measured with 10 nm resolution from  $0.23\ \mu\text{m}$  to  $0.6\ \mu\text{m}$ , for 10 m range resolution along the optical path (see [10] for more details). Besides, meter-scale experiments were performed with a Ti:Sa CPA laser system providing  $\sim 60\ \text{GW}$  pulses (9 mJ,  $\sim 150\ \text{fs}$ ) centered at  $0.81\ \mu\text{m}$ . The 12 mm diameter beam freely propagated over 6.1 m and was focused with a  $f = 5\ \text{m}$  convergent mirror, so as to produce a single filament at a distance of about 3.3 m from the mirror. The UV-visible part of the supercontinuum, reflected from the edge of a glass plate set near the filament, was measured with a photomultiplier tube attached to a monochromator, providing 7 nm spectral resolution. We checked carefully that no white light was generated in the glass plate. Each point of the spectra was integrated over 128 laser shots.

The spectral evolution resulting from the first setup is recalled from [10] in Fig. 1a. At 105 m, a 50 nm broad THG band appears around  $0.27\ \mu\text{m}$ . From 135 m, the spectrum changes into an ultrabroad, continuous UV-visible plateau, which forms a hump in the wavelength domain  $0.27 \leq \lambda \leq 0.5\ \mu\text{m}$ . This hump persists at longer distances, whereas UV components become more depleted (see Fig. 6 of [10]). As shown

in Fig. 1b, the same behavior develops over much shorter distances from a single filament created with the second experimental setup. At short distances close to the nonlinear focus (filamentation onset distance, noted  $z_c \simeq 3.3\ \text{m}$ ), SPM widely broadens the pump spectrum. At  $\Delta z = z - z_c \simeq 1.3\ \text{m}$  from the focus, a 20 nm THG band appears around  $0.27\ \mu\text{m}$ . This spectral enlargement is comparable with that detected in the laboratory [8] over some tens of cm and more recently in [9] by increasing the beam energy. About 2 m later ( $\Delta z \simeq 3.2\ \text{m}$ ), THG is depleted and a continuous UV-visible plateau appears, creating a hump in the  $0.3\text{--}0.5\ \mu\text{m}$  region. At further distances, this plateau was observed to hold its shape, far beyond the end of the filament.

Figures 1a and b exhibit the same spectral dynamics. Major changes, however, occur over longer distances in the Lidar configuration, because multifilamentation takes place in the Teramobile bundle that conveys high (TW) powers. The fact that long-range Lidar propagation and laboratory-scaled experiments develop comparable SCG can be explained by the generic dynamics of a single filament. Differences in the longitudinal scales are explained as follows. In Fig. 1a, the broad TW beam breaks up into multiple filaments, each having a typical length of a few meters and individual power of  $\sim 10\ \text{GW}$  [15]. The Lidar beam then consists of the incoherent superposition of  $\sim 100$  independent filaments, randomly nucleated along the propagation axis. The build-up in wavelengths arises over longer intervals in this configuration ( $\Delta z \sim 30\ \text{m}$ ), because most filaments are not aligned on the same Fourier profile in the early filamentation stage. Reaching a quasi-coherent state consumes several tens of meters along the optical path, in order to modify the total spectrum noticeably. The similarity in the spectral shapes of Fig. 1 confirms these properties and, thereby, raises the conjecture stated in [10].

## 3 Modelling

To reproduce these spectral dynamics, we performed numerical simulations using the model equations of [10], which couple the slowly-varying envelopes of the fundamental

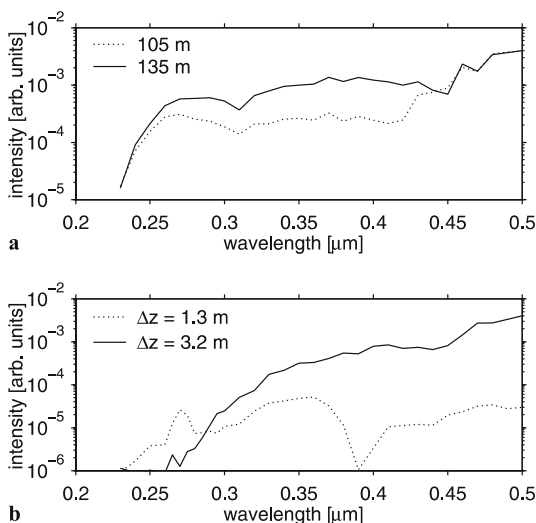


**FIGURE 1** Spectra in the wavelength domain  $0.2 \leq \lambda \leq 0.5\ \mu\text{m}$  for different propagation distances. (a) Spectra developing over 135 m measured by Lidar arrangement [10]; (b) Experimental data from laboratory measurements. In (b),  $\Delta z$  is the longitudinal distance from the nonlinear focus  $z_c \simeq 3.3\ \text{m}$  (filamentation onset distance). Spectral intensity at  $0.5\ \mu\text{m}$  is fixed to  $4 \times 10^{-3}$  times that of the fundamental [6], except for  $\Delta z = 1.3\ \text{m}$  where its value is two decades below ( $3 \times 10^{-5}$ )

wave ( $\mathcal{E}_\omega$ ) with the TH one ( $\mathcal{E}_{3\omega}$ ) as

$$\frac{\partial \mathcal{E}_j}{\partial z} = \left( i\beta_j \nabla_\perp^2 - \alpha_j \frac{\partial}{\partial t} - i \frac{k_j''}{2} \frac{\partial^2}{\partial t^2} - i\delta_j \right) \times \mathcal{E}_j + \mathcal{F}_j + \mathcal{P}_j, \quad (1)$$

where  $j = \omega, 3\omega$ . In (1),  $z$  is the propagation variable,  $t$  is the time coordinate retarded in the pump frame, and  $\nabla_\perp^2 = r^{-1} \partial_r r \partial_r$ ;  $\alpha_{3\omega} = \Delta v^{-1}$ , where  $\Delta v = [v_g(3\omega)^{-1} - v_g(\omega)^{-1}]^{-1} = 0.44$  cm/fs is the group-velocity mismatch responsible for temporal walk-off ( $\alpha_\omega = 0$ ),  $\beta_{3\omega} = \beta_\omega/3 = 1/6k_0$  with  $k_0 = 2\pi/\lambda_\omega$ ;  $k_\omega'' = 0.2$  fs<sup>2</sup>/cm and  $k_{3\omega}'' = 1$  fs<sup>2</sup>/cm are the coefficients for group-velocity dispersion (GVD) and  $\delta_{3\omega} = \Delta k \equiv 3k(\omega) - k(3\omega) = -5$  cm<sup>-1</sup> is the wave vector mismatch ( $\delta_\omega = 0$ ). The function  $\mathcal{F}_j$  represents the optical nonlinearities, involving self-phase, cross-phase modulations and four-wave mixing:

$$\mathcal{F}_\omega = ik_0 n_2 \times (R(t)\mathcal{E}_\omega + 2|\mathcal{E}_{3\omega}|^2 \mathcal{E}_\omega + \mathcal{E}_\omega^{*2} \mathcal{E}_{3\omega}) \quad (2)$$

$$\mathcal{F}_{3\omega} = ik_0 n_2 \left( 3 \frac{n_2^{3\omega}}{n_2} |\mathcal{E}_{3\omega}|^2 \mathcal{E}_{3\omega} + 6|\mathcal{E}_\omega|^2 \mathcal{E}_{3\omega} + \mathcal{E}_\omega^3 \right) \quad (3)$$

$$R(t) = \frac{1}{2} |\mathcal{E}_\omega|^2 + \frac{\tau_K^{-1}}{2} \times \int_{-\infty}^t e^{-(t-t')/\tau_K} |\mathcal{E}_\omega(t')|^2 dt'. \quad (4)$$

The function  $\mathcal{P}_j$  describes the plasma response with free electron density  $\varrho$  as

$$\mathcal{P}_j = -i \frac{\beta_j k_0^2}{\varrho_c} \varrho \mathcal{E}_j - \frac{\sigma_j}{2} \varrho \mathcal{E}_j - \frac{\beta_j^{(K_j)}}{2} |\mathcal{E}_j|^{2K_j-2} \mathcal{E}_j \quad (5)$$

$$\frac{\partial \varrho}{\partial t} = \sum_{j=\omega, 3\omega} (\varrho_{\text{int}} - \varrho) \sigma_{(K_j)} |\mathcal{E}_j|^{2K_j} + \frac{\sigma_j}{U_i} \varrho |\mathcal{E}_j|^2, \quad (6)$$

where  $K_j$ ,  $\sigma_{(K_j)}$  and  $\beta_j^{(K_j)}$  denote the number of photons for IR and UV wavelengths, multiphoton ionization rates and related absorption losses for dioxygen molecules, respectively. Plasma response includes avalanche ionization with cross-sections  $\sigma_j$ . Eqs. (1)–(6),

whose values of the physical parameters can be found in [10], were numerically integrated in radial symmetry to compute the spectra emitted by a single filament at the propagation distances experimentally scanned in Fig. 1b.

For comparison, we also performed computations of the  $\omega$  component alone, undergoing self-steepening and chromatic dispersion. These effects being responsible for a strong blue-shift of fs spectra in air [11, 12], they may possibly inhibit the influence of THG and cause by themselves UV-visible SCG. In that case, the envelope  $\mathcal{E}_\omega$  is governed by the equation:

$$\frac{\partial \mathcal{E}_\omega}{\partial z} = \frac{i}{2k_0} T^{-1} \nabla_\perp^2 \mathcal{E}_\omega + i \hat{D} \mathcal{E}_\omega - \frac{ik_0}{2\varrho_c} T^{-1} \varrho \mathcal{E}_\omega - \frac{\sigma_\omega}{2} \varrho \mathcal{E}_\omega + ik_0 n_2 TR(t) \mathcal{E}_\omega - \frac{\beta_\omega^{(K_\omega)}}{2} |\mathcal{E}_\omega|^{2K_\omega-2} \mathcal{E}_\omega, \quad (7)$$

where  $\varrho$  obeys (6) for the IR pulse only, with the parameters chosen above.

$\hat{D} = \sum_{n=2}^5 (k^{(n)}/n!) (i\partial_t)^n$  is the dispersion operator, with coefficients  $k^{(n)} \equiv \partial^n k / \partial \omega^n |_{\omega=\omega_0}$  computed from the Sellmeier formula for air ( $k''' = 0.1$  fs<sup>3</sup>/cm) established in [16]. This model moreover accounts for space-time focusing ( $T^{-1} \nabla_\perp^2 \mathcal{E}$ ) and self-steepening ( $T|\mathcal{E}|^2 \mathcal{E}$ ), where  $T \equiv 1 + (i/\omega_0) \partial_t$  [17].

#### 4 Results and discussion

With (1)–(6) we simulated one filament starting from a Gaus-

sian pulse with waist  $w_0 = 0.5$  mm, FWHM duration of 150 fs and power  $P_{\text{in}} \simeq 10$  GW. Figure 2a shows its spectral evolution at different distances after the nonlinear focus  $z_c \simeq 0.4$  m. The plotted quantity is the normalized spectral intensity integrated in space versus the distance  $\Delta z$  from  $z_c$ . Self-focusing first induces SPM in the fundamental pulse. At  $\Delta z = 1.3$  m, the TH component broadens in turn around  $0.27$   $\mu\text{m}$  and experiences a significant “redshift”. At  $\Delta z \geq 3$  m, the spectrum is increased by about one decade at visible wavelengths, while UV components become more attenuated. Spectral distortions similar to Fig. 1b develop over comparable distances shifted from the self-focus point,  $\Delta z = z - z_c$ . They agree with the experimental data, apart from oscillations created by interferences between different peaks appearing in the pulse profile. Such oscillations are smoothed in the experimental spectra, measured with a resolution of 7 nm and averaged over 128 shots. Some differences, however, exist before the hump in wavelengths fully develops. At  $\Delta z = 1.3$  m, the dip located at  $\sim 0.39$   $\mu\text{m}$  in the experimental spectrum is shifted back to  $0.32$   $\mu\text{m}$  in its numerical counterpart, and the spectral intensity at UV wavelengths fluctuates within one decade. In spite of these minor discrepancies, which we attribute to limitations of radial simulations vs the experimental pulse shape and to the implicit assumption of narrow spectral bandwidths used in (1), our numerical results offer

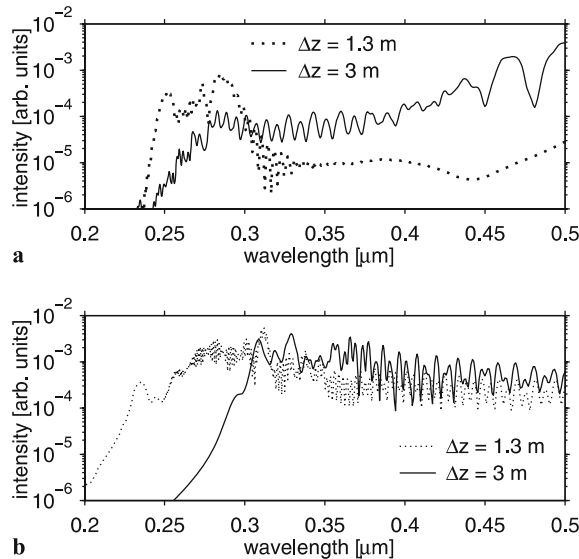
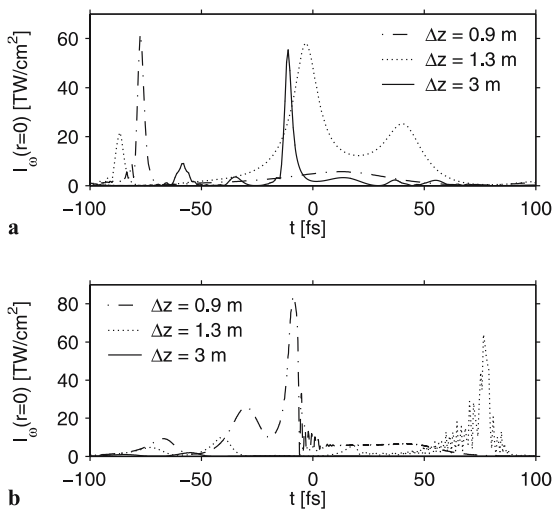


FIGURE 2 Spectra numerically computed from (a) (1)–(6) and (b) (7) vs. intervals  $\Delta z$  from the focus  $z_c = 0.4$  m



**FIGURE 3** Temporal profiles at  $\Delta z = 0.9$  m (*dash-dotted curves*), at  $\Delta z = 1.3$  m (*dotted curves*) and  $\Delta z = 3$  m (*solid curves*) for (a) the model accounting for THG without self-steepening and chromatic dispersion (1); (b) Temporal profiles computed from (7) at the same distances

a rather good agreement with meter-range experiments. They also reproduce the long-distance spectral behavior recalled in Fig. 1a, as already noticed in [10].

Figure 2b shows the same pieces of information computed from (7). A strong extent of the generated white light develops towards the blue side of the spectra and saturates around  $0.2 \mu\text{m}$ , in agreement with former theoretical predictions [12]. However, simulated at the same intervals  $\Delta z$ , the spectral dynamics changes significantly, compared with Figs. 1b and 2a. The first discrepancy concerns the early spectral broadening of the generated TH, which cannot be described by the single-wave equation (7). While the lower bound of the measured spectra yields the UV cut-off  $\lambda_{c.o.} \simeq 0.23 \mu\text{m}$ , the continuum computed from (7) clearly penetrates the far-UV regions  $< 0.2 \mu\text{m}$ . The second discrepancy lies in the build-up of wavelengths. Whereas THG forms a plateau of wavelengths dramatically increasing in intensity from  $0.25 \mu\text{m}$  to  $0.5 \mu\text{m}$ , the opposite characterizes the spectral dynamics computed from the model (7), i.e., the strong blue-shift created by self-steepening hardly changes in intensity from low to larger wavelengths and remains one decade below the experimental value of the intensity measured at  $0.5 \mu\text{m}$ . As a result, the model equations (1)–(6) accounting for THG offers a better description of white-light emission and SCG than (7).

Finally, we briefly compare the temporal pulse profiles of the pump pulse governed by the two models (we recall that TH distributions in time fol-

low the fundamental ones, as shown in [7, 10]). Figure 3a shows three characteristic stages in the pulse evolution, linked to the spectral broadenings plotted in Fig. 2a. We observe that the pump intensity ( $I_0$ ) exceeds  $2 \times 10^{13} \text{ W/cm}^2$ , which agrees with the threshold given in [8]. First a leading peak with sharp edge arises, which asymmetrically broadens the spectra with an early redshift in both components ( $\Delta z = 0.9$  m). The pulse is then recentered near  $t = 0$  with smoother temporal gradients, which relaxes the spectrum to the blue side ( $\Delta z = 1.3$  m). A last focusing event enables the merging of both spectral components from  $\Delta z = 3$  m. Figure 3b shows temporal profiles computed from the model (7) at analogous distances. Here, the pulse undergoes shock dynamics within a sharp trailing edge caused by self-steepening [18]. This dynamics produces the spectral extent of the fundamental towards the lowest UV regions, up to  $\Delta z = 1.3$  m (see also [11] on this point). This extent diminishes more and more, as the pulse spreads out and smoothes its distribution in time ( $\Delta z = 3$  m). The temporal distortions plotted in Fig. 3 thus justify the different spectral dynamics promoted by the numerical models (1) and (7).

## 5 Conclusion

In conclusion, we have shown that the propagation of femtosecond pulses in air is strongly influenced by the nonlinear dynamics of the third harmonic component. Coupling between the pump field and TH develops an

important spectral broadening in the wavelength domain  $0.23 \leq \lambda \leq 0.5 \mu\text{m}$ , which favors supercontinuum generation. Spectral dynamics are identical over meter-range scales as well as over  $\sim 100$  m and beyond. THG dominates over chromatic dispersion and self-steepening in the build-up of wavelengths. This property was evidenced by direct simulations, which showed that including THG improves the qualitative agreement of the numerical results with experiments. Although the focus of this paper mostly concerned results and simulations at meter-range distances, we recalled for the reader's benefit Lidar spectra over more than 100 m (Fig. 1a), showing modest changes in the general spectral shapes. Even if we were not able to simulate realistic broad beams so far away, reproducing reasonable agreement upon meter-scale distances make us fairly confident that the physics involved in SCG is mainly captured by the model equation (1).

**ACKNOWLEDGEMENTS** Experiments were performed in the framework of the Teramobile Project, funded jointly by CNRS and DFG.

## REFERENCES

- 1 A. Braun, G. Korn, X. Liu, D. Du, J. Squier, G. Mourou, *Opt. Lett.* **20**, 73 (1995)
- 2 B. La Fontaine, F. Vidal, Z. Jiang, C.Y. Chien, D. Comtois, A. Desparois, T.W. Johnston, J.-C. Kieffer, H. Pépin, and H.P. Mercure, *Phys. Plasmas* **6**, 1615 (1999)
- 3 M. Rodriguez, R. Bourayou, G. Méjean, J. Kasparian, J. Yu, E. Salmon, A. Scholz, B. Stecklum, J. Eislöffel, U. Laux, A.P. Hatzes, R. Sauerbrey, L. Wöste, J.-P. Wolf, *Phys. Rev. E* **69**, 036607 (2004)
- 4 S.L. Chin, S. Petit, F. Borne, K. Miyazaki, *Jpn. J. Appl. Phys.* **38**, L126 (1999)
- 5 O. Kosareva, V.P. Kandidov, A. Brodeur, C.Y. Chien, S.L. Chin, *Opt. Lett.* **22**, 1332 (1997)
- 6 J. Kasparian, J. Kasparian, R. Sauerbrey, D. Mondelain, S. Niedermeier, J. Yu, J.-P. Wolf, Y.-B. André, M. Franco, B. Prade, S. Tzortzakos, A. Mysyrowicz, M. Rodriguez, H. Wille, L. Wöste, *Opt. Lett.* **25**, 1397 (2000)
- 7 N. Aközbeke, A. Iwasaki, A. Becker, M. Scallora, S.L. Chin, C.M. Bowden, *Phys. Rev. Lett.* **89**, 143901 (2002)
- 8 H.H. Yang, J. Zhang, J. Zhang, L.Z. Zhao, Y.J. Li, H. Teng, Y.T. Li, Z.H. Wang, Z.L. Chen, Z.Y. Wei, J.X. Ma, W. Yu, Z.M. Sheng, *Phys. Rev. E* **67**, 015401 (2003)
- 9 F. Théberge, W. Liu, Q. Luo, S.L. Chin, *Appl. Phys. B: Lasers and Optics* **80**, 221 (2005)
- 10 L. Bergé, S. Skupin, G. Méjean, J. Kasparian, J. Yu, S. Frey, E. Salmon, J.-P. Wolf, *Phys. Rev. E* **71**, 016602 (2005)

- 11 N. Aközbek, M. Scalora, C.M. Bowden, S.L. Chin, *Opt. Commun.* **191**, 353 (2001)
- 12 M. Kolesik, G. Katona, J.V. Moloney, E.M. Wright, *Appl. Phys. B: Lasers and Optics* **77**, 185 (2003)
- 13 H. Wille, M. Rodriguez, J. Kasparian, D. Mondelain, J. Yu, A. Mysyrowicz, R. Sauerbrey, J.-P. Wolf, L. Wöste, *Eur. Phys. Jour. Appl. Phys.* **20**, 183 (2002)
- 14 R.M. Measures (Ed.), In: *Laser remote sensing – Fundamentals and applications* (Wiley, New York 1984)
- 15 L. Bergé, S. Skupin, F. Lederer, G. Méjean, J. Yu, J. Kasparian, E. Salmon, J.-P. Wolf, M. Rodriguez, L. Wöste, R. Bourayou, R. Sauerbrey, *Phys. Rev. Lett.* **92**, 225002 (2004)
- 16 E.R. Peck, K. Reeder, *J. Opt. Soc. Am.* **62**, 958 (1972)
- 17 T. Brabec, F. Krausz, *Phys. Rev. Lett.* **78**, 3282 (1997)
- 18 G.P. Agrawal (Ed.), *Nonlinear Fiber Optics*, 3rd Edn. (Academic Press 2001) pp. 274

R. ACKERMANN<sup>1,2</sup>  
G. MÉCHAIN<sup>4</sup>  
G. MÉJEAN<sup>1</sup>  
R. BOURAYOU<sup>3</sup>  
M. RODRIGUEZ<sup>2</sup>  
K. STELMASZCZYK<sup>2</sup>  
J. KASPARIAN<sup>1,✉</sup>  
J. YU<sup>1</sup>  
E. SALMON<sup>1</sup>  
S. TZORTZAKIS<sup>4</sup>  
Y.-B. ANDRÉ<sup>4</sup>  
J.-F. BOURRILLON<sup>5</sup>  
L. TAMIN<sup>5</sup>  
J.-P. CASCELLI<sup>5</sup>  
C. CAMPO<sup>5</sup>  
C. DAVOISE<sup>5</sup>  
A. MYSYROWICZ<sup>4</sup>  
R. SAUERBREY<sup>3</sup>  
L. WÖSTE<sup>2</sup>  
J.-P. WOLF<sup>1</sup>

## Influence of negative leader propagation on the triggering and guiding of high voltage discharges by laser filaments

<sup>1</sup> Teramobile, LASIM, UMR CNRS 5579, Université Lyon 1, 43 boulevard du 11 Novembre 1918, 69622 Villeurbanne Cedex, France

<sup>2</sup> Teramobile, Institut für Experimentalphysik, FU Berlin, Arnimallee 14, 14195 Berlin, Germany

<sup>3</sup> Teramobile Project, Institut für Optik und Quantenelektronik, Friedrich-Schiller-Universität Jena, Max-Wien-Platz 1, 07743 Jena, Germany

<sup>4</sup> Teramobile, LOA, UMR CNRS 7639, ENSTA-Ecole Polytechnique, Centre de l'Yvette, Chemin de la Hunière, 91761 Palaiseau Cedex, France

<sup>5</sup> Centre d'Essais Aéronautique de Toulouse, 47 rue Saint-Jean, BP 53123, 31131 Balma Cedex, France

Received: 3 October 2005

Published online: 17 December 2005 • © Springer-Verlag 2005

**ABSTRACT** The triggering and guiding of negative discharges using filaments induced by a femtosecond-terawatt laser pulse have been studied in sphere-plane gaps up to 4.5 meters. Fast-frame camera pictures allow the evaluation of the influence of the negative leader propagation on the triggering and guiding process. We show that the plasma channel can either trigger a space-leader discharge or act as a guiding path for the negative leader head. For the latter case the results suggest a linear dependence of the guided lengths up to 2.4 m, while the formation of a space-leader reduces this guided length by up to 50%. This effect is explained by the limited plasma lifetime of the filament that is measured to be about 1  $\mu$ s.

**PACS** 52.80.Mg; 52.38.-r; 52.25.Dg; 72.65.Jx

### 1 Introduction

Lightning control by lasers has been a dream of scientists since the 1970's. Early approaches focussed on powerful CO<sub>2</sub>-lasers [1, 2], but as the air plasma is opaque at the laser-wavelength  $\lambda = 10.6 \mu\text{m}$  (critical density  $n_c \approx 10^{19} \text{cm}^{-3}$ ), large plasma extensions are hardly achievable. Therefore, the application of ultrashort laser pulses has become more popular in recent years, as they provide plasma generation via Multi-Photon-Ionization at moderate pulse energies [3–7]. The opacity problem is avoided by typical laser wavelengths in the NIR or UV [8], e.g.,  $n_c \approx 2 \times 10^{21} \text{cm}^{-3}$  at 800 nm.

The first approach to trigger lightning was to replace or extend an existing lighting rod by the laser filament near to the ground. As in this case, the last step of lightning is the emergence of an upward moving positive leader, most of the investigations have focussed on this type of leaders, e.g., using a bi-foci lens to produce a 2 m long plasma channel [5, 9]. However, in weakly focussed beams a dynamic balance of the nonlinear Kerr-effect and plasma generation [10–13] allows plasma channels at distances up to several kilometers [14]. Such filaments may be in contact with lightning leaders, 90% of which have negative polarity [15]. Therefore, negative discharges have raised much attention in the last years [4, 6, 16, 17].

In laboratory experiments the main property of negative discharges compared to the positive polarity is the existence of the so called space-stem, a propagating plasma that originates from negative streamers [18–21]. The space-stem acts as a source for both negative and positive streamers, branching towards both electrodes, and propagates towards the ground electrode in a self-reproducing way. When the space-stem has reached the ground electrode, the breakdown is initiated. For gaps greater than about 2 m the space-stem can transform itself into a space-leader whose positive leader head propagates towards the cathode [18, 20]. Therefore, the negative discharge develops stepwise by the connection of the space-leader to the electrode-leader. A stepped propagation is also observed for negative lightning leaders which exhibit similar mechanisms to laboratory discharges [20].

Previous experiments have shown that negative discharges can be guided and triggered by laser filaments in long air gaps up to 3.8 m [6]. Triggering is characterized by the reduction of the voltage inducing 50% breakdown probability ( $U_{50}$ ). Besides, negative and positive streamers have been observed at

✉ Fax: +33-472 445871, E-mail: jerome.kasparian@lasim.univ-lyon1.fr

the borders of a 5 cm long plasma channel in a 30 cm gap under negative voltage pulses [4, 22]. In this paper we present new experimental results about the triggering and guiding of negative discharges in gaps up to 4.5 m. Fast-frame camera pictures show the space-leader formation and the negative leader propagation for different configurations. Finally, taking into account earlier results obtained in [6], the influence of the space-leader formation on the achievable guided lengths will be discussed.

## 2 Experimental setup

The experiments were conducted using the Marx high-voltage generator of the Centre d'Essais Aéronautiques de Toulouse, France. This device delivered a voltage pulse of negative polarity up to 2.7 MV. Its rise time was 2  $\mu\text{s}$ , and the fall time was about 50  $\mu\text{s}$ . A plane (5 m height and 10 m width) ground electrode was placed perpendicular to the beam axis, while the high voltage electrode was a sphere with 8 cm diameter. The distance between both electrodes was adjusted from 2.3 m to 4.5 m.

Discharges were guided using the Teramobile [23, 24], a mobile laser system delivering pulses of 250 mJ energy with pulse durations down to 100 fs. The center wavelength was 800 nm and the repetition rate 10 Hz. The laser was installed inside the high-voltage facility, with its beam aligned with the electrodes. The laser beam was tangent to the HV electrode and went through a small hole drilled into the ground electrode to avoid ablation. The beam was slightly focussed ( $f \approx 23$  m) by a telescope so that the filaments covered the whole gap. The number of filaments was estimated to be 25 by applying a resistivity measurement technique as reported in [25]. This filament number is consistent with the observation of the beam profile on a screen [26]. The peak electron density is estimated to be  $3 \times 10^{16} \text{ cm}^{-3}$  [25]. Typically, the filamentation started 1 m upstream from the high voltage electrode. A negative chirp was applied resulting in an initial pulse duration of 500 fs, as this led to the maximum trig-

gering efficiency. The delay of the laser was varied between 1  $\mu\text{s}$  before and 2.6  $\mu\text{s}$  after the beginning of the high voltage pulse.

Fast-frame camera pictures and records of the voltage and current at the high voltage electrode were used to investigate the different steps of the discharge development, while still photographs allowed the determination of their geometrical characteristics.

## 3 Experimental results and discussion

We first characterized the regime far above the distance threshold for the formation of space-leaders [18–20] at a gap distance of 4.5 m. Figure 1 shows a set of fast-frame camera pictures (a), the corresponding records of the voltage and current (b) and a still picture (c) of a partially guided discharge triggered by the laser under these conditions. The peak voltage was 2.2 MV, and the laser was shot 1.2  $\mu\text{s}$  after the beginning of the high voltage pulse. We checked that only triggered discharges could occur. No free discharge could be observed up to 2.7 MV, which was the limit of the generator performance. On the first fast-frame camera picture in Fig. 1a one can see that a space-leader has developed about 1 m away from the high voltage electrode, and its positive leader head propagates towards the cathode. The propagation velocity of the positive leader, averaged from 11 picture series, amounts to  $(2.4 \pm 0.5) \times 10^6$  m/s independent of the gap length. This is in line with previous measurements on guided leaders [5, 6]. After the connection of the space-leader to the electrode leader, the new leader head at the position of the space-leader continues its propagation towards the ground electrode, at first guided over some distance and then in a free propagation. The delay between the laser pulse and the first occurrence of the space-leader on the fast-frame pictures has been measured to be  $(800 \pm 300)$  ns, averaged over seven shots at this gap distance.

The current oscillograms show that the connection of the space-leader to the electrode leader causes a strong cur-

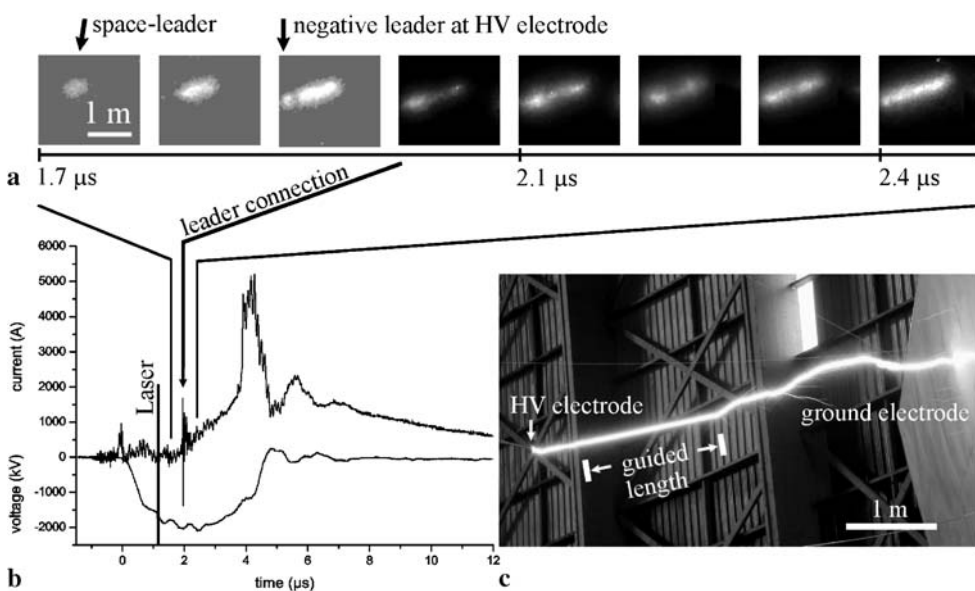


**FIGURE 1** (a) a sequence of fast-frame camera pictures zoomed into the first part of the gap to show space-leader formation, (b) the corresponding records of the high voltage and current and (c) a still photograph of a partially guided discharge in a 4.5 m gap. The exposure time of each fast-frame picture was 40 ns with a delay of 50 ns between each

rent pulse of about 1 kA, followed by a current rise lasting about 2  $\mu$ s, until the final jump occurs [20,21]. The corresponding charge consumption reached up to 400  $\mu$ C m<sup>-1</sup> before breakdown for guided space-leader discharges. This value is twice as much as for free discharges without space-leader formation, for which we measured (150  $\pm$  30)  $\mu$ C m<sup>-1</sup> at 3.4 m gap distance and a peak voltage of 2.3 MV  $\approx$   $U_{50}$ , in line with the value of 158  $\mu$ C m<sup>-1</sup> reported elsewhere [19].

As described above, space-leaders require gaps of about 2 m [18, 20]. In order to investigate the guided space-leader formation near to this threshold, the gap distance was reduced to 2.3 m. The peak voltage level was set to 2.0 MV  $\approx$  1.2  $\times$   $U_{50}$  leading to a breakdown probability of 100% even without laser. The laser delay was set to 1.2  $\mu$ s after the

start of the voltage pulse. Under these conditions both unguided and guided discharges occurred, and we observed two competing processes with respect to the occurrence of space-leaders.

The first case (Fig. 2) is similar to the mechanism described above for the 4.5 m gap. However, probably due to the stronger electric field, the space-leader frequently starts to propagate towards the ground electrode, before the connection to the electrode leader has been established. Although the space-leader formation lies out of the limited time-window of the fast-frame camera, the delay between the laser pulse and this formation appears to be shorter than in the 4.5 m gap determined above, since it is below 450 ns.

In the second case (Fig. 3) the streamers and the spacestem entirely bridge the gap leading to the initiation of the

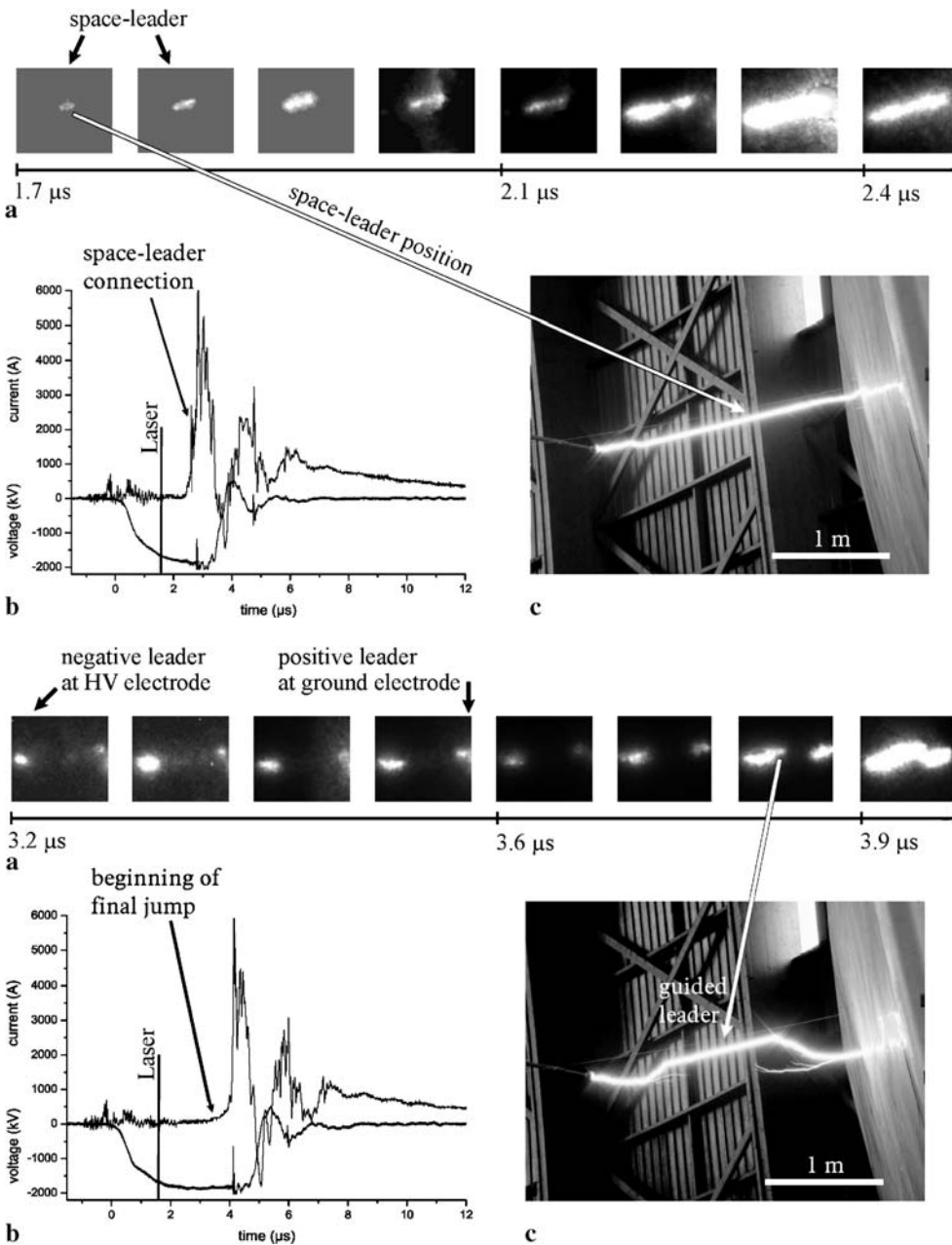


**FIGURE 2** (a) a sequence of fast-frame camera pictures for a triggered space-leader in a 2.3 m gap, (b) oscillograms of a space-leader discharge under similar conditions for a laser delay of 1.7  $\mu$ s and (c) a still photograph of the discharge

**FIGURE 3** (a) a sequence of fast-frame camera pictures for a guided electrode leader in a 2.3 m gap, (b) oscillograms of a discharge with a guided electrode leader under similar conditions for a laser delay of 1.7  $\mu$ s and (c) a still photograph of the discharge

final jump. This can be identified by the positive leader starting at the ground electrode (see Fig. 3a) and the increasing current marked in Fig. 3b. The negative electrode leader appears about  $2.5 \mu\text{s}$  after the start of the voltage pulse on the fast-frame pictures (not shown). No space-leader develops in this case, but the leader can still be partially guided, as can be seen on the last but one camera picture in Fig. 3a.

Comparing the time scales in Figs. 2a and 3a, one notices that the space-leader occurs about  $1.5 \mu\text{s}$  before the initiation of the final jump in the case of the guided electrode leader. This suggests that the space-stem and streamers interact with the plasma channel generated by the laser during their propagation to the ground electrode. The streamer to leader transition of a natural discharge is generally considered to result from electron detachment and heating of the electrons transported into the gap by the streamers [21, 27]. Therefore, the triggering of a space-leader could be explained by a contribution of the electrons of the filament to this process in the vicinity of the space-stem and its streamers. This may result in a thermal expansion of the filament during the first hundreds of nanoseconds after the laser, as reported on a smaller scale [28]. The smaller delay between the laser pulse and the space-leader formation at 2.3 m compared to the 4.5 m gap would then be explained by the higher level of the electric field. However, since the streamers are less luminous than the leader head, a camera with a higher dynamic range and spatial resolution would be required to reveal an interaction of the filament with the space-stem and streamers.

Also shown in Figs. 2b and 3b are the voltage and current records for both types of discharges indicating the different time scales and the absence of the current peak in the case where the electrode leader is guided.

The above results show that the laser is able to provoke a space-leader discharge if it is shot, before the final jump is initiated. In contrast to the observations on a small scale [4] the position of the space-leader does not necessarily correspond to the position of the guided part of the discharge (see Fig. 2).

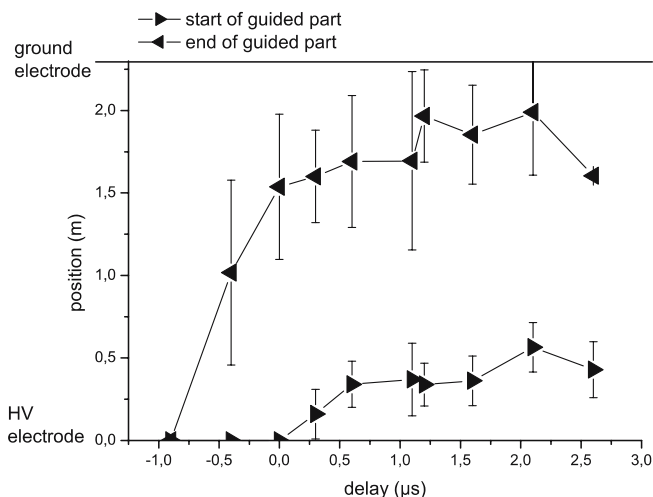


**FIGURE 4** Parameters of the guided parts of the discharge in a 2.3 m gap at voltage levels of about 2.0 MV. The error bars indicate the standard deviation

Besides the streamer and leader propagation, the plasma lifetime [29, 30] is a key parameter for extrapolating the laboratory results to real-scale lightning control, because it limits the effective length of the plasma channel. This lifetime was estimated in two ways. Changing the laser delay relative to the voltage pulse in a 2.3 m gap (Fig. 4), we observed no triggered or guided event if the laser was shot more than  $1 \mu\text{s}$  before the beginning of the voltage pulse, showing that the plasma channel has vanished within a few microseconds, before a sufficient electric field can be reached.

The second approach is based on the evaluation of the fast-frame camera pictures of the 4.5 m gap. As can be seen on Fig. 1a the space-leader propagates in the plasma channel first towards the high voltage electrode, until it connects to the electrode leader and then towards the ground electrode. This propagation begins  $t_d = 800 \text{ ns}$  after the laser pulse and occurs at a speed of  $v_g = 2.4 \times 10^6 \text{ m/s}$ . Therefore, the guided length, which corresponds to the path propagated by the space-leader before the plasma channel has vanished, is  $x_g = v_g(t_p - t_d)$  where  $t_p$  is the plasma lifetime. It has been measured to be  $t_p = (1.3 \pm 0.4) \mu\text{s}$  from an average over seven events. The obtained plasma durations are much shorter than the 10  $\mu\text{s}$  lifetime of the ionized channel observed for a stronger focus ( $f \approx 5 \text{ m}$ ) [5].

However, Fig. 3a shows that the electrode leader can still be guided, although it develops more than  $2.5 \mu\text{s}$  after the laser pulse, i.e., at a time beyond the free plasma lifetime. In fact, the leader follows the guided path of the streamer, which has propagated earlier, first freely, before the laser was shot, then guided by the filament. The statistics over 13 shots of guided electrode leaders show that the end of the guided part does not exceed a distance of 1.5 m downstream from the high voltage electrode. The streamer velocity can be estimated from the fast frame pictures to be not less than  $0.7 \times 10^6 \text{ m/s}$ . When the laser arrives  $1.2 \mu\text{s}$  after the start of the voltage pulse, the streamers have propagated at least 80 cm into the gap. At this point, the streamer generated plasma is heated. If the heating is sufficient, a space-leader could be initiated. This is consistent with the fact that the space-leader is located at  $(1.0 \pm 0.2) \text{ m}$  downstream from the high-voltage electrode (averaged over 10 shots) independently from the gap length. If no space-leader is initiated, the streamers can interact with the laser filament during additional 70 cm on their way to the ground electrode if one considers a plasma lifetime of  $1 \mu\text{s}$  as determined above. This leads to the observed limitation of 1.5 m for guided electrode leaders.

Figure 5 shows the guided lengths as a function of the gap length for laser delays between 0 and  $2.6 \mu\text{s}$ . The data are averaged over all shots for which a space-leader can be seen on the fast-frame pictures. The guided length reaches 1.6 m for the 2.3 m gap and drops to about 1.2 m at 4.5 m gap length. The longer guiding for the 2.3 m gap can be explained by the reduced delay before space-leader formation, as described above (450 vs 800 ns). Figure 5 also displays results from earlier experiments with a laser delay between 2.4 and  $5 \mu\text{s}$  in a sphere-plane gap with distances between 1.2 m and 3.8 m under negative voltage pulses with a rising time of  $1.2 \mu\text{s}$  [6]. This shorter rising time further increases the delay between the high voltage max-

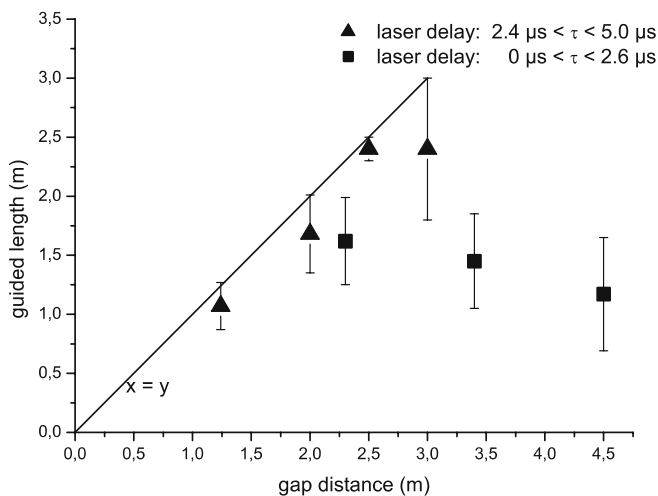


**FIGURE 5** The mean values of the total guided lengths as a function of the gap distance.  $\tau$  denotes the time delay between the laser, the beginning of the voltage pulse, the error bars indicate the standard deviation. The results for laser delays between 2.4 and 5.0  $\mu\text{s}$  were obtained in an earlier experiment [6]

imum and the laser pulse. The experiments had been performed at moderate voltage levels so that all observed discharges were triggered by the laser. In these conditions the guided length increases linearly up to 2.4 m where a saturation seems to occur. Considering the plasma lifetime of 1  $\mu\text{s}$  determined above, this suggests that the emerged electrode leader connects to the plasma channel without a delay as was observed for guided positive leaders [31]. The above condition of moderate voltage levels is essential to achieve optimum guided lengths, since at higher voltages the electrode leader is initiated before the laser. Therefore, the propagating electrode leader would connect to the filament at some point between the electrodes (see Fig. 3a): Then the discharge would be guided only from this point on.

#### 4 Conclusion

We have studied the triggering and guiding of negative discharges with long plasma filaments in sphere-plane gaps from 2.3 m to 4.5 m. The laser is able to provoke a space-leader if it is shot, before the final jump is initiated. The plasma lifetime relevant for triggering and guiding of discharges is about 1  $\mu\text{s}$ . In the case of space-leader formation this lifetime limits the guided length to the meter range due to a delay of several hundreds of nanoseconds between the laser pulse and the occurrence of the space-leader. If the electrode leader is guided by the plasma channel, the results suggest that the guided lengths are limited to 2.4 m due to the plasma lifetime and a measured leader velocity of  $2.4 \times 10^6$  m/s.

However, in view of real scale lightning applications of this technique, numerical modeling [8] as well as recent experimental results [17, 32] show that the plasma lifetime can be enhanced by propagating a second laser pulse along the filament, improving the effective length of the filament for guiding.

With regard to a fundamental understanding of the negative discharge development, further investigation, based on

more statistical accumulation and sensitive camera devices, could help to reveal the processes leading to the occurrence of a space-leader, especially to observe directly an interaction of the space-stem and streamers with the laser produced plasma channel.

**ACKNOWLEDGEMENTS** This work has been performed within the Teramobile project, funded jointly by the CNRS, DFG, and French and German ministries of Research and of Foreign affairs. The Teramobile web site is [www.teramobile.org](http://www.teramobile.org). K.S. acknowledges support from Humboldt Foundation.

#### REFERENCES

- M. Miki, Y. Aihara, T. Shindo, J. Phys. D: Appl. Phys. **26**, 1244 (1993)
- M. Miki, T. Shindo, Y. Aihara, J. Phys. D: Appl. Phys. **29**, 1984 (1996)
- H. Pépin, D. Comtois, F. Vidal, C.-Y. Chien, A. Desparois, T.W. Johnston, J.-C. Kieffer, B. La Fontaine, F. Martin, F.A.M. Rizk, C. Potvin, P. Couture, H.P. Mercure, A. Bondiou-Clergerie, P. Lalande, I. Gallimberti, Physics of Plasmas **8**, 2532 (2001)
- B. La Fontaine, F. Vidal, D. Comtois, C.-Y. Chien, A. Desparois, T.W. Johnston, J.-C. Kieffer, H.P. Mercure, H. Pépin, F.A.M. Rizk, IEEE Transactions on Plasma Science **27**, 688 (1999)
- D. Comtois, H. Pépin, F. Vidal, F.A.M. Rizk, C.-Y. Chien, T.-W. Johnston, J.-C. Kieffer, B. La Fontaine, F. Martin, C. Potvin, P. Couture, H.P. Mercure, A. Bondiou-Clergerie, P. Lalande, I. Gallimberti, IEEE Transactions on Plasma Science **31**, 377 (2003)
- M. Rodriguez, R. Sauerbrey, H. Wille, L. Wöste, T. Fujii, Y.-B. André, A. Mysyrowicz, L. Klingbeil, K. Rethmeier, W. Kalkner, J. Kasparian, E. Salmon, J. Yu, J.-P. Wolf, Opt. Lett. **27**, 772 (2002)
- S.L. Chin, K. Miyazaki, Jpn. J. Appl. Phys. **38**, 2011 (1999)
- X.M. Zhao, J.-C. Diels, C.Y. Wang, J.M. Elizondo, IEEE J. Quantum Electron. **QE-31**, 3, 599 (1995)
- D. Comtois, H. Pépin, F. Vidal, F.A.M. Rizk, C.-Y. Chien, T.W. Johnston, J.-C. Kieffer, B. La Fontaine, F. Martin, C. Potvin, P. Couture, H. Mercure, A. Bondiou-Clergerie, P. Lalande, I. Gallimberti, IEEE Transactions on Plasma Science **31**, 387 (2003)
- A. Braun, G. Korn, X. Liu, D. Du, J. Squier, G. Mourou, Opt. Lett. **20**, 73 (1995)
- H. Schillinger, R. Sauerbrey, Appl. Phys. B **68**, 753 (1999)
- A. Talebpour, M. Abdel-Fattah, S. Chin, Opt. Commun. **183**, 479 (2000)
- J. Kasparian, R. Sauerbrey, S.L. Chin, Appl. Phys. B **71**, 877 (2000)
- M. Rodriguez, R. Bourayou, G. Méjean, J. Kasparian, J. Yu, E. Salmon, A. Scholz, B. Stecklum, J. Eislöf, U. Laux, A.P. Hatzes, R. Sauerbrey, L. Wöste, J.-P. Wolf, Phys. Rev. E **69**, 036607 (2004)
- M.A. Uman, *The Lightning Discharge* (Dover Publications 2001)
- R. Ackermann, K. Stelmaszczyk, P. Rohwetter, G. Méjean, E. Salmon, J. Yu, J. Kasparian, G. Méchain, V. Bergmann, S. and Schaper, B. and Weise, T. Kumm, K. Rethmeier, W. Kalkner, L. Wöste, J.P. Wolf, Appl. Phys. Lett. **85**, 5781 (2004)
- G. Méjean, R. Ackermann, J. Kasparian, E. Salmon, J. Yu, J.P. Wolf, K. Rethmeier, W. Kalkner, P. Rohwetter, K. Stelmaszczyk, L. Wöste, submitted to Appl. Phys. Lett. (2005) to be published
- Les Renardières Group, Electra **74**, 67 (1981)
- T. Reess, P. Ortega, A. Gibert, P. Domens, P. Pignolet, J. Phys. D: Appl. Phys. **28**, 2306 (1995)
- P. Ortega, P. Domens, A. Gibert, B. Hutzler, G. Riquel, J. Phys. D: Appl. Phys. **27**, 2379 (1994)
- G.L. Bacchiega, A. Gazzani, M. Bernardi, I. Gallimberti, A. Bondiou, International Aerospace and Ground Conference on Lightning and Static Electricity, Mannheim, (1994), pp. 13–22
- F. Vidal, D. Comtois, C.-Y. Chien, A. Desparois, B. La Fontaine, T.W. Johnston, J.-C. Kieffer, H.P. Mercure, H. Pépin, F.A.M. Rizk, IEEE Transactions on Plasma Science **28**, 418 (2000)
- H. Wille, M. Rodriguez, J. Kasparian, D. Mondelain, J. Yu, A. Mysyrowicz, R. Sauerbrey, J.-P. Wolf, L. Wöste, Europ. Phys. J. - Appl. Phys. **20**, 183 (2002)
- J. Kasparian, M. Rodriguez, G. Méjean, J. Yu, E. Salmon, H. Wille, R. Bourayou, S. Frey, Y.-B. André, A. Mysyrowicz, R. Sauerbrey, J.-P. Wolf, L. Wöste, Science **301**, 61 (2003)
- S. Tzortzakis, M.A. Franco, Y.-B. André, A. Chiron, B. Lamouroux, B.S. Prade, A. Mysyrowicz, Phys. Rev. E, Rapid Commun. **60**, 3505 (1999)

- 26 L. Bergé, S. Skupin, F. Lederer, G. Méjean, J. Yu, J. Kaparian, E. Salmon, J.P. Wolf, M. Rodriguez, L. Wöste, R. Bourayou, R. Sauerbrey, *Phys. Rev. Lett.* **92**, 225 002 (2004)
- 27 A. Bondiou, I. Gallimberti, *J. Phys. D: Appl. Phys.* **27**, 1252 (1994)
- 28 S. Tzortzakis, B. Prade, M. Franco, A. Mysyrowicz, S. Hüller, P. Mora, *Phys. Rev. E* **64**, 057 401 (2001)
- 29 S. Tzortzakis, B. Prade, M. Franco, A. Mysyrowicz, *Opt. Commun.* **181**, 123 (2000)
- 30 H. Yang, J. Zhang, Y. Li, J. Zhang, Y. Li, Z. Chen, H. Teng, Z. Wei, Z. Sheng, *Phys. Rev. E* **66**, 016 406 (2002)
- 31 B. La Fontaine, D. Comtois, C.-Y. Chien, A. Desparois, F. Génin, G. Jarry, T. Johnston, J.-C. Kieffer, F. Martin, R. Mawassi, H. Pépin, F.A.M. Rizk, F. Vidal, C. Potvin, P. Couture, H.P. Mercure, *J. Appl. Phys.* **88**, 610 (2000)
- 32 Z.Q. Hao, J. Zhang, Y.T. Li, X. Lu, X.H. Yuan, Z.Y. Zheng, Z.H. Wang, W.J. Ling, Z.Y. Wei, *Appl. Phys. B* **80**, 627 (2005)

A reprint from  
**American Scientist**  
the magazine of Sigma Xi, The Scientific Research Society

This reprint is provided for personal and noncommercial use. For any other use, please send a request to Permissions, American Scientist, P.O. Box 13975, Research Triangle Park, NC, 27709, U.S.A., or by electronic mail to [perms@amsci.org](mailto:perms@amsci.org). ©Sigma Xi, The Scientific Research Society and other rightsholders

# Filaments of Light

*Pulsed terawatt lasers create some surprising effects when shone through the air—including the channeling of light*

Jérôme Kasparian

Next time you give a presentation about your research, take a close look at the laser pointer you're holding in your hand. How big is the beam coming out of it? And how large is the spot that it forms? The answers will, of course, hinge on the particular laser pointer you're wielding and the distance between podium and screen. Typical values might be a few millimeters for the beam as it exits the aperture of the pointer and a centimeter or so for the circle of light it casts across the auditorium. It takes only a smattering of physical intuition to guess the reason: Diffraction causes the beam to diverge. The actual cause may be a little more complicated, because some laser pointers include a lens that makes the light converge at a fixed distance from the tip, which leads the beam to spread out beyond this focal point—more so than if only diffraction had operated.

Imagine now that your laser pen packed a more powerful punch—say

---

*Jérôme Kasparian is an investigator in Jean-Pierre Wolf's group at the Laboratoire de spectrométrie ionique et moléculaire (LASIM), part of France's Centre national de la recherche scientifique and Université Claude Bernard Lyon 1. He received his Ph.D. in 1997 at the LASIM, where he studied lidar remote sensing and the optical properties of aerosols. He then joined the Institute for Optics and Quantum Electronics at the Friedrich Schiller Universität in Jena, Germany, where his main interest was the nonlinear optics and propagation of ultrashort, high-power laser pulses through the atmosphere. He participated in launching the French-German Teramobile collaboration before returning to Lyon as the coordinator of this project. Address: Laboratoire de spectrométrie ionique et moléculaire, UMR CNRS 5579, Université Claude Bernard Lyon 1, 43 boulevard du 11 novembre 1918, F-69622 Villeurbanne Cedex, France. Internet: jkaspari@lasim.univ-lyon1.fr*

that the intensity of the beam was a whopping  $10^{12}$  times that of a typical pointer. What then would the beam do as it crossed the room? (It's clear enough what it'll do when it hits the screen—quickly burn a hole). The answer, it turns out, is anything but intuitive. A laser of sufficient intensity traveling through air will—all by itself—engineer a narrow channel, one perhaps a tenth of a millimeter wide, over which light will propagate for tens or even hundreds of meters. Such filaments of laser light were first created a little more than a decade ago, and investigators are just now beginning to explore a variety of applications for them—mapping atmospheric pollutants, characterizing materials at a distance, perhaps one day even controlling lightning.

## Let There Be (White) Light

Two separate physical phenomena account for the strange filamentary propagation of high-power laser light. The first is self-focusing, which comes about because the refractive index of air depends on the intensity of light passing through it, a phenomenon known as the optical Kerr effect. As a consequence, when one sends high-power laser light through the atmosphere, the center of the beam (where light intensity is highest) passes through gas that has a higher refractive index than the air located just off axis. The result is the same as if you had shot the beam through a convex lens, which has more glass (with its high refractive index) at the center than at the margins. Physicists refer to this configuration, sensibly enough, as a "Kerr lens." For a laser with an 800-nanometer wavelength operating in air, a Kerr lens develops whenever the beam power exceeds a few gigawatts.

The more a laser is focused by such a Kerr lens, the higher the intensity becomes. And as the intensity rises, the focusing gets even stronger, boosting the intensity of light still further. Eventually, something has to give—and it does. When the light intensity reaches somewhere between  $10^{13}$  and  $10^{14}$  watts per square centimeter, a nonlinear process called *multiphoton ionization* comes into play. The oxygen and nitrogen molecules in air are then able to absorb many photons at once, stripping electrons from their parent atoms, forming a plasma.

Although Kerr-lens focusing and the ensuing creation of plasma could, in theory, be brought about using a laser that operates continuously at extreme power levels, in practice, it proves much easier to achieve the necessary oomph using short bursts—the shorter the better. Common sense explains why: For a laser pulse of a given energy, the more limited the duration, the higher the peak intensity. So with the laser's energy concentrated in a brief pulse, the focusing effect is strong even though the average power in the beam is modest.

There's a second reason to use very short bursts: The ability of a laser to ionize the air remains high, but the average density of electrons created is low, allowing the beam to propagate through them. (Electron density will be relatively low when the pulses are too short to shoot the released electrons into nearby gas molecules, releasing more electrons, which then would bash into other molecules and so forth in a process called *cascade ionization*.) Electrons are present in sufficient numbers, however, to decrease the refractive index of the air containing them, which results in the equiva-

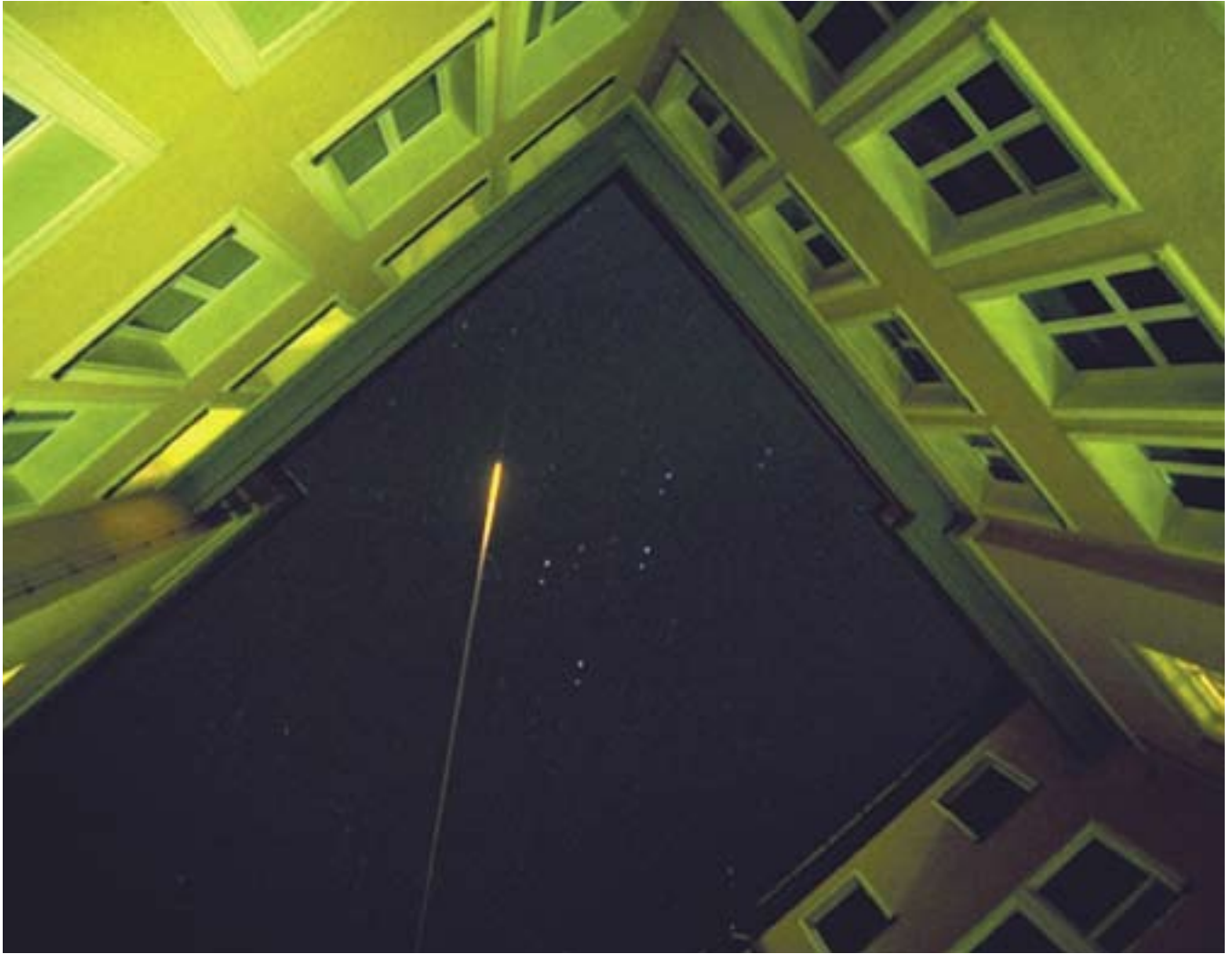


**Figure 1.** A laser projecting very intense pulses of light through the atmosphere is able to induce some intriguing optical effects. Here the beam of such a laser is manipulated to focus high in the atmosphere. Although the beam from a less powerful laser would diverge above this point, when the radiation is sufficiently intense, nonlinear processes in the atmosphere channel the light into many parallel filaments, which convey the light farther upward while scattering a portion of it back toward the ground. Unlike the infrared beam from which it originates, these filaments of light contain a wide range of colors, making them visible to the naked eye. (Photograph courtesy of Carsten Wedekind.)

lent of a diverging lens and tends to defocus the beam.

Either phenomenon considered alone—the focusing of a Kerr lens or the defocusing induced by the electrons in a blob of plasma—would prevent high-power laser pulses from propagating very far through the air. But it turns out that the two opposing effects can be made to balance, allowing the beam to travel over large distances without either diverging or collapsing. Instead, the energy is channeled along a narrow filament of light.

What happens when the intensity of laser light used is turned up higher than the critical value for filamentation to begin? You might guess that the light filament formed would become thicker and thicker, perhaps to the point of being better described as

a “light rope.” But that is not what happens. Instead, several localized filaments emerge. That is, hiking the peak power of the laser pulses that are applied increases the number of filaments that result without notably influencing the individual intensity or the energy each filament carries.

Whether present singly or in bunches, these threadlike shafts of light exhibit another surprising property as well: Even though the laser used to create them produces essentially monochromatic light, each filament contains a broad range of wavelengths—what students of optics call “a white-light supercontinuum.” The transformation into white light is easy enough to understand once you realize that a pulsed laser doesn’t instantly switch on and off. Rather, the oscillatory electric and

magnetic fields carried in each pulse gradually build to a maximum intensity and then diminish. That property alone explains some of the spectral broadening—basic physics dictating that the bandwidth of a pulse can be no less than the reciprocal of its duration. But that principle explains only a small part of the whitening effect. More important is the fact that the refractive index of the air containing the pulse is proportional to the intensity of the light. So where the intensity of light is highest (in the middle of the pulse), so is the refractive index, which causes the highest intensity light waves to be retarded with respect to the lower intensity waves that travel ahead and behind. The result is a distortion to the pulse envelope and the creation of light that contains both longer and

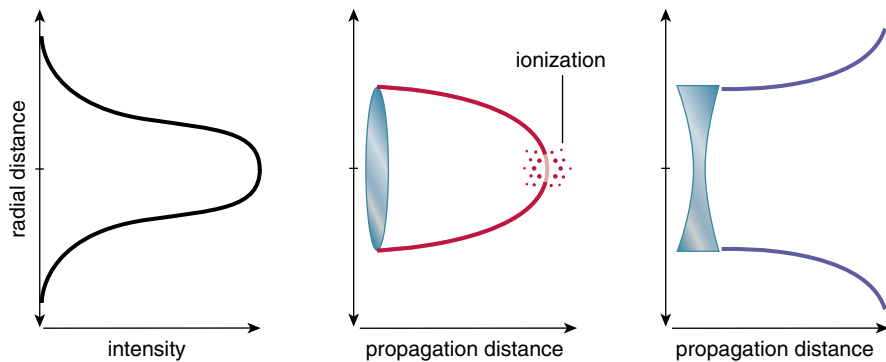


Figure 2. Light in a laser beam is of highest intensity at the center and decreases with radial distance away from the axis of propagation (left). Because the refractive index of air increases with the intensity of light passing through it (the optical Kerr effect), a high-intensity laser beam shone through the atmosphere encounters the functional equivalent of a convex lens, causing the beam to converge (center). The intensity eventually becomes sufficient to ionize the air (speckled pattern). The electrons released in this process decrease the refractive index of the air, mimicking a concave lens and causing the beam to diverge (right).

shorter wavelengths than what the laser itself puts out. The range of different wavelengths that arise from this and other nonlinear effects makes the illumination essentially white.

As if the existence of narrow filaments and their ability to generate white light weren't bizarre enough, another surprising phenomenon has been found to take place: A significant part of the white-light supercontinuum appears to be emitted backward! This back-directed light is the result of partial self-reflection of the forward-traveling beam, which experiences changes in refractive index along the axis of the filament as a result of the focusing and defocusing taking place. And just like with the beam of

a flashlight shone on a double-glazed window, each change in refractive index produces a partial reflection.

### Stepping Out

The laser-research consortium that I coordinate was established in 1999, when French teams led by Jean-Pierre Wolf at the Laboratoire de spectrométrie ionique et moléculaire (part of the Université Claude Bernard Lyon I) and André Mysyrowicz at Laboratoire d'optique appliquée (part of the École polytechnique in Palaiseau) joined forces with German groups led by Ludger Wöste at the Freie Universität Berlin and Roland Sauerbrey at the Friedrich Schiller Universität in Jena, Germany. Our aim

was to create an experimental laser that could be brought into the field to study how light filaments propagate over greater distances than one can possibly arrange in the lab and to develop ways to use them for probing the atmosphere. A laser of this sort allows for the remote examination of gaseous or aerosol pollutants released, say, from automobiles or industrial installations. And it can be used to study the formation of water droplets in clouds.

It was clear early on that pursuing such investigations demands mobility, yet the high-power pulsed lasers then available took up most of a room—not something one could easily pack up and move. The solution was to install a laser of this type in a standard 20-foot-long freight container, which could be carried by truck (or by ship) as needed anywhere in the world and operated even in adverse weather conditions. We call this portable terawatt laser system the “Teramobile.”

The laser we use is quite sophisticated. It sends out short pulses of infrared light (800-nanometer wavelength) 10 times per second. Each pulse is only 70 femtoseconds (70 millionths of a nanosecond) long when it exits the laser and carries 350 millijoules of energy. The peak power works out to 5 terawatts ( $5 \times 10^{12}$  watts). My colleagues and I have been experimenting with this laser for several years, working mostly on schemes for measuring the composition of atmospheric trace gases as well as the abundance and nature of aerosol particles.

Several optical techniques for probing such properties of the atmosphere already exist, methods that go by such complicated names as “Fourier-transform infrared spectroscopy,” “differential optical absorption spectroscopy” and “light detection and ranging” (lidar). The Teramobile laser adds the possibility of carrying out such studies using one or more white-light laser filaments instead of the usual sources of light—ordinary (monochromatic) lasers or in some cases the natural illumination that the Sun or Moon provides.

Although laser filaments do not suffer the diminution in intensity that accompanies the spreading of a conventional laser beam, members of the Teramobile team were concerned at the outset of our investigations that these narrow channels of light might easily be blocked by raindrops or atmospheric dust. So we carefully

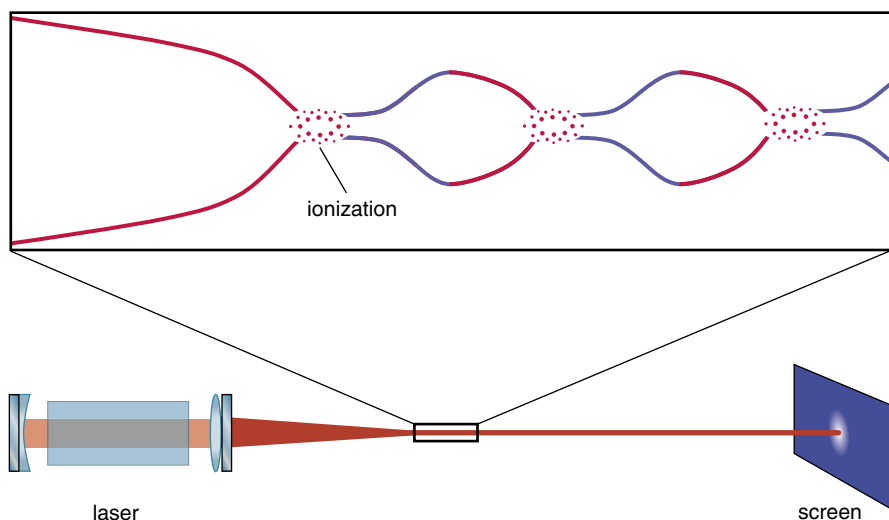


Figure 3. The self-focusing that arises from the Kerr effect (red) and the defocusing that results from the subsequent ionization (blue) together act to channel light into a distinct filament, which is roughly 0.1 millimeter in diameter. This filament of light can project tens or even hundreds of meters without diverging.

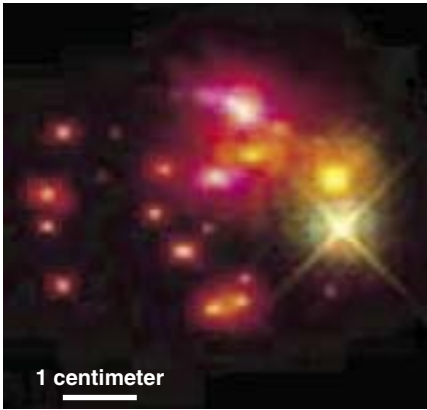


Figure 4. Increasing the power level of the laser used to create a filament of light does not increase the diameter of this conduit; rather, multiple filaments form, shown here projected on a screen. (Image courtesy of the Teramobile Project.)

studied the interaction of light filaments with such aerosol particles, introducing droplets of various sizes into the light path. It turned out that our worries were unjustified. We discovered that opaque droplets as large as 100 micrometers in diameter do not obstruct the propagation of a light filament, although they are about as large as the filament itself. At the same time we were doing these studies, See Leang Chin and his

coworkers at the Université Laval in Québec, found that a laser filament cannot be sent through a hole, even one that is several times the diameter of the filament.

This counterintuitive result is explained by the fact that a filament of light is not simply a tube through which all the photons flow; rather, it reflects a dynamic balance within the much more diffuse beam that surrounds it, something I like to call a “photon bath,” which acts as an energy reservoir feeding the filament when it encounters an obstacle. Thus, blocking the propagation of a filament in one place naturally spawns a new filament elsewhere within the wider beam. Numerical simulations by Jerome V. Moloney and his coworkers at the University of Arizona and by Luc Bergé at Commissariat à l’énergie atomique (CEA, the French atomic energy agency) in Bruyères le Châtel show this effect well.

Light filaments sent into the sky can thus traverse a cloud so long as the accompanying photon bath makes it through. Small-scale laboratory tests had suggested that laser filaments should be able to pass through a typical cumulus or stratocumulus cloud without being visibly affected. My

colleagues and I found similar results when we scaled up the experiment using the Teramobile beam and an open cloud chamber producing a 10-meter-long cloud of 1-micrometer droplets. Light filaments were visible exiting the fog, even for a concentration of almost 100,000 droplets per cubic centimeter, meaning that one filament must have hit an average of 2,000 droplets for each meter it traveled.

### Up, Up and Away

To determine whether filaments of light could indeed penetrate high into the atmosphere, the scientists on the Teramobile project did the obvious: We tried it. After directing the Teramobile laser vertically upward, we studied the beam from the ground using the 2-meter-diameter astronomical telescope at Thüringer Landessternwarte in Tautenburg. Because the laser was located some distance from the telescope, we were able to obtain side-on images of the beam by virtue of Rayleigh scattering (the scattering of light off air molecules, which among other things causes the sunlit sky to appear blue). The pictures we took also revealed the pattern cast by the beam when it impinged on the bottom of clouds or layers of diffuse haze. These experiments,

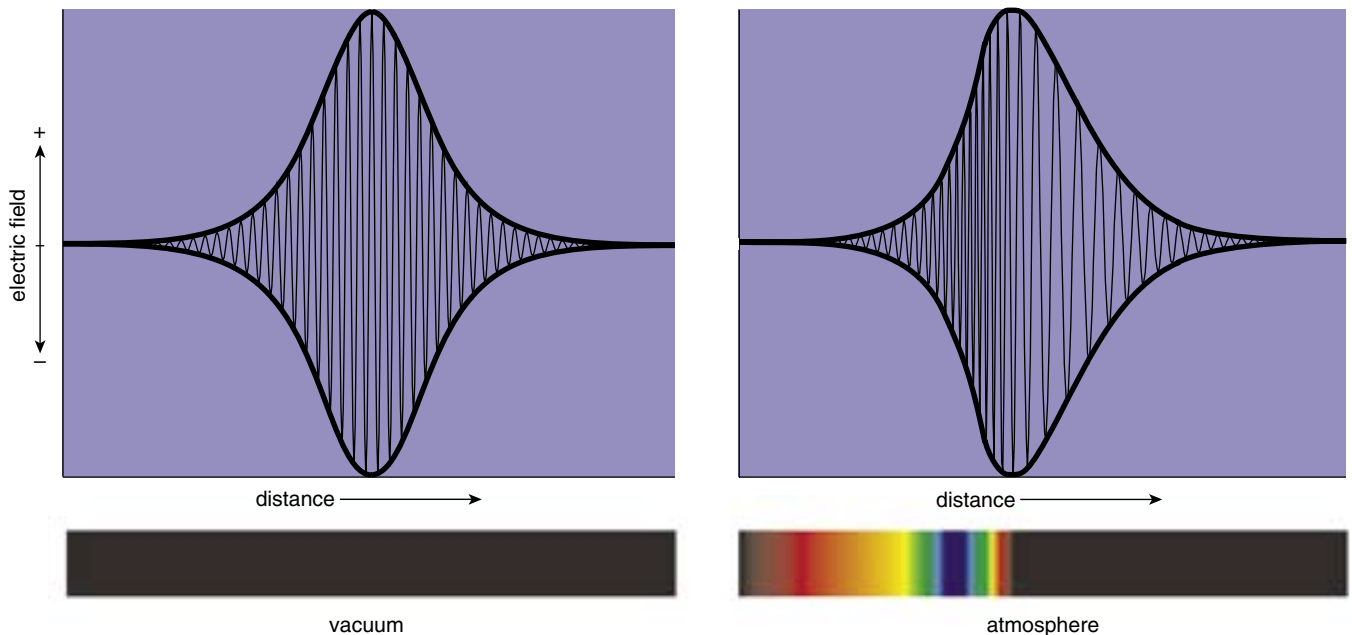


Figure 5. Terawatt lasers used to induce nonlinear optical effects pack their energy into vanishingly short pulses—ones that last for only a few hundred femtoseconds ( $10^{-15}$  second). During any one pulse, the electric and magnetic fields first grow to some peak intensity and then diminish (*top left*). Were it sent through empty space, a pulse of infrared light would have a symmetric envelope (*heavy line*) containing electromagnetic waves of variable amplitude but with a uniform infrared wavelength, meaning that this light would remain invisible to the eye (*bottom left*). But in the atmosphere, the Kerr effect causes the highest amplitude waves within the pulse to slow relative to the smaller amplitude ones that come before and after (*top right*). The resulting distortion creates a range of wavelengths (that is, colors) not present originally (*bottom right*). The combination of many colors is then perceived as white light.

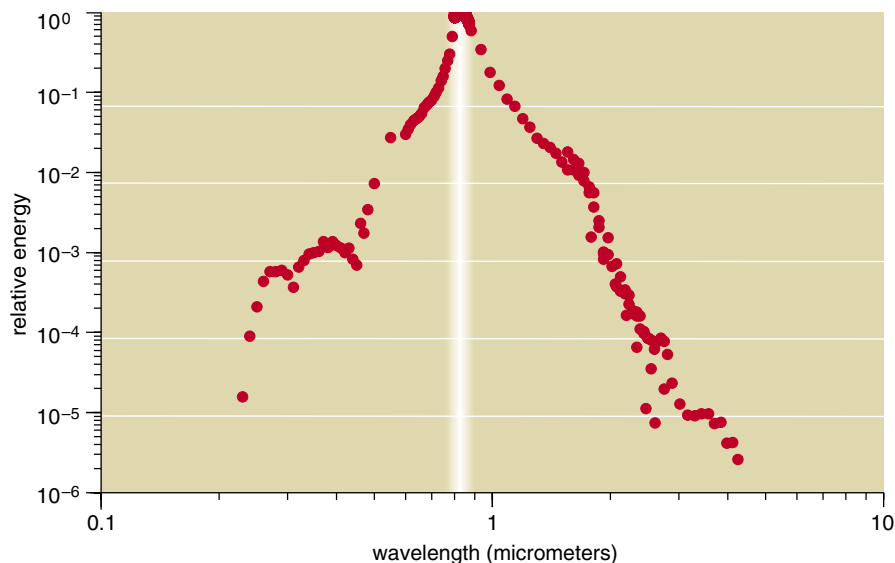


Figure 6. Although only a narrow range of infrared wavelengths (*white band*) are present originally in the beam from the author's terawatt laser, the temporal Kerr effect broadens the spectrum considerably (*red dots*).

which were carried out in 2002, demonstrated for the first time an ability to bring light to a tight focus as far as 2 kilometers away from the laser source, at which point distinct filaments can propagate for hundred of meters. And although the reach of these high-intensity filaments is currently limited to such distances, the Teramobile laser is able to throw diffuse white light as high as 18 kilometers—that is, well into the stratosphere.

Having such a far reach holds great promise for probing the physical and chemical makeup of the atmosphere. Investigators have long applied lasers for this purpose, often using one or more refinements to the basic lidar technique, whereby a pulsed laser is directed into the air, and the backscattered light is measured as a function of time. Performing these measurements with a temporal resolution of, say, between one and ten nanoseconds provides a depth resolution of a few meters or less. Such observations, which are often obtained while sweeping the beam from side to side, allow for the construction of three-dimensional maps of atmospheric aerosols or trace gases.

Currently, the most popular way to detect such gases (often pollutants) remotely is a technique called DIAL, shorthand for "Differential Absorption Lidar." The strategy is to compare the lidar signals obtained at two slightly different wavelengths, one being set exactly to an absorption line in

the spectrum of the pollutant under scrutiny. Seeing a diminution in the amount of light returned at that wavelength but not at a slightly different wavelength attests to the presence of the targeted trace gas and rules out the possibility that something more mundane (say, clouds or haze) had obscured the light scattered back toward the observation station.

The problem with the DIAL method is that it can only be used to map trace gases that exhibit a narrow absorption

line that is free of interference from the absorption spectra of other atmospheric components. This requirement limits its application severely. Worse, the need to tune the laser wavelength exactly to the absorption line makes it impossible to measure more than one pollutant at a time. And it makes DIAL blind to the presence of an unanticipated pollutant. Using the Teramobile laser or its equivalent for lidar should provide a better way to probe the sky, because the telescope can then gather light containing many wavelengths, not just one or two, and the resulting absorption spectra would reveal a wealth of information about the air this light passed through.

A similar tactic could one day be applied, for example, to characterize the nucleation of water droplets and their subsequent maturation in clouds. Measurements of droplet growth and density could allow meteorologists to forecast when rain or snow will form, or this information could be used to determine how much of the sunlight falling on a given cloud reflects back into space. Why use a ground-based laser for such investigations? Droplet nucleation and growth take place over just of a few tens of minutes, so making the required measurements from research aircraft is generally too expensive to consider, and weather-balloon soundings are typically too infrequent to provide helpful observa-

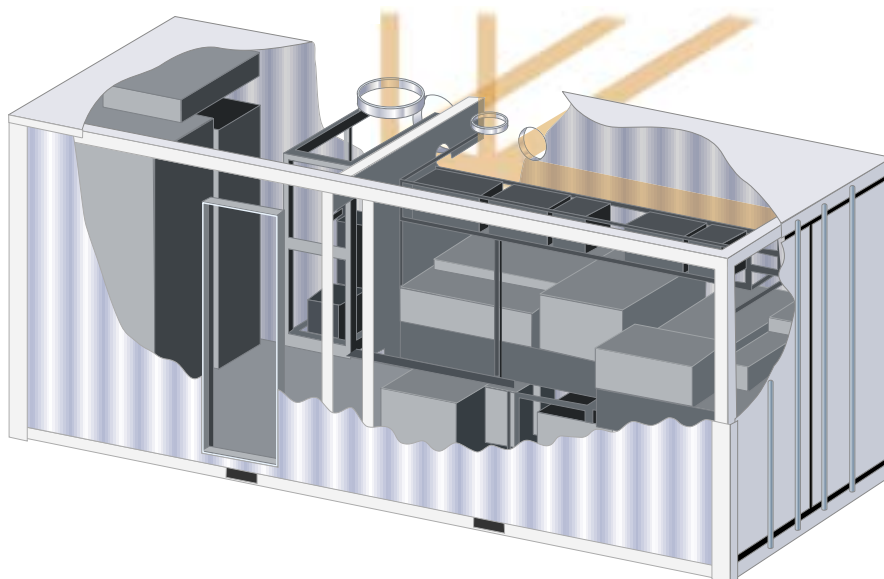


Figure 7. The Teramobile laser system consists of a 20-foot shipping container filled with the sophisticated equipment needed to generate a terawatt-class pulsed laser. Windows on one side and on the top allow the beam (*orange*) to be sent either horizontally or vertically. Adjustable optical elements on the output of the laser permit the focal distance to be varied so that filamentation can be made to begin a variable distance away.

tions. Optical remote-sensing techniques are clearly the most straightforward avenue for conducting such research, and the capabilities of the Teramobile laser in its white-light lidar mode are quite promising in this regard.

### Bug Zapper Extraordinaire

The fact that the Kerr effect can transform a high-power infrared laser into a remote source of white light opens the door to a number of exciting applications. For example, the tendency for some of the light to be reflected backward suggests that we could create an artificial “guide star” for use in adjusting astronomical telescopes equipped with adaptive optics. But there are other nonlinear optical effects of the Teramobile laser that can be exploited as well. One is something called *multiphoton fluorescence*.

In normal fluorescence, a substance, say the phosphor powder that coats the inside of a fluorescent lamp, absorbs high-energy photons (typically in the ultraviolet) and releases lower-energy photons (having, usually, visible-light wavelengths). In multiphoton fluorescence, two or more low-energy photons are absorbed simultaneously, raising an electron’s energy level enough to allow a single high-energy photon to be given off when the electron returns to its original state. But because the chance of an atom absorbing two photons at once is quite low, light of very high intensity (that is, containing a very large number of photons) is



Figure 8. In an experiment to test how well the Teramobile system works when the air is not clear, an artificial cloud of water droplets was formed within this 10-meter-long pipe. To the delight of the author and his colleagues, the droplets did not block the propagation of light filaments. Why not? Although such droplets may extinguish a filament in one position, the scattered photons then contribute to the formation of a new filament elsewhere. (Photograph courtesy of Alexis Gratié/DAVM/Université Lyon 3.)

needed. The pulsed Teramobile laser provides just such light, which proves a great boon for remotely sensing certain compounds using the phenomenon of multiphoton fluorescence.

In a 2002 experiment, my colleagues and I showed that the Teramobile beam and detection apparatus could sense biological aerosols at a distance.

The motivation was to be able to map a cloud, say, of bacteria (perhaps given off during some industrial mishap or even a biological attack) and to identify potentially pathogenic agents among the various background atmospheric aerosols, among which may be more mundane organic particles such as soot or pollen.

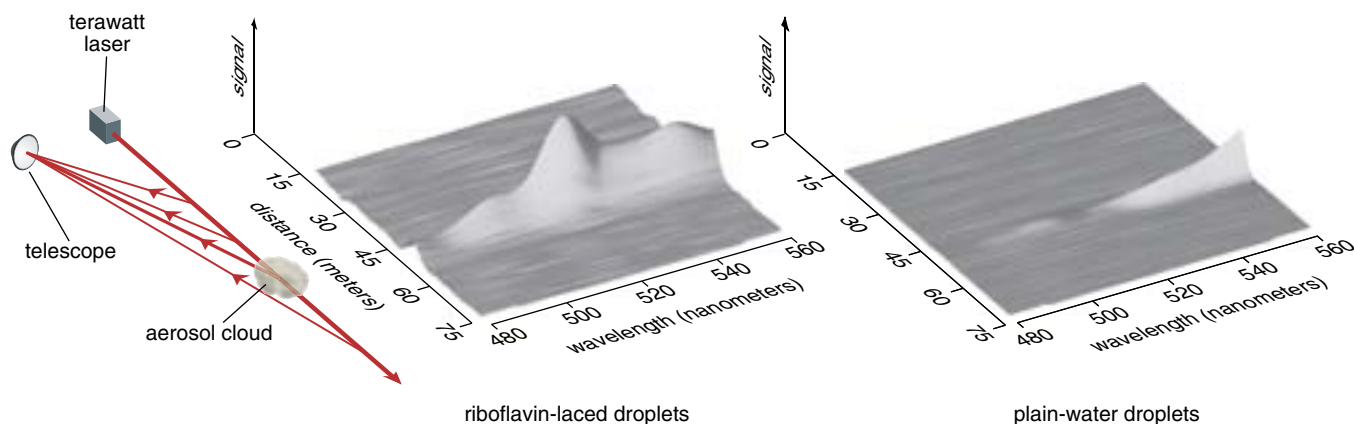
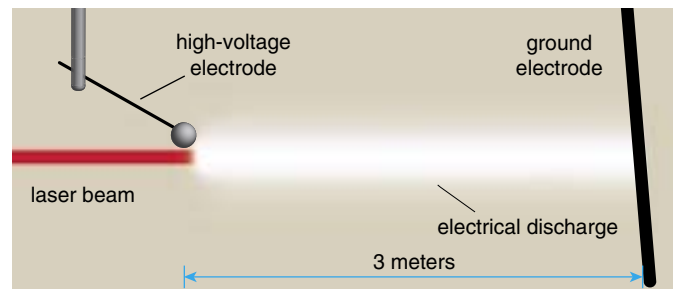


Figure 9. In 2002, the Teramobile laser was used to probe a cloud of water droplets that were laced with the biomolecule riboflavin so as to mimic the biological aerosols that might be released, say, in an accident or a terrorist attack. Spectral measurements of the light returned from the cloud (*left*) easily distinguish it from an equivalent cloud made of ordinary water droplets (*right*). Although lower-power lasers could also be used to detect biological aerosols in this way, they would have to emit light with a shorter wavelength and would thus be more prone to attenuation, limiting the distance over which they could operate.



Figure 10. Experiments with the Teramobile laser are advancing a decades-old quest to be able to trigger lightning discharges on command and to control their paths in such a way as to avoid damage on the ground. Here a normally erratic electrical discharge (top left), one created in a high-voltage test facility located at the Technische Universität Berlin, is successfully channeled along the path of ionization created by the laser beam (top right). Although the distance between electrodes in this test is only 3 meters (bottom right), advances in laser technology might one day allow real lightning discharges to be manipulated over distances large enough to protect people and property. (Photographs courtesy of the Teramobile Project.)



Our test used water droplets sized to mimic bacteria and laced with the compound riboflavin, which fluoresces at visible wavelengths when it absorbs two infrared photons, producing a characteristic spectrum in the backscattered light. The experiment, carried out on a cloud located about 45 meters from the Teramobile laser, showed that it was easy to distinguish such a plume from a cloud of pure water droplets. With refinement, this technique could, potentially, be quite sensitive. We calculated that a laser tuned to excite two-photon fluorescence in the amino acid tryptophan would boost sensitivity by a factor of 10, allowing concentrations of as little as 10 bacteria per cubic centimeter to be detected 4 kilometers away. Although lidar systems based on normal fluorescence could also be used to probe for biological agents, the laser employed would have to operate at a shorter wavelength and thus be more prone to attenuation, limiting the distance over which it could function effectively.

The ability of laser filaments to deliver high-intensity light at substantial distances also opens the door to other very interesting applications. For example, it becomes possible to conduct elemental analyses of the surfaces of metals, plastics, minerals or liquids from an appreciable distance, using a variation of a technique called *laser-induced breakdown spectroscopy*. For that, a powerful laser is focused on the material of interest, causing some of it to be transformed into plasma. The emission spectrum of the glowing plasma can then be analyzed, revealing the na-

ture of the substrate, with a detection limit that can be as little as a few parts per million for some elements. This method is currently used for such applications as the identification of highly radioactive nuclear waste and for monitoring the composition of molten alloys, because the tests can be performed without having to touch the sample. Imagine being able to do such probing from a large distance away! Normally, diffraction limits the intensity of light that can be focused on a remote target. But laser filaments can deliver intensities that are higher than the ablation threshold of many types of materials, at distances of hundreds of meters or even kilometers.

Another application under investigation may prove more spectacular yet—the control of lightning strikes. Lightning has always fascinated people, in part because of its unpredictable nature and destructive power—qualities that make these electrical discharges very difficult to study. Investigators from Electricité de France and CEA partially overcame those obstacles in the 1970s, when they developed a technique to trigger lightning on command using small rockets trailing thin wires. If shot upward at the right moment, the rockets and the wires they unspooled behind them served to initiate and channel the flow of electric current.

One outgrowth of this work was the idea of using a high-intensity laser to ionize air along the beam, thus forming a conducting channel of plasma that could replace the rocket-

hoisted wires. The first attempts, mounted in the 1970s and '80s, used lasers that produced nanosecond-long pulses. Those experiments were unsuccessful, however, because the plasma created by such lasers is largely opaque, which keeps the beam from extending a conductive path very far. But recently this field of research has seen renewed interest, because lasers can now provide higher intensities in shorter pulses, thereby avoiding the severe absorption that would otherwise occur. In particular, the team of Henri Pépin (Institut national de la recherche scientifique) and Hubert P. Mercure (Hydro-Québec) in Montreal have obtained quite promising results, using pulsed lasers to trigger and guide high-voltage discharges over several meters in the laboratory.

Spectacular experiments with the Teramobile system, installed in a high-voltage facility at the Technische Universität Berlin, showed that laser filaments can trigger and guide electric discharges over distances exceeding 4 meters. Moreover, the breakdown voltage is typically reduced by 30 percent. My colleagues and I have also shown that rain (or rather simulated rain) does not prevent the laser filaments from triggering these huge sparks. Research now focuses on the possibility of extending the lifetime of the plasma and increasing the length over which it is able to guide a discharge. Although the control of real lightning remains science fiction for the moment, recent progress in laser technology has brought this three-decade-old dream much closer to reality.

Over the past few years, the capabilities of terawatt-class lasers have improved markedly, while size and cost have come down. At the same time, physicists have made great strides in understanding the non-linear propagation of these high-power laser pulses in air. The rapidity of this progress suggests that Teramobile-type lasers, or systems like it, might soon be used widely, not just by scientists in the course of their research but for any number of military, commercial or public-safety applications.

## Bibliography

- Kasparian, J, M. Rodriguez, G. Méjean, J. Yu, E. Salmon, H. Wille, R. Bourayou, S. Frey, Y.-B. André, A. Mysyrowicz, R. Sauerbrey, J.-P. Wolf and L. Wöste. 2003. White-light filaments for atmospheric analysis. *Science* 301:61–64.
- Wille, H. M. Rodriguez, J. Kasparian, D. Mondelain, J. Yu, A. Mysyrowicz, R. Sauerbrey, J.-P. Wolf and L. Wöste. 2002. Teramobile: A mobile femtosecond-terawatt laser and detection system. *European Physical Journal—Applied Physics* 20:183–190.
- Kasparian, J, S. Frey, G. Méjean, E. Salmon, J. Yu, J.-P. Wolf, R. Bourayou, J.-C. Luderer, M. Rodriguez, H. Wille and L. Wöste. 2005.

Femtosecond white-light lidar. In *Laser Remote Sensing*. Ed. T. Fujii and T. Fukuchi. New York: Marcel Dekker.

For relevant Web links, consult this issue of *American Scientist Online*:

<http://www.americanscientist.org/IssueTOC/issue/821>

## Laser noise reduction in air

Pierre Béjot

Groupe de Physique Appliquée, Université de Genève, 20 rue de l'École de Médecine, CH 1211 Genève, Switzerland

Jérôme Kasparian,<sup>a)</sup> Estelle Salmon, and Roland Ackermann

Laboratoire de Spectrométrie Ionique et Moléculaire, UMR CNRS 5579, Université Lyon 1, 43 Boulevard du 11 Novembre 1918, F69622 Villeurbanne Cedex, France

Nicolas Gisin and Jean-Pierre Wolf

Groupe de Physique Appliquée, Université de Genève, 20 rue de l'École de Médecine, CH 1211 Genève, Switzerland

(Received 13 February 2006; accepted 11 May 2006; published online 21 June 2006)

Fluctuations of the white-light supercontinuum produced by ultrashort laser pulses in self-guided filaments (spatiotemporal solitons) in air are investigated. We demonstrate that correlations exist within the white-light supercontinuum, and that they can be used to significantly reduce the laser intensity noise by filtering the spectrum. More precisely, the fundamental wavelength is anticorrelated with the wings of the continuum, while conjugated wavelength pairs on both sides of the continuum are strongly correlated. Spectral filtering of the continuum reduces the laser intensity noise by 1.2 dB, showing that fluctuations are rejected to the edges of the spectrum. © 2006 American Institute of Physics. [DOI: 10.1063/1.2216402]

Considerable interest has recently been devoted to quantum optics and nonlinear effects in transparent media. Second order nonlinearity ( $\chi^2$ ) processes in parametric generators have been the model of choice in this respect, where both photon correlation and squeezing were first demonstrated. Recent studies showed that both phenomena also occurred for temporal solitons in optical fibers.<sup>1,2</sup> The origin of the correlations in the generated continuum is intrinsic to the ( $\chi^3$ ) self-phase-modulation process.<sup>3</sup> For sufficient laser intensity, self-organized spatiotemporal solitons form even in the air. These self-generated light filaments propagate over several hundreds of meters and give rise to an exceptionally broad continuum.<sup>4</sup> In this letter, we report the observation of both spectral correlations in the continuum and laser noise reduction for filaments propagating in air. These results, which remain in the classical domain of correlations and noise reduction, open perspectives for high precision remote measurements of atmospheric molecules or for the transmission of encrypted information.<sup>5</sup> For instance, water vapor concentration and atmospheric temperature profile measurements require a precision better than 1% to be useful for global warming models. A significant source of noise in light detection and ranging (LIDAR) measurements, besides atmospheric fluctuations, is laser noise. A low noise broadband laser covering several absorption bands of H<sub>2</sub>O would therefore be an ideal source for such measurements (the carrier wavelength would then be slightly shifted to 830 nm).

Filaments<sup>6</sup> arise in the nonlinear propagation of ultrashort, high-power laser pulses in transparent media. They result from a subtle balance between Kerr-lens focusing and defocusing by self-induced plasma. In the atmosphere, filaments have been observed over several hundreds of meters, up to a few kilometers away from the laser source,<sup>7</sup> even in perturbed conditions such as clouds<sup>8</sup> or turbulence.<sup>9</sup> These properties open the way to atmospheric applications,<sup>4</sup> such as

LIDAR remote sensing, laser-induced breakdown spectroscopy (LIBS), lightning control, or free space communications. Up to now, filamentation has been studied extensively, but only from the classical point of view. Quantum optics of both self-guiding and white-light generation by self-phase modulation (SPM) and the resulting correlations in the spectrum of the white-light continuum have not been described so far. Here, we demonstrate that correlations exist within the white-light supercontinuum, and that they can be used to significantly reduce the laser intensity noise by filtering the spectrum. These results on nonlinear optics in the air show that, even at very high intensities, the broadened spectrum is the result of interactions of the type  $\omega_1 + \omega_2 = \omega_3 + \omega_4$ , which are the origin of the observed correlations. In particular, in the first phase of the spectral broadening process, the most intensity is at  $\omega_0$ , and we expect correlations for  $2\omega_0 = \omega_1 + \omega_2$ .

The experimental setup is depicted in Fig. 1. A chirped pulse amplification (CPA) Ti:sapphire laser system delivered 200 fs pulses of typically 1 mJ, at 22.5 Hz repetition rate. The central wavelength of the laser was set at 805 and 817 nm depending on the alignment, with an initial band-

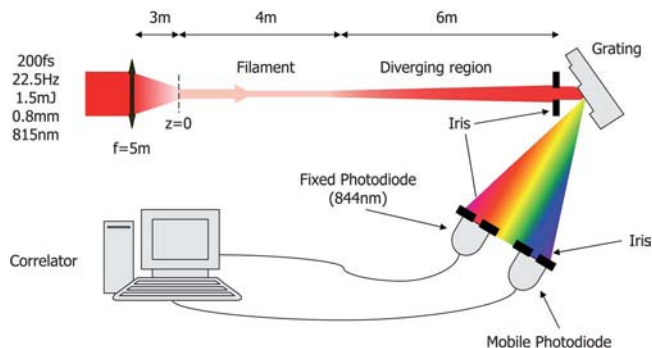


FIG. 1. (Color online) Low loss experimental setup used for the measurement of correlations within the light supercontinuum generated by filaments.

<sup>a)</sup>Electronic mail: jkaspari@lasim.univ-lyon1.fr

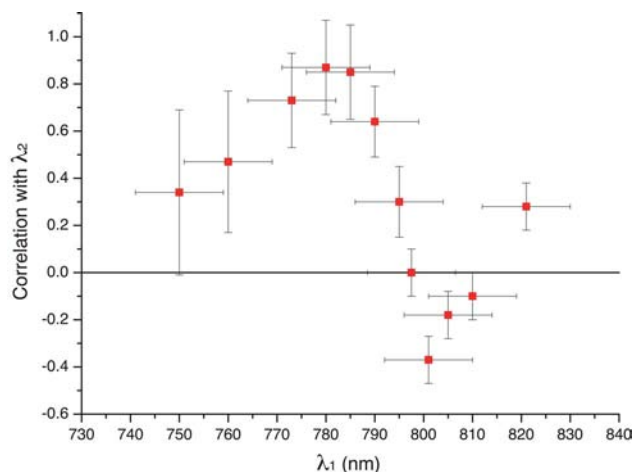


FIG. 2. (Color online) Demonstration of correlations within the continuum spectrum. Strong correlations are observed for the wavelengths  $\lambda_1$  conjugated to the fixed wavelength channel about  $\lambda_2=844$  nm, while anticorrelation is observed with the fundamental spectrum centered on  $\lambda_0=805$  nm.

width of 8 nm. The beam was focused by a spherical mirror of 5 m focal length, yielding a nonlinear focus (filament onset)  $\sim 3$  m downstream of the spherical mirror: This nonlinear focus was defined as origin of the propagation axis ( $z=0$ ). The filament length was  $\sim 4$  m. At  $z=10$  m, the continuum generated by the filament was dispersed by a diffraction grating (order 1 blazed, efficiency of 0.9 at 810 nm), and two photodiodes (quantum efficiency of 0.93 at 810 nm) selected two specific spectral channels (9 nm bandwidth). The correlation coefficient between these two wavelength channels was numerically evaluated for each time series (5000 shots). Reference conditions without nonlinear propagation were obtained by using a plane mirror instead of the spherical one in order to avoid filamentation.

In a second experiment, the filament was scattered on an achromatic target and analyzed by a spectrometer (1 nm resolution) between 785 and 845 nm. We recorded 5000 spectra, normalized them to unity and used them to compute the cross-correlation map across the spectrum. In a third experiment, we directly measured the laser intensity noise reduction factor. For this, we used the “low loss” grating setup and a single photodiode recorded a 20 000-shot time series of the integrated spectrum over different spectral intervals. The standard deviation, for both focused (filamenting) and unfocused (reference) conditions, was computed to quantify the noise reduction due to the SPM correlations within the filament.

Figure 2 displays the cross correlation of the white-light continuum with one fixed wavelength at  $\lambda_2=844$  nm as measured with the setup of Fig. 1. The central wavelength of the fundamental spectrum was  $\lambda_0=805$  nm in this experiment. As expected from the quantum point of view, where two photons at the fundamental wavelength  $\lambda_0$  are converted into a pair of photons at wavelengths  $\lambda_1$  and  $\lambda_2$ , with  $2/\lambda_0 = 1/\lambda_1 + 1/\lambda_2$ , a strong correlation ( $C_{\lambda_1\lambda_2}=0.85$ ) is observed at the conjugate wavelength of the fixed wavelength. In contrast, the fundamental, which is depleted when the white light is generated, is anticorrelated ( $C_{\lambda_0\lambda_1}=-0.4$ ). The typical number of photons measured in the experiment is  $10^8$  per shot. In order to determine whether the correlations are classical or quantum, we evaluated the “Gemellity Factor”.<sup>10</sup>  $G = (F_1 + F_2)/2 - \sqrt{C_{12}^2 F_1 F_2 + (F_1 - F_2)^2/4}$ , where  $F_1$  and  $F_2$  are

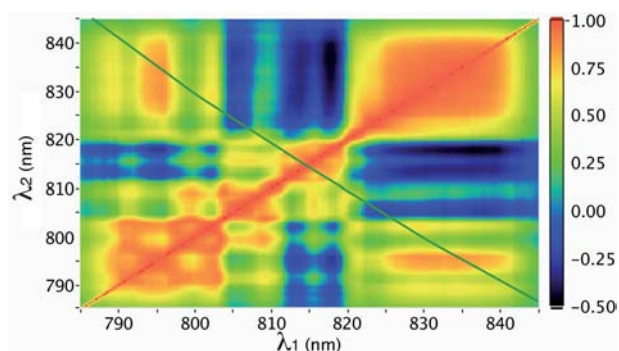


FIG. 3. (Color online) 2D Map of spectral correlations within the filament continuum. The green line corresponds to the wavelength pairs that satisfy the relation  $2/\lambda_0=1/\lambda_1+1/\lambda_2$  with  $\lambda_0=815$  nm.

the Fano factors of the two wavelengths, i.e., the ratio of the signal noise at the considered wavelength over the shot noise.<sup>11</sup>  $G$  amounts to  $10^7$ , i.e., much greater than unity, for any wavelength pair within the 760–844 nm range. Hence, although the number of detected photons is moderate and the losses in this first experiment are limited, the observed correlations are classical and represent the correlation between the instantaneous fluctuations of the different photon fluxes.

The occurrence of correlations within the spectrum was further confirmed by considering the whole map of cross correlations (Fig. 3), as obtained from the second setup, which involves high losses. In this experiment,  $\lambda_0=815$  nm. Positive correlations are observed in regions corresponding to nearly conjugated wavelengths, as well as in the trivial case of  $\lambda_1=\lambda_2$  axis. In contrast, negative correlations form a dark cross centered on the fundamental wavelength. In other words, the generation of the white-light photons requires a depletion of the fundamental photon number. It is interesting to notice that structures (lines) appear in the map, in both the positive and the negative correlation regions. This behavior can be interpreted as cascades of four-photon mixing processes, where one (or both) of the conjugated wavelengths is (are) involved in a consecutive process, destroying the initial correlations. Moreover, the probability of cascading depends on the spectral intensity, which is related to the broadening itself.

Spectrally filtering the supercontinuum around  $\lambda_0=805$  nm (785–820 nm) and comparing the intensity fluctuations between the filamenting and the reference (linearly propagating) beams (setup 3) demonstrated a reduction of the intensity noise power (i.e., the variance of the recorded photocurrent) by 1.2 dB. In contrast, a spectral range restricted to one side of the fundamental wavelength  $\lambda_0$  (814–849 nm) yielded no noise reduction. As observed in the case of fibers, SPM rejects the fluctuations to the edges of the spectrum.

Considering the very high intensity involved to generate filaments in air, these results are particularly unexpected. In particular, it is remarkable that the presence of the self-induced plasma, which stabilizes the filamentation process, has no significant effect on the correlations in the spectrum.

As a conclusion, we have demonstrated that the broadband continuum generated by spatiotemporal solitons propagating in air (filaments) exhibits strong correlations. Although obtained at very high intensities, these correlations are the scars of quantum four-photon interactions. As fluctuations are rejected to the edges of the spectrum, spectral

filtering of the continuum allowed a reduction of the laser intensity noise by 1.2 dB, still well above the shot noise. Moreover, the characteristics of the spectral filter were not optimized in this demonstration experiment, and higher compression ratios can be expected. These results might open a new range of applications, such as high precision LIDAR measurements of atmospheric pollutants or transmission schemes in optical communications.

The authors gratefully acknowledge H. Zbinden (Université de Genève), C. Fabre (ENS, Paris), and G. Leuchs (Universität Erlangen) for very fruitful discussions.

<sup>1</sup>S. Spälter, N. Korolkova, F. König, A. Sizmann, and G. Leuchs, *Phys. Rev. Lett.* **81**, 786 (1998).

<sup>2</sup>T. Opatny, N. Korolkova, and G. Leuchs, *Phys. Rev. A* **66**, 053813 (2002).

<sup>3</sup>L. Boivin, F. X. Kärtner, and H. A. Haus, *Phys. Rev. Lett.* **73**, 240 (1994).

<sup>4</sup>J. Kasparian, M. Rodriguez, G. Méjean, J. Yu, E. Salmon, H. Wille, R. Bourayou, S. Frey, Y.-B. André, A. Mysyrowicz, R. Sauerbrey, J.-P. Wolf, and L. Wöste, *Science* **301**, 61 (2003).

<sup>5</sup>T. C. Ralph, *Phys. Rev. A* **61**, 010303 (1999).

<sup>6</sup>A. Braun, G. Korn, X. Liu, D. Du, J. Squier, and G. Mourou, *Opt. Lett.* **20**, 73 (1995).

<sup>7</sup>M. Rodriguez, R. Bourayou, G. Méjean, J. Kasparian, J. Yu, E. Salmon, A. Scholz, B. Stecklum, J. Eislöffel, U. Laux, A. P. Hatzes, R. Sauerbrey, L. Wöste, and J.-P. Wolf, *Phys. Rev. E* **69**, 036607 (2004).

<sup>8</sup>G. Méjean, J. Kasparian, J. Yu, E. Salmon, S. Frey, J.-P. Wolf, S. Skupin, A. Vinçotte, R. Nuter, S. Champeaux, and L. Bergé, *Phys. Rev. E* **72**, 026611 (2005).

<sup>9</sup>R. Ackermann, G. Méjean, J. Kasparian, J. Yu, E. Salmon, and J.-P. Wolf, *Opt. Lett.* **31**, 86 (2006).

<sup>10</sup>N. Treps and C. Fabre, *Laser Phys.* **15**, 187 (2005), e-print quant-ph/0407214.

<sup>11</sup>U. Fano, *Phys. Rev.* **72**, 26 (1947).

## Optimal control of filamentation in air

Roland Ackermann, Estelle Salmon, Noëlle Lascoux, and Jérôme Kasparian<sup>a)</sup>  
*Téramobile, LASIM UMR CNRS 5579, Université Lyon 1, 43 Bd du 11 Novembre 1918,  
 F-69622 Villeurbanne Cedex, France*

Philipp Rohwetter, Kamil Stelmaszczyk, Shaohui Li, Albrecht Lindinger, and Ludger Wöste  
*Téramobile, Institut für Experimentalphysik, FU Berlin, Arnimalle 14, D-14195 Berlin, Germany*

Pierre Béjot, Luigi Bonacina, and Jean-Pierre Wolf  
*GAP, Université de Genève, 20 Rue de l'École de Médecine, CH 1211 Genève, Switzerland*

(Received 4 July 2006; accepted 5 September 2006; published online 27 October 2006)

The authors demonstrate optimal control of the propagation of ultrashort, ultraintense (multiterawatt) laser pulses in air over distances up to 36 m in a closed-loop scheme. They optimized three spectral ranges within the white-light continuum as well as the ionization efficiency. Optimization results in signal enhancements by typical factors of 2 and 1.4 for the target parameters. The optimization results in shorter pulses by reducing their chirp in the case of white-light continuum generation, while they correct the pulse from its defects and set the filamentation onset near the detector as far as air ionization is concerned. © 2006 American Institute of Physics. [DOI: 10.1063/1.2363941]

When propagating in air, high-power ultrashort laser pulses undergo filamentation.<sup>1</sup> Filaments result from a dynamic balance between Kerr-lens focusing and defocusing by self-induced plasma generation. In the atmosphere, filaments have been observed up to a few kilometers away from the laser source.<sup>2</sup> They can be generated and propagated even in perturbed conditions such as clouds<sup>3</sup> or turbulence.<sup>4</sup> Their ability to generate a “white-light laser”<sup>5</sup> by self-phase modulation (SPM) as well as long conducting plasma channels opens the way to atmospheric applications.<sup>6</sup>

The possibility of controlling to a certain extent the basic features of the propagation of ultrashort laser pulses has been demonstrated recently. Besides the long-known effect of an initial focusing of the beam,<sup>7</sup> the effects of the initial pulse chirp,<sup>2,8–11</sup> spatial filtering,<sup>12</sup> beam profile,<sup>13</sup> pulse energy,<sup>14</sup> initial focus,<sup>15</sup> and polarization<sup>16</sup> have been investigated. However, since numerical simulation of the propagation of high-power, large-diameter laser pulses is time consuming, it is generally not possible to define the best laser conditions to optimize a specific property of the filaments. The advent of spatial light modulators (SLMs) and acousto-optical modulators made a target optimization of ultrashort laser pulses possible by addressing their spectral components independently, applying specific phase shifts or modulating their intensities. This ability was applied for coherent control of atomic and molecular interactions.<sup>17,18</sup> Since the large number of parameters at play in such optimization prevents in most cases any explicit calculation of the optimal pulse shape, nondeterministic algorithms such as genetic algorithms are widely used to maximize or minimize a predefined experimental parameter.<sup>19</sup> In return, the optimal shape found by the algorithm is often considered to bear information about the physical process at play.<sup>20</sup>

The spectral amplitude and phase dependence of the pulse is expected to affect the filamentation process via different mechanisms.

- (1) The envelope intensity profile determines the nonlinear focusing process of the beam.
- (2) Propagation in air induces group velocity dispersion, which can be precompensated by spectral phase control.
- (3) SPM originates from the intensity variations within the laser pulse envelope. A shaped pulse with steeper intensity fronts will therefore experience a more efficient energy conversion into the white-light continuum.
- (4) Multiphoton ionization of air molecules is sensitive to the spectral and temporal pulse characteristics; hence the control of these parameters may result in a change in the dynamic balance between Kerr effect and plasma defocusing, affecting the filamentation process itself.
- (5) Retarded Kerr effect might also play a role in the optimal pulse shape.

Notice, moreover, that pulse shaping and closed-loop optimization could also be used to improve the selectivity of multiphoton-excited fluorescence lidar for bioaerosol detection<sup>21</sup> or remote laser induced breakdown spectroscopy<sup>22,23</sup> in the future.

Recently, the use of closed-loop optimization to set the position of filaments in dye-doped water<sup>24</sup> or the yield of second-harmonic generation<sup>25</sup> was reported. In this letter, we demonstrate the optimal control of the propagation of ultrashort, ultraintense (multiterawatt) laser pulses in air over distances up to 36 m. We independently optimized three spectral regions within the white-light continuum as well as the ionization efficiency. We show that the optimized pulse shapes retrieved after the optical and the air-ionization measurements bear the signatures of the different physical mechanisms at the basis of the two processes.

The experiments were performed using the *Téramobile* laser,<sup>8</sup> which delivered 150 fs pulses of 210 mJ centered around 785 nm at a repetition rate of 10 Hz. Light from the supercontinuum was scattered on a neutral diffusive screen located 36 m away from the laser and focused onto a photomultiplier by a 20 cm telescope installed close to the laser in a lidar configuration. The signal in three different spectral bands (360±5, 400±5, and 500±5 nm) was the optimizing

<sup>a)</sup>Electronic mail: jkaspari@lasim.univ-lyon1.fr

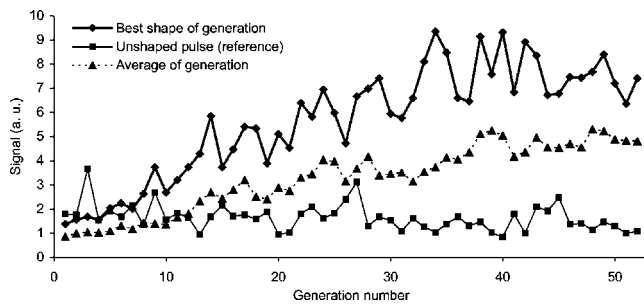


FIG. 1. Typical optimization of the white-light continuum, in the 355–365 nm spectral region.

variable in the optical experiments. Alternatively, optimizations were performed on the electron density, recorded by sonometric measurements<sup>26,27</sup> after 28 m propagation of the laser beam. In both experiments, the signal was averaged over 50 shots.

Closed-loop optimizations<sup>19</sup> were performed using a genetic algorithm<sup>28</sup> and a liquid crystal SLM ( $2 \times 128$  pixels, CRI) placed in the Fourier plane of an afocal 4- $f$  setup.<sup>29,30</sup> The SLM provides a high-resolution spectral shaping of the pulse, but its intrinsic low damage threshold imposed to set it between the stretcher and the regenerative amplifier of the chirped pulse amplification (CPA) laser chain. In this configuration, the amplification distorts the pulse shape applied to the SLM. However, this does not prevent the optimization, since the closed-loop algorithm suppresses the need for an explicit knowledge of the pulse behavior after it leaves the pulse shaper. Instead, the pulse distortions imposed by the amplification are part of the system to optimize. The pulse shaper was used exclusively to control the spectral phase, allowing maximal transmission of the light on each pixel. To reduce the search space, neighboring pixels were binned in sets of 4, resulting in 32 effective pixels. At each generation, 30 individuals were investigated. To correct for possible drifts of the laser or the atmosphere along the optimization process, a reference signal (unshaped pulse) was recorded at the end of each generation.

Convergence to an optimum pulse shape was achieved after typically 40–60 generations and resulted in an increase in the signal compared to that generated by the reference pulse, for all optimizations performed. The enhancement factor was typically 2 (with a single event yielding a factor of 5) for white light and 1.4 for ionization. As shown in Fig. 1, in the case of the white-light continuum, convergence is achieved in spite of very significant variations of the reference signal over time, showing that the genetic algorithm is able to learn even in a noisy environment. Here, the noise is

mainly due to the fluctuations of the 10 Hz laser system, although drifts in the atmosphere also play a role. We checked that repeated optimizations of the same parameter yield comparable results.

Optimizing the white-light continuum (e.g., at 360 nm) from a slightly chirped pulse mainly results in a quadratic phase partly correcting this chirp [see dotted lines in Figs. 2(a) and 2(b)] at the output port of the laser. The chirp is characterized by the slope of the pulse ridge in the time-frequency plane of the Wigner plot. The larger slope of this ridge in the optimized pulse, corresponding to a faster sweep of the wavelengths within the pulse, is the signature for a shorter, less chirped pulse. However, the optimization does not only correct a chirp but instead yields a rich pulse shape [Fig. 2(b)], which was observed to yield up to 20% more signal than could be obtained by tuning the grating compressor to optimize the chirp correction.<sup>8</sup> Maximizations of the white light at all wavelengths considered yield similar phase masks (i.e., the same optimal pulses), resulting in comparable relative signals at different wavelengths and similar spectra of the continuum around the fundamental (between 600 and 900 nm). This latter observation is unexpected, since different pulse shapes would result in different intensity gradient within the pulse envelope and hence in different broadening by SPM. The fact that similar pulse shapes maximize both the generation of the 400 nm and other wavelengths within the continuum indicates that all wavelengths are generated by SPM, while any possible contribution from second-harmonic generation (SHG) to the signal at 400 nm is negligible, even on the surface of the screen, where inversion symmetry is broken so that SHG is not forbidden. Note that our result contrasts with that obtained in the bulk, where, e.g., Schumacher<sup>31</sup> demonstrated the independent optimization of different wavelengths within the supercontinuum. The difference stems from the fact that filamentation is a much more complex process than only SPM in bulk media, as it invokes stabilization of different nonlinear effects such as plasma generation.

In contrast to the optimization of the white-light generation, the optimized pulse for ionization is stretched compared to the initial pulse [Figs. 2(c) and 2(d)], resulting in a longer pulse (800 fs instead of 150 fs typically), as can be seen from the broader extent of the pulse along the temporal axis in the optimized pulse [Fig. 2(d)]. The resulting lower peak power pushes the filament onset away from the laser output. As shown in Fig. 3, the number of filaments increases steeply at the location of the microphone, which is consistent with our previous observation that the sound is maximal at the beginning of the filaments.<sup>26</sup> In other words, the genetic

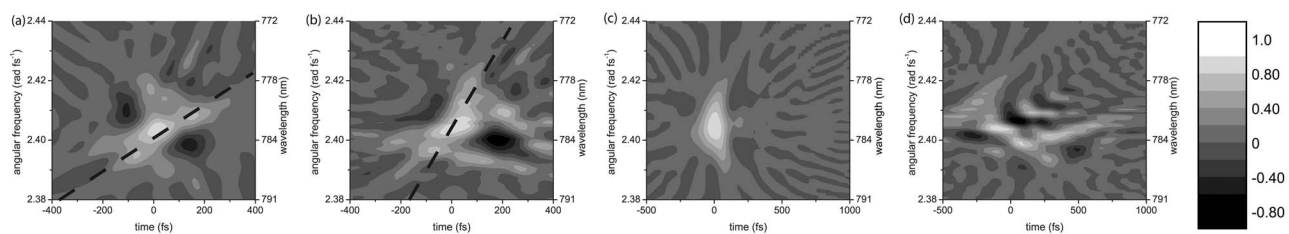


FIG. 2. Normalized Wigner plot of the pulse before (a) and after (b) maximization of the white light at 360 nm, and before (c) and after (d) maximization of the electron density in the filaments. Initial pulses are retrieved from SHG-FROG measurements, while optimized pulses are retrieved from the initial pulses by simulating the geometry of the pulse shaper. Panels (a) and (c) differ because of day-to-day laser fluctuations. The gray scale given on the left is common to all plots.

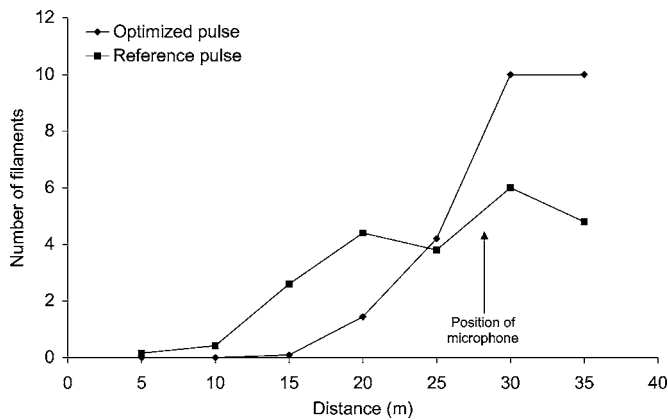


FIG. 3. Filament number as a function of the propagation distance, after optimization for the plasma density and for an unshaped pulse.

algorithm maximizes the plasma generation by maximizing the number of filaments at the location of the detector and setting their onset in this region. Indeed, the filament number increases by a factor of 1.7, close to the factor of 1.4 observed for the ionization signal. This is accomplished essentially by adjusting the chirp and correcting for the discrepancies from a Fourier-transform limited pulse. Moreover, further coherent control enhancing the multiphoton ionization of the air at the onset of the filaments may stem from the complex structure of the Wigner plot of the optimized pulse [Fig. 2(d)]. The change in the filament onset is consistent with the positions observed for chirped pulse of similar duration.<sup>8</sup>

In conclusion, we have demonstrated the optimization of nonlinear processes occurring over long distances in the propagation of multiterawatt laser pulses. Both the generation of visible wavelengths within the white-light continuum and the ionization efficiency at a fixed distance were increased by a factor of 2 and 1.4, respectively, by using optimal control procedures. Although the observed enhancement factor is modest compared to both other results in laboratory conditions and the needs for practical applications, our results demonstrate that pulse shaping can still be performed with high-energy laser pulses, even in relatively unfavorable conditions, including a noisy system and low repetition rate limiting the number of available laser shots per acquisition and hence the number of free parameters.

Nevertheless, the analysis of the optimized shapes shows that optimization of the white-light continuum is achieved by cleaning the pulse shape. Optimizing specific wavelengths within the white-light continuum results in optimizing the whole continuum. On the other hand, optimizing the ionization level at a specific distance mainly results in moving the filamentation onset close to the target location. This finding agrees with the previous observation that electron density decreases along the filament length.<sup>26</sup> Optimizing white-light continuum generation or air ionization within the filaments can be very advantageous for a wide range of applications, including lidar remote sensing, remote light induced breakdown spectroscopy, or the control of high-voltage discharges or lightning.

This work has been performed within the *Teramobile* project, funded jointly by the CNRS, DFG, as well as the

French Agence Nationale pour la Recherche under the Grant No. NT05-1\_43175. The Teramobile web site is [www.teramobile.org](http://www.teramobile.org).

- <sup>1</sup>A. Braun, G. Korn, X. Liu, D. Du, J. Squier, and G. Mourou, *Opt. Lett.* **20**, 73 (1995).
- <sup>2</sup>M. Rodriguez, R. Bourayou, G. Méjean, J. Kasparian, J. Yu, E. Salmon, A. Scholz, B. Stecklum, J. Eislöffel, U. Laux, A. P. Hatzes, R. Sauerbrey, L. Wöste, and J.-P. Wolf, *Phys. Rev. E* **69**, 036607 (2004).
- <sup>3</sup>G. Méjean, J. Kasparian, J. Yu, E. Salmon, S. Frey, J.-P. Wolf, S. Skupin, A. Vinçotte, R. Nuter, S. Champeaux, and L. Bergé, *Phys. Rev. E* **72**, 026611 (2005).
- <sup>4</sup>R. Ackermann, G. Méjean, J. Kasparian, J. Yu, E. Salmon, and J.-P. Wolf, *Opt. Lett.* **31**, 86 (2006).
- <sup>5</sup>S. L. Chin, S. Petit, F. Borne, and K. Miyazaki, *Jpn. J. Appl. Phys., Part 2* **38**, L126 (1999).
- <sup>6</sup>J. Kasparian, M. Rodriguez, G. Méjean, J. Yu, E. Salmon, H. Wille, R. Bourayou, S. Frey, Y.-B. André, A. Mysyrowicz, R. Sauerbrey, J.-P. Wolf, and L. Wöste, *Science* **301**, 61 (2003).
- <sup>7</sup>E. L. Dawes and J. H. Marburger, *Phys. Rev.* **179**, 862 (1969).
- <sup>8</sup>H. Wille, M. Rodriguez, J. Kasparian, D. Mondelain, J. Yu, A. Mysyrowicz, R. Sauerbrey, J.-P. Wolf, and L. Wöste, *Eur. Phys. J.: Appl. Phys.* **20**, 183 (2002).
- <sup>9</sup>G. Méchain, A. Couairon, Y.-B. André, C. D'Amico, M. Franco, B. Prade, S. Tzortzakos, A. Mysyrowicz, and R. Sauerbrey, *Appl. Phys. B: Lasers Opt.* **79**, 379 (2004).
- <sup>10</sup>G. Méchain, C. D'Amico, Y.-B. André, S. Tzortzakos, M. Franco, B. Prade, A. Mysyrowicz, A. Couairon, E. Salmon, and R. Sauerbrey, *Opt. Commun.* **247**, 171 (2005).
- <sup>11</sup>I. S. Golubtsov, V. P. Kandidov, and O. G. Kosareva, *Quantum Electron.* **33**, 525 (2003).
- <sup>12</sup>V. P. Kandidov, N. Akosbek, M. Scarola, O. G. Kosareva, A. V. Nyakk, Q. Luo, S. A. Hosseini, and S. L. Chin, *Appl. Phys. B: Lasers Opt.* **80**, 267 (2005).
- <sup>13</sup>G. Fibich and B. Ilan, *J. Opt. Soc. Am. B* **17**, 1749 (2000).
- <sup>14</sup>G. Méjean, J. Kasparian, J. Yu, E. Salmon, S. Frey, J.-P. Wolf, S. Skupin, A. Vinçotte, R. Nuter, S. Champeaux, and L. Bergé, *Phys. Rev. E* **72**, 026611 (2005).
- <sup>15</sup>S. Skupin, L. Bergé, U. Peschel, F. Lederer, G. Méjean, J. Yu, J. Kasparian, E. Salmon, J. P. Wolf, M. Rodriguez, L. Wöste, R. Bourayou, and R. Sauerbrey, *Phys. Rev. E* **70**, 046602 (2004).
- <sup>16</sup>H. Yang, J. Zhang, Q. Zhang, Z. Hao, Y. Li, Z. Zheng, Z. Wang, Q.-L. Dong, X. Lu, Z. Wei, Z.-M. Sheng, J. Yu, and W. Yu, *Opt. Lett.* **30**, 534 (2005).
- <sup>17</sup>D. Goswami, *Phys. Rep.* **374**, 385 (2002), and references therein.
- <sup>18</sup>M. Dantus and V. V. Lozovoy, *Chem. Rev. (Washington, D.C.)* **104**, 1813 (2004), and references therein.
- <sup>19</sup>R. S. Judson and H. Rabitz, *Phys. Rev. Lett.* **68**, 1500 (1992).
- <sup>20</sup>A. Bartelt, S. Minemoto, C. Lupulescu, S. Vaida, and L. Wöste, *Eur. Phys. J. D* **16**, 127 (2001).
- <sup>21</sup>G. Méjean, J. Kasparian, J. Yu, S. Frey, E. Salmon, and J.-P. Wolf, *Appl. Phys. B: Lasers Opt.* **78**, 535 (2004).
- <sup>22</sup>K. Stelmasczyk, P. Rohwetter, G. Méjean, J. Yu, E. Salmon, J. Kasparian, R. Ackermann, J.-P. Wolf, and L. Wöste, *Appl. Phys. Lett.* **85**, 3977 (2004).
- <sup>23</sup>M. Y. Shverdin, S. N. Goda, G. Y. Yin, and S. E. Harris, *Opt. Lett.* **31**, 1331 (2006).
- <sup>24</sup>G. Heck, J. Sloss, and R. J. Levis, *Opt. Commun.* **259**, 216 (2006).
- <sup>25</sup>T. Baumert, T. Brixner, V. Seyfried, M. Strehle, and G. Gerber, *Appl. Phys. B: Lasers Opt.* **65**, 779 (1997).
- <sup>26</sup>J. Yu, D. Mondelain, J. Kasparian, E. Salmon, S. Geffroy, C. Favre, V. Boutou, and J. P. Wolf, *Appl. Opt.* **42**, 7117 (2003).
- <sup>27</sup>S. A. Hosseini, J. Yu, Q. Luo, and S. L. Chin, *Appl. Phys. B: Lasers Opt.* **79**, 519 (2004).
- <sup>28</sup>T. Back and H. Schwefel, *Evol. Comput.* **1**, 1 (1993).
- <sup>29</sup>A. M. Weiner, D. E. Leaird, J. S. Patel, and J. R. Wullert, *IEEE J. Quantum Electron.* **28**, 908 (1992).
- <sup>30</sup>S. Vajda, A. Bartelt, C. Kaposta, T. Leisner, C. Lupulescu, S. Minemoto, P. Rosendo-Francisco, and L. Wöste, *Chem. Phys.* **267**, 231 (2001).
- <sup>31</sup>D. Schumacher, *Opt. Lett.* **27**, 451 (2002).

## Optimal control of filamentation in air

Roland Ackermann, Estelle Salmon, Noëlle Lascoux, and Jérôme Kasparian<sup>a)</sup>  
*Téramobile, LASIM UMR CNRS 5579, Université Lyon 1, 43 Bd du 11 Novembre 1918,  
 F-69622 Villeurbanne Cedex, France*

Philipp Rohwetter, Kamil Stelmazczyk, Shaohui Li, Albrecht Lindinger, and Ludger Wöste  
*Téramobile, Institut für Experimentalphysik, FU Berlin, Arnimalle 14, D-14195 Berlin, Germany*

Pierre Béjot, Luigi Bonacina, and Jean-Pierre Wolf  
*GAP, Université de Genève, 20 Rue de l'École de Médecine, CH 1211 Genève, Switzerland*

(Received 4 July 2006; accepted 5 September 2006; published online 27 October 2006)

The authors demonstrate optimal control of the propagation of ultrashort, ultraintense (multiterawatt) laser pulses in air over distances up to 36 m in a closed-loop scheme. They optimized three spectral ranges within the white-light continuum as well as the ionization efficiency. Optimization results in signal enhancements by typical factors of 2 and 1.4 for the target parameters. The optimization results in shorter pulses by reducing their chirp in the case of white-light continuum generation, while they correct the pulse from its defects and set the filamentation onset near the detector as far as air ionization is concerned. © 2006 American Institute of Physics. [DOI: 10.1063/1.2363941]

When propagating in air, high-power ultrashort laser pulses undergo filamentation.<sup>1</sup> Filaments result from a dynamic balance between Kerr-lens focusing and defocusing by self-induced plasma generation. In the atmosphere, filaments have been observed up to a few kilometers away from the laser source.<sup>2</sup> They can be generated and propagated even in perturbed conditions such as clouds<sup>3</sup> or turbulence.<sup>4</sup> Their ability to generate a “white-light laser”<sup>5</sup> by self-phase modulation (SPM) as well as long conducting plasma channels opens the way to atmospheric applications.<sup>6</sup>

The possibility of controlling to a certain extent the basic features of the propagation of ultrashort laser pulses has been demonstrated recently. Besides the long-known effect of an initial focusing of the beam,<sup>7</sup> the effects of the initial pulse chirp,<sup>2,8–11</sup> spatial filtering,<sup>12</sup> beam profile,<sup>13</sup> pulse energy,<sup>14</sup> initial focus,<sup>15</sup> and polarization<sup>16</sup> have been investigated. However, since numerical simulation of the propagation of high-power, large-diameter laser pulses is time consuming, it is generally not possible to define the best laser conditions to optimize a specific property of the filaments. The advent of spatial light modulators (SLMs) and acousto-optical modulators made a target optimization of ultrashort laser pulses possible by addressing their spectral components independently, applying specific phase shifts or modulating their intensities. This ability was applied for coherent control of atomic and molecular interactions.<sup>17,18</sup> Since the large number of parameters at play in such optimization prevents in most cases any explicit calculation of the optimal pulse shape, nondeterministic algorithms such as genetic algorithms are widely used to maximize or minimize a predefined experimental parameter.<sup>19</sup> In return, the optimal shape found by the algorithm is often considered to bear information about the physical process at play.<sup>20</sup>

The spectral amplitude and phase dependence of the pulse is expected to affect the filamentation process via different mechanisms.

- (1) The envelope intensity profile determines the nonlinear focusing process of the beam.
- (2) Propagation in air induces group velocity dispersion, which can be precompensated by spectral phase control.
- (3) SPM originates from the intensity variations within the laser pulse envelope. A shaped pulse with steeper intensity fronts will therefore experience a more efficient energy conversion into the white-light continuum.
- (4) Multiphoton ionization of air molecules is sensitive to the spectral and temporal pulse characteristics; hence the control of these parameters may result in a change in the dynamic balance between Kerr effect and plasma defocusing, affecting the filamentation process itself.
- (5) Retarded Kerr effect might also play a role in the optimal pulse shape.

Notice, moreover, that pulse shaping and closed-loop optimization could also be used to improve the selectivity of multiphoton-excited fluorescence lidar for bioaerosol detection<sup>21</sup> or remote laser induced breakdown spectroscopy<sup>22,23</sup> in the future.

Recently, the use of closed-loop optimization to set the position of filaments in dye-doped water<sup>24</sup> or the yield of second-harmonic generation<sup>25</sup> was reported. In this letter, we demonstrate the optimal control of the propagation of ultrashort, ultraintense (multiterawatt) laser pulses in air over distances up to 36 m. We independently optimized three spectral regions within the white-light continuum as well as the ionization efficiency. We show that the optimized pulse shapes retrieved after the optical and the air-ionization measurements bear the signatures of the different physical mechanisms at the basis of the two processes.

The experiments were performed using the *Téramobile* laser,<sup>8</sup> which delivered 150 fs pulses of 210 mJ centered around 785 nm at a repetition rate of 10 Hz. Light from the supercontinuum was scattered on a neutral diffusive screen located 36 m away from the laser and focused onto a photomultiplier by a 20 cm telescope installed close to the laser in a lidar configuration. The signal in three different spectral bands (360±5, 400±5, and 500±5 nm) was the optimizing

<sup>a)</sup>Electronic mail: jkaspari@lasim.univ-lyon1.fr

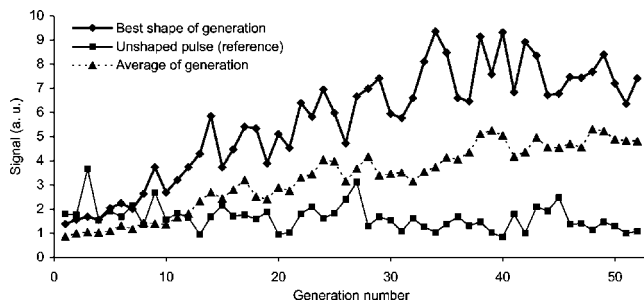


FIG. 1. Typical optimization of the white-light continuum, in the 355–365 nm spectral region.

variable in the optical experiments. Alternatively, optimizations were performed on the electron density, recorded by sonometric measurements<sup>26,27</sup> after 28 m propagation of the laser beam. In both experiments, the signal was averaged over 50 shots.

Closed-loop optimizations<sup>19</sup> were performed using a genetic algorithm<sup>28</sup> and a liquid crystal SLM ( $2 \times 128$  pixels, CRI) placed in the Fourier plane of an afocal 4- $f$  setup.<sup>29,30</sup> The SLM provides a high-resolution spectral shaping of the pulse, but its intrinsic low damage threshold imposed to set it between the stretcher and the regenerative amplifier of the chirped pulse amplification (CPA) laser chain. In this configuration, the amplification distorts the pulse shape applied to the SLM. However, this does not prevent the optimization, since the closed-loop algorithm suppresses the need for an explicit knowledge of the pulse behavior after it leaves the pulse shaper. Instead, the pulse distortions imposed by the amplification are part of the system to optimize. The pulse shaper was used exclusively to control the spectral phase, allowing maximal transmission of the light on each pixel. To reduce the search space, neighboring pixels were binned in sets of 4, resulting in 32 effective pixels. At each generation, 30 individuals were investigated. To correct for possible drifts of the laser or the atmosphere along the optimization process, a reference signal (unshaped pulse) was recorded at the end of each generation.

Convergence to an optimum pulse shape was achieved after typically 40–60 generations and resulted in an increase in the signal compared to that generated by the reference pulse, for all optimizations performed. The enhancement factor was typically 2 (with a single event yielding a factor of 5) for white light and 1.4 for ionization. As shown in Fig. 1, in the case of the white-light continuum, convergence is achieved in spite of very significant variations of the reference signal over time, showing that the genetic algorithm is able to learn even in a noisy environment. Here, the noise is

mainly due to the fluctuations of the 10 Hz laser system, although drifts in the atmosphere also play a role. We checked that repeated optimizations of the same parameter yield comparable results.

Optimizing the white-light continuum (e.g., at 360 nm) from a slightly chirped pulse mainly results in a quadratic phase partly correcting this chirp [see dotted lines in Figs. 2(a) and 2(b)] at the output port of the laser. The chirp is characterized by the slope of the pulse ridge in the time-frequency plane of the Wigner plot. The larger slope of this ridge in the optimized pulse, corresponding to a faster sweep of the wavelengths within the pulse, is the signature for a shorter, less chirped pulse. However, the optimization does not only correct a chirp but instead yields a rich pulse shape [Fig. 2(b)], which was observed to yield up to 20% more signal than could be obtained by tuning the grating compressor to optimize the chirp correction.<sup>8</sup> Maximizations of the white light at all wavelengths considered yield similar phase masks (i.e., the same optimal pulses), resulting in comparable relative signals at different wavelengths and similar spectra of the continuum around the fundamental (between 600 and 900 nm). This latter observation is unexpected, since different pulse shapes would result in different intensity gradient within the pulse envelope and hence in different broadening by SPM. The fact that similar pulse shapes maximize both the generation of the 400 nm and other wavelengths within the continuum indicates that all wavelengths are generated by SPM, while any possible contribution from second-harmonic generation (SHG) to the signal at 400 nm is negligible, even on the surface of the screen, where inversion symmetry is broken so that SHG is not forbidden. Note that our result contrasts with that obtained in the bulk, where, e.g., Schumacher<sup>31</sup> demonstrated the independent optimization of different wavelengths within the supercontinuum. The difference stems from the fact that filamentation is a much more complex process than only SPM in bulk media, as it invokes stabilization of different nonlinear effects such as plasma generation.

In contrast to the optimization of the white-light generation, the optimized pulse for ionization is stretched compared to the initial pulse [Figs. 2(c) and 2(d)], resulting in a longer pulse (800 fs instead of 150 fs typically), as can be seen from the broader extent of the pulse along the temporal axis in the optimized pulse [Fig. 2(d)]. The resulting lower peak power pushes the filament onset away from the laser output. As shown in Fig. 3, the number of filaments increases steeply at the location of the microphone, which is consistent with our previous observation that the sound is maximal at the beginning of the filaments.<sup>26</sup> In other words, the genetic

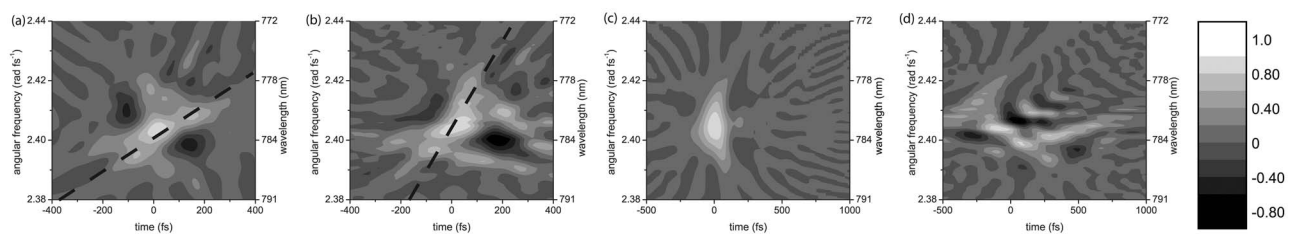


FIG. 2. Normalized Wigner plot of the pulse before (a) and after (b) maximization of the white light at 360 nm, and before (c) and after (d) maximization of the electron density in the filaments. Initial pulses are retrieved from SHG-FROG measurements, while optimized pulses are retrieved from the initial pulses by simulating the geometry of the pulse shaper. Panels (a) and (c) differ because of day-to-day laser fluctuations. The gray scale given on the left is common to all plots.

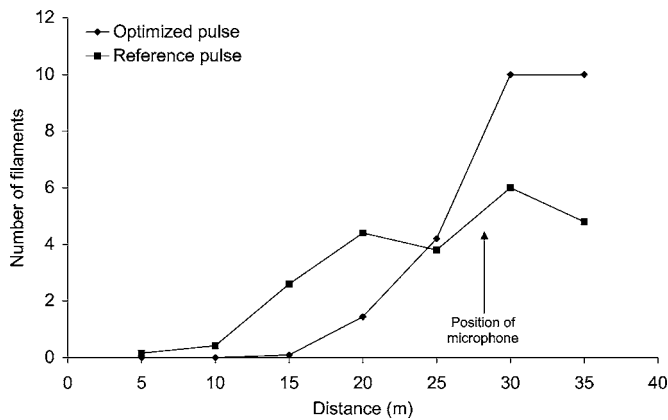


FIG. 3. Filament number as a function of the propagation distance, after optimization for the plasma density and for an unshaped pulse.

algorithm maximizes the plasma generation by maximizing the number of filaments at the location of the detector and setting their onset in this region. Indeed, the filament number increases by a factor of 1.7, close to the factor of 1.4 observed for the ionization signal. This is accomplished essentially by adjusting the chirp and correcting for the discrepancies from a Fourier-transform limited pulse. Moreover, further coherent control enhancing the multiphoton ionization of the air at the onset of the filaments may stem from the complex structure of the Wigner plot of the optimized pulse [Fig. 2(d)]. The change in the filament onset is consistent with the positions observed for chirped pulse of similar duration.<sup>8</sup>

In conclusion, we have demonstrated the optimization of nonlinear processes occurring over long distances in the propagation of multiterawatt laser pulses. Both the generation of visible wavelengths within the white-light continuum and the ionization efficiency at a fixed distance were increased by a factor of 2 and 1.4, respectively, by using optimal control procedures. Although the observed enhancement factor is modest compared to both other results in laboratory conditions and the needs for practical applications, our results demonstrate that pulse shaping can still be performed with high-energy laser pulses, even in relatively unfavorable conditions, including a noisy system and low repetition rate limiting the number of available laser shots per acquisition and hence the number of free parameters.

Nevertheless, the analysis of the optimized shapes shows that optimization of the white-light continuum is achieved by cleaning the pulse shape. Optimizing specific wavelengths within the white-light continuum results in optimizing the whole continuum. On the other hand, optimizing the ionization level at a specific distance mainly results in moving the filamentation onset close to the target location. This finding agrees with the previous observation that electron density decreases along the filament length.<sup>26</sup> Optimizing white-light continuum generation or air ionization within the filaments can be very advantageous for a wide range of applications, including lidar remote sensing, remote light induced breakdown spectroscopy, or the control of high-voltage discharges or lightning.

This work has been performed within the *Teramobile* project, funded jointly by the CNRS, DFG, as well as the

French Agence Nationale pour la Recherche under the Grant No. NT05-1\_43175. The Teramobile web site is [www.teramobile.org](http://www.teramobile.org).

- <sup>1</sup>A. Braun, G. Korn, X. Liu, D. Du, J. Squier, and G. Mourou, *Opt. Lett.* **20**, 73 (1995).
- <sup>2</sup>M. Rodriguez, R. Bourayou, G. Méjean, J. Kasparian, J. Yu, E. Salmon, A. Scholz, B. Stecklum, J. Eislöffel, U. Laux, A. P. Hatzes, R. Sauerbrey, L. Wöste, and J.-P. Wolf, *Phys. Rev. E* **69**, 036607 (2004).
- <sup>3</sup>G. Méjean, J. Kasparian, J. Yu, E. Salmon, S. Frey, J.-P. Wolf, S. Skupin, A. Vinçotte, R. Nuter, S. Champeaux, and L. Bergé, *Phys. Rev. E* **72**, 026611 (2005).
- <sup>4</sup>R. Ackermann, G. Méjean, J. Kasparian, J. Yu, E. Salmon, and J.-P. Wolf, *Opt. Lett.* **31**, 86 (2006).
- <sup>5</sup>S. L. Chin, S. Petit, F. Borne, and K. Miyazaki, *Jpn. J. Appl. Phys., Part 2* **38**, L126 (1999).
- <sup>6</sup>J. Kasparian, M. Rodriguez, G. Méjean, J. Yu, E. Salmon, H. Wille, R. Bourayou, S. Frey, Y.-B. André, A. Mysyrowicz, R. Sauerbrey, J.-P. Wolf, and L. Wöste, *Science* **301**, 61 (2003).
- <sup>7</sup>E. L. Dawes and J. H. Marburger, *Phys. Rev.* **179**, 862 (1969).
- <sup>8</sup>H. Wille, M. Rodriguez, J. Kasparian, D. Mondelain, J. Yu, A. Mysyrowicz, R. Sauerbrey, J.-P. Wolf, and L. Wöste, *Eur. Phys. J.: Appl. Phys.* **20**, 183 (2002).
- <sup>9</sup>G. Méchain, A. Couairon, Y.-B. André, C. D'Amico, M. Franco, B. Prade, S. Tzortzakos, A. Mysyrowicz, and R. Sauerbrey, *Appl. Phys. B: Lasers Opt.* **79**, 379 (2004).
- <sup>10</sup>G. Méchain, C. D'Amico, Y.-B. André, S. Tzortzakos, M. Franco, B. Prade, A. Mysyrowicz, A. Couairon, E. Salmon, and R. Sauerbrey, *Opt. Commun.* **247**, 171 (2005).
- <sup>11</sup>I. S. Golubtsov, V. P. Kandidov, and O. G. Kosareva, *Quantum Electron.* **33**, 525 (2003).
- <sup>12</sup>V. P. Kandidov, N. Akosbek, M. Scarola, O. G. Kosareva, A. V. Nyakk, Q. Luo, S. A. Hosseini, and S. L. Chin, *Appl. Phys. B: Lasers Opt.* **80**, 267 (2005).
- <sup>13</sup>G. Fibich and B. Ilan, *J. Opt. Soc. Am. B* **17**, 1749 (2000).
- <sup>14</sup>G. Méjean, J. Kasparian, J. Yu, E. Salmon, S. Frey, J.-P. Wolf, S. Skupin, A. Vinçotte, R. Nuter, S. Champeaux, and L. Bergé, *Phys. Rev. E* **72**, 026611 (2005).
- <sup>15</sup>S. Skupin, L. Bergé, U. Peschel, F. Lederer, G. Méjean, J. Yu, J. Kasparian, E. Salmon, J. P. Wolf, M. Rodriguez, L. Wöste, R. Bourayou, and R. Sauerbrey, *Phys. Rev. E* **70**, 046602 (2004).
- <sup>16</sup>H. Yang, J. Zhang, Q. Zhang, Z. Hao, Y. Li, Z. Zheng, Z. Wang, Q.-L. Dong, X. Lu, Z. Wei, Z.-M. Sheng, J. Yu, and W. Yu, *Opt. Lett.* **30**, 534 (2005).
- <sup>17</sup>D. Goswami, *Phys. Rep.* **374**, 385 (2002), and references therein.
- <sup>18</sup>M. Dantus and V. V. Lozovoy, *Chem. Rev. (Washington, D.C.)* **104**, 1813 (2004), and references therein.
- <sup>19</sup>R. S. Judson and H. Rabitz, *Phys. Rev. Lett.* **68**, 1500 (1992).
- <sup>20</sup>A. Bartelt, S. Minemoto, C. Lupulescu, S. Vaida, and L. Wöste, *Eur. Phys. J. D* **16**, 127 (2001).
- <sup>21</sup>G. Méjean, J. Kasparian, J. Yu, S. Frey, E. Salmon, and J.-P. Wolf, *Appl. Phys. B: Lasers Opt.* **78**, 535 (2004).
- <sup>22</sup>K. Stelmasczyk, P. Rohwetter, G. Méjean, J. Yu, E. Salmon, J. Kasparian, R. Ackermann, J.-P. Wolf, and L. Wöste, *Appl. Phys. Lett.* **85**, 3977 (2004).
- <sup>23</sup>M. Y. Shverdin, S. N. Goda, G. Y. Yin, and S. E. Harris, *Opt. Lett.* **31**, 1331 (2006).
- <sup>24</sup>G. Heck, J. Sloss, and R. J. Levis, *Opt. Commun.* **259**, 216 (2006).
- <sup>25</sup>T. Baumert, T. Brixner, V. Seyfried, M. Strehle, and G. Gerber, *Appl. Phys. B: Lasers Opt.* **65**, 779 (1997).
- <sup>26</sup>J. Yu, D. Mondelain, J. Kasparian, E. Salmon, S. Geffroy, C. Favre, V. Boutou, and J. P. Wolf, *Appl. Opt.* **42**, 7117 (2003).
- <sup>27</sup>S. A. Hosseini, J. Yu, Q. Luo, and S. L. Chin, *Appl. Phys. B: Lasers Opt.* **79**, 519 (2004).
- <sup>28</sup>T. Back and H. Schwefel, *Evol. Comput.* **1**, 1 (1993).
- <sup>29</sup>A. M. Weiner, D. E. Leaird, J. S. Patel, and J. R. Wullert, *IEEE J. Quantum Electron.* **28**, 908 (1992).
- <sup>30</sup>S. Vajda, A. Bartelt, C. Kaposta, T. Leisner, C. Lupulescu, S. Minemoto, P. Rosendo-Francisco, and L. Wöste, *Chem. Phys.* **267**, 231 (2001).
- <sup>31</sup>D. Schumacher, *Opt. Lett.* **27**, 451 (2002).

# Spatial mode cleaning by femtosecond filamentation in air

B. Prade, M. Franco, and A. Mysyrowicz

Laboratoire d'Optique Appliquée, Ecole Nationale Supérieure de Techniques Avancées, Ecole Polytechnique, CNRS UMR 7639, Palaiseau F-91761, France

A. Couairon

Centre de Physique Théorique, École Polytechnique, CNRS UMR 7644, Palaiseau F-91128, France

H. Buersing, B. Eberle, M. Krenz, and D. Seiffer

FGAN-Forschungsinstitut für Optronik und Mustererkennung, Research Institute for Optronics and Pattern Recognition, D-76275 Ettlingen, Germany

O. Vasseur

Office National d'Etudes de Recherches Aéropatiales, Département d'Optique Théorique et Appliquée, Palaiseau, F-91761 France

Received April 12, 2006; revised May 29, 2006; accepted May 31, 2006;  
posted June 14, 2006 (Doc. ID 69906); published August 9, 2006

By studying the conical emission of a blue femtosecond laser filament in air, it is shown that self-improvement of the beams' spatial mode quality occurs for a self-guided laser pulse. © 2006 Optical Society of America

OCIS codes: 190.5940, 190.7110, 010.1300.

A significant reshaping of the characteristics of intense femtosecond laser pulses takes place during their nonlinear propagation in air and other gases.<sup>1</sup> The beam first shrinks because of self-focusing and then maintains an  $\sim 100\ \mu\text{m}$  diameter and a peak intensity close to  $10^{13}\ \text{W}/\text{cm}^2$  over a distance longer than the Rayleigh length. This self-guiding reflects a competition between self-focusing and the defocusing action due to the abrupt onset of multiphoton ionization of air molecules. Optical pulses undergoing filamentation carry other interesting self-actions in terms of spectrum and pulse duration. For instance, the pulse experiences self-compression down to nearly the single-cycle limit.<sup>2-4</sup> Remarkably, the emerging pulse conserves the phase relation between the carrier wave and the pulse envelope, making it a very attractive source for generating even shorter laser pulses in the attosecond range.<sup>2</sup> The spectrum of the pulse displays an important broadening due largely to self-phase modulation induced by the self-steepened back edge of the pulse. Part of this broadband emission is in the form of a characteristic colored conical emission (CE) surrounding the filament core, with bluer frequencies on the outside rings.<sup>5</sup> By analyzing the self-guided pulse in the far field, we demonstrate another interesting effect occurring in air during filamentation, namely, a significant improvement of the beam quality of the emerging pulse, which takes the form of a single transverse mode.

The incident pulse was obtained by frequency doubling the output of a CPA Ti:sapphire laser. The incident laser pulse power at 406 nm (duration, 40 fs; pulse energy, 1 mJ; beam waist, 1.5 mm) was focused with a converging mirror of focal length  $f=5.66\ \text{m}$ . Typical shot-to-shot intensity variations were of the

order of  $\pm 5\%$ . To characterize the beam convergence, the strongly attenuated laser pulse intensity profile was first carefully measured at two locations before the geometric focus. From these data, the geometric focus of the low-intensity beam was determined from linear diffraction theory to be 5.66 m after the focusing mirror. At high intensity ( $I_0 \sim 1\ \text{GW}/\text{cm}^2$ ), slightly above the onset of filamentation, the laser pulse diameter shrinks to a diameter of  $\sim 100\ \mu\text{m}$  3 m before the geometric focus and then maintains this small diameter over 2 m. A total loss by 20% of the beam energy occurs during this propagation stage.

We have examined the far-field pattern of the emerging beam at a distance of 20 m after beam collapse. The emerging beam takes the form of an intense core surrounded by weaker radiation forming the CE. A striking feature is the excellent quality of the CE. This is shown in Fig. 1, which compares the spatial profile of the CE [Fig. 1(a)] with the total beam profile at the same distance [Fig. 1(b)]. The total beam comprises the nonfilamentary part of the

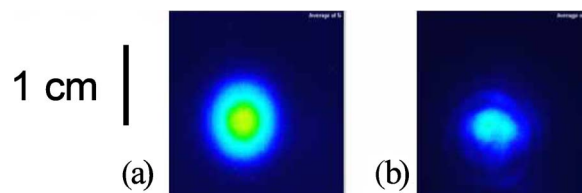


Fig. 1. (Color online) CE and laser pattern measured after 20 m of propagation in air. (a) Surrounding CE only, with the power spectrum close to that of the incident laser pulse removed by a color filter placed at  $z=10\ \text{m}$ . The wavelengths between 380 and 420 nm have been removed. (b) Total laser beam (strongly attenuated) at the same distance (false colors).

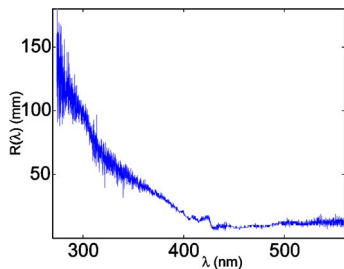


Fig. 2. (Color online) Radius of the CE (half-width at half-maximum) as a function of wavelength measured at 15 m.

beam, the filament core, and the much weaker CE. The conical spatial profile shown in Fig. 1(a) corresponds to a fundamental transverse radiation mode, while the nonfilamentary part of the beam around 400 nm exhibits a poorer beam quality. We have measured the diameter of the CE for different wavelengths with a spectrograph and a CCD camera. Each wavelength has a corresponding quasi-Gaussian profile, the half-width of which is plotted in Fig. 2. Bluer wavelengths exhibit larger diameters, giving rise to the appearance of colored rings, while the CE is absent from the visible part of the spectrum. This allows us to estimate the diameter of the beam around 400 nm that corresponds to the filamentary mode that produces the CE. The fraction of the incoming beam energy that couples into this transverse mode is found to be about 30%. This corresponds to 8 times the critical power estimated from the formula  $P_{cr} = 3.77\lambda^2 / 8\pi n_0 n_2$ , where  $\lambda$  is the laser wavelength,  $n_0$  is the refractive index, and  $n_2$  is the nonlinear Kerr coefficient at  $\lambda$ .<sup>6</sup> Moll *et al.*<sup>7</sup> reported a similar effect occurring during the collapse of a short pulse propagating in a dense dielectric medium. They found a universal behavior with the beam shape becoming highly radially symmetric when approaching the collapse region. They discussed this effect in terms of the beam's being driven into a Townes mode when the pulse approaches the collapse region. Our results confirm this symmetrization effect in a gas and further show that the high-quality mode is maintained over a large distance exceeding 15 m beyond the collapse location. We compared the measured beam profiles at different distances with those obtained by numerically solving the nonlinear Schrödinger (NLS) equation describing the propagation of an intense pulse in the envelope approximation.<sup>8,9</sup> Interestingly, the experimental results could be reproduced only if an input pulse energy of 0.3 mJ was introduced in the simulations. This corresponds to the fraction of energy coupled in the filamentary mode, as discussed above. All other laser parameters were taken from the experimental conditions. Figure 3(a) shows the calculated peak intensity of the pulse as a function of the propagation distance, together with the free electron density resulting from multiphoton ionization, while Fig. 3(b) shows the evolution of the beam width, computed as contours of the fluence distribution at various levels of the peak fluence. Despite the apparent equilibrium that maintains a constant filament width over 2 m, two distinct bursts of electron density indicate the

competition between self-focusing and plasma defocusing taking place in the filament, among other effects.

Figure 4 compares the calculated and the measured fluence profiles at 20 m. It clearly shows the presence of an intense core surrounded by the weaker CE. The fluence profiles between 3 and 5 m were estimated from microburns of undeveloped photographic plates to be of the order of 100  $\mu\text{m}$ , in agreement with the simulations.

Another stringent test of the validity of the simulations concerns the spectral domain. The measured spectrum of the filament core at 20 m, integrated over many shots, is shown in Fig. 5, together with a numerical simulation. There is excellent agreement, except for the lack of fringes in the measured spectrum. However, we observed fluctuations in the fringe pattern from shot to shot. When integrated over several shots, such fluctuations wash out the fringe pattern. We also note that the UV extension (below 300 nm) corresponds to a large angle component in the CE with a radius of the order of 10 cm (see Fig. 2), which is not reproduced in the simulations.

The origin of the fluctuations of the fringe pattern was determined by simulations in which the input intensity was slightly varied around the nominal value. The fringe pattern depends sensitively on the exact intensity. This is illustrated in Fig. 6 by two simulations performed with identical input conditions, except for a change of intensity by 10%. These spectra

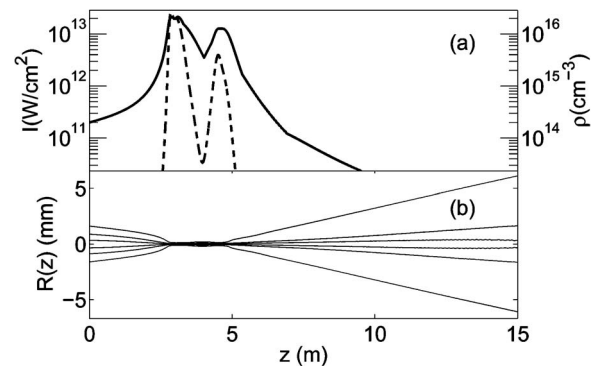


Fig. 3. (a) Calculated peak intensity (solid curve) of the pulse at 406 nm as a function of propagation distance. Also shown is the density of generated free electrons (dashed curve). (b) Calculated beam width as a function of distance. The curves correspond to contours for the fluence distribution at 90%, 50% and 10% of the maximum fluence at each distance.

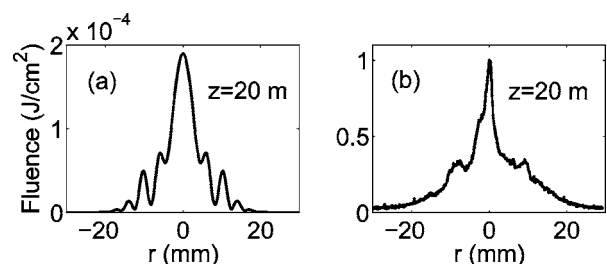


Fig. 4. (a) Calculated and (b) measured beam intensity profile at 20 m, showing the presence of a narrow core surrounded by a weaker ring.

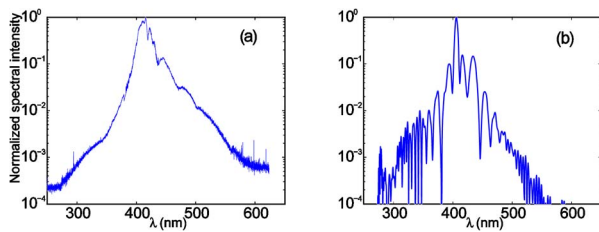


Fig. 5. (Color online) (a) Spectrum of the filament measured on axis after 15 m of propagation. The recorded spectrum is averaged over 100 laser shots (collecting angle, 0.16 mrad). (b) Numerical simulation obtained with an incident laser energy of 0.4 mJ.

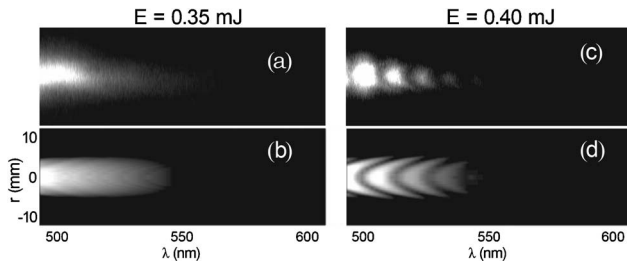


Fig. 6. Comparison between (a), (c) measured and (b), (d) calculated  $r$ - $\lambda$  diagram at 10 m for two incident pulse energies. The grayscale is logarithmic with a 2 decade dynamic range.

reproduce rather faithfully the measured single-shot spectra, including the radial expansion of the spectrum with the fishbone structure, as shown in Fig. 6. A similar fishbone structure was obtained from laser pulses undergoing filamentation in various condensed media<sup>10</sup> and was interpreted as a manifestation of the pulse splitting in time that occurs during the filamentation process. Note that close to the filamentation threshold a more uniform spectrum with fewer fringes is observed.

The universality of the filamentation phenomenon, as well as the mode cleaning effect reported in this work, suggests that filaments correspond to attractors of the dynamics of the NLS equation that involve cylindrically symmetric eigensolutions. Recently, several authors proposed that X-waves play a key role in filamentation in water.<sup>10-14</sup> Nonlinear X-waves are nondiffracting and nondispersive spatially and temporally extended solutions to the NLS equation with a characteristic X-shaped extension both in the spectral domain  $k_{\perp}$  versus  $\omega$  and in the space-time domain ( $r$  versus  $t$ ).<sup>15</sup> Nonlinear X-waves are particularly robust because the losses occurring inside the core are replenished by energy drawn from the extended tails.<sup>11</sup> These structures are spontaneously generated by filaments in condensed media<sup>13</sup> and have led to an interpretation of the associated phenomenon of CE in terms of a four-wave mixing process that involves two highly localized pump waves and two X-waves.<sup>16</sup> The wavelength-dependent angle of the CE measured in different condensed media or in air was shown to be fully determined by the dis-

persion of the medium.<sup>17</sup> Several simulation results show that far fields exhibit characteristic X-shaped extensions of the laser energy in the region beyond the nonlinear focus<sup>12,14,18</sup> that support the interpretation that mode self-cleaning in air is associated with the generation of a nonlinear X-wave.

In summary, this study reveals a striking new feature associated with filamentation, namely, improved beam quality. Filaments therefore bear remarkable properties in the time (pulse self-compression), frequency (spectrum broadening), and spatial (mode improvement) domains, making them a unique light source for applications.

A. Couairon's e-mail address is [couairon@cpht.polytechnique.fr](mailto:couairon@cpht.polytechnique.fr)

## References

1. A. Couairon, A. Mysyrowicz, K. Yamanouchi, S. L. Chin, P. Agostini, and G. Ferrante, in *Progress in Ultrafast Intense Laser Science* (Springer, 2006), pp. 235-258.
2. C. P. Hauri, W. Kornelis, F. W. Helbing, A. Heinrich, A. Couairon, A. Mysyrowicz, J. Biegert, and U. Keller, *Appl. Phys. B: Photophys. Laser Chem.* **79**, 673 (2004).
3. A. Couairon, M. Franco, A. Mysyrowicz, J. Biegert, and U. Keller, *Opt. Lett.* **30**, 2657 (2005).
4. A. Couairon, J. Biegert, C. P. Hauri, W. Kornelis, F. W. Helbing, U. Keller, and A. Mysyrowicz, *J. Mod. Opt.* **53**, 75 (2005).
5. E. T. J. Nibbering, P. F. Curley, G. Grillon, B. S. Prade, M. A. Franco, F. Salin, and A. Mysyrowicz, *Opt. Lett.* **21**, 62 (1996).
6. J. H. Marburger, *Prog. Quantum Electron.* **4**, 35 (1975).
7. K. D. Moll, A. L. Gaeta, and G. Fibich, *Phys. Rev. Lett.* **90**, 203902 (2003).
8. T. Brabec and F. Krausz, *Phys. Rev. Lett.* **78**, 3282 (1997).
9. G. Méchain, A. Couairon, M. Franco, B. Prade, and A. Mysyrowicz, *Phys. Rev. Lett.* **93**, 035003 (2004).
10. D. Faccio, P. Di Trapani, S. Minardi, A. Bramati, F. Bragheri, C. Liberale, V. Degiorgio, A. Dubietis, and A. Matijosius, *J. Opt. Soc. Am. B* **22**, 862 (2005).
11. A. Dubietis, E. Gaižauskas, G. Tamošauskas, and P. Di Trapani, *Phys. Rev. Lett.* **92**, 253903 (2004).
12. M. Kolesik, E. M. Wright, and J. V. Moloney, *Phys. Rev. Lett.* **92**, 253901 1 (2004).
13. D. Faccio, A. Matijosius, A. Dubietis, R. Piskarskas, A. Varanavičius, E. Gaižauskas, A. Piskarskas, A. Couairon, and P. Di Trapani, *Phys. Rev. E* **72**, 037601 (2005).
14. A. Couairon, E. Gaižauskas, D. Faccio, A. Dubietis, and P. Di Trapani, *Phys. Rev. E* **73**, 016608 (2006).
15. C. Conti, S. Trillo, P. Di Trapani, G. Valiulis, A. Piskarskas, O. Jedrkiewicz, and J. Trull, *Phys. Rev. Lett.* **90**, 170406 (2003).
16. D. Faccio, M. Porras, A. Dubietis, F. Bragheri, A. Couairon, and P. Di Trapani, *Phys. Rev. Lett.* **96**, 193901 (2006).
17. D. Faccio, M. A. Porras, A. Dubietis, A. Tamošauskas, E. Kučinskas, A. Couairon, and P. Di Trapani, *Opt. Commun.* (2006), doi:10.1016/j.optcom.2006.04.062.
18. M. Kolesik, E. M. Wright, and J. V. Moloney, *Opt. Express* **13**, 10729 (2005).

# Femtosecond filamentation in air at low pressures: Part I: Theory and numerical simulations

A. Couairon<sup>a,\*</sup>, M. Franco<sup>b</sup>, G. Méchain<sup>b</sup>, T. Olivier<sup>b</sup>, B. Prade<sup>b</sup>, A. Mysyrowicz<sup>b</sup>

<sup>a</sup> Centre de Physique Théorique, École Polytechnique, CNRS UMR 7644, F-91128, Palaiseau Cedex, France

<sup>b</sup> Laboratoire d'Optique Appliquée, École Nationale Supérieure des Techniques Avancées-École Polytechnique, CNRS UMR 7639, F-91761 Palaiseau Cedex, France

Received 10 March 2005; received in revised form 27 August 2005; accepted 30 August 2005

## Abstract

We investigate numerically the influence of the pressure on femtosecond filamentation in air. We show that femtosecond filamentation occurs at low pressure and compute the features of the plasma channel generated in the wake of the pulse. We discuss the influence of the pulse duration, chirp and input beam shape on the length of the plasma channels. These calculations constitute a prerequisite for laboratory experiments over short distances as well as for vertical femtosecond filamentation at high altitude on which light detection and ranging techniques or lightning protection rely.

© 2005 Elsevier B.V. All rights reserved.

PACS: 42.25.Bs; 42.65.Jx; 42.65.Sf; 52.38.Hb

## 1. Introduction

The propagation in gases or in condensed media of femtosecond laser pulses with powers exceeding the critical power for self-focusing  $P_{\text{cr}} \equiv 3.77\lambda^2/8\pi n_0 n_2$  (3 GW in air at  $\lambda = 800$  nm) [1] generates specific structures called filaments [2–4]. A filament possesses a narrow central core (diameter of about 100  $\mu\text{m}$  in air) surrounded by a laser energy reservoir [5]. Powerful beams usually form multiple filaments fed by this energy reservoir. Their global evolution involves a dynamical competition between several physical effects. Diffraction, Kerr self-focusing, photo-ionization, multiphoton absorption participate in the dynamics. The pulse temporal profile is also significantly modified due to group velocity dispersion, self-phase modulation and self-steepening.

Several applications rely on specific properties of femtosecond filaments. Three properties are particularly interest-

ing: (i) Light filaments can propagate horizontally over distances exceeding 2 km [6–8] and vertically over distances presumably reaching several kilometers [9,10]. (ii) Light filaments produce, via self-phase modulation, a white light continuum [3,11,12]. For instance, light detection and ranging (LIDAR) techniques use both properties and allow the detection of pollutants in the atmosphere when the laser pulse is launched in the sky and the backscattered light is collected by a telescope and analyzed [13]. (iii) Light filaments produce ionized channels in their wake. The triggering and guiding of electric discharges by a filament has been demonstrated in the laboratory, over distances of several meters [14–18], see [19] for a review. These scales must be extended to hundreds of meters for practical applications.

Both for lightning protection and LIDAR applications, the pressure evolves from the atmospheric pressure to a few tenths of bars at an altitude of 10 km. It has been shown recently that a control of filamentation can be achieved over horizontal kilometeric distances by varying the chirp of the input pulse [7,8]. In order to achieve a control of the filamentation process in the atmosphere, the properties

\* Corresponding author. Tel.: +33 1 69 33 47 24; fax: +33 1 69 33 30 08.  
E-mail address: [couairon@cphr.polytechnique.fr](mailto:couairon@cphr.polytechnique.fr) (A. Couairon).

of filaments must be studied in detail as a function of the pressure.

The aim of the present paper is to present theoretical investigations on femtosecond filaments propagating in air at various pressures from 0.1 to 1 atm. This study shows the influence of various control parameters of the input pulse. Calculations are performed for pulse durations of 60 fs, 120 fs and 500 fs, with the longest durations obtained by chirping the shortest pulse. The influence of the shape of the input beam is also studied. This parameter is shown to play an important role in the physics of filamentation. In particular, the length of the plasma column generated in the wake of the pulse vary with the shape of the input beam and can be significantly enhanced by using diaphragmed input beams with steep intensity gradients. The general trends show the existence of low pressure filaments, as well as the increase in the length of the plasma channels at lower pressures. The simulations also show that a chirp in the input pulse allows the generation of a plasma channel from a nonlinear focus located at a larger distance without significant change in the channel length. Finally, the numerical results show that femtosecond filamentation can occur at low pressures ( $0.2 \leq p \leq 1$  atm), which corresponds to altitudes higher than 10 km.

The outline of this paper is the following: First, we present the physical model in Section 2. In Section 3, we present numerical results about the propagation of laser pulses in air at low pressures and the generation of plasma channels. In Section 4, we present results showing the influence of the pulse duration. The influence of the beam focusing is studied in Section 5. The influence of the shape of the input beam is shown in Section 6. Finally, conclusions and outlook are given in Section 7.

## 2. Numerical simulations

The numerical code used in this study relies on the physical model developed for the propagation of an intense pulse in noble gases or air [7,8,20–23], fused silica [24–26], and liquids [27–29].

We model the linearly polarized beam with cylindrical symmetry around the propagation axis  $z$  by the envelope  $\mathcal{E}$  of the electric field  $\mathbf{E}$ , written as  $\mathbf{E} = \text{Re}[\mathcal{E} \exp(ikz - i\omega_0 t)]$ , where  $k = n_0 \omega_0 / c$  and  $\omega_0$  are the wavenumber and frequency of the carrier wave and  $n_0$  denotes the refraction index of air. In the following, these quantities correspond to a laser wavelength of 800 nm. The input pulses were modeled by Gaussians with energy  $E_{\text{in}}$  and a temporal FWHM duration  $\tau_{\text{FWHM}}$  (temporal half width  $t_p$ ):

$$\mathcal{E}(r, t, 0) = \mathcal{E}_0 \exp\left(-\frac{r^n}{w_0^n} - \frac{t^2}{t_p^2} - i\frac{kr^2}{2f} - iC\frac{t^2}{t_p^2}\right). \quad (1)$$

The input power is computed from the energy and pulse duration  $P_{\text{in}} = E_{\text{in}}/t_p \sqrt{\pi/2}$  and the input intensity is computed from the input power, the transverse waist  $w_0$  and the shape of the beam. For a Gaussian beam ( $n = 2$ ),

$\mathcal{E}_0^2 = 2P_{\text{in}}/\pi w_0^2$  whereas for a super-Gaussian beam  $\mathcal{E}_0^2 = [P_{\text{in}}/2\pi w_0^2] \times [n2^{2/n}/\Gamma(2/n)]$ . The quantity  $f$  denotes the curvature of the input beam and  $C$  the chirp of the input pulse, linked to the minimum pulse duration (according to the laws of Gaussian optics)  $t_p^{\text{min}} = t_p/\sqrt{1+C^2}$  and the second order derivative  $\phi^{(2)} = Ct_p^2/2(1+C^2)$ .

We have performed various set of experiments using diaphragmed beams. In order to mimic input beams obtained in usual experiments on filamentation, the numerical simulation can start either with Gaussian or super-Gaussian beams. Their feet can also be masked by requiring  $\mathcal{E}(r, t, z = 0) = 0$  for  $r > r_{\text{mask}}$  so as to model a circular aperture.

Two coupled equations describe the evolution of the envelope of the electric field and the electron density. The scalar envelope  $\mathcal{E}(r, t, z)$  is assumed to be slowly varying in time. It evolves along the propagation axis  $z$  according to the nonlinear envelope equation [30], expressed in the frequency domain:

$$\hat{U} \frac{\partial \hat{\mathcal{E}}}{\partial z} = i \left[ \frac{\nabla_{\perp}^2}{2k} + \frac{k}{2} \left( \frac{n^2 \omega^2}{k^2 c^2} - \hat{U}^2 \right) \right] \hat{\mathcal{E}} + \text{TF}\{N(\mathcal{E})\}, \quad (2)$$

where  $\hat{\mathcal{E}}(r, \omega, z) = \text{TF}\{\mathcal{E}(r, t, z)\}$ ,  $\hat{U}(\omega) \equiv 1 + (\omega - \omega_0)/kv_g$ ,  $v_g \equiv \partial\omega/\partial k|_{\omega_0}$  denotes the group velocity and  $\text{TF}\{N(\mathcal{E})\}$  denotes the time-Fourier transform of the nonlinear terms. Eq. (2) accounts for diffraction in the transverse plane, group velocity dispersion and high-order dispersive terms exactly computed by means of a Sellmeier dispersion relation for the refraction index  $n(\omega)$  of air. The operator  $\hat{U}$  in front of  $\partial/\partial z$  in Eq. (2) accounts for space-time focusing (see [30,31]). A small  $\omega - \omega_0$  expansion of the quantity

$$\hat{U}^{-1} \left( \frac{n^2 \omega^2}{k^2 c^2} - \hat{U}^2 \right) \sim \frac{k''}{k} (\omega - \omega_0)^2 + \frac{k'''}{3k} (\omega - \omega_0)^3 + \dots \quad (3)$$

leads to the second and third order dispersive coefficients  $k'' \equiv \partial^2 k / \partial \omega^2|_{\omega_0} = 0.2 \text{ fs}^2/\text{cm}$  and  $k''' \equiv \partial^3 k / \partial \omega^3|_{\omega_0} = 0.1 \text{ fs}^3/\text{cm}$  at 800 nm. Eq. (2) can be written in the time domain by using the retarded time  $t \equiv t_{\text{lab}} - z/v_g$  and by neglecting the high-order dispersive terms:

$$\frac{\partial \mathcal{E}}{\partial z} = \left[ \frac{i}{2k} U^{-1} \nabla_{\perp}^2 - i \frac{k''}{2} \frac{\partial^2 \mathcal{E}}{\partial t^2} + \frac{k'''}{6} \frac{\partial^3 \mathcal{E}}{\partial t^3} \right] \mathcal{E} + U^{-1} N(\mathcal{E}), \quad (4)$$

where  $U \equiv (1 + \frac{i}{kv_g} \frac{\partial}{\partial t})$  and the nonlinear effects include the optical Kerr effect with a nonlocal term corresponding to delayed Raman–Kerr optical shock response [32,33], self-steepening, plasma absorption, plasma defocusing and multiphoton absorption:

$$N(\mathcal{E}) = ik_0 n_2 T^2 \left[ (1 - f_R) |\mathcal{E}(t)|^2 + f_R \int_{-\infty}^t d\tau R(\tau - t) |\mathcal{E}(\tau)|^2 \right] \times \mathcal{E}(t) - \frac{\sigma}{2} (1 + i\omega_0 \tau_c) \rho \mathcal{E} - T \frac{\beta_K}{2} \left( 1 - \frac{\rho}{\rho_{\text{at}}} \right) |\mathcal{E}|^{2K-2} \mathcal{E}. \quad (5)$$

The operator  $T \equiv 1 + \frac{i}{\omega_0} \frac{\partial}{\partial t}$  in front of the Kerr term is responsible for the self-steepening of the pulse [31,34,35]. Self-focusing related to the Kerr effect occurs for pulses with  $P_{\text{in}}$  above  $P_{\text{cr}} = 3$  GW. This critical value corresponds to the nonlinear refraction index of air  $n_2 = 3.2 \times 10^{-19}$  cm<sup>2</sup>/W at  $p = 1$  bar, which we used in our simulations. From [32,36], the response function that accounts for the delayed Raman contribution in the Kerr effect may be written as

$$R(t) = \Omega^2 \tau_s \exp\left(-\frac{t}{\tau_d}\right) \times \sin\left(\frac{t}{\tau_s}\right),$$

with the characteristic times  $\tau_d = 70$  fs and  $\tau_s = 63$  fs,  $\Omega^2 = \tau_s^{-2} + \tau_d^{-2} = 21$  THz, and fraction  $f_R = 0.5$ .

For plasma absorption, the cross-section for inverse bremsstrahlung follows the Drude model [37] and reads

$$\sigma = \frac{ke^2}{n_0^2 \omega_0^2 \epsilon_0 m} \times \frac{\omega_0 \tau_c}{1 + \omega_0^2 \tau_c^2}, \quad (6)$$

where the momentum transfer collision time  $\tau_c = 350$  fs at  $p = 1$  bar. Since  $\tau_c \gg \omega_0^{-1} = 0.42$  fs, the classical plasma defocusing term is retrieved in Eq. (5):

$$-i \frac{\sigma \omega_0 \tau_c \rho \mathcal{E}}{2} \sim -i \frac{k\rho}{2n_0^2 \rho_c} \mathcal{E},$$

where  $\rho_c$  denotes the critical plasma density above which the plasma becomes opaque.

The evolution equation for the electron density reads

$$\frac{\partial \rho}{\partial t} = \sigma_K |\mathcal{E}|^{2K} (\rho_{\text{at}} - \rho) + \frac{\sigma}{U_i} \rho |\mathcal{E}|^2. \quad (7)$$

The first term on the right-hand side of Eq. (7) describes free electron generation via multiphoton ionization of oxygen with neutral atom density  $\rho_{\text{at}} = 0.2\rho_{\text{air}}$ , involving  $K \equiv \langle \frac{U_i}{\hbar\omega_0} + 1 \rangle$  photons. The quantity  $U_i = 12.06$  eV denotes the ionization potential of oxygen molecules and  $\langle \cdot \rangle$  denotes the integer part. At 800 nm,  $K = 8$  photons are necessary and the photoionization rate of oxygen molecules is computed in the framework of Keldysh's general formulation [38] revisited by Mishima et al. [39] so as to take into account a specific preexponential factor for diatomic molecules. In the multiphoton ionization regime  $W_{\text{PI}} = \sigma_K |\mathcal{E}|^{2K}$ , where  $\sigma_K = 3.7 \times 10^{-96}$  s<sup>-1</sup> cm<sup>16</sup> W<sup>-8</sup>. The multiphoton absorption cross-section reads as  $\beta_K = \sigma_K \times K\hbar\omega_0 \rho_{\text{at}} = 3.7 \times 10^{-95}$  cm<sup>13</sup> W<sup>-7</sup>. The second term in Eq. (7) accounts for avalanche ionization.

Some of the parameters in this model vary with the pressure of the gas. The values given above corresponds to a gas of 1 atm and their variation with the pressure in the range 0.1–10 atm is as follows:

$$n_2 = n_{2,0} \times p, \quad \tau_c = \tau_{c,0}/p, \quad \sigma = \sigma_0 \times \frac{p(1 + \omega_0^2 \tau_{c,0}^2)}{p^2 + \omega_0^2 \tau_{c,0}^2},$$

$$\rho_{\text{at}} = \rho_{\text{at},0} \times p, \quad \beta_K = \beta_{K,0} \times p,$$

where  $p$  is expressed in atm and the index 0 denotes atmospheric pressure at sea level. These expressions show that

the nonlinear dynamics is not expected to be trivially rescaled with air pressure, which enters in the plasma induced defocusing and plasma absorption terms with a different power than in other nonlinear terms. Therefore, the numerical investigation is important in order to reveal the changes in the competition between the nonlinear effects when the pressure varies.

Our numerical code contains several numerical scheme as explained in [23]. One of the most efficient follows a standard split step Crank–Nicholson scheme applied to each frequency corresponding to the Fourier decomposition in time of the pulse. It is clearly a formidable computational task to propagate a pulsed beam over large distances due to the wide range of spatial and temporal scales involved. Adaptive unevenly distributed mesh grids allow us to adjust the resolution to this wide range going from the micron scale to a few centimeters and from a fraction of fs to ps durations [8]. Usually, a resolution of 5–10  $\mu\text{m}$  in the transverse direction and 1–3 fs in the time direction is sufficient for most weakly nonlinear situations whereas much higher resolution is achieved around the peak intensities, with this adaptive mesh, when necessary. The gain in computational time corresponds to a factor of 10 when this standard Crank–Nicholson–Fourier scheme is used with an adaptive mesh, compared to the case of a mesh with constant step sizes.

### 3. Long distance propagation of collimated beams at low pressures

Laser pulses of 50 mJ energy and 120 fs duration (FWHM) are first shown to lead to filamentation over long distances when they propagate in air at low pressures from 0.2 to 1 atm. The restriction to cylindrical symmetry might seem questionable in the case of large peak input powers because a real beam is inherently non-homogeneous and undergoes beam-breakup and multiple filamentation. We investigate however the ideal case where a perfectly clean, and possibly powerful, input beam is launched and leads to a single filament. Among the reasons, there is the fact that our (3+1)D simulation code does not lead to a symmetry breaking when it is initiated by a pulsed cylindrically symmetric beam, without noise. The break-up of a powerful beam into multiple beamlets which eventually evolve into filaments actually depends on the level of input noise, as recently shown in [40]. The nonlinear saturation of the growing beamlets can also prevent the formation of a fully developed multifilamentation pattern as predicted by linear stability analyses [41,42]. In addition, a large number of (3+1)D simulations would be necessary to perform various statistical realizations and obtain a valuable information about the multiple filaments initiated with a white noise, which is beyond the scope of the present paper. We therefore describe the physics of a single filament in interaction with its surrounding energy reservoir. This is relevant even if the filament is produced by a pulse with high peak input power since several experimental situations show that

multiple filaments in air interact through their mutual energy reservoir [7,8,21,43].

Fig. 1 shows simulation results for the fluence, intensity, electron density and beam width obtained from a collimated Gaussian input beam with  $n = 2$  and  $w_0 = 14$  mm launched in air at three different pressures. Figs. 1(a1)–(a3) correspond to the lowest pressure of 0.2 bar. The fluence profile in Fig. 1(a1) shows a light filament exhibiting several peaks and radiation losses emitted from the core at each of these peaks. The filament starts at  $z = 80$  m and propagates beyond 250 m. At low pressures between 0.6 and 1 bar, Figs. 1(b1) and (c1) also show evidence of an extended filamentation, with refocusing peaks located at distances larger than 300 m. The peak intensity and the peak electron density are plotted as functions of the propagation distance in Figs. 1(a2), (b2), (c2). They reach saturation at the levels  $2 \times 10^{13}$  W/cm<sup>2</sup> and  $2\text{--}10 \times 10^{15}$  cm<sup>-3</sup>. The ratio of the saturation levels for the electron density obtained at different pressures follows the ratio of the gas pressures. This effect is due to intensity clamping

as explained in Section 5. The nonlinear focus beyond which the plasma string is generated is located at smaller propagation distances when the pressure is increased. This effect is well explained by the fact that the critical power for self-focusing scales as  $1/p$ , and therefore decreases when the pressure increases. Thus, the location of the nonlinear focus decreases because it is closer to the laser when the effective ratio  $P_{\text{in}}^{\text{eff}}/P_{\text{cr}}$  is large. As shown in [44] the position of the nonlinear focus  $z_{\text{nf}}$  as a function of  $P_{\text{in}}^{\text{eff}}/P_{\text{cr}}$  follows a Marburger-like scaling law when a Raman contribution is present in the Kerr effect:

$$z_{\text{nf}} = \frac{0.367z_{\text{R}}}{\sqrt{[(\max_t P_{\text{in}}^{\text{eff}}(t)/P_{\text{cr}})^{1/2} - 0.852]^2 - 0.0219}}, \quad (8)$$

where  $z_{\text{R}}$  denotes the Rayleigh length and

$$P_{\text{in}}^{\text{eff}}(t) = P_{\text{in}}[(1 - f_{\text{R}}) \exp(-2t^2/t_p^2) + f_{\text{R}} \int_{-\infty}^t R(t' - t) \times \exp(-2(t'/t_p)^2) dt']. \quad (9)$$

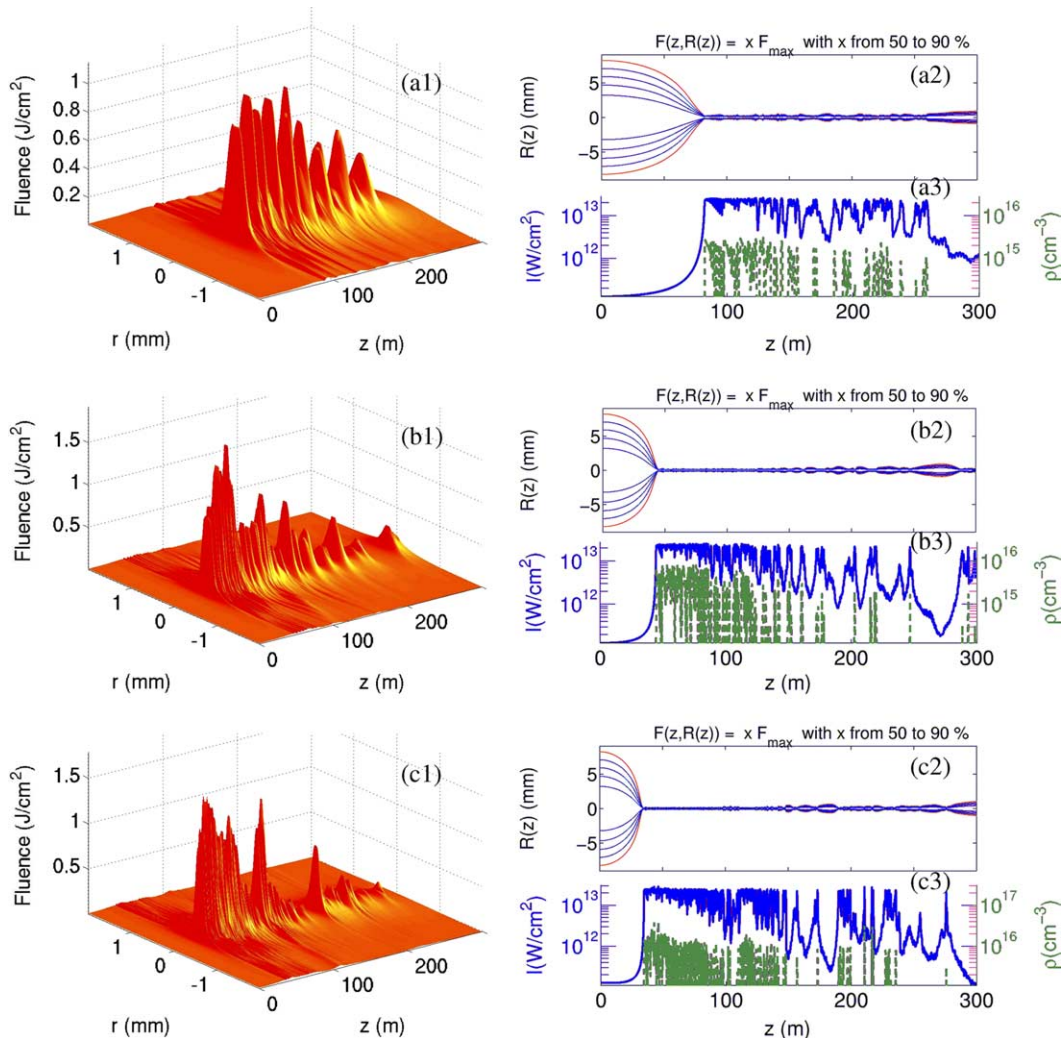


Fig. 1. Propagation of a 50 mJ, 120 fs laser pulse in the atmosphere at (a) 0.2 bar, (b) 0.6 bar and (c) 1 bar. The input beam is a collimated Gaussian with  $w_0 = 14$  mm. (a1), (b1), (c1) Fluence profile as a function of the propagation distance. (a2), (b2), (c2) Intensity (continuous curve, left axis) and electron density (dashed curve, right axis) vs.  $z$ . (a3), (b3), (c3) Beam width vs.  $z$ . The levels correspond to a fraction of the maximum fluence, from 50% to 90%.

We have also performed numerical simulations (not shown) with a continuously decreasing pressure with altitude, so as to model a vertical propagation. In these simulations,  $p$  varies with the altitude according to the simple isothermal model (between 0 and 11 km):  $p = p_0 \exp(-(z - z_0)/z_p)$ , where  $z_p \equiv RT/Mg \simeq 8$  km. Since the typical filamentation scale of about 100 m is much smaller than  $z_p$ , no significant changes in the filament and plasma channels were obtained in comparison with the case of a constant low pressure. Filamentation occurs over several hundreds of meters in both cases with discontinuous plasma channels.

#### 4. Influence of the chirp of the input pulse on the plasma channel

Another parameter playing a crucial role is duration of the input pulse. When experiments are performed with a single laser, the pulse duration is controlled by modifying the chirp of the input pulse. Usually, the propagation of ultrashort laser pulses over long distances is achieved by precompensation of the group velocity dispersion of air. This is done by means of a negative chirp in the initial pulse, which therefore becomes longer and consequently, contains less power. A theoretical analysis of the filamentation length with chirped pulses satisfying these conditions has been done in [45]. This analysis shows that the filamentation length is enhanced for large negative chirps, provided the dispersive-compression length (defined as the distance necessary to compress the chirped pulse owing to group velocity dispersion) slightly exceeds the self-focusing distance (defined by Eq. (8)). This result is in agreement with experimental results in [8]. Fig. 2 shows a comparison between the plasma channels generated by numerical simulation of the propagation of chirped and non chirped pulses (minimum duration of  $t_p = 120$  fs), with either collimated or focused Gaussian input beams (focal length of  $f = 50$  m), 50 mJ energy and  $w_0 = 14$  mm. Fig. 2(a) corresponds to a non-chirped pulse and collimated beam: the nonlinear focus is located at a distance of 30 m from the source, which is comparable to the value  $z_{\text{nf}} = 31$  m predicted by Eq. (8). The plasma channel generated on axis is not continuous but appears by bursts. Its total length, defined as the distance over which the on-axis electron density exceeds  $10^{15} \text{ cm}^{-3}$ , is about 69 m. The propagation of a pulse with the same parameters except for the chirp  $\phi^{(2)} = -3 \times 10^4 \text{ fs}^2$  (corresponding to an input duration of 500 fs) shows that the nonlinear focus is located at 75 m from the source and the generated plasma channel is still discontinuous with a total length of about 47 m (Fig. 2(b)). Here, the dispersive compression length is about 1.5 km, much larger than the self-focusing length. By using pulses with the same energy and minimum duration, a negative chirp therefore delays the beginning of filamentation as expected but the extension of the generated plasma channel is only slightly smaller in agreement with the analysis in [45]. It

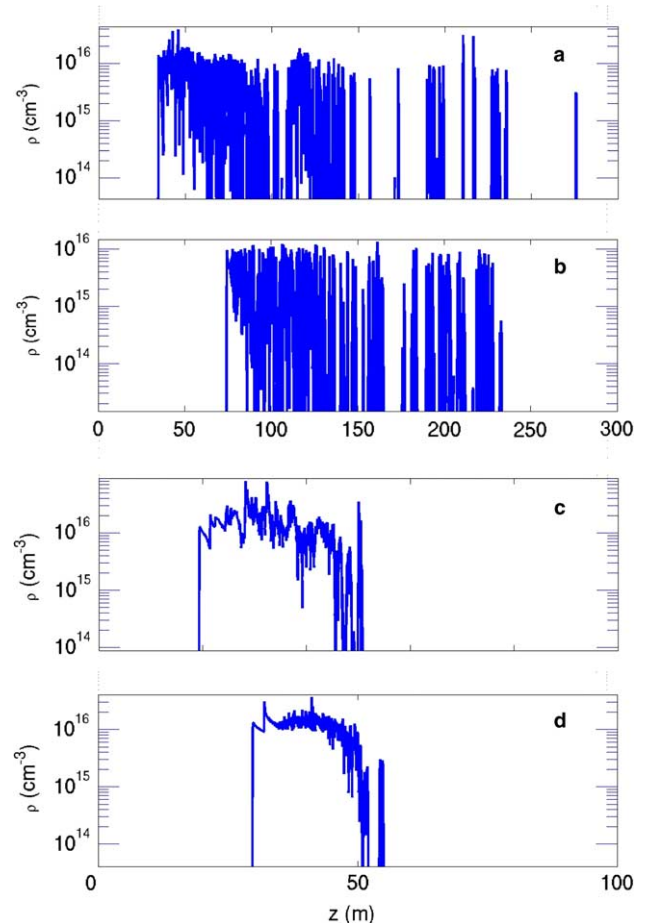


Fig. 2. Influence of the initial chirp on the plasma channel. (a) The input beam is Gaussian with  $w_0 = 14$  mm,  $E_{\text{in}} = 50$  mJ; the input pulse is not chirped with  $t_p = 120$  fs. (b) Same conditions as in (a) with a chirp of  $-3 \times 10^4 \text{ fs}^2$  (input pulse duration of 500 fs). (c) Same conditions as in (a) with a focused beam corresponding to a focal length  $f = 50$  m. (d) Same conditions as in (c) with a chirp of  $-3 \times 10^4 \text{ fs}^2$ . Note that (a), (b) and (c), (d) have different scales for the propagation distance.

is worth noting that these simulations model single shot experiments. In an experiment, very close plasma bursts would be measured as a single continuous plasma channel, first because shot to shot fluctuations might lead to a natural averaging process and second because the measurement technique itself averages the electron density over a short centimetric scale.

#### 5. Propagation of focused beams at low pressures

Figs. 2(c) and (d) show the electron density generated on-axis for the same pulses as in Section 4 except that the beam is now focused by a lens of focal length  $f = 50$  m. The plasma channel generated with the unchirped pulse is now continuous. The focusing lens therefore facilitates the connection of the electron bursts into a single 28 m long channel, which starts closer to the laser. As in the case of the collimated beam, the chirped pulse associated with the focused beam generates a 21 m long continuous plasma channel but the beginning of the filament is

delayed (see Fig. 2(d)). The chirp of the input pulse therefore not only allows a shift of the beginning of filamentation but also a control of its length, whereas its continuity is controlled by the focal length. By tuning independently the focal length and the chirp, it is possible to produce various type of plasma channels. In practice, the choice of these parameters will depend whether a specific application needs a discontinuous plasma channels cover-

ing a large distance or a continuous plasma channel over a shorter range. In particular, a lens compresses the filamentation dynamics along the longitudinal direction. When a pulsed collimated beam generates the filament, it leads to successive focusing defocusing cycles reflecting the competition between the optical Kerr effect, multiphoton absorption and plasma induced defocusing. The periodicity between the pinching points of the beam, and

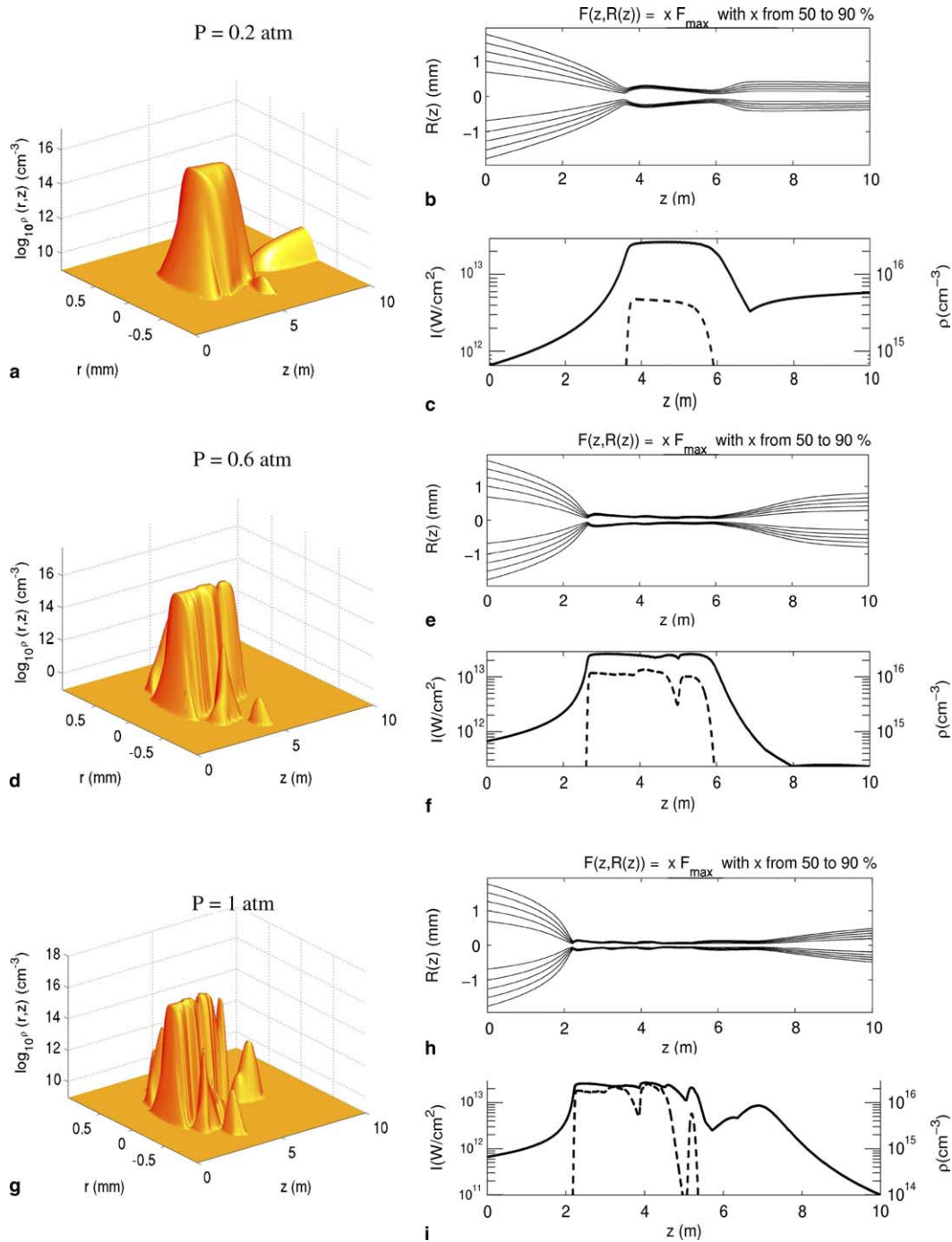


Fig. 3. Plasma channel generated in the wake of the ultrashort pulse for a Gaussian input beam with  $w_0 = 3$  mm,  $E_{\text{in}} = 6$  mJ,  $f = 6$  m,  $\tau_{\text{FWHM}} = 60$  fs. (a)  $p = 0.2$  atm, (d)  $p = 0.6$  atm and (g)  $p = 1$  atm. (b) Beam diameter as a function of the propagation distance  $z$  for  $p = 0.2$  atm. (e) and (h) same as in (b) for  $p = 0.6$  and  $p = 1$  atm. (c) Intensity (continuous line, left axis) and electron density (dashed line, right axis) vs.  $z$  for  $p = 0.2$  atm. (f) and (i) same as in (c) for  $p = 0.6$  and  $p = 1$  atm.

thus the continuity of the plasma, depends on the input conditions. A pulsed beam with the same parameters, focused by a lens, will clearly produce a plasma channel with a shorter periodicity, located between the nonlinear focus and the position of the focus of the lens. If the focal length is sufficiently short, the plasma channel can become continuous. However, it is well known that it can also extend beyond the focus of the lens [46] with possible refocusing at larger distances.

It is therefore also interesting to study filamentation over laboratory scales since a prerequisite for experiments about long distance filamentation is to test the predictions of the calculations over shorter distances achievable in the laboratory. A forthcoming paper will describe laboratory experiments performed by using focal lengths in the meter range [47].

The following results corresponds to smaller energies and focused beams as used in laboratory experiments. Fig. 3 shows a comparison between the plasma channels numerically computed for  $p = 0.2$ ,  $p = 0.6$  and  $p = 1$  atm. These results are obtained for a Gaussian input beam with  $w_0 = 3$  mm, a focal length of 6 m and an input energy of 6 mJ. The pulse duration is  $\tau_{\text{FWHM}} = 60$  fs. Figs. 3(a), (d) and (g) show nearly connected plasma channels. The plasma strings undergo slight structural changes when the pressure is increased from 0.2 to 1 atm. The beam diameters shown in Figs. 3(b) (e) and (h) show that the nonlinear focus beyond which the filament starts is located farther on the propagation axis when the pressure is low. The maximum intensity shown in continuous line in Figs. 3(c), (f) and (i) slightly exceeds  $10^{13}$  W/cm<sup>2</sup> but has comparable values in the three cases. The intensity clamping governed by a local balance between the index changes  $n_2 I$  and  $-\rho/2\rho_c$  is indeed insensitive to the pressure because both  $n_2$  and  $\rho$  are proportional to the pressure. This result follows from the fact that the electron density is mainly given by its multiphoton contribution, in which case it scales as  $\rho \simeq \sigma_K I^K \rho_{\text{at},p}$ . The maximum intensity therefore scales as  $I \simeq (2n_2\rho_c/\sigma_K \rho_{\text{at},p})^{1/(K-1)}$  which does not depend on the pressure since  $n_2/\rho_{\text{at}} = n_{2,0}/\rho_{\text{at},0}$ , all other parameters being pressure independent. In contrast, the same scaling for the electron density shows that  $\rho \propto p$ . The maximum electron density shown in dashed curve on the same Figs. 3(c) and (i) is thus in the ratio 1/5 as it should be from the ratio of the pressures. The on-axis electron density increases with pressure. Computation at larger pressures ( $p > 1$  atm) shows that the plasma channel becomes discontinuous (not shown).

The diameter of the ionized plasma channel is larger at lower pressure. As a result, integration of the electron density over the transverse dimension, i.e., the number of charges per centimeter exhibits only a smooth variation with pressure. Figs. 4(a)–(c) indeed show that the number of charges per cm which in principle is directly proportional to the electric conductivity of the plasma, reaches  $10^{13}$  cm<sup>-1</sup> for all pressures. The set of curves in each graph in Fig. 4 correspond to various integration radii (10, 50,

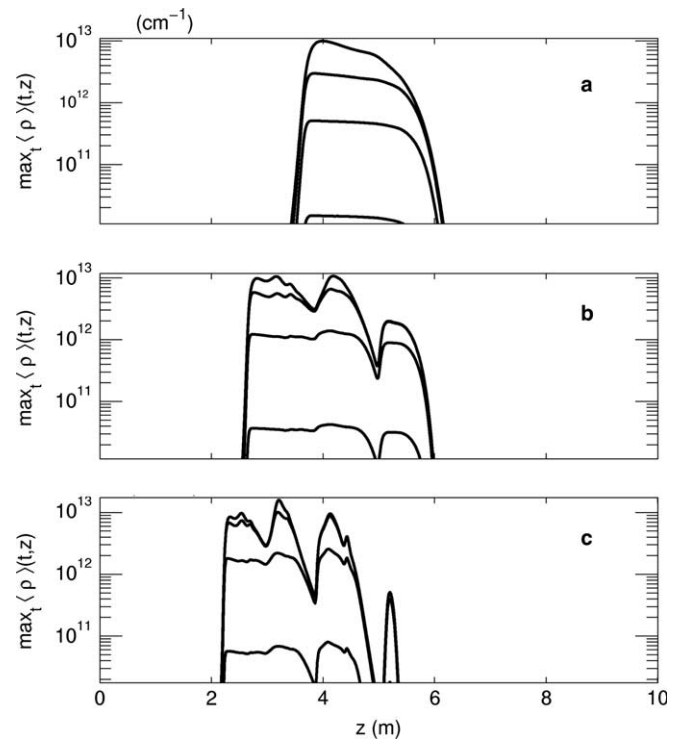


Fig. 4. Number of electrons per length unit as a function of the air pressure. The parameters are the same as in Fig. 3. (a)  $p = 0.2$  atm, (b)  $p = 0.6$  atm, (c)  $p = 1$  atm. The curves on each graph correspond to different integration radii: 10, 50, 100  $\mu\text{m}$  and the whole beam.

100  $\mu\text{m}$ ), the curve at the highest level reflecting the number of charges per cm in the whole beam.

## 6. Influence of the input beam shape on the plasma column

Other input beam profiles have been used in the simulations. The general trends are recovered with all the beam profiles but some structural modifications of the plasma channels generated by the pulse occur. Fig. 5 shows the integrated electron density, i.e., the number of electrons per cm as a function of the propagation distance and the gas pressure for three different input beam profiles. The pulse has an energy of 5.4 mJ with a duration of 130 fs (FWHM). The focal length is  $f = 2$  m. With a Gaussian input beam (see dotted curves in Fig. 5), the integrated electron density exhibits a 60 cm long main channel before the focus of the lens, reaching a few  $10^{13}$  cm<sup>-1</sup>. At 1 atm, two secondary plasma channels, nearly two orders of magnitude below the main channel, are formed further on the propagation axis (Fig. 5(a)). When the pressure decreases, the length of the principle plasma channel decreases. With a super-Gaussian input beam of order  $n = 50$  (see continuous curves in Fig. 5), the main plasma channel is more spiky and a longer averaged plasma channel starting closer to the focus of the lens is obtained at an optimal pressure of 0.6 atm (Fig. 5(b)). With a diaphragmed Gaussian beam (dashed curves in Fig. 5), the same behavior is obtained except that the low level plasma channel extending beyond

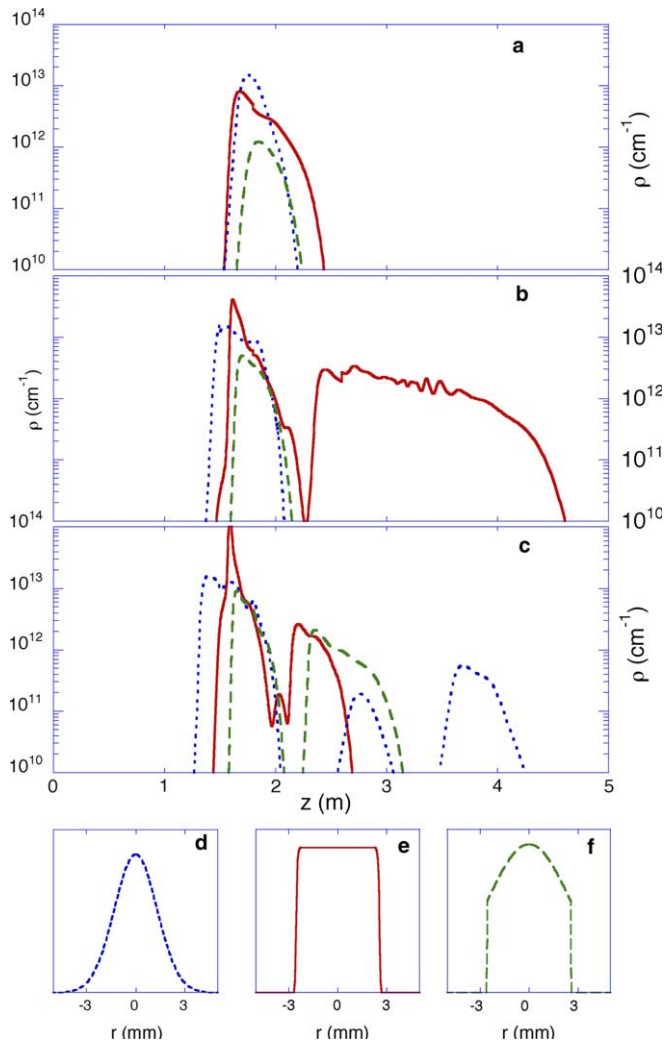


Fig. 5. Number of electrons per length unit as a function of the air pressure for various input beam profiles. The pulse parameters are  $E_{\text{in}} = 5.4$  mJ,  $t_p = 130$  fs,  $f = 2$  m. (a)  $p = 0.2$  atm, (b)  $p = 0.6$  atm, (c)  $p = 1$  atm. The different beam shapes are indicated by dotted, continuous, or dashed curves: dotted  $\equiv$  Gaussian input beam with  $w_0 = 2.6$  mm (shown in (d)); continuous  $\equiv$  super-Gaussian input beam with  $w_0 = 2.6$  mm and  $n = 50$  (shown in (e)); dashed  $\equiv$  diaphragmed Gaussian input beam with  $w_0 = 5.2$  mm and  $r_{\text{mask}} = 2.6$  mm (shown in (f)).

the linear focus of the lens has a maximum length at a larger pressure than with a super-Gaussian input beam.

These results show that the shape of the input beam provides another sensitive control parameter for the length of the plasma channel.

## 7. Discussion and conclusion

The results show that femtosecond filamentation can occur at low pressures ( $0.2 \leq p \leq 1$  atm), which corresponds to altitudes up to  $\sim 11$  km. The effect of lowering the pressure modifies mainly the self-focusing stage during the propagation of the ultra-short pulse. The length of the plasma string does not change significantly in the range of pressure from 0.2 to 1 atm. Below 0.2 bar, the length is strongly reduced but this reflects the fact that

the power is lower than the critical power for self-focusing. Indeed, the non-linear index of refraction  $n_2$  related to the optical Kerr effect depends on the gaz density:  $n_2 \propto p$ . Therefore, as the critical power  $P_{\text{cr}}$  is inversely proportional to the non-linear index  $n_2$ ,  $P_{\text{cr}}$  is inversely proportional to the gaz pressure. Hence, as the pressure decreases, the critical power increases and consequently the filament appears at a distance closer to the geometrical focus of the lens (or farther from the laser with collimated beams).

A second result concern the features of filamentation when the shape of the input beam vary. We have shown that this parameter, which is experimentally accessible, plays an important role in filamentation. For instance, it is possible to increase by a factor of two the length of the plasma channel generated in the wake of the ultrashort laser pulse, simply by introducing steep intensity gradients at the periphery of the input beam.

Finally, with a constant energy per pulse and a constant duration, the chirp of the input pulse has been shown to be of little influence on the length of the plasma channel generated by filamentation. However, if the input pulse is stretched by introducing a chirp, the power of the input beam is lowered and therefore, the beginning of filamentation is delayed in agreement with [7,8,45].

In conclusion, we have investigated by numerical simulations the influence of the pressure on filamentation. The calculations indicate the crucial influence of the shape of the input beam. In contrast, when the input pulse duration and power are constant, a chirp has little influence on filamentation. However, a chirp can be used as a control parameter to modify the duration of the input pulse and its power, which delays the beginning of filamentation and reduces the total length of the plasma channel. The plasma channel, however, may be discontinuous with bursts spread over a long distance. In a previous study [7,8], we have shown that large negative chirps allow an increase of the spread the plasma channels generated by horizontal propagation of ultrashort laser pulses at 1 atm. Finally, simulations of vertical filamentation with varying pressure have revealed filamentation over several hundreds of meters accompanied by disconnected plasma channels with a maximum electron density of  $10^{16} \text{ cm}^{-3}$ .

## References

- [1] J.H. Marburger, Prog. Quantum Electron. 4 (1975) 35.
- [2] A. Braun, G. Korn, X. Liu, D. Du, J. Squier, G. Mourou, Opt. Lett. 20 (1995) 73.
- [3] E.T.J. Nibbering, P.F. Curley, G. Grillon, B.S. Prade, M.A. Franco, F. Salin, A. Mysyrowicz, Opt. Lett. 21 (1996) 62.
- [4] A. Brodeur, C.Y. Chien, F.A. Ilkov, S.L. Chin, O.G. Kosareva, V.P. Kandidov, Opt. Lett. 22 (1997) 304.
- [5] M. Mlejnek, M. Kolesik, E.M. Wright, J.V. Moloney, Phys. Rev. Lett. 83 (1999) 2938.
- [6] B.L. Fontaine, F. Vidal, Z. Jiang, C.Y. Chien, D. Comtois, A. Desparois, T.W. Johnston, J.-C. Kieffer, H. Pépin, Phys. Plasmas 6 (1999) 1615.

- [7] G. Méchain, A. Couairon, Y.-B. André, C. D'Amico, M. Franco, B. Prade, S. Tzortzakis, A. Mysyrowicz, R. Sauerbrey, *Appl. Phys. B* 79 (2004) 379.
- [8] G. Méchain, C. D'Amico, Y.-B. André, S. Tzortzakis, M. Franco, B. Prade, A. Mysyrowicz, A. Couairon, E. Salmon, R. Sauerbrey, *Opt. Commun.* 247 (2005) 171.
- [9] L. Wöste, C. Wedekind, H. Wille, P. Rairoux, B. Stein, S. Nikolov, C. Werner, S. Niedermeier, F. Ronneberger, H. Schillinger, et al., *Laser Optoelektron.* 29 (1997) 51.
- [10] M. Rodriguez, R. Bourayou, G. Méjean, J. Kasparian, J. Yu, E. Salmon, A. Scholz, B. Stecklum, J. Eislöffel, U. Laux, et al., *Phys. Rev. E* 69 (2004) 036607.
- [11] J. Kasparian, R. Sauerbrey, D. Mondelain, S. Niedermeier, J. Yu, J.-P. Wolf, Y.-B. André, M. Franco, B. Prade, S. Tzortzakis, et al., *Opt. Lett.* 25 (2000) 1397.
- [12] V.P. Kandidov, I.S. Golubtsov, O.G. Kosareva, *Quantum Electron.* 34 (2004) 348.
- [13] P. Rairoux, H. Schillinger, S. Neirdeimer, M. Rodriguez, F. Ronneberger, R. Sauerbrey, B. Stein, D. Waite, C. Wedekind, H. Wille, et al., *Appl. Phys. B* 71 (2000) 573.
- [14] D. Comtois, C.Y. Chien, A. Desparois, F. Génin, G. Jarry, T.W. Johnston, J.-C. Kieffer, B.L. Fontaine, F. Martin, R. Mawassi, et al., *J. Appl. Phys.* 76 (2000) 819.
- [15] B.L. Fontaine, D. Comtois, C.Y. Chien, A. Desparois, F. Génin, G. Jarry, T.W. Johnston, J.-C. Kieffer, F. Martin, R. Mawassi, et al., *J. Appl. Phys.* 88 (2000) 610.
- [16] P. Rambo, J. Schwarz, J.-C. Diels, *J. Opt. A* 3 (2001) 146.
- [17] S. Tzortzakis, B. Prade, M. Franco, A. Mysyrowicz, S. Hüller, P. Mora, *Phys. Rev. E* 64 (2001) 057401.
- [18] M. Rodriguez, R. Sauerbrey, H. Wille, L. Wöste, T. Fujii, Y.-B. André, A. Mysyrowicz, L. Klingbeil, K. Rethmeier, W. Kalkner, et al., *Opt. Lett.* 27 (2002) 772.
- [19] N. Khan, N. Mariun, I. Aris, J. Yeak, *New J. Phys.* 4 (2002) 61.1.
- [20] M. Mlejnek, E.M. Wright, J.V. Moloney, *Opt. Lett.* 23 (1998) 382.
- [21] G. Méchain, A. Couairon, M. Franco, B. Prade, A. Mysyrowicz, *Phys. Rev. Lett.* 93 (2004) 035003.
- [22] A. Couairon, G. Méchain, S. Tzortzakis, M. Franco, B. Lamouroux, B. Prade, A. Mysyrowicz, *Opt. Commun.* 225 (2003) 177.
- [23] A. Couairon, S. Tzortzakis, L. Bergé, M. Franco, B. Prade, A. Mysyrowicz, *J. Opt. Soc. Am. B* 19 (2002) 1117.
- [24] S. Tzortzakis, M. Franco, B. Prade, A. Mysyrowicz, A. Couairon, L. Bergé, *Phys. Rev. Lett.* 87 (2001) 213902.
- [25] L. Sudrie, A. Couairon, M. Franco, B. Lamouroux, B. Prade, S. Tzortzakis, A. Mysyrowicz, *Phys. Rev. Lett.* 89 (2002) 186601.
- [26] A. Couairon, L. Sudrie, M. Franco, B. Prade, A. Mysyrowicz, *Phys. Rev. B* 71 (2005) 125435.
- [27] Q. Feng, J.V. Moloney, A.C. Newell, E.M. Wright, K. Cook, P.K. Kennedy, D.X. Hammer, B.A. Rockwell, C.R. Thompson, *IEEE J. Quantum Electron.* 33 (1997) 127.
- [28] M. Kolesik, E.M. Wright, J.V. Moloney, *Phys. Rev. Lett.* 92 (2004) 253901.
- [29] A. Dubietis, E. Gaižauskas, G. Tamošauskas, P.D. Trapani, *Phys. Rev. Lett.* 92 (2004) 253903.
- [30] T. Brabec, F. Krausz, *Phys. Rev. Lett.* 78 (1997) 3282.
- [31] A.L. Gaeta, *Phys. Rev. Lett.* 84 (2000) 3582.
- [32] R.H. Stolen, J.P. Gordon, W.J. Tomlison, H.A. Haus, *J. Opt. Soc. Am. B* 6 (1989) 1159.
- [33] G.K.L. Wong, Y.R. Shen, *Phys. Rev. A* 10 (1974) 1277.
- [34] A.A. Zozulya, S.A. Diddams, T.S. Clement, *Phys. Rev. A* 58 (1998) 3303.
- [35] A.A. Zozulya, S.A. Diddams, A.G.V. Engen, T.S. Clement, *Phys. Rev. Lett.* 82 (1999) 1430.
- [36] J.-F. Ripoche, G. Grillon, B. Prade, M. Franco, E. Nibbering, R. Lange, A. Mysyrowicz, *Opt. Commun.* 135 (1997) 310.
- [37] E. Yablonovitch, N. Bloembergen, *Phys. Rev. Lett.* 29 (1972) 907.
- [38] L.V. Keldysh, *Sov. Phys. JETP* 20 (1965) 1307.
- [39] K. Mishima, M. Hayashi, J. Yi, S.H. Lin, H.L. Selzle, E.W. Schlag, *Phys. Rev. A* 66 (2002) 033401.
- [40] G. Fibich, È. Eisenmann, B. Ilan, Y. Erlich, M. Fraenkel, Z. Henis, A.L. Gaeta, A. Zigler, *Opt. Exp.* 13 (2005) 5897.
- [41] A.J. Campillo, S.L. Chapiro, B.R. Suydam, *Appl. Phys. Lett.* 23 (1973) 628.
- [42] A.J. Campillo, S.L. Chapiro, B.R. Suydam, *Appl. Phys. Lett.* 24 (1973) 178.
- [43] W. Liu, J.-F. Gravel, F. Théberge, A. Becker, S.L. Chin, *Appl. Phys. B* 80 (2005) 857.
- [44] A. Couairon, *Eur. Phys. J. D* 27 (2003) 159.
- [45] I.S. Golubtsov, V.P. Kandidov, O.G. Kosareva, *Quantum Electron.* 33 (2003) 525.
- [46] H.R. Lange, G. Grillon, J.-F. Ripoche, M.A. Franco, B. Lamouroux, B.S. Prade, A. Mysyrowicz, E.T.J. Nibbering, A. Chiron, *Opt. Lett.* 23 (1998) 120.
- [47] G. Méchain, T. Olivier, M. Franco, A. Couairon, B. Prade, A. Mysyrowicz, *Opt. Commun.* (submitted).

# Femtosecond filamentation in air at low pressures. Part II: Laboratory experiments

G. Méchain<sup>a,\*</sup>, T. Olivier<sup>a</sup>, M. Franco<sup>a</sup>, A. Couairon<sup>b</sup>, B. Prade<sup>a</sup>, A. Mysyrowicz<sup>a</sup>

<sup>a</sup> *Laboratoire d'Optique Appliquée, ENSTA École Polytechnique, CNRS UMR 7639, F-91761 Palaiseau Cedex, France*

<sup>b</sup> *Centre de Physique Théorique, École Polytechnique, CNRS UMR 7644, F-91128 Palaiseau Cedex, France*

Received 30 August 2005; received in revised form 15 October 2005; accepted 15 October 2005

## Abstract

We present experimental studies of filamentation of a femtosecond laser pulse in air at low pressures. The evolution of the filament has been studied by measuring along the propagation axis the conductivity and the sub-THz emission from the plasma channel. We show experimentally that the filamentation process occurs at pressures as low as 0.2 atm in agreement with numerical simulations. Experimental and numerical results [A. Couairon, M. Franco, G. Méchain, T. Olivier, B. Prade, A. Mysyrowicz, *Opt. Commun.*, submitted for publication] are compared and the possible sources of discrepancy are discussed.

© 2005 Elsevier B.V. All rights reserved.

*PACS:* 42.25.Bs; 42.65.Jx; 52.38.Hb; 52.70.Ds

*Keywords:* Femtosecond filamentation; Beam-trapping; Laser–plasma interactions; Conductivity measurements

## 1. Introduction

The propagation of femtosecond laser pulses carrying several times the critical power for self-focusing [2] leads to a particular type of propagation called filamentation, which has been studied both theoretically and experimentally during the past decade [3–7]. This filamentation or self-channeling of the beam takes place via a dynamic competition between beam self-focusing due to the optical Kerr effect and beam defocussing due to photo-ionization when the pulse intensity becomes high enough to induce multiphoton absorption. Other effects are involved in this complex dynamics such as diffraction, group velocity dispersion, self-phase modulation and pulse self-steepening, the combination of which leads to a strong pulse restructuring. This is also at the origin of an important spectral broadening (white continuum emission). Filamentation in air allows intense IR femtosecond pulses to prop-

agate over very long distances, reaching hundreds of meters [8–10]. Using appropriate temporal chirps, the onset of the filament as well as its length can be controlled [9,10]. The white light continuum emitted by the filament can be used to probe the atmosphere with LIDAR techniques [11–13]. Moreover, the plasma column created by filamentation has been used to trigger and guide electric discharges and might possibly be used for lighting protection [14–19]. For such applications, vertical propagation should be achieved to high altitudes. Thus, the study of filamentation at low pressures is important.

In this paper, we present laboratory studies of filamentation as a function of pressure, down to 0.2 atm, which corresponds to altitudes higher than 10 km. These filamentation studies have been performed in a single filament configuration. The measurements presented here concern mainly air conductivity measurements [20–22]. However, because we found some disagreements between our results and simulations, we have performed additional measurements using heterodyne radiometric detection in the sub-THz range [23–31]. Both experimental techniques yield similar results.

\* Corresponding author. Tel.: +33 1 69 31 97 02; fax: +33 1 69 31 99 96.  
E-mail address: [gregoire.mechain@ensta.fr](mailto:gregoire.mechain@ensta.fr) (G. Méchain).

The experimental setup and the methods, procedures and conditions of the measurements are described in Section 2. In Section 3, the data are presented and compared with the numerical studies of Ref. [1]. We focus especially on the behavior of the filament length as a function of pressure.

## 2. Experimental setup and measurement methods

The experimental setup is presented in Fig. 1. The laser system is a Ti:sapphire CPA (Chirp Pulse Amplification) laser system operating at 10 Hz and delivering a maximum output power of 0.2 TW per pulse. The pulse duration has been characterized using an autocorrelation setup and is equal to 130–135 fs (FWHM). The beam at the output of the compressor is roughly Gaussian with a waist equal to 10.4 mm. This beam is truncated by a circular aperture whose radius is equal to 4.5 mm in order to have a more stable beam shape with a perfect circular symmetry. A Galilean telescope further reduces the beam by a factor roughly equal to 2. The final laser beam profile after the telescope has been characterized by a calibrated CCD-camera. Fig. 2 represents this beam profile, fitted by a super-Gaussian profile whose radius at  $1/e^2$  is equal to 2.32 mm.

After the telescope, the laser beam is focused inside a tube assembly by using a converging lens having a two meter focal length. The air pressure inside the tube can be controlled from 0.2 to 1 atm. The tube consists in a 1.5 m glass tube followed by metallic tubes of various lengths. A special cell with two electrodes can be inserted to allow conductivity measurements at various distances and pressures. These measurements are performed by recording the electric conduction of the plasma channel using the method described in a previous work [20]. A voltage of 800 V is applied between two copper electrodes drilled in their center and separated by 25 mm (see Fig. 1). The conducting plasma column formed by the self-guided pulse closes the electric circuit. The peak of the induced current between the electrodes is measured through a load resistance  $R = 8.2 \text{ k}\Omega$  linked to a fast digital oscilloscope (1-GHz bandwidth). All curves presented here have been obtained using the same procedure. Each point represents the average on three measurements. Each mea-

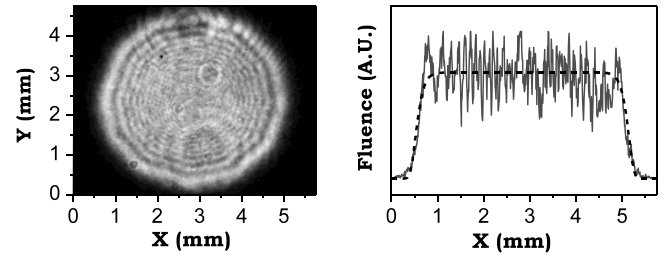


Fig. 2. Left: Beam profile measured with a calibrated CCD camera just before the focusing lens. Right: Fluence profile taken along the horizontal diameter of the beam (solid line) and super-Gaussian fit (dashed line) following the relationship  $I(r) \propto \exp[-2(\frac{r}{w_0})^n]$ , with  $n = 22$  and  $w_0 = 2.32 \text{ mm}$ .

surement corresponds to the highest value obtained in a consecutive series of 100 laser shots.

The sub-terahertz radiation emitted by the plasma channel has been detected via an heterodyne radiometer. The detailed description of the detector is reported in Ref. [32]. The detection frequency is  $91(\pm 3) \text{ GHz}$ . The detector is aligned perpendicularly to the plasma channel direction. The emission of the electromagnetic pulse (EMP) is collected inside the corrugated horn of a radiometer with two Teflon lenses, with a focal length equal to 80 mm. The lenses are transparent in the spectral range of interest and have a corrugated structure to avoid reflections. In order to perform the radiometric measurements at different pressures, a cross-shaped tube with two Teflon windows facing one another is used and can be set at different positions along the plasma channel.

In order to correlate the radiometric measurements and the conductivity measurements, we have first compared both signals, pulse after pulse, at a given position (170 cm from the focusing lens) where the conductivity is quite high. The results of these fluctuation and correlation studies is represented in Fig. 3. As can be noticed, the correlation is excellent. Another comparison is performed by measuring the plasma length with both methods (see Fig. 4), showing again good agreement. As a conclusion, the radiometric measurements validate the conductivity measurements. Only the conductivity measurements will be presented in the rest of this paper, since the radiometric measurements have a smaller dynamic range.

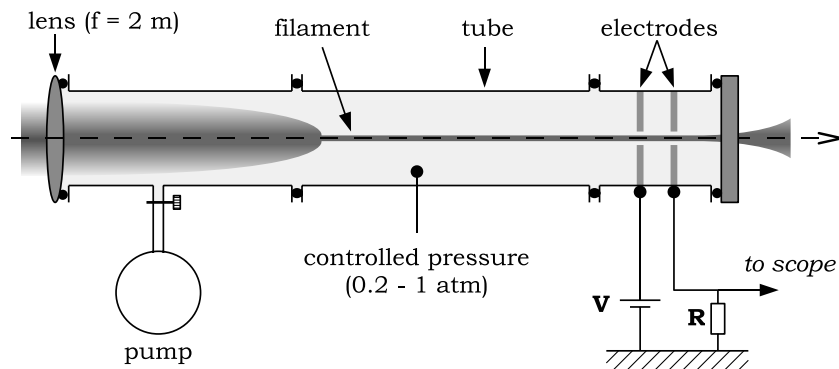


Fig. 1. Experimental setup used for low pressure measurements of the conductivity of the filament.

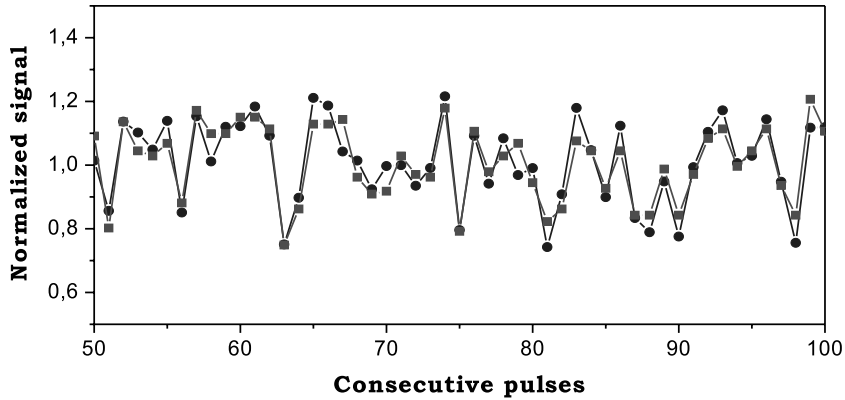


Fig. 3. Measurement of the conductivity (circles) and radiometric heterodyne signal radiated at 91 GHz (squares) recorded simultaneously at the same position.

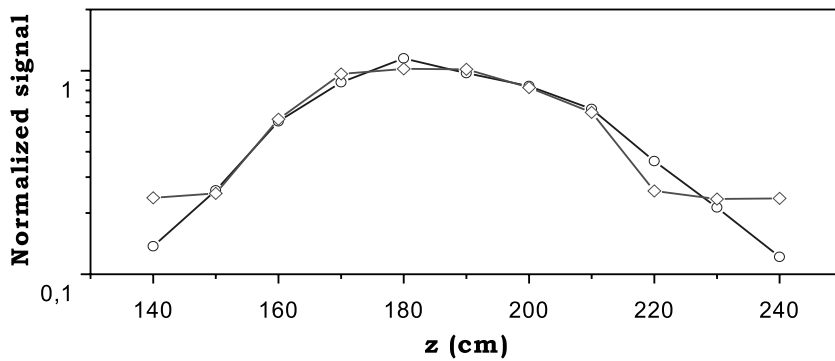


Fig. 4. Filament characterization: Comparison between conductivity measurements and radiometric heterodyne measurements (diamonds = radiometric measurement, circles = conductivity measurement).

**3. Experimental results and discussion**

The measurements, presented in Fig. 5, were performed with an incident energy of 3.7 mJ, which is the

maximum energy that produces a single plasma channel. One notices several features. First, the filamentation subsists even at our lowest pressure of 0.2 atm. Second, the maximum signal is clamped to the same value. Finally,

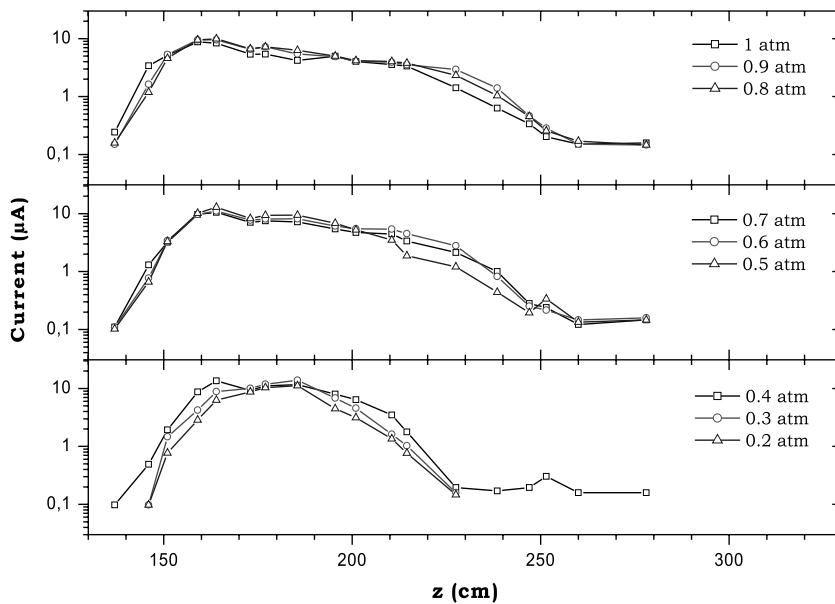


Fig. 5. Evolution of the conductivity of the filament along the optical axis with an energy equal to 3.7 mJ/pulse.  $z$  is the distance from the focusing lens. The presented signal corresponds to the current in the load resistance. The measurements have been performed for different pressures inside the tube, varying from 0.2 to 1 atm.

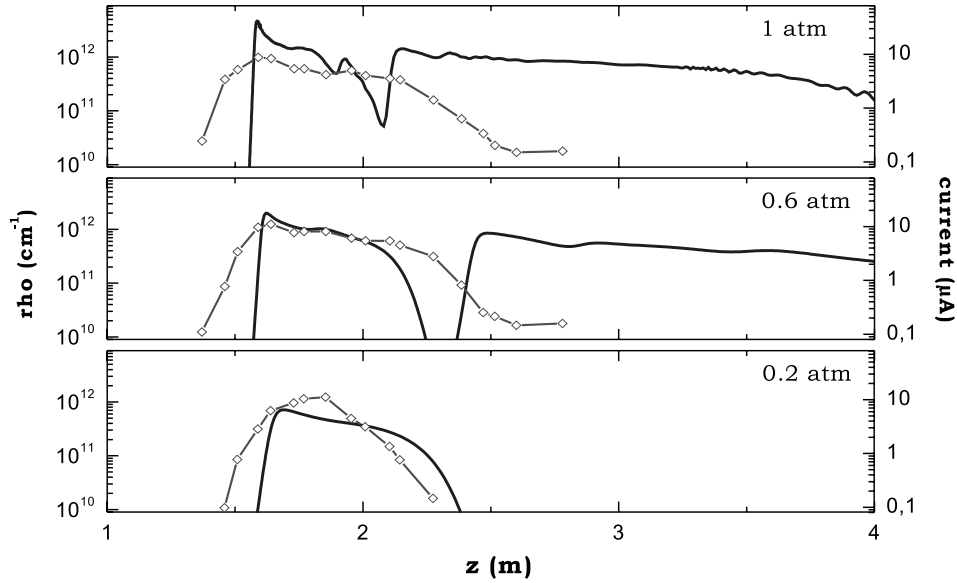


Fig. 6. Comparison between the experimental results at 3.7 mJ (diamonds, scale on the right axis) and numerical simulations (line, scale on the left axis) of the number of electrons per length unit ( $\rho$ ) for 3 pressures (0.2, 0.6 and 1 atm). A super-Gaussian beam profile is used as in Fig. 7.

the total length of the filament diminishes at the lowest pressures.

Using the method and the numerical model described in Ref. [1], we have performed numerical simulations adapted to our experimental setup and conditions. Fig. 6 represents simulations that have been performed for three different representative pressures: 0.2, 0.6 and 1 atm using a super-Gaussian initial beam shape which closely fits the measured beam profile.

We now compare the results of Fig. 5 to the numerical results. In Fig. 6, we plot the experimental results obtained with a pulse energy of 3.7 mJ at three representative pressures together with numerical simulations. As can be seen, the numerical results reproduce well the first portion of the filament including the magnitude of the signal and the location of the start of the filament. The discrepancy concerning the total length of the plasma column for 0.6 and 1 atm appear when we introduce the super-Gaussian input beam in the simulations. A Gaussian input beam, although farther from the experimental input beam leads to a good

agreement for the length of the plasma channel. We also note that by reducing the pulse energy by a factor of two with the super-Gaussian beam, the extension of the plasma channel vanishes (see Fig. 7), we retrieve the experimental data. From the observed discrepancy, we conclude first of all that the modulations in the input beam which are produced by the circular aperture have an influence in the dynamics and cannot simply be considered as noise and averaged. Second, the ionization rates in our model are computed from the Keldysh formulation taken in the multiphoton limit. Some authors correct these rates by numerical factors to approach the effective ionization rates [33]. The length of the plasma channel, in particular the presence of a refocusing clearly depend on these rates. A closer inspection of the numerical data explains why the measured air resistivity is approximately constant for all pressures. The diameter of the plasma column increases with decreasing pressure while the on-axis electron density decreases correspondingly, keeping the integrated electron density approximately constant. On the other hand, the experimental signal is proportional to the number of charges integrated over a plasma channel cross-section.

#### 4. Conclusion

Following the simulations performed in part one, we studied experimentally the behavior of femtosecond light filaments in air at low pressures. The possibility of filamentation in air at pressures as low as 0.2 atm has been demonstrated. This corresponds to a vertical propagation at an altitude greater than 10 km, which is fundamental for LIDAR or lightning triggering applications. Besides, the reduction of the plasma channel length has been observed as the pressure decreases, which validates the simulations performed in Ref. [1]. Experimentally, the effect of the

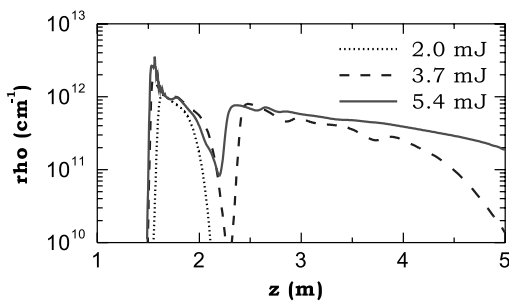


Fig. 7. Numerical simulations of the number of electrons per length unit ( $\rho$ ) for three different incident energies: 2, 3.7 and 5.4 mJ. The pressure is 0.6 atm. A super-Gaussian beam profile,  $I(r) \propto \exp[-2(\frac{r}{w_0})^n]$ , with  $n = 22$  and  $w_0 = 2.32$  mm, is used.

pressure on the position of the onset of the filament follows that predicted by Marburger's law for the position of the nonlinear focus which is shifted a few cm toward the focus of the lens when pressure decreases to 0.2 atm. In addition, we note both experimentally and theoretically that the maximum conductivity level is clamped to a value that is almost not affected by the pressure variation. The simulations performed with input beams roughly mimicking the experimental intensity profile predict that plasma columns are longer than measured. This discrepancy in the length of the plasma channel indicated that not only the averaged intensity profile could affect the propagation dynamics but also the diffraction rings introduced by the inverse telescope. The ionization rates were also found to play a key role in the formation of an extended plasma channel.

## References

- [1] A. Couairon, M. Franco, G. Méchain, T. Olivier, B. Prade, A. Mysyrowicz, *Opt. Commun.*, submitted for publication.
- [2] J.H. Marburger, *Prog. Quant. Electron.* 4 (1975) 35.
- [3] A. Braun, G. Korn, X. Liu, D. Du, J. Squier, G. Mourou, *Opt. Lett.* 20 (1) (1995) 73.
- [4] E.T.J. Nibbering, P.F. Curley, G. Grillon, B.S. Prade, M.A. Franco, F. Salin, A. Mysyrowicz, *Opt. Lett.* 21 (1) (1996) 62.
- [5] A. Brodeur, C.Y. Chien, F.A. Ilkov, S.L. Chin, O.G. Kosareva, V.P. Kandidov, *Opt. Lett.* 22 (5) (1997) 304.
- [6] H.R. Lange, G. Grillon, J.-F. Ripoche, M.A. Franco, B. Lamouroux, B.S. Prade, A. Mysyrowicz, E.T.J. Nibbering, A. Chiron, *Opt. Lett.* 23 (2) (1998) 120.
- [7] M. Mlejnek, M. Kolesik, E.M. Wright, J.V. Moloney, *Phys. Rev. Lett.* 83 (15) (1999) 2938.
- [8] B. La Fontaine, F. Vidal, Z. Jiang, C.Y. Chien, D. Comtois, A. Desparois, T.W. Johnston, J.-C. Kieffer, H. Pépin, *Phys. Plasmas* 6 (1999) 1615.
- [9] G. Méchain, A. Couairon, Y.-B. André, C. D'Amico, M. Franco, B. Prade, S. Tzortzakis, A. Mysyrowicz, R. Sauerbrey, *Appl. Phys. B* 79 (2004) 379.
- [10] G. Méchain, C. D'Amico, Y.-B. André, S. Tzortzakis, M. Franco, B. Prade, A. Mysyrowicz, A. Couairon, E. Salmon, R. Sauerbrey, *Opt. Commun.* 247 (2005) 171.
- [11] L. Wöste, C. Wedekind, H. Wille, P. Rairoux, B. Stein, S. Nikolov, C. Werner, S. Niedermeier, F. Ronneberger, H. Schillinger, R. Sauerbrey, *Laser Optoelektron.* 29 (5) (1997) 51.
- [12] P. Rairoux, H. Schillinger, S. Neirdeimer, M. Rodriguez, F. Ronneberger, R. Sauerbrey, B. Stein, D. Waite, C. Wedekind, H. Wille, L. Wöste, C. Ziener, *Appl. Phys. B* 71 (2000) 573.
- [13] M. Rodriguez, R. Bourayou, G. Méjean, J. Kasparian, J. Yu, E. Salmon, A. Scholz, B. Stecklum, J. Eislöffel, U. Laux, A.P. Hatzes, R. Sauerbrey, L. Wöste, J.-P. Wolf, *Phys. Rev. E* 69 (2004) 036607.
- [14] D. Comtois, C.Y. Chien, A. Desparois, F. Génin, G. Jarry, T.W. Johnston, J.-C. Kieffer, B. La Fontaine, F. Martin, R. Mawassi, H. Pépin, F.A.M. Rizk, F. Vidal, P. Couture, H.P. Mercure, C. Potvin, A. Bondiou-Clergerie, I. Gallimberti, *J. Appl. Phys.* 76 (7) (2000) 819.
- [15] B. La Fontaine, D. Comtois, C.Y. Chien, A. Desparois, F. Génin, G. Jarry, T.W. Johnston, J.-C. Kieffer, F. Martin, R. Mawassi, H. Pépin, F.A.M. Risk, F. Vidal, C. Potvin, P. Couture, H.P. Mercure, *J. Appl. Phys.* 88 (2) (2000) 610.
- [16] P. Rambo, J. Schwarz, J.-C. Diels, *J. Opt. A* 3 (2001) 146.
- [17] S. Tzortzakis, B. Prade, M. Franco, A. Mysyrowicz, S. Hüller, P. Mora, *Phys. Rev. E* 64 (2001) 057401.
- [18] M. Rodriguez, R. Sauerbrey, H. Wille, L. Wöste, T. Fujii, Y.-B. André, A. Mysyrowicz, L. Klingbeil, K. Rethmeier, W. Kalkner, J. Kasparian, E. Salmon, J. Yu, J.-P. Wolf, *Opt. Lett.* 27 (2002) 772.
- [19] N. Khan, N. Mariun, I. Aris, J. Yeak, *New J. Phys.* 4 (61) (2002) 1.
- [20] S. Tzortzakis, M.A. Franco, Y.-B. André, A. Chiron, B. Lamouroux, B.S. Prade, A. Mysyrowicz, *Phys. Rev. E* 60 (1999) R3505.
- [21] H. Schillinger, R. Sauerbrey, *Appl. Phys. B* 68 (1999) 753.
- [22] H.D. Ladouceur, A.P. Baranavski, D. Lohrmann, P.W. Grounds, P.G. Girardi, *Opt. Commun.* 189 (2001) 107.
- [23] C.-C. Cheng, E.M. Wright, J.V. Moloney, *Phys. Rev. Lett.* 97 (2001) 213001 1.
- [24] G. Shvets, I. Kaganovich, E. Startsev, *Phys. Rev. Lett.* 89 (13) (2002) 139301.
- [25] C.-C. Cheng, E.M. Wright, J.V. Moloney, *Phys. Rev. Lett.* 89 (13) (2002) 139302.
- [26] V.T. Tikhonchuk, *Phys. Rev. Lett.* 89 (20) (2002) 209301.
- [27] P. Sprangle, J.R. Peñano, B. Hafizi, C.A. Kapetanacos, *Phys. Rev. E* 69 (6) (2004) 066415.
- [28] J.R. Peñano, P. Sprangle, B. Hafizi, A. Ting, D.F. Gordon, C.A. Kapetanacos, *Phys. Plasmas* 11 (5) (2004) 2865.
- [29] W. Hoyer, A. Knorr, J. Moloney, E. Wright, M. Kira, W. Koch, *Phys. Rev. Lett.* 94 (11) (2005) 115004.
- [30] A. Proulx, A. Talebpour, S. Petit, S.L. Chin, *Optics Commun.* 174 (2000) 305.
- [31] G. Méchain, S. Tzortzakis, B. Prade, M. Franco, A. Mysyrowicz, B. Leriche, *Appl. Phys. B* 77 (2003) 707.
- [32] S. Tzortzakis, G. Méchain, G. Palatano, Y.-B. André, M. Franco, B. Prade, A. Mysyrowicz, *Opt. Lett.* 27 (21) (2002) 1944.
- [33] A. Talebpour, J. Yang, S.L. Chin, *Opt. Commun.* 163 (1–3) (1999) 29.

## High current permanent discharges in air induced by femtosecond laser filamentation

A. Houard, C. D'Amico, Y. Liu, Y. B. Andre, M. Franco, B. Prade, and A. Mysyrowicz<sup>a)</sup>  
*Laboratoire d'Optique Appliquée, ENSTA, Ecole Polytechnique, CNRS UMR 7639, 91761  
 Palaiseau, France*

E. Salmon  
*LASIM, Université Lyon 1, CNRS UMR 5579, 69622 Villeurbanne, France*

P. Pierlot and L.-M. Cleon  
*Agence d'Essai Ferroviaire, SNCF, 21 Av. du Président Allende, 94407 Vitry-sur-Seine, France*

(Received 19 February 2007; accepted 4 April 2007; published online 27 April 2007)

Filaments created in air by an intense femtosecond laser pulse in the presence of an electric field generate a highly conductive permanent plasma column. © 2007 American Institute of Physics.

[DOI: [10.1063/1.2734396](https://doi.org/10.1063/1.2734396)]

There is currently a wide interest in the process of femtosecond laser filamentation in air (for a recent review see Ref. 1). During its propagation in air, an intense short IR laser pulse first undergoes self-focusing, because of the optical Kerr effect, until the peak intensity on axis becomes high enough ( $\sim 5 \times 10^{13}$  W/cm<sup>2</sup>) to ionize air molecules. The ionization process involves the simultaneous absorption of eight to ten infrared photons. It has therefore a threshold-like behavior and a strong clamping effect on the intensity in the self-guided pulse. A dynamical competition then starts taking place between the self-focusing effect due to the optical Kerr effect and the defocusing effect due to the created plasma. As a result, the pulse maintains a small beam diameter and high peak intensity over large distances. In the wake of the self-guided pulse, a plasma column is created with an initial density of  $10^{16}$ – $10^{17}$  e/cm<sup>3</sup> over a distance which depends on initial laser conditions. This length is typically 1 m for a pulse initial power close to the minimum value  $P_{cr}$  required for filamentation (5 GW for an IR pulse at 800 nm under normal air conditions) and can reach hundreds of meters at higher powers.

It has been demonstrated that this plasma column is able to trigger and guide high voltage electric discharges between two electrodes in contact with the plasma column.<sup>2,3</sup> Remarkably, there is a noticeable delay between the arrival of the laser pulse and the initiation of the discharge. A model has been developed which reproduces quantitatively this delayed initiation of the discharge in laboratory experiments.<sup>2</sup> In short, the short-lived plasma leads, in the presence of an electric field, to Joule heating of a thin air column. After plasma recombination, the expansion of the heated air column leads to a central depression canal, which initiates and guides the electric discharge. Up to 4 m long electric discharges have been produced with megavolt applied voltage.<sup>4–6</sup> Although many features of these long discharges were similar to those carried on a centimeter scale in the laboratory, and therefore point out to a similar thermally driven discharge initiation, the more complex boundary conditions of the experiment prevented meaningful simulations to test the model.

There are many potential applications of filament-triggered discharges (laser lightning rod, fast switch for high voltage connection, etc.). In this letter, we address another potential application, namely, the contactless capture of current. A crucial requirement for such an application is the resistivity of the produced plasma, which must remain low in order to minimize unwanted power dissipation. Other important questions concern the amount of current such a discharge is able to carry, and the plasma lifetime, which should be long enough so that the plasma column is sustained between successive laser shots even at a low repetition rate. In order to address these questions, experiments have been performed using the Teramobile laser in conjunction with electric power facility designed to test the motors of high-speed trains (TGV).

The Teramobile laser is a mobile chirp pulse amplification laser system based on titanium:sapphire technology delivering pulses of 100 fs duration, with a peak power of several terawatts and a repetition rate of 10 Hz.<sup>7</sup> The laser beam was focused in air with a telescope of 25 m focal length. This led to the formation of a bundle of about 40 plasma filaments over a distance of  $\sim 5$  m. Two electrodes consisting of cylindrical copper blocks of 3 cm diameter were placed 2 m beyond the beginning of the filaments. At this point the diameter of the filament bundle was  $\sim 7$  mm. It crossed through a 5 mm diameter hole pierced in the first electrode and impinged on the second electrode. The distance between the two electrodes could be varied between 3 and 60 mm. In some experiments, both electrodes were pierced, letting the filament bundle through, with no significant change in the results. The electric voltage applied across the electrodes was either dc voltage of 4 kV or ac of 20 kV. In all measurements, we checked that no spontaneous discharge occurred in the absence of a laser pulse. The current flowing through the plasma when triggered by the laser generated filaments was measured with a coaxial shunt (Fig. 1).

Experiments were also carried out with first electrode hole diameters of 4 and 3 mm with no significant change in the results. However, we could not reach the limit of a single filament because of alignment difficulties.

A typical result in the case of a 3 kV dc voltage is shown in Fig. 2(a) for an electrode separation of 4 mm. One notices a sudden drop (within the detection time resolution of

<sup>a)</sup>Electronic mail: [andre.mysyrowicz@ensta.fr](mailto:andre.mysyrowicz@ensta.fr)

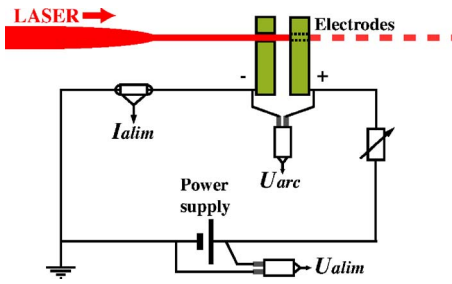


FIG. 1. (Color online) Experimental setup.

$\sim 2$  ms) of the voltage across the electrodes while simultaneously the current reaches 250 A, the maximum value allowed by the power supply. The power dissipation in the plasma was around 8 kW, yielding an Ohmic resistance of less than  $0.1 \Omega/\text{cm}$ . This high conductivity is maintained for the duration of the applied voltage (1.2 s). If the voltage is applied for a longer duration, melting of the electrodes occurs. The melting is accompanied by a thermally driven displacement of the plasma to the top of the electrodes. In this case, the dissipation in the discharge increases significantly, as shown in Fig. 2(b). A triggering rate of 80% was obtained for several hundreds of attempts. In no case, a spontaneous discharge occurred in the absence of a laser shot.

Experiments were also carried out with ac voltage. Figure 3(a) shows the current flowing through the electrodes with a peak voltage of 20 kV at 50 Hz. After the onset of filamentation, the applied voltage drops to near zero and a 50 Hz alternative current flows between the electrodes. The high conducting discharge could be obtained over a distance of up to 6 cm, with a peak current again limited by the power supply. The average power dissipation in the ac mode was 8000 W for a current of 8.9 A rms, yielding an average resistance  $R/l \sim 25 \Omega/\text{cm}$ . Triggering of the discharge occurred preferentially when the negative voltage crest was synchronous with the laser pulse. Triggering on the positive crest was also observed, but with less statistical success. In some instances, we observed the discharge occurring at the peak of the negative crest while the laser was coincident with the positive crest [see Fig. 3(b)].

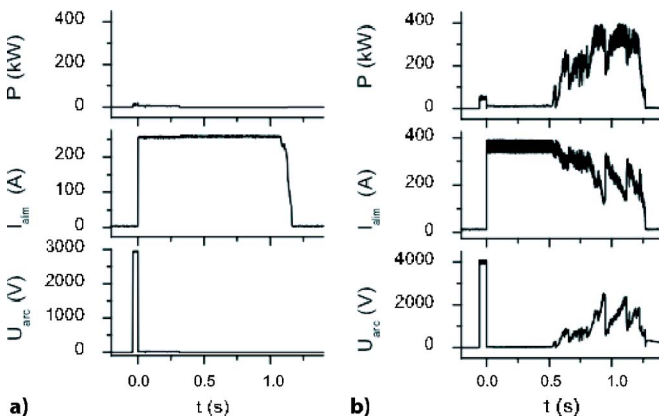


FIG. 2. (Color online) (a) Evolution of the voltage ( $U_{\text{arc}}$ ), current flowing ( $I_{\text{alim}}$ ), and dissipated power ( $P$ ) between the two electrodes. The voltage is applied during 1.5 s and the laser pulse arrived at  $t=0$  s. The current discharge is triggered by the laser filaments. (b) Evolution of the voltage ( $U_{\text{arc}}$ ), current flowing ( $I_{\text{alim}}$ ), and dissipated power ( $P$ ) between the electrodes when the guided discharge transforms into an arc (at  $t=0.5$  s).

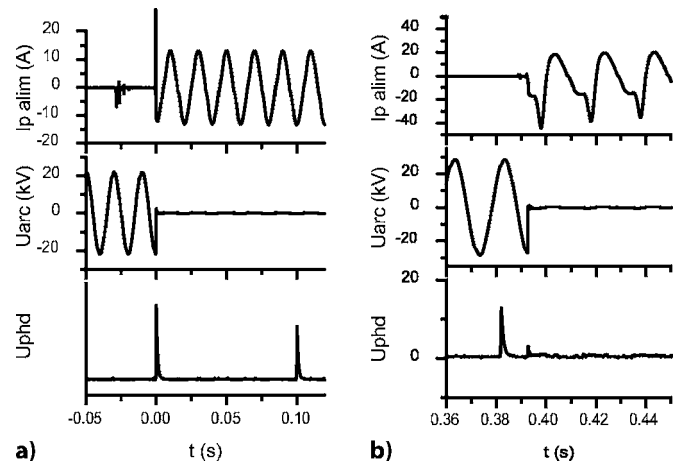


FIG. 3. (Color online) (a) Evolution of the ac voltage across the electrodes ( $U_{\text{arc}}$ ) and current flowing between the electrodes ( $I_{p \text{ alim}}$ ). At the bottom the photodiode signal ( $U_{\text{phd}}$ ) also gives the arrival time of the laser pulse on the electrode. Here  $t=0$  s correspond to the formation of the trigger laser filament. (b) Same experiment but with a delay between the laser pulse and the discharge initiation.

To discuss the results we first note that the applied voltage obviously converts the initial cold, low-density plasma into a high conducting, high temperature, and long-lived plasma column. One can estimate the final plasma temperature by noting that in order to account for the measured plasma resistance, one must assume that all molecules in air become singly ionized. In this case, the plasma conductivity  $\sigma$  ( $\Omega^{-1} \text{cm}^{-1}$ ) can be expressed with the Spitzer formula,<sup>8</sup>

$$\sigma = \frac{l}{RS} = \frac{n_e e^2}{m_e v_{ei}} = 1.53 \times 10^{-4} \frac{T_e^{3/2}}{Z \ln \Lambda},$$

where  $n_e$  is the electron density,  $v_{ei}$  the electron-ion collision frequency,  $T_e$  is the electronic temperature (in K), and  $\ln \Lambda$  is the Coulomb logarithm,

$$\ln \Lambda = 23 - \ln \left( \frac{Z \sqrt{n_e}}{(T_e)^{3/2}} \right).$$

For  $n_e = 10^{19} \text{cm}^{-3}$ ,  $Z=1$ ,  $S=2 \text{cm}^2$ , and  $R/l = 0.17 \Omega \text{cm}^{-1}$ , we obtain a temperature  $T_e = 3.5 \times 10^4 \text{K} \sim 3 \text{eV}$ .

Concerning the kinetics of plasma evolution, from a low-density initial plasma ( $n_e \sim 10^{16} - 10^{17} \text{cm}^{-3}$ ) to a fully ionized plasma, we note that in some instances the discharge was observed with a significant delay  $dt \approx 10 \text{ms}$  [see Fig. 3(b)]. We therefore tentatively attribute the initiation of the discharge to the same mechanism, as discussed in Ref. 3, namely, a thermally induced effect.

In conclusion, the plasma generated by femtosecond laser filaments has a low Ohmic resistivity, and it is able to carry a large current, either dc or ac over a long time  $>1$  s. These features are promising for applications such as the contactless capture of current.

The authors are grateful to M. Pellet from DGA and to Steffan Hüller for fruitful discussions.

<sup>1</sup>A. Couairon and A. Mysyrowicz, Phys. Rep. **441**, 47 (2007).

<sup>2</sup>S. Tzortzakis, M. Franco, Y.-B. André, A. Chiron, B. Lamouroux, B. Prade, and A. Mysyrowicz, Phys. Rev. E **60**, R3505 (1999).

- <sup>3</sup>S. Tzortzakis, B. Prade, M. Franco, A. Mysyrowicz, S. Hüller, and P. Mora, *Phys. Rev. E* **64**, 057401 (2001).
- <sup>4</sup>M. Rodriguez, R. Sauerbrey, H. Wille, L. Wöste, T. Fujii, Y.-B. André, A. Mysyrowicz, J. Kasparian, E. Salmon, J. Yu, and J.-P. Wolf, *Opt. Lett.* **27**, 772 (2002).
- <sup>5</sup>R. Ackermann, G. Méchain, G. Méjean, R. Bourayrou, M. Rodriguez, K. Stelmaszczyk, J. Kasparian, J. Yu, E. Salmon, S. Tzortzakis, Y.-B. André, J.-F. Bourrillon, L. Tamin, J.-P. Cascelli, C. Campo, C. Davoise, A. Mysyrowicz, R. Sauerbrey, L. Wöste, and J.-P. Wolf, *Appl. Phys. B: Lasers Opt.* **82**, 561 (2006).
- <sup>6</sup>R. Ackermann, K. Stelmaszczyk, P. Rohwetter, G. Mejean, E. Salmon, J. Yu, G. Mechain, J. Kasparian, V. Bergmann, S. Schaper, B. Weise, T. Kumm, K. Rethmeier, W. Kalkner, J.-P. Wolf, and L. Wöste, *Appl. Phys. Lett.* **85**, 23 (2004).
- <sup>7</sup>H. Wille, M. Rodriguez, J. Kasparian, D. Mondelain, J. Yu, A. Mysyrowicz, R. Sauerbrey, J. P. Wolf, and L. Wöste, *Eur. Phys. J.: Appl. Phys.* **20**, 183 (2002).
- <sup>8</sup>L. Spitzer, *Physics of Fully Ionized Gases* (Interscience, New York, 1955), 91.

P. BÉJOT<sup>1,2</sup>  
J. KASPARIAN<sup>2,✉</sup>  
E. SALMON<sup>2</sup>  
R. ACKERMANN<sup>2</sup>  
J.-P. WOLF<sup>1</sup>

# Spectral correlation and noise reduction in laser filaments

<sup>1</sup> GAP, Université de Genève, 20 rue de l'École de médecine, 1211 Genève, Switzerland

<sup>2</sup> LASIM, UMR CNRS 5579, Université Lyon 1, 43 bd du 11 Novembre 1918, 69622 Villeurbanne Cedex, France

Received: 30 October 2006

Published online: 31 January 2007 • © Springer-Verlag 2007

**ABSTRACT** Intensity correlations and noise reduction are observed and characterized in the broadband supercontinuum generated by spatio-temporal solitons propagating in air, i.e., in filamentation of ultrashort laser pulses. Large correlations and reduction of the laser noise are observed already at the first steps of the filamentation process, while further propagation results in cascaded  $\chi^{(3)}$  broadening processes and yield complex correlation maps. The spectral range yielding an optimal laser noise reduction of 3.6 dB is found to cover 10 nm around the fundamental wavelength.

**PACS** 42.65.Jx; 42.65.Tg; 42.65.Ky; 42.50.Lc

## 1 Introduction

Recent studies on optical fibers showed that spectral correlations and squeezing occur in temporal solitons [1–8]. The origin of correlations in the intensity fluctuations within the white light continuum is intrinsic to spectral broadening by  $\chi^{(3)}$  Kerr effect [9, 10]. Such  $\chi^{(3)}$  broadening includes both self-phase modulation (SPM), cross-phase modulation (CPM) and four-wave mixing (FWM). SPM and CPM correspond to the deformation of the temporal envelope of the pulse, while FWM describes the interaction of two incident waves at wavelengths  $\lambda_0$  and  $\lambda'_0$ , which are converted into a pair of photons at the conjugated wavelengths  $\lambda_1$  and  $\lambda_2$ , for which the energy conservation imposes  $1/\lambda_0 + 1/\lambda'_0 = 1/\lambda_1 + 1/\lambda_2$ . Both SPM and FWM result in typical correlation maps within the spectrum at the exit of the fiber. The wavelengths within the side of the continuum appear anticorrelated with the incident one, while pairs of conjugated wavelengths are strongly correlated [1]. Such correlation maps are very well reproduced by numerical simulations in optical fibers [11]. These simulations also show that photons originating from  $\chi^{(3)}$  broadening can in turn undergo subsequent cascaded  $\chi^{(3)}$ -induced events. The resulting depletion of the corresponding wavelengths results in a more complex correlation map within the continuum [12]. This process occurs at further propagation distances and higher pulse energy,

i.e., for higher order solitons. For sufficiently short pulses, phase correlations have been observed within the continuum, i.e., the continuum has a high coherence [13, 14], although such phase correlations are beyond the scope of the present work.

Although remaining in the classical domain, intensity correlations within the white-light continuum, as well as laser noise compression, have also recently been observed in the case of spatio-temporal solitons, namely self-guided filaments generated in the air by high-power, ultrashort laser pulses [15]. Filaments [16] arise in the non-linear propagation of ultrashort, high-power laser pulses in transparent media. They result from a dynamic balance between Kerr-lens focusing and defocusing by self-induced plasma generation. In the atmosphere, filaments have been observed over several hundreds of meters, up to a few kilometers away from the laser source [17]. They can be generated and propagated even in perturbed conditions such as clouds [18] or turbulence [19]. These properties open the way to atmospheric applications [20], such as LIDAR remote sensing, laser-induced breakdown spectroscopy (LIBS) [21], lightning control [22] and free space communications. For example, high sensitivity multi-pollutant detection with a “white-light LIDAR” [20] would greatly benefit of a reduced shot-to-shot noise on the supercontinuum intensity due to the recently observed noise reduction [15].

As described above, the generation of the supercontinuum originates from cascaded  $\chi^{(3)}$  events. At the beginning of the process, the fundamental radiation  $\omega_0$  generates photon pairs at  $\omega_1$  and  $\omega_2$ , such that  $2\omega_0 = \omega_1 + \omega_2$ . However, once the continuum intensity is sufficient, the generated wavelengths in turn can undergo four-wave mixing. Therefore, a given wavelength can be generated through a large number of pathways and correlations within the spectrum may be reduced or even lost after some propagation distance.

In this paper, we extend the previous experimental results [15] by investigating the build-up and the evolution of correlations observed within the spectrum of the white-light continuum, with propagation and for increasing beam power. These results are compared with simple simulations based on SPM. Moreover, the influence of the integration window within the spectrum of the supercontinuum is investigated, providing an optimal filtering scheme for laser noise reduction in laser filaments.

✉ Fax: +33 472445871, E-mail: jkaspari@lasim.univ-lyon1.fr

## 2 Experimental setup

The experimental setup is depicted in Fig. 1. A CPA (chirped pulse amplification) Ti:sapphire laser system delivered 200 fs pulses at 22.5 Hz repetition rate, centered at 815 nm, with  $\sim 10$  mm beam diameter (at  $1/e^2$  level). The pulse energy could be varied from 1 to 6 mJ. The beam was focused by a spherical mirror with 5 m focal length, yielding a non-linear focus (filament onset)  $\sim 3$  m downstream of the spherical mirror. The spherical mirror was defined as the origin of the propagation axis ( $z = 0$ ). The filament length was  $\sim 4$  m. At given distances  $z$  comprised between 2 and 12 m, the beam was scattered on a spectrally neutral target, and the light was collected with a fiber into a spectrometer providing 0.3 nm resolution between 725 and 900 nm. In each experimental condition, 5000 spectra were recorded, normalized to 1 and used to compute the cross-correlation map of the intensity fluctuations across the spectrum. The correlation between two wavelengths  $\lambda_1$  and  $\lambda_2$ , was calculated as:

$$C(\lambda_1, \lambda_2) = \frac{V(n_1 + n_2) - (V(n_1) + V(n_2))}{2\sqrt{V(n_1)V(n_2)}}, \quad (1)$$

where  $V(x)$  is the variance of variable  $x$  and  $n_i$  the photon number (or, equivalently, the intensity), at the wavelength  $\lambda_i$ .

## 3 Results and discussion

### 3.1 Correlations of the intensity fluctuations

Figure 2 displays the map of cross-correlations of the intensity fluctuations before the onset of the filaments

((a),  $z = 2$  m), shortly after it ((b),  $z = 3.5$  m), and at the filament end ((c),  $z = 8$  m). Before filamentation, correlations are limited to the region corresponding to  $\lambda_1 = \lambda_2$ . The regions of negative correlation are due to a slight jitter of the fundamental wavelength, as suggested by numerical simulations (see below). Once filamentation occurs ( $z \geq 3$  m, i.e., only 0.5 m propagation within the filament, see Fig. 2b), SPM is initiated, and positive correlations are observed in regions corresponding to nearly conjugated wavelengths ( $2\omega_0 = \omega_1 + \omega_2$ ). In contrast, negative correlations form a dark cross centered on the fundamental wavelength. In other words, the generation of the white-light photons requires depletion of the number of photons about the fundamental wavelength. This behavior is the signature for a simultaneous generation of both the Stokes and the anti-Stokes components of the continuum originating from the depletion of the fundamental wavelength of the incident laser [15]. Further propagation of the filament (Fig. 2c) results in a more complicated structure of the correlation map, with stripes of positive and negative correlations appearing around the fundamental wavelength. These stripes are due to the typical oscillatory structure of the supercontinuum generated by  $\chi^{(3)}$  broadening, which results from the beating of the waves generated at each wavelength in two slices of the pulse which have the same time derivative of the intensity [23]. After the filament end, the correlation map does not evolve anymore since the laser intensity is too low to allow further  $\chi^{(3)}$  broadening.

The same evolution is observed when the laser power is progressively increased while the measurement is performed at a fixed position downstream of the filament ( $z = 12$  m, Fig. 3). At low input beam power (1.3 mJ/pulse, i.e., 6.5 GW,

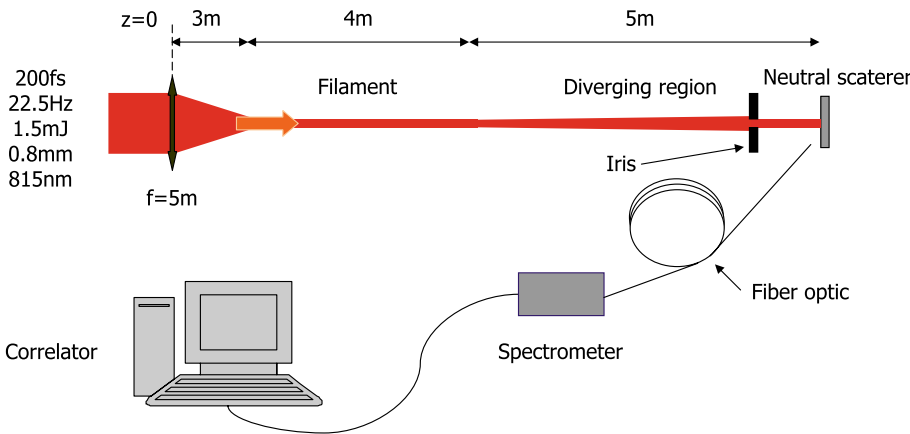


FIGURE 1 Experimental setup

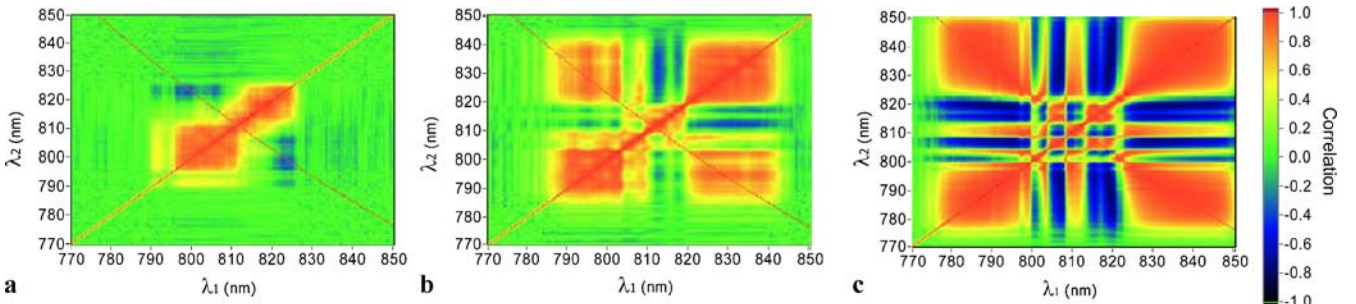


FIGURE 2 Correlation map within the white-light spectrum at the fixed peak power of 6.5 GW ( $\sim$  twice the critical power for filamentation). (a) Before filamentation ( $z = 2$  m); (b) filamentation onset ( $z = 3.5$  m); (c) filament end ( $z = 8$  m)

only twice the critical power for filamentation in air [24]), the pattern typical of a single-step SPM process (Fig. 3a) is observed. Increasing the laser power allows cascaded  $\chi^{(3)}$  broadening events resulting in much more complex patterns (Fig. 3b, 9 GW), and even the disappearance of the correlation between conjugated wavelengths (Fig. 3c, 16 GW). These complex patterns correspond to highly structured spectra of the continuum, as displayed under the correlation maps of Fig. 3.

These results show that intensity correlations within the spectrum of the white-light supercontinuum are generated in the course of self-guided filamentation. The absorption and (incoherent) scattering of light by the plasma which is generated within the filaments does not prevent correlations within the spectrum of the continuum. This is further confirmed by comparing the observed correlations maps (see e.g., Fig. 2b) with numerical simulations for temporal solitons (i.e., in fibers) performed by Schmidt et al. [11]. Although they do not take ionization nor other higher order processes into account, these simulations yield the same characteristic pattern in which each wavelength is correlated with its conjugate but anticorrelated with the fundamental wavelength.

The agreement of these calculations with our experimental results is fairly good, although the spatial resolution of our experiment does not allow observing the longitudinal fluctuations of the correlation map. Moreover, according to the simulations, the square regions with positive correlation in Fig. 2, as well as the positive stripes within the negative correlation cross, stem from higher-order solitons. Now, we observe experimentally such patterns for high powers and/or long propagation distances, i.e., when cumulative broadening occurs.

To further assess the critical role of  $\chi^{(3)}$  broadening in the generation of correlations, we performed a simple simulation of the correlation map. Here, the propagation of the self-guided filament is not described in detail. Instead, only the effect of laser noise on SPM generation is considered. The initial electrical field is defined by its carrier frequency and envelope:

$$E(z, t) = E_0 \cos(\omega_0 t - \Delta\varphi(z, t)) \exp(-t^2/2\tau^2), \quad (2)$$

where  $t = T - z/c$  is the reduced time,  $T$  is the absolute time,  $z$  is the position along the propagation axis,  $c$  is the velocity of light,  $\omega_0$  the frequency of the carrier wave, and  $\tau$  the pulse duration. The envelope  $E(t) = E_0 \exp(-t^2/2\tau^2)$  is used to compute the dephasing  $\Delta\varphi(z, t)$  due to Kerr effect after a propagation distance  $z$  for each temporal slice of the pulse:

$$\Delta\varphi(z, t) = n_2 I z = n_2 E^2(t) z, \quad (3)$$

where  $n_2$  is the non-linear refractive index ( $n_2 = 4 \times 10^{-19} \text{ cm}^2/\text{W}$  in the air at 800 nm [25]). A Fourier transform of the deformed carrier yields the resulting spectrum. To simplify the calculation, we consider that the intensity within the filament is strictly clamped for a given shot [26], so that the SPM-generated spectrum can be calculated within one iteration.

We repeated the calculation for initial intensities and wavelengths randomly fluctuating around the nominal parameters of the experiments (200 fs pulses at 815 nm, with a mean intensity of  $3.3 \times 10^{16} \text{ W/m}^2$ ). The intensity was normally distributed with a standard deviation of  $4.3 \times 10^{15} \text{ W/m}^2$ , as estimated from the experimental data. Moreover, a slight jitter of 0.3 nm on the central wavelength has been added. This fluctuation corresponds to a jitter of the central wavelength between two pixels of the spectrometer. The resulting set of 500 simulated spectra yielded a correlation map, calculated with the same procedure as for experimental data. Figure 4 displays the resulting correlation maps for several propagation distances, similar to those of the experimental results displayed in Fig. 2, namely before filamentation, 0.5 m after the beginning of filamentation and at the filament end, respectively.

The calculated results are very similar to the experimental ones, showing that the dominant process is actually SPM and that the ionization does not jeopardize the correlations in spite of its higher order nonlinearity and lack of coherence (as ionization is not taken into account). Note that the large regions of positive correlation away from the fundamental wavelength stem from the fact that, away from the oscillatory spectrum around the fundamental, both wings of the continuum are generated simultaneously, all the more efficiently that the incident intensity is higher.

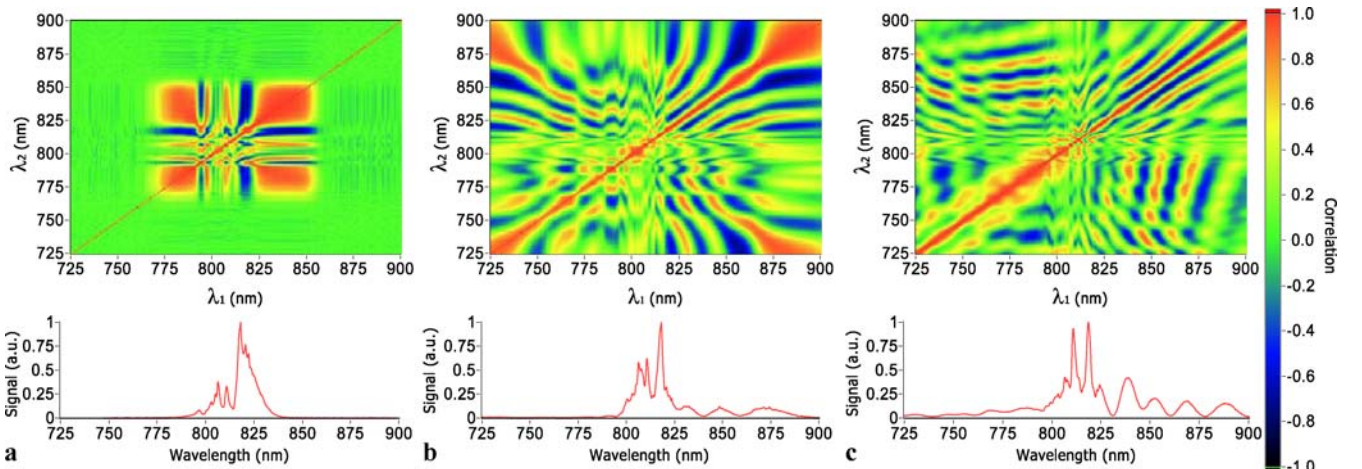


**FIGURE 3** Correlation map within the white-light spectrum at a fixed position  $z = 12$  m, beyond the filament end. (a)  $P = 6.5$  GW, twice the critical power for filamentation; (b)  $P = 9$  GW; (c)  $P = 16$  GW. The panel below each correlation map displays the spectrum of the continuum at the considered power

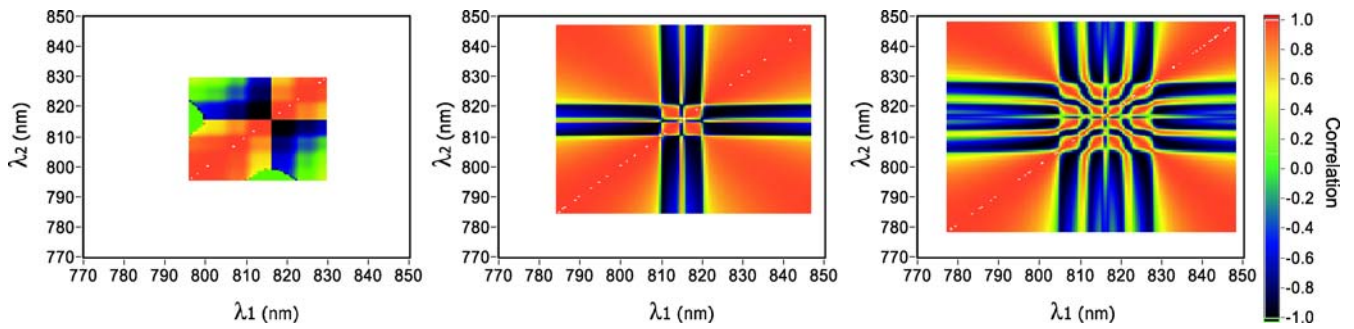


FIGURE 4 Simulated correlation map. (a) Before filamentation ( $z = 2$  m); (b) filamentation onset ( $z = 3.5$  m); (c) filament end ( $z = 8$  m)

### 3.2 Laser noise reduction

The occurrence of correlations within the spectrum allows us to expect noise reduction for adequately selected spectral regions. We have recently reported a laser noise reduction of 1.2 dB in filaments, even though the filter (flat gate open from 785 to 820 nm) was not optimized [15]. The noise reduction of the spectrally filtered filament supercontinuum is defined as  $-10 \log \left( \frac{V(I_{\text{filament}})}{V(I_{\text{ref}})} \right)$ , where  $I_{\text{filament}}$  and  $I_{\text{ref}}$  are the intensities associated with the filament and the unfocused laser beam taken as reference, respectively, integrated over the considered spectral interval. In order to estimate the highest level of compression that would be achievable using filaments, we sought for an optimal filter, restricting ourselves to square bandpass filters within the 750–880 nm spectral range, and considering experimental data with 6.5 GW peak power, corresponding to Fig. 2. The spectral range yielding maximal noise reduction is 809–819 nm, i.e., centered on the incident laser wavelength (815 nm). This range is independent of the propagation distance within the filament. The noise reduction over this optimal spectral range increases from 0.69 dB shortly after the filament onset, to 3.6 dB at the filament end. This value is three times more than reported in [15]. Moreover, it is comparable with the squeezing observed in fibers after correction for the detection losses (e.g., 4.1 dB in microstructured fibers [27] and 3.2 or 3.7 dB for classical fibers [28, 29]), although in our experiment the conditions are far from sub-shot noise. Therefore, soliton propagation in laser-generated self-guided filaments can be expected to be a good candidate for laser-noise reduction.

## 4 Conclusion

As a summary, we have characterized the correlations of the intensity fluctuations and the noise reduction observed in the broadband supercontinuum generated by spatio-temporal solitons propagating in air (filamentation). Large correlations and reduction of the noise is observed already at the first steps of the filamentation process, before multi-step  $\chi^{(3)}$  broadening. Multi-step  $\chi^{(3)}$  broadening results in more complex correlation patterns without reducing the maximum correlation values. An optimal noise squeezing of 3.6 dB is obtained for a 10 nm wide spectral range centered on the fundamental wavelength.

**ACKNOWLEDGEMENTS** We gratefully acknowledge N. Gisin, H. Zbinden (Université de Genève), C. Fabre (ENS, Paris), G. Leuchs (Universität Erlangen) and J. Dudley (Université de Franche-Comte) for very fruitful discussions.

## REFERENCES

- 1 S. Spälter, N. Korolkova, F. König, A. Sizmann, G. Leuchs, Phys. Rev. Lett. **81**, 786 (1998)
- 2 T. Opatrny, N. Korolkova, G. Leuchs, Phys. Rev. A **66**, 053813 (2002)
- 3 S.J. Carter, P.D. Drummond, M.D. Reid, R.M. Shelby, Phys. Rev. Lett. **58**, 1841 (1987)
- 4 M. Rosenbluh, R.M. Shelby, Phys. Rev. Lett. **66**, 153 (1991)
- 5 K. Bergman, H.A. Haus, Opt. Lett. **16**, 663 (1991)
- 6 K. Bergman, C.R. Doerr, H.A. Haus, M. Shirasaki, Opt. Lett. **18**, 643 (1993)
- 7 K. Bergman, H.A. Haus, E.P. Ippen, M. Shirasaki, Opt. Lett. **19**, 290 (1994)
- 8 N. Nishizawa, S. Kume, M. Mori, T. Goto, A. Miyauchi, Japan. J. Appl. Phys. **33**, 138 (1994)
- 9 L. Boivin, F.X. Kärtner, H.A. Haus, Phys. Rev. Lett. **73**, 240 (1994)
- 10 A. Mecozzi, P. Kumar, Opt. Lett. **22**, 1232 (1997)
- 11 E. Schmidt, L. Knöll, D.-G. Welsch, Phys. Rev. A **59**, 2442 (1999)
- 12 E. Schmidt, L. Knöll, D.-G. Welsch, M. Zielonka, F. König, A. Sizmann, Phys. Rev. Lett. **85**, 3801 (2000)
- 13 M. Bellini, T.W. Hänsch, Opt. Lett. **25**, 1049 (2000)
- 14 J.W. Nicholson, M.F. Yan, Opt. Express **12**, 679 (2004)
- 15 P. Béjot, J. Kasparian, E. Salmon, R. Ackermann, N. Gisin, J.-P. Wolf, Appl. Phys. Lett. **88**, 251112 (2006)
- 16 A. Braun, G. Korn, X. Liu, D. Du, J. Squier, G. Mourou, Opt. Lett. **20**, 73 (1995)
- 17 M. Rodriguez, R. Bourayou, G. Méjean, J. Kasparian, J. Yu, E. Salmon, A. Scholz, B. Stecklum, J. Eislöffel, U. Laux, A.P. Hatzes, R. Sauerbrey, L. Wöste, J.-P. Wolf, Phys. Rev. E **69**, 036607 (2004)
- 18 G. Méjean, J. Kasparian, J. Yu, E. Salmon, S. Frey, J.-P. Wolf, S. Skupin, A. Vinçotte, R. Nuter, S. Champeaux, L. Bergé, Phys. Rev. E **72**, 026611 (2005)
- 19 R. Ackermann, G. Méjean, J. Kasparian, J. Yu, E. Salmon, J.-P. Wolf, Opt. Lett. **31**, 86 (2006)
- 20 J. Kasparian, M. Rodriguez, G. Méjean, J. Yu, E. Salmon, H. Wille, R. Bourayou, S. Frey, Y.-B. André, A. Mysyrowicz, R. Sauerbrey, J.-P. Wolf, L. Wöste, Science **301**, 61 (2003)
- 21 K. Stelmaszczyk, P. Rohwetter, G. Méjean, J. Yu, E. Salmon, J. Kasparian, R. Ackermann, J.-P. Wolf, L. Wöste, Appl. Phys. Lett. **85**, 3977 (2004)
- 22 R. Ackermann, K. Stelmaszczyk, P. Rohwetter, G. Méjean, E. Salmon, J. Yu, J. Kasparian, G. Méchain, V. Bergmann, S. Schaper, B. Weise, T. Kumm, K. Rethmeier, W. Kalkner, J.-P. Wolf, L. Wöste, Appl. Phys. Lett. **85**, 5781 (2004)
- 23 G.P. Agrawal, *Nonlinear Fiber Optics*, 3rd edn. (Academic Press, San Diego, New York, 1995), p. 102
- 24 Y.R. Shen, *The Principles of Nonlinear Optics* (John Wiley and Sons, New York, 1984)
- 25 X.M. Zhao, P. Rambo, J.-C. Diels, QELS'95 **16**, 178 (1995)
- 26 A. Becker, N. Aközbek, K. Vijayalakshmi, E. Oral, C.M. Bowden, S.L. Chin, Appl. Phys. B **73**, 287 (2001)
- 27 M. Fiorentino, J.E. Sharping, P. Kumar, A. Porzio, R.S. Windeler, Opt. Lett. **27**, 649 (2002)
- 28 S. Spälter, M. Burk, U. Ströbner, A. Sizmann, G. Leuchs, Opt. Express **2**, 77 (1998)
- 29 S.R. Friberg, S. Machida, M.J. Werner, A. Levanon, T. Mukai, Phys. Rev. Lett. **77**, 3775 (1996)

## 32 TW atmospheric white-light laser

P. Béjot, L. Bonacina, J. Extermann, M. Moret, and J. P. Wolf

*GAP-Biophotonics, University of Geneva, 20 rue de l'École de Médecine, Geneva 1211, Switzerland*

R. Ackermann, N. Lascoux, R. Salamé, E. Salmon, and J. Kasparian<sup>a)</sup>

*CNRS-LASIM UMR 5579-Université Claude Bernard Lyon 1, Bât. A. Kastler, 43 Bd. du 11 Novembre 1918, F-69622 Villeurbanne Cedex, France*

L. Bergé, S. Champeaux, and C. Guet

*CEA/DAM Ile de France, BP 12, 91680 Bruyères-le-Châtel, France*

N. Blanchot, O. Bonville, A. Boscheron, P. Canal, M. Castaldi, O. Hartmann, C. Lepage, L. Marmande, E. Mazataud, G. Mennerat, L. Patissou, V. Prevot, D. Raffestin, and J. Ribolzi

*Commissariat à l'Énergie Atomique—Centre d'Études Scientifiques et Techniques d'Aquitaine (CEA/CESTA), BP n°2, 33114 Le Barp, France*

(Received 12 February 2007; accepted 19 February 2007; published online 10 April 2007)

Ultrahigh power laser pulses delivered by the Alisé beamline (26 J, 32 TW pulses) have been sent vertically into the atmosphere. The highly nonlinear propagation of the beam in the air gives rise to more than 400 self-guided filaments. This extremely powerful bundle of laser filaments generates a supercontinuum propagating up to the stratosphere, beyond 20 km. This constitutes the highest power “atmospheric white-light laser” to date. © 2007 American Institute of Physics.

[DOI: [10.1063/1.2722564](https://doi.org/10.1063/1.2722564)]

Highly nonlinear effects are expected to prevent long distance propagation of ultrashort and ultraintense laser pulses in the atmosphere. Kerr self-focusing should lead to catastrophic collapse, while laser-induced plasma should defocus the beam. However, at the subjoule and terawatt levels, a subtle balance between Kerr focusing and defocusing by the induced plasma leads to “laser filaments”<sup>1</sup> that are stable over many tens of meters<sup>2</sup> and produce a coherent supercontinuum.<sup>3</sup> We investigated the scalability of this propagation well beyond these energies and powers by launching 26 J, 32 TW laser pulses delivered by the Alisé beamline of the CEA-CESTA in the atmosphere. We show that filamentation still occurs at these extreme levels. More than 400 filaments simultaneously generate a supercontinuum propagating up to the stratosphere, beyond 20 km.

Compared with the propagation of most intense pulses investigated so far using the *Teramobile* facility<sup>4</sup> (400 mJ, 5 TW), we increased the power and energy by one and almost two orders of magnitude, respectively. At the extreme power levels delivered by the Alisé beamline, it is a particular challenge to understand laser propagation. The nonlinear Schrödinger equation used to model the propagation at terawatt levels<sup>5</sup> may be altered by higher order terms, which would prevent the formation of filamentary structures. For instance, over the critical plasma density, inverse bremsstrahlung would stop the beam propagation. Potential applications of filaments stem from their unique properties; the ability of generating a “white-light laser”<sup>3</sup> that can be used in light detection and ranging (Lidar) systems to remotely detect atmospheric pollutants<sup>6</sup> or bioaerosols,<sup>7</sup> creating long conducting plasma channels for lightning control applications,<sup>8,9</sup> and delivering intensities up to  $10^{14}$  W/cm<sup>2</sup> at kilometeric distances.<sup>10</sup>

We investigated the vertical propagation in air of pulses from the Alisé laser facility.<sup>11</sup> Alisé was used in a chirped pulse amplification configuration with six stages of Nd:phosphate amplifiers. It provides compressed pulses of up to 26 J energy centered at the wavelength  $\lambda_0 = 1053$  nm, with a spectral width of 3 nm full width at half maximum (FWHM). During the experiment, the pulse duration was varied from 520 fs to 65 ps FWHM. We investigated pulses up to 32 TW peak power, corresponding to about 5000 times the critical power for self-focusing [ $P_{cr} = \lambda_0^2 / (2\pi n_2) \approx 5.8$  GW at 1053 nm, considering  $n_2 \sim (3-4) \times 10^{-19}$  cm<sup>2</sup>/W in the air<sup>12</sup>]. The beam was emitted vertically into the atmosphere, either collimated (natural divergence of 10  $\mu$ rad) or slightly focused through lenses ( $f = 16$  m or  $f = 300$  m) installed at the exit of the grating compressor. Laser diagnostics included a beam profile analyzer, a single-shot autocorrelator, and a streak camera. A frequency-doubled Nd:YAG (yttrium aluminum garnet) laser, collinear to the Alisé beam, was used as a reference for quantitative estimation of the conversion efficiency into the white-light supercontinuum.

The backscattered white-light signal was detected by a slightly off-axis (50 cm) Lidar system consisting of a 20 cm telescope equipped with detectors sensitive in three spectral ranges in the visible and near-infrared regions. Further spectral selectivity was achieved by using bandpass filters. Simultaneously, the beam was imaged from the side, from an off-axis distance of 5–30 m, by a color-frame, digital charge coupled device camera (Nikon D70).

Once pulses are launched into the air, Kerr effect is initiated in the beam. For the ultrahigh powers ( $P \gg 100P_{cr}$ ), as is the case in our experiment, multifilamentation occurs through modulational instability that breaks up the beam into periodic cells over very short propagation distances  $z_{fil} \approx 2P_{cr} / (\lambda_0 I_0) \approx 1-3$  m for an incident intensity  $I_0 \sim 4-6 \times 10^{11}$  W/cm<sup>2</sup>. This breakup results in an overall honey-

<sup>a)</sup>Electronic mail: [jkaspari@lasim.univ-lyon1.fr](mailto:jkaspari@lasim.univ-lyon1.fr)

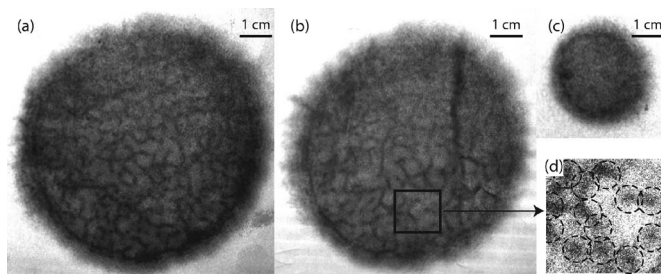


FIG. 1. Beam profile after  $\sim 11$  m propagation (a)  $f=\infty$  ( $2550P_{cr}$ , 420 filaments), (b)  $f=300$  m ( $2200P_{cr}$ , 290 filaments), and (c)  $f=15$  m ( $3180P_{cr}$ , no filaments distinguishable). (d) Detail of the filamentary structure of (b). Gray circles highlight the filaments.

comb beam structure, the cells of light being separated by “bridges.”<sup>13–15</sup> These structures appear as dark straight lines on the beam profile recorded on a photosensitive paper after only 11 m propagation (Fig. 1). Along these structures, hot spots can be observed, which correspond to the onset of mature individual filaments [see Fig. 1(d)]. Their high intensity is confirmed by their ability to locally ablate the surface of a paper screen within a single shot. Calibrated ablation tests showed that the intensity within the filaments is slightly higher than the clamped intensity of  $5 \times 10^{13}$  W/cm<sup>2</sup> observed in subjoule beams at 800 nm.<sup>16</sup> This finding suggests that even at multijoule energies, the filamentation process is governed by the dynamic balance between Kerr effect and plasma defocusing. Hundreds of filaments are observed within the beam profile unless the beam is focused too strongly [Fig. 1(c)]. We counted typically one filament for each 3.5–7.5 critical power  $P_{cr}$ , very close to that observed at lower power with the Teramobile ( $5P_{cr}$  per filament),<sup>17</sup> although the latter experiments were performed at a wavelength of 800 nm instead of 1.05  $\mu$ m.

The occurrence of self-guided filaments shows that, as is the case for lower pulse energy, Kerr lens self-focusing does not cause the beam to collapse, but instead promotes a dynamic balance with defocusing induced by the electron plasma generated at the nonlinear foci. This allows the beam to propagate collimated at long distances in spite of strong self-focusing. Filaments generated in the beam emit the white-light continuum forward as a white-light laser,<sup>3</sup> which was clearly visible to the naked eye, propagating to high altitudes in the zenith direction as a collimated beam. Moreover, the laser supercontinuum was observed on Lidar signals over the whole visible spectrum, from 300 to 850 nm, showing that its spectrum is extremely broad. Figure 2 displays the white-light Lidar signal detected in the 300–475 nm spectral region as a function of altitude. Although the acquisition is single shot, the signal can be observed up to 20 km in the stratosphere. This is all the more remarkable that the considered spectral region is more than 600 nm away from the fundamental laser wavelength. This spectacular result constitutes the most powerful Lidar signal acquired so far and definitely assesses the capability of 30 TW pulses to propagate over kilometer-range distances.

To efficiently exploit the possibilities opened by multi-joule pulses in the atmosphere, one critically needs to control their propagation. For this reason, we investigated the effect of the pulse duration on the filament location (onset distance and filamentation length). This was performed by adjusting the laser *chirp*, i.e., by tailoring the pulses so that the spectral components of the ultrashort laser beam are launched in a

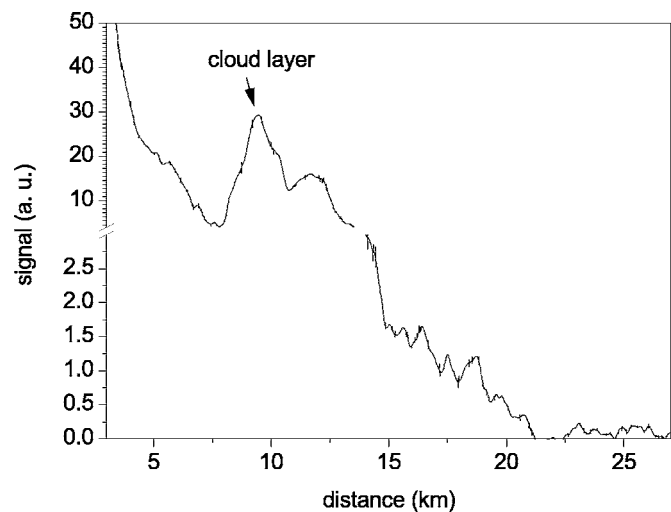


FIG. 2. Single-shot white-light Lidar signal in the 300–470 nm spectral region, displaying signals up to 20 km in spite of a cloud layer (cirrus) around 10 km. Note the dual intensity scale.

sequence, resulting in overall longer pulses with reduced peak power.<sup>4</sup> The effect of chirp on filamentation clearly appears when comparing images of the beam in the visible spectral region (Fig. 3). Filamentation can be identified as regions where a source term for white light is detected. Such a source term is indicated by an increase of the white-light signal compared to the reference YAG laser, which provides a reference for intensity normalization. We observe white light already at the bottom of the image (19 m) for all chirps. However, larger chirps lower the peak powers and yield less efficient white-light conversion per unit length. The shortest pulses of the series (570 fs, i.e., 32 TW) yield shorter filamentation (filament end at 100 m), while 2.1 ps pulses (9 TW) push the filamentation end 350 m away from the laser source. The observed altitude dependence on the pulse duration of the laser beam shows that filamentation of ultra-high power, multijoule laser pulses can be controlled remotely by changing the laser parameters as is currently performed on smaller laser classes.

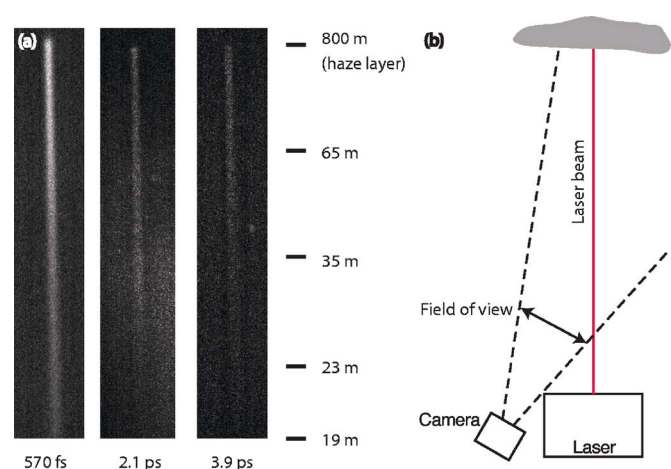


FIG. 3. (Color online) Chirp dependence of the filament onset. (a) Side image of the beam. Signal corresponding to larger initial chirps (lower peak powers) rises more slowly but over longer distances: The white light is still generated at higher altitudes, although filamentation is weaker in this case. (b) Observation geometry.

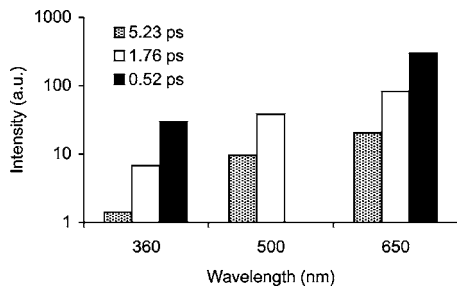


FIG. 4. Averaged Lidar returns from 200 to 300 m as a function of the wavelength and chirp. The emitted pulse energy is  $\sim 15$  J.

Practical applications of ultrashort lasers in the atmosphere require to control not only the filamentation location but also the build-up of the white-light continuum. We compared (Fig. 4) the Lidar signal in three spectral regions of the continuum (360, 500, and 650 nm, with 10 nm bandwidth) for three chirp values. The analysis shows that the chirp almost does not affect the ratios between different wavelengths. This means that the shape of the spectrum of the continuum generated in the filaments is comparable. Moreover, the signal detected at a given wavelength (hence, the generation efficiency of the white light at this wavelength, at the fixed incident pulse energy of 15 J) is almost inversely proportional to the pulse duration. The reference YAG signal permits us to estimate the absolute value of the signal at 650 nm for the shorter pulses (520 fs) to be 2.2 mJ, corresponding to a conversion efficiency of  $\sim 1.5 \times 10^{-5} \text{ nm}^{-1}$  for 31 TW laser pulses. Considering the width of the continuum and its expected exponential decay<sup>18</sup> away from the fundamental wavelength, this figure leads us to estimate that the overall conversion efficiency from the fundamental into the continuum amounts to a few percent. This conversion efficiency is smaller than may have been expected from extrapolations based on previous measurements at 800 nm at lower power and energy.<sup>18</sup>

Although longer fundamental wavelengths could have been expected to yield more spectral broadening,<sup>19,20</sup> this observation can be understood when considering that the intensity within the filaments is clamped and that their number, which is proportional to the power, does not influence much the white-light spectrum.<sup>21</sup> Spectral broadening is thus governed by the time gradients of the intensity through nonlinear phase variations. These gradients are sharper for shorter pulses, which then yield more efficient broadening.<sup>22</sup> Therefore, further optimization of the white-light generation would require one to increase the peak power by shortening the laser pulses, even at the cost of a reduced pulse energy.

As a conclusion, we have shown that ultraintense laser beams up to 30 TW, 20 J generate multiple (up to 400) filaments through processes remarkably similar to those observed for subjoule pulses.<sup>4</sup> Although conversion into the supercontinuum is less efficient than with shorter pulses (a

few percent), the white light propagates up to the stratosphere, i.e., beyond 20 km, constituting the highest power white-light laser to date. These results are encouraging for the use of multijoule, ultrashort laser pulses in both future nonlinear white-light Lidars or applications requiring the remote delivery of high intensities, such as lightning control.

This work was partly funded by the Délégation Générale à l'Armement (Grant No. 05.34.034) and the Agence Nationale de la Recherche (Grant No. NT05-1\_43175).

- <sup>1</sup>A. Braun, G. Korn, X. Liu, D. Du, J. Squier, and G. Mourou, *Opt. Lett.* **20**, 73 (1995).
- <sup>2</sup>B. La Fontaine, F. Vidal, Z. Jiang, C. Y. Chien, D. Comtois, A. Desparois, T. W. Johnston, J.-C. Kieffer, H. Pépin, and H. P. Mercure, *Phys. Plasmas* **6**, 1615 (1999).
- <sup>3</sup>S. L. Chin, S. Petit, F. Borne, and K. Miyazaki, *Jpn. J. Appl. Phys., Part 2* **38**, L126 (1999).
- <sup>4</sup>J. Kasparian, M. Rodriguez, G. Méjean, J. Yu, E. Salmon, H. Wille, R. Bourayou, S. Frey, Y.-B. André, A. Mysyrowicz, R. Sauerbrey, J.-P. Wolf, and L. Wöste, *Science* **301**, 61 (2003).
- <sup>5</sup>L. V. Keldysh, *Sov. Phys. JETP* **20**, 1307 (1965).
- <sup>6</sup>R. Bourayou, G. Méjean, J. Kasparian, M. Rodriguez, E. Salmon, J. Yu, H. Lehmann, B. Stecklum, U. Laux, J. Eislöffel, A. Scholz, A. P. Hatzes, R. Sauerbrey, L. Wöste, and J.-P. Wolf, *J. Opt. Soc. Am. B* **22**, 369 (2005).
- <sup>7</sup>G. Méjean, J. Kasparian, J. Yu, S. Frey, E. Salmon, and J.-P. Wolf, *Appl. Phys. B: Lasers Opt.* **78**, 535 (2004).
- <sup>8</sup>R. Ackermann, K. Stelmaszczyk, P. Rohwetter, G. Méjean, E. Salmon, J. Yu, J. Kasparian, G. Méchain, V. Bergmann, S. Schaper, B. Weise, T. Kumm, K. Rethmeier, W. Kalkner, J. P. Wolf, and L. Wöste, *Appl. Phys. Lett.* **85**, 5781 (2004).
- <sup>9</sup>G. Méjean, R. Ackermann, J. Kasparian, E. Salmon, J. Yu, J.-P. Wolf, K. Rethmeier, W. Kalkner, P. Rohwetter, K. Stelmaszczyk, and L. Wöste, *Appl. Phys. Lett.* **88**, 021101 (2006).
- <sup>10</sup>M. Rodriguez, R. Bourayou, G. Méjean, J. Kasparian, J. Yu, E. Salmon, A. Scholz, B. Stecklum, J. Eislöffel, U. Laux, A. P. Hatzes, R. Sauerbrey, L. Wöste, and J.-P. Wolf, *Phys. Rev. E* **69**, 036607 (2004).
- <sup>11</sup>N. Blanchot, D. Le Goff, I. Le Goff, P. Manac'h, E. Mazataud, M. Nicolaizeau, M. Padois, L. Videau, D. Villate, and L. Voisin, *Conference on Laser and Electro-Optics, CWB4, 2002* (unpublished).
- <sup>12</sup>E. T. J. Nibbering, G. Grillon, M. A. Franco, B. S. Prade, and A. Mysyrowicz, *J. Opt. Soc. Am. B* **14**, 650 (1997).
- <sup>13</sup>Gadi Fibich, Shmuel Eisenmann, Boaz Ilan, Yossi Erlich, Moshe Fraenkel, Zohar Henis, Alexander Gaeta, and Arie Zigler, *Opt. Express* **13**, 5897 (2005).
- <sup>14</sup>A. J. Campillo, S. L. Shapiro, and B. R. Suydam, *Appl. Phys. Lett.* **24**, 178 (1974).
- <sup>15</sup>S. Champeaux and L. Bergé, *Opt. Lett.* **31**, 1301 (2006).
- <sup>16</sup>A. Becker, N. Aközbe, K. Vijayalakshmi, E. Oral, C. M. Bowden, and S. L. Chin, *Appl. Phys. B: Lasers Opt.* **73**, 287 (2001).
- <sup>17</sup>G. Méjean, J. Kasparian, J. Yu, E. Salmon, S. Frey, J.-P. Wolf, S. Skupin, A. Vinçotte, R. Nuter, S. Champeaux, and L. Bergé, *Phys. Rev. E* **72**, 026611 (2005).
- <sup>18</sup>J. Kasparian, R. Sauerbrey, D. Mondelain, S. Niedermeier, J. Yu, J.-P. Wolf, Y.-B. André, M. Franco, B. Prade, A. Mysyrowicz, S. Tzortzakakis, M. Rodriguez, H. Wille, and L. Wöste, *Opt. Lett.* **25**, 1397 (2000).
- <sup>19</sup>A. Couairon and L. Bergé, *Phys. Rev. Lett.* **88**, 135003 (2002).
- <sup>20</sup>S. Champeaux and L. Berge, *Phys. Rev. E* **68**, 066603 (2003).
- <sup>21</sup>G. Méjean, J. Kasparian, J. Yu, S. Frey, E. Salmon, J. P. Wolf, L. Bergé, and S. Skupin, *Appl. Phys. B: Lasers Opt.* **82**, 341 (2006).
- <sup>22</sup>N. Aközbe, S. A. Trushin, A. Baltuska, W. Fuß, E. Goulielmakis, K. Kosma, F. Krausz, S. Panja, M. Uiberacker, W. E. Schmid, A. Becker, M. Scalora, and M. Bloemer, *New J. Phys.* **8**, 177 (2006).

# Coherent and incoherent radial THz radiation emission from femtosecond filaments in air

C. D'Amico, A. Houard, M. Franco, B. Prade, A. Mysyrowicz

Laboratoire d'Optique Appliquée, ENSTA, Ecole Polytechnique, CNRS UMR 7639, Palaiseau, 91761 France.  
[andre.mysyrowicz@ensta.fr](mailto:andre.mysyrowicz@ensta.fr)

**Abstract:** We show that the THz radiation emitted in the radial direction by a femtosecond filament created in air is linearly polarized and coherent. By applying an electric field along the filament axis this THz radiation is strongly enhanced and becomes incoherent and not polarized.

©2007 Optical Society of America

**OCIS codes:** (190.5530) Pulse propagation and solitons, (350.5400) Plasmas, (350.7420) Waves

---

## References and Links

1. C.-C. Cheng, E. M. Wright, and J. V. Moloney, "Generation of electromagnetic pulses from plasma channels induced by Femtosecond Light Strings," *Phys. Rev. Lett.* **87**, 213001 (2001).
2. S. Tzortzakis, G. Méchain, G.-B. Patalano, Y.-B. André, M. Franco, B. Prade, A. Mysyrowicz, J.-M. Munier, M. Gheudin, G. Beaudin, P. Encrenaz, "Coherent subterahertz radiation from femtosecond infrared filaments in air," *Opt. Lett.* **27**, 1944 (2002).
3. G. Méchain, S. Tzortzakis, B. Prade, M. Franco, A. Mysyrowicz, B. Leriche, "Calorimetric detection of THz radiation from femtosecond filaments in air," *Appl. Phys. B* **77**, 707 (2003).
4. P. Sprangle, J. Peñano, B. Hafizi, and C. Kapetanacos, "Ultrashort laser pulses and electromagnetic pulse generation in air and on dielectric surfaces," *Phys. Rev. E* **69**, 066415 (2004).
5. G. Shvets, I. Kaganovich, and E. Startsev, "Comment on "Generation of Electromagnetic Pulses from Plasma Channels Induced by Femtosecond Light Strings,"" *Phys. Rev. Lett.* **89**, 139301 (2002).
6. C.-C. Cheng, E. M. Wright, and J. V. Moloney, "Reply to the Comment by Gennady Shvets, Igor Kaganovich, and Edward Startsev," *Phys. Rev. Lett.* **89**, 139302 (2002).
7. V. T. Tikhonchuk, "Comment on "Generation of Electromagnetic Pulses from Plasma Channels Induced by Femtosecond Light Strings,"" *Phys. Rev. Lett.* **89**, 209301 (2002).
8. W. Hoyer, A. Knorr, J. V. Moloney, E. M. Wright, M. Kira, S. W. Koch, "Photoluminescence and terahertz emission from femtosecond laser-induced plasma channels," *Phys. Rev. Lett.* **94**, 115004 (2005).
9. D. Strickland and G. Mourou, "Compression of amplified chirped optical pulses," *Opt. Commun.* **56**, 219 (1985).
10. H. Wille, M. Rodriguez, J. Kasparian, D. Mondelain, J. Yu, A. Mysyrowicz, R. Sauerbrey, J. P. Wolf, and L. Wöste, "Teramobile: a mobile femtosecond-terawatt laser and detection system," *Eur. Phys. J. AP* **20**, 183 (2002).
11. T. Löffler, F. Jacob, and H. G. Roskos, "Generation of terahertz pulses by photoionization of electrically biased air," *Appl. Phys. Lett.* **77**, 453 (2000).
12. A. Beker, N. Aközbeke, K. Vijayalakshmi, E. Oral, C. M. Bowden, S. L. Chin, "Intensity clamping and re-focusing of intense femtosecond laser pulses in nitrogen molecular gas," *Appl. Phys. B* **73**, 287 (2001).
13. S. Tzortzakis, B. Prade, M. Franco, A. Mysyrowicz, S. Hüller, and P. Mora, "Femtosecond laser-guided electric discharge in air," *Phys. Rev. E* **64**, 057401 (2001).
14. S. Tzortzakis, B. Prade, M. Franco, and A. Mysyrowicz, "Time-evolution of the plasma channel at the trail of a self-guided IR femtosecond laser pulse in air," *Opt. Commun.* **181**, 123 (2000).

---

## 1. Introduction

An intense femtosecond laser pulse propagating in air undergoes filamentation. During filamentation, a long low density plasma column is produced. It has been predicted that this plasma column should emit THz radiation in a direction perpendicular to the filament axis [1]. This prediction has been verified experimentally [2, 3], although the physical model underlying this prediction has been disputed [4-8]. Besides the original interpretation in terms of longitudinal plasma oscillations induced by radiative pressure [1], other models assign the THz emission to a Cerenkov-like process arising from the ionization front driven by the ponderomotive force of the laser pulse [4], or to the energy relaxation by inelastic scattering of the produced free electrons [8]. Important information allowing to distinguish among these

processes, particularly the last one, can be obtained from the polarization and coherence properties of the THz emission.

In this manuscript, we study the polarization and coherence properties of the radial THz radiation from a filament in air. We also measure the THz emission when a voltage is applied to the plasma column. A considerable increase of the emission is observed in this last case. This increase is accompanied by a drastic change in the polarization and the loss of coherence of the emission, indicating a new mechanism for its origin. We discuss a possible origin of this incoherent emission.

## 2. Experimental set-up and polarization of the radial THz emission

The experimental set up is shown in Fig. 1. Two different lasers were used in the experiment. The first is a laboratory CPA [9] laser chain delivering 120 fs long optical pulses at 800 nm with a maximum energy per pulse of 10 mJ, at a repetition rate of 10 Hz. In this case a single femtosecond filament is created by focusing the laser beam in air with a 2 m-focal lens. The second laser is the Teramobile [10], delivering 100 fs long pulses at 10 Hz with an energy per pulse of 200 mJ. The Teramobile laser pulse is focused with a telescope, the focal length of which can be varied from 10 m up to infinity. For these experiments we set the telescope focal length at 18 m. In this case approximately 40 filaments are produced in a bundle of  $\sim 8$  mm diameter.

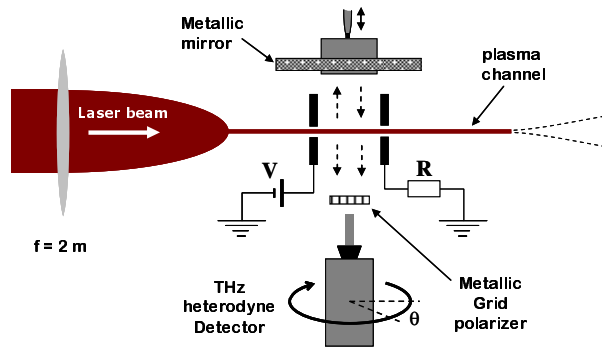


Fig. 1. Experimental Set-up. See the text for a detailed description.

The THz radiation emitted by the plasma filament is detected by means of a heterodyne detector placed perpendicularly to the filament direction. The local frequency of the heterodyne detector is 91 GHz. The detected frequencies are comprised between 88 and 94 GHz with a rejection filter at 91 GHz, to avoid feedback resonances. A waveguide in front of the detector channels the THz radiation to the detector. To perform a measurement of the polarization of the THz emission, we use a linear polarizer consisting of a specially designed metallic grid in front of the heterodyne waveguide. Using the unpolarized emission from a cw thermal source as a test, we first observed that a rotation of the waveguide and detector with respect to the grid polarizer yields a Malus law. This indicates that the waveguide plus detector system acts as a linear polarizer along the polarization axis of the detection. We then oriented the ensemble either parallel or perpendicular to the filament axis.

The result is shown in Fig. 2 for a single filament. We find the THz component to be linearly polarized along the filament axis. Figure 2 clearly shows that the component of the THz electric field perpendicular to the filament direction is zero (continuous line in the Fig. 2). We also verified that the THz signal is independent of the polarization direction of the laser beam producing the filament. The same polarization properties were found with multi-filament configuration using the Teramobile laser beam.

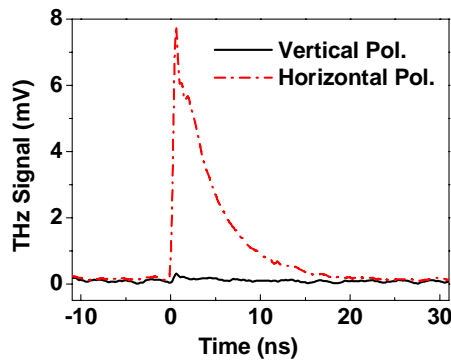


Fig. 2. Polarization properties of the THz field in absence of applied electric field. The graph shows both perpendicular (solid line) and parallel (dotted line) components of the THz field (the time axis represents the response of our detection system).

### 3. Study of the coherence properties of the radial THz signal

In order to monitor the coherence of the emission, we measured the interference between the THz emitted from one side of the filament and that emitted from the opposite side, after reflection on a movable perpendicular mirror (see set-up in Figs. 1 and 5(a)). We expect, for a coherent source, to observe an interference pattern with a period of one-half wavelength ( $\lambda / 2$ ). In the present experiment, the frequencies detected by the heterodyne system are comprised between 88 and 94 GHz ( $91 \pm 3$  GHz). We expect therefore an interference pattern with a period of  $1.65 \pm 0.05$  mm. Results are shown in Fig. 3(a). By moving the metallic mirror we get an interference pattern with a period of  $\lambda / 2$  ( $1.6 \pm 0.2$  mm) as expected, with a good contrast as shown in Fig. 3(a). The visibility of the fringe pattern is better than 0.5. The coherence length of the detector is 5cm. The mirror is placed at 20cm from the filament and is moved back over 1cm. The length that gives the delay between the waves emitted from the two opposite sides is therefore 42cm, almost one order of magnitude longer than the detector coherence length. We conclude therefore that the fringes we observe are a proof of the coherence (first order) of the emitted radiation.

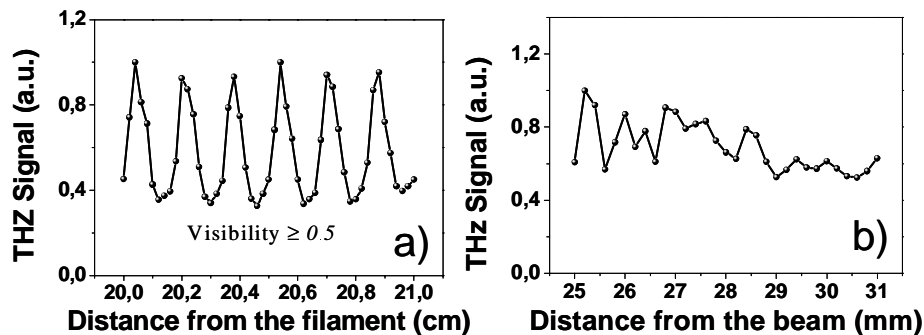


Fig. 3. Coherence properties of the THz radiation in the case of a single filament (a) and in the case of the multi-filamentation with the Teramobile laser beam (b). The x axis indicates the distance between the filament and the reflecting mirror.

Repeating the same experiment with the Teramobile laser, we notice the absence of fringes, as shown in Fig. 3(b). This can be understood simply by noting that the signal is the sum from many filaments which are not located at the same distance from the detector and/or reflecting mirror. The superposition of phase shifted emissions washes out the fringe pattern even if each individual filament emits coherent THz radiation. Nevertheless, the linear polarized nature of the emission subsists, because the emission from each individual filament remains polarized.

#### 4. Radial THz emission in presence of a DC longitudinal electric field

In a second experiment, we applied an electric potential difference  $V$  (see Figs. 1 and 5(a)) to a portion of the filament by means of two copper electrodes separated by 4 cm and placed along the midsection of the filament. Each electrode has a 2 mm-diameter hole in its center to let the filament pass through. The current  $I_R$  flowing through an external resistor  $R$  of 10  $\Omega$  could be measured when the electric circuit was short-circuited by the plasma channel. With a distance of 4 cm between the electrodes the applied static voltage could be varied from  $V=0$  kV up to about  $V=120$  kV before having a spontaneous electric discharge in air starting at the edges of the electrodes.

Results are shown in Fig. 4(a). The THz radiation energy increases quadratically as a function of the applied DC voltage. With an applied electric field of 3 kV/cm we find a THz signal larger than for an un-charged filament by more than one order of magnitude. A plot of the maximum current signal as a function of the DC voltage applied between the electrodes gives a linear dependence, as shown in Fig. 4(b).

A study of the polarization pattern of the emission in the presence of the DC field, using the same procedure as described above, shows that it is unpolarized. Both perpendicular and parallel components of the signal have the same order of magnitude, as shown in Fig. 5(b).

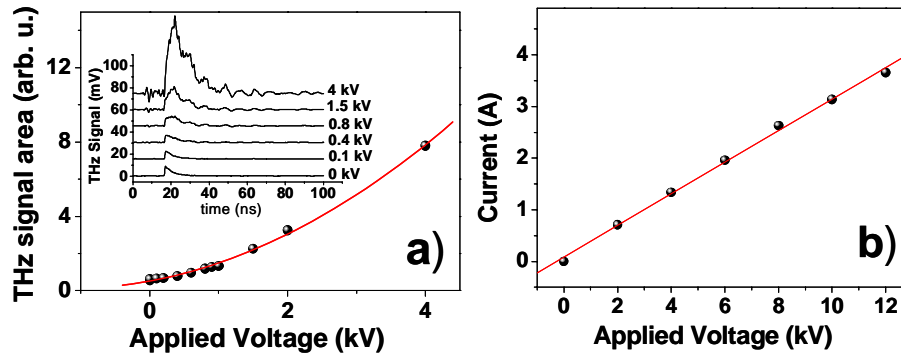


Fig. 4. Evolution of the horizontal component of the THz signal (a) and the peaks of the current signal (b) with the applied voltage. In the graph of the Fig. 4(a) the area of the THz signals in the inset is plotted as function of the applied voltage, the experimental data are well fitted by a quadratic law (continuous line).

Performing the interference experiment with a single filament, we found that the interference fringes disappear in presence of the applied potential difference, indicating the presence of an incoherent radiation. This result is shown in Fig. 5(c). We have verified that the peculiar geometry of our source (thin string) cannot induce polarization or/and interference effects by repeating the experiment with a 200  $\mu\text{m}$  thick heated metallic wire. No polarization or obvious interference was found from this source.

#### 5. Explanation of the results by means of a phenomenological model

We have considered several mechanisms for the new THz signal. Löffler, *et al.* [11] have previously observed an intense THz emission in the presence of an electric field by strongly focusing an intense femtosecond laser pulse in air. In the experiment of Löffler, *et al.*, the external electric field was parallel to the laser field in contrast to our experiments. They attribute the THz emission to the tunneling regime of ionization, when the laser intensity reaches  $10^{15}$  W/cm<sup>2</sup>. In our case, the THz radiation is emitted by a plasma channel created by filamentation. The laser intensity in the filament is well known to be clamped to a maximum value of about  $5 \times 10^{13}$  W/cm<sup>2</sup> [12]. At such intensities, the ionization mechanism can still be adequately described by a multi-photon perturbation regime. Therefore we conclude that tunneling ionization we observe is not responsible for the enhanced THz emission.

Both the polarization and interference experiments indicate the onset of a new emission mechanism by the electrically charged filament. Moreover, the THz signal in presence of the DC electric field appears with a delay of about 2ns with respect to the signal without electric field. It can be clearly seen from the graph of Fig. 6. When a weak potential difference is applied between the two electrodes, we can distinguish two peaks on the signal. The first peak, around zero, does not depend on the electric field intensity and keeps its polarization direction. The second peak depends on the electric field intensity and is not polarized.

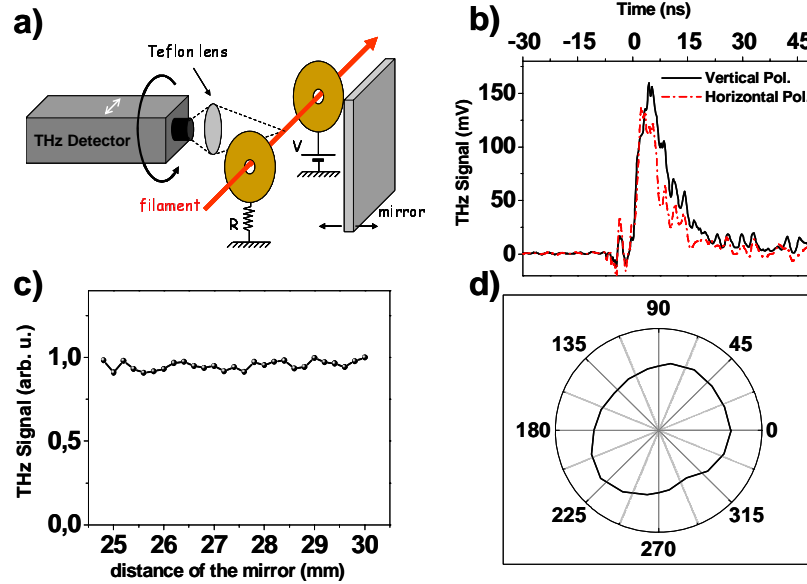


Fig. 5. Polarization properties of the THz field in presence of applied electric field. a) Scheme of the polarization and coherence experiment. Figure 5(b) shows both perpendicular (solid line) and parallel (dotted line) components of the THz field. Figure 5(c) shows the absence of interference of the THz radiation emitted by a charged filament. Figure 5(d) shows the complete polarization diagram of the THz radiation emitted by a single charged filament.

The most likely explanation is based on Joule heating of the charged plasma column, generating a thin hot air wire. This mechanism was investigated by our group in 2001 [13]. Using time-resolved diffractometry technique [14], we showed that the Joule heating of a thin air column and its subsequent expansion is responsible for the initiation of guided discharges by filaments. We estimate the increase of the temperature of the air column as follows. The maximum dissipated energy in the air column is given by  $\Delta E_j \approx \Delta P_j \cdot \tau$ , where  $\tau$  is the lifetime of the plasma, which is of the order of 1 ns [14] and  $\Delta P_j = V \cdot I$ , where  $I$  is the current flowing in the circuit. From the graph in the Fig. 4(b) we obtain  $\Delta E_j \approx \Delta P_j \cdot \tau \approx 3 \cdot 10^4 \text{ W} \times 10^{-9} \text{ s} = 30 \mu\text{J}$ . Finally, we have  $\Delta T = \Delta E_j / (M \cdot C_p) \approx 100 \text{ K}$  where  $C_p \approx 1 \text{ J} \cdot \text{g}^{-1} \cdot \text{K}^{-1}$  is the specific heat capacity of the air and  $M \approx 1.6 \cdot 10^{-7} \text{ g}$  where  $M = \rho(\pi r_f^2 L)$  is the mass of the heated air column where  $\rho = 10^{-3} \text{ g} \cdot \text{cm}^{-3}$  is the air density,  $r_f = 50 \mu\text{m}$  the filament radius and  $L = 4 \text{ cm}$  the distance between the two electrodes. This calculation is made assuming a constant air pressure and is in agreement with the increase of the temperature of the air column extracted from the analysis of time-resolved diffractometry in Ref. [14]. We therefore attribute the increase of THz emission with applied electric field, as well as the unpolarized and incoherent character of this new THz emission to the same heating process with the subsequent black body radiation from the heated air column.

Under such a hypothesis we can estimate the total power emitted in space by the heated air in the 100 GHz range. According to Wien's law the maximum emission frequency for a

black-body at 400 K is around 23.6 THz. Therefore, at the detection frequency of 91 GHz, the Black-body law is well approximated by the Rayleigh-Jeans law. We can then calculate the total power emitted in total space by the filament by using the following formula:

$$\Delta P = \frac{4\pi^2 RL}{c^2} \nu_c^2 k_B \Delta T \Delta \nu. \quad (2)$$

This formula represents the Rayleigh-Jeans law integrated over the emitting surface  $2\pi r_f L$  of the filament and multiplied by the detected frequency range  $\Delta \nu = 6 \text{ GHz}$ .  $\Delta T$  is the variation of temperature responsible for the emission and  $\nu_c = 91 \text{ GHz}$ . The coefficient  $k_B = 1.38 \times 10^{-23} \text{ J} \cdot \text{K}^{-1}$  is the Boltzmann's constant. For an increasing of temperature of  $\Delta T = 100 \text{ K}$  we can estimate from Eq. (2) that the total power emitted by the 10 kV charged filament in the 6 GHz range around 91 GHz is about  $\Delta P = 60 \text{ pW}$ .

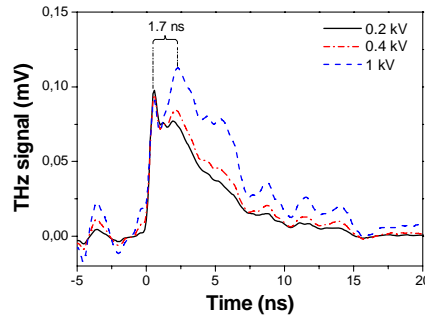


Fig. 6. Signal of the radial THz emission from the filament in presence of a weak electric field applied along the filament. The second peak of the signal increases as the electric field increases. The first peak does not depend on the applied electric field. The delay between the two peaks for weak applied electric fields is about 2ns.

Finally, returning to the THz emission in the absence of electric field, we note that its coherence properties are consistent with the Cherenkov mechanism proposed by Sprangle, *et al.* [4] but is not consistent with the mechanism proposed in Ref. [8]. We can estimate that the total power emitted in the absence of applied field is one order of magnitude less than the power from the thermal emission in the presence of an external field. Therefore we estimate the total power emitted by the un-charged filament to be about 6 pW, in agreement with the model of Ref. [4]. As pointed out by Sprangle, *et al.* [4], the emitted pulse duration should be of the order of 50 ps and have a spectrum extending over several THz.

## 6. Conclusion

In conclusion, we have shown that the radial THz emission from a single plasma filament in air is linearly polarized along the filament axis and is coherent. When the filament is electrically charged, an order of magnitude increase of the signal is observed. This is accompanied by a loss of coherence and a depolarization, showing that it corresponds to the appearance of a new emission mechanism. We interpret the new emission as due to the blackbody radiation of a thin air column left after the plasma has recombined.

## Acknowledgments

Part of the results was obtained with the Teramobile laser. Teramobile is a joint CNRS – DFG project involving the universities of Berlin, Jena, Lyon and Palaiseau. We acknowledge the invaluable help of Y. B. André and E. Salmon and a valuable discussion with Dr. Yi Liu.

## Terahertz Radiation Source in Air Based on Bifilamentation of Femtosecond Laser Pulses

Y. Liu, A. Houard, B. Prade, S. Akturk, and A. Mysyrowicz\*

*Laboratoire d'Optique Appliquée, ENSTA, Ecole Polytechnique, Teramobile project, CNRS UMR 7639, Palaiseau, 91761, France*

V. T. Tikhonchuk

*Centre Lasers Intenses et Applications, Université Bordeaux I; CNRS; CEA, UMR 5107, Talence, 33405 France*

(Received 11 June 2007; published 25 September 2007)

A new terahertz (THz) source in air based on the bifilamentation of femtosecond laser pulses is reported. This THz radiation is 1 order of magnitude more intense than the transition-Cherenkov THz emission from femtosecond laser filaments reported recently and shows different angular and polarization properties. We attribute it to the emission from a bimodal transmission line created by two plasma filaments.

DOI: [10.1103/PhysRevLett.99.135002](https://doi.org/10.1103/PhysRevLett.99.135002)

PACS numbers: 52.59.Ye, 41.60.-m, 52.25.Os, 52.38.Hb

THz spectroscopy is rapidly emerging as a new domain with rich implications in both fundamental and applied sciences. However, up to now, a major obstacle for its use has been the strong attenuation (100 dB/km) that THz radiation experiences while propagating in air, due to the presence of water vapor. Recently, a method of generating THz was demonstrated which provides a solution to this problem [1]. It was shown that a femtosecond laser pulse undergoing filamentation emits a strong THz pulse confined in a narrow cone oriented along the forward direction. By simple manipulation on the laser pulse undergoing filamentation, it is possible to place the filament formation, hence the THz radiation source, in the immediate proximity of a remote sample. Therefore, in terms of effective irradiance at long distance, this method easily surpasses other known THz sources in spite of the fact the overall efficiency of the transition-Cherenkov emission is relatively low. A first demonstration showed the production of THz at a distance of 30 meters from the laser. Another advantage of this method is its extreme simplicity: filamentation being a self-action does not require any precise alignment.

The physical origin of the THz radiation was attributed to a transition-Cherenkov emission process from the electron current pulse propagating in the wake of the laser pulse along the plasma filament. A short laser pulse undergoing filamentation forms a plasma channel in its wake due to the interplay between the Kerr-like focusing in air and defocusing on plasma electrons. The generated plasma is weakly ionized (typically, about 0.1% of the oxygen molecules in air are ionized) yet it is strongly collisional, since the gas pressure is atmospheric. The ponderomotive force of the laser pulse produces in plasma an electron current oscillating at a frequency around 1 THz (the density of free electrons produced by filamentation is  $\sim 3 \times 10^{16} \text{ cm}^{-3}$ ). This longitudinal plasma oscillation is strongly damped (relaxation time  $\sim 300$  fs). Therefore, this current pulse can be assimilated to a dipole oriented along the propagation axis and moving at the speed of light. For a finite

length of filament, the moving dipole emits a radially polarized, broadband electromagnetic radiation due to the Cherenkov-like effect in a cone of the aperture determined by the ratio of the filament length to the emission wavelength. Excellent agreement is found between the measured radiation pattern at around 100 GHz and the predictions from the theoretical model.

In this Letter we present new results where a similar forward oriented THz emission is produced in air. However, its physical origin is different, which is manifested in higher intensity and different angular distribution and polarization. It is obtained by sending a sequence of two femtosecond IR laser pulses separated by less than 3 ns, forming two overlapping filaments in air. The first and second pulses individually produce the transition-Cherenkov THz emission described above. However, surprisingly, the magnitude of the THz radiation from the pulse sequence is larger by more than 1 order of magnitude (see Fig. 1). The radiation pattern is also different: the maximum of radiation intensity is on the propagation axis (see Fig. 2), and its polarization is strictly linear, instead of being radially polarized. However, the polarization direction does not depend upon the polarization directions of either laser pulses.

The laser used in our experiments was the Teramobile system, which provides 150-fs pulse at 800 nm with as much as 300 mJ of energy per pulse [2], or a 100 Hz Ti:sapphire laser delivering 50 fs pulses at 800 nm with a maximum energy of 15 mJ per pulse. In the experiments, the output femtosecond pulse was split into two pulses by a Mach-Zehnder interferometer so that the time delay between the two pulses could be continuously adjusted. After the interferometer, the collinearly propagating pulses were focused by the same convex lens to form two spatially overlapping filaments (see inset in Fig. 1). The filament length depends on the focusing conditions. It was varied from 5 to 50 cm in the present experiment.

The forward THz radiation was reflected by a centrally pierced metallic mirror positioned at the end of filament.

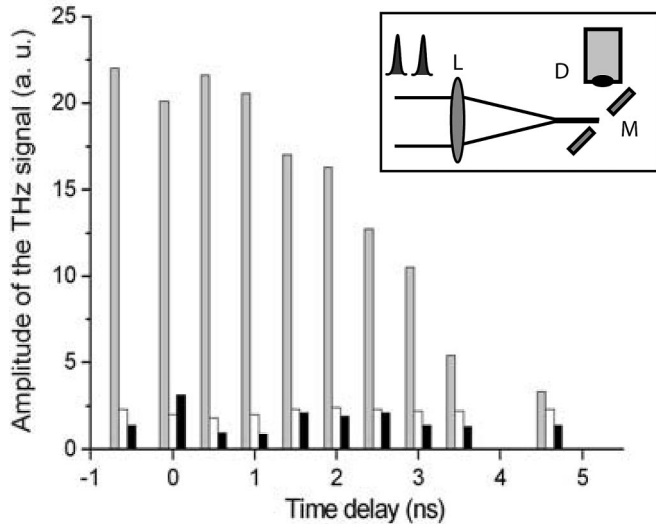


FIG. 1. Amplitude of the THz signal as a function of the time delay between the two IR pulses. The signal generated by the first and the second pulse individually is also shown. The gray, white, and black bars denote the THz signal produced by the pulse sequence, the first pulse, and the second pulse, respectively. Inset: the schematic setup of the experiments, L: convex lens, D: heterodyne terahertz detector, M: metallic mirror with a 1-cm-hole on the center.

The mirror collected the THz radiation while transmitting the filament core through the central hole with a diameter of 1 cm. The reflected THz radiation was focused by a Teflon lens and detected with a heterodyne detector, which is sensitive to the 91 GHz frequency component. In this way, the entire forward THz radiation at this wavelength was collected except the leakage of the THz through the hole on the mirror center.

The amplitude of the THz signal obtained with the pulse sequence from the “Teramobile” laser is shown in Fig. 1 as a function of the time delay between the two IR pulses in the case of focal length  $f = 2$  m. The energy of the first and second pulses was 3.7 and 2.8 mJ, respectively. The THz signals produced individually by each of the two pulses are also shown. With both pulses, an enhancement of the THz radiation by more than 1 order of magnitude is observed for time delays shorter than 1 ns. Close to zero time delay, the enhancement is slightly reduced. With larger time delays, the enhanced THz emission decreases gradually, and it becomes equal to the sum of the individual THz signals for delays exceeding 4.6 ns.

To measure the angular pattern of the emission, the pierced mirror was removed and a waveguide for the THz radiation was used instead of the Teflon lens [1]. The angular distribution of this THz emission was measured by rotating the detector in the horizontal plane around a point on the filament axis. In Fig. 2, the THz radiation patterns from single and double IR pulse filaments are presented. We notice that the maximum radiation

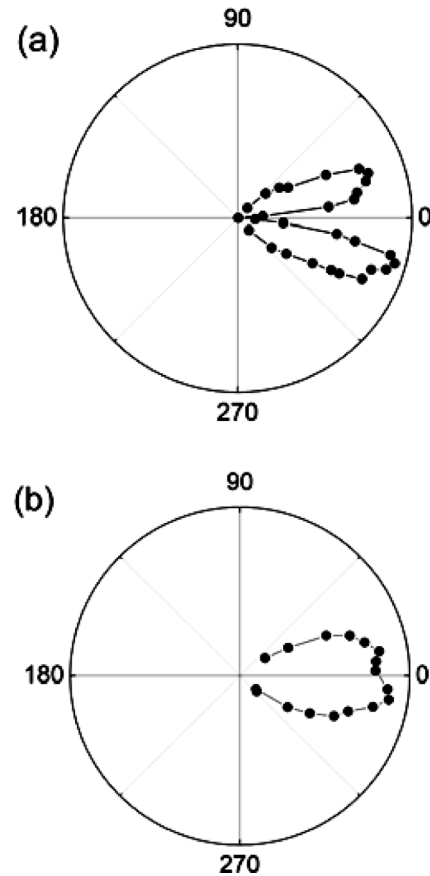


FIG. 2. (a) Angular distribution of THz radiation from single IR pulse filament, (b) angular distribution of the THz from the bifilamentation. Both figures are not to the same scale.

intensity obtained with two pulses lies along the propagation axis, in contrast to the single pulse case.

We also measured the polarization properties of this new THz emission. Inside the THz detector, a rectangular waveguide acts as a linear polarizer. Correspondingly, the polarization of the THz wave can be measured by rotating the detector around its axis. The THz signal yields a Malus’ law, which indicates that the THz radiation is linearly polarized. The polarization direction of the THz radiation was found to be independent on the polarization directions of both IR pulses. However, we observed that the polarization direction changed day by day and was very sensitive to the alignment of the two IR pulses. This feature will be discussed later in detail.

These three observations indicate that the physical origin of the THz radiation generated by the double pulse is different from the transition-Cherenkov mechanism. We have explored several possibilities to elucidate its origin:

(1) *THz emission from the second IR pulse amplified by the plasma formed by the first pulse.*—Since the enhancement of THz radiation is observed for time delays of up to a few ns between the two pulses, it obviously points out to a retarded effect connected to the presence of a plasma

produced by the first pulse. It is therefore conceivable that the plasma left by the first pulse acts as an amplifying medium for the transition-Cherenkov THz produced by the second pulse. Amplification could be due for instance to a Raman gain or an induced emission from inverted population of excited vibrational-rotational states of air molecules. In order to check this hypothesis, we have repeated the double pulse experiment in a noble gas (Xe) and found a similarly greatly enhanced emission. We can therefore exclude the Raman or inversion mechanisms, which do not occur in a monoatomic gas.

(2) *THz generation in a stratified plasma.*— It has been predicted that a short laser pulse propagating in a periodically varying (stratified) plasma can generate electromagnetic radiation in the THz domain [3], if the modulation period is of the order of a few hundred microns. However, such a modulation cannot be created spontaneously in the time between two pulses. The plasma oscillations created by the first pulse are decaying in a time scale less than 1 ps, and they cannot induce any specific large-scale plasma motion. Moreover, the plasma column is expected to be fairly homogeneous along the filament because of the strong clamping effect upon the pulse intensity [4]. Therefore, this undulator effect is not likely at the origin of the THz emission in our experiments.

(3) *Geometric effect.*—The fact that the direction of the polarization of the THz signal is sensitive to the alignment of the interferometer generating the two laser pulses gave us a clue to the origin of the THz emission. Namely, it should correspond to the geometry of two plasma filaments. To verify this hypothesis, we have done the following experiments. First, we have produced two perfectly collinear laser pulses. This was done by manipulating the optical spectrum inside the compressor of the CPA laser system which delivers 50 fs pulse, such that two exactly collinear pulses separated by 80 fs are produced at the output as a single beam. With such a sequence of two pulses, two perfectly overlapping plasma columns are produced but no nonlinear enhancement of the THz generation was observed. Second, resorting again to the Mach-Zehnder interferometer, we have analyzed more closely the superposition pattern of the filament tracks produced by both pulses. This was performed by introducing a glass plate in the middle part of the laser filament and examining *post mortem* the produced permanent damage. We observed an elongated damage pattern corresponding to two partially overlapping filaments. The elongated axis of the pattern was always aligned along the THz polarization direction. Two typical results are shown in Fig. 3. The distance between the centers of two filaments is of the order of 100  $\mu\text{m}$ .

Having identified the crucial parameter in the experiment, we now discuss the physical origin and characteristics of the enhanced forward directed THz emission. In the case of a single pulse the amplitude of the plasma wave

excited by the ponderomotive force of a short laser pulse ( $\omega_{pe}\tau_L < \pi$ ) can be estimated as  $E_p \approx \omega_{pe}^2 U_p \tau_L / ec$ , where  $\omega_{pe}$  is the plasma frequency,  $U_p$  is the laser pulse ponderomotive potential, and  $\tau_L$  is the laser pulse duration. This current has only the axial component since the plasma filament is axially symmetric and is independent upon the laser pulse polarization. It has a length of the order of the damping length  $c/\nu_e \approx 100 \mu\text{m}$ , where  $\nu_e$  is the electron collision frequency, and it propagates with the light velocity  $c$  along the filament of length  $l$ . Such a current cannot generate an electromagnetic emission exactly in the axial direction. The optimum emission angle depends on the ratio of the radiation wavelength  $\lambda$  to the filament length:  $\theta \approx \sqrt{\lambda/l}$ .

Things look different in the case of two pulses. The first plasma filament stays intact (the plasma recombination time is a few ns), and another filament is created by the second laser pulse beside it. This arrangement of two parallel plasma columns can be assimilated to a transmission line, which supports two types of waves: the longitudinal plasma wave, propagating in each wire independently, and an electromagnetic TM mode with the electric field in the plane of the two wires (the components  $E_x$  and  $E_z$ ) and the magnetic field directed perpendicular to this plane (the component  $B_y$ ). This mode propagates with the light velocity and the coupling between the wires is achieved by the mutual conductance  $C$  and inductance  $L$  (per unit length of the line). In our case the current  $I$ , created by the laser pulse ponderomotive force in the second filament, induces the tension  $V$  between the wires according to the Faraday law,  $\partial V/\partial z = -L\partial I/\partial t$ . This

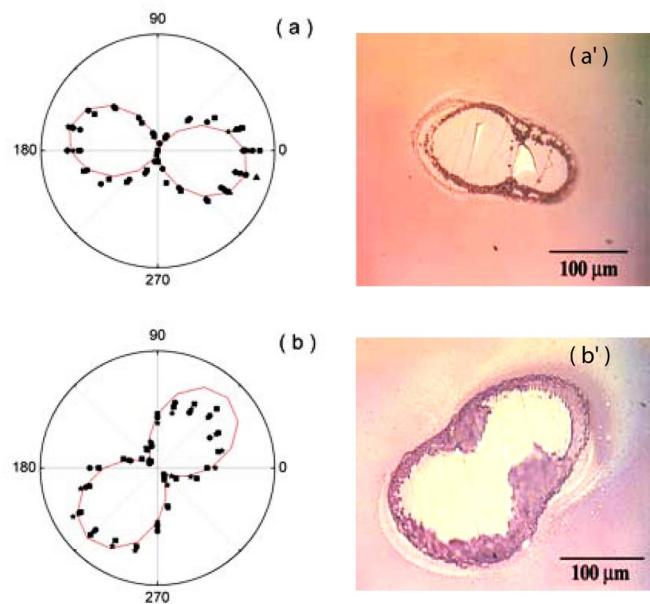


FIG. 3 (color online). THz polarization and damage pattern of the bifilament on a glass plate. The solid line in (a) and (b) are fitted by Malus' law.

tension is related to the linear density of electric charge,  $Q = CV$ . Moreover, the charge conservation implies the continuity equation,  $\partial Q/\partial t = -\partial I/\partial z$ . Combining these two equations one finds the telegrapher's equation:

$$\frac{\partial^2 V}{\partial t^2} = \frac{1}{CL} \frac{\partial^2 V}{\partial z^2}.$$

It is well known in electrodynamics (see, for example, [5]) that the product  $CL = 1/c^2$  for any transmission line, and  $L = (\mu_0/4\pi)[1 + 4 \ln(d/a)]$ , where  $d$  is the distance between the wires and  $a$  is the wire radius. This equation describes an electromagnetic pulse propagating with the light velocity along the line. Having in mind that the electric current is driven by the laser pulse ponderomotive force,  $I \simeq \varepsilon_0 \omega E_p \pi a^2$ , the estimate for the tension amplitude reads:  $V \simeq cLI \simeq a^2 E_p \omega / c$ .

This wave is, however, confined within the line, because the main electric current is propagating in the axial direction. To explain the axially directed electromagnetic emission one has to account for the perpendicular current between the wires,  $j_x \simeq \sigma V/d$ , where  $\sigma = e^2 n_e / m_e (\nu_e - i\omega)$  is the plasma conductivity. This current exists only if the filaments are not completely separated and there is some plasma between them, that is,  $d \sim a$ .

Having these estimates in hand, one can easily describe the general characteristics of the electromagnetic emission from the bifilament. First, it is confined within a cone of angle  $\theta \simeq \sqrt{\lambda/l}$  with the maximum along the laser beam propagation direction. In contrast to the emission of a longitudinal current from a single filament, which is proportional to  $\ln(l/\lambda)$ , the emission intensity from a pair of filaments is linearly proportional to the length  $l$  [6]. For the parameters of experiment ( $l = 20$  cm and  $\lambda = 3$  mm) it gives a factor of 10 for the intensity enhancement. Second, the polarization is linear, lying in the plane of plasma filaments. The spectrum attains its maximum at the plasma frequency ( $\sim 1$  THz) and it extends towards longer wavelengths decreasing as  $1/\lambda^2$ . The maximum delay between two laser pulses for which enhancement is observed is explained by the lifetime of the first plasma filament. The recombination time is of the order of 3–4 ns in air. Finally, the total emitted energy depends on the filament lengths and dimensions. The maximum energy which can be emitted, is limited by the total energy of the plasma wave:

$W_{\max} \simeq \varepsilon_0 E_p^2 a^2 l$ . It increases as the square of laser pulse intensity and duration.

In conclusion, we observed a new THz radiation based on bifilamentation of two femtosecond pulses in air. This THz radiation is found to be 1 order of magnitude more intense than our recently reported transition-Cherenkov THz radiation from the plasma filaments. Moreover, this THz wave is radiated in a small angle confined in the direction of the laser propagation and it is linearly polarized. We confirmed that the polarization plane of the THz was determined by the relative position of the two filaments, which actually provides an extremely simple method to control the THz polarization. The physical origin and the basic characteristics of the process are explained with a simple model of a transmission line formed by a pair of neighboring plasma filaments. Like the transition-Cherenkov mechanism of the THz emission from laser-created filaments, it is a simple and flexible method of generation of electromagnetic radiation in the THz domain to illuminate a remote target. This new THz source should be beneficial for applications such as the THz tomography.

We are grateful to Ciro D'Amico and Michel Franco for many stimulating discussions. Partial support by a grant from CNRS and DGA is acknowledged.

---

\*andre.mysyrowicz@ensta.fr.

- [1] C. D'Amico, A. Houard, M. Franco, B. Prade, A. Mysyrowicz, A. Couairon, and V.T. Tikhonchuk, *Phys. Rev. Lett.* **98**, 235002 (2007).
- [2] H. Wille, M. Rodriguez, J. Kasparian, D. Mondelain, J. Yu, A. Mysyrowicz, R. Sauerbrey, J.P. Wolf, and L. Wöste, *Eur. Phys. J. Appl. Phys.* **20**, 183 (2002).
- [3] L.M. Gorbunov and A.A. Frolov, *JETP* **83**, 967 (1996).
- [4] A. Becker, N. Aközbek, K. Vijayalakshmi, E. Oral, C.M. Bowden, and S.L. Chin, *Appl. Phys. B* **73**, 287 (2001).
- [5] L.D. Landau and E.M. Lifshitz, *Electrodynamics of Continuous Media, translated*, edited by J.B. Sykes and J.S. Bell (Pergamon, Oxford, 1960).
- [6] X. Xie, J. Xu, J. Dai, and X-C. Zhang, *Appl. Phys. Lett.* **90**, 141104 (2007). The authors report a similar THz emission in air using two femtosecond laser pulses. However, the short focal length used leads to very short filaments, giving a THz enhancement by a factor of 2.5 only.

## Conical Forward THz Emission from Femtosecond-Laser-Beam Filamentation in Air

C. D'Amico, A. Houard, M. Franco, B. Prade, and A. Mysyrowicz\*

*Laboratoire d'Optique Appliquée, ENSTA, Ecole Polytechnique, CNRS UMR 7639, Palaiseau, 91761 France*

A. Couairon

*Centre de Physique Théorique, CNRS, Ecole Polytechnique, F-91128 Palaiseau, France*

V. T. Tikhonchuk

*Centre Lasers Intenses et Applications, Université Bordeaux I, CEA, CNRS, UMR 5107, Talence, 33405 France*

(Received 21 February 2007; published 7 June 2007)

We attribute a strong forward directed THz emission from femtosecond laser filaments in air to a transition-Cherenkov emission from the plasma space charge moving behind the ionization front at light velocity. Distant targets can be easily irradiated by this new source of THz radiation.

DOI: [10.1103/PhysRevLett.98.235002](https://doi.org/10.1103/PhysRevLett.98.235002)

PACS numbers: 52.38.Hb, 41.60.-m, 42.65.Tg, 52.25.Os

For a long time, the THz region ( $10^{11}$ – $10^{13}$  Hz, wavelengths from 30  $\mu\text{m}$  to 3 mm) has remained the last unexplored bastion between visible and long wavelength electromagnetic radiation, due to the lack of efficient emitters and receptors. However, this situation changed dramatically during the last decade, and THz radiation rapidly became an important research tool for atoms, molecules, semiconductors, high-temperature superconductors, biomedical tissues, organic chemical materials, cellular structures, etc. Numerous applications of THz radiation have been proposed in areas such as biomedical diagnostics, tomographic imaging, security screening, and chemical identification [1].

Most of the advances are tied to the use of nonlinear optical techniques to produce THz radiation. So far, the most established nonlinear technique has been optical field rectification, which achieves frequency down conversion of laser pulses [2]. The optical rectification of a femtosecond pulse (duration  $\sim 100$  fs) leads to a coherent pulse in the desired frequency range, since the Fourier transform of the rectified pulse envelope yields a carrier frequency  $\delta\nu \approx 1/\delta\tau \approx 10^{13}$  Hz. Optical rectification was achieved first via the second order polarizability  $P_i(\omega) = \chi_{ijk}^{(2)}(\omega, \omega + \omega', -\omega')E_j(\omega + \omega')E_k^*(\omega')$  induced in a nonlinear medium lacking inversion symmetry, where  $\omega$  and  $\omega'$  are the THz and optical frequencies, respectively. ZnTe has proved to be a particularly suitable material because of its good transparency window in the THz region and because of the accidental phase matching between the phase velocities of THz radiation and 800 nm, the central wavelength of femtosecond laser pulses based on the well developed Ti:sapphire technology.

Optical rectification has also been achieved via a third order nonlinear process. By mixing two femtosecond laser pulses at frequencies  $\omega$  and  $2\omega$  with a proper phase relation, the inversion symmetry of the medium seen by the total field is effectively broken and optical rectification of

the pulse envelope becomes possible even in a centrosymmetric Kerr medium [3]. This technique, described by the third order nonlinear susceptibility  $\chi_{ijkl}^{(3)}(\omega, 2\omega' + \omega, -\omega', -\omega')$ , is particularly attractive because normal air or other common gases can be used as a rectifying medium. Very recently, THz production in air via a third order optical rectification process was shown to be strongly enhanced by the presence of a plasma generated by one of the incident laser pulses [4]. THz signals with field strength greater than 400 kV/cm have been reported in air [5]. Still, the production of THz radiation by optical rectification in air remains a difficult task requiring precise alignments. Another major challenge to overcome before the THz frequency domain becomes widely used for applications is the transfer of THz radiation over long distances  $l \gg 1$  m. The peak intensity of short THz pulses is attenuating rapidly during propagation because of air group velocity dispersion, beam diffraction, and absorption by water vapor. Most THz experiments so far are performed over small distances in the laboratory under controlled air conditions to avoid humidity.

In this Letter, we report generation of THz emission in air by a mechanism different from optical rectification, which offers the advantage of extreme simplicity. This emission is in the form of a strongly collimated THz beam in the forward direction, which we attribute to a combined transition-Cherenkov radiation generated by the space charge created behind the ionization front and moving in the wake of the laser pulse at light velocity. It uses normal air as the generation medium and requires a single femtosecond laser beam without precise alignment procedure. More importantly, the THz source can be easily positioned in the vicinity of a distant target, possibly kilometers away, thereby solving the problem of transporting THz radiation in air. In terms of effective irradiance of a distant target, this new THz source surpasses other THz sources by orders of magnitude. We have developed a

theoretical model which reproduces well the observed characteristics of the THz emission. It calculates the long wavelength radiation emitted by a dipole source moving with the light velocity in the wake of the intense femto-second pulse. The dipolelike charge distribution which is oriented along the propagation axis results from a combination of the ionization process and the ponderomotive force induced by the incident laser pulse.

The key feature is filamentation of fs laser pulses in air [6]. Femtosecond filamentation occurs spontaneously when a short intense laser pulse is launched through a transparent medium with a power above a critical value  $P_{\text{cr}} = 3.72\lambda^2/8\pi n_0 n_2$ , where  $n_0$  and  $n_2$  are, respectively, the refractive index and optical Kerr constant at the laser frequency. In air, the threshold power  $P_{\text{cr}} \approx 5$  GW is easily achieved by commercially available low repetition rate Ti:sapphire lasers. Filaments are the product of a dynamic competition between several linear and nonlinear effects. For our purpose, the most important nonlinear effects are the optical Kerr effect, which tends to focus the intense beam upon itself, and the plasma defocusing action, which happens whenever the laser intensity on axis has increased sufficiently for the multiphoton ionization of air molecules to occur. In the zone of nonlinear interaction, this competition leads to a high peak intensity and a small average beam diameter  $d \sim 100 \mu\text{m}$  over a long distance when compared to the Rayleigh (diffraction) length of  $\sim 4$  cm at the wavelength of 800 nm. For this reason, the propagating pulse is often called a self-guided pulse. Filaments on a large scale are remarkably robust and largely insensitive to initial laser conditions, provided a smooth focusing geometry (focal length  $> 1$  m) is achieved. The “self-guided” pulse leaves in its wake a long thin plasma column with an initial electron density  $n_e$  of the order of  $10^{16} \text{ cm}^{-3}$ . This plasma wake is generated over a typical distance of 1 m for an input laser power slightly above the critical power. It can reach hundreds of meters at higher input powers.

It has been pointed out [7] that the plasma strings formed during filamentation should emit THz radiation in a direction perpendicular to the filament axis, because the radiation pressure excites longitudinal plasma oscillations at the plasma frequency  $\omega_{\text{pe}} = \sqrt{n_e e^2 / m_e \epsilon_0} = 10^{13} \text{ rad s}^{-1}$ . Radial THz emission has been observed experimentally [8]. Its origin has been recently reinterpreted by Sprangle *et al.* [9] as being due to the ponderomotive force of the laser pulse rather than the radiation pressure. The peak amplitude of the radial THz field is estimated to be of the order of 5 kV/cm [9]. The nature of the THz emission we report here is different. Instead of being emitted radially, it is confined to a very narrow cone in the forward direction (see the right side of Fig. 1). We have compared the forward and radial emission from filaments at a distance of 5 cm from the middle section of the filament source and found the former to be more intense by more than 2 orders

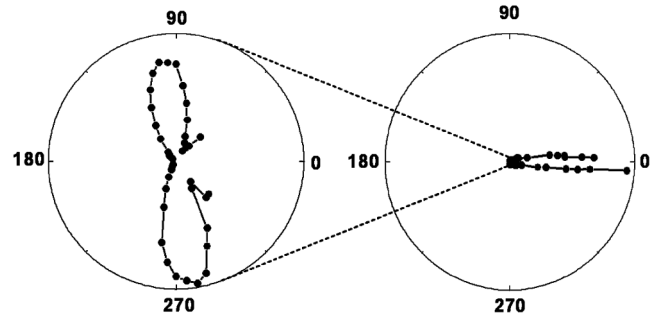


FIG. 1. Comparison between the radial (left side) and forward (right side) THz emission from a filament. Detection of the radial emission requires a reduction by 1 order of magnitude of the distance between filament and detector.

of magnitude, as shown in Fig. 1. Furthermore, the forward THz radiation displays unusual polarization properties, which are incompatible with third order optical rectification in air.

The experimental setup is shown in Fig. 2. The laser is a Ti:sapphire chirped pulse amplification system operating at 10 Hz and delivering pulses of 150 fs duration. In the experiment, the central part of the beam is selected by means of a 5 mm diameter diaphragm, yielding an energy of 4 mJ per pulse. A single filament is created by focusing the laser pulses in air with a 2 m focal lens. We detect one spectral component of the broadband THz radiation emitted by the plasma filament by means of a heterodyne detector operating either at 91 or 110 GHz. The radiation diagram of the THz emission is obtained by rotating the detector around a point on the filament axis (see Fig. 2). To measure the polarization properties of the THz forward emission, we use a linear polarizer consisting of a specially designed metallic grid in front of the heterodyne detection system which itself acts as a linear polarizer. By rotating this grid polarizer we measured the amplitude of the signal as a function of the grid polarization angle [see Fig. 3(a)]. The THz forward emission yields a squared Malus law, indicating that the signal has a linear polarization. The direction of this polarization is independent of the laser

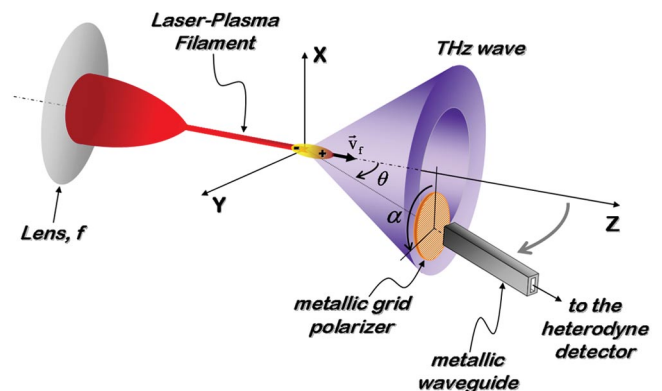


FIG. 2 (color). Experimental setup (schematic).

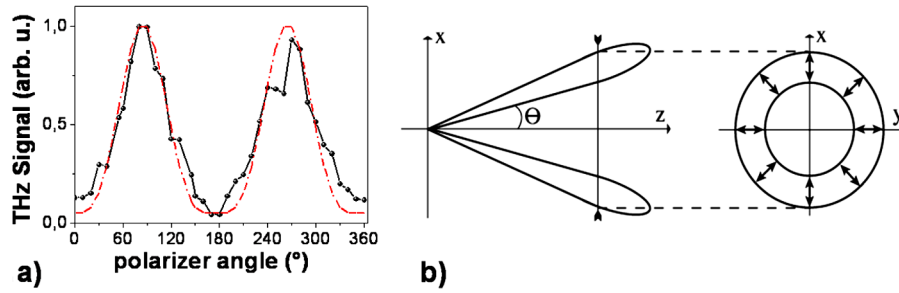


FIG. 3 (color online). Polarization of the THz forward emission measured at  $\theta = 10^\circ$  with a focal lens of 75 cm, obtained by rotating a grid linear polarizer in front of the heterodyne detector. The heterodyne detector itself acts also as a linear polarizer. The THz emission yields a squared Malus Law:  $I \propto \sin^4(\theta)$  (dotted line), indicating that the polarization of the THz signal is perpendicular to the emission cone surface. (b) Recapitulates the polarization diagram of the THz emission.

polarization. It lies in the plane defined by the laser axis  $z$  and the detection axis. The polarization properties of the THz radiation are summarized in Fig. 3(b). In Fig. 4, we show the THz radiation diagram measured for different laser focusing distances. One notices a larger opening of the radiation cone with a smaller focal distance. A narrow forward collimated THz beam is obtained with the focal lengths larger than 1 m, when the plasma channel is maintained over a length of a few tens of a centimeter.

In view of its polarization properties, the THz emission cannot be assigned to a mechanism implying the oscillation of a free electron cloud driven by the linearly polarized electric field of the laser, since one would expect the

electric vector of the THz radiation to depend on the laser polarization vector. One can therefore exclude the mechanism based on the optical rectification via a four-wave or higher order mixing process. We attribute the origin of the THz radiation to a combined “transition-Cherenkov” emission by a dipolelike electric charge oriented along the propagation axis, and moving at the light velocity behind the self-guided laser pulse in the medium. During filamentation, the laser ponderomotive force creates a dipolelike charge separation behind the ionization front [10]. This is due to the fact that the plasma formed during filamentation is weakly ionized but remains strongly collisional. According to the estimates of Ref. [9], the electron-

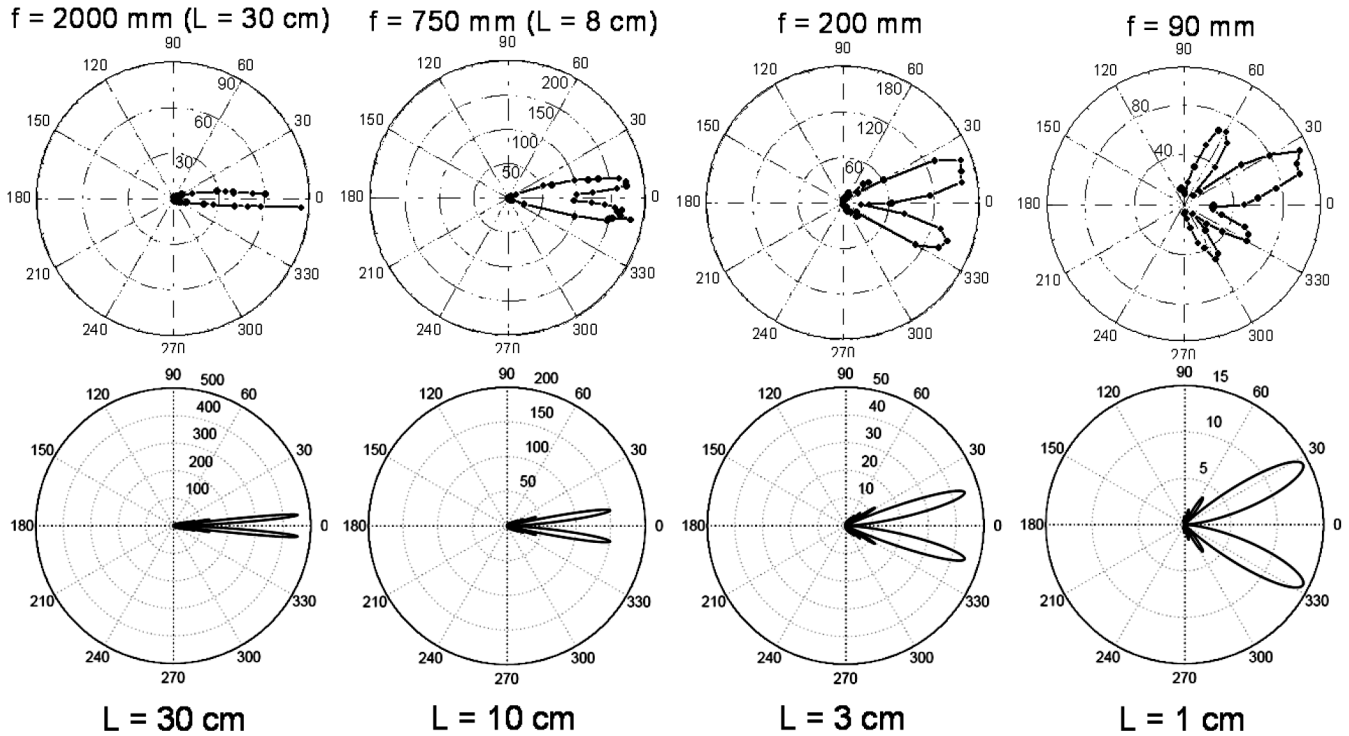


FIG. 4. Emission diagrams  $I(\theta)$  for the THz signal obtained with different focal lengths for the laser. Upper curves: experimental results. Lower curves: calculations. The filament plasma length  $L$  ( $f = 2000$  and  $f = 750$  mm) is obtained from direct measurement. Simulations yield similar values. Relative THz intensities are indicated for each diagram.

atom collision time at ambient air pressure is on the order of 0.1–0.2 ps, which is shorter than the plasma wave period. Therefore the wake field contains effectively 1–2 oscillations and looks like an electric dipole moving with the laser pulse. The dipole length  $l$  is of the order of the plasma wave damping length ( $\sim 30\text{--}100\ \mu\text{m}$ ), which is shorter than the emission wavelength,  $\lambda \approx 3\ \text{mm}$ . Because of this, the emission efficiency is smaller than the common Cherenkov emission by the factor  $(l/\lambda)^2$ .

Another important difference from the common Cherenkov emission is the fact that in our case, the emitting charges are moving with the laser pulse at the light velocity  $c$  in a medium where the refractive index  $N(\omega)$  is very close to 1. This reduces the emission efficiency, but does not suppress it completely, if one takes into account the finite length of the emission. In this respect, the mechanism of THz emission holds also some features of transition—radiation [11]. According to a recent analysis of the Cherenkov emission of electrons [12], the emitted THz field intensity is proportional to the logarithm of the medium length  $L$ , in the case of a charge moving at the light velocity in the medium, whereas it is proportional to  $L$  in the case of the common Cherenkov emission. An analysis similar to that of Ref. [12], for the wake field created by the laser pulse provides the spectral intensity of the electromagnetic emission at the frequency  $\omega$  and at the angle  $\theta$  with respect to the laser propagation axis, which reads as

$$\frac{d^2W}{d\omega d\Omega} = \frac{r_e E_l^2 \omega^2 \nu_e^2}{16\pi^2 m_e c^3 \omega_0^4 \theta^2} \sin^2(\omega L \theta^2 / 4c). \quad (1)$$

Here,  $r_e$  and  $m_e$  are the electron classical radius and mass,  $\nu_e$  is the electron collision frequency,  $E_l$  is the laser pulse energy, and  $\omega_0$  is the laser frequency. Note that the emission efficiency depends on the length of the plasma filament and on the square of the laser energy. It is also broadband since it is limited by the plasma frequency and the frequency of electron collisions to a few THz bandwidth.

The angular emission patterns for a THz field wavelength of 3 mm calculated from Eq. (1) are shown in Fig. 4 (bottom) for different medium lengths  $0.3\ \text{cm} < L < 30\ \text{cm}$ . The characteristic angle of the most intense lobe depends on  $L$  as  $\theta_{\max} = \sqrt{\lambda/L}$ . The adopted values of  $L$  correspond to the measured or calculated plasma length achieved during filamentation for the corresponding focusing geometries, as shown at the top of Fig. 4.

To test the potential of this forward THz conical emission to reach high intensities on distant targets, we have also measured the THz emission from filaments generated with the Teramobile laser [13]. In this case, the input laser power (2 TW) largely exceeds the critical power for fila-

mentation ( $\sim 5\ \text{GW}$ ). As a consequence, a bundle of approximately 40 filaments with the same energy was produced at a distance of 30 m from the laser. A THz signal in the forward direction was detected at this distance with an intensity increased by a factor 40 when compared to the single filament. This is in agreement with the proposed interpretation, as the spectral intensity of the THz emission is proportional to the sum of the filaments energy. With the Teramobile laser, we have demonstrated that the distance where filamentation occurs can be varied over several hundreds of meters by introducing a chirp to precompensate the group velocity dispersion in air [14]. Therefore, the THz source can be easily moved close to a remote target. By steering the laser beam one can achieve the THz mapping of the remote object. Filament generated THz radiation could thus find applications in biomedical imaging [1].

In conclusion, the space charge generated in the wake of the laser pulse undergoing filamentation produces an electromagnetic emission in the THz domain, which is interpreted as a transition-Cherenkov-type radiation. This is a robust phenomenon, which may find various applications due to its simplicity and flexibility.

---

\*Electronic address: andre.mysyrowicz@ensta.fr

- [1] E. Pickwell and V. P. Wallace, *J. Phys. D* **39**, R301 (2006) (medical applications); Y. C. Shen *et al.*, *Appl. Phys. Lett.* **86**, 241116 (2005) (security screening); Hua Zhong, Albert Redo-Sanchez, and X.-C. Zhang, *Opt. Express* **14**, 9130 (2006) (chemical identification).
- [2] M. Bass, P. A. Franken, J. F. Ward, and G. Weinreich, *Phys. Rev. Lett.* **9**, 446 (1962); Ajay Nahata, Aniruddha S. Welling, and Tony F. Heinz, *Appl. Phys. Lett.* **69**, 2321 (1996).
- [3] D. J. Cook and R. M. Hochstrasser, *Opt. Lett.* **25**, 1210 (2000).
- [4] M. Kress *et al.*, *Opt. Lett.* **29**, 1120 (2004); Xu Xie, J. Dai, and X.-C. Zhang, *Phys. Rev. Lett.* **96**, 075005 (2006).
- [5] T. Bartel *et al.*, *Opt. Lett.* **30**, 2805 (2005).
- [6] For a recent review on filamentation, see A. Couairon and A. Mysyrowicz, *Phys. Rep.* **441**, 47 (2007).
- [7] C. C. Cheng, E. M. Wright, and J. V. Moloney, *Phys. Rev. Lett.* **87**, 213001 (2001).
- [8] G. Méchain *et al.*, *Appl. Phys. B* **77**, 707 (2003).
- [9] P. Sprangle, J. Peñano, B. Hafizi, and C. Kapetanios, *Phys. Rev. E* **69**, 066415 (2004).
- [10] A. Proulx, A. Talebpour, S. Petit, and S. L. Chin, *Opt. Commun.* **174**, 305 (2000).
- [11] T. Takahashi *et al.*, *Phys. Rev. E* **62**, 8606 (2000).
- [12] J. Zheng, C. X. Yu, Z. J. Zheng, and K. A. Tanaka, *Phys. Plasmas* **12**, 093105 (2005).
- [13] J. Kasparian *et al.*, *Science* **301**, 61 (2003).
- [14] G. Méchain *et al.*, *Opt. Commun.* **247**, 171 (2005).

## Forward THz radiation emission by femtosecond filamentation in gases: theory and experiment

C D Amico<sup>1</sup>, A Houard<sup>1</sup>, S Akturk<sup>1</sup>, Y Liu<sup>1</sup>, J Le Bloas<sup>2</sup>,  
M Franco<sup>1</sup>, B Prade<sup>1</sup>, A Couairon<sup>3</sup>, V T Tikhonchuk<sup>2</sup>  
and A Mysyrowicz<sup>1,4</sup>

<sup>1</sup> Laboratoire d'Optique Appliquée, ENSTA, Ecole Polytechnique,  
CNRS UMR 7639, Palaiseau, 91761 France

<sup>2</sup> Centre Laser Intenses et Applications, Université Bordeaux 1, CNRS,  
CEA, Talence, 33405 France

<sup>3</sup> Centre de Physique Théorique, CNRS, Ecole Polytechnique,  
F-91128 Palaiseau, France

E-mail: [ciro.damico@ensta.fr](mailto:ciro.damico@ensta.fr) and [Andre.Mysyrowicz@ensta.fr](mailto:Andre.Mysyrowicz@ensta.fr)

*New Journal of Physics* **10** (2008) 013015 (18pp)

Received 27 September 2007

Published 17 January 2008

Online at <http://www.njp.org/>

doi:10.1088/1367-2630/10/1/013015

**Abstract.** A transition–Cherenkov electromagnetic emission by a femtosecond laser pulse propagating in a self-induced plasma channel in air has been very recently proposed as mechanism for production of terahertz (THz) radiation in the forward direction. In this paper, we study in detail the theory of the transition–Cherenkov process. The theoretical model is developed and compared with recent experimental results for several gases.

<sup>4</sup> Author to whom any correspondence should be addressed.

**Contents**

<b>1. Introduction</b>	<b>2</b>
<b>2. Femtosecond laser filamentation</b>	<b>3</b>
<b>3. Theoretical model for forward THz emission</b>	<b>4</b>
3.1. Plasma wave excitation in the wake of laser pulse . . . . .	5
3.2. Electromagnetic emission from the plasma wake . . . . .	6
<b>4. Forward THz generation and measurement in air</b>	<b>9</b>
4.1. Remote forward THz source created in air by focusing TW laser pulses . . . . .	10
<b>5. Experimental results on forward THz emission by filamentation in noble gases</b>	<b>12</b>
<b>6. Comparison of the conversion efficiencies of forward THz emission in noble gases and in air</b>	<b>13</b>
<b>7. Forward THz emission and above threshold ionization (ATI) processes</b>	<b>14</b>
<b>8. Conclusions</b>	<b>16</b>
<b>Acknowledgment</b>	<b>17</b>
<b>References</b>	<b>17</b>

**1. Introduction**

The region of the electromagnetic spectrum with frequencies between  $10^{11}$  and  $10^{13}$  Hz, commonly called the terahertz (THz) region, has remained unexplored for a very long time due to the lack of efficient generation and detection techniques. Heterodyne techniques, commonly used to detect microwave radiation ( $10^9$ – $10^{10}$  Hz), could not be used to detect THz radiation, because of the lack of THz local oscillators. Worse, ‘THz photons’ are not energetic enough to induce photoelectric effects in materials, making photoelectric effect based detection techniques unpractical.

This situation has changed in the last few decades and the THz domain has witnessed significant attention and improvements. New techniques have been developed for both generation and detection of THz radiation. Among other methods, the optical rectification process in non centro-symmetric crystals has been shown to produce THz radiation. In this method, the fundamental frequency  $\omega$  of an infrared femtosecond laser pulse (duration  $\tau_L \approx 100$  fs) is down-converted to the THz frequency  $\omega'$  via the second-order susceptibility:  $P_i(\omega') = \chi_{ijk}^{(2)}(\omega', \omega' + \omega, -\omega)E_j(\omega' + \omega)E_k^*(\omega)$ . This conversion gives a coherent THz pulse, since the Fourier transform of the rectified pulse envelope yields a carrier frequency of about 10 THz [1]. For this process, ZnTe and GaAs crystals are mostly used, thanks to their favorable transmission and phase matching behaviors.

Optical rectification can generate THz radiation in centro-symmetric media, such as gases, as well. In this case, the fundamental frequency is mixed with the second harmonic, in a third-order process:  $P_i^{(3)0}(t) \propto \chi_{ijkl}^{(3)}E_j^{2\omega}(t)E_k^\omega(t)E_l^\omega(t)$ . Likewise, in an inverse process, the THz radiation can be mixed with the fundamental and give rise to second-harmonic generation, yielding a method for detection:  $P_i^{(3)2\omega}(t) \propto \chi_{ijkl}^{(3)}E_j^\omega(t)E_k^\omega(t)E_l^0(t)$  [2, 3]. This detection and generation scheme is particularly attractive since it could use ubiquitous air for both generation and detection, with a very good efficiency. A THz signal with estimated field strength greater

than  $400 \text{ kV cm}^{-1}$  has been recently reported [4]. Note that in this case, the high conversion process in the gas needs the presence of a plasma.

The THz generation via optical rectification in gases has some limitations. Firstly, it requires precise alignments; making its use a difficult task. Secondly, due to water vapor, the THz radiation is significantly attenuated during propagation in air. This poses a challenge for long distance propagation and remote detection.

Generation of radial THz radiation by filamentation of femtosecond laser pulses in air has also been predicted [5]–[7] and experimentally demonstrated [8] in recent years. The mechanism that gives rise to the radial THz radiation by a filament has been a controversial subject. Cheng *et al* [5] proposed that the radial THz emission is due to the plasma oscillations induced by the pulse radiation pressure and the emission is coherent. According to Sprangle *et al* [6], however, the emission is due to some components of the pulse ionization front, which have superluminal velocities and give rise to Cherenkov radiation. One also expects the THz emission to be coherent in this case. Another model, as described in [7], is based on the scattering of electrons by ions in the plasma, and predicts an incoherent bremsstrahlung-like THz radiation. In addition to the predicted temporal coherence, D'Amico *et al* [9] demonstrated that the radially emitted THz radiation from the filament has very good spatial coherence properties.

Despite the controversies on the explanation of its mechanism, generation of THz radiation by filamentation received immediate attention since it requires almost no alignment; and more importantly since it potentially resolves the challenge of transmitting THz over long distances. The filaments can be generated over controllable distances, up to several hundreds of metres in air, by adjusting the input pulse parameters [10, 11]. Transmitting the filament consequently transmits the accompanying THz radiation, as well.

In a recent work [12], a novel THz emission process from femtosecond filaments in air has been reported. As opposed to the earlier works, which showed radially emitted THz from filaments, this process gives rise to a relatively collimated emission in the laser propagation direction. The physical mechanism behind this process is attributed to combined transition–Cherenkov radiation.

In this work, we present a comprehensive theoretical analysis and experimental study and of the forward THz emission from filaments. We begin by a brief summary on filamentation, long distance laser propagation and forward THz generation. We then present a detailed discussion of the theoretical model explaining the THz emission as transition–Cherenkov radiation. Next, we present experimental results on THz generation from filaments in air and noble gases (argon, krypton and xenon) and compare the corresponding conversion rates. Due to the involvement of the electron collision cross-section in the process, the highest conversion efficiency is found in xenon, in agreement with the theoretical model. We also used the relative conversion efficiencies to estimate the kinetic energy of electrons in the multiphoton ionization process during filamentation.

## 2. Femtosecond laser filamentation

Filamentation denotes a peculiar phenomenon related to the propagation of a beam of light through a medium without apparent diffraction. Counteracting the natural spreading of the beam is possible with intense laser pulses owing to the optical Kerr effect, which causes a change of the refraction index in the medium proportional to the beam intensity. The core of the beam,

more intense than the wings, induces a spatial phase profile equivalent to that of a focusing lens, resulting in self-focusing of the beam. In contrast with a lens, however, the effect is cumulative but self-focusing overcomes diffraction and eventually leads to a catastrophic collapse only if the beam power exceeds a critical threshold.

With the advent of chirped pulse amplification [13], ultrashort laser pulses became easily available with peak powers exceeding this threshold. Filamentary propagation of laser pulses in air was observed in 1995 [14] and led to numerous works since this observation. For a review about filamentation process see [15].

One of the distinguishing features of filaments is their ability to generate tenuous plasmas in the wake of the propagating pulse, which in turn modifies the narrowband laser pulse into a broadband pulse [16, 17]. This opens up the possibility of a wholly new set of applications ranging from the pulse compression and generation of extreme ultraviolet radiation [18]–[21] to the remote generation of THz radiation [12]. In addition, filaments have numerous interesting properties. For instance, the plasma strings can be concatenated to enlarge their total length [22]; filaments can be amplified in suitable media [23, 24]; the combination of plasma string generation with the organization of multiple filaments into rings or arrays [25] was predicted to serve as a photonic crystal to guide radar signals [26].

Although the initial interpretation of a balance between the Kerr self-focusing and both the self-attenuating natural diffraction and plasma-induced defocusing is still a debated topic (see for instance, the recent interpretation based on the excitation of dispersion- and diffraction-free modes [27]–[34]), the conditions to control the filamentation process and the generation of a plasma string with given features from terawatt laser pulses are well identified at least in the laboratory, making the option of using filaments as sources of THz radiation very attractive.

### 3. Theoretical model for forward THz emission

It has been predicted in [5] that the plasma channel formed by the laser pulse propagating in air should emit THz radiation perpendicularly to the filament axis. The underlying physical process was interpreted as originating from the radiation pressure of the laser pulse that induces longitudinal plasma oscillations, with frequency equal to the plasma frequency. For an electron density typically obtained in filaments,  $n_e = 10^{16} \text{ cm}^{-3}$ , the plasma frequency lies in the THz region,  $\omega_{pe} = \sqrt{n_e e^2 / m_e \epsilon_0} \approx 6 \times 10^{12} \text{ rad s}^{-1}$ . Sprangle *et al* [6] have highlighted the main role of the ponderomotive force in the THz emission by plasma strings. In their model, the radial THz electric field is estimated to be about  $5 \text{ kV cm}^{-1}$ , in the near field.

Here, we review the predictions of our theoretical model which provides the basis for interpreting the measurements of the radial as well as the forward components in the angular diagram of THz emission. Our model predicts a conical THz emission by a Cherenkov-like process of the electric current moving in the plasma channel behind the ionizing laser pulse. Similarly to the Cherenkov emission of an electric charge moving faster than the light group velocity, the emission is localized on the surface of a cone oriented in the propagation direction, it has a radial polarization, and the source size is much smaller than the emission wavelength. However, there are two main differences in the process: firstly, there is no net charge in the plasma channel. The ponderomotive force of the laser pulse produces the charge separation, but the wake is neutral as a whole, i.e. the moving source in our case is a dipole-like structure. The interference between the emissions of the positive and negative charges decreases the emission efficiency, but does not suppress it completely. Secondly, the THz source in our case is generated

even if the velocity of the ionization front is exactly the light velocity. Therefore, the radiation would not exist in an infinite plasma string; it is actually generated due to the finite length of the filament, which also defines the emission angle. In that sense it resembles transition radiation but it is more efficient, as we will see later in this section. Note finally that the refraction index of the weakly ionized air is slightly smaller than 1, making the source slightly superluminal. Therefore, the THz radiation is also partly generated by a Cherenkov-like mechanism, although superluminality is not strictly necessary, as in the Sprangle model [7].

Our theoretical development contains two parts. Firstly, we recall the theory of the plasma wave generation in the plasma channel and present estimates of it for the parameters of our experiment. Secondly, we present a model of the electromagnetic emission of the moving plasma wave from the channel and estimate the spectrum and the energy of the emitted signal.

### 3.1. Plasma wave excitation in the wake of laser pulse

Let us consider a motion of electrons in the plasma channel created by the laser pulse. According to the studies on filamentation of ultra short laser pulses in air [15], we consider an infrared laser pulse of duration  $\sim 100$  fs, focused in a spot of radius  $\sim 100 \mu\text{m}$  and creating a plasma channel of radius  $\sim 40\text{--}60 \mu\text{m}$  and a few cm or a few tens of cm long. The self-guided pulse is shaped like a pancake since its length  $\sim 10\text{--}15 \mu\text{m}$  is shorter than both its radius and the plasma column radius; therefore, it is sufficient to describe the motion of electrons in a one-dimensional model, along the laser propagation axis  $z$ . The longitudinal electric field  $E_z$  created in the plasma string is described by the wave equation

$$\partial_t^2 E_z + \nu_e \partial_t E_z + \omega_{pe}^2 E_z = S_z, \quad (1)$$

where  $\nu_e$  is the electron collision frequency,  $\omega_{pe} = \sqrt{e^2 n_e / m_e \epsilon_0}$  is the electron plasma frequency and the source term,  $S_z$ , has been derived by Sprangle *et al* [6]:

$$S_z(r, z, t) \approx \frac{e\omega_{pe}^2}{2\epsilon_0 m_e \omega_0^2 c} \left( \frac{2\nu_e}{c} + \frac{2}{c\omega_{pe}^2} \frac{\partial \omega_{pe}^2}{\partial t} - \frac{\partial}{\partial z} \right) I_L, \quad (2)$$

where  $I_L$  is the laser pulse intensity. The dominant terms in the source are the first term proportional to the collision frequency, which accounts for the radiation pressure created by the laser pulse and the third term involving the spatial derivative, which accounts for the ponderomotive force. The temporal variation of the electron density takes place only in the head of pulse and can be neglected. The general solution to equation (1) in the reference frame of the laser pulse,  $\tau = t - z/c$ , takes the following form:

$$E_z(\tau) \propto \frac{e\omega_{pe}}{2\epsilon_0 m_e c^2 \omega_0^2} \int_0^{\tau_L} d\tau' e^{-\nu_e(\tau-\tau')/2} \sin(\omega_{pe}(\tau-\tau')) \left( \frac{\partial}{\partial \tau'} + 2\nu_e \right) I_L(\tau'). \quad (3)$$

Here, we supposed that the electron collision frequency is small compared to the plasma frequency,  $\nu_e < \omega_{pe}$ . An example of the plasma wave electric field created in the wake of a laser pulse is shown in figure 1 for typical parameters of our experimental conditions:  $\nu_e = 1.3 \text{ ps}^{-1}$ , the laser pulse duration  $\tau_L = 120 \text{ fs}$  and  $\omega_{pe} = 10 \text{ ps}^{-1}$ .

The plasma wave pulse is rather short, it contains 2–3 oscillations and damps out within 1 ps time. The maximum amplitude is about  $200 \text{ V cm}^{-1}$  for a laser pulse intensity

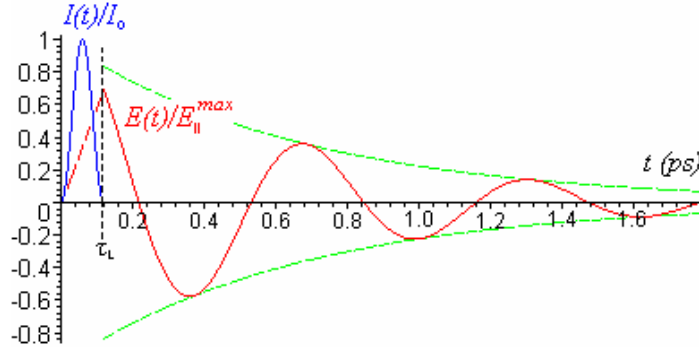


**Figure 1.** Temporal profile of the longitudinal electric field in the plasma (red curve) created in the wake of a sine shaped laser pulse, the profile of which is shown in blue curve.

of  $24 \text{ TW cm}^{-2}$ . The general form for the maximum field amplitude can be calculated from equation (3) for the sine laser pulse intensity,  $I_L(\tau) = I_0 \sin^2(\pi \tau / \tau_L)$ . Then  $E_z^{\text{max}}$  becomes:

$$E_z^{\text{max}} = \frac{2\pi^2 e \omega_{\text{pe}} I_0 \sin(\omega_{\text{pe}} \tau_L / 2)}{\varepsilon_0 m_e c^2 \omega_0^2 (4\pi^2 - \omega_{\text{pe}}^2 \tau_L^2)}. \quad (4)$$

The optimum condition for the plasma wake excitation  $\omega_{\text{pe}} \tau_L = 2\pi$  is achieved for the pulse duration that equals the plasma wave period,  $E_z^{\text{max}} = \pi e \omega_{\text{pe}} I_0 / 4 \varepsilon_0 m_e c^2 \omega_0^2$ . It can reach a few  $\text{kV cm}^{-1}$  for our parameters. From the maximum amplitude of the wake field, the total pulse energy transferred to the plasma wave can be estimated as  $W_p \approx \pi \rho_0^2 \varepsilon_0 |E_z^{\text{max}}|^2 L$ , which is of the order of  $10^{-10} \text{ J}$ , much less than the energy deposited for the ionization.

The calculation of the electromagnetic emission is performed from the Fourier spectrum of the electric current associated with this plasma wave,  $j_z(\omega) = i \varepsilon_0 \omega E_z(\omega)$ , which can be written as:

$$j_z \omega = - \frac{e \omega \omega_{\text{pe}}^2 (\omega + 2i\nu_e)}{2m_e c^2 \omega_0^2 (\omega^2 - \omega_{\text{pe}}^2 + i\nu_e \omega)} I_\omega, \quad (5)$$

where  $I_\omega$  is the Fourier spectrum of the laser pulse intensity. The current spectrum has a pronounced maximum at the plasma frequency, and it behaves as a linear function for low frequencies,  $\omega \ll \omega_{\text{pe}}$ ,  $\nu_e, \tau_L^{-1}$ :

$$j_z \omega = \frac{i e \omega \nu_e \tau_L}{2m_e c^2 \omega_0^2} I_0. \quad (6)$$

This is the frequency domain corresponding to our measurements. It is important to notice that the current in this spectral range is proportional to the electron collision frequency and the laser pulse flux,  $I_0 \tau_L$ , but does not depend on the plasma density.

### 3.2. Electromagnetic emission from the plasma wake

In this derivation, we are following the recent publication by Zheng *et al* [35] where the effect of the finite orbit length on the Cherenkov emission of a charged particle has been considered.

The radiated field can be calculated directly from the well-known expression for the vector potential  $\mathbf{A}$  created by a current  $\mathbf{j}$  [36]:

$$\mathbf{A}(\mathbf{r}, t) = \frac{\mu_0}{4\pi} \int d^3r' \frac{\mathbf{j}(\mathbf{r}', t')}{|\mathbf{r} - \mathbf{r}'|}, \quad t' = t - \frac{|\mathbf{r} - \mathbf{r}'|}{c}, \quad (7)$$

where  $t-t'$  is the time for the field to travel from the point of emission to the point of observation. By considering the far field,  $r \gg r'$ ,  $c/\omega$ , this formula takes a simple form for the Fourier component of the vector potential

$$\mathbf{A}_\omega(\mathbf{r}) = \mu_0 \frac{e^{ikr}}{4\pi r} \mathbf{j}_{\omega,k}, \quad (8)$$

where  $\mathbf{k} = \mathbf{n} \omega/c$ , is the field wave vector and  $\mathbf{n}$  is the unit vector in the radial direction. (In fact, we measured the signal at a distance of the order of 10 cm, comparable to the length of the plasma channel  $r \approx r'c/\omega$ . The predictions of the theoretical model will be therefore compared only qualitatively with experimental results.)

For our case, where the current is in the axial direction, the magnetic field,  $\mathbf{B} = \text{curl } \mathbf{A}$ , has only the azimuthal component,  $\mathbf{B}_\varphi = -ikA_z \sin \theta$ . Correspondingly, the radiation field is zero on the laser axis,  $\theta = 0$ . The electric field is then perpendicular to  $\mathbf{n}$  and  $\mathbf{B}$ , i.e. the emission has a radial polarization.

Since the radius of the plasma column  $\rho_0$  is smaller than the emission wavelength, one can assume a  $\delta$ -function distribution of the current in the radial direction. From the axial current distribution in the pulse frame given by equation (1), the Fourier component of the current reads:

$$j_{z,\omega}(\boldsymbol{\rho}, z) = \pi \rho_0^2 \delta(\rho) e^{i\omega z/c} j_z(\omega, z). \quad (9)$$

While taking the spatial Fourier transform of the current one has to account for the finite length of the emission zone  $L$  in the axial direction. The energy spectral density of electromagnetic radiation emitted in the unit solid angle then reads:

$$\frac{d^2W}{d\omega d\Omega} = \frac{cr^2}{\pi\mu_0} |B_\omega|^2 = \frac{|j_z(\omega)|^2}{4\pi\epsilon_0c} \frac{\rho_0^4 \sin^2 \theta}{(1 - \cos \theta)^2} \sin^2 \left( \frac{L\omega}{2c} (1 - \cos \theta) \right). \quad (10)$$

This constitutes our principal result describing the angular and spectral distribution of the radiation as a product of two factors. The frequency spectrum is shown in figure 2 (left). It has a maximum at the plasma frequency, corresponding to a few THz, and a broad low frequency tail decreasing as  $\omega^{-2}$ . The angular distribution contains multiple lobes, the angular positions of which are defined by the condition:  $4L \sin^2 \theta/2 = N\lambda$ . Here,  $\lambda = 2\pi c/\omega$  is the emission wavelength and  $N$  is an integer. The lobe  $N = 1$  is the strongest and corresponds to the cone opening angle

$$\theta \approx \sqrt{\lambda/L}. \quad (11)$$

It is shown in figure 2 (right) for the case  $L\omega/c = 200$ .

The energy spectral density of the total emission follows from equation (10) by integrating over angles

$$\frac{dW}{d\omega} = \frac{\rho_0^4}{2\epsilon_0c} |j_z(\omega)|^2 [\gamma - 1 + \ln 2L\omega/c], \quad (12)$$

where  $\gamma$  is the constant of Euler. In fact, the term  $\gamma - 1$  accounts for the emission in the first lobe and the logarithmic term is the contribution from other angles, which is much less intense than

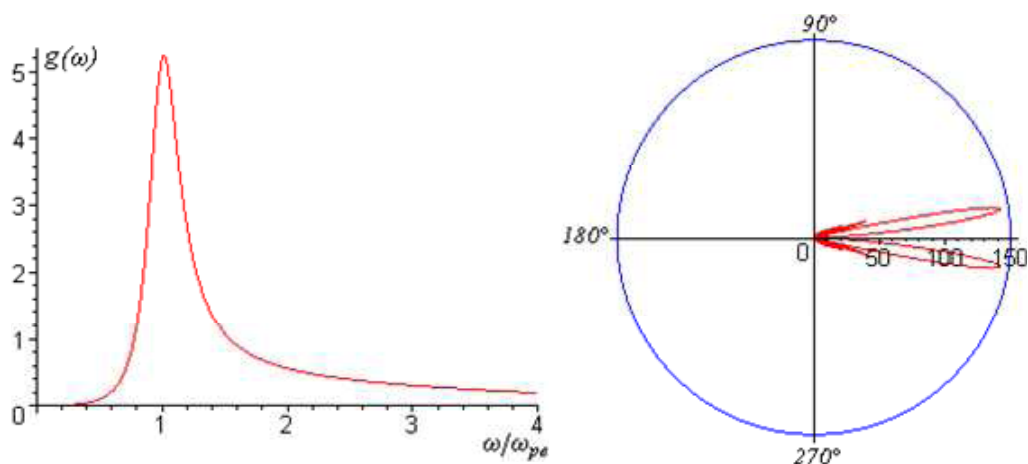


**Figure 2.** Spectrum (left) and the angular distribution (right) of the electromagnetic emission.

the main conical emission in the first lobe as it is distributed over all directions. In this respect, the model presented above for the conversion of plasma waves into electromagnetic waves also explains the emission observed at large angles,  $\theta \approx \pi/2$  [6]. As a consequence, the energy of the electromagnetic emission within the cone is independent of the filament length, which defines only the emission angle. These features are quite different from those of the standard Cherenkov emission for which the energy is proportional to the length of the particle trajectory.

According to equations (6) and (12), the energy spectral density of the electromagnetic emission in the long wavelength domain is proportional to the square of the laser pulse energy and the square of the electron collision frequency. The emission efficiency should therefore increase for gases which contain big atoms, such as xenon where the effective cross-section of elastic electron collisions is larger than in air and in other noble gases.

Finally, by taking the integral in equation (12) over frequency one can estimate the total energy of the electromagnetic emission:

$$W = \frac{r_e \omega_{pe}^6}{16m_e c^3 \omega_0^4 \nu_e} (I_0 \tau_L \pi \rho_0^2)^2 [\gamma + \ln(2L\omega_{pe}/c) - 1], \quad (13)$$

where  $r_e = \mu_0 e^2 / 4\pi m_e$  is the classical electron radius. The emitted energy is proportional to the square of the laser pulse energy, the third power of the electron density and it is inversely proportional to the electron collision frequency. The spectrum width of the THz emission is smaller for gases with a low electron collision frequency.

For the parameters of our experiment, the total electromagnetic energy in the THz domain is predicted to be relatively small, about  $10^{-14}$  J, corresponding to the emission efficiency of about  $10^{-11}$ , which is actually due to a low conversion of the laser beam into the plasma wake. In the present example, about 2% of the plasma wave energy is converted into the electromagnetic emission. This is a quite reasonable number if one accounts for the high electron collision rate and therefore, for a strong collisional dissipation of the plasma wave.

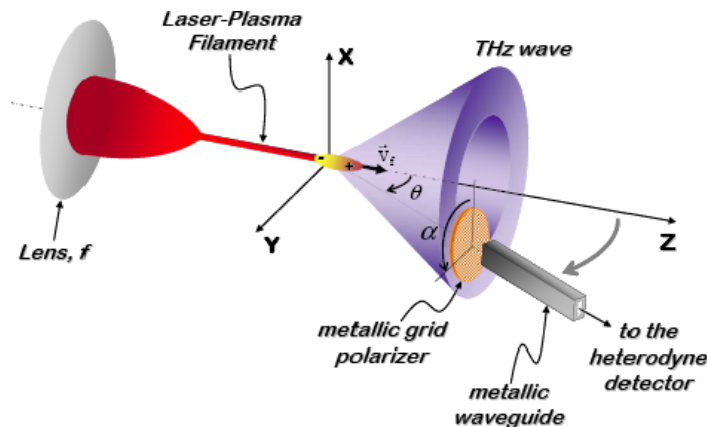


**Figure 3.** Experimental set-up used for THz generation and measurement.

#### 4. Forward THz generation and measurement in air

The experimental set-up used for the study of THz generation by filaments is shown in figure 3. The laser source is a Ti:sapphire CPA (chirped pulse amplification) system operating at 10 Hz and delivering pulses of 150 fs duration. A single filament is formed by focusing 4 mJ ( $\sim 27$  GW) femtosecond laser pulses in air using a 2 m focal lens. In the experiment, the central part of the beam traversing the lens is selected by means of a 5 mm diameter diaphragm, yielding a super-Gaussian spatial profile. We detect a specific spectral component of the broadband THz radiation emitted by the plasma filament with a heterodyne detector operating either at 91 or 110 GHz (0.1 THz).

The predictions of the theoretical model have been experimentally verified by measuring the forward THz radiation in air in this low frequency range. Concerning the polarization properties, the direction of the THz electric field is perpendicular to the detection axis, it lies on the plane common to both detection and filament axes, and it does not depend on the laser pulse polarization direction. By symmetry considerations, we conclude that the radiation is radially polarized, as predicted by the transition-Cherenkov model.

Most of the measurements were done with the heterodyne detector at 0.1 THz, but we also recently measured the spectral distribution of the produced THz pulse between 0.1 and 3 THz with calorimetric detection [37]. The THz forward radiation from the filament was collected with an off-axis parabola, and the collimated THz beam was sent to the bolometer at 4 K (see description of the detector in [38]). By inserting several calibrated band-pass and low-pass filters we were able to confirm that most of the THz pulse energy is emitted in the spectral region above 1 THz, and that its spectral distribution follows qualitatively the prediction of the theoretical model.

At low frequencies the general formula (10) can be approximated by:

$$\frac{d^2 W}{d\Omega d\omega} \propto \frac{E_f^2 v_c^2 \omega^2}{\theta^2} \sin^2 \left( \frac{L\theta^2}{4c} \omega \right), \quad (14)$$

where  $E_f$  is the energy contained in the self-guided pulse. This formula describes the THz angular emission diagram at low frequencies. The aperture angle of the emission cone is inversely proportional to the square root of the plasma channel length, as was previously pointed out. We measured the plasma channel length, under different focusing conditions, by recording

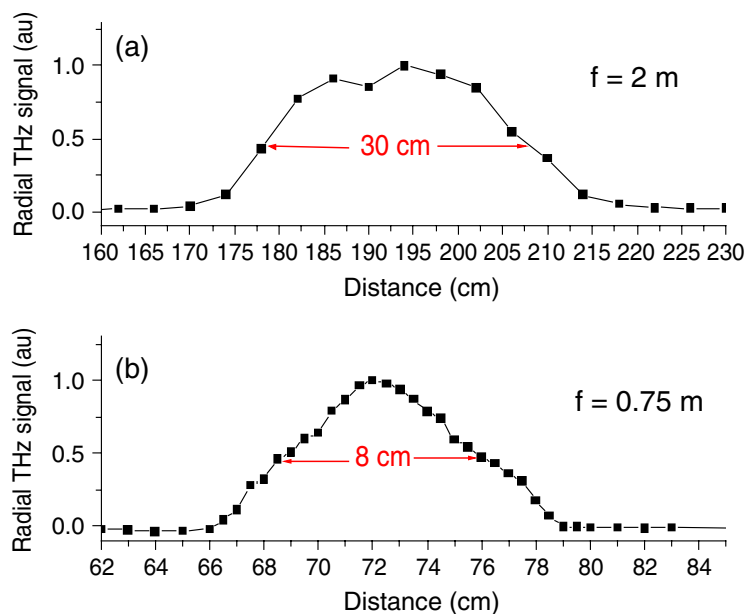


**Figure 4.** Radial THz signal as function of the propagation distance, measured along the filament for two different focal length lenses:  $f = 2$  m (a) and  $f = 0.75$  m (b). The full width at half maximum (FWHM) is the length of the obtained plasma channels.

the radial THz emission, under the reasonable assumption that the locally measured emission requires the presence of plasma. In figure 4, the results of measurements are shown for two different focal lengths, 2000 and 750 mm. In the first case, the self-guided laser pulse creates a 30 cm long plasma channel and in the second case it is 8 cm.

For each set of focusing conditions we have recorded the angular diagram by rotating the detector around a fixed point along the filament axis, as shown in figure 3. We have compared the measured and calculated emission diagrams for different lengths of filament, finding a very good agreement between theory and experiment. In particular, the law  $\theta \approx \sqrt{\lambda/L}$  for the maximum emission angle has been experimentally verified. In figure 5, we show the comparison between the measured and calculated emission diagrams for an 8 cm long filament.

#### 4.1. Remote forward THz source created in air by focusing TW laser pulses

To test the potential of this forward THz conical emission to reach high intensities on distant targets, we have also measured the THz emission from filaments generated with the Teramobile laser [39]. In this case, the pulse peak power was 2 TW. The laser pulse was focused by means of a telescope with the focal length of 20 m. The laser beam splits in a multi-filamentary structure before collapsing in a large bundle, which generates a 5 mm diameter and 4 m long plasma column, around the focus. The measurement of forward THz emission was performed by means of the 0.1 THz heterodyne detector. We obtained in this case a strong THz signal and the corresponding emission angular diagram is shown in figure 6. The detector was placed 2.5 m away from the rotation point along the laser axis. Due to the experimental difficulties resulting from the long plasma channel and large beam size, we measured the THz radiation only on one

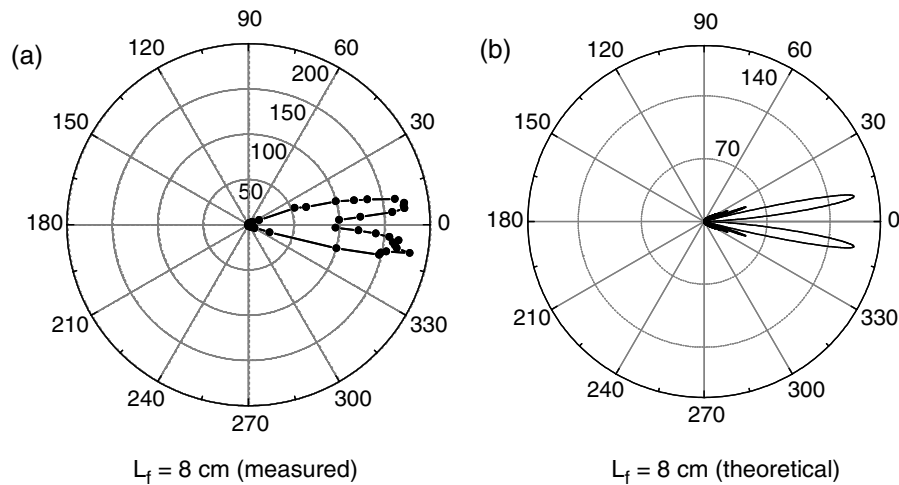


**Figure 5.** Comparison between experimental (a) and theoretical (b) THz emission angular diagrams for an 8 cm long filament.

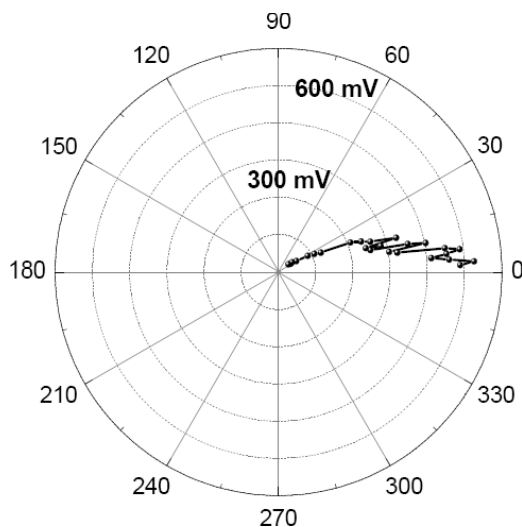


**Figure 6.** Experimental angular diagram (measured only between  $0^\circ$  and  $180^\circ$ ) of THz radiation created at long distance (20 m) with a TW laser (Teramobile).

side of the beam. Note that, overall, the measured angular distribution matches the theoretical model. The fine structures result from the fact that for the long plasma channels involved, the measurement position is not quite in the far-field. Taking into account the measurement position, by comparing the signal levels for the pulse peak powers of 27 GW shown above and 2 TW, we estimate, for the latter case, a forward emission with energy of two to three orders of magnitude stronger than the former. The energy needed for the pulse to create a large plasma column is about one to two orders of magnitude larger than in the case of one filament, where we created a  $100\text{--}200\ \mu\text{m}$  large plasma column. Now, following the transition–Cherenkov model, the radiated power in unit solid angle is proportional to the square of the energy of the self-guided pulse that creates the plasma (equation (14)), therefore we expect the radiation to be

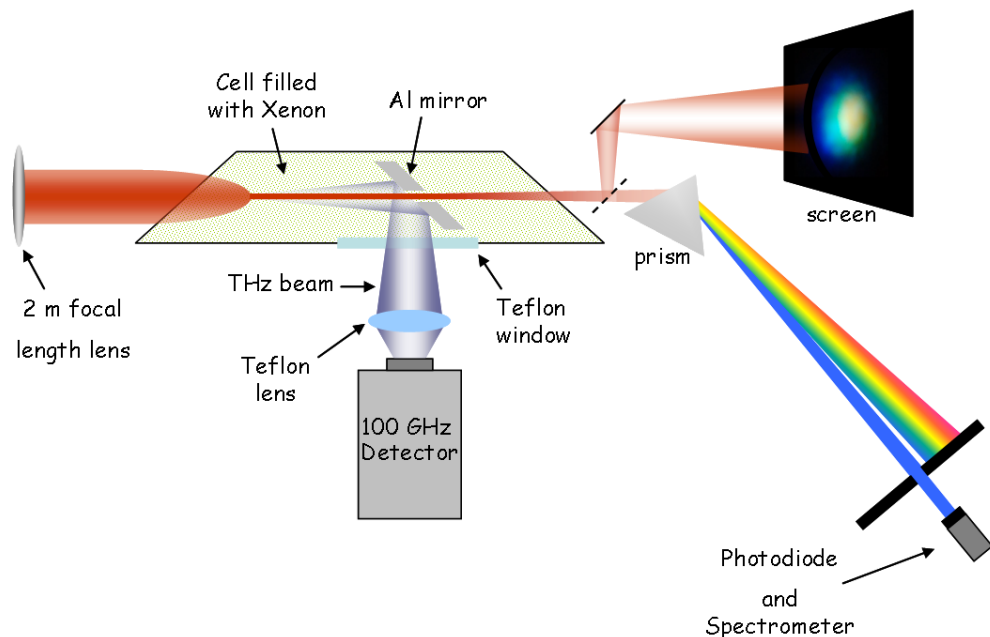


**Figure 7.** Experimental set-up used to detect, at the same time, the THz emission and the conical emission of the filament in gases.

between 100 and 1000 times stronger in the case of a large plasma column. A study of the polarization properties of the emitted radiation showed a radial polarization, as in the previous experiments.

## 5. Experimental results on forward THz emission by filamentation in noble gases

In this section, we present our experimental study of the THz emission from filamentation in noble gases. In most of our experiments, we used xenon, except that at the end of this section we present a comparison between xenon, argon and krypton. Figure 7 shows the experimental set-up that we used for the measurements in this section. The laser system is a Ti:sapphire CPA, which can deliver pulses with energies up to 15 mJ (at 100 Hz), with duration of  $\sim 40$  fs, centered at 800 nm wavelength. The pulses were focused with a 2 m focal length lens into a 1.5 m long gas cell. The gas pressure was kept around 1 atm. In order to avoid the absorption of the forward THz radiation by the exit window, we used a  $45^\circ$  aluminium mirror, with a half-circle hole at the top, to reflect the THz beam. The reflected half of the THz cone then passes through the Teflon wall of the cell, and is detected by the heterodyne 0.1 THz detector.

We first investigate the dependence of the THz radiation on the pulse energy. The integration over the solid angle of the equation (14) gives:

$$\Delta W \propto E_f^2 v_e^2 v^2 \ln \left( \frac{2\pi L v}{c} \right) \Delta v, \quad (15)$$

where  $v = 0.1$  THz, is the signal frequency and  $\Delta v = 6$  GHz is the bandwidth of our heterodyne detector. As the intensity of the laser pulse in the filament is defined by the filamentation process, we conclude that the efficiency of the forward THz emission should be proportional to the square

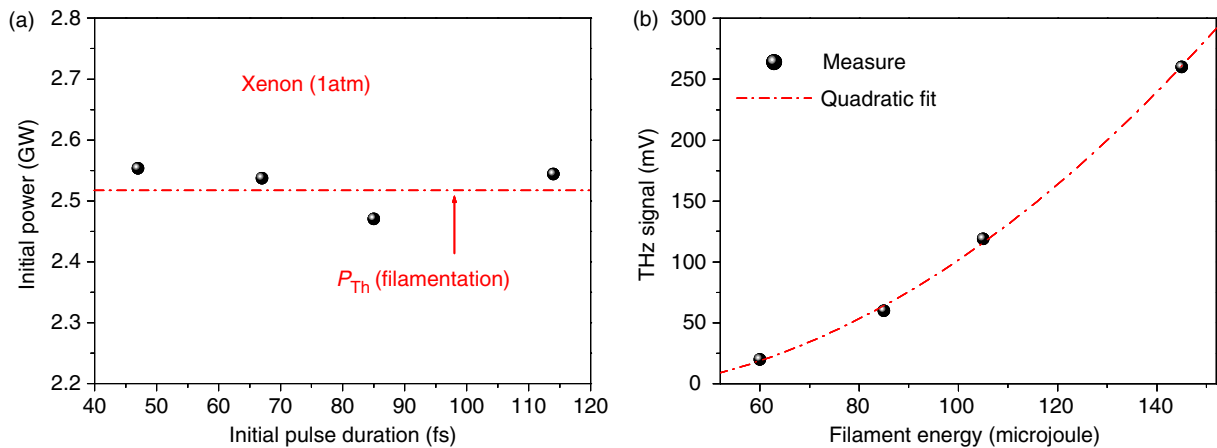


**Figure 8.** Measured THz signal (back dots) as a function of the filament energy, along with quadratic fit (dash-dotted line).

of the pulse energy, the square of the electron–neutral collision frequency and the logarithm of the filament length.

In order to examine the agreement of the theory with the experimental results, we varied the pulse duration in the range 40–120 fs, by adjusting the bandwidth at the compressor part of the CPA system, and kept the input power around the threshold for filamentation in xenon (about 2.5 GW) (see figure 8(a)). For different durations we measured the input and output pulse energies and found nearly constant transmission in accordance with Dubietis *et al* [40]. For the mono-atomic gases involved, the critical power does not change with the pulse duration. Thus changing the duration of the input pulse allowed us to change the energy contained in the filament. In figure 8(b), we present the measured THz signal as a function of the filament energy and observe a quadratic dependence, in accordance with the theory (see equation (15)).

In these experiments, we also observed a bright ‘blue spot’ after filamentation, emitted in the laser direction, but slightly off-axis (see inset of figure 9). The spectrum of the spot is centered at a wavelength of 400 nm, corresponding to the second harmonic of the input signal. Since the gases that we use are all centro-symmetric, we attribute this second harmonic generation (SHG) to the mixing of the generated THz signal with the fundamental, in a third order nonlinear process. This process can be described with the polarizability:  $P_i^{(3)2\omega}(t) \propto \chi_{ijkl}^{(3)} E_j^\omega(t) E_k^\omega(t) E_l^0(t)$  [41]. During the filamentation, the laser pulse can split into multiple pulses; hence, the THz generated at the peak of the pulse can interact with the trailing portion of the pulse. To confirm this, we spatially and spectrally filtered the SHG, and measured its relative strength with respect to the strength of the emitted THz. As shown in figure 9, we observe that the SHG signal is linearly proportional to the THz, as expected from the equation above.

## 6. Comparison of the conversion efficiencies of forward THz emission in noble gases and in air

In order to study the dependence of THz generation on the electron collision frequency, we measured the forward THz signal emitted from filaments in xenon, argon, krypton and air, all at atmospheric pressure. For each case, we also measured the energy in the filament coming out of

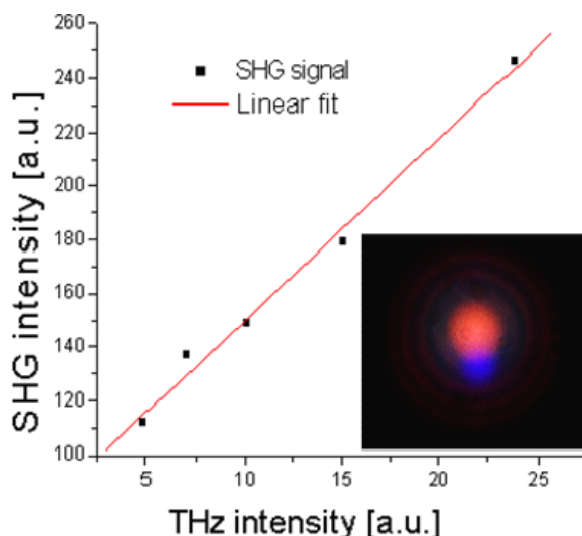


**Figure 9.** SHG signal versus the THz signal. The linear dependence of these two signals is an indication of SHG by the third-order mixing of the fundamental and THz pulses. The inset is a photographic picture of the conical emission coming from the filament. The blue spot that gives SHG signals is emitted off-axis and exhibits a 400 nm centered frequency spectrum.

**Table 1.** THz signal and filament energy measured for four different gases.

Gas ( $p = 1$ atm)	THz signal (mV)	Filament energy ( $\mu$ J)
Air	90	700
Ar	51	410
Kr	61	300
Xe	44	100

the cell by selecting the core with an aperture. In table 1, we show the measured values of the THz signal and the filament energy.

In light of the theoretical considerations presented above, one can assume the same temporal length of the emitted THz pulse in the different noble gases. Therefore, the relative conversion rates can be estimated by dividing the THz signal by the energy in the filament. From table 1, we can find the following ratios between the conversion rates:  $\eta_{\text{Ar}}/\eta_{\text{Air}} \approx 1$ ,  $\eta_{\text{Kr}}/\eta_{\text{Air}} \approx 1.6$  and  $\eta_{\text{Xe}}/\eta_{\text{Air}} \approx 3.4$ . These relative conversion ratios qualitatively match our expectation from the theory, as equation (15) predicts that the THz energy increases with the electron collision cross-section, as discussed in more detail below.

## 7. Forward THz emission and above threshold ionization (ATI) processes

In this section, we present a more detailed and quantitative study of the relative conversion efficiencies. We can express the electron–neutral atom collision frequency as  $\nu_e = n_a v_e \sigma_m$ , where  $v_e$  is the mean electron velocity,  $n_a$  the gas neutral atom density and  $\sigma_m$  the momentum

transfer cross section (MTCS) of electrons. Equation (15) can therefore be written as:

$$\Delta W \propto E_f^2 n_a^2 v_e^2 \sigma_m^2 v^2 \ln \left( \frac{2\pi L_f v}{c} \right) \Delta v. \quad (16)$$

The density of neutral atoms, for a given pressure, is the same for all considered gases. The power of the THz emission has a logarithmic and therefore weak dependence on the filament length,  $L_f$ , hence can be neglected. As a result, the ratio between the emitted THz power and the squared filament energy is only proportional to  $\sigma_m^2$  and the squared average electron velocity, i.e. the averaged electron kinetic energy,  $T \propto v_e^2$ . Therefore, one can compare the electron MTCSs for different gases by writing:

$$\frac{\sqrt{T'} \sigma'_m(T')}{\sqrt{T} \sigma_m(T)} = \frac{E}{E'} \sqrt{\frac{S'_{\text{THz}}}{S_{\text{THz}}}}, \quad (17)$$

where  $\sqrt{T/T'} = v_e/v'_e$  and  $S_{\text{THz}} \propto P_{\text{THz}}$  is the measured THz signal. We can write the electron kinetic energy for an  $s$ -photon ATI process [42] as  $T = \sum_s \alpha_s (n+s) \eta \omega - (U_i + U_p)$ , where  $\eta \omega$  is the photon energy and  $s$  is the number of above-threshold photons. The integer number  $n = \text{mod}[(U_i + U_p)/\eta \omega + 1]$  is the minimum number of photons needed to ionize the atom. In this formula  $\alpha_s$  is the probability of having an  $s$ -photon ATI process,  $U_i$  is the ionization energy of the atom or molecule and  $U_p = e^2 I_L / 2 \epsilon_0 m_e c \omega^2$  is the ponderomotive potential [43] given by the laser pulse intensity  $I_L$ . In general, in the range of intensities reached during filamentation, the ponderomotive potential is of the order of a few eV and cannot be neglected.

For a given pair of gases, the right-hand side of equation (17) is completely determined by the experimental values given in table 1. For the left-hand side, we assume that the averaged electron kinetic energy is nearly the same in all three noble gases. To justify this, we first recall that the intensity within a filament is clamped to a certain level given by equation (20) in [15]. The clamped intensity value in krypton is slightly higher than in xenon ( $I \approx 3 \times 10^{13} \text{ W cm}^{-2}$  in krypton,  $I \approx 1.2 \times 10^{13} \text{ W cm}^{-2}$  in xenon). On the other hand, from previous works on ATI processes [44] we can infer that in order to have electrons with the same average kinetic energy, one needs slightly higher intensity in krypton than in xenon because of the higher ionization potential of krypton. Hence, the difference in the clamped intensities approximately balances the average electron kinetic energies. The same argument also holds for the Xe/Ar and Kr/Ar pairs. The averaged electron kinetic energies in the considered gases are thus reasonably considered to be roughly the same; hence, we can write  $T/T' \approx 1$ . Equation (17) then becomes:

$$\frac{\sigma'_m(T)}{\sigma_m(T)} \approx \frac{E}{E'} \sqrt{\frac{S'_{\text{THz}}}{S_{\text{THz}}}}. \quad (18)$$

Figure 10 shows a graphical examination of this equation. The MTCS ratios are plotted as functions of the electron kinetic energy, by comparing Xe/Ar (solid line), Xe/Kr (dotted line) and Kr/Ar (dash-dotted line) by using the MTCS values reported by Hunter *et al* [45] and by Frost and Phelps [46]. The values we measured are represented by dots in the graph of figure 10, and at the same time they determine the right-hand side of equation (18). The experimental data of figure 10 have fixed  $y$ -coordinates, while the electron kinetic energy ( $x$ -axis) is unknown. Therefore, the best fit of the measured points on the graphs gives a reasonably good estimation of the electron kinetic energy in our experiments.

As can be seen from figure 10, the best agreement is found for electron energies around 3 eV, but the zone between 2 and 4 eV still provides good results. We note that the zone

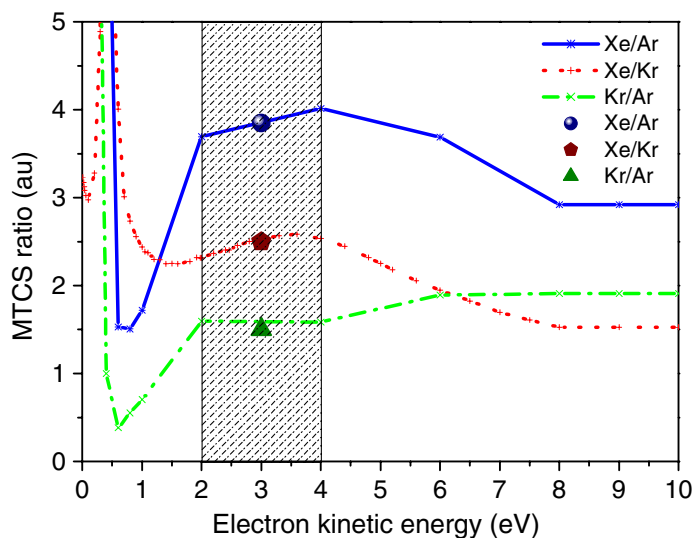


**Figure 10.** Graphical method used to examine equation (17). The solid, dotted and dash-dotted lines are the MTCS ratios for the comparison of Xe/Ar, Xe/Kr and Kr/Ar, respectively. The symbols represent our measurements. The symbols have  $y$ -axis values fixed by the measurement; they are translated along the  $x$ -axis (electron kinetic energy) in order to find the energy range in which we have the best agreement with the values reported in the literature. The best fit is found in the energy range 2–4 eV.

between 2 and 4 eV implies 1-photon and 2-photon ATI processes at a wavelength of 800 nm. Therefore, we conclude that 1-photon and 2-photon ATI processes can explain our experimental observation of forward THz emission during filamentation in rare gases. If one considers the intensity reached during filamentation processes in noble gases ( $\sim 10^{13} \text{ W cm}^{-2}$ ), 1-photon and/or 2-photon ATI processes are expected with a high probability, as previously pointed out for longer pulse durations [44, 47].

We conclude that the forward THz emission is strongly tied to the ATI processes during the filamentation in rare gases. In particular, a high order ATI process, in the electron energy range 1–4 eV, should give a stronger forward THz emission. This can be particularly interesting for molecular gases, where the MTCS can exhibit resonances, due to the different rotational and vibrational states of molecules.

## 8. Conclusions

In this paper, we described the origin of the THz radiation from the filaments created by intense femtosecond laser pulses propagating in gases. Both the conical and radial components of THz emission have been attributed to the same effect, namely the transition–Cherenkov process. The space charge is generated at the pulse’s peak intensity; the ponderomotive force of the laser field separates the charges, generating dipole-like structures, oscillating in the wake of the laser pulse. Since the ionization front moves with the laser at the speed of light, this gives rise to emission resembling transition and Cherenkov radiations. The theory of the transition–Cherenkov emission process has been developed and the spectrum and angular

distribution of the radiation has been calculated. THz experiments performed in air, xenon, krypton and argon have been compared with the theory. The THz radiation pattern is in excellent agreement with calculations. Furthermore, the THz emitted energy is shown to increase as the square of the laser pulse energy, as expected. Relative THz efficiencies measured in different gases depend on the electron–neutral atom collision frequency. From the relative efficiencies, it is possible to extract the initial electron kinetic energy during the multiphoton ionization process. It is shown that ATI plays an important role in the THz generation.

## Acknowledgment

This work has been partially supported by DGA and CNRS, France.

## References

- [1] Bass M, Franken P A, Ward J F and Weinreich G 1962 *Phys. Rev. Lett.* **9** 446
- Nahata A, Welling A S and Heinz T F 1996 *Appl. Phys. Lett.* **69** 2321
- [2] Dai J, Xie X and Zhang X-C 2006 *Phys. Rev. Lett.* **97** 103903
- [3] Cook D J and Hochstrasser R M 2000 *Opt. Lett.* **25** 1210
- [4] Bartel T, Gaal P, Reimann K, Woerner M and Elsaesser T 2005 *Opt. Lett.* **30** 2805
- [5] Cheng C C, Wright E M and Moloney J V 2001 *Phys. Rev. Lett.* **87** 213001
- [6] Sprangle P, Peñano J, Hafizi B and Kapetanacos C 2004 *Phys. Rev. E* **69** 066415
- [7] Hoyer W, Knorr A, Moloney J V, Wright E M, Kira M and Koch S W 2005 *Phys. Rev. Lett.* **94** 115004
- [8] Tzortzakis S *et al* 2002 *Opt. Lett.* **27** 1944
- [9] D'Amico C, Houard A, Franco M, Prade B and Mysyrowicz A 2007 *Opt. Express* **15** 15274
- [10] Méchain G, D'Amico C, André Y-B, Tzortzakis S, Franco M, Prade B, Mysyrowicz A, Couairon A, Salmon E and Sauerbrey R 2005 *Opt. Commun.* **247** 171
- [11] Golubtsov I S, Kandidov V P and Kosareva O G 2003 *Quantum Electron.* **33** 525
- [12] D'Amico C, Houard A, Franco M, Prade B, Couairon A, Tikhonchuk V T and Mysyrowicz A 2007 *Phys. Rev. Lett.* **98** 235002
- [13] Strickland D and Mourou G 1985 *Opt. Commun.* **56** 219
- [14] Braun A, Korn G, Liu X, Du D, Squier J and Mourou G 1995 *Opt. Lett.* **20** 73
- [15] Couairon A and Mysyrowicz A 2007 *Phys. Rep.* **441** 47
- [16] Tzortzakis S, Franco M, André Y-B, Chiron A, Lamouroux B, Prade B and Mysyrowicz A 1999 *Phys. Rev. E* **60** R3505
- [17] Couairon A 2003 *Phys. Rev. A* **68** 015801
- [18] Hauri C P, Kornelis W, Helbing F W, Couairon A, Mysyrowicz A, Biegert J and Keller U 2004 *Appl. Phys. B* **79** 673
- [19] Couairon A, Biegert J, Hauri C P, Kornelis W, Helbing F W, Keller U and Mysyrowicz A 2006 *J. Mod. Opt.* **53** 75
- [20] Chakraborty H S, Gaarde M B and Couairon A 2006 *Opt. Lett.* **31** 3662
- [21] Zaïr A, Guandalini A, Schapper F, Holler M, Biegert J, Gallmann L, Keller U, Couairon A, Franco M and Mysyrowicz A 2007 *Opt. Express* **15** 5394
- [22] Couairon A, Méchain G, Tzortzakis S, Franco M, Lamouroux B, Prade B and Mysyrowicz A 2003 *Opt. Commun.* **225** 177
- [23] Philip J, D'Amico C, Chériaux G, Couairon A, Prade B and Mysyrowicz A 2005 *Phys. Rev. Lett.* **95** 163901
- [24] D'Amico C, Prade B, Franco M and Mysyrowicz A 2006 *Appl. Phys. B* **85** 49
- [25] Méchain G, Couairon A, Franco M, Prade B and Mysyrowicz A 2004 *Phys. Rev. Lett.* **93** 035003
- [26] Musin R R, Shneider M N, Zheltikov A M and Miles R B 2007 *Appl. Opt.* **46** 5593

- [27] Kolesik M, Wright E M and Moloney J V 2004 *Phys. Rev. Lett.* **92** 253901
- [28] Faccio D, Matijosius A, Dubietis A, Piskarkas R, Varanavicius A, Gaizauskas E, Piskarkas A, Couairon A and Di Trapani P 2005 *Phys. Rev. E* **72** 037601
- [29] Couairon A, Gaizauskas E, Faccio D, Dubietis A and Di Trapani P 2006 *Phys. Rev. E* **73** 016608
- [30] Faccio D, Averchi A, Couairon A, Dubietis A, Piskarskas R, Matijosius A, Bragheri F, Porras M A, Piskarskas A and Di Trapani P 2006 *Phys. Rev. E* **74** 047603
- [31] Faccio D, Porras M A, Dubietis A, Tamosauskas G, Kucinskas E, Couairon A and Di Trapani P 2006 *Opt. Commun.* **265** 672
- [32] Faccio D, Porras M A, Dubietis A, Bragheri F, Couairon A and Di Trapani P 2006 *Phys. Rev. Lett.* **96** 193901
- [33] Bragheri F, Faccio D, Couairon A, Matijosius A, Tamosauskas G, Varanavicius A, Degiorgio V, Piskarskas A and Di Trapani P 2007 *Phys. Rev. A* **76** 025801
- [34] Porras M A, Parola A, Faccio D, Couairon A and Di Trapani P 2007 *Phys. Rev. A* **76** 011803
- [35] Zheng J, Yu C X, Zheng Z J and Tanaka K A 2005 *Phys. Plasmas* **12** 093105
- [36] Jackson J D 1965 *Classical Electrodynamics* 3rd edn (New York: Wiley)
- [37] Houard A, Liu Y, Prade B, Mysyrowicz A and Leriche B 2007 *Appl. Phys. Lett.* **91** 241105
- [38] Méchain G *et al* 2003 *Appl. Phys. B* **77** 707
- [39] Kasparian J *et al* 2003 *Science* **301** 61
- [40] Dubietis A, Couairon A, Kucinskas E, Tamosauskas G, Gaizauskas E, Faccio D and Di Trapani P 2006 *Appl. Phys. B* **84** 439
- [41] Cook D J, Chen J X, Morlino E A and Hochstrasser R M 1999 *Chem. Phys. Lett.* **309** 221
- [42] Agostini P, Fabre F, Mainfray G and Petit F 1979 *Phys. Rev. Lett.* **42** 1127
- [43] Bucksbaum P H, Freeman R R, Bashkansky M and McIlrath T J 1987 *J. Opt. Soc. Am.* **4** 760
- [44] McIlrath T J, Bucksbaum P H, Freeman R R and Bashkansky M 1987 *Phys. Rev. A* **35** 4611
- [45] Hunter S R, Carter J G and Christophorou G 1988 *Phys. Rev. A* **38** 5539
- [46] Frost L S and Phelps A V 1964 *Phys. Rev.* **136** A1538
- [47] Freeman R R, Bucksbaum P H, Milchberg H, Darack S, Schumacher D and Geusic M E 1987 *Phys. Rev. Lett.* **59** 1092

# Electric events synchronized with laser filaments in thunderclouds

Jérôme Kasparian<sup>1,2,\*</sup>, Roland Ackermann<sup>1</sup>, Yves-Bernard André<sup>3</sup>, Grégoire Méchain<sup>3</sup>, Guillaume Méjean<sup>1</sup>, Bernard Prade<sup>3</sup>, Philipp Rohwetter<sup>4</sup>, Estelle Salmon<sup>1</sup>, Kamil Stelmaszczyk<sup>4</sup>, Jin Yu<sup>1</sup>, André Mysyrowicz<sup>3</sup>, Roland Sauerbrey<sup>5</sup>, Ludger Wöste<sup>4</sup>, Jean-Pierre Wolf<sup>1,2</sup>

<sup>1</sup> Teramobile, Université Lyon 1; CNRS; LASIM UMR 5579, bât. A. Kastler, 43 Bd du 11 novembre 1918, F-69622 Villeurbanne Cedex, France.

<sup>2</sup> GAP, Université de Genève, 20 rue de l'École de Médecine, CH-1211 Genève 4, Switzerland

<sup>3</sup> Teramobile, Laboratoire d'Optique Appliquée, UMR CNRS 7639, ENSTA—Ecole Polytechnique, Centre de l'Yvette, Chemin de la Humière, F-91761 Palaiseau Cedex, France

<sup>4</sup> Teramobile, Institut für Experimentalphysik, Freie Universität Berlin, Arnimallee 14, D-14195 Berlin, Germany

<sup>5</sup> Forschungszentrum Dresden - Rossendorf, Bautzner Landstrasse 128, 01328 Dresden, Germany

\*Corresponding author: [jerome.kasparian@physics.unige.ch](mailto:jerome.kasparian@physics.unige.ch)

**Abstract:** We investigated the possibility to trigger real-scale lightning using ionized filaments generated by ultrashort laser pulses in the atmosphere. Under conditions of high electric field during two thunderstorms, we observed a statistically significant number of electric events synchronized with the laser pulses, at the location of the filaments. This observation suggests that corona discharges may have been triggered by filaments.

©2008 Optical Society of America

**OCIS codes:** (010.1300) Atmospheric propagation; (140.7090) Ultrafast lasers; (190.5940) Self-action effects; (190.7110) Ultrafast nonlinear optics; (350.5400) Plasmas; (999.9999) Lightning control

---

## References and links

1. R. Fieux, C. Gary, and P. Hubert, "Artificially Triggered Lightning above Land," *Nature* **257**, 212-214 (1975).
2. V. A. Rakov, M. A. Uman, and K. J. Rambo, "A review of ten years of triggered-lightning experiments at Camp Blanding, Florida," *Atmos. Res.* **76**, 503-517 (2005).
3. M. Miki, Y. Aihara, and T. Shindo, "Development of long gap discharges guided by a pulsed CO<sub>2</sub> laser," *J. Phys. D: Appl. Phys.* **26**, 1244-1252 (1993).
4. S. Uchida, Y. Shimada, H. Yasuda, S. Motokoshi, C. Yamanaka, T. Yamanaka, Z. Kawasaki, and K. Tsubakimoto, "Laser-triggered lightning in field experiments," *J. Opt. Technol.* **66**, 199-202 (1999).
5. A. Braun, G. Korn, X. Liu, D. Du, J. Squier, and G. Mourou, "Self-channeling of high-peak-power femtosecond laser pulses in air," *Opt. Lett.* **20**, 73-75 (1995).
6. S. L. Chin, S. A. Hosseini, W. Liu, Q. Luo, F. Theberge, N. Akozbek, A. Becker, V. P. Kandidov, O. G. Kosareva, and H. Schroeder, "The propagation of powerful femtosecond laser pulses in optical media: physics, applications, and new challenges," *Can. J. Phys.* **83**, 863-905 (2005).
7. L. Bergé, S. Skupin, R. Nuter, J. Kasparian, and J.-P. Wolf, "Ultrashort filaments of light in weakly-ionized, optically-transparent media," *Rep. Prog. Phys.* **70**, 1633-1713 (2007).
8. A. Couairon and A. Mysyrowicz, "Femtosecond filamentation in transparent media," *Phys. Rep.* **441**, 47-189 (2007).
9. J. Kasparian and J.-P. Wolf, "Physics and applications of atmospheric nonlinear optics and filamentation," *Opt. Express* **16**, 466-493 (2008).
10. J. Kasparian, M. Rodriguez, G. Méjean, J. Yu, E. Salmon, H. Wille, R. Bourayou, S. Frey, Y.-B. André, A. Mysyrowicz, R. Sauerbrey, J.-P. Wolf, and L. Wöste, "White-Light Filaments for Atmospheric Analysis," *Science* **301**, 61-64 (2003).
11. M. Mlejnek, E. M. Wright, and J. V. Moloney, "Power dependence of dynamic spatial replenishment of femtosecond pulses propagating in air," *Opt. Express* **4**, 223-228 (1999).
12. S. Skupin, L. Bergé, U. Peschel, F. Lederer, G. Méjean, J. Yu, J. Kasparian, E. Salmon, J. P. Wolf, M. Rodriguez, L. Wöste, R. Bourayou, and R. Sauerbrey, "Filamentation of femtosecond light pulses in the air: Turbulent cells versus long-range clusters," *Phys. Rev. E* **70**, 046602 (2004).

13. J. Kasparian, R. Sauerbrey, and S. L. Chin, "The critical laser intensity of self-guided light filaments in air," *Appl. Phys. B* **71**, 877-879 (2000).
14. X. M. Zhao, J.-C. Diels, C. Y. Wang, and J. M. Elizondo, "Femtosecond ultraviolet laser pulse induced lightning discharges in gases," *IEEE J. Quantum Electron.* **31**, 599-612 (1995).
15. M. Rodriguez, R. Bourayou, G. Méjean, J. Kasparian, J. Yu, E. Salmon, A. Scholz, B. Stecklum, J. Eislöffel, U. Laux, A. P. Hatzes, R. Sauerbrey, L. Wöste, and J.-P. Wolf, "Kilometer-range non-linear propagation of femtosecond laser pulses," *Phys. Rev. E* **69**, 036607 (2004).
16. G. Méjean, J. Kasparian, J. Yu, E. Salmon, S. Frey, J.-P. Wolf, S. Skupin, A. Vinçotte, R. Nuter, S. Champeaux, and L. Bergé, "Multifilamentation transmission through fog," *Phys. Rev. E* **72**, 026611 (2005).
17. G. Méchain, G. Méjean, R. Ackermann, P. Rohwetter, Y.-B. André, J. Kasparian, B. Prade, K. Stelmaszyk, J. Yu, E. Salmon, W. Winn, L. A. V. Schlie, A. Mysyrowicz, R. Sauerbrey, L. Wöste, and J.-P. Wolf, "Propagation of fs-TW laser filaments in adverse atmospheric conditions," *Appl. Phys. B* **80**, 785-789 (2005).
18. R. Salamé, N. Lascoux, E. Salmon, J. Kasparian, and J. P. Wolf, "Propagation of laser filaments through an extended turbulent region," *Appl. Phys. Lett.* **91**, 171106 (2007).
19. H. Wille, M. Rodriguez, J. Kasparian, D. Mondelain, J. Yu, A. Mysyrowicz, R. Sauerbrey, J.-P. Wolf, and L. Wöste, "Teramobile: a mobile femtosecond-terawatt laser and detection system," *Eur. Phys. J. - Appl. Phys.* **20**, 183-190 (2002).
20. P. Hubert, P. Laroche, A. Eybertberard, and L. Barret, "Triggered Lightning in New-Mexico," *J. Geophys. Res. Atmospheres* **89**, 2511-2521 (1984).
21. R. B. Standler and W. P. Winn, "Effects of Coronae on Electric-Fields beneath Thunderstorms," *Quart. J. R. Met. Soc.* **105**, 285-302 (1979).
22. W. Rison, R. J. Thomas, P. R. Krehbiel, T. Hamlin, and J. Harlin, "A GPS-based three-dimensional lightning mapping system: Initial observations in central New Mexico," *Geophys. Res. Lett.* **26**, 3573-3576 (1999).
23. M. Rodriguez, R. Sauerbrey, H. Wille, L. Wöste, T. Fujii, Y.-B. André, A. Mysyrowicz, L. Klingbeil, K. Rethmeier, W. Kalkner, J. Kasparian, E. Salmon, J. Yu, and J.-P. Wolf, "Megavolt discharges triggered and guided with laser filaments," *Opt. Lett.* **27**, 772-774 (2002).
24. M. Stanley, P. R. Krehbiel, D. Davis, C. B. Moore, J. Mathis, W. P. Winn, W. Rison, M. Brook, V. Idone, and J. Payne, *EOS, Transactions. AGU* **75**, 104 (1994).
25. P. R. Krehbiel, X. M. Shao, M. Stanley, G. Gray, S. McCrary, R. Scott, J. Lopez, C. R. Rhodes, and D. Holden, "Interferometer observations of natural and triggered lightning at Langmuir Laboratory," *EOS, Transactions. AGU* **75**, 99 (1994).
26. B. La Fontaine, F. Vidal, D. Comtois, C.-Y. Chien, A. Deparois, T. W. Johnston, J.-C. Kieffer, H. P. Mercure, H. Pépin, and F. A. M. Rizk, "The influence of electron density on the formation of streamers in electrical discharges triggered with ultrashort laser pulses," *IEEE Trans. Plasma Sci.* **27**, 688-700 (1999).
27. S. Tzortzakis, B. Prade, M. Franco, and A. Mysyrowicz, "Time evolution of the plasma channel at the trail of a self-guided IR femtosecond laser pulse in air," *Opt. Commun.* **181**, 123-127 (2000).
28. P. Rambo, J. Schwarz, and J.-C. Diels, "High-voltage electrical discharges induced by an ultrashort-pulse UV laser system," *J. of Opt. A: Pure Appl. Opt.* **3**, 146-158 (2001).
29. G. Méjean, R. Ackermann, J. Kasparian, E. Salmon, J. Yu, J.-P. Wolf, K. Rethmeier, W. Kalkner, P. Rohwetter, K. Stelmaszyk, and L. Wöste, "Improved laser triggering and guiding of megavolt discharges with dual fs-ns pulses," *Appl. Phys. Lett.* **88**, 021101 (2006).
30. H. Yang, J. Zhang, Y. Li, J. Zhang, Y. Li, Z. Chen, H. Teng, Z. Wei, and Z. Sheng, "Characteristics of self-guided laser plasma channels generated by femtosecond laser pulses in air," *Phys. Rev. E* **66**, 016406 (2002).
31. Z. Hao, J. Zhang, Y. T. Li, X. Lu, X. H. Yuan, Z. Y. Zheng, Z. H. Wang, W. J. Ling, and Z. Y. Wei, "Prolongation of the fluorescence lifetime of plasma channels in air induced by femtosecond laser pulses," *Appl. Phys. B* **80**, 627-630 (2005).
32. T. B. Petrova, H. D. Ladouceur, and A. P. Baronavski, "Numerical modeling of the electrical breakdown and discharge properties of laser-generated plasma channels," *Phys. Rev. E* **76**, 066405 (2007).
33. P. Bédot, L. Bonacina, J. Extermann, M. Moret, J. P. Wolf, R. Ackermann, N. Lascoux, R. Salamé, E. Salmon, J. Kasparian, L. Bergé, S. Champeaux, C. Guet, N. Blanchot, O. Bonville, A. Boscheron, P. Canal, M. Castaldi, O. Hartmann, C. Lepage, L. Marmande, E. Mazataud, G. Mennerat, L. Patissou, V. Prevot, D. Raffestin, and J. Ribolzi, "32 Terawatt Atmospheric White-Light Laser," *Appl. Phys. Lett.* **90**, 151106 (2007).

## 1. Introduction

Lightning has always been considered as fascinating but hazardous. Extensive work has been dedicated to the quantitative understanding of this natural phenomenon, with only limited success. In particular, its randomness makes *in situ* measurements difficult, raising the need to trigger lightning strikes at predetermined times and locations where instruments are available. Small rockets pulling thin wires into the high-field regions below thunderclouds can achieve such triggering [1, 2]. But the number of available rockets is limited, and several seconds elapse between the launch of a rocket and the triggered lightning strike.

To overcome these drawbacks, the use of lasers has been considered since the 1970's although without success. [3] The hot and dense plasma produced by such lasers absorbs the tail of the laser pulse and prevents the formation of the long plasma channels required to guide lightning strikes. Even by focusing four laser beams at the top of a lightning tower and using a solid target to produce a dense plasma, Uchida *et al.* [4] observed only two lightning strikes when the lasers were shot. Moreover, these events cannot be unambiguously attributed to an effect of the laser because the laser pulses were triggered only upon detection of naturally initiated descending leaders.

The advent of high-power, ultrashort (~100 fs) lasers renewed the perspective of laser-controlled lightning. Such systems generate efficient multiphoton/tunnel ionization of the air even at moderate energy (typically a few mJ per pulse), while they are too short to induce cascading ionization. The balance between Kerr self-focusing and defocusing by this plasma results in self-guided filaments [5-10]. More powerful lasers generate multiple filaments, which start and end randomly within a filamentation bundle of length up to hundreds of meters [11, 12]. They form channels of cold and underdense plasma with an electron density  $N_e \approx 10^{15} \text{ cm}^{-3}$  [13], several orders of magnitude above the required free electron density for lightning initiation in the atmosphere ( $N_{\text{init}} \approx 5 \times 10^{11} \text{ cm}^{-3}$  [14]). We have recently shown that such conducting filaments can be generated away from the laser source [15], propagate in clouds or turbulent atmospheres [16-18], and trigger and guide high-voltage discharges even in artificial rain [9, 10].

In this paper, we report *in-situ* investigations of the effect of laser filaments on electric activity in a thunderstorm. The observation of a statistically significant number of radiofrequency (RF) pulses associated with electric events in clouds, collocated and synchronized with the filaments, suggests that the laser has induced electric activity in the thunderclouds.

## 2. Experimental methods

We investigated the effect of femtosecond plasma channels of moderate energy on thunderclouds during a field campaign at the Langmuir Laboratory (New Mexico, USA, See Fig. 1), which provides a fully equipped facility with high lightning occurrence.

The *Teramobile* femtosecond-terawatt laser [19] was fired from the ridge of South Baldy Peak, 3209 m above sea level, at coordinates N33.98° and W107.2°. The laser was triggered at a repetition rate  $f = 10 \text{ Hz}$  (*i.e.* every  $T = 100 \text{ ms}$ ) by an internal clock, independently from the thunderstorm activity. It emitted a collimated (unfocused) beam, leaning southwards 70° above horizontal. The laser beam diameter was 3 cm, and the energy per pulse was 270 mJ at a center wavelength of 800 nm. The laser pulses, of 150 fs initial duration, were negatively chirped to 600 fs. Based on previous experiments with the same laser system [15] as well as control measurements performed at the campaign location [17] we determined that the above-described laser setup generates multiple filamentation with significant ionization over a typical length of 100 m, a few hundreds of meters above ground.

We investigated two thunderstorms (labelled T1 and T2, respectively) on September 24 (20:50 to 22:40 UTC) and September 25 (21:34 to 23:20 UTC), 2004. We focused the analysis on times when the electric field would have been sufficient to trigger lightning using rockets, *i.e.* exceeded 10 kV/m [20]. To account for the faster decrease of the electric field at ground level than a few meters above [21], we considered the maximum value of the electric

field, measured at ground level by a field mill, over a running 20 s time interval rather than its instantaneous value. During T1, the high-electric field criterion was achieved during 135 s, corresponding to 1350 laser pulses, in several time frames between 21:23 and 21:28. During T2, the relevant times lasted for 115 s (1150 laser pulses) in 3 periods: 21:48-21:52, around 23:07, and 23:14-23:15.

We analyzed the raw data from five Lightning Mapping Array (LMA) [22] receivers located within 1 km distance from the laser (See Fig. 1). Such receivers detect radiofrequency (RF) pulses at 63 MHz, generated by the electric activity in the atmosphere, with a time accuracy of 40 ns. For each node of a 100 x 100 m grid within a 2 x 2 km area around the laser, we shifted the clock of each receiver in order to account for its distance to the considered location. Each electric event in the atmosphere is then characterized by a set of RF pulses detected simultaneously (within  $\pm 167$  ns, *i.e.* 100 m horizontal resolution) by all of the 5 receivers. This data analysis technique allows to consider sets of RF sources with a delay mismatch corresponding to distances up to 100 m. Therefore, it is well suited to detect possible RF sources spreading over many tens of meters, as could be the case for events distributed along a filament, *i.e.* over a length up to 100 m. The delay mismatch between the times of arrival of the signals on the different receivers was evaluated for each event detected during T1.

Because the laser is fired independently from the electric activity in the clouds, temporal correlations of the electric events detected by the LMA with the laser operation can provide indications for an effect of the laser. At each location, we sought electric events temporally separated by entire multiples of  $T = 1/f$  within an uncertainty of  $t = 2$  ms. This 2 ms time delay has been chosen as a safe value to account for both the drift of the laser master clock over the duration of the thunderstorms, as well as possible delays between a laser pulse and an electric event it could trigger. In particular, typical discharge propagation speeds of  $10^5$ - $10^6$  m/s [23] correspond to sub-ms to ms-range delays for the typical 100 m scale of the filaments.

Electric activity in clouds is a random process, so that a temporal correlation between the electric activity in the thunderclouds and the laser pulses may be obtained by chance. We therefore estimated, at each location within the investigated area, the probability  $\alpha_{sync}$  that the observed number of synchronized events may have been obtained by chance among random events, rather than being due to an effect of the laser. This estimation yields the corresponding confidence level  $1 - \alpha_{sync}$ , where  $\alpha_{sync}$  can be understood as the risk of error when concluding that the observed pulses are related with the laser pulses.

Alternatively, we periodically blocked the laser beam for  $t_{OFF} = 3$  to 10 s and recorded the ratio of the number of events while the laser was emitted and blocked, respectively. Comparing this ratio with the one that could be expected in the case of random pulses yields the confidence level  $1 - \alpha_{excess}$  for this second observable.

The  $\alpha$  values have been calculated as follows. Observing, at a given location,  $n$  selected events among  $N$  is likely to be due to an effect of the laser only if the corresponding single-sided confidence level  $1 - \alpha$  (where  $\alpha$  is the *a priori* probability that at least  $n$  events are selected among  $N$  random ones) is high. If the *a priori* probability for an individual random event to be selected is  $p$ , then:

$$\alpha = \sum_{n'=n}^N p^{n'} \cdot (1-p)^{(N-n')} \cdot \frac{N!}{n'!(N-n)!} = \beta(n, N-n+1, p)$$

where  $\beta$  denotes the incomplete beta function. When observing  $n_{ON}$  events during the time  $t_{ON}$  with the laser firing, and  $n_{OFF}$  events in the time  $t_{OFF}$  without laser, the selection probability is  $p = t_{ON} / (t_{ON} + t_{OFF})$ , so that  $1 - \alpha_{excess} = 1 - \beta(n_{ON}, n_{OFF} + 1, t_{ON} / (t_{ON} + t_{OFF}))$ . Similarly, if  $n$  events among  $N$  are separated by entire multiples of  $T$  within  $t = 2$  ms, the confidence level of the corresponding single-sided statistical test is the probability of detecting by chance  $n$  or

more synchronized events among  $N$  random events:  $1 - \alpha_{\text{sync}} = 1 - \sum_{k=1}^{T/t} R_k$ , where  $R_k = R_1 \cdot (1 - R_{k-1})$ ,  $R_0 = 1$  and  $R_1 = \beta(n, N - n + 1, t/T)$ . Here, the summation accounts for the fact that the absolute time of the train of laser pulses is unknown, so that any time delay should be considered.

### 3. Results and discussion

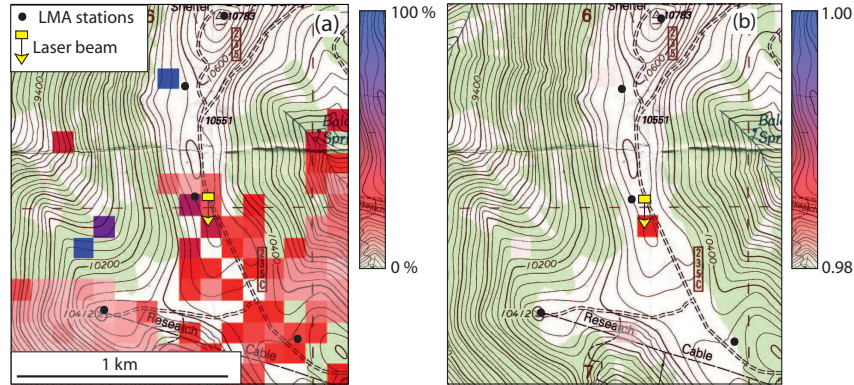


Fig. 1. Statistical analysis of the electric events detected during thunderstorm T1. (a) Rate of pulses synchronized with the laser repetition rate; (b) Corresponding statistical confidence level ( $1 - \alpha_{\text{sync}}$ , see text for details). The color scale is transparent below 98 % (*i.e.* for error risks above 2 %), leaving the topographical background uncovered. The arrow head indicates the location of the laser-induced plasma channel, while its tail marks the laser emitter. Topographic background courtesy of US Geological Survey.

Fig. 1 displays the result of the statistical analysis of thunderstorm T1. At the location of the laser filaments (arrow head), 43 % (3 out of 7, Fig. 1(a)) of the pulses are synchronized with the laser repetition rate. This rate may appear pretty low, especially when considering that higher rates are observed at several other locations of the map. However, performing the statistical test described above at each location draws a fully different picture (Fig. 1(b)). The confidence level shows high statistical significance ( $1 - \alpha_{\text{sync}} = 0.987$ ) only at the location of the laser filaments, suggesting that the laser did indeed induce the observed electric events. This statistical significance is achieved in spite of the limited number of events, especially if we compare with the 1350 laser pulses launched into the atmosphere during the considered 135 s time frame. This significance stems from the fact that the time jitter allowed between synchronized pulses is much shorter than the time between two consecutive laser pulses (2 ms vs 100 ms). Similar results are obtained for Thunderstorm T2 (3 synchronized pulses out of 10 in 115 s,  $1 - \alpha_{\text{sync}} = 0.958$ ). In the latter case the effect is slightly shifted northwards due to a drift in the plasma filaments along the laser beam and the uncertainties in the triangulation algorithm. No effect was observed when the electric field was low or negative. Therefore, our results suggest that a small fraction (0.24 % of the laser pulses, *i.e.* ~1 event/minute) of the plasma filaments have initiated electric events in a strong positive (upward pointing) electric field.

Moreover, more electric events are observed when the laser is fired than when it is blocked (Fig. 2). During T1, 7 pulses are detected at the laser location during a total  $t_{\text{ON}} = 135$  s, and none during  $t_{\text{OFF}} = 72$  s when the laser is blocked, corresponding to a significant effect within a confidence level  $1 - \alpha_{\text{excess}} = 0.95$ . Again, similar results (10 pulses in  $t_{\text{ON}} = 115$  s vs none in  $t_{\text{OFF}} = 84$  s,  $1 - \alpha_{\text{excess}} = 0.998$ ) are observed for T2.

The laser filaments do not extend to the ground, so that they can be compared with a rocket-pulled wire not connected to the ground. While the potential upward positive leader

can be invisible to the LMA [24, 25], the associated negative downward leader propagating from the bottom of the wire (resp. filament) and dart leaders that later propagate from the cloud down to the initial positive leader channel, shall emit detectable pulses. However, the delay mismatch between the RF pulses detected on the different LMA detectors for some events correspond to some tens of meters. Such mismatches suggest spatially spread events, such as corona discharges at the tips of individual filaments within the bundle of multiple filamentation.

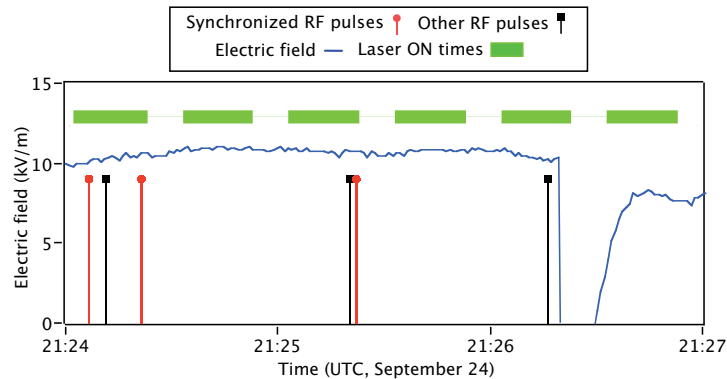


Fig. 2. Electric events during a high-field period of thunderstorm T1. Triggered events contribute to the excess of detected events when the laser is shot (green blocks)

The very limited effect of the plasma channel left behind by the filaments, which did not trigger full lightning strike, is due to their limited lifetime of  $\sim 1 \mu\text{s}$  [26, 27], corresponding to an effective length on the meter-scale for a leader propagating at a speed of a few  $10^6 \text{ m/s}$  [23]. Since wires of a few tens of meters are sufficient for rocket triggering of lightning, the plasma lifetime has to be enhanced up to several tens of  $\mu\text{s}$ . This could be achieved by a subsequent nanosecond, multi-Joule laser pulse [14, 28]. Recently, we have even shown in the laboratory that a frequency-doubled YAG pulse of moderate energy (200 mJ) is sufficient to improve the ability of femtosecond filaments to trigger high-voltage discharges on the meter-scale [29]. Sequences of ultrashort pulses at 800 nm have also been proposed to improve the plasma lifetime [30, 31]. The definition of the optimal pulse sequence is still an open question, relying on throughout modeling of the temporal evolution of the plasma channel created by the laser in an electric field. [32] Other available parameters include the pulse energy and beam profile. While the latter is difficult to control over long distances in the highly perturbed propagation conditions encountered in thunderstorms, an increased pulse energy could yield more filaments over longer distances [33], thus possibly improving the effect of the laser on the electric field.

To implement and optimize such improved laser schemes in a field campaign, an observable is required to assess for the influence of each investigated parameter. In that purpose, a sensitive detection system with adequate spatial and temporal resolution, as was provided by the LMA, is a key element for such field experiments. The effect of the laser, as faint as it may be, can then be monitored as a function of each experimental parameter in order to drive the experimental work and optimize the laser effect. In that regard, our results constitute a step towards laser-controlled lightning.

#### 4. Conclusion

As a conclusion, we have investigated the influence of ultrashort laser filaments on thunderclouds. Our results suggest that plasma filaments generated in the atmosphere by ultrashort laser pulses can trigger electric events in thunderclouds under high positive electric field, although the efficiency achieved in our experiment is low. This result constitutes a step

towards laser-controlled lightning. The triggering of actual lightning strikes requires further development, in particular to enhance the plasma lifetime and density within the filament *e.g.* using sequences of laser pulses. Also, improving the laser repetition rate will enhance the time rate of triggered events. A factor of 10 could be achieved if using the TW-lasers with repetition rates of 100 Hz or more that are becoming available.

### **Acknowledgements**

This work has been performed in the framework of the *Teramobile* collaboration ([www.teramobile.org](http://www.teramobile.org)), funded jointly by the CNRS, DFG, French and German ministries of Foreign affairs, Agence Nationale de la Recherche (ANR, grant # NT05-1\_43175), Fonds national suisse de la recherche scientifique (FNS, grants #200021-111688/1 and 200021-116198/1), and the Swiss Secrétariat d'État à l'Éducation et à la Recherche (COST P18 action C06.0114). The authors also acknowledge AFOSR and AFRL/DE for their financial support to the experimental campaign. K. S. acknowledges financial support by the Alexander von Humboldt Foundation. We would like to warmly thank the team of the Langmuir Laboratory at the New Mexico Institute of Mining and Technology, and especially Graydon Aulich, Gary Coppler, James Dinallo, Harald Edens, Steven Hunyady, Sandy Kieft, Dan Klingsmith, William Rison, Ron Thomas, and William Winn for their constant support and fruitful discussions all along the campaign and data analysis. Constructive discussions with L.A.(Vern) Schlie at AFRL/DE, as well as the efficient administrative support by Anne Gourlan at Lasim were also highly appreciated.

# Progress towards lightning control using lasers

**Jérôme Kasparian**

jerome.kasparian@unige.ch

**Roland Ackermann**

**Yves-Bernard André**

**Grégoire Méchain**

**Guillaume Méjean**

**Bernard Prade**

**Philipp Rohwetter**

**Estelle Salmon**

**Kamil Stelmaszczyk**

**Jin Yu**

**André Mysyrowicz**

**Roland Sauerbrey**

**Ludger Wöste**

**Jean-Pierre Wolf**

Teramobile, Université de Lyon; Université Lyon 1; CNRS; LASIM UMR 5579, bât. A. Kastler, 43 Bd du 11 novembre 1918, F-69622 Villeurbanne Cedex, France

GAP, Université de Genève, 20 rue de l'École de Médecine, CH-1211 Genève 4, Switzerland

Teramobile, Université de Lyon; Université Lyon 1; CNRS; LASIM UMR 5579, bât. A. Kastler, 43 Bd du 11 novembre 1918, F-69622 Villeurbanne Cedex, France

Teramobile, Laboratoire d'Optique Appliquée, UMR CNRS 7639, ENSTA—Ecole Polytechnique, Centre de l'Yvette, Chemin de la Hunière, F-91761 Palaiseau Cedex, France

Teramobile, Laboratoire d'Optique Appliquée, UMR CNRS 7639, ENSTA—Ecole Polytechnique, Centre de l'Yvette, Chemin de la Hunière, F-91761 Palaiseau Cedex, France

Teramobile, Université de Lyon; Université Lyon 1; CNRS; LASIM UMR 5579, bât. A. Kastler, 43 Bd du 11 novembre 1918, F-69622 Villeurbanne Cedex, France

Teramobile, Laboratoire d'Optique Appliquée, UMR CNRS 7639, ENSTA—Ecole Polytechnique, Centre de l'Yvette, Chemin de la Hunière, F-91761 Palaiseau Cedex, France

Teramobile, Institut für Experimentalphysik, Freie Universität Berlin, Arnimallee 14, D14195 Berlin, Germany

Teramobile, Université de Lyon; Université Lyon 1; CNRS; LASIM UMR 5579, bât. A. Kastler, 43 Bd du 11 novembre 1918, F-69622 Villeurbanne Cedex, France

Teramobile, Institut für Experimentalphysik, Freie Universität Berlin, Arnimallee 14, D14195 Berlin, Germany

Teramobile, Université de Lyon; Université Lyon 1; CNRS; LASIM UMR 5579, bât. A. Kastler, 43 Bd du 11 novembre 1918, F-69622 Villeurbanne Cedex, France

Teramobile, Laboratoire d'Optique Appliquée, UMR CNRS 7639, ENSTA—Ecole Polytechnique, Centre de l'Yvette, Chemin de la Hunière, F-91761 Palaiseau Cedex, France

Forschungszentrum Dresden - Rossendorf, Bautzner Landstrasse 128, 01328 Dresden, Germany

Teramobile, Institut für Experimentalphysik, Freie Universität Berlin, Arnimallee 14, D14195 Berlin, Germany

GAP, Université de Genève, 20 rue de l'École de Médecine, CH-1211 Genève 4, Switzerland

Lightning research needs on-demand lightning strikes, because of the random character of natural lightning. Lasers have been proposed as alternatives to the current technique using rocket-pulled wires, because they would expectedly provide more flexibility. However, high-energy, nanosecond lasers cannot provide long connected plasma channels. In contrast, we recently reported the triggering of electric events in thunderclouds using ultrashort laser pulses. Further improvements of the laser pulse sequence and experimental geometry are discussed. [DOI: 10.2971/jeos.2008.08035]

**Keywords:** lightning, ultrashort laser, self-guiding, laser filaments, plasma

## 1 INTRODUCTION

Attempts to provide natural rather than divine interpretations of lightning began in the 17<sup>th</sup> Century with René Descartes, followed in the 18<sup>th</sup> Century by Thomas-François Dalibard and Benjamin Franklin. The former demonstrated that lightning is an electrical phenomenon, in an experiment initially proposed by the latter, who also conceived the first lightning rod [1]. In the 20<sup>th</sup> Century, photography and the cathode ray tube oscilloscope allowed the trajectory of lightning strikes to be observed, and the corresponding voltage and intensity to

be measured, i.e.  $\sim 100$  MV and  $\sim 30$  kA, respectively [2]. Today's instruments provide an even more precise view of the processes at play in the physics of lightning.

Lightning strikes occur after charges are generated by collisions between ice and/or water particles within thunderclouds, and separated by vertical winds, with speeds up to 20 m/s. The electric field originating from this separation between positive charges at the cloud top and negative charges

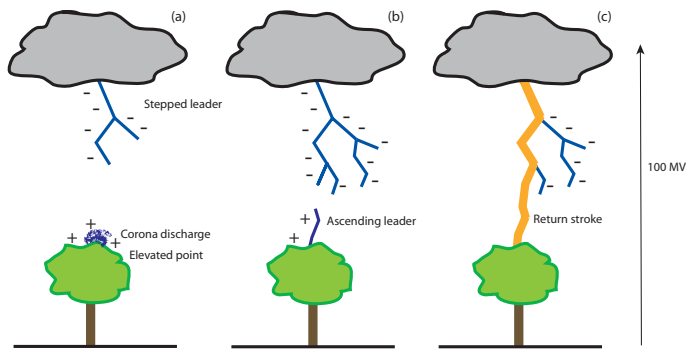


FIG. 1 Mechanism of lightning initiation: (a) stepped leader formation; (b) initiation of an upward leader; (c) return stroke

at its bottom reaches up to 10 to 15 kV/m at ground level, and 50 kV/m some hundreds of meters above. Such high field initiates corona discharges which develop into streamers, which in turn connect and form an ionized channel, or *leader* (Figure 1(a)). The leader progresses downwards in several branches, by steps of a few tens of meters, with typical rest times of 100  $\mu$ s between two steps (Figure 1(b)). If a leader branch reaches close to an elevated point such as a tree, a building or a mountain ridge, an upward leader starts, propagates upwards and connects to the descending leader, allowing a *return stroke*, with a typical intensity of 30 kA, to flow from the ground to the cloud (Figure 1(c)). The return stroke lasts a few tenths of a second and constitutes the visible part of the lightning strike.

## 2 ATTEMPTS TO TRIGGER LIGHTNING USING HIGH-ENERGY LASERS

Lightning is a random process in both the spatial and temporal domains. But field experiments require lightning strikes at the very location of instruments, which moreover need synchronization. Therefore, they require some extent of control of the lightning strikes. Several groups [3, 4] developed on-demand lightning initiation by rockets pulling a thin conducting wire, which triggers a lightning strike and guides it to the ground. Conducting wires sections as short as a few tens of meters proved almost as efficient as longer ones, and limit the perturbation to the lightning mechanism. However, rockets lack flexibility, since they cannot be aimed at specific cloud regions and are available in limited number.

Soon after their discovery, lasers were proposed as potential triggers for lightning, that could offer more flexibility than rockets, including beam steering and virtually continuous operation. Such proposition generated extensive work, both theoretical and experimental [5]. Laser sparks were typically produced by CO<sub>2</sub> lasers, with energies up to several kJ [6] and a typical pulse duration of 50 ns [7]. Such high energy heats the channel up to 4000°C, and therefore reduces the gas density to the 0.1 atm range, resulting in efficient air ionization. But the dense plasma generated by the leading edge of the pulse absorbs its tail, resulting in high pulse energy losses and blocking further propagation, hence preventing the generation of a connected plasma channel longer than a few meters.

Field experiments on the shore of the Sea of Japan in a period of intense winter low-cloud thunderstorms confirmed this limitation [8]. Three lasers were used. One 1 kJ CO<sub>2</sub> laser was focused on a dielectric target at the top of a 50 m high tower constructed on a 200 m high hill, while a second one was focused near to the generated ablation plume to form a 2 m long plasma spark. A third, ultraviolet laser produced a weakly ionized plasma channel slightly offset from the tower, intended to direct the leader to the cloud. The lasers were triggered when the initiation of cloud discharges, considered as the precursor of the descending lightning strikes, was detected. The authors reported two successful attempts, although the statistical significance of their result is not clear.

## 3 CONTROL OF HIGH-VOLTAGE DISCHARGES USING ULTRASHORT LASERS

The advent of lasers providing ultrashort, high-power pulses changed the perspective for laser-induced lightning. In contrast to longer pulses, ultrashort laser pulses in air form plasma channels, or self-guided *filaments* [9]–[13] with a length up to 100 m [14] at a distance from several meters up to several kilometres from the laser source [15]. This process originates from a dynamic balance between Kerr self-focusing and the defocusing effect of the free electrons of the plasma generated at the self-focus location. Steering the beam allows to aim the ionized plasma channel at the most active part of a thundercloud. Furthermore, filaments can propagate almost unperturbed in adverse conditions such as rain [16], fog [17], turbulence [18, 19] or reduced pressure [16], which makes them highly suitable for atmospheric applications.

Both infrared [20, 21] and ultraviolet [22] ultrashort laser pulses have been shown to trigger high-voltage discharges in strongly focused configurations. Later, the *Teramobile* laser [23] installed in a high-voltage facility generated self-guided filaments, which triggered (Figure 2) and guided 1.8 MV discharges over up to 4.5 m [24]–[26] (Figure 3) using 300 mJ

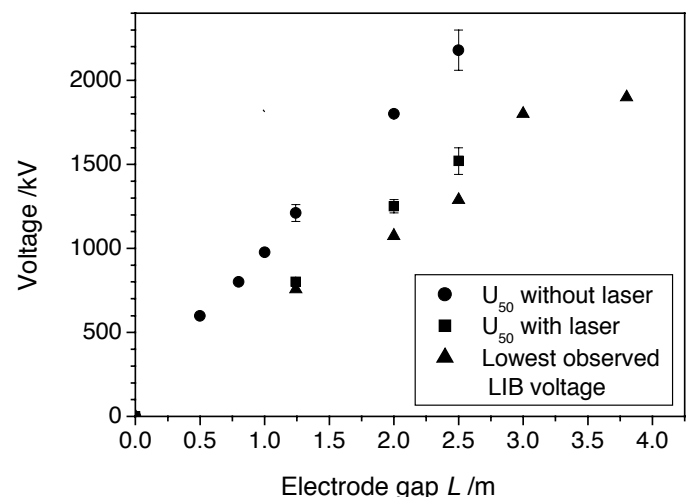


FIG. 2 Laser triggering of high-voltage discharges: Median breakdown voltage ( $U_{50}$ ) with and without laser. The lowest breakdown voltage observed (LIB) is also plotted [24].

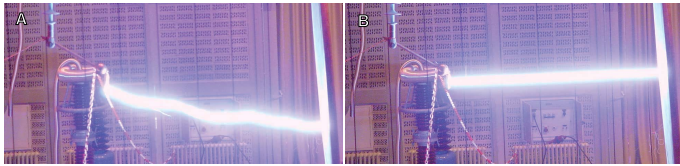


FIG. 3 Laser guiding of high-voltage discharges. (a) Free discharge over 3 m, without laser filaments. Note the erratic path. (b) Straight discharge guided along laser filaments [25].

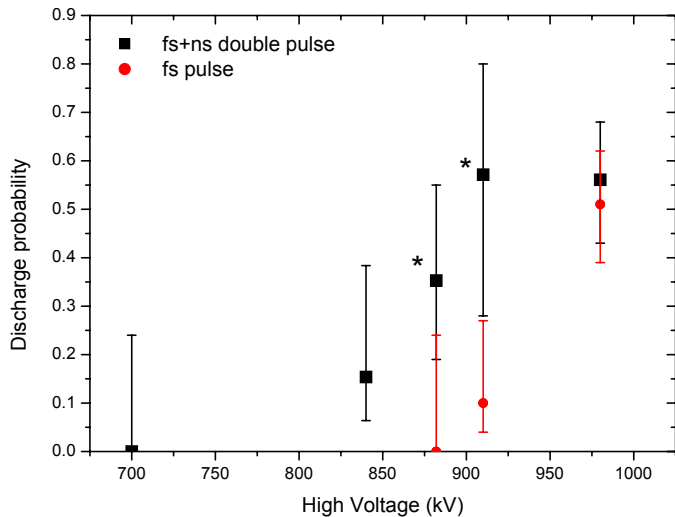


FIG. 4 Triggering probability of high-voltage discharges with both a single fs pulse alone and a dual (fs+ns) pulse with the maintaining pulse at 532 nm. \* denotes a statistically significant effect of the maintaining laser for individual points [28].

pulses centered at 790 nm. Even artificial rain does not prevent the laser filaments from triggering discharges [27]. Moreover, a subsequent YAG laser pulse of moderate energy (sub-Joule) at 532 nm increases the triggering effect of the infrared femtosecond laser [28, 29] (Figure 4) by extending the plasma lifetime, improving the triggering to the atmosphere. This approach relies on avalanche ionization, re-heating and photodetaching electrons of the plasma channel by subsequent pulses, either in the nanosecond [22] or in the femtosecond regime [30, 31]. Although none of these processes alone has a significant contribution, they can contribute to the switching to a regime where increased electron density, more efficient Joule heating and reduced electron attachment efficiency at higher temperatures sustain each other in a positive feedback loop.

#### 4 FIELD EXPERIMENTS WITH FEMTOSECOND LASER FILAMENTATION

Following the demonstration of both the capability of laser filaments to propagate in realistic atmospheric conditions and their ability to trigger high-voltage electric discharges, the effect of femtosecond plasma channels of moderate energy on thunderclouds was investigated during a field campaign [32] at the Langmuir Laboratory (New Mexico, USA, see Figure 5), which provides a fully equipped facility with high lightning occurrence.

The *Teramobile* laser [23] emitted a collimated beam, leaning

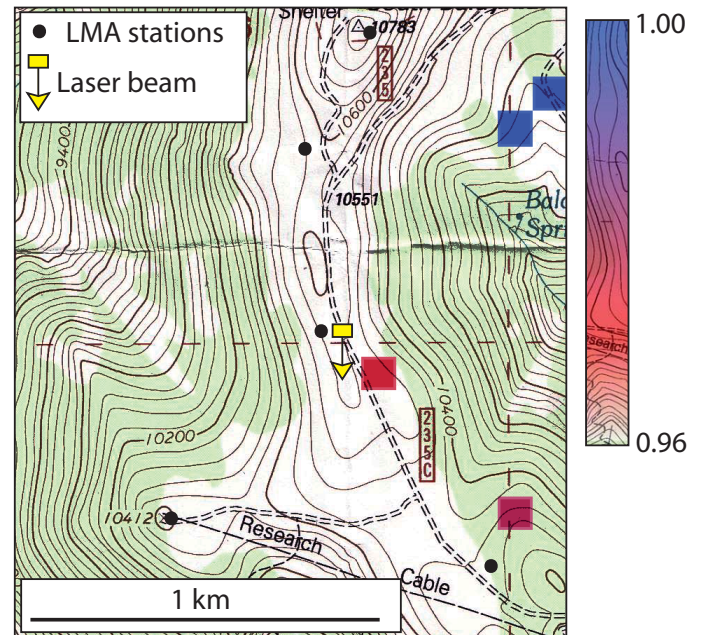


FIG. 5 Statistical confidence level of the electric events synchronized with the laser pulses during a thunderstorm on September 25, 2004. The colour scale is transparent below 96 % (i.e. for error risks above 4 %), leaving the topographical background uncovered. Topographic background courtesy of US Geological Survey.

southwards  $70^\circ$  above horizontal from the ridge of South Baldy Peak, 3209 m above sea level, at a repetition rate of 10 Hz. The laser beam diameter was 3 cm, and the energy per pulse was 270 mJ at a central wavelength of 800 nm. The laser pulses were negatively chirped to 600 fs in order to generate multiple filamentation with significant ionization over a typical length of 100 m, a few hundreds of meters above the ground. The data analysis focused on a total time of 250 s during two thunderstorms, when the electric field would have been sufficient to trigger lightning using rockets.

An array of five radiofrequency (RF) receivers located within 1 km distance from the laser (see Figure 5) detected the electric activity in the atmosphere [33]. Triangulation based on the times of arrival of the RF pulses on the detectors yielded a location and time stamping of the cloud activity which generated them. Delay mismatches up to 300 ns were accepted between the detectors, to allow the detection of events distributed over a length up to 100 m (i.e. the expected filamentation length) along the laser beam.

Since the laser is fired independently from the electric activity in the clouds, and natural electric activity in clouds is a random process, we sought for temporal correlations between the electric events detected by the LMA and the laser pulses. A significant correlation appears as a strong indication of an effect of the laser, with a confidence level defined by a comparison between the number of observed synchronized events and the number of random events that would expectedly happen to be synchronized by pure chance.

Figure 5 displays the result of this statistical analysis for a storm on September 25, 2004. At the location of the laser filaments (arrow head) within the spatial resolution of the data processing, 30% (3 out of 10) of the pulses are synchro-

nized with the laser repetition rate. The probability to obtain the same number of synchronized events by chance is only 2.4%, meaning that the statistical confidence level is as high as 97.6%. The delay mismatch between the RF pulses detected on the different LMA detectors for some events correspond to some tens of meters, typical of spatially spread events, such as corona discharges at the tips of individual filaments within the bundle of multiple filaments. Similar results are obtained during the second thunderstorm, while no effect was observed when the electric field was low or negative.

These results suggest that a small fraction (0.24%, i.e.  $\sim 1$  event/minute) of the plasma filaments have initiated electric events in a strong positive (upward pointing) electric field [32]. This result constitutes a step towards laser-controlled lightning, but the low efficiency achieved in this experiment requires further development.

## 5 OPTIMIZATION OF THE FILAMENT EFFECT IN THUNDERSTORMS

The very limited effect of the plasma channel left behind by the filaments, which did not trigger lightning strikes to the ground, appears to be due to their low electron density as well as the limited plasma lifetime of  $\sim 1 \mu\text{s}$  [34, 35], corresponding to an effective length on the meter-scale for a leader propagating at a speed of a few  $10^6$  m/s [24]. Since wires of a few tens of meters are sufficient for rocket triggering of lightning, the plasma lifetime has to be enhanced up to several tens of  $\mu\text{s}$ . As discussed above, this may be achieved by emitting a pulse sequence, with a YAG laser pulse [22, 28, 29] or a train of femtosecond pulses [30, 31] launched after the initial ultrashort pulse. The definition of the optimal pulse sequence is still an open question, relying on extensive modelling of the temporal evolution of the plasma channel created by the laser in an electric field [36]. Other available parameters include the pulse energy and beam profile. While the latter is difficult to control over long distances in the highly perturbed propagation conditions encountered in thunderstorms, higher pulse energies could yield more filaments over longer distances [37] thus possibly improving the effect of the laser on the electric field.

The emission geometry is also subject to optimization. Hints in this direction have recently been proposed [38]. This model considers filaments as passive conductors, which suddenly emerge from the space charge accumulated around the ground, as rockets do if their speed is sufficient, resulting in an enhanced electric field favourable for lightning initiation. The treatment of filaments as static conductors is supported by an estimation of a  $\sim 0.1 \mu\text{s}$  loading time of the RC circuit formed by the ground, filament, and cloud base. Such loading time is longer than the picosecond timescale of electron attachment, but shorter than the microsecond lifetime of the plasma channel. Therefore, filaments can be assumed to intercept all leaders in their vicinity, within a distance  $r = 10 I^{2/3} \sim 100$  m for an intensity  $I = 30$  kA of the lightning strike [2]. Once it interacts with the descending leader and generates an upward positive leader, the plasma

channel is considered to be stabilized by the current flowing through it [39].

Based on these assumptions, phenomenological Monte-Carlo simulations of a descending leader above a flat ground were used to illustrate the impact of several configuration parameters with and without tower [38]. Due to a limited region of influence and a poor duty cycle related to the short plasma lifetime as compared with typical repetition rates of terawatt lasers, a fixed, vertical laser beam triggered independently from the cloud activity appears to have a hardly measurable effect on the thundercloud. A few events at most may be accessible, which could explain the very small number of events observed during the *Teramobile* field campaign [32].

However, the flexibility of the laser technique could drastically improve this low efficiency. The laser beam could be triggered and steered according to a real-time detector, as used by Uchida *et al.* [8] to detect and locate the advent of descending leaders. This approach improves the duty cycle by a factor of 100 to 1000, since all laser shots will then be able to intercept a descending leader. Moreover, the steering capability extends the volume of influence of the laser, and therefore increases the number of accessible descending leaders by a typical factor of 10, even for conservative filament heights of a few hundreds of meters [38]. Intercepting several tens to a few hundreds of shots in one single season therefore appears accessible. Such numbers are sufficient to achieve the statistical significance required for a field campaign to be conclusive. It could also constitute a quantitative improvement as compared with the yield of the rocket technique.

## 6 CONCLUSION

Although initiated 50 years ago, the effort to control lightning using lasers has not yet reached its goal of triggering and guiding lightning strikes on demand to the ground. However, recent results obtained with the femtosecond-terawatt *Teramobile* laser renew the expectations that ultrashort laser pulses may be good candidates to achieve this challenge. Further improvement requires optimized plasma filaments generated by the ultrashort laser pulses. In particular, pulse sequences, as well as a higher pulse power, are expected to enhance both the electron density and plasma lifetime. Active triggering and steering of the laser upon the detection of leader initiation in the clouds shall also improve dramatically the volume accessible to the filaments, as well as their duty cycle. Macroscopic number of triggered events could therefore be expected in a near future.

## ACKNOWLEDGEMENTS

This work has been performed in the framework of the *Teramobile* collaboration ([www.teramobile.org](http://www.teramobile.org)), funded jointly by the CNRS, DFG, French and German ministries of Foreign affairs, Agence Nationale de la Recherche (ANR, grant # NT05-1.43175), Fonds national suisse de la recherche scientifique (FNS, grants #200021-111688/1 and 200021-116198/1), and the

Swiss Secrétariat d'État à l'Éducation et à la Recherche (COST P18 action C06.0114).

## References

- [1] E. Philip Krider, "Benjamin Franklin and the First Lightning Conductors" *Proc. Int. Comm. Hist. Met.* **1**, 1-13 (2004).
- [2] C. Gary, *La foudre: nature, histoire, risques et protection* (Dunod, Paris, 2004).
- [3] R. Fieux, C. Gary, and P. Hubert, "Artificially Triggered Lightning above Land" *Nature* **257**, 212-214 (1975).
- [4] V. A. Rakov, M. A. Uman, and K. J. Rambo, "A review of ten years of triggered-lightning experiments at Camp Blanding, Florida" *Atmos. Res.* **76**, 503-517 (2005).
- [5] E. M. Bazelyan, and Yu P. Raizer, "The mechanism of lightning attraction and the problem of lightning initiation by lasers" *Phys-Usp+* **43**, 701 (2000).
- [6] V. Apollonov *et al.* AHPLA'99 Paper 3886-34
- [7] M. Miki, Y. Aihara, and T. Shindo, "Development of long gap discharges guided by a pulsed CO<sub>2</sub> laser" *J. Phys. D Appl. Phys* **26**, 1244-1252 (1993).
- [8] S. Uchida, Y. Shimada, H. Yasuda, S. Motokoshi, C. Yamanaka, T. Yamanaka, Z. Kawasaki, and K. Tsubakimoto, "Laser-triggered lightning in field experiments" *J. Opt. Technol.* **66**, 199-202 (1999).
- [9] A. Braun, G. Korn, X. Liu, D. Du, J. Squier, and G. Mourou, "Self-channeling of high-peak-power femtosecond laser pulses in air" *Opt. Lett.* **20**, 73-75 (1995).
- [10] S. L. Chin, S. A. Hosseini, W. Liu, Q. Luo, F. Theberge, N. Akozbek, A. Becker, V. P. Kandidov, O. G. Kosareva, and H. Schroeder, "The propagation of powerful femtosecond laser pulses in optical media: physics, applications, and new challenges" *Can. J. Phys.* **83**, 863-905 (2005).
- [11] L. Bergé, S. Skupin, R. Nuter, J. Kasparian, and J.-P. Wolf, "Ultra-short filaments of light in weakly-ionized, optically-transparent media" *Rep. Prog. Phys.* **70**, 1633-1713 (2007).
- [12] A. Couairon, and A. Mysyrowicz, "Femtosecond filamentation in transparent media" *Phys. Rep.* **441**, 47-189 (2007).
- [13] J. Kasparian, and J.-P. Wolf, "Physics and applications of atmospheric nonlinear optics and filamentation" *Opt. Express* **16**, 466-493 (2008).
- [14] B. La Fontaine, F. Vidal, Z. Jiang, C. Y. Chien, D. Comtois, A. Desparois, T. W. Johnson, J.C. Kieffer, and H. Pépin, "Filamentation of ultrashort pulse laser beams resulting from their propagation over long distances in air" *Phys. Plasmas* **6**, 1615-1621 (1999).
- [15] M. Rodriguez, R. Bourayou, G. Méjean, J. Kasparian, J. Yu, E. Salmon, A. Scholz, B. Stecklum, J. Eislöffel, U. Laux, A. P. Hatzes, R. Sauerbrey, L. Wöste, and J.-P. Wolf, "Kilometer-range non-linear propagation of femtosecond laser pulses" *Phys. Rev. E* **69**, 036607 (2004).
- [16] G. Méchain, G. Méjean, R. Ackermann, P. Rohwetter, Y.-B. André, J. Kasparian, B. Prade, K. Stelmaszczyk, J. Yu, E. Salmon, W. Winn, L. A. V. Schlie, A. Mysyrowicz, R. Sauerbrey, L. Wöste, and J.-P. Wolf, "Propagation of fs-TW laser filaments in adverse atmospheric conditions" *Appl. Phys. B* **80**, 785-789 (2005).
- [17] G. Méjean, J. Kasparian, J. Yu, E. Salmon, S. Frey, J.-P. Wolf, S. Skupin, A. Vinçotte, R. Nuter, S. Champeaux, and L. Bergé, "Multifilamentation transmission through fog" *Phys. Rev. E* **72**, 026611 (2005).
- [18] R. Ackermann, G. Méjean, J. Kasparian, J. Yu, E. Salmon, and J.-P. Wolf, "Laser filaments generated and transmitted in highly turbulent air" *Opt. Lett.* **31**, 86-88 (2006).
- [19] R. Salamé, N. Lascoux, E. Salmon, J. Kasparian, and J. P. Wolf, "Propagation of laser filaments through an extended turbulent region" *Appl. Phys. Lett.* **91**, 171106 (2007).
- [20] H. Pépin, D. Comtois, F. Vidal, C. Y. Chien, A. Desparois, T. W. Johnston, J. C. Kieffer, B. La Fontaine, F. Martin, F. A. M. Rizk, C. Potvin, P. Couture, H. P. Mercure, A. Bondiou-Clergerie, P. Lalande, and I. Gallimberti, "Triggering and guiding high-voltage large-scale leader discharges with sub-joule ultrashort laser pulses" *Phys. Plasmas* **8**, 2532-2539 (2001).
- [21] D. Comtois, C. Y. Chien, A. Desparois, F. Gérin, G. Jarry, T. W. Johnston, J. C. Kieffer, B. La Fontaine, F. Martin, R. Mawassi, H. Pépin, F. A. M. Rizk, F. Vidal, P. Couture, H. P. Mercure, C. Potvin, A. Bondiou-Clergerie, and I. Gallimberti, "Triggering and guiding leader discharges using a plasma channel created by an ultrashort laser" *Appl. Phys. Lett.* **76**, 819-821 (2000).
- [22] P. Rambo, J. Schwartz, and J.-C. Diels, "High-voltage electrical discharges induced by an ultrashort-pulse UV laser system" *J. Opt. A - Pure Appl. Op.* **3**, 146-158 (2001).
- [23] H. Wille, M. Rodriguez, J. Kasparian, D. Mondelain, J. Yu, A. Mysyrowicz, R. Sauerbrey, J.-P. Wolf, and L. Wöste, "Teramobile: a mobile femtosecond-terawatt laser and detection system" *Eur. Phys. J.-Appl. Phys.* **20**, 183-190 (2002).
- [24] M. Rodriguez, R. Sauerbrey, H. Wille, L. Wöste, T. Fujii, Y.-B. André, A. Mysyrowicz, L. Klingbeil, K. Rethmeier, W. Kalkner, J. Kasparian, E. Salmon, J. Yu, and J.-P. Wolf, "Megavolt discharges triggered and guided with laser filaments" *Opt. Lett.* **27**, 772-774 (2002).
- [25] J. Kasparian, M. Rodriguez, G. Méjean, J. Yu, E. Salmon, H. Wille, R. Bourayou, S. Frey, Y.-B. André, A. Mysyrowicz, R. Sauerbrey, J.-P. Wolf, and L. Wöste, "White-Light Filaments for Atmospheric Analysis" *Science* **301**, 61-64 (2003).
- [26] R. Ackermann, G. Méchain, G. Méjean, R. Bourayou, M. Rodriguez, K. Stelmaszczyk, J. Kasparian, J. Yu, E. Salmon, S. Tzortzakis, Y.-B. André, J.-F. Bourrillon, L. Tamin, J.P. Cascelli, C. Campo, C. Davoise, A. Mysyrowicz, R. Sauerbrey, L. Wöste, and J.-P. Wolf, "Wolf, Influence of negative leader propagation on the triggering and guiding of high voltage discharges by laser filaments" *Appl. Phys. B.* **82**, 561-566 (2006).
- [27] R. Ackermann, K. Stelmaszczyk, P. Rohwetter, G. Méjean, E. Salmon, J. Yu, J. Kasparian, G. Méchain, V. Bergmann, S. Schaper, B. Weise, T. Kumm, K. Rethmeier, W. Kalkner, J.P. Wolf, and L. Wöste, "Triggering and guiding of megavolt discharges by laser-induced filaments under rain conditions" *Appl. Phys. Lett.* **85**, 5781-5783 (2004).
- [28] G. Méjean, R. Ackermann, J. Kasparian, E. Salmon, J. Yu, J.-P. Wolf, K. Rethmeier, W. Kalkner, P. Rohwetter, K. Stelmaszczyk, and L. Wöste, "Improved laser triggering and guiding of megavolt discharges with dual fs-ns pulses" *Appl. Phys. Lett.* **88**, 021101 (2006).
- [29] X. M. Zhao, J.-C. Diels, C. Y. Wang, and J. M. Elizondo, "Femtosecond ultraviolet laser pulse induced lightning discharges in gases" *IEEE J. Quantum Elect.* **31**, 599-612 (1995).
- [30] Z. Hao, J. Zhang, Y. T. Li, X. Lu, X. H. Yuan, Z. Y. Zheng, Z. H. Wang, W. J. Ling, Z. Y. Wei, "Prolongation of the fluorescence lifetime of plasma channels in air induced by femtosecond laser pulses" *Appl. Phys. B* **80**, 627-630 (2005).
- [31] H. Yang, J. Zhang, Y. Li, J. Zhang, Y. Li, Z. Chen, H. Teng, Z. Wei, and Z. Sheng, "Characteristics of self-guided laser plasma channels generated by femtosecond laser pulses in air" *Phys. Rev. E* **66**, 016406 (2002).

- [32] J. Kasparian, R. Ackermann, Y.-B. André, G. Méchain, G. Méjean, B. Prade, P. Rohwetter, E. Salmon, K. Stelmaszczyk, J. Yu, A. Mysyrowicz, R. Sauerbrey, L. Wöste, and J.P. Wolf, "Electric events synchronized with laser filaments in thunderclouds" *Opt. Express* **16**, 5757 (2008).
- [33] W. Rison, R. J. Thomas, P. R. Krehbiel, T. Hamlin, and J. Harlin, "A GPS-based three-dimensional lightning mapping system: Initial observations in central New Mexico" *Geophys. Res. Lett.* **26**, 3573-3576 (1999).
- [34] B. La Fontaine, F. Vidal, D. Comtois, C.-Y. Chien, A. Deparois, T. W. Johnston, J.C. Kieffer, H. P. Mercure, H. Pépin, and F. A. M. Rizk, "The influence of electron density on the formation of streamers in electrical discharges triggered with ultrashort laser pulses" *IEEE T. Plasma Sci.* **27**, 688-700 (1999).
- [35] S. Tzortzakis, B. Prade, M. Franco, and A. Mysyrowicz, "Time evolution of the plasma channel at the trail of a self-guided IR femtosecond laser pulse in air" *Opt. Commun.* **181**, 123-127 (2000).
- [36] T. B. Petrova, H. D. Ladouceur, and A. P. Baronavski, "Numerical modeling of the electrical breakdown and discharge properties of laser-generated plasma channels" *Phys. Rev. E* **76**, 066405 (2007).
- [37] P. Béjot, L. Bonacina, J. Extermann, M. Moret, J. P. Wolf, R. Ackermann, N. Lascoux, R. Salamé, E. Salmon, J. Kasparian, L. Bergé, S. Champeaux, C. Guet, N. Blanchot, O. Bonville, A. Boscheron, P. Canal, M. Castaldi, O. Hartmann, C. Lepage, L. Marmande, E. Mazataud, G. Mennerat, L. Patissou, V. Prevot, D. Raffestin, and J. Ribolzi, "32 Terawatt Atmospheric White-Light Laser" *Appl. Phys. Lett.* **90**, 151106 (2007).
- [38] J. Kasparian, and J.-P. Wolf, "On lightning control using lasers" *Prog. Ultra. Int. Laser Sci.* **5** to be published.
- [39] T. B. Petrova, H. D. Ladouceur, and A. P. Baronavski, "Nonequilibrium dynamics of laser-generated plasma channels" *Phys. Plasmas* **15**, 053501 (2008).

## Cross compression of light bullets by two-color cofilamentation

Pierre Béjot,<sup>1,\*</sup> Jérôme Kasparian,<sup>1,2</sup> and Jean-Pierre Wolf<sup>1</sup>

<sup>1</sup>*GAP-Biophotonics, Université de Genève, 20 rue de l'École de Médecine, 1211 Geneva 4, Switzerland*

<sup>2</sup>*Université Lyon 1, CNRS, LASIM UMR 5579, bâtiment A. Kastler, 43 Boulevard du 11 novembre 1918, F-69622 Villeurbanne Cedex, France*

(Received 14 April 2008; published 2 October 2008)

The cofilamentation of two ultrashort laser pulses at 800 and 400 nm in argon is numerically shown to counteract their temporal splitting. The output pulses are as short as 15 and 6.5 fs, respectively, without any postprocess compression or stringent alignment. The simultaneous generation of two sub-millijoule (160 and 15  $\mu$ J, respectively) sub-six-cycle pulses at  $\omega$  and  $2\omega$  is of particular interest for attosecond science.

DOI: [10.1103/PhysRevA.78.043804](https://doi.org/10.1103/PhysRevA.78.043804)

PACS number(s): 42.65.Tg

Increasing interest has recently been devoted to the generation of single attosecond pulses, because they allow phenomena such as coherent molecular dynamics or Rydberg orbital motion to be probed with attosecond time resolution [1]. However, the generation of attosecond pulses requires few- or even single-cycle driving pulses, causing in turn strong attention to few-cycle pulse (FCP) generation [2–5].

Self-guided filaments induced by ultrashort laser pulses in gases [6–9] provide an efficient way to produce such FCPs. A first approach consists in stopping the filamentation by a gas pressure gradient, before pulse splitting occurs. But this approach requires a complex gas cell design and a careful control of the longitudinal location of filamentation [10]. Alternatively, filaments can generate a broad spectrum by self-phase-modulation (SPM). This continuum is then temporally compressed by chirped mirrors or a pulse shaper [11]. This recompression stage requires both careful design and alignment. Moreover, the spectral width of the continuum is critical.

The use of a dual-color pulse can improve this bandwidth. Recently, numerical simulations suggested that a weak seed pulse at frequency  $\omega_s$  copropagating with a filament at  $\omega_0$  can generate an ultrabroad continuum at  $\omega_{\text{FWM}}=2\omega_0-\omega_s$  through four-wave mixing (FWM) and produce a FCP at 545 nm without any postcompression stage [12]. The induced light bullet can then propagate over about 0.25 m, much farther than expected by consideration of the group-velocity dispersion. The interplay between self-phase-modulation and cross-phase modulation (XPM) between two pulses at different wavelengths (e.g., 400 and 800 nm) copropagating in a gas-filled hollow-core fiber [13,14] also generates an ultrabroad continuum in the visible region. The same SPM-XPM interplay was also demonstrated in the case of copropagating filaments, resulting in an ultrabroad continuum in either the deep uv [3,15] or the far infrared [16]. However, the output bandwidth and time duration of the initial pulses has not been characterized so far.

In addition to enhancing the spectral broadening, the use of a two-color pair of ultrashort pulses at frequencies  $\omega$  and  $2\omega$  breaks the temporal symmetry of the electric field. Therefore, the emission of attosecond pulses in the cutoff photon

energy region takes place every full cycle instead of every half cycle and the duration requirements for the driving pulse are reduced by a factor of 2, allowing the use of multicycle pulses [17–22].

Hence, the simultaneous generation of a two-color pair of ultrabroadband pulses at both  $\omega$  and  $2\omega$  would help both stages of the attosecond pulse generation: the generation of the FCP and the subsequent production of single attosecond pulses in the higher harmonics. In this paper, we show numerically that the cofilamentation of two laser pulses at  $\lambda_{\mathbf{R}}=800$  nm and  $\lambda_{\mathbf{B}}=400$  nm in argon indeed generates a pair of intense, sub-six-cycle pulses in a two-color field, meeting the requirements for attosecond pulse generation. Moreover, contrary to existing experimental schemes, this two-color dual pulse is obtained without any temporal postcompression stage or complex gas cell design, leading the way to a practical experimental implementation.

We consider two collinearly polarized incident electric fields at  $\lambda_{\mathbf{B}}$  (labeled  $\mathbf{B}$ ) and  $\lambda_{\mathbf{R}}$  ( $\mathbf{R}$ ) with cylindrical symmetry around the propagation axis  $z$ . The scalar envelopes are assumed to vary slowly in time and along  $z$ . The two fields are coupled by XPM only: Four-wave mixing effects such as  $2\omega_{\mathbf{B}} \pm \omega_{\mathbf{R}}$ ,  $2\omega_{\mathbf{R}} \pm \omega_{\mathbf{B}}$  are not taken into account in this discussion because, due to the short coherence length (28  $\mu$ m to 2.8 mm, depending on the considered wavelength set, i.e., much shorter than the typical 2.5 cm length of the filaments considered in this work), they induce a negligible depletion of the incident pulses. It should also be noted that the FWM efficiency is kept very low ( $10^3$  times lower than the  $\mathbf{R}$  pulse intensity) by the short associated coherence length [25]. Higher-order processes are also neglected. The two scalar envelopes evolve according to the coupled propagation equations (1) and (2) directly derived from the non-linear unidirectional pulse propagation equation [23] for two copropagating pulses [24]:

$$\begin{aligned} \partial_z \varepsilon_{\mathbf{B}} = & \frac{i}{2k_{\mathbf{B}}} \Delta_{\perp}^2 \varepsilon_{\mathbf{B}} - i \frac{k_{\mathbf{B}}''}{2} \partial_t^2 \varepsilon_{\mathbf{B}} - i \Delta_{1/\nu} \partial_t \varepsilon_{\mathbf{B}} + \frac{ik_{\mathbf{B}}}{n_{\mathbf{B}}} (n_{2\mathbf{B}} |\varepsilon_{\mathbf{B}}|^2 \\ & + n_{\text{cross}} |\varepsilon_{\mathbf{R}}|^2) \varepsilon_{\mathbf{B}} - \frac{ik_{\mathbf{B}}}{2n_{\mathbf{B}}^2 \rho_{c_{\mathbf{B}}}} \rho \varepsilon_{\mathbf{B}} - \frac{1}{2} \sigma_{\mathbf{B}} \rho \varepsilon_{\mathbf{B}} \\ & - \frac{\beta_{\mathbf{B}}^{K_{\mathbf{B}}}}{2} |\varepsilon_{\mathbf{B}}|^{2K_{\mathbf{B}}-2} \varepsilon_{\mathbf{B}}, \end{aligned} \quad (1)$$

\*pierre.bejot@unige.ch

TABLE I. Input parameters of the simulations. The difference in the focal length between **R** and **B** is caused by the longitudinal chromatic aberration of the lens.

	$\lambda_{\mathbf{B}}=400$ nm	$\lambda_{\mathbf{R}}=800$ nm
Energy (mJ)	0.2	1
$\Delta t_{\text{FWHM}}$ (fs)	30	30
$\sigma_r$ (mm)	6	6
Chirp (fs <sup>2</sup> )	0	0
$f$ (m)	1	1.04
Initial delay (fs)	0	0
Pressure (bar)	1	1

$$\begin{aligned} \partial_z \varepsilon_{\mathbf{R}} = & \frac{i}{2k_{\mathbf{R}}} \Delta_{\perp}^2 \varepsilon_{\mathbf{R}} - i \frac{k_{\mathbf{R}}''}{2} \partial_t^2 \varepsilon_{\mathbf{R}} + \frac{ik_{\mathbf{R}}}{n_{\mathbf{R}}} (n_{2\mathbf{R}} |\varepsilon_{\mathbf{R}}|^2 + n_{\text{cross}} |\varepsilon_{\mathbf{B}}|^2) \varepsilon_{\mathbf{R}} \\ & - \frac{ik_{\mathbf{R}}}{2n_{\mathbf{R}} \rho c_{\mathbf{R}}} \rho \varepsilon_{\mathbf{R}} - \frac{1}{2} \sigma_{\mathbf{R}} \rho \varepsilon_{\mathbf{R}} - \frac{\beta_{\mathbf{R}}^{\text{KR}}}{2} |\varepsilon_{\mathbf{R}}|^2 k_{\mathbf{R}}^{-2} \varepsilon_{\mathbf{R}}, \end{aligned} \quad (2)$$

where  $t$  refers to the retarded time in the reference frame of **R** and the notations are as described in [25]. In Eq. (1),  $\Delta_{1/v} = \frac{1}{v_{s\mathbf{B}}} - \frac{1}{v_{s\mathbf{R}}}$  is the walkoff constant between **R** and **B**. The plasma density  $\rho$  is coupled to both electric fields through:

$$\partial_t \rho = \left( \sum_{l=\mathbf{B},\mathbf{R}} \sigma_{K_l} |\varepsilon_l|^2 k_l \right) \left( 1 - \frac{\rho}{\rho_{\text{at}}} \right) + \frac{1}{U} \sum_{l=\mathbf{B},\mathbf{R}} \sigma_l \rho |\varepsilon_l|^2 - \alpha \rho^2, \quad (3)$$

where  $\alpha$  is the recombination time constant. The values of the physical parameters are similar to those of [25]. The input electric field envelopes are modeled in focused geometry by two Gaussian profiles. Both the linear chirp of the pulses and their initial delay [which is positive when **R** reaches the focal region ( $z=1$  m) before **B**] are set in the frequency space.

We integrated Eqs. (1) and (2) with a Fourier split-step scheme. The linear terms (diffraction and dispersion) are computed in the Fourier space over a half step in a fully implicit scheme [26]. The nonlinear terms are directly computed in the physical space over a second half step using a Runge-Kutta procedure. Equation (3) was integrated by a Euler scheme. We used a fixed 8192-point temporal grid, providing a resolution of 0.25 fs, and an adaptive grid in both the transverse and  $z$  dimensions [27], with a transverse resolution down to 1.5  $\mu\text{m}$  where filamentation occurs. The simulation input parameters match those of the experiments described in [25], as summarized in Table I.

To precisely identify the contribution of cofilamentation, we compared the results of numerical simulations of the independent filamentation of both **B** and **R** with the case where the two pulses copropagate, with the same initial conditions. Figure 1 displays the effect of cofilamentation on both the quadratic radius and the intensity in the center of the beams. While **R** is little affected by the cofilamentation in the considered conditions, **B** is refocused twice by cross Kerr focusing. In this process, the photon bath [28,29] of **R** signifi-

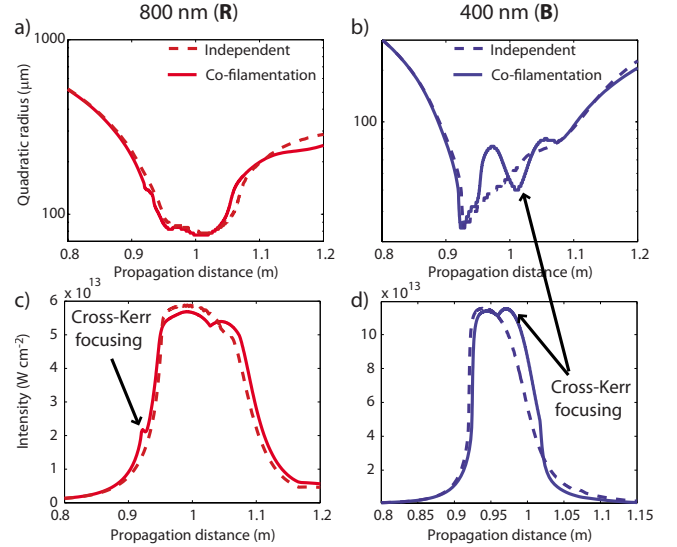


FIG. 1. (Color online) Quadratic radii of 800 (a) and 400 (b) nm pulses as a function of propagation distance for both stand-alone propagation and cofilamentation. When the two pulses copropagate, a second focusing cycle is observed at  $z=102$  cm. Correspondingly, the intensity of 800 (c) [400 (d)] nm increases at  $z=0.93$  (1) m as **B** (**R**) experiences filamentation due to the cross-Kerr-focusing.

cantly contributes, through a  $\chi^{(3)}$  process, to the refocusing of the copropagating **B** pulse. In contrast to **B**, **R** is moderately affected by the cofilamentation. This is due to the fact that the **B** transverse dimension is larger than that of **R** throughout almost the whole propagation (typically 100 vs 25  $\mu\text{m}$ ), so that the nonlinear cross effects averaged over the whole **R** cross section remain small. The clamped intensity of both pulses is almost unaffected by cofilamentation and amounts to  $11 \times 10^{13}$   $\text{W cm}^{-2}$  for **B** and  $6 \times 10^{13}$   $\text{W cm}^{-2}$  for **R** over a few centimeters.

As shown in Fig. 2, the cofilamentation also strongly influences the temporal shape of **B**. The independent propaga-

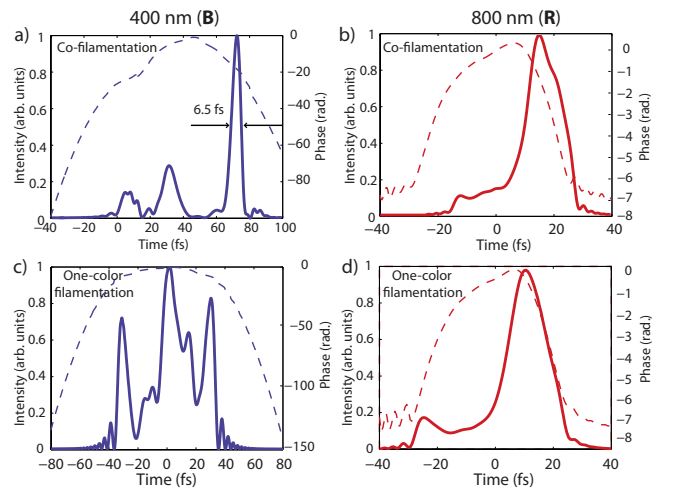


FIG. 2. (Color online) Temporal intensity (solid line) and phase (dashed line) of the 400 (a) and 800 (b) nm pulses after 150 cm propagation, in the case of cofilamentation. Independent propagation is displayed in (c) and (d).

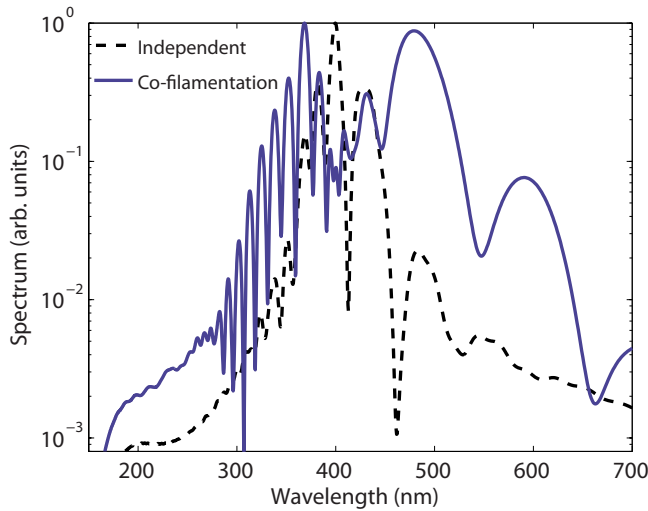


FIG. 3. (Color online) Spectrum around 400 nm. Cofilamentation drastically enhances the spectral broadening through XPM.

tion of **B** gives rise to multiple pulse splitting, resulting in a series of sharp spikes spanning over 100 fs, which would fully prevent single attosecond pulse generation. In contrast, cross Kerr focusing, as well as defocusing and absorption of each pulse by the plasma generated by the other one, partially blocks pulse splitting, generating a 6.5 fs short pulse (4.9 cycles) with little quadratic phase dependency. In the high-intensity temporal region, the phase exhibits an almost linear temporal dependency which indicates a central frequency shift of **B** (the negative slope indicates a central frequency blueshift as can be noticed in Fig. 3). In addition to this slight blueshift, the spectrum of the continuum is greatly broadened as compared with the case of the stand-alone **B** filament (Fig. 3). As in the case of the spatial domain, cofilamentation affects **R** marginally, although it typically reduces the pedestal intensity by a factor of 2 and increases the contrast ratio between the almost FCP (15 fs, i.e., 5.6 cycles) fluence and its pedestal by 2.5.

The space-time plots of Fig. 4 give more insight into the cofilamentation spatiotemporal dynamics. The drastic reduction of pulse splitting as well as the cross Kerr focusing appear clearly. After **B** has experienced multiple pulse splitting, the **R**-induced plasma diffracts and absorbs all the **B** spikes, which temporally occur after **R**. Simultaneously, the (cross) Kerr effect focuses both the **B** and **R** energy reservoirs located around the filaments. Moreover, the effect of cofilamentation on **R** can be seen in Fig. 4(b) at the distance  $z=94$  cm, where the plasma generated by **B** defocuses the trailing edge of **R**. Without any postcompression, **R** is composed of only 5.6 cycles (15 fs), while **B** contains about 4.9 cycles (6.5 fs) at  $z=150$  cm with a contrast 3.5, 50 cm after the filamentation process. At this distance, **R** (**B**) intensity is as high as 1 (0.3) TW cm<sup>-2</sup> corresponding to a bullet energy of 160 (13)  $\mu$ J transversely integrated over 2 mm and disregarding the pedestal. Moreover, the extremely short FWHM time duration of the two light bullets remains stable over more than 20 cm, as expected for temporal solitonlike structures. It may be noted that the above results were recorded in the center of the beam, although the two pulses are

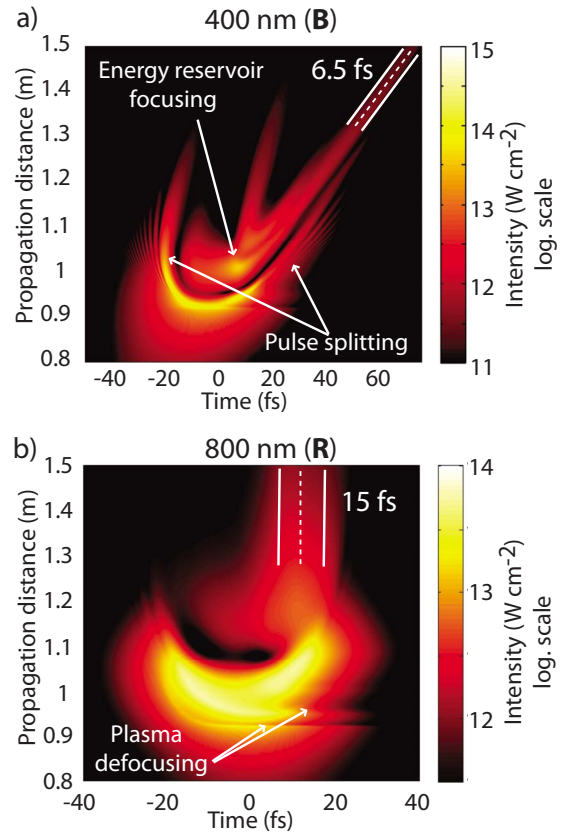


FIG. 4. (Color online) Temporal shape of **B** (a) and **R** (b) as a function of the distance when the two pulses copropagate. The durations of the two pulses [full width at half maximum (FWHM)] remain stable over more than 20 cm from  $z=1.3$  to 1.5 m. Note that the walkoff between the two pulses delays **B** in the **R** frame.

transversely inhomogeneous. However, real experiments tackle such inhomogeneities and select the shortest and spectrally broadest regions of the beam by selecting the center of the beam using a pinhole. Therefore, we expect that our calculations are representative of future experiments, which could greatly benefit from the self-aligned character of the proposed technique, as well as the fact that it requires no postcompression. Such advantages, together with its reasonable energy conversion efficiency, make our approach experimentally very attractive as compared with techniques providing a higher yield, but at the cost of more elaborate

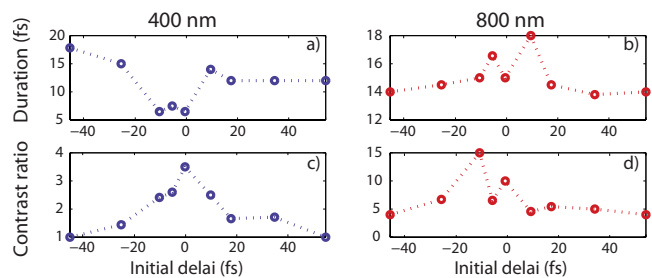


FIG. 5. (Color online) **B** (a) and **R** (b) FWHM duration and contrast ratio (c), (d) after the cofilamentation ( $z=150$  cm). Positive delays correspond to the situation where **R** reaches the focal region ( $z=1$  m) before **B**.

setups such as hollow waveguides and chirp mirror recompression [30].

The time delay between the pulses, and hence their temporal overlap in the interaction region, critically influences their cofilamentation, and in particular the FWHM duration and the contrast ratio of the two copropagating pulses (Fig. 5). While an adequate delay almost inhibits the pulse splitting of the **B** pulse, a detuned delay may have the opposite effect, resulting in a comb of sharp peaks. While the **R** duration is less sensitive to the delay, a perfect overlap yields a threefold increase of the contrast ratio of **R**. Other parameters, like the relative intensities of the two pulses, their wavelength, or the focal length they encounter, are also expected to influence cofilamentation. For example, although such development is beyond the scope of this work, we expect that it would be possible to better compress the **R** pulse by adjusting the relative location of the focus of **R** and **B**.

As a conclusion, we have numerically demonstrated a method to simultaneously generate two sub-six-cycle pulses with subjoule energy. The cross Kerr focusing governing cofilamentation drastically reduces the pulse splitting, resulting in almost few-cycle pulses at both  $\omega$  and  $2\omega$ , which could act as a pair of driving pulses for attosecond pulse generation. The fairly good energy conversion efficiency of this self-aligned and self-recompressed method makes it attractive for practical experiments.

This work was supported by the Swiss NSF (Contracts No. 200021-111688 and No. 200021-116198 and R'équip program), and the Swiss SER in the framework of COST P18 (Action C06.0114), as well as the Boninchi and Schimideiny Foundations. We gratefully acknowledge L. Bonacina for very fruitful discussions and M. Moret for his computational support.

- 
- [1] M. Hentschel, R. Kienberger, C. Spielmann, G. A. Reider, N. Milosevic, T. Brabec, P. Corkum, U. Heinzmann, M. Drescher, and F. Krausz, *Nature (London)* **414**, 509 (2001).
- [2] A. Couairon, J. Biegert, C. Hauri, W. Kornelis, F. Helbing, U. Keller, and A. Mysyrowicz, *J. Mod. Opt.* **53**, 75 (2006).
- [3] T. Fuji, T. Horio, and T. Suzuki, *Opt. Lett.* **32**, 2481 (2007).
- [4] A. Zair, A. Guandalini, F. Schapper, M. Holler, J. Biegert, L. Gallmann, A. Couairon, M. Franco, A. Mysyrowicz, and U. Keller, *Opt. Express* **15**, 5394 (2007).
- [5] S. Trushin, K. Kosma, W. Fuss, and E. Schmid, *Opt. Lett.* **32**, 2432 (2007).
- [6] L. Bergé, S. Skupin, R. Nuter, J. Kasparian, and J.-P. Wolf, *Rep. Prog. Phys.* **70**, 1633 (2007).
- [7] J. Kasparian and J.-P. Wolf, *Opt. Express* **16**, 466 (2008).
- [8] A. Couairon and A. Mysyrowicz, *Phys. Rep.* **441**, 47 (2007).
- [9] J. Kasparian *et al.*, *Science* **301**, 61 (2003).
- [10] A. Mysyrowicz, A. Couairon, and U. Keller, *New J. Phys.* **10**, 025023 (2008).
- [11] C. Hauri, W. Kornelis, F. Helbing, A. Heinrich, A. Couairon, A. Mysyrowicz, J. Biegert, and U. Keller, *Appl. Phys. B: Lasers Opt.* **79**, 673 (2004).
- [12] L. Berge and S. Skupin, *Phys. Rev. Lett.* **100**, 113902 (2008).
- [13] E. Matsubara, K. Yamane, T. Sekikawa, and M. Yamashita, *J. Opt. Soc. Am. B* **24**, 985 (2007).
- [14] N. Karasawa, R. Morita, H. Shigekawa, and M. Yamashita, *Opt. Lett.* **25**, 183 (2000).
- [15] Y. Zheng *et al.*, *Opt. Lett.* **33**, 233 (2008).
- [16] T. Fuji and T. Suzuki, *Opt. Lett.* **32**, 3330 (2007).
- [17] T. Pfeifer, M. Gallmann, M. Abel, D. Neumark, and S. Leone, *Opt. Lett.* **31**, 975 (2006).
- [18] Z. Zeng, Y. Cheng, X. Song, R. Li, and Z. Xu, *Phys. Rev. Lett.* **98**, 203901 (2007).
- [19] S. Zamith, Y. Ni, A. Gurtler, L. Noordam, H. Muller, and M. Vrakking, *Opt. Lett.* **29**, 2303 (2004).
- [20] C. M. Kim, I. J. Kim, and C. H. Nam, *Phys. Rev. A* **72**, 033817 (2005).
- [21] Y. Oishi, M. Kaku, A. Suda, F. Kannari, and K. Midorikawa, *Opt. Express* **14**, 7230 (2006).
- [22] H. Mashiko, S. Gilbertson, C. Li, S. D. Khan, M. M. Shakya, E. Moon, and Z. Chang, *Phys. Rev. Lett.* **100**, 103906 (2008).
- [23] M. Kolesik and J. V. Moloney, *Phys. Rev. E* **70**, 036604 (2004).
- [24] L. Bergé, S. Skupin, G. Mejean, J. Kasparian, J. Yu, S. Frey, E. Salmon, and J. P. Wolf, *Phys. Rev. E* **71**, 016602 (2005).
- [25] P. Béjot, J. Kasparian, and J.-P. Wolf, *Opt. Express* **16**, 14115 (2008).
- [26] W. Press, B. Flannery, S. Teukolsky, and W. Vetterling, *Numerical Recipes* (Cambridge University Press, Cambridge, U.K., 1989).
- [27] P. Béjot, C. Bonnet, V. Boutou, and J.-P. Wolf, *Opt. Express* **15**, 13295 (2007).
- [28] F. Courvoisier, V. Boutou, J. Kasparian, E. Salmon, G. Mejean, J. Yu, and J. P. Wolf, *Appl. Phys. Lett.* **83**, 213 (2003).
- [29] G. Mejean *et al.*, *Phys. Rev. E* **72**, 026611 (2005).
- [30] A. Cavalieri *et al.*, *Nature (London)* **449**, 1029 (2007).

# Dual-color co-filamentation in Argon

Pierre Béjot<sup>1,\*</sup>, Jérôme Kasparian<sup>1,2</sup>, Jean-Pierre Wolf<sup>1</sup>

(1) *Université de Genève, GAP-Biophotonics, 20 rue de l'Ecole de Médecine, 1211 Geneva 4, Switzerland*

(2) *Université Lyon 1; CNRS; LASIM UMR 5579, bât. A. Kastler, 43 Bd du 11 novembre 1918, F-69622 Villeurbanne Cedex, France*

[pierre.bejot@physics.unige.ch](mailto:pierre.bejot@physics.unige.ch)

**Abstract:** We investigate both experimentally and theoretically the mechanisms driving the co-filamentation of two ultrashort laser pulses at 800 and 400 nm in Argon. The cross-Kerr lens and cross-phase modulation between the two filaments of different colors bridging both the continuum spectra and the plasma channels induced by the individual pulses. This dual-color filamentation also results in the simultaneous generation of two few-cycle pulses at both 800 and 400 nm, providing a potential way to generate attosecond pulses.

© 2008 Optical Society of America

**OCIS codes:** (190.7110) Ultrafast nonlinear optics; (320.6629) Supercontinuum generation; (260.3230) Ionization; (320.5520) Pulse compression; (190.5940) Self-action effects; (260.5950) Self-focusing

---

## References and links

1. T. Pfeifer, M. Gallmann, M.J. Abel, D.M Neumark, and S.R Leone. Single attosecond pulse generation in the multicycle-driver regime by adding a weak second-harmonic field. *Opt. Lett.* **31**, 975-977, (2006).
2. M. Hentschel, R. Kienberger, Ch. Spielmann, G. A. Reider, N. Milosevic, T. Brabec, P. Corkum, U. Heinzmann, M. Drescher, and F. Krausz. Attosecond metrology. *Nature (London)* **414**, 509-513, (2001).
3. H.S. Chakraborty, M.B. Gaarde, and A. Couairon. Single attosecond pulses from high harmonics driven by self-compressed filaments. *Opt. Lett.* **31**, 3662-3664, (2006).
4. T. Brixner, N. H. Damrauer, P. Niklaus, and G. Gerber. Photosensitive adaptive femtosecond quantum control in the liquid phase. *Nature (London)* **414**, 57-60, (2001).
5. J. Kasparian, M. Rodriguez, G. Mejean, J. Yu, E. Salmon, H. Wille, R. Bourayou, S. Frey, Y. B. Andre, A. Mysyrowicz, R. Sauerbrey, J. P. Wolf, and L. Woste. White-light filaments for atmospheric analysis. *Science* **301**, 61-64, (2003).
6. A. Couairon and A. Mysyrowicz. Femtosecond filamentation in transparent media. *Phys. Rep.* **44**, 47-189, (2007).
7. L. Bergé, S. Skupin, R. Nuter, J. Kasparian, and J.-P. Wolf. Ultrashort filaments of light in weakly ionized, optically transparent media. *Rep. Prog. Phys.* **70**, 1633-1713, (2007).
8. J. Kasparian and J.-P. Wolf. Physics and applications of atmospheric nonlinear optics and filamentation. *Opt. Express* **16**, 466-493, (2008).
9. T. Fuji, T. Horio, and T. Suzuki. Generation of 12 fs deep-ultraviolet pulses by four-wave mixing through filamentation in neon gas. *Opt. Lett.* **32**, 2481-2483, (2007).
10. A. Zair, A. Guandalini, F. Schapper, M. Holler, J. Biegert, L. Gallmann, A. Couairon, M. Franco, A. Mysyrowicz, and U. Keller. Spatio-temporal characterization of few-cycle pulses obtained by filamentation. *Opt. Express* **15**, 5394-5404, (2007).
11. S.A Trushin, K. Kosma, W. Fuss, and E. Schmid. Sub-10-fs supercontinuum radiation generated by filamentation of few-cycle 800 nm pulses in argon. *Opt. Lett.* **32**, 2432-2434, (2007).
12. X. Chen, X. Li, J. Liu, P. Wei, X. Ge, R. Li, and Z. Xu. Generation of 5 fs, 0.7 mJ pulses at 1 KHz through cascade filamentation. *Opt. Lett.* **32**, 2402-2404, (2007).
13. T. Fuji and T. Suzuki. Generation of sub-two-cycle mid-infrared pulses by four-wave mixing through filamentation in air. *Opt. Lett.* **32**, 3330-3332, (2007).

14. C.P. Hauri, W. Kornelis, F.W. Helbing, A. Heinrich, A. Couairon, A. Mysyrowicz, J. Biegert, and U. Keller. Generation of intense, carrier-envelope phase-locked few-cycle laser pulses through filamentation. *Appl. Phys. B*, **79**, 673-677, (2004).
15. A. Couairon, J. Biegert, C.P. Hauri, W. Kornelis, F.W. Helbing, U. Keller, and A. Mysyrowicz. Self-compression of ultra-short laser pulses down to one optical cycle by filamentation. *J. Mod. Opt.* **53**, 75-85, (2006).
16. A. Couairon, M. Franco, A. Mysyrowicz, J. Biegert, and U. Keller. Pulse self-compression to the single-cycle limit by filamentation in a gas with a pressure gradient. *Opt. Lett.* **30**, 2657-2659, (2005).
17. C.P. Hauri, A. Guandalini, P. Eckle, W. Kornelis, J. Biegert, and U. Keller. Generation of intense few-cycle laser pulses through filamentation-parameter dependence. *Opt. Express* **13**, 7541-7547, (2005).
18. P. Bejot, J. Kasparian, E. Salmon, R. Ackermann, and J. P. Wolf. Spectral correlation and noise reduction in laser filaments. *Appl. Phys. B* **87**, 1-4, (2007).
19. J. Scharz, P. Rambo, and J.-C. Diels. Ultraviolet filamentation in air. *Optics Communication* **180**, 383-390, (2000).
20. P. Béjot, C. Bonnet, V. Boutou, and J.-P. Wolf. Laser noise compression by filamentation at 400 nm in argon. *Opt. Express* **15**, 13295-13309, (2007).
21. E. Matsubara, K. Yamane, T. Sekikawa, and M. Yamashita. Generation of 2.6 fs optical pulses using induced-phase modulation in a gas-filled hollow fiber. *J. Opt. Soc. Am. B* **24**, 985-989, (2007).
22. H. Wille, M. Rodriguez, J. Kasparian, D. Mondelain, J. Yu, A. Mysyrowicz, R. Sauerbrey, J. P. Wolf, and L. Woste. Teramobile: A mobile femtosecond-terawatt laser and detection system. *Eur. Phys. J.: Appl. Phys.* **20**, 183-190, (2002).
23. S. Skupin, L. Bergé, U. Peschel, F. Lederer, G. Mejean, J. Yu, J. Kasparian, E. Salmon, J. P. Wolf, M. Rodriguez, L. Woste, R. Bourayou, and R. Sauerbrey. Filamentation of femtosecond light pulses in the air: Turbulent cells versus long-range clusters. *Phys. Rev. E* **70**, 046602, (2004).
24. G. Fibich and B. Ilan. Self-focusing of elliptic beams: an example of the failure of the aberrationless approximation. *J. Opt. Soc. Am. B* **17**, 1749-1758, (2000).
25. D. Walter, S. Eyring, J. Lobhreiher, R. Spitzenpfel, and C. Spielmann. Spatial optimization of filaments. *Appl. Phys. B*, **88**, 175-178, (2007).
26. R. Ackermann, E. Salmon, N. Lascoux, J. Kasparian, P. Rohwetter, K. Stelmaszyk, S. H. Li, A. Lindinger, L. Woste, P. Bejot, L. Bonacina, and J. P. Wolf. Optimal control of filamentation in air. *Appl. Phys. Lett.* **89**, 171117, (2006).
27. M. Kolesik, D.E. Roskey, and Moloney J.V. Conditional femtosecond pulse collapse for white-light and plasma delivery to a controlled distance. *Opt. Lett.* **32**, 2753-2755, (2007).
28. N. Karasawa, R. Morita, H. Shigekawa, and M. Yamashita. Generation of intense ultrabroadband optical pulses by induced phase modulation in an argon-filled single-mode hollow waveguide. *Opt. Lett.* **25**, 183-185, (2000).
29. Z. Zeng, Y. Cheng, X. Song, R. Li, and Z. Xu. Generation of an extreme ultraviolet supercontinuum in a two-color laser field. *Phys. Rev. Lett.* **98**, 203901, (2007).
30. S. Zamith, Y. Ni, A. Gurtler, L.D. Noordam, H.G Muller, and M.J.J Vrakking. Control of atomic ionization by two-color few-cycle pulses. *Opt. Lett.* **29**, 2303-2305, (2004).
31. C.M. Kim, I.J. Kim, and C.H. Nam. Generation of a strong attosecond pulse train with an orthogonally polarized two-color laser field. *Phys. Rev. A* **72**, 033817, (2005).
32. Y. Oishi, M. Kaku, A. Suda, F. Kannari, and K. Midorikawa. Generation of extreme ultraviolet continuum radiation driven by a sub-10-fs two-color field. *Opt. Express* **14**, 7230-7237, (2006).
33. W.G. Wagner, H.A. Haus, and J.H. Marburger. Large-scale self-trapping of optical beams in the paraxial ray approximation. *Phys. Rev.* **175**, 256-266, (1968).
34. NIST Atomic Spectra Database [http://physics.nist.gov/PhysRefData/ASD/lines\\_form.html](http://physics.nist.gov/PhysRefData/ASD/lines_form.html)
35. M. Kolesik and J.V. Moloney. Nonlinear optical pulse propagation simulation: From maxwell's to unidirectional equations. *Phys. Rev. E* **70**, 036604, (2004).
36. M. Kolesik, E.M. Wright, A. Becker, and J.V. Moloney. Simulation of third-harmonic and supercontinuum generation for femtosecond pulses in air. *Appl. Phys. B*, **85**, 531-538, (2006).
37. H. Ehrhardt, Kh. Hesselba, K. Jung, E. Schubert, and K. Willmann. Electron-impact ionization of argon - measurements of triple differential cross-sections. *J. Phys. B* **7**, 69-78, (1974).
38. E.R. Peck and D.J. Fischer. Dispersion of argon. *J. Opt. Soc. Am.* **54**, 1362-1364, (1964).
39. V. Mizrahi and D.P. Shelton. Dispersion of nonlinear susceptibilities of Ar,  $N_2$ , and  $O_2$  measured and compared. *Phys. Rev. Lett.* **55**, 696-699, (1985).
40. M. Mlejnek, E. M. Wright, and J. V. Moloney. Femtosecond pulse propagation in argon: A pressure dependence study. *Phys. Rev. E* **58**, 4903-4910, (1998).
41. Y.P Raizer. Plasma physics. Springer, Berlin Plasma Physics, (1994).
42. A. Couairon, S. Tzortzakis, L. Bergé, M. Franco, B. Prade, and A. Mysyrowicz. Infrared femtosecond light filaments in air: simulations and experiments. *J. Opt. Soc. Am. B* **19**, 1117-1131, (2002).
43. W.H. Press, B.P. Flannery, S.A. Teukolsky, and W.T. Vetterling. Numerical recipes. Cambridge University Press, Cambridge Numerical Recipes, (1989).
44. A. Chiron, B. Lamouroux, R. Lange, J. F. Ripoche, M. Franco, B. Prade, G. Bonnaud, G. Riazuelo, and A. Mysy-

- rowicz. Numerical simulations of the nonlinear propagation of femtosecond optical pulses in gases. *European Physical Journal D* **6**, 383-396, (1999).
45. M. Rodriguez, R. Sauerbrey, H. Wille, L. Woste, T. Fujii, Y. B. Andre, A. Mysyrowicz, L. Klingbeil, K. Rethmeier, W. Kalkner, J. Kasparian, E. Salmon, J. Yu, and J. P. Wolf. Triggering and guiding megavolt discharges by use of laser-induced ionized filaments. *Opt. Lett.* **27**, 772-774, (2002).
  46. J. Kasparian, R. Ackermann, Y.-B. Andre, G. Méchain, G. Mejean, B. Prade, P. Rohwetter, E. Salmon, K. Stelmaszczyk, J. Yu, A. Mysyrowicz, R. Sauerbrey, L. Woste, and J.-P. Wolf. Electric events synchronized with laser filaments in thunderclouds. *Opt. Express* **16**, 5757-5763, (2008).
  47. S. Tzortzakis, G. Méchain, G. Patalano, M. Franco, B. Prade, and A. Mysyrowicz. Concatenation of plasma filaments created in air by femtosecond infrared laser pulses. *Appl. Phys. B* **76**, 609-612, (2003).
  48. W. Liu, F. Gravel, J. F. Theberge, A. Becker, and S.L. Chin. Background reservoir: its crucial role for long-distance propagation of femtosecond laser pulses in air. *Appl. Phys. B* **80**, 857-860, (2005).
  49. J.E. Rothenberg. Pulse splitting during self-focusing in normally dispersive media. *Opt. Lett.* **17**, 583-585, (1992).
  50. A Couairon, G. Méchain, S. Tzortzakis, M. Franco, B. Lamouroux, B. Prade, and A. Mysyrowicz. Propagation of twin laser pulses in air and concatenation of plasma strings produced by femtosecond infrared filaments. *Opt. Comm.* **225**, 177-192, (2003).
- 

## 1. Introduction

Strong interest has been recently devoted to few-cycle pulses (FCP) generation for their properties in both the spectral and time domains. In the time domain, their very short duration can be used to generate high harmonics in rare gases, a step to produce XUV attosecond pulses in order to probe, with attosecond time resolution, phenomena [1, 2, 3] such as coherent molecular dynamics or Rydberg orbital motion. In the Fourier reciprocal space, their octave-broad spectrum can be used in spectroscopy [4] or white-light Lidar applications [5].

Filamentation [6, 7, 8], resulting from the dynamic balance between Kerr self-focusing and defocusing on laser-induced plasma, is now recognized as an efficient way to produce such ultrashort pulses [9, 10, 11, 12, 13, 14, 15, 16, 17]. Moreover, filament-based experiments do not need fine alignment as is the case of capillary-based setups.

Up to now, both experimental and theoretical investigations have focused on filamentation in the infrared (800 nm) and ultraviolet (248 nm) regions [6, 7, 8, 15, 18, 19]. However, recent results showed that filamentation of 400 nm pulses in Argon can also produce a very broad spectrum [20]. Unfortunately, filamentation at 400 nm yields a limited energy on the wings of the continuum induced by self-phase modulation (SPM) [21], which restricts the theoretical minimum pulse duration achievable by this method.

A great deal of effort has been devoted to the control of the plasma channel and the white-light generated during filamentation [8]. Chirp [22], energy, beam size and shape [23], ellipticity [24], spectral and spatial shaping [25, 26] have been investigated. Recently, another way to control filamentation has been proposed theoretically: the two-color filamentation, or *conditional femtosecond pulse collapse* [27] for white-light and plasma delivery to a controlled distance. Launching 600 nm and 800 nm pulses with an adequate time-delay, and a power just below the critical power allows, with the help of air dispersion, to control the location of the filamentation onset.

Such two-color dual filamentation approach could also overcome the limited energy on the wings of the white-light continuum. By combining two pulses with different central wavelength (e.g. 800 nm and 400 nm) in a gas-filled hollow core fiber, the interplay of both XPM and SPM results in a broader spectrum than SPM alone [21, 28]. Two-color filamentation was also used to generate ultrashort deep-ultraviolet (200 nm and 266 nm) [9] or mid-infrared pulses [13] by four-wave mixing (FWM). These processes are very efficient because both pulses are clamped to intensities as high as  $5 \cdot 10^{13} \text{ W.cm}^{-2}$  over several Rayleigh lengths. Moreover, the use of two single-cycle pulses, at frequencies  $\omega$  and  $2\omega$  can enhance the generation of high harmonics, as compared to a single pulse [1, 29, 30, 31, 32]. Simultaneously generating single-cycle pulses

at both 800 nm and 400 nm is therefore particularly promising for attosecond and high-field physics.

In this paper, we study both experimentally and theoretically two-color (800 nm and 400 nm) filamentation in Argon. We show that an adequate time-delay results in co-filamentation of the two pulses, yielding a single, strongly broadened spectrum and opening the way to the simultaneous generation of 400 nm and 800 nm FCP. Moreover, the two-color co-filamentation generates a much longer connected plasma channel than that generated by each of the filaments individually, which could be useful to trigger and control high voltage discharges.

## 2. Materials and methods

### 2.1. Experimental setup

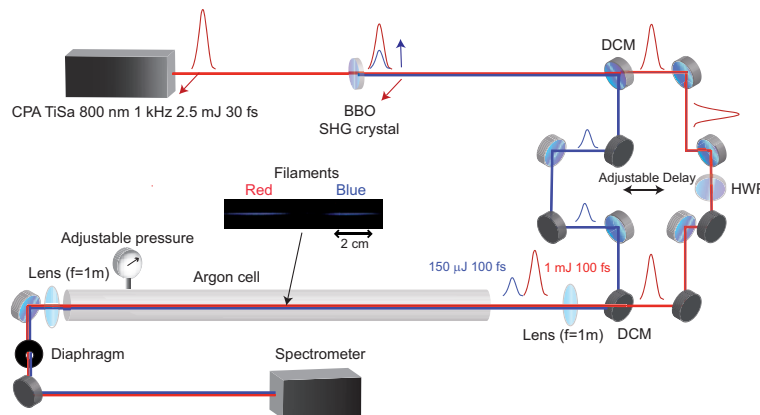


Fig. 1. Experimental setup. DCM: Dichroic mirror. HWP: Half-waveplate.

The experimental setup is shown in Fig. 1. A Ti:Sa amplifier system (Hidra, Coherent Inc.), delivers 2.5 mJ (stability: 0.5 % rms), 800 nm pulses at a 1 kHz repetition rate. The seed pulse is shaped by a Dazzler in order to shorten the output pulse down to 30 fs. The beam is frequency-doubled to 400 nm using a 0.5 mm thick BBO crystal, providing a typical output energy of 150 – 300 μJ. The remaining NIR (labeled as beam "R", about 1 mJ) and the blue ("B") pulses are separated by a dichroic mirror (DCM). The R polarization is rotated by a zero-order waveplate (WP) and its delay relative to B is adjusted by a delay line, after which the two beams are recombined with another DCM (DCM2). Then, the two collinear beams are focused by a  $f = 1$  m lens in a 2 m long cell filled with 2 bar Argon. We determined the zero-delay between both pulses by optimizing the sum-frequency generation at 266 nm in a 200 μm thick BBO crystal. When either of the two pulses propagates into the cell, a single plasma channel of 2.5 cm length is generated. Such short channel may stem from the moderate initial beam quality, in both the temporal and spatial dimensions. However, as in particular numerical simulations below will show, the actual filaments are longer than the 2.5 cm-long section where the electron density is sufficient to be observed visually, up to beyond 10 cm. As expected from the Marburger formula [33] considering the lens longitudinal chromatic aberration, the B and R filaments start at  $z_B = 90$  cm and  $z_R = 97$  cm, respectively,  $z$  being the propagation distance. The two beams are then collimated at the cell exit by a  $f = 1$  m lens. The core (4 mm in diameter) of the beams are redirected to a spectrometer (Ocean Optics, HR4000, 0.5 nm resolution). Besides, the plasma channels are characterized by side images recorded with a

RGB color-frame digital camera (Nikon D80), with a resolution of about  $30 \mu\text{m}$ . The signal was averaged over 3 s, corresponding to 3000 laser pulses. We checked that the collected light was unpolarized and shows no axial dependence, which excludes both Rayleigh scattering and third-order susceptibility processes, and warrants that only the plasma fluorescence is recorded. To avoid scattered light from either the **R** or the **B** filaments, we considered the green layer ( $450 - 600 \text{ nm}$ ) of the RGB pictures, where several fluorescence emission lines of nitrogen are present, although the main fluorescence signal is in the  $650 - 950 \text{ nm}$  range [34].

## 2.2. Numerical methods

The high intensity within the filaments, as well as their reduced transverse dimension ( $\simeq 100 \mu\text{m}$ ) prevent in-situ measurements. To get insight into the highly non-linear co-filamentation process beyond the experimentally available data, we developed a numerical model aimed at reproducing the actual experimental conditions as closely as possible.

More precisely, we consider two collinearly polarized incident electric fields at  $\lambda_b = 400 \text{ nm}$  and  $\lambda_r = 800 \text{ nm}$  with cylindrical symmetry around the propagation axis  $z$ . They write  $\Re\{\varepsilon_i \exp[i(k_i z - \omega_i t)]\}$ , where  $k_i = \frac{2\pi n_i}{\lambda_i}$  and  $\omega_i = \frac{2\pi c}{\lambda_i}$  ( $i = \mathbf{R}, \mathbf{B}$ ) are the carrier wave number and the frequency, in the slowly varying envelope approximation [35]. This separation of the **R** and **B** radiations is acceptable as long as their spectra do not overlap [36]. Each field is propagated within a classical non-linear Schrödinger equation (NLSE) [7], while their interaction occurs through cross-phase modulation (XPM). We therefore, neglect all phenomena such as  $2\omega_b \pm \omega_r$ ,  $2\omega_r \pm \omega_b$ , as well as higher order processes. The two scalar envelopes evolve according to the coupled propagation equations (1-2):

$$\partial_z \varepsilon_{\mathbf{B}} = \frac{i}{2k_{\mathbf{B}}} \Delta_{\perp}^2 \varepsilon_{\mathbf{B}} - i \frac{k_{\mathbf{B}}''}{2} \partial_t^2 \varepsilon_{\mathbf{B}} - i \Delta_{\frac{1}{v}} \partial_t \varepsilon_{\mathbf{B}} + \frac{ik_{\mathbf{B}}}{n_{\mathbf{B}}} \left( n_{2\mathbf{B}} |\varepsilon_{\mathbf{B}}|^2 + n_{\text{cross}} |\varepsilon_{\mathbf{R}}|^2 \right) \varepsilon_{\mathbf{B}} \quad (1)$$

$$\begin{aligned} & - \frac{ik_{\mathbf{B}}}{2n_{\mathbf{B}}^2 \rho_{c\mathbf{B}}} \rho \varepsilon_{\mathbf{B}} - \frac{1}{2} \sigma_0 \rho \varepsilon_{\mathbf{B}} - \frac{\beta_{\mathbf{B}}^{K_{\mathbf{B}}}}{2} |\varepsilon_{\mathbf{B}}|^{2K_{\mathbf{B}}-2} \varepsilon_{\mathbf{B}} \\ \partial_z \varepsilon_{\mathbf{R}} = & \frac{i}{2k_{\mathbf{R}}} \Delta_{\perp}^2 \varepsilon_{\mathbf{R}} - i \frac{k_{\mathbf{R}}''}{2} \partial_t^2 \varepsilon_{\mathbf{R}} + \frac{ik_{\mathbf{R}}}{n_{\mathbf{R}}} \left( n_{2\mathbf{R}} |\varepsilon_{\mathbf{R}}|^2 + n_{\text{cross}} |\varepsilon_{\mathbf{B}}|^2 \right) \varepsilon_{\mathbf{R}} \quad (2) \\ & - \frac{ik_{\mathbf{R}}}{2n_{\mathbf{R}}^2 \rho_{c\mathbf{R}}} \rho \varepsilon_{\mathbf{R}} - \frac{1}{2} \sigma_{\mathbf{R}} \rho \varepsilon_{\mathbf{R}} - \frac{\beta_{\mathbf{R}}^{K_{\mathbf{R}}}}{2} |\varepsilon_{\mathbf{R}}|^{2K_{\mathbf{R}}-2} \varepsilon_{\mathbf{R}} \end{aligned}$$

where  $t$  refers to the retarded time in the reference frame of the  $800 \text{ nm}$  pulse  $t \rightarrow t - \frac{z}{v_{g\mathbf{R}}}$  with  $v_{g\mathbf{R}} = \frac{\partial \omega}{\partial k} |_{\omega_{\mathbf{R}}}$  corresponding to the group velocity of the  $800 \text{ nm}$  carrier envelope. The terms on the right-hand side of Eq. 1 account for spatial diffraction, second order dispersion, temporal walkoff due to the group-velocity dispersion of the two envelopes, instantaneous self and cross Kerr effects, plasma defocusing and absorption, respectively (Table 1). The Kerr response of Argon is assumed to be instantaneous [6]. In (1),  $\Delta_{\frac{1}{v}} = \frac{1}{v_{g\mathbf{B}}} - \frac{1}{v_{g\mathbf{R}}}$  is the walkoff constant and  $\rho_{c_i} = \frac{\omega_i m_e \varepsilon_0}{q_e^2}$  corresponds to the critical plasma density above which the plasma becomes opaque. In addition, the constant  $\sigma_i = \frac{k_i e^2}{\omega_i m_e \varepsilon_0} \frac{\tau}{1 + (\omega \tau)^2}$  denotes the cross-section for electron-neutral inverse bremsstrahlung ( $\tau$  is the electron-atom relaxation time) and  $\beta_i^{K_i}$  corresponds to the coefficient of multiphoton absorption,  $K_i$  being the minimal number of photons necessary to ionize Argon. This quantity is calculated as  $K_i = \text{mod}(\frac{U}{\hbar \omega_i}) + 1$  ( $K_{\mathbf{R}} = 11$  and  $K_{\mathbf{B}} = 6$ ), where  $U$

is the ionization potential of Argon ( $U = 15.76 \text{ eV}$  [37]).  $\beta^{K_i}$  is expressed as  $\beta^{K_i} = K_i \hbar \omega_i \rho_{at} \sigma_{K_i}$  where  $\rho_{at}$  is the Argon density and  $\sigma_{K_i}$  is the multiphoton ionization cross section.

The dynamic of the electric field is coupled with the plasma density  $\rho$  by the multiphoton ionization. Hence, the plasma density  $\rho$  follows the equation:

$$\partial_t \rho = \left( \sum_{l=\mathbf{B},\mathbf{R}} \sigma_{K_l} |\varepsilon_l|^{2K_l} \right) \left( 1 - \frac{\rho}{\rho_{at}} \right) + \frac{1}{U} \sum_{l=\mathbf{B},\mathbf{R}} \sigma_l \rho |\varepsilon_l|^2 - \alpha \rho^2 \quad (3)$$

where  $\alpha$  is the recombination time constant.

Table 1. Physical parameters used in the model ( $p$  accounts for the relative gas pressure:  $p = \frac{P}{1\text{bar}}$ )

	$\lambda_{\mathbf{B}} = 400 \text{ nm}$	$\lambda_{\mathbf{R}} = 800 \text{ nm}$
$k'' \text{ (fs}^2 \cdot \text{cm}^{-1}\text{)}$	0.49 $p$ [38]	0.21 $p$
$n_2 \text{ (m}^2 \text{W}^{-1}\text{)}$	4.9. $p 10^{-23}$ [39]	3.2. $p 10^{-23}$
$n_{\text{cross}} \text{ (m}^2 \text{W}^{-1}\text{)}$	1. $p 10^{-23}$	
$K$	6	11
$\beta^K \text{ (m}^{2K-3} \text{W}^{1-K}\text{)}$	1.95. $p 10^{-88}$	3.32. $p 10^{-176}$
$\sigma^K \text{ (s}^{-1} \text{cm}^{2K} \text{W}^{-K}\text{)}$	2.79. $p 10^{-72}$ [6]	5.06. $p 10^{-140}$
$\sigma(1\text{bar}) \text{ (m}^2\text{)}$	2.53 $10^{-24}$	1.01 $10^{-23}$
$\rho_c \text{ (m}^{-3}\text{)}$	6.4 $10^{27}$	1.74 $10^{27}$
$\alpha \text{ (m}^{-3} \text{s}^{-1}\text{)}$	7 $10^{-13}$ [40]	
$\tau \text{ (s)}$	1.9 $10^{-13} p^{-1}$ [41]	

Table 2. Input parameters used in the model. The different focal length for the 800 nm ( $\mathbf{R}$ ) and 400 nm ( $\mathbf{B}$ ) pulses account for longitudinal chromatic aberration of the focusing length used in the experiments.

	$\lambda_{\mathbf{B}} = 400 \text{ nm}$	$\lambda_{\mathbf{R}} = 800 \text{ nm}$
<i>Energy (mJ)</i>	0.150	1
$\Delta t_{FWHM} \text{ (fs)}$	50	30
$\sigma_r \text{ (mm)}$	6	6
<i>Chirp (fs<sup>2</sup>)</i>	-100	-330
$f \text{ (m)}$	1	1.04
<i>Pressure (bar)</i>	2	

The initial conditions are chosen to match the experimental parameters, as summarized in Table 2. We chose an initial plasma density of  $10^9 e^- \cdot \text{cm}^{-3}$  [42]. The input electric field envelopes are modeled in focused geometry by two Gaussian profiles with input power  $P_{in_i}$  as

$$\varepsilon_i(r, t, 0) = \sqrt{\frac{2P_{in_i}}{\pi\sigma_{ri}^2}} \cdot \exp\left(-\frac{r^2}{\sigma_{ri}^2} - \frac{t^2}{\tau_i^2} + i\frac{k_i r^2}{2f_i}\right) \quad (4)$$

where  $\sigma_{ri}$  is the intensity quadratic radius,  $\tau_i = \Delta t_{FWHM} / (\sqrt{2 \ln(2)})$  and  $f_i$  is the focal length of the  $\lambda_i$  pulse. Both the initial delay imposed between the two pulses and the linear chirp of the pulses are set in the frequency space:

$$\epsilon_{\mathbf{R}}(r, \omega, 0) \rightarrow \epsilon_{\mathbf{B}}(r, \omega, 0) \cdot \exp(i\omega\Delta_t) \cdot \exp(iC_{\mathbf{B}}^2 \omega^2) \quad (5)$$

$$\epsilon_{\mathbf{R}}(r, \omega, 0) \rightarrow \epsilon_{\mathbf{R}}(r, \omega, 0) \cdot \exp(iC_{\mathbf{R}}^2 \omega^2) \quad (6)$$

Here,  $\Delta_t$  represents the time delay between the two pulses,  $C_{\mathbf{B}}$  ( $C_{\mathbf{R}}$ ) is the linear chirp parameter of the initial  $\lambda_{\mathbf{B}}$  ( $\lambda_{\mathbf{R}}$ ) pulse.

The above equations have been integrated with a Fourier Split-Step scheme in which all the linear terms are computed in the Fourier space over a half-step while the nonlinear terms are directly computed in the physical space over a second half-step using a Runge-Kutta procedure. To integrate the linear terms of the equation along the  $z$  axis, *i.e.* diffraction and dispersion, we used a fully implicit scheme [43], more stable than the Euler method [44]. On the other hand, for the plasma Eq. (3), an Euler scheme is sufficiently robust. Adaptive steps were used in both the spatial transverse and longitudinal dimensions. The temporal and spatial resolutions at the filament location were  $0.25$  fs and  $1.5$   $\mu\text{m}$ , respectively. We checked that increasing the 2D grid resolution does not influence the final results.

### 3. Results and discussion

#### 3.1. Spectral bridging by co-filamentation

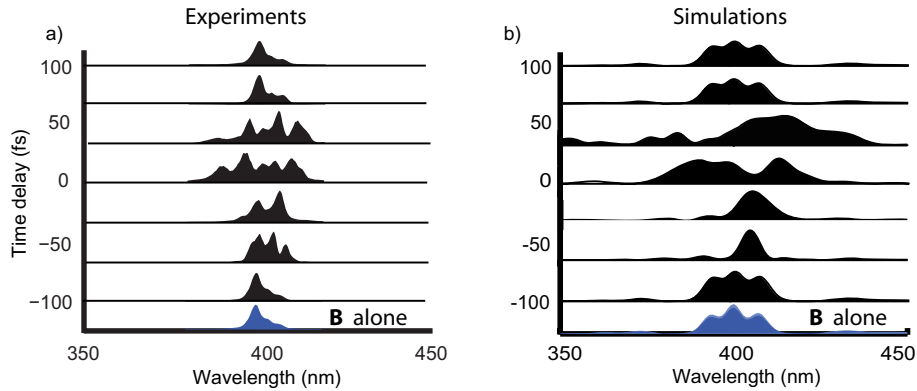


Fig. 2. 400 nm pulse spectrum as function of the relative delay between the pulses centered at 400 nm and 800 nm. The time delay is positive when the NIR pulse ( $\mathbf{R}$ ) is launched after the blue one ( $\mathbf{B}$ ). The spectrum at the bottom of each series corresponds to the  $\mathbf{B}$  pulse alone. (a) Experimental results, integrated over 4 mm diameter; (b) Numerical simulations. The broader numerical spectrum stems from the consideration of the filament center only, where the broadening is strongest, as well as the non-perfect temporal and spatial profiles of the experimental pulse

When one of the beams propagates independently, spectral broadening is only due to SPM and, to a lesser extent, to the plasma-induced nonlinear phase shift. In the case of dual-color co-filamentation, additional XPM-induced nonlinear phase shift broadens the continuum. Figure 2 displays both the experimental and the theoretical spectrum of the  $\mathbf{B}$  filament output spectrum

as a function of the delay with the **R** pulse. A fine delay tuning allows to control the shape of the blue spectrum output. The numerical results agree qualitatively with the experimental ones, except for the spectral width of the continuum. The simulated spectral broadening critically depends on the delay between the two pulses, as is the case for the experimental data. Comparable delays also yield the same relative broadening. The difference in the absolute spectral width is due to the fact that the experimental data integrate the spectrum over a 4 mm wide region, while the numerical results consider the spectrum in the filament center, where the broadening is strongest. The presence of a pre-pulse in the experiment [17] and an imperfect transverse intensity profile may also contribute to this difference.

The numerical simulations also reproduce well the shape and central wavelength of the **B** spectrum when the delay between both pulses is varied. Launching **R** 50 fs (*i.e.*, a delay comparable with the pulse duration) before (resp. after) **B** enhances the red (resp. blue) part of **B**. This can be qualitatively understood by considering that the instantaneous frequency in a  $\chi^{(3)}$  medium is approximately  $\omega(t) = \omega_0 - \frac{n_2 * \lambda}{c} \frac{\partial I}{\partial t}$  with  $n_2 > 0$  in Argon so that the spectrum is shifted towards the blue (resp. red) in the trailing (resp. leading) edge of the pulse, when  $dI/dt$  is negative (resp. positive). Depending on the sign of the delay, either the leading or trailing part of the considered pulse interacts with the other pulse, resulting in a selective enhancement of the corresponding spectrum side.

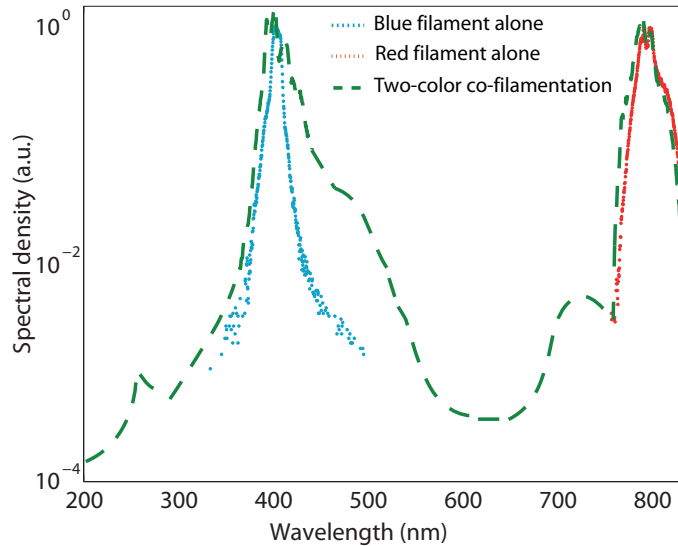


Fig. 3. (a) Experimentally observed influence of co-filamentation on the output spectrum of the supercontinuum. Co-filamentation broadens individual continuum spectra, especially in the blue region, and connects them into a continuum spanning 2 octaves (200 nm - 800 nm). The peak at 266 nm originates from the  $\chi^{(3)}$  mixing  $\frac{1}{266} = \frac{1}{400} + \frac{1}{400} - \frac{1}{800}$

Figure 3 displays the full experimental spectrum of the **B** and **R** pulses, as well as that of the connected continuum generated by the co-propagation of the **B** and **R** with a perfect temporal overlap (0 fs delay). Besides broadening the continuum around the **B** and **R** wavelengths, it also bridges those two continua into a single continuous spectrum spanning over two octaves, which raises the expectation that the corresponding pulses may be as short as 1.4 fs FWHM. Co-propagation also results in a peak at 266 nm, which is not generated by any of the filaments alone (therefore excluding third harmonic generation by the **R** pulse), originating from the  $\chi^{(3)}$

mixing  $\frac{1}{266} = \frac{1}{400} + \frac{1}{400} - \frac{1}{800}$  [9]. This mixing process even enhances the spectral broadening down to at least 240 nm, limited by the spectral range of the detection.

### 3.2. Bridging of plasma channels by co-filamentation

When the laser intensity exceeds a few  $10^{12} \text{ W.cm}^{-2}$ , Argon ionizes. The resulting plasma stabilizes the filaments in a dynamic balance with the Kerr effect. Moreover, the plasma decreases the local medium resistivity, which is of high importance to control high-voltage discharges [45] or lightning [46]. Long, highly conductive plasma "wires" are therefore highly desirable in order to increase the triggering and guiding efficiency of the filaments.

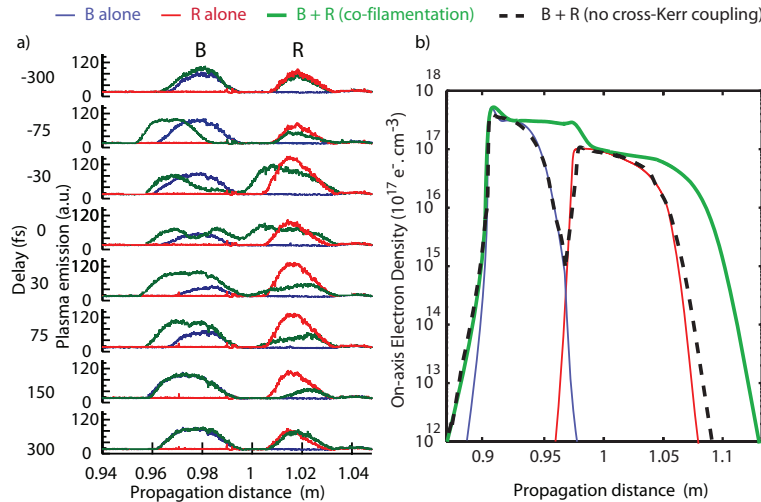


Fig. 4. a) Experimental plasma channel length for several delays. For well adjusted delay, the two plasma channel are concatenated and form a longer plasma channel without any non-ionized region. Blue: **B** induced plasma channel. Red: **R** induced plasma channel. b) Theoretical on-axis plasma channel density for both individual filaments, co-propagating filaments, and collinear filaments without cross-Kerr coupling.

Figure 4(a) depicts the qualitative profile of the electron density as a function of the propagation distance, for several delays between the **R** and **B** filaments. As long as the pulses do not temporally overlap, the resulting plasma density is the sum of the contributions of the two pulses propagating individually, with two 2.5 cm long plasma channels, separated by a 2 cm long non-ionized (therefore, isolating) region. When the pulses overlap, the two plasma columns do not only connect, but the gap between them is filled by a continuous plasma channel. In other words, co-filamentation bridges the individual plasma channels into a 9 cm long channel, corresponding to a 3.6-fold increase of the length as compared with the individual filaments. It is indeed remarkable that this bridging is obtained by the addition of the **B**, which accounts for only 13 % of the overall energy involved in the experiment. The same lever effect is observed in the numerical simulations (Fig. 4(b)). It results in a decrease of the filament resistivity between  $z_1 = 0.9 \text{ m}$  and  $z_2 = 1.07 \text{ m}$ , which is proportional to  $\int_{z_1}^{z_2} 1/\rho(z) dz$ : The co-filamentation reduces this resistivity by a factor 6, as compared to the independent propagation of the individual pulses, *i.e.* when they do not temporally overlap. Such situation contrasts with the concatenation of two plasma channels generated by two collinear 800 nm pulses of similar 4 mJ pulse energy [47]. In the latter case, an electrical connection is achieved between two filaments, but the end of the first filament is located very close to the onset of the second one.

The resulting doubling of the electrically connected plasma channel length therefore appears as a straightforward effect of the double available energy, rather than of a non-linear interaction between two co-filamenting pulses.

Partial temporal overlap results in intermediate results. The addition of **R** behaves as a supplementary energy reservoir [48] and yields an additional cross-Kerr focusing which shifts the onset of the **B** filaments toward the laser source. Reciprocally, **B** contributes to focusing **R**, but its plasma also defocuses and absorbs **R**. The outcome of these opposite effects depends on the sign of the delay between the pulses. If **R** is launched after **B**, the plasma left behind by **B** tends to defocus the **R** pulse, so that the **R** filament starts later and has a lower plasma density. On the opposite, if **R** is launched before **B**, the cross-Kerr focusing dominates. The resulting plasma channel is more intense and shifts upstream. Therefore, the plasma channel length, density and location can be controlled by adjusting the time delay between the two pulses.

To further demonstrate the contribution of the non-linear coupling between the co-filamenting pulses, we performed the same experiment with two pulses of orthogonal polarization. Such configuration resulted in a much weaker coupling than between pulses with parallel polarization. This weaker coupling stems from the fact that the non-diagonal terms of the third-order susceptibility  $\chi^{(3)}$  tensor amount to one third of the value of the diagonal ones. As a consequence, co-filamentation is much less efficient for pulses of orthogonal polarization, in contrast to the concatenation of plasma channels generated by two collinear 800 nm pulses [47], which is independent from the relative polarization of the two pulses [50]. The key role of non-linear coupling between the co-filamenting pulses is also demonstrated by the fact that the numerical simulations do not need to include two-color multiphoton ionization to reproduce the experimentally observed bridging of the plasma channels. On the other hand, setting the non-linear interaction term to zero in the simulations leads to the disappearance of the bridging (see dotted line in Fig. 4(b)).

The need for a non-linear coupling between the two co-filamenting pulses sets the upper limit to the non-ionized gaps that may be bridged by co-filamentation. Such coupling requires a simultaneous high intensity of both the **R** and **B** pulses, colocated in the non-ionized gap region. Therefore, gaps much longer than the length of the individual filaments will not be able to be bridged by co-filamentation.

### 3.3. Spatio-temporal dynamics of copropagation

To get a better insight on the physics of co-filamentation, we simulated the temporal and transverse intensity mappings, which exhibit rich spatio-temporal deformations in the course of this dual-color process. Figs. 5 and 6 display the **R** (resp. **B**) calculated intensity as a function of time and radial location, for several propagation distances. In both figures, the first column corresponds to the filamentation of a single color pulse, while the second shows the result of the co-filamentation process. The initial delay between the two pulses is set to 10 fs (*i.e.*, the **B** precedes the **R** pulse by 10 fs). These simulations show in particular that the **R** filament diameter is larger than that of **B** (250  $\mu m$  vs. 30  $\mu m$ ), so that the latter is submitted to cross-Kerr effect on a fraction of its cross-section only, while the full **B** filament is influenced by the **R** one. This difference in diameters therefore explains why **R** is more affected than **B** by co-filamentation, from the points of view of both the continuum spectrum and the plasma channels length and position.

The mechanism of co-filament-assisted spectral broadening of **B** is also well illustrated by the simulations. When the **B** intensity reaches the multiphoton ionization threshold, the **R** pulse core is both absorbed by multiphoton absorption and diffracted by the plasma. The cross-Kerr lens generated by the blue filament shifts the **R** focus upstream. Then ( $z = 96$  cm), if **R** is not present, **B** filament intensity decreases because of both plasma absorption and group-velocity

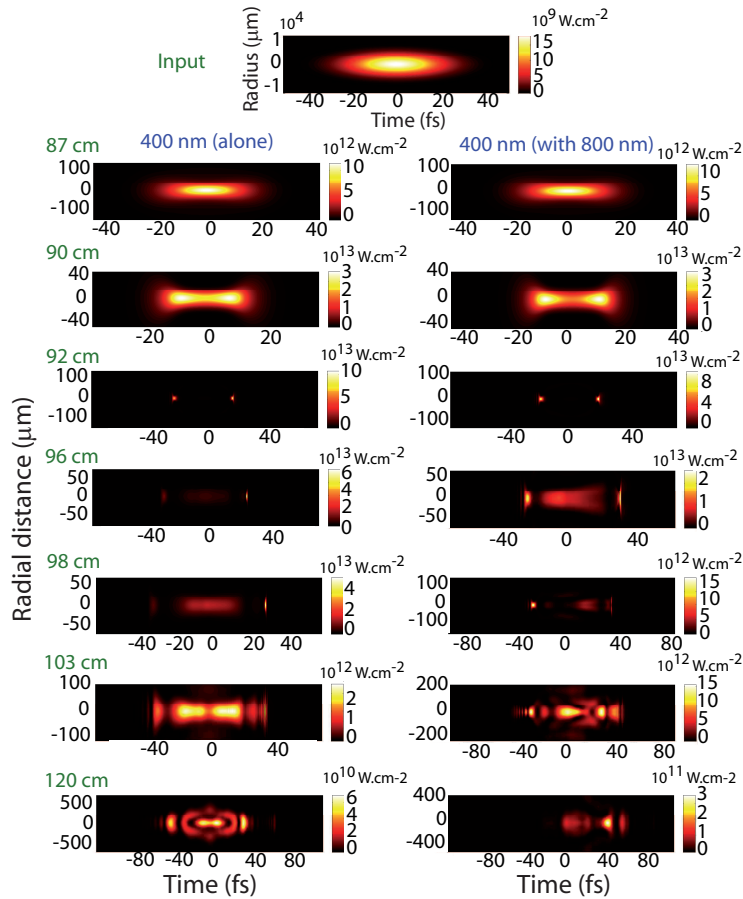


Fig. 5. One- or two-color filamentation dynamic for the 400 nm (**B**) pulse. Left: **B** intensity for several distances when propagating alone. Right: **B** intensity for the same distances when the **R** filament copropagates

dispersion. **B** then splits in the time domain [49] and its spectrum significantly broadens. Conversely, if the **R** pulse is present, the spiky blue pulse experiences more nonlinear phase shift due to the combined effects of XPM and the plasma blue shift, which broadens the spectrum. The shape of the resulting continuum depends on the delay between the two pulses and determines which of the spikes in the **B** pulse experiences the **R**-induced phase shift.

As could be expected from the width of the spectrum corresponding to the co-propagating pulses (Fig. 3), co-filamentation even leads to the formation of almost FCP (about 10 fs FWHM for both pulses, see Figs. 5 and 6 at  $z = 120$  cm) without requiring the pulse post-processing which is usually needed when generating FCP by filamentation [14]. Moreover, in view of attosecond pulse generation, the simultaneous availability of both **R** and **B** FCP could help the generation of such XUV pulses.

Further optimization of the co-filamentation may be obtained in the future by investigating the effect of the gas type and pressure. Also, atmospheric applications can reasonably be envisioned since the filamentation conditions in Argon are, to the first order, comparable to those of air, and the pressure investigated in the present work, namely 2 bars, is of the same order of

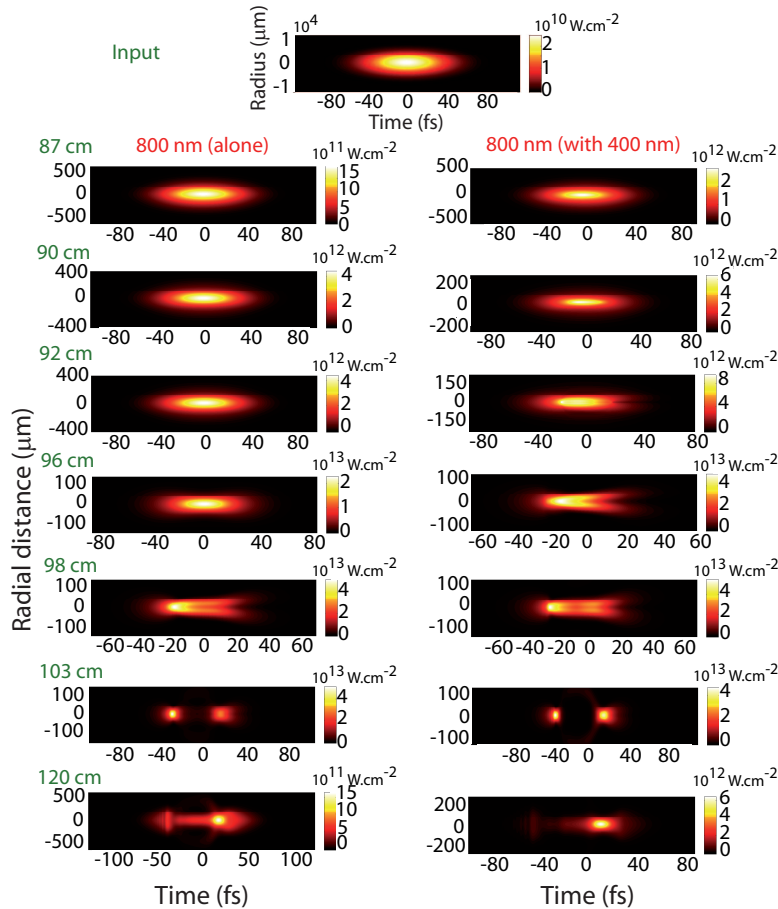


Fig. 6. One- or two-color filamentation dynamic for the **R** pulse. Left: **R** intensity for several distances when propagating alone. Right: **R** intensity for the same distances when the **B** filament copropagates

magnitude as the atmospheric pressure. However, if considering long-distance propagation and high-energy beams, the influence of the modulational instability of already multifilamenting beam onto the interaction between the two pulses will have to be investigated. The corresponding expectedly very rich physics is however beyond the scope of the present paper.

#### 4. Conclusion

We investigated both experimentally and theoretically the two-color co-filamentation of ultrashort laser pulses at 400 nm (**B**) and 800 nm (**R**). Temporally overlapping the two pulses bridges their two filaments. It results in both a spectacular enhancement of the spectral broadening over two octaves, and a connected plasma more than 3 times longer than the initial ones. Moreover, the generation of twin almost-few-cycle pulses at both **B** and **R** could provide an elegant way to produce attosecond pulses generation without any post-processing such as chirp compensation or phase shaping. The pulses with extremely broad spectra could also be used for the coherent control of states spanning over a large energy interval[4]. The extended plasma channel length could also be useful for the control of high-voltage discharges and lightning [46].

## **Acknowledgments**

This work was supported by the Swiss NSF (contracts 200021-111688 and 200021-116198), and the Swiss SER in the framework of COST P18 (Action C06.0114), as well as the Boninchi and Schmideiny foundations. We gratefully acknowledge L. Bonacina for very fruitful discussions. We also thank M. Moret for his computational support.

# Ultrafast gaseous “half-wave plate”

P. Béjot, Y. Petit, L. Bonacina, J. Kasparian<sup>#</sup>, M. Moret, and J.-P. Wolf\*

GAP, Université de Genève, 20 rue de l'École de Médecine, CH-1211 Genève 4, Switzerland

<sup>#</sup> Also with Teramobile, Université Lyon 1; CNRS; LASIM UMR 5579, bât. A. Kastler, 43 Bd du 11 novembre 1918, F-69622 Villeurbanne Cedex, France

\*Corresponding author: [jean-pierre.wolf@physics.unige.ch](mailto:jean-pierre.wolf@physics.unige.ch)

**Abstract:** We demonstrate that filaments generated by ultrashort laser pulses can induce a remarkably large birefringence in Argon over its whole length, resulting in an ultrafast “half-wave plate” for a copropagating probe beam. This birefringence originates from the difference between the nonlinear refractive indices induced by the filament on the axes parallel and orthogonal to its polarization. An angle of 45° between the filament and the probe polarizations allows the realization of ultrafast Kerr-gates, with a switching time ultimately limited by the duration of the filamenting pulse.

©2008 Optical Society of America

**OCIS codes:** (140.7090) Ultrafast lasers; (190.7110) Ultrafast nonlinear optics; (260.1440) Birefringence; (190.3270) Kerr effect; (190.5940) Self-action effects

---

## References and links

1. A. Braun, G. Korn, X. Liu, D. Du, J. Squier, and G. Mourou, "Self-channeling of high-peak-power femtosecond laser pulses in air," *Opt. Lett.* **20**, 73-75 (1995).
2. S. L. Chin, S. A. Hosseini, W. Liu, Q. Luo, F. Theberge, N. Akozbek, A. Becker, V. P. Kandidov, O. G. Kosareva, and H. Schroeder, "The propagation of powerful femtosecond laser pulses in optical media: physics, applications, and new challenges," *Can. J. Phys.* **83**, 863-905 (2005).
3. L. Bergé, S. Skupin, R. Nuter, J. Kasparian, and J.-P. Wolf, "Ultrashort filaments of light in weakly-ionized, optically-transparent media," *Rep. Prog. Phys.* **70**, 1633-1713 (2007).
4. A. Couairon and A. Mysyrowicz, "Femtosecond filamentation in transparent media," *Phys. Rep.* **441**, 47-189 (2007).
5. J. Kasparian and J.-P. Wolf, "Physics and applications of atmospheric nonlinear optics and filamentation," *Opt. Express* **16**, 466-493 (2008).
6. J. Kasparian, M. Rodriguez, G. Méjean, J. Yu, E. Salmon, H. Wille, R. Bourayou, S. Frey, Y.-B. André, A. Mysyrowicz, R. Sauerbrey, J.-P. Wolf, and L. Wöste, "White-Light Filaments for Atmospheric Analysis," *Science* **301**, 61-64 (2003).
7. J. Kasparian, R. Ackermann, Y.-B. André, G. Méchain, G. Méjean, B. Prade, P. Rohwetter, E. Salmon, K. Stelmazczyk, J. Yu, A. Mysyrowicz, R. Sauerbrey, L. Wöste, and J.-P. Wolf, "Electric events synchronized with laser filaments in thunderclouds," *Opt. Express* **16**, 5757 (2008).
8. C. P. Hauri, W. Kornelis, F. W. Helbing, A. Couairon, A. Mysyrowicz, J. Biegler, and U. Keller, "Generation of intense, carrier-envelope phase-locked few-cycle laser pulses through filamentation," *Appl. Phys. B* **79**, 673-677 (2004).
9. S. A. Trushin, K. Kosma, W. Fuss, and W. E. Schmid, "Sub-10-fs supercontinuum radiation generated by filamentation of few-cycle 800 nm pulses in argon," *Opt. Lett.* **32**, 2432-2434 (2007).
10. S. Petit, A. Talebpour, A. Proulx, and S. L. Chin, "Polarization dependence of the propagation of intense laser pulses in air," *Opt. Commun.* **175**, 323-327 (2000).
11. G. Fibich and B. Ilan, "Self-focusing of circularly polarized beams," *Phys. Rev. E* **67**, 036622 (2003).
12. H. Yang, J. Zhang, Q. J. Zhang, Z. Q. Hao, Y. T. Li, Z. Y. Zheng, Z. H. Wang, Q. L. Dong, X. Lu, Z. Y. Wei, Z. M. Sheng, J. Yu, and W. Yu, "Polarization-dependent supercontinuum generation from light filaments in air," *Opt. Lett.* **30**, 534-536 (2005).
13. M. Kolesik, J. V. Moloney, and E. M. Wright, "Polarization dynamics of femtosecond pulses propagating in air," *Phys. Rev. E* **64**, 046607 (2001).
14. S. Tzortzakis, B. Prade, M. Franco, and A. Mysyrowicz, "Time evolution of the plasma channel at the trail of a self-guided IR femtosecond laser pulse in air," *Opt. Commun.* **181**, 123-127 (2000).
15. J. P. Geindre, P. Audebert, A. Rousse, F. Fallies, J. C. Gauthier, A. Mysyrowicz, A. Dossantos, and G. Hamoniaux, "Frequency-Domain Interferometer for Measuring the Phase and Amplitude of a Femtosecond Pulse Probing a Laser-Produced Plasma," *Opt. Lett.* **19**, 1997-1999 (1994).
16. Y. H. Chen, S. Varma, I. Alexeev, and H. M. Milchberg, "Measurement of transient nonlinear refractive index in gases using xenon supercontinuum single-shot spectral interferometry," *Opt. Express* **15**, 7458-7467 (2007).

17. M. Mlejnek, E. M. Wright, and J. V. Moloney, "Femtosecond pulse propagation in argon: A pressure dependence study," *Phys. Rev. E* **58**, 4903-4910 (1998).
18. P. B ejot, C. Bonnet, V. Boutou, and J.-P. Wolf, "Laser noise compression by filamentation at 400 nm in argon," *Opt. Express* **15**, 13295-13309 (2007).
19. G. P. Agrawal, *Nonlinear Fiber Optics* (Academic Press, San Diego, 2001).
20. J. Kasparian, R. Sauerbrey, and S. L. Chin, "The critical laser intensity of self-guided light filaments in air," *Appl. Phys. B* **71**, 877-879 (2000).
21. P. Sprangle, E. Esarey, and B. Hafizi, "Propagation and stability of intense laser pulses in partially stripped plasmas," *Phys. Rev. E* **56**, 5894-5907 (1997).
22. A. Becker, N. Ak ozbek, K. Vijayalakshmi, E. Oral, C. M. Bowden, and S. L. Chin, "Intensity clamping and re-focusing of intense femtosecond laser pulses in nitrogen molecular gas," *Appl. Phys. B* **73**, 287-290 (2001).
23. B. La Fontaine, F. Vidal, Z. Jiang, C. Y. Chien, D. Comtois, A. Desparois, T. W. Johnson, J.-C. Kieffer, and H. P epin, "Filamentation of ultrashort pulse laser beams resulting from their propagation over long distances in air," *Phys. plasmas* **6**, 1615-1621 (1999).
24. M. Rodriguez, R. Bourayou, G. M ejean, J. Kasparian, J. Yu, E. Salmon, A. Scholz, B. Stecklum, J. Eisl offel, U. Laux, A. P. Hatzes, R. Sauerbrey, L. W oste, and J.-P. Wolf, "Kilometer-range non-linear propagation of femtosecond laser pulses," *Phys. Rev. E* **69**, 036607 (2004).
25. G. M echain, A. Couairon, Y.-B. Andr e, C. D'amico, M. Franco, B. Prade, S. Tzortzakis, A. Mysyrowicz, and R. Sauerbrey, "Long-range self-channeling of infrared laser pulses in air: a new propagation regime without ionization," *Appl. Phys. B* **79**, 379 (2004).
26. G. M ejean, J. Kasparian, J. Yu, E. Salmon, S. Frey, J.-P. Wolf, S. Skupin, A. Vin otte, R. Nuter, S. Champeaux, and L. Berg e, "Multifilamentation transmission through fog," *Phys. Rev. E* **72**, 026611 (2005).
27. G. M echain, G. M ejean, R. Ackermann, P. Rohwetter, Y.-B. Andr e, J. Kasparian, B. Prade, K. Stelmaszczyk, J. Yu, E. Salmon, W. Winn, L. A. V. Schlie, A. Mysyrowicz, R. Sauerbrey, L. W oste, and J.-P. Wolf, "Propagation of fs-TW laser filaments in adverse atmospheric conditions," *Appl. Phys. B* **80**, 785-789 (2005).
28. R. Salam e, N. Lascoux, E. Salmon, J. Kasparian, and J. P. Wolf, "Propagation of laser filaments through an extended turbulent region," *Appl. Phys. Lett.* **91**, 171106 (2007).

## 1. Introduction

The propagation of laser filaments in gases is now well understood as a dynamic balance between Kerr self-focusing and defocusing on laser-generated plasma [1-5]. Filaments have been characterized in detail in many regards, in particular from the spectral, temporal and spatial point of view. They are able to deliver high intensities (several  $10^{13}$  W/cm<sup>2</sup>) over distances far beyond the diffraction limit, therefore providing unique capabilities for applications like atmospheric remote sensing [6], lightning control [7] or few-cycle pulses generation [8, 9].

However, polarization has been left apart in the investigations to date, except for a few pioneering works [10-13] dealing with the influence of the incident polarization on the filament themselves. Studies of filament-induced changes in the refractive index of air have only considered long-lasting effects (nanoseconds to microseconds) of the plasma left behind the pulse [14, 15]. Self-induced birefringence has been observed to generate refractive index changes  $\Delta n$  in the  $10^{-5}$  range [16] for ultrashort lasers focused into gases. The resulting phase shift remains, however, marginal as diffraction restricts the effect to a Rayleigh length of about 100  $\mu$ m around the beam waist position. In this Letter, we demonstrate that the unique interaction length and the high-intensity conveyed by laser filaments in a rare gas, namely Argon, are sufficient to induce a "half-wave plate" effect, rotating the incident linear polarization of a non-filamenting probe pulse by an arbitrarily selected angle.

## 2. Experimental setup and numerical methods

A sketch of the experiment is displayed in Fig. 1. Slightly chirped driving (800 nm, 1 mJ, 100 fs) and probe (400 nm, 1  $\mu$ J, 100 fs) pulses, both linearly polarized and slightly focused ( $f = 1$  m), propagate collinearly in an Argon-filled cell of 2 m length. While the driving pulse generates a single filament, the probe pulse propagates linearly in absence of the driving pulse. The relative delay between the two pulses can be adjusted by a delay line. The zero delay was determined using a sum-frequency autocorrelation. A zero-order half-wave plate is

used to set the input polarization of the driving pulse, taken as the reference ( $x$  axis,  $\theta = 0^\circ$ ). At the output of the cell, the intensity of a small portion of the probe beam is selected by a pinhole (1 mm diameter) to avoid birefringence inhomogeneities related to the beam intensity transverse profile, and measured through a polarizer (Glan cube). The time-integrated signal, as a function of the polarizer orientation, bears both the ellipticity and the polarization axis of the output probe pulse. In particular, a linear polarization appears as a squared cosine function.

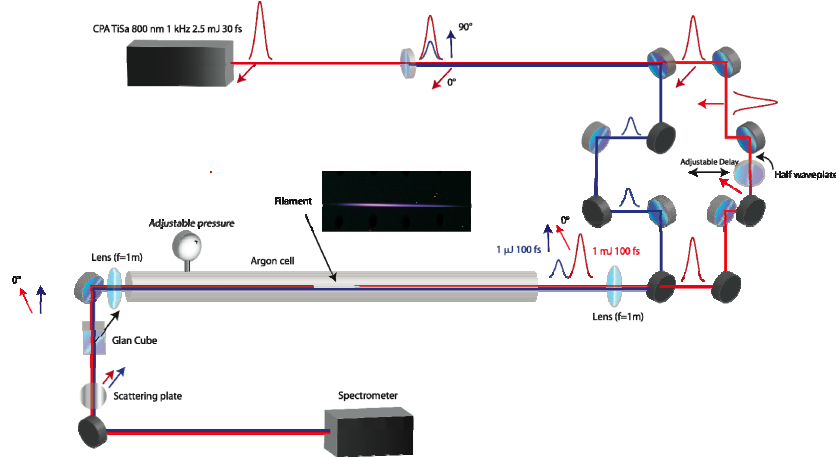


Fig. 1. Experimental setup. The polarization of the driving pulse (filamenting pulse, red) is set relative to that of the probe pulse (blue) before their interaction in the Argon cell. The driving and the probe beams are separated by a spectrometer and their polarization is analyzed by rotating a Glan cube.

We also compare the experimental results with numerical simulations based on a 2D+1 model, where the scalar envelope  $\varepsilon = \varepsilon(r, z, t)$ , with cylindrical symmetry around the propagation axis, evolves according to the Non-Linear Schrödinger Equation (NLSE) as derived by Mlejnek *et al.* [17]:

$$\partial_z \varepsilon = \frac{i}{2k_0} \Delta_\perp^2 \varepsilon - \frac{ik''}{2} \partial_t^2 \varepsilon + \frac{ik_0 n_2}{n_0} |\varepsilon|^2 \varepsilon - \frac{ik_0}{2n_0^2 \rho_c} \rho \varepsilon - \frac{1}{2} \sigma \rho \varepsilon - \frac{\beta^K}{2} |\varepsilon|^{2K-2} \varepsilon \quad (1)$$

where  $t$  refers to the retarded time in the reference frame  $t \rightarrow t - z/v_g$  of the pulse with  $v_g$  corresponding to the group velocity of the carrier envelope. The terms on the right-hand side of the equation account for spatial diffraction, second order dispersion, instantaneous Kerr effect, plasma defocusing through refraction, absorption, and losses due to multiphoton absorption, respectively.  $\rho_c = \omega_0 m_e \varepsilon_0 / e^2$  corresponds to the critical plasma density above which the plasma becomes opaque ( $1.7 \times 10^{21} \text{ cm}^{-3}$  at 800 nm). In addition, the constant  $\sigma = ke^2 \tau / (\omega m_e \varepsilon_0 (1 + \omega^2 \tau^2))$  represents the cross-section for electron-neutral inverse Bremsstrahlung ( $\tau$  is the electron-atom relaxation time constant) and  $\beta^K$  corresponds to the coefficient of multiphoton absorption,  $K$  being the minimal number of photons necessary to ionize the medium, Argon in our case.  $\beta^K$  is expressed as  $\beta^K = \hbar K \omega_0 \rho_{at} \sigma_K$  where  $\rho_{at}$  is the Argon density,  $n_2$  is the non-linear refractive index of Argon (at 1 atm,  $n_2 = 3.2 \times 10^{-19} \text{ cm}^2/\text{W}$  at 800 nm and  $n_2 = 4.9 \times 10^{-19} \text{ cm}^2/\text{W}$  at 400 nm) and  $\sigma_K$  is the multiphoton ionization cross-section. The dynamics of the electric field is coupled to the plasma density  $\rho$  by the multiphoton ionization process. The Argon ionization follows the equation:

$$\partial_t \rho = \sigma_K (\rho_{at} - \rho) |\varepsilon|^{2K} + \frac{\sigma}{U_i} \rho |\varepsilon|^2 - \alpha \rho^2 \quad (2)$$

By numerically solving the NLSE with a Fourier Split-Step scheme in a fully implicit method [18] with input parameters corresponding to our experiment ( $E = 750 \mu\text{J}$ ,  $\Delta t_{\text{FWHM}} = 30 \text{ fs}$ , and a residual chirp of  $330 \text{ fs}^2$ ), we calculated the evolution of the pulse intensity profile as a function of propagation distance  $z$  for each considered Argon pressure.

### 3. Results and discussion

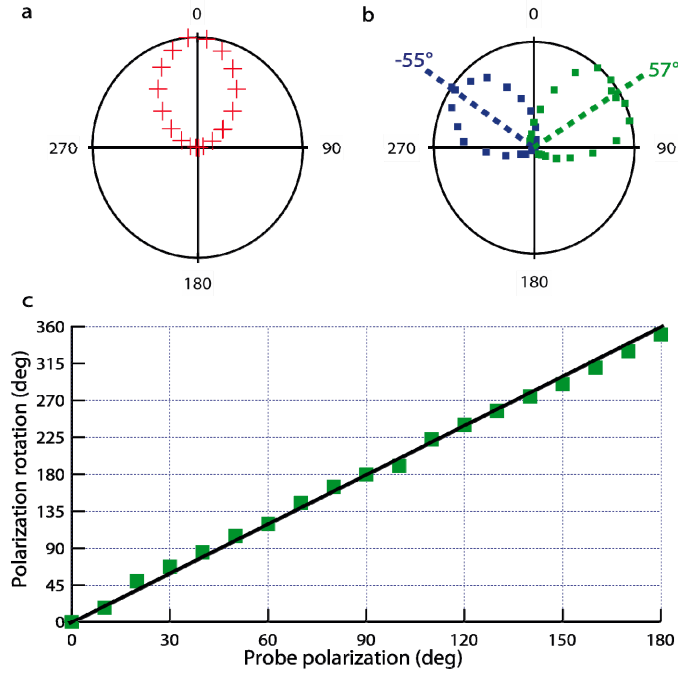


Fig. 2. Filament-induced birefringence leading to a half-wave plate behavior in 3-bar Argon. (a)-(b) Polar plot of the intensity transmitted as a function of the analyzing polarizer angle. For clarity, only half of the pattern is shown, the other half being given by symmetry. (a) Driving pulse (filament) polarization set at  $0^\circ$ . (b) Input (blue,  $-55^\circ$ ) and output (green,  $57^\circ$ ) polarizations of the probe pulse. Co-propagation with the filament rotates the probe polarization by  $112^\circ$ . The squared *cosine* patterns are signatures for linearly polarized light (c) Experimental rotation of the probe polarization as a function of its initial value (green dots): The influence of the filament-induced effective  $\lambda_{\text{probe}}/2.1$  plate agrees remarkably well with the behavior of an ideal half-wave plate, displayed for reference (solid line).

Figure 2 illustrates the experimentally measured alteration of the probe beam polarization at the exit of the cell (filled with 3 bars Argon) when its initial polarization is set at  $-55^\circ$  with respect to the driving beam polarization and the two pulses temporally overlap. After the interaction, the probe beam polarization remains highly linear with a contrast ratio  $(I_{\text{max}}^{\text{probe}} - I_{\text{min}}^{\text{probe}}) / (I_{\text{max}}^{\text{probe}} + I_{\text{min}}^{\text{probe}})$  as high as 98.4%, but rotated to  $57 \pm 2^\circ$ , symmetrical to the initial one with regard to that of the filamenting pump beam. This probe polarization flipping is the same as would be expected with a half-wave plate inserted in the probe beam path with its neutral axis at  $0^\circ$ . More precisely, the observed filament-induced birefringence corresponds to a  $\lambda_{\text{probe}}/2.1$  “waveplate”, *i.e.* the difference in the optical paths between the parallel and the perpendicular components of the probe beam amounts  $1/2.1$  optical cycle. Such a remarkably large dephasing therefore provides a way to tilt the linear polarization of an ultrashort laser

pulse by a controlled amount: The angle of rotation of the probe polarization is twice the angle that is initially set between the input probe pulse polarization and the driving beam polarization, which undergoes filamentation, as shown in Fig 2(c). Notice, in particular, that choosing a 45° angle between the polarizations of the driving and probe beams flips the probe polarization by 90° at the cell exit. Setting the polarizer perpendicular to the initial probe polarization allows then to switch the probe beam intensity on and off.

The polarization of the probe pulse is only affected within a short range of time delays between the two pulses (200 fs), corresponding to the measured cross-correlation between the pump undergoing filamentation and the probe beam. The effect is maximum when the two pulses temporally overlap. This observation is consistent with the fact that the optical Kerr effect in a monoatomic rare gas like Argon is instantaneous. The duration of the observed “filament-induced Kerr gate” is thus fully controlled by that of the driving laser pulse. Further experiments using few-cycle pulses as driving lasers could therefore lead to optical gates with unprecedented time resolution.

The mechanism of the observed filament-induced birefringence can be explained by the difference in the non-linear refractive indices generated by the driving laser pulse along its polarization axis and the orthogonal axis, respectively. More precisely, the driving field  $E^{filament}$ , polarized along the  $x$ -axis (therefore implying  $E_y^{filament} = 0$ ), induces a symmetry breaking in the optical response of the isotropic Argon gas. The non-linear Kerr polarizations of the probe beam along  $x$  and  $y$  respectively read [19]:

$$P_{XPM,x}^{probe} = \frac{3\epsilon_0}{2} \chi_{xxxx}^{(3)} |E_x^{filament}|^2 E_x^{probe} \quad (3)$$

$$P_{XPM,y}^{probe} = \frac{3\epsilon_0}{2} \chi_{yyxx}^{(3)} |E_x^{filament}|^2 E_y^{probe} \quad (4)$$

where XPM stands for the probe Cross-Phase Modulation induced by the filamenting pulse, and the non-linear elements  $\chi_{ijkl}^{(3)} = \chi_{ijkl}^{(3)}(\lambda_{probe}; \lambda_{probe}, \lambda_{pump}, -\lambda_{pump})$  are related to the considered cross-Kerr process. All the other non-linear Kerr polarization terms are negligible here, as the ratio of the probe and driving beam energies is  $10^{-3}$ . As the dominant contribution to the  $\chi^{(3)}$  tensor in atomic gases like Argon is governed by the electronic cloud response (*i.e.* by the atomic nonlinear polarizability), and since the filament and probe frequencies are far from any resonant transition of Argon, we can consider that  $\chi_{xxxx}^{(3)} = 3\chi_{yyxx}^{(3)}$  [19]. As a consequence, the filament-induced birefringence is:

$$\Delta n_{XPM}^{probe} = \frac{1}{2n_0} \left( \frac{3}{2} \text{Re}(\chi_{xxxx}^{(3)} - \chi_{yyxx}^{(3)}) \right) |E_x^{filament}|^2 = n_2^{XPM} I^{filament} \quad (5)$$

with

$$n_2^{XPM} = \text{Re}(\chi_{xxxx}^{(3)}) / (n_0^2 \epsilon_0 c) = 4n_2 / 3 \quad (6)$$

Here,  $n_2^{XPM}$  is the XPM non-linear refractive index of Argon,  $I^{filament}$  the intensity within the filament,  $n_0 = 1.0003$  the linear refractive index of Argon at the probe frequency for experimental pressures at room temperature,  $\epsilon_0$  the vacuum permittivity and  $c$  the speed of light in vacuum.  $n_2$  is the “usual” non-linear refractive index as used *e.g.* in Eq. (1). Integrated over the whole interaction length, this birefringence induces a dephasing between the probe beam components along the fast and slow polarization axes of:

$$\Delta\varphi_{XPM}^{probe} = 2\pi \int \Delta n_{XPM}^{probe} dz / \lambda_{probe} = 2\pi n_2^{XPM} \int I^{filament}(z) dz / \lambda_{probe} \quad (7)$$

As is usual in filamentation models, the third-order susceptibility of the plasma (ions and electrons) is not taken into account, because (i) electrons only have a significant contribution in the relativistic regime [20] and (ii) the small relative abundance of ions relative to neutral molecules (typically  $10^{-4}$  [21]) and the fact that their third-order susceptibility is smaller than that of neutrals and does not deviate by more than one order of magnitude [20] prevents them from having any measurable contribution.

$\Delta\phi_{XPM}^{probe}$  varies with the nonlinear refractive index  $n_2^{XPM}$ , and hence, with the Argon pressure in the cell at a fixed temperature. The measured birefringence at different Argon pressures is presented in Fig. 3 and Fig. 4. As described above, a pressure close to 3 bars (precisely  $3.3\pm 0.2$  bars) permits to generate an ideal half-wave plate. For lower pressures, an elliptical polarization is observed. A fit of the angular pattern of the output polarization (Figs. 3(b)-3(d)) yields a contrast ratio of 67.7% at 1 bar, 39.5% at 2 bar and 98.4% at 3 bar, as well as the orientation of their ellipticity main axis, which amounts to  $-51\pm 3^\circ$ ,  $71\pm 5^\circ$  and  $57\pm 2^\circ$  respectively. This elliptical polarization is the signature for a smaller dephasing  $\Delta\phi_{XPM}^{probe}$ , corresponding to  $\lambda_{probe}/8.3$  at 1 bar and  $\lambda_{probe}/3.4$  at 2 bar, respectively, Fig. 5(a).

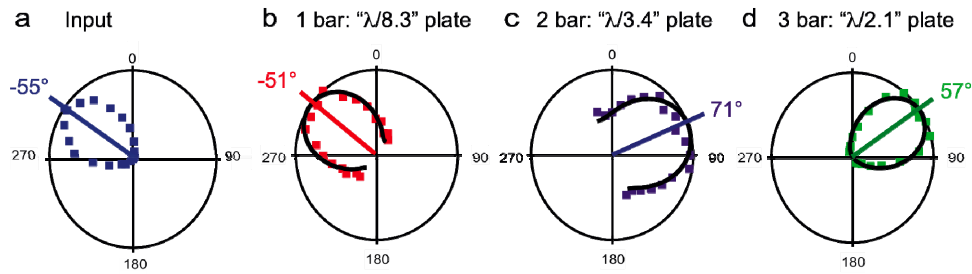


Fig. 3. Pressure dependence of the filament-induced birefringence. (a). Input probe polarization; (b)-(d). Output probe beam polarization for 1, 2 and 3 bar respectively. The black solid lines are fits assuming elliptical polarizations.

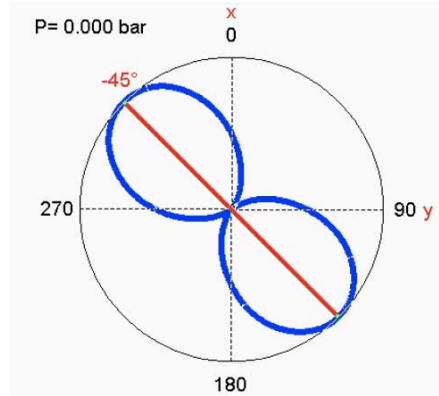


Fig. 4. (1.3 MB) Movie of the pressure dependence of the output polarization diagram of a probe beam driven by an ultrashort laser filament. The movie displays, for each pressure, the simulated signal of the probe beam as a function of the orientation of a polarizer downstream of the interaction region between the drive and pump pulses.

To gain more insight into the pressure dependence, we compared the experimental results with the output of the numerical simulations providing the longitudinal intensity profile at the different pressures, and thus the corresponding birefringence  $\Delta n_{XPM}^{probe}$  through Eq. (5). This dephasing depends linearly on the Argon pressure, in excellent agreement with the experimental data (Fig. 5(a)) for a value of  $n_2^{XPM}$  proportional to the Argon pressure and equal

to  $1.6 \times 10^{-20} \text{ cm}^2/\text{W}$  at 1 atm. This value lies below that expected from Eq. (6). Such underestimation is due to the fact that the calculations overestimate the pump intensity, because they consider that of the beam center while the actual intensity is lower in the beam region selected by the pinhole. Further work is required to provide a quantitative transverse profile of filament-induced birefringence and achieve a better quantitative agreement.

As can be seen on Fig. 5(b), our simulations show that higher pressures (*i.e.* higher  $n_2^{SPM}$  values) result in longer filaments with lower intensity clamping [21, 22]. These opposite effects roughly compensate each other when calculating the integral  $\int I^{filament}(z) dz$ , so that the dephasing  $\Delta\varphi_{XPM}^{probe} = 2\pi n_2^{XPM} \int I^{filament}(z) dz / \lambda_{probe}$  varies like  $n_2^{XPM}$ , *i.e.* with the Argon pressure.

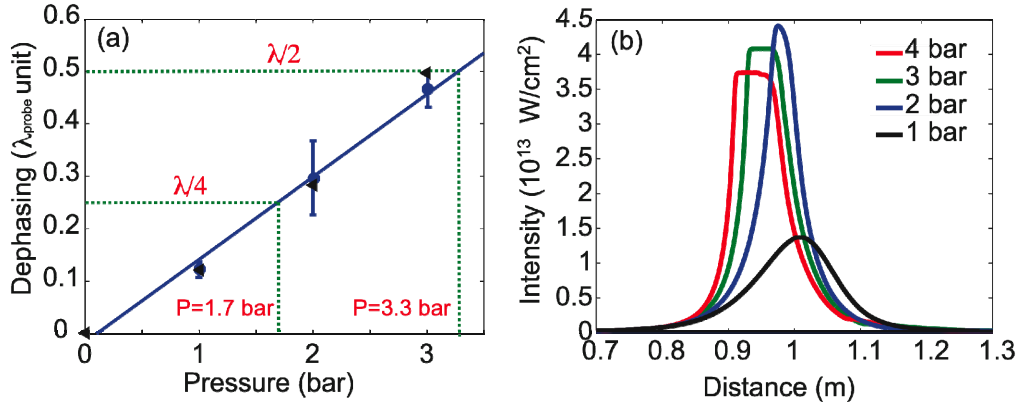


Fig. 5. (a). Experimental (circles) and simulated (triangular) pressure dependence of the filament-induced dephasing. (b). Evolution of the intensity at the filament center with the propagation distance, depending on the pressure.

As the dephasing depends monotonically on the pressure, any  $\Delta\varphi_{XPM}^{probe}$  value may be generated by choosing an adequate Argon pressure. For example, an interpolation of the experimental data presented in Fig. 5 suggests that an equivalent “ $\lambda/4$  plate” can be generated for  $1.7 \pm 0.1$  bar. Even further tuning of the birefringence could be obtained by a careful choice of the investigated position within the beam profile, because of the transverse intensity gradients which are expected to generate transverse birefringence variations.

## Conclusion

In conclusion, we have demonstrated that laser-generated self-guided filaments can induce substantial birefringence in near-atmospheric pressure gases. An angle of  $45^\circ$  between the filament and the probe polarizations allows the realization of Kerr-gates, with an unprecedented switching time ultimately limited by the duration of the filamenting pulse. An optical ultrafast switch could even be initiated remotely by self-guided filaments in the atmosphere [6, 23-25], even in perturbed conditions [26-28], opening new perspectives for remote optical ultrafast data transmission and processing, *e.g.* remote ultrafast optical logical gates.

## Acknowledgments

This work was supported by the Swiss NSF (contract 200021-111688 and R’equip program), and the Swiss SER in the framework of COST P18 action C06.0114, as well as the Boninchi and Schmeideiny foundations.

## Effects of atmospheric turbulence on remote optimal control experiments

J. Extermann, P. Béjot, L. Bonacina,<sup>a)</sup> P. Billaud, J. Kasparian,<sup>b)</sup> and J.-P. Wolf  
*Université de Genève, GAP-Biophotonics, 20 rue de l'École de Médecine, 1211 Geneva 4, Switzerland*

(Received 31 October 2007; accepted 5 January 2008; published online 28 January 2008)

Distortions of ultrashort laser pulses propagating through turbulence are investigated both experimentally and numerically. As expected, a strong correlation is found between temporal distortions and local intensity on the speckle pattern. We suggest that the localization of distortions in low-intensity regions may favor remote control strategies based on nonlinear interactions with respect to those based on linear schemes. © 2008 American Institute of Physics.

[DOI: 10.1063/1.2838308]

Atmospheric applications of ultrashort and ultraintense lasers have recently emerged as a novel and very active field of research. On one side, the use of filamentation in air as coherent white light source for Light Detection and Ranging of atmospheric species has been proven as an attractive method.<sup>1,2</sup> On the other side, time-resolved and coherent control schemes have recently been used to efficiently discriminate between aerosol particles that exhibit identical spectral signatures.<sup>3,4</sup> There is now a particular interest to apply control schemes, such as fluorescence depletion and multipulse impulsive Raman spectroscopy,<sup>5</sup> directly in the atmosphere, especially since first field applications were demonstrated within the Teramobile project.<sup>1,6</sup> However, transmitting an optimally shaped pulse over long distance through the atmosphere is not fully straightforward. Although optimal control can be used to control filamentation in the field,<sup>7</sup> no demonstration of the applicability of quantum control of molecular species at a distance has been reported yet. Among the processes that may affect the propagation of an ultrashort laser pulse, thermal turbulence is likely the most effective in preventing remote control techniques. In fact, contrary to dispersion and Kerr-related effects, distortions induced by turbulence cannot be avoided by a sensible choice of the pulse characteristics, or precompensated,<sup>8,9</sup> due to their random nature. Pointing variation and wavefront distortions (speckles) of nanosecond or cw laser beams induced by atmospheric turbulence have been extensively studied.<sup>10</sup> In this paper, we investigate both experimentally and numerically how turbulence affects the properties of linearly propagating femtosecond laser pulses.

The measurements were carried out under stable environmental conditions (relative humidity  $\leq 40\%$ , temperature of 20 °C) with an amplified 1 KHz Ti:sapphire laser system delivering 2.5 mJ, 30 fs pulses with a beam diameter of  $\sim 12$  mm at  $1/e^2$  and curvature radius  $R = -15$  m. After propagating over a distance of  $d_1 = 3.8$  m, the beam goes across a highly turbulent region generated by the perpendicular flow of a hot air blower ( $T \leq 500$  °C with 500 l/min flux, output air velocity of 20 m/s, angular divergence of 20°). The perturbation intensity is controlled by varying the distance between the blower and the beam axis. The strength of the perturbation, represented by the structure parameter of the refractive index  $C_n^2$ , was determined by measuring the

variance in pointing angle of a He-Ne laser collinear with the femtosecond beam.<sup>11</sup> The turbulence range achievable by the experiment [ $C_n^2 = (7-15) \times 10^{-9} \text{ m}^{-2/3}$ ] represents a very strong perturbation, a few orders of magnitude higher than those typically encountered in the atmosphere.<sup>12</sup> After passing through the turbulent region, the pulses propagate for an additional distance  $d_2 = 3.7$  m before being characterized by a single shot autocorrelator (by sampling a 28 mm<sup>2</sup> portion in the center of the beam profile) or imaged by a digital charge coupled device camera equipped with a  $f = 105$  mm objective (spatial resolution 150  $\mu\text{m}/\text{pixel}$ , 10 ms exposure time). Alternatively, we characterized individual wavefront regions (0.25 mm<sup>2</sup>) by frequency resolved optical gating (FROG) inserting in the beam path a random phase plate. This time-invariant perturbation allowed multishot acquisition. We measured by interferometry that the plate introduces an average phase difference of  $\sim 4\pi/3$  among two points on the wavefront separated by 2 mm, an analogous estimate for a perturbation strength of  $C_n^2 = 9.6 \times 10^{-10} \text{ m}^{-2/3}$  gives  $\sim 2\pi/3$ .

To complement the experimental measurements, we numerically simulated the propagation of a linearly polarized Gaussian pulse centered at  $\lambda_0 = 800$  nm with wavefront curvature and radii matching the experimental values. Every spectral component is first propagated in free space, supposed to be linear and homogeneous, along a distance  $d_1$ . Then, to simulate the passage through turbulence, we apply a phase screen generated according to the Kolmogorov theory<sup>13</sup> for the different  $C_n^2$  values. Finally, the pulse spectral components are propagated again in free space for an additional distance  $d_2$ .

As shown in Figs. 1(a) (experiment) and 1(b) (simulation), the beam profile is spatially distorted in a typical speckle pattern as a result of the propagation through turbulence. The experimental and simulated wavefronts bear a strong resemblance, especially considering that the former is the superposition of ten successive laser shots. The strongly inhomogeneous distribution of intensity, ranging from  $10^{-3}$  to 2 times that of the unperturbed wavefront, results from the superposition of the multiple interferences among beam portions experiencing different phase shifts through turbulence repeated at each wavelength in the bandwidth.<sup>14</sup> Beside spatial distortions, we investigated also global temporal modifications, as reported in Fig. 1(c). Pulse autocorrelation widths averaged over 50 independent laser shots show a clear increase with turbulence strength. The experimental datapoints (squares) are normalized by the duration of a pulse propagating the same distance in the unperturbed laboratory atmo-

<sup>a)</sup>Electronic mail: luigi.bonacina@physics.unige.ch.

<sup>b)</sup>Also at Université Lyon 1, CNRS, LASIM UMR 5579, 43 bd du 11 Novembre, 69622 Villeurbanne Cedex, France.

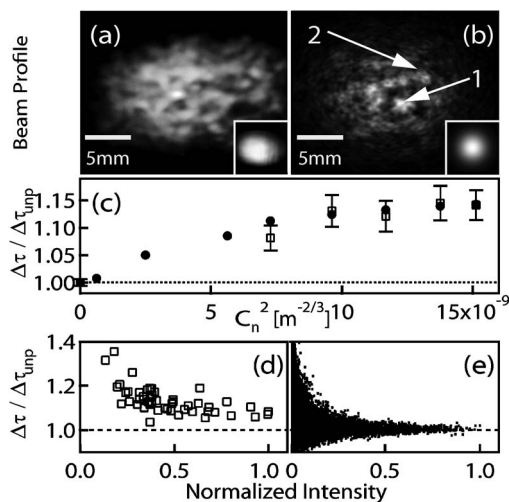


FIG. 1. (a) Experimental and (b) simulated beam profile. Arrows indicate the (1) strong and (2) the weak intensity spots. In the insets, the beam profiles in absence of artificial turbulence. (c) Pulse duration normalized to that of a pulse propagating the same distance in absence of turbulence as a function of turbulence strength, from experiment ( $\square$ ) and simulation ( $\bullet$ ). Relative pulse duration as a function of pulse intensity at fixed  $C_n^2 = 9.6 \times 10^{-10} \text{ m}^{-2/3}$  from experiment (D) and simulation (E).

sphere,  $\Delta\tau_{\text{unp}}$ . Note that this duration does not correspond to that of a Fourier limited pulse. We derived from the simulation a comparable quantity by calculating the average of the temporal second moment of different beam portions normalized by the unperturbed value (circles). Note that, even in presence of strong perturbations, the average relative variation  $\Delta\tau / \Delta\tau_{\text{unp}}$  does not exceed 15%. The quantitative agreement between experiment and calculations over the whole range of turbulence strengths investigated, authorizes to extend the simulations to the  $C_n^2 = (2-7) \times 10^{-9} \text{ m}^{-2/3}$  range, which was not accessible in the experiment.

Figs. 1(d) and 1(e) compare the results of experiment and simulation by plotting the relative distortion of pulse duration as a function of the local wavefront intensity. The observed temporal distortions are strongly correlated with intensity, evidencing that the major deviations from the unperturbed case are concentrated in weak intensity regions. Pulse duration converges to the unperturbed one ( $\Delta\tau / \Delta\tau_{\text{unp}} = 1$ ) as intensity increases.

We can gather more insight by investigating locally the spectral and temporal characteristics of regions of different intensities on the beam profile. As mentioned above, these measurements required the use of a random phase plate, which entails a much higher distortion than that generated by the hot air blow. In Fig. 2, we report two illustrative experimental temporal  $I(t)$  and spectral  $I(\lambda)$  profiles retrieved by inverting multishots FROG measurements from regions of different intensities: high [(a), (c)] and low [(b), (d)]. Similarly, Fig. 3 displays characteristic examples of simulated  $I(t)$ ,  $I(\lambda)$ , and Wigner plot of strong [(a), (c), and (e)] and of weak [(b), (d), and (f)] intensity regions. The inspection of these traces further confirms the strong correlation between local intensity and pulse distortions. In low-intensity regions, the existence of substructures in the temporal profiles and major spectral alterations is clearly apparent from the plots. Conversely, for high intensities, little or no distortions are present and the traces almost perfectly overlap with those calculated for a pulse propagating in the

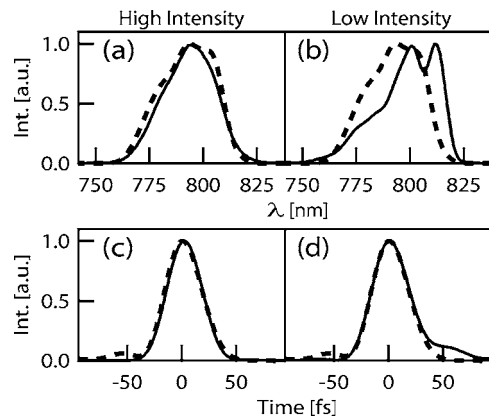


FIG. 2. Solid lines: experimental  $I(\lambda)$  and  $I(t)$  retrieved inverting the multi shot FROG measurement of [(a) and (c)] high and [(b) and (d)] weak intensity spots on the wavefront. Dotted lines: corresponding traces for a pulse propagating without turbulence over the same distance.

absence of turbulence (dotted lines). Simulation allowed us to determine that in the intense spots, the effect of multiple interferences accounts for minor amplitude deviations in both  $I(t)$  and  $I(\lambda)$ , not exceeding a few percent fraction of the relative intensity. These observations altogether are consistent with a scenario where interferences act similarly at all wavelengths: in a defined portion of the beam profile, the spectral components experience a similar phase shift when passing through turbulence. Such a condition holds exclusively because of the narrow bandwidth of the femtosecond laser pulse (35 nm) as compared with the wavelength dependence of the index of refraction of air,  $n_{\text{air}}$ .

By integrating  $I(t)$  across the beam profile, we conclude that the overall pulse duration is only slightly affected by turbulence: 6% on the temporal second moment with respect to the unperturbed situation for  $C_n^2 = 9.6 \times 10^{-10} \text{ m}^{-2/3}$ . This  $C_n^2$  value is four orders of magnitude higher than typical atmospheric conditions. In the approximation of constant tur-

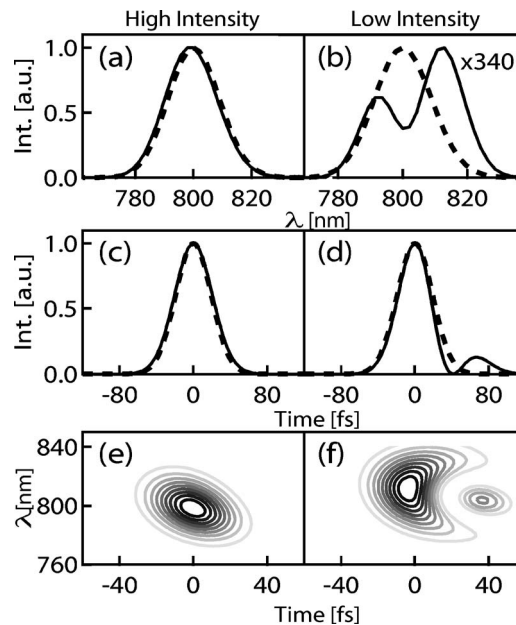


FIG. 3. [(a) and (b)] Simulated  $I(\lambda)$ , [(c) and (d)]  $I(t)$ , and [(e) and (f)] Wigner representation of the pulse characteristics in the high (left column) and low (right column) intensity spots on the beam profiles indicated by arrows 1 and 2 in Fig. 1(b).

bulence over the propagation length,<sup>15</sup> using a standard value<sup>12</sup> for strong atmospheric turbulence ( $C_n^2=2.5 \times 10^{-13} \text{ m}^{-2/3}$ ), we can extrapolate that comparable pulse distortions should appear after kilometeric propagation. However, the strong assumptions prevent a more quantitative estimation.

To conclude, the effect of atmospheric turbulence on linearly propagating femtosecond laser pulses can be simply treated as the superposition of interferences independently acting on the components of the pulse spectrum. Bright spots on the wavefront correspond to weakly perturbed regions, which essentially maintain the spectral and temporal properties of the original pulse. The degree of alteration anticipated for actual atmospheric propagation (<6%) does not constitute an overwhelming limitation but it is a factor to take into account to design robust remote control applications. A partial compensation to the effects of turbulence can be achieved by adopting control strategies based on multiple-photon interactions, as nonlinear power dependence limits higher order interactions within intense beam regions, where the original spectral and temporal pulse features are conserved. In analogy with what is currently done in astronomy,<sup>16</sup> one can also envisage to use adaptive optical components to realize real-time wavefront correction; taking into consideration the weak spectral dependence over pulse bandwidth of  $n_{\text{air}}$ , we suggest that this way not only spatial but also temporal distortions of femtosecond pulses can be actively compensated for.

Our work was supported by the Swiss NSF (Contract No. 200021-111688) and Swiss SER in the framework of COST P18 and Boninchi Foundation, Geneva. We thank

Amplitude Technology for the autocorrelator and S. Waldis for the phase-plate characterization.

- <sup>1</sup>J. Kasparian, M. Rodriguez, G. Mejean, J. Yu, E. Salmon, H. Wille, R. Bourayou, S. Frey, Y. B. Andre, A. Mysyrowicz, R. Sauerbrey, J. P. Wolf, and L. Woste, *Science* **301**, 61 (2003).
- <sup>2</sup>H. L. Xu, J. F. Daigle, Q. Luo, and S. L. Chin, *Appl. Phys. B: Lasers Opt.* **82**, 655 (2006).
- <sup>3</sup>F. Courvoisier, V. Boutou, V. Wood, A. Bartelt, M. Roth, H. Rabitz, and J. P. Wolf, *Appl. Phys. Lett.* **87**, 063901 (2005).
- <sup>4</sup>F. Courvoisier, V. Boutou, L. Guyon, M. Roth, H. Rabitz, and J. P. Wolf, *J. Photochem. Photobiol., A* **180**, 300 (2006).
- <sup>5</sup>D. Pestov, R. K. Murawski, G. O. Ariunbold, X. Wang, M. C. Zhi, A. V. Sokolov, V. A. Sautenkov, Y. V. Rostovtsev, A. Dogariu, Y. Huang, and M. O. Scully, *Science* **316**, 265 (2007).
- <sup>6</sup>G. Mejean, J. Kasparian, E. Salmon, J. Yu, J. P. Wolf, R. Bourayou, R. Sauerbrey, M. Rodriguez, L. Woste, H. Lehmann, B. Stecklum, U. Laux, J. Eisloffel, A. Scholz, and A. P. Hatzes, *Appl. Phys. B: Lasers Opt.* **77**, 357 (2003).
- <sup>7</sup>R. Ackermann, E. Salmon, N. Lascoux, J. Kasparian, P. Rohwetter, K. Stelmaszczyk, S. H. Li, A. Lindinger, L. Woste, P. Bejot, L. Bonacina, and J. P. Wolf, *Appl. Phys. Lett.* **89**, 171117 (2006).
- <sup>8</sup>H. Wille, M. Rodriguez, J. Kasparian, D. Mondelain, J. Yu, A. Mysyrowicz, R. Sauerbrey, J. P. Wolf, and L. Woste, *Eur. Phys. J.: Appl. Phys.* **20**, 183 (2002).
- <sup>9</sup>I. Pastirk, X. Zhu, R. M. Martin, and M. Dantus, *Opt. Express* **14**, 8885 (2006).
- <sup>10</sup>J. Goodman, *Statistical Optics* (Wiley, New York, 2000).
- <sup>11</sup>R. Ackermann, G. Mejean, J. Kasparian, J. Yu, E. Salmon, and J. P. Wolf, *Opt. Lett.* **31**, 86 (2006).
- <sup>12</sup>S. Bendersky, N. S. Kopeika, and N. Blaunstein, *Appl. Opt.* **43**, 4070 (2004).
- <sup>13</sup>C. M. Harding, R. A. Johnston, and R. G. Lane, *Appl. Opt.* **38**, 2161 (1999).
- <sup>14</sup>W. J. Liu and C. H. Zhou, *Appl. Opt.* **44**, 6506 (2005).
- <sup>15</sup>R. Salamé, N. Lascoux, E. Salmon, R. Ackermann, J. Kasparian, and J.-P. Wolf, *Appl. Phys. Lett.* **91**, 171106 (2007).
- <sup>16</sup>R. Foy, A. Migus, F. Biraben, G. Grynberg, P. R. McCullough, and M. Tallon, *Astron. Astrophys. Suppl. Ser.* **111**, 569 (1995).

# Filament-Induced Birefringence in Argon<sup>1</sup>

Y. Petit<sup>a,\*</sup>, P. Béjot<sup>a</sup>, L. Bonacina<sup>a</sup>, J. Kasparian<sup>b</sup>, M. Moret<sup>a</sup>, and J.-P. Wolf<sup>a</sup>

<sup>a</sup> *GAP, Université de Genève, 20 rue de l’Ecole de Médecine, CH-1211 Genève 4, Switzerland*

<sup>b</sup> *Teramobile, Université Lyon 1; CNRS; LASIM UMR 5579, bât. A. Kastler, 43 Bd du 11 novembre 1918, F-69622 Villeurbanne Cedex, France*

\*e-mail: Yannick.petit@unige.ch

Received September 30, 2008

**Abstract**—We demonstrate that a driving ultrashort laser pulse undergoing filamentation can induce a remarkably large birefringence in Argon, resulting in an ultrafast “half-wave plate” for a copropagating non-filamenting probe beam. Such femtosecond birefringence, which originates from the difference between the nonlinear refractive indices induced by the filament on the axes parallel and orthogonal to its own polarization, opens the way to potential ultrafast Kerr-gates whose ultimate time-duration is only restricted by the duration of the driving pulse. We also show that the induced birefringence is transversely inhomogeneous, resulting from the intensity profile of the driving pulse.

PACS numbers: 42.65.Re, 42.65.Sf, 42.65.Jx

DOI: 10.1134/S1054660X09020273

## 1. INTRODUCTION

The propagation of laser beams undergoing filamentation in gases is now a well understood process, resulting from a dynamical balance between Kerr self-focusing and defocusing on laser-generated plasma [1–5]. Detailed characterizations have been performed on the spectral, temporal and spatial behavior of filaments. These light structures provide unique capabilities for applications like atmospheric remote sensing [6], lightning control [5, 7], few-cycle pulses generation [8–10], as they can deliver high intensities (several  $10^{13}$  W/cm<sup>2</sup>) over distances far beyond the usual diffraction limit.

Up to now, polarization has been somehow left apart in investigations to date. A few pioneering works studied the influence of the incident polarization on the filament themselves [11–14]. Filament-induced changes in the refractive index of air have only been considered for long-lasting effects (nanoseconds to microseconds) of the plasma left behind the pulse [15, 16]. Even if self-induced birefringence has been observed to generate refractive index changes  $\Delta n$  in the  $10^{-5}$  range for ultrashort lasers focused into gases [17], the resulting phase shift remains marginal as diffraction restricts the effect to a Rayleigh length of about 100  $\mu$ m around the beam waist position.

In this paper, we demonstrate that the unique interaction length and the high-intensity conveyed by laser filaments in a rare gas, Argon here, can induce a “half-wave plate” effect, providing the ability to rotate the incident linear polarization of a non-filamenting probe pulse by an arbitrarily chosen angle. We also show that the transverse intensity distribution of the filamenting

beam leads to an inhomogeneous birefringence across the probe beam profile. Consequently, the femtosecond birefringence profile presents an inhomogeneous transverse distribution within the probe profile. Such consideration could be an appropriate method for non-destructive measurement of the distribution of the longitudinally-integrated intensity profile of the filament.

## 2. EXPERIMENTAL SETUP

The experimental setup has been described in detail in [18] (Fig. 1). A Ti:Sa amplifier system associated with a delay line and a BBO doubling crystal delivers two slightly chirped pulses, respectively red (800 nm, 1 mJ, 100 fs) and blue (400 nm, 1  $\mu$ J, 100 fs), with a tunable time delay. The red pulse polarization is rotated by a zero-order waveplate (WP), and its orientation is taken as reference ( $x$  axis,  $\theta = 0^\circ$ ). The two beams are slightly focused by a 1 m focal lens in a 2 m long cell filled with tunable pressure Argon.

The driving (red) pulse generates a single filament, whereas the probe (blue) pulse propagates linearly in absence of the driving pulse. We measured the time-integrated probe intensity of each pulse as a function of the output polarizer orientation, for chosen positions in the beam profile. Using this technique, a linear polarization appears as a squared cosine function, as described in Figs. 2a and 2b. We used a 0.5 nm resolution monochromator to discriminate between the two pulses.

We also compared the experimental results with numerical simulations based on a 2D + 1 model, as described in detail before [18–20]. We considered pump input parameters corresponding to our experiment (i.e., an energy  $E = 750$   $\mu$ J, a Fourier-limited pulse duration  $\Delta t_{\text{FWHM}} = 30$  fs, and a residual chirp of

<sup>1</sup> The article is published in the original.

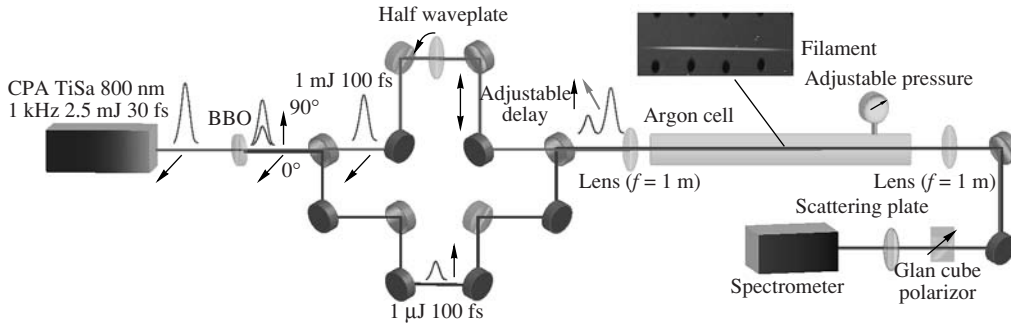


**Fig. 1.** Experimental setup. DCM: Dichroic mirror. HWP: half-wave plate. The linear polarization of the red pulse (800 nm) is set relative to that of the blue pulse (400 nm) before their interaction in the Argon cell. These copropagating beams are separated by a spectrometer their polarization is analyzed by rotating a Glan cube. Diaphragm is shortly open for the experiments described in Sections 3 and 5, and fully open for Section 6 [18].

330 fs<sup>2</sup>), and we calculated the evolution of the pump pulse intensity profile as a function of propagation distance  $z$  for each considered Argon pressure.

### 3. FILAMENT-INDUCED ULTRAFAST HALF-WAVE PLATE

Figure 2 illustrates the experimentally measured modification of the probe beam polarization at the exit of the cell (filled with a 3 bar Argon pressure) when its initial polarization is set at  $\alpha_{\text{input}} = -55^\circ$  with respect to the driving beam polarization and the two pulses temporally overlap. After the interaction, the probe beam polarization remains highly linear with a contrast ratio  $(I_{\text{max}}^{\text{probe}} - I_{\text{min}}^{\text{probe}})/(I_{\text{max}}^{\text{probe}} + I_{text{min}}^{\text{probe}})$  as high as 98.4%, but rotated to  $\alpha_{\text{output}} = 57 \pm 2^\circ$ , symmetrical to the initial one with regard to that of the filamenting pump beam. This probe polarization flipping is the same as would be obtained with a half-wave plate inserted in the probe beam path with its neutral axis at  $0^\circ$ . More precisely, the observed filament-induced birefringence corresponds to a  $\lambda_{\text{probe}}/2.1$  “waveplate,” i.e., the difference in the optical paths between the parallel and the perpendicular components of the probe beam amounts  $1/2.1$  optical cycle at 400 nm. Such a remarkably large dephasing provides a way to tilt the linear polarization of an ultrashort laser pulse by a controlled amount: the angle of rotation of the probe polarization is twice the angle that is initially set between the input probe pulse polarization and the filamenting pump pulse polarization. In particular, choosing a  $45^\circ$  angle between the polarizations of the driving and probe beams flips the probe polarization by  $90^\circ$  at the cell exit. Setting the polarizer perpendicular to the initial probe polarization allows then to switch the probe beam intensity on and off by switching the driving pulse on and off.

As shown in Fig. 3, this polarization switching critically depends on the time delay between the two pulses (200 fs), corresponding to the measured cross-correlation between the pump undergoing filamentation and the probe beam. Moreover, the birefringence depen-

dence with the delay is symmetric with respect to time reversal, which is consistent with the fact that the optical Kerr effect in a monoatomic rare gas like Argon is instantaneous. The duration of the observed “filament-induced Kerr gate” is thus fully controlled by that of the driving laser pulse. Using few-cycle pulses as driving lasers could therefore lead to optical gates with unprecedented time resolution (Fig. 4). Such gates could convert information encoded in the temporal intensity profile of the driving pulse into the temporal polarization profile of the probe beam [21].

### 4. THEORETICAL DESCRIPTION

The mechanism of the observed filament-induced birefringence can be explained by the difference in the nonlinear refractive indices generated by the driving laser pulse along its polarization axis and the orthogo-

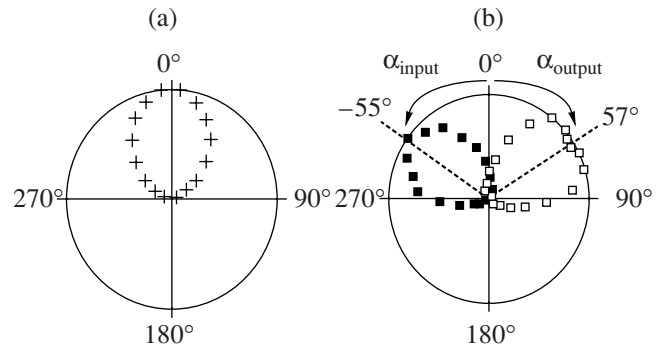


**Fig. 2.** Polar plot of the intensity transmitted as a function of the analyzing polarizer angle, for a 3 bar Argon pressure. For clarity, only half of the pattern is shown, the other half being given by symmetry. (a) Driving pulse (filament) polarization set at  $0^\circ$ . (b) Input (blue,  $\alpha_{\text{input}} = -55^\circ$ ) and output (green,  $\alpha_{\text{output}} = 57^\circ$ ) polarizations of the probe pulse. Co-propagation with the filament flips the probe polarization to an axis symmetrically around the driving pulse polarization. The squared *cosine* patterns are signatures for linearly polarized light [18].

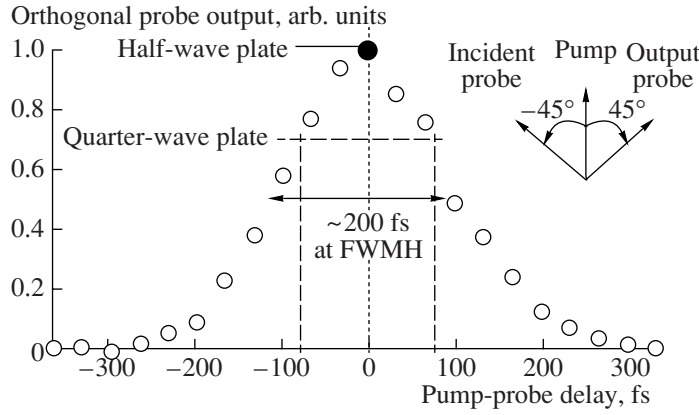


**Fig. 3.** Output probe intensity measured with a polarizer orthogonal to the probe beam input polarization, as a function of the pump-probe delay. Here, a pump polarization at  $45^\circ$  and a 3 bar Argon pressure of 3 bar are considered [21]. Possibility to perform quarter-wave plate for  $\pm 80$  fs delays, as the transmission of the orthogonal probe output is  $\sqrt{2}/2$ .

nal axis, respectively. More precisely, the driving field  $E_x^{\text{filament}}$ , polarized along the  $x$ -axis (therefore implying  $E_y^{\text{filament}} = 0$ ), induces a symmetry breaking in the optical response of the isotropic Argon gas. The nonlinear Kerr polarizations of the probe beam along  $x$  and  $y$  respectively read [22]:

$$P_{\text{XMP}, x}^{\text{probe}} = \frac{3\varepsilon_0}{2} \chi_{xxxx}^{(3)} |E_x^{\text{filament}}|^2 E_x^{\text{probe}}, \quad (1)$$

$$P_{\text{XMP}, y}^{\text{probe}} = \frac{3\varepsilon_0}{2} \chi_{yyxx}^{(3)} |E_x^{\text{filament}}|^2 E_y^{\text{probe}}, \quad (2)$$

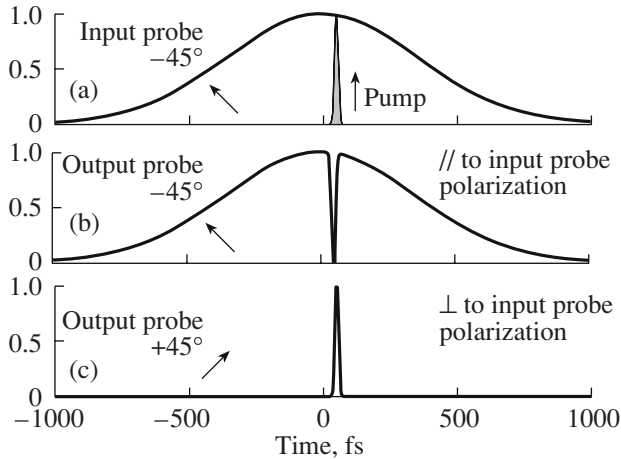


**Fig. 4.** Principle of an ultrafast Kerr-gate based on a filamenting pump beam. (a) Long probe beam and ultrashort pump beam, with linear polarizations at  $45^\circ$  from each other. (b, c) Output probe intensity, respectively parallel and orthogonal to the incident probe polarization [21].

where XPM stands for the probe Cross-Phase Modulation induced by the filamenting pulse, and the nonlinear elements  $\chi_{ijkl}^{(3)} = \chi_{ijkl}^{(3)}(\lambda_{\text{probe}}; \lambda_{\text{probe}}, \lambda_{\text{pump}}, -\lambda_{\text{pump}})$  are related to the considered cross-Kerr process. All the other nonlinear Kerr polarization terms are negligible here, as the ratio of the probe and driving beam energies is  $10^{-3}$ . The dominant contribution to the  $\chi^{(3)}$  tensor in atomic rare gases, like Argon, is governed by the electronic cloud response (i.e., by the atomic nonlinear polarizability). The plasma contribution to  $\chi^{(3)}$  is neglected because of the relatively low concentration of ions with respect to neutral molecules (typically  $10^{-4}$  [23]), and because free electrons only have a significant contribution in the relativistic regime [24]. Since the filament and probe frequencies are far from any resonant transition in the case of Argon, we can consider that  $\chi_{xxxx}^{(3)} = 3\chi_{yyxx}^{(3)}$  [22]. As a consequence, the filament-induced birefringence is:

$$\begin{aligned} \Delta n_{\text{XPM}}^{\text{probe}} &= \frac{1}{2n_0} \left( \frac{3}{2} \text{Re}(\chi_{xxxx}^{(3)} - \chi_{xyxy}^{(3)}) \right) |E_x^{\text{filament}}|^2 \\ &= n_2^{\text{XPM}} I^{\text{filament}} \end{aligned} \quad (3)$$

with

$$n_2^{\text{XPM}} = \text{Re}(\chi_{xxxx}^{(3)}) / (n_0^2 \varepsilon_0 c) = 4n_2/3. \quad (4)$$

Here,  $n_2^{\text{XPM}}$  is the XPM nonlinear refractive index of Argon,  $I^{\text{filament}}$  the intensity within the filament,  $n_0 = 1.0003$  the linear refractive index of Argon at the probe frequency for experimental pressures at room temperature,  $\varepsilon_0$  the vacuum permittivity and  $c$  the speed of light in vacuum,  $n_2$  is the “usual” nonlinear refractive index as defined, e.g., in [2–5]. Integrated over the whole interaction length, this birefringence induces a dephas-

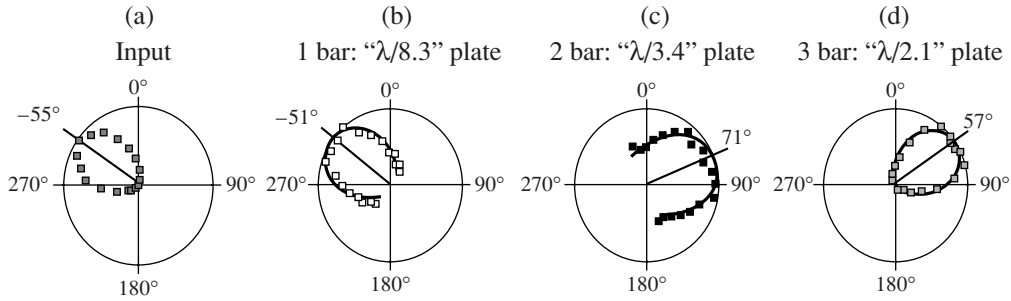


**Fig. 5.** Pressure dependence of the filament-induced birefringence. (a) Input probe polarization; (b–d) Output probe beam polarization for 1, 2, and 3 bar respectively. The black solid lines are fits assuming elliptical polarizations [18].

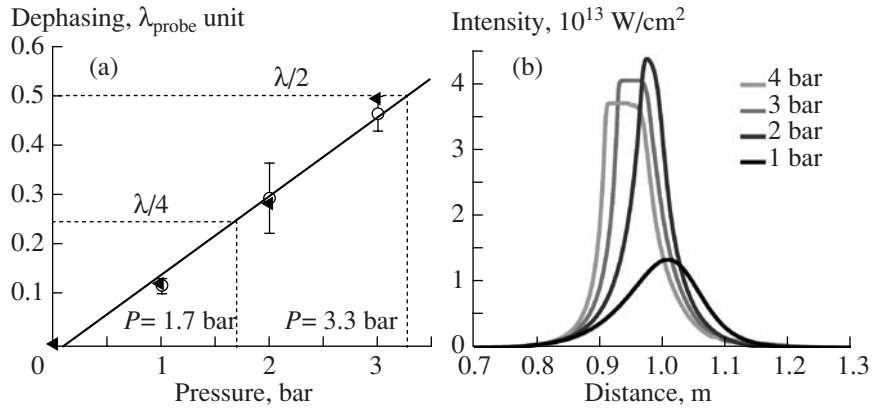


**Fig. 6.** (a) Experimental (circles) and simulated (triangular) pressure dependence of the filament-induced dephasing. (b) Evolution of the intensity at the filament center with the propagation distance, depending on the pressure [18].

ing between the probe beam components along the fast and slow polarization axes of:

$$\begin{aligned} \Delta\phi_{\text{XPM}}^{\text{probe}} &= 2\pi \int \Delta n_{\text{XPM}}^{\text{probe}} dz / \lambda_{\text{probe}} \\ &= 2\pi n_2^{\text{XPM}} \int I^{\text{filament}}(z) dz / \lambda_{\text{probe}}. \end{aligned} \quad (5)$$

## 5. PRESSURE DEPENDENCE OF INDUCED BIREFRINGENCE

The filamented-induced dephasing  $\Delta\phi_{\text{XPM}}^{\text{probe}}$  varies with the nonlinear refractive index  $n_2^{\text{XPM}}$ , and hence, with the Argon pressure in the cell at a fixed temperature at 21°. The measured birefringence at different Argon pressures is presented in Fig. 5. A pressure close to 3 bar (precisely  $3.3 \pm 0.2$  bar) permits to generate an ideal half-wave plate. For lower pressures, an elliptical polarization is observed. A fit of the angular pattern of the output polarization (Figs. 5b–5d) yields a contrast ratio of 67.7% at 1 bar, 39.5% at 2 bar and 98.4% at 3 bar, as well as the orientation of their ellipticity main axis, which amounts to  $\alpha_{\text{output}} = -51^\circ \pm 3^\circ$ ,  $71^\circ \pm 5^\circ$ , and  $57^\circ \pm 2^\circ$ , respectively. This elliptical polarization is the

signature for a smaller dephasing  $\Delta\phi_{\text{XPM}}^{\text{probe}}$ , corresponding to  $\lambda_{\text{probe}}/8.3$  at 1 bar and  $\lambda_{\text{probe}}/3.4$  at 2 bar, respectively, Fig. 5a.

To gain more insight into the pressure dependence, we compared the experimental results with the output of the numerical simulations providing the longitudinal intensity profile at the different pressures, and thus the corresponding birefringence  $\Delta n_{\text{XPM}}^{\text{probe}}$  through Eq. (3). This dephasing depends linearly on the Argon pressure, in excellent agreement with the experimental data (Fig. 6a) for a value of  $n_2^{\text{XPM}}$  proportional to the Argon pressure and equal to  $1.6 \times 10^{-20}$  cm<sup>2</sup>/W at 1 atm. This value lies below that expected from Eq. (4). Such underestimation is due to the fact that the calculations overestimate the pump intensity, because simulations consider that of the beam center while the actual measurement is integrated over 1 mm diameter. Moreover, the temporal walk-off of both pulses due to group-velocity dispersion in Argon is not taken into account in our calculations. Further work is required to provide quantitative transverse and temporal profiles of filament-induced birefringence, and achieve a better quantitative agreement.

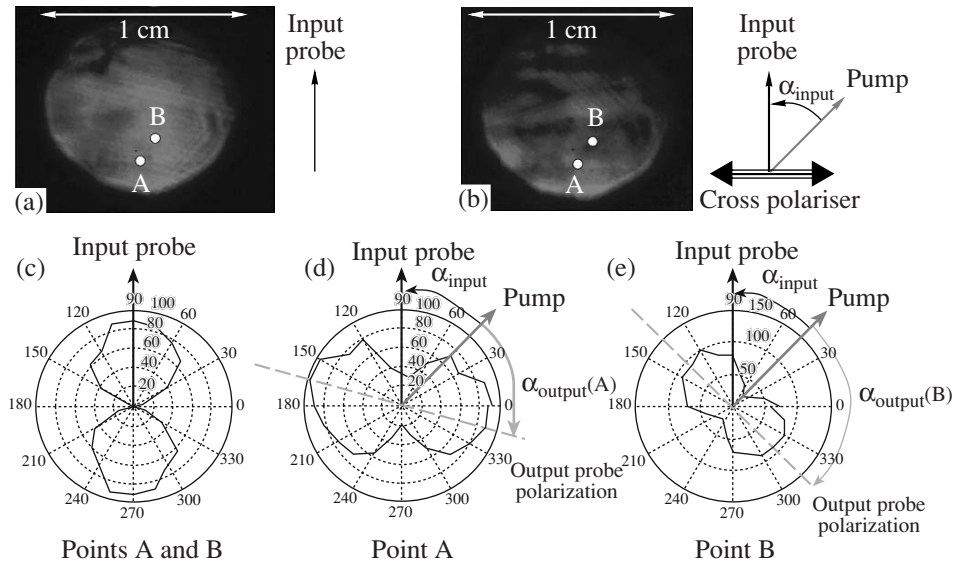


**Fig. 7.** Inhomogeneous distribution of the filament-induced ultrafast birefringence resulting from the profile of the pump intensity. (a) Intensity profile of the homogeneously polarized input probe beam. (c) Both points A and B exhibit the same linear polarization. (b) Output probe beam intensity distribution measured through a polarizer orthogonal to the incident probe polarization ( $\alpha_{\text{input}}(\text{A}) = \alpha_{\text{input}}(\text{B}) = -45^\circ$  with respect to the pump polarization). The inhomogeneous pump intensity profile is transferred to the pump polarization. As a result, the angular polarization distributions at points A and B are different:  $\alpha_{\text{output}}(\text{A}) = +60^\circ$  (d) and  $\alpha_{\text{output}}(\text{B}) = +90^\circ$  (e), respectively [21].

As can be seen on Fig. 6b, our simulations show that higher pressures (i.e., higher  $n_2^{\text{SPM}}$  values) result in longer filaments with lower intensity clamping [24, 25]. These opposite effects roughly compensate each other when calculating the integral  $\int I^{\text{filament}}(z) dz$ , so that the dephasing  $\Delta\phi_{\text{XPM}}^{\text{probe}} = 2\pi n_2^{\text{XPM}} \int I^{\text{filament}}(z) dz / \lambda_{\text{probe}}$  varies like  $n_2^{\text{XPM}}$ , i.e., with a linear dependence with Argon pressure.

As the filament-induced dephasing depends monotonically on pressure, any  $\Delta\phi_{\text{XPM}}^{\text{probe}}$  value may be generated by choosing an adequate Argon pressure. For example, an interpolation of the experimental data presented in Fig. 6 suggests that an equivalent “ $\lambda/4$  plate” can be generated for  $1.7 \pm 0.1$  bar.

## 6. TRANSVERSE DISTRIBUTION OF INDUCED BIREFRINGENCE

The filament-induced dephasing  $\Delta\phi_{\text{XPM}}^{\text{probe}}$  given in Eq. (5) results from the integration of the filament intensity over its whole copropagation with the probe beam. Since the intensity profile of the filamenting beam is far from homogeneous,  $\Delta\phi_{\text{XPM}}^{\text{probe}}$  also exhibits a transverse distribution, which will be transferred onto the probe polarization profile, as displayed in Fig. 7 for a 3 bar Argon pressure. In order to illustrate such mod-

ification of the probe polarization distribution, we selected two distinct points of the probe transverse profile, noted A and B on Fig. 7: while they have the same linear polarization before the interaction with the filament (Fig. 7c), they bear different elliptical polarizations after copropagation (Figs. 7d, 7e). Their contrast ratios are equivalent around 67%, but their main axes have different orientations with respect to the direction of the filamenting pulse polarization ( $\alpha_{\text{output}}(\text{A}) = +60^\circ$  and  $\alpha_{\text{output}}(\text{B}) = +90^\circ$ , respectively, while  $\alpha_{\text{input}}(\text{A}) = \alpha_{\text{input}}(\text{B}) = \alpha_{\text{input}} = -45^\circ$ ). This transverse distribution of the induced birefringence bears valuable information about the transverse intensity distribution in the filament, although this information is integrated over the whole co-propagation distance. Further investigations are to be performed to quantitatively describe the complete filament-induced birefringence pattern distribution.

## 7. CONCLUSIONS

In conclusion, we have demonstrated that laser-generated self-guided filaments can induce significant birefringence in near-atmospheric pressure gases. An angle of  $45^\circ$  between the filament and the probe polarizations allows the realization of Kerr-gates, with an unprecedented switching time ultimately limited by the duration of the filamenting pulse. An optical ultrafast switch could even be initiated remotely by self-guided filaments in the atmosphere [6, 26–28], even in perturbed conditions [29–31], opening new perspectives for

remote optical ultrafast data transmission and processing, e.g., remote ultrafast optical logical gates.

Moreover, we have shown that the transverse probe polarization distribution, which originates from the transverse intensity profile of the filament, is transferred onto the transverse probe beam polarization distribution, as a result of the transverse distribution of the Kerr-induced birefringence. The resulting polarization map can be used as a diagnostics to analyze the filament internal structure and intensity profile.

#### ACKNOWLEDGMENTS

This work was supported by the Swiss NSF (contract 200021-111688 and R'equip program), and the Swiss SER in the framework of COST P18 action C06.0114, as well as the Boninchi and Schmideyn foundations.

#### REFERENCES

1. A. Braun, G. Korn, X. Liu, et al., *Opt. Lett.* **20**, 73 (1995).
2. S. L. Chin, S. A. Hosseini, W. Liu, et al., *Can. J. Phys.* **83**, 863 (2005).
3. L. Bergé, S. Skupin, R. Nuter, et al., *Rep. Prog. Phys.* **70**, 1633 (2007).
4. A. Couairon, and A. Mysyrowicz, *Phys. Rep.* **441**, 47 (2007).
5. J. Kasparian, and J.-P. Wolf, *Opt. Express* **16**, 466 (2008).
6. J. Kasparian, M. Rodriguez, G. Méjean, et al., *Science* **301**, 61 (2003).
7. J. Kasparian, R. Ackermann, Y.-B. André, et al., *Opt Express* **16**, 5757 (2008).
8. C. P. Hauri, W. Komelis, F. W. Helbing, et al., *Appl. Phys. A* **79**, 673 (2004).
9. S. A. Trushin, K. Kosma, W. Fuss, et al., *Opt. Lett.* **32**, 2432 (2007).
10. P. Béjot, J. Kasparian, and J.-P. Wolf, *Opt. Express* **16**, 14115 (2008).
11. S. Petit, A. Talebpour, A. Proulx, et al., *Opt. Commun.* **175**, 323 (2000).
12. G. Fibich and B. Ilan, *Phys. Rev. E* **67**, 036622 (2003).
13. H. Yang, J. Zhang, Q. J. Zhang, et al., *Opt. Lett.* **30**, 534 (2005).
14. M. Kolesik, J. V. Moloney, and E. M. Wright, *Phys. Rev. E* **64**, 046607 (2001).
15. S. Tzortzakis, B. Prade, M. Franco, et al., *Opt Commun.* **181**, 123 (2000).
16. J. P. Geindre, P. Audebert, A. Rousse, et al., *Opt. Lett.* **19**, 1997 (1994).
17. Y. H. Chen, S. Varma, I. Alexeev, et al., *Opt. Express* **15**, 7458 (2007).
18. P. Béjot, Y. Petit, L. Bonacina, et al., *Opt Express* **16**, 14115 (2008).
19. M. Mlejnek, E. M. Wright, and J. V. Moloney, *Phys. Rev. E* **58**, 4903 (1998).
20. P. Béjot, C. Bonnet, V. Boutou, et al., *Opt. Express* **15**, 13295 (2007).
21. Y. Petit, P. Béjot, L. Bonacina, et al., in *Proc. of the 17th Intern. Laser Physics Workshop LPHYS'08, Trondheim, Norway, 30 June–4 July, 2008*.
22. G. P. Agrawal, *Nonlinear Fiber Optics* (Academic, San Diego, 2001).
23. J. Kasparian, R. Sauerbrey, and S. L. Chin, *Appl. Phys. A* **71**, 877 (2000).
24. P. Sprangle, E. Esarey, and B. Hafizi, *Phys. Rev. E* **56**, 5894 (1997).
25. A. Becker, N. Aközbek, K. Vijayalakshmi, et al., *Appl. Phys. A* **73**, 287 (2001).
26. B. La Fontaine, F. Vidal, Z. Jiang, et al., *Phys. Plasmas* **6**, 1615 (1999).
27. M. Rodriguez, R. Bourayou, G. Méjean, et al., *Phys. Rev. E* **69**, 036607 (2004).
28. G. Méchain, A. Couairon, Y.-B. André, et al., *Appl. Phys. A* **79**, 379 (2004).
29. G. Méjean, J. Kasparian, J. Yu, et al., *Phys. Rev. E* **72**, 026611 (2005).
30. G. Méchain, G. Méjean, R. Ackermann, et al., *Appl. Phys. A* **80**, 785–789 (2005).
31. R. Salamé, N. Lascoux, E. Salmon, et al., *Appl. Phys. Lett.* **91**, 171106 (2007).

# Multiple filamentation of non-uniformly focused ultrashort laser pulses

Z.Q. Hao · R. Salamé · N. Lascoux · E. Salmon ·  
P. Maioli · J. Kasparian · J.-P. Wolf

Received: 14 July 2008 / Revised version: 24 October 2008  
© Springer-Verlag 2008

**Abstract** We propose the impingement of non-uniform wavefront curvature as a simple way to improve the longitudinal homogeneity of the plasma density along filaments generated by ultrashort laser pulses. We characterize multiple filamentation of a multiterawatt beam with different wavefront curvatures applied to specific regions in the transverse beam profile. In adequate conditions, the filamenting region is more homogeneously ionized, in the longitudinal direction, than in the case of uniform focusing. Moreover, the ionization maximum is located between the middle and the two thirds of the filaments in all investigated chirps and focus configurations.

**PACS** 42.65.Jx · 42.65.Re · 52.38.Hb

## 1 Introduction

There is great interest in the filamentation of ultra-intense femtosecond laser pulses propagating in the atmosphere [1–5] and its potential applications [5, 6], such as lightning

control [7, 8], pulse self-compression [9, 10], remote laser-induced breakdown spectroscopy (LIBS) [11, 12], or remote sensing [13–15]. Filamentation arises from a dynamic balance between Kerr self-focusing and defocusing by the laser-generated plasma in the propagation medium. When the beam power exceeds the critical power for filamentation ( $P_{cr} \sim 3$  GW in air at 800 nm), multiple filaments are generated at distances up to some kilometers away from the laser source [16] and can propagate over hundreds of meters [17].

Extensive efforts have been dedicated to the control of filamentation, in particular in view of increasing the filamentation length, distance, and the ionization efficiency within them, as is required for most of the above-cited applications. Several parameters have been investigated, including the pulse chirp, expanding and focusing the beam by a telescope [18], the pulse energy [19], beam ellipticity [20] and astigmatism [21], polarization [22], pulse shaping [23] or wavefront control using a deformable mirror [24], a pinhole [25] or a mesh [26]. In this paper, we propose non-uniform focusing of the beam as a simple way to improve the longitudinal homogeneity of long filaments. We show that the filamentation from transverse beam regions with different wavefront curvatures can interact and sustain each other, resulting in adequate conditions in long filaments with a longitudinally more homogeneous ionization than would be obtained with uniform beam focusing.

## 2 Experimental setup

The experiments were conducted with the Teramobile system [18] emitting 300 mJ pulses centered at 800 nm. We investigated positively and negatively chirped pulses, respectively anticompensating and compensating group velocity

---

Z.Q. Hao · R. Salamé · N. Lascoux · E. Salmon · P. Maioli ·  
J. Kasparian  
Université de Lyon, Lyon Cedex 07, France

Z.Q. Hao · R. Salamé · N. Lascoux · E. Salmon · P. Maioli ·  
J. Kasparian  
LASIM UMR 5579, Université Lyon 1, CNRS, bâtiment  
A. Kastler, 43 boulevard du 11 novembre 1918, 69622  
Villeurbanne, France

J. Kasparian (✉) · J.-P. Wolf  
GAP-Biophotonics, University of Geneva, 20 rue de l'École  
de Médecine, Geneva 1211, Switzerland  
e-mail: [jerome.kasparian@unige.ch](mailto:jerome.kasparian@unige.ch)

dispersion (GVD) in air. The typical second-order dispersion terms up to  $k'' = 2 \times 10^4 \text{ fs}^2$  yield durations ranging from 100 to 460 fs. These values, respectively, correspond to 190 to 1000  $P_{\text{cr}}$  for 260–300 mJ energy per pulse. An all-reflective telescope of adjustable focus expanded the beam diameter to 15 cm at  $1/e^2$  and allowed to adjust its focusing before transmitting it horizontally into 130 m of free atmosphere. Two geometries were investigated. In the first one, one side of the beam was focused by a semi-circular lens of focal length  $f_{1/2} = 35 \text{ m}$ . In the second one, the central portion of the beam was focused by a  $f_c = 30$  or  $f_c = 40 \text{ m}$  lens of 5 cm diameter, typically enclosing 20% of the beam energy for an assumed Gaussian profile. The average intensity of the beam region concerned by the central lens was twice that of the beam edge. In both cases, the lens was inserted at the output of the expanding telescope. The other side (respectively, the outer ring) of the beam profile was left unaffected, i.e., it was governed only by diffraction and the focus  $f_T$  of the expanding telescope. Filamentation in each condition was characterized by the cracking noise of the beam on a paper screen [27]. This criterion is representative of the ionization density which is a highly relevant parameter in view of lightning control applications. It is more demanding than, e.g., the observation of bright hot spots in the beam profile, so that the filament lengths given below may appear underestimated as compared with other works [28]. In each condition, the begin and end position of the filamenting region were recorded, as well as the position of the most intense sound emission on the target, which is representative of the highest plasma density.

### 3 Results and discussions

Figure 1 displays, as a reference, the typical extension of the filamenting region generated by the beam of uniform wavefront curvature, with three foci ( $f_T = 30, 40$  and  $150 \text{ m}$ , respectively) of the emitting telescope, and several chirps. As is well known [18], the location of the filamentation onset depends on the initial chirp value through both the compensation of group-velocity dispersion (GVD) and the initial peak power. It is also constrained by the geometrical term arising from the emitting telescope. Stronger focusing results in less chirp dependence because it corresponds to a higher relative contribution of the geometrical term in the Marburger formula [29]. More focused beams also generate a shorter filament bundle. Moreover, the geometrical focus of the emitting telescope defines the location of the highest plasma concentration within a few meters. The almost parallel beam ( $f_T = 150 \text{ m}$ ) generates a longer filamenting region, which is limited by the available propagation field. Therefore, in the following, we mainly focus on the situation where  $f_T = 40 \text{ m}$ , where the effect of non-uniform wavefront curvature is more likely to be significant.

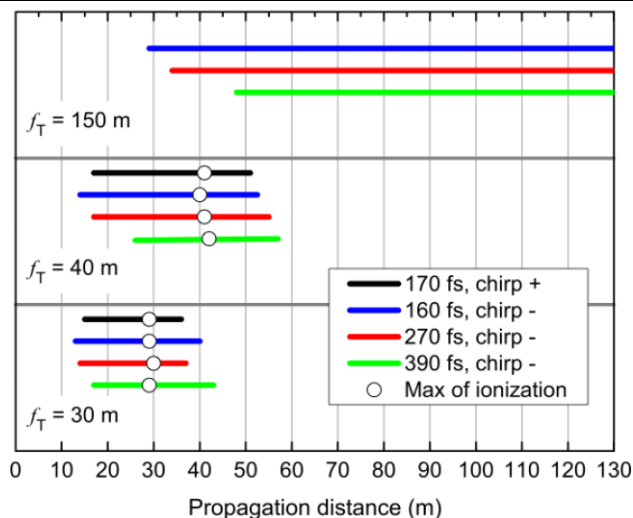


**Fig. 1** Filamentation range and position of strongest ionization of the full beam ( $E = 300 \text{ mJ}$ ) as a function of chirp and initial focusing. Positive and negative chirps, respectively, correspond to the anticompensation and compensation of the group velocity dispersion of air

The effect of focusing ( $f_{1/2} = 35 \text{ m}$ ) one side of the beam superimposed over the uniform focusing by the emitting telescope ( $f_T = 40 \text{ m}$ ), for 260 mJ pulses, is shown in Fig. 2. The observation of the beam profile (see the inset in Fig. 2) in the filamenting region permits to unambiguously assign each filament to a given half of the beam. Surprisingly, the sharp phase jump induced by the edge of the semi-circular lens along the beam diameter does not couple the two beam sides through diffraction, nor generates a line of filament at the border between the two wavefront curvature domains. The side that is only focused by the emitting telescope generates a shorter filament bundle than the whole beam with the same wavefront curvature and energy (260 mJ), as plotted in the upper part of the figure. This reduced length is due to the fact that it only carries half of the total beam energy. The position of the ionization maximum, however, is very little affected, and lies shortly after the middle of the filamenting region. This observation confirms that the location of the highest plasma density is mainly governed by geometrical focusing considerations rather than by self-focusing. The beam side with the supplementary focusing generates an even shorter filament bundle, with a shorter self-focusing distance. Depending on the chirp, these two filamenting regions can overlap, providing a long ionized region. Moreover, since the filament bundle is focused, it converges towards the center of the beam. Therefore, filaments from both beam sides overlap and cannot be distinguished any more, as indicated by the dotted sections in Fig. 2. They can be considered as one single plasma bundle. In particular, the longitudinal and transverse gap between the two bundle sections is small compared to the typical scales of high-voltage discharges to be considered in

**Fig. 2** Effect on the filamenting range and position of the maximum of ionization frequency of a supplementary focusing ( $f_{1/2} = 35$  m) of one half of the beam profile, on top of the focusing by the emitting telescope ( $f_T = 40$  m). Negative chirps correspond to the compensation of the group velocity dispersion of air. The total energy per pulse is 260 mJ. *Inset:* beam profile on a screen at a propagation distance  $z \sim 25$  m

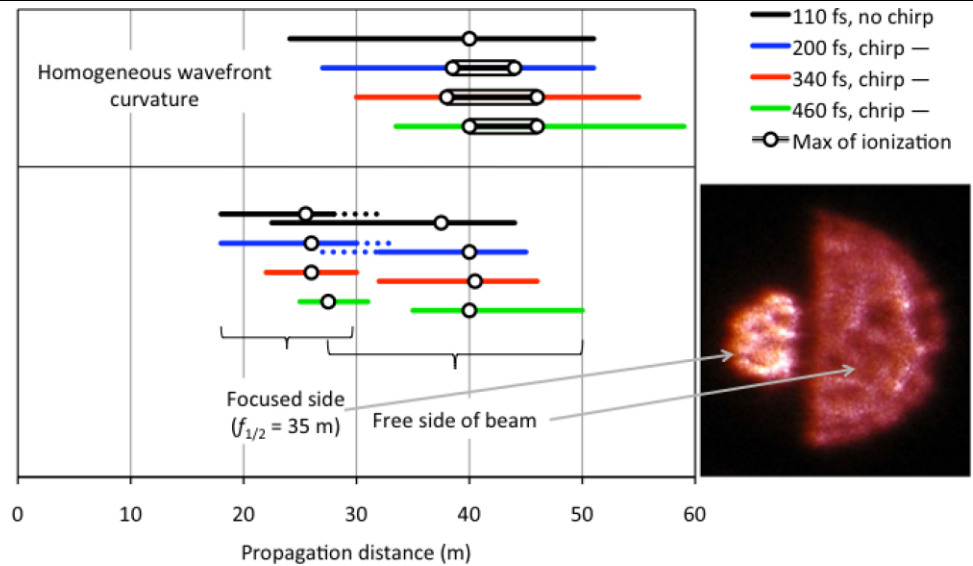
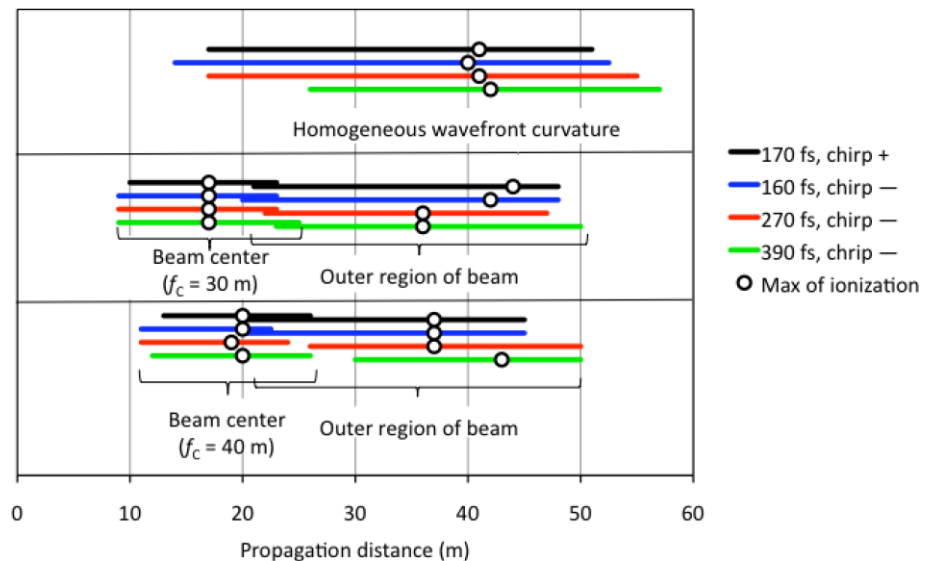


**Fig. 3** Effect on the filamenting range and position of the maximum of ionization frequency of a supplementary focusing ( $f_c = 30$  m and  $f_c = 40$  m) of the center of the beam profile, on top of the focusing by the emitting telescope ( $f_T = 40$  m), for a pulse energy of 300 mJ. Positive and negative chirps, respectively, correspond to the anticompensation and compensation of the group velocity dispersion of air



applications. The longitudinal ionization profile in this filamenting region has two maxima, each being governed by the initial wavefront curvature of one side of the initial beam profile. Such two-maxima structure results in a more homogeneous ionization along the length of the filament bundle, than would be obtained with a single maximum related to a uniform wavefront curvature. Similar results are obtained for a more focused beam ( $f_T = 30$  m) as well as for an almost collimated beam ( $f_T = 150$  m). The strong influence of the non-uniform wavefront curvature applied to the beam contrasts with that of classical astigmatism, which only marginally influences the location of the filamenting region of the beam [21].

Figure 3 displays the effect of central lenses of 5 cm diameter with focal lengths  $f_c = 30$  m and  $f_c = 40$  m placed in the center of an already focused beam ( $f_T = 40$  m) with

300 mJ per pulse. Visual observation of the beam profile on a screen during its propagation confirms that filaments are first initiated in the inner (more focused) region of the beam, and later on the edges of the beam, which is less focused and intrinsically carries less intensity than its center. The locations of the filamentation onset and of the ionization maximum depend very little on the initial pulse chirp. Moreover, the filament bundles respectively generated by the external and inner part of the profile overlap well for all investigated chirps. The overall beam self-focusing and the focused geometry together lead the filament bundle from the beam edge to converge toward the beam center [30]. Its energy reservoir therefore merges with that of the central bundle. The resulting common photon bath re-feeds both central and peripheral filaments. Such process contributes to the

observed improved longitudinal homogeneity of the plasma generated by the filaments over several tens of meters.

The overlap between the filament bundles generated in the inner and outer beam regions critically depend on the ability of the outer region to reach the beam center before the inner filaments vanish. The focal length of the central part of the beam contributes to this matching through (i) the length of the filamenting region in the center of the beam and (ii) the offset that it imposes to the filament onset, as compared with that of the outer region. The wavefront curvature of the outer region and the beam power also contribute to this match since they govern the onset position of the outer filament bundle. This need for interaction of the photon baths of both inner and outer regions of the beam profile explains the difference between the effects of transverse and radial variations of the wavefront curvature. While in the former case the two sides of the beam interact very little, they are geometrically forced to merge after some propagation distance in the concentric configuration. Therefore, the latter is more favorable to generate a long ionized section with higher longitudinal homogeneity.

When the respective wavefront curvatures of the outer ring and the center of the beam are far off (e.g.,  $f_T = 150$  m and  $f_c = 40$  m, not shown), self-focusing of the outer part is not sufficient to focus a significant energy on the beam axis before the end of the strongly focused central filament bundle. Therefore, its power cannot contribute to the photon bath in the beam center. As a result, no extension of the filamenting length is observed.

#### 4 Conclusions

A non-uniform wavefront curvature of ultrashort, ultra-intense laser pulses propagating in air significantly affect the location, length of the generated filament bundles, as well as the longitudinal homogeneity of their plasma density. Adequate laser parameters almost connect the filament bundles, providing a more homogeneous ionization than for a uniformly focused beam. While the precise result depends on the initial focus and chirp of the beam, this improved plasma longitudinal homogeneity is qualitatively observed over a wide range of energy and chirp. It is of high interest for applications requiring long plasma channels, as is the case for lightning control [8]. By applying a different wavefront curvature on different regions of the beam profile, it can also be seen as an easy technique for rough spatial pulse shaping [24, 31], allowing a better use of the energy reservoir [25, 30] of the beam.

**Acknowledgements** The authors acknowledge funding from the Agence Nationale de la Recherche (ANR, grant No. NT05-1\_43175), Fonds National Suisse de la Recherche Scientifique (FNS, grants Nos. 200021-111688/1 and 200021-116198/1), and the Swiss Secrétariat d'État à l'Éducation et à la Recherche in the framework of the COST P18 project "The Physics of Lightning Flash and its Effects".

#### References

1. A. Braun, G. Korn, X. Liu, D. Du, J. Squier, G. Mourou, Self-channeling of high-peak-power femtosecond laser pulses in air. *Opt. Lett.* **20**, 73–75 (1995)
2. S.L. Chin, S.A. Hosseini, W. Liu, Q. Luo, F. Theberge, N. Akozbek, A. Becker, V.P. Kandidov, O.G. Kosareva, H. Schroeder, The propagation of powerful femtosecond laser pulses in optical media: physics, applications, and new challenges. *Can. J. Phys.* **83**, 863–905 (2005)
3. L. Bergé, S. Skupin, R. Nuter, J. Kasparian, J.-P. Wolf, Ultrashort filaments of light in weakly-ionized, optically-transparent media. *Rep. Prog. Phys.* **70**, 1633–1713 (2007)
4. A. Couairon, A. Mysyrowicz, Femtosecond filamentation in transparent media. *Phys. Rep.* **441**, 47–189 (2007)
5. J. Kasparian, J.-P. Wolf, Physics and applications of atmospheric nonlinear optics and filamentation. *Opt. Express* **16**, 466–493 (2008)
6. J. Kasparian, M. Rodriguez, G. Méjean, J. Yu, E. Salmon, H. Wille, R. Bourayou, S. Frey, Y.-B. André, A. Mysyrowicz, R. Sauerbrey, J.-P. Wolf, L. Wöste, White-light filaments for atmospheric analysis. *Science* **301**, 61 (2003)
7. H. Pépin, D. Comtois, F. Vidal, C.Y. Chien, A. Desparois, T.W. Johnston, J.C. Kieffer, B. La Fontaine, F. Martin, F.A.M. Rizk, C. Potvin, P. Couture, H.P. Mercure, A. Bondiou-Clergerie, P. Lalande, I. Gallimberti, Triggering and guiding high-voltage large-scale leader discharges with sub-joule ultrashort laser pulses. *Phys. Plasmas* **8**, 2532–2539 (2001)
8. J. Kasparian, R. Ackermann, Y.-B. André, G. Méchain, G. Méjean, B. Prade, P. Rohwetter, E. Salmon, K. Stelmaszczyk, J. Yu, A. Mysyrowicz, R. Sauerbrey, L. Wöste, J.-P. Wolf, Electric events synchronized with laser filaments in thunderclouds. *Opt. Express* **16**, 5757–5763 (2008)
9. A. Couairon, M. Franco, A. Mysyrowicz, J. Biegert, U. Keller, Pulse self-compression to the single-cycle limit by filamentation in a gas with a pressure gradient. *Opt. Lett.* **30**, 2657 (2005)
10. P. Béjot, J. Kasparian, J.-P. Wolf, Cross-compression of light bullets by two-color co-filamentation. *Phys. Rev. A* **78**, 043804 (2008)
11. K. Stelmaszczyk, P. Rohwetter, G. Méjean, J. Yu, E. Salmon, J. Kasparian, R. Ackermann, J.P. Wolf, L. Wöste, Long-distance remote laser-induced breakdown spectroscopy using filamentation in air. *Appl. Phys. Lett.* **85**, 3977 (2004)
12. J.-F. Daigle, G. Méjean, W. Liu, F. Théberge, H.L. Xu, Y. Kamali, J. Bernhardt, A. Azarm, Q. Sun, P. Mathieu, G. Roy, J.-R. Simard, S.L. Chin, Long range trace detection in aqueous aerosol using remote filament-induced breakdown spectroscopy. *Appl. Phys. B* **87**, 749 (2007)
13. G. Méjean, J. Kasparian, J. Yu, S. Frey, E. Salmon, J.-P. Wolf, Remote detection and identification of biological aerosols using a femtosecond terawatt lidar system. *Appl. Phys. B* **78**, 535–537 (2004)
14. G. Méjean, J. Kasparian, E. Salmon, J. Yu, J.-P. Wolf, R. Bourayou, R. Sauerbrey, M. Rodriguez, L. Wöste, H. Lehmann, B. Stecklum, U. Laux, J. Eislöffel, A. Scholz, A.P. Hatzes, Towards a supercontinuum-based infrared Lidar. *Appl. Phys. B* **77**, 357 (2003)
15. R. Bourayou, G. Méjean, J. Kasparian, M. Rodriguez, E. Salmon, J. Yu, H. Lehmann, B. Stecklum, U. Laux, J. Eislöffel, A. Scholz, A.P. Hatzes, R. Sauerbrey, L. Wöste, J.-P. Wolf, White-light filaments for multiparameter analysis of cloud microphysics. *J. Opt. Soc. Am. B* **22**, 369 (2005)
16. M. Rodriguez, R. Bourayou, G. Méjean, J. Kasparian, J. Yu, E. Salmon, A. Scholz, B. Stecklum, J. Eislöffel, U. Laux, A.P. Hatzes, R. Sauerbrey, L. Wöste, J.-P. Wolf, Kilometer-range nonlinear propagation of femtosecond laser pulses. *Phys. Rev. E* **69**, 036607 (2004)

17. B. La Fontaine, F. Vidal, Z. Jiang, C.Y. Chien, D. Comtois, A. Desparois, T.W. Johnson, J.-C. Kieffer, H. Pépin, Filamentation of ultrashort pulse laser beams resulting from their propagation over long distances in air. *Phys. Plasmas* **6**, 1615–1621 (1999)
18. H. Wille, M. Rodriguez, J. Kasparian, D. Mondelain, J. Yu, A. Mysyrowicz, R. Sauerbrey, J.-P. Wolf, L. Wöste, Teramobile: a mobile femtosecond-terawatt laser and detection system. *Eur. Phys. J. Appl. Phys.* **20**, 183–190 (2002)
19. G. Méchain, C. D'Amico, Y.-B. André, S. Tzortzakis, M. Franco, B. Prade, A. Mysyrowicz, A. Couairon, E. Salmon, R. Sauerbrey, Range of plasma filaments created in air by a multi-terawatt femtosecond laser. *Opt. Commun.* **247**, 171 (2005)
20. A. Dubietis, G. Tamošauskas, G. Fibich, B. Ilan, *Opt. Lett.* **29**, 1126 (2004)
21. S. Eisenmann, E. Louzon, Y. Katzir, T. Palchan, A. Zigler, Y. Sivan, G. Fibich, Multiple filamentation induced by input-beam ellipticity. *Opt. Express* **15**, 2779 (2007)
22. G. Fibich, B. Ilan, Multiple filamentation of circularly polarized beams. *Phys. Rev. Lett.* **89**, 013901 (2002)
23. R. Ackermann, E. Salmon, N. Lascoux, J. Kasparian, P. Rohwetter, K. Stelmaszczyk, S. Li, A. Lindinger, L. Wöste, P. Béjot, L. Bonacina, J.-P. Wolf, Optimal control of filamentation in air. *Appl. Phys. Lett.* **89**, 171117 (2006)
24. Z. Jin, J. Zhang, M.H. Xu, X. Lu, Y.T. Li, Z.H. Wang, Z.Y. Wei, X.H. Yuan, W. Yu, Control of filamentation induced by femtosecond laser pulses propagating in air. *Opt. Express* **13**, 10424 (2005)
25. W. Liu, J.F. Gravel, F. Théberge, A. Becker, S.L. Chin, Background reservoir: its crucial role for long-distance propagation of femtosecond laser pulses in air. *Appl. Phys. B* **80**, 857–860 (2005)
26. H. Schroeder, J. Liu, S.L. Chin, From random to controlled small-scale filamentation in water. *Opt. Express* **12**, 4768 (2004)
27. G. Fibich, S. Eisenmann, B. Ilan, A. Ziegler, Control of multiple filamentation in air. *Opt. Lett.* **29**, 1772 (2004)
28. G. Méchain, A. Couairon, Y.-B. André, C. D'Amico, M. Franco, B. Prade, S. Tzortzakis, A. Mysyrowicz, R. Sauerbrey, Long-range self-channeling of infrared laser pulses in air: A new propagation regime without ionization. *Appl. Phys. B* **79**, 379 (2004)
29. J.H. Marburger, E.L. Dawes, Dynamical formation of a small-scale filament. *Phys. Rev. Lett.* **21**, 556 (1968)
30. S. Skupin, L. Bergé, U. Peschel, F. Lederer, G. Méjean, J. Yu, J. Kasparian, E. Salmon, J.P. Wolf, M. Rodriguez, L. Wöste, R. Bourayou, R. Sauerbrey, Filamentation of femtosecond light pulses in the air: Turbulent cells versus long-range clusters. *Phys. Rev. E* **70**, 046602 (2004)
31. P. Rohwetter, M. Queisser, K. Stelmaszczyk, M. Fechner, L. Wöste, Laser multiple filamentation control in air using a smooth phase mask. *Phys. Rev. A* **77**, 013812 (2008)

# Ultraviolet-visible conical emission by multiple laser filaments

P. Maioli<sup>1,\*</sup>, R. Salamé<sup>1</sup>, N. Lascoux<sup>1</sup>, E. Salmon<sup>1</sup>, P. Bédot<sup>2</sup>, J. Kasparian<sup>1,2</sup>,  
and J.-P. Wolf<sup>2</sup>

<sup>1</sup>Université de Lyon, Université Lyon 1, CNRS, LASIM UMR 5579, bâtiment A. Kastler,  
43 boulevard du 11 novembre 1918, F-69622 Villeurbanne, France

<sup>2</sup>GAP-Biophotonics, University of Geneva, 20 rue de Médecine, Geneva 1211, Switzerland

\*Corresponding author: [paolo.maioli@lasim.univ-lyon1.fr](mailto:paolo.maioli@lasim.univ-lyon1.fr)

**Abstract:** We characterized the angular distribution of the supercontinuum emission from multiple infrared laser filaments propagating in air over long distances, from the infrared (1080 nm) to ultraviolet (225 nm). These experimental data suggest that the X-Waves modeling or Cerenkov emission, rather than phase matching of four-wave mixing, could explain the conical emission. We also estimate the total light conversion efficiency from the original laser wavelength into the white-light continuum.

©2008 Optical Society of America

**OCIS codes:** (190.7110) Ultrafast nonlinear optics; (320.6629) Supercontinuum generation; (190.5940) Self-action effects; (260.5950); Self-focusing

---

## References and links

1. L. Bergé, S. Skupin, R. Nuter, J. Kasparian, and J.-P. Wolf, "Ultrashort filaments of light in weakly ionized, optically transparent media," *Rep. Prog. Phys.* **70**, 1633-1713 (2007).
2. S. L. Chin, S. A. Hosseini, W. Liu, Q. Luo, F. Théberge, N. Aközbek, A. Becker, V. P. Kandidov, O. G. Kosareva, and H. Schroeder, "The propagation of powerful femtosecond laser pulses in optical media: physics, applications, and new challenges," *Can. J. Phys.* **83**, 863-905 (2005).
3. A. Couairon and A. Mysyrowicz, "Femtosecond filamentation in transparent media," *Phys. Rep.* **441**, 47-189 (2007).
4. J. Kasparian and J.-P. Wolf, "Physics and applications of atmospheric nonlinear optics and filamentation," *Opt. Express* **16**, 466-493 (2007).
5. J. Kasparian, M. Rodriguez, G. Méjean, J. Yu, E. Salmon, H. Wille, R. Bourayou, S. Frey, Y.-B. André, M. Franco, B. Prade, A. Mysyrowicz, and R. Sauerbrey, "White-light filaments for atmospheric analysis," *Science* **301**, 61-64 (2003).
6. H. Pépin, D. Comtois, F. Vidal, C. Y. Chien, A. Desparois, T. W. Johnston, J. C. Kieffer, B. La Fontaine, F. Martin, F. A. M. Rizk, C. Potvin, P. Couture, H. P. Mercure, A. Bondiou-Clergerie, P. Lalande, and I. Gallimberti, "Triggering and guiding high-voltage large-scale leader discharges with sub-joule ultrashort laser pulses," *Phys. Plasmas* **8**, 2532-2539 (2001).
7. X. M. Zhao, J.-C. Diels, C. Y. Wang, and M. Elizondo, "Femtosecond ultraviolet laser pulse induced lightning discharges in gases," *IEEE J. Quantum Electron.* **31**, 599-612 (1995).
8. G. Méjean, R. Ackermann, J. Kasparian, E. Salmon, J. Yu, and J.-P. Wolf, "Improved laser triggering and guiding of megavolt discharges with dual fs-ns pulses," *Appl. Phys. Lett.* **88**, 021101 (2006).
9. J. Kasparian, R. Ackermann, Y.-B. André, G. Méchain, G. Méjean, B. Prade, P. Rohwetter, E. Salmon, K. Stelmaszczyk, J. Yu, A. Mysyrowicz, R. Sauerbrey, L. Wöste, and J.-P. Wolf, "Electric events synchronized with laser filaments in thunderclouds," *Opt. Express* **16**, 5757-5763 (2008).
10. R. R. Alfano and S. L. Shapiro, "Observation of Self-Phase Modulation and Small-Scale Filaments in Crystals and Glasses," *Phys. Rev. Lett.* **24**, 592-594 (1970).
11. A. Brodeur and S. L. Chin, "Ultrafast white-light continuum generation and self-focusing in transparent condensed media," *J. Opt. Soc. Am. B* **16**, 637-650 (1999).
12. A. L. Gaeta, "Catastrophic Collapse of Ultrashort Pulses," *Phys. Rev. Lett.* **84**, 3582-3585 (2000).
13. P. Bédot, J. Kasparian, and J.-P. Wolf, "Cross-compression of light bullets by two-color co-filamentation," *Phys. Rev A* **78**, 043804 (2008).
14. C. D'Amico, A. Houard, M. Franco, B. Prade, A. Mysyrowicz, A. Couairon, and V. T. Tikhonchuk, "Conical Forward THz Emission from Femtosecond-Laser-Beam Filamentation in Air," *Phys. Rev. Lett.* **98**, 235002 (2007).

15. H. Xiong, H. Xu, Y. Fu, Y. Cheng, Z. Xu, and S. L. Chin, "Spectral evolution of angularly resolved third-order harmonic generation by infrared femtosecond laser-pulse filamentation in air," *Phys. Rev. A* **77**, 043802 (2008).
16. M. Kolesik, E. M. Wright, A. Becker, and J. V. Moloney, "Simulation of third-harmonic and supercontinuum generation for femtosecond pulses in air," *Appl. Phys. B* **85**, 531-538 (2006).
17. M. Kolesik, E. M. Wright, and J. V. Moloney, "Supercontinuum and third-harmonic generation accompanying optical filamentation as first-order scattering processes," *Opt. Lett.* **32**, 2816-2818 (2007).
18. H. Wille, M. Rodriguez, J. Kasparian, D. Mondelain, J. Yu, A. Mysyriwicz, R. Sauerbrey, J.-P. Wolf, and L. Wöste, "Teramobile: A mobile femtosecond-terawatt laser and detection system," *Eur. Phys. J. Appl. Phys.* **20**, 183-190 (2002).
19. G. Méjean, J. Kasparian, J. Yu, E. Salmon, S. Frey, J.-P. Wolf, S. Skupin, A. Vinçotte, R. Nuter, S. Champeaux, and L. Bergé, "Multifilamentation transmission through fog," *Phys. Rev. E* **72**, 026611 (2005).
20. E. T. J. Nibbering, P. F. Curley, G. Grillon, B. S. Prade, M. A. Franco, F. Salin, and A. Mysyrowicz, "Conical emission from self-guided femtosecond pulses in air," *Opt. Lett.* **21**, 62-64 (1996).
21. O. G. Kosareva, V. P. Kandidov, A. Brodeur, and S. L. Chin, "Conical emission from laser plasma interactions in the filamentation of powerful ultrashort laser pulses in air," *Opt. Lett.* **22**, 1332-1334 (1997).
22. I. Golub, "Optical characteristics of supercontinuum generation," *Opt. Lett.* **15**, 305-307 (1990).
23. Q. Xing, K. M. Yoo, and R. R. Alfano, "Conical emission by four-photon parametric generation by using femtosecond laser pulses," *Appl. Opt.* **32**, 2087-2089 (1993).
24. G. G. Luther, A. C. Newell, J. V. Moloney, and E. M. Wright, "Short-pulse conical emission and spectral broadening in normally dispersive media," *Opt. Lett.* **19**, 789-791 (1994).
25. M. Kolesik, E. M. Wright, and J. V. Moloney, "Dynamic Nonlinear X Waves for Femtosecond Pulse Propagation in Water," *Phys. Rev. Lett.* **92**, 253901 (2004).
26. D. Faccio, M. Porras, A. Dubietis, F. Bragheri, A. Couairon, and P. Di Trapani, "Conical Emission, Pulse Splitting, and X-Wave Parametric Amplification in Nonlinear Dynamics of Ultrashort Light Pulses," *Phys. Rev. Lett.* **96**, 193901 (2006).
27. D. Faccio, A. Averchi, A. Lotti, P. Di Trapani, A. Couairon, D. Papazoglou, and S. Tzortzakis, "Ultrashort laser pulse filamentation from spontaneous XWave formation in air," *Opt. Express* **16**, 1565-1570 (2008).
28. G. Méjean, J. Kasparian, J. Yu, S. Frey, E. Salmon, J.-P. Wolf, L. Bergé, and S. Skupin, "UV-Supercontinuum generated by femtosecond pulse filamentation in air: Meter-range experiments versus numerical simulations," *Appl. Phys. B* **82**, 341-345 (2006).
29. L. Bergé, S. Skupin, G. Méjean, J. Kasparian, J. Yu, S. Frey, E. Salmon, and J.-P. Wolf, "Supercontinuum emission and enhanced self-guiding of infrared femtosecond filaments sustained by third-harmonic generation in air," *Phys. Rev. E* **71**, 016602 (2005).
30. M. Rodriguez, R. Bourayou, G. Méjean, J. Kasparian, J. Yu, E. Salmon, A. Scholz, B. Stecklum, J. Eislöffel, U. Laux, A. P. Hatzes, R. Sauerbrey, L. Wöste, and J.-P. Wolf, "Kilometer-range nonlinear propagation of femtosecond laser pulses," *Phys. Rev. E* **69**, 036607 (2004).
31. S. Skupin, L. Bergé, U. Peschel, F. Lederer, G. Méjean, J. Yu, J. Kasparian, E. Salmon, J.-P. Wolf, M. Rodriguez, L. Wöste, R. Bourayou, and R. Sauerbrey, "Filamentation of femtosecond light pulses in the air: Turbulent cells versus long-range clusters," *Phys. Rev. E* **70**, 046602 (2004).
32. E.R. Peck and K. Reeder, "Dispersion of Air," *J. Opt. Soc. Am.* **62**, 958-962 (1972).
33. D. Faccio, A. Averchi, A. Couairon, M. Kolesik, J. V. Moloney, A. Dubietis, G. Tamosauskas, P. Polesana, A. Piskarskas, and P. Di Trapani, "Spatio-temporal reshaping and X Wave dynamics in optical filaments," *Opt. Express* **15**, 13077-13095 (2007).
34. D. Faccio, A. Lotti, M. Kolesik, J. V. Moloney, S. Tzortzakis, A. Couairon, and P. Di Trapani, "Spontaneous emergence of pulses with constant carrier-envelope phase in femtosecond filamentation," *Opt. Express* **16**, 11103-11114 (2008).
35. M. Aldener, S. S. Brown, H. Stark, J. S. Daniel, and A. R. Ravishankara, "Near-IR absorption of water vapor: Pressure dependence of line strengths and an upper limit for continuum absorption," *J. Mol. Spectrosc.* **232**, 223-230 (2005).
36. S. Roy, T. R. Meyer, and J. R. Gord, "Broadband coherent anti-Stokes Raman scattering spectroscopy of nitrogen using a picosecond modeless dye laser," *Opt. Lett.* **30**, 3222-3224 (2005).
37. F. Théberge, M. Châteauneuf, V. Ross, P. Mathieu, and J. Dubois, "Ultrabroadband conical emission generated from the ultraviolet up to the far-infrared during the optical filamentation in air," *Opt. Lett.* **33**, 2515-2517 (2008).

---

## 1. Introduction

Propagation of high energy femtosecond laser beams in the atmosphere has drawn a considerable attention both for the study of fundamental characteristics of filaments [1-4] and for the development of many applications like atmospheric remote sensing [5] or triggering and guiding of electric discharges in the prospect of lightning control [6-9]. Femtosecond intense laser pulses can propagate in the atmosphere over several Rayleigh lengths as self-

guided filaments. The basic mechanism of self-guiding consists of a dynamic balance between the nonlinear Kerr effect in air, which self-focuses the beam until ionization of oxygen molecules by multiphoton absorption, and the defocusing effect of plasma, which prevents optical collapse and sustains long-distance propagation. Besides this basic image, many nonlinear physical processes accompany filamentation, e.g. spectral broadening by self-phase modulation [10, 11], self-compression [12, 13], generation of THz radiation [14] or third-harmonic generation [15-17]. Moreover, when the pulse power largely exceeds the critical power ( $P_{crit} \sim 3$  GW in air at 800 nm), multiple filamentation occurs [18], with a number of filaments proportional to the power [19].

A visually spectacular effect associated with filamentation is conical emission [20, 21]. It generates a wealth of coloured rings around the beam in the forward direction, whose peak wavelength decreases from infrared to ultraviolet with increasing distance from the propagation axis. The mechanism at the root of conical emission is still debated. It may imply Cerenkov radiation [20, 22], self-phase modulation (SPM) [21], four-wave mixing (FWM) [23, 24] or X-Waves modelling [25-27]. The first experimental measurements of conical emission in air have been performed in the 500-700 nm range [20, 21]. More recently, Méjean *et al.* estimated a divergence of the UV conical emission, although this estimation was based on indirect observation [28, 29]. In addition, the first high-resolution angle-wavelength spectrum of air filaments and the link with X-Waves was recently introduced [27].

In this Letter, we extend the measurement of conical emission to the ultraviolet, down to 225 nm. Moreover, we show that conical emission is not modified by multiple filamentation, as had been suggested based on indirect observations [30].

## 2. Experimental setup

Figure 1 shows the experimental setup. Intense femtosecond pulses at  $\lambda_o = 800$  nm (FWHM 23 nm) were generated by the Teramobile facility [18] whose laser system consists of a Ti:Sa oscillator followed by a chirped pulse amplification (CPA) chain. The compressed pulses, of 100 fs pulse duration at a 10 Hz repetition rate, had energies of 305 mJ. The corresponding peak power is 3 TW, *i.e.* 1000  $P_{crit}$ , which yields a few tens of filaments. The amplified femtosecond beam, with an initial diameter of 15 cm, was focused by a sending telescope ( $f = +42$  m), leading to a filamentation onset at  $z_{f1} = 30$  m and a filamentation length of 22 m until  $z_{f2} = 52$  m. Downstream of the filaments, at  $z = 82.5$  m, 86 m and 106 m respectively, we measured the forward-emitted spectrum as a function of the transverse distance from the beam center, hence of the emission angle  $\theta$  over  $\pm 8$  mrad. At each angle, the spectrum was recorded between 225 and 1080 nm with 0.4 nm resolution by a computer-interfaced spectrometer (OceanOptics HR2000+), whose input optical fiber was oriented toward the incoming laser source and swept across the beam profile.

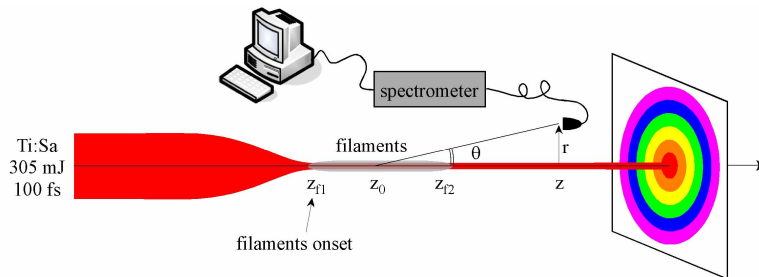


Fig. 1. Experimental setup. A fiber collector is swept across the beam downstream of the filamenting region and the collected conical emission is analyzed on a spectrometer.

To correctly record the spectra in spite of their high dynamics (8 orders of magnitude), we employed different neutral filters with high optical density (up to OD 4.0) and varied the integration time from 1 s to 65 s (10 to 650 laser shots). For most of the positions, we acquired

at least two spectra: one with higher optical density and shorter integration time, to avoid saturation when measuring the intense 800 nm peak, and another with lower densities and longer integration times, for resolving very weak conical emission features at remote wavelengths. Data were smoothed by running averages over 10 adjacent points, *i.e.* over 4 nm.

### 3. Results and discussion

The data recorded at distances  $z = 82.5$  m, 86 m and 106 m yield consistent angles if considering that the origin of the conical emission lies at  $z_0 = 44.5$  m, which lies equally spaced between  $z_{f1}$  and  $z_{f2}$ , *i.e.* in the middle of the filamenting region. This suggests that conical emission is generated all along the filamenting region, a picture consistent with the dynamical replenishment model, in which relatively short filaments are generated randomly all along the filamenting region [31] and independently emit conical emission.

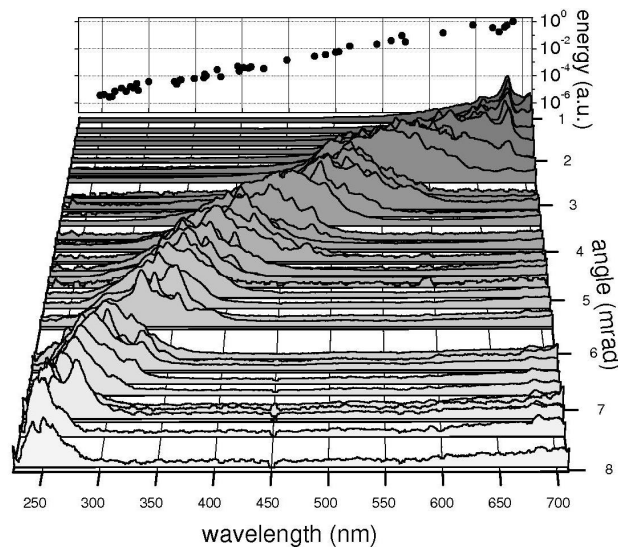


Fig. 2. Main graph: Normalized light intensity spectra as a function of angle  $\theta$  with respect to the axis of propagation. The spectral dependence of conical emission angle is clearly visible (see also Fig. 3). Back panel: integrated energy of the conical emission as a function of wavelength.

Figure 2 displays the forward-emitted spectra over the 225-710 nm region as a function of  $\theta$ . Each spectrum is independently normalized to unity. The energy of the conical emission peak is also displayed as a function of wavelength on the rear panel of Fig. 2. It is obtained by integrating the intensity of the un-normalized spectra over the wavelength as well as spatially over the ring (*i.e.*, over  $2\pi$  on the azimuthal angle). The peak of conical emission shifts from 250 nm up to the fundamental wavelength, and broadens from 20 to 140 nm (FWHM inferred from Lorentzian fits) for decreasing values of  $\theta$ . Note that no conical emission was observed in the infrared between 800 and 1080 nm.

Figure 3 displays the wavelength dependence of the conical emission, as extracted from Fig. 2. Our data agree well with previous ones obtained in the case of single filamentation by Nibbering *et al.* [20] and Kosareva *et al.* [21] between 500 and 700 nm. In particular, the conical emission angle decreases regularly with increasing wavelength. Note that our measurements are a convolution of the emission angles from individual filaments and of the divergence of the filament bundle. Due to the overall beam refocusing near the focus [30], this divergence is smaller than initial geometrical beam divergence of 1.8 mrad (half angle), but could not be quantitatively determined in our experiment. This error shall be below  $\Delta\theta = 1$  mrad, in line with observations over longer distances [30]. Hence, our data show that

the indirect measurements of Méjean *et al.* [28, 29] underestimated the conical emission angles, especially in the 300 - 450 nm range, by approximately 2 mrad. The origin of this underestimation could lie in an improper modelling of their Lidar geometrical compression.

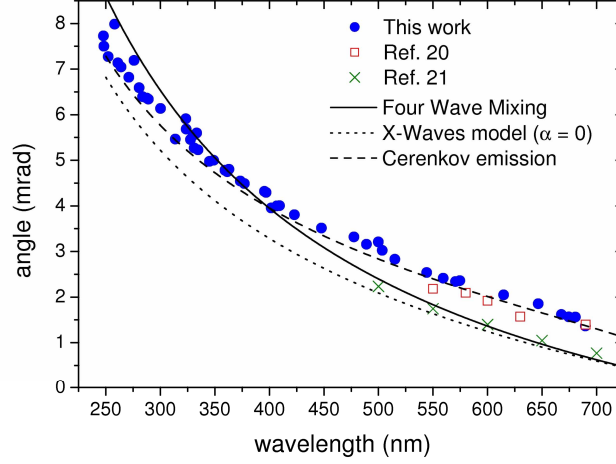


Fig. 3. Conical emission angle versus central wavelength.

We compared our data with the respective angular dispersion of conical emission predicted by FWM [24], X-Waves stationary solutions [27] and by the Cerenkov emission interpretation [20]. In the case of FWM, phase matching imposes the following angular dispersion of conical emission:

$$\theta = \sqrt{k_0''/k_0} \Omega, \quad (1)$$

where  $k(\omega) = n(\omega)\omega/c$  ( $\omega = 2\pi c/\lambda$  being the frequency and  $n(\omega)$  the refractive index of air, given by [32]),  $\Omega = \omega - \omega_0$  is the difference between the generated frequency and the input pump frequency and  $k_0'' = \partial^2 k(\omega)/\partial \omega^2|_{\omega_0}$  [24]. On the other hand, according to the X-Waves solution theory [27], the angle  $\theta$  is given by:

$$\theta = \sqrt{1 - \left( \frac{k_0 + \Omega/v_g}{k(\omega)} \right)^2} \approx 1 - \frac{1}{2k(\omega)^2} \left( k_0 + \frac{\Omega}{v_g} \right)^2, \quad (2)$$

where  $v_g = 1/(k_0' - \alpha)$  is the filament group velocity and  $\alpha$  is a free fit parameter which accounts for the input conditions [33], which we set to zero in our curve. This is equivalent to considering  $v_g = 1/k_0' \equiv v_c$ , where  $v_c$  is the laser pulse group velocity at the carrier frequency.

In the case of Cerenkov emission [20], the same dispersion relation writes:

$$\cos(\theta) = \frac{1}{k(\omega)} \left( k_0 + \frac{n_0}{c} \Omega \right). \quad (3)$$

Note that by introducing the series expansion  $\cos(\theta) = (1 - \theta^2 + \dots)^{1/2}$  in Eq. (3) we obtain the same approximate expression as in Eq. (2) for the particular case  $v_g = c/n_0 \equiv v_\phi$ . In other words, the Cerenkov relation can be considered as a sub-case of the more general X-Waves relation when the filament group velocity  $v_g$  equals the carrier frequency phase velocity  $v_\phi$ . While the three models fit the previous data adequately, our extension of the data to the UV partially lifts the ambiguity. Our data show that the measured CE spectra are well reproduced by using the Cerenkov expression, *i.e.* by putting  $v_g = v_\phi$  in the X Waves relation [34]. On the other hand, the FWM predicts a slope significantly different from that of the experimental

data, especially under 450 nm. Our measurements therefore suggest that the latter process alone is not sufficient to fit data. In addition, when points are shifted downward to correct for the beam divergence ( $\Delta\theta \leq 1$  mrad), X-Waves dispersion relation of Eq. (2) always fits the data precisely by using a value of  $\alpha$  ranging from 0 to  $2 \cdot 10^{-14}$  s/m.

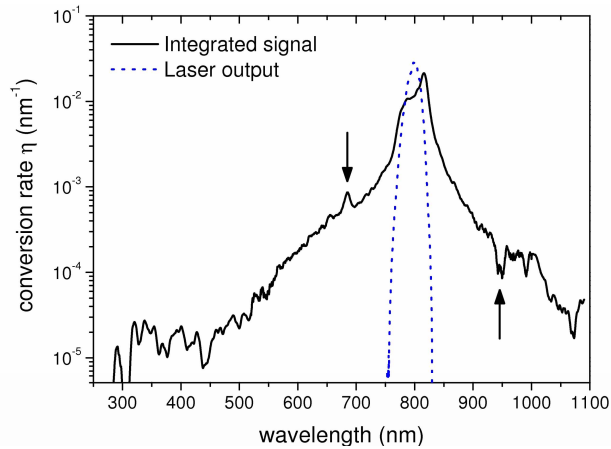


Fig. 4. Conversion efficiency from the fundamental wavelength into white light. Arrows point coherent anti-Stokes Raman scattering (CARS) emission and water vapor absorption.

By integrating the intensity spectra over the full  $\theta$  angle distribution *i.e.* from  $-8$  to  $8$  mrad, and normalizing by the total beam energy, we calculated for the first time the absolute conversion efficiency from the fundamental wavelength of the incident laser into the white-light continuum. Fig. 4 displays the conversion efficiency rate per spectral unit,  $\eta(\lambda)$ , expressed in  $\text{nm}^{-1}$ , which describes the amount of the incident energy at  $800$  nm which is converted into an infinitesimal wavelength range centered at  $\lambda$  (resolution  $4$  nm). The spectrum after propagation is centered at  $806$  nm, slightly red-shifted as compared with the incident carrier wavelength at  $800$  nm. In addition, it features both the water vapor absorption line at  $940$  nm ( $3\nu$  polyad vibrational states of  $\text{H}_2\text{O}$ ) [35] and the coherent anti-Stokes Raman scattering (CARS) emission of  $\text{N}_2$  at  $678$  nm, corresponding to a Raman shift of  $2329$   $\text{cm}^{-1}$  from the  $806$  nm central wavelength [36]. The observation of these spectral features illustrates the capability of the supercontinuum to provide a suitable light source for both absorption and Raman spectroscopy in the atmosphere.

#### 4. Conclusion

As a conclusion, we have characterized the conical emission from multiple filamentation down to  $225$  nm in the ultraviolet. The data prolong well the previously existing ones, while we observed no conical emission between  $800$  and  $1080$  nm. Our data exclude the phase-matching of FWM as the only mechanism driving conical emission in the UV, and favor X-Waves modeling and Cerenkov emission. They are also useful for applications which require a good characterization of the emission geometry, such as white-light Lidar.

#### Acknowledgments

The authors acknowledge funding from the Agence Nationale de la Recherche (ANR, grant # NT05-1\_43175), Fonds national suisse de la recherche scientifique (FNS, grants #200021-111688/1 and 200021-116198/1), and the Swiss Secrétariat d'État à l'Éducation et à la Recherche in the framework of the COST P18 project "The physics of Lightning Flash and its Effects".

Note: after acceptance of this paper, we became aware of complementary measurements of conical emission in the infrared up to  $14$   $\mu\text{m}$  [37].

intriguing possibility. Mutations in the tumor suppressor gene *VHL* that are associated with qualitatively different tumor predispositions (pheochromocytoma versus clear cell renal carcinoma) appear to be associated with quantitative differences in impairment of HIF regulation (10–12). Conceivably, matching of cellular context to a relatively precise, quantitatively restricted, level of HIF activation (that is the consequence of an IDH1 Arg<sup>132</sup> mutation) is necessary for glioblastoma multiforme predisposition. If true, then alteration of such a balance, through metabolic interventions that target  $\alpha$ -KG, might offer a therapeutic or preventive strategy.

Finally, although Zhao *et al.* provide an explanation for dominant mutational inactivation of IDH1, they do not completely explain why the pathogenic effects are restricted to Arg<sup>132</sup>. Other arginine residues (Arg<sup>100</sup> and Arg<sup>109</sup> in human IDH1) are implicated in isocitrate binding (13), and in recom-

binant porcine IDH1, mutations at all these sites are inactivating (14). Perhaps the proposed disruption of subunit cooperation is restricted to Arg<sup>132</sup> mutations, or Arg<sup>132</sup> mutations in some way favor the heterodimerization that is required for dominant inactivation. Alternatively, Arg<sup>132</sup> mutations might have some quantitatively specific effect on enzyme inhibition that is necessary for oncogenic predisposition.

On the other hand, could there be a primary genetic explanation? Mutational predisposition at CG dinucleotides can explain the common Arg<sup>132</sup>  $\rightarrow$  His substitution but not all of the other mutations. Moreover, Yan *et al.* recently sequenced the homologous exon of the *IDH2* gene in tumors that did not contain an *IDH1* mutation, and found nine mutations at the equivalent Arg<sup>172</sup>, a residue that is encoded by a codon not containing the CG dinucleotide (3). This mutation was shown to be inactivating, although neither

dominant inactivation nor effects on HIF were tested. Further studies to test this and other (non-disease-associated) mutations in the model proposed by Zhao and colleagues should be of great interest.

#### References

1. D. W. Parsons *et al.*, *Science* **321**, 1807 (2008).
2. S. Zhao *et al.*, *Science* **324**, 261 (2009).
3. H. Yan *et al.*, *N. Engl. J. Med.* **360**, 765 (2009).
4. F. E. Bleeker *et al.*, *Hum. Mutat.* **30**, 7 (2009).
5. J. Balsas *et al.*, *Acta Neuropathol.* **116**, 597 (2008).
6. C. B. Thompson, *N. Engl. J. Med.* **360**, 813 (2009).
7. E. Gottlieb, I. P. Tomlinson, *Nat. Rev. Cancer* **5**, 857 (2005).
8. C. Loenarz, C. J. Schofield, *Nat. Chem. Biol.* **4**, 152 (2008).
9. Y. Shi, J. R. Whetstone, *Mol. Cell* **25**, 1 (2007).
10. W. G. Kaelin Jr., *Nat. Rev. Cancer* **8**, 865 (2008).
11. L. Li *et al.*, *Mol. Cell. Biol.* **27**, 5381 (2007).
12. K. Knauth, C. Bex, P. Jemth, A. Buchberger, *Oncogene* **25**, 370 (2006).
13. X. Xu *et al.*, *J. Biol. Chem.* **279**, 33946 (2004).
14. S. Soundar, B. L. Danek, R. F. Colman, *J. Biol. Chem.* **275**, 5606 (2000).

10.1126/science.1173362

## APPLIED PHYSICS

# Laser Beams Take a Curve

Jérôme Kasparian and Jean-Pierre Wolf

The properties usually associated with laser beams are illustrated by laser pointers, which are monochromatic (red or green), coherent (they create speckle patterns), and directional (the beam travels in a straight line). However, the advent of laser sources that emit ultrashort laser pulses has changed this simple picture: These sources are broadband and may maintain coherence for very short times—just for one or a few cycles of the electric field. These sources are so intense that, when traveling through a medium such as air, they can ionize atoms and create plasmas. On page 229 of this issue, Polynkin *et al.* (1) exploit linear optical effects of laser beams with complex profiles, as well as nonlinear effects that arise at high intensities, to create laser beams that can form plasma channels whose paths curve as they propagate.

Laser beams with complex profiles (that have multiple maxima and minima and are not a single peak) can curve in part because energy can flow between components within these beams. Polynkin *et al.* use a beam profile based on the Airy function, which has its own history in optics—it was introduced in

the study of rainbows. A two-dimensional (2D) Airy beam (2, 3) (see the figure, panel A) can be prepared by inserting an active element such as a matrix of liquid crystals oriented so as to tailor the distribution of phase in the plane perpendicular to the beam. This Airy profile is asymmetrical and its intensity is strongly localized in a main peak on one side of the beam profile.

As the beam propagates, interferences between the phases in different locations in the beam profile impose a curved trajectory to the main peak in the Airy profile. This interference effect is linear—it depends neither on the beam intensity nor on interactions with the propagation medium. Viewed head on, the pulse would appear to swing from the left and back to the right. However, the beam's center of mass still propagates on a straight line (the red line in panel A) because the energy fraction contained in the long trail on the other side of the beam balances the main Airy peak.

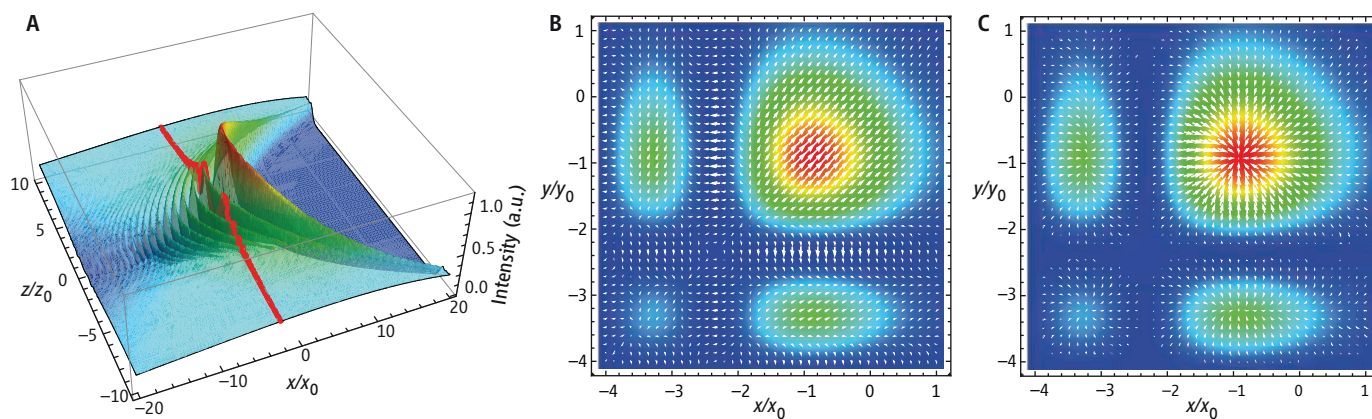
A further remarkable property of the Airy beam is that it is “self-healing”: If part of the beam hits an opaque object, energy flows from the rest of the beam profile and reconstructs the original asymmetric pattern (4). A similar self-healing effect occurs in high-intensity laser beams that form self-guided

Complex energy flows within laser beams can cause them to curve as they travel.

plasma channels, also called filaments (5–8). A dynamic balance develops between the nonlinear optical Kerr effect, which changes the refractive index of its propagation medium to create a virtual converging lens, and diffraction by the self-generated plasma, which creates long plasma channels. If a laser filament impinges on a particle, the scattered light is released into the periphery of the profile, where it contributes to the optical Kerr effect, thereby reconstructing the filament shortly after the interaction (9). This self-healing capability may allow high-intensity laser beams to access remote locations and to be transmitted through clouds and turbulence, opening the way to atmospheric applications (8, 10).

Polynkin *et al.* combined the complex profile of an Airy beam with nonlinear optical effects to create plasma channels that can turn and follow the shape (or “caustic”) shown in panel A of the figure; the plasma forms only in the high-intensity region of the main peak. A key issue is whether the natural (linear) energy flow (see the figure, panel B) that displaces the transverse beam will dominate the nonlinearly induced energy flow from the optical Kerr effect, which attracts energy toward the plasma filament (see the figure, panel C) and feeds it during its propagation.

GAP-Biophotonics, University of Geneva, 20, rue de l'École de Médecine, 1211 Geneva 4, Switzerland. E-mail: jerome.kasparian@unige.ch; jean-pierre.wolf@unige.ch



**Laser beams taking turns.** (A) A laser pulse with an Airy profile propagates in the  $z$  direction (normalized units). The main peak emerges from an initially broad profile, accelerates toward the exterior of the beam while progressively growing up to  $z = 0$ , and then loses intensity until it is absorbed in a resurgent broad maximum. The red line is the straight trajectory of the beam's center of gravity. (B and C) Energy flows in the curving beams of Polynkin *et al.* (B) Linear and (C) nonlinear (Kerr effect) energy flow (white arrows) across the beam profile. The

same normalized color scale as in (A) is used to illustrate a 2D Airy beam (damping coefficient  $\alpha = 0.1$ ;  $z = 0$ ). While the linear Airy flow pushes the main peak of the profile toward the top-right corner of the graph, independently from the incident intensity, the Kerr effect tends to attract the energy toward this main peak, with an efficiency proportional to the local intensity. The competition between the two processes causes deformations of the plasma channels generated in Airy beams at high intensity.

At moderate intensities, the transverse energy flux is dominated by the Airy regime, but at higher intensities, the Kerr contribution establishes an attractor at the beam's main peak, and tends to let the beam move straight rather than follow the Airy caustic. However, the curved plasma channels observed by Polynkin *et al.*—both in their experiments and in the numerical integration of the nonlinear Schrödinger equation—show that such a regime is not reached in the filaments in gases, where the intensity ranges from  $10^{13}$  to  $10^{14}$  W/cm<sup>2</sup> (11).

Thus, the Airy regime will dominate in most realistic experimental conditions in air. In particular, the observed curved plasma channel compares well to the electron density that would be generated by the intensity of a linearly propagating Airy beam. This density can be estimated as the eighth power of the intensity profile, which takes into account the ionization of oxygen driven by multiple absorption of photons (11). However, the longitudinal asymmetry of the curved plasma channel and the bifurcations observed both experimentally and numerically by Polynkin *et al.* show that the Kerr effect cannot be fully neglected at this intensity level.

Because the trajectory of the curved plasma channels roughly follow that of the Airy beam, their length and curvature suffer from the same limitations related to the intensity drop of the main peak along its propagation path. The maximum achievable deviation from a straight path scales linearly with the initial beam size  $w_0$ , but the propagation distance required to reach a given deviation scales with  $w_0^2$ . Sending a macro-

scopic Airy beam around a corner thus appears difficult. For example, an Airy beam with a main peak of  $w_0 = 1$ -cm width and an optimal value of the confinement factor  $a$  (in this case, 0.05) would need to propagate more than 2.8 km before reaching its maximum deviation of only 24 cm.

Nevertheless, Airy beams carrying high intensities provide a wealth of attractive applications at smaller geometrical scales. Self-bent beams could be used to manufacture curved waveguides in transparent bulk media, in a way similar to permanent optical waveguides inscription in fused silica using filaments (6). The ability of controlling curvature would allow for the realization of complex guiding structures in three dimensions, with applications such as wavelength division multiplexers, beam splitters, and couplers. A beam main peak of  $\sim 10$   $\mu\text{m}$  could be deviated by  $\sim 25$  times its size, meaning that it would have moved off a straight trajectory by 250  $\mu\text{m}$  after less than 3-mm propagation.

A further striking advantage of Airy-driven curved propagation, compared to Kerr-driven propagation, is its applicability in vacuum. A curved beam in vacuum, especially at high intensity, could open new ways of achieving long interaction lengths with particle beams, acceleration of protons and electrons on controlled trajectories, or efficient coupling with beams of x-rays or gamma-rays.

The use of Airy beams in the context of high-power pulses and self-channeling further builds on a recent trend to apply specific beam shapes, such as X-waves (12), Bessel beams (13), or axially or radially

polarized beams (14), to exploit their remarkable properties already developed in the linear regime. Depending on the specific beam shape considered, such properties may include nondiffractiveness, self-healing, transverse acceleration, or the generation of a zero electric field at the beam center. When these methods are used with higher-power sources, nonlinear effects such as self-guiding further extend their scope for applications. Examples include tailoring the spectrum of the “white light” generated in the filaments for atmospheric remote sensing, or using filaments and their associated plasma to divert lightning strikes from sensitive targets, such as airports and industrial plants (15).

#### References and Notes

1. P. Polynkin, M. Kolesik, J. V. Moloney, G. A. Siviloglou, D. N. Christodoulides, *Science*, **324**, 229 (2009).
2. M. V. Berry, N. L. Balazs, *Am. J. Phys.* **47**, 264 (1979).
3. I. M. Besieris, A. M. Shaarawi, *Opt. Lett.* **32**, 2447 (2007).
4. J. Broky, G. A. Siviloglou, A. Dogariu, D. N. Christodoulides, *Opt. Express* **16**, 12880 (2008).
5. S. L. Chin *et al.*, *Can. J. Phys.* **83**, 863 (2005).
6. A. Couairon, A. Mysyrowicz, *Phys. Rep.* **441**, 47 (2007).
7. L. Bergé, S. Skupin, R. Nuter, J. Kasparian, J. P. Wolf, *Rep. Prog. Phys.* **70**, 1633 (2007).
8. J. Kasparian, J.-P. Wolf, *Opt. Express* **16**, 466 (2008).
9. F. Courvoisier *et al.*, *Appl. Phys. Lett.* **83**, 213 (2003).
10. J. Kasparian *et al.*, *Science* **301**, 61 (2003).
11. J. Kasparian, R. Sauerbrey, S. L. Chin, *Appl. Phys. B* **71**, 877 (2000).
12. D. Faccio *et al.*, *Phys. Rev. Lett.* **96**, 193901 (2006).
13. P. Polesana, M. Franco, A. Couairon, D. Faccio, P. Di Trapani, *Phys. Rev. A* **77**, 043814 (2008).
14. R. Martínez-Herrero, P. M. Mejias, S. Bosch, *Opt. Commun.* **281**, 3046 (2008).
15. J. Kasparian *et al.*, *Opt. Express* **16**, 5757 (2008).
16. This work was supported by the Swiss NSF, contract 200021-116198/1.

10.1126/science.1172244

# Lightning control by lasers

Powerful lightning strikes pose a significant threat to buildings and people, but imagine if it were possible to control and direct them with a laser beam. *Nature Photonics* spoke to Jérôme Kasparian, a researcher from the University of Geneva and co-ordinator of the Teramobile project, about the idea.

The idea of firing an intense laser beam into a thundercloud to induce lightning and guide it back to a preferred location on the ground may sound far-fetched, but such a practice could one day be commonplace for protecting important buildings such as power plants or airports. In recent years, European scientists working on the Teramobile project (see Box 1) have demonstrated that intense, ultrashort laser pulses can ionize the air to create a virtual conductive path for guiding an electrical discharge along a straight line of several metres in a laboratory. The next stage is to build a laser 10 times as powerful, 'Teramobile 2', which, it is hoped, will allow a similar effect high in the sky. *Nature Photonics* spoke to Jérôme Kasparian about progress so far.

## ■ How did the idea for using lasers for controlling lightning come to mind?

This idea of triggering lightning using lasers is almost as old as the laser itself. Before long there were laser powers sufficient to ionize the air, and early on people realized that this

would create a conducting path for electrical charge which could assist the triggering of lightning.

The first attempts took place as early as the 1970s in Russia and Japan, using huge CO<sub>2</sub> lasers, strongly focused, which generated a plasma spark but were not very successful. The problem was that the plasma was very localized and strongly absorbed the laser energy, thus preventing further propagation and the creation of a long ionization channel. There were a lot of laboratory experiments; in addition a Japanese team tried an experiment in the atmosphere in real conditions with three huge lasers focused near the top of a lightning tower. However, this was a huge system and not very effective.

## ■ What helped the idea to become more realistic?

What has happened between the early studies and now is the advent of CPA [chirped pulsed amplification] lasers, which allow the creation of ultrashort and high-power pulses beyond the terawatt level. They

allow a self-guiding propagation regime known as filamentation. In this regime there is a dynamic balance between the nonlinear Kerr effect (self-focusing) and the effect of free electrons, which have a negative contribution on the refractive index and tend to defocus the beam. This gives a balance between the self-focusing and defocusing of the beam, resulting in self-guiding. With a sub-joule laser it is possible to make filaments tens or even hundreds of metres long with an electron density of 10<sup>15</sup> or even 10<sup>16</sup> electrons per cubic centimetre. Today, there are several groups working on similar ideas using different configurations, including the group of Pépin and Mercure in Quebec, the group of Diels at the University of New Mexico, and our Teramobile group, which is a European collaboration. Everyone is working on the idea of having a long ionized channel that can trigger and guide discharges. Several groups have been doing small-scale experiments over a few centimetres or few tens of centimetres, and then there have been very impressive experiments by the group in Quebec. We have also done some experiments in the lab using real filaments over a few metres at a few megavolts, as well as conducting field trials.

## ■ My understanding is that the principle of using lasers for lightning control has been well demonstrated in the lab, but what about field trials?

It is not really straightforward going from the lab to the field. A big issue is with the lifetime of the plasma you generate. It is limited to the microsecond range. The discharge establishes at a speed of typically a few metres per microsecond, which means that after the discharge has propagated a few metres the track has disappeared. As a consequence, the pulse duration limits the effective length of the channel. We took our laser and went to the Langmuir Laboratory of New Mexico Tech, which is a permanent station for lightning studies. The visual observation did not give any results because we were at pretty high altitude at 3,000 metres and in the clouds at that time, and the camera could not see anything, but we could use the lightning



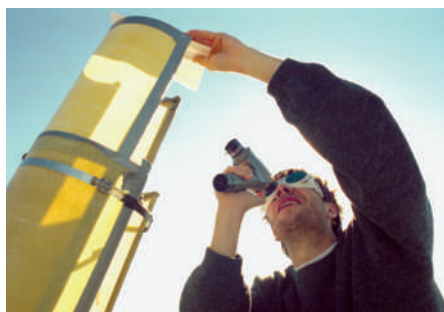
© ISTOCKPHOTO.COM/AIPHOTO

In the future, intense lasers may be able to provide control of electrical activity inside thunderclouds. Experiments in the laboratory and field trials have shown in principle that this is feasible, but more powerful lasers are needed to actually trigger and guide lightning.

mapping array of Langmuir Laboratory, a network of radiofrequency detectors. Any discharge radiates a broad spectrum of radiofrequency radiation which can be detected. There were thirteen detectors spread over the region and we used the five closest to our lasers. These detectors detect precisely the time of arrival of each laser pulse and by triangulation you can reconstruct the three-dimensional position of each event. You have to remember that this detection technique detects not only the lightning strike but all of the electric activity in the cloud. What we did was to correlate the electric activity with the position of the laser beam and the time when the laser was pulsed with a precise repetition rate of 10 times per second. We were able to correlate an excess of electrical activity with the location and time of the laser pulses. These events correlated with the laser are quite faint events; they are not actually lightning strikes.

#### ■ So what's next?

The main limitation to overcome is the limited lifetime of the plasma channel. We need to get an effective channel length of a few tens of metres to trigger the lightning. This length scale has been confirmed by experiments using rockets with conductive wire tails of various lengths. Such a short channel would also be better for us because we don't want to have the channel come all the way down to the laser from the point of view of the damage to the equipment or us — we are sitting underneath in the laser control room. To create plasma channels



Jérôme Kasparian, leader of the Teramobile team, adjusts the beam path of the Teramobile laser.

with a length of a few tens of metres, we need a more powerful laser. We are working on Teramobile 2, which will be a 10 times more powerful laser. However, it is not only a matter of brute force; we are also trying to be cleverer and not just shoot 10 times more power but organize this power in a train of 10 pulses, sharing the full power of the laser. The idea is that the first pulse would better establish the channel and the subsequent ones would maintain it. The burst mode will be something very innovative, as will a mobile laser providing 30 TW pulses. We will benefit from the fact that CPA technology has improved a lot in the past 10 years, so we can simply get more power from the current CPA technology. The technology is evolving towards smaller systems, especially with diode-pumped lasers. Most of the size of the systems is due to the pump lasers. From the energy point of view it is pretty

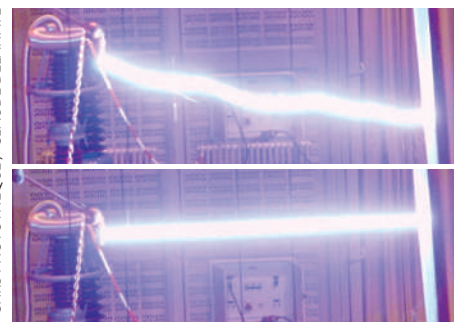


Image of a high-voltage electrical discharge, that is, artificial lightning, over a distance of 3 m with (straight path) and without (erratic path) the assistance of a guiding laser filament.

inefficient. Eventually, I guess that there will be directly diode-pumped femtosecond systems. You can really imagine that in a few years the laser technology will allow us to have such a mobile terawatt laser in a van. It is hard to say exactly when Teramobile 2 will be ready, but I guess it is a matter of a few years.

#### ■ How could you ensure that the discharge doesn't come directly back to the laser itself?

In fact this is not a big problem because you can control the distance from which the conducting channel begins. If you insert a grounded conductor in the laser path before it gets back to the laser, the discharge will go to this component. There are two variants. One is to use a grounded metallic mirror to reflect the beam and the discharge will go to the ground through the mirror; or you aim with the laser via the top of a classical lightning rod so that the discharge will go to the rod instead of following the conducting beam.

#### ■ What are the benefits of using lasers for controlling lightning over schemes such as using rockets with conducting tail wires?

The rockets work pretty well — every second shot can be effective. However, you have a limited number of rockets and you cannot easily aim at the place in the clouds that you want to activate. With a laser, you can aim it and work it continuously so it would provide much more flexibility. Although a laser scheme might be too expensive for individual homes, for critical facilities such as power plants or airports it could be used to direct a laser strike away to a preferred location. Of course this is in the longer term.

INTERVIEW BY OLIVER GRAYDON

### Box 1 | The Teramobile project

The Teramobile laser project was launched in 1999 and became operational in 2001. It is a very powerful mobile terawatt-class Ti:sapphire laser which uses chirped pulse amplification to generate intense ultrashort pulses (see specifications below) for atmospheric studies. The laser comprises a Ti:sapphire oscillator and a Nd:YAG pumped Ti:sapphire amplification chain made of a regenerative amplifier and two four-pass amplifiers. It concentrates the state-of-the-art laser technology in a 20-foot standard freight container, allowing field measurement campaigns. It is an international project initiated jointly by a French–German collaboration of CNRS (France) and DFG (Germany). Switzerland has now joined the consortium. It is now funded by ANR and the Swiss FNS and involves five research institutes in Berlin, Dresden,

Lyon, Palaiseau and Geneva. The laser system itself was built by Thales Laser of France. The Teramobile laser is used for investigating nonlinear propagation of femtosecond-terawatt laser pulses over long distances in the atmosphere, and their applications to atmospheric research. This includes Lidar remote sensing of atmospheric pollutants as well as lightning protection and triggering by a mobile terawatt laser system.

#### Teramobile specifications

Centre wavelength: 800 nm  
Pulse energy: 350 mJ  
Peak power: 5 TW  
Pulse duration: 70 fs to 2 ps  
Repetition rate: 10 Hz  
Output beam diameter: 50 mm  
Size: 3.5 m × 2.2 m  
Weight: 10 tonnes

## White-light symmetrization by the interaction of multifilamenting beams

K. Stelmaszczyk,<sup>1</sup> P. Rohwetter,<sup>1</sup> Y. Petit,<sup>2</sup> M. Fechner,<sup>1</sup> J. Kasparian,<sup>2,\*</sup> J.-P. Wolf,<sup>2</sup> and L. Wöste<sup>1</sup>

<sup>1</sup>*Institut für Experimentalphysik, Freie Universität Berlin, Arnimallee 14, D14195 Berlin, Germany*

<sup>2</sup>*GAP-Biophotonics, Université de Genève, 20 rue de l'École de Médecine, 1211 Geneva 4, Switzerland*

(Received 8 April 2009; published 29 May 2009)

We show experimentally that the interaction of two multifilamenting beams in fused silica with incidence angles up to a few degrees results in an increase in the symmetry of the continuum emission from  $D_2$  to  $C_\infty$  around the axis of symmetry between the two beams. We observe an intense white disk between the locations of the individual conical emission patterns, reducing the conical emission in each of them. We attribute this behavior to an enhanced self-phase modulation in the interference region between the two beams. This frequency conversion depletes by more than 40% the energy initially available in the photon bath to feed filaments.

DOI: 10.1103/PhysRevA.79.053856

PACS number(s): 42.65.Jx, 42.65.Tg, 42.65.Ky

### I. INTRODUCTION

Nonlinearity is known as capable to increase the symmetry of physical systems. This is, e.g., the case in the self-similar optical collapse, in which any incident beam profile submitted to Kerr self-focusing self-converts into a circular Townes profile [1].

Self-focusing can ultimately result in filamentation, which is due to a dynamic balance between the Kerr self-focusing and defocusing on the plasma generated at the nonlinear focus [2–6]. When the incident beam power largely exceeds the critical power  $P_{cr}$  of the propagation material ( $P_{cr} \approx 2.3$  MW in fused silica at 800 nm [7]), the beam profile breaks up into many cells, each one yielding one single filament. These filaments generated across the beam profile were shown to be coherent with one another, which allows them to interact. These interactions can take the form of repulsion or attraction of neighboring filaments [8–12] or interference of their conical emission [13]. Moreover, the interaction of the two incident laser photon baths can also lead to the attraction or repulsion of the resulting filaments of each individual beam, depending on their relative phase [14,15]. Adequate tuning of the relative incidence angle even allows the filaments from the two beams to merge into a central one [11], or to exchange energy, resulting in a partial extinction of the conical emission [16].

In this paper, we investigate the interaction of two multifilamenting beams in fused silica with incident angles up to a few degrees. We show that this interaction results in an increase in symmetry of the continuum emission from  $D_2$  to  $C_\infty$  around the axis of symmetry between the two beams. An intense white disk is observed between the locations of the individual conical emission patterns, reducing or even almost suppressing the conical emission in each of them. We attribute this behavior to an enhanced self-phase modulation (SPM) in the interaction region, where the interference between the two beams redistributes the local wave vectors into a broad angular distribution. Frequency conversion depletes the energy initially available in the photon bath to feed fila-

ments, similarly to the competition already observed in the case of a single beam [17].

The observed on-axis generation of the white light, while a significant fraction of the fundamental still propagates a few degrees apart, could be useful for spectroscopic applications to geometrically select the supercontinuum emission and reject this undeviated fraction of the fundamental wavelength.

### II. EXPERIMENTAL SETUP

The experimental setup is depicted in Fig. 1. A femtosecond chirped-pulse amplification laser operating at  $\lambda_0 = 800$  nm wavelength generates a train of pulses at a repetition rate of 10 Hz. The energy of each individual pulse is 20 mJ with a duration of 130 fs. The laser beam is divided in two parts by a thin 50:50% beam splitter. The most intense central part from each beam is selected by circular apertures of 2 mm diameter, letting, respectively, 1.2 and 1.3 mJ of energies to pass through. The beams then interact inside a 20-mm-thick fused silica block. The optimal temporal overlap is adjusted by translating a bending mirror in one arm. Visual observation as well as true-color imaging from the top of the fused silica block showed the occurrence of multiple filamentation when the two beam propagate independently as well as when they overlap temporally.

The interaction between the beams was investigated at four incidence angles  $2\theta'_0 = 3.0^\circ, 3.2^\circ, 3.8^\circ,$  and  $4.5^\circ$  (full angles) in air, corresponding to  $2\theta_0 = 2.1^\circ, 2.2^\circ, 2.6^\circ,$  and  $3.1^\circ$  in the fused silica block, respectively. The far-field pat-

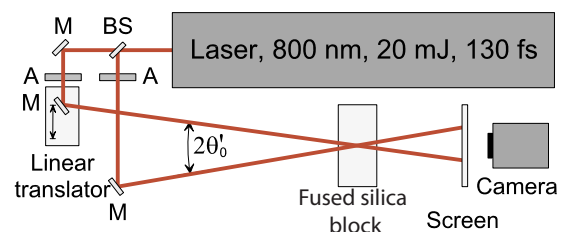


FIG. 1. (Color online) Experimental setup: BS: beam splitter, A: circular aperture, and M: mirror.

\*jerome.kasparian@unige.ch

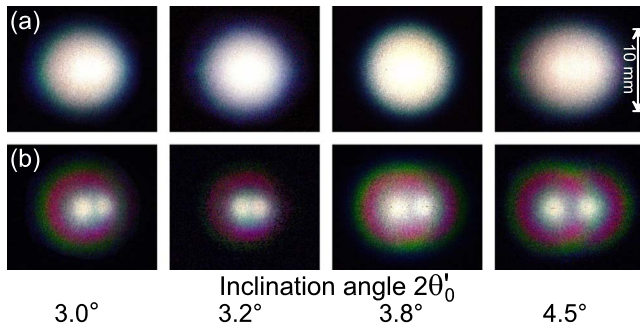


FIG. 2. (Color online) Far-field beam image on a screen at a distance of 40 mm from the fused silica block as a function of the angle between the incident beams (a) with and (b) without temporal overlap between the pulses.

tern of the white-light emission was recorded with a color-frame digital camera, on a diffusing screen placed 40 mm behind the substrate. Besides, the spectrum of the emitted continuum was analyzed using a miniature spectrometer, with 0.34 nm resolution. In order to record the full dynamics of the spectrum, which spans over more than 4 orders of magnitude, different neutral density filters were used for different spectral ranges, which were then cross normalized to reconstruct the full spectra. The emitted light was collected by a Teflon integrating sphere. The angular distribution of the white-light spectrum was recorded by horizontally translating the sphere across the plane defined by the two incident beams, at a distance of 275 mm from the fused silica block. In this configuration, the 5 mm input port of the integrating sphere provided an angular resolution of  $1^\circ$ .

### III. EXPERIMENTAL RESULTS

Figure 2 displays such far-field image. Without interaction, each beam propagates independently and yields a small ( $\approx 3\text{--}4$  nm) white spot with the corresponding conical emission [see also Figs. 3(a) and 3(c)]. In contrast, the interaction of the two pulses yields remarkably strong white light and a much broader ( $\sim 10$  nm) circular spot encompassing the positions of both beams [Fig. 3(b)]. In addition, the conical emission disappears. The white color of the spot as well as its size and shape are very similar for all investigated inci-

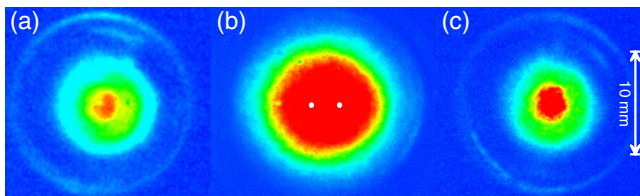


FIG. 3. (Color online) Intensity distribution of the white-light generation at 436 nm, for an incidence angle of  $2\theta'_0 = 3.5^\circ$ . (a) Non-interacting left beam, (b) two interacting beams, and (c) noninteracting right beam. The intensity scale is normalized independently for each of the image. Reduction in conical emission is clearly visible for interacting beams (b), where the two white dots indicate the positions of individual beams respective to the white-light spot.

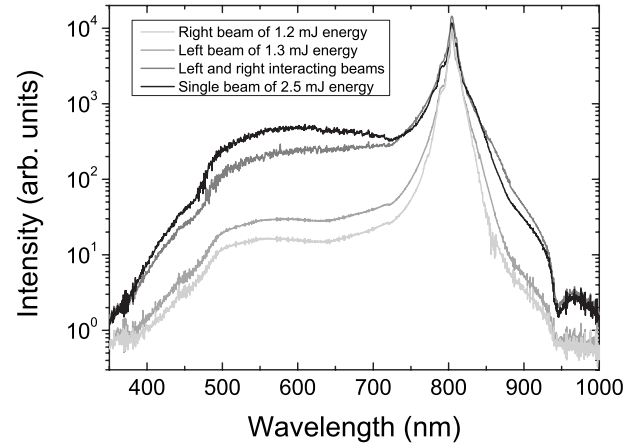


FIG. 4. Influence of the two-beam interaction on the white-light spectrum. The spectra are assembled from several spectrum sections recorded with different optical density filters and normalized to each other.

dence angles. At larger incidences the efficiency of the white-light emission is noticeably lower and the transition from a circular to elliptical spot profile is observed. This tendency is already visible in Fig. 2(a) for  $2\theta'_0 = 4.5^\circ$ .

The generation of a bright white spot qualitatively observed on the screen, as mentioned above, indeed corresponds to a tenfold increase in the supercontinuum generation in the 450–700 nm region, as well as around 900 nm, as compared with the individually propagating beams (Fig. 4). This spectral broadening is practically independent from the incidence angle over the whole investigated interval of incidence angles. The two interacting beams generate white-light continuum almost as efficiently as one single beam that would bear their whole energy, depleting the fundamental wavelength by more than 40%.

Both with and without interactions between the beams, the angular distribution of the white-light spectrum (Fig. 5) is dominated by the peak at the fundamental wavelength around  $\pm 1.6^\circ$ , i.e., at the original location of each incident beam. However, the interaction results in a reduction in the fundamental emission at  $0^\circ$  and a transversely more homogeneous spectrum, between  $-3^\circ$  and  $+3^\circ$ . This homogeneity corresponds to the visual observation of an homogeneous white spot on a screen in the far field. Also, the conical emission [dotted line on panel (a)] disappears almost completely when the two beams overlap temporally.

### IV. DISCUSSION

The observed generation of a white-light disk in the forward direction may at once remind us of the interaction [14,15] or even the merging [11] of the filaments from two crossing beams. However, such merging occurs at very small incident angles, typically 20–30 times smaller than in our experiment [11]. Moreover, we observed neither evidence of filament merging into new filaments oriented along the  $z$  axis on photographs taken from the top of the fused silica block nor conical emission, i.e., concentric colorful rings coaxial with the forward-emitted white light. We therefore conclude

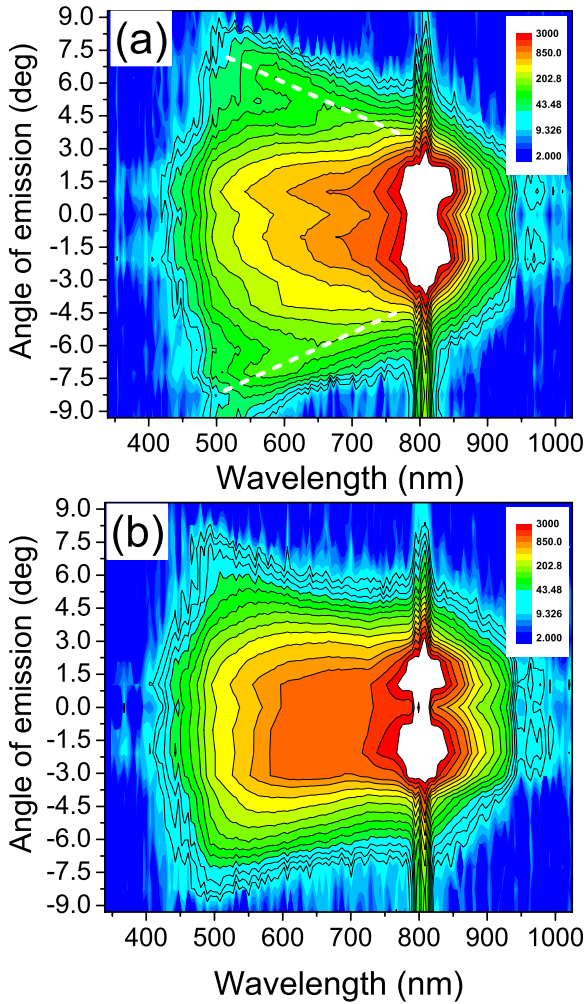


FIG. 5. (Color online) Angular distribution of the white-light spectrum for (a) noninteracting and (b) interacting beams with an incident angle of  $2\theta'_0=3.2^\circ$  ( $2\theta_0=2.2^\circ$ ). Both graphs share the same logarithmic scale in intensity. Note that the interaction results in (i) a strong reduction in the conical emission [dotted lines in panel (a)], (ii) the generation of an homogeneous spectrum between  $-1.5^\circ$  and  $1.5^\circ$ , as shown by the wide flat region of panel (b), and (iii) a reduced fundamental intensity at  $0^\circ$ , as shown by a narrowing of the white (saturated) region of panel (b).

that the process at play does not specifically depend on the occurrence of filamentation.

Instead, we interpret our observations based on a partial inhibition of filamentation due to a more efficient white-light continuum generation in the photon bath where the two beams interact through SPM and cross-phase modulation (XPM). The observed efficient depletion of the fundamental wavelength by the white-light generation reduces its power available to feed the filaments. This results in a less efficient filamentation and hence in a sharp decrease in the brightness of the associated conical emission at the exit of the fused silica block.

In the interaction region, the interference between the two beams redistributes the directions of the wave vectors, thus losing the initial  $D_2$  symmetry defined by the two incident beams. Instead, the wide range of wave-vector directions re-

sults in a revolution ( $C_\infty$ ) symmetry around the  $z$  axis, independently of the incidence angle. Moreover, due to the relatively large incidence angle, no interference pattern can be resolved in the far field. This is consistent with the report by Corsi *et al.*, who reported such interference with a narrower incidence angle and observed that the white-light fringes tend to merge when the angle increases above  $0.5^\circ$  [18].

The interference between the two beams does not only impact the spatial symmetry of the supercontinuum emission, but also its intensity, locally doubling the incident electric field, i.e., quadrupling the incident intensity. Note that the transient grating [19] originating from the interference pattern has a typical step of  $\lambda_0/2 \sin(\theta_0) \sim 15 \mu\text{m} \gg \lambda_0$ , yielding a typical width of  $2\theta_0 \sim 3^\circ$  for the zero-order spot, so that no fringes are visible within the spot on the screen. On the other hand, illuminating a glass block with a cylindrical lens also resulted in a similar circular spot, although the incident angles  $\theta_0$  continuously range from  $-5^\circ$  to  $5^\circ$ , thus blurring any interference pattern. We can therefore exclude diffraction on this interference pattern as the origin of the observed circular white spot.

The above discussion in terms of SPM can easily be transposed in terms of four-wave mixing (FWM), since both formalisms and SPM provide equivalent descriptions of the same physical processes if the wavelengths are quasidegenerate and the main active process is the conversion of the central wavelength into the supercontinuum. In a first step, we shall address the change in symmetry from  $D_2$  to  $C_\infty$ . In FWM, two photons at  $\lambda_1$  and  $\lambda_2$  mix up to generate two photons at  $\lambda_3$  and  $\lambda_4$ . In this process, the energy conservation imposes  $\omega_1 + \omega_2 = \omega_3 + \omega_4$  ( $\omega_i$  being the frequency associated with  $\lambda_i$ ), while the phase matching condition sets  $\vec{k}_1 + \vec{k}_2 = \vec{k}_3 + \vec{k}_4$ , where  $k_i = 2\pi n_i / \lambda_i$ . As a consequence the plane defined by  $\vec{k}_3$  and  $\vec{k}_4$  can spin around  $\vec{k}_1 + \vec{k}_2$ , adding one degree of freedom to the system. If the wavelengths of the incident photons lie within the spectral peak of the incident fundamental pulse,  $k_1 \sim k_2 \sim k_0$ , the direction of  $\vec{k}_1 + \vec{k}_2$  is close to the  $z$  axis. This degree of freedom is characterized by the angle  $\phi_3$  between the planes, respectively, defined by  $(\vec{k}_1, \vec{k}_2)$  and  $(\vec{k}_3, \vec{k}_4)$  and results in a circular ( $C_\infty$ ) symmetry of the emission.

However, such circular symmetry in a process driven by phase matching would at first be expected to generate colored rings rather than a white circular spot. Such spot can be understood if we consider quasidegenerate FWM events, i.e., with all  $\lambda_i$  close to  $\lambda_0$ . Such events have a very high occurrence probability due to an efficient pumping and seeding by the fundamental wavelength itself and intrinsic phase matching. However, their net impact on the pulse spectrum is negligible because many events of opposite directions statistically compensate each other. As a consequence, quasidegenerate FWM events are not considered in usual conditions. In our configuration with crossing beams, however, spectrally quasidegenerate events must be considered because they result in the emission of photons within the incident fundamental spectral peak, but in directions outside those of the initial beams so that it yields a net geometrical effect. More specifically, the output photons at wavelengths  $\lambda_3$  and  $\lambda_4$  are emitted at angles

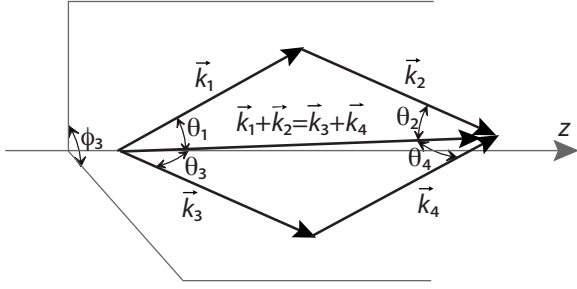


FIG. 6. Definition of the geometry of the proposed interpretation in terms of FWM

$$\theta_3 = \arccos\left(\frac{k_3^2 - k_4^2 + (k_1 + k_2)^2 \cos^2 \theta_0}{2k_3(k_1 + k_2)\cos \theta_0}\right), \quad (1)$$

$$\theta_4 = \arccos\left(\frac{k_4^2 - k_3^2 + (k_1 + k_2)^2 \cos^2 \theta_0}{2k_4(k_1 + k_2)\cos \theta_0}\right), \quad (2)$$

as derived from the cosine theorem in the triangle formed by  $\vec{k}_1 + \vec{k}_2 \approx (k_1 + k_2)\cos \theta_0 \vec{u}_z$ ,  $\vec{k}_3$ , and  $\vec{k}_4$  (Fig. 6).  $\theta_3$  and  $\theta_4$  obviously depend on  $\lambda_1$  and  $\lambda_2$ , so that the spectral width of the incident pulses provides a supplementary spatial degree of freedom. Scanning those wavelengths across the input spectrum therefore yields the angular distribution of the emission of  $\lambda_3$  and  $\lambda_4$ . Furthermore, since FWM events are cascading, Eqs. (1) and (2) will iteratively increase the two-dimensional divergence of the fundamental wavelength, in a process similar to that recently described by Majus *et al.* [20].

We simulated such geometric broadening of the incident peaks for up to 50 cascaded FWM events. In each step,  $\lambda_1$  and  $\lambda_2$  are scanned from 775 to 825 nm, and generation of photons at  $\lambda_3$  set to  $\lambda_3 = 2\lambda_0 - \lambda_1$  is considered, with  $\lambda_0 = 800$  nm. The generation efficiency is assumed to be proportional to the intensity of  $\lambda_1$  and  $\lambda_2$  in the initial spectrum. The same processing is iterated, assuming that the spectrum is unaffected by the considered processes, by bootstrapping  $\theta_3$  as the input  $\theta_0$  for the next iteration. As displayed in Fig. 7, the fundamental radiation spreads over a wide angular range. The photon bath in the initial direction of the beams, available to sustain filamentation within those beams, is clearly depleted, while the two beams merge into a more homogeneous angular distribution of the fundamental wavelength, which bridges the gap between the two beams after typically 40 iterations.

It should be noted that, in this simple calculation, only the efficiently seeded in-plane FWM events have been taken into account. However, the emission can occur in any plane around the  $z$  axis. As a consequence, a supplementary degree of freedom should be considered, yielding an even faster and more efficient spatial broadening. Moreover, our simulation is restricted to the fundamental wavelength of the incident beams due to computing limitations, but it could in principle be extended to the full spectrum of the white-light con-

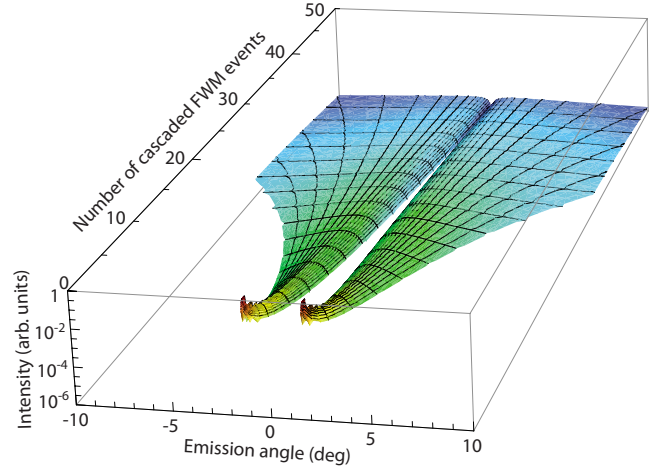


FIG. 7. (Color online) Angular broadening of the incident pulses. The plot displays the calculated intensity integrated over the 775–825 nm range as a function of the angle, for up to 50 cascaded FWM events (see text for details).

tinuum. It would then obviously yield a similar angular spreading of the beam, resulting in the bright white spot observed in the experiments.

## V. CONCLUSION

In conclusion, we have shown that two ultrashort beams crossing at an angle of a few degrees in fused silica with adequate relative delay result in a qualitative change in the emission pattern of the continuum. While this pattern is composed of two sets of conical emission rings when the two beams propagate independently, their interaction results in a bright white circular spot, encompassing the directions of the two incident beams. This pattern change is the signature of SPM within the field resulting from the interference of the two incident beams. Moreover, the spectral broadening of the photon bath competes with the feeding of filamentation, largely reducing its contribution to the final far-field pattern.

The difference in the emission geometry of the white-light continuum and of the fundamental wavelength allows us to geometrically select the supercontinuum for spectroscopic applications of the white-light supercontinuum, such as remote sensing [3,21] or supercontinuum cavity ring-down spectroscopy [22]. For example, in our experimental arrangement, the overall losses in the blue green (BG) part of the spectrum can be less than 20–30 %, while a 2-mm-thick BG colored glass filter would reject 50–60 % of the light in the same spectral region.

## ACKNOWLEDGMENTS

This work was supported by the Swiss NSF (Contracts No. 200021-111688 and No. 200021-116198 and R'equip program). We greatly acknowledge fruitful discussions with Dr. Bruno Schmidt about the arrangement of the experimental setup.

- [1] K. D. Moll, A. L. Gaeta, and G. Fibich, *Phys. Rev. Lett.* **90**, 203902 (2003).
- [2] A. Braun, G. Korn, X. Liu, D. Du, J. Squier, and G. Mourou, *Opt. Lett.* **20**, 73 (1995).
- [3] J. Kasparian and J.-P. Wolf, *Opt. Express* **16**, 466 (2008).
- [4] L. Bergé, S. Skupin, R. Nuter, J. Kasparian, and J.-P. Wolf, *Rep. Prog. Phys.* **70**, 1633 (2007).
- [5] A. Couairon and A. Mysyrowicz, *Phys. Rep.* **441**, 47 (2007).
- [6] S. L. Chin, S. A. Hosseini, W. Liu, Q. Luo, F. Theberge, N. Akozbek, A. Becker, V. P. Kandidov, O. G. Kosareva, and H. Schroeder, *Can. J. Phys.* **83**, 863 (2005).
- [7] S. Tzortzakis, L. Sudrie, M. Franco, B. Prade, A. Mysyrowicz, A. Couairon, and L. Bergé, *Phys. Rev. Lett.* **87**, 213902 (2001).
- [8] L. Bergé, M. R. Schmidt, J. J. Rasmussen, P. L. Christiansen, and K. Ø. Rasmussen, *J. Opt. Soc. Am. B* **14**, 2550 (1997).
- [9] C. Ren, R. G. Hemker, R. A. Fonseca, B. J. Duda, and W. B. Mori, *Phys. Rev. Lett.* **85**, 2124 (2000).
- [10] S. A. Hosseini, Q. Luo, B. Ferland, W. Liu, S. L. Chin, O. G. Kosareva, N. A. Panov, N. Aközbeq, and V. P. Kandidov, *Phys. Rev. A* **70**, 033802 (2004).
- [11] T.-T. Xi, X. Lu, and J. Zhang, *Phys. Rev. Lett.* **96**, 025003 (2006).
- [12] Ma Yuan-Yuan, Lu Xin, Xi Ting-Ting, Hao Zuo-Qiang, Gong Qi-Huang, and Zhang Jie, *Chin. Phys.* **16**, 2731 (2007).
- [13] S. L. Chin, S. Petit, W. Liu, A. Iwasaki, M. C. Nadeau, V. P. Kandidov, O. G. Kosareva, and K. Y. Andrianov, *Opt. Commun.* **210**, 329 (2002).
- [14] A. A. Ishaaya, T. D. Grow, S. Ghosh, L. T. Vuong, and A. L. Gaeta, *Phys. Rev. A* **75**, 023813 (2007).
- [15] Y. Y. Ma, X. Lu, T. T. Xi, Q. H. Gong, and J. Zhang, *Appl. Phys. B: Lasers Opt.* **93**, 463 (2008).
- [16] A. C. Bernstein, M. Mc Cormick, G. M. Dyer, J. C. Sanders, and T. Ditmire, *Phys. Rev. Lett.* **102**, 123902 (2009).
- [17] D. Faccio, A. Averchi, A. Couairon, A. Dubietis, R. Piskarskas, A. Matijosius, F. Bragheri, M. A. Porras, A. Piskarskas, and P. Di Trapani, *Phys. Rev. E* **74**, 047603 (2006).
- [18] C. Corsi, A. Tortora, and M. Bellini, *Appl. Phys. B: Lasers Opt.* **78**, 299 (2004).
- [19] H. J. Eichler, P. Gunter, and D. W. Pohl, *Laser-Induced Dynamic Gratings* (Springer, Berlin, 1986).
- [20] D. Majus, V. Jukna, G. Valiulis, and A. Dubietis, *Phys. Rev. A* **79**, 033843 (2009).
- [21] J. Kasparian, M. Rodriguez, G. Méjean, J. Yu, E. Salmon, H. Wille, R. Bourayou, S. Frey, Y.-B. André, A. Mysyrowicz, R. Sauerbrey, J.-P. Wolf, and L. Wöste, *Science* **301**, 61 (2003).
- [22] K. Stelmaszczyk, P. Rohwetter, M. Fechner, M. Queiβer, A. Czyżewski, T. Stacewicz, and L. Wöste, *Opt. Express* **17**, 3673 (2009).

# Curved plasma channels: Kerr lens and Airy prism

Jérôme Kasparian  
jerome.kasparian@unige.ch

Université de Genève, GAP-Biophotonics, 20 rue de l'Ecole de Médecine, 1211 Geneva 4, Switzerland

Jean-Pierre Wolf

Université de Genève, GAP-Biophotonics, 20 rue de l'Ecole de Médecine, 1211 Geneva 4, Switzerland

We analytically calculate the transverse energy fluxes that would be respectively induced in high-power Airy beams by the Kerr self-focusing and the Airy profile itself if they were the only active process. Under experimental conditions representative of laser filamentation experiments of high-power ultrashort laser pulses in air and condensed media, the Kerr lens induces transverse energy fluxes much larger than the Airy "prism" at the main peak. As a consequence, the curved plasma channels in Airy beams are not only a plasma spark on a curved focus, but indeed self-guided filaments, and their curved trajectory appears as a perturbation due to the linear Airy propagation regime. [DOI: 10.2971/jeos.2009.09039]

**Keywords:** beam trapping, self-focusing and defocusing, self-phase modulation, wavefronts and ray tracing

## 1 INTRODUCTION

Airy beams are non-centrosymmetric, non-diffractive beams [1, 2] providing an apparent curved propagation. This lateral acceleration stems from their two-dimensional spatial intensity and phase profile,

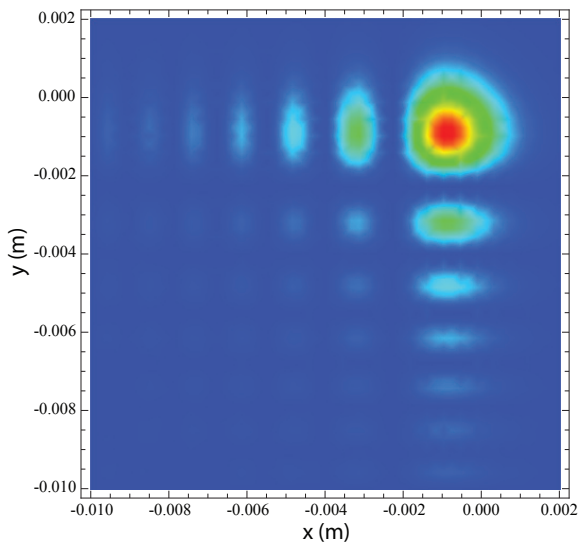
$$\begin{aligned}
 E_{Airy}(x, y, z) = \exp & \left[ a \frac{x+y}{x_0} - a \frac{z^2}{k^2 x_0^4} \right. \\
 & \left. + i \left( a^2 \frac{z}{k x_0^2} + \frac{z(x+y)}{2k x_0^3} - \frac{z^3}{6k^3 x_0^6} \right) \right] \\
 & \times Ai \left( \frac{x}{x_0} + ia \frac{z}{k x_0^2} - \frac{z^2}{4k^2 x_0^4} \right) \\
 & \times Ai \left( \frac{y}{x_0} + ia \frac{z}{k x_0^2} - \frac{z^2}{4k^2 x_0^4} \right) \quad (1)
 \end{aligned}$$

where  $E$  is the electric field envelope,  $x$  and  $y$  the transverse coordinates,  $z$  the propagation coordinate,  $x_0$  is an arbitrary transverse scale (typically of the order of the diameter of the main peak at  $z = 0$ ),  $k = 2\pi/\lambda$  is the wavenumber,  $\lambda$  the wavelength, and  $a$  a damping coefficient.

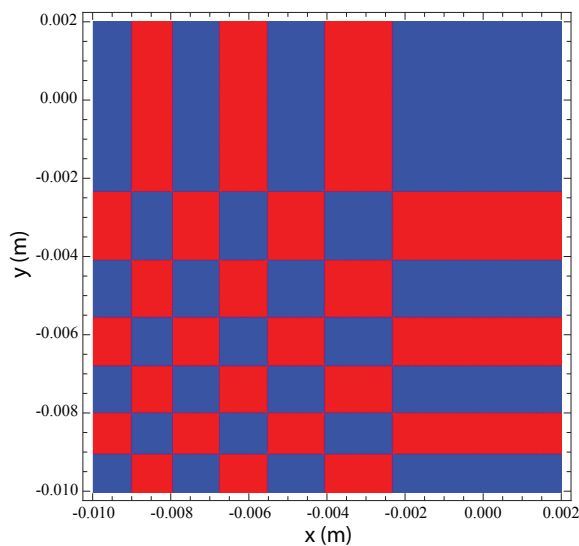
$Ai(u) = \frac{1}{\pi} \int_0^\infty \cos(t^3/3 + ut) dt$  is the Airy function of first kind and solution to the differential equation  $v'' - vu = 0$ . At  $z \sim 0$ , a significant fraction of the light intensity is localized in a main peak of width on the order of  $x_0$  on one side of the beam profile. The remaining intensity spreads on the other side in a wide trail featuring oscillations with a slow damping (Figure 1(a)). The phases of these intensity oscillations are alternatively 0 and  $\pi$  (Figure 1(b)) so that their interference results in the well-known curved trajectory of the main peak. Since the trail simultaneously spreads away from the beam center of mass, the latter still propagates on a straight line, so that the Ehrenfest theorem is not violated [1, 3]. A "true" Airy profile ( $a = 0$ ) bears an infinite power

due to a non-converging transverse intensity integral on the trail side. As a consequence, practical realizations correspond to the range  $0 < a \leq 0.3$ , where the typical Airy beam behaviour, especially the lateral acceleration, is maintained over a finite propagation distance. This distance decreases for increasing values of  $a$  until the Airy behaviour disappears above  $a \geq 0.3$ . Although Airy profiles have been known for decades, they have attracted considerable interest recently following the first experimental realization [2] of an Airy-shaped optical beam. Such realization opened the way to applications such as the transport of particles or their sweeping out of a predefined volume [4]. The interest further rose with the generation of an Airy beam at a high intensity [5], sufficient to observe plasma channels. Close to  $z = 0$ , the main Airy peak concentrates most of the beam energy on around 1% of the surface of the beam profile. As a consequence, one could expect that the Airy propagation regime acts like a linear focusing resulting in a plasma spark at the main peak, playing the role of a (curved) linear focus. Alternatively, the observed curved plasma channel could be seen as the result of self-guided laser filamentation [6]–[10] with a trajectory bent by the Airy profile. Filamentation is a non-linear propagation regime observed for high-power, ultrashort laser pulses. It stems from a dynamic balance between Kerr self-focusing of the beam and defocusing by the self-generated plasma at the non-linear focus. This process occurs in the most intense region of the beam profile, therefore on the main peak in the case of an Airy profile [5].

The Kerr effect, at the root of filamentation, acts as a Kerr "lens" which tends to establish an inward-pointing energy flux towards the most intense region of the beam profile. On the other hand, the propagation of a beam with an Airy profile is characterized by an outward-pointing displacement of the main peak and hence in an energy flux oriented towards



(a)



(b)

FIG. 1 (a) Intensity and (b) Phase of a typical two-dimensional Airy profile with a damping coefficient  $a = 0.1$ , at a propagation distance  $z = 0$ , for  $x_0 = 1$  mm.

one side of the beam. Recently, we suggested that a combination of Kerr- and Airy-generated energy fluxes governs the filamentation within Airy beams [11].

In this paper, we quantify the relative effects of the Airy profile and Kerr lens on propagation, and more specifically on the transverse Poynting vector, i.e. the transverse energy flow. We show that the Airy profile acts like a prism and induces a much smaller transverse Poynting vector than the Kerr lens. This domination is stronger in usual condensed media such as water or glass, and even higher in a highly non-linear medium such as  $\text{CS}_2$ . We therefore conclude that self-guiding actually occurs within the main Airy beam so that one can actually describe the curved plasma channels observed by Polynkin et al. [5] as curved self-guided filaments.

## 2 RESULTS AND DISCUSSION

We evaluated the transverse energy fluxes that would be respectively generated by the Kerr lens and the Airy profile, if they would be the only process at play in the propagation of the pulse. They are defined at any location in space by the transverse component of the Poynting vector  $\vec{\Pi} = \frac{1}{\mu_0} \vec{E} \times \vec{B}$ , which in the paraxial approximation, amounts to

$$\langle \vec{\Pi}_{\perp}(x, y, z) \rangle = \frac{1}{k} I(x, y, z) \vec{\nabla}_{\perp} \phi(x, y, z) \quad (2)$$

where  $I$  is the local intensity and  $\phi$  the local phase of the beam. The phase shift of a temporal slice of the pulse due to the Kerr effect is given in the paraxial approximation and at any  $(x, y, z)$  by  $\phi^{(Kerr)} = kn_2 \int_0^z I(x, y, z) dz$  [8, 9]. Here  $n_2$  is the nonlinear refractive index ( $n_2^{(air)} = 2.4 \times 10^{-19} \text{ cm}^2/\text{W}$  in air [13]). The Kerr effect is most efficient where the intensity is strongest, i.e. close to  $z = 0$  on the main peak of the Airy profile. If filamentation is initiated, it will maintain the intensity (and hence the Kerr lens) at high levels over its whole length. We therefore focus our analysis below on the highest-intensity region where the conditions are more favorable to the onset of filamentation, and consider that, if filament occurs, the discussion can be extended to the whole filament length. Over a short propagation distance around  $z = 0$ , we may neglect the longitudinal variation of the intensity and write  $\phi^{(Kerr)} \approx n_2 I k z$ . As a consequence, the Poynting vector that would be induced by the Kerr lens alone is

$$\begin{aligned} \langle \vec{\Pi}_{\perp}^{(Kerr)}(x, y, z) \rangle &= \frac{1}{k} I(x, y, z) \vec{\nabla}_{\perp} (n_2 I(x, y, z) k z) \\ &= n_2 I(x, y, z = 0) z \vec{\nabla}_{\perp} I(x, y, z = 0) \end{aligned} \quad (3)$$

where  $I$  is the intensity of the Airy field envelope as defined in Eq. (1).

In the region close to  $x = 0, y = 0$ , where the main Airy peak lies, a numerical analysis shows that the local Taylor series deviates quickly from the Airy function because the steep peaks in this region (see Figure 1) result in strong values of the successive derivatives. In contrast, the asymptotic development of the Airy function near to  $+\infty$  provides a good approximation of the phase gradient of the Airy profile even close to the origin, because the smooth shape of the function beyond zero corresponds to very small values of the derivatives over this whole region. As a consequence,

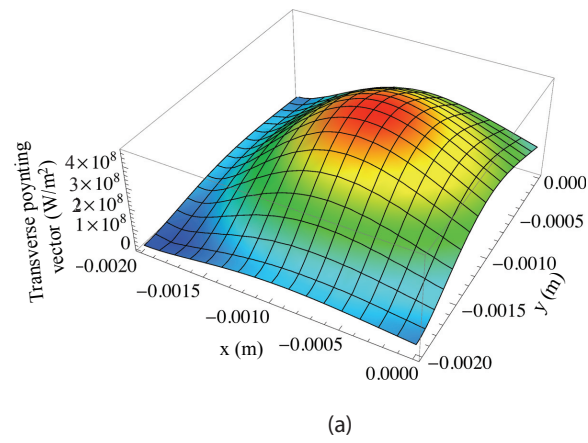
$$Ai(u)[u \rightarrow \infty] \sim \frac{\exp\left[-\frac{2}{3}u^{3/2}\right]}{2\sqrt{\pi}u^{1/4}} \quad (4)$$

so that to the first order in the transverse coordinates  $x$  and  $y$ , the Airy profile tends to

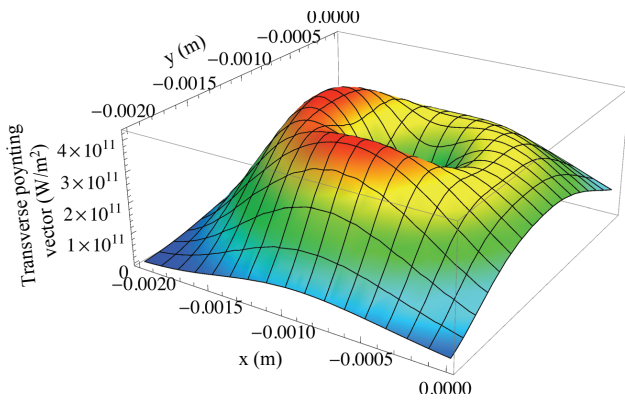
$$E_{Airy}(x, y, z)[x, y \rightarrow \infty] \sim \frac{\exp\left[a \frac{x+y}{x_0} - \frac{2}{3} \left[\left(\frac{x}{x_0}\right)^{3/2} + \left(\frac{y}{x_0}\right)^{3/2}\right] + i \frac{(x+y)z}{2kx_0^3}\right]}{\sqrt{x_0} 4\pi(xy)^{1/4}} \quad (5)$$

As a consequence, as soon as  $z/kx_0^2$  and  $a$  are small compared to  $x$  and to 1, the phase of the Airy profile is given by

$$\phi_{Airy}(x, y, z)[x, y \rightarrow \infty] \sim \frac{(x+y)z}{2kx_0^3} \quad (6)$$



(a)



(b)

FIG. 2 Norm of the Poynting vector that would be respectively generated by (a) Airy and (b) Kerr contributions on the main peak if they were the only process at play. The calculation is performed in air, for  $a = 0.1$ ,  $x_0 = 1$  mm,  $z = 1$  mm,  $\lambda = 800$  nm,  $I = 5 \times 10^{17}$  W/m<sup>2</sup>.

Since the phase depends linearly on the transverse coordinates  $x$  and  $y$ , the Airy regime is equivalent to inserting a prism with an apex angle proportional to  $z$ , on the path of the main peak. The transverse Poynting vector that would be induced by the Airy profile considered alone then writes

$$\begin{aligned} \langle \vec{\Pi}_{\perp}^{(Airy)}(x, y, z) \rangle &= \frac{1}{k} I(x, y, z) \vec{\nabla}_{\perp} \phi_{Airy}(x, y, z) \\ &\approx \frac{z}{2k^2 x_0^3} I(x, y, z = 0) (\vec{u}_x + \vec{u}_y) \end{aligned} \quad (7)$$

where  $\vec{u}_x$  and  $\vec{u}_y$  are the unit vectors along the  $x$  and  $y$  axes, respectively. Figure 2 displays both  $|\vec{\Pi}_{\perp}^{(Airy)}|$  and  $|\vec{\Pi}_{\perp}^{(Kerr)}|$ , given by Eqs. (3) and (7), in the region of interest to our study and for  $x_0 = 1$  mm at a wavelength of 800 nm. Poynting vectors are non-additive because of interference effects so that these two values cannot in principle be considered as two independent components of the total Poynting vector at play in a nonlinear Airy beam. However, their ratio (Figure 3) can be seen as an indication of the relative efficiency of the Airy prism and the Kerr lens in the considered region. This ratio amounts to

$$\begin{aligned} \eta(x, y, z) &= \frac{\Pi_{\perp}^{(Kerr)}(x, y, z)}{\Pi_{\perp}^{(Airy)}(x, y, z)} \\ &\approx \sqrt{2} k^2 x_0^3 n_2 |\vec{\nabla}_{\perp} I(x, y, z = 0)| \end{aligned} \quad (8)$$

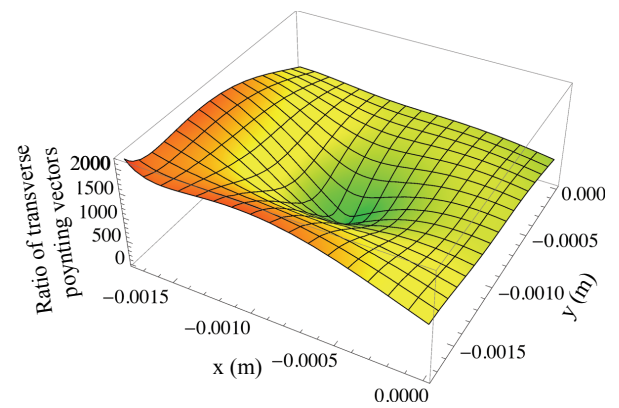


FIG. 3 Ratio  $\eta$  of the norm of Poynting vector that would be respectively generated by the Kerr lens and the Airy prism if alone. The calculation is performed in air for  $a = 0.1$ ,  $x_0 = 1$  mm,  $z = 1$  mm,  $\lambda = 800$  nm,  $I = 5 \times 10^{17}$  W/m<sup>2</sup>.

The transverse dependence of  $\eta$  for  $\frac{z}{kx_0^2} \ll 1$  is only governed by the intensity profile. Moreover,  $\eta$  is to the first order independent from  $z$ . We numerically checked this independence for  $0 < z \leq x_0$  and  $0 \leq a \leq 0.5$ . Moreover, Eq. (8) confirms that  $\eta$  is highest where the intensity gradient is strongest. As a consequence, the Kerr lens is most likely to dominate the propagation in this region. We calculated the  $\eta$  ratio there, as a function of the attenuation factor  $a$ , for an intensity of  $5 \times 10^{13}$  W/cm<sup>2</sup> typical of the intensity clamping in laser filaments in air [12]. As clearly appears on Figures 3 and 4,  $\eta \gg 1$  for any value of  $a$  allowing an Airy acceleration of the main peak. In other words, the Kerr effect and its associated self-guiding of laser filaments are strong enough to occur within the main Airy peak in spite of the lateral acceleration that it is experiencing. This provides a clear evidence that the curved plasma channels observed by Polynkin et al. [5] are not just ionization at the high-intensity main peak of the Airy profile, but indeed correspond to self-guiding within this peak. The Airy propagation regime acts like a perturbation on this self-guiding. This perturbation results in a curved trajectory, in a way similar to turbulence deviating the filaments without destroying them [14]. One can therefore consider that filamentation and transverse Airy acceleration, hence the Kerr lens and Airy prism, are decoupled to the first order and impose their effect on the beam almost independently from each other. This decoupling is favored by the fact that the Airy- and Kerr-generated Poynting vectors have very different magnitudes, which prevents them from efficiently interfering.

$\eta$  is directly proportional to both  $n_2$  and the intensity. It therefore strongly depends on the propagation medium. While  $I$  is clamped to  $5 \times 10^{13}$  W/cm<sup>2</sup> in air [12], the non-linear refractive indexes of glass and in water are  $n_2^{(glass)} = 3.2 \times 10^{-16}$  cm<sup>2</sup>/W [15] and  $n_2^{(water)} \approx 2.7 \times 10^{-16}$  cm<sup>2</sup>/W [16], respectively. The intensity in self-guided filaments in those media is clamped around  $I \sim 15$  TW/cm<sup>2</sup> [15]. The  $\eta$  ratio is therefore 1000 times higher in condensed media as compared with air. In CS<sub>2</sub>,  $n_2$  is typically 100 times stronger than in water [17]. Although experimental values of the clamped intensity have not been reported to date, we can expect that it will be comparable to that in other condensed media like water or glass.

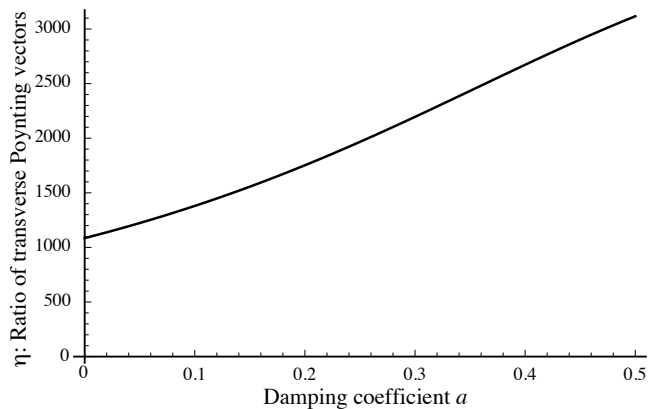


FIG. 4 Ratio  $\eta$  of the norm of Poynting vector that would be respectively generated by the Kerr lens and the Airy prism if alone. The calculation is performed in air at the location of maximum intensity gradient, as a function of  $a$  for  $x_0 = 1$  mm,  $z = 1$  mm,  $\lambda = 800$  nm,  $I = 5 \times 10^{17}$  W/m<sup>2</sup>.

As a consequence,  $\eta$  will be close to  $10^8$ . With such high domination of the Kerr lens over the Airy prism, their decoupling might be challenged, which could affect the trajectory of the main Airy peak, or even lead the filament to leave the curved trajectory. The description of this propagation regime is out of scope of this paper. However, an experimental study as well as two- or three-dimensional numerical simulations would be of high interest to describe it in more detail.

The influence of wavelength on  $\eta$  is mainly due to the  $k^2$  factor of Eq. (8), since the variation of  $n_2$  with wavelength is smooth. However, since  $\eta \gg 1$ , sweeping the wavelength from the NIR to the near UV will not invert the ratio of the influences of Kerr lens and Airy prism. Eq. (8) also shows that  $\eta$  is proportional to  $x_0^3$ . As a consequence, large beam sizes correspond to a higher Kerr-induced Poynting vector. While the numerical examples above correspond to  $x_0 = 1$  mm, Airy peaks of dimensions comparable with those of a filament (hence,  $x_0 \sim 100$   $\mu$ m) would result in comparable magnitudes of the effects of the Airy and Kerr contributions in air. In this case, interferences may become significant and one may expect that filament would be seriously perturbed and that self-guiding may be challenged by the Airy prism. Again, this regime is beyond the scope of this work.

### 3 CONCLUSION

As a conclusion, the Kerr lens induces transverse energy fluxes much larger than the Airy profile, in any experimental condition representative of the filamentation of high-power, ultrashort laser pulses in air. This effect is even more marked in water and glass, and even further in the highly non-linear material CS<sub>2</sub>. Due to this domination, self-guiding can occur almost unperturbed within the Airy peak. The curved plasma channels observed within them are therefore genuine self-guided filaments, on which the Airy propagation regime acts like a decoupled perturbation resulting in a curved trajectory.

### ACKNOWLEDGEMENTS

This work was supported by the Swiss NSF, contracts 200021-116198 and 200021-125315.

### References

- [1] M. V. Berry, and N. L. Balazs, "Nonspreading wave packets" *Am. J. Phys.* **47**, 264-267 (1979).
- [2] G. A. Siviloglou, J. Broky, A. Dogariu, and D. N. Christodoulides, "Observation of accelerating Airy beams" *Phys. Rev. Lett.* **99**, 213901 (2007).
- [3] I. M. Besieris, and A. M. Shaarawi, "A note on an accelerating finite energy Airy beam" *Opt. Lett.* **32**, 2447-2449 (2007).
- [4] J. Baumgartl, M. Mazilu, and K. Dholakia, "Optically mediated particle clearing using Airy wavepackets" *Nat. Photonics* **2**, 675-678 (2008).
- [5] P. Polynkin, M. Kolesik, J. V. Moloney, G. A. Siviloglou, and D. N. Christodoulides, "Curved plasma channel generation using ultra-intense Airy beams in air" *Science* **324**, 229-232 (2009).
- [6] A. Braun, G. Korn, X. Liu, D. Du, J. Squier, and G. Mourou, "Self-channeling of high-peak-power femtosecond laser pulses in air" *Opt. Lett.* **20**, 73-75 (1995).
- [7] S. L. Chin, S. A. Hosseini, W. Liu, Q. Luo, F. Theberge, N. Aközbek, A. Becker, V. P. Kandidov, O. G. Kosareva, and H. Schröder, "The propagation of powerful femtosecond laser pulses in optical media: physics, applications, and new challenges" *Can. J. Phys.* **83**, 863-905 (2005).
- [8] L. Bergé, S. Skupin, R. Nuter, J. Kasparian, and J.-P. Wolf, "Ultrashort filaments of light in weakly-ionized, optically-transparent media" *Rep. Prog. Phys.* **70**, 1633-1714 (2007).
- [9] A. Couairon, and A. Mysyrowicz, "Femtosecond filamentation in transparent media" *Phys. Rep.* **441**, 47-189 (2007).
- [10] J. Kasparian, and J.-P. Wolf, "Physics and applications of atmospheric nonlinear optics and filamentation" *Opt. Express* **16**, 466-493 (2008).
- [11] J. Kasparian, and J.-P. Wolf, "Laser beams take a curve" *Science* **324**, 194-195 (2009).
- [12] J. Kasparian, R. Sauerbrey, and S. L. Chin, "The critical laser intensity of self-guided light filaments in air" *Appl. Phys. B-Lasers O.* **71**, 877-879 (2000).
- [13] V. Loriot, P. Béjot, E. Hertz, O. Faucher, B. Lavorel, S. Henin, J. Kasparian, and J.-P. Wolf, "Higher-order Kerr terms allowing ionization-free filamentation in air" submitted to *Phys. Rev. Lett.* (2009).
- [14] R. Salamé, N. Lascoux, E. Salmon, J. Kasparian, and J.-P. Wolf, "Propagation of laser filaments through an extended turbulent region" *Appl. Phys. Letts.* **91**, 171106 (2007).
- [15] S. Skupin, and L. Bergé, "Self-guiding of femtosecond light pulses in condensed media: Plasma generation versus chromatic dispersion" *Physica D* **220**, 14-30 (2006).
- [16] J. Liu, H. Schroeder, S. L. Chin, R. Li, and Z. Xu, "Nonlinear propagation of fs laser pulses in liquids and evolution of supercontinuum generation" *Opt. Express* **13**, 10248-10259 (2005).
- [17] P. D. Maker, R. W. Terhune, and C. M. Savage, "Intensity-Dependent Changes in the Refractive Index of Liquids" *Phys. Rev. Lett.* **12**, 507-509 (1964).

# Optical rogue wave statistics in laser filamentation

Jérôme Kasparian<sup>1\*</sup>, Pierre Béjot<sup>1</sup>, Jean-Pierre Wolf<sup>1</sup> and John M. Dudley<sup>2</sup>

<sup>1</sup>GAP GAP-Biophotonics, University of Geneva, 20, 1211 Geneva 4 Switzerland

<sup>2</sup>Institut FEMTO-ST, UMR 6174 CNRS-Université de Franche-Comté, Besançon, France

\*jerome.kasparian@unige.ch

**Abstract:** We experimentally observed optical rogue wave statistics during high power femtosecond pulse filamentation in air. We characterized wavelength-dependent intensity fluctuations across 300 nm broadband filament spectra generated by pulses with several times the critical power for filamentation. We show how the statistics vary from a near-Gaussian distribution in the vicinity of the pump to a long tailed “L-shaped” distribution at the short wavelength and long wavelength edges. The results are interpreted in terms of pump noise transfer via self-phase modulation.

©2009 Optical Society of America

**OCIS codes:** (190.4380) Nonlinear optics, four-wave mixing; (190.5530) Pulse propagation and solitons; (190.5940) Self-action effects; (190.7110) Ultrafast nonlinear optics

---

## References and links

1. D. R. Solli, C. Ropers, P. Koonath, and B. Jalali, “Optical rogue waves,” *Nature* **450**, 1054 (2007).
2. A. I. Dyachenko and V. E. Zakharov, “Modulation instability of Stokes wave implies a freak wave,” *JETP Lett.*, **81**, 255-259 (2005).
3. J. M. Dudley, G. Genty, and B. J. Eggleton, “Harnessing and control of optical rogue waves in supercontinuum generation,” *Opt. Express* **16**, 3644-3651 (2008).
4. D. R. Solli, C. Ropers, and B. Jalali, “Active control of optical rogue waves for stimulated supercontinuum generation,” *Phys. Rev. Lett.* **101**, 233902 (2008).
5. G. Genty, J. M. Dudley, and B. J. Eggleton, “Modulation control and spectral shaping of optical fiber supercontinuum generation in the picosecond regime,” *Appl. Phys. B* **94**, 187-194 (2009).
6. C. Lafargue, J. Bolger, G. Genty, F. Dias, J. M. Dudley, and B. J. Eggleton, “Direct detection of optical rogue waves energy statistics in supercontinuum generation,” *Electron. Lett.* **45**, 217-219 (2009).
7. N. Akhmediev, A. Ankiewicz, and M. Taki, “Waves that appear from nowhere and disappear without a trace,” *Phys. Lett. A* **373**, 675-678 (2009).
8. N. Akhmediev, J. M. Soto-Crespo, and A. Ankiewicz, “Extreme waves that appear from nowhere: on the nature of rogue waves,” *Phys. Lett. A* (2009).
9. D. Borlaug, S. Fathpour, and B. Jalali, “Extreme value statistics and the Pareto distribution in silicon photonics,” arXiv:0809.2565v1 [Phys. Optics] (2008).
10. K. Hammani, C. Finot, J. M. Dudley, and G. Millot, “Optical rogue-wave fluctuations in fiber Raman amplifiers,” *Opt. Express* **16**, 16467-16474 (2008).
11. S. L. Chin, S. A. Hosseini, W. Liu, Q. Luo, F. Théberge, N. Akozbek, A. Becker, V. P. Kandidov, O. G. Kosareva, and H. Schroeder, “The propagation of powerful femtosecond laser pulses in optical media: physics, applications, and new challenges,” *Can. J. Phys.* **83**, 863-905 (2005).
12. A. Couairon and A. Mysyrowicz. “Femtosecond filamentation in transparent media,” *Phys. Rep.* **44**, 47-189, (2007).
13. L. Bergé, S. Skupin, R. Nuter, J. Kasparian, and J.-P. Wolf. “Ultrashort filaments of light in weakly ionized, optically transparent media,” *Rep. Prog. Phys.* **70**, 1633-1713 (2007).
14. J. Kasparian and J.-P. Wolf. Physics and applications of atmospheric nonlinear optics and filamentation. *Opt. Express* **16**, 466-493, (2008).
15. P. Béjot, J. Kasparian, E. Salmon, R. Ackermann, and J.-P. Wolf, “Spectral correlation and noise reduction in laser filaments,” *Appl. Phys. B* **87**, 1-4 (2007).
16. S. Coles, *An Introduction to Statistical Modeling of Extreme Values* (Springer-Verlag, London, 2001).
17. V. Pareto, *Manuale di economia politica con una introduzione alla scienza sociale* (Societa Editrice Libreria, Milano 1906)

18. S. Bendersky, N. S. Komeika, and N. Blaunstein, "Atmospheric Optical Turbulence Over Land in Middle East Coastal Environments: Prediction Modeling and Measurements," *Appl. Opt.* **43**, 4070-4079 (2004)
19. R. Salamé, N. Lascoux, E. Salmon, J. Kasparian, and J. P. Wolf, "Propagation of laser filaments through an extended turbulent region," *Appl. Phys. Lett.* **91**, 171106-171106 (2007).

## 1. Introduction

There has recently been much interest in the study of extreme value or "rogue" events in nonlinear optics. Such events are associated with characteristic heavy tailed "L-shaped" probability distributions where – in stark contrast to Gaussian statistics – events much larger than the mean occur with significant probability. Initial interest in this area began in late 2007 with experiments reporting extreme value events in fiber supercontinuum generation associated with the generation of high power soliton pulses [1]. These experiments attracted widespread attention because they were carried in a regime where the spectral broadening was seeded by modulation instability, allowing important links to be made with mechanisms potentially underlying the formation of oceanic rogue waves [2].

Within the optics community, these results rapidly initiated studies into techniques for supercontinuum stabilization in the presence of noise [3-6]. Complementary work has explored non-soliton mechanisms for rogue wave formation in optical fibers, associated with the propagation dynamics and collisions of nonlinear breathers [7-8]. Aside from systems where direct analogy with oceanic waves can be drawn, other research has found that long-tailed distributions with similar extreme value or rogue wave-like statistics can appear in systems such as fiber Raman amplification and silicon photonics [9-10].

In this paper, we report a further example of nonlinear propagation exhibiting long tailed statistics characteristic of extreme value processes, thus confirming that such behavior may be very widespread in optical systems. Specifically, we study intensity fluctuations across the spectrum of a self-guided optical filament generated with pulses close to the critical power for filamentation in air [11-14]. In contrast to the experiments in fiber supercontinuum generation [1], we do not characterize the ultrafast temporal structure of the filament fluctuations, but rather characterize the wavelength dependence of the shot-to-shot intensity fluctuations across the generated filament spectrum. Our results show how the statistics vary from a near-Gaussian distribution near the center of the spectrum to long-tailed at the short wavelength and long wavelength edges. A simple numerical model is used to interpret these results in terms of pump noise transfer via self-phase modulation.

## 2. Experimental set-up

The experimental setup has been previously described in detail in [15], but is shown in Fig. 1 for completeness. A CPA (Chirped Pulse Amplification) Ti:Sapphire laser system delivers 200 fs pulses with pulse energy in the 1-6 mJ range (5-30 GW peak power). The centre wavelength is 815 nm and the beam diameter (at  $1/e^2$  level) is around 10 mm.

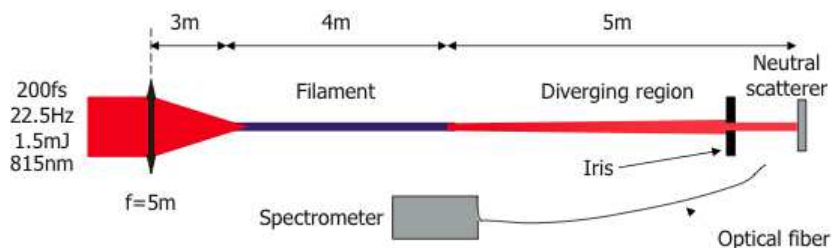


Fig. 1. Experimental setup

The beam was focused by a spherical mirror with 5 m focal length, yielding a non-linear focus (filament onset)  $\sim 3$  m downstream of the spherical mirror. Self-guided filaments

typically 4 m long were generated. A pinhole selected the supercontinuum emitted by the filament, rejecting the surrounding “photon bath” and conical emission. We checked that the filament pointing stability was sufficient to prevent truncation of the supercontinuum by the iris. The supercontinuum was then scattered onto a spectrally neutral target, and the scattered light was collected using a fiber. Its spectrum was recorded at 3 nm resolution using a fiber spectrometer. For a range of different power levels as described below, an ensemble of 5000 spectra was sampled. The sampling rate of  $\sim 5$  Hz was lower than the source repetition rate because of detection latency time of 200 ms, but each measured spectrum corresponded to one distinct input pulse with no averaging effect. We can record individual spectra in this way because of the low repetition rate of the source, and this represents a complementary technique to the ultrafast detection techniques that have been used to characterize soliton rogue wave events with high repetition rate fiber sources.

### 3. Experimental results

Figure 2(a) shows a series of experimentally measured spectra obtained at the filament output for a pulse peak power of  $P_0 = 15 \text{ GW} = 5 P_{cr}$ , where  $P_{cr} = 3 \text{ GW}$  is the critical self-focusing power for air. We plot only 500 realizations from the full ensemble for clarity. As expected under these pumping conditions, the mean spectrum (bold line) exhibits significant spectral broadening. However, it is also clear from the distribution of individual spectra (gray curves) that there are considerable shot-to-shot fluctuations at wavelengths away from the 815 nm pump. Towards the spectral edges, this leads to considerable jitter in the overall filament spectral width. The qualitative differences in the fluctuations near the pump and at the edges are illustrated in Fig. 2(b) and (c) which shows the equivalent time series of the filtered intensity at wavelengths of 815 nm and 630 nm respectively.

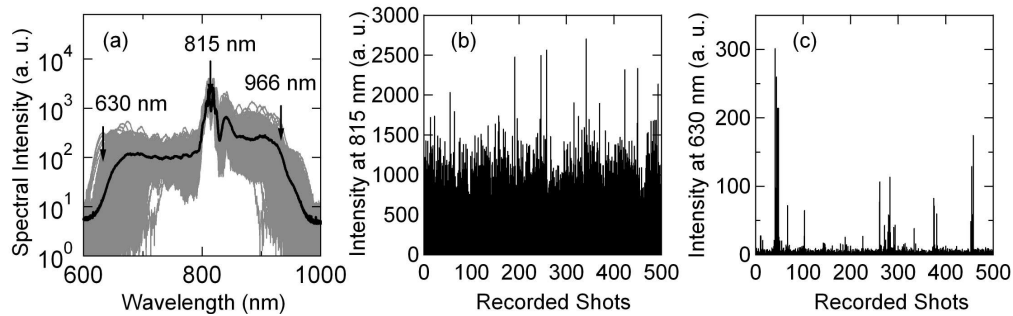


Fig. 2. (a) Typical series of 500 individual spectra (gray traces), together with the calculated mean over the same 500-shot ensemble (bold line). These results were measured at the output of a filament generated by a 15 GW (*i.e.*  $5 P_{cr}$ ) pump. (b) and (c) show time series of the intensity at (b) 815 nm in the spectrum center, and (c) 630 nm on the spectrum edge.

These noise properties were examined in more quantitative detail by calculating the histograms of the intensity fluctuations at the three different wavelengths marked on Fig. 2(a). These results are shown in Fig. 3, and clearly show significant differences between the spectral centre and wings. Specifically, At 815 nm near the pump, we see a near-Gaussian distributed fluctuations, whereas on the edges of the supercontinuum at 630 nm and 966 nm, L-shaped long-tailed histograms characteristic of extreme-value behavior are observed. Although a detailed analysis of the exact nature of these statistical properties is outside the scope of this paper, we have checked that these histograms are fitted (at 5% confidence levels) by distributions such as Weibull or Pareto that are commonly associated with long tailed behavior [16]. Note that the null hypothesis of a Gaussian distribution fit to these histograms was rejected even at the 20% confidence level.

To gain improved insight into the mechanisms leading to these extreme non-Gaussian distributions, we have also characterized the distribution of the intensity fluctuations at all

wavelengths across the spectrum, not only at specific wavelengths shown in Fig. 3. Significantly, such a full analysis of the wavelength dependence of the fluctuations is possible with our particular setup that allows a large number of shot-to-shot spectral measurements, but has not been possible in the earlier work studying fiber supercontinuum generation at higher repetition rates.

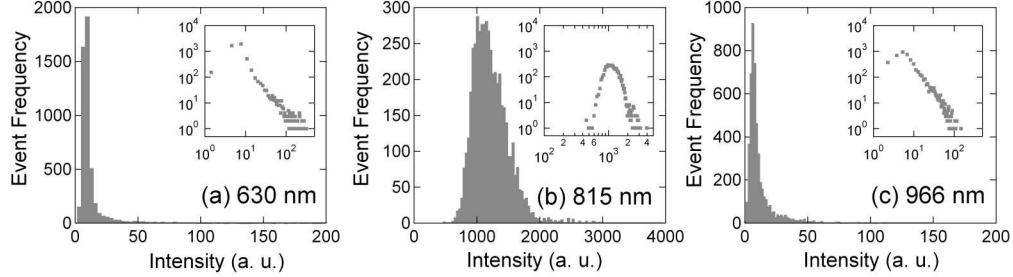


Fig. 3. Histograms at (a) 630 nm (b) 815 nm and (c) 966 nm. Insets show the same data on a log-log representation to highlight the differences in the distributions – while the distribution in (b) is bell-shaped, the distributions on the edges exhibit L-shaped characteristics.

To perform such a wavelength-dependent analysis, we introduce a long-tailed “Pareto-like” metric that can be readily computed from the experimental data. Specifically, we recall that long tailed distributions are often characterized by relationships such as the Pareto Principle which states that a large fraction (typically 80%) of the events or effects under study are associated with a small (typically 20%) of the causative factors [17]. Of course, the two quantities compared in the Pareto ratio are dimensionally different, and the ratio of 80/20 is arbitrary, but it is nonetheless a very useful concept to characterize the tendency of a particular distribution to exhibit extreme value or long-tailed characteristics. In quantitative terms, we consider the ensemble of spectra obtained  $[I_n(\lambda)]$  with  $n = 1 \dots N$  ( $N = 5000$  in our case). At the considered wavelength  $\lambda_0$  we sort the spectra by decreasing values so that  $I_0(\lambda_0) > I_1(\lambda_0) > I_2(\lambda_0) > \dots > I_N(\lambda_0)$  and then compute the “Pareto Metric” at  $\lambda_0$ , defined by:

$$M(\lambda_0) = \frac{\sum_{i=1}^{kN} I_i(\lambda_0)}{\sum_{i=1}^N I_i(\lambda_0)} \quad (1)$$

where the first sum corresponds the  $kN$  most intense measurements at the considered wavelength, with  $k = 0.2$  is taken for consistency with the Pareto Principle. In physical terms, this yields the contribution of the  $kN$  most intense measurements to the average signal. The lowest possible value of the metric is  $M = k$  in the case of a uniform distribution,  $M \approx 0.44$  for a Gaussian distribution, whilst values of  $M > 0.5$  indicate substantial deviation from Gaussian statistics and the development of an asymmetric long-tailed probability density function.

Figure 4 shows our results characterising the wavelength dependence of the intensity fluctuations in this manner. Here we plot both the evolution of the mean filament spectrum and the corresponding metric  $M(\lambda)$  for a range of input peak powers. There are two main points to draw from these results. Firstly, the metric  $M$  is higher towards the spectral edges than near the centre, confirming the association between nonlinear spectral broadening and deviation from Gaussian statistics. Secondly (and quantitatively) the metric increases to  $M > 0.5$  where we see characteristic long-tailed histogram behavior for power levels exceeding  $3.7 P_{cr}$  and, moreover, the maximum value of  $M$  anywhere across the spectrum also increases with power, taking values of 0.52, 0.62 and 0.73 for power levels of  $3.7 P_{cr}$ ,  $5 P_{cr}$  and  $5.5 P_{cr}$  respectively. These results extend those shown in Fig. 3 in clearly showing the difference in intensity distributions as a continuous function of wavelength across the spectrum.

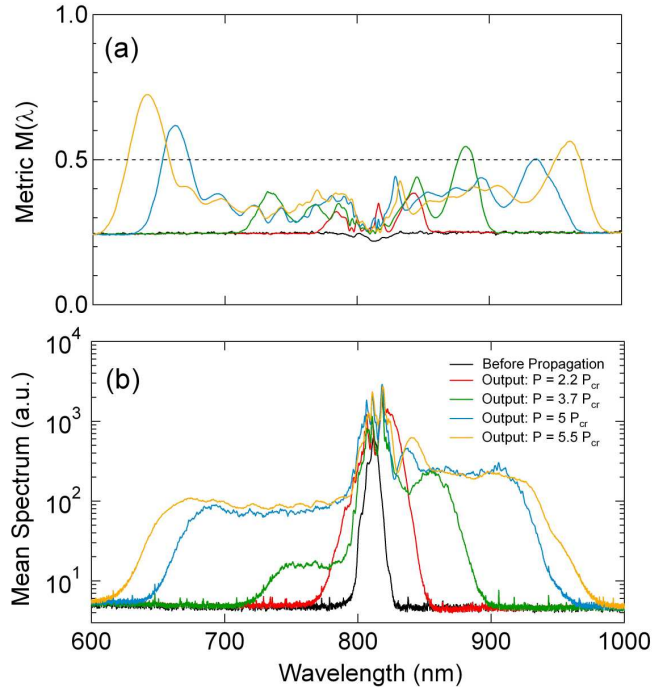


Fig. 4. Filament spectra for peak powers as shown. (a) plots the wavelength-dependence of the metric  $M(\lambda)$  and (b) shows the corresponding spectra. Values of  $M > 0.5$  (dotted line) indicate the development of a long tail on the probability distribution.

#### 4. Discussion and interpretation

The increase in the Pareto metric towards the spectrum edges of the spectrum and with higher input power indicates strong correlation between nonlinear spectral broadening in the filament and the appearance of long-tailed statistics. This is a further example of an optical system in which nonlinearity generates extreme-value behaviour, complementing other recent studies in other systems [9, 10]. Significantly, although a complete description of filament supercontinuum generation is complex, a satisfactory qualitative interpretation of our results above can be obtained assuming that spectral broadening is dominated by self-phase modulation (SPM). We have numerically calculated the output spectrum after SPM by calculating the intensity-dependent non-linear phase imposed to each temporal slice of the pulse and computing the Fourier transform of the output electric field. The considered intensity of  $5 \times 10^{13} \text{ W/cm}^2$  [11-14], propagation distance of 5 cm (typical of the distance over which the initial SPM-dominated broadening occurs), pulse duration of 100 fs, and nonlinear refractive index of air,  $n_2 = 2.84 \times 10^{-19} \text{ cm}^2/\text{W}$  were typical of filamentation. We performed 1000 realisations with Gaussian-distributed intensity noise (at  $\pm 2\%$  standard deviation) and wavelength jitter ( $\pm 3 \text{ nm}$  standard deviation), yielding an ensemble of 1000 spectra.

The mean spectrum and the corresponding Pareto-metric from Eq. (1) are shown in Fig. 5. Although we would not expect a simplified SPM-based model to be quantitatively accurate, the results nonetheless show that noise-driven SPM broadening provides a good qualitative description of the spectral characteristics measured in our experiments. In particular, the increase in the M-metric towards the spectral edges and the associated deviation from Gaussian to long-tailed L-shaped statistics are well-reproduced in our simulations. Reproducing the simulation with different intensity and wavelength jitters, we found that both parameters combine additively to generate a L-shaped statistics. However, for intensity and wavelength noises typical of CPA laser chains, the individual contribution of the wavelength jitter contributes more efficiently to the generation of an L-shaped statistics.

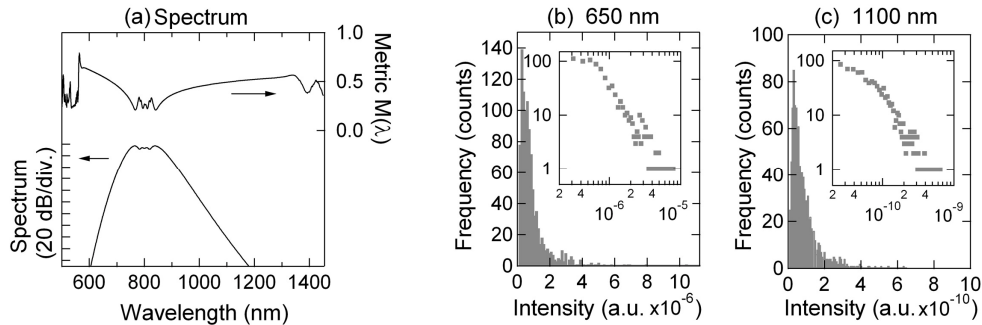


Fig. 5. (a) Mean spectrum (log scale, left axis) and Pareto metric  $M(\lambda)$  (right axis) for 1000 realizations of noise-induced SPM. Peak spectral intensity is 57 dB. (b) and (c) Histograms of spectral intensities at 650 nm and 1100 nm respectively. Insets use a log-log representation.

It is important to stress, however, that although these results are certainly suggestive of the dominant role of SPM in transforming Gaussian pump noise into L-shaped statistics, the filamentation process itself involves a number of other processes whose role necessitates further study. In particular, we note that our experimental filtering of conical emission from the measurements may potentially exclude noise contributions due to plasma effects.

We also investigated experimentally the effect of additional noise sources in the system, specifically inserting a strong turbulence area ( $C_n^2 \gg 10^9 \text{ m}^{-2/3}$ ,  $\sim 10^4$  times the highest atmospheric values [18]) over 1 m along the propagation region. We previously reported that filaments propagate almost unaffected in such conditions [19]. We observed that the turbulence leads to two competing effects depending on input power. In the low-power regime ( $2.9 P_{cr}$ ), turbulence affects only marginally the spectral dependence of the Pareto-metric in Fig. 4(b). At higher power ( $7.5 P_{cr}$ ), strong turbulence destroys typically 90 % of the filaments. The intensity distribution in a given wavelength range is therefore governed by whether or not a filament is formed. In this distribution, high intensities at any wavelength correspond to the occurrence of a filament, whose formation can then be considered as an extreme (“rogue”) event. The intensity distribution is therefore L-shaped not only on the edges of the spectrum, but also over the *whole* spectrum, including around the central wavelength where the Pareto-metric increases beyond 0.5.

## 5. Conclusions

The major result presented here has been the experimental observation of optical rogue wave statistics in the self-guided filamentation of high-power femtosecond pulses propagating in both still and highly turbulent air. Our experiments are in contrast to the ultrafast measurement techniques used to directly characterize rogue wave soliton pulses on the long wavelength edge of fiber supercontinuum spectra. Rather, we record an ensemble of broadband filament spectra and characterize the wavelength-dependence of the intensity fluctuations across the 300 nm broad white-light continuum. By introducing a convenient Pareto-like metric, we have shown how the statistics vary from a near-Gaussian distribution in the vicinity of the pump to a long tailed “L-shaped” distribution at the short wavelength and long wavelength edges. Based on a simple numerical model, we have interpreted our results in terms of pump noise transfer via self-phase modulation.

## Acknowledgements

This work was supported by the *Institut Universitaire de France*, the *Agence Nationale de la Recherche* Project MANUREVA (ANR-08-SYSC-019), the *Fonds National Suisse de la Recherche Scientifique* (FNS, grant #200021-116198/1), and the *Swiss Secrétariat d’État à l’Éducation et à la Recherche* in the framework of the COST P18 project “The Physics of Lightning Flash and its Effects”.

# Contribution of water droplets to charge release by laser filaments in air

Stefano Henin, Yannick Petit, Denis Kiselev, Jérôme Kasparian,<sup>a)</sup> and Jean-Pierre Wolf  
*Groupe de Physique Appliquée, Université de Genève, 20 rue de l'École de Médecine,  
 CH1211 Genève 4, France*

(Received 17 June 2009; accepted 12 August 2009; published online 4 September 2009)

We measured the electric charge release from single water microdroplets illuminated by ultrashort laser filaments in air. This charge is up to 600 times larger than from a comparable filament volume in air. In contrast, for atmospheric droplet concentrations and sizes, the volume-averaged overall droplet contribution to the charge is small as compared with that of the filaments along its whole propagation path. © 2009 American Institute of Physics. [DOI: 10.1063/1.3220066]

Self-guided filaments are generated by ultrashort laser pulses<sup>1–4</sup> through a dynamic balance between Kerr self-focusing and defocusing by the free electrons released from the propagation medium by the pulse itself. Filaments can propagate over distances beyond 100 m,<sup>5</sup> be initiated remotely<sup>6</sup> and propagate through fogs and clouds,<sup>7,8</sup> turbulence,<sup>9</sup> or reduced pressures.<sup>10</sup> Hence, they are ideally suited for atmospheric applications.<sup>4,11</sup> In particular, charges released by the filaments provide an electrically conducting path for high-voltage discharges<sup>12</sup> or lightning control,<sup>13</sup> and assist water nucleation<sup>11</sup> in the atmosphere in a similar way as cosmic rays or other ionizing particles do.<sup>14</sup>

In wet meteorological conditions or under rain, droplets hit by the laser ionize and contribute to the generation of electric charges in the atmosphere. On the timescale of the pulse duration, spherical droplets focus the beam onto a nanometric hot spot, where the ionization efficiency is strongly increased.<sup>15</sup> Then, the droplet explodes within a few microseconds<sup>16</sup> due to the energy released by the pulse. At this time, both the local charge release at the hot spot and the charge stabilization close to the particle surface yield an inhomogeneous charge distribution within the droplet. As a consequence, individual fragments resulting from droplet explosion bear a net charge, which can further ionize the surrounding atmosphere. Up to now, this charge had neither been estimated nor considered in models of filamentation in the atmosphere.

In this letter, we estimate the contribution of water droplets to the laser-induced electric charge release along laser filaments. We show that it is much higher than the charge released by a comparable volume of the filament in air. However at typical atmospheric droplet densities, their spatially averaged contribution is smaller than that of air. As a consequence, the charges released by the droplet either rapidly neutralize each other or can be considered as a secondary process in lightning control experiments using laser filaments.

The Helvetera platform<sup>17</sup> delivered laser pulses of up to 27.5 mJ energy and 65 fs Fourier-limited duration (420 GW peak power) at a wavelength of 800 nm and 100 Hz repetition rate. The slightly diverging beam ( $f/D=1400$ ) had an initial diameter of  $2 \times 2.4$  mm. In a first configuration (Fig. 1), the laser was slightly focused by an  $f=2.8$  m lens. 1-m-long laser filaments started at the nonlinear focus

$\sim 3.5$  m downstream, between two planar electrodes of  $1 \times 1$  cm that were swept along the beam. Alternatively, the beam was strongly focused between the electrodes by an  $f=5$  cm lens.

One electrode was set to a potential of +2 kV, while the other one was grounded through a 27 k $\Omega$  resistor. The time-integrated voltage at the resistor, measured with 12.5 kHz bandwidth, yielded the total collected charge, assuming a constant dielectric permittivity.

A piezoelectric nozzle (Microdrop MD K 140, and MD E 201H driver) launched  $\sim 100$   $\mu\text{m}$  diameter water droplets, synchronized so that each laser shot hit a droplet between the electrodes. The data acquisition was triggered by a sonometric detector<sup>18</sup> recording the acoustic shockwave of the droplet explosion to ensure its presence in the beam. The experiment was performed at atmospheric pressure, 20–22 °C temperature and relative humidity of 30–35%.

We detected charge only on the high-voltage (positive) electrode, excluding the detection of positive ions. The laser conditions had little influence on the time of flight (TOF) of the collected charges, excluding fragments which ejection speed strongly depends on the incident laser intensity.<sup>16</sup> Finally, we collected almost no free electrons, since their mobility ( $10^4$   $\text{cm}^2/\text{s V}$  in air<sup>19</sup>) would lead to a TOF of 25 ns to the positive electrode, much longer than the picosecond time scale of attachment. In contrast, the average TOF of the detected charge carriers amounts to 50–65  $\mu\text{s}$ , consistent with the  $\text{cm}^2/\text{s V}$  range of the  $\text{O}_2^-$  ions mobility in a weakly ionized plasma.<sup>19</sup> Our relatively slow measurement therefore mostly focuses on the  $\text{O}_2^-$  ions, which are representative of the charge generated in the filaments.<sup>20</sup> More precisely, the electron density after the laser shot is governed by

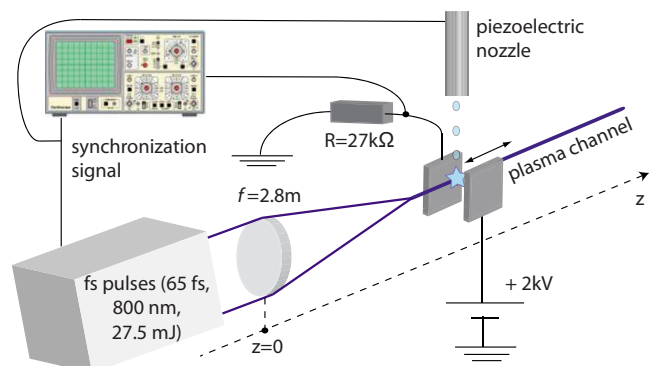


FIG. 1. (Color online) Experimental setup.

<sup>a)</sup>Electronic mail: jerome.kasparian@unige.ch.

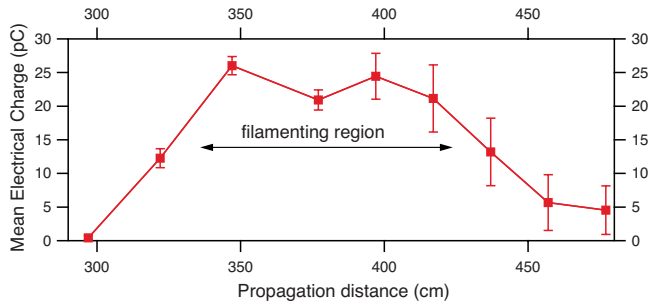


FIG. 2. (Color online) Longitudinal dependence of the charge collected from laser filaments in air, following the typical charge distribution in filaments. Error bars: one standard deviation over 150 measurements.

$dN_e/dt = -\eta N_e - \beta N_e^2$ , where  $\eta$  and  $\beta$ , respectively, represent the attachment to  $O_2$  molecules (yielding  $O_2^-$  ions) and the recombination with positive ions. In air at atmospheric pressure,  $\eta = 7.5 \times 10^6 \text{ s}^{-1}$  and  $\beta = 3.9 \times 10^{-8} \text{ cm}^3 \text{ s}^{-1}$ ,<sup>21</sup> so that 5.8% of the electrons undergo attachment and generate  $O_2^-$  ions.

The longitudinal dependence of the charge collected along a bundle of 3–5 filaments in air, for 22 mJ pulses of 65 fs Fourier-limited duration (Fig. 2) follows the typical plasma density in filaments.<sup>18</sup> This confirms that our measurement is representative of the charge generated in the filament and validates the detection technique. Considering three plasma channels with a typical electron density of  $10^{16} \text{ cm}^{-3}$  in the  $10 \mu\text{m}$  diameter core of the filaments, the 1 cm long filament section located between the electrodes bear  $\sim 3.8 \text{ nC}$ . We therefore collect almost 0.5% of the initial electron density, i.e., almost 9% of the generated  $O_2^-$  ions. This limited collection efficiency is due to a partial neutralization of the  $O_2^-$  ions by recombination during their TOF to the electrodes.<sup>22</sup>

Inserting a  $100 \mu\text{m}$  droplet in the middle of the filament bundle ( $z = 375 \text{ cm}$ ) increases the collected charge by several pC [Fig. 3(a)]. The droplet contribution steeply increases from 8 to 24 pC above 120 GW incident power, i.e., when the pulse intensity reaches several hundreds of  $\text{GW}/\text{cm}^2$ , sufficient to fragment the droplets<sup>16</sup> even if they are not hit by the filament itself. Below 120 GW, the charge release by the droplet is almost constant, consistent with the intensity clamping within the filaments.<sup>23</sup> The threefold increase in the charge released by the droplet, as compared with the 1 cm long section of the filaments bundle, corresponds to a local 600-fold increase for a comparable volume.

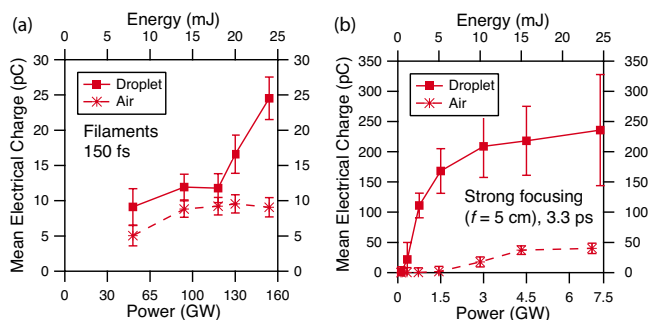


FIG. 3. (Color online) Power dependence of the charge collected in air with or without laser-droplet interaction. (a) Self-guided filaments generated by a slightly chirped pulse. (b) Focused beam ( $f = 50 \text{ mm}$ ). Error bars: one standard deviation over 500 measurements.

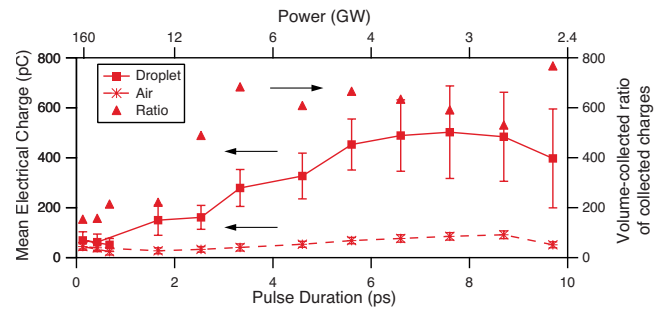


FIG. 4. (Color online) Chirp dependence of the charge emission by air and water droplets under illumination by strongly focused laser pulses of 24 mJ energy. Right scale: relative increase in the collected charge due to the laser-droplet interaction.

In contrast, the charge emitted by the droplet in a strongly focused incident beam [Fig. 3(b)] continuously varies with the incident power until 3 GW ( $2 \times 10^{14} \text{ W}/\text{cm}^2$  at the  $80 \mu\text{m}$  diameter waist) and then saturates, reaching a value about ten times the charge released in air in similar focusing conditions. Such enhancement corresponds to a factor of 900 when comparing with an equivalent volume of air illuminated by a strongly focused beam. The continuous increase in the emitted charge is due to the fact that the intensity at the focus is proportional to the incident power, contrary to the clamped intensity of the filaments.

Although the *local* charge release by the droplets is strong as compared to that released by the filaments in the air, the *spatially averaged* contribution is moderate. A typical cloud density of 1 droplet/ $\text{mm}^3$  (Ref. 24) corresponds to 10 droplets per meter along a  $100 \mu\text{m}$  diameter filament. The droplets therefore cover only 0.1% of the filament volume, which averages their 600-fold local enhancement in the charge release to only 60% of the total generated charge. Typical atmospheric cloud particles are however 10 to 100 times smaller than in our experiments, and therefore release much less charges. As a consequence, the contribution of atmospheric droplets to the charge release is marginal in the action of ultrashort laser pulses in the atmosphere, e.g., in the context of lightning triggering. However, they could locally contribute to the droplet growth through electrostatic collapse resulting in larger, more stable droplets.

Both the absolute charge emitted by a droplet and its relative contribution to the total generated charge are higher for longer, chirped pulses up to 3.5 ps (Fig. 4). Longer pulses ionize water more efficiently by allowing cascade ionization, contrary to subpicosecond pulses. The charge release in the air depends less on the pulse duration, since the contribution of avalanche ionization for durations below 10 ps keeps moderate (e.g., 12% for  $I = 10^{12} \text{ W}/\text{cm}^2$ ). As a consequence, self-compression in the filaments<sup>25</sup> is expected to limit the charge release efficiency of the droplets illuminated by filaments, and therefore to reduce the contribution of atmospheric aerosols to the ionization. Moreover, since the pulse duration inside the filaments depends little on that of the incident pulses, the initial chirp of the pulses does not influence much the charge released by the filaments in air.

As a conclusion, we have characterized the contribution of individual water droplets to the electric charge generated in air by filamenting as well as strongly focused ultrashort laser pulses. Droplets of  $100 \mu\text{m}$  diameter significantly enhance the local charge generation under filament illumina-

tion, up to a factor of 600 at the droplet scale. However, actual atmospheric aerosols have a negligible space-averaged contribution to the atmospheric ionization and their influence on the action of laser filaments on the electric activity of thunderclouds is negligible. The electrostatic collapse of droplets of opposite charge may however contribute to droplet growth in subsaturated atmospheres<sup>11</sup>

This work has been funded by the Swiss FNS (Grant Nos. 200021-116198 and 200021-125315) and SER (Grant No. COST P18 action C06.0114).

- <sup>1</sup>S. L. Chin, S. A. Hosseini, W. Liu, Q. Luo, F. Theberge, N. Akozbek, A. Becker, V. P. Kandidov, O. G. Kosareva, and H. Schroeder, *Can. J. Phys.* **83**, 863 (2005).
- <sup>2</sup>A. Couairon and A. Mysyrowicz, *Phys. Rep.* **441**, 47 (2007).
- <sup>3</sup>L. Bergé, S. Skupin, R. Nuter, J. Kasparian, and J.-P. Wolf, *Rep. Prog. Phys.* **70**, 1633 (2007).
- <sup>4</sup>J. Kasparian and J.-P. Wolf, *Opt. Express* **16**, 466 (2008).
- <sup>5</sup>B. La Fontaine, F. Vidal, Z. Jiang, C. Y. Chien, D. Comtois, A. Desparois, T. W. Johnson, J.-C. Kieffer, and H. Pépin, *Phys. Plasmas* **6**, 1615 (1999).
- <sup>6</sup>M. Rodriguez, R. Bourayou, G. Méjean, J. Kasparian, J. Yu, E. Salmon, A. Scholz, B. Stecklum, J. Eislöffel, U. Laux, A. P. Hatzes, R. Sauerbrey, L. Wöste, and J.-P. Wolf, *Phys. Rev. E* **69**, 036607 (2004).
- <sup>7</sup>F. Courvoisier, V. Boutou, J. Kasparian, E. Salmon, G. Méjean, J. Yu, and J.-P. Wolf, *Appl. Phys. Lett.* **83**, 213 (2003).
- <sup>8</sup>G. Méjean, J. Kasparian, J. Yu, E. Salmon, S. Frey, J.-P. Wolf, S. Skupin, A. Vinçotte, R. Nuter, S. Champeaux, and L. Bergé, *Phys. Rev. E* **72**, 026611 (2005).
- <sup>9</sup>R. Salamé, N. Lascoux, E. Salmon, J. Kasparian, and J. P. Wolf, *Appl. Phys. Lett.* **91**, 171106 (2007).
- <sup>10</sup>G. Méchain, G. Méjean, R. Ackermann, P. Rohwetter, Y.-B. André, J. Kasparian, B. Prade, K. Stelmaszczyk, J. Yu, E. Salmon, W. Winn, L. A. Schlie, A. Mysyrowicz, R. Sauerbrey, L. Wöste, and J.-P. Wolf, *Appl. Phys. B: Lasers Opt.* **80**, 785 (2005).
- <sup>11</sup>J. Kasparian, M. Rodriguez, G. Méjean, J. Yu, E. Salmon, H. Wille, R. Bourayou, S. Frey, Y.-B. André, A. Mysyrowicz, R. Sauerbrey, J.-P. Wolf, and L. Wöste, *Science* **301**, 61 (2003).
- <sup>12</sup>M. Rodriguez, R. Sauerbrey, H. Wille, L. Wöste, T. Fujii, Y.-B. André, A. Mysyrowicz, L. Klingbeil, K. Rethmeier, W. Kalkner, J. Kasparian, E. Salmon, J. Yu, and J.-P. Wolf, *Opt. Lett.* **27**, 772 (2002).
- <sup>13</sup>J. Kasparian, R. Ackermann, Y.-B. André, G. Méchain, G. Méjean, B. Prade, P. Rohwetter, E. Salmon, K. Stelmaszczyk, J. Yu, A. Mysyrowicz, R. Sauerbrey, L. Wöste, and J.-P. Wolf, *Opt. Express* **16**, 5757 (2008).
- <sup>14</sup>F. Yu, *Atmos. Chem. Phys.* **6**, 5193 (2006).
- <sup>15</sup>V. Boutou, C. Favre, S. C. Hill, Y. L. Pan, R. K. Chang, and J. P. Wolf, *Appl. Phys. B: Lasers Opt.* **75**, 145 (2002).
- <sup>16</sup>A. Lindinger, J. Hagen, L. D. Socaciu, T. M. Bernhardt, L. Wöste, D. Duft, and T. Leisner, *Appl. Opt.* **43**, 5263 (2004).
- <sup>17</sup>A detailed description of the laser system can be found under: <http://www.gap.unige.ch/biophotonics/helvetica.htm>.
- <sup>18</sup>J. Yu, D. Mondelain, J. Kasparian, E. Salmon, S. Geffroy, C. Favre, V. Boutou, and J. P. Wolf, *Appl. Opt.* **42**, 7117 (2003).
- <sup>19</sup>M. Yamaura, N. Hayashi, S. Ihara, S. Satoh, and C. Yamabe, *J. Appl. Phys.* **95**, 6007 (2004).
- <sup>20</sup>B. La Fontaine, F. Vidal, D. Comtois, C.-Y. Chien, A. Deparois, T. W. Johnston, J.-C. Kieffer, H. P. Mercure, H. Pépin, and F. A. M. Rizk, *IEEE Trans. Plasma Sci.* **27**, 688 (1999).
- <sup>21</sup>T. B. Petrova, H. D. Ladouceur, and A. P. Baronavski, *Phys. Plasmas* **15**, 053501 (2008).
- <sup>22</sup>S. Tzortzakis, B. Prade, M. Franco, and A. Mysyrowicz, *Opt. Commun.* **181**, 123 (2000).
- <sup>23</sup>J. Kasparian, R. Sauerbrey, and S. L. Chin, *Appl. Phys. B: Lasers Opt.* **71**, 877 (2000).
- <sup>24</sup>H. R. Pruppacher and J. D. Klett, *Mircophysics of Clouds and Precipitation* (Kluwer, Dordrecht, 1997).
- <sup>25</sup>A. Couairon, M. Franco, A. Mysyrowicz, J. Biegert, and U. Keller, *Opt. Lett.* **30**, 2657 (2005).

## Higher-Order Kerr Terms Allow Ionization-Free Filamentation in Gases

P. Béjot,<sup>1,2</sup> J. Kasparian,<sup>1,\*</sup> S. Henin,<sup>1</sup> V. Loriot,<sup>2</sup> T. Vieillard,<sup>2</sup> E. Hertz,<sup>2</sup> O. Faucher,<sup>2</sup> B. Lavorel,<sup>2</sup> and J.-P. Wolf<sup>1</sup>

<sup>1</sup>*Université de Genève, GAP-Biophotonics, 20 rue de l'École de Médecine, 1211 Geneva 4, Switzerland*

<sup>2</sup>*Laboratoire Interdisciplinaire CARNOT de Bourgogne (ICB), UMR 5209 CNRS-Université de Bourgogne, BP 47870, 21078 Dijon Cedex, France*

(Received 6 May 2009; revised manuscript received 8 February 2010; published 12 March 2010)

We show that higher-order nonlinear indices ( $n_4, n_6, n_8, n_{10}$ ) provide the main defocusing contribution to self-channeling of ultrashort laser pulses in air and argon at 800 nm, in contrast with the previously accepted mechanism of filamentation where plasma was considered as the dominant defocusing process. Their consideration allows us to reproduce experimentally observed intensities and plasma densities in self-guided filaments.

DOI: 10.1103/PhysRevLett.104.103903

PACS numbers: 42.65.Jx, 37.10.Vz, 42.65.Tg, 78.20.Ci

The filamentation of ultrashort laser pulses in gases [1] has attracted a lot of interest in recent years because of its physical interest as well as its potential applications [2–5]. Filaments are self-channeled structures propagating over many Rayleigh lengths without diffraction. They are generally considered to stem from a dynamic balance between Kerr focusing and defocusing by the plasma generated at the nonlinear focus. Numerical simulations based on this balance report a core intensity of several  $10^{13}$  W/cm<sup>2</sup> and typical electron densities of several  $10^{16}$  cm<sup>-3</sup> [3,4]. Consequently, plasma ionization is generally admitted as necessary for an ultrashort pulse to experience self-channeling in gases.

But the plasma density provided by this description of filamentation appears overestimated as compared with experimental measurements. As reviewed in [6], such measurements are dispersed over several orders of magnitude, especially due to different focusing conditions and divergent assumptions about the core diameter of the filaments, but the electron density in a filament generated by a slightly focused beam is more likely to amount to  $10^{14}$ – $10^{15}$  cm<sup>-3</sup> [6]. This value, as well as the discrepancy by more than 1 order of magnitude with numerical simulations, was recently confirmed [7]. The observation of so-called plasma-free filamentation [8,9], as well as the consideration that a balance between the instantaneous Kerr term and the time-integrated plasma contribution implies strongly asymmetric pulse shapes [10], periodically led to challenge the role of plasma in laser filamentation.

However, up to now, no other process seriously challenged plasma as the main defocusing process balancing the Kerr self-focusing. Nurhuda *et al.* proposed that the saturation of the nonlinear susceptibility  $\chi^{(3)}$  should be taken into account [11]. Such saturation can be described as negative higher-order Kerr terms. The nonlinear index of air induced by high-power femtosecond laser pulses can be written as  $\Delta n_{\text{Kerr}} = n_2 I + n_4 I^2 + n_6 I^3 + n_8 I^4 + \dots$ , where  $I$  is the incident intensity and the  $n_{2*j}$  coefficients are related to  $\chi^{(2*j+1)}$  susceptibilities. This nonlinear index

is generally truncated after its first term,  $n_2$  [2–5], mostly because of the lack of data about the values of the subsequent terms.

Numerical works have investigated the influence of the quintic nonlinear response on the propagation dynamics in gases, although without knowledge of its value [12–16]. They showed that  $n_4$  is negative; i.e., the  $\chi^{(5)}$  susceptibility is a defocusing term. It tends to stabilize the propagation of ultrashort laser pulses in air and to decrease both the electron density and the maximal on-axis intensity. Consequently, the losses due to multiphoton absorption (MPA), which lead to the end of the filamentation, are reduced and pulse self-channeling is sustained over longer distances. However, plasma generation still appeared as necessary for filament stabilization. Moreover, the value of  $n_4$  was set arbitrarily, which limits the conclusiveness of these studies. Finally, the lack of data prevented any evaluation of a possible effect of the further-order nonlinear refractive indices.

However, the higher-order Kerr indices have recently been measured in N<sub>2</sub>, O<sub>2</sub>, and Ar by Loriot *et al.* [17]. The reader is referred to this work for a detailed description of this experimental determination. In this Letter, we investigate their influence on numerical simulations of laser filamentation. We show that their values are sufficient to provide the dominant contribution to the defocusing terms of self-channeling. Their implementation in numerical simulations yields the experimentally observed plasma density. As a consequence, contrary to previously held beliefs, a plasma is not required for the observation of filamentation. Rather, plasma generation can be considered as a by-product of the self-guiding of laser filaments.

We implemented these nonlinear coefficients into a numerical model describing the propagation of ultrashort high-power pulses [18]. We consider a linearly polarized incident electric field at  $\lambda_0 = 800$  nm with cylindrical symmetry around the propagation axis  $z$ . The scalar envelope  $\varepsilon(r, t, z)$ , assumed to vary slowly in time and along  $z$ , evolves according to the propagation equation:

TABLE I. Coefficients of the nonlinear refractive index expansion of N<sub>2</sub> and O<sub>2</sub> at 1 bar pressure, and interpolation to air, as used in the present work [17].

Species	$n_2(10^{-19} \text{ cm}^2/\text{W})$	$n_4(10^{-33} \text{ cm}^4/\text{W}^2)$	$n_6(10^{-46} \text{ cm}^6/\text{W}^3)$	$n_8(10^{-59} \text{ cm}^8/\text{W}^4)$
N <sub>2</sub>	1.1 ± 0.2	-0.5 ± 0.27	1.4 ± 0.15	-0.44 ± 0.04
O <sub>2</sub>	1.6 ± 0.35	-5.2 ± 0.5	4.8 ± 0.5	-2.1 ± 0.14
Air	1.2 ± 0.23	-1.5 ± 0.3	2.1 ± 0.2	-0.8 ± 0.06

$$\partial_z \varepsilon = \frac{i}{2k_0} \Delta_{\perp} \varepsilon - i \frac{k''}{2} \partial_t^2 \varepsilon + i \frac{k_0}{n_0} \left( \sum_{j=1}^4 n_{2^*j} |\varepsilon|^{2^*j} \right) \varepsilon - i \frac{k_0}{2n_0^2 \rho_c} \rho \varepsilon - \frac{\varepsilon}{2} \sum_{l=O_2, N_2} \left( \sigma_l \rho + \frac{W_l(|\varepsilon|^2) U_l}{|\varepsilon|^2} (\rho_{\text{at}_l} - \rho) \right) \quad (1)$$

where  $k_0 = 2\pi n_0/\lambda_0$  and  $\omega_0 = 2\pi c/\lambda_0$  are the wave number and the angular frequency of the carrier wave, respectively,  $n_0$  is the linear refractive index at  $\lambda_0$ ,  $k'' = \frac{\partial^2 k}{\partial \omega^2} |_{\omega_0}$  is the second order dispersion coefficient,  $\rho_{\text{at}}$  the neutral atoms density,  $\rho$  the electron density,  $\rho_c = \epsilon_0 m \omega_0^2 / e^2$  is the critical electron density,  $m$  being the electron mass and  $e$  its charge.  $W_l(|\varepsilon|^2)$  and  $\sigma_l$  are the photoionization probability and the inverse Bremsstrahlung cross section of species  $l$  respectively (with ionization potential  $U_l$ ), and  $t$  refers to the retarded time in the reference frame of the pulse. The right-hand terms of Eq. (1) account for spatial diffraction, second order group-velocity dispersion (GVD), instantaneous nonlinear effects (i.e., the nonlinear refractive index of air, up to the  $n_8$  term), plasma defocusing, inverse Bremsstrahlung and multiphoton absorption, respectively. As compared with previously published data [17], we used values of the higher-order refractive indices (Table I) incorporating the correction for the coherent artifact [19], i.e., adequately subtracting its electronic contribution at play in the original measurement of Ref. [17]. This correction results in dividing each  $n_{2^*j}$  term by  $j + 1$ . Owing to the short pulse duration (30 fs) used in the simulations, the delayed orientational response is disregarded. The

propagation dynamics of the electric field is coupled with the density of the electrons originating from the ionization of both O<sub>2</sub> and N<sub>2</sub>:  $\rho = \rho_{O_2} + \rho_{N_2}$ . This density is governed by the multispecies generalized Keldysh-PPT (Perelomov-Popov-Terent'ev) formulation [3,6].

We used this model to simulate the propagation of an ultrashort pulse typical of laboratory-scale experiments: 1 mJ energy, 30 fs FWHM pulse duration without initial chirp (hence, about 3.9 critical powers  $P_{\text{cr}}$ ), an initial waist of  $\sigma_r = 4$  mm, a focal length  $f = 1$  m and a pressure of 1 bar. Figures 1 and 2 compare the numerical results of the full model implementing Kerr terms up to  $n_8$  and of the classical model, where the Kerr term is truncated to  $n_2$ . Both models lead to self-guided filaments. The full model yields a lower maximum intensity (31.6 TW/cm<sup>2</sup> vs 78 TW/cm<sup>2</sup>), although these values lie within the range of published experimental data in comparable conditions [2–5]. On the other hand, the full model predicts an electron density 40 times below the classical one ( $1.1 \times 10^{15} \text{ cm}^{-3}$  vs  $4.2 \times 10^{16} \text{ cm}^{-3}$ ). While the latter value is comparable with the output of other numerical works [2–5], the full model agrees with the available experimental measurements of the electron density [6,7].

Note that, with the considered parameters, the full model yields a more strict intensity clamping than the classical one [20]. It predicts an intensity constant within 20% over 15 cm (vs 9.5 cm in the case of the classical model), a length well comparable to experimental data reported to date in air for mJ pulses [3,4,21,22]. This stricter clamping can be explained by the lower electron density, which results in weaker multiphoton losses, allowing a slower decay of the filament intensity and ionization. The full model also yields a narrower output spectrum (Fig. 3),

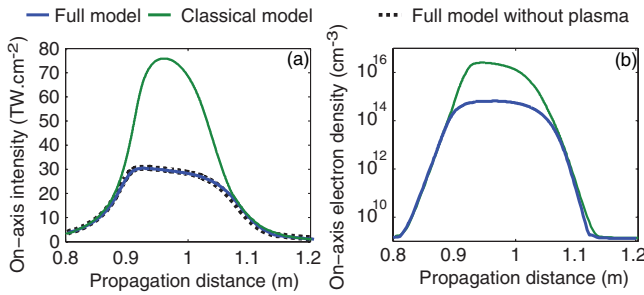


FIG. 1 (color online). (a) On-axis intensity and (b) plasma density as a function of the propagation distance for the classical model (considering only  $n_2$  term of the Kerr index and the plasma defocusing), the full model, as well as the full model without plasma.

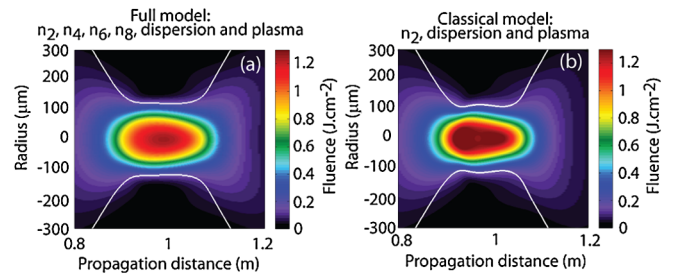


FIG. 2 (color online). Fluence distribution in air as a function of the propagation distance for the full model (a) and the classical model including  $n_2$ , ionization and GVD only (b). The white lines display the quadratic radius as a function of the propagation distance.

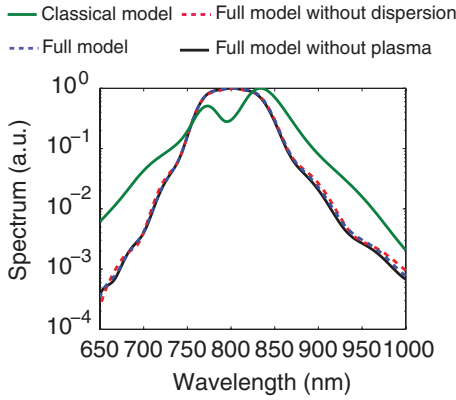


FIG. 3 (color online). Spectrum after 2 m propagation in air at atmospheric pressure.

which better fits experimental data in air [3,4]. It should therefore be considered as the reference model for numerical simulations of filamentation. Note that the almost symmetric shape of the spectrum is due to the neglect of self-steepening

On the other hand, neglecting the ionization in the full model [see Fig. 1(a)] almost does not affect the simulation output. This shows that, in contrast to the classical understanding of filamentation in gases, the self-guiding process and plasma generation are almost decoupled. Instead, the negative higher-order nonlinear indices  $n_4$  and  $n_8$  constitute the dominant regularization terms leading to filamentation in air at atmospheric pressure. This limited influence of the ionization on the filamentation dynamics when higher-order nonlinear indices are adequately considered sheds a new light on the possibility of ionization-free filamentation [8], which appears as a natural possibility in the context of the full model. Still, the dominant contribution of higher-order Kerr terms does not prevent ionization [Fig. 1(b)], which may contribute, e.g., to the conical emission.

We checked that the above conclusions are not restricted to a particular set of values of the nonlinear refractive indices. Indeed, qualitatively comparable results have been obtained when varying the indices by several tens of percent, comparable with the experimental uncertainties on the nonlinear indices. Furthermore, to compare the above molecular results with an atomic gas where no molecular orientation occurs, we performed simulations for argon, where the ionization potential is close to that of the air molecules [23], thus behaving in a similar manner as far as ionization is concerned. As in the case of air, we refined the corresponding indices to take the coherent artifact into account. The resulting values are summarized in Table II. Like in air, the full model yields lower filament

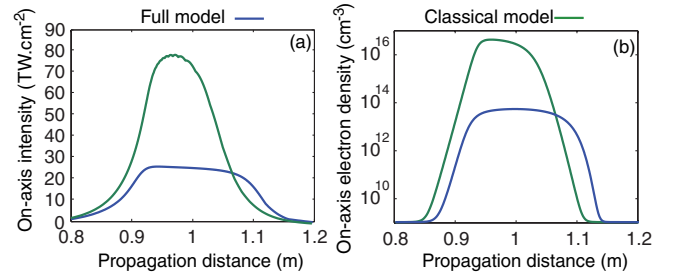


FIG. 4 (color online). (a) On-axis intensity and (b) plasma density as a function of the propagation distance for the classical model (considering only  $n_2$  term of the Kerr index and the plasma defocusing) and the full model, in Argon under 1 bar pressure.

intensity ( $28.5 \text{ TW/cm}^2$  vs  $80.9 \text{ TW/cm}^2$ ) and electron density ( $5.2 \times 10^{13} \text{ cm}^{-3}$  vs  $4.1 \times 10^{16} \text{ cm}^{-3}$ ) than the classical model (Fig. 4). Also, the evolution of the fluence profile as a function of propagation distance (Fig. 5) is quite similar in both models.

The space-time dynamics shows more differences between the full and the classical models (Fig. 6). In both cases, the pulse splits into two subpulses around 1.05 m propagation, but the full model predicts an almost symmetrical temporal profile pattern all along propagation, while the classical model yields a largely asymmetric one. This behavior illustrates the different temporal dynamics of higher-order Kerr terms as compared with the plasma generation. The former is an instantaneous phenomenon depending only on the intensity. In contrast, the plasma generated during the pulse accumulates, resulting in an ever growing contribution. As a consequence, the leading edge of the pulse propagates in a low plasma density while the trailing edge is more defocused by the much higher electron concentration it encounters. Moreover, the lower losses due to the lower plasma density in the full model allows a slight refocusing cycle around 1.15 m, which is not predicted by the classical model. The results of the full model stay unaffected when the plasma is not taken into account (e.g., the peak intensity only increases by 0.6%), which confirms that the filamentation process, including the pulse splitting is indeed driven by the higher-order Kerr terms when they are considered.

These differences in time-space dynamics illustrate the interest of implementing all orders of the Kerr effect in numerical simulations of filamentation in gases. Since successive terms  $n_{2*j}I^j$  of the Kerr index are of alternate signs and have comparable values at an intensity of about  $30\text{--}35 \text{ TW/cm}^2$  [17], the inclusion of all terms up to  $n_8$  in air (resp.  $n_{10}$  in argon) is necessary to adequately simulate the propagation of filamenting ultrashort pulses.

TABLE II. Coefficients of the nonlinear refractive index expansion of Ar at 1 bar pressure, as used in the present work [17].

$n_2(10^{-19} \text{ cm}^2/\text{W})$	$n_4(10^{-33} \text{ cm}^4/\text{W}^2)$	$n_6(10^{-45} \text{ cm}^6/\text{W}^3)$	$n_8(10^{-59} \text{ cm}^8/\text{W}^4)$	$n_{10}(10^{-74} \text{ cm}^{10}/\text{W}^5)$
$1.0 \pm 0.09$	$-0.37 \pm 1$	$0.4 \pm 0.05$	$-1.7 \pm 0.1$	$8.8 \pm 0.5$

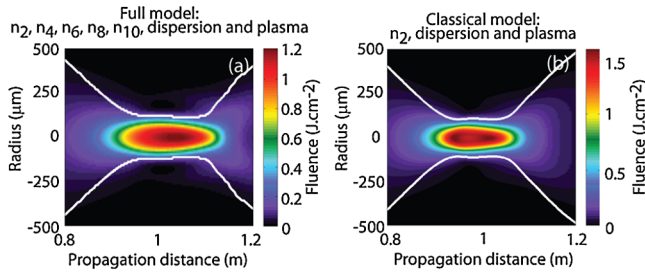


FIG. 5 (color online). Fluence distribution in 1 bar Argon as a function of the propagation distance for the full model (a), and the classical model including  $n_2$ , ionization and GVD only (b).

The observation that ionization, as well as GVD, almost do not affect the results of the full model provides an opportunity to speed up the numerical simulations. Neglecting the ionization typically cuts the computation time by a factor of 3 with little impact on the result in the conditions shown above. A parametric study would be necessary to determine the conditions, and especially the wavelengths and materials where such approximation is legitimate. Such study shall compare the intensities yielding a dynamic balance of the Kerr terms on one side, and between Kerr and plasma contributions on the other side. In air, where these intensities amount to  $31.6 \text{ TW/cm}^2$  and  $\sim 78 \text{ TW/cm}^2$ , respectively, the lower intensity for pure Kerr balance ensures the domination of the latter process. Depending on the respective values of the higher-order nonlinear indexes and ionization rates, the respective balance intensities may switch, leading to the domination of the Kerr-plasma balance.

In conclusion, we have shown that the recently measured higher-order nonlinear indices of air (up to  $n_8$ ) or argon (up to  $n_{10}$ ) dominate both the focusing and defocusing terms implied in the self-guiding of ultrashort laser pulses in these gases. As a consequence, contrary to previously held beliefs, a plasma is not required to generate filamentation in gases, and its generation is quite decoupled from the self-guiding process. Instead, filamentation is, at least in the considered conditions, governed by higher-order nonlinear indices. The usual definition of a filament as a

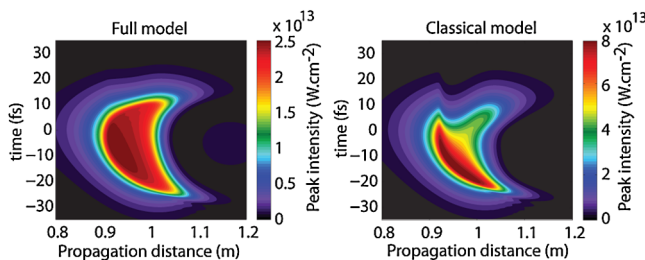


FIG. 6 (color online). Space-time dynamics of filamentation in 1 bar Argon for the full model (a), and the classical model including  $n_2$ , ionization and GVD only (b). Both models yield pulse splitting around 1.05 m propagation distance, but the full model where filamentation is driven by the instantaneous Kerr effect results in a more symmetrical temporal dynamics.

dynamic balance between the  $n_2$  Kerr self-focusing and defocusing on the plasma shall therefore be revisited. Filamentation in gases rather appears as a nonlinear self-guided propagation regime sustained by a dynamic balance between nonlinear self-focusing and defocusing effects. Depending on experimental conditions, the latter can include higher-order Kerr terms and free electrons with respective weights depending on the propagation medium considered.

This work was supported by the Conseil Régional de Bourgogne, the ANR *COMOC*, the *FASTQUAST* ITN Program of the 7th FP, the Swiss NSF (Contracts No. 200021-111688, No. 200021-116198 and R'equip program), as well as the SER in the framework of the Cost P18 program (Contract No. C06.0114).

\*jerome.kasparian@unige.ch

- [1] A. Braun, G. Korn, X. Liu, D. Du, J. Squier, and G. Mourou, *Opt. Lett.* **20**, 73 (1995).
- [2] S. L. Chin *et al.*, *Can. J. Phys.* **83**, 863 (2005).
- [3] L. Bergé, S. Skupin, R. Nuter, J. Kasparian, and J.-P. Wolf, *Rep. Prog. Phys.* **70**, 1633 (2007).
- [4] A. Couairon and A. Mysyrowicz, *Phys. Rep.* **441**, 47 (2007).
- [5] J. Kasparian and J.-P. Wolf, *Opt. Express* **16**, 466 (2008).
- [6] J. Kasparian, R. Sauerbrey, and S. L. Chin, *Appl. Phys. B* **71**, 877 (2000).
- [7] F. Theberge, W. W. Liu, P. T. Simard, A. Becker, and S. L. Chin, *Phys. Rev. E* **74**, 036406 (2006).
- [8] G. Méchain *et al.*, *Appl. Phys. B* **79**, 379 (2004).
- [9] A. Dubietis, E. Gaizauskas, G. Tamosauskas, and P. Di Trapani, *Phys. Rev. Lett.* **92**, 253903 (2004).
- [10] G. Stibenz, N. Zhavoronkov, and G. Steinmeyer, *Opt. Lett.* **31**, 274 (2006).
- [11] M. Nurhuda, A. Suda, and K. Midorikawa, *New J. Phys.* **10**, 053006 (2008).
- [12] N. Aközbek, M. Scalora, C. M. Bowden, and S. L. Chin, *Opt. Commun.* **191**, 353 (2001).
- [13] A. Couairon, *Phys. Rev. A* **68**, 015801 (2003).
- [14] A. Vinçotte and L. Bergé, *Phys. Rev. A* **70**, 061802(R) (2004).
- [15] G. Fibich and B. Ilan, *Opt. Lett.* **29**, 887 (2004).
- [16] M. Centurion, Y. Pu, M. Tsang, and D. Psaltis, *Phys. Rev. A* **71**, 063811 (2005).
- [17] V. Loriot, E. Hertz, O. Faucher, and B. Lavorel, *Opt. Express* **17**, 13429 (2009); *Opt. Express* **18**, 3011(E) (2010).
- [18] P. Béjot, C. Bonnet, V. Boutou, and J.-P. Wolf, *Opt. Express* **15**, 13295 (2007).
- [19] J.-L. Oudar, *IEEE J. Quantum Electron.* **19**, 713 (1983).
- [20] A. Becker, N. Aközbek, K. Vijayalakshmi, E. Oral, C. M. Bowden, and S. L. Chin, *Appl. Phys. B* **73**, 287 (2001).
- [21] S. A. Hosseini, J. Yu, Q. Luo, and S. L. Chin, *Appl. Phys. B* **79**, 519 (2004).
- [22] G. Méchain, T. Olivier, M. Franco, A. Couairon, B. Prade, and A. Mysyrowicz, *Opt. Commun.* **261**, 322 (2006).
- [23] V. Loriot, E. Hertz, B. Lavorel, and O. Faucher, *J. Phys. B* **41**, 015604 (2008).

# Saturation of the filament density of ultrashort intense laser pulses in air

S. Henin · Y. Petit · J. Kasparian · J.-P. Wolf · A. Jochmann · S.D. Kraft · S. Bock · U. Schramm · R. Sauerbrey · W.M. Nakaema · K. Stelmaszczyk · P. Rohwetter · L. Wöste · C.-L. Soulez · S. Mauger · L. Bergé · S. Skupin

Received: 11 February 2010 / Published online: 16 March 2010  
© Springer-Verlag 2010

**Abstract** We experimentally and numerically characterize multiple filamentation of laser pulses with incident intensities of a few TW/cm<sup>2</sup>. Propagating 100 TW laser pulses over 42 m in air, we observe a new propagation regime where the filament density saturates. As also evidenced by numerical simulations in the same intensity range, the total number of filaments is governed by geometric constraints and mutual interactions among filaments rather than by the available power in the beam.

## 1 Introduction

The propagation of ultrashort intense laser pulses in air or other transparent media is characterized by filamentation

[1–5], a self-sustained propagation regime where a dynamical balance is established between Kerr-lens self-focusing and defocussing by further nonlinear processes like interaction with plasma generated at the nonlinear focus or other higher-order saturation effects [6]. Filamentation is now well characterized from the milli-Joule to the sub-Joule levels, corresponding to powers from the GW up to the TW for pulse durations in the fs range. Recently, we demonstrated that filamentation still occurs at the multi-J level [7], displaying similar physics as at lower energies. However, this experiment was conducted with relatively long pulses between 520 fs and 65 ps. Moreover, the beam was emitted vertically, so that filaments were observed indirectly by imaging or LIDAR (Light Detection and Ranging) from the ground. Therefore, a direct comparison of multi-TW pulse dynamics with the experimentally reported results at much lower powers and shorter pulse durations (30–200 fs) was not straightforward.

A prominent property classically attributed to filamentation is the linear dependency of the filament number with the input power. As early as 1973, Campillo et al. [8] theoretically predicted from the cubic Schrödinger equation that self-focusing cells should each contain a number of critical powers,  $P_{cr}$ , depending on their shape, with a minimum of  $6.7P_{cr}$  in the case of square cells. In the context of self-channeling of femtosecond filaments, several experimental data collected from different laser systems confirmed a linear dependence of the filament number with power, with one filament per  $\sim 5P_{cr}$  ( $P_{cr} \approx 4$  GW in air at 800 nm). Such value was observed close to the filamentation threshold [9–11], in the multiple-filamentation regime of TW-class lasers [12], as well as in the case of multi-TW, multi-Joule experiments (26 J, 32 TW) [7].

In this work, we investigate the horizontal propagation of a 3 J, 100 TW (30 fs) laser pulse over 42 m in air. We char-

---

S. Henin · Y. Petit · J. Kasparian (✉) · J.-P. Wolf  
Teramobile, GAP, Université de Genève, 20 rue de l'Ecole de  
Médecine, 1211 Genève 4, Switzerland  
e-mail: [jerome.kasparian@unige.ch](mailto:jerome.kasparian@unige.ch)

A. Jochmann · S.D. Kraft · S. Bock · U. Schramm · R. Sauerbrey  
Forschungszentrum Dresden-Rossendorf, Bautzner Landstraße  
400, 01328 Dresden, Germany

W.M. Nakaema · K. Stelmaszczyk · P. Rohwetter · L. Wöste  
Teramobile, Institut für Experimentalphysik, Freie Universität  
Berlin, Arnimallee 14, 14195 Berlin, Germany

C.-L. Soulez · S. Mauger · L. Bergé  
CEA, DAM, DIF, 91297 Arpajon, France

S. Skupin  
Max Planck Institute for the Physics of Complex Systems,  
01187 Dresden, Germany

S. Skupin  
Institute of Condensed Matter Theory and Optics, Friedrich  
Schiller University, 07742 Jena, Germany

acterize the density of the high-intensity filaments, which substantially deviates from the above-recalled linear dependency. This deviation results from the saturation of the filament number per unit surface of the transverse beam profile, based on the typical cross-section of the photon bath surrounding the filament cores along their self-guiding. Dimensions of this cross-section put an upper limit on the local filament density, which becomes almost independent of the input power along the self-guiding range. While our finding challenges the previously established linearity rule, it provides new evidence that both the filament occupation constraints inside photon baths and their mutual interaction are key ingredients of the multifilamentation dynamics. Three-dimensional numerical simulations confirm these features by reproducing the major experimental patterns at comparable incident intensities over smaller beam scales.

## 2 Material and methods

Experiments were performed using the Ti:Sa chirped pulse amplification chain at Forschungszentrum Dresden-Rossendorf. The laser provided up to 3 J, 100 TW pulses of 30 fs duration, at a repetition rate of 10 Hz and central wavelength of 800 nm. The pulse energy was adjusted by rotating a half-waveplate associated with a polarizer before the grating compressor. The beam was transported in a vacuum tube to the experimental hall, where it was launched, collimated (i.e. as a parallel beam) with a diameter of  $\sim 10$  cm,

through a 6 mm thick fused silica window, into 42 m of free propagation in air. The dispersion in the window was pre-compensated by adequately adjusting the grating compressor of the laser system.

The multiple filamentation of the beam was characterized by both single-shot burns on photosensitive paper (Kodak Linagraph 1895, see Fig. 1), and single-shot still photographs on an optically neutral screen, recorded by a CCD camera equipped with density filters. Each filament in the beam profile was then individually identified on the images or burns, as a bright or a black spot, respectively, and located by its transverse coordinates relative to the centre of the beam. The same process, performed on either of the red, green or blue layers of the CCD camera or the burn images, yielded consistent filament numbers, with typically 10% deviations. Based on this filament identification, we computed the local filament density at any location across the laser beam.

Densitometry measurements on the red layer of the CCD camera images provided fluence profiles of the beam, which were calibrated by integrating this profile over the transverse plane at the considered propagation distance  $z$  and normalizing through the input pulse energy, neglecting the losses along propagation. This method mainly focuses on the photon bath and discards the most intense part of the filaments, which occupy a small fraction of the profile and whose fluence is truncated by the dynamics of the detector. The fluence profile is converted into intensity by dividing all flu-

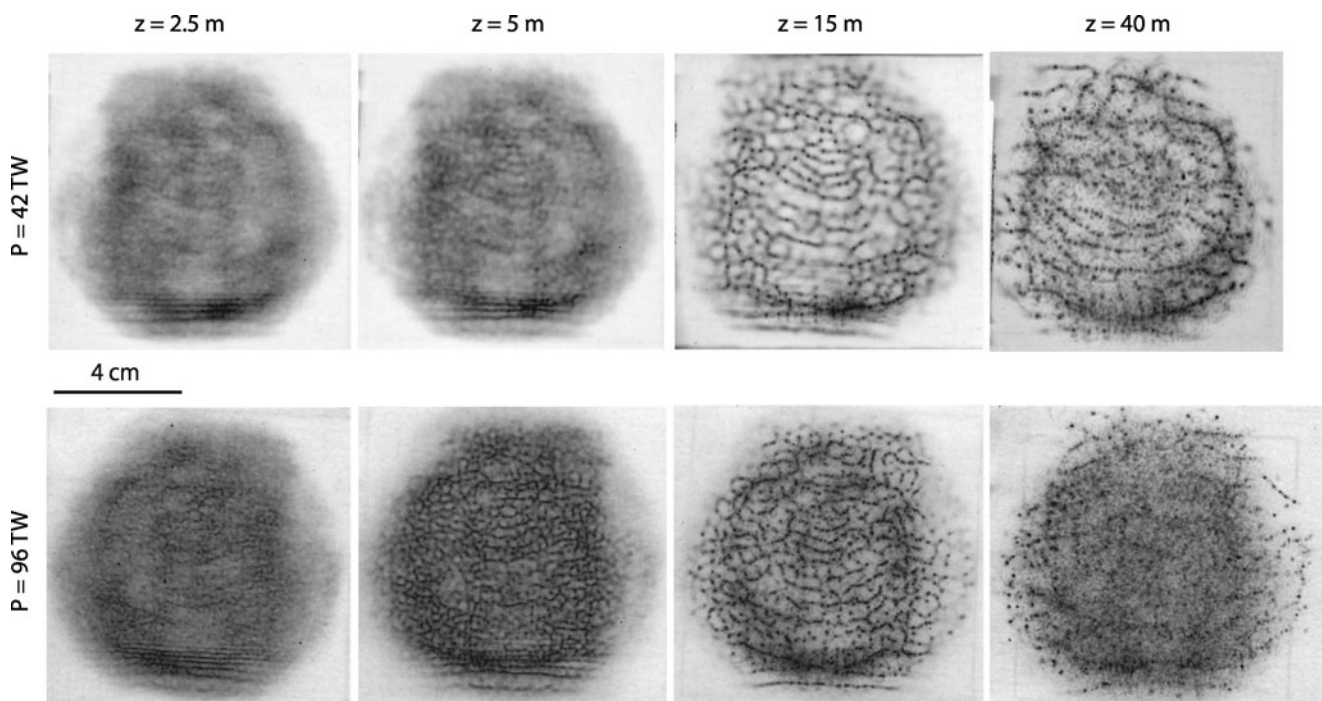


**Fig. 1** Beam profiles on burn paper of multi-TW, 30 fs pulses propagating in air, as a function of the incident power and propagation distance. Most filaments appear on lines along which filaments are spaced by a few mm

ence values by the pulse duration, which is assumed to be close to the initial one, since the photon bath is barely affected by plasma temporal distortions.

To get more insight into the mechanism leading to the saturation of the filament density, we performed a spatially resolved analysis of the measured intensity profiles. We sampled the beam profile into 187 square elementary surfaces of  $6.6 \text{ mm} \times 6.6 \text{ mm}$ . In each elementary surface at location  $\mathbf{r}$ , we counted the filament number, which, divided by the elementary surface provided the local density of filaments  $N(\mathbf{r})$ . Moreover, the intensity profile from the densitometry, numerically averaged over the elementary surface, provided the local photon bath intensity  $I_{\text{bath}}(\mathbf{r})$ . We next compute the ratio  $p(\mathbf{r}) = I_{\text{bath}}(\mathbf{r})/N(\mathbf{r})$  in each elementary surface. This ratio corresponds to the power per filament in the considered surface, around the considered transverse position  $\mathbf{r}$  in the beam. Owing to the transverse dimension of the beam and the fact that interactions between self-focusing cells are local, we consider the 187 elementary surfaces as almost independent. Sorting the elementary surfaces according to their intensity and averaging the values of  $N(\mathbf{r})$  for each value of  $I_{\text{bath}}$  yield the average value  $N(I_{\text{bath}})$  and thereby the mean value of  $p$  for any  $I_{\text{bath}}$ :  $p(I_{\text{bath}})$ , which will be plotted in Fig. 4.

To understand the mechanism of filament saturation along the self-guiding stage, we also integrated the standard propagation model (so-called Nonlinear Envelope Equation [3]) in complete space and time resolved (3 + 1)-dimensional geometry. This model governs the laser electric field envelope  $E$  with intensity  $I = |E|^2$  and a source equation describes plasma generation. The propagation equations take into account chromatic dispersion of air, space-time focusing and self-steepening terms, and nonlinear (cubic) polarization with Kerr index  $n_2 = 2.5 \times 10^{-19} \text{ cm}^2/\text{W}$  ( $P_{\text{cr}} = 4 \text{ GW}$ ) including an instantaneous part and a Raman-delayed contribution in ratio 1/2. This choice of parameters particularly suits ultrashort infrared pulses with durations  $\leq 50 \text{ fs}$  [13, 14], undergoing plasma coupling and multiphoton absorption losses. The source equation govern-

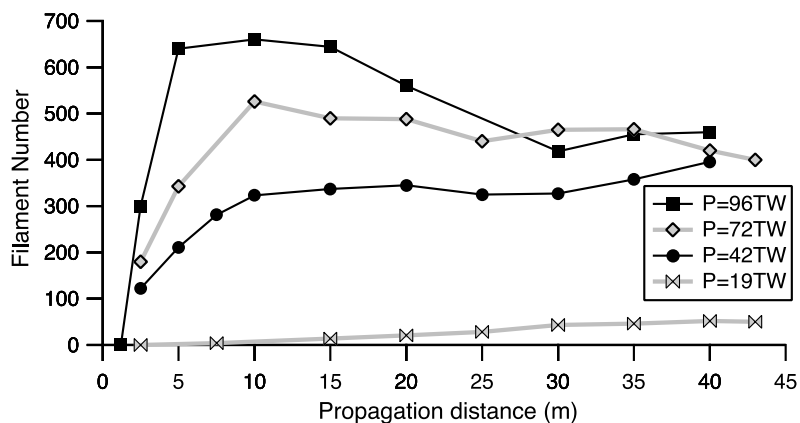
ing the free electron density  $\rho$  includes a photo-ionization rate approached by  $W(I) = \sigma_K I^K$  with cross-section  $\sigma_K = 2.9 \times 10^{-99} \text{ s}^{-1} \text{ cm}^{2K}/\text{W}^K$  ( $K = 8$  is the minimum photon number requested for ionization of  $\text{O}_2$  molecules at the laser wavelength  $\lambda_0 = 800 \text{ nm}$ ), together with avalanche ionization depending on an electron collision time of 350 fs. Electron recombination is neglected over the short time scale of the pulses.

### 3 Results and discussion

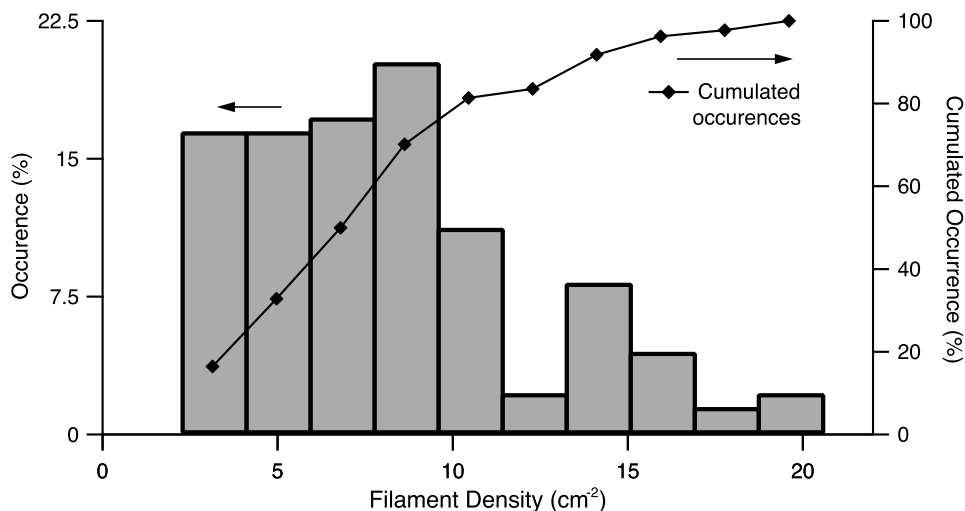
Figure 1 displays typical multifilamentation patterns at propagation distances up to  $z = 40 \text{ m}$ . The filamentary cells are organized in quasi-parallel strings mutually separated by a few mm. In each string, the filaments, identified as the most spiky structures, are separated by 1–2 mm from each other. These strings can be composed of optical cells with lower fluence, which are therefore not identified as intense filaments. The total number of filaments in the beam profile is displayed in Fig. 2 as a function of the propagation distance and the incident power. Up to 700 intense filaments are generated in the beam profile. Although this number may appear large in absolute value, it remains modest compared with the power involved. At 800 nm, an incident power close to 100 TW typically corresponds to  $25,000P_{\text{cr}}$ , which would be expected to generate up to 5000 filaments at the rate of  $5P_{\text{cr}}$  per filament. Actually, the filament number appears to be divided by a factor of almost 10 at all investigated input energies. From Figs. 1 and 2, we can see that the total number of filaments remains in the same order of magnitude over several meters. The focal spot produces a universal pattern involving a reduced number of ordered hot spots.

Figure 3 displays statistics about the local filament density  $N(\mathbf{r})$  over all elementary grid surfaces of  $6.6 \text{ mm} \times 6.6 \text{ mm}$  across the beam profile of the 96 TW pulse after 15 m of propagation. Consistent with the strong saturation of the filament number in the overall beam, the local filament density is limited to  $N_{\text{fil}} \sim 10 \text{ filaments}/\text{cm}^2$ , a value

**Fig. 2** Filament number as a function of the propagation distance and energy



**Fig. 3** Occurrence distribution of the local filament density at the propagation distance  $z = 15$  m for the 96 TW pulse



exceeded in only 20% of the elementary surfaces. This density corresponds to a typical distance of  $\sim 3$  mm between the nearest filaments. For comparison, a photon bath intensity of  $10^{13}$  W/cm<sup>2</sup> would yield a density of  $\sim 500$  filaments/cm<sup>2</sup> at the classical rate of  $5P_{\text{cr}}$ /filament. This reduced filament density was observed all along the available propagation distances, up to 42 m, as well as when reducing the incident pulse energy or chirping the incident pulses.

Due to the strong inhomogeneity of the background intensity profile across the beam,  $I_{\text{bath}}$  spans over a range of more than one order of magnitude, providing the opportunity to investigate the filament density  $N$  as a function of intensity over this range. Figure 4 displays this information, showing the ratio  $p(I_{\text{bath}}) = I_{\text{bath}}/N(I_{\text{bath}})$  as defined in the previous section and expressed in units of  $P_{\text{cr}}$ . This presentation facilitates the estimation of the power required to generate a filament in given conditions. For example, a constant power of  $5P_{\text{cr}}$ /filament, observed at low incident intensities, would result in the horizontal dotted line displayed in Fig. 4. Clearly, experimental data substantially deviate from this trend as soon as  $I_{\text{bath}}$  exceeds a few  $10^{11}$  W/cm<sup>2</sup>, showing that the saturation of the filament density does not only occur in the overall beam, but also in the local dynamics of the filamentary cells. Data reported from the literature [7, 11, 12, 15] are also plotted for reference: They fit well with our present data and show that current high-power laser systems can reach this saturation regime (see the “Helvetera” data), which had however not been identified so far.

It is well-known from both theory [16, 17] and experiments [18, 19] that isolated filaments form, besides their inner core, a surrounding photon bath with transverse dimensions of several hundreds of  $\mu\text{m}$ . Consequently, filaments in principle require a minimum surface of several mm<sup>2</sup> to develop. This cross-section corresponds to millimeter-range spacing between filaments, under which neighboring optical cells weakly interact. The mutual attraction of filaments

located a few mm apart has already been well described [20–25]. In our experiments, since we did not focus the beam, neighboring filaments can be expected to emerge in phase since they are issued from the same beam, so that interactions will be mainly attractive. In fact, we expect that in the merging process, robust filaments conveying the highest intensity will “absorb” the less intense optical cells. Therefore, underlying the saturation mechanism that limits the filament density, the interaction between filaments, initiated by their overlapping photon baths, can result in the merging of the “in excess” filaments. This merging mechanism here involves the Kerr self-focusing effect, altered by plasma generation and related losses, acting all together on interacting cells which occupy a few mm<sup>2</sup> in the beam profile at distances where the filamentation is most active. This process can be compared to that observed in the case of two beams crossing in glass, where the interferences in the photon bath reduce the available energy for filamentation and therefore decrease the filament number [26].

Thus, filaments do not only require a minimal power of  $5P_{\text{cr}}$  to be initiated, but also a minimum surface to develop and survive with their own photon bath. This minimum surface can be determined as the counterpart of the upper limit of the filament density of  $N_{\text{fil}} \sim 10$  cm<sup>-2</sup> observed in the data of Fig. 3. On this basis, we can express the fact that the filament density  $N(\mathbf{r})$  around the position  $\mathbf{r}$  (e.g., the center of one elementary surface inside the beam) is limited by both of these constraints. An approximate description can therefore be provided by the evaluation:

$$N(\mathbf{r}) = \min[I_{\text{bath}}(\mathbf{r})/5P_{\text{cr}}; N_{\text{fil}}]. \quad (1)$$

Accordingly, the number of critical powers required to generate a filament expresses in terms of the input beam power  $P_{\text{in}}$  as

$$I_{\text{bath}}(\mathbf{r})/[N(\mathbf{r})P_{\text{cr}}] = \max[5; I_{\text{bath}}(\mathbf{r})/(N_{\text{fil}}P_{\text{cr}})]. \quad (2)$$

**Fig. 4** Experimental data and model (2) of the local filament density as a function of the local photon bath intensity  $I_{\text{bath}}$  at  $z = 15$  m for the 96 TW pulse. Previously published data in different experimental conditions are displayed for reference: Multi-TW, 100 fs pulses (Teramobile laser) [12], multijoule, picosecond pulses (Alisé laser) [7], a TW, 30 fs laser (Helvetera system) [15], and a mJ, 120 fs laser (single filamentation) [11]

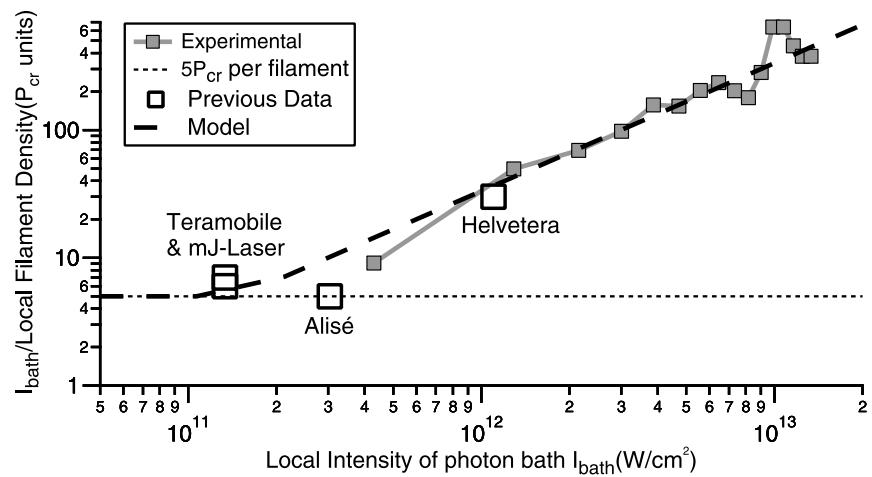
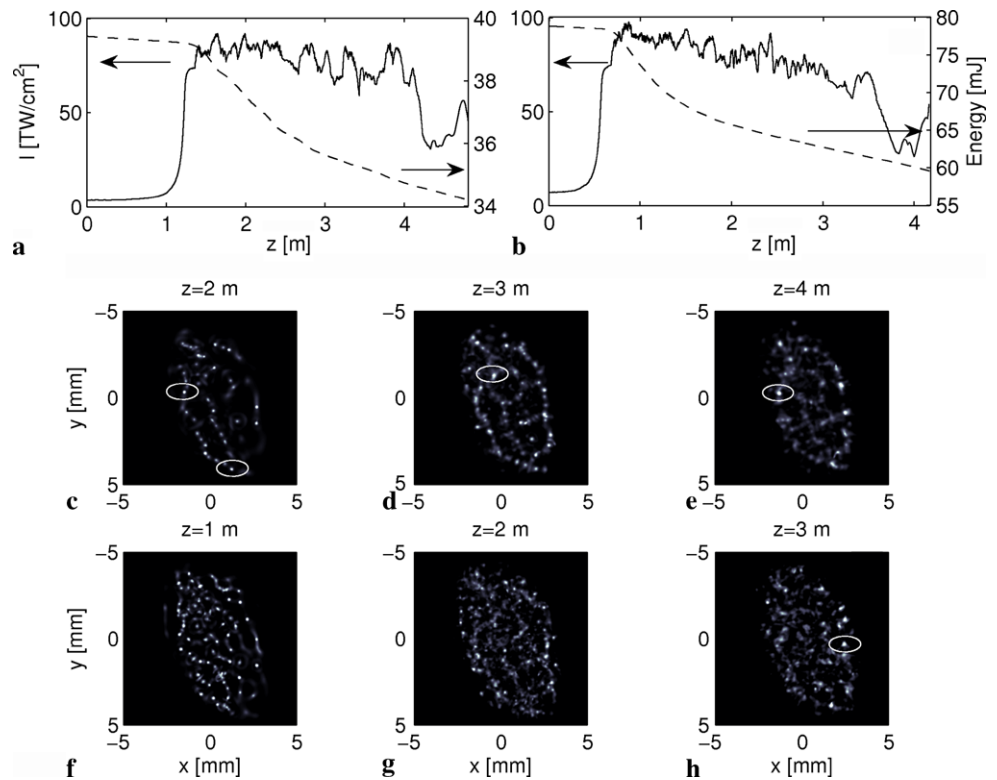


**Fig. 5** Peak intensities (solid curves, units on the left-hand side axis) and energy losses (dashed curves, units on the right-hand side axis) for the beams with (a)  $300P_{\text{cr}}$  and (b)  $600P_{\text{cr}}$  computed numerically using  $1/e^2$  beam waist of 5 mm in air. (c, d, e) and (f, g, h) show their respective fluence distributions in the (x, y) plane. White ellipses exemplify intense filaments with highest fluence



The low-intensity case of (1) and (2) corresponds to standard power regimes, while the high-intensity case is for the first time examined in this work. Figure 4 compares the outcome of this simple model with the experimental data. Despite the simplicity of the model, the agreement is excellent, showing the validity of the simple model proposed to predict the filament density at high intensities.

Our measurements therefore define a new filamentation regime, where the filament number density saturates at high input optical powers. This result apparently contradicts previous observations showing longer filamentation ranges and higher  $N_2$  fluorescence when the beam diameter is reduced [27–29]. However, these works did not directly measure the

number of filaments, but rather the  $N_2$  fluorescence emitted backwards in LIDAR configuration. In fact, closely packed filaments may here be issued from the merging of several filament germs and be longer and/or more intense, yielding a stronger signal integrated along the filamenting range.

The saturation of the filament density is also well evidenced by (3 + 1)-dimensional numerical simulations, whose results are summarized in Figs. 5 and 6. Due to the limitations of current computer capabilities, we could not simulate the  $\sim 100 \text{ cm}^2$  of the beam shown in Fig. 1 with adequate transverse resolution. Rather, we considered a smaller beam, with a long-axis beam waist of 5 mm at  $1/e^2$ , comparable to the size of the elementary surfaces used in the

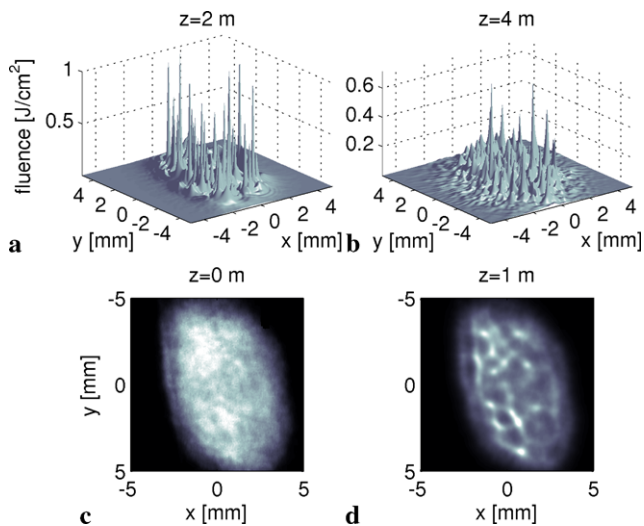


**Fig. 6** Surface plots of the transverse fluence profiles of the  $300P_{\text{cr}}$  beam at (a)  $z = 2$  m and (b)  $z = 4$  m. Image cuts of the fluence profiles of the  $300P_{\text{cr}}$  beam at (a)  $z = 0$  and (b)  $z = 1$  m

analysis of the experimental data. Since this size is close to the focal spots examined in [30], we used a fluence profile previously simulated in Fig. 9 of that work and recalled in Fig. 6(c). In order to investigate the saturation of the filament number at high intensities comparable to those of the experiments, this profile was scaled to a power of  $P_{\text{in}} = 300P_{\text{cr}}$  or  $P_{\text{in}} = 600P_{\text{cr}}$ . These values correspond to a peak intensity of 3.5 and 7 TW/cm<sup>2</sup>, respectively, comparable to that of the experimental measurements. We therefore cannot expect to reproduce systematically the multifilamentation pattern of Fig. 1, but rather to test the evolution of the filament number along the self-channeling range. Simulations ran over 256 processors and guaranteed fine resolution in both space ( $\Delta x = \Delta y = 1 \mu\text{m}$ ) and time ( $\Delta t = 0.6$  fs), with an adaptive step  $\Delta z$  along the propagation axis.

Figure 5(a) and (b) show the peak pulse intensities (solid curves) and energy losses owing to plasma generation (dashed curves) along the 4 m long propagation range, followed by pulse relaxation. The plasma density forms an almost flat plateau around the peak value  $\rho_{\text{max}} = 5 \times 10^{16} \text{ cm}^{-3}$  (not shown). Importantly, the energy losses become more pronounced at higher incident peak powers: Over the first three meters after the nonlinear focus, the relative energy loss due to plasma generation is about 10% for the  $300P_{\text{cr}}$  pulses, whereas it reaches 20% for  $600P_{\text{cr}}$ . Furthermore, Fig. 5(c, d, e) and (f, g, h) display the fluence patterns at distances beyond the nonlinear focus. Fluence is here truncated at the maximum level of 1 J/cm<sup>2</sup>, in order to discriminate better between optical structures with high and low local intensities.

Similarly to the experimental observation, filaments emerge near to the nonlinear focus along quasi-parallel lines within the profile. These lines stem from the initial beam inhomogeneities, from which small-scaled filaments emerge

(see the “optical pillars” scenario in Ref. [30]). As expected, more cells appear in the fluence pattern with double input power. Near the nonlinear focus, we count around 46 and 116 cells at  $z = 2$  and 1 m for the  $300$  and  $600P_{\text{cr}}$  beams, respectively. These filament numbers are compatible with the 60 and 120 filaments predicted by the classical estimation of  $5P_{\text{cr}}$  per filament. However, in the beam with  $300P_{\text{cr}}$ , only 20 of them (the brightest spots) are capable to exceed a fluence of 0.5 J/cm<sup>2</sup>, as detailed in Fig. 6(a). A couple of meters beyond, due to energy exchanges and active plasma defocussing [22], the weak cells are absorbed by the photon bath surrounding the strongest filaments, among which 8 can still reach the same fluence level [Fig. 6(b)] within the beam surface of  $\sim 0.5 \text{ cm}^2$ . With double power, more intense filaments are created near focus, but their number relaxes to quite similar values, i.e., around 9–10 filaments two meters after the nonlinear focus. Such process clearly illustrates the saturation of the filament density at very high incident intensities. Note the strong evacuation of energy in the beam with higher power, so that both fluence patterns become more resembling at  $z = 4$  m. Their geometric structure emphasizes more clearly the quasi-parallel lines of filaments, mutually spaced by  $\approx 2\text{--}3$  mm from each other. Scaled to  $25,000P_{\text{cr}}$ , this estimation should correspond to  $\sim 400\text{--}1600$  filaments, in reasonable agreement with the experiments (Fig. 2). Furthermore, a numerical evaluation of the  $300P_{\text{cr}}$  beam background intensity,  $I_{\text{bath}} \approx 3.2 \text{ TW/cm}^2$ , that supports the filamentary spikes with mean density of 16–20 intense filaments/cm<sup>2</sup> beyond the nonlinear focus, yields between 40 and  $50P_{\text{cr}}$ , which holds the comparison with the curve inferred from (2) and plotted in Fig. 4.

Considering the different transverse scales of the beams, we suggest that a comparison with the experimental data requires to scale the propagation distance according to the nonlinear focal lengths, which we estimate to be approximately 15 and 1.5 m in the case of the experiments and numerical simulations, respectively. Figure 6(c) and (d) illustrate the transverse fluence patterns in the early Kerr stage of the  $300P_{\text{cr}}$  beam. Before the nonlinear focus, Kerr-induced modulational instability breaks up the focal spot into primary cells mutually separated by the optimum transverse wavelength  $\lambda_{\text{opt}} = w_0 \lambda_0 (\pi / n_2 P_{\text{in}})^{1/2} \approx 1.3 \text{ mm}$  [7, 11] along the highest intensity zones of the input beam. So, the initial beam defects do condition the location of the mm-spaced strings which will further be amplified.

These numerical results confirm the experimental findings, showing that over long propagation distances, the number of atmospheric high-intensity filaments becomes independent of the initial pulse intensity and power. Light spots thus tend to exhibit similar distance of mutual separation in the mm range. Energy losses, although relatively small, help the filaments to be distributed into an “equilibrium”

pattern involving a smaller density of hot spots than in classical expectations. Small-scaled filaments are embedded inside mm-spaced strings, which are primarily designed by the fluctuations of the initial beam profile. Hence, filamentary ultrashort broad pulses tend to self-organize into a robust macroscopic ordered structure, which departs to some extent from the optically-turbulent light guide scenario proposed in Ref. [31].

Going back to the fusion mechanism recalled in the previous section, two filaments modeled as Gaussians of waist  $w_{\text{fil}} \approx 150 \mu\text{m}$  are distinguishable if their initial separation distance  $\delta$  exceeds  $2^{1/2}w_{\text{fil}}$ . In purely Kerr media, they are expected to coalesce if their individual power is larger than  $P_{\text{cr}}/4$  but remains below critical [20]. In the presence of nonlinear saturation (plasma defocussing), however, filaments with an initial distance  $\delta \leq 10^{1/2}w_{\text{fil}}$  can merge up to a power  $P_{\text{fil}} \leq 1.35P_{\text{cr}}$  [30]. In this case, nonlinear losses relax these constraints as the filaments reach lower, near-critical powers allowing merging even from larger separation distances. Multiphoton absorption thus promotes the mutual coalescence of filaments from separation distances larger than  $10^{1/2}w_{\text{fil}} \approx 0.5 \text{ mm}$ , i.e., over the mm scale. These arguments indicate that, at the very best, only one filament can be expected to occupy an area of about  $1 \text{ mm}^2$  inside the focal spot in plasma regime, which thereby justifies the experimental and numerical observations.

#### 4 Conclusion

We have investigated experimentally and numerically the multiple filamentation of high-intensity ultrashort laser pulses over 42 m in air. The filament density substantially deviates from usual linear variation with peak power, exhibiting a saturation of the filament number density across the beam profile. This saturation can be understood by considering the interaction of neighboring filaments, resulting in their mutual attraction when they are closer than a few mm from their nearest neighbors. Three-dimensional numerical simulations confirm this saturation mechanism and specify two characteristic processes in the filament dynamics: First, quasi-parallel strings of filaments are preconditioned by the initial modulations at the top of the incident beam. Second, along the propagation range promoting plasma generation and multiabsorption losses, filamentary cells bearing the highest fluences become mutually separated by mm-range distances, above which their possible fusion ceases.

**Acknowledgements** This work was granted access to the HPC resources of CCRT under the allocation 2009-x2009106003 made by GENCI (Grand Equipement National de Calcul Intensif). We acknowledge financial support from the Swiss National Science Foundation (FNS, Grants 200021-116198 and 200021-125315).

#### References

1. J. Kasparian, M. Rodriguez, G. Méjean, J. Yu, E. Salmon, H. Wille, R. Bourayou, S. Frey, Y.-B. André, A. Mysyrowicz, R. Sauerbrey, J.-P. Wolf, L. Wöste, *Science* **301**, 61 (2003)
2. A. Couairon, A. Mysyrowicz, *Phys. Rep.* **44**, 47 (2007)
3. L. Bergé, S. Skupin, R. Nuter, J. Kasparian, J.-P. Wolf, *Rep. Prog. Phys.* **70**, 1633 (2007)
4. J. Kasparian, J.-P. Wolf, *Opt. Express* **16**, 466 (2008)
5. S.L. Chin, S.A. Hosseini, W. Liu, Q. Luo, F. Théberge, N. Aközbek, A. Becker, V.P. Kandidov, O.G. Kosareva, H. Schroeder, *Can. J. Phys.* **83**, 863 (2005)
6. P. Bédot, J. Kasparian, S. Henin, V. Loriot, T. Vieillard, E. Hertz, O. Faucher, B. Lavorel, J.-P. Wolf, *Phys. Rev. Lett.* **104**, 103903 (2010)
7. P. Bédot, L. Bonacina, J. Extermann, M. Moret, J.P. Wolf, R. Ackermann, N. Lascoux, R. Salamé, E. Salmon, J. Kasparian, L. Bergé, S. Champeaux, C. Guet, N. Blanchot, O. Bonville, A. Boscheron, P. Canal, M. Castaldi, O. Hartmann, C. Lepage, L. Marmande, E. Mazataud, G. Mennerat, L. Patissou, V. Prevot, D. Raffestin, J. Ribolzi, *Appl. Phys. Lett.* **90**, 151106 (2007)
8. A.J. Campillo, S.L. Shapiro, B.R. Snydam, *Appl. Phys. Lett.* **23**, 628 (1973)
9. A.C. Bernstein, J.-C. Diels, T.S. Luk, T.R. Nelson, A. McPherson, S.M. Cameron, *Opt. Lett.* **28**, 2354 (2003)
10. W. Liu, S.L. Chin, *Opt. Express* **13**, 5750 (2005)
11. R. Salamé, N. Lascoux, E. Salmon, J. Kasparian, J.P. Wolf, *Appl. Phys. Lett.* **91**, 171106 (2007)
12. G. Méjean, J. Kasparian, J. Yu, E. Salmon, S. Frey, J.-P. Wolf, S. Skupin, A. Vinçotte, R. Nuter, S. Champeaux, L. Bergé, *Phys. Rev. E* **72**, 026611 (2005)
13. A. Couairon, S. Tzortzakis, L. Bergé, M. Franco, B. Prade, A. Mysyrowicz, *J. Opt. Soc. Am. B* **19**, 1117 (2002)
14. S. Champeaux, L. Bergé, D. Gordon, A. Ting, J. Peñano, P. Sprangle, *Phys. Rev. E* **77**, 036406 (2008)
15. S. Henin, Y. Petit, D. Kiselev, J. Kasparian, J.-P. Wolf, *Appl. Phys. Lett.* **95**, 091107 (2009)
16. S. Skupin, L. Bergé, U. Peschel, F. Luderer, *Phys. Rev. Lett.* **93**, 023901 (2004)
17. M. Kolesik, J.V. Moloney, *Opt. Lett.* **29**, 590 (2004)
18. F. Courvoisier, V. Boutou, J. Kasparian, E. Salmon, G. Méjean, J. Yu, J.-P. Wolf, *Appl. Phys. Lett.* **83**, 213 (2003)
19. W. Liu, F. Théberge, E. Arévalo, J.-F. Gravel, A. Becker, S.L. Chin, *Opt. Lett.* **30**, 2602 (2005)
20. L. Bergé, M.R. Schmidt, J. Juul Rasmussen, P.L. Christiansen, K.O. Rasmussen, *J. Opt. Soc. Am. B* **14**, 2550 (1997)
21. L. Bergé, C. Gouédard, J. Schjodt-Eriksen, H. Ward, *Physica D (Amsterdam)* **176**, 181 (2003)
22. S.A. Hosseini, Q. Luo, B. Ferland, W. Liu, S.L. Chin, O.G. Kosareva, N.A. Panov, N. Aközbek, V.P. Kandidov, *Phys. Rev. A* **70**, 033802 (2004)
23. C. Ren, R.G. Hemker, R.A. Fonseca, B.J. Duda, W.B. Mori, *Phys. Rev. Lett.* **85**, 2124 (2000)
24. Y.-Y. Ma, X. Lu, T.-T. Xi, Q.-H. Gong, J. Zhang, *Appl. Phys. B* **93**, 463 (2008)
25. E. D'Asaro, S. Heidari-Bateni, A. Pasquazi, G. Assanto, J. Gonzalez, J. Solis, C.N. Afonso, *Opt. Express* **17**, 17150 (2009)
26. K. Stelmaszczyk, P. Rohwetter, Y. Petit, M. Fechner, J. Kasparian, J.-P. Wolf, L. Wöste, *Phys. Rev. A* **79**, 053856 (2009)
27. O.G. Kosareva, N.A. Panov, N. Aközbek, V.P. Kandidov, Q. Luo, S.A. Hosseini, W. Liu, J.F. Gravel, G. Roy, S.L. Chin, *Appl. Phys. B, Lasers Opt.* **82**, 111 (2006)

28. Q. Luo, S.A. Hosseini, W. Liu, J.F. Gravel, O.G. Kosareva, N.A. Panov, N. Akozbek, V.P. Kandidov, G. Roy, S.L. Chin, *Appl. Phys. B, Lasers Opt.* **80**, 35 (2005)
29. J.F. Daigle, O. Kosareva, N. Panov, M. Bégin, F. Lessard, C. Marceau, Y. Kamali, G. Roy, V. Kandidov, S. Chin, *Appl. Phys. B, Lasers Opt.* **94**, 249 (2008)
30. S. Skupin, L. Bergé, U. Peschel, F. Lederer, G. Méjean, J. Yu, J. Kasparian, E. Salmon, J.P. Wolf, M. Rodriguez, L. Wöste, R. Bourayou, R. Sauerbrey, *Phys. Rev. E* **70**, 046602 (2004)
31. M. Mlejnek, M. Kolesik, J.V. Moloney, E.M. Wright, *Phys. Rev. Lett.* **83**, 2938 (1999)

# Laser-induced water condensation in air

Philipp Rohwetter<sup>1</sup>, Jérôme Kasparian<sup>2\*</sup>, Kamil Stelmaszczyk<sup>1</sup>, Zuoqiang Hao<sup>3</sup>, Stefano Henin<sup>2</sup>,  
Noëlle Lascoux<sup>3</sup>, Walter M. Nakaema<sup>1</sup>, Yannick Petit<sup>2</sup>, Manuel Queißer<sup>1</sup>, Rami Salamé<sup>3</sup>,  
Estelle Salmon<sup>3</sup>, Ludger Wöste<sup>1</sup> and Jean-Pierre Wolf<sup>2</sup>

**Triggering rain on demand is an old dream of mankind, with a huge potential socio-economical benefit. To date, efforts have mainly focused on cloud-seeding using silver salt particles. We demonstrate that self-guided ionized filaments generated by ultrashort laser pulses are also able to induce water-cloud condensation in the free, sub-saturated atmosphere. Potential contributing mechanisms include photo-oxidative chemistry and electrostatic effects. As well as revealing the potential for influencing or triggering water precipitation, laser-induced water condensation provides a new tool for the remote sensing of nucleation processes in clouds.**

Global warming and stratospheric ozone depletion have demonstrated that human activities can significantly alter the climate of Earth. However, the potential to locally alter or even control the weather is still the subject of intensive debate<sup>1,2</sup>. There have been long-standing efforts dedicated to seeding clouds<sup>3</sup> with silver salt particles to encourage precipitation. Here, we demonstrate that self-guided ionized filaments<sup>4–8</sup> generated by ultrashort laser pulses are also able to induce water cloud condensation in the free, sub-saturated atmosphere. In additional laboratory experiments under both saturated and sub-saturated conditions, we estimate a water uptake rate of up to  $5 \text{ mg cm}^{-3} \text{ s}^{-1}$  in the active volume of the filament-induced plasma channels. We briefly discuss possible mechanisms that could contribute to this observed laser-induced water condensation, although further investigations are needed to fully clarify their roles. Laser-based condensation provides a new tool for the remote sensing of nucleation processes in clouds and may even open up the possibility of influencing or triggering water precipitation.

Self-guided laser filaments result from a nonlinear propagation regime of ultra-short laser pulses. Beyond a critical power ( $P_{\text{cr}} = 3 \text{ GW}$  in air at a wavelength of 800 nm), the beam self-focuses due to the optical Kerr effect until its intensity is sufficient to allow multiphoton ionization of air molecules, generating a cold plasma. At this point, the released free electrons (typically  $10^{15}$ – $10^{16} \text{ cm}^{-3}$ ) and the negative higher-order Kerr terms<sup>9</sup> tend to defocus the beam and dynamically balance Kerr self-focusing. As a result, one or several self-guided filaments<sup>10</sup> with a diameter of 100  $\mu\text{m}$  are generated over distances much longer than the Rayleigh length, up to hundreds of metres<sup>11</sup>. Filaments can be initiated at predefined remote distances<sup>12</sup> and propagate through adverse conditions including fog and clouds<sup>10</sup>, turbulence<sup>13,14</sup> or reduced pressures<sup>15</sup>. They are therefore well suited for atmospheric applications<sup>4,7</sup>, even in perturbed atmospheres.

We recently demonstrated that laser filaments can trigger corona discharges within thunderclouds<sup>16</sup>, opening the way to lightning control applications. With the present demonstration of water condensation, self-guided filaments also raise new hopes that laser-assisted local weather modification may be achieved, which, in contrast to cloud-seeding using rockets, could be operated continuously and would be free of environmental side effects.

## Experiments

As detailed in the Methods, experiments were conducted both in the free atmosphere and under controlled conditions in a diffusion cloud chamber filled with ambient air. A bundle of 20 to 30 self-guided filaments was generated by the Teramobile femtosecond-terawatt laser<sup>17</sup>, which provided 220-mJ pulses with a duration of 60 fs (3.5 TW peak power) at a central wavelength of 800 nm and a repetition rate of 10 Hz. The filamentation onset was adjusted by providing a negative chirp to the emitted laser pulse, so that the group velocity dispersion (GVD) in the air recompressed the pulse at a distance chosen for the interaction with the air mass under investigation, either in the atmospheric cloud chamber or in the free atmosphere.

## Results and discussion

Highly reproducible filament-induced water condensation trails were observed with the naked eye (see Fig. 1a,b and Supplementary Movie) when the filaments were launched into the atmospheric cloud chamber at a saturation of  $S = 2.3 \pm 0.7$  (that is, a relative humidity,  $\text{RH} = 230 \pm 70\%$ ) and a temperature  $T = -24 \text{ }^\circ\text{C}$ . In ten experiments, we were able to confirm this qualitative observation by recording the corresponding evolution of droplet density and size distribution using a Malvern Spraytec aerosol particle sizer (see typical result in Fig. 1c,d). The particle sizer gave access to particles greater than 2.4  $\mu\text{m}$  only, so the condensation nuclei (CN) and cloud condensation nuclei (CCN) could not be detected. The initial size distribution featured three modes at diameters of 4, 50 and 250  $\mu\text{m}$ . The droplet density in each size class fluctuated significantly due to the residual air turbulence in the chamber and the corresponding inhomogeneous distribution of the pre-existing aerosols. However, a Student *t*-test comparing the measured signals before and after the laser shot confirmed that the observed effect has a statistical significance of  $1 - \alpha > 0.9995$ . After the laser was fired, the average diameter of the small particles grew to 6  $\mu\text{m}$ , and their density dropped by half, a change well beyond the fluctuations recorded before the laser pulse. The total water content of this smaller mode therefore remained almost constant. The decrease of this mode is most probably due to the coalescence of droplets, particularly the bigger ones. This coalescence process is sustained by the mutual attraction of

<sup>1</sup>Teramobile, Institut für Experimentalphysik, Freie Universität Berlin, Arnimallee 14, D-14195 Berlin, Germany, <sup>2</sup>Teramobile, GAP, Université de Genève, 20 rue de l'École de Médecine, CH-1211 Genève 4, Switzerland, <sup>3</sup>Teramobile, Université Lyon 1; CNRS; LASIM UMR 5579, bâtiment A. Kastler, 43 Boulevard du 11 novembre 1918, F-69622 Villeurbanne Cedex, France. \*e-mail: jerome.kasparian@unige.ch

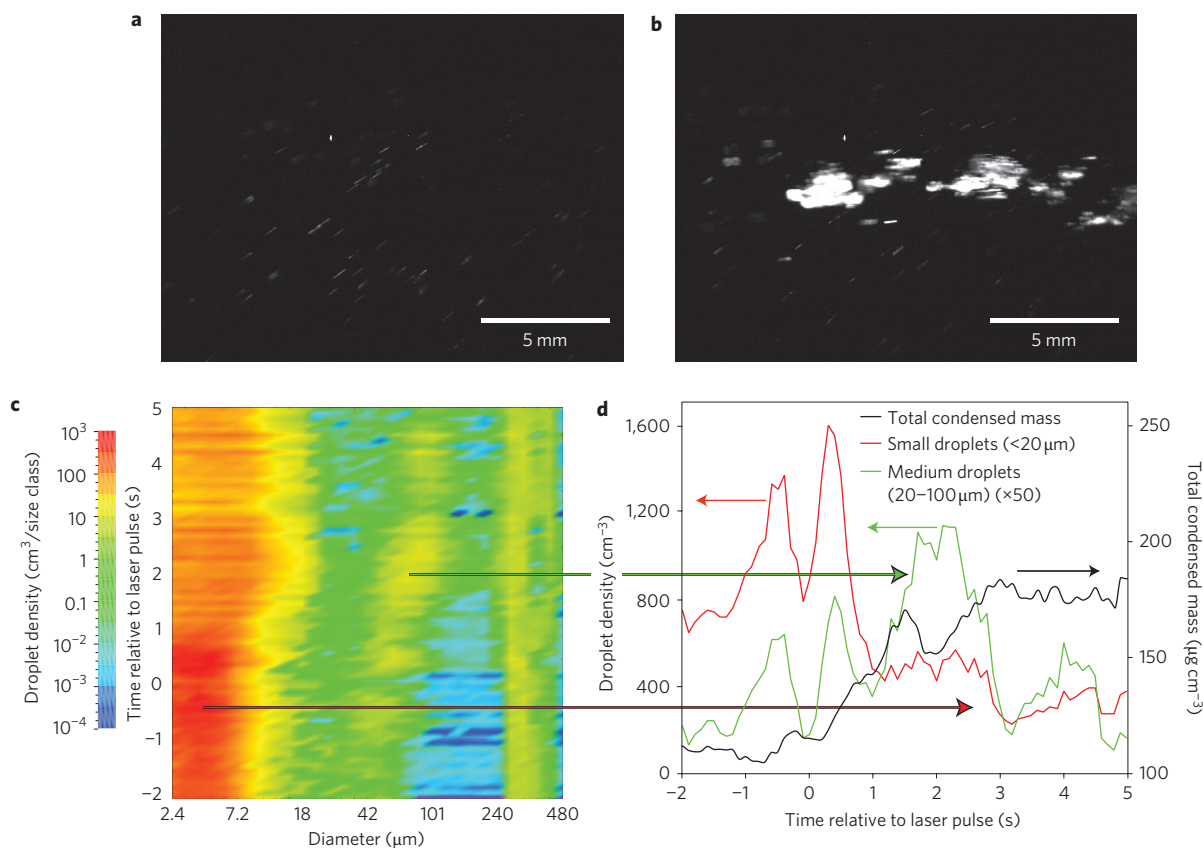


**Figure 1 | Laser-induced condensation in an atmospheric cloud chamber ( $T = -24\text{ }^{\circ}\text{C}$  and  $\text{RH} = 230\%$ ).** **a,b**, View inside the chamber before (**a**) and after (**b**) firing a set of three laser shots at 100-ms intervals. The laser filaments induce macroscopically visible droplet condensation, as is evident from the massive increase in light scattering (see also the Supplementary Movie). **c,d**, Effect of a pair of laser shots launched in the chamber at  $t = 0$  and  $t = 0.1$  s. Temporal evolution of the particle size distribution (**c**) and the amount of small and medium droplets (**d**, left axis) as well as the total condensed water mass (**d**, right axis) per unit volume. The arrows indicate the correspondence between the modes of the size distribution on panel **c**, and the curves displaying their mode-integrated droplet density on panel **d**.

particles bearing opposite net charges generated in amounts of  $10^{15}$ – $10^{16}$  charges  $\text{cm}^{-3}$  by the filaments<sup>18</sup>.

Simultaneously, the density of the mode around  $50\text{ }\mu\text{m}$  doubled. Figure 1c clearly shows that this mode does not develop from smaller droplets, because these two modes remain distinct throughout the growth sequence. Rather, the sudden rise in the medium mode shortly after the laser fired probably stems from the laser-induced fragmentation of droplets from the larger mode at  $250\text{ }\mu\text{m}$ . The  $50\text{-}\mu\text{m}$  droplets then grew to  $80\text{ }\mu\text{m}$  within 3 s. Simultaneously, the biggest mode also grew towards  $400\text{ }\mu\text{m}$ . As a consequence of this growth, the total atmospheric content of condensed water, as determined by integrating the volume of the droplets over the measured size distribution and averaging over the beam, increased by half ( $+70\text{ }\mu\text{g cm}^{-3}$ ). Considering that the  $100\text{-}\mu\text{m}$  filaments only occupy 0.5% of the laser beam volume, the local increase within the filament active volume amounted to a factor of 100 ( $15\text{ mg cm}^{-3}$ ), that is,  $5\text{ mg cm}^{-3}\text{ s}^{-1}$  over the 3 s of growth time. Such results provide clear evidence of filament-assisted condensation. The final droplet diameter of  $80\text{ }\mu\text{m}$  was twice as big as that predicted by a diffusive growth model for pure water under thermodynamically stable conditions<sup>19</sup> (that is, growth limited by the local depletion of water vapour). Their growth rate of  $10\text{ }\mu\text{m s}^{-1}$  was four times faster, probably due to Wilson-type<sup>20</sup> enhancement of the growth rate of the droplets charged by their exposure to the high-charge density generated by the filaments.

However, the Wilson mechanism is not the only mechanism that can explain laser-induced water vapour condensation, because a dramatic and highly reproducible effect was also observed

in sub-saturated conditions (Fig. 2). We varied the relative humidity in the chamber between 70 and 90% and the temperature between 20 and  $60\text{ }^{\circ}\text{C}$ . The observation of an increase in probe light scattering was governed by the water content of the atmosphere rather than by the relative humidity. Condensation was observed only when this was above  $80\text{ }\mu\text{g cm}^{-3}$  provided the relative humidity exceeded 75%. In such conditions, a 30-s series of 300 multifilamenting laser pulses resulted in an immediate rise in the scattering signal by a factor of 10, followed by a slower increase up to a factor of 25 with a time constant  $\tau \approx 4\text{ s}$  (Fig. 2). Such a steep rise again provides clear evidence of an increase in droplet size and number density in the chamber, consistent with observations with the naked eye. Moreover, saturation of the growth rate is typical of a process limited by vapour depletion and the diffusion rate of vapour into the beam region. In contrast, lower water vapour concentrations did not allow substantial condensation even at  $\text{RH} = 95\%$ . The requirement for condensable water before a visible effect is seen shows that it is water vapour condensation indeed that is observed.

This condensation is not affected by the heat deposited by the laser filaments into the air. A typical filament<sup>5–8</sup> with an intensity of  $50\text{ GW cm}^{-2}$ , diameter of  $100\text{ }\mu\text{m}$  and pulse duration of 100 fs carries 0.4 mJ of energy. Even if this energy was totally absorbed over a 10-m length of air, the specific heat of  $1\text{ kJ kg}^{-1}\text{ K}^{-1}$  and the density of  $1.2\text{ kg m}^{-3}$  would yield a temperature increase limited to 3.3 K. In fact, only a small fraction of the filament energy is absorbed, so heating of the air can be neglected in the analysis of our results, and the ambient temperature can be considered as representative of the conditions within the filaments.

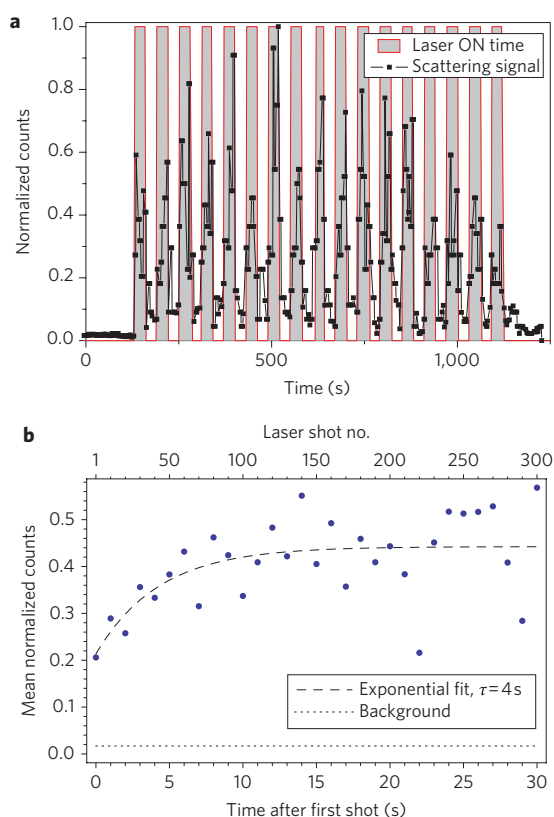


**Figure 2 | Laser-induced condensation in a sub-saturated atmospheric cloud chamber ( $T = 60\text{ }^{\circ}\text{C}$ ,  $\text{RH} = 75\text{--}85\%$ ), observed through the scattered signal at  $90^{\circ}$ .** **a**, High reproducibility of the effect over repeated laser on/off cycles of 300 laser shots each. **b**, Rise time (time constant  $\tau \approx 4\text{ s}$ ) of the light scattered by the growing droplets, averaged over the 17 cycles of panel **a**.

This negligible heating of the air contrasts with the high electron temperature in the plasma filament, which can reach up to 6,000 K (refs 5–8). It should be noted that, due to the small transverse dimension of the filaments, the slight local heating of the air results in large temperature gradients, leading to the development of a shockwave<sup>21</sup>. The corresponding expansion of the air might contribute to the condensation process.

Note also that the fragmentation of pre-existing water droplets into smaller ones increases the scattering signal. We quantified this effect by modelling the laser-induced droplet fragmentation, considering that each mother droplet absorbs an amount of energy proportional to its cross-section, part of which is turned into additional surface energy during fragmentation. A one-step fragmentation model based on a maximum entropy principle results in a Poissonian size distribution of the fragments of each mother droplet<sup>22</sup>. By treating this distribution as continuous, even in cases where it contained only a few tens of daughter particles<sup>23</sup>, we found that the contribution of laser-induced droplet fragmentation to the effect observed in the sub-saturated cloud chamber was marginal, regardless of whether nonlinear absorption or linear absorption were considered. Instead, the observed condensation may be understood by remembering that the atmospheric cloud chamber is filled with ambient air. Therefore, in the urban environment of the laboratory (including aerosols and gaseous pollutants) and in the presence of the high-intensity laser field, photochemically or charge-assisted mechanisms contribute significantly to droplet formation<sup>24–26</sup>.

To provide a definitive demonstration of the capability of laser filaments to trigger condensation, not only in controlled laboratory

conditions but also in real atmospheric conditions, we performed open-field experiments (Fig. 3a) in the late autumn of 2008 in Berlin, Germany, under conditions of polar air mass, providing a high relative humidity ( $\text{RH} = 90\text{--}93\%$ ) together with low level of background aerosols (70 km horizontal visibility). The laser was launched vertically into the atmosphere, at a repetition rate of 5 Hz. The filaments were most active between heights of 45 and 75 m. Their strength then decreased over a few tens of metres beyond this range. The aerosol content of the atmosphere was monitored by LIDAR (light detection and ranging)<sup>27</sup> using a low-power frequency-doubled Nd:YAG laser at 10 Hz repetition rate. This allowed the performance of differential measurements of the changes induced by the terawatt laser pulses preceding the LIDAR pulses (Fig. 3a). The LIDAR return signals provide range-resolved measurements of the total volume backscattering coefficient  $\beta$ , which comprises a molecular contribution (Rayleigh scattering is subtracted in the data processing) and an aerosol contribution (Mie scattering). This aerosol backscattering coefficient  $\beta_{\text{Mie}}$  is defined as<sup>27</sup>

$$\beta_{\text{Mie}} = \int_0^{\infty} N(r) \frac{d\sigma(n, r)}{d\Omega} \Big|_{\theta=\pi} dr \quad (1)$$

where  $N(r)$  is the number density of droplets of size  $r$ , and  $d\sigma(n, r)/d\Omega|_{\theta=\pi}$  is the size- and refractive index-dependent backscattering differential cross-section of the particles.  $\beta_{\text{Mie}}$  therefore provides information averaged over all aerosol types and sizes within the probed volume.

The LIDAR measurements were taken 1 ms after firing the terawatt laser pulses. This time delay, much shorter than typical droplet growth times, was imposed by a lateral wind sweeping the air ionized by the filaments out of the detection volume. As already mentioned above, the filaments occupy a fraction of only  $2.5 \times 10^{-4}$  of the air volume probed by the LIDAR. Despite those difficulties and atmospheric fluctuations, the beam-averaged value of  $\beta_{\text{Mie}}$  at the height of the filaments was up to 0.5% higher when following a filamenting laser pulse than without filaments (Fig. 3b). This increase corresponds to a local enhancement of Mie scattering by a factor of 20 within the filaments, from  $\beta_{\text{Mie}} = 1 \times 10^{-6} \text{ m}^{-1} \text{ sr}^{-1}$  to  $2 \times 10^{-5} \text{ m}^{-1} \text{ sr}^{-1}$ . The latter value is typical of haze<sup>27</sup>, in spite of a growth time of 1 ms, much shorter than the signal rise time identified in the sub-saturated chamber (Fig. 2b). Because  $\beta_{\text{Mie}}$  is a measure of all kinds of aerosols, one could argue that only sulphate and nitrate CN or CCN were observed. However, the results of the experiment in the sub-saturated chamber discussed above show that the laser filaments also cause the subsequent condensation of water droplets provided enough water vapour is available in the atmosphere.

The statistical significance of the observed effect was assessed by a Mann–Whitney U-test, comparing the sets of LIDAR signals following a filamenting pulse with the reference LIDAR signals. The null-hypothesis of this non-parametric test is that the two samples are drawn from a single population, so their probability distributions are equal. It therefore makes no assumption about the shape of the underlying distribution(s) and is insensitive to outliers. The Mann–Whitney test can be seen as assessing for differences in medians of the considered distributions. Statistically significant results ( $\alpha < 0.01$ , where  $1 - \alpha$  is the confidence level) were obtained between 6:00 and 6:30, when temperature and relative humidity were  $2.9\text{ }^{\circ}\text{C}$  and 90%, respectively.

Afterwards, the meteorological conditions changed. A reduction in the visibility, a slow increase in the relative humidity up to 93% over 2 h and a rise in the absolute value of the LIDAR signal suggested an increase in the background concentration of water aerosols. Correlatively, the effect of filament-induced condensation on the backscattering signal faded into the background. The fact

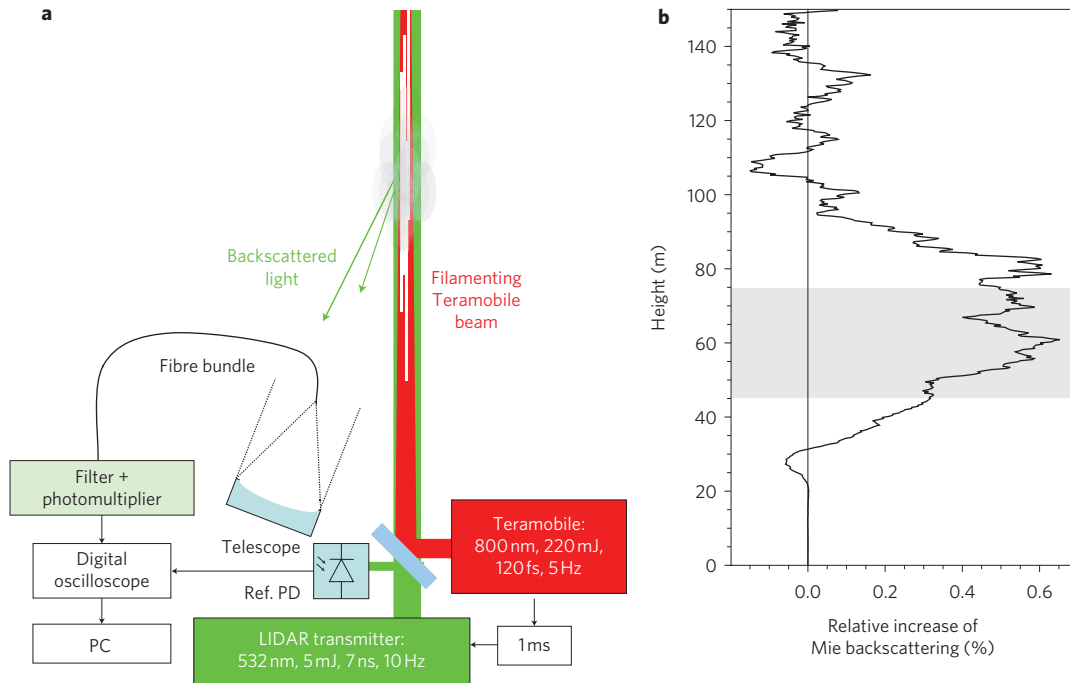


**Figure 3 | Laser-induced condensation experiment in the atmosphere.** **a**, Experimental set-up. The Teramobile laser (red) is fired 1 ms before the LIDAR pulse (green) measuring the aerosol content of the atmosphere. **b**, Time-averaged relative increase of the Mie backscattering coefficient  $\beta_{\text{Mie}}$  measured between 6:00 and 6:30 with and without firing the Teramobile laser. The signal enhancement at the height of the filaments (the most active filamenting region at 45–75 m is shaded) is a clear indication for filament-induced condensation.

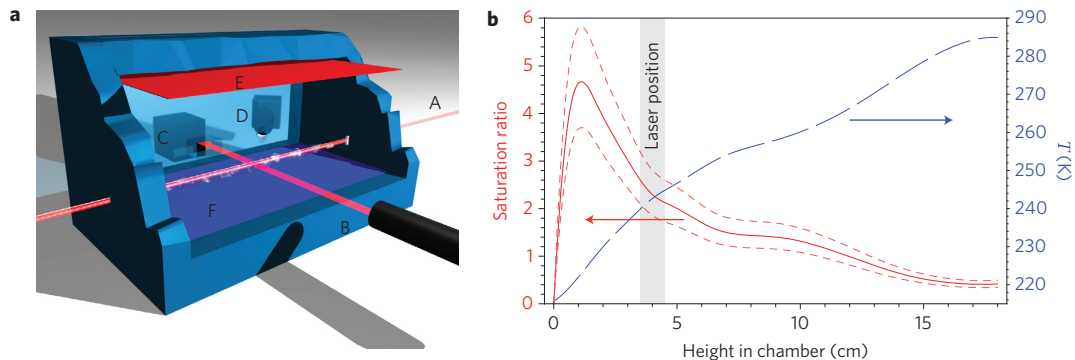


**Figure 4 | Atmospheric diffusion chamber for laboratory experiments.** **a**, Experimental set-up (schematic). A, Teramobile beam; B, particle sizer laser beam; C, particle sizer receiver unit; D, imaging charge-coupled device camera; E, heat and vapour source; F, cold bottom plate. **b**, Measured vertical temperature (blue, right scale) and derived supersaturation profile (red, left scale) in the chamber. The dashed lines correspond to the worst-case combinations of  $2\sigma$  temperature and chamber top saturation measurement errors. The grey region indicates the position of the laser beam.

that the observed effects depend on the weather conditions excludes a systematic experimental flaw. Furthermore, we can exclude direct contribution of the filament plasma to the LIDAR signal, because the lifetime of the plasma generated by the filaments does not exceed the microsecond timescale, well below the millisecond interval between the pump and the probe pulses<sup>28</sup>.

As in the cloud chamber experiment, we checked that the enhancement of the LIDAR signal by the laser filaments could not be explained by laser-induced aerosol fragmentation. First, the observed effect decreases when the background LIDAR signal increases, that is, when more water droplets are available for fragmentation. The above-described model of droplet fragmentation quantitatively confirmed this qualitative argument. Based on very high-visibility conditions and air-mass back trajectories<sup>29</sup>, we considered an initial maritime haze size distribution<sup>30</sup>. The visibility provided the water droplet concentration, which was equal to  $136 \text{ mm}^{-3}$ . Alternative rural, remote continental and urban size

distributions were also considered, without affecting the result qualitatively. Between 8 and 400 fragments per mother droplet were considered, with refractive indices in the range 1.3–1.5 commonly encountered in hazes<sup>31</sup>. Even if an overestimation of the filament number (100) and diameter ( $200 \mu\text{m}$ ) were taken into account in the calculations, we found that fragmentation could increase the Mie backscattering coefficient by at most 0.1–0.2%. Thus, fragmentation does not provide the dominant contribution to the observed effect in the atmospheric experiments.

Systematic parametric measurements would be required to better understand and optimize the complex processes at play in our observations. Although such a study is beyond the scope of the present work, some important facts have to be considered. Each filament generates a cold plasma<sup>5–8</sup> with  $10^{15}$ – $10^{16}$  electrons  $\text{cm}^{-3}$  (ref. 5), that is, an average charge generation rate of  $10^{11}$  charges  $\text{cm}^{-3} \text{ s}^{-1}$  at a repetition rate of 10 Hz. Most of these electrons attach to ions within a few picoseconds while, typically,

$10^{13} \text{ cm}^{-3}$  of them attach to  $\text{O}_2$  molecules to form  $\text{O}_2^-$  ions, which last for several microseconds<sup>5</sup>. These oxygen ions can form Wilson clusters<sup>24</sup> with high efficiency due to the extremely high initial concentration of  $\text{O}_2^-$ , even without photoactivation. Direct multiphoton water photolysis<sup>25</sup> can further contribute to this process because the intensity of  $\sim 50 \text{ GW cm}^{-2}$  in the filaments allows processes that are usually only considered for UV lasers. However, thermally driven chemical reactions are not to be considered, because, as discussed above, the plasma generated by the filaments is cold<sup>5–8</sup>.

The exceptionally high charge density could also result in a production rate of oxidizing molecules such as  $\text{O}_3$  and  $\cdot\text{OH}$  radicals that is orders of magnitude above the natural rates found in the atmosphere. The resulting  $\cdot\text{OH}$ , together with the  $\text{O}_2^-$  ions mentioned above, will rapidly produce Wilson clusters<sup>25</sup>, oxidize  $\text{SO}_2$  (refs 26,32) and  $\text{NO}_2$  into  $\text{H}_2\text{SO}_4$  and  $\text{HNO}_3$ , respectively, and assist their heterogeneous nucleation as well as that of volatile organic species. Such processes are indeed compatible with the millisecond timescale of the observed process. Most of these aerosols are highly hygroscopic and will later serve as CCN, allowing the growth of water droplets in adequate humidity conditions, as demonstrated in the sub-saturated cloud chamber experiment. However, at the time of the probe pulse, the scattering efficiencies are still low because the droplets have not had time to grow.

## Conclusions

As a conclusion, we have experimentally demonstrated that self-guided filaments generated by ultrashort laser pulses can assist water condensation, even in an undersaturated free atmosphere. Potential contributing mechanisms include photo-oxidative chemistry and electrostatic effects. The phenomenon provides a new and attractive tool for remote characterization of the humid atmosphere and cloud formation. In addition, it may even provide the potential to influence or trigger water precipitation using continuously operating lasers rather than rockets.

## Methods

The Teramobile femtosecond–terawatt laser<sup>17</sup> used to generate the filaments provided 220-mJ pulses of 60-fs duration at 800 nm, with a repetition rate of 10 Hz. The beam formed a bundle of 20–30 filaments. In laboratory experiments, it was launched through a diffusion chamber<sup>33</sup> (Fig. 4a) filled with ambient air, as single shots or in bursts of up to 30 s in duration. The filaments typically started a few metres before the chamber, which was positioned  $\sim 15$  m away from the laser output. A strong temperature gradient was maintained in the chamber volume of  $0.6 \times 0.3 \times 0.2 \text{ m}^3$  by using a cold base plate that was kept at  $-60^\circ \text{C}$  by indirect contact with a liquid-nitrogen reservoir, and a thermostated circulator heated to  $10^\circ \text{C}$  at the top of the chamber. Water vapour from a reservoir at the top of the chamber diffused towards the bottom plate. We estimated the relative humidity at the top of the chamber to be  $42 \pm 10\%$  by measuring the evaporation time of  $51 \pm 1$  min of sessile water drops with an initial volume of  $2 \mu\text{l}$  (ref. 34). The typical vertical temperature profile, measured with a K-type thermocouple, is shown in Fig. 1b. This profile was used to estimate the supersaturation profile, assuming steady state<sup>35</sup> and a zero water vapour concentration at the bottom of the chamber. The supersaturation was estimated to be  $S \approx 4$  near the bottom of the chamber, consistent with the fact that we operated the chamber slightly below the threshold of sensitivity to cosmic rays<sup>36</sup>. The resulting supersaturation in the interaction region was  $S = 2.3 \pm 0.7$  at a temperature of  $T \approx -24^\circ \text{C}$ . Sub-saturated conditions were obtained by installing a water reservoir that was maintained above  $100^\circ \text{C}$  at the top of the cloud chamber while its bottom was circulator cooled to  $+11^\circ \text{C}$ . The relative humidity at the position of the beam was monitored with a capacitance hygrometer. It ranged between 75 and 85% ( $S = 0.75\text{--}0.85$ ) at a local temperature of  $\sim 60^\circ \text{C}$ .

The water aerosol density in the atmospheric cloud chamber was observed with the naked eye and monitored by launching a low-power continuous wave (c.w.) laser (Nd:YAG, 532 nm, 10 mW) across the path of the pump beam and observing the scattering at  $90^\circ$  or  $45^\circ$ . Scattering is a signature of water droplets, because Rayleigh scattering by air molecules within the cell is negligible at atmospheric pressure over the considered metre scale. Alternatively, the particle size distribution was monitored by measuring the angular distribution of the scattered light of a He:Ne laser in the forward direction using a Malvern Spraytec particle sizer. The data were inverted using Mie theory, while considering the dominant particles to be spherical water droplets.

The atmospheric experiment was performed at night in late autumn of 2008 in Berlin ( $52^\circ 27' 24'' \text{ N}$ ,  $13^\circ 17' 38'' \text{ E}$ , 55 m above sea level), under conditions of

incoming arctic cold air ( $2.9^\circ \text{C}$ ) and initially strong westerly winds at an atmospheric pressure of  $\sim 995$  hPa, with a relative humidity initially stable at 90% over 1 h and then slowly rising to 93% over 2 h. The horizontal visibility and wind speed and direction were measured 33 and 39 m above ground, respectively, 1,140 m east of the experimental location. Temperature and relative humidity were recorded upwind at 620 m in the east–south–east direction away from the experimental site. The initial horizontal standard visibility was  $\sim 70$  km, indicating an exceptionally low background of aerosol scatterers. This value was used to calibrate the aerosol-related fraction of the atmospheric backscattering coefficient from the LIDAR signals.

In this experiment (Fig. 3), the Teramobile beam was expanded to a diameter of 10 cm and launched vertically into the free atmosphere at a repetition rate of 5 Hz. The pulses were chirped and the beam slightly focused to maximize the strength of multiple filamentation at a distance of 60 m. Backscattering from the atmosphere was probed with a LIDAR using a 5-mJ YAG laser beam at 532 nm, pulsed at 10 Hz, emitted collimated with a beam diameter of 4 cm, and overlapped with the Teramobile beam on a dichroic mirror. This overlap was checked at 0 and 60 m by folding the beams horizontally, ensuring that the strongly filamenting region was effectively superposed with the probe beam.

The probe beam alternately measured the backscattering 1 ms following a Teramobile shot and then in unaffected atmosphere 100 ms following the shot. The horizontal wind speed of  $2.5\text{--}5 \text{ m s}^{-1}$  ensured that each pulse (resp. pulse pair) interacted with a fresh air column. Single-shot LIDAR transients were collected with a 11.4-cm-diameter,  $f = 500$  mm telescope (4 mrad field of view), 20 cm off the axis of the laser beam, detected by a photomultiplier tube equipped with a narrowband (1 nm bandwidth full-width at half-maximum (FWHM) at 532 nm) interference filter, and recorded on a digital oscilloscope used as a transient recorder (500 MHz bandwidth). Each individual LIDAR signal was normalized by the pulse energy of the probe pulses, as recorded using a high-speed photodiode. The inclination between the axes of the laser beams and of the telescope provided 100% overlap around 60 m, in the filamenting region. We integrated the LIDAR signals generated by probe pulses over the most active filamenting region, between altitudes of 45 and 75 m (shaded region of Fig. 3), and compared those following a Teramobile pulse with reference pulses.

Received 11 November 2009; accepted 8 March 2010;  
published online 2 May 2010

## References

- Qiu, J. & Cressey, D. Taming the sky. *Nature* **453**, 970–974 (2008).
- US National Research Council. *Critical Issues in Weather Modification Research* (National Academies, 2003).
- Langmuir, I. Growth of particles in smokes and clouds and the production of snow from supercooled clouds. *Science* **106**, 505 (1947).
- Kasparian, J. *et al.* White-light filaments for atmospheric analysis. *Science* **301**, 61–64 (2003).
- Couairon, A. & Mysyrowicz, A. Femtosecond filamentation in transparent media. *Phys. Rep.* **44**, 47–189 (2007).
- Bergé, L., Skupin, S., Nuter, R., Kasparian, J. & Wolf, J.-P. Ultrashort filaments of light in weakly-ionized, optically-transparent media. *Rep. Prog. Phys.* **70**, 1633–1713 (2007).
- Kasparian, J. & Wolf, J.-P. Physics and applications of atmospheric nonlinear optics and filamentation. *Opt. Express* **16**, 466–493 (2008).
- Chin, S. L. *et al.* The propagation of powerful femtosecond laser pulses in optical media: physics, applications and new challenges. *Can. J. Phys.* **83**, 863–905 (2005).
- Béjot, P. *et al.* Higher-order Kerr terms allow ionization-free filamentation in air. *Phys. Rev. Lett.* **104**, 103903 (2010).
- Méjean, G. *et al.* Multifilamentation transmission through fog. *Phys. Rev. E* **72**, 026611 (2005).
- La Fontaine, B. *et al.* Filamentation of ultrashort pulse laser beams resulting from their propagation over long distances in air. *Phys. Plasma* **6**, 1615–1621 (1999).
- Rodriguez, M. *et al.* Kilometer-range non-linear propagation of femtosecond laser pulses. *Phys. Rev. E* **69**, 036607 (2004).
- Chin, S. L. *et al.* Filamentation of femtosecond laser pulses in turbulent air. *Appl. Phys. B* **74**, 67–76 (2002).
- Salamé, R., Lascoux, N., Salmon, E., Kasparian, J. & Wolf, J.-P. Propagation of laser filaments through an extended turbulent region. *Appl. Phys. Lett.* **91**, 171106 (2007).
- Méchain, G. *et al.* Propagation of fs-TW laser filaments in adverse atmospheric conditions. *Appl. Phys. B* **80**, 785–789 (2005).
- Kasparian, J. *et al.* Electric events synchronized with laser filaments in thunderclouds. *Opt. Express* **16**, 5757–5763 (2008).
- Wille, H. *et al.* Teramobile: a mobile femtosecond–terawatt laser and detection system. *Eur. Phys. J.—Appl. Phys.* **20**, 183–190 (2002).
- Kasparian, J., Sauerbrey, R. & Chin, S. L. The critical laser intensity of self-guided light filaments in air. *Appl. Phys. B* **71**, 877–879 (2000).
- Pruppacher, H. R. & Klett, J. D. *Microphysics of Clouds and Precipitation* (Kluwer Academic Publishing, 1997).

20. Wilson, C. T. R. On a method of making visible the paths of ionising particles through a gas. *Proc. R. Soc. Lond. A* **85**, 285–288 (1911).
21. Yu, J. *et al.* Sonographic probing of laser filaments in air. *Appl. Opt.* **42**, 7117–7117 (2003).
22. Cohen, R. D. Shattering of a liquid drop due to impact. *Proc. R. Soc. Lond. A* **435**, 483–503 (1991).
23. Villermaux, E. Fragmentation. *Annu. Rev. Fluid Mech.* **39**, 419–446 (2007).
24. Byers Brown, W. Photonucleation of water vapour in the presence of oxygen. *Chem. Phys. Lett.* **235**, 94–98 (1995).
25. Clark, I. D. & Noxon, J. F. Particle formation during water-vapor photolysis. *Science* **174**, 941–944 (1971).
26. He, F. & Hopke, P. K. SO<sub>2</sub> oxidation and H<sub>2</sub>O–H<sub>2</sub>SO<sub>4</sub> binary nucleation by radon decay. *Aerosol Sci. Technol.* **23**, 411–421 (1995)
27. Measures, R. M. *Laser Remote Sensing—Fundamentals and Applications* (Wiley Interscience, 1984).
28. Tzortzakis, S., Prade, B., Franco, M. & Mysyrowicz, A. Time evolution of the plasma channel at the trail of a self-guided IR femtosecond laser pulse in air. *Opt. Commun.* **181**, 123–127 (2000).
29. Aeronet project, NASA, back trajectory data for stations Leipzig (D), Hamburg (D), and Belsk (Pl), <http://croc.gsfc.nasa.gov/aeronet/>.
30. Jaenicke, R. Tropospheric aerosol, in *Aerosol–Cloud–Climate* (Hobbs, P. V., ed.) (Academic Press, 1993).
31. Quentzel, H., Ruppertsberg, G. H. & Schellhase, R. Calculations about the systematic error of the visibility-meters measuring scattered light. *Atmos. Environ.* **9**, 587–601 (1975).
32. Caffrey, P. *et al.* In-cloud oxidation of SO<sub>2</sub> by O<sub>3</sub> and H<sub>2</sub>O<sub>2</sub>: cloud chamber measurements and modelling of particle growth. *J. Geophys. Res.* **106**, 27587–27601 (2001).
33. Langsdorf, A. Jr. A continuously sensitive diffusion cloud chamber. *Rev. Sci. Instrum.* **10**, 91–103 (1939).
34. Schönfeld, F., Graf, K. H., Hardt, S. & Butt, H. J. Evaporation dynamics of sessile liquid drops in still air with constant contact radius? *Int. J. Heat Mass Transfer* **51**, 3696–3699 (2008).
35. Saavedra, I. On the theory of the diffusion cloud chamber. *Nucl. Instrum.* **3**, 85–89 (1958).
36. Tohmfor, G. & Volmer, M. Die keimbildung unter dem einfluß elektrischer ladungen. *Annalen der Physik* **425**, 109–131 (1938).

### Acknowledgements

The authors would like to acknowledge J. Kirkby of CERN for fruitful discussions, I. Sorge of Institut für Meteorologie, FU-Berlin, Germany, for providing weather data, and T. L. Kucsera (GEST) at NASA/Goddard for back-trajectories (available at the [aeronet.gsfc.nasa.gov](http://aeronet.gsfc.nasa.gov) website). This work was supported by the Deutsche Forschungsgemeinschaft, Agence Nationale de la Recherche (Project ANR-05-Blan-0187), the Fonds National Suisse de la Recherche Scientifique (FNS, grant nos. 200021-116198 and 200021-125315), and the Swiss Secrétariat d'État à l'Éducation et à la Recherche in the framework of the COST P18 project 'The Physics of Lightning Flash and its Effects'.

### Author contributions

All authors contributed extensively to the work presented in this paper. More specifically, P.R., J.K., K.S., L.W. and J.-P.W. conceived and designed the study. P.R., K.S., Z.H., S.H., N.L., W.N., Y.P., M.Q., R.S. and E.S. performed the experiments. P.R., J.K. and K.S. analysed the data, and J.K., L.W. and J.-P.W. wrote the paper.

### Additional information

The authors declare no competing financial interests. Supplementary information accompanies this paper at [www.nature.com/naturephotonics](http://www.nature.com/naturephotonics). Reprints and permission information is available online at <http://npg.nature.com/reprintsandpermissions/>. Correspondence and requests for materials should be addressed to J.K.

# Generalized Miller Formulæ

W. Ettoumi, Y. Petit, J. Kasparian\*, and J.-P. Wolf

Université de Genève, GAP-Biophotonics, 20 rue de l'École de Médecine, 1211 Geneva 4,  
Switzerland

[\\*jerome.kasparian@unige.ch](mailto:*jerome.kasparian@unige.ch)

**Abstract:** We derive the spectral dependence of the non-linear susceptibility of any order, generalizing the common form of Sellmeier equations. This dependence is fully defined by the knowledge of the linear dispersion of the medium. This finding generalizes the Miller formula to any order of non-linearity. In the frequency-degenerate case, it yields the spectral dependence of non-linear refractive indices of arbitrary order.

© 2010 Optical Society of America

**OCIS codes:** (120.4530) Optical constants; (190.0190) Nonlinear optics; (190.3270) Kerr effect; (190.7110) Ultrafast nonlinear optics.

---

## References and links

1. R. W. Boyd, *Nonlinear optics*, (Academic Press, 2008).
2. J. M. Dudley, G. Genty, and S. Coen, "Supercontinuum generation in photonic crystal fiber," *Rev. Mod. Phys.* **78**, 1135 (2006).
3. M. Soljačić and J. D. Joannopoulos, "Enhancement of nonlinear effects using photonics crystals," *Nature Mater.* **3**, 211 (2004).
4. V. Loriot, E. Hertz, O. Faucher, and B. Lavorel, "Measurement of high-order Kerr refractive index of major air components," *Opt. Express* **16**, 13429 (2009).
5. P. Béjot, J. Kasparian, S. Henin, V. Loriot, T. Vieillard, E. Hertz, O. Faucher, B. Lavorel, and J.-P. Wolf, "Higher-order Kerr terms allow ionization-free filamentation in air," submitted to *Phys. Rev. Lett.*
6. A. Braun, G. Korn, X. Liu, D. Du, J. Squier, and G. Mourou, "Self-channeling of high-peak-power femtosecond laser pulses in air," *Opt. Lett.* **20**, 73 (1995).
7. S. L. Chin, S. A. Hosseini, W. Liu, Q. Luo, F. Theberge, N. Aközbek, A. Becker, V. P. Kandidov, O. G. Kosareva, and H. Schroeder, "The propagation of powerful femtosecond laser pulses in optical media: physics, applications, and new challenges," *Can. J. Phys.* **83**, 863 (2005).
8. L. Bergé, S. Skupin, R. Nuter, J. Kasparian, and J.-P. Wolf, "Ultrashort filaments of light in weakly-ionized, optically-transparent media," *Rep. Prog. Phys.* **70**, 1633 (2007).
9. A. Couairon and A. Mysyrowicz, "Femtosecond filamentation in transparent media," *Phys. Rep.* **441**, 47 (2007).
10. J. Kasparian and J.-P. Wolf, "Physics and applications of atmospheric nonlinear optics and filamentation," *Opt. Express* **16**, 466 (2008).
11. R. C. Miller, "Optical second harmonic generation in piezoelectric crystals," *Appl. Phys. Lett.* **5**, 17 (1964).
12. V. Mizrahi and D. P. Shelton, "Dispersion of Nonlinear Susceptibilities of Ar, N<sub>2</sub>, and O<sub>2</sub> Measured and Compared," *Phys. Rev. Lett.* **55**, 696 (1985).
13. A. Owyong, Ph.D. thesis, California Institute of Technology, 1972 (unpublished).
14. J. Zhang, Z. H. Lu, and L. J. Wang, "Precision refractive index measurements of air, N<sub>2</sub>, O<sub>2</sub>, Ar, and CO<sub>2</sub> with a frequency comb," *Appl. Opt.* **47**, 3143 (2008).
15. B. Boulanger, Y. Petit, P. Segonds, C. Félix, B. Ménaert, J. Zaccaro, and G. Aka, "Absorption and fluorescence anisotropies of monoclinic crystals : the case of Nd:YCOB," *Opt. Express* **16**, 7997 (2008).
16. J. A. Armstrong, N. Bloembergen, J. Ducuing, and P. S. Pershan, "Interactions between Light Waves in a Non-linear Dielectric," *Phys. Rev.* **127**, 1918 (1962).

---

## 1. Introduction

Non-linear optics [1] relies on the knowledge of the non-linear susceptibilities (or, alternatively, the non-linear indices) of the propagation media. This description is generally truncated to the

first term, *i.e.* the second-order susceptibility in non-centrosymmetric media, or the third-order susceptibility in centrosymmetric ones. However, the increase of the available laser powers as well as the investigation of systems like optical fibers [2] or photonic crystals [3] where the confinement of the light increases its intensity raise the need to consider higher-order processes. Recently, the non-linear refractive indices of O<sub>2</sub>, N<sub>2</sub> were measured up to  $n_8$  (*i.e.* the 9<sup>th</sup>-order susceptibility  $\chi^{(9)}$ ) and in Ar up to  $n_{10}$  (*i.e.*  $\chi^{(11)}$ ) at 800 nm [4]. Furthermore, we demonstrated [5] that they must be considered in the description of the filamentation of ultrashort pulses [6–10]. This result, which was unexpected, provides a clear illustration of this need, and of the associated requirement to evaluate these terms at any wavelength. But systematic measurements over the spectrum are out of reach of present experimental capabilities. A theoretical support is therefore required to extend the existing experimental results to any frequency, which would provide a new insight into non-linear optics.

Such relation was provided by Miller in the case of the second-order susceptibility. He observed that in many crystals the knowledge of  $\chi^{(2)}$  for one single triplet of frequencies ( $\omega'_0; \omega'_1, \omega'_2$ ) and the dispersion relation of the medium is sufficient to determine  $\chi^{(2)}$  for any triplet of frequencies ( $\omega_0; \omega_1, \omega_2$ ) [11]:

$$\frac{\chi^{(2)}(\omega_0; \omega_1, \omega_2)}{\chi^{(2)}(\omega'_0; \omega'_1, \omega'_2)} = \frac{\chi^{(1)}(\omega_0)\chi^{(1)}(\omega_1)\chi^{(1)}(\omega_2)}{\chi^{(1)}(\omega'_0)\chi^{(1)}(\omega'_1)\chi^{(1)}(\omega'_2)} \quad (1)$$

Mizrahi and Shelton later suggested that the Miller formula could be extended to the non-linear index  $n_2$ , *i.e.* to the third-order frequency-degenerate non-linearity [12]. However, they did not demonstrate this result in their article, but rather referred to an unpublished work [13].

In this Letter, we explicitly derive the spectral dependence of the non-linear susceptibility of any order, generalizing the common form of Sellmeier equations. We show that this spectral dependence is fully defined by the knowledge of the linear dispersion of the medium. As a consequence, the Miller formula [Eq. (1)] [11] can be extended to any order of non-linearity. In the frequency-degenerate case, this finding yields the spectral dependence of non-linear refractive indices of arbitrary order, confirming and widely generalizing Mizrahi and Shelton's statement about  $\chi^{(3)}$  [12].

## 2. Derivation of generalized Miller formulæ

### 2.1. Electrons in an anharmonic oscillator

Elucidating the spectral dependence of the electric susceptibility requires to consider the equation of motion of an electron located at  $\vec{r}$  in a three-dimensional potential  $V(\vec{r})$ .  $V$  can be expanded as a 3-dimensional Taylor series around the equilibrium position  $\vec{r} = \vec{0}$ :

$$V(\vec{r}) = V(\vec{0}) + \sum_{i+j+k \geq 2} \frac{x^i y^j z^k}{i! j! k!} \left[ \frac{d^{i+j+k} V}{\partial x^i \partial y^j \partial z^k} \right]_{\vec{r}=\vec{0}} \quad (2)$$

where the summation begins at  $q \equiv i + j + k = 2$  since  $\left[ \frac{\partial V}{\partial x} \right]_{x=0} = \left[ \frac{\partial V}{\partial y} \right]_{y=0} = \left[ \frac{\partial V}{\partial z} \right]_{z=0} = 0$  by definition of the equilibrium position. As a consequence, the electron experiences a force equal to

$$\vec{F}(\vec{r}) = -\vec{\nabla} V(\vec{r}) = - \sum_{q \geq 2} \left( \frac{\frac{x^{i-1} y^j z^k}{(i-1)! j! k!}}{\frac{x^i y^{j-1} z^k}{i! (j-1)! k!}} \right) \left[ \frac{\partial^q V}{\partial x^i \partial y^j \partial z^k} \right]_{\vec{r}=\vec{0}} \quad (3)$$

The macroscopic polarization along the axes  $x$ ,  $y$  and  $z$  are respectively  $P_x = -Nex$ ,  $P_y = -Ney$  and  $P_z = -Nez$ ,  $N$  being the local density of electrons and  $-e$  their charge. Equation (3)

therefore rewrites:

$$\vec{F}(\vec{r}) = - \sum_{q \geq 2} \left( \frac{-1}{Ne} \right)^{q-1} \begin{pmatrix} P_x^{i-1} P_y^j P_z^k \\ (i-1)! j! k! \\ P_x^i P_y^{j-1} P_z^k \\ i! (j-1)! k! \\ P_x^i P_y^j P_z^{k-1} \\ i! j! (k-1)! \end{pmatrix} \left[ \frac{\partial^q V}{\partial x^i \partial y^j \partial z^k} \right]_{\vec{r}=\vec{0}} \quad (4)$$

or, equivalently:

$$\vec{F}(\vec{r}) = - \sum_{q \geq 1} \left( \frac{-1}{Ne} \right)^q \frac{P_x^i P_y^j P_z^k}{i! j! k!} \begin{pmatrix} \frac{\partial^{q+1} V}{\partial x^{i+1} \partial y^j \partial z^k} \\ \frac{\partial^{q+1} V}{\partial x^i \partial y^{j+1} \partial z^k} \\ \frac{\partial^{q+1} V}{\partial x^i \partial y^j \partial z^{k+1}} \end{pmatrix}_{\vec{r}=\vec{0}} \quad (5)$$

We introduce the  $(q+1)^{th}$  rank tensor  $Q^{(q)}$ , which elements are given by:

$$\begin{pmatrix} Q_{x;x^{(i)},y^{(j)},z^{(k)}}^{(q)} \\ Q_{y;x^{(i)},y^{(j)},z^{(k)}}^{(q)} \\ Q_{z;x^{(i)},y^{(j)},z^{(k)}}^{(q)} \end{pmatrix} \equiv \frac{(-1)^q}{m \times i! j! k!} \begin{pmatrix} \frac{\partial^{q+1} V}{\partial x^{i+1} \partial y^j \partial z^k} \\ \frac{\partial^{q+1} V}{\partial x^i \partial y^{j+1} \partial z^k} \\ \frac{\partial^{q+1} V}{\partial x^i \partial y^j \partial z^{k+1}} \end{pmatrix}_{\vec{r}=\vec{0}} \quad (6)$$

where, for example,  $x^{(i)}$  indicates that the coordinate  $x$  appears  $i$  times in the index list of the considered tensor element. As a consequence, the classical equation of motion of the electron becomes:

$$\frac{d^2 \vec{P}}{dt^2} + \bar{\gamma} \frac{d\vec{P}}{dt} + \bar{\omega}_e^2 \vec{P} + Ne \sum_{q=1}^{\infty} Q^{(q)} : \bigotimes_{l=1}^q \frac{\vec{P}}{Ne} = \frac{Ne^2}{m} \vec{E}(t) \quad (7)$$

where  $:$  denotes the contracted product and  $\bigotimes$  the tensorial product.  $\vec{E}$  is the driving electric field,  $\bar{\omega}_e^2 = \begin{pmatrix} \omega_{e,x}^2 & 0 & 0 \\ 0 & \omega_{e,y}^2 & 0 \\ 0 & 0 & \omega_{e,z}^2 \end{pmatrix}$  is the eigenfrequency matrix of the considered medium, which is diagonal provided  $x$ ,  $y$ , and  $z$  are the principal axes of the optical frame of the medium (*e.g.*  $\omega_{e,x} = \sqrt{\frac{1}{m} \frac{\partial^2 V}{\partial x^2}}$ ), and the matrix  $\bar{\gamma}$  stands for the linear absorption. No multiphoton absorption is considered here. Note that a medium symmetry of at least  $K \times C_2$  (*i.e.* a crystal with at least orthorhombic symmetry, or a statistically isotropic medium like air) allows to simultaneously diagonalize  $\bar{\omega}_e^2$  and  $\bar{\gamma}$  in the optical frame [15].

A perturbative solution of Eq. (7) is searched as:

$$\vec{P} = \sum_{l=1}^{\infty} \alpha^l \vec{P}^{(l)} \quad (8)$$

where  $\alpha \in ]0..1[$  is a free parameter. The series begins at 1, assuming  $\vec{P}^{(0)} = \vec{0}$ . Inserting it in Eq. (7) and equating the terms in  $\alpha^q$  yields a set of equations

$$\frac{d^2 \vec{P}^{(1)}}{dt^2} + \bar{\gamma} \frac{d\vec{P}^{(1)}}{dt} + \bar{\omega}_e^2 \vec{P}^{(1)} = \frac{Ne^2}{m} \vec{E}(t) \quad (9)$$

and,  $\forall q \geq 2$ ,

$$\frac{d^2 \vec{P}^{(q)}}{dt^2} + \bar{\gamma} \frac{d\vec{P}^{(q)}}{dt} + \bar{\omega}_e^2 \vec{P}^{(q)} = -Ne Q^{(q)} : \bigotimes_{u=1}^q \frac{\vec{P}^{(1)}}{Ne} \quad (10)$$

Note that in the right-hand side of Eq. (10), we have deliberately omitted the terms in  $\otimes_{\Sigma q'_u=q} (P^{(q'_u)})$ , with  $q > q'_u > 1$ . These terms imply non-linear polarizations in the construction of the considered higher-order non-linear polarization and hence correspond to cascades of frequency mixings, like *e.g.* in the generation of third harmonic by frequency-doubling the fundamental wavelength and then mixing it with its second-harmonic. Consistently, in the identification of the non-linear susceptibilities in Eq. (20), only single-step mixing will be taken into account.

## 2.2. Sellmeier equations

If  $\bar{\bar{\Omega}}$  can be diagonalized (*i.e.* if the medium symmetry is at least  $K \times C_2$  or absorption can be neglected), Eq. (9) defining the linear polarization is purely vectorial and can be solved on each axis independently. Omitting the indices displaying the axis of the considered polarization, we write  $P^{(1)}(t) = \int_{-\infty}^{+\infty} P_0^{(1)}(\omega) e^{i\omega t} d\omega$  and  $E(t) = \int_{-\infty}^{+\infty} E_0(\omega) e^{i\omega t} d\omega$ , where, following the usual notation, positive frequencies denote incident ones and negative frequencies are emitted ones. Introducing the spectral dependency parameter  $\Omega(\omega) = \omega_e^2 - \omega^2 + i\omega\gamma$  yields

$$\int_{-\infty}^{+\infty} \Omega(\omega) P_0^{(1)}(\omega) e^{i\omega t} d\omega = \frac{Ne^2}{m} \int_{-\infty}^{+\infty} E_0(\omega) e^{i\omega t} d\omega \quad (11)$$

which implies, for any frequency  $\omega_0$  of the emitted field:

$$P_0^{(1)}(\omega_0) = \frac{Ne^2}{m} \frac{E_0(\omega_0)}{\Omega(\omega_0)} \quad (12)$$

Hence, the linear susceptibility at frequency  $\omega_0$  is:

$$\chi^{(1)}(\omega_0) = \frac{1}{\Omega(\omega_0)} \frac{Ne^2}{m\epsilon_0} = \frac{Ne^2}{m\epsilon_0(\omega_e^2 - \omega_0^2 + i\omega_0\gamma)} \quad (13)$$

which defines the spectral dependence of  $\chi^{(1)}$  on any principal axis. If absorption can be neglected ( $\gamma \sim 0$ ) and  $\chi^{(1)} \ll 1$ , Eq. (13) takes a form similar to a typical Sellmeier formula:  $n^2 - 1 = \frac{A}{B - 1/\lambda^2}$ , where  $n^2 = 1 + \chi^{(1)}$ .

## 2.3. Uniaxial generalized Miller formulae

Equation (10) can be reduced to a scalar form provided the polarization is excited along one single principal axis. We will first focus on this case which simplifies the writing and thus helps focusing the discussion on the the physical aspects, without altering the principle of the derivation. Omitting the index corresponding to the axis, the scalar form of Eq. (10) reads, for any  $q \geq 2$ :

$$\frac{d^2 P^{(q)}}{dt^2} + \gamma \frac{dP^{(q)}}{dt} + \omega_e^2 P^{(q)} = -NeQ^{(q)} \left( \frac{P^{(1)}}{Ne} \right)^q \quad (14)$$

Since  $P^{(q)}(t) = \int_{-\infty}^{+\infty} P_0^{(q)}(\omega) e^{i\omega t} d\omega$ , Eq. (14) rewrites:

$$\int_{-\infty}^{+\infty} \Omega(\omega) P_0^{(q)}(\omega) e^{i\omega t} d\omega = -\frac{Q^{(q)}}{(Ne)^{q-1}} \left( \int_{-\infty}^{+\infty} P_0^{(1)}(\omega) e^{i\omega t} d\omega \right)^q \quad (15)$$

$$= -\frac{Q^{(q)}}{(Ne)^{q-1}} \iint \dots \iint \prod_{l=1}^q (P_0^{(1)}(\omega_l) e^{i\omega_l t} d\omega_l) \quad (16)$$

Identifying the terms at an arbitrary frequency  $\omega_0$  on both sides of the equation, we obtain:

$$P_0^{(q)}(\omega_0) = -\frac{Q^{(q)}}{\Omega(\omega_0)(Ne)^{q-1}} \iint \dots \iint \delta\left(\sum_{l=0}^q \omega_l = 0\right) \times \prod_{l=1}^q \left(P^{(1)}(\omega_l) d\omega_l\right) \quad (17)$$

$$P_0^{(q)}(\omega_0) = -Ne \left(\frac{e}{m}\right)^q \frac{Q^{(q)}}{\Omega(\omega_0)} \sum_{\sum_{l=0}^q \omega_l = 0} \left(\prod_{l=1}^q \frac{E_0(\omega_l)}{\Omega(\omega_l)}\right) \quad (18)$$

Let us now consider the construction of a wave at  $\omega_0$  from a set of  $q' \leq q$  incident waves at frequencies  $\omega_1, \dots, \omega_{q'}$ , each algebraic frequency  $\omega_l$  being implied  $u_l$  times in the process:  $\sum_{l=1}^{q'} u_l = q$ , while energy conservation imposes  $\sum_{l=1}^{q'} u_l \omega_l = \omega_0$ . In this case,

$$P_0^{(q)}(\omega_0) = -Ne \left(\frac{e}{m}\right)^q \frac{Q^{(q)}}{\Omega(\omega_0)} C_q^{u_1, \dots, u_{q'}} \prod_{l=1}^{q'} \left(\frac{E_0(\omega_l)}{\Omega(\omega_l)}\right)^{u_l} \quad (19)$$

where  $C_q^{u_1, \dots, u_{q'}} = q! / (u_1! \times \dots \times u_{q'}!)$  is the number of combinations achievable from  $q'$  sets of  $u_1, \dots, u_{q'}$  objects, respectively. The terms of Eq. (18) corresponding to each combination of frequencies conserving energy can be identified with the expression of the non-linear polarization using the  $(q+1)^{th}$  rank tensor.

$$P_0^{(q)}(\omega_0) = \varepsilon_0 C_q^{u_1, \dots, u_{q'}} \chi^{(q)}(\omega_0; \omega_1, \dots, \omega_{q'}) \prod_{l=1}^{q'} E_0^{u_l}(\omega_l) \quad (20)$$

As stated above, consistently with Eq. (14) we do not consider here the cascaded processes. Therefore, the identification yields:

$$\chi^{(q)}(\omega_0; \omega_1, \dots, \omega_q) = -Ne \left(\frac{e}{m}\right)^q \frac{Q^{(q)}}{\varepsilon_0 \prod_{l=0}^q \Omega(\omega_l)} \quad (21)$$

$$= \frac{m\varepsilon_0^q}{N^q e^{q+1}} Q^{(q)} \prod_{l=0}^q \chi^{(1)}(\omega_l) \quad (22)$$

This expression provides a general description of the non-linear susceptibility of any order, provided the shape of the potential  $V$  is known. In practice, this potential is rarely known, but it is independent from the excitation frequency. The spectral dependence of the above expression is therefore only driven by  $\Omega$ , *i.e.* the spectral dependence of the first-order susceptibilities. As a consequence, in a given medium, *the knowledge of both the frequency dependence of the linear susceptibility and of the  $q^{th}$ -order susceptibility for a specific set of wavelengths is sufficient to extrapolate this susceptibility to any other set of wavelengths*, through the relation:

$$\frac{\chi^{(q)}(\omega_0; \omega_1, \dots, \omega_q)}{\chi^{(q)}(\omega'_0; \omega'_1, \dots, \omega'_q)} = \frac{\prod_{l=0}^q \Omega(\omega'_l)}{\prod_{l=0}^q \Omega(\omega_l)} = \frac{\prod_{l=0}^q \chi^{(1)}(\omega_l)}{\prod_{l=0}^q \chi^{(1)}(\omega'_l)} \quad (23)$$

When applied to  $\chi^{(2)}$ , this generalized Miller formula immediately reduces to the original one of Eq. (1) [11].

#### 2.4. Three-dimensionnal Miller formulæ

While the one-dimensional treatment of Eqs. (14)–(23) provides an easy writing of the derivation, the same sequence can be applied to solve Eq. (10) in the general three-dimensional case.

Products simply have to be transposed to the adequate tensorial products. The identification of the spectral components of the Fourier expression of  $\vec{P}^{(q)}$  and  $\otimes \vec{P}^{(1)}$  yields a three-dimensional equivalent of Eq. (18):

$$\bar{\bar{\Omega}}(\omega_0) \vec{P}_0^{(q)}(\omega_0) = -Ne \left(\frac{e}{m}\right)^q Q^{(q)} : \left( \otimes_{l=1}^q \frac{\vec{P}^{(1)}(\omega_l)}{Ne} \right) \quad (24)$$

In media with at least  $K \times C_2$  symmetry, or if absorption can be neglected,  $\bar{\bar{\Omega}}$  is diagonal so that this expression can easily be identified with the counterpart of Eq. (20) expressing the non-linear polarization in terms of non-linear susceptibility:

$$\vec{P}_0^{(q)}(\omega_0) = \varepsilon_0 \chi^{(q)} : \otimes_{l=1}^q \vec{E}(\omega_l) \quad (25)$$

$$\frac{\chi_{v;x^{(i)},y^{(j)},z^{(k)}}^{(q)}(\omega_0; \omega_1, \dots, \omega_q)}{\chi_{v;x^{(i)},y^{(j)},z^{(k)}}^{(q)}(\omega'_0; \omega'_1, \dots, \omega'_q)} = \frac{\prod_{l=0}^q \Omega_{v_l}(\omega'_l)}{\prod_{l=0}^q \Omega_{v_l}(\omega_l)} \quad (26)$$

$$= \frac{\prod_{l=0}^q \chi_{v_l}^{(1)}(\omega_l)}{\prod_{l=0}^q \chi_{v_l}^{(1)}(\omega'_l)} \quad (27)$$

where each index  $v_l$  denotes either the  $x$ ,  $y$ , or  $z$  axis. The spectral dependence of  $\chi^{(q)}$  only depends on the product of the  $\Omega_{v_l}(\omega_l)$ , meaning that all frequencies commute. This property, together with the fact that the  $\Omega(\omega)$  are even functions as soon as absorption can be neglected, provides a direct evidence and generalization to arbitrary orders of the ABDP relations. These relations state that as soon as  $\bar{\bar{\Omega}}$  can be diagonalized,  $\omega_0$  commutes with any  $\omega_l$  in the expression of  $\chi^{(2)}$  and  $\chi^{(3)}$  [16].

### 2.5. Application to non-linear refractive indices

In the case of frequency-degenerate interactions of odd order excited along one single principal axis, the susceptibility tensor reduces to  $\chi^{(2p+1)}(\omega_0) \equiv \frac{2^{p+1} p! (p+1)!}{(2p+1)!} \frac{(n_0^2(\omega_0) \varepsilon_0 c^2)^p}{n_0(\omega_0)} n_{2p}(\omega_0)$ , which defines the  $p^{\text{th}}$ -order non-linear refractive index  $n_{2p}$ . Therefore, the knowledge of the dispersion curve for the linear susceptibility and the measurement of  $\chi^{(2p+1)}$  at one single frequency  $\omega'_0$  are sufficient to provide  $\chi^{(2p+1)}$  at any frequency  $\omega_0$  thanks to Eq. (23):

$$\frac{\chi^{(2p+1)}(\omega_0)}{\chi^{(2p+1)}(\omega'_0)} = \left( \frac{\Omega(\omega'_0)}{\Omega(\omega_0)} \right)^{2p+2} = \left( \frac{\chi^{(1)}(\omega_0)}{\chi^{(1)}(\omega'_0)} \right)^{2p+2} \quad (28)$$

or equivalently, if absorption can be neglected, in terms of the real parts of the non-linear refractive indices:

$$\frac{n_{2p}(\omega_0)}{n_{2p}(\omega'_0)} = \left( \frac{n_0^2(\omega_0) - 1}{n_0^2(\omega'_0) - 1} \right)^{2p+2} \quad (29)$$

As an illustration, Fig. 1 displays the values of  $n_2$  through  $n_8$  for  $N_2$ ,  $O_2$  and Ar, based on the measurements of Loriot *et al.* at 800 nm [4] as corrected by B ejot *et al.* [5], extrapolated to the whole spectrum using Eq. (28).

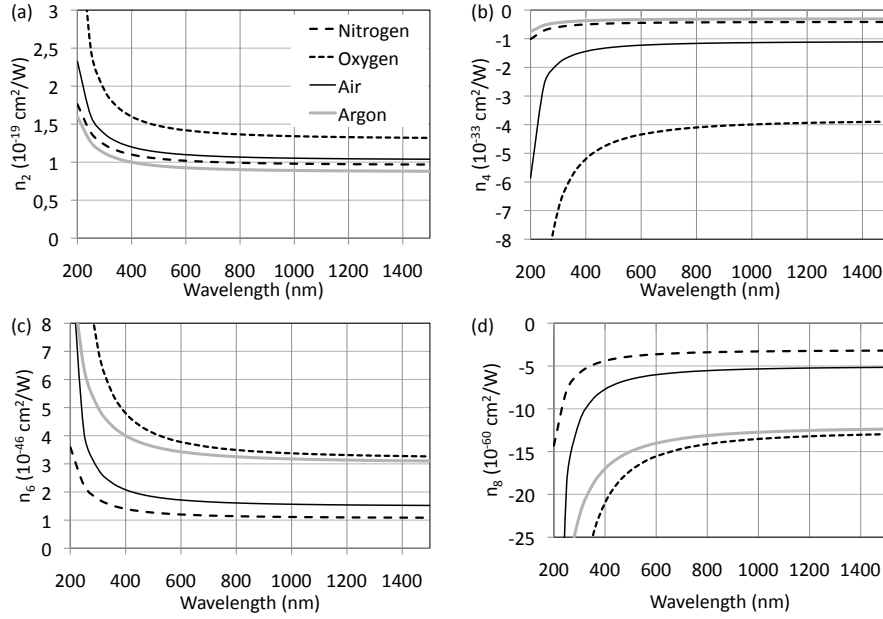


Fig. 1. Spectral dependence of the non-linear refractive indices (a)  $n_2$ , (b)  $n_4$ , (c)  $n_6$ , and (d)  $n_8$  of  $O_2$ ,  $N_2$ , air and Ar at atmospheric pressure.

### 3. Generalization to mixes and multiple resonance frequencies

Up to now, we have only considered the case of a single type of oscillators. However, in actual media (*e.g.* in mixes like the air, where both  $N_2$  and  $O_2$  get polarized, or in crystals where several oscillation modes can be excited) several eigenfrequencies  $\omega_{e,l}$  may contribute. In this case, the polarization  $\vec{P}$  can be defined as  $\sum \vec{P}_l$ , where  $l$  denotes the types of oscillators, or species. If the coupling between the oscillators can be neglected, the above derivation applies to each oscillator type independently, and the resulting refractive index will be given by the Lorentz-Lorenz model. For example the Sellmeier equation of air reads [14]:

$$10^8(n_0 - 1) = 8015.514 + \frac{2368616}{128.7459 - 1/\lambda^2} + \frac{19085.73}{50.01974 - 1/\lambda^2} \quad (30)$$

where the wavelength  $\lambda$  is expressed in  $\mu\text{m}$ . Obviously, the terms of Eq. (30) respectively correspond to  $N_2$ , with a resonance at  $1/\lambda^2 \sim 128.7\mu\text{m}^{-2}$  (*i.e.*  $\lambda = 88$  nm):

$$10^8(n_{0,N_2} - 1) = 8736.28 + \frac{2398095.2}{128.7 - 1/\lambda^2} \quad (31)$$

and to  $O_2$ , with  $1/\lambda^2 \sim 50\mu\text{m}^{-2}$  (*i.e.*  $\lambda = 141$  nm) [14]:

$$10^8(n_{0,O_2} - 1) = 15532.45 + \frac{456402.97}{50.0 - 1/\lambda^2} \quad (32)$$

In such cases, the generalized Miller formulæ of Eq. (23) cannot be applied to the material or the mix as a whole. Instead, they must be applied to each susceptibility-order of each oscillator type. The non-linear susceptibilities of the whole material will then be deduced from those of the individual oscillator types through the Lorentz-Lorenz model. Figure 1 displays the result of this treatment in the case of air.

#### 4. Conclusion

In conclusion, we have explicitly derived the spectral dependence of the non-linear susceptibility of any order, generalizing the common form of Sellmeier equations, in both frequency-degenerate and non-degenerate systems. This spectral dependence is fully defined by the knowledge of the linear dispersion of the medium. As a consequence, the Miller formula [Eq. (1)] [11] can be generalized to any order of non-linearity and any tensor element of non-linear susceptibilities as soon as the material has at least  $K \times C_2$  symmetry and negligible absorption. In particular, the spectral dependence of non-linear refractive indices of any order can be deduced from their value at one single frequency and the dispersion curve of the medium. Such knowledge is of particular value in nonlinear optics implying confined light leading to very-high intensities, as, *e.g.* in fiber optics [2] filamentation [7–10], or photonic crystals [3].

#### Acknowledgments

This work was supported by the Swiss NSF (contracts 200021-116198 and 200021-125315).

# Arbitrary-order nonlinear contribution to self-steepening

Jérôme Kasparian,<sup>1,\*</sup> Pierre Béjot,<sup>2</sup> and Jean-Pierre Wolf<sup>1</sup>

<sup>1</sup>Université de Genève, GAP-Biophotonics, 20 Rue de l'École de Médecine, 1211 Geneva 4, Switzerland

<sup>2</sup>Laboratoire Interdisciplinaire Carnot de Bourgogne (ICB), UMR 5209, CNRS-Université de Bourgogne, 9 Avenue Alain Savary, BP 47 870, F-21078 Dijon Cedex, France

\*Corresponding author: jerome.kasparian@unige.ch

Received June 1, 2010; revised July 8, 2010; accepted July 15, 2010;  
posted July 26, 2010 (Doc. ID 129224); published August 13, 2010

On the basis of the recently published generalized Miller formulas, we derive the spectral dependence of the contribution of arbitrary-order nonlinear indices to the group-velocity index. We show that in the context of laser filamentation in gases, all experimentally accessible orders (up to the ninth-order nonlinear susceptibility  $\chi^{(9)}$  in air and  $\chi^{(11)}$  in argon) have contributions of alternative signs and similar magnitudes. Moreover, we show both analytically and numerically that the dispersion term of the nonlinear indices must be considered when computing the intensity-dependent group velocity. © 2010 Optical Society of America  
OCIS codes: 190.3270, 190.7110, 120.4530.

Nonlinear optics [1] relies on the nonlinear properties of the propagation medium, among which the successive orders of the nonlinear susceptibility are essential parameters. However, due to the difficulty in measuring them experimentally, their knowledge is generally limited to the first nonzero order ( $\chi^{(2)}$  or  $\chi^{(3)}$ , depending on medium symmetry). Furthermore, the available laser sources drastically limit the wavelengths available for such measurements, so that reliable dispersion curves for higher-order susceptibilities cannot be deduced from the sparse experimental data available to date.

The lack of data led to the neglect of these higher order Kerr terms in most numerical simulations of, e.g., both self-guided filaments in ultrashort intense laser pulses [2–5] or the propagation of high-intensity pulses in hollow-core fibers [6]. Similarly, the Kerr contribution to the group velocity is most generally limited to the third order and treated as dispersionless in the lack of data about its dispersion [3,4]. Recently, however, the measurement of the higher-order refractive indices up to  $n_8$  in  $N_2$  and  $O_2$ , and up to  $n_{10}$  in argon [7,8], followed by the generalization of the Miller formulas [9] to any order of nonlinearity [10], provided a new insight into the spectral dependence of the nonlinear refractive index at high incident intensity.

This allowed us to show that these terms cannot be neglected and can even provide the dominant contribution stabilizing the self-guided filaments [11]. Furthermore, in argon-filled hollow-core fibers, these terms are necessary to obtain quantitative agreement of numerical simulations with experimental data [12,13]. But these works focused on the contribution of higher-order Kerr terms to phase velocity. The contribution of the spectral dispersion of higher-order indices to group velocity was not considered, although it can be expected to impact the propagation, and in particular the self-steepening term.

Here we derive an explicit expression for the contribution of any order of the nonlinear refractive indices to the group-velocity index. We show that in filamentation, all nonlinear orders of the group-velocity index can have similar orders of magnitude and must be considered. Furthermore, especially in the UV, the dispersion of the nonlinear indices cannot be neglected when calculating self-steepening.

At arbitrary intensity  $I$  and frequency  $\omega$ , the refractive index can be expressed as [1]

$$n(\omega) = n_0(\omega) + n_2(\omega)I + n_4(\omega)I^2 + \dots = \sum_{j=0}^{\infty} n_{2j}(\omega)I^j. \quad (1)$$

In gases, where  $n - 1 \ll 1$ , the refractive index  $n(\omega) = \sqrt{1 + \sum_{j=0}^{\infty} \chi^{(2j+1)}(\omega)I^j}$  can be approximated by [1]

$$n_0(\omega) \approx 1 + \frac{1}{2}\chi^{(1)}(\omega), \quad (2)$$

$$n_{2j}(\omega) \approx Z^{(2j+1)}\chi^{(2j+1)}(\omega), \quad (3)$$

where  $\chi^{(2j+1)}$  is the  $(2j + 1)$ th-order nonlinear susceptibility and the  $Z^{(2j+1)}$  are frequency-independent factors. If a pulse can be described as a carrier wave modulated by an envelope with a sufficiently narrow spectrum to allow neglect of the envelope deformations over short distances, then a group-velocity index can be defined as

$$n_g(\omega) = \frac{c}{v_g} = n(\omega) + \omega \frac{dn}{d\omega}, \quad (4)$$

where  $v_g$  is the group velocity and  $c$  is the speed of light in vacuum. Defining  $Z^{(1)} = 1/2$  and considering Eqs. (1)–(3),  $n_g$  is rewritten:

$$n_g(\omega) = \sum_{j=0}^{\infty} \left( n_{2j}(\omega) + \omega \frac{dn_{2j}}{d\omega} \right) I^j \equiv \sum_{j=0}^{\infty} n_{g,2j} I^j, \quad (5)$$

$$\approx 1 + \sum_{j=0}^{\infty} Z^{(2j+1)} \left( \chi^{(2j+1)}(\omega) + \omega \frac{d\chi^{(2j+1)}}{d\omega} \right) I^j. \quad (6)$$

Identifying the terms for each power of the intensity, we obtain the contribution of each order of nonlinearity to the group-velocity index:

$$n_{g,0}(\omega) - 1 \approx \frac{1}{2} \left( \chi^{(1)} + \omega \frac{d\chi^{(1)}(\omega)}{d\omega} \right), \quad (7)$$

$$\forall j \geq 1, \quad n_{g,2j}(\omega) \approx Z^{(2j+1)} \left( \chi^{(2j+1)} + \omega \frac{d\chi^{(2j+1)}(\omega)}{d\omega} \right). \quad (8)$$

The first expression corresponds to the usual linear contribution, while the first term in the expression of the group-velocity index  $n_{2,g}$  corresponds to the classical self-steepening term [1,14,15]. Within the elastically bound electron model, the susceptibility of the arbitrary order is given up to any order by the generalized Miller formulas [10]:

$$\chi^{(1)}(\omega) = \frac{Ne^2}{m\epsilon_0(\omega_0^2 - \omega^2 + i\omega_0\gamma)}, \quad (9)$$

$$\forall q \geq 2, \quad \chi^{(q)}(\omega) = \frac{Ne}{\epsilon_0} \left( \frac{e}{m} \right)^q Q^{(q)} \frac{1}{\Omega(\omega)^{q+1}}, \quad (10)$$

where  $m$  and  $-e$  are the electron mass and charge,  $\epsilon_0$  is the permittivity of vacuum,  $N$  is the density of dipoles in the propagation medium,  $\gamma$  is the width of the resonance at frequency  $\omega_0$ , and  $Q^{(q)}$  describes the potential well where the electron oscillates;  $\Omega(\omega) = \omega_0^2 - \omega^2 + i\omega_0\gamma$ . Inserting these expressions into Eqs. (7) and (8) yields

$$n_{g,0}(\omega) - 1 \approx (n_0(\omega) - 1) \frac{\omega_0^2 + \omega^2 + i\omega_0\gamma}{\omega_0^2 - \omega^2 + i\omega_0\gamma}, \quad (11)$$

$$\forall j \geq 1, \quad n_{g,2j}(\omega) \approx n_{2j}(\omega) \frac{\omega_0^2 + (4j+3)\omega^2 + i\omega_0\gamma}{\Omega(\omega)}. \quad (12)$$

These equations provide a general expression of each nonlinear contribution to the group-velocity index  $n_g$ . As a consequence, it allows evaluation of the impact of higher-order Kerr terms on self-steepening in the context of laser filamentation in gases or the propagation of ultrashort pulses in hollow fibers. In the following, we consider the propagation of high-intensity pulses in transparent media, far from resonance. In this case,  $|\omega_0 - \omega| \gg \gamma$ , so that  $\omega_0^2 + \omega^2 > |\omega_0^2 - \omega^2| \gg \omega_0\gamma$ . The imaginary parts of Eqs. (11) and (12) become negligible:

$$n_{g,0}(\omega) - 1 \approx (n_0(\omega) - 1) \frac{\omega_0^2 + \omega^2}{\omega_0^2 - \omega^2}, \quad (13)$$

$$n_{g,2j}(\omega) \approx n_{2j} \frac{\omega_0^2 + (4j+3)\omega^2}{\omega_0^2 - \omega^2}. \quad (14)$$

Note that the negative values obtained for  $\omega > \omega_0$  correspond to the well-known region of the negative group-velocity index [16]. Figure 1 displays the spectral

dependence from Eq. (14), based on the recent experimental measurements of  $n_{2j}$  at 800 nm [7,8,11], extrapolated to the whole visible spectrum by applying generalized Miller formulas [10] and the dispersion data of Zhang *et al.* [17].

From Eqs. (13) and (14), we can estimate the ratio of the successive terms of the group-velocity index

$$\frac{n_{g,2}I}{n_{g,0} - 1} = \frac{n_2I}{n_0 - 1} \frac{\omega_0^2 + 7\omega^2}{\omega_0^2 + \omega^2}, \quad (15)$$

$$\forall j \geq 1, \quad \frac{n_{g,2j+2}I^{j+1}}{n_{g,2j}I^j} = \frac{n_{2j+2}I}{n_{2j}} \frac{\omega_0^2 + (4j+7)\omega^2}{\omega_0^2 + (4j+3)\omega^2}. \quad (16)$$

The second factor of Eqs. (15) and (16) is of the order of 1. Therefore, the orders of magnitude of the ratio of successive terms are driven by the ratio of the nonlinear indices  $n_{2j}$ , multiplied by  $I$ . The values displayed in Fig. 1 imply that, for  $I < 10^{14}$  W/cm<sup>2</sup>,  $n_{2j}I^j \ll n_0 - 1$ . Self-steepening is, therefore, as well known [14,15], a second-order term in the nonlinear Schrödinger equation (NLSE) describing the nonlinear propagation of light in a nonlinear transparent medium. Furthermore, all known terms in  $n_{2j}I^j$  have alternate signs and comparable orders of magnitude [7,8,10]. The same, therefore, applies to the terms in  $n_{g,2j}I^j$ , which must all be taken into account when describing self-steepening e.g., in the context of filamentation, where the intensity is clamped around  $5 \times 10^{13}$  W/cm<sup>2</sup> [18,19], or of the propagation in hollow fibers.

Equation (14) provides an estimation of the error performed when neglecting the dispersion term in the contribution of the higher-order indices to the group-velocity index. Figure 2 displays the relative error  $1 - n_{2j}/n_{g,2j}$  implied at atmospheric pressure when neglecting the dispersion terms of the Kerr contributions to the group velocity. The calculations are based on the same data as in Fig. 1. As is clear from Eq. (14), this error decreases for longer wavelengths, where dispersion is smoother. At 800 nm, it amounts to  $\sim 20\%$  and may be considered acceptable, although not negligible. However, at blue or UV

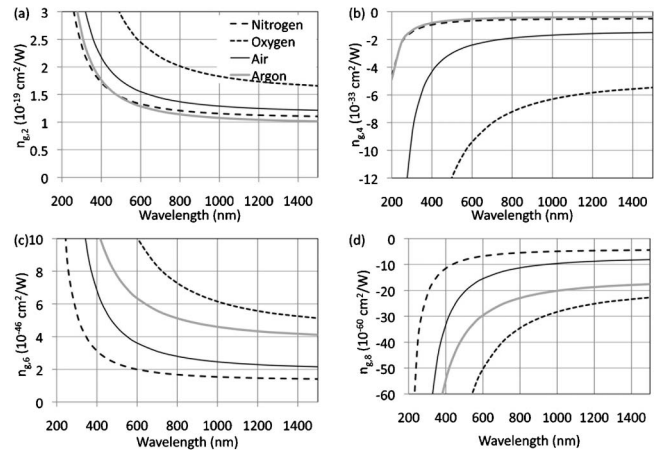


Fig. 1. Spectral dependence of the nonlinear group-velocity indices: (a)  $n_{g,2}$ , (b)  $n_{g,4}$ , (c)  $n_{g,6}$ , and (d)  $n_{g,8}$  of O<sub>2</sub>, N<sub>2</sub>, air, and Ar at 1 atm.

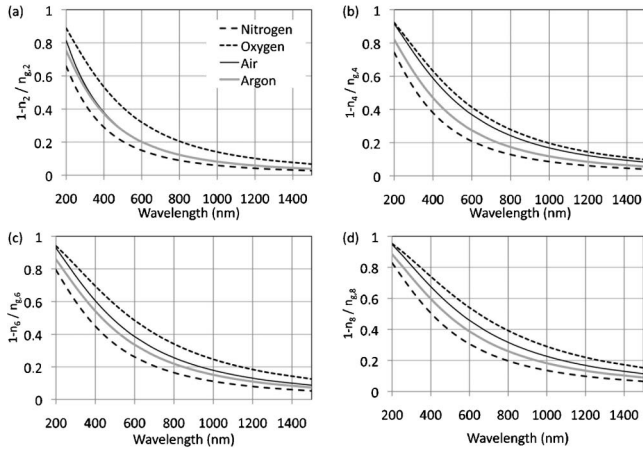


Fig. 2. Relative error induced when neglecting the dispersion of the Kerr terms in the group velocity: (a)  $1 - n_2/n_{g,2}$ , (b)  $1 - n_4/n_{g,4}$ , (c)  $1 - n_6/n_{g,6}$ , and (d)  $1 - n_8/n_{g,8}$  of  $O_2$ ,  $N_2$ , air, and Ar at 1 atm.

wavelengths, the dispersion term dominates and must be considered in the equations.

Numerical simulations of the propagation of a 35 fs pulse in a 1-m-long hollow-core fiber filled with 1.4 bars argon, confirm this finding. As described in detail earlier [13], the model implements the NLSE, including the higher-order Kerr terms. We compared the code output with and without the contribution of the higher-order indices to the group-velocity index up to the term in  $n_{10}$ , i.e., the terms of Eq. (6) for  $1 \leq j \leq 5$ . As can be seen in Fig. 3, the consideration of the full steepening term affects the spectrum by deforming the pulse

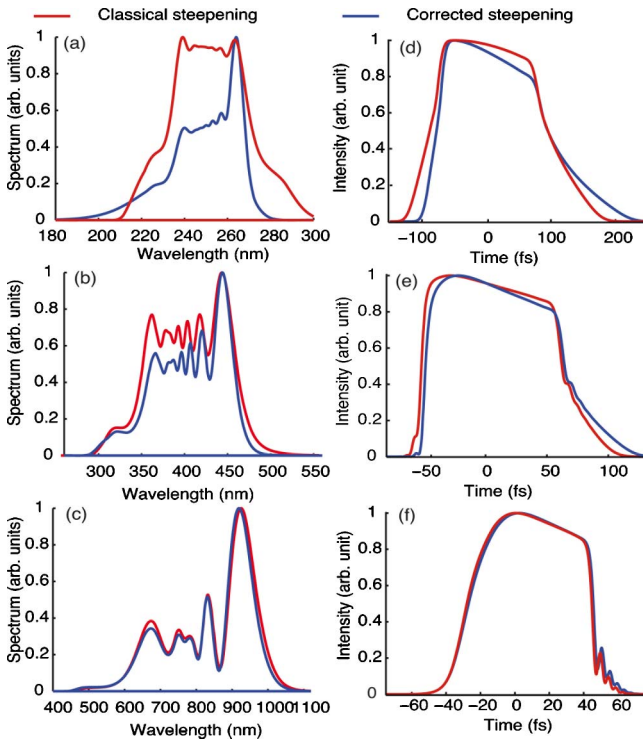


Fig. 3. (Color online) Influence of the higher-order indices contribution to the group-velocity index on the propagation of a 35 fs pulse with fixed  $n_2(\lambda)I$  in a 1-m-long hollow-core fiber filled with 1.4 bars argon: (a), (d) 250 nm, 286  $\mu\text{J}$ ; (b), (e) 400 nm, 360  $\mu\text{J}$ ; and (c), (f) 800 nm, 400  $\mu\text{J}$ .

envelope. It simultaneously redshifts the central part of the spectrum and blueshifts its edges. Furthermore, as predicted by the analytic calculations, the contribution of the dispersion of the higher-order Kerr terms is larger in the UV and negligible in the IR. These terms must, therefore, be considered in numerical simulations, especially while investigating spectral broadening.

In conclusion, based on the recent generalization of the Miller formulas, we have estimated the contribution of higher-order indices to the group-velocity index. These contributions define the self-steepening term of the NLSE. They have alternate signs and comparable absolute values in intensity regimes typical of filamentation. All nonlinear terms must, therefore, be considered in the evaluation of the self-steepening of ultrashort intense laser pulses propagating in transparent Kerr media. Furthermore, we demonstrate both analytically and numerically that their spectral dispersion cannot be neglected either, especially at shorter wavelengths.

This work was supported by the Swiss National Science Foundation (contract 200021-125315) and the French Agence Nationale de la Recherche ("Control of molecular processes in contact with an environment" project).

## References

1. R. W. Boyd, *Nonlinear Optics* (Academic, 2008).
2. S. L. Chin, S. A. Hosseini, W. Liu, Q. Luo, F. Théberge, N. Aközbe, A. Becker, V. P. Kandidov, O. G. Kosareva, and H. Schroeder, *Can. J. Phys.* **83**, 863 (2005).
3. L. Bergé, S. Skupin, R. Nuter, J. Kasparian, and J.-P. Wolf, *Rep. Prog. Phys.* **70**, 1633 (2007).
4. A. Couairon and A. Mysyrowicz, *Phys. Rep.* **441**, 47 (2007).
5. J. Kasparian and J.-P. Wolf, *Opt. Express* **16**, 466 (2008).
6. J. M. Dudley, G. Genty, and S. Coen, *Rev. Mod. Phys.* **78**, 1135 (2006).
7. V. Loriot, E. Hertz, O. Faucher, and B. Lavorel, *Opt. Express* **17**, 13429 (2009).
8. V. Loriot, E. Hertz, O. Faucher, and B. Lavorel, *Opt. Express* **18**, 3011 (2010).
9. R. C. Miller, *Appl. Phys. Lett.* **5**, 17 (1964).
10. W. Ettoumi, Y. Petit, J. Kasparian, and J.-P. Wolf, *Opt. Express* **18**, 6613 (2010).
11. P. Béjot, J. Kasparian, S. Henin, V. Loriot, T. Vieillard, E. Hertz, O. Faucher, B. Lavorel, and J.-P. Wolf, *Phys. Rev. Lett.* **104**, 103903 (2010).
12. B. E. Schmidt, P. Béjot, M. Giguère, A. D. Shiner, C. Trallero-Herrero, E. Bisson, J. Kasparian, J.-P. Wolf, D. M. Villeneuve, J.-C. Kieffer, P. B. Corkum, and F. Légaré, *Appl. Phys. Lett.* **96**, 121109 (2010).
13. P. Béjot, B. E. Schmidt, J. Kasparian, J.-P. Wolf, and F. Légaré, *Phys. Rev. A* **81**, 063828 (2010).
14. N. Aközbe, M. Scalora, C. M. Bowden, and S. L. Chin, *Opt. Commun.* **191**, 353 (2001).
15. I. S. Golubtsov and O. G. Kosareva, *J. Opt. Technol.* **69**, 462 (2002).
16. R. W. Boyd and D. J. Gauthier, *Science* **326**, 1074 (2009).
17. J. Zhang, Z. H. Lu, and L. J. Wang, *Appl. Opt.* **47**, 3143 (2008).
18. J. Kasparian, R. Sauerbrey, and S. L. Chin, *Appl. Phys. B* **71**, 877 (2000).
19. A. Becker, N. Aközbe, K. Vijayalakshmi, E. Oral, C. M. Bowden, and S. L. Chin, *Appl. Phys. B* **73**, 287 (2001).

## Production of ozone and nitrogen oxides by laser filamentation

Yannick Petit, Stefano Henin, Jérôme Kasparian,<sup>a)</sup> and Jean-Pierre Wolf

GAP Biophotonics, Université de Genève, 20 rue de l'École de Médecine, CH1211 Genève 4, Switzerland

(Received 4 June 2010; accepted 21 June 2010; published online 15 July 2010)

We have experimentally measured that laser filaments in air generate up to  $10^{14}$ ,  $3 \times 10^{12}$ , and  $3 \times 10^{13}$  molecules of  $O_3$ ,  $NO$ , and  $NO_2$ , respectively. The corresponding local concentrations in the filament active volume are  $10^{16}$ ,  $3 \times 10^{14}$ , and  $3 \times 10^{15}$   $cm^{-3}$ , and allows efficient oxidative chemistry of nitrogen, resulting in concentrations of  $HNO_3$  in the parts per million range. The latter forming binary clusters with water, our results provide a plausible pathway for the efficient nucleation recently observed in laser filaments. © 2010 American Institute of Physics.

[doi:10.1063/1.3462937]

In their propagation through transparent media, ultrashort laser pulses can generate self-guided filaments.<sup>1-4</sup> Filamentation stems from a dynamic balance between Kerr self-focusing on one side, and defocusing by both higher-order (negative) Kerr terms,<sup>5</sup> and the free electrons originating from the ionization of the propagation medium by the pulse itself. Filaments, which can be longer than 100 m,<sup>6</sup> be initiated remotely<sup>7</sup> and propagate through clouds<sup>8</sup> and turbulence,<sup>9</sup> are ideally suited for atmospheric applications<sup>4,10</sup> like lightning control,<sup>11</sup> or laser-assisted water nucleation.<sup>12</sup>

In subsaturated atmospheres, the latter effect cannot be explained by the Wilson mechanism<sup>13</sup> in which the charges stabilize charge-transfer complexes of  $H_2O^+O_2^-$ , on which droplets grow. Rather, the observed effect may imply binary nucleation of  $HNO_3$ ,<sup>14-16</sup> which according to the extended Köhler theory stabilizes the growing droplets of binary mixtures, similar to observations in cloud chambers for binary  $H_2SO_4-H_2O$ .<sup>17,18</sup> Assessing this pathway requires a precise knowledge of the physicochemistry of the filaments. In this paper, we measure the generation of three key gases, namely  $O_3$ ,  $NO$ , and  $NO_2$  by laser filaments. Filaments produce large amounts of these trace gases, allowing efficient oxidative chemistry of nitrogen and resulting in concentrations of  $HNO_3$  in the multiparts per million range, which may account for the efficient droplet nucleation induced by laser filaments in sub-saturated atmospheres.<sup>12</sup>

The experiments (Fig. 1) were conducted on the Helvetiera platform, which delivered laser pulses of up to 12 mJ energy and 80 fs Fourier-limited duration (150 GW peak power) at a wavelength of 800 nm and 100 Hz repetition rate. A chopper reduced this rate by a factor of 40 in most experiments (i.e., an average of 2.5 pulses/s) to limit the concentration in the cell and reduce the chemical reactions between the generated species as well as to avoid saturation of the measurement devices. The incident pulse duration was varied by detuning the laser compressor to induce a chirp. The beam ( $2 \times 2.4$  cm cross section) was focused by an  $f=2.8$  m lens to generate one to two filaments in a 2 m long Plexiglas cell of 2 cm diameter with 250  $\mu m$  thin fused silica windows. Fresh air from the room entered freely the cell at one of its ends. At its other end, the air was continuously pumped in parallel through polyethylene tubes by an

ozone analyzer (Horiba APOA-350E) at a flow of 2.2 l/min and a NOx analyzer (Monitor laboratories 8840) at a flow of 0.5 l/min. Although in the filaments, ozone and NOx are partly ionized, the transit time of  $\sim 10$  s through the sampling circuit ensures that they are neutralized before entering the analyzers, so that ionized species are measured together with neutral ones.

All measurements were performed once steady state was reached in the cell. We checked that all measurements were linear with the number of laser shots per unit time. If we neglect chemical reactions among the NOx and  $O_3$  during the transit to the analyzers, the variation in the measured concentration  $C_i$  of species  $i$  depends on the generation of this species by the laser beam (source term  $S_i$ ) and its dilution by the flow  $F$  through the cell.

$$V \times dC_i/dt = S_i - F \times C_i. \quad (1)$$

In a steady state, the source term reads the following:

$$S_i = C_i \times F. \quad (2)$$

Volumic generation rates and the resulting concentrations are then evaluated by dividing  $S_i$  by the total filament volume, corresponding to two filaments of 0.5 m length and of 100  $\mu m$  diameter, i.e., a total volume of 4  $mm^3$ . In Eqs. (1) and (2), we have neglected the losses and source terms due to chemical reactions, especially the oxidation of  $NO$  and  $NO_2$  by ozone<sup>17</sup>



as well as on the walls of the cell, mainly the degradation of ozone into  $O_2$  on the wall surface, as follows:

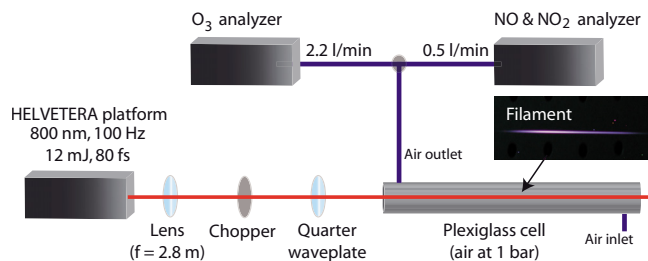


FIG. 1. (Color online) Experimental setup.

<sup>a)</sup>Electronic mail: jerome.kasparian@unige.ch.

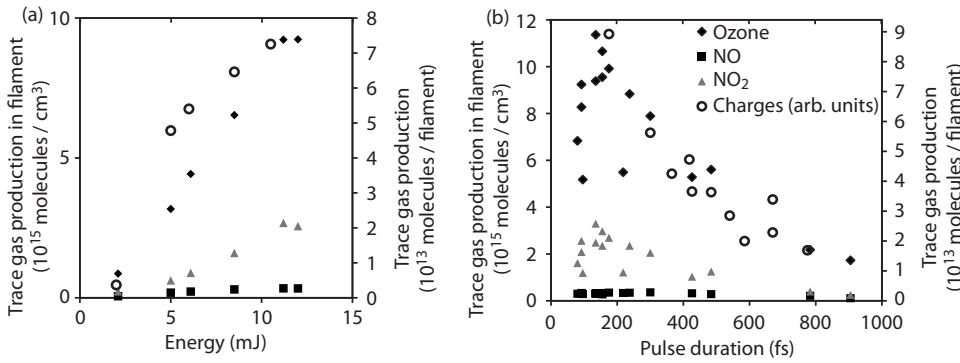


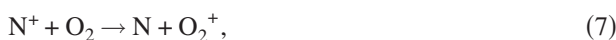
FIG. 2. Generation of O<sub>3</sub>, NO, and NO<sub>2</sub> in laser filaments as a function of (a) the incident energy for a pulse duration of 80 fs and (b) the pulse duration for a pulse of 11.2 mJ energy.



We, therefore, measure a lower limit for the production of O<sub>3</sub> and NO by the laser filaments. On the other hand, the effect on NO<sub>2</sub> is more complex, since Reactions (3) and (4) have opposite effects. These contributions are discussed at the end of the present manuscript. In parallel with the concentration of trace gases, we measured the relative efficiency of charge release by the filaments, as detailed in Ref. 19.

Figure 2 displays the generation rate per unit volume of O<sub>3</sub>, NO, and NO<sub>2</sub> in the filament as a function of the incoming pulse energy and duration. Obviously, the filaments produce considerable amounts of these trace gases. For 2.5 shots/s, the concentrations averaged over the cell volume reach 200 ppb of O<sub>3</sub> and 50 ppb of NO<sub>2</sub>, one order of magnitude above typical atmospheric values and even higher than the alert level in most countries. They correspond to the generation of extremely high concentrations within the filament volume: 400 ppm (10<sup>16</sup> cm<sup>-3</sup>) of ozone and 100 ppm of NO<sub>2</sub> (3 × 10<sup>14</sup> cm<sup>-3</sup>), respectively.

The production of O<sub>3</sub>, NO, and NO<sub>2</sub> increases quite linearly with pulse energy, with a threshold between 1 and 2 mJ, corresponding to the filamentation threshold in our experimental conditions. It is proportional to that of electrons for various pulse durations and energies (Fig. 2). Linearly polarized pulses yield 19% more ozone, 33% more NO, and 68% more NO<sub>2</sub>, consistent with the fact that a linear polarization is more favorable to filamentation than a circular one,<sup>20</sup> resulting, in our setup, in twice as much charge generation than circularly polarized pulses. These data show that NOx and ozone are mainly produced in the filaments, hence in plasma, rather than in the photon bath. The corresponding pathways may therefore be activated by photodissociation, ionization, or electron impact onto O<sub>2</sub> and N<sub>2</sub> molecules. The very complex chemistry occurring in air plasmas<sup>21,22</sup> prevents us to isolate one single scheme, although three of them are more likely to contribute significantly to the formation of NO. The first one relies on the N<sup>+</sup> ions, which are highly reactive with O<sub>2</sub>, with a rate constant as high as 5 × 10<sup>-10</sup> cm<sup>3</sup>/s at 300 K. Note that, throughout this work, we use of the rate constants at room temperature because the filaments are known to negligibly heat the heavy species of the plasma.<sup>2,3</sup> The branching ratios are 43%, 51%, and 6% between the reactions, as follows<sup>23</sup>:



Alternatively, the recombination of electrons with N<sub>2</sub><sup>+</sup>, can break the N–N bond and lead to the following<sup>24</sup>:



The excited nitrogen atom can also be generated by the following<sup>21</sup>:



The activated nitrogen atoms will then react with oxygen molecules, as follows:



Besides Reactions (6) and (11), O<sup>\*</sup> is also produced by the following<sup>25</sup>



The oxygen atoms immediately react with oxygen molecules, as follows:



Ozone will then oxidize NO into NO<sub>2</sub> through reaction (3). Although the main reaction paths are identified above, simulations of the measured concentrations using rate equations is currently impossible because of the very riche chemical dynamics at play<sup>21</sup> and of the lack of data on the initial N<sup>\*</sup>, N<sub>2</sub><sup>\*</sup>, N<sup>+</sup>, and N<sub>2</sub><sup>+</sup> concentrations in the filaments. However, since the concentration of O<sub>3</sub>, NO, and NO<sub>2</sub> are closely related to that of the electrons, a process initiation by Reactions (6)–(9) is more likely than (10). The very high concentrations O<sub>3</sub> and NO<sub>2</sub> in the filament volume allow an efficient chemistry. In particular, the equilibrium<sup>17</sup>



is governed by  $K_{14} = [\text{N}_2\text{O}_5] / ([\text{NO}_2][\text{NO}_3]) = 3 \times 10^{-11}$  cm<sup>3</sup> at 298 K. N<sub>2</sub>O<sub>5</sub> immediately reacts with water, as follows:



Given the rate constant  $k_4 = 3 \times 10^{-17}$  cm<sup>3</sup>/s of Reaction (4),<sup>17</sup> the extremely high NO<sub>2</sub> and ozone concentrations in the filaments could generate up to 6 × 10<sup>14</sup> molecules/cm<sup>3</sup>/s of NO<sub>3</sub>, a production rate comparable with that of NO<sub>2</sub> in our experiments. Considering the equilibrium constant K<sub>14</sub> and the reaction rate  $k_{15} = 3 \times 10^{-4}$  s<sup>-1</sup>, Reactions (4), (14), and (15) clearly result in the generation of N<sub>2</sub>O<sub>5</sub>, hence HNO<sub>3</sub>, in the parts per million range, or even higher. Binary HNO<sub>3</sub>–H<sub>2</sub>O clusters<sup>16</sup> then form, grow into condensation nuclei and allow macroscopic

droplet formation and net uptake of water from the atmosphere. Reactions (6)–(15) provide a large excess of condensation nuclei as compared with the droplet densities of at most some  $10^3 \text{ cm}^{-3}$  observed in our recent nucleation experiments.<sup>12</sup> Chemistry therefore appears as the dominant process in laser-induced condensation in subsaturated atmospheres. At least, that relevant species are available in amounts largely sufficient to explain the observed condensation.

Up to now, we have neglected the losses due to Reactions (3)–(5). Since all species are generated simultaneously, their concentrations can be considered as roughly proportional (as is also visible on Fig. 2) so that the reaction rates depend on the square of the considered concentration. Under this assumption, the rate Eq. (1) rewrites, for each species  $i$ , as follows:

$$V \times dC_i/dt = S_i - k_i C_i^2 - FC_i, \quad (16)$$

so that in the steady state,

$$C_i = (-F + \sqrt{F^2 + 4k_i S_i})/2k_i. \quad (17)$$

Comparing results in two conditions with identical source term and different pumping rates (hence, sampling flows) yields

$$k_i = (C_{i,1}F_1 - C_{i,2}F_2)/(C_{i,2}^2 - C_{i,1}^2). \quad (18)$$

In the case of ozone, we measured  $[O_3]_1=314 \text{ ppb}$  for  $F_1=2.2 \text{ l/min}$  and  $[O_3]_2=285 \text{ ppb}$  for  $F_2=2.7 \text{ l/min}$ , which yields  $k_{O_3}=4.5 \text{ l/min/ppm}$ . Implementing this correction increases the source term by at most 10%: the losses due to ozone depletion via chemical processes in the flow cell is not the main source of error. Furthermore,  $[NO_2]_1=124 \text{ ppb}$  for  $F_1=0.5 \text{ l/min}$  and  $[NO_2]_2=32 \text{ ppb}$  for  $F_2=2.7 \text{ l/min}$ , result in  $k_{NO_2}=1.7 \text{ l/min/ppm}$ , so that the correction is limited to 1.3%, showing that the main sources and sinks of  $NO_2$ , i.e., respectively Reactions (3) and (4), approximately balance each other. Losses due to chemistry therefore affect little our measurements of both  $NO_2$  and  $O_3$ . These effects are of the same order of magnitude or larger than the long-term drift of the gas analyzers over the time span of the measurements. The concentrations at the output of the cell, and hence the production rates of  $O_3$  and  $NO_2$  (right scales in Fig. 2) can therefore be trusted within typically 10%. On the other hand, the molecule concentrations in the filament volume (left scale in Fig. 2) rely on the estimation of typical filament diameters,<sup>1–4</sup> which may be trusted within a factor of 2. However, the excess of  $HNO_3$  by orders of magnitudes as compared to the amounts required to explain the observed laser-induced water condensation<sup>12</sup> ensures the validity of our qualitative conclusion in spite of this relatively large quantitative uncertainty.

The depletion of NO was estimated by considering the rate  $k_3=1.9 \times 10^{-14} \text{ cm}^3/\text{s}$  of Reaction (3) (Ref. 17) and the concentration retrieved in the filaments. We find a depletion rate  $d[NO]/[NO]dt=k_3 \times [O_3]=200 \text{ s}^{-1}$ . As a consequence, the NO produced is almost completely oxidized into  $NO_2$  within 50 ms due to the extremely high ozone concentration. This confirms that Reaction (3) is far from being the limiting factor in the generation of  $HNO_3$ .

As a conclusion, we have experimentally measured that laser filaments in air generate up to  $10^{14}$ ,  $3 \times 10^{12}$ , and  $3 \times 10^{13}$  molecules of  $O_3$ , NO, and  $NO_2$ , respectively. The

corresponding local concentrations in the filament active volume are  $10^{16}$ ,  $3 \times 10^{14}$ , and  $3 \times 10^{15} \text{ cm}^{-3}$  and allow efficient oxidative chemistry of nitrogen, resulting in concentrations of  $HNO_3$  in the parts per million range. The latter forming binary clusters with water, our results provide a plausible pathway for the efficient nucleation observed in laser filaments, especially in subsaturated atmospheres.

We gratefully acknowledge B. Lazarrotto (Service de la Protection de l'Air de Geneve) for supplying the trace gas analyzers. This work was supported by the Swiss NSF (Contract No. 200021-125315).

<sup>1</sup>S. L. Chin, S. A. Hosseini, W. Liu, Q. Luo, F. Theberge, N. Akozbek, A. Becker, V. P. Kandidov, O. G. Kosareva, and H. Schroeder, *Can. J. Phys.* **83**, 863 (2005).

<sup>2</sup>A. Couairon and A. Mysyrowicz, *Phys. Rep.* **441**, 47 (2007).

<sup>3</sup>L. Bergé, S. Skupin, R. Nuter, J. Kasparian, and J.-P. Wolf, *Rep. Prog. Phys.* **70**, 1633 (2007).

<sup>4</sup>J. Kasparian and J.-P. Wolf, *Opt. Express* **16**, 466 (2008).

<sup>5</sup>P. Béjot, J. Kasparian, S. Henin, V. Lorient, T. Vieillard, E. Hertz, O. Faucher, B. Lavorel, and J.-P. Wolf, *Phys. Rev. Lett.* **104**, 103903 (2010).

<sup>6</sup>B. La Fontaine, F. Vidal, Z. Jiang, C. Y. Chien, D. Comtois, A. Desparois, T. W. Johnson, J.-C. Kieffer, and H. Pépin, *Phys. Plasmas* **6**, 1615 (1999).

<sup>7</sup>M. Rodriguez, R. Bourayou, G. Méjean, J. Kasparian, J. Yu, E. Salmon, A. Scholz, B. Stecklum, J. Eislöffel, U. Laux, A. P. Hatzes, R. Sauerbrey, L. Wöste, and J.-P. Wolf, *Phys. Rev. E* **69**, 036607 (2004).

<sup>8</sup>G. Méjean, J. Kasparian, J. Yu, E. Salmon, S. Frey, J.-P. Wolf, S. Skupin, A. Vinçotte, R. Nuter, S. Champeaux, and L. Bergé, *Phys. Rev. E* **72**, 026611 (2005).

<sup>9</sup>R. Salamé, N. Lascoux, E. Salmon, J. Kasparian, and J. P. Wolf, *Appl. Phys. Lett.* **91**, 171106 (2007).

<sup>10</sup>J. Kasparian, M. Rodriguez, G. Méjean, J. Yu, E. Salmon, H. Wille, R. Bourayou, S. Frey, Y.-B. André, A. Mysyrowicz, R. Sauerbrey, J.-P. Wolf, and L. Wöste, *Science* **301**, 61 (2003).

<sup>11</sup>J. Kasparian, R. Ackermann, Y.-B. André, G. Méchain, G. Méjean, B. Prade, P. Rohwetter, E. Salmon, K. Stelmaszczyk, J. Yu, A. Mysyrowicz, R. Sauerbrey, L. Wöste, and J.-P. Wolf, *Opt. Express* **16**, 5757 (2008).

<sup>12</sup>P. Rohwetter, J. Kasparian, K. Stelmaszczyk, S. Henin, N. Lascoux, W. M. Nakaema, Y. Petit, M. Queißer, R. Salamé, E. Salmon, Z. Q. Hao, L. Wöste, and J.-P. Wolf, *Nat. Photonics* **4**, 451 (2010).

<sup>13</sup>W. Byers Brown, *Chem. Phys. Lett.* **235**, 94 (1995).

<sup>14</sup>V.-M. Kerminen, A. S. Wexler, and S. Potukuchi, *J. Geophys. Res.* **102**, 3715 (1997).

<sup>15</sup>T. Koop, B. Luo, U. M. Biermann, P. J. Crutzen, and T. Peter, *J. Phys. Chem. A* **101**, 1117 (1997).

<sup>16</sup>F. Yu, *Atmos. Chem. Phys.* **6**, 5193 (2006).

<sup>17</sup>J. H. Seinfeld and S. N. Pandis, *Atmospheric Chemistry and Physics—From Air Pollution to Climate Change*, 2nd ed. (Wiley, New York, 2006).

<sup>18</sup>J. Duplissy, M. B. Enghoff, K. L. Aplin, F. Arnold, H. Aufmhoff, M. Avngaard, U. Baltensperger, T. Bondo, R. Bingham, K. Carslaw, J. Curtis, A. David, B. Fastrup, S. Gagné, F. Hahn, R. G. Harrison, B. Kellert, J. Kirkby, M. Kulmala, L. Laakso, A. Laaksonen, E. Lillestol, M. Lockwood, J. Mäkelä, V. Makhmutov, N. D. Marsh, T. Nieminen, A. Onnela, E. Pedersen, J. O. P. Pedersen, J. Polny, U. Reichl, J. H. Seinfeld, M. Sipilä, Y. Stozhkov, F. Stratmann, H. Svensmark, J. Svensmark, R. Veenhof, B. Verheggen, Y. Viisanen, P. E. Wagner, G. Wehrle, E. Weingartner, H. Wex, M. Wilhelmsson, and P. M. Winkler, *Atmos. Chem. Phys.* **10**, 1635 (2010).

<sup>19</sup>S. Henin, Y. Petit, D. Kiselev, J. Kasparian, and J.-P. Wolf, *Appl. Phys. Lett.* **95**, 091107 (2009).

<sup>20</sup>G. Fibich and B. Ilan, *Phys. Rev. E* **67**, 036622 (2003).

<sup>21</sup>I. A. Kossyi, A. Yu. Kostinsky, A. A. Matveyev, and V. P. Silakov, *Plasma Sources Sci. Technol.* **1**, 207 (1992).

<sup>22</sup>H. L. Xu, A. Azarm, J. Bernhardt, Y. Kamali, and S. L. Chin, *Chem. Phys.* **360**, 171 (2009).

<sup>23</sup>I. Dotan, P. M. Hierl, R. A. Morris, and A. A. Viggiano, *Int. J. Mass Spectrom. Ion Process.* **167–168**, 223 (1997).

<sup>24</sup>J. N. Bardsley, *J. Phys. B* **1**, 365 (1968).

<sup>25</sup>O. V. Bragin'skiy, A. N. Vasilieva, K. S. Klopovskiy, A. S. Kovalev, D. V. Lopaev, O. V. Proshina, T. V. Rakhimova, and A. T. Rakhimov, *J. Phys. D: Appl. Phys.* **38**, 3609 (2005).

# Mobile source of high-energy single-cycle terahertz pulses

A.G. Stepanov · S. Henin · Y. Petit · L. Bonacina ·  
J. Kasparian · J.-P. Wolf

Received: 15 July 2010  
© Springer-Verlag 2010

**Abstract** The *Teramobile* laser facility was used to realize the first mobile source of high-power THz pulses. The source is based on a tilted-pulse-front pumping THz generation scheme optimized for application of terawatt laser pulses. Generation of 50- $\mu$ J single-cycle electromagnetic pulses centered at 0.19 THz with a repetition rate of 10 Hz was obtained for incoming 700-fs 120-mJ near-infrared laser pulses. The corresponding laser-to-THz photon conversion efficiency is approximately 100%.

## 1 Introduction

THz waves have attracted considerable interest in recent years owing to their prospective applications in different scientific and industrial fields [1, 2]. Some of these applications require ultrashort THz pulses of high peak power, such as for nonlinear optics and spectroscopy in the THz frequency range and for recently developed time-resolved spectroscopy with THz pump [3–7]. To date, the highest THz peak power (100 MW) has been achieved with accelerator-based sources [3]. These sources have a number of obvious disadvantages typical for large-scale facilities. Several table-top techniques based on femtosecond lasers have been tested for obtaining high-power near-single-cycle THz pulses, including photoconductive switches, optical

rectification and, more recently, four-wave mixing in air/gas plasma [8]. For most of these techniques the generation of THz pulses with an average frequency of  $\sim 1$  THz and peak power of more than 1 MW is problematic owing to the low laser-to-THz conversion efficiency and the inherently limited laser pulse power that can be applied for THz generation. In contrast to other techniques, the tilted-pulse-front pumping (TPFP) THz generation scheme [9, 10] allows an increase in pump laser power to the terawatt level while retaining relatively high energy-conversion efficiency ( $\geq 0.1\%$ ). Recently, a few TFPF schemes optimized for the generation of extremely high-power ( $\geq 100$  MW) single-cycle THz pulses have been proposed [11–13].

Several THz applications, such as environmental studies, stand-off THz imaging and spectroscopy for security purposes and point-to-point communications, require mobile sources of high-power THz radiation with a central frequency of 0.1–0.5 THz [1, 2]. This spectral region is particularly attractive because of the relatively low absorption by molecular water in ambient air, which allows propagation of the THz radiation for up to several kilometers under typical atmospheres [14]. Recently, we demonstrated that 30- $\mu$ J single-cycle pulses with an average frequency of 0.3 THz can be obtained in a TFPF THz generation scheme pumped by a femtosecond terawatt laser [15]. Although generally bulky, high-intensity lasers can be made mobile and can even be used for field and outdoor experiments, as demonstrated by the pioneering work of the *Teramobile* consortium [16, 17], which performed numerous field experiments with 100-fs, 4-TW laser pulses. Therefore, such high-intensity laser sources represent good candidates for stand-off and field experiments.

In this letter we report the generation of 50- $\mu$ J single-cycle pulses centered at 0.19 THz by a TFPF scheme using the *Teramobile* laser system as the pump source. To the best

---

A.G. Stepanov  
Institute for Spectroscopy RAS, Fizicheskaya Str. 5, Troitsk,  
Moscow Region 142190, Russia  
e-mail: [andrei\\_g\\_stepanov@yahoo.com](mailto:andrei_g_stepanov@yahoo.com)

S. Henin · Y. Petit · L. Bonacina · J. Kasparian · J.-P. Wolf (✉)  
GAP-Biophotonics, Université de Genève, Rue de l'École de  
Médecine 20, Genève 1211, Switzerland  
e-mail: [jean-pierre.wolf@unige.ch](mailto:jean-pierre.wolf@unige.ch)

of our knowledge, these are the highest-energy single-cycle THz pulses achieved using a laser-based technique. Moreover, as the pulses were obtained with a mobile laser system, this represents the first demonstration of a mobile source of high-power single-cycle THz pulses.

## 2 Experimental set-up

The THz generation set-up (Fig. 1) was installed inside the *Teramobile* laser container. As proposed previously [12, 15], the laser beam cross-section was elliptically shaped before pulse-front tilting to reduce the propagation distance for both the laser and THz pulses inside the lithium niobate crystal and to avoid distortion of the large-aperture laser pulse at the tilting pulse front [11, 12]. Using a telescope consisting of two cylindrical mirrors with a focal length of 550 and 175 mm, respectively for this purpose, we obtained a  $40 \times 10$  mm ( $1/e^2$ ) laser cross-section profile. The long dimension of the laser cross-section was mainly limited by the 30-mm height of the LiNbO<sub>3</sub> crystal. After the cylindrical telescope, the THz generation set-up was similar to that used in our previous work [15].

The absolute value of the THz pulse energy was measured using a room-temperature pyroelectric detector (Coherent, Moletron J4-05). The same detector model was previously used by other research groups to measure 100- $\mu$ J THz pulses obtained with an accelerator-based source [3] and  $\mu$ J-level pulses generated by optical rectification in ZnTe [5]. Below 1 THz, diffraction and the spectral dependence of the absorber placed on the pyroelectric crystal may result in a decrease in detector sensitivity, so that our measurements provide a lower limit of the absolute energy value in this frequency range. In contrast to previous measurements [3, 5], we did not focus the THz beam on the active area of the detector. The intensity profile for the THz beam cross-section ( $21 \times 15$  mm ( $1/e^2$ ) at a distance of 5 mm from the crystal output surface) was measured by scanning with the detector. To obtain THz pulse energy, the scanning data were deconvoluted for the active area of the detector and integrated.

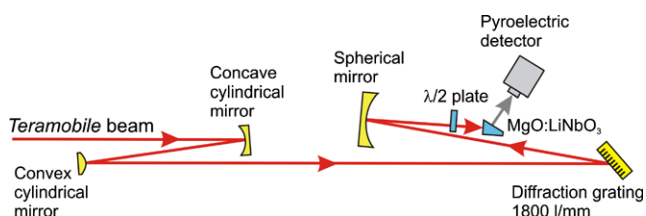


**Fig. 1** Schematic of the tilted-pulse-front pumping terahertz generation set-up optimized for application of terawatt laser pulses

## 3 Results and discussion

The maximum laser pulse energy of 120 mJ used for THz generation in these experiments was limited by the dimensions of the LiNbO<sub>3</sub> crystal. Figure 2 shows the dependence of the THz pulse energy on the duration of 120-mJ laser pulses. The laser pulse duration was varied by shifting the diffraction grating of the laser compressor (i.e. by laser pulse chirping) as previously described [16].

THz pulses with the highest energy (50  $\mu$ J) were achieved with negatively chirped laser pulses of 120 mJ for 700 fs. The use of close to transform-limited 140-fs laser pulses results in a 30% decrease in generation efficiency. One of the most probable explanations for this behavior is self-phase modulation of a 140-fs laser pulse along the propagation distance of 6 m in air from the laser compressor to the THz generation set-up. The presence of self-phase modulation of 140-fs laser pulses is unambiguously indicated by a decrease at 804 nm and increases at 789 and 814 nm in the laser pulse spectra measured just before the THz generation set-up (Fig. 3). These spectral features disappeared when the laser pulses were chirped; moreover, they were not observed immediately after the compressor output. The specific mechanism of the decrease in THz generation efficiency resulting from self-phase modulation is beyond the scope of the present study.

Measurements of the THz pulse energy as a function of the 140-fs laser pulse energy reveal a quadratic dependence up to laser pulse energy of 70 mJ (Fig. 4). A further increase in pulse energy results in saturation of the quadratic dependence (not shown in Fig. 4), which is most probably related to self-phase modulation of the laser pulse, as discussed above.

The temporal profile of the THz pulses was characterized by electro-optic sampling using a 0.5-mm ZnTe crys-

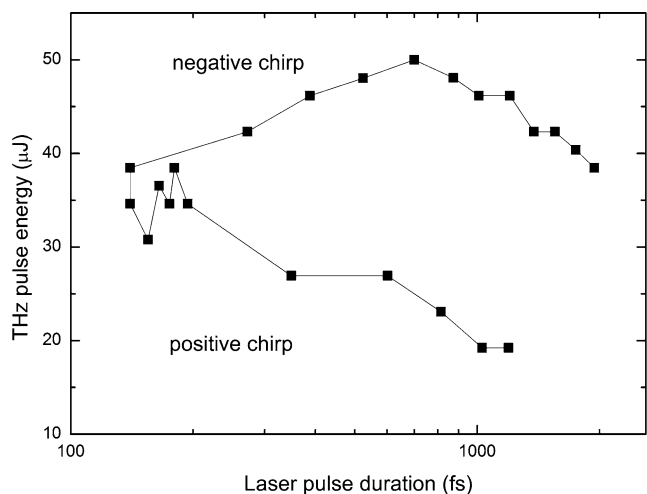


**Fig. 2** THz pulse energy as a function of the duration of 120-mJ laser pulses

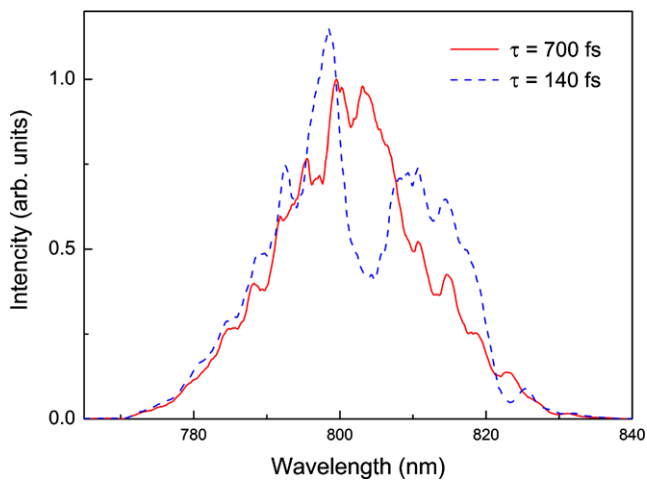


**Fig. 3** Spectra of close to transform-limited 140-fs laser pulses (*solid line*) and negatively chirped 700-fs laser pulse (*dashed line*) after propagation over a distance of 6 m in air

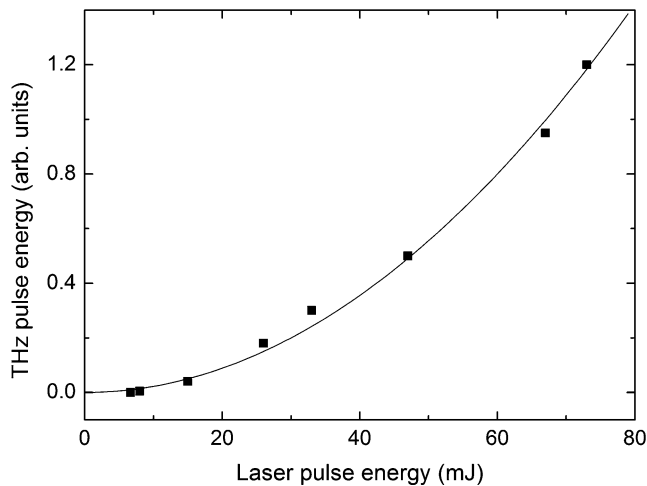


**Fig. 4** THz pulse energy as a function of the energy of incident 140 fs transform-limited pulses

tal as a sensor, which was placed at a distance of 150 mm from the THz output surface of the LiNbO<sub>3</sub> crystal. Figure 5 shows electro-optic signals and the corresponding spectra of 50- and 44- $\mu$ J THz pulses generated by 700-fs, 120-mJ and 500-fs, 80-mJ laser pulses, respectively.

The THz pulse spectra observed in our experiments are slightly narrower and red-shifted compared with spectra obtained by model calculations for transform-limited laser pulses [13]. The red-shift and spectral narrowing probably result from the pulse chirping applied for THz generation. It should also be noted that according to model calculations [13], the average frequency and width of THz pulse spectra can be increased by up to 1.2 and 1.6 THz (FWHM), respectively, by decreasing the laser pulse duration to 50 fs.

The laser-to-terahertz energy-conversion efficiency calculated from the laser pulse energy incident on the crystal

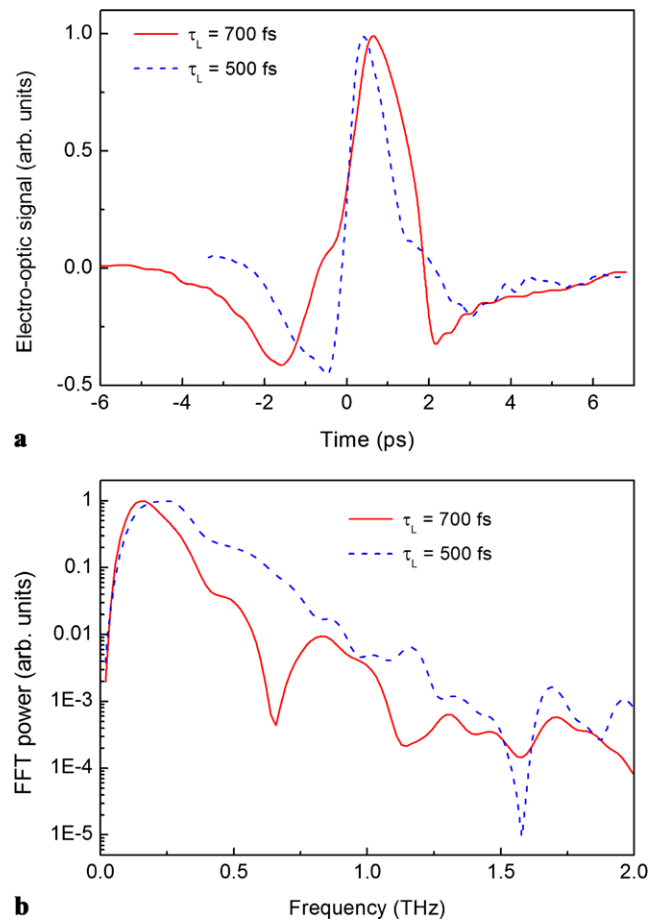


**Fig. 5** (a) Normalized electro-optic signals and (b) power spectra obtained for incident laser pulses of 120 mJ for 700 fs (*solid line*) and 80 mJ for 500 fs (*dashed line*)

surface and the THz pulse energy measured was  $5.0 \times 10^{-4}$ . This value is comparable with the conversion efficiencies reported for generation of 10- $\mu$ J-scale near-single-cycle THz pulses by TFPF [4, 15]. The photon conversion efficiency was approximately 100%. Note that this value could exceed 100% due to cascaded  $\chi^{(2)}$  processes [18, 19].

## 4 Conclusions

In summary, we have demonstrated the first mobile source of high-power THz pulses based on a TFPF THz generation scheme combined with the *Teramobile* laser facility. Application of 700-fs, 120-mJ laser pulses yielded 50- $\mu$ J single-cycle THz pulses with an average frequency of 0.19 THz. This source can be used for stand-off applications such as nonlinear THz atmospheric research and THz LIDAR systems.

**Acknowledgements** We acknowledge financial support from the Swiss National Science Foundation (Grant 20021-125315) and the Switzerland-Russia S&T Cooperation Programme “Generation and Applications of High Power Terahertz Waves”.

## References

1. D. Mittleman (ed.), *Sensing with Terahertz Radiation* (Springer, Berlin, 2003)
2. X.-C. Zhang, J. Xu, *Introduction to THz Wave Photonics* (Springer, Boston, 2010)
3. Y. Shen, T. Watanabe, D.A. Arena, C.-C. Kao, J.B. Murphy, T.Y. Tsang, X.J. Wang, G.L. Carr, *Phys. Rev. Lett.* **99**, 043901 (2007)
4. J. Hebling, K.-L. Yeh, M.C. Hoffmann, K.A. Nelson, *IEEE J. Sel. Top. Quantum Electron.* **14**, 345 (2008)
5. L. Razzari, F.H. Su, G. Sharma, F. Blanchard, A. Ayesheshim, H.-C. Bandulet, R. Morandotti, J.-C. Kieffer, T. Ozaki, M. Reid, F.A. Hegmann, *Phys. Rev. B* **79**, 193204 (2009)
6. J. Liu, X.-C. Zhang, *Phys. Rev. Lett.* **103**, 235002 (2009)
7. H. Hirori, M. Nagai, K. Tanaka, *Phys. Rev. B* **81**, 081305 (2010)
8. K. Reimann, *Rep. Prog. Phys.* **70**, 1597 (2007)
9. J. Hebling, G. Almási, I.Z. Kozma, J. Kuhl, *Opt. Express* **10**, 1161 (2002)
10. A.G. Stepanov, J. Hebling, J. Kuhl, *Appl. Phys. Lett.* **83**, 3000 (2003)
11. L. Pálfalvi, J.A. Fülöp, G. Almási, J. Hebling, *Appl. Phys. Lett.* **92**, 171107 (2008)
12. A.G. Stepanov, *Opt. Spectrosc.* **107**, 529 (2009)
13. J. A Fülöp, L. Pálfalvi, G. Almási, J. Hebling, *Opt. Express* **18**, 12311 (2010)
14. Y. Kasai, T. Seta, *J. Natl. Inst. Inf. Commun. Technol.* **55**, 73 (2008)
15. A.G. Stepanov, L. Bonacina, S.V. Chekalin, J.-P. Wolf, *Opt. Lett.* **33**, 2497 (2008)
16. H. Wille, M. Rodriguez, J. Kasparian, D. Mondelain, J. Yu, A. Mysyrowicz, R. Sauerbrey, J.-P. Wolf, L. Wöste, *Eur. Phys. J., Appl. Phys.* **20**, 183 (2002)
17. J. Kasparian, M. Rodriguez, G. Méjean, J. Yu, E. Salmon, H. Wille, R. Bourayou, S. Frey, Y.-B. André, A. Mysyrowicz, R. Sauerbrey, J.-P. Wolf, L. Wöste, *Science* **301**, 61 (2003)
18. K.L. Vodopyanov, *Opt. Express* **17**, 2263 (2006)
19. M. Nagai, M. Jewariya, Y. Ichikawa, H. Ohtake, T. Sugiura, Y. Uehara, K. Tanaka, *Opt. Express* **17**, 11543 (2009)

# Mobile source of high-energy single-cycle terahertz pulses

A.G. Stepanov · S. Henin · Y. Petit · L. Bonacina ·  
J. Kasparian · J.-P. Wolf

Received: 15 July 2010 / Published online: 20 August 2010  
© Springer-Verlag 2010

**Abstract** The *Teramobile* laser facility was used to realize the first mobile source of high-power THz pulses. The source is based on a tilted-pulse-front pumping THz generation scheme optimized for application of terawatt laser pulses. Generation of 50- $\mu$ J single-cycle electromagnetic pulses centered at 0.19 THz with a repetition rate of 10 Hz was obtained for incoming 700-fs 120-mJ near-infrared laser pulses. The corresponding laser-to-THz photon conversion efficiency is approximately 100%.

## 1 Introduction

THz waves have attracted considerable interest in recent years owing to their prospective applications in different scientific and industrial fields [1, 2]. Some of these applications require ultrashort THz pulses of high peak power, such as for nonlinear optics and spectroscopy in the THz frequency range and for recently developed time-resolved spectroscopy with THz pump [3–7]. To date, the highest THz peak power (100 MW) has been achieved with accelerator-based sources [3]. These sources have a number of obvious disadvantages typical for large-scale facilities. Several table-top techniques based on femtosecond lasers have been tested for obtaining high-power near-single-cycle THz pulses, including photoconductive switches, optical

rectification and, more recently, four-wave mixing in air/gas plasma [8]. For most of these techniques the generation of THz pulses with an average frequency of  $\sim 1$  THz and peak power of more than 1 MW is problematic owing to the low laser-to-THz conversion efficiency and the inherently limited laser pulse power that can be applied for THz generation. In contrast to other techniques, the tilted-pulse-front pumping (TPFP) THz generation scheme [9, 10] allows an increase in pump laser power to the terawatt level while retaining relatively high energy-conversion efficiency ( $\geq 0.1\%$ ). Recently, a few TFPF schemes optimized for the generation of extremely high-power ( $\geq 100$  MW) single-cycle THz pulses have been proposed [11–13].

Several THz applications, such as environmental studies, stand-off THz imaging and spectroscopy for security purposes and point-to-point communications, require mobile sources of high-power THz radiation with a central frequency of 0.1–0.5 THz [1, 2]. This spectral region is particularly attractive because of the relatively low absorption by molecular water in ambient air, which allows propagation of the THz radiation for up to several kilometers under typical atmospheres [14]. Recently, we demonstrated that 30- $\mu$ J single-cycle pulses with an average frequency of 0.3 THz can be obtained in a TFPF THz generation scheme pumped by a femtosecond terawatt laser [15]. Although generally bulky, high-intensity lasers can be made mobile and can even be used for field and outdoor experiments, as demonstrated by the pioneering work of the *Teramobile* consortium [16, 17], which performed numerous field experiments with 100-fs, 4-TW laser pulses. Therefore, such high-intensity laser sources represent good candidates for stand-off and field experiments.

In this letter we report the generation of 50- $\mu$ J single-cycle pulses centered at 0.19 THz by a TFPF scheme using the *Teramobile* laser system as the pump source. To the best

---

A.G. Stepanov  
Institute for Spectroscopy RAS, Fizicheskaya Str. 5, Troitsk,  
Moscow Region 142190, Russia  
e-mail: [andrei\\_g\\_stepanov@yahoo.com](mailto:andrei_g_stepanov@yahoo.com)

S. Henin · Y. Petit · L. Bonacina · J. Kasparian · J.-P. Wolf (✉)  
GAP-Biophotonics, Université de Genève, Rue de l'École de  
Médecine 20, Genève 1211, Switzerland  
e-mail: [jean-pierre.wolf@unige.ch](mailto:jean-pierre.wolf@unige.ch)

of our knowledge, these are the highest-energy single-cycle THz pulses achieved using a laser-based technique. Moreover, as the pulses were obtained with a mobile laser system, this represents the first demonstration of a mobile source of high-power single-cycle THz pulses.

## 2 Experimental set-up

The THz generation set-up (Fig. 1) was installed inside the *Teramobile* laser container. As proposed previously [12, 15], the laser beam cross-section was elliptically shaped before pulse-front tilting to reduce the propagation distance for both the laser and THz pulses inside the lithium niobate crystal and to avoid distortion of the large-aperture laser pulse at the tilting pulse front [11, 12]. Using a telescope consisting of two cylindrical mirrors with a focal length of 550 and 175 mm, respectively for this purpose, we obtained a  $40 \times 10$  mm ( $1/e^2$ ) laser cross-section profile. The long dimension of the laser cross-section was mainly limited by the 30-mm height of the LiNbO<sub>3</sub> crystal. After the cylindrical telescope, the THz generation set-up was similar to that used in our previous work [15].

The absolute value of the THz pulse energy was measured using a room-temperature pyroelectric detector (Coherent, Moletron J4-05). The same detector model was previously used by other research groups to measure 100- $\mu$ J THz pulses obtained with an accelerator-based source [3] and  $\mu$ J-level pulses generated by optical rectification in ZnTe [5]. Below 1 THz, diffraction and the spectral dependence of the absorber placed on the pyroelectric crystal may result in a decrease in detector sensitivity, so that our measurements provide a lower limit of the absolute energy value in this frequency range. In contrast to previous measurements [3, 5], we did not focus the THz beam on the active area of the detector. The intensity profile for the THz beam cross-section ( $21 \times 15$  mm ( $1/e^2$ ) at a distance of 5 mm from the crystal output surface) was measured by scanning with the detector. To obtain THz pulse energy, the scanning data were deconvoluted for the active area of the detector and integrated.

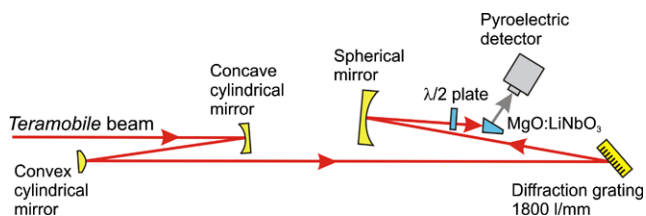


**Fig. 1** Schematic of the tilted-pulse-front pumping terahertz generation set-up optimized for application of terawatt laser pulses

## 3 Results and discussion

The maximum laser pulse energy of 120 mJ used for THz generation in these experiments was limited by the dimensions of the LiNbO<sub>3</sub> crystal. Figure 2 shows the dependence of the THz pulse energy on the duration of 120-mJ laser pulses. The laser pulse duration was varied by shifting the diffraction grating of the laser compressor (i.e. by laser pulse chirping) as previously described [16].

THz pulses with the highest energy (50  $\mu$ J) were achieved with negatively chirped laser pulses of 120 mJ for 700 fs. The use of close to transform-limited 140-fs laser pulses results in a 30% decrease in generation efficiency. One of the most probable explanations for this behavior is self-phase modulation of a 140-fs laser pulse along the propagation distance of 6 m in air from the laser compressor to the THz generation set-up. The presence of self-phase modulation of 140-fs laser pulses is unambiguously indicated by a decrease at 804 nm and increases at 789 and 814 nm in the laser pulse spectra measured just before the THz generation set-up (Fig. 3). These spectral features disappeared when the laser pulses were chirped; moreover, they were not observed immediately after the compressor output. The specific mechanism of the decrease in THz generation efficiency resulting from self-phase modulation is beyond the scope of the present study.

Measurements of the THz pulse energy as a function of the 140-fs laser pulse energy reveal a quadratic dependence up to laser pulse energy of 70 mJ (Fig. 4). A further increase in pulse energy results in saturation of the quadratic dependence (not shown in Fig. 4), which is most probably related to self-phase modulation of the laser pulse, as discussed above.

The temporal profile of the THz pulses was characterized by electro-optic sampling using a 0.5-mm ZnTe crys-

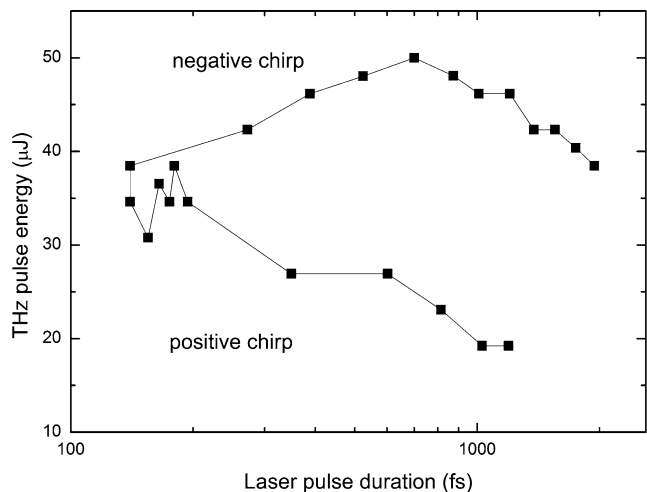


**Fig. 2** THz pulse energy as a function of the duration of 120-mJ laser pulses

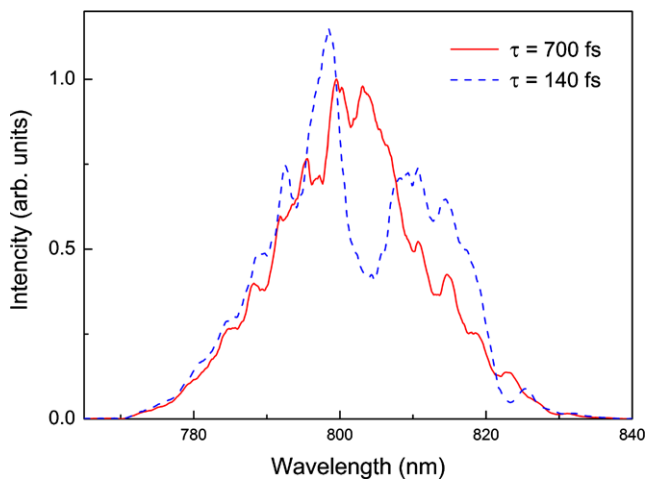


**Fig. 3** Spectra of close to transform-limited 140-fs laser pulses (*solid line*) and negatively chirped 700-fs laser pulse (*dashed line*) after propagation over a distance of 6 m in air

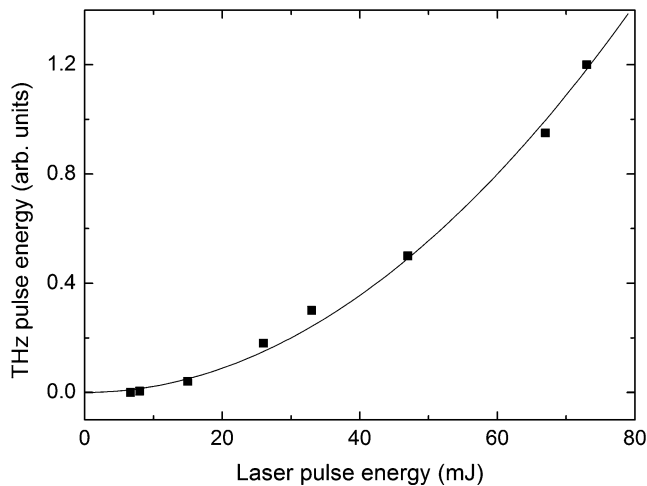
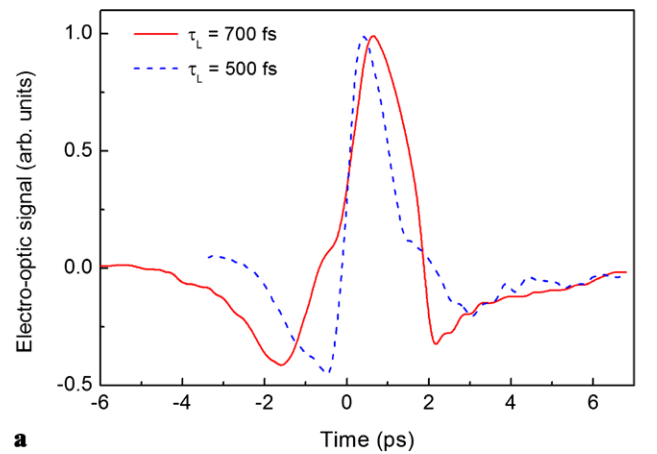


**Fig. 4** THz pulse energy as a function of the energy of incident 140 fs transform-limited pulses

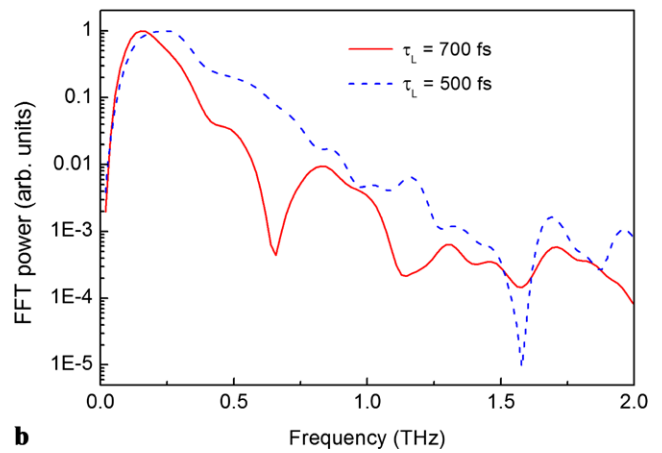
tal as a sensor, which was placed at a distance of 150 mm from the THz output surface of the LiNbO<sub>3</sub> crystal. Figure 5 shows electro-optic signals and the corresponding spectra of 50- and 44- $\mu$ J THz pulses generated by 700-fs, 120-mJ and 500-fs, 80-mJ laser pulses, respectively.

The THz pulse spectra observed in our experiments are slightly narrower and red-shifted compared with spectra obtained by model calculations for transform-limited laser pulses [13]. The red-shift and spectral narrowing probably result from the pulse chirping applied for THz generation. It should also be noted that according to model calculations [13], the average frequency and width of THz pulse spectra can be increased by up to 1.2 and 1.6 THz (FWHM), respectively, by decreasing the laser pulse duration to 50 fs.

The laser-to-terahertz energy-conversion efficiency calculated from the laser pulse energy incident on the crystal



**a**



**b**

**Fig. 5** (a) Normalized electro-optic signals and (b) power spectra obtained for incident laser pulses of 120 mJ for 700 fs (*solid line*) and 80 mJ for 500 fs (*dashed line*)

surface and the THz pulse energy measured was  $5.0 \times 10^{-4}$ . This value is comparable with the conversion efficiencies reported for generation of 10- $\mu$ J-scale near-single-cycle THz pulses by TFPF [4, 15]. The photon conversion efficiency was approximately 100%. Note that this value could exceed 100% due to cascaded  $\chi^{(2)}$  processes [18, 19].

## 4 Conclusions

In summary, we have demonstrated the first mobile source of high-power THz pulses based on a TFPF THz generation scheme combined with the *Teramobile* laser facility. Application of 700-fs, 120-mJ laser pulses yielded 50- $\mu$ J single-cycle THz pulses with an average frequency of 0.19 THz. This source can be used for stand-off applications such as nonlinear THz atmospheric research and THz LIDAR systems.

**Acknowledgements** We acknowledge financial support from the Swiss National Science Foundation (Grant 20021-125315) and the Switzerland-Russia S&T Cooperation Programme “Generation and Applications of High Power Terahertz Waves”.

## References

1. D. Mittleman (ed.), *Sensing with Terahertz Radiation* (Springer, Berlin, 2003)
2. X.-C. Zhang, J. Xu, *Introduction to THz Wave Photonics* (Springer, Boston, 2010)
3. Y. Shen, T. Watanabe, D.A. Arena, C.-C. Kao, J.B. Murphy, T.Y. Tsang, X.J. Wang, G.L. Carr, *Phys. Rev. Lett.* **99**, 043901 (2007)
4. J. Hebling, K.-L. Yeh, M.C. Hoffmann, K.A. Nelson, *IEEE J. Sel. Top. Quantum Electron.* **14**, 345 (2008)
5. L. Razzari, F.H. Su, G. Sharma, F. Blanchard, A. Ayesheshim, H.-C. Bandulet, R. Morandotti, J.-C. Kieffer, T. Ozaki, M. Reid, F.A. Hegmann, *Phys. Rev. B* **79**, 193204 (2009)
6. J. Liu, X.-C. Zhang, *Phys. Rev. Lett.* **103**, 235002 (2009)
7. H. Hirori, M. Nagai, K. Tanaka, *Phys. Rev. B* **81**, 081305 (2010)
8. K. Reimann, *Rep. Prog. Phys.* **70**, 1597 (2007)
9. J. Hebling, G. Almási, I.Z. Kozma, J. Kuhl, *Opt. Express* **10**, 1161 (2002)
10. A.G. Stepanov, J. Hebling, J. Kuhl, *Appl. Phys. Lett.* **83**, 3000 (2003)
11. L. Pálfalvi, J.A. Fülöp, G. Almási, J. Hebling, *Appl. Phys. Lett.* **92**, 171107 (2008)
12. A.G. Stepanov, *Opt. Spectrosc.* **107**, 529 (2009)
13. J. A Fülöp, L. Pálfalvi, G. Almási, J. Hebling, *Opt. Express* **18**, 12311 (2010)
14. Y. Kasai, T. Seta, *J. Natl. Inst. Inf. Commun. Technol.* **55**, 73 (2008)
15. A.G. Stepanov, L. Bonacina, S.V. Chekalin, J.-P. Wolf, *Opt. Lett.* **33**, 2497 (2008)
16. H. Wille, M. Rodriguez, J. Kasparian, D. Mondelain, J. Yu, A. Mysyrowicz, R. Sauerbrey, J.-P. Wolf, L. Wöste, *Eur. Phys. J., Appl. Phys.* **20**, 183 (2002)
17. J. Kasparian, M. Rodriguez, G. Méjean, J. Yu, E. Salmon, H. Wille, R. Bourayou, S. Frey, Y.-B. André, A. Mysyrowicz, R. Sauerbrey, J.-P. Wolf, L. Wöste, *Science* **301**, 61 (2003)
18. K.L. Vodopyanov, *Opt. Express* **17**, 2263 (2006)
19. M. Nagai, M. Jewariya, Y. Ichikawa, H. Ohtake, T. Sugiura, Y. Uehara, K. Tanaka, *Opt. Express* **17**, 11543 (2009)

**Mechanism of hollow-core-fiber infrared-supercontinuum compression with bulk material**P. Béjot,<sup>1,\*</sup> B. E. Schmidt,<sup>2,†</sup> J. Kasparian,<sup>3</sup> J.-P. Wolf,<sup>3</sup> and F. Legaré<sup>2</sup><sup>1</sup>Laboratoire Interdisciplinaire CARNOT de Bourgogne, UMR 5209 CNRS-Université de Bourgogne, BP 47870, F-21078 Dijon Cedex, France<sup>2</sup>Institut National de la Recherche Scientifique, Centre Énergie Matériaux et Télécommunications, 1650 Boulevard Lionel-Boulet, Varennes, Québec J3X1S2, Canada<sup>3</sup>GAP-Biophotonics, Université de Genève, 20 rue de l'École de Médecine, CH-1211 Geneva 4, Switzerland

(Received 23 March 2010; published 28 June 2010)

We numerically investigate the pulse compression mechanism in the infrared spectral range based on the successive action of nonlinear pulse propagation in a hollow-core fiber followed by linear propagation through bulk material. We found an excellent agreement of simulated pulse properties with experimental results at 1.8  $\mu\text{m}$  in the two-optical-cycle regime close to the Fourier limit. In particular, the spectral phase asymmetry attributable to self-steepening combined with self-phase modulation is a necessary prerequisite for subsequent compensation by the phase introduced by glass material in the anomalous dispersion regime. The excellent agreement of the model enabled simulating pressure and wavelength tunability of sub-two cycles in the range from 1.5 to 4  $\mu\text{m}$  with this cost-efficient and robust approach.

DOI: 10.1103/PhysRevA.81.063828

PACS number(s): 42.65.Re, 42.65.Jx

**I. INTRODUCTION**

The ability to study molecular dynamics was one motivation to improve chirped pulse amplification (CPA) [1] in terms of reduced pulse duration and increased energy since the early 1990s. The key ingredient for reducing the pulse duration to few optical cycles at high power levels lies in additional spectral broadening through either (i) nonlinear propagation in hollow-core-fiber (HCF) [2] and laser-induced (co-)filaments [3–5] or (ii) ultrabroadband optical parametric amplification (OPA) [6] and OPCPA [7]. However, the main challenge remains in controlling the spectral phase of the ultrabroadband spectrum. Conventional prism or grating configurations have been demonstrated for pulse compression to few optical cycles. However, prisms suffer from higher-order distortions and nonlinear effects at high peak powers, while gratings introduce losses. Active devices such as spatial light modulators offer full control over the spectral phase but are elaborate experimentally [8] and also induce high losses. The established state of the art for high-power, carrier-envelope phase (CEP), stable, few-cycle pulse generation consists of chirped mirrors typically being used subsequently to induce broadening in a HCF.

Based on those achievements at 800 nm wavelength, the development of attosecond technology in the framework of high-order harmonic generation (HHG) during the past decade accessed a previously unexplored time scale down to currently 80 as [9]. Because the extension of the XUV spectrum scales as  $I\lambda^2$  [10,11], reliable sources delivering high intensities  $I$  at longer wavelengths  $\lambda$  of the driving laser are required to generate shorter attosecond pulses. The present article numerically investigates the mechanism of a cost-efficient approach for compression of intense IR few-cycle pulses that has been recently demonstrated experimentally [12]. This technique is based on spectral broadening in an argon-filled HCF followed by compression using anomalous dispersion of fused silica (FS) which introduces negative group delay

dispersion (GDD) in this IR spectral range. The motivation of the present numerical study is to explain why the compression is not limited by third-order dispersion (TOD), which is positive for all materials. By the help of one-dimensional propagation simulations, we identified the exact compression mechanism. The action in argon of the Kerr effect up to the 10th order combined with dispersion and self-steepening generates a spectral asymmetry whose phase is adequately opposed to the one subsequently introduced by linear anomalous propagation through FS. Note that this technique differs from [13], where the propagation inside the output window has to be nonlinear to compress the pulse after the propagation cell.

**II. EXPERIMENTAL AND NUMERICAL METHODS**

The experimental setup employed to demonstrate the new compression concept [12] is depicted in Fig. 1. It shows the IR source which is a fluorescence-seeded, high-energy OPA (HE-TOPAS, Light Conversion) pumped by 7-mJ, 40-fs pulses from a Ti:Sa CPA. The OPA Idler wavelength is tuned to 1.83  $\mu\text{m}$  providing a pulse duration of 73 fs and 0.93 mJ of pulse energy. The IR laser beam is coupled to a HCF (400  $\mu\text{m}$  in diameter, 1.4 bar argon pressure) using a  $f = 1\text{-m}$  plano-convex lens. Lens and cell windows are made of  $\text{CaF}_2$  to introduce minimal dispersion to the OPA pulses. Due to Fresnel losses on the uncoated glass surfaces, approximately 0.82 mJ is coupled into the fiber. The pure fiber transmission is estimated to be 65% and the output beam is collimated using an  $R = 2\text{-m}$  concave silver mirror. Pulses are then recompressed by a single pass through a 3-mm FS glass plate. Their characterization is carried out with a home-built second-harmonic-generation–frequency-resolved optical gating (SHG-FROG) specially designed for few-cycle pulse measurement [14]. The experimental data appear as red circles in Fig. 2 as a reference for the numerical simulations (solid blue curve). Figure 2(a) shows the broadened spectra after the HCF with its corresponding spectral phase before compensation by the FS plate in (c). On the other hand, the spectral phase in (d) includes the contribution of nonlinear propagation in the fiber plus the linear propagation through FS in the

\* pierre.bejot@u-bourgogne.fr

† schmidt@emt.inrs.ca

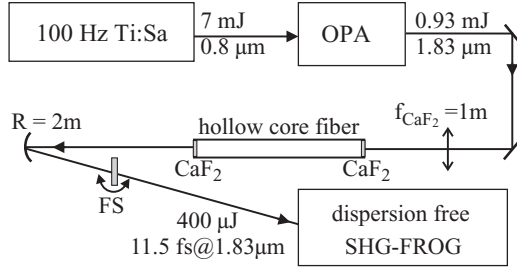


FIG. 1. Experimental setup. Idler pulses from a high-energy OPA are propagated in a hollow-core fiber filled with 1.4 bar argon. The broadband pulses are subsequently compressed by linear propagation through a fused silica (FS) plate of 3 mm thickness.

anomalous dispersion regime. Experimentally, this flat phase is determined by varying the glass thickness by steps of 0.5 mm and small angular tilts, which lead to the generation of 11.5-fs pulses displayed in Fig. 2(b). This excellent compression to only 1.14 times the FL (10.1 fs) is surprising even though the GDD of FS is negative in the anomalous dispersion regime. As discussed in [12], the TOD, which is positive for all gases, would be expected to broaden a FL pulse to almost 15 fs (1.5 times the FL) after passing the FS and CaF<sub>2</sub> if it was the only process in play.

To bring insight into the compression mechanism, we precisely modeled the nonlinear propagation in the HCF, as well as the linear propagation through the glass, according to the experimental conditions. Let us consider a linearly polarized incident electric field  $E = \text{Re } e\{\varepsilon(z,t) \exp[i(k_0 z - \omega_0 t)]\}$  at wavelength  $\lambda_0 = 1.83 \mu\text{m}$  traveling in a HCF filled with argon along the propagation axis  $z$ .  $k_0 = 2\pi n_0/\lambda_0$  and  $\omega_0 = 2\pi c/\lambda_0$  are the wave number and the frequency of the carrier wave, respectively. The refractive index  $n$  is evaluated according to the Sellmeier equation of argon at 1 bar [15] and its pressure dependence is given by

TABLE I. Nonlinear indexes of argon at  $1.83 \mu\text{m}$  used in the model ( $p$  accounts for the relative gas pressure:  $p = \frac{P}{1 \text{ bar}}$ ).  $\alpha$  accounts for the fiber optical losses.

$n_2$	$n_4$	$n_6$	$n_8$	$n_{10}$	$\alpha$
$10^{-24}$	$10^{-42}$	$10^{-58}$	$10^{-75}$	$10^{-94}$	$\text{m}^{-1}$
$\text{m}^2 \text{W}^{-1}$	$\text{m}^4 \text{W}^{-2}$	$\text{m}^6 \text{W}^{-3}$	$\text{m}^8 \text{W}^{-4}$	$\text{m}^{10} \text{W}^{-5}$	$\text{m}^{-1}$
$9.73p$	$-3.55p$	$3.78p$	$-1.59p$	$8.10p$	$0.43p$

$n(p) = \sqrt{1 + p[n(p=1)^2 - 1]}$ , where  $p = P/1 \text{ bar}$  accounts for the relative pressure. The scalar envelope  $\varepsilon(r,t,z)$  is assumed to be slowly varying in time and along  $z$ . In the frequency domain, it therefore evolves according to the nonlinear Schrödinger equation (NLSE) [16],

$$\partial_z \tilde{\varepsilon} = \tilde{D} \tilde{\varepsilon} + ik_0 T \tilde{\Delta} n \varepsilon - \frac{\tilde{\alpha}}{2} \tilde{\varepsilon}, \quad (1)$$

where  $\tilde{\varepsilon}$  is the Fourier transform of  $\varepsilon$ . The terms on the right-hand side of Eq. (1) account for dispersion [ $\tilde{D}(\omega) = k(\omega) - k_0 - k_1(\omega - \omega_0)$ ], self-steepening ( $T = 1 + i\tau_{\text{shock}}\partial_t$ , where  $\tau_{\text{shock}} \simeq 1/\omega_0$ ), instantaneous Kerr effects ( $\Delta n = \sum_{m=1}^5 n_{2m} |\varepsilon|^{2m}$  includes the contribution of higher nonlinear indexes up to  $n_{10}$ ), and optical losses  $\alpha$ . The  $n_{2m}$  coefficients are related to  $\chi^{(2m+1)}$  susceptibilities and have been reported in a recent article [17] at 800 nm. We then extrapolated these indexes at  $1.83 \mu\text{m}$  by using generalized Miller formulas [18], providing the spectral dependence of the  $n_{2m}$  coefficients from the knowledge of the linear dispersion. The calculated nonlinear refractive indexes used in this article are summarized in Table I. Losses  $\alpha$  have been estimated from the experimental measurements described in [12]. Equation (1) is valid even for subcycle pulses [19]. Finally, we numerically checked that ionization does not play a role in the process. According to PPT theory, the plasma density for the considered intensities is lower than  $10^{11} \text{ cm}^{-3}$ , inducing a refractive index change four orders lower than the Kerr-induced one.

The input electric field envelope is modeled by a Gaussian profile as

$$\varepsilon(t,0) = \sqrt{\frac{2P_{\text{in}}}{\pi\sigma_r^2}} \exp\left(-\frac{t^2}{\sigma_t^2}\right), \quad (2)$$

where  $P_{\text{in}}$  denotes for the initial peak power,  $\sigma_r$  is the intensity quadratic radius, and  $\sigma_t = \Delta t_{\text{FWHM}}/\sqrt{2 \ln(2)}$  ( $\Delta t_{\text{FWHM}}$  is the full width at half maximum of temporal intensity).  $P_{\text{in}}$  is then calculated as  $P_{\text{in}} = \sqrt{\frac{2}{\pi}} \frac{E_{\text{in}}}{\sigma_r}$ ,  $E_{\text{in}}$  being the pulse energy. The initial conditions are chosen to match the experimental parameters of [12], as summarized in Table II.

Equation (1) is solved with a split-step Fourier algorithm for 1 m fiber length. At each propagation step, the dispersion terms are computed in the frequency domain, whereas both the nonlinear contributions and the self-steepening are treated

TABLE II. Initial conditions used in the model, corresponding to the experiments driven in [12].

$E_{\text{in}}$ (mJ)	$\Delta t_{\text{FWHM}}$ (fs)	$\sigma_r$ ( $\mu\text{m}$ )	$P_{\text{in}}$ (GW)
0.82	73	210	10.5

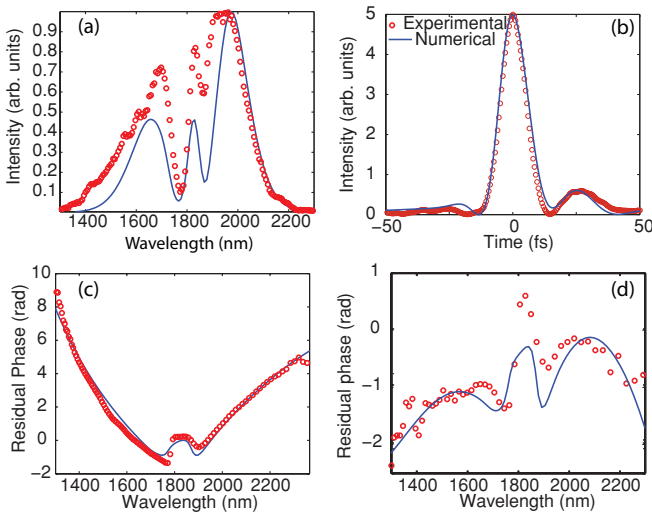


FIG. 2. (Color online) Comparison between experimental (red circles) and theoretical (solid blue line) results. (a) Power spectrum for propagation in argon at pressure of 1.4 bar, (c) spectral phase of the pulse before and (d) after compensation with 3-mm FS. The temporal intensity profile of the compressed pulse is shown in (b).

in the time domain. The self-steepening is solved by using a second-order Runge-Kutta procedure. Moreover, we ensured that increasing the temporal resolution does not change our numerical results.

In order to reproduce experimental conditions, we then apply the spectral phase function induced by both the 1-mm CaF<sub>2</sub> output window and the FS plates with different thicknesses. This function is calculated according to the Sellmeier equations giving the spectral dependence of the CaF<sub>2</sub> and FS refractive indexes [20,21]. In addition, we checked experimentally that no spectral broadening occurs when the fiber is empty, that is, the propagation within the CaF<sub>2</sub> plates remains linear.

### III. RESULTS AND DISCUSSION

Figure 2 compares the experimental and numerical results at a glance. It displays the broadened power spectrum after nonlinear propagation (a), the corresponding spectral phase before (c) and after (d) compression with 3 mm FS. Measured and simulated temporal intensities after compression are shown in (b). The crucial task of the numerical work was to determine the origin for the asymmetry of (i) the spectral shape in (a) and (ii) the phase which is then efficiently compensated by glass material in the anomalous dispersion regime shown in (d). The excellent match for nonlinear propagation according to the full model given by Eq. (1) and subsequent compression with bulk material revealed that SPM, self-steepening, and higher-order Kerr terms during propagation in the fiber are the three relevant nonlinear effects for describing the experimental observations. The aim of the current section is to discuss their respective contributions to the final compression with a simple FS plate. We stress the fact that simulations match exactly experimental conditions. The low peak power of 10.5 GW, which is less than one-third the critical power for self-focusing in argon ( $\approx 37$  GW at 1.4 bar), prevents spatiotemporal pulse collapse and thus fully justifies the 1D + 1 modeling.

#### A. Pulse compression to few optical cycles

Before having a closer look at the details of the nonlinear propagation, we numerically describe the compression by linear propagation through a bulk material in the anomalous dispersion regime. Due to self-steepening, the asymmetric spectral shape of Fig. 2(a) is accompanied by an asymmetric spectral phase. This uncompensated phase after the fiber assembly but before the FS plate is shown in Fig. 3(a) as a red line. In the temporal domain it causes the trailing edge to be more abrupt than the leading one, producing a strong asymmetry in the temporal intensity profile plotted in Fig. 3(b). Its FWHM pulse duration is about 75 fs after the CaF<sub>2</sub> window, close to the 68 fs measured experimentally but far longer than the FL of 11.3 fs. Obviously, the output spectral phase is predominantly positively chirped, as expected from SPM-induced broadening. Pure SPM induces a spectral phase that is typically approximated by a quadratic function and therefore can be compensated because the GDD of both FS and CaF<sub>2</sub> is negative in the anomalous dispersion regime. Thus, a pulse which has experienced Kerr-induced spectral broadening can be temporally compressed by travel through an adequate

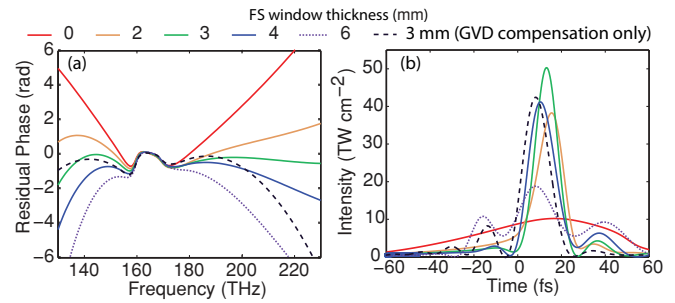


FIG. 3. (Color online) Pulse compression for the spectrum of Fig. 2 by adding different amounts of FS. The color coding for the spectral phases in (a) corresponds to the temporal intensities in (b). Comparing the green with the black dashed plot demonstrates the effect of uncompensated TOD components.

FS plate, as depicted in Fig. 3. The figure illustrates the effect of different glass thicknesses on the spectral phase and corresponding time profile whereby the complete phase introduced by FS is calculated according to the Sellmeier equation. The best compression is obtained using a 2.77-mm FS plate and leads to a pulse duration of 10.9 fs, which corresponds to about 1.8 optical cycles at 1.83  $\mu\text{m}$ . Moreover, we calculated that using a 3-mm FS plate leads to a pulse duration of 11.1 fs. The agreement is excellent, even quantitatively, since the shortest experimentally measured duration was 11.5 fs along with a FL of 10.1 fs. Moreover, the contrast between the main pulse and satellite pulses remains relatively high (about 11), in both experiment and simulation. However, this situation worsens if only the GDD is compensated for. To demonstrate this, we calculated compression taking into account only the negative GDD of 3-mm FS instead of taking the full Sellmeier formula into account (short-dashed line in Fig. 3). Apparently, the compression cannot reach the FL mainly because of remaining higher-order dispersion, which is not fully compensated by FS, as depicted in Fig. 3(a). That means if the negative TOD component after nonlinear propagation is not compensated by the bulk material, the pulse duration increases to 13.5 fs.

#### B. Mechanism study: Respective contributions of the processes in play

Starting from the initial conditions summarized in Table II the nonlinear propagation was simulated investigating different nonlinear effects. As expected, the third-order Kerr term ( $n_2$  in Table I), typically referred to as SPM, is the driving force for spectral broadening [16]. After 1 m of propagation the broadened spectrum symmetrically spans over 1  $\mu\text{m}$  (from 1.3 to 2.3  $\mu\text{m}$ ), as can be seen in Fig. 4(a). Even though spectral bandwidth and FL pulse durations are comparable with those of the experiment, the spectral shape and phase are not adequately reproduced (data not shown). On the other hand, the full model corresponding to the solid line in Fig. 2 including self-steepening and higher-order Kerr terms exhibits different propagation dynamics, as illustrated in Fig. 4(b), and yields remarkable agreement with the experiment result.

To track the contribution of different nonlinear effects, we successively introduced them in the numerical model and compare the corresponding outcomes. Table III summarizes the characteristic lengths  $L_x$  of all processes taken into

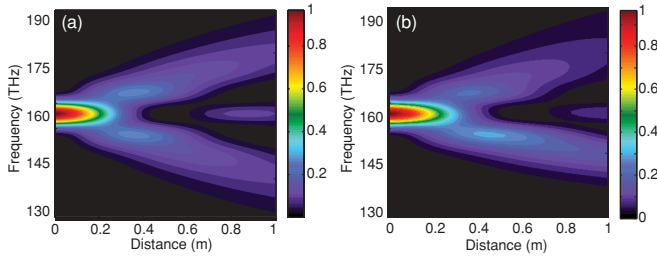


FIG. 4. (Color online) Spectral evolution as a function of propagation distance for the simple case considering only  $n_2$  in (a) and for the full model in (b). The latter clearly resembles an asymmetry because of self-steepening, which tends to promote the higher-frequency region.

account. As expected, the main process driving the pulse propagation (i.e., the process with the shortest characteristic length) is the total Kerr effect, whereas the gas dispersion remains negligible. As shown in [22], even if the first order remains most important during the propagation, it appears that the higher-order Kerr contributions have a non-negligible effect, leading to a refractive index saturation at an intensity of  $19 \text{ TW cm}^{-2}$  and even a negative nonlinear refractive index for intensities higher than  $27 \text{ TW cm}^{-2}$ .

Moreover, as depicted in Table III, self-steepening is not the main process driving the pulse propagation since its characteristic length  $L_{\text{steepening}}$  is about 50 times longer than those of the Kerr effect. In any case, since  $L_{\text{steepening}}$  is comparable with the fiber length, it cannot be neglected. In that section, we investigate how the steepening modifies the final result, and in particular the compression.

As mentioned earlier, the simple case of pure SPM, which only takes into account the first-order Kerr term, is not appropriate for explaining the results of Fig. 2. To find the nonlinear pulse-shaping mechanism that allows for subsequent compression with bulk material, we investigate the effect of the following three models:

- (i) Kerr model: Includes higher-order Kerr effects but without self-steepening (green dashed-dotted line in Fig. 5);
- (ii) Reduced model: Includes only the third-order Kerr effect and self-steepening (dashed blue line in Fig. 5);
- (iii) Full model: Includes higher-order (up to 11th) Kerr terms and self-steepening (red solid line in Fig. 5).

TABLE III. Characteristic lengths of the different processes taking place during the propagation.

Nonlinear effect	Characteristic length	Distance (m)
Kerr (3rd order)	$ c/(\omega_0 n_2  \varepsilon ^2) $	0.136
Kerr (5th order)	$ c/(\omega_0 n_4  \varepsilon ^4) $	2.38
Kerr (7rd order)	$ c/(\omega_0 n_6  \varepsilon ^6) $	0.142
Kerr (9th order)	$ c/(\omega_0 n_8  \varepsilon ^8) $	0.217
Kerr (11th order)	$ c/(\omega_0 n_{10}  \varepsilon ^{10}) $	2.7
Kerr (full)	$ c/(\omega_0 \sum_{m=1}^5 n_{2m}  \varepsilon ^{2m}) $	0.112
Self-steepening	$ c\sigma_t/(\sum_{m=1}^5 n_{2m}  \varepsilon ^{2m}) $	5
Dispersion	$ \sigma_t^2/k^{(2)} $	156

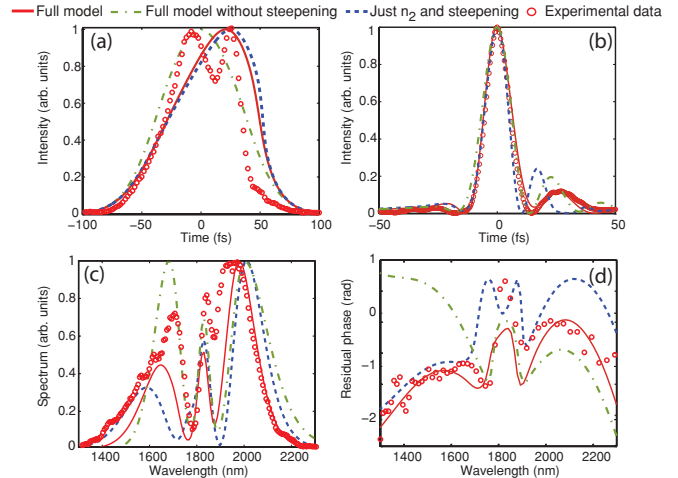


FIG. 5. (Color online) Comparison of the three numerical models with experimental measurements. (a,b) Time profile of (a) the uncompressed and (b) the compressed pulses. (c) Broadened power spectrum and (d) its associated phase when the pulse is compressed.

Above all, one can see that using the pure Kerr model is not sufficient for accurately describing the output spectral shape or its phase. In particular, it is obvious from Fig. 5(d) that the phase in the blue part of the spectrum strongly deviates from the experiment. This also reflects as a longer pulse duration of 12.9 fs and a reduced contrast ratio between main and satellite pulses.

Accounting for self-steepening is the key advance of the reduced model (blue line), which enables modeling an asymmetric spectral shape and phase being much closer to the experimental one than the the Kerr model. However, small discrepancies of the spectral peak positions in combination with additional phase modulations around the center wavelength lead to an enhanced postpulse appearing at shorter delay than that seen in the experiment.

For the considered experimental conditions, the full model describes the broadening process to a much higher degree of accurateness, as is evident when comparing the result with experimental data. The spectral shape, both compressed and uncompressed phase, as well as the temporal intensity, match perfectly except for a small deviation of the blue spectral peak height and the cutoff on the blue side are reduced. The latter might explain a slightly longer FL of 10.8 fs in the simulation compared to the 10.1 fs in the experiment. However, the phase in the same region agrees very well and so does the temporal appearance of main and satellite pulses.

Residual discrepancies could originate from the approximation in the steepening term  $\tau_{\text{shock}} \simeq \frac{1}{\omega_0}$ . In particular, it has been demonstrated that for quite a broad spectrum  $\tau_{\text{shock}}$  has to be corrected as  $\tau_{\text{shock}} = \frac{1}{\omega_0} - \frac{\partial \ln[A_{\text{eff}}(\omega)]}{\partial \omega} |_{\omega_0}$  [23], where  $A_{\text{eff}}(\omega)$  is the effective area. This correction induces a change in the spectrum asymmetry and could indeed explain the difference between experiments and numerical results in Fig. 5. Moreover, spatiotemporal couplings which intrinsically cannot be taken into account in 1D simulations or excitation of higher-order transverse modes cannot be totally ruled out for explaining these discrepancies.

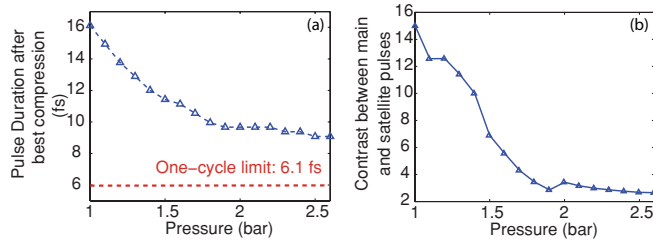


FIG. 6. (Color online) Pressure dependence of (a) minimal pulse duration achievable by compression with optimized FS thickness in each case and (b) ratio between main and satellite pulse intensities.

However, this correction does not affect the bottom line of the numerical investigations. Our results prove that neglecting self-steepening leads to underestimating the compression efficiency (the best compression gives 12.9 fs, that is, 2.1 cycles) and the contrast between the main and the satellite pulses (about 5), indicating that self-steepening induces an opposite contribution to the positive TOD of the FS plate. Moreover, as in [22], it appears that the higher-order Kerr terms have to be included in order to quantitatively reproduce experiments.

### C. Parameters dependence

Enforced by the quantitative agreement of our full model, we performed a parameter study in order to find the optimal conditions to generate single-cycle IR pulses with a clean temporal shape (i.e., without any post- or prepulses). In that regard, we investigate how the compression behaves as functions of both wavelength and argon pressure. Adjusting the pressure is a very handy method for controlling the spectral broadening, simply because  $n_2$  is proportional to the pressure. Indeed, a higher pressure is expected to broaden the spectrum even more, leading in turn to shorter compressed pulses, provided an adequate FS plate can compensate for potentially more complex spectral phases induced by both SPM and self-steepening as the pulse spectrum gets broader and broader. In addition, when aiming for even shorter XUV attosecond pulses, few-cycle driving fields in the IR region are strongly desirable simply because the extension of the XUV spectrum is proportional to the kinetic energy of the accelerated electron scaling as  $I\lambda^2$ . In that framework, we have extended our analysis to longer wavelengths, and

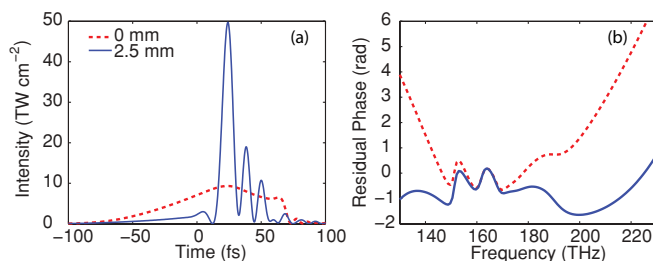


FIG. 7. (Color online) (a) Temporal profile and (b) residual spectral phase of the pulse for a pressure of 2.6 bar without (dashed red line) and with (blue line) the best compression leading to a FWHM duration of 1.25 cycles.

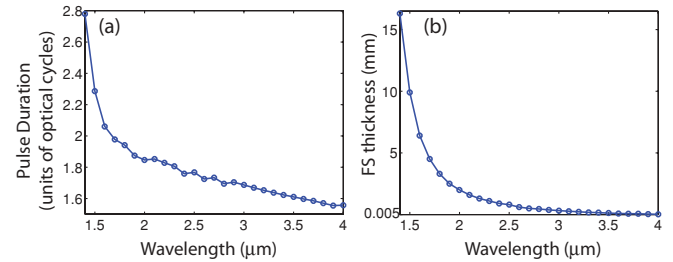


FIG. 8. (Color online) (a) Temporal duration (in cycle units) at different wavelengths of pulses compressed with an optimal FS thickness. The best FS thicknesses are displayed in (b). Note that the CaF<sub>2</sub> exit window is taken into account.

we discuss the efficiency of the method to generate single-cycle pulses in the 1.4- to 4- $\mu\text{m}$  spectral region.

#### 1. Pressure dependence at 1.83 $\mu\text{m}$

We first performed calculations as a function of pressure according to the experimental conditions (i.e., setting the other parameters like in the experimental conditions being discussed in the first section). As depicted in Fig. 6(a), a higher pressure leads to a shorter main pulse, however, at the cost of the growth of satellite pulses in the trailing edge of the pulse [see Fig. 6(b)]. For instance, the best compression with a FS plate at a pressure of 2.6 bar is about 7.5 fs, which is less than 1.25 cycles. However, as depicted in Fig. 7, the nonlinear induced spectral phase cannot be fully compensated by the FS plate, causing the birth of several satellite pulses. Moreover, increasing the pressure above 2.6 bar enhances those satellite pulses without reducing the main pulse duration. In other words, a trade-off between the pulse duration and contrast of main and satellite pulses has to be accepted due to uncompensated higher-order dispersion.

#### 2. Wavelength dependence at 1.4 bar pressure

In this section, we describe how the compression behaves as the pulse central wavelength is varied for all other parameters, keeping the same initial conditions of the first section. Figure 8(a) displays the pulse duration as a function of the pulse central wavelength and shows the scalability for generating sub-two-cycle pulses with this very simple compression technique at least from 1.7 to 4  $\mu\text{m}$ . Nevertheless, as depicted in Fig. 8, the compression ability below 1.7  $\mu\text{m}$  diminishes, mainly because the zero second-order dispersion wavelength lies at around 1.3  $\mu\text{m}$ . On the contrary, the ratio  $k_2/k_3$  of FS being higher at longer wavelengths, the propagation through the FS plate leads in turn to a better compression at longer central wavelengths. However, since the nonlinear refractive index  $n_2$  decreases as the wavelength increases and since the same  $B$  integral [ $B = n_2 \int_0^L I(z) dz$ ] has to be accumulated to obtain an equivalent spectral broadening, it appears that the compression at longer wavelengths is limited at this pressure mainly because of the limited spectral broadening.

## IV. CONCLUSION

In this article, we have identified the mechanisms allowing for pulse compression of IR pulses in a FS plate after

spectral broadening in an argon-filled HCF. We have described numerically a technique for generating tunable sub-two-cycle pulses in the range from 1.5 to 4  $\mu\text{m}$ , which have been also demonstrated experimentally at 1.83  $\mu\text{m}$  center wavelength. In particular, the comparison between experiment and simulations revealed self-steepening as a key process, as well as a significant contribution from higher-order Kerr terms. Compression is simply achieved by propagating the pulse through a FS plate, which exhibits negative GDD in the IR range, after nonlinear propagation in a standard HCF setup. Our numerical simulations show that self-steepening allows a better compression than expected due to SPM only because steepening induces a negative third-order component which partially compensates the positive TOD of FS. Moreover, we have identified the processes involved in the spectral broadening process. Thus, it appears that higher-order Kerr terms have an important impact to adequately fit the experimental results. Moreover, the excellent quantitative agreement of our model with respect to the experiments driven at 1.83  $\mu\text{m}$  allowed us to discuss the optimal parameters for generating

sub-two-cycle pulses in the 1.5- to 4- $\mu\text{m}$  range. Such a tunable, few-cycle IR source will be useful in the scope of attosecond pulse generation experiments, where the cutoff frequency of the XUV radiations quadratically depends on the pump wavelength.

#### ACKNOWLEDGMENTS

This work was supported by the ANR COMOC and the Swiss NSF (Contract Nos. 200021-116198 and 200021-125315). Experiments were carried out at the Advanced Laser Light Source (ALLS) at INRS in Varennes (Canada) and the support of the Canada Foundation for Innovation, the Canadian Institute for Photonic Innovations, the Natural Sciences and Engineering Research Council of Canada, and the Fonds Québécois de la Recherche sur la Nature et les Technologies is greatly acknowledged. We gratefully acknowledge the fruitful discussions with D. M. Villeneuve and Paul Corkum, as well as the help and the time spent on the laser system by François Poitras and Antoine Laramée.

- 
- [1] D. Strickland and G. Mourou, *Opt. Commun.* **56**, 219 (1985).
- [2] M. Nisoli, S. Stagira, S. DeSilvestri, O. Svelto, S. Sartania, Z. Cheng, M. Lenzner, C. Spielmann, and F. Krausz, *Appl. Phys. B* **65**, 189 (1997).
- [3] C. P. Hauri, W. Kornelis, F. W. Helbing, A. Heinrich, A. Couairon, A. Mysyrowicz, J. Biegert, and U. Keller, *Appl. Phys. B* **79**, 673 (2004).
- [4] S. Skupin, G. Stibenz, L. Bergé, F. Lederer, T. Sokollik, M. Schnurer, N. Zhavoronkov, and G. Steinmeyer, *Phys. Rev. E* **74**, 056604 (2006).
- [5] P. Béjot, J. Kasparian, and J.-P. Wolf, *Phys. Rev. A* **78**, 043804 (2008).
- [6] M. Nisoli, S. Stagira, S. De Silvestri, O. Svelto, G. Valiulis, and A. Varanavicius, *Opt. Lett.* **23**, 630 (1998).
- [7] X. Gu *et al.*, *Opt. Express* **17**, 62 (2009).
- [8] M. Yamashita, K. Yamane, and R. Morita, *IEEE J. Quantum Electron.* **12**, 213 (2006).
- [9] E. Goulielmakis *et al.*, *Science* **320**(5883), 1614 (2008).
- [10] P. B. Corkum and F. Krausz, *Nat. Phys.* **3**, 381 (2007).
- [11] P. B. Corkum, *Phys. Rev. Lett.* **71**, 1994 (1993).
- [12] B. E. Schmidt *et al.*, *Appl. Phys. Lett.* (to be published).
- [13] L. Bergé, S. Skupin, and G. Steinmeyer, *Phys. Rev. A* **79**(3), 033838 (2009).
- [14] A. Baltuška, M. S. Pshenichnikov, and D. A. Wiersma, *Opt. Lett.* **23**, 1474 (1998).
- [15] M. J. Weber, *Handbook of Optical Materials* (CRC Press, Boca Raton, FL, 2003).
- [16] G. P. Agrawal, *Nonlinear Fiber Optics*, 3rd ed. (Academic Press, San Diego, 2001).
- [17] V. Loriot, E. Hertz, O. Faucher, and B. Lavorel, *Opt. Express* **17**, 13429 (2009); **18**, 3011(E) (2010).
- [18] W. Ettoumi, Y. Petit, J. Kasparian, and J.-P. Wolf, *Opt. Express* **18**, 6613 (2010).
- [19] G. Genty, P. Kinsler, B. Kibler, and J. M. Dudley, *Opt. Express* **15**, 5382 (2007).
- [20] *Handbook of Optics*, 2nd ed. (McGraw-Hill, Columbus, OH, 1994), Vol. 2.
- [21] I. H. Malitson, *J. Opt. Soc. Am.* **55**, 1205 (1965).
- [22] P. Béjot, J. Kasparian, S. Henin, V. Loriot, T. Vieillard, E. Hertz, O. Faucher, B. Lavorel, and J.-P. Wolf, *Phys. Rev. Lett.* **104**, 103903 (2010).
- [23] B. Kibler, J. M. Dudley, and S. Coen, *Appl. Phys. B* **81**, 337 (2005).

## Spectral dependence of purely-Kerr-driven filamentation in air and argon

W. Ettoumi,<sup>1</sup> P. Béjot,<sup>2</sup> Y. Petit,<sup>1</sup> V. Loriot,<sup>2,3</sup> E. Hertz,<sup>2</sup> O. Faucher,<sup>2</sup> B. Lavorel,<sup>2</sup> J. Kasparian,<sup>1,\*</sup> and J.-P. Wolf<sup>1</sup>

<sup>1</sup>Université de Genève, GAP-Biophotonics, 20 rue de l'École de Médecine, 1211 Geneva 4, Switzerland

<sup>2</sup>Laboratoire Interdisciplinaire Carnot de Bourgogne (ICB), UMR 5209 CNRS-Université de Bourgogne, 9 Av. A. Savary, Boîte Postale 47 870, F-21078 DIJON Cedex, France

<sup>3</sup>Instituto de Química Física Rocasolano, CSIC, C/Serrano, 119, 28006 Madrid, Spain

(Received 4 May 2010; published 21 September 2010; publisher error corrected 27 September 2010)

Based on numerical simulations, we show that higher-order nonlinear indices (up to  $n_8$  and  $n_{10}$ , respectively) of air and argon have a dominant contribution to both focusing and defocusing in the self-guiding of ultrashort laser pulses over most of the spectrum. Plasma generation and filamentation are therefore decoupled. As a consequence, ultraviolet wavelength may not be the optimal wavelength for applications requiring to maximize ionization.

DOI: [10.1103/PhysRevA.82.033826](https://doi.org/10.1103/PhysRevA.82.033826)

PACS number(s): 42.65.Jx, 42.65.Tg, 78.20.Ci

The filamentation of high-power ultrashort laser pulses is generally described as a dynamic balance between Kerr self-focusing and the defocusing by the plasma generated at the nonlinear focus [1–5]. In this description, the Kerr-induced change in the refractive index is truncated to the first term  $n_2 I$ , where  $I$  is the local intensity. However, at higher intensities, the development has to be extended to higher-order terms in  $I$  so that the real part of the refractive index at any frequency  $\omega$  writes

$$n(\omega) = n_0(\omega) + \Delta n_{\text{Kerr}}(\omega) = n_0(\omega) + \sum_{j \geq 1} n_{2j}(\omega) I^j, \quad (1)$$

where the  $n_{2j}(\omega)$  coefficients are related to the  $(2j + 1)$ -th-order susceptibility tensor  $\chi^{(2j+1)}(\omega)$ , in the degenerate case where all considered fields are at frequency  $\omega$ :

$$n_{2j}(\omega) = \frac{(2j + 1)!}{2^{j+1} j! (j + 1)!} \frac{1}{[n_0^2(\omega) \epsilon_0 c]^j} \text{Re}[\chi^{(2j+1)}(\omega)]. \quad (2)$$

In the past years, several numerical works have investigated the influence of the quintic nonlinear response on the filamentation dynamics at a wavelength of 800 nm, although without knowledge of its actual value [6–10]. They suggested that this term was defocusing, but considered it as marginal. Recently, the measurement of the higher-order Kerr indices at a wavelength of 800 nm up to  $n_8$  in air and  $n_{10}$  in argon [11] showed that they have alternate signs, and are therefore alternatively focusing and defocusing. Furthermore, by implementing these terms in a numerical simulation of filamentation, we have recently shown that the defocusing terms  $n_4$  and  $n_8$ , rather than the plasma, provide the main regularizing process in the filamentation of 30-fs pulses in air at 800 nm so that plasma generation and propagation equations are almost decoupled [12]. This finding provides an explanation for measurements of plasma-free filamentation [13,14] and predicts symmetrical temporal pulse shapes, in contrast with a balance between the instantaneous Kerr term and the time-integrated plasma contribution, which implies strongly asymmetric pulse shapes [15]. It also explains

the discrepancy, by almost 2 orders of magnitude, between experimentally measured and numerically derived electron densities within filaments. While the experiments yield some  $10^{14} \text{ cm}^{-3}$  [16,17], the numerical simulations require a few  $10^{16} \text{ cm}^{-3}$  to balance the  $n_2 I$  Kerr self-focusing term [3,4]. The consideration of the higher-order Kerr terms also turned out to be necessary to obtain a quantitative agreement between numerical simulations and experimental results about the propagation of ultrashort infrared (IR) pulses in an argon-filled hollow-core fiber [18,19].

However, the ionization rates are higher at shorter wavelengths so that ionization is generally believed to be much stronger in the case of ultraviolet (UV) filamentation [20], while its low efficiency in the IR would expectedly prevent self-guiding of filaments. But the recently derived generalized Miller formulas [21] predict larger absolute values of the higher-order nonlinear indices at shorter wavelengths, with faster spectral dependencies for the higher orders. As a consequence, the relative contribution to self-guiding cannot be easily extrapolated from qualitative discussions.

In this paper, we numerically investigate these relative contributions from the near UV to the near infrared (NIR). Using the values of the  $n_{2j}$  indices at any wavelength as obtained from the generalized Miller formulas [21], and the values recently measured at 800 nm [11], we simulate the filamentation of laser pulses from 300 to 1600 nm in air and argon. We show that filaments are efficiently generated at all wavelengths, even in the IR. Moreover, the plasma marginally contributes to self-guiding in the filamentation of 30-fs laser pulses in argon for wavelengths typically longer than 400 nm. In air, where the ionization of oxygen is about 100 times more efficient than in argon, the Kerr terms still provide the largest defocusing contribution, although the plasma contribution can be neglected over the whole propagation length only in the IR. This finding strongly impacts the plasma generation. We also find that UV wavelengths are not optimal to maximize ionization in a filament.

Numerical simulations are performed, as described in detail in Ref. [12], by solving a nonlinear Schrödinger equation (NLSE) taking the higher-order Kerr terms into account. The reduced scalar envelope  $\varepsilon$  defined such that  $|\varepsilon(r, z, t)|^2 = I(r, z, t)$ ,  $I$  being the intensity, is assumed to vary slowly in

\*jerome.kasparian@unige.ch

time and along  $z$ :

$$\begin{aligned} \partial_z \varepsilon = & \frac{i}{2k} \Delta_{\perp} \varepsilon - i \frac{k''}{2} \partial_r^2 \varepsilon \\ & + \left(1 + \frac{i}{\omega} \frac{\partial}{\partial t}\right) i \frac{k}{n_0} \left( \sum_{j \geq 1} n_{2j} |\varepsilon|^{2j} \right) \varepsilon - i \frac{k}{2n_0^2 \rho_c} \rho \varepsilon \\ & - \frac{\varepsilon}{2} \sum_{\ell=O_2, N_2} \left[ \sigma_{\ell}(\omega) \rho + \frac{W_{\ell}(|\varepsilon|^2, \omega) U_{\ell}}{|\varepsilon|^2} (\rho_{nt_{\ell}} - \rho) \right], \end{aligned} \quad (3)$$

where  $\omega$  and  $k = n_0 \omega / c$  are the angular frequency and wave number of the carrier wave,  $k''$  accounts for the linear group-velocity dispersion (GVD),  $\rho$  is the electron density,  $\rho_{nt_{\ell}}$  is the density of neutral molecules of species  $\ell$ ,  $\rho_c = m_e \epsilon_0 \omega / q_e^2$  is the critical plasma density and  $m_e$  and  $q_e$  are the mass and charge of the electron,  $n_0$  is the linear refractive index at  $\lambda$ ,  $W_{\ell}(|\varepsilon|^2)$  is the photoionization rate of species  $\ell$  with ionization potential  $U_{\ell}$ ,  $\sigma_{\ell}$  is the cross section for avalanche ionization as defined below in Eq. (8), and  $t$  refers to the retarded time in the reference frame of the pulse. The right-hand terms of Eq. (3) account for spatial diffraction, second-order GVD, Kerr self-focusing (including the self-steepening term), defocusing by the higher-order nonlinear refractive indices, plasma defocusing, inverse bremsstrahlung, and multiphoton absorption, respectively. We neglect the delayed orientational response, which for pulses longer than 100 fs would increase the self-focusing term [3,4] and affect the ionization efficiency of  $N_2$  and  $O_2$  molecules by less than 20% and 10%, respectively [22,23]. These opposite effects are negligible in the numerical simulations for 30-fs pulse duration, and do not affect qualitatively the following discussion even for longer pulses. We also neglect space-time focusing. However, in the following, we mainly focus on the self-guiding process, peak intensity, and ionization, which are little affected by this approximation.

The spectral dependence of the NLSE (3) stems from the plasma contribution as well as the dispersion of the linear ( $n_0$ ) and nonlinear ( $n_{2j}$ ) refractive indices. The latter can be deduced at any frequency  $\omega$  from those of  $O_2$  and  $N_2$  at the same frequency by following the Lorenz-Lorentz relation, which links the refractive index of a mix of nonpolar gases to its components [24],

$$\frac{n_{\text{mix}}^2(\omega) - 1}{n_{\text{mix}}^2(\omega) + 2} = \sum \rho_i \frac{n_i^2(\omega) - 1}{n_i^2(\omega) + 2}, \quad (4)$$

where  $n(\omega)$  is defined in Eq. (1) and  $\rho_i$  denotes the relative abundance of the species  $i$  in the mix. Considering that  $\Delta n_{\text{Kerr}} \ll 1$ , a first-order development of Eq. (4) yields, for any order  $j$ :

$$n_{2j, \text{Air}}(\omega) = 0.79 n_{2j, N_2}(\omega) + 0.21 n_{2j, O_2}(\omega). \quad (5)$$

The values of the  $n_{2j}$  for argon, nitrogen, and oxygen can be calculated at any frequency  $\omega$  from their values measured at  $\lambda_0 = 800$  nm [11] and the dispersion curves in

those gases [25], through the generalized Miller formula [21] expressed in term of nonlinear refractive indices:

$$n_{2j}(\omega) = n_{2j}(\omega_0) \left[ \frac{n_0^2(\omega) - 1}{n_0^2(\omega_0) - 1} \right]^{2(j+1)}. \quad (6)$$

While  $n_{8, \text{Air}}$  varies by a factor of 2 between 300 and 1600 nm, ionization displays an even much steeper spectral dependence. More specifically, the temporal evolution of the electron density is given by

$$\frac{\partial \rho}{\partial t} \approx \sum_{\ell=O_2, N_2} \left[ W_{\ell}(I, \omega) \rho_{0, nt_{\ell}} + \frac{\sigma_{\ell}(\omega)}{U_{\ell}} I \rho \right], \quad (7)$$

where  $\rho_{0, nt_{\ell}}$  is the initial density of neutral molecules of species  $\ell$ . Here, attachment to neutral molecules and recombination with positive ions have been neglected owing to the short pulse durations considered in this paper. The cross section for avalanche ionization is calculated on the basis of Drude's theory [3]:

$$\sigma_{\ell}(\omega) = \frac{q_e^2}{m_e \epsilon_0 n_0(\omega) c v_{e, \ell} \left(1 + \frac{\omega^2}{v_{e, \ell}^2}\right)} \quad (8)$$

$$\approx \frac{q_e^2 v_{e, \ell}}{\omega^2 m_e \epsilon_0 n_0(\omega) c}, \quad (9)$$

where  $v_{e, \ell}$  is the mean-collisional frequency of an electron with the species  $\ell$  (i.e., the average electron velocity, divided by the mean-free path of an electron, assuming that only species  $\ell$  is present), and  $c$  is the speed of light. At atmospheric pressure in air,  $v_{e, O_2} = 1/(1.75 \text{ ps})$ ,  $v_{e, N_2} = 1/(440 \text{ fs})$ , and  $v_{e, Ar} = 1/(350 \text{ fs})$ . The multiphoton and tunnel ionization rates are given by the multispecies generalized Keldysh-Perelomov, Popov, Terent'ev formulation [3,16],

$$\begin{aligned} W_{\ell}(|\varepsilon|^2, \omega) = & \frac{4\sqrt{2}}{\pi} |C_{n_{\ell}^*, l_{\ell}^*}|^2 \left( \frac{4\sqrt{2} U_{\ell}^{3/2}}{E_p \sqrt{1 + \gamma_{\ell}^2}} \right)^{2n_{\ell}^* - 3/2 - |m_{\ell}|} \\ & \times \frac{f(l_{\ell}, m_{\ell})}{|m_{\ell}|!} e^{-2v_{\ell}} \left( \sinh^{-1}(\gamma_{\ell}) - \frac{\gamma_{\ell} \sqrt{\gamma_{\ell}^2 + 1}}{1 + 2\gamma_{\ell}^2} \right) \\ & \times U_{\ell} \frac{\gamma_{\ell}^2}{1 + \gamma_{\ell}^2} \sum_{\kappa_{\ell} \geq v_{\ell}}^{+\infty} e^{-\alpha_{\ell}(\kappa_{\ell} - v_{\ell})} \Phi_m(\sqrt{\beta_{\ell}(\kappa_{\ell} - v_{\ell})}), \end{aligned} \quad (10)$$

where, expressed in atomic units,  $E_p = |\varepsilon| \sqrt{2/(\epsilon_0 c)}$ ,  $\gamma_{\ell} = \omega \sqrt{2U_{\ell}} / E_p$ ,  $v_{\ell} = U_{\ell} [1 + 1/(2\gamma_{\ell}^2)] / (\hbar \omega)$ ,  $\beta_{\ell} = 2\gamma_{\ell} / \sqrt{1 + \gamma_{\ell}^2}$ ,  $\alpha_{\ell} = 2[\sinh^{-1}(\gamma_{\ell}) - \gamma_{\ell} / \sqrt{1 + \gamma_{\ell}^2}]$ , and  $\Phi_m(x) = e^{-x^2} \int_0^x (x^2 - y^2)^{|m_{\ell}|} e^{y^2} dy$ .  $n_{\ell}^* = Z_{\ell} / \sqrt{2U_{\ell}}$  is the effective quantum number,  $l_{\ell}^* = n_{\ell}^* - 1$ ,  $l_{\ell}$ , and  $m_{\ell}$  are the orbital momentum and the magnetic quantum number, respectively. In air,  $l_{\ell} = m_{\ell} = 0$  [26].  $Z_{\ell}$  is the residual ion charge accounting for the difference between the  $O_2$  and  $N_2$  molecules and their atomic counterparts. These empirical coefficients  $Z_{O_2} = 0.53$  and  $Z_{N_2} = 0.9$  have been measured at 800 nm [27] and are expected to be independent from the wavelength. Since argon

is an atomic gas,  $Z_{\text{Ar}} = 1$ . The factors  $|C_{n_\ell^*, l_\ell^*}|$  and  $f(l_\ell, m_\ell)$  are

$$|C_{n_\ell^*, l_\ell^*}| = \frac{2^{2n_\ell^*}}{n_\ell^* \Gamma(n_\ell^* + l_\ell^* + 1) \Gamma(n_\ell^* - l_\ell^*)}, \quad (11)$$

$$f(l_\ell, m_\ell) = \frac{(2l_\ell + 1)(l_\ell + |m_\ell|)!}{2^{|m_\ell|} |m_\ell|! (l_\ell - |m_\ell|)!}. \quad (12)$$

To quantify the relative contributions of the higher-order Kerr terms ( $n_4$ – $n_{10}$ ) and of the ionization to the defocusing, which balances the self-focusing, we define the instantaneous ratio  $\xi$  between the refractive index changes induced by both of these contributions at any location  $\vec{r}$ :

$$\xi(\vec{r}, t) = \left| \sum_{j \geq 2} n_{2j} I(\vec{r}, t)^j \right| / \frac{\rho(\vec{r}, t)}{2n_0 \rho_c}. \quad (13)$$

This expression is, in fact, the ratio of the magnitude of the two defocusing terms in the propagation equation (3), namely, those accounting for higher-order Kerr terms and plasma defocusing, respectively. When considering the overall action of both effects on the whole pulse duration, we define a pulse-integrated value of  $\xi$ :

$$\bar{\xi}(\vec{r}) = \int \left| \sum_{j \geq 2} n_{2j} I(\vec{r}, t)^j \right| |\varepsilon(\vec{r}, t)| dt / \int \frac{\rho(\vec{r}, t)}{2n_0 \rho_c} |\varepsilon(\vec{r}, t)| dt. \quad (14)$$

We numerically integrated the propagation equation (3) for an ultrashort pulse typical of laboratory-scale filamentation experiments: 30-fs Fourier-limited full width at half-maximum pulse duration, a peak power of 6.5 critical powers  $P_{\text{cr}} = \lambda^2/4\pi n_2$ , a beam diameter of  $\sigma_r = 4$  mm, a focal length  $f = 1$  m, and a pressure of 1 bar of either air or argon. The main results are displayed in Fig. 1.

Our simulations yield filamentation over the whole investigated spectral range (300–1600 nm), reproducing experimental observations from the UV [28,29] to the mid IR [30]. As visible in Figs. 1(a) and 1(b), the clamping intensity, filament onset, and filament length are very similar in air and argon over the whole considered spectral length for a given incident reduced power  $P/P_{\text{cr}}$ . Moreover, longer wavelengths yield longer filaments with an earlier onset. Furthermore, the output spectrum after 1.5-m propagation [panels (e) and (f)] is broader for longer wavelengths. As a result, the relative broadening, defined as the ratio of the output spectral width to the initial frequency  $\Delta\omega/\omega_0$  is almost constant across the spectrum. Spectral properties appear very similar in air and argon.

In contrast, the electron density is approximately ten times higher in the former than in the latter. The spectral dependence of the electron density is very nonmonotonic [panels (c) and (d)]. On one hand, due to steps in the number of photons required for ionization, the electron density is not a monotonic function of the wavelength. For instance, ionization in air is almost two times more efficient at 793 nm than at 815 nm (see Fig. 2). On the other hand, contrary to expectations that shorter wavelengths should result in stronger ionization, a maximum in the peak electron density is observed in the 610-nm range in the case of air, and around 470 nm in argon [Figs. 1(c), 1(d), and 4(a)]. Away from this maximum, the peak electron density

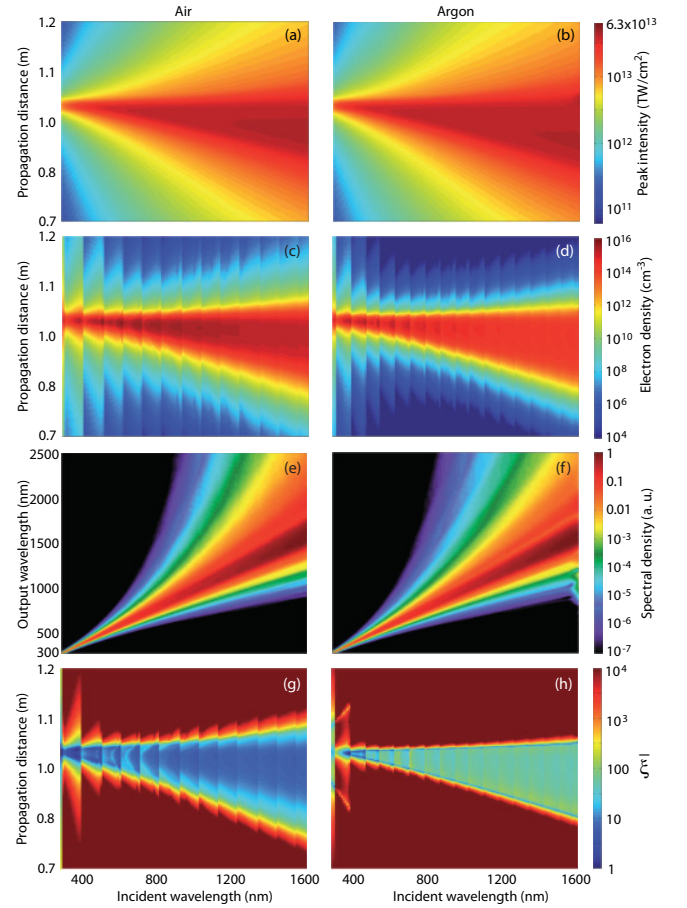


FIG. 1. (Color) Maximum on-axis intensity (a), (b), electron density (c), (d), spectral broadening (e), (f), and pulse-averaged contributions of the higher-order Kerr and plasma contributions to the nonlinear refractive index [(g), (h), see text for details], as a function of the wavelength and propagation distance in air (a), (c), (e), (g) and argon (b), (d), (f), (h).

decreases within a dynamics of typically 1 order of magnitude. This unexpected behavior stems from the convolution of the respective spectral dependences of (i) the ionization rate  $W$ , which increases at shorter wavelengths and (ii) the peak intensity, which decreases in the UV. This decrease is due to the fact that, according to Eq. (6) and considering the typical dispersion curves in gases, the higher-order indices increase faster, in absolute values, when the frequency increases. As a consequence, the clamping intensity canceling the Kerr effect  $I_{\Delta n_{\text{Kerr}}=0}$  is lower, as shown in Fig. 3.

The spectral dependence of the peak electron density by more than 1 order of magnitude, also evidenced in Fig. 4(a), appears in contradiction with numerical results obtained without considering the higher-order Kerr terms [31], which predict almost similar electron densities, close to  $10^{16} \text{ cm}^{-3}$ , at the three investigated wavelengths (248, 800, and 1550 nm). Since the latter results were obtained with longer pulses (127 fs) of slightly lower power than in our paper, a direct quantitative comparison cannot be performed. However, we expect that the qualitative difference between our results and those of Ref. [31] are due to the inclusion of the higher-order

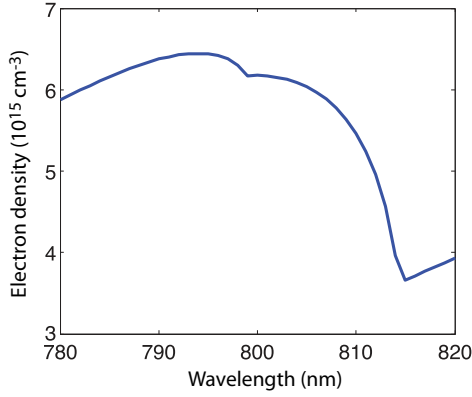


FIG. 2. (Color online) Wavelength dependence close to 800 nm of the electron density generated by a 30-fs pulse of constant intensity 50 TW.

Kerr terms in our model, and thus illustrate the influence of the latter.

The very similar behavior, except for the plasma density, of two gases with comparable values of the nonlinear refractive indices but significantly different ionization potentials, suggests that filamentation is driven by the higher-order Kerr terms rather than by plasma, not only at 800 nm as evidenced recently [12], but also on the whole investigated spectral range in both air and argon. Indeed, the on-axis  $\xi$  ratio [Figs. 1(g), and 1(h)] exceeds 1 in all considered conditions. Furthermore, the higher-order Kerr terms strongly dominate the filamentation dynamics ( $\xi > 10$ ) at all wavelengths above  $\lambda \sim 400$  nm in argon and above  $\lambda \sim 600$  nm in air, although, due to the thresholds induced by the steps in photon numbers required to ionize oxygen [see Eq. (10)], the evolution of this behavior is not strictly monotonic. Due to the domination of the higher-order Kerr terms, the latter will govern the intensity within the filaments so that the ionization is mostly decoupled from the filamentation dynamics.

It should be noted that Miller formulas are sometimes considered to underestimate dispersion [32]. However, such correction to the dispersion curve of higher-order Kerr terms would result in a larger absolute value of the high-order Kerr

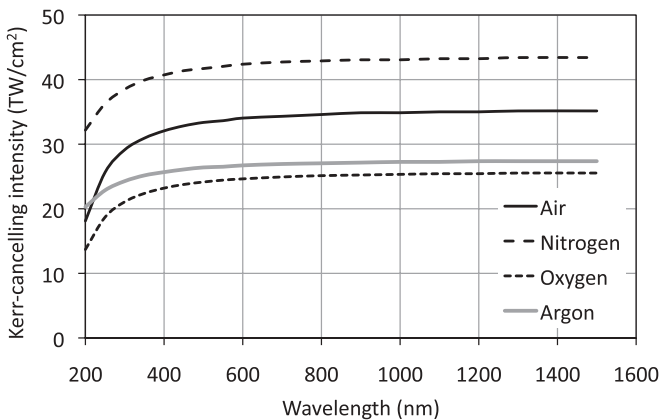


FIG. 3. Wavelength dependence of the clamping intensity canceling the Kerr effect  $I_{\Delta n_{\text{Kerr}}=0}$ , in  $\text{O}_2$ ,  $\text{N}_2$ , air, and Ar, based on the dispersion of the higher-order Kerr indices from Eq. (6).

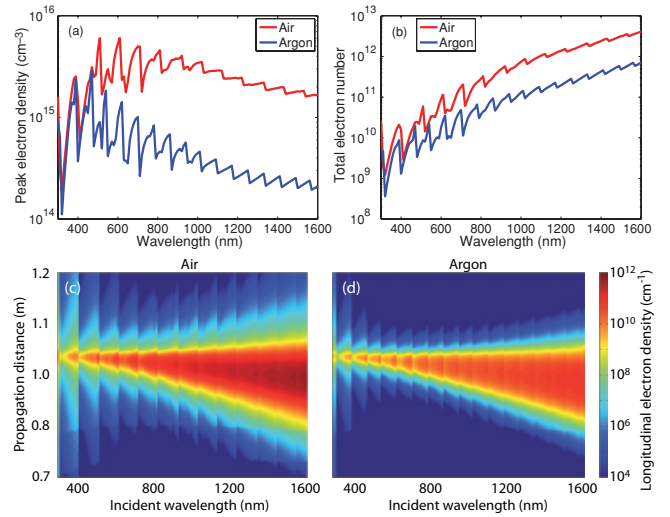


FIG. 4. (Color) Wavelength dependence of ionization in laser filamentation. (a) Peak electron density; (b) total number of electrons; (c), (d) transverse-integrated longitudinal electron density in air and argon, representative of the electric conductivity of the filament. Note the difference with Figs. 1(c) and 1(d), which is due to the larger filament diameter in the IR.

indices in the UV. In this case,  $I_{\Delta n_{\text{Kerr}}=0}$  will be even lower in the UV. In other words, the curves of Fig. 3 will decrease faster on the left side of the graph. As a consequence, the higher-order Kerr indices will have an even more dominant contribution to the self-guiding, as compared to that of plasma. Such larger dispersion would therefore qualitatively reinforce our conclusion about the domination of defocusing higher-order Kerr terms over the plasma defocusing.

This new vision of filamentation provides straightforward interpretation for experimental observations that the spectral broadening mostly occurs at the beginning of the filaments, while the spectrum is little affected in the main region of self-guided propagation [33]. This is due to the fact that, in the self-guided propagation, the intensity is clamped close to  $I_{\Delta n_{\text{Kerr}}=0}$  so that the spectral counterpart of this Kerr effect, self-phase modulation, is also waved out. The earlier onset of filamentation for longer wavelengths is compatible with the Marburger formula [34], which predicts that the nonlinear focal length describing self-focusing is inversely proportional to the wavelength. Furthermore, the longer filaments in the IR appear to stem from the lower peak electron density [Fig. 4(a)].

The very smooth dispersion curve of both air and argon above 500 nm [21] results in a very slow variation of this clamping intensity  $I_{\Delta n_{\text{Kerr}}=0}$  (Fig. 3) and explains the quasiconstant clamping intensity observed over this spectral range.

The availability of simulations at constant reduced power  $P/P_{\text{cr}}$  over a broad spectral range allows to discuss the choice of wavelength to optimize the filaments properties for specific purposes. As described earlier, the spectral dependence of the electron generation contrasts strongly with the common expectation that, due to a more efficient ionization, UV wavelengths should ionize the propagation medium more efficiently.

However, the peak electron density is not directly relevant for typical atmospheric applications. For example, laser-assisted water condensation [35], can be expected to require the largest possible value of the total generated charge. This total charge is obtained by integrating the plasma density over the filament length and cross section [Fig. 4(b)]. Here, the longer filaments in the IR as well as their larger diameters result in an unanticipated larger total charge at longer wavelengths.

Applications such as lightning control [36] require the longest possible filaments with the higher conductivity [i.e., a high longitudinal (transversely integrated) electron density]. Long wavelengths simultaneously optimize both of these properties [Figs. 4(c) and 4(d)]. In that regard, UV lasers providing short filaments with a small diameter and decreasing transverse-integrated electron densities would expectedly be less efficient than the commonly used titanium:sapphire lasers around 800 nm, while wavelengths further in the IR should even be more efficient. IR is also very attractive because it would allow to work in the telecommunication spectral region (1.55  $\mu\text{m}$ ), where optical components are available and eye-safety standards are much more favorable for atmospheric applications than in the rest of the NIR and visible spectral region.

In conclusion, applying generalized Miller formulas to estimate arbitrary-order nonlinearities from the IR to the UV spectrum, we have shown that higher-order nonlinear indices (up to  $n_8$  in air and  $n_{10}$  in argon) have a dominant

contribution to both the focusing and the defocusing terms implied in the self-guiding of 30-fs laser pulses in air, at all wavelengths between 300 and 1600 nm. As a consequence, the plasma generation is almost decoupled from the self-guiding of filaments over the whole visible and IR spectral range. Instead, filaments can be considered as a self-guiding regime mostly governed in air and argon by the balance between the alternate signs of the nonlinear indices, respectively resulting in Kerr self-focusing and self-defocusing.

Moreover, a systematic investigation at constant reduced power  $P/P_{\text{cr}}$  as a function of wavelength provides hints to choose optimal wavelengths for generating filaments optimized for a specific application. In particular, we have shown that, contrary to previous expectations, the IR is more favorable than the commonly used 800-nm wavelength if long ionized filaments or high total amounts of charges are required. This raises the hope to further improve the spectacular results [5,35,36] recently obtained with titanium:sapphire lasers. Moreover, the higher eye-safety threshold in the telecommunication window at 1.55  $\mu\text{m}$  is favorable for the practical development of the envisioned applications in free space.

This work was supported by the Conseil Régional de Bourgogne, the ANR *COMOC*, the *FASTQUAST* ITN Program of the 7th FP, and the Swiss NSF (Contracts No. 200021-116198 and No. 200021-125315).

- 
- [1] A. Braun, G. Korn, X. Liu, D. Du, J. Squier, and G. Mourou, *Opt. Lett.* **20**, 73 (1995).
- [2] S. L. Chin, S. A. Hosseini, W. Liu, Q. Luo, F. Theberge, N. Aközbeke, A. Becker, V. P. Kandidov, O. G. Kosareva, and H. Schroeder, *Can. J. Phys.* **83**, 863 (2005).
- [3] L. Bergé, S. Skupin, R. Nuter, J. Kasparian, and J.-P. Wolf, *Rep. Prog. Phys.* **70**, 1633 (2007).
- [4] A. Couairon and A. Mysyrowicz, *Phys. Rep.* **441**, 47 (2007).
- [5] J. Kasparian and J.-P. Wolf, *Opt. Express* **16**, 466 (2008).
- [6] N. Aközbeke, M. Scalora, C. M. Bowden, and S. L. Chin, *Opt. Commun.* **191**, 353 (2001).
- [7] A. Vinçotte and L. Bergé, *Phys. Rev. A* **70**, 061802(R) (2004).
- [8] G. Fibich and B. Ilan, *Opt. Lett.* **29**, 887 (2004).
- [9] L. Bergé, S. Skupin, G. Méjean, J. Kasparian, J. Yu, S. Frey, E. Salmon, and J. P. Wolf, *Phys. Rev. E* **71**, 016602 (2005).
- [10] J.-F. Zhang, Q. Tian, Y.-Y. Wang, C.-Q. Dai, and L. Wu, *Phys. Rev. A* **81**, 023832 (2010).
- [11] V. Loriot, E. Hertz, O. Faucher, and B. Lavorel, *Opt. Express* **17**, 13429 (2009); **18**, 3011(E) (2010).
- [12] P. Béjot, J. Kasparian, S. Henin, V. Loriot, T. Vieillard, E. Hertz, O. Faucher, B. Lavorel, and J.-P. Wolf, *Phys. Rev. Lett.* **104**, 103903 (2010).
- [13] G. Méchain *et al.*, *Appl. Phys. B* **79**, 379 (2004).
- [14] A. Dubietis, E. Gaizauskas, G. Tamosauskas, and P. Di Trapani, *Phys. Rev. Lett.* **92**, 253903 (2004).
- [15] G. Stibenz, N. Zhavoronkov, and G. Steinmeyer, *Opt. Lett.* **31**, 274 (2006).
- [16] J. Kasparian, R. Sauerbrey, and S. L. Chin, *Appl. Phys. B: Lasers Opt.* **71**, 877 (2000).
- [17] F. Théberge, W. Liu, P. T. Simard, A. Becker, and S. L. Chin, *Phys. Rev. E* **74**, 036406 (2006).
- [18] B. E. Schmidt *et al.*, *Appl. Phys. Lett.* **96**, 121109 (2010).
- [19] P. Béjot, B. E. Schmidt, J. Kasparian, J.-P. Wolf, and F. Legaré, *Phys. Rev. A* **81**, 063828 (2010).
- [20] J. Schwarz, P. Rambo, and J.-C. Diels, *Opt. Commun.* **180**, 383 (2000).
- [21] W. Ettoumi, Y. Petit, J. Kasparian, and J.-P. Wolf, *Opt. Express* **18**, 6613 (2010).
- [22] I. V. Litvinyuk, K. F. Lee, P. W. Dooley, D. M. Rayner, D. M. Villeneuve, and P. B. Corkum, *Phys. Rev. Lett.* **90**, 233003 (2003).
- [23] Z. X. Zhao, X. M. Tong, and C. D. Lin, *Phys. Rev. A* **67**, 043404 (2003).
- [24] C. J. F. Böttcher, *Theory of Electric Polarisation* (Elsevier, Amsterdam, 1978).
- [25] J. Zhang, Z. H. Lu, and L. J. Wang, *Appl. Opt.* **47**, 3143 (2008).
- [26] R. Nuter and L. Bergé, *J. Opt. Soc. Am. B* **23**, 874 (2006).
- [27] A. Talebpour, J. Yang, and S. L. Chin, *Opt. Commun.* **163**, 29 (1999).
- [28] J. Schwarz, P. Rambo, J.-C. Diels, M. Kolesik, E. M. Wright, and J. V. Moloney, *Opt. Commun.* **180**, 383 (2000).
- [29] S. Tzortzakis, B. Lamouroux, A. Chiron, M. Franco, B. Prade, A. Mysyrowicz, and S. D. Moustazis, *Opt. Lett.* **25**, 1270 (2000).
- [30] C. P. Hauri *et al.*, *Opt. Lett.* **32**, 868 (2007).
- [31] S. Skupin and L. Bergé, *Opt. Commun.* **280**, 173 (2007).
- [32] V. Mizrahi and D. P. Shelton, *Phys. Rev. Lett.* **55**, 696 (1985).
- [33] D. Mondelain, Ph.D. thesis, Université Lyon I, 2001 (unpublished) [<http://tel.archives-ouvertes.fr/tel-00396346/fr/>].
- [34] E. L. Dawes and J. H. Marburger, *Phys. Rev.* **179**, 862 (1969).
- [35] P. Rohwetter *et al.*, *Nature Photon.* **4**, 451 (2010).
- [36] J. Kasparian *et al.*, *Opt. Express* **16**, 5757 (2008).

# Compression of 1.8 $\mu\text{m}$ laser pulses to sub two optical cycles with bulk material

Bruno E. Schmidt,<sup>1,2,a)</sup> Pierre Béjot,<sup>3</sup> Mathieu Giguère,<sup>1</sup> Andrew D. Shiner,<sup>2</sup> Carlos Trallero-Herrero,<sup>2</sup> Éric Bisson,<sup>1</sup> Jérôme Kasparian,<sup>4</sup> Jean-Pierre Wolf,<sup>4</sup> David M. Villeneuve,<sup>2</sup> Jean-Claude Kieffer,<sup>1</sup> Paul B. Corkum,<sup>2</sup> and François Légaré<sup>1,a)</sup>

<sup>1</sup>Centre Énergie Matériaux et Télécommunications, Institut National de la Recherche Scientifique, 1650 Boulevard Lionel-Boulet, Varennes, Quebec J3X1S2, Canada

<sup>2</sup>Joint Laboratory for Atto-Second Science, University of Ottawa/NRC, 100 Sussex Drive, Ottawa, Ontario K1A 0R6, Canada

<sup>3</sup>Laboratoire Interdisciplinaire CARNOT de Bourgogne, UMR 5209 CNRS, Université de Bourgogne, BP 47870, 21078 Dijon Cedex, France

<sup>4</sup>GAP-Biophotonics, Université de Genève, 20 rue de l'École de Médecine, 1211 Geneva 4, Switzerland

(Received 20 January 2010; accepted 17 February 2010; published online 25 March 2010)

We demonstrate a simple scheme to generate 0.4 mJ 11.5 fs laser pulses at 1.8  $\mu\text{m}$ . Optical parametrically amplified pulses are spectrally broadened by nonlinear propagation in an argon-filled hollow-core fiber and subsequently compressed to 1.9 optical cycles by linear propagation through bulk material in the anomalous dispersion regime. This pulse compression scheme is confirmed through numerical simulations. © 2010 American Institute of Physics. [doi:10.1063/1.3359458]

In the past decade, attosecond technology based on high harmonic generation has been developed permitting ultrafast measurements with  $\sim 100$  as temporal resolution.<sup>1-3</sup> Further reduction in the duration of isolated attosecond pulses and higher photon energies requires intense longer-wavelength carrier envelope phase (CEP) stable few-cycle pulses. Those requirements can be fulfilled using the Idler of a white light seeded optical parametric amplifier (OPA)<sup>4</sup> with an appropriate pulse compression scheme. In this letter, we demonstrate a robust approach for pulse compression at 1.8  $\mu\text{m}$  to below two optical cycle duration.

Different approaches to generate intense IR few-cycle laser pulses have been demonstrated as follows: (1) 0.74 mJ 15.6 fs at 2.1  $\mu\text{m}$  using an optical parametric chirped-pulse amplifier (OPCPA),<sup>5</sup> (2) pulse self-compression by filamentation; 0.27 mJ 17.9 fs at 2.1  $\mu\text{m}$ <sup>6</sup> and 1.5 mJ 19.8 fs at 1.5  $\mu\text{m}$ ,<sup>7</sup> (3) 1.2 mJ 17 fs at 1.5  $\mu\text{m}$  utilizing difference frequency generation of few-optical-cycle 800 nm laser pulses followed by type II parametric amplification,<sup>8</sup> and (4) 0.4 mJ 13.1 fs at 1.4  $\mu\text{m}$  using spectral broadening in a hollow-core fiber (HCF) and dispersion compensation with chirped mirrors.<sup>9</sup>

In this letter, we demonstrate the generation of 0.4 mJ 11.5 fs laser pulses at 1.8  $\mu\text{m}$ . Similar to our recent work using the OPA Signal wavelength,<sup>9</sup> we spectrally broaden the Idler via nonlinear propagation in a HCF. Instead of chirped mirrors or adaptive devices for dispersion compensation, we show that laser pulses can be efficiently compressed utilizing solely the properties of fused silica (FS) in the anomalous dispersion regime below the third order dispersion (TOD) limit of bulk material. Although compression with glass in the anomalous dispersion regime was applied to mid-IR wavelengths ( $\sim 6$   $\mu\text{m}$ ),<sup>10</sup> the authors discussed the limitation of bulk material compression to be applicable to multi-cycle pulses only.

The present approach distinguishes itself from previous setups in the reduced complexity, as shown in the sketch of the experimental layout in Fig. 1(a). The IR laser pulses are generated with a superfluorescence-seeded three stage OPA (HE-TOPAS, Light conversion) pumped by 7 mJ, 45 fs Ti:Sa pulses. A conversion efficiency of 35% (Signal+Idler) with 3% intensity fluctuation is typically achieved at the OPA output. At 1.83  $\mu\text{m}$ , the spectral full width at half maximum (FWHM) is 67 nm corresponding to a TL of 73 fs. This OPA spectrum, shown as shaded gray in Fig. 1(b), is measured with an Ocean Optics NIR 256 spectrometer corrected for spectral sensitivity. The IR laser beam is coupled into a 1 m long HCF (400  $\mu\text{m}$  in diameter, argon pressure of  $140 \pm 10$  kPa, 1 mm CaF<sub>2</sub> windows) using a  $f=1$  m plano-convex CaF<sub>2</sub> lens. At the output, the laser beam is collimated

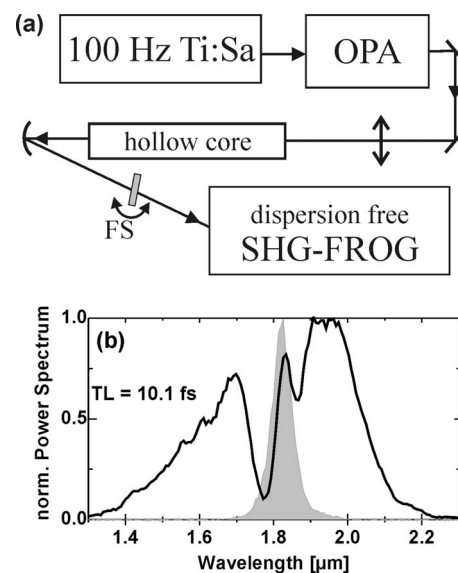


FIG. 1. (a) Experimental layout comprising a CPA pumped high energy OPA whose spectrum is broadened via propagation in a HCF. (b) Experimental spectra of the OPA Idler before (shaded gray) and after broadening (solid black). An asymmetric broadening towards the blue spectral side is visible.

<sup>a)</sup>Authors to whom correspondence should be addressed. Electronic addresses: schmidt@emt.inrs.ca and legare@emt.inrs.ca.

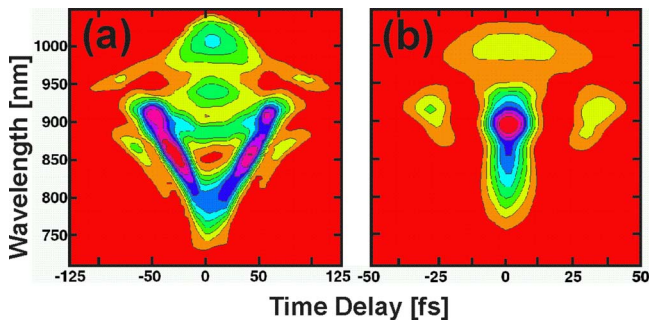


FIG. 2. (Color online) Experimental SHG-FROG traces for the uncompressed pulse after propagation in the HCF (a) corresponds to a pulse duration of 68 fs. Propagation through 3 mm of FS leads to a compressed 11.5 fs pulse depicted in (b) on a different time scale.

with an  $R=2$  m concave silver mirror. As shown by the solid line of Fig. 1(b), with 0.89 mJ at the input of the HCF, significant spectral broadening is observed corresponding to a TL of 10.1 fs. This spectrum clearly shows an asymmetry with wider extension towards shorter wavelengths.

Complete pulse characterization is carried out with a home built SHG-FROG (second harmonic generation frequency resolved optical grating).<sup>11</sup> Beam splitting is attained by geometrical beam separation to achieve ultrabroadband and dispersion free operation.<sup>12</sup> A high degree of phase matching and negligible geometrical temporal smear<sup>13</sup> is obtained by achromatically focusing both optical arms with a 500 mm focal length convex silver mirror into a Type I BBO crystal ( $\theta=21^\circ$ ) of 10  $\mu\text{m}$  thickness. The SHG-FROG spectrograms are measured with a USB2000 spectrometer from Ocean Optics and corrected for spectral sensitivity. In addition, spectral distortion of the ultrabroadband SHG is accounted for by applying a cubic correction function to the measured SHG-FROG spectrogram.<sup>13</sup>

After spectral broadening in the HCF, the pulse must be temporally compressed. At 800 nm, this is commonly carried out with chirped mirrors which are not available at 1.8  $\mu\text{m}$ . Fortunately, the unique characteristics of the 1.8  $\mu\text{m}$  source mean that the negative group delay dispersion (GDD) of FS is able to compensate for the spectral phase introduced by self-phase modulation (SPM) in argon. Because the zero dispersion of FS lies at  $\sim 1.3$   $\mu\text{m}$ , it exhibits negative GDD throughout the entire spectral range of interest. Once the appropriate FS thickness is found, a small angular tilt of the glass is sufficient to obtain the shortest pulse duration. In this manner a compression factor of 6.5 is achieved compared to the OPA output pulses.

The pulse duration immediately after the evacuated fiber was measured to be 75 fs [Fig. 3(c), gray line] in agreement with the TL (73 fs) of the OPA spectra presented in Fig. 1(b) as shaded gray. Inserting argon leads to significant broadening and the corresponding SHG-FROG traces of the uncompressed and fully compressed pulses are shown in Fig. 2. Surprisingly, linear propagation through a simple piece of FS is sufficient to achieve excellent compression. Figure 3 presents the reconstructed electric field in the spectral (a, b) and the temporal domains (c). The direction of the time axis was determined by comparing the spectral phase with and without the 3 mm FS. The asymmetric shape of the reconstructed power spectrum [solid black line in Fig. 3(a)] is in reasonable agreement with the measured one given by the black squares. The spectral phase for the compressed pulse [black

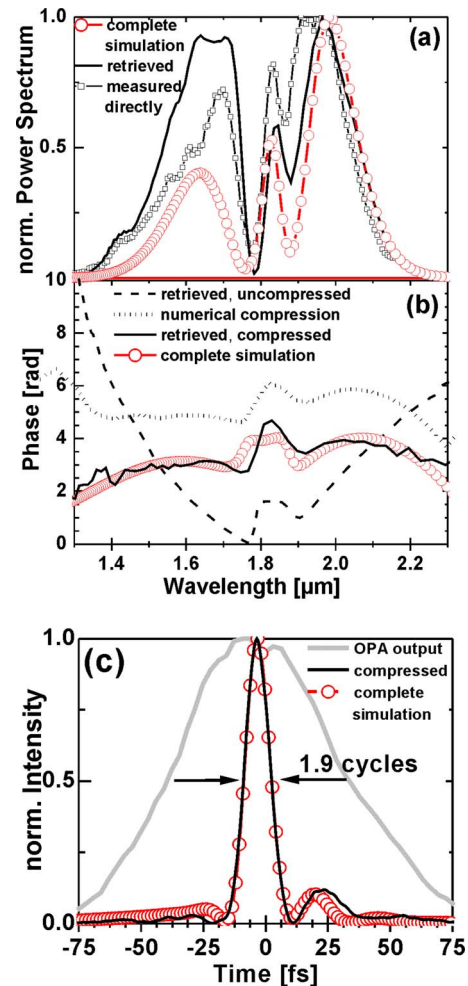


FIG. 3. (Color online) (a) Power spectral densities after nonlinear propagation in the HCF. (b) SHG-FROG retrieved spectral phases for uncompressed (black dashed line) and compressed pulses (black solid line) are compared with full numerical simulations (circles). The spectral phase named numerical compression (black dotted line) has been obtained by numerically propagating the retrieval of the uncompressed pulse (dashed line) through 3 mm of FS. (c) Temporal intensities corresponding to the spectra given above whereby compression down to 11.5 fs is achieved with 3 mm FS after the HCF.

solid line in Fig. 3(b)] is significantly flattened with respect to the uncompressed phase (black dashed line). In the case of pure SPM, one would expect symmetric broadening of the power spectrum around the fundamental accompanied by a symmetric phase function. However, the uncompensated phase [black dashed line] is slightly steeper on the red side compared with the blue side. This spectral asymmetry of the uncompensated pulse corresponds to a temporal asymmetry whereby the pulse exhibits a much steeper trailing edge than the leading one. Linear propagating this pulse through 3 mm of FS generates a very short 11.5 fs pulse [solid black line in Fig. 3(c)]. The fairly clean compressed pulse contains 78% of total energy in the main part and the FWHM duration is only 1.14 times the TL duration of 10.1 fs. Residual higher order phases which are not compensated by the bulk compressor are likely to cause the small pedestals on both sides of the main pulse. We mention that in addition to the rather clean temporal shape on the femtosecond time scale, the present approach is free of superfluorescence background as was reported in case of OPCPA.<sup>5</sup> When the seed is blocked in the OPA, no light is observed at the output of the fiber.

It is pointed out that this almost TL and relatively clean temporal shape is remarkable because it denotes dispersion compensation not only of the GDD but also of the TOD to a large extent. Most of the commonly used glasses, like FS, exhibit normal dispersion ( $GDD > 0$ ) below  $1 \mu\text{m}$  and anomalous dispersion ( $GDD < 0$ ) beyond the zero dispersion wavelength centered between  $1.2\text{--}2 \mu\text{m}$ . Thus bulk material is potentially suitable for pulse compression of IR laser pulses. However, all glasses exhibit positive TOD throughout their entire transmission range. Uncompensated TOD causes any femtosecond pulse to deviate from the TL pulse shape even if the GDD is zero. For instance, assuming a Gaussian shape at center wavelength of  $1.83 \mu\text{m}$ , a TOD of only  $1000 \text{ fs}^3$  ( $3 \text{ mm FS}$  plus  $1 \text{ mm CaF}_2$ ) causes a TL pulse to broaden from  $10.1$  to  $14.7 \text{ fs}$ . To confirm that linear propagation through bulk material (intensity  $\approx 5 \times 10^9 \text{ W/cm}^2$ ) compresses the pulse after the HCF, we calculated the spectral phase introduced by  $3 \text{ mm}$  of FS according to the Sellmeier equation. This phase was then added to the retrieved phase of the uncompressed pulse [black dashed curve in Fig. 3(b)]. The result [black dotted line in Fig. 3(b)] matches the retrieved phase of the compressed pulse. On the one hand, this numerical cross check proves the compression mechanism due to linear propagation in FS. On the other hand, it also demonstrates the reliability of the SHG-FROG retrieval though the retrieved power spectrum shows a lower peak on the blue side when compared to the directly measured spectrum. However, by comparing the retrieved spectral phase of compressed and uncompressed pulse we obtain the exact refractive index of FS in the range from  $1.4$  to  $2.2 \mu\text{m}$ . Now the question about the origin of the negative TOD component arises. To address this question, two possible explanations are discussed.

On the one hand, our experimental results might be viewed in the context of pulse self-compression. This explanation can be ruled out since we have to add  $3 \text{ mm}$  of FS subsequent to the HCF setup to obtain the shortest pulse. At  $1.8 \mu\text{m}$ , FS provides significant negative GDD ( $-68 \text{ fs}^2/\text{mm}$ ). Furthermore, in contrast to experimentally observed self-compression,<sup>6,7,14,15</sup> the laser power of  $10 \text{ GW}$  in our experiment is roughly two times below the estimated critical power for self-focusing.

On the other hand, the pronounced spectral asymmetry suggests that self-steepening<sup>15–17</sup> of the pulse takes place in addition to SPM. This temporal reshaping of the trailing edge then leads to an asymmetric spectral phase opposed to the positive TOD of bulk material. To prove this qualitative explanation, we performed numerical simulations. The nonlinear Schrödinger equation<sup>18</sup> was solved in one dimension where the action of self-steepening could be turned on and off numerically. Numerical results based on exact experimental conditions like input pulse duration, pulse energy, and pressure are given by the circles in Fig. 3 and a detailed description is in preparation for a longer article.<sup>19</sup> Briefly, if self-steepening is neglected, it was not possible to simulate an asymmetric power spectrum as shown in Fig. 3(a). Contrary, the symmetry of the spectrum is broken because of self-steepening which is known to promote the higher frequency region of the spectrum.<sup>15</sup> It furthermore enables calculating an asymmetric phase like the dashed curve of Fig. 3(b). Its linear propagation through  $3 \text{ mm}$  of FS leads to the plot shown by the circles in Fig. 3(b) which is in excellent

agreement with the experimentally retrieved phase [solid black line]. The corresponding temporal intensity [circles in Fig. 3(c)] closely resembles the experimentally retrieved pulse. Neglecting self-steepening leads to a pulse duration of  $14.4 \text{ fs}$  with an increased pedestal.

In conclusion, we have demonstrated a very simple and robust approach for the generation of submillijoule two-cycle  $1.8 \mu\text{m}$  laser pulses via nonlinear propagation in a HCF followed by dispersion compensation utilizing the anomalous dispersion of bulk material. This straight forward approach was confirmed by numerical simulations that demonstrate the action of self-steepening is to generate a spectral phase opposite to that of FS. At the moment, our sub two-cycle laser pulses are not CEP stabilized, but this is feasible using the Idler of a white light seeded OPA.<sup>4</sup>

We are very grateful for the help and the time spent on the laser system by François Poitras and Antoine Laramée. The authors acknowledge the support of the Canada Foundation for Innovation, the Canadian Institute for Photonic Innovations, the Natural Sciences and Engineering Research Council of Canada, and the Fonds Québécois de la Recherche sur la Nature et les Technologies.

<sup>1</sup>M. Hentschel, R. Kienberger, Ch. Spielmann, G. A. Reider, N. Milosevic, T. Brabec, P. B. Corkum, U. Heinzmann, M. Drescher, and F. Krausz, *Nature (London)* **414**, 509 (2001).

<sup>2</sup>G. Sansone, E. Benedetti, F. Calegari, C. Vozzi, L. Avaldi, R. Flammini, L. Poletto, P. Villoresi, C. Altucci, R. Vellota, S. Stagira, S. De Silvestri, and M. Nisoli, *Science* **314**, 443 (2006).

<sup>3</sup>E. Goulielmakis, M. Schultze, M. Hofstetter, V. S. Yakovlev, J. Gagnon, M. Uiberacker, A. L. Aquila, E. M. Gullikson, D. T. Attwood, R. Kienberger, F. Krausz, and U. Kleineberg, *Science* **320**, 1614 (2008).

<sup>4</sup>A. Baltuška, T. Fuji, and T. Kobayashi, *Phys. Rev. Lett.* **88**, 133901 (2002).

<sup>5</sup>X. Gu, G. Marcus, Y. Deng, T. Metzger, C. Teisset, N. Ishii, T. Fuji, A. Baltuška, R. Butkus, V. Pervak, H. Ishizuki, T. Taira, T. Kobayashi, R. Kienberger, and F. Krausz, *Opt. Express* **17**, 62 (2009).

<sup>6</sup>C. P. Hauri, R. B. Lopez-Martens, C. I. Blaga, K. D. Schultz, J. Cryan, R. Chirla, P. Colosimo, G. Doumy, A. M. March, C. Roedig, E. Sistrunk, J. Tate, J. Wheeler, L. F. Di Mauro, and E. P. Power, *Opt. Lett.* **32**, 868 (2007).

<sup>7</sup>O. D. Mücke, S. Ališauskas, A. J. Verhoef, A. Pugžlys, A. Baltuška, V. Smilgevičius, J. Pocius, L. Giniūnas, R. Danielius, and N. Forget, *Opt. Lett.* **34**, 2498 (2009).

<sup>8</sup>C. Vozzi, F. Calegari, E. Benedetti, S. Gasilov, G. Sansone, G. Cerullo, M. Nisoli, S. De Silvestri, and S. Stagira, *Opt. Lett.* **32**, 2957 (2007).

<sup>9</sup>M. Giguère, B. E. Schmidt, A. D. Shiner, M.-A. Houle, H.-C. Bandulet, G. Tempea, D. M. Villeneuve, J.-C. Kieffer, and F. Légaré, *Opt. Lett.* **34**, 1894 (2009).

<sup>10</sup>N. Demirdöven, M. Khalil, O. Golonzka, and A. Tokmakoff, *Opt. Lett.* **27**, 433 (2002).

<sup>11</sup>R. Trebino, K. W. DeLong, D. N. Fittinghoff, J. N. Sweetser, M. A. Krum-bügel, B. A. Richman, and D. J. Kane, *Rev. Sci. Instrum.* **68**, 3277 (1997).

<sup>12</sup>I. Z. Kozma, P. Baum, U. Schmidhammer, S. Lochbrunner, and E. Riedle, *Rev. Sci. Instrum.* **75**, 2323 (2004).

<sup>13</sup>A. Baltuška, M. S. Pshenichnikov, and D. A. Wiersma, *Opt. Lett.* **23**, 1474 (1998).

<sup>14</sup>N. L. Wagner, E. A. Gibson, T. Popmintchev, I. P. Christov, M. M. Murnane, and H. C. Kapteyn, *Phys. Rev. Lett.* **93**, 173902 (2004).

<sup>15</sup>G. Yang and Y. R. Shen, *Opt. Lett.* **9**, 510 (1984); G. Stibenz, N. Zhavoronkov, and G. Steinmeyer, *Opt. Lett.* **31**, 274 (2006).

<sup>16</sup>N. Aközbe, M. Scalora, C. M. Bowden, and S. L. Chin, *Opt. Commun.* **191**, 353 (2001).

<sup>17</sup>A. L. Gaeta, *Phys. Rev. Lett.* **84**, 3582 (2000).

<sup>18</sup>G. P. Agrawal, *Nonlinear Fiber Optics*, 3rd ed. (Academic, San Diego (2001)).

<sup>19</sup>P. Béjot, B. E. Schmidt, J. Kasparian, J.-P. Wolf, P. B. Corkum, and F. Légaré, "IR pulse compression with bulk material: Experiments versus simulations," (unpublished).

# From higher-order Kerr nonlinearities to quantitative modeling of third and fifth harmonic generation in argon

P. Béjot,<sup>1</sup> E. Hertz,<sup>1</sup> B. Lavorel,<sup>1</sup> J. Kasparian,<sup>2</sup> J.-P. Wolf,<sup>2</sup> and O. Faucher<sup>1,\*</sup>

<sup>1</sup>Laboratoire Interdisciplinaire CARNOT de Bourgogne (ICB), UMR 5209 CNRS-Université de Bourgogne BP 47870, 21078 Dijon Cedex, France

<sup>2</sup>Université de Genève, GAP-Biophotonics, 20 rue de l'École de Médecine, 1211 Geneva 4, Switzerland

\*Corresponding author: Olivier.Faucher@u-bourgogne.fr

Received December 9, 2010; revised January 21, 2011; accepted January 23, 2011;  
posted February 9, 2011 (Doc. ID 139397); published March 8, 2011

The recent measurement of negative higher-order Kerr effect (HOKE) terms in gases has given rise to a controversial debate, fed by its impact on short laser pulse propagation. By comparing the experimentally measured yield of the third and fifth harmonics, with both an analytical and a full comprehensive numerical propagation model, we confirm the absolute and relative values of the reported HOKE indices. © 2011 Optical Society of America

OCIS codes: 320.2250, 190.2620, 320.7110.

In a recent experiment, we have shown that the electronic optical Kerr effect in Ar, N<sub>2</sub>, O<sub>2</sub>, and air exhibits a highly nonlinear behavior versus the applied intensity [1,2], resulting in a saturation of the nonlinear refractive index observed at moderate intensity, followed by a sign inversion at higher laser intensity. This observation has a substantial impact on the propagation of ultrashort and ultraintense laser pulses, especially in the context of laser filamentation [3–6], where the higher-order Kerr effect (HOKE), rather than the defocusing contribution of the free electrons, can play a key role in the self-guiding process [7], especially at long wavelengths [8] and for short pulses [9]. However, this issue is still controversial [10–12]. Therefore, an independent confirmation of our measurement of the HOKE is still needed. Recently, Kolesik *et al.* [10] have proposed such a test, based on the comparison of the yields of the third harmonic (TH) and the fifth harmonic (FH) radiations generated by the nonlinear frequency upconversion of a short and intense laser pulse in air. Based on numerical simulations, they suggested that, considering the HOKE indices, “the relative strength of the FH to the TH should reach values of the order of 10<sup>-1</sup>” while, if omitting them, “this ratio should be about 4–5 orders smaller” [10].

So far, no measurement of the yield of the FH versus the TH have been achieved in air. However, Kosma *et al.* [13] measured the yields of TH and FH produced by a short and intense laser pulse in argon. The present Letter aims at confronting the results of this experiment with predictions based on the HOKE in argon [1,2].

In the first part, we confirm the ratio of the recently measured nonlinear indices [1,2] based on the analytical description of the harmonic generation. In the second part, a comprehensive model, including linear and nonlinear propagation effects such as dispersion, self-phase modulation, ionization, and Kerr effect, is presented.

For a focused laser beam propagating linearly, the harmonic power of the  $q$ th harmonic in the perturbative regime is given by

$$P_q = A_q N^2 |J_q(b\Delta k)|^2, \quad (1)$$

where  $N$  is the atomic density of the medium and

$$A_q = \frac{q\omega_1^2}{4n_q^\ell (n_1^\ell)^q (\epsilon_0\pi)^{q-1} c^q w_0^{2q-2}} (\chi^{(q)})^2 P_1^q, \quad (2)$$

with  $P_1$ ,  $\omega_1$ , and  $w_0$  the power, the angular frequency, and the beam waist of the incident beam, respectively [14,15].  $\chi^{(q)}$  is the  $q$ th-order microscopic nonlinear susceptibility ( $q = 3, 5$ ) given in SI units,  $n_j^\ell$  are the linear refractive indices at the fundamental ( $j = 1$ ) and harmonic frequencies ( $j = 3, 5$ ),  $\epsilon_0$  is the permittivity of the vacuum, and  $c$  is the speed of light.  $J_q$  is a dimensionless function that accounts for the phase matching

$$J_q = \int_{-2f/b}^{2(L-f)/b} d\xi \frac{\exp(-ib\Delta k\xi/2)}{(1+i\xi)^{q-1}}, \quad (3)$$

with  $\Delta k = k_q - qk_1 = \frac{2\pi q}{\lambda_1} (n_q^\ell - n_1^\ell)$  the phase mismatch (with  $n_q^\ell - n_1^\ell$  proportional to the pressure) and  $k_j$  ( $j = 1, q$ ) the wave vectors,  $b$  the confocal parameter,  $L$  the length of the static cell, and  $f$  the position of the focus with respect to the entrance of the static cell [16]. According to Eqs. (1) and (2), the ratio of the FH to the TH power is

$$\frac{P_5}{P_3} \approx \frac{5}{3\epsilon_0^2\pi^2 c^2 w_0^4} \left(\frac{\chi^{(5)}}{\chi^{(3)}}\right)^2 \left(\frac{N_5|J_5|}{N_3|J_3|}\right)^2 P_1^2, \quad (4)$$

where  $n_j^\ell$  have been approximated to unity in Eq. (2).  $N_3$  and  $N_5$  refer to the different atomic densities at the pressures maximizing the harmonic conversion for the third and fifth orders, respectively. This equation provides a direct relationship between the power ratio of the harmonics and the ratio of the corresponding nonlinear susceptibilities. The latter are related to the nonlinear refractive indices through the relation [8]

$$n_{2j} = \frac{(2j+1)!}{2^{j+1}j!(j+1)!} \frac{1}{((n_1^\ell)^2 \epsilon_0 c)^j} \chi_{\text{Kerr}}^{(2j+1)}, \quad (5)$$

so that

$$\frac{P_5}{P_3} \approx \frac{3}{5\pi^2 w_0^4} \left(\frac{n_4}{n_2}\right)^2 \left(\frac{N_5 |J_5|}{N_3 |J_3|}\right)^2 P_1^2. \quad (6)$$

In the experiment by Kosma *et al.*,  $b = 7.8$  cm,  $w_0 = 100$   $\mu$ m,  $L = 1.8$  cm,  $f = L/2$ , and the wavelength  $\lambda_1 = 810$  nm [13]. The fundamental power, calculated from the input energy  $E_1 = 710$   $\mu$ J and the pulse duration  $\tau_1 = 12$  fs, is  $P_1 = 59$  GW. They observed that the pressure maximizing the TH power ranged between 160 [13] and 250 mbar [17] for similar experimental conditions. One single maximum, around 50 mbar, is observed for the FH. The maximum energies of the TH and FH measured at the respective optimal pressures reported in [13] are 140 and 4 nJ, respectively, while the pulse duration was estimated to be 11 fs for both harmonics [13,17]. This leads to the power ratio  $P_5/P_3 = 0.028$ . According to Eq. (6), where  $J_q$  of Eq. (3) has been calculated using  $n_1^l = 1.00028$ ,  $n_3^l = 1.00030$ , and  $n_5^l = 1.00035$  for the values of the refractive index of argon at 1 bar at 810, 270, and 162 nm, respectively [18], the corresponding ratio of the HOKE indices is  $|n_4/n_2| = 6.8 \times 10^{-19}$  m<sup>2</sup>/W. This value confirms, within a factor of 2 compatible with the experimental error, the ratio of the experimental HOKE indices  $n_2 = 10^{-23}$  m<sup>2</sup>/W<sup>1</sup> and  $n_4 = -3.6 \times 10^{-42}$  m<sup>4</sup>/W<sup>2</sup> [1,2], resulting in  $|n_4/n_2| = 3.6 \times 10^{-19}$  m<sup>2</sup>/W. The agreement is remarkable, especially considering the simplicity of the analytical model used.

Further comparison with the experiment was performed by computing the value of  $N^2 |J_q|^2$  as a function of the argon pressure relying on Eq. (3) (Fig. 1). This function should reflect the pressure dependence of the harmonic powers. The analytical model predicts a maximum at about 300 mbar for the TH, in line with the experimental results. It yields three maxima between 0 and 400 mbar for the FH, the first of them close to the observed optimum pressure for the FH. This oscillatory structure, which is due to the periodic phase matching, was not observed in the experiments [19] probably due to nonlinear propagation effects, which are not considered in the analytical model.

To overcome these limitations and take into account the perturbations of the fundamental pulse during its propagation through the gas sample, as well as the effect of the HOKE indices on the phase matching, we have solved

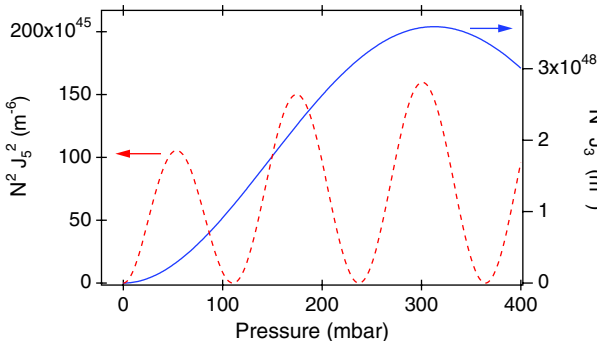


Fig. 1. (Color online) Analytical calculation of the pressure dependence of the third (solid blue line) and fifth (dashed red line) harmonics in argon.

the unidirectional pulse propagation equation for the experimental conditions of Kosma *et al.* More precisely, assuming a cylindrical symmetry around the propagation axis  $z$ , the angularly resolved spectrum  $\tilde{E}(k_\perp, \omega)$  of the real electric field  $E(r, t)$  follows the equation [20]

$$\partial_z \tilde{E} = ik_z \tilde{E} + \frac{1}{2k_z} \left( \frac{i\omega^2}{c^2} \tilde{P}_{\text{NL}} - \frac{\omega}{\epsilon_0 c^2} \tilde{J} \right), \quad (7)$$

where  $k_z = \sqrt{k^2(\omega) - k_\perp^2}$ ,  $\tilde{P}_{\text{NL}}$  and  $\tilde{J}$  are the angularly resolved nonlinear polarization and the free charge induced current spectrum, respectively, and  $k(\omega) = \frac{n(\omega)\omega}{c}$ .

The nonlinear polarization  $P_{\text{NL}}$  is evaluated in the time domain as  $P_{\text{NL}} = \chi^{(3)} E^3 + \chi^{(5)} E^5 + \chi^{(7)} E^7 + \chi^{(9)} E^9 + \chi^{(11)} E^{11}$ . Because the nonlinear polarization is defined from the real electric field, Eq. (7) captures without any modifications all frequency-mixing processes induced by the total field. For numerical stability concerns, we considered only the part responsible for the refractive index change around  $\omega_0$ , neglecting harmonics generation induced by the terms proportional to  $E^7$ ,  $E^9$ , and  $E^{11}$ . The current induced by the free charges is calculated in the frequency domain as  $\tilde{J} = \frac{e^2 \nu_e + i\omega}{m_e \nu_e^2 + \omega^2} \tilde{\rho} e$ , where  $e$  and  $m_e$  are the electron charge and the mass, respectively,  $\nu_e$  is the effective collisional frequency, and  $\rho$  is the electron density, which is evaluated as

$$\partial_t \rho = W(I)(\rho_{\text{at}} - \rho) + \frac{\sigma}{U_i} I - \beta \rho^2, \quad (8)$$

where  $W(I)$  is the ionization probability evaluated with the Keldysh–PPT (Perelomov, Popov, Terent’ev) model [4],  $\rho_{\text{at}}$  is the atomic number density,  $\sigma$  is the inverse Bremsstrahlung cross section,  $\beta$  is the recombination constant (negligible on the time scale investigated in the present work), and  $I$  is proportional to the time-averaged  $\langle E^2 \rangle$ .

Figure 2 displays the harmonics intensity as a function of argon pressure for an input pulse and a detection geometry matching the experimental parameters: 12 fs pulse duration (FWHM), 700  $\mu$ J input energy, and a beam radius of 4 mm before focusing. In order to mimic the experiment, the pulse first propagates in a vacuum up to the position of the cell (99.1 cm after the  $f = 1$  m lens). After

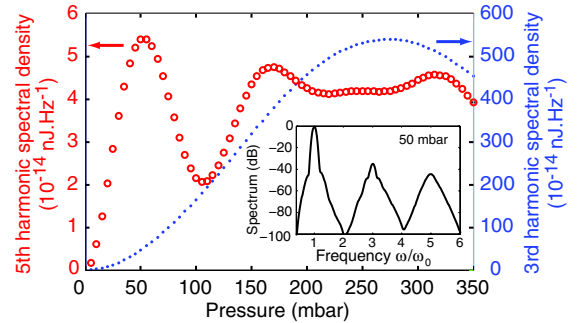


Fig. 2. (Color online) Numerical calculation of the pressure dependence of the third (dotted blue line) and fifth (open circles) harmonics in argon integrated over the full radial distribution. To be compared with Fig. 3 of [13]. The spectrum calculated at 50 mbar is shown in the inset.

this focusing step, the pulse propagates over 1.8 cm in the argon cell. The optimal pressure for the FH is 50 mbar, in full agreement with the experiment [13]. The reduction of the second and third maxima of the FH, as compared to Fig. 1, results from the phase mismatch introduced by the HOKE at high pressure. The TH yield is maximal at 260 mbar, similar to the value reported in [17]. In full agreement with the experiment by Kosma *et al.* [13], the ratio at 50 mbar is about 0.1 and becomes even larger at reduced pressures. Furthermore, the total FH and TH energies at their respective optimum pressures are 6 and 218 nJ, in good agreement with the experimental values of 4 and 140 nJ, where losses due to the setup lead to a slight underestimation of the output energies [13].

If the HOKE is not considered in the model, the ratio of the FH to the TH at a pressure of 50 mbar drops to 0.017, and the FH and TH energies are respectively 1.7 and 584 nJ: These values are inconsistent with the experimental results of Kosma *et al.* Furthermore, contrary to the experimental observations [19], the FH would exhibit strong maxima at 160 and 250 mbar. These discrepancies show that the HOKE is necessary to reproduce the experimental results [13,17], further validating their measured values [1,2]. Note that the ratio of 0.017 strongly depends on the propagation distance, so that it cannot be directly compared to that of 10,000 predicted by Kolesik *et al.* for the “classical” model over an unspecified propagation distance. For a propagation length of 220  $\mu\text{m}$ , 80 times shorter than in our work but consistent with neglecting the phase matching, our calculation indeed predicts a ratio of 10,000.

In conclusion, as recently suggested in [10], we have compared the recent experimental measurements of the TH and FH yields in argon [13] with both analytical and numerical simulations. These results agree quantitatively with the measured high-order Kerr indices [1,2]. This conclusion is supported by the following findings. First, the harmonic yield reported in argon by Kosma *et al.* at the pressure that optimized the fifth harmonic leads to a ratio of about 0.1 between the fifth and the third harmonics. This ratio implies a ratio of the Kerr indices consistent with our measurement of the HOKE indices within their uncertainty range [1,2]. Second, the analytical model based on our HOKE indices reproduces the pressure maximizing the TH, as well as the first pressure maximum of the fifth harmonic yield. Third, a full numerical propagation model accounting for the dispersion and nonlinear effects such as ionization and higher-order Kerr effects quantitatively reproduces the ratio of the harmonic yields observed in the experiment, as well as the pressure dependence of both the third and fifth

harmonics. It even reproduces the absolute harmonics intensity within a fairly good accuracy.

The authors are grateful to Werner Fuss and Kyriaki Kosma for fruitful discussions and critical reading of the manuscript. This work was supported by the Conseil Régional de Bourgogne, the Agence Nationale pour la Recherche (ANR) *COMOC*, the *FASTQUAST* Marie Curie Initial Training Networks (ITN) Program of the Seventh Framework Program and the Swiss National Science Foundation (SNSF), contract 200021-125315.

## References

1. V. Loriot, E. Hertz, O. Faucher, and B. Lavorel, *Opt. Express* **17**, 13429 (2009).
2. V. Loriot, E. Hertz, O. Faucher, and B. Lavorel, *Opt. Express* **18**, 3011 (2010).
3. S. L. Chin, S. A. Hosseini, W. Liu, Q. Luo, F. Théberge, N. Aközbe, A. Becker, V. P. Kandidov, O. G. Kosareva, and H. Schröder, *Can. J. Phys.* **83**, 863 (2005).
4. L. Bergé, S. Skupin, R. Nuter, J. Kasparian, and J.-P. Wolf, *Rep. Prog. Phys.* **70**, 1633 (2007).
5. A. Couairon and A. Mysyrowicz, *Phys. Rep.* **441**, 47 (2007).
6. J. Kasparian and J.-P. Wolf, *Opt. Express* **16**, 466 (2008).
7. P. Béjot, J. Kasparian, S. Henin, V. Loriot, T. Vieillard, E. Hertz, O. Faucher, B. Lavorel, and J.-P. Wolf, *Phys. Rev. Lett.* **104**, 103903 (2010).
8. W. Ettoumi, P. Béjot, Y. Petit, V. Loriot, E. Hertz, O. Faucher, B. Lavorel, J. Kasparian, and J.-P. Wolf, *Phys. Rev. A* **82**, 033826 (2010).
9. V. Loriot, P. Béjot, W. Ettoumi, Y. Petit, J. Kasparian, S. Henin, E. Hertz, B. Lavorel, O. Faucher, and J.-P. Wolf, “On negative higher-order Kerr effect and filamentation,” *Laser Phys.* (to be published).
10. M. Kolesik, E. M. Wright, and J. V. Moloney, *Opt. Lett.* **35**, 2550 (2010).
11. P. Polynkin, M. Kolesik, E. M. Wright, and J. V. Moloney, “Global fits of the minimal universal extra dimensions scenario,” arxiv.org, <http://arxiv.org/abs/1010.2023v2>.
12. M. Kolesik, D. Mirell, J.-C. Diels, and J. V. Moloney, *Opt. Lett.* **35**, 3685 (2010).
13. K. Kosma, S. A. Trushin, W. E. Schmid, and W. Fuss, *Opt. Lett.* **33**, 723 (2008).
14. R. W. Boyd, *Nonlinear Optics*, 3rd ed. (Academic, 2008).
15. J. Reintjes and C. Y. She, *Opt. Commun.* **27**, 469 (1978).
16. G. C. Bjorklund, *IEEE J. Quantum Electron.* **11**, 287 (1975).
17. K. Kosma, S. A. Trushin, W. Fuss, and W. E. Schmid, *Phys. Chem. Chem. Phys.* **11**, 172 (2009).
18. A. Bideau, Y. Guern, R. Abjean, and A. Johannin-Gilles, *J. Quant. Spectrosc. Radiat. Transfer* **25**, 395 (1981).
19. W. Fuss, Max-Planck-Institut für Quantenoptik, D-85741 Garching, Germany (personal communication, 2010).
20. M. Kolesik and J. V. Moloney, *Phys. Rev. E* **70**, 036604 (2004).

## Transition from Plasma-Driven to Kerr-Driven Laser Filamentation

P. Béjot,<sup>1,2,\*</sup> E. Hertz,<sup>1</sup> J. Kasparian,<sup>2,†</sup> B. Lavorel,<sup>1</sup> J.-P. Wolf,<sup>2</sup> and O. Faucher<sup>1</sup>

<sup>1</sup>Laboratoire Interdisciplinaire Carnot de Bourgogne (ICB), UMR 5209 CNRS-Université de Bourgogne, BP 47870, F-21078 Dijon Cedex, France

<sup>2</sup>GAP-Biophotonics, Université de Genève, 20 rue de l'École de Médecine, 1211 Geneva 4, Switzerland  
(Received 7 March 2011; revised manuscript received 15 April 2011; published 14 June 2011)

While filaments are generally interpreted as a dynamic balance between Kerr focusing and plasma defocusing, the role of the higher-order Kerr effect (HOKE) is actively debated as a potentially dominant defocusing contribution to filament stabilization. In a pump-probe experiment supported by numerical simulations, we demonstrate the transition between two distinct filamentation regimes at 800 nm. For long pulses (1.2 ps), the plasma substantially contributes to filamentation, while this contribution vanishes for short pulses (70 fs). These results confirm the occurrence, in adequate conditions, of filamentation driven by the HOKE rather than by plasma.

DOI: 10.1103/PhysRevLett.106.243902

PACS numbers: 42.65.Jx, 37.10.Vz, 42.65.Tg, 78.20.Ci

Filamentation [1–4] is a self-guided propagation regime typical of high-power lasers, offering spectacular potential applications [5] like rainmaking [6] and lightning control [7]. We recently challenged its long-established mechanism by measuring the higher-order Kerr effect (HOKE) in gases, implying that the nonlinear refractive index must be written as  $\Delta n_{\text{Kerr}} = \sum n_{2j} I^j$ , where the nonlinear indices  $n_{2j}$  are related to the  $(2j + 1)$ th electric susceptibility  $\chi^{(2j+1)}$ . The inversion of  $\Delta n_{\text{Kerr}}$ , due to negative  $n_4$  and  $n_8$  terms in air and argon, leads to a defocusing Kerr effect at an intensity close to that present within filaments [8,9]. As a consequence, the HOKE can ensure self-defocusing in filaments and balance Kerr self-focusing [10], in place of the plasma, especially for short pulses [9]. This result raised an active controversy [11–16] in the lack of direct experimental confirmation.

Quantitative differences between the predictions of filamentation models including or disregarding the HOKE are not sufficient to distinguish between them. The intensity within filaments ( $\sim 50 \text{ TW/cm}^2$  [17]) is compatible with regularization by either the plasma [18] or the HOKE [10], which balance the Kerr self-focusing in the same intensity range. Furthermore the electron density is difficult to measure and highly dependent on initial conditions, resulting in a wide spread of the reported values from  $10^{12}$  to  $10^{17} \text{ cm}^{-3}$  [18], although the latest measurements range from  $\sim 10^{15} \text{ cm}^{-3}$  [19] to a few  $10^{16} \text{ cm}^{-3}$  [13].

In the present Letter, we therefore focus on experimental conditions where *qualitatively different behaviors* of plasma- and HOKE-driven filamentation allows us to unambiguously distinguish between them. This discrimination proceeds from the intrinsically different temporal dynamics of these nonlinear defocusing contributions. While the Kerr effect is instantaneous at the time scale of the pulse envelope, the free electrons accumulated throughout the pulse duration survive for tens of picoseconds after the laser pulse has passed [20,21]. In an

atomic gas like argon, where no spatiotemporal modification of the refractive index due to molecular alignment occurs, two pulses separated by a few picoseconds can therefore only be coupled if the free electron density left by the first one is sufficient to affect the second one. This allows us to distinguish between two scenarios. If the plasma is the dominant mechanism for the self-guiding of the pump pulse, then the electron density produced in its wake necessarily affects the probe filament. On the contrary, if the HOKE terms are predominant, then the probe filament is insensitive to the presence of the pump.

Based on these different temporal dynamics, we unambiguously observe experimentally the all-Kerr-driven filamentation of ultrashort laser pulses, as well as the transition to a plasma-driven filamentation regime in the case of long pulses. This new perspective on the filamentation physics critically revises the discussion of the optimal laser parameters for applications ranging from laser-controlled atmospheric experiments to harmonics generation [22,23].

In our experimental setup (Fig. 1), two orthogonally polarized copropagating laser pulses centered at 800 nm

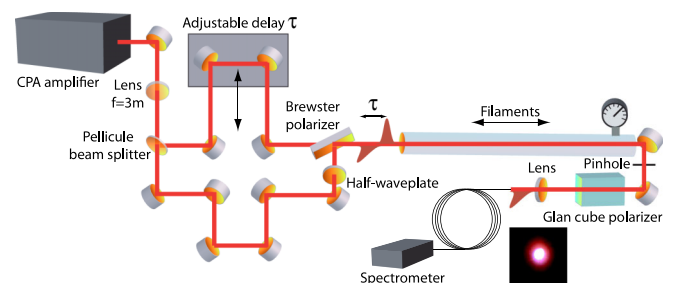


FIG. 1 (color online). Experimental setup. Two orthogonally polarized identical pulses with an adjustable delay are focused in an argon-filled cell. At the output of the cell, the probe spectrum is selected by a Glan cube polarizer and analyzed with a spectrometer.

are loosely focused by a  $f = 3$  m lens in a 2 m-long gas cell filled with argon. We investigate both short pulses (70 fs, 600  $\mu$ J, 3 bar) and long pulses (1.2 ps, 6 mJ, 5 bar), keeping the peak power of each pulse equal to 2.5 critical powers. At this power level, each pulse produces a single filament when propagating alone. The probe pulse is temporally delayed with regard to the pump by  $\tau$  ( $\tau = 1$  ps for short pulses and  $\tau = 2$  ps for long pulses).

The influence of the plasma left by the pump on the probe filament is characterized by observing changes in its spectrum. The filament output spectrum is selected in the far-field ( $z \sim 2$  m) by a pinhole excluding the conical emission and most of the photon bath, and analyzed with a spectrometer (Ocean Optics HR4000, providing 0.5 nm resolution and 14 bits of dynamic range) after separating the two pulses at the cell exit using a Glan-Thomson polarizer. To improve the signal-to-noise over the whole considered spectral range, each spectrum is reconstructed by assembling data from 3 spectral ranges. For each range, the integration time was adjusted between 2 and 2000 pulses to ensure the use of the full dynamics of the spectrometer in every spectral region. The resulting spectra were then averaged over 20 realizations. The change in the probe spectra induced by the pump pulse is characterized by calculating the contrast  $C(\lambda) = [S_1(\lambda) - S_0(\lambda)] / [S_1(\lambda) + S_0(\lambda)]$  between the spectral densities with ( $S_1$ ) and without ( $S_0$ ) the pump pulse at each wavelength  $\lambda$ .

Since the spatial overlap all along the propagation is crucial for the relevance of the measurements, it is optimized by maximizing the interference pattern produced by the unfocused pulses both before and after the cell. It is also confirmed by the occurrence of multiple filamentation at zero delay, which is set by optimizing frequency doubling in a BBO crystal placed before the cell. Moreover, we checked that the alignment is conserved when translating the probe pulse from  $\tau = 0$  ps to  $\tau = 1$  ps ( $\tau = 2$  ps) by inserting a 200  $\mu$ m (400  $\mu$ m) thick glass window in the path of the short (long) pump pulse, delaying it by 1 ps (2 ps) and checking that the multifilamentation is restored. Let us note that the action of the pump pulse on the probe filaments may induce a longitudinal or transverse displacement. Such coupling, however, would mean that the plasma strongly affect the filamentation dynamics close to the nonlinear focus, where a substantial part of the white-light continuum is generated. It would therefore result in significant changes in the output spectra. Finally, no broadening is recorded in vacuum, confirming that neither input nor output windows of the cell have significant contributions on the spectral broadening.

As shown in Fig. 2(a), the spectrum of the filament generated by a 1.2 ps long-pulse narrows when it is preceded by a pump filament  $\tau = 2$  ps ahead of it. This coupling demonstrates that the probe pulse propagates through a preionized medium with a free electron density providing a significant negative contribution to the

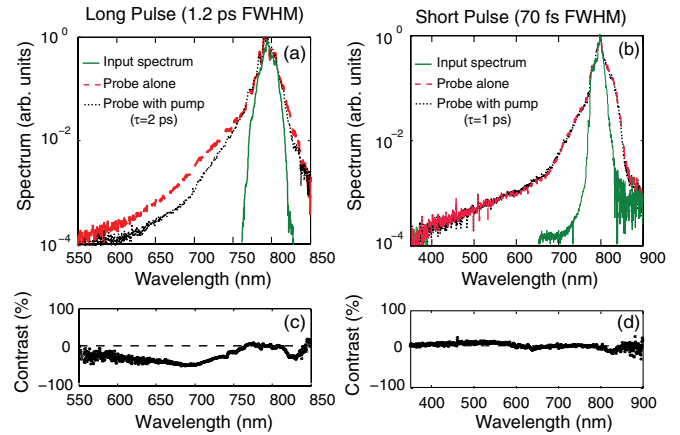


FIG. 2 (color online). (a),(b) Experimental spectra of the filaments generated by a long (1.2 ps, a) and short (70 fs, b) pulse conveying 2.5 critical powers, both with and without a pump pulse  $\tau = 2$  ps and  $\tau = 1$  ps ahead of it, respectively. This delay ensures that the pump pulse can only influence the probe pulse through the defocusing free electrons left behind by the pump. The input spectra are also given for reference. (c)–(d) Contrast between the spectra with and without pump pulse. The probe pulse is affected by the plasma left by the pump pulse only in the long-pulse regime.

refractive index, i.e., a non-negligible defocusing term: As expected from the Kerr-plasma balance model, the plasma density generated in the filament substantially contributes to the self-guiding. In this framework, the narrower spectrum of the probe filament is easily explained by the supplementary plasma density left by the pump pulse, which decreases the clamping intensity ensuring the balance in the probe pulse between Kerr self-focusing and defocusing by the plasma, and consequently reduces the efficiency of its spectral broadening.

Conversely, in the case of short pulses [70 fs, Fig. 2(b)], the spectrum of the probe is nearly insensitive to the plasma left by the pump. The decoupling between the two pulses separated by a delay ( $\tau = 1$  ps) too short to allow electron recombination unambiguously shows that the plasma density left in the wake of the pump pulse is too weak to significantly affect the filamentation process in the considered conditions. Plasma therefore plays no role in filamentation of 70 fs pulses, which is instead driven by the HOKE as predicted numerically [10]. Note that, if the two pulses overlap temporally ( $\tau = 0$ ), their coupling is restored due to cross-phase modulation, confirming that the two pulses indeed overlap both longitudinally and transversely. These results therefore provide the experimental demonstration of the transition from plasma-driven filamentation in the case of long pulses to HOKE-driven filamentation for shorter pulses, as expected from theoretical considerations [9].

In order to support this qualitative discussion and provide a closer look on the physical process at play, we numerically investigate the propagation of the pulses in

the present experimental conditions. In a first step, we simulate the propagation of the pump pulse. The plasma density left behind this pulse is then used as an initial condition for calculating the probe pulse propagation.

The numerical model considers linearly polarized incident electric fields at a wavelength  $\lambda_0 = 800$  nm with cylindrical symmetry around the propagation axis  $z$ . According to the unidirectional pulse propagation equation [24], the scalar envelope  $\varepsilon(r, t, z)$  [defined such that  $|\varepsilon(r, z, t)|^2 = I(r, z, t)$ ,  $I$  being the intensity] evolves in the frame traveling at the pulse velocity according to

$$\partial_z \tilde{\varepsilon} = i[\sqrt{k^2(\omega) - k_\perp^2} - k'\omega] \tilde{\varepsilon} + \frac{1}{\sqrt{k^2(\omega) - k_\perp^2}} \left( \frac{i\omega^2}{c^2} \tilde{P}_{\text{NL}} - \frac{\omega}{2\epsilon_0 c^2} \tilde{J} \right) - \tilde{\alpha}, \quad (1)$$

where  $c$  is the velocity of light in vacuum,  $\omega$  is the angular frequency,  $k(\omega) = n(\omega)\omega/c$ ,  $k'$  its derivative at  $\omega_0 = 2\pi c/\lambda_0$ ,  $n(\omega)$  is the linear refractive index at the frequency  $\omega$ ,  $k_\perp$  is the spatial angular frequency.  $P_{\text{NL}}$  is the nonlinear polarization,  $J$  is the free-charge induced current and  $\alpha$  is the nonlinear losses induced by photoionization.  $\tilde{f}$  denotes simultaneous temporal Fourier and spatial Hankel transforms of function  $f$ :  $\tilde{f} = \int_0^\infty \int_{-\infty}^\infty r J_0(k_\perp r) f(r, t) e^{i\omega t} dt dr$ , where  $J_0$  is the zeroth order Bessel function and  $f \equiv \varepsilon$ ,  $P_{\text{NL}}$ ,  $J$ , or  $\alpha$ .  $P_{\text{NL}}$  is evaluated as  $P_{\text{NL}} = \sum n_{2j} |\varepsilon|^{2j} \varepsilon$ , where  $n_{2j}$  are the  $j$ th-order nonlinear refractive indices as measured in [8]. The current is evaluated as  $\tilde{J} = \frac{e^2}{m_e} (\nu_e + i\omega) \tilde{\rho} \varepsilon / (\nu_e^2 + \omega^2)$ , where  $e$  and  $m_e$  are the electron charge and mass, respectively,  $\epsilon_0$  is the vacuum permittivity,  $\nu_e$  is the effective electronic collisional frequency, and  $\rho$  is the electron density. Finally,  $\alpha = [W(|\varepsilon|^2) U_i (\rho_{\text{at}} - \rho) / (2|\varepsilon|^2)] \varepsilon$ ,  $\rho_{\text{at}}$  is the neutral atoms density,  $W(|\varepsilon|^2)$  is the

photo-ionization probability modeled by the PPT (Perelomov, Popov, Terent'ev) formulation, with ionization potential  $U_i$ .

The propagation dynamics of the electric field is coupled with the electron density  $\rho$ , calculated as [2]

$$\partial_t \rho = W(|\varepsilon|^2) (\rho_{\text{at}} - \rho) + \frac{\sigma}{U_i} \rho |\varepsilon|^2 - \beta \rho^2, \quad (2)$$

where  $\beta$  is the electron recombination rate and  $\sigma$  is the inverse Bremsstrahlung cross-section of argon, also accounting for avalanche ionization. The output spectrum is integrated over 2 mrad around the beam center to match the experimental conditions.

The full model including the contribution of the HOKE together with the plasma response reproduces remarkably well the experimentally observed behavior. In particular, as displayed in Fig. 3, the spectral broadening of the long probe pulse is reduced when the pump pulse precedes it, in a ratio comparable with the experimental data, while the filament generated by the 70 fs probe pulse is unaffected by the pump pulse. In contrast, disregarding the HOKE (Fig. 4) would lead us to expect that the filament output spectrum generated by probe pulses of any duration should be affected by the presence of the pump pulse, in contradiction with the experimental results. Furthermore, this truncated model inadequately predicts the wings of the spectral broadening, even for a single pulse. Comparing both Figs. 3 and 4 with Fig. 2 clearly illustrates the need to consider the HOKE in numerical simulations of laser filamentation, even in the plasma-driven, long-pulse filamentation regime.

This need is illustrated by comparing the electron densities predicted by both models. While the truncated model yields  $10^{17} \text{ cm}^{-3}$  for both 1.2 ps and 70 fs pulses, the full

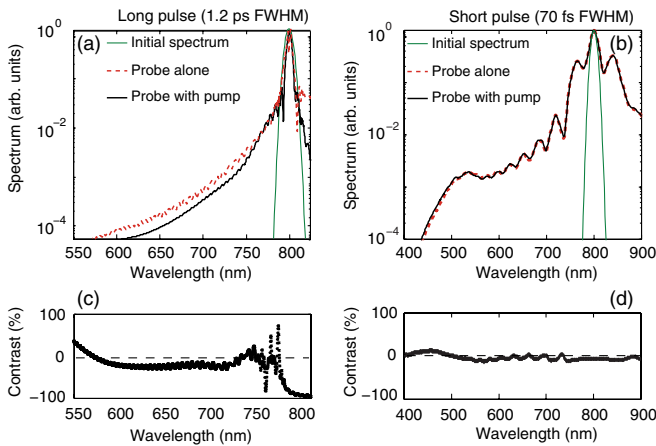


FIG. 3 (color online). (a),(b) Spectra of the filaments generated by the long (a) and short (b) pulse, simulated by the full numerical model considering the HOKE. (c–d) Contrast between the spectra with and without pump pulse. The probe pulse is affected by the plasma left by the pump pulse only in the long-pulse regime.

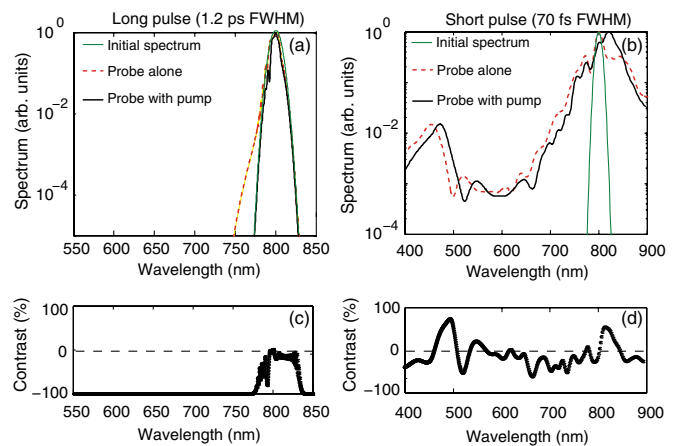


FIG. 4 (color online). (a),(b) Spectra of the filaments generated by the long (a) and short (b) pulse, simulated by the truncated numerical model disregarding the HOKE. (c–d) Contrast between the spectra with and without pump pulse. The probe pulse is affected by the plasma left by the pump pulse whatever the pulse duration.

model yields  $4 \times 10^{16} \text{ cm}^{-3}$  and  $10^{15} \text{ cm}^{-3}$ , respectively. This strong dependence of the plasma contribution on the pulse duration explains both the contrasted behaviors observed in our experiment between the plasma- and HOKE-driven filamentation regimes, but also the wide spread of the experimentally measured electron densities in filaments [13,18,19]. Furthermore, we can estimate the relative contributions of HOKE and plasma to defocusing by considering the ratio  $\xi = \Delta n_{\text{HOKE}}/\Delta n_{\text{plasma}}$  of the HOKE- to plasma-induced refractive index change. For short pulses (70 fs), this ratio keeps well above 1 all along the filament length ( $\xi \geq 39$ ), illustrating the negligible contribution of plasma to the filamentation process. In contrast, for 1.2 ps this ratio keeps close to 1 ( $\xi \geq 0.72$ , except for a spike with  $\xi = 0.24$  at the very filament onset), confirming that, while plasma provides the major defocusing contribution, the HOKE are far from negligible even in these conditions.

As a conclusion, a pump-probe experiment allowed us to unambiguously observe experimentally the theoretically predicted HOKE-driven filamentation for ultrashort pulses [10], as well as the transition from this regime to the long-known plasma-driven filamentation regime for long pulses [9]. This transition is similar to that observed in the context of high-order harmonic generation (HHG), where the use of too long pulses results in gas ionization instead of HHG [23]. Furthermore, comparing our results with numerical simulations shows that, even in the plasma-driven filamentation regime of the present work, the contribution of the HOKE to the propagation dynamics cannot be neglected. This finding provides a better understanding of filamentation, and therefore allows us to improve its modeling. It further confirms the relevance of the measured HOKE [8,9], with implications ranging from spectral broadening in optical fibers [25] to the generation of few-cycle pulses [26], atmospheric applications [5–7], or fermionic light [27].

This work was supported by the ANR COMOC ANR-07-BLAN-0152-01, FASTQUAST ITN Program of the seventh FP and the Swiss NSF (contract number 200021-125315). We acknowledge L. Bonacina, A. Rondi, J. Extermann, and M. Moret for their experimental support.

---

\*pierre.bejot@unige.ch

†jerome.kasparian@unige.ch

- [1] A. Braun, G. Korn, X. Liu, D. Du, and J. Squier, and G. Mourou, *Opt. Lett.* **20**, 73 (1995).
- [2] A. Couairon and A. Mysyrowicz, *Phys. Rep.* **441**, 47 (2007).
- [3] S. L. Chin, S. A. Hosseini, W. Liu, Q. Luo, F. Théberge, N. Aközbek, A. Becker, V. P. Kandidov, O. G. Kosareva, and H. Schroeder, *Can. J. Phys.* **83**, 863 (2005).
- [4] L. Bergé, S. Skupin, R. R. Nuter, J. Kasparian, and J.-P. Wolf, *Rep. Prog. Phys.* **70**, 1633 (2007).
- [5] J. Kasparian and J.-P. Wolf, *Opt. Express* **16**, 466 (2008).
- [6] P. Rohwetter, J. Kasparian, K. Stelmasczyk, Z. Q. Hao, S. Henin, N. Lascoux, W. M. Nakaema, Y. Petit, M. M. Queisser, R. Salamé, E. Salmon, L. Wöste, and J.-P. Wolf, *Nat. Photon.* **4**, 451 (2010).
- [7] J. Kasparian, R. Ackermann, Y.-B. André, G. Méchain, G. Méjean, B. Prade, P. Rohwetter, E. Salmon, K. Stelmasczyk, J. Yu, A. Mysyrowicz, R. Sauerbrey, L. Wöste, and J.-P. Wolf, *Opt. Express* **16**, 5757 (2008).
- [8] V. Loriot, E. Hertz, O. Faucher, and B. Lavorel, *Opt. Express* **17**, 13429 (2009); *Opt. Express* **18**, 3011(E) (2010).
- [9] V. Loriot, P. Béjot, W. Ettoumi, Y. Petit, J. Kasparian, S. Henin, E. Herz, B. Lavorel, O. Faucher, and J.-P. Wolf, [arXiv:1011.0841v1](https://arxiv.org/abs/1011.0841v1) [Laser Phys. (to be published)].
- [10] P. Béjot, J. Kasparian, S. Henin, V. Loriot, T. Vieillard, E. Hertz, O. Faucher, B. Lavorel, and J.-P. Wolf, *Phys. Rev. Lett.* **104**, 103903 (2010).
- [11] M. Kolesik, E. M. Wright, and J. V. Moloney, *Opt. Lett.* **35**, 2550 (2010).
- [12] M. Kolesik, D. Mirell, J.-C. Diels, and J. V. Moloney, *Opt. Lett.* **35**, 3685 (2010).
- [13] Y.-H. Chen, S. Varma, T. M. Antonsen, and H. M. Milchberg, *Phys. Rev. Lett.* **105**, 215005 (2010).
- [14] C. Brée, A. Demircan, and G. Steinmeyer, *Phys. Rev. Lett.* **106**, 183902 (2011).
- [15] P. Béjot, E. Hertz, B. Lavorel, J. Kasparian, J.-P. Wolf, and O. Faucher, *Opt. Lett.* **36**, 828 (2011).
- [16] O. Kosareva, J.-F. Daigle, N. Panov, T. Wang, S. Hosseini, S. Yuan, G. Roy, V. Makarov, and S. L. Chin, *Opt. Lett.* **36**, 1035 (2011).
- [17] A. Becker, N. Aközbek, K. Vijayalakshmi, E. Oral, C. M. Bowden, and S. L. Chin, *Appl. Phys. B* **73**, 287 (2001).
- [18] J. Kasparian, R. Sauerbrey, and S. L. Chin, *Appl. Phys. B* **71**, 877 (2000).
- [19] F. Théberge, W. W. Liu, P. T. Simard, A. Becker, and S. L. Chin, *Phys. Rev. E* **74**, 036406 (2006).
- [20] S. Tzortzakis, B. Prade, M. Franco, and A. Mysyrowicz, *Opt. Commun.* **181**, 123 (2000).
- [21] V. Loriot, E. Hertz, B. Lavorel, and O. Faucher, *J. Phys. B* **41**, 015604 (2008).
- [22] S. Suntsov, D. Abdollahpour, D. G. Papazoglou, and S. Tzortzakis, *Opt. Express* **17**, 3190 (2009).
- [23] A. L’Huillier, K. J. Schafer, and K. C. Kulander, *J. Phys. B* **24**, 3315 (1991).
- [24] M. Kolesik and J. V. Moloney, *Phys. Rev. E* **70**, 036604 (2004).
- [25] T. Popmintchev, M.-C. Chen, P. Arpin, M. M. Murnane, and H. C. Kapteyn, *Nat. Photon.* **4**, 822 (2010).
- [26] C. P. Hauri, W. Kornelis, F. W. Helbing, A. Couairon, A. Mysyrowicz, J. Biegler, and U. Keller, *Appl. Phys. B* **79**, 673 (2004).
- [27] D. Novoa, H. Michinel, and D. Tommasini, *Phys. Rev. Lett.* **105**, 203904 (2010).

# On Negative Higher-Order Kerr Effect and Filamentation<sup>1</sup>

V. Lorient<sup>a, b</sup>, P. Béjot<sup>a, c</sup>, W. Ettoumi<sup>c</sup>, Y. Petit<sup>c</sup>, J. Kasparian<sup>c, \*</sup>, S. Henin<sup>c</sup>,  
E. Hertz<sup>a</sup>, B. Lavorel<sup>a</sup>, O. Faucher<sup>a, \*\*</sup>, and J.-P. Wolf<sup>c</sup>

<sup>a</sup> *Laboratoire Interdisciplinaire Carnot de Bourgogne (ICB), UMR 5209 CNRS-Université de Bourgogne, 9 Av. A. Savary, BP 47 870, F-21078 Dijon Cedex, France*

<sup>b</sup> *Instituto de Química Física Rocasolano, CSJC, C/Serrano, 119, 28006 Madrid, Spain*

<sup>c</sup> *Université de Genève, GAP-Biophotonics, 20 rue de l'École de Médecine, 1211 Geneva 4, Switzerland*

\*e-mail: jerome.kasparian@unige.ch

\*\*e-mail: olivier.faucher@u-bourgogne.fr

Received October 28, 2010; in final form, November 11, 2010; published online June 4, 2011

**Abstract**—As a contribution to the ongoing controversy about the role of higher-order Kerr effect (HOKE) in laser filamentation, we first provide thorough details about the protocol that has been employed to infer the HOKE indices from the experiment. Next, we discuss potential sources of artifact in the experimental measurements of these terms and show that neither the value of the observed birefringence, nor its inversion, nor the intensity at which it is observed, appear to be flawed. Furthermore, we argue that, independently on our values, the principle of including HOKE is straightforward. Due to the different temporal and spectral dynamics, the respective efficiency of defocusing by the plasma and by the HOKE is expected to depend substantially on both incident wavelength and pulse duration. The discussion should therefore focus on defining the conditions where each filamentation regime dominates.

**DOI:** 10.1134/S1054660X11130196

## 1. INTRODUCTION

While potentially spectacular applications like rainmaking or the control of lightning [1–3] as well as the generation of THz radiation [4] attract much attention on the filamentation of ultrashort laser pulses, a controversy has recently been raised about the physical mechanism at the root of this phenomenon. Filaments are generally described as a dynamic balance between Kerr self-focusing and defocusing by the plasma generated at the non-linear focus [5–8]. The recent measurement of higher-order Kerr effect (HOKE) indices of alternate signs in air and argon [9] led us to propose that these terms provide the main defocusing effect, so that ionization and self-guiding are almost decoupled [10], at least in the visible and infrared regions [11]. Based on numerical work, and in the lack of knowledge of their values, these terms had already been assumed to contribute to defocusing, but only marginally [12–16]. Our unexpected prediction has therefore been actively challenged [17–19].

The controversy simultaneously focuses on two questions: the validity of the experimental measurement of the HOKE indices, and the validity of a filamentation model based on them. It is fed by the difficulty to perform quantitative measurements in filaments, due to the high intensity within them. This difficulty prevents one to directly test the contribution of the HOKE to filamentation. In this paper, we address these two aspects, with the aim of making the controversy as factual as possible by summarizing the

facts and the open questions on this subject. In a first section, we establish the methodology used for extracting the HOKE terms from the experiment and discuss several potential artifacts in the experimental measurement of the HOKE terms, the values of which are critical to evaluate their contribution to filamentation. In a second section, we discuss the relevance and the physical consequences of the introduction of the HOKE in the description of filamentation. We suggest that the contribution of the HOKE on the filamentation process strongly depends on the incident wavelength and pulse duration. More specifically, longer wavelengths and shorter pulses are more sensitive to the HOKE, while defocusing by the plasma is favored in the case of shorter wavelengths and long pulses.

## 2. ON THE MEASUREMENT OF THE HOKE INDICES

The key result reported by Lorient et al. [9] is the saturation and inversion of the instantaneous (i.e., at least, much shorter than the experimental resolution of  $\sim 100$  fs) non-linear refractive index at high intensities, which we phenomenologically described as HOKE terms from  $n_4 I^2$  to  $n_8 I^4$  in air (resp., to  $n_{10} I^5$  in argon). These terms have been obtained by a numerical fit on the experimental data. The implications to filamentation rely on two aspects of the measurement. On one hand, the fact that the Kerr effect can saturate and even become negative at high intensities enable all-Kerr driven self-guiding as described in [10]. On the other hand, this result can only have practical

<sup>1</sup> The article is published in the original.

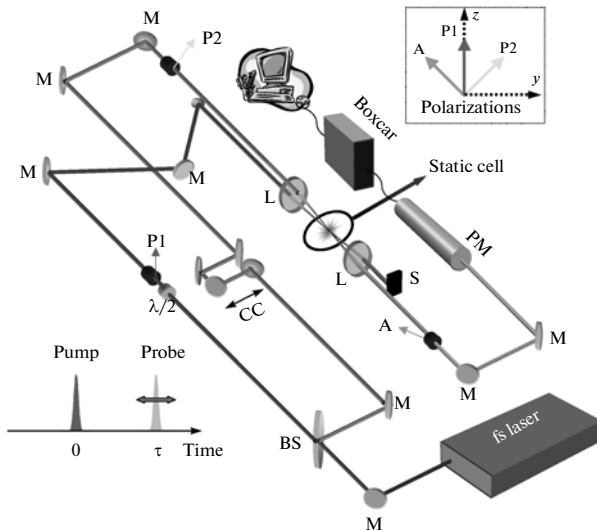


**Fig. 1.** Experimental setup for time-resolved birefringence measurements. M: Mirror, BS: Beam Splitter, L: Lens ( $f=20$  cm), CC: Corner Cube, P: Polarizer, A: Analyzer, S: Beam stop, PM: Photo multiplier. The relative polarizations of the pump (P1), probe (P2), and signal-field (A) are shown in the inset.

implications on filamentation if this inversion occurs at an intensity  $I_{\Delta n_{\text{Kerr}}=0}$  below or close to the clamping intensity predicted by the usual filamentation model relying on the balance between Kerr self-focusing and defocusing by the free electrons, i.e.,  $I_{\text{crit}} \approx 5 \times 10^{13}$  W/cm<sup>2</sup> in air [20, 21]. If  $I_{\Delta n_{\text{Kerr}}=0}$  is higher, the Kerr inversion will not occur in laser filaments, and will therefore play a negligible role in filamentation. We shall therefore describe in this section the experimental protocol that has been used in order to determine the intensity and extract the HOKE indices from the experimental sets of data, but also discuss potential sources of artifact affecting the measurement of these negative HOKE indices.

### 2.1. Measurement Protocol

In the experiment reported in [9], the transient birefringence of a molecular or atomic gas sample has been measured using a time-resolved polarization technique depicted in Fig. 1. The setup allows to carry out two types of detection: homodyne and heterodyne. In the former, the signal is related to the squared amplitude of the birefringence (amplitude-sensitive detection), whereas in the latter it is related to the birefringence itself (amplitude and phase sensitive detection). The heterodyne detection therefore provides the sign of the birefringence. In practice it is implemented by introducing between the cell and the analyzer a phase plate producing a static birefringence (see [9]). The measurements are based on the comparison between two optical Kerr contributions induced by the

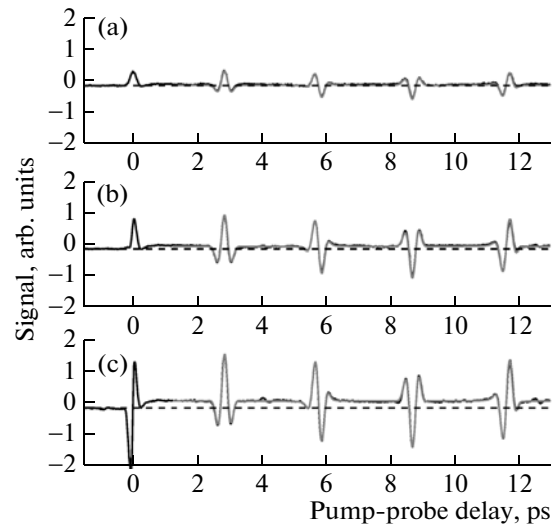


**Fig. 2.** Pump-probe birefringence signals (black solid lines) recorded in static cell filled with 0.1 bar of O<sub>2</sub> at room temperature. The energy of the pump pulse is 26 (a), 56 (b), and 96 μJ (c). Numerical fits of the postpulse signals (red solid lines) used, to evaluate the effective intensity in the experiment:  $\bar{I} = 8$  (a), 20 (b), and 34 TW/cm<sup>2</sup> (c), respectively (see text). The simulations are based on Eq. (1). The horizontal dashed-lines represent the zero signal.

field; the electronic Kerr contribution resulting from the deformation of the electronic cloud and the reorientation of the molecular dipole due to molecular alignment [22], respectively. This section provides details about the procedure that has been followed in order to extract the HOKE indices from this experiment.

**2.1.1. Intensity calibration.** A special attention has been paid to the estimation of the laser intensity experienced by the molecules or atoms present within the interaction volume. This intensity was inferred from the measurement of the field-free alignment [23, 24]. The last, also named post-pulse alignment, is described by  $\langle \cos^2\theta \rangle(t) - 1/3$ , with  $\theta$  the angle between the molecule axis and the field direction and where  $\langle \rangle$  denotes the expectation value averaged over the thermal distribution of molecules [25]. It is well established that both the structural shape of the alignment revivals and the permanent alignment are very sensitive to the initially applied laser intensity [26]. Below saturation of the alignment, the value of  $\langle \cos^2\theta \rangle$  at the revivals of alignment increases linearly with the applied intensity [25, 27], whereas between revivals (i.e., for permanent alignment) it grows first quadratically and then linearly with the intensity. Field-free alignment therefore provides an accurate and unambiguous estimation of the laser intensity in the gas.

Figure 2 shows the time-resolved birefringence signal of O<sub>2</sub> at different laser energies recorded with an heterodyne detection. Pure heterodyne detection pro-

vides a post-pulse signal  $S_{\text{hete}}$  proportional to the convolution of the probe intensity  $I_{\text{pr}}(t)$  with  $(\langle \cos^2 \theta \rangle(t) - 1/3)$  [9, 28]:

$$S_{\text{hete}}(t) \propto I_{\text{pr}}(t) \otimes \frac{3\rho\Delta\alpha}{4n_0\epsilon_0} \left( \langle \cos^2 \theta \rangle(t) - \frac{1}{3} \right), \quad (1)$$

with  $\Delta\alpha$  the polarizability anisotropy,  $\rho$  the gas density,  $n_0$  the linear refractive index,  $\epsilon_0$  the dielectric constant of vacuum, and  $\otimes$  denotes the convolution. The permanent alignment offsets the baseline for positive delays. This offset increases with the intensity. Because of the intensity profile of the pump and probe beams, the signal measured in the experiment results from a spatial averaging. Using a space-averaged calculation (i.e., a 3D model) we have checked numerically that the volume effect can be adequately taken into account in a simpler 1D calculation just by using an effective intensity. In fact, considering a gaussian beam profile, a peak laser intensity  $I_{\text{peak}}$ , and a crossing angle of about  $4^\circ$  between the pump and probe beams [9], the field-free alignment signal integrated over the volume can be approximated by the signal produced at the effective intensity  $\bar{I}$  defined as

$$\bar{I} \approx I_{\text{peak}}/1.7. \quad (2)$$

This approximation allows to save computer time when fitting the experimental data.

Figure 2 also shows the results of the simulations that have been used to fit the effective intensities. The temporal envelope  $I_{\text{pr}}(t)$  of the probe beam has been described by a gaussian function of duration slightly above 100 fs (FWHM) in order to account for the crossing of the two beams. The fact that the simulations reproduce very well both the revivals and the permanent alignment supports the analysis based on the effective intensity.

The intensity determined as described above has been double-checked by comparing its value to the one estimated from the measurement of the beam waist, the incident energy, and the pulse duration. The estimation was supported by (i) the limited gas pressure in the static cell (0.1 bar, except for measurements at or below 1 TW/cm<sup>2</sup>), (ii) the limited power of the incident beam  $P = 1.8 \text{ GW} \ll P_{\text{cr}} = 80 \text{ GW}$ , where  $P_{\text{cr}}$  is the critical power for nitrogen, as well as the low value of the nonlinear phase accumulated during propagation (less than 0.10 and 0.14 rad for N<sub>2</sub> and O<sub>2</sub>) respectively), and (iii) the focused geometry ( $f = 20 \text{ cm}$ ), which limits self-channeling that would induce changes in the beam profile. This ensures that the propagation was mostly linear in the experiment, allowing to estimate the intensity therein from the measurement of the beam waist conducted at low energy. Figure 3 reports the effective intensities obtained by the two independent methods in the case of oxygen. The error bars on the measured intensity (solid circles) results from the uncertainties on the

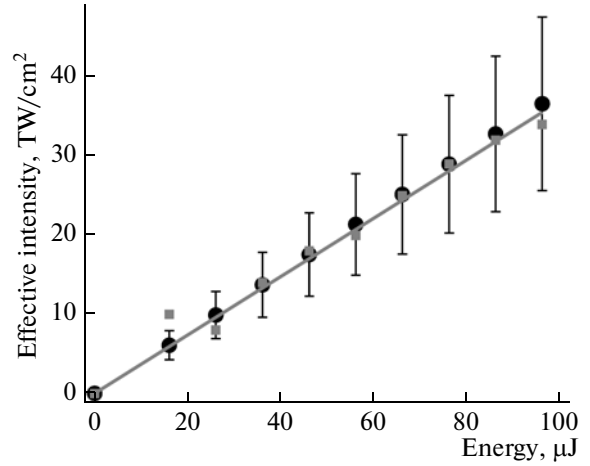


Fig. 3. Effective intensity  $\bar{I}$  fitted on the postpulse alignment signal in O<sub>2</sub> (red solid squares) compared to the intensity estimated from the measurement of the pulse/beam characteristics (black solid circles). Linear regression of the fitted intensity on the measured pulse energy (red solid line).

measured energy ( $\pm 5\%$ ), pulse duration ( $\pm 10\%$ ), and beam waist ( $\pm 15\%$ ). The red solid line corresponds to a linear regression of the intensities fitted on the post-pulse alignment signal. It allows to estimate an uncertainty of  $\pm 10\%$  (at 3 standard deviations) in the determination of the intensities. We can therefore exclude flaws in the intensity determination beyond this order of magnitude.

**2.1.2. Determination of the lowest-order Kerr index ( $n_2$ ).** The measurement of the lowest-order Kerr index has been conducted at low energy in order to avoid any influence from the HOKE terms. In order to ensure a good signal-to-noise ratio despite the weakness of the birefringence signal, an homodyne detection, that offers a better sensitivity than the heterodyne one, has been employed. In the case of a homodyne detection, the signal is given by [9]

$$S_{\text{homo}}(t) \propto I_{\text{pr}}(t) \otimes \left( \frac{3\rho\Delta\alpha}{4n_0\epsilon_0} \left( \langle \cos^2 \theta \rangle(t) - \frac{1}{3} \right) + \frac{2}{3} n_2^{\text{cross}} I(t) \right)^2, \quad (3)$$

where the lowest-order electronic Kerr response  $n_2^{\text{cross}}$  has been added to the retarded rotational response resulting from the alignment. Here, it is worth mentioning that the signal measured in our experiment results from the cross-coupling between two distinguishable laser beams, namely the pump and probe beams. The coefficients  $n_2^{\text{cross}} = 2 \times n_2$ , with  $n_2$  the standard self-induced Kerr index, therefore describes the non-linear refractive index due to cross-Kerr effect. The correspondence between cross-Kerr and

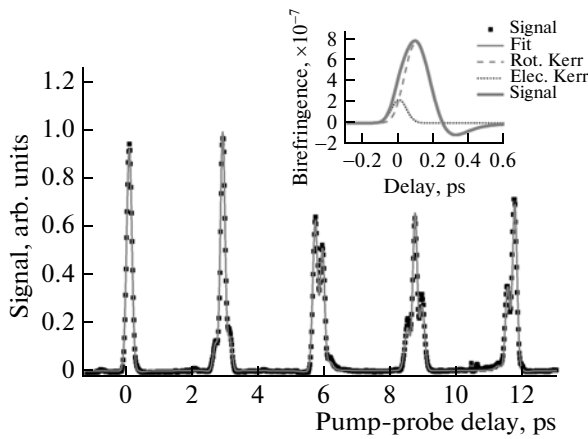


**Fig. 4.** Homodyne birefringence signal (black solid squares) recorded in 1 bar of  $O_2$  at room temperature and numerical fit (red solid line). The effective intensity of the pump is  $1 \text{ TW/cm}^2$ . In the inset, the total birefringence (red solid line) resulting from the electronic (blue dotted line) and rotational (green dashed line) Kerr contributions.

Kerr indices is given in [9]. Finally, the factor  $2/3$  results from the different values of the Kerr index experienced by the probe field along directions parallel ( $\parallel$ ) and perpendicular ( $\perp$ ) to the pump field, respectively, with  $n_{2\parallel} = 3 \times n_{2\perp}$ . This relation is valid when the intrapulse alignment can be neglected so that the medium can be viewed as isotropic during the pump excitation [29]. The approximation is justified for the investigated molecules and the relatively short pulse duration used in the experiment compared to the rotational period. For instance, in  $N_2$  or  $O_2$ , the orientational Kerr contribution to  $n_2$  calculated from the elements of the hyper-polarizability tensor [30] is less than 5% at the maximum peak intensity investigated in the experiment.

Since the permanent alignment can be neglected in the low intensity regime, both rotational and electronic contributions exhibit a linear dependency on the applied pump intensity  $I$ , which therefore acts as an amplitude factor on the overall signal.  $n_2^{\text{cross}}$  was hence determined independently from the knowledge of this intensity. Figure 4 shows the time-resolved birefringence signal recorded in  $O_2$  at low intensity. For all recorded data, the value of  $n_2$  has been evaluated

**Table 1.** Correction factors for the volume effect defined as  $c_{2j} = \bar{n}_{2j}^{\text{cross}} / n_{2j}^{\text{cross}}$ , with  $n_{2j}^{\text{cross}}$  and  $\bar{n}_{2j}^{\text{cross}}$  the HOKE terms and its corresponding effective value, respectively

$n_{2j}^{\text{cross}}$	$n_4^{\text{cross}}$	$n_6^{\text{cross}}$	$n_8^{\text{cross}}$	$n_{10}^{\text{cross}}$
$c_{2j}$	1.04	1.30	1.45	2.66

through deconvolution of the rotational response from the signal. First, the postpulse signal was adjusted by Eq. (3) with  $n_2^{\text{cross}} = 0$ , using a low intensity value as a fixed parameter and an amplitude factor as a free parameter. This allows to evaluate the contribution of the rotational term close to the zero delay, and only relies on the knowledge of the molecular polarisability ( $\Delta\alpha = 4.60$  and  $7.25 \text{ au}$  for  $N_2$  and  $O_2$ , respectively).

Next, the signal was adjusted using  $n_2^{\text{cross}}$  as a free parameter. As described in [9], measurements in argon have been calibrated with the postpulse signal recorded independently in  $N_2$  in the same experimental conditions. The data presented in Table 1 of [9] result from statistics performed over 50, 30, and 8 data samples recorded at low intensity (i.e.,  $I < 1 \text{ TW/cm}^2$ ) in  $N_2$ ,  $O_2$ , and Ar, respectively.

**2.1.3. Determination of the higher-order Kerr indices.** All HOKE indices have been determined by the use of an heterodyne detection that is phase sensitive and therefore allows to recover the sign of each term. When considering HOKE terms up to the fifth power of the applied intensity  $I$ , the heterodyne birefringence signal is given by [9]

$$S_{\text{hete}}(t) \propto I_{\text{pr}}(t) \otimes \left( \Delta n_{\text{rot}}(t) + \frac{2}{3} n_2^{\text{cross}} I(t) + \frac{4}{5} n_4^{\text{cross}} I(t)^2 + \frac{6}{7} n_6^{\text{cross}} I(t)^3 + \frac{8}{9} n_8^{\text{cross}} I(t)^4 + \frac{10}{11} n_{10}^{\text{cross}} I(t)^5 \right), \quad (4)$$

with  $\Delta n_{\text{rot}}(t) = 3\rho\Delta\alpha/4n_0\epsilon_0 \left( \langle \cos^2\theta \rangle(t) - \frac{1}{3} \right)$ . We have

generalized the relation  $n_{2j\parallel} = (2j+1)n_{2j\perp}$  with  $j \in \mathbb{N}^*$ , verified for  $n_2$  and  $n_4$  [31], to higher orders. As mentioned in the previous section, this approximation results from neglecting the intrapulse alignment considering the medium as isotropic during the interaction with the pump.

Although the determination of  $n_2^{\text{cross}}$  is straightforward, since it is independent from  $I$ , the evaluation of the HOKE indices is complicated by the fact that spatial averaging depends on the non-linearity order. As in Subsection 2.1.1, in order to avoid the prohibitively large use of computer time, the deconvolution of the HOKE from the signal has been achieved by fitting the experimental data with a 1D model. However, in order to evaluate the influence of the volume effect, different 3D simulations of Eq. (4) have been preliminary performed. First, Eq. (4) has been truncated to the second power of  $I$  (i.e.,  $n_6^{\text{cross}}, \dots, n_{10}^{\text{cross}} = 0$ ) and then spatially integrated. Second, the 1D model, in which  $n_4^{\text{cross}}$  was

replaced beforehand by the effective index  $\bar{n}_4^{\text{cross}}$ , has been used to fit the previous numerical result using the effective intensity defined in Subsection 2.1.1 as a fixed parameter and  $\bar{n}_4^{\text{cross}}$  as a free parameter. For the next HOKE index  $n_6^{\text{cross}}$ , the same procedure has been applied. The result of the 3D calculation including  $n_4^{\text{cross}}$  and  $n_6^{\text{cross}}$  has been fitted with the 1D model with  $\bar{n}_4^{\text{cross}}$  fixed,  $\bar{n}_6^{\text{cross}}$  being the free parameter. This approach has been repeated successively for each HOKE index up to  $n_{10}^{\text{cross}}$ . In order to check that the ratios between the HOKE indices and their respective effective values were independent from the intensity, different numerical tests have been performed over the intensity range considered experimentally. The ratio between the HOKE indices and the effective values that account for the volume effect are given in Table 1. Since both  $n_2$  and the alignment depend linearly on the intensity, the correction factor for  $n_2$  is  $c_2 = 1$  (i.e.,  $\bar{n}_2^{\text{cross}} = n_2^{\text{cross}}$ ).

Figure 5 displays the time-resolved birefringence signals recorded in  $N_2$  from low to high intensity. The simulations have been performed using the  $n_{2j}^{\text{cross}}$  coefficients first reported in [9], determined as detailed above. Like in  $O_2$  and Ar, the electronic Kerr contribution to the birefringence signal (i) scales linearly with the intensity at low intensity where  $n_2^{\text{cross}}$  dominates, (ii) then saturates at moderate intensity, and finally (iii) reverses its sign and becomes highly non-linear at high intensity where the HOKE dominates. To avoid correlation between the  $n_{2j}^{\text{cross}}$  coefficients in the least square fitting procedure, the different orders were fitted successively.  $\bar{n}_4^{\text{cross}}$  was first adjusted with  $n_2^{\text{cross}}$  fixed and  $\bar{n}_{2j>4}^{\text{cross}} = 0$ , from a set of 14 (resp., 10 and 11) data recorded in  $N_2$  (resp.,  $O_2$  and Ar) at an effective intensity  $\bar{I} \leq 27 \text{ TW/cm}^2$  (resp., 20 and 24  $\text{TW/cm}^2$ ). Due to the predominant value of  $\bar{n}_8^{\text{cross}}$  compared to  $\bar{n}_6^{\text{cross}}$ , it has not been possible to isolate an intensity window where these two indices could be fitted independently. They have therefore been determined simultaneously, with  $n_2^{\text{cross}}$  and  $\bar{n}_4^{\text{cross}}$  fixed and  $\bar{n}_{10}^{\text{cross}} = 0$ , from a set of 24 (resp., 10 and 26) data recorded in  $N_2$  (resp.,  $O_2$  and Ar) at  $27 < \bar{I} < 50 \text{ TW/cm}^2$  (resp.,  $20 < \bar{I} < 35 \text{ TW/cm}^2$  and  $24 < \bar{I} < 45 \text{ TW/cm}^2$ ). For the same reason, the last term  $\bar{n}_{10}^{\text{cross}}$ , necessary only in argon, has been fitted together with  $\bar{n}_6^{\text{cross}}$  and  $\bar{n}_8^{\text{cross}}$ .

In order to reduce the errors bars, the records mentioned above have also been used in order to fit the

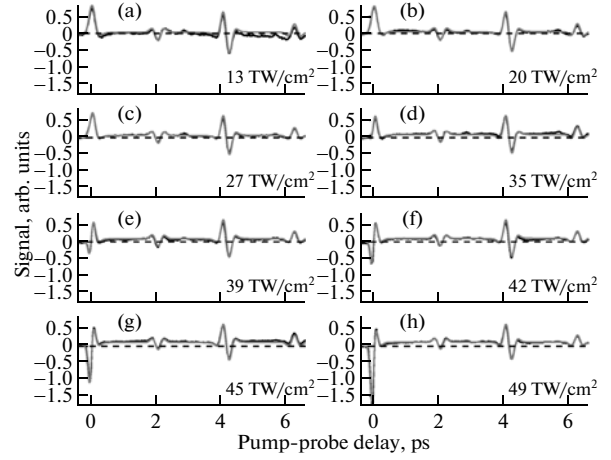


**Fig. 5.** Intensity dependence of the birefringence signals (black solid lines) recorded in static cell filled with 0.1 bar of  $N_2$  at room temperature. Numerical simulations of Eq. (4) (red solid lines) where  $n_{2j}^{\text{cross}}$  and  $I$  have been replaced by the effective values  $\bar{n}_{2j}^{\text{cross}}$  and  $\bar{I}$ , respectively (see text).  $\bar{I} = 13$  (a), 20 (b), 27 (c), 35 (d), 39 (e), 42 (f), 45 (g), and 49  $\text{TW/cm}^2$  (h).

HOKE indices on the two-dimensional data displaying birefringence signal as a function of intensity and time delay. Figure 6 displays a comparison between the experimental data set and the numerical simulations resulting from the fitting procedure. The good agreement between observations and calculations confirms the values of the HOKE indices retrieved as detailed above, as evidenced in particular by the fact that they overcome the rotational response (see positive signal at positive delays for  $N_2$  and  $O_2$ ) at large intensity.

## 2.2. Is the Observed Inversion Due to Negative HOKE?

Negative non-linear indices generated by high-power laser pulses are generally attributed to a contribution of the free electrons, given by the Drude model [6]:

$$\Delta n_{\text{plasma}} = -\frac{\rho}{2n_0\rho_{\text{crit}}}, \quad (5)$$

where  $\rho$  is the electronic density,  $n_0$  is the linear refractive index,  $\rho_{\text{crit}} = \frac{\epsilon_0 m_e \omega_l^2}{e^2}$  is the critical plasma density ( $\rho_{\text{crit}} = 1.75 \times 10^{27} \text{ m}^{-3}$  at 800 nm),  $\epsilon_0$  is the permittivity of vacuum,  $m_e$  is the electron mass,  $\omega_l$  is the laser angular frequency, and  $e$  the elementary charge.

As described in the previous section, our measurements were performed in a pump-probe configuration where the pump beam intensity is sufficient to partially ionize the gas, so that the free electrons contribute negatively to the refractive index. To cancel this free

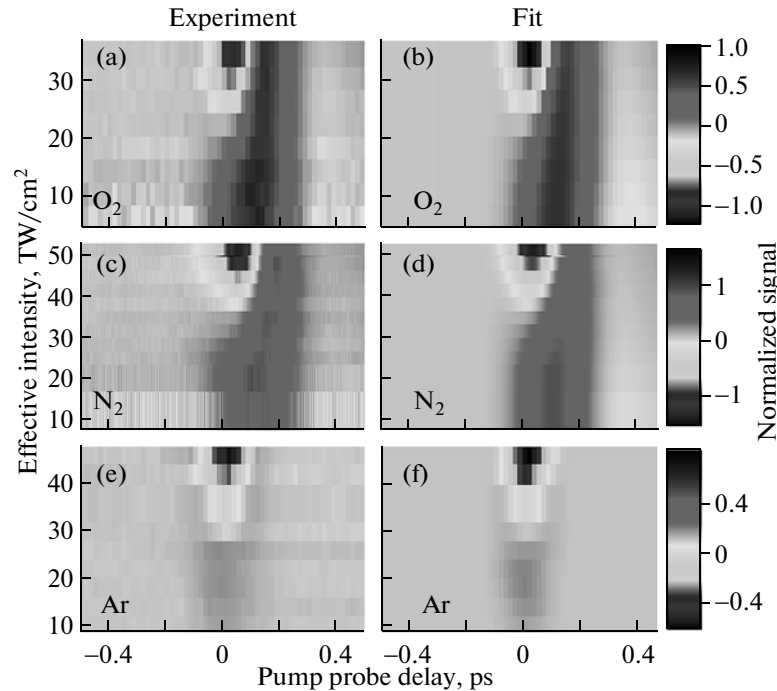


**Fig. 6.** Time-resolved birefringence signals recorded for different effective intensities  $\bar{I}$  in O<sub>2</sub> (a), N<sub>2</sub> (c), and Ar (e). Numerical fits of the O<sub>2</sub> (b), N<sub>2</sub> (d), and Ar (f) data normalized for each intensity to the maximum amplitude of the postpulse signal (not shown), except for argon.

electron contribution, we measured the transient variation of the *birefringence* rather than the variation of the refractive index itself. This approach is supported by the general belief that non relativistic plasmas are not birefringent, even at the time scale of the laser-medium interaction [29]. However, since this statement has never been proved rigorously to date, we discuss below the potential plasma contribution on each time scale.

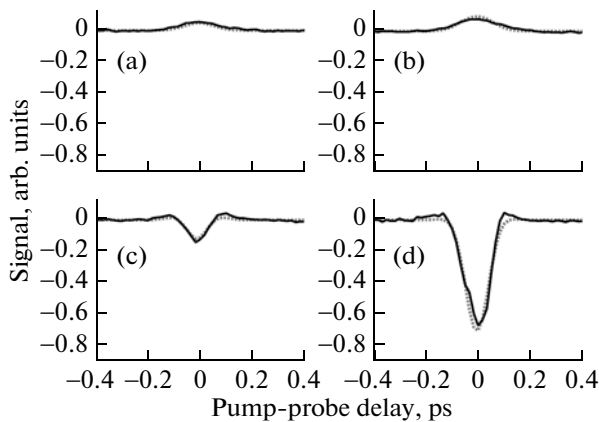


**Fig. 7.** Time-resolved birefringence signals (solid lines) recorded for different effective intensities  $\bar{I} = 10$  (a), 21 (b), 28 (c), and 43 TW/cm<sup>2</sup> (d) in argon. Numerical fits are displayed as red dotted lines.

**2.2.1. Postpulse plasma contribution.** The birefringence induced by a high-intensity ultrashort pulse in argon is not maintained after the pulse has passed [32–34]. A direct contribution of the plasma to the medium birefringence would have the same lifetime as the plasma, i.e., at least several picoseconds [35]. It can therefore be excluded.

This negligible birefringence of the plasma is further confirmed by the temporal dependence of the birefringence in our experiments. In the case of argon (see Fig. 7) the birefringence goes down to zero for time delays larger than  $\sim 200$  fs, i.e., as soon as the two pulses do not overlap anymore. In the case of oxygen and nitrogen (see Figs. 2 and 5, respectively), the birefringence observed at positive delays between the revivals of alignment is perfectly reproduced by the molecular permanent alignment described in Subsection 2.1.1.

**2.2.2. Intrapulse plasma contribution.** Considering that the free electrons accumulate over the pulse duration, their potential contribution to the nonlinear birefringence should produce an asymmetric temporal profile, as depicted in Fig. 8. In contrast, for a symmetric pulse like we used in [9], the Kerr contribution to the refractive index is symmetrical in time. The relative contribution of the plasma to the birefringence would be therefore defined by the asymmetry of the birefringence profile around time  $t = 0$ . Such asymme-

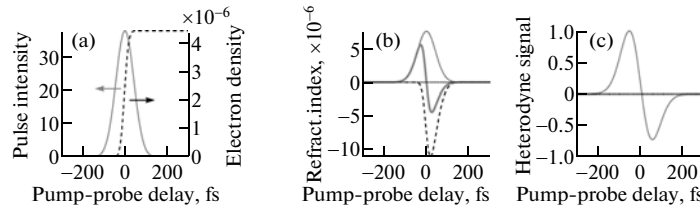


**Fig. 8.** (a) Pulse intensity (grey line) and electron density (black dotted line) calculated in argon along the pulse duration (100 fs) for a peak intensity of  $28 \text{ TW/cm}^2$ . (b) Corresponding refractive index produced by a positive Kerr effect (dotted line), an hypothetical negative Kerr effect resulting from accumulated free electrons, (black dashed line), and both contributions (grey solid line). (c) Heterodyned signal resulting from both contributions.

try is not observed in our experiment, as evidenced for example by the data in argon displayed in Fig. 7.

Besides the free electrons, the plasma is made of ions. Their susceptibility can be estimated according to Sprangle et al. [36]:

$$\frac{\chi_{\text{ion}}^{(3)}}{\chi_{\text{neutral}}^{(3)}} \approx \left( \frac{\text{IP}_{\text{neutral}}}{\text{IP}_{\text{ion}}} \right)^3, \quad (6)$$

where  $\text{IP}_x$  denotes the ionization potential of species  $x$ , as detailed in Table 2. Assuming that the refractive index variation of the ions is three times larger along the laser polarization axis than perpendicular to it, as is the case for the neutrals, the contribution of the ions is about 10 to 20% lower than that of neutrals for the same partial pressure. At the maximum intensity used our experiment, the ionization is restricted to 1% at most [37], so that the ions cannot, in any case, contribute to more than 0.2% to the observed birefringence. Moreover, as discussed above for the electrons, any contribution from the ions would result in an asymmetric temporal profile.

Finally, ionization can deplete the ground state population to the benefit of excited bound and continuum states. Both processes can result in a large modification of the refractive index [38–40]. Moreover, for intensities close to the inversion of the refractive index, the ionization takes place at the frontier between multiphoton and tunneling ionization regimes. Besides depletion of the ground state, ionization might contribute to the HOKE through the fast-moving electrons recolliding with the atomic or molecular core, as described by the three-step model [41]. The resulting oscillation of the induced dipole responsible for high harmonic generation [42] could lead to large nonlinearities in the Kerr effect. Since we consider a process occurring within an optical cycle, this potential effect can be considered as instantaneous as compared with the time scale of the pulse. Calculations of the dipole induced by a strong laser field could, therefore contribute to interpret the effect observed in our experiment.

**2.2.3. Two-beam coupling.** Another artifact that could be raised is the energy exchange between the two crossing laser pulses, known as two-beam coupling [29, 43]. First, we should mention that the signal provided by heterodyne detection used in the high-order Kerr measurement is in principle free from any two-beam coupling contribution. In fact, pure heterodyne detection results from the difference between two data sets recorded in the same conditions, except for opposite phases of a local oscillator [44, 45]. Second, for femtosecond pulses with identical spectra, two-beam coupling requires a frequency chirp and a finite time response of the nonlinear refractive index [46]. The very fast excitation combined with the small residual frequency chirp of our pulses can only lead to a marginal amount of two-beam coupling through the purely electronic Kerr response. Finally, and most importantly, the time profile resulting from two-beam coupling should be asymmetric with respect to the pump-probe delay. This was not observed in our experiment, as previously mentioned (see, e.g., Fig. 7). Consequently, the influence of two-beam coupling on our experimental results can be confidently disregarded.

### 3. HOKE- AND PLASMA-DRIVEN FILAMENTATION REGIMES

Improving models by considering higher-order of the relevant processes is a quite natural approach in all branches of physics. Higher-order optical non-linearity is well-known, giving rise e.g. to higher harmonics [29] and should therefore be included in the propagation equations, unless it is proven that it induces a neg-

**Table 2.** Ionization potentials of neutral and ionized nitrogen, oxygen, and argon

Species	N <sub>2</sub>	O <sub>2</sub>	Ar
IP <sub>neutral</sub> , eV	15.6	12.07	15.8
IP <sub>ion</sub> , eV	27.12	24.14	27.6
$\frac{\chi_{\text{ion}}^{(3)}}{\chi_{\text{neutral}}^{(3)}}$	0.19	0.125	0.185

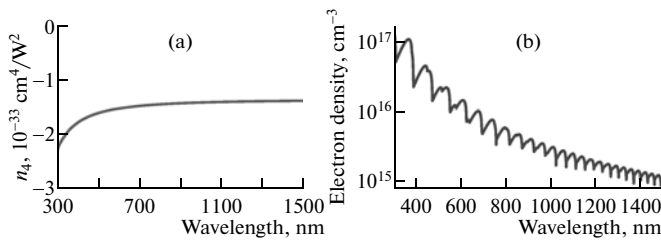


**Fig. 9.** (a) Dispersion of the fifth-order Kerr index ( $n_4$ ) [48] and (b) electron density generated in air by a 30 fs pulse of constant intensity  $50 \text{ TW/cm}^2$ . Note that the vertical scales are respectively linear and logarithmic.

ligible effect in the considered situation. In the context of filamentation, such development was already tried several years ago [12–16], although the significance of those works was limited by the lack of experimental knowledge of the magnitude of these terms.

This magnitude constitutes the key question arising about their role in laser filamentation. Considering the wide range of wavelengths, pulse durations, incident energies and focusings investigated in the last ten years [5–8], we expect that no unique dominant effect can be identified for all conditions. Rather, four regularizing terms exist in the full non-linear Schrödinger equation (NLSE) [10], with relative contributions depending on the experimental conditions. Three of them (defocusing by the HOKE and by the free electrons, as well as diffraction) are spatial, while group-velocity dispersion (GVD) is temporal.

The latter two are independent on intensity. Diffraction cannot be the dominant regularizing factor in filamentation, which it can only occur beyond the self-focusing  $P_c$ , defined as the power required for the self-focusing to dominate diffraction. Furthermore, due to the limited bandwidths at play and the relatively low dispersion of usual gases in the near infrared, the contribution of GVD is very small in usual filamenting conditions, especially on the short distances of the laboratory. However, for few-cycle pulses centered in the UV, the bandwidth and the dispersion increase, so that GVD may play a substantial role as it does, e.g., in water [47].

In most usual cases, defocusing by plasma and/or the HOKE will therefore be the main regularizing terms. The relative contributions of the HOKE and the plasma-induced refractive index change can be characterized as the ratio of the corresponding terms in the NLSE, at any location  $\mathbf{r}$  and time  $t$  [11]:

$$\xi(\mathbf{r}, t) = \left| \sum_{j \geq 2} n_{2j} I(\mathbf{r}, t)^j \right| / \frac{\rho(\mathbf{r}, t)}{2n_0 \rho_{\text{crit}}} \quad (7)$$

The overall action of both effects on the whole pulse duration is described by the pulse-integrated value of  $\xi$ :

$$\bar{\xi}(\mathbf{r}) = \frac{\int \left| \sum_{j \geq 2} n_{2j} I(\mathbf{r}, t)^j \right| \times |\varepsilon(\mathbf{r}, t)| dt}{\int \frac{\rho(\mathbf{r}, t)}{2n_0 \rho_{\text{crit}}} |\varepsilon(\mathbf{r}, t)| dt}, \quad (8)$$

where  $\varepsilon$  is the reduced scalar envelope defined such that  $|\varepsilon|^2 = I$  [11].

Both HOKE and plasma defocusing generate a negative non-linear refractive index. However, they differ by three aspects. First, multiphoton ionization requires 8 photons in  $\text{O}_2$  and 11 photons in  $\text{N}_2$  and Ar, so that the corresponding non-linearity is of 8th- or 11th order. In contrast, over the intensity range relevant for filamentation, orders up to 4 (resp. 5) only have to be considered in air (resp. argon), as discussed in Subsection 2.1.3. Secondly, the Kerr effect has a time constant of a few fs at most, shorter than the pulse duration, while the plasma density accumulates over whole duration of the same pulse. Finally, both terms increase in absolute values for higher frequencies, but the Kerr effect shows a relatively slow dispersion over the visible spectral range [48], while the increase of the ionization rates is much faster [6], as illustrated in Fig. 9 in the case of air.

One can therefore expect that the plasma will tend to provide the dominant defocusing contribution on the short-wavelength side, while the HOKE should be favoured on the long-wavelength side. Indeed, we observed this transition in a recent numerical work [11]. As a consequence, one can consider as a general rule that the regularizing process will be defocusing by the free electrons for short wavelengths ( $\lambda \leq 300\text{--}400 \text{ nm}$ ) and by the HOKE for longer wavelengths. The discussion should therefore focus on defining the border between “long” and “short” wavelengths, rather than on the existence of the HOKE. Still, the position of this transition depends little on the value of the HOKE indices since the ionization coefficients cover several orders of magnitude over the spectrum.

Similarly, as a consequence of the different temporal dynamics of the plasma and the HOKE, the pulse duration will strongly impact their respective contribution to defocusing. The longer the pulse, the more efficient the accumulation of plasma, and consequently its relative contribution to defocusing. Indeed, as shown in Fig. 10a, numerical calculations using the model described in [11] and relying on the generalized non-linear Schrödinger equation and ionization rates given by the multi-species generalized Keldysh–Perelemov, Popov, Terent’ev (PPT) formulation [6], the plasma contribution is marginal ( $\xi \gg 1$ ) over most of the duration of a short pulse. It only plays a significant role at the very tail of the pulse, where the intensity has decreased close to zero. Its contribution to the overall

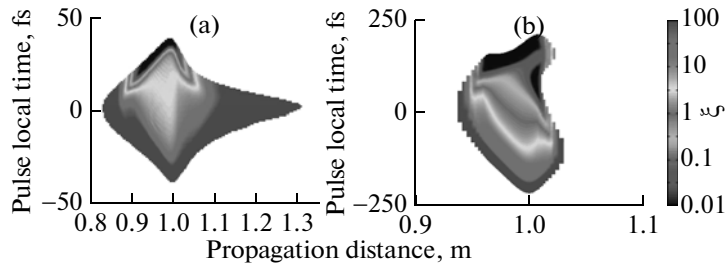


**Fig. 10.** Numerical simulation of the space-time dynamics of the on-axis ratio  $\xi(r=0)$  of the respective contributions of higher-order Kerr terms and plasma to defocusing (see text for detail). The white regions correspond to irrelevant values due to the low intensity ( $I < I_{\max}/e^2$ ). Pulse durations are (a) 30 fs ( $\bar{\xi}_{\min}(r=0) = 3.3$  at  $z = 98.7$  cm) and (b) 250 fs ( $\bar{\xi}_{\min}(r=0) = 0.5$  at  $z = 99.8$  cm). Note the asymmetric temporal shape due to the plasma accumulation, contrasting with the symmetric pulse shape related with the domination of the instantaneous HOKE in panel (a).

pulse propagation is therefore negligible, as evidenced by a high on-axis value of  $\bar{\xi}_{\min}(r=0) = 3.3$  for a 30 fs pulse. In contrast, for a longer pulse (250 fs, Fig. 10b), the plasma efficiently accumulates earlier in the pulse and is significant already in its high-intensity region. It therefore contributes significantly ( $\bar{\xi}_{\min}(r=0) = 0.5$  for a 250 fs pulse) to the propagation of long pulses, resulting in particular in an asymmetric temporal pulse shape. The published values of the HOKE indices suggest that the border between the two regimes lies at a few hundreds of fs at 800 nm. The two regimes are therefore experimentally accessible with the current laser technology, which may explain the contradicting results obtained among the available experimental work. Furthermore, the transition between them is smooth, so that in adequate conditions both processes contribute with similar magnitudes. Again, the discussion should focus on the domains of the long- and short pulse regime rather than on seeking for one single universally dominating mechanism.

The different regimes discussed above can be displayed schematically as a “phase diagram” (Fig. 11). In this graph, the axis have been left blank on purpose to ensure the generality, independently of the mea-

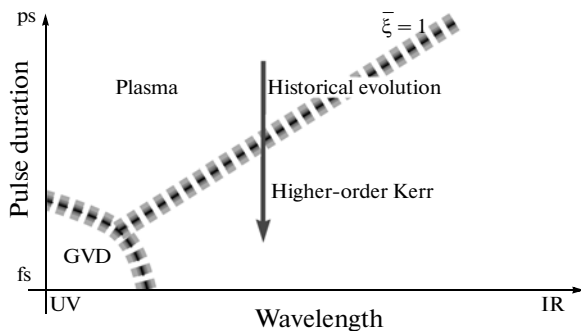


**Fig. 11.** Schematic “Phase diagram” of the dominating defocusing mechanisms at play in filamentation.

surement of the HOKE terms. From a practical point of view, the transition between the regimes corresponds to the equality of the contributions of plasma and HOKE to defocusing ( $\bar{\xi} = 1$ ). The historical trend over the last 10 years includes a substantial shortening of the pulses, from 100–200 fs in the late 1990s and early 2000s to  $\sim 30$  fs nowadays. According to our results, this shortening corresponds to a transition between “long” and “short” pulses, i.e., from plasma- to HOKE-regularized filaments, which might explain why HOKE had been considered marginal up to now.

#### 4. CONCLUSIONS

As a conclusion, we have discussed the details of the recent measurement of the HOKE indices [9] and excluded a range of potential artifacts, confirming the reliability of these experimental data. Furthermore, we have shown that, due to different temporal and spectral dynamics of the plasma- and HOKE-induced defocusing, the former should be dominant for long pulses at short-wavelengths, while the latter will dominate for short pulses at long wavelengths. We therefore suggest that the controversy about the mechanism of filamentation should turn from a qualitative discussion of which effect dominates, to a more quantitative discussion about the domains of relevance of each process.

#### ACKNOWLEDGMENTS

This work was supported by the Conseil Régional de Bourgogne, the ANR *COMOC*, the *FASTQUAST* ITN Program of the 7th FP and the Swiss NSF (contracts 200021-125315 and 200021-125315-2).

#### REFERENCES

1. J. Kasparian, M. Rodriguez, G. Méjean, J. Yu, E. Salmon, H. Wille, R. Bourayou, S. Frey, Y.-B. André, A. Mysyrowicz, R. Sauerbrey, J.-P. Wolf, and L. Wöste, *Science* **301**, 61 (2003).

2. J. Kasparian, R. Ackermann, Y.-B. André, G. Méchain, G. Méjean, B. Prade, P. Rohwetter, E. Salmon, K. Stelmaszczyk, J. Yu, A. Mysyrowicz, R. Sauerbrey, L. Wöste, and J.-P. Wolf, *Opt. Express* **16**, 5757 (2008).
3. P. Rohwetter, J. Kasparian, K. Stelmaszczyk, Z. Hao, S. Henin, N. Lascoux, W. M. Nakaema, Y. Petit, M. Queißer, R. Salamé, E. Salmon, L. Wöste, and J.-P. Wolf, *Nature Photon.* **4**, 451 (2010).
4. S. Tzortzakis, G. Méchain, G. Pantalano, Y. B. André, B. Prade, M. Franco, A. Mysyrowicz, J. M. Munier, M. Gheudin, G. Beaudin, and P. Encrenaz, *Opt. Lett.* **27**, 1944 (2002).
5. S. L. Chin, S. A. Hosseini, W. Liu, Q. Luo, F. Théberge, N. Aközbebek, A. Becker, V. P. Kandidov, O. G. Kosareva, and H. Schröder, *Can. J. Phys.* **83**, 863 (2005).
6. L. Bergé, S. Skupin, R. Nuter, J. Kasparian, and J.-P. Wolf, *Rep. Prog. Phys.* **70**, 1633 (2007).
7. A. Couairon and A. Mysyrowicz, *Phys. Rep.* **441**, 47 (2007).
8. J. Kasparian and J.-P. Wolf, *Opt. Express* **16**, 466 (2008).
9. V. Loriot, E. Hertz, O. Faucher, and B. Lavorel, *Opt. Express* **17**, 13429 (2009); *Opt. Express* **18**, 3011(E) (2010).
10. P. Béjot, J. Kasparian, S. Henin, V. Loriot, T. Vieillard, E. Hertz, O. Faucher, B. Lavorel, and J.-P. Wolf, *Phys. Rev. Lett.* **104**, 103903 (2010).
11. W. Ettoumi, P. Béjot, Y. Petit, V. Loriot, E. Hertz, O. Faucher, B. Lavorel, J. Kasparian, and J. Wolf, *Phys. Rev. A* **82**, 033826 (2010).
12. N. Aközbebek, M. Scalora, C. M. Bowden, and S. L. Chin, *Opt. Commun.* **191**, 353 (2001).
13. A. Vinçotte and L. Bergé, *Phys. Rev. A* **70**, 061802(R) (2004).
14. G. Fibich and B. Ilan, *Opt. Lett.* **29**, 887 (2004).
15. L. Bergé, S. Skupin, G. Méjean, J. Kasparian, J. Yu, S. Frey, E. Salmon, and J. P. Wolf, *Phys. Rev. E* **71**, 016602 (2005).
16. J.-F. Zhang, Q. Tian, Y.-Y. Wang, C.-Q. Dai, and L. Wu, *Phys. Rev. A* **81**, 023832 (2010).
17. M. Kolesik, E. M. Wright, and J. V. Moloney, *Opt. Lett.* **35**, 2550 (2010).
18. P. Polynkin, M. Kolesik, E. M. Wright, and J. V. Moloney, arXiv:1010.2303v1 [physics.optics] (2010).
19. A. Teleki, E. M. Wright, and M. Kolesik, *Phys. Rev. A* **82**, 065801 (2010).
20. J. Kasparian, R. Sauerbrey, and S. L. Chin, *Appl. Phys. B* **71**, 877 (2000).
21. A. Becker, N. Aközbebek, K. Vijayalakshmi, E. Oral, C. M. Bowden, and S. L. Chin, *Appl. Phys. B* **73**, 287 (2001).
22. H. Stapelfeldt and T. Seideman, *Rev. Mod. Phys.* **75**, 543 (2003).
23. T. Seideman, *Phys. Rev. Lett.* **83**, 4971 (1999).
24. F. Rosca-Pruna and M. J. J. Vrakking, *Phys. Rev. Lett.* **87**, 153902 (2001).
25. V. Renard, M. Renard, A. Rouzé, S. Guérin, H. R. Jauslin, B. Lavorel, and O. Faucher, *Phys. Rev. A* **70**, 033420 (2004).
26. V. Renard, M. Renard, S. Guérin, Y. T. Pashayan, B. Lavorel, O. Faucher, and H. R. Jauslin, *Phys. Rev. Lett.* **90**, 153601 (2003).
27. A. Rouzé, V. Renard, B. Lavorel, and O. Faucher, *J. Phys. B* **38**, 2329 (2005).
28. V. Loriot, P. Tzallas, E. P. Benis, E. Hertz, B. Lavorel, D. Charalambidis, and O. Faucher, *J. Phys. B* **40**, 2503 (2007).
29. R. W. Boyd, *Nonlinear Optics*, 3rd ed. (Academic, Boston, 2008).
30. J. R. Lalanne, A. Ducasse, and S. Kielich, *Laser-Molecule Interaction: Laser Physics and Molecular Nonlinear Optics* (Wiley, New York, 1996).
31. J. Arabat and J. Etchepare, *J. Opt. Soc. Am. B* **10**, 2377 (1993).
32. P. Béjot, Y. Petit, L. Bonacina, J. Kasparian, M. Moret, and J.-P. Wolf, *Opt. Express* **16**, 7564 (2008).
33. Y. Petit, P. Béjot, L. Bonacina, J. Kasparian, M. Moret, and J.-P. Wolf, *Laser Phys.* **19**, 336 (2009).
34. C. Marceau, S. Ramakrishna, S. Génier, T.-J. Wang, Y. Chen, F. Théberge, M. Châteauneuf, J. Dubois, T. Seideman, and S. L. Chin, *Opt. Commun.* **283**, 2732 (2010).
35. S. Tzortzakis, B. Prade, M. Franco, and A. Mysyrowicz, *Opt. Commun.* **181**, 123 (2000).
36. P. Sprangle, E. Esarey, and B. Hafizi, *Phys. Rev. E* **56**, 5894 (1997).
37. A. Talebpour, J. Yang, and S. L. Chin, *Opt. Commun.* **163**, 29 (1999).
38. M. Nurhuda, A. Suda, and K. Midorikawa, *Phys. Rev. A* **66**, 041802 (2002).
39. M. Nurhuda, A. Suda, and K. Midorikawa, *New J. Phys.* **10**, 053006 (2008).
40. C. Brée, A. Demircan, and G. Steinmeyer, "Saturation of the All-Optical Kerr Effect," WIAS Preprint no 1540 (2010), available from [http://www.wias-berlin.de/preprint/1540/wias\\_preprints\\_1540.pdf](http://www.wias-berlin.de/preprint/1540/wias_preprints_1540.pdf) (to be published in *Phys. Rev. Lett.*).
41. P. B. Corkum, *Phys. Rev. Lett.* **71**, 1994 (1993).
42. J. Itatani, J. Levesque, D. Zeidler, H. Niikura, H. Pepin, J. C. Kieffer, P. B. Corkum, and D. M. Villeneuve, *Nature* **432**, 867 (2004).
43. A. Dogariu, T. Xia, D. J. Hagan, A. A. Said, E. W. Van Stryland, and N. Bloembergen, *J. Opt. Soc. Am. B* **14**, 796 (1997).
44. C. Minhaeng, D. Mei, N. F. Scherer, G. R. Fleming, and S. Mukamel, *J. Chem. Phys.* **99**, 2410 (1993).
45. B. Lavorel, O. Faucher, M. Morgen, and R. Chaux, *J. Raman Spectrosc.* **31**, 77 (2000).
46. S. Smolorz and F. Wise, *J. Opt. Soc. Am. B* **17**, 1636 (2000).
47. A. Dubietis, E. Gaizauskas, G. Tamosauskas, and P. D. Trapani, *Phys. Rev. Lett.* **92**, 253903 (2004).
48. W. Ettoumi, Y. Petit, J. Kasparian, and J.-P. Wolf, *Opt. Express* **18**, 6613 (2010).

## Influence of pulse duration, energy, and focusing on laser-assisted water condensation

Y. Petit,<sup>1</sup> S. Henin,<sup>1</sup> J. Kasparian,<sup>1,a)</sup> J. P. Wolf,<sup>1</sup> P. Rohwetter,<sup>2</sup> K. Stelmaszczyk,<sup>2</sup> Z. Q. Hao,<sup>2</sup> W. M. Nakaema,<sup>2</sup> L. Wöste,<sup>2</sup> A. Vogel,<sup>3</sup> T. Pohl,<sup>3</sup> and K. Weber<sup>3</sup>

<sup>1</sup>*Teramobile, GAP, Université de Genève, 20 rue de l'École de Médecine, CH-1211 Genève 4, Switzerland*

<sup>2</sup>*Teramobile, Institut für Experimentalphysik, Freie Universität Berlin, Arnimallee 14, D-14195 Berlin, Germany*

<sup>3</sup>*Department of Mechanical and Process Engineering, Environmental Measurement Techniques, University of Applied Sciences, Düsseldorf, Josef-Gockeln-Str. 9, D-40474 Dusseldorf, Germany*

(Received 15 November 2010; accepted 5 January 2011; published online 26 January 2011)

We investigate the influence of laser parameters on laser-assisted water condensation in the atmosphere. Pulse energy is the most critical parameter. Nanoparticle generation depends linearly on energy beyond the filamentation threshold. Shorter pulses are more efficient than longer ones with saturation at  $\sim 1.5$  ps. Multifilamenting beams appear more efficient than strongly focused ones in triggering the condensation and growth of submicronic particles, while polarization has a negligible influence on the process. The data suggest that the initiation of laser-assisted condensation relies on the photodissociation of the air molecules rather than on their photoionization. © 2011 American Institute of Physics. [doi:10.1063/1.3546172]

Self-guided filaments<sup>1–5</sup> generated by ultrashort laser pulses have recently been proposed as candidates to assist the condensation of water in the atmosphere<sup>6</sup> as an alternative to cloud seeding by dispersing small particles of carbonic ice, AgI, or salts.<sup>7</sup> The mechanism behind laser-assisted condensation most probably relies on photochemically activated processes, implying binary H<sub>2</sub>O-HNO<sub>3</sub> nucleation. Indeed, it was recently discovered that O<sub>3</sub>, NO, and NO<sub>2</sub> are generated in laser filaments in amounts largely sufficient to produce HNO<sub>3</sub> in the multi-ppm range.<sup>8</sup> Besides unveiling the mechanism of the phenomenon, the influence of the laser parameters is a key question for maximizing it and thus for obtaining macroscopic effects in the atmosphere.

In this work, we investigate *in situ* a wide range of laser energies (0–165 mJ), pulse durations (240 fs–3.3 ps), polarizations (linear and circular), and beam geometry (strong and loose focusing) and characterize their influence on filament-induced water condensation in the atmosphere. We show that pulse energy, and to a lesser extent pulse duration, strongly affects the particle yield. In contrast, the impact of focusing is moderate, while the polarization of the incident beam has little influence on the particle generation efficiency. The different dependences of laser-induced condensation and ionization suggest that the activation of laser-assisted condensation relies on the photodissociation of the air molecules rather than their photoionization.

Experiments were performed under atmospheric conditions of 8–12 °C and 66%–80% relative humidity on the shore of the Rhône River close to Geneva (46°12' North, 6°5' East, and 380 m above sea level). This location was chosen to take benefit of the relatively warm water flow from the Lake of Geneva acting as a heat buffer, resulting in a local humidity enhancement.

Water vapor condensation was initiated by the *Teramobile* mobile femtosecond-terawatt laser system,<sup>9</sup> providing up

to 165 mJ pulses of 240 fs duration at a central wavelength of 800 nm and a repetition rate of 10 Hz. The beam was expanded to a 10 cm diameter and slightly focused by a built-in expanding telescope. After  $\sim 15$  m of horizontal propagation 1.2 m above ground, the beam generated about 10 filaments in the atmosphere at the nonlinear focus. Alternatively, the beam was strongly focused on the measurement region using a  $f=1$  m lens.

Energy was attenuated by a half-wave plate associated with a polarizer inserted at the output of the main amplifier ahead of the compressor. The polarization was switched from linear to circular by a quarter-wave plate installed at the compressor exit. Furthermore, the pulse duration was adjusted by varying the distance between the gratings of the laser compressor so as to impose a linear chirp on the laser pulses, as described earlier.<sup>9</sup>

The measurements focused on the most intense filamenting region, which was shielded from external wind by an open protection chamber. The efficiency of the laser in aerosol generation was characterized by measuring the aerosol size distribution and number density with an aerosol spectrometer (Grimm 1.107, Grimm Aerosol Technik GmbH & Co., Germany) sampling at a 2 cm distance from the laser filaments. This device measured the size distribution in 31 classes from 250 nm to 32  $\mu$ m diameter. It was coupled with a nanoparticle sensor (Grimm Nanocheck 1.320, Grimm Aerosol Technik GmbH & Co., Germany). Alternating measurements in the filament-free atmosphere provided the particle background number density as a reference. Cross-check measurements using a condensation particle counter (TSI Model 3007, TSI Incorporated, Minnesota) allowed us to ensure that this measurement is free from artifacts due, e.g., to the electric charge deposited by the filaments on the particles.<sup>10</sup> Simultaneously, the measurement of the shock-wave by a sonometric setup described in detail before provided an estimation of the ionization of the air.<sup>11</sup> When relevant, the statistical significance of the difference between experimental conditions was assessed by performing a Stu-

<sup>a)</sup>Electronic mail: jerome.kasparian@unige.ch.

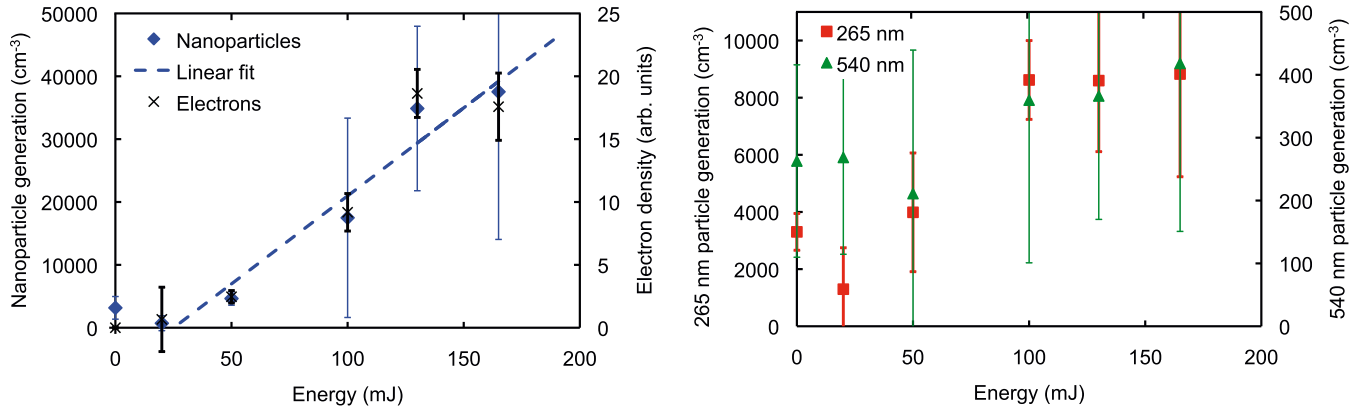


FIG. 1. (Color online) Energy dependence of the generation of (a) nanometric (25 nm) and (b) submicrometric particles by laser pulses of 240 fs duration. Atmospheric conditions are 80% relative humidity and 12 °C. Error bars display the standard deviation on three experimental realizations for each point. The linear fit on panel (a) evidences the linear dependence of the nanometric particle generation on the input energy.

dent test providing the risk  $\alpha$  that the two results are due to Gaussian sampling fluctuations.<sup>12</sup>

As shown in Fig. 1(a), the generation of nanoparticles (20–300 nm) depends almost linearly on the incident pulse energy, above a threshold of 25 mJ corresponding to the filamentation threshold in our conditions. This linear dependence is evidenced by the agreement ( $R^2=0.95$ ) of the linear fit (dashed curve) with the experimental data in spite of their error bars. This agreement is not further improved by considering higher-order polynomials. The energy dependence of the nanoparticles is parallel to that of the free electron release and stems from the linear scaling of the filament number, and hence of the active volume, with the incident power.<sup>13</sup> The effect of the laser on the concentration of larger particles (250–500 nm) depends less on energy [Fig. 1(b)], consistent with the fact that the growth of these particles, which is governed by diffusion-limited condensation, is limited not only by the presence of condensation nuclei but also by the available water vapor contents in the atmosphere around them.

The laser-assisted generation of nanometric particles on the chirp does not depend on the sign of the chirp but only on the pulse duration. This dependence displays two regimes (Fig. 2). Under up to  $\sim 1.5$  ps, it decreases regularly parallel to the electron release. Beyond this pulse duration, the particle generation efficiency stabilizes while the electron generation continues to decrease. Submicronic particles typically exhibit the same variation, although the measurement uncertainty is larger due to lower particle densities in those size classes (Fig. 2(b)). The decoupling between the efficiencies of nanoparticle generation and ionization suggests that the initiation of the laser action relies on photodissociative processes rather than the photoionization of the molecules of the

air. These photodissociative processes generate ozone and NO<sub>2</sub> from the molecules of the air, subsequently releasing HNO<sub>3</sub> in the atmosphere. Only seven photons are required to photodissociate N<sub>2</sub>, as compared with 11 photons to ionize it into N(<sup>2</sup>D<sup>0</sup>)+N(<sup>4</sup>S<sup>0</sup>).<sup>14,15</sup> Photodissociation, therefore, depends less on the intensity than photoionization, allowing its efficiency to decrease less for longer pulses. Conversely, attachment contributes to decreasing the electron density beyond a few picoseconds. Note that the ionization of the condensed particles contributes negligibly to the total charge.<sup>10</sup>

In the considered atmospheric conditions, the incident polarization has little influence, if any, on the laser-assisted condensation process (Fig. 3) within the uncertainty of the measurement: The difference between the linear and circular polarization is not statistically significant (within  $\alpha \leq 0.025$ ) for any size class. As a consequence, the ratio of the effect of pulses with both polarizations lies close to unity. This result can be understood by considering that circular polarization yields less filaments,<sup>16,17</sup> which are, however, longer and more intense,<sup>18</sup> so that the overall efficiency is little affected.

Finally, as displayed in Fig. 4, a loosely focused beam allowing multiple filamentation yields up to 2.5 times more particles of 400 nm than its strongly focused counterpart. The analysis of 12 realizations of the same experiment shows that this difference is statistically significant up to 600 nm but vanishes for larger particles due to the small particle counts. In particular, the apparent larger yield of particles in the 2–3  $\mu$ m region may very well be an artifact due to sampling fluctuations.

The higher efficiency of filaments may appear surprising at first sight, considering the high nonlinearity of the processes at play and the fact that the intensity is clamped to

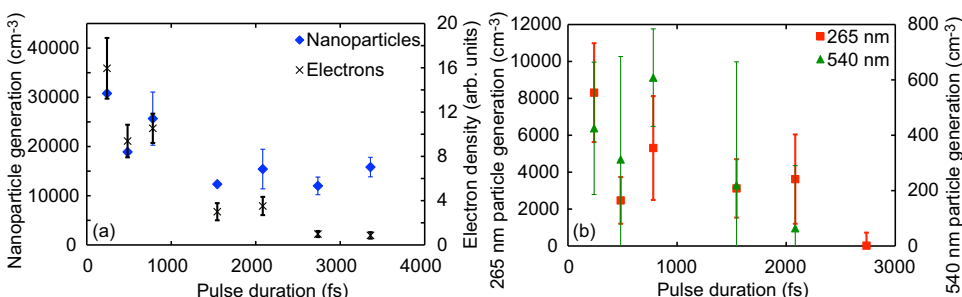


FIG. 2. (Color online) Pulse duration dependence of the generation of (a) nanometric (25 nm) and (b) submicrometric particles by laser pulses of 150 mJ. Atmospheric conditions are 90%–96% relative humidity and 8 °C. Error bars display the standard deviation on three measurements.

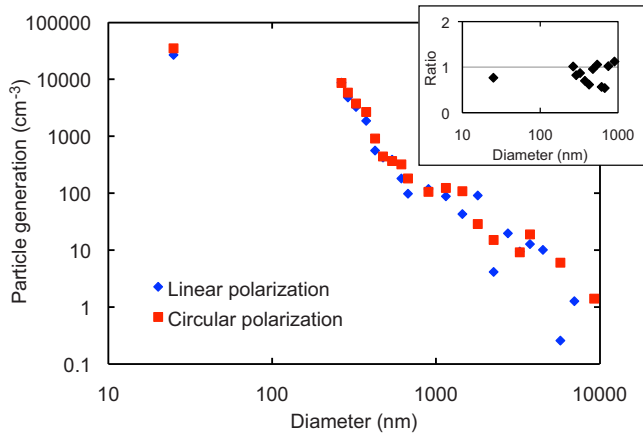


FIG. 3. (Color online) Effect of the laser filaments on the particle concentration for linear and circular incident polarizations of a 130 mJ and 240 fs pulse. Atmospheric conditions are 12 °C and 80% relative humidity. Inset: Ratio of the two curves from the main panel.

$\sim 5 \times 10^{13} \text{ W/cm}^2$ .<sup>19,20</sup> For example, the focused beam yields three to 20 times more free electrons than its multifilamenting counterpart. However, the  $\sim 10$  filaments in the latter activate a much larger volume than the strongly focused beam does. Besides the filament volume of 50 mm<sup>3</sup>, the active species like HNO<sub>3</sub> generated by the filaments spread around them and activate the surrounding volume. This more spread volume also contains a larger amount of water vapor and is therefore more favorable to the diffusion-limited growth of the particles.

As a conclusion, after investigating laser-induced water vapor nucleation in the real atmosphere under various laser conditions, we observed that both the nucleation of nanoparticles and their growth to submicrometric sizes strongly depend on the incident energy with a linear dependence beyond

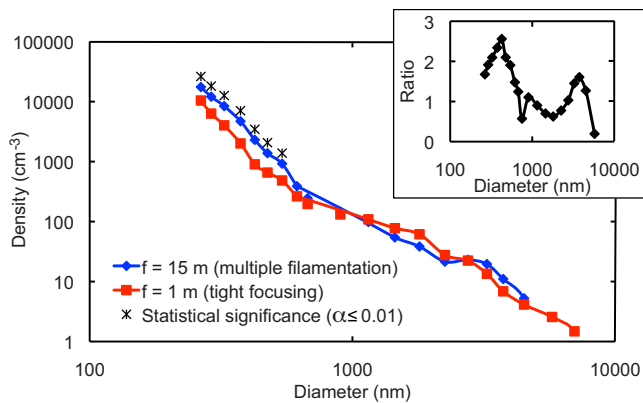


FIG. 4. (Color online) Comparison of the efficiencies of tight ( $f=1$  m) and loose ( $f=15$  m, leading to multiple filamentation) laser pulses of 150 mJ for 240 fs. Atmospheric conditions are 66% relative humidity and 12 °C. Inset: Ratio of the two curves from the main panel.

the threshold of filamentation. Shorter pulses appear to be more efficient in assisting condensation, although the efficiency stabilizes above 1.5 ps. The polarization showed no influence on the efficiency, while the wider volume of a multifilamenting beam appears to be more favorable to the generation of droplets up to 600 nm. The discrepancy between the behaviors of the particle generation and ionization suggest that the first steps of laser-assisted condensation rely more on photodissociation than on photoionization of the air molecules. These results are of key interest to dimension laser systems to optimize laser-assisted condensation.

This work was supported by the Deutsche Forschungsgemeinschaft and the Fonds National Suisse de la Recherche Scientifique (FNS Grant Nos. 200021-125315 and 200021-125315-2).

<sup>1</sup>J. Kasparian, M. Rodriguez, G. Méjean, J. Yu, E. Salmon, H. Wille, R. Bourayou, S. Frey, Y.-B. André, A. Mysyrowicz, R. Sauerbrey, J.-P. Wolf, and L. Wöste, *Science* **301**, 61 (2003).

<sup>2</sup>A. Couairon and A. Mysyrowicz, *Phys. Rep.* **441**, 47 (2007).

<sup>3</sup>L. Bergé, S. Skupin, R. Nuter, J. Kasparian, and J.-P. Wolf, *Rep. Prog. Phys.* **70**, 1633 (2007).

<sup>4</sup>J. Kasparian and J.-P. Wolf, *Opt. Express* **16**, 466 (2008).

<sup>5</sup>S. L. Chin, S. A. Hosseini, W. Liu, Q. Luo, F. Théberge, N. Aközbe, A. Becker, V. P. Kandidov, O. G. Kosareva, and H. Schröder, *Can. J. Phys.* **83**, 863 (2005).

<sup>6</sup>P. Rohwetter, J. Kasparian, K. Stelmasczyk, Z. Hao, S. Henin, N. Lascoux, W. M. Nakaema, Y. Petit, M. Queißer, R. Salamé, E. Salmon, L. Wöste, and J.-P. Wolf, *Nat. Photonics* **4**, 451 (2010).

<sup>7</sup>I. Langmuir, *Science* **106**, 505 (1947).

<sup>8</sup>Y. Petit, S. Henin, J. Kasparian, and J.-P. Wolf, *Appl. Phys. Lett.* **97**, 021108 (2010).

<sup>9</sup>H. Wille, M. Rodriguez, J. Kasparian, D. Mondelain, J. Yu, A. Mysyrowicz, R. Sauerbrey, J.-P. Wolf, and L. Wöste, *Eur. Phys. J.: Appl. Phys.* **20**, 183 (2002).

<sup>10</sup>S. Henin, Y. Petit, D. Kiselev, J. Kasparian, and J.-P. Wolf, *Appl. Phys. Lett.* **95**, 091107 (2009).

<sup>11</sup>J. Yu, D. Mondelain, J. Kasparian, E. Salmon, S. Geffroy, C. Favre, V. Boutou, and J.-P. Wolf, *Appl. Opt.* **42**, 7117 (2003).

<sup>12</sup>W. H. Press, S. A. Teukolsky, W. T. Vetterling, and B. P. Flannery, *Numerical Recipes in C: The Art of Scientific Computing* (Cambridge University Press, Cambridge, England, 1992).

<sup>13</sup>G. Méjean, J. Kasparian, J. Yu, E. Salmon, S. Frey, J.-P. Wolf, S. Skupin, A. Vinçotte, R. Nuter, S. Champeaux, and L. Bergé, *Phys. Rev. E* **72**, 026611 (2005).

<sup>14</sup>P. G. Richards, D. G. Torr, and M. R. Torr, *J. Geophys. Res.* **86**, 1495 (1981).

<sup>15</sup>E. C. Zipf, P. J. Espy, and C. F. Boyle, *J. Geophys. Res.* **85**, 687, DOI:10.1029/JA085iA02p00687 (1980).

<sup>16</sup>G. Fibich and B. Ilan, *Phys. Rev. E* **67**, 036622 (2003).

<sup>17</sup>L. Bergé, C. Gouédard, J. Schjødt-Eriksen, and H. Ward, *Physica D* **176**, 181 (2003).

<sup>18</sup>S. Petit, A. Talebpour, A. Proulx, and S. L. Chin, *Opt. Commun.* **175**, 323 (2000).

<sup>19</sup>J. Kasparian, R. Sauerbrey, and S. L. Chin, *Appl. Phys. B: Lasers Opt.* **71**, 877 (2000).

<sup>20</sup>A. Becker, N. Aközbe, K. Vijayalakshmi, E. Oral, C. M. Bowden, and S. L. Chin, *Appl. Phys. B: Lasers Opt.* **73**, 287 (2001).

**1-J white-light continuum from 100-TW laser pulses**

Yannick Petit,<sup>1</sup> Stefano Henin,<sup>1</sup> Walter M. Nakaema,<sup>2</sup> Pierre Béjot,<sup>1</sup> Axel Jochmann,<sup>3</sup> Stephan D. Kraft,<sup>3</sup> Stefan Bock,<sup>3</sup> Ulrich Schramm,<sup>3</sup> Kamil Stelmaszczyk,<sup>2</sup> Philipp Rohwetter,<sup>2</sup> Jérôme Kasparian,<sup>1,\*</sup> Roland Sauerbrey,<sup>3</sup> Ludger Wöste,<sup>2</sup> and Jean-Pierre Wolf<sup>1</sup>

<sup>1</sup>*Teramobile, GAP, Université de Genève, 20 rue de l'Ecole de Médecine, CH-1211 Genève 4, Switzerland*

<sup>2</sup>*Teramobile, Institut für Experimentalphysik, Freie Universität Berlin, Arnimallee 14, D-14195 Berlin, Germany*

<sup>3</sup>*Forschungszentrum Dresden-Rossendorf, Bautzener Landstraße 400, D-01328, Germany*

(Received 10 November 2010; published 7 January 2011)

We experimentally measured the supercontinuum generation using 3-J, 30-fs laser pulses and measured white-light generation at the level of 1 J. Such high energy is allowed by a strong contribution to the continuum by the photon bath, as compared to the self-guided filaments. This contribution due to the recently observed congestion of the filament number density in the beam profile at very high intensity also results in a wider broadening for positively chirped pulses rather than for negatively chirped ones, similar to broadening in hollow-core fibers.

DOI: [10.1103/PhysRevA.83.013805](https://doi.org/10.1103/PhysRevA.83.013805)

PACS number(s): 42.65.Jx, 42.65.Ky

**I. INTRODUCTION**

The propagation of ultrashort laser pulses in air or other transparent media is characterized by filamentation [1–5], a propagation regime where a dynamical balance is established between Kerr self-focusing and defocusing by further nonlinear processes. The plasma generated at the nonlinear focus is generally considered as the main process in that regard, although we recently suggested that the higher-order Kerr effect could play this role [6], in particular for longer wavelengths [7] and/or shorter pulses [8]. Filamentation is now well characterized from the mJ, GW level to the sub-J, TW levels, with potential major atmospheric applications such as lightning triggering and control or laser-induced condensation [9,10].

Recently, we demonstrated that filamentation still occurs at multi-J levels [11], with similar physics as at lower powers. However, at intensities above  $1-2 \times 10^{11}$  W/cm<sup>2</sup>, we observed a change in the spatial dynamics of multifilamentation [12]. Below this threshold, the number of filaments is proportional to the incident power  $P$ , one filament being generated per  $5-7P_{\text{cr}}$  available in the incident pulse [13]. The critical power for filamentation  $P_{\text{cr}}$ , which is close to 3 GW in air at 800 nm, is the minimum incident power required for the self-focusing to balance diffraction. In this regime, filaments are typically 100–1000 times more intense than the surrounding photon bath ( $5 \times 10^{13}$  W/cm<sup>2</sup> [14,15] vs some  $10^{10}$  W/cm<sup>2</sup>) and roughly concentrate 10% of the total beam fluence although covering only a few  $10^{-4}$  of the total beam surface [2,3]. As a consequence of such difference in intensity levels, the contribution of filaments to the nonlinear behavior of the beam is so dominant that the contribution of the photon bath can be fully neglected.

In contrast, above  $1-2 \times 10^{11}$  W/cm<sup>2</sup>, the filament number is governed by the surface of the beam profile. As a consequence, filaments cover a constant fraction of the beam surface. Since their intensity is still clamped, the fraction of the beam fluence carried by the filaments decreases, the photon bath intensity increases. It can even exceed the TW/cm<sup>2</sup>

level, reducing the intensity ratio between the filaments and the bath to one order of magnitude [12]. Furthermore, filaments have been observed to be connected by regions of higher intensity within the photon bath. In this regime, a substantial contribution of the photon bath to the nonlinearity can therefore be expected.

In this article, we investigate the spectral broadening along the horizontal propagation of a 3-J, 100-TW laser pulse over 42 m in air. We measure a conversion efficiency of several tens of percentage points, resulting in up to 1 J of white-light continuum. Furthermore, in this high-intensity regime, the effect of the chirp is opposite to the standard behavior in the usual low-intensity filamentation regime, but rather comparable to that observed in hollow-core fibers, where a positive chirp yields more spectral broadening than a negative one [16,17]. Finally, we observe a line at 771 nm, which we interpret as a Rabi-shifted oxygen atomic multiplet OI line.

**II. EXPERIMENTAL SETUP**

Experiments were performed using the Ti:Sa chirped-pulse amplification (CPA) chain of the Forschungszentrum Dresden-Rossendorf providing up to 3-J, 100-TW pulses of 30 fs duration, at the repetition rate of 10 Hz and central wavelength of 800 nm. The initial spectrum was 60 nm broad (full width at half maximum). The pulse energy was adjusted by using a half-wave plate and a polarizer before the grating compressor. The pulses were transported in a vacuum tube to a 42-m-long experimental hall, where they were launched into air, collimated (i.e., as a parallel beam) with a diameter of  $\sim 10$  cm, through a 6-mm-thick fused silica window. Detuning the compressor allowed us to impose a chirp onto the pulses. In the following, the chirp values always refer to the exit of the output window.

The pulses underwent multiple filamentation in the high-intensity regime, as described in detail elsewhere [12], that is, with a relatively low filament number as compared with the available power, and a high photon bath intensity. The beam-averaged spectrum was collected on a diffusive screen using a 10- $\mu\text{m}$  core fiber of 25° aperture (full angle), fixed 50 cm away from the screen. It was analyzed by an OceanOptics USB4000 spectrometer providing 0.27-nm resolution over the

\*jerome.kasparian@unige.ch

200-to-1100-nm range. Spectral calibration of the spectrometer was checked to be better than 1 nm for two specific wavelengths of HeNe laser at 632.8 nm and frequency-doubled Nd:YAG laser at 532 nm. The spectra were numerically averaged over two to three single-shot acquisitions and corrected by the spectral response of the spectrometer.

We quantitatively characterized the spectral broadening using three independent approaches: (i) the full width at  $1/e^2$ ; (ii) the second moment of the intensity distribution; and (iii) the efficiency of the supercontinuum generation, that is, the ratio of the energy in the continuum ( $\lambda < 765$  nm and  $\lambda > 845$  nm) to the total incident pulse energy. These three approaches yielded similar results and dependencies, so that in the following we mainly focus on the generation efficiency.

The analysis of the experimental data was supported by numerical simulations of the output spectrum after the pulse propagation. In order to compare the respective contributions of the photon bath and the filaments to the spectral broadening, we independently investigated two regimes. In the first one, we considered a photon bath without filamentation, by performing  $1D + 1$  (propagation distance and time) simulations based on the unidirectional pulse propagation equation described in Ref. [18]. In the second regime, we simulated a filamenting beam in a  $2D + 1$  (propagation distance, radial distance, and time) propagation model based on the nonlinear Schrödinger equation as detailed in [7].

### III. RESULTS AND DISCUSSION

The afore-mentioned limited number of filaments, relative to the incident power of the laser pulses, could have been expected to reduce the white-light generation efficiency. However, we do not observe such reduction. Rather, the white-light generation appears quite as efficient as in previous experiments in the low-intensity regime (300 mJ, 100 fs) using the Teramobile laser [19] (Fig. 1).

In particular, in the present experiment, the exponential decrease on the wings of the spectrum is comparable with that of the spectrum in experiments at lower intensity [19] (130 nm/decade vs 140 nm/decade on the blue side of the spectrum). Still, considering the incident energy in the present work, the comparable conversion efficiency of several tens of percentage points (see Fig. 3) results in an unprecedented supercontinuum energy of up to the joule level.

We also observed that the filament number appears to have very little influence on the white-light conversion efficiency and that positive chirps are more favorable to spectral broadening than negative ones. As shown in Figs. 2 and 3, at a fixed energy or power, the more positive chirps (+100 fs) yield up to twice as much spectral broadening as its negative counterpart. This finding is unexpected since (i) the supercontinuum is generally considered to originate from the filaments, and (ii) negative chirps lead to self-compression due to group-velocity dispersion and are expected to yield a higher peak power and thus to generate more white-light by increasing the temporal variations of the intensity, as well as by favoring the formation of filaments. For example, 100-fs negatively chirped pulses result in almost Fourier-limited pulses after 42 m of propagation. In contrast, positively chirped pulses spread temporally all along their propagation.

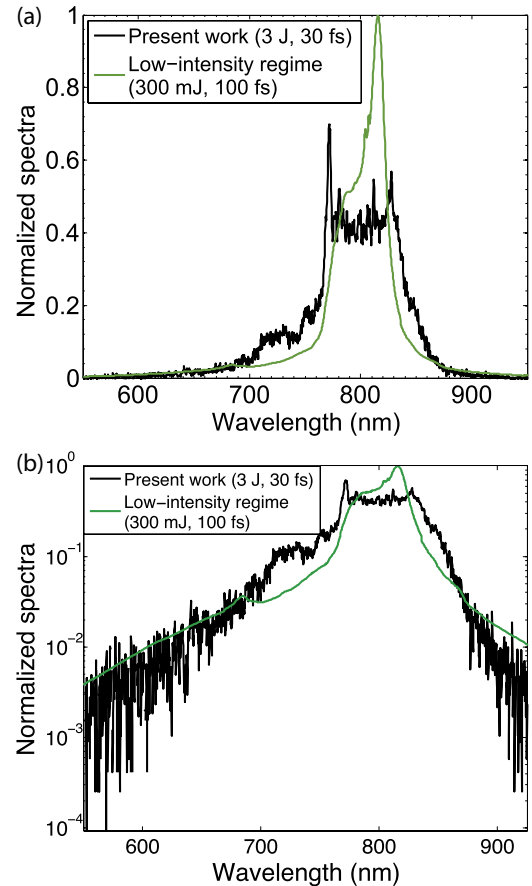


FIG. 1. (Color online) Efficiency of the white-light generation by a 2.53-J, 30-fs, Fourier-limited laser pulse in 10-cm beam diameter after 42 m of propagation, and by the Teramobile laser (300 mJ, 100 fs in 5-cm beam diameter) after the filamenting region ( $z \sim 40$  m) [19]. Both spectra are normalized to their total area: (a) linear scale; (b) logarithmic scale.

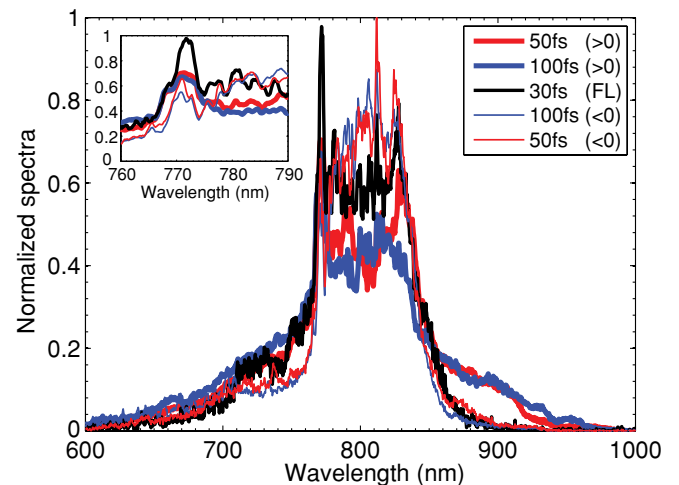


FIG. 2. (Color online) Spectra generated after 42-m propagation of a 2.53-J pulse of 30-fs Fourier-limited (FL) duration and the same pulse both positively and negatively chirped (50- and 100-fs pulse durations). All spectra have the same normalization factor, so that their amplitudes can be compared. (Inset) Blowup of the 760-to-790-nm spectral region, exhibiting a peak at 771.5 nm for Fourier-limited and positively chirped pulses.

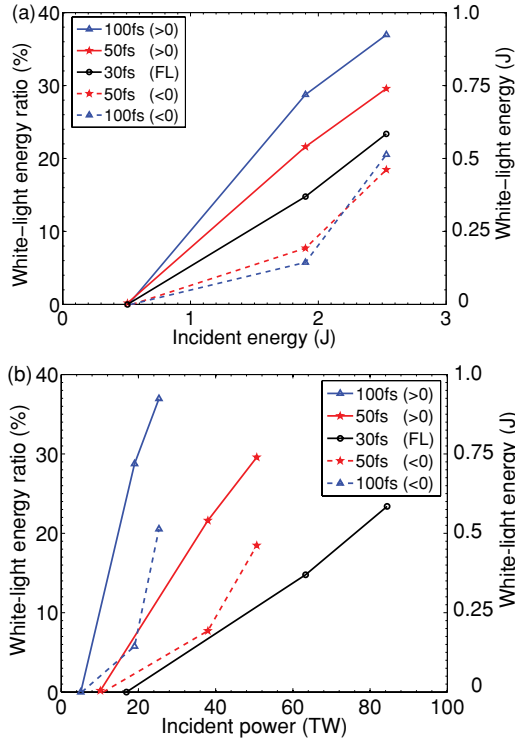


FIG. 3. (Color online) Conversion efficiency and corresponding energy of the white-light continuum after 42-m propagation of a 2.53-J pulse, as a function of incident pulse energy (a) and power (b). The continuum is defined as the spectral range out of the 765-to-845-nm spectral range.

These observations can, however, be understood by considering the role of the photon bath in the white-light generation. A rough evaluation of this contribution can be obtained by considering the classical expression of the spectral broadening by self-phase modulation,

$$\frac{\Delta\omega}{\omega_0} = n_2 \frac{dI}{dt} \frac{z}{c}, \quad (1)$$

where  $\Delta\omega$  is the frequency shift,  $\omega_0$  is the incident frequency,  $n_2 = 1.1 \times 10^{-19} \text{ cm}^2/\text{W}$  [20] is the nonlinear refractive index of air,  $I$  is the incident intensity,  $z$  is the propagation distance, and  $c$  is the speed of light. After  $z = 42 \text{ m}$ , the intensity of the photon bath ( $I \sim 1 \text{ TW}/\text{cm}^2$  [12]) yields  $\Delta\omega/\omega_0 \sim 0.5$ , showing that the self-phase modulation of the photon bath yields sufficient spectral broadening to account for the spectra observed in our experiment. Note that the use of a larger value of  $n_2$  (e.g.,  $3.2 \times 10^{-19} \text{ cm}^2/\text{W}$  [2]) would result in an ever-wider broadening. This contribution can indeed be observed in real-color photographs of the beam on a screen (Fig. 4). It will even be enhanced on the high-intensity regions connecting the filaments.

Since the detection system collects light from the whole beam profile, the recorded spectrum can be considered, to the first order, as the weighted sum of the contributions from the photon bath and from the filaments. The weight of any portion of the beam profile  $S$  is the integral of the fluence over its area. In other words, the respective contributions of the filaments and the photon bath to the observed spectrum are roughly proportional to the total energy they respectively carry.

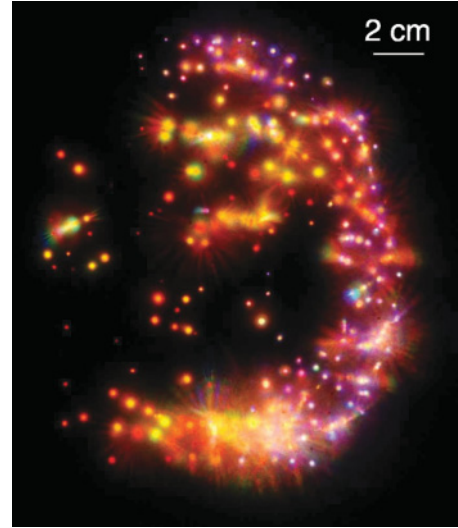


FIG. 4. (Color online) Beam profile on a screen of a 30-fs, 1.65-J pulse after 15-m propagation, that is, at the beginning of the filamenting region. The white contribution from the photon bath is clearly visible.

In our high-intensity regime, comparing the contributions to spectral broadening of 500 filaments of  $100 \mu\text{m}$  diameter and  $5 \times 10^{13} \text{ W}/\text{cm}^2$  with that of  $80 \text{ cm}^2$  of photon bath conveying  $1 \text{ TW}/\text{cm}^2$  yields an energy ratio of 98%/2% in favor of the photon bath. Furthermore, as discussed earlier, the latter is widely broadened. Therefore, in spite of their locally more efficient broadening, the filaments will provide a minor source of spectral broadening in this configuration.

In contrast, at lower intensity, for example, under the “low-intensity” conditions displayed in Fig. 1, the contribution of 50 filaments has to be compared with a bath typically conveying a few TW. In this case, the filaments bear  $\sim 10\%$  of the total beam power and will therefore contribute substantially to the overall spectrum. Furthermore, in the latter case the photon bath intensity of  $\sim 0.1 \text{ TW}/\text{cm}^2$  only allows a marginal relative spectral broadening within it. As a result, the photon bath contribution to the spectral broadening is marginal, as commonly observed in experiments at lower intensity [19].

Considering that the photon bath is the main source of spectral broadening provides a clear interpretation of our observation that positively chirped pulses efficiently generate white light. In the photon bath, especially over long propagation distances, the main nonlinearity at play is self-phase modulation (SPM), which shifts the leading edge of the pulse to longer wavelengths and the trailing edge to shorter wavelengths. In positively chirped pulses, the leading edge already bears the longer wavelengths, and the shorter wavelengths are on the trailing edge. This time-dependent frequency offset within the pulse is therefore reinforced by SPM. On the other hand, if the pulse is negatively chirped, SPM redshifts its blueshifted leading edge and blueshifts its redshifted trail. A positive chirp is therefore more favorable to the spectral broadening than a negative chirp. Our results show that, under our conditions, this effect overrides the pulse temporal recompression or spreading due to group-velocity dispersion.

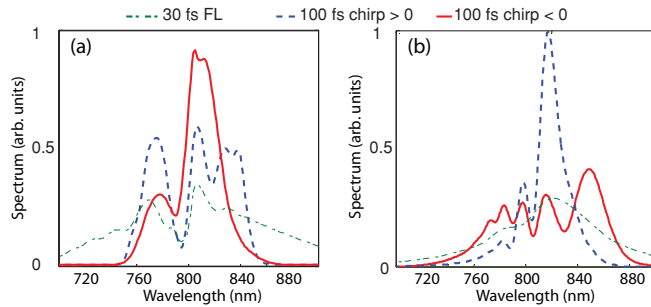


FIG. 5. (Color online) Simulated transversely integrated spectrum for pulses of 30 fs, Fourier-limited, and 100 fs, positively and negatively chirped. (a)  $1D + 1$ ,  $30 \text{ mJ/cm}^2$  ( $1 \text{ TW/cm}^2$  for 30-fs pulses); (b)  $2D + 1$ ,  $0.81 \text{ mJ}$  ( $9 P_{\text{cr}}$  for 30-fs pulses).

This mechanism leading to wider spectral broadening for positive chirps has already been observed in hollow-core fibers [16,17]. Indeed, supercontinuum generation by the photon bath can be expected to be an essentially one-dimensional problem, quite similar to propagation in a fiber. Such regime is also similar to the one observed in the case of two beams crossing each other in glass, where substantial SPM within the photon bath depleted the power available for filament generation and hence reduced the filament number [21].

Chirp therefore provides a convenient way of controlling the width of the supercontinuum generated by high-intensity laser pulses. Such control can be used to maximize the generated bandwidth, as is required, for example, for multispectral Lidar applications [1,4], but also to concentrate the white light over a restricted spectral region around the fundamental wavelength for specific applications [22].

The contrast between the high- and low-intensity regimes is illustrated in Fig. 5, which displays the simulated spectra generated by the photon bath and by a filamenting beam. In the  $1D + 1$  code, representative of the photon bath after 42 m propagation, with  $30 \text{ mJ/cm}^2$ , a positive chirp yields more broadening in the 750-to-850-nm spectral region in qualitative agreement with the experimental observations. However, the broader spectrum obtained for FT-limited pulses provides a conversion efficiency (as defined in Fig. 3) of 50%, vs 10% for 100-fs, positively chirped pulses and 5% for 100-fs, negatively chirped pulses, which does not quantitatively reproduce our experimental results. This deviation could be due to the fact that our model treats the photon bath as homogeneous, disregarding the interactions between the filaments, especially the higher-intensity strings along which they are organized [12]. However, adequately considering these structures would

require three-dimensional modeling of the full beam, which is well beyond our current computing capabilities.

In contrast, in the  $2D + 1$  simulation of a filamenting beam on a reduced scale compatible with computing capabilities ( $0.81 \text{ mJ}$ , i.e.,  $9 P_{\text{cr}}$  at 30 fs, propagation distance 1.5 m), the main effect of the chirp is to affect the well-known shift the central beam wavelength [23]. Furthermore, a negatively chirped pulse broadens the spectrum more efficiently than a positively chirped one. The chirp dependence of our experimental data regarding the spectral broadening therefore supports the preceding conclusion that the photon bath rather than the filaments provides the main contribution to the observed spectral broadening at the  $\text{TW/cm}^2$  intensity level investigated in the present work.

As shown in the inset of Fig. 2, our experimental data exhibit a sharp line at 771.5 nm. This line is clearly visible for Fourier-limited and positively chirped pulses, with up to a few percentage points of the total spectrum energy. It is much weaker for negative chirps. This line may be the oxygen atomic multiplet  $\text{OI}(3p^5P-3s^5S)$  centered at 777.4 nm in the plasma generated in air by the filaments [24,25]. This line would subsequently be Rabi-shifted due to the high intensity, as recently observed by Compton *et al.* [26]. The influence of the chirp could be understood by considering that the proposed process requires two steps: (i) the formation of excited atomic oxygen and (ii) the stimulation of the emission by the same incident pulse. Since the excitation mainly occurs at the peak of the pulse where the intensity is highest, stimulation would mainly occur on the trail of the pulse. It would therefore be more efficient if the blue side of the spectrum is still significant on this trail, that is, for positively chirped pulses. If this interpretation can be confirmed, the observation of a Rabi shift may suggest that further unexpected effect occurs in the high-intensity multifilamentation regime, although such effects are beyond the scope of the present work.

#### IV. CONCLUSION

As a conclusion, by investigating the supercontinuum generation from 3-J, 30-fs laser pulses, we have observed the occurrence of a high-intensity filamentation regime where the photon bath, rather than the filaments as in the case of lower intensity, provides most of the spectral broadening. As a consequence, similar to broadening in hollow-core fibers, the widest spectral broadening is observed for positively chirped pulses rather than for negatively chirped ones. The substantial contribution of the photon bath also allows the generation of an unprecedented level of 1 J of supercontinuum.

[1] J. Kasparian *et al.*, *Science* **301**, 61 (2003).  
 [2] A. Couairon and A. Mysyrowicz, *Phys. Rep.* **441**, 47 (2007).  
 [3] L. Bergé, S. Skupin, R. Nuter, J. Kasparian, and J.-P. Wolf, *Rep. Prog. Phys.* **70**, 1633 (2007).  
 [4] J. Kasparian and J.-P. Wolf, *Opt. Express* **16**, 466 (2008).

[5] S. L. Chin, S. A. Hosseini, W. Liu, Q. Luo, F. Théberge, N. Aközbeke, A. Becker, V. P. Kandidov, O. G. Kosareva, and H. Schroeder, *Can. J. Phys.* **83**, 863 (2005).  
 [6] P. Bédot, J. Kasparian, S. Henin, V. Loriot, T. Vieillard, E. Hertz, O. Faucher, B. Lavorel, and J.-P. Wolf, *Phys. Rev. Lett.* **104**, 103903 (2010).

- [7] W. Ettoumi, P. B ejot, Y. Petit, V. Lorient, E. Hertz, O. Faucher, B. Lavorel, J. Kasparian, and J.-P. Wolf, *Phys. Rev. A* **82**, 033826 (2010).
- [8] V. Lorient, P. B ejot, W. Ettoumi, Y. Petit, J. Kasparian, S. Henin, E. Hertz, B. Lavorel, O. Faucher and J.-P. Wolf (to be published in Laser Physics.), e-print [arXiv:1011.0841v1](https://arxiv.org/abs/1011.0841v1).
- [9] J. Kasparian *et al.*, *Opt. Express* **16**, 5757 (2008).
- [10] P. Rohwetter *et al.*, *Nat. Photon.* **4**, 451 (2010).
- [11] P. B ejot *et al.*, *Appl. Phys. Lett.* **90**, 151106 (2007).
- [12] S. Henin *et al.*, *Appl. Phys. B* **100**, 77 (2010).
- [13] G. M ejan *et al.*, *Phys. Rev. E* **72**, 026611 (2005).
- [14] J. Kasparian, R. Sauerbrey, and S. L. Chin, *Appl. Phys. B: Lasers Opt.* **71**, 877 (2000).
- [15] A. Becker, N. Ak ozbek, K. Vijayalakshmi, E. Oral, C. M. Bowden, and S. L. Chin, *Appl. Phys. B* **73**, 287 (2001).
- [16] Z. Zhu and T. G. Brown, *Opt. Express* **12**, 689 (2004).
- [17] J. M. Dudley, G. Genty, and S. Coen, *Rev. Mod. Phys.* **78**, 1135 (2006).
- [18] P. B ejot, B. E. Schmidt, J. Kasparian, J.-P. Wolf, and F. Legar e, *Phys. Rev. A* **81**, 063828 (2010).
- [19] P. Maioli, R. Salam e, N. Lascoux, E. Salmon, P. B ejot, J. Kasparian, and J.-P. Wolf, *Opt. Express* **17**, 4726 (2009).
- [20] V. Lorient, E. Hertz, O. Faucher, and B. Lavorel, *Opt. Express* **17**, 13429 (2009); **18**, 3011(E) (2010).
- [21] K. Stelmaszczyk, P. Rohwetter, Y. Petit, M. Fechner, J. Kasparian, J.-P. Wolf, and L. W oste, *Phys. Rev. A* **79**, 053856 (2009).
- [22] V. P. Kandidov, O. G. Kosareva, I. S. Golubtsov, W. Liu, A. Becker, N. Akozbek, C. M. Bowden, and S. L. Chin, *Appl. Phys. B* **77**, 149 (2003).
- [23] A. M. Zheltikov, *Phys. Rev. A* **79**, 023823 (2009).
- [24] P. Rambo, J. Schwarz, and J.-C. Diels, *J. Opt. A* **3**, 146 (2001).
- [25] Y. E. Geints, A. M. Kabanov, G. G. Matvienko, V. K. Oshlakov, A. A. Zemlyanov, S. S. Golik, and O. A. Bukin, *Opt. Lett.* **35**, 2717 (2010).
- [26] R. Compton, A. Filin, D. A. Romanov, and R. J. Levis, *Phys. Rev. Lett.* **103**, 205001 (2009).

ARTICLE

Received 18 Mar 2011 | Accepted 28 Jul 2011 | Published 30 Aug 2011

DOI: 10.1038/ncomms1462

# Field measurements suggest the mechanism of laser-assisted water condensation

S. Henin<sup>1</sup>, Y. Petit<sup>1</sup>, P. Rohwetter<sup>2</sup>, K. Stelmaszczyk<sup>2</sup>, Z.Q. Hao<sup>2</sup>, W.M. Nakaema<sup>2</sup>, A. Vogel<sup>3</sup>, T. Pohl<sup>3</sup>, F. Schneider<sup>4</sup>, J. Kasparian<sup>1</sup>, K. Weber<sup>3</sup>, L. Wöste<sup>2</sup> & J.-P. Wolf<sup>1</sup>

Because of the potential impact on agriculture and other key human activities, efforts have been dedicated to the local control of precipitation. The most common approach consists of dispersing small particles of dry ice, silver iodide, or other salts in the atmosphere. Here we show, using field experiments conducted under various atmospheric conditions, that laser filaments can induce water condensation and fast droplet growth up to several  $\mu\text{m}$  in diameter in the atmosphere as soon as the relative humidity exceeds 70%. We propose that this effect relies mainly on photochemical formation of p.p.m.-range concentrations of hygroscopic  $\text{HNO}_3$ , allowing efficient binary  $\text{HNO}_3\text{-H}_2\text{O}$  condensation in the laser filaments. Thermodynamic, as well as kinetic, numerical modelling based on this scenario semiquantitatively reproduces the experimental results, suggesting that particle stabilization by  $\text{HNO}_3$  has a substantial role in the laser-induced condensation.

<sup>1</sup> Teramobile, GAP, Université de Genève, rue de l'École de Médecine 20, CH-1211 Genève 4, Switzerland. <sup>2</sup> Teramobile, Institut für Experimentalphysik, Freie Universität Berlin, Arnimallee 14, D-14195 Berlin, Germany. <sup>3</sup> Department of Mechanical and Process Engineering, Environmental Measurement Techniques, University of Applied Sciences, Düsseldorf, Josef-Gockeln-Str. 9, D-40474, Düsseldorf, Germany. <sup>4</sup> Grimm Aerosol Technik GmbH, Dorfstraße 9, D- 83404 Ainring, Germany. Correspondence and requests for materials should be addressed to J.K. (email: jerome.kasparian@unige.ch).

Owing to their impact on key human activities like agriculture, strong efforts have been dedicated in the last 70 years to seed clouds by dispersing small particles of dry ice, AgI, or other salts in the atmosphere<sup>1</sup>. However, the efficiency of these techniques is still debated<sup>2,3</sup>. Recently, self-guided ionized filaments<sup>4–8</sup>, generated by ultrashort laser pulses, have been proposed as an alternative approach to trigger water condensation<sup>9</sup>.

Laser filaments are self-sustained light structures of typically 100  $\mu\text{m}$  diameter and up to hundreds of meters in length, widely extending the traditional linear diffraction limit. Their formation stems from an intensity-dependent refractive index modification of the propagation medium, known as the Kerr effect, and is due to third-order nonlinear polarization of the medium. It results in self-focusing of the beam, until the intensity rises sufficiently for ionizing the air. The self-generated plasma<sup>4–8</sup> and/or negative higher order Kerr effect<sup>10</sup> balance the self-focusing, resulting in self-guided propagation. Filaments convey an intensity as high as  $5 \times 10^{13} \text{ W cm}^{-2}$  over long distances<sup>11</sup>, ionizing and photo-oxidising<sup>12</sup> the air. Both of these effects could be expected to assist water condensation. However, the Thomson process<sup>13,14</sup>, triggered by charges and typical of the Wilson chamber<sup>15</sup>, is irrelevant to the atmosphere because it requires supersaturation<sup>16,17</sup>. Furthermore, we recently observed that laser-induced condensation and electron densities have different behaviours as a function of the incident laser power<sup>18</sup>.

Here, on the basis of field experiments performed under various atmospheric conditions, we show that laser filaments can induce water condensation and droplet growth up to several  $\mu\text{m}$  in diameter in the atmosphere as soon as the relative humidity (RH) exceeds 70%. We propose that the local photochemical formation of p.p.m.-range concentrations of hygroscopic  $\text{HNO}_3$  substantially contributes to this effect by enabling efficient binary  $\text{HNO}_3\text{-H}_2\text{O}$  condensation in the laser filaments. Thermodynamic as well as kinetic numerical modelling supports this interpretation. These results offer key information to optimize the water condensation process.

## Results

**Laser-induced rise of particle density.** We investigated atmospheric water condensation initiated by the Teramobile mobile femtosecond–Terawatt laser system<sup>19</sup> operating continuously and generating  $\sim 10$  filaments over typically 15–20 m. We shielded the latter from wind by an open chamber and sampled the aerosols alternatively at 2 cm distance from the filaments and in background atmospheric conditions. Comparing the corresponding particle densities clearly evidences the laser-induced increase of the particle number in each size class, even far below water vapour saturation (Fig. 1a–d). The most spectacular effect is observed on nanoparticles of  $\sim 25 \text{ nm}$  diameter. For example, at 75% RH, the nanoparticle density typically increased by  $5 \times 10^4\text{--}10^5 \text{ cm}^{-3}$  (3–6 times the background concentration), while 10  $\mu\text{m}$  particles increased by a few particles per litre (up to 30% of background). Note that these are averaged values over the volume of the protection chamber, that is, after dilution by a factor of 200–400 as compared with the active filament volume (see below). As a result, the size distribution is shifted to the larger sizes (Fig. 1e), evidencing the laser-induced growth of the particles. Furthermore, these particles do not re-evaporate significantly. For example, 25-nm-diameter particles have been observed to last over at least 20 min, limited by the diffusion out of the measurement chamber (see blue line in Fig. 2c).

**Influence of atmospheric conditions.** Atmospheric conditions have specific and contrasted influence on the laser-assisted yield of different particle sizes. As illustrated in Figure 3, RH is positively correlated with the generation of particles below 400 nm, and negatively correlated above, whereas the opposite correlations are observed in the case of temperature. Conversely, water vapour volume mixing ratio (VMR) is anticorrelated with particles under 500 nm, positively correlated with particles above 3  $\mu\text{m}$ , and uncorrelated with the generation of particles in the 600 nm–3  $\mu\text{m}$  range.

This contrasted behaviour defines three size ranges. The first one regards nanoparticles (25 nm median diameter, as compared with

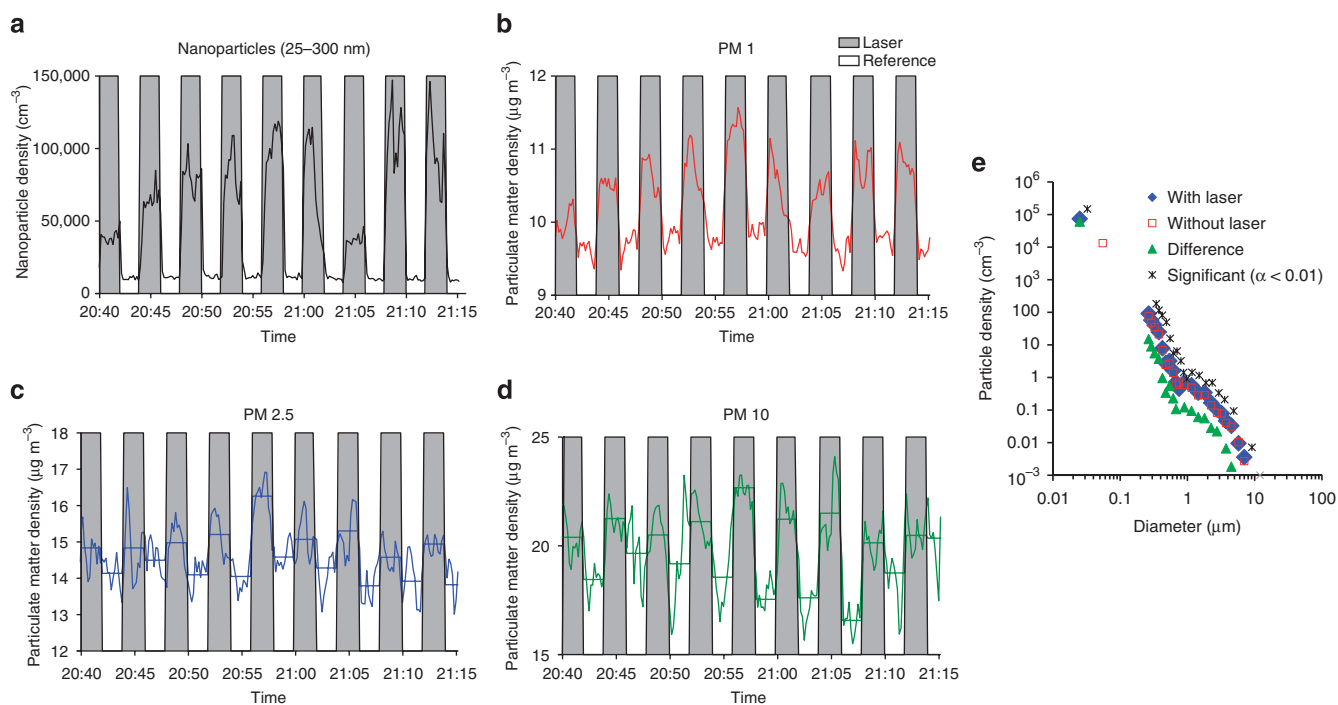


**Figure 1 | Laser filaments-induced condensation in sub-saturated conditions.** (75% RH, 13°C). (a–d) Sampling of air alternatively close to the laser (grey) and in background atmosphere. PM<sub>x</sub> denotes particulate matter of aerodynamic diameter  $x \mu\text{m}$  or less. On panels **c** and **d**, the average values are superimposed over the raw data. (e) Corresponding size distributions. Stars mark sizes for which a Student test yielded a statistical significance of at least  $1 - \alpha > 0.99$  for the difference between laser and reference conditions.

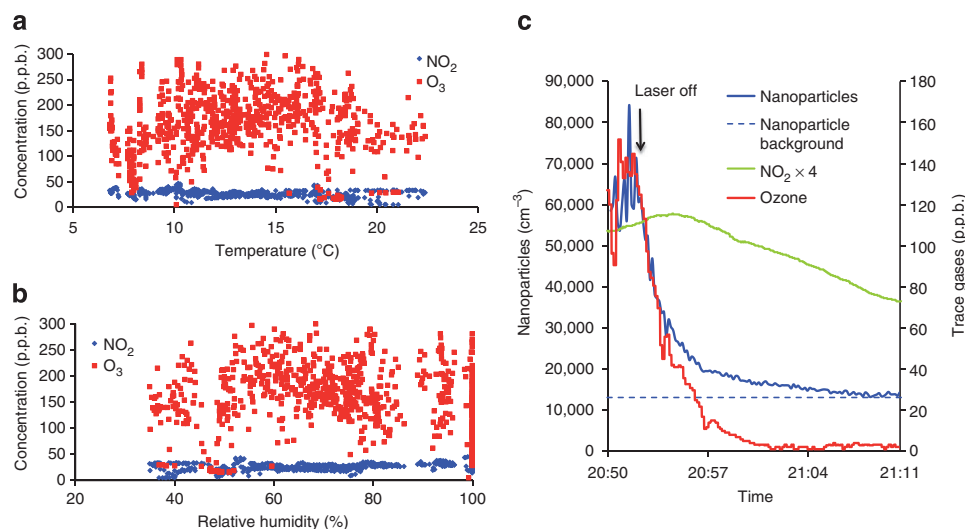


**Figure 2 | Laser generation of trace gases.** (a,b) Laser-induced concentrations of ozone and  $\text{NO}_2$  as a function of (a) temperature and (b) relative humidity. (c) Temporal evolution of the concentration of nanoparticles,  $\text{NO}_2$  and ozone close to the laser filaments in the protection chamber when the laser is switched off (black arrow). Nanoparticles correspond to the 25–300 nm range, with a measured median diameter close to the lower limit of 25 nm.

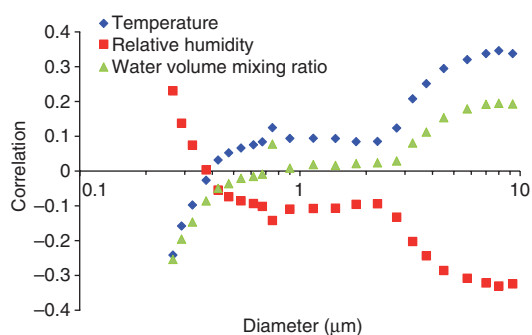


**Figure 3 | Size-dependence of the influence of atmospheric parameters on laser-induced particles.** The graph displays the correlation of temperature, relative humidity, and water mixing ratio in the atmosphere, with the laser-induced increase of particle concentration in each size class. Correlations are calculated over the whole campaign duration, each 4-minutes cycle comparing the particle concentration close to the laser filaments with that in the background (Fig. 1a–d) being considered as an individual data point.

55 nm in the background), the concentration of which is increased by the laser in all conditions encountered during the campaign. Their increase is positively correlated with both relative and absolute humidity (Fig. 4b,c), and negatively correlated with temperature (Fig. 4a). Particles in the 230–400 nm range feature a second regime. The effect of the laser on their concentration decreases with increasing absolute humidity (Fig. 4f) and temperature (Fig. 4d). Conversely, it is negligible below 50% RH, and increases when RH rises up to 100% (Fig. 4e). The dependences vanish for diameters close to 500 nm (Fig. 4g,h,i), and reverse above, defining the third regime (Fig. 4j,k,l). Note, however, that the increase of micrometer-sized particles rises again when approaching 100% RH.

**Trace gas measurements.** Typical  $\text{O}_3$  and  $\text{NO}_2$  concentrations were, respectively, 200 p.p.b. and 25 p.p.b. in the open chamber, when the laser was operating, independent of the temperature and humidity (Fig. 2a,b). Considering the diffusion of the gases in the chamber and through its openings, the dilution factor between the filament volume and the chamber amounts to 200–400. The measured

concentrations are therefore in line with laboratory results<sup>12</sup>, as expected resulting in a  $\text{HNO}_3$  concentration in the p.p.m. range or above inside the filaments. Figure 2c displays the decay time of these gases, as well as of nanoparticles, after the laser is switched off. The comparable time constants for gases and particles suggests that the decay is mostly governed by dilution through the chamber apertures and owing to the airflow induced by the air sampling of the aerosol and gas sensors. The ozone concentration decreases to its background level in 10 min, faster than the nanoparticles (20 min) while  $\text{NO}_2$  exhibits a retarded effect typical of a secondary product generated by the oxidation of NO by ozone, which also speeds up the decay of the latter. The same behaviour was observed reproducibly over more than 30 experimental realizations.

**$\text{NO}_3^-$  contents in laser-induced particles.** As displayed in Figure 5, ionic chromatography of laser-induced particles impacted on filters reveals high concentrations of  $\text{HNO}_3$ , detected as dissolved  $\text{NO}_3^-$  ions, regardless of the particle size. This concentration is one to two orders of magnitude above that of  $\text{SO}_4^{2-}$  ions in the same particles. Smaller amounts of  $\text{NO}_2^-$  ions are also detected.

## Discussion

The three different regimes observed for nanoparticles, sub-micronic, and micrometric particles suggest the following condensation mechanism. The laser initiates particle nucleation or activates pre-existing nanometer-sized particles. This nucleation from the gas phase may occur via multicomponent nucleation of sulphuric acid<sup>20–23</sup>, although it is beyond the scope of the present work in which no data is available on particles smaller than 25 nm. It results in the accumulation of ~25 nm particles inside the filaments. Such particles can grow, if the RH is sufficient to ensure their stability. Once they reach ~500 nm, their subsequent evolution is expectedly limited by diffusion of water molecules, which may explain why the growth of these particles requires high VMR, hence higher temperature, as illustrated by the correlation of both these parameters with bigger particles. On the other hand, the depletion of the humidity by the water uptake results in the negative correlation between RH and these micrometric particles.

This scenario requires a highly efficient stabilizing mechanism to prevent the particles from re-evaporating well below 100% RH. This mechanism may be provided by the strong impact of the laser filaments on the local chemical composition of the atmosphere.

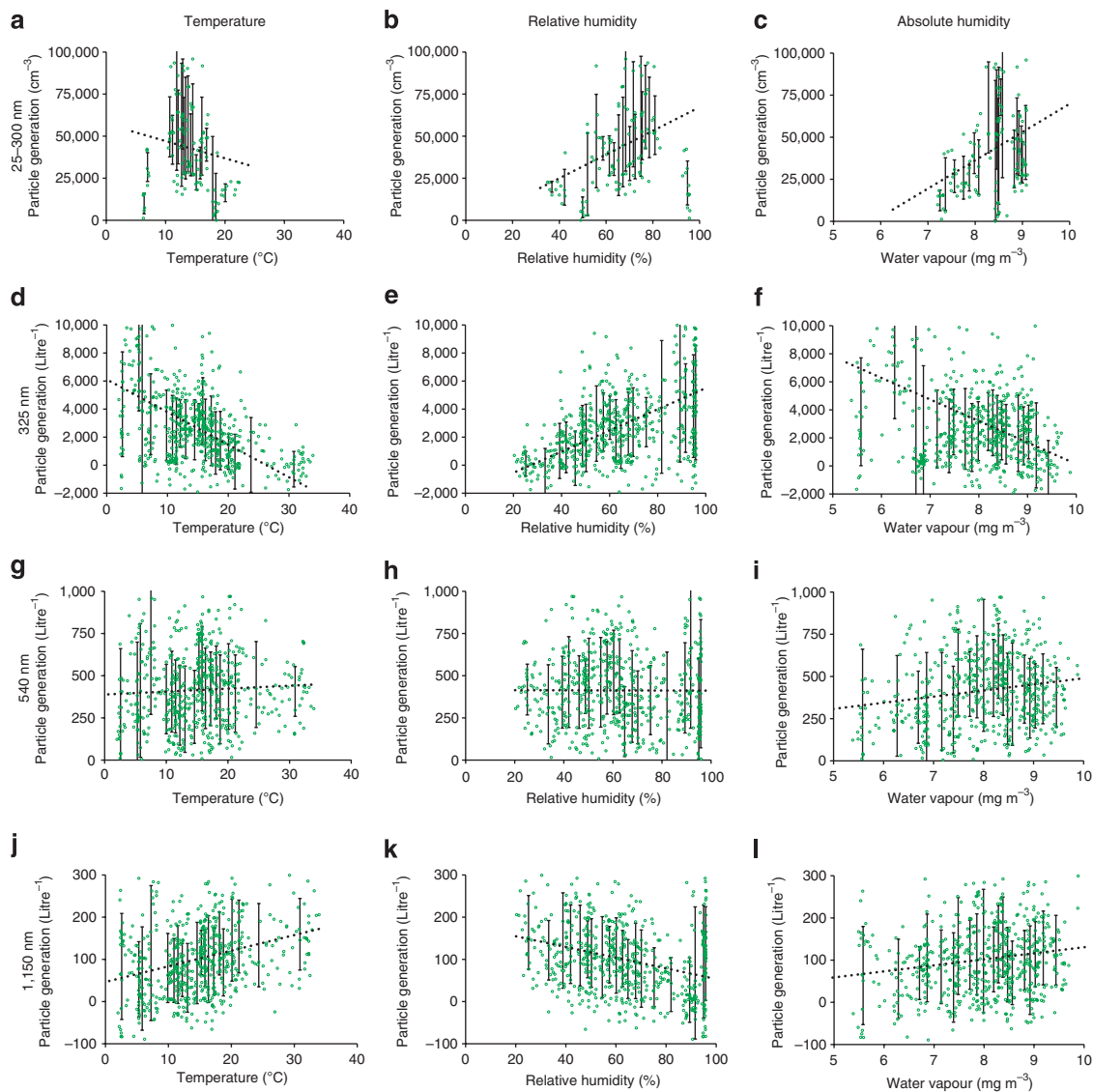


**Figure 4 | Impact of the atmospheric conditions on laser-induced particles.** Effect of laser filaments on the number density of nanoparticles (25–300 nm in diameter) (first regime, panels **a–c**), 325 nm (second regime, panels **d–f**), 540 nm (transition from second to third regime, panels **g–i**), 1.15  $\mu\text{m}$  (third regime, panels **j–l**), as a function of temperature (**a,d,g,j**), RH (**b,e,h,k**), and water vapour concentration (**c,f,i,l**). For each size class, the difference in number density between the conditions with and without laser of each measurement cycle (Fig. 1a–d) has been considered as an individual data point, displayed as a dot on each panel of the present figure as a function of a specific atmospheric parameter. Error bars are calculated by sorting the individual measurements by increasing values of the considered atmospheric parameter, and computing one standard deviation for successive blocks encompassing 5% of the measurements. Dotted lines display linear fits of the data.

In particular, the estimated  $\text{HNO}_3$  concentration inside laser filaments is typically 1,000 times the p.p.b. levels at which the highly hygroscopic  $\text{HNO}_3$  is known to stabilize water droplets in the atmosphere slightly below 100% RH (ref. 20). We can therefore expect efficient stabilization at much lower RH through binary  $\text{HNO}_3$ – $\text{H}_2\text{O}$  condensation.

The dilution factor of 200–400 between the filament active volume ( $\sim 10$  filaments of  $100\ \mu\text{m}$  typical diameter) and the protection chamber leads us to estimate that  $\sim 2 \times 10^7\ \text{cm}^{-3}$  nanoparticles, and some  $10^5\ \text{cm}^{-3}$  microparticles are generated in the filaments by each laser shot. Notice that up to  $10^{11}$  ozone molecules ( $8 \times 10^{-11}\ \text{g}$ ) and  $2.5 \times 10^{10}$   $\text{NO}_2$  molecules ( $2 \times 10^{-11}\ \text{g}$ ) are available for each nanoparticle. Consequently, even larger particle sizes (several micrometers) could be stabilized by the resulting  $\text{HNO}_3$ . These concentrations are therefore compatible with a pathway based on the binary condensation of  $\text{HNO}_3$ – $\text{H}_2\text{O}$  particles.

We performed numerical simulations to evaluate to what extent this binary  $\text{HNO}_3$ – $\text{H}_2\text{O}$  condensation model can explain the experimental data. Figure 6a displays the resulting Köhler plot, that is, the equilibrium RH over the ternary  $\text{HNO}_3$ – $\text{H}_2\text{O}$ – $\text{NH}_4\text{NO}_3$  droplet surface, as a function of its diameter, in conditions representative of those encountered within the laser filaments. Water-vapour uptake dominates evaporation, if the RH is higher than its equilibrium value, that is, for conditions above the curve. This value decreases down to 75% RH for a  $\text{HNO}_3$  concentration of 4 p.p.m., allowing droplets from several tens of nm to a few  $\mu\text{m}$  to grow at RH well below 100% and to shift towards the right of the plot until they reach an ascending branch of the Köhler curve at several  $\mu\text{m}$ , consistent with the experimental data. This effect persists over the whole range of temperatures encountered in the experiment, although its effectiveness significantly decreases at rising temperatures. In particular, a higher humidity is required to stabilize the particles in warmer

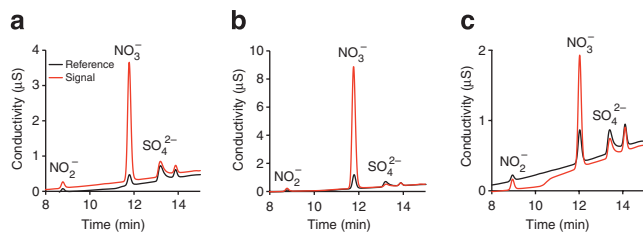


**Figure 5 | Anionic contents of laser-induced particles.** Anions are detected in the laser-induced particles by semi-quantitative ionic chromatography of particles impacted on filters with a pore of 15 nm (a), 50 nm (b) and 1 µm (c). The curves display the current detected by the chromatograph as a function of the ion transit time, characteristic of each species, for both the particles impacted on filters, and reference conditions without laser.

air. We checked that the condensation germs had no impact on the Köhler plots of particles above 80 nm, where the salt core is largely diluted (compare dotted and solid lines on Fig. 6a), so that our results can be expected to be also representative of situations with other nucleation germs implying for example, electric charges or sulphur compounds.

A 15 nm salt core stabilizes the smaller particles, as shown by the positive slope of the Köhler curves for diameters below 40 nm (see solid curves on Fig. 6a). This positive slope, which arrests the growth of the particles, constitutes a growth barrier if the RH is below the local maximum of the Köhler curve, and could therefore explain the median diameter of 25 nm observed by the nanoparticle counter, irrespective of the RH. Because RH influences the height of the Köhler maximum, and therefore the droplet capability to step over it, the Köhler plots provide a reasonable interpretation of the positive correlation between RH and the generation of particles of several hundreds of nm (Fig. 4e), as well as the rise of the generation of micrometer-sized particles at RH close to 100% (Fig. 4k).

Similar results are obtained over the whole range of temperatures encountered during our campaign (2–36°C). The calculated effect of the laser decreases with increasing temperature, in agreement with the negative correlation observed in the experiments between the generation of small particles and temperature (Fig. 4a). The final droplet size is limited by both the amount of HNO<sub>3</sub> made available by the laser filaments and the water vapour VMR. Water vapour depletion occurs when the droplets exceed a few µm in diameter. This depletion is more pronounced for lower temperatures, which correspond to lower water vapour concentration for a given RH, and explains positive correlation between the concentration of larger droplets and both absolute humidity (Fig. 4l) and temperature (Fig. 4j).

The laser-generated HNO<sub>3</sub> does not only allow the droplets to grow at a moderate relative humidity, but also drastically speeds up their growth. We reproduced this acceleration in Kulmala's model<sup>24</sup> in which we released the assumption of near-saturation ambient vapour pressures owing to the multi-p.p.m. HNO<sub>3</sub> concentration in the gas phase. As displayed on Figure 6b, in conditions representative of our experiments, the droplets typically reach a micrometer-sized diameter within ~1 s or less. Similar results have been obtained over the ranges of temperature, RH and HNO<sub>3</sub> concentrations representative of our experimental conditions. This fast growth is consistent with the observation of an almost instantaneous effect (on the second-scale) of the laser in the present experiments, as well as in former laboratory results<sup>9</sup>. In adequate conditions (see, for example, the green curve in Figure 6b), the model even predicts a diameter increase by up to 20% within 1 ms.

However, such growth is not sufficient to explain the previously observed increase of Lidar (light detection and ranging)

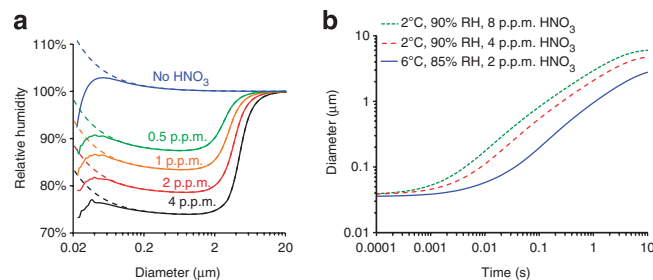


**Figure 6 | Simulation of the droplet stability conditions and growth after the laser shot.** (a) Köhler plots for a droplet density of 1,000 cm<sup>-3</sup>, at T = 6°C and 1,013.25 hPa. Curves from top to bottom correspond to 0, 0.5, 1, 2, and 4 p.p.m. initial concentration of gaseous HNO<sub>3</sub>; Solid lines: Droplets including a 15 nm NH<sub>4</sub>NO<sub>3</sub> core; Dashed lines: Droplets without salt core. (b) Growth of 1,000 cm<sup>-3</sup> ternary HNO<sub>3</sub>-H<sub>2</sub>O-NH<sub>4</sub>NO<sub>3</sub> particles with a 25 nm dissolved NH<sub>4</sub>NO<sub>3</sub> core. A micrometer-sized diameter is reached within ~1 s or faster.

backscattering signal only 1 ms after the filaments were shot<sup>9</sup>. This discrepancy illustrates the limitations of our model at the very short time scales, when the ionized and excited species within the laser-generated plasma, as well as local transient temperature jumps induced by the laser<sup>25</sup> strongly modify the atmospheric chemistry. Furthermore, we disregard the nucleation of new particles as well as contributions of H<sub>2</sub>SO<sub>4</sub> formed by photo-oxidation of the atmospheric SO<sub>2</sub> (refs 20–23), of the charges released by the filaments<sup>26</sup>, of mineral or organic condensation nuclei, which may be activated and made hygroscopic by the high laser-generated ozone concentrations<sup>12</sup>, or of other yet to be identified mechanisms. Furthermore, the information provided by the backscattering coefficient is integrated over the whole size distribution, including nanometric condensation nuclei, the formation of which is not considered in this work. Consequently, the outcome of our model cannot be directly compared with our previous size-unresolved Lidar results<sup>9</sup>.

As a conclusion, investigations and modelling of laser-induced water vapour condensation, under various atmospheric conditions, show that laser filaments drastically increase the number density of 25 nm particles and their growth, within a few seconds, up to stable micrometric particles, even at RH as low as 70%. These nanoparticles grow in particular by condensing water vapour and HNO<sub>3</sub> from the atmosphere strongly modified by the laser. They form stable micrometer-sized particles that persist over at least 20 min, demonstrating that the condensation is not transient during the laser pulse, but rather a process allowing the particle growth to stable micrometer-sized droplets. Numerical modelling based on binary HNO<sub>3</sub>-H<sub>2</sub>O condensation semi-quantitatively reproduces the experimental results, although it neglects any contribution of sulphuric acid, the laser-released charges, or the activation pre-existing condensation nuclei. The simulations predict fast particle growth, their stability at low RH, and the influence of the atmospheric conditions, which confirms the substantial contribution of binary HNO<sub>3</sub>-H<sub>2</sub>O condensation in the laser filaments. Although further work is needed to characterize the nucleation of new particles, these results provide a semi-quantitative interpretation to the laser-induced condensation and define favourable atmospheric conditions for laser-assisted condensation and provide a theoretical understanding for this phenomenon. As a consequence, they open the way to applications in the real atmosphere, from remote sounding of the atmosphere to laser-based rainmaking or rain prevention.

## Methods

**Experimental conditions.** Experiments were performed in 28 runs, for a total of 133 hours of records from fall 2009 to spring 2010 on the bank of the Rhône River

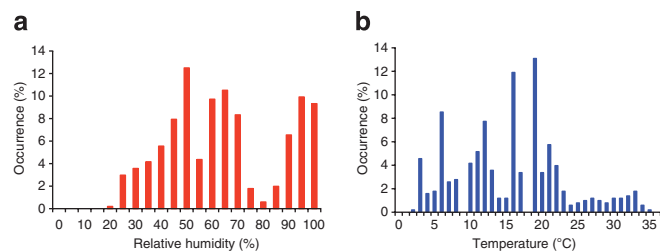


**Figure 7 | Occurrence distribution of the atmospheric conditions during the measurements.** The histograms display the statistical distribution of (a) relative humidity and (b) temperature over the whole data set acquired during the campaign, each 4-minutes measurement cycle (Fig. 1a–d) being treated as an individual datum.

close to Geneva (46°12' North, 6°5' East, 380 m above sea level). This location was chosen to get the benefit from the relatively warm water flow from the Lake of Geneva acting as a heat buffer, locally increasing the RH. As detailed in Figure 7, data were acquired in a wide variety of atmospheric conditions: RH from 35 to 100%, temperature between 2 and 36°C. Furthermore, experiments at all times of the day and the night ensured that both phases of increase and decrease of temperature and RH have been recorded.

**Experimental setup.** The experimental setup is depicted schematically in Figure 8. Water condensation was initiated by the Teramobile mobile femtosecond-Terawatt laser system<sup>19</sup>. The laser was operated continuously and provided up to 160 mJ pulses of 240 fs unchirped duration at a central wavelength of 800 nm and a repetition rate of 10 Hz. The beam was expanded to 10 cm diameter and slightly focused ( $f \sim 20$  m) by a built-in expanding telescope. At the nonlinear focus, that is, after  $\sim 15$  m of horizontal propagation 1.2 m above ground, the beam generated some 10 filaments in the atmosphere. Filamentation spanned over typically 15–20 m, as inferred from both visual observation on a screen and the emission of a shockwave recorded by a microphone<sup>27</sup>. The region around the filament onset was shielded from wind by an open protection chamber (32 cm  $\times$  36 cm  $\times$  56 cm; surface-to-volume ratio 0.15 cm<sup>-1</sup>) where the atmosphere was analysed. This open chamber was internally coated with aluminium, and featured two circular apertures of 6 cm diameter to let the laser through.

**Characterization of aerosol particles.** After allowing typically 5 min (that is, 3,000 shots) to stabilize the aerosol and trace gas concentrations, the aerosols were sampled inside the chamber, at 2 cm distance from the filaments. Their size distribution and density were characterized using an aerosol size spectrometer (Grimm 1.107) coupled with a nanoparticle sensor (Grimm Nanocheck 1.320). The former measured the size distribution in 31 classes from 250 nm up to 32  $\mu$ m based on the angular pattern of light scattering, and the latter counted and evaluated the count median diameter of nanoparticles between 25 and 300 nm by measuring the nanocurrent induced by the flow of particles after they are electrically charged in a corona discharge. Reference conditions were recorded alternatively with the laser conditions.

The measurements were double-checked by intercomparing the results with other aerosol detectors. These include a second nanoparticle detector (Grimm Nanocheck 1.108), a second aerosol spectrometer (Grimm 1.107), as well as elastic optical scattering of a 1 mW continuous-wave frequency-doubled YAG laser at 532 nm. We also checked that consistent results were obtained using a condensation particle counter (TSI Model 3007), which is insensitive to the particle charge, showing that the measurement of the nanoparticles is not affected by the charges deposited on them by the filaments<sup>28</sup>. The statistical significance of the difference between experimental conditions was assessed by performing a Student test to calculate the risk  $\alpha$  that the two results be due to Gaussian sampling fluctuations<sup>29</sup>.

To ensure that the observed generation of nanoparticles is not an artefact due to the protection chamber, we performed complementary measurements without it, alternatively switching the laser on and off and sampling the aerosols at the same position. Although in this configuration we were restricted to a qualitative analysis of the data due to the perturbation by the wind airflow across the filaments, the results were consistent with the main records. We also checked that the chamber did not significantly affect the temperature and RH by performing simultaneous measurements inside and outside.

We verified that the measured effect of the laser on the particle concentration is not correlated with the background particle concentrations, excluding a substantial contribution of artefacts related to the laser-induced fragmentation of pre-existing particles. The correlation between two series of values,  $x$  and  $y$ , is defined, as usual, as  $\sigma_{xy}/\sigma_x \sigma_y$ , where  $\sigma_x$  and  $\sigma_y$  denote the standard deviation of the series  $x$  and  $y$ , respectively, and  $\sigma_{xy}$  denotes their covariance. Substantial influence of background organic compounds was also ruled out by checking that car or ship engines

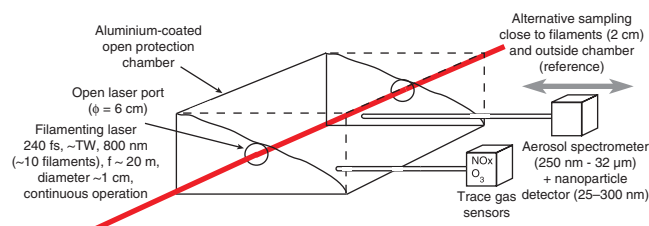


**Figure 8 | Experimental setup.** The laser filaments (red) are shielded from wind by an open protection chamber. This chamber is internally coated with aluminium and offers two widely open ports to let the laser through. Trace gases are monitored continuously in the protection chamber by dedicated sensors. The effect of the laser on aerosols is measured by sampling the particles using aerosol spectrometers and a nanoparticle detector, alternatively close to the laser filaments and in the background.

running in the vicinity of our setup had minimal influence on our results; however, for safety, we disregarded the corresponding data in the analysis of our results.

**Chemical analysis of aerosol particles.** We characterized the chemical composition of the aerosols produced in the laser filaments by aspirating them at a flow of 1.2 l min<sup>-1</sup> during 2 h of continuous laser operation and impacting them on polycarbonate membrane filters (Nuclepore Track-Etch) with 1  $\mu$ m, 50 nm, or 15 nm pore sizes. Reference samples were collected without laser. Soluble particles were then dissolved by immersing the filters for 15 h in HPLC-grade water, including 15 min in an ultrasonic bath. The anions dissolved in the resulting solutions were analysed by an ionic chromatograph (ICS 3000).

**Trace gas measurements.** The influence of the atmospheric conditions on the generation of the precursors of HNO<sub>3</sub>, namely NO, NO<sub>2</sub> and ozone, was investigated by recording the gas concentrations in the protection chamber around the filament. Standard analysers monitored the concentration of O<sub>3</sub> (UV Photometric Analyser Model 49, Thermo Environmental Instruments, featuring a reaction time of 20 s) as well as NO<sub>2</sub> and NO (Chemiluminescent nitrogen oxides analyser AC 31 M, Environnement S.A., 15 s reaction time) in the vicinity of the filaments.

**Modelling of particle stability.** We modelled the droplet stability within the size range accessible to our experimental system, that is, above 25 nm in diameter, leaving the initial particle nucleation beyond the scope of the present work. We adapted the extended Köhler theory<sup>30</sup> to handle the multi-p.p.m. concentrations of HNO<sub>3</sub> generated by laser filaments<sup>12</sup> as well as the full experimental range of RH. The Köhler theory describes the equilibria between evaporation and condensation of both water vapour and HNO<sub>3</sub>. It explicitly takes into account the Kelvin effect, which substantially shifts the equilibrium between evaporation and condensation because of the curvature-dependent surface energy. We neglected charge effects as well as species left in excited states in the plasma, and considered the condensational growth of a monodisperse cloud of spherical binary HNO<sub>3</sub>-H<sub>2</sub>O droplets. Within this framework, the composition- and curvature-dependent partial pressures at equilibrium are expressed as:

$$p_{\infty,i}(T, m_j) = p_{\text{sat},i}(T, m_j) \exp\left(\frac{4\sigma(T, m_j)v_i(T, m_j)}{k_B T D_p(T, m_j)}\right) \quad (1)$$

where  $k_B$  is Boltzmann's constant,  $T$  denotes the temperature, and  $p_{\infty,i}$  is the partial vapour pressure of species  $i$  (that is, H<sub>2</sub>O or HNO<sub>3</sub>). The partial molecular volumes  $v_i$ , the saturation partial vapour pressures  $p_{\text{sat},i}$  over a flat solution with the same composition as the droplet, the droplet density  $\rho$  and diameter  $D_p$ , and the surface tension  $\sigma$  are calculated from the temperature  $T_{\text{sol}}$  and the partial masses  $m_i$  of the considered species in the liquid phase by using the thermodynamic E-AIM 'model II' (<http://www.aim.env.uea.ac.uk/aim/aim.php>)<sup>31–33</sup>. The index  $j$  denotes the dependence on all involved species. Optionally, the droplets were doped with a NH<sub>4</sub>NO<sub>3</sub> core accounting for typical nucleation germs<sup>30,34</sup>. For given salt core and water masses, we determined the equilibrium partition of HNO<sub>3</sub> between the gas and liquid phases, in a closed system (that is for a fixed number of HNO<sub>3</sub> and H<sub>2</sub>O molecules determined in the initial conditions). Equation (1) was then used to determine the equilibrium water vapour pressure over the corresponding droplet, defining the corresponding point in the Köhler plot.

**Kinetic modelling of particle growth.** The kinetic modelling of the droplet growth relies on the implementation of the full Kulmala's model<sup>24</sup>, in which we suppressed the assumption of near-saturation ambient vapour pressures owing to the low RH to handle, together with high HNO<sub>3</sub> concentrations in the gas phase. Mass and heat transfers between a given spherical droplet and the atmosphere are described by the classical transition regime equations<sup>35</sup>, including corrections for molecular

diffusivities and thermal conductivity. These corrections extend the applicability of the continuum description to droplet sizes approaching the thermal molecular mean free path.

$$\frac{dm_i}{dt} = \frac{2\pi D_i(T) M_i D_p(T, m_j)}{R} f(\text{Kn}, \alpha_{m,i}) \times \left( \frac{p_{i,\infty}}{T_\infty} - \frac{p_{\text{sat},i}(T)}{T_a} \exp \left\{ \frac{4\sigma v_i(T, m_j)}{k_B T_a D_p(T, m_j)} \right\} \right) \quad (2)$$

$$\frac{dT_a}{dt} = \frac{\sum_i q_i(T_a) dm_i / dt - 2\pi D_p(T_a, m_j) f(\text{Kn}, \alpha_T) k_{\text{air}}(T_a - T_\infty)}{c_{\text{sol}}(T_a) \sum_i m_i} \quad (3)$$

Here,  $R$  is the universal gas constant,  $T_\infty$  the background temperature,  $T_a$  the droplet temperature,  $k_{\text{air}}$  the thermal conductivity of air,  $c_{\text{sol}}$  the specific heat capacity of the liquid phase.  $D_i$  denotes the diffusivity of species  $i$  in air,  $M_i$  its molar mass,  $q_i$  its latent heat of evaporation from the mixed solution. In these expressions, heating of the atmosphere by the laser has been neglected, because it is known to keep below a few degrees<sup>5–8</sup>.  $f(\text{Kn}, \alpha)$  is the Fuchs–Sutugin correction factor<sup>20</sup>

$$f(\text{Kn}, \alpha) = \frac{0.75\alpha(1 + \text{Kn})}{\text{Kn}^2 + \text{Kn} + 0.282\alpha\text{Kn} + 0.75\alpha} \quad (4)$$

where  $\text{Kn}$  is the Knutzen number<sup>20</sup> (that is, the ratio of the molecular mean free path to the droplet radius). The mass and thermal accommodation coefficients  $\alpha_{m,i}$  and  $\alpha_T$  describe non-unity sticking probability of molecules of species  $i$  impinging the particle surface, and imperfect thermal coupling due to gas kinetic effects, respectively. We set them to unity, following the recommendation of Laaksonen *et al.* in the context of growth rate modelling<sup>36</sup>. The specific heat capacity  $c_{\text{sol}}$  of the liquid phase is approximated by that of pure water, whereas the thermal conductivity of the atmosphere is approximated as that of pure air<sup>35</sup>. The effective latent heats of evaporation  $q_i$ , depend on the particle composition due to the exothermic dissolution of gaseous  $\text{HNO}_3$ . They are obtained from the equilibrium vapour pressures calculated with the E-AIM model, using the Clausius–Clapeyron equation:

$$q_i(T, m_j) = \frac{RT^2}{M_i} \frac{dp_{\text{sat},i}(T, m_j)}{p_{\text{sat},i}(T, m_j) dT} \quad (5)$$

Using this expression neglects the distortion of the saturation vapour pressures due to the Kelvin effect, which however causes a relative change of the latent heats remaining below ~1% even for droplet diameters as small as 10 nm (ref. 35). Finally, owing to the low total condensed mass per air volume (typically 0.1% for a droplet density of 1,000 cm<sup>-3</sup> and 1 μm diameter), we neglect the impact of the latent heats of condensation and evaporation on the temperature of the reservoir.

## References

- Langmuir, I. Growth of particles in smokes and clouds and the production of snow from supercooled clouds. *Science* **106**, 505–505 (1947).
- Qiu, J. & Cressey, D. Taming the sky. *Nature* **453**, 970–974 (2008).
- US National Research Council. *Critical Issues in Weather Modification Research* (National Academies, 2003).
- Kasparian, J. *et al.* White-light filaments for atmospheric analysis. *Science* **301**, 61–64 (2003).
- Couairon, A. & Mysyrowicz, A. Femtosecond filamentation in transparent media. *Phys. Rep.* **44**, 47–189 (2007).
- Bergé, L., Skupin, S., Nuter, R., Kasparian, J. & Wolf, J.-P. Ultrashort filaments of light in weakly-ionized, optically-transparent media. *Rep. Prog. Phys.* **70**, 1633–1713 (2007).
- Kasparian, J. & Wolf, J.-P. Physics and applications of atmospheric nonlinear optics and filamentation. *Opt. Express* **16**, 466–493 (2008).
- Chin, S. L. *et al.* The propagation of powerful femtosecond laser pulses in optical media: physics, applications, and new challenges. *Can. J. Phys.* **83**, 863–905 (2005).
- Rohwetter, P. *et al.* Laser-induced water condensation in air. *Nature Photon.* **4**, 451–456 (2010).
- Béjot, P. *et al.* Higher-order Kerr terms allow ionization-free filamentation in gases. *Phys. Rev. Lett.* **104**, 103903 (2010).
- Rodriguez, M. *et al.* Kilometer-range non-linear propagation of femtosecond laser pulses. *Phys. Rev. E* **69**, 036607 (2004).
- Petit, Y., Henin, S., Kasparian, J. & Wolf, J.-P. Production of ozone and nitrogen oxides by laser filamentation. *Appl. Phys. Lett.* **97**, 021108 (2010).
- Thomson, J. J. *Conduction of Electricity through Gases* (Cambridge University Press, London, 1906).
- Tohmfor, G. & Volmer, M. Die Keimbildung unter dem Einfluß elektrischer Ladungen. *Ann. Phys.* **425**, 109–131 (1938).
- Wilson, C. T. R. On a method of making visible the paths of ionising particles through a gas. *Proc. R. Soc. Lond. A* **85**, 285–288 (1911).

- Yu, F. Modified Kelvin–Thomson equation considering ion–dipole interaction: Comparison with observed ion-clustering enthalpies and entropies. *J. Chem. Phys.* **122**, 084503–084508 (2005).
- Winkler, P. M., *et al.* Heterogeneous Nucleation Experiments Bridging the Scale from Molecular Ion Clusters to Nanoparticles. *Science* **319**, 1374 (2008).
- Petit, Y. *et al.* Influence of pulse duration, energy, and focusing on laser-assisted water condensation. *Appl. Phys. Lett.* **98**, 041105 (2011).
- Wille, H. *et al.* Teramobile: a mobile femtosecond-terawatt laser and detection system. *Eur. Phys. J. – Appl. Phys.* **20**, 183–190 (2002).
- Seinfeld, J. H. & Pandis, S. N. *Atmospheric Chemistry and Physics—From Air Pollution to Climate Change*. (2nd edn, Wiley, 2006).
- Yu, F. & Turco, F. P. From molecular clusters to nanoparticles: Role of ambient ionization in tropospheric aerosol formation. *J. Geophys. Res.* **106**, 4797–4814 (2001).
- Duplissy, J. *et al.* Results from the CERN pilot CLOUD experiment. *Atmos. Chem. Phys.* **10**, 1635–1647 (2010).
- Yu, F. From molecular clusters to nanoparticles: second-generation ion-mediated nucleation model. *Atmos. Chem. Phys.* **6**, 5193–5211 (2006).
- Kulmala, M., Laaksonen, A., Korhonen, P., Vesala, T., Ahonen, T. & Barrett, J. C. The effect of atmospheric nitric acid vapor on cloud condensation nucleus activation. *J. Geophys. Res.* **98**, 22949–22958 (1993).
- Miles, R. E. H., Knox, K. J., Reid, J. P., Laurain, A. M. C. & Mitchem, L. Measurements of mass and heat transfer at a liquid water surface during condensation or evaporation of a subnanometer thickness layer of water. *Phys. Rev. Lett.* **105**, 116101 (2010).
- Hirsikko, A. *et al.* Atmospheric ions and nucleation: a review of observations. *Atmos. Chem. Phys.* **11**, 767–798 (2011).
- Yu, J. *et al.* Sonographic probing of laser filaments in air. *Appl. Opt.* **42**, 7117–7120 (2003).
- Henin, S., Petit, Y., Kiselev, D., Kasparian, J. & Wolf, J.-P. Contribution of water droplets to charge release by laser filaments in air. *Appl. Phys. Lett.* **95**, 091107 (2009).
- Press, W. H., Teukolsky, S. A., Vetterling, W. T. & Flannery, B. P. *Numerical Recipes in C: The Art of Scientific Computing*. (Cambridge University Press, 1992).
- Laaksonen, A., Korhonen, P., Kulmala, M. & Charlson, R. J. Modification of the Köhler equation to include soluble trace gases and slightly soluble substances. *J. Atmos. Sci.* **55**, 853 (1998).
- Clegg, S. L., Brimblecombe, P. & Wexler, A. S. A thermodynamic model of the system  $\text{H}^+ - \text{NH}_4^+ - \text{SO}_4^{2-} - \text{NO}_3^- - \text{H}_2\text{O}$  at tropospheric temperatures. *J. Phys. Chem. A* **102**, 2137–2154 (1998).
- Dutcher, C. S., Wexler, A. S. & Clegg, S. L. Surface Tensions of Inorganic Multicomponent Aqueous Electrolyte Solutions and Melts. *J. Phys. Chem. A* **114**, 12216–12230 (2010).
- Clegg, S. L. & Wexler, A. S. Densities and apparent molar volumes of atmospherically important electrolyte solutions. I. The solutes  $\text{H}_2\text{SO}_4$ ,  $\text{HNO}_3$ ,  $\text{HCl}$ ,  $\text{Na}_2\text{SO}_4$ ,  $\text{NaNO}_3$ ,  $\text{NaCl}$ ,  $(\text{NH}_4)_2\text{SO}_4$ ,  $\text{NH}_4\text{NO}_3$ , and  $\text{NH}_4\text{Cl}$  from 0 to 50 °C, including extrapolations to very low temperature and to the pure liquid state, and  $\text{NaHSO}_4$ ,  $\text{NaOH}$  and  $\text{NH}_3$  at 25 °C. *J. Phys. Chem.* **115**, 3393–3460 (2010).
- Vlasenko, A., Sjogren, S., Weingartner, E., Stemmler, K., Gäggeler, H. W. & Ammann, M. Effect of humidity on nitric acid uptake to mineral dust aerosol particles. *Atmos. Chem. Phys.* **6**, 2147–2160 (2006).
- Pruppacher, H. R. & Klett, J. D. *Microphysics of Clouds and Precipitation*, (Kluwer Academic Publishers, 1997).
- Laaksonen, A., Vesala, T., Kulmala, M., Winkler, P. M. & Wagner, P. E. Commentary on cloud modelling and the mass accommodation coefficient of water. *Atmos. Chem. Phys.* **5**, 461–464 (2005).

## Acknowledgements

We gratefully acknowledge Thomas Leisner (Karlsruhe Institute of Technology) for fruitful discussions. The expert assistance of D. Palomino and S. Stoll (Faurel Institute, University of Geneva) for the ionic chromatography was very much appreciated. This work was supported by the Deutsche Forschungsgemeinschaft and the Fonds National Suisse de la Recherche Scientifique (FNS, grant No. 200021-125315 and NCCR MUST program).

## Author contributions

All authors contributed extensively to the work presented in this paper. More specifically, S.H., Y.P., J.K. and J.-P.W. conceived and designed the study. S.H., Y.P., P.R., K.S., Z.Q.H., W.M.N., A.V., T.P., F.S. and J.K. performed the experiments. S.H., Y.P. and J.K. analysed the data, P. R. developed the numerical model and performed the simulations, and J.K. and J.-P.W. wrote the paper.

## Additional information

**Competing financial interests:** The authors declare no competing financial interests.

**Reprints and permission** information is available online at <http://npg.nature.com/reprintsandpermissions/>

**How to cite this article:** Henin, S. *et al.* Field measurements suggest the mechanism of laser-assisted water condensation. *Nat. Commun.* 2:456 doi: 10.1038/ncomms1462 (2011).

**License:** This work is licensed under a Creative Commons Attribution–NonCommercial–Share Alike 3.0 Unported License. To view a copy of this license, visit <http://creativecommons.org/licenses/by-nc-sa/3.0/>